

Transactions of the ASME®

HEAT TRANSFER DIVISION

Chairman, J. B. KITTO, JR.
Secretary, O. A. PLUMB
Technical Editor, R. VISKANTA (1995)
Associate Technical Editors,
Y. BAYAZITOGU (1995)
R. O. BUCKIUS (1993)
W. A. FIVELAND (1994)
L. S. FLETCHER (1994)
W. L. GROSSHANDLER (1995)
C. E. HICKOX, JR. (1995)
F. P. INCROPERA (1993)
J. H. KIM (1993)
J. R. LLOYD (1995)
T. W. SIMON (1995)
R. J. SIMONEAU (1993)
L. C. WITTE (1994)

BOARD ON COMMUNICATIONS

Chairman and Vice President
R. D. ROCKE

Members-at-Large

T. BARLOW, W. BEGELL, T. F. CONRY,
T. DEAR, J. KITTO, R. MATES,
W. MORGAN, E. M. PATTON,
S. PATULSKI, R. E. REDER,
A. VAN DER SLUYS, F. M. WHITE

President, J. A. FALCON
Executive Director,
D. L. BELDEN
Treasurer,
ROBERT A. BENNETT

PUBLISHING STAFF

Mng. Dir., Publ.,
CHARLES W. BEARDSLEY
Managing Editor,
CORNELIA MONAHAN
Sr. Production Editor,
VALERIE WINTERS
Production Assistant,
MARISOL ANDINO

Transactions of the ASME, *Journal of Heat Transfer* (ISSN 0022-1481) is published quarterly (Feb., May, Aug., Nov.) for \$165.00 per year by The American Society of Mechanical Engineers, 345 East 47th Street, New York, NY 10017. Second class postage paid at New York, NY and additional mailing offices. POSTMASTER: Send address changes to Transactions of the ASME, *Journal of Heat Transfer*, c/o THE AMERICAN SOCIETY OF MECHANICAL ENGINEERS, 22 Law Drive, Box 2300, Fairfield, NJ 07007-2300.

CHANGES OF ADDRESS must be received at Society headquarters seven weeks before they are to be effective. Please send old label and new address.

PRICES: To members, \$40.00, annually; to nonmembers, \$165.00.

Add \$24.00 for postage to countries outside the United States and Canada.

STATEMENT from By-Laws. The Society shall not be responsible for statements or opinions advanced in papers or . . . printed in its publications (B7.1, para. 3).

COPYRIGHT © 1993 by The American Society of Mechanical Engineers. Authorization to photocopy material for internal or personal use under circumstances not falling within the fair use provisions of the Copyright Act is granted by ASME to libraries and other users registered with the Copyright Clearance Center (CCC) Transactional Reporting Service provided that the base fee of \$3.00 per article is paid directly to CCC, 27 Congress St., Salem, MA 01970. Request for special permission or bulk copying should be addressed to Reprints/Permission Department. INDEXED by Applied Mechanics Reviews and Engineering Information, Inc. Canadian Goods & Services Tax Registration #126148048.

Journal of Heat Transfer

Published Quarterly by The American Society of Mechanical Engineers

VOLUME 115 • NUMBER 1 • FEBRUARY 1993

ANNOUNCEMENTS

- 2 *Journal of Heat Transfer Referees—1992*
- 5 Editorial
- 200 Change of address form for subscribers
- 246 Errata on a previously published paper by N. Kasagi, Y. Tomita, and A. Kuroda
- 282 Call for papers: 10th International Heat Transfer Conference
- Inside back cover Information for authors

TECHNICAL PAPERS

Heat Conduction

- 7 Microscale Heat Conduction in Dielectric Thin Films
A. Majumdar
- 17 Electron and Phonon Thermal Conduction in Epitaxial High- T_c Superconducting Films
K. E. Goodson and M. J. Flik
- 26 Multidimensional Inverse Heat Conduction Using the Monte Carlo Method
A. Haji-Sheikh and F. P. Buckingham
- 34 Laser Beam Welding With Simultaneous Gaussian Laser Preheating
Y.-N. Liu and E. Kannatey-Asibu, Jr.
- 42 Heat Transfer Within a Concrete Slab Applying the Microwave Decontamination Process
W. Li, M. A. Ebadian, T. L. White, and R. G. Grubb
- 51 Maximum Temperatures in Diamond Heat Spreaders Using the Surface Element Method
J. V. Beck, A. M. Osman, and G. Lu

Forced Convection

- 58 Heat Transfer and Friction Factor Measurements in Ducts With Staggered and In-Line Ribs
Ying-Jong Hong and Shou-Shing Hsieh
- 66 Local Heat Transfer Behavior and Its Impact on a Single-Row, Annularly Finned Tube Heat Exchanger
X. Hu and A. M. Jacobi
- 75 Optimal Arrays of Pin Fins and Plate Fins in Laminar Forced Convection
A. Bejan and A. M. Morega
- 82 Effects of Sodium and Potassium Chlorides on Silica Fouling
S. H. Chan, Z. J. Chen, and P. He

Liquid Jet Impingement

- 91 Convective Heat Transfer Enhancement Due to Intermittency in an Impinging Jet
D. A. Zumbrennen and M. Aziz
- 99 Stagnation-Point Heat Transfer During Impingement of Laminar Liquid Jets: Analysis Including Surface Tension
Xin Liu, L. A. Gabour, and J. H. Lienhard V
- 106 Correlating Equations for Impingement Cooling of Small Heat Sources With Single Circular Liquid Jets
D. J. Womac, S. Ramadhyani, and F. P. Incropera
- 116 Conjugate Heat Transfer From a Heated Disk to a Thin Liquid Film Formed by a Controlled Impinging Jet
A. Faghri, S. Thomas, and M. M. Rahman

Natural Convection

- 124 Thermal Drag and Critical Heat Flux for Natural Convection of Air in Vertical Parallel Plates
Zeng-Yuan Guo and Xiao-Bo Wu
- 130 Unsteady Boundary Layer Free Convection Flow Over Horizontal Cylinder and Sphere Embedded in a Stratified Medium
R. K. Tripathi and G. Nath
- 133 Natural Convection in a Partial Sector-Shaped Enclosure: Experimental Results
N. Al-ani and M. W. Nansteel
- 140 Investigation of Natural Convection Heat Transfer in Converging Channel Flows Using a Specklegram Technique
K. D. Kihm, J. H. Kim, and L. S. Fletcher

(Contents continued)

- 149 Natural Convection From L-Shaped Corners With Adiabatic and Cold Isothermal Horizontal Walls
D. Angirasa and R. L. Mahajan
- 158 Natural Convection Between Two Horizontal Cylinders in an Adiabatic Circular Enclosure
C. J. Ho, W. S. Chang, and C. C. Wang
- 166 Natural Convection in the Inclined, Cranked Thermosyphon
G. S. H. Lock and J. Fu
- 173 Heat Transfer Characteristics of the Single-Phase, Elbow Thermosyphon
G. S. H. Lock and D. Ladoon

Radiative Transfer

- 178 Transient Optical Transmission Measurement in Excimer-Laser Irradiation of Amorphous Silicon Films
H. K. Park, X. Xu, C. P. Grigoropoulos, N. Do, L. Klees, P. T. Leung, and A. C. Tam
- 184 Discrete Ordinates Solutions of Nongray Radiative Transfer With Diffusely Reflecting Walls
J. A. Menart, HaeOk Skarda Lee, and Tae-Kuk Kim
- 194 Refractive Index Effects on Radiation in an Absorbing, Emitting, and Scattering Laminated Layer
R. Siegal and C. M. Spuckler

Evaporation and Boiling

- 201 Investigation of an Evaporating Extended Meniscus Based on the Augmented Young-Laplace Equation
S. DasGupta, J. A. Schonberg, and P. C. Wayner, Jr.
- 209 On the Use of Monolayers to Reduce Evaporation From Stationary Water Pools
T. D. Tang, M. T. Pauken, S. M. Jeter, and S. I. Abdel-Khalik
- 215 Nucleation Site Density in Forced Convection Boiling
L. Z. Zeng and J. F. Klausner
- 222 Effects of Heating Surface Materials on a Liquid-Solid Contact State in a Sessile Drop-Boiling System
S. Inada and W.-J. Yang
- 231 Flashing Inception in Water During Rapid Decompression
E. Elias and P. L. Chambré

Heat Pipes

- 239 Simulation of the Early Startup Period of High-Temperature Heat Pipes From the Frozen State by a Rarefied Vapor Self-Diffusion Model
Y. Cao and A. Faghri
- 247 A Numerical Analysis of High-Temperature Heat Pipe Startup From the Frozen State
Y. Cao and A. Faghri

Materials Processing

- 255 Magnetized Fiber Orientation Control in Solidifying Composites: Numerical Simulation
G. S. Dulikravich, B. Kosovic, and S. Lee

TECHNICAL NOTES

- 263 Laplace Transform Solution for Heat Transfer in Composite Walls With Periodic Boundary Conditions
M. F. Zedan and A. M. Mujahid
- 266 Development of an Algebraic Model to Predict the Heat Transfer for Turbulent Flow in a Rod Bundle
Nae-Hyun Kim, Sang-Keun Lee, and Si-Hwan Kim
- 269 Solidification of a Flowing Liquid Inside a Pipe Subject to Radiation and Convection
B. T. F. Chung, S. Gulati, and A. K. Dalmia
- 272 Relations for Local Radiative Heat Transfer Between Rectangular Boundaries of an Absorbing-Emitting Medium
R. Siegal
- 276 Mass Transfer Effects on the Unsteady Forced and Free Convective Flow Through a Porous Medium Past an Infinite Vertical Isothermal Plate
V. M. Soundalgekar, R. M. Lahurikar, and S. G. Pohaneekar
- 278 Prediction of Spatial and Temporal Distributions of Frost Growth on a Flat Plate Under Forced Convection
Y.-X. Tao and R. W. Besant

JOURNAL OF HEAT TRANSFER POLICY ON REPORTING UNCERTAINTIES IN EXPERIMENTAL MEASUREMENTS AND RESULTS

The JOURNAL OF HEAT TRANSFER (JHT) has, for some time, recognized the need to prepare a set of guidelines on estimating experimental uncertainty. This was warranted for two major reasons: to ensure uniformity of presenting experimental data, and to raise the authors' awareness regarding the importance of giving a more precise statement about their measurement uncertainties.

The JHT Editorial Board has reached the consensus that the guidelines recently adopted by the *Journal of Fluids Engineering* (JFE) are sound and can be modified for use by the JHT authors and readers. The JFE guidelines can be found in its Vol. 113, September 1991, pp. 313–314. The JFE editors have discussed the subject thoroughly to reach an agreement on their guidelines. Much of the guideline material described below was adopted from the JFE guidelines with few modifications. The example, drawn from a simple heat transfer problem, is added. It is hoped that the guidelines and example will help the authors prepare their papers and the referees review the papers on a consistent basis.

The example, suggested by H. W. Coleman, a principal author of the JFE statement on experimental uncertainties, is gratefully appreciated. Suggestions and comments by R. J. Moffat are also gratefully appreciated.

Jong H. Kim and Terrence W. Simon,
Associate Technical Editors
Raymond Viskanta, Technical Editor

Guidelines

An uncertainty analysis of experimental measurements is necessary for the results to be used to their fullest value. Authors submitting papers for publication to this journal are required to describe the uncertainties in their experimental measurements and in the results calculated from those measurements. The journal suggests that all uncertainty evaluation be performed in accordance with a 95 percent confidence interval. If estimates are made at a confidence level other than 95 percent, adequate explanation of the techniques and rationalization for the choice of confidence interval should be provided.

For each result presented, the presentation of the experimental data should include the following information:

- 1 The precision limit, P . The $\pm P$ interval about a nominal result (single or averaged) is the experimenter's 95 percent confidence estimate of the band within which the mean of many such results would fall, if the experiment was repeated many times under the same conditions using the same equipment. The precision limit is thus an estimate of the lack of repeatability caused by random errors and unsteadiness.
- 2 The bias limit, B . The bias limit is an estimate of the magnitude of the fixed, constant error. It is assigned with the understanding that the experimenter is 95 percent confident that the true value of the bias error, if known, would be less than $|B|$.
- 3 The uncertainty, U . The $\pm U$ interval about the nominal result is the band within which the experimenter is 95 percent confident that the true value of the result lies. The 95 percent confidence uncertainty is calculated from

$$U = [B^2 + P^2]^{1/2} \quad (1)$$

- 4 A brief description of, or reference to, the methods used for the uncertainty analysis.

The estimates of precision limits and bias limits should be made over a representative time interval for the experiment.

The following additional information should be presented, preferably in tabular form:

- 1 The precision and bias limits for each variable and parameter used.
- 2 The equations by which each result was calculated.
- 3 A statement comparing the observed scatter in results on repeated trials (if performed) with the expected scatter ($\pm P$) based on the uncertainty analysis.

A discussion of sources of experimental error in the body of the text without the above does not satisfy our requirement. All reported data must show uncertainty estimates. All figures reporting new data should show uncertainty estimates of those data either on the figure itself or in the caption.

A list of references on the topic is provided below.

Example

Consider an experiment in which an air-cooled device is being tested and it is desired to determine the rate of heat transfer, q , to the cooling air. This might be accomplished by measuring the mass flow rate, m , and the inlet and outlet air temperatures, T_i and T_o , and computing:

$$q = mc(T_o - T_i) \quad (2)$$

where c is the constant-pressure specific heat of air.

The 95 percent confidence uncertainty, U_q , in the experimental result, q , is given by the following combination of a precision (random) contribution to the uncertainty of q , P_q , and a bias contribution to the uncertainty of q , B_q :

$$U_q = \sqrt{P_q^2 + B_q^2} \quad (3)$$

These two contributions can be evaluated separately in terms of the sensitivity coefficients of the result, q , to the measured quantities (e.g., $\partial q / \partial m$) following the propagation equation of Kline and McClintock (1955),

$$P_q^2 = \left(\frac{\partial q}{\partial m}\right)^2 P_m^2 + \left(\frac{\partial q}{\partial c}\right)^2 P_c^2 + \left(\frac{\partial q}{\partial T_o}\right)^2 P_{T_o}^2 + \left(\frac{\partial q}{\partial T_i}\right)^2 P_{T_i}^2 \quad (4)$$

and

$$B_q^2 = \left(\frac{\partial q}{\partial m}\right)^2 B_m^2 + \left(\frac{\partial q}{\partial c}\right)^2 B_c^2 + \left(\frac{\partial q}{\partial T_o}\right)^2 B_{T_o}^2 + \left(\frac{\partial q}{\partial T_i}\right)^2 B_{T_i}^2 + 2\left(\frac{\partial q}{\partial T_o}\right)\left(\frac{\partial q}{\partial T_i}\right)B'_{T_o}B'_{T_i} \quad (5)$$

where B'_{T_o} and B'_{T_i} are the portions of B_{T_o} and B_{T_i} that arise from identical error sources (such as the calibration error for thermocouples that were calibrated using the same standards, equipment, and procedures) and are therefore presumed to be perfectly correlated.

Using Eq. (2) to evaluate the derivatives, defining $\Delta T = T_o - T_i$, and rearranging, one obtains

$$\left(\frac{P_q}{q}\right)^2 = \left(\frac{P_m}{m}\right)^2 + \left(\frac{P_c}{c}\right)^2 + \left(\frac{P_{T_o}}{\Delta T}\right)^2 + \left(\frac{P_{T_i}}{\Delta T}\right)^2 \quad (6)$$

and

$$\left(\frac{B_q}{q}\right)^2 = \left(\frac{B_m}{m}\right)^2 + \left(\frac{B_c}{c}\right)^2 + \left(\frac{B_{T_o}}{\Delta T}\right)^2 + \left(\frac{B_{T_i}}{\Delta T}\right)^2 - 2\left(\frac{B'_{T_o}}{\Delta T}\right)\left(\frac{B'_{T_i}}{\Delta T}\right) \quad (7)$$

These derivatives could be evaluated numerically, using the data reduction program, or analytically.

The precision limits, P_m , P_{T_o} , and P_{T_i} , can each be calculated as 2 times the standard deviation of unsteadiness of a set of observations of m , T_o , and T_i , respectively, measured with the apparatus in normal running condition. These terms must include the process unsteadiness; instrument unsteadiness (or imprecision) is not sufficient. A sufficiently large number of samples (>30) should be taken over a sufficiently long sampling period, relative to the longest period of the unsteadiness, in order for unsteadiness values to be representative of the process. The precision limit of the specific heat, P_c , would arise due to the variation in the average temperature used to enter the property table or curvefit. Evaluation requires determining the relationship between c and T . In most practical cases, this term would be negligible, relative to the other precision limit terms.

The bias limits, B_m , B_{T_o} , and B_{T_i} , are each determined either by calibration tests conducted before and after the experiment or by combining, by the root-sum-square method, estimates of elemental bias errors that influence the measurement of the respective variables. The elemental bias errors include the estimated bias errors of the calibration standards and in the calibration procedure, and less-than-perfect curve fitting of the calibration data. One component of the bias limit, B_c , is the "fossilized" error, which represents the bias error inherent in the specific heat taken from a table of properties. It is due to errors that may have arisen in the measurements of those properties and in the tabulation of the results. Such contributions are usually at least 0.25–0.5 percent, and are often much larger than that (Coleman and Steele, 1989).

In estimating the precision limits and bias limits for a variable, the true definition of the variable must be acknowledged.

For example, in Eq. (2), the temperatures T_o and T_i represent the bulk mean air temperatures at the outlet and inlet cross sections, respectively. If point measurements of temperature are used to represent T_o and T_i in Eq. (2), then a bias error (which Moffat (1988) calls a "conceptual bias") occurs that is equal to the difference between the measured temperatures (T_o and T_i) and the bulk mean temperatures at the outlet and inlet cross sections, respectively. A correction must be made for that difference and the bias error evaluation should include an estimate of the residual uncertainty in that correction in addition to the bias errors from the probe calibration, etc.

Consider the situation in which the bias limits in the temperature measurements are uncorrelated and are estimated as 0.5°C and the bias limit on the specific heat property value is 0.5 percent. The estimated bias error of the mass flow meter system is specified as "0.25 percent of reading from 10 to 90 percent of full scale." Discussion with the manufacturer reveals that this is a fixed error estimate (it cannot be reduced by taking the average of multiple readings and is, thus, truly a bias error), and B_m is taken as 0.0025 times the value of m . For $\Delta T = 20^\circ\text{C}$, Eq. (7) gives:

$$\frac{B_q}{q} = \sqrt{(0.0025)^2 + (0.005)^2 + \left(\frac{0.5^\circ\text{C}}{20^\circ\text{C}}\right)^2 + \left(\frac{0.5^\circ\text{C}}{20^\circ\text{C}}\right)^2} = 0.036 \quad (= 3.6 \text{ percent}) \quad (8)$$

Obviously, the bias limits on the temperature measurements are dominant for the specific case considered. Notice that if the bias errors in the two temperature measurements were totally correlated, the last term on the right side of Eq. (7) would cancel the third and fourth terms and then B_q/q would be 0.0056 instead of 0.036.

If the random errors and process unsteadiness were such that the precision limit for q , P_q , calculated from Eq. (5), was 2.7 percent, the overall uncertainty in the determination of q , U_q , would be:

$$\frac{U_q}{q} = \sqrt{\left(\frac{B_q}{q}\right)^2 + \left(\frac{P_q}{q}\right)^2} = \sqrt{(0.036)^2 + (0.027)^2} = 0.045 = 4.5 \text{ percent} \quad (9)$$

References and Recommended Readings

- Abernethy, R. B., Benedict, R. P., and Dowdell, R. B., 1985, "ASME Measurement Uncertainty," *ASME Journal of Fluids Engineering*, Vol. 107, pp. 161–164.
- Coleman, H. W., and Steele, W. G., 1989, *Experimentation and Uncertainty Analysis for Engineers*, Wiley, New York.
- Kline, S. J., and McClintock, F. A., 1953, "Describing Uncertainties in Single-Sample Experiments," *Mechanical Engineering*, Vol. 75, Jan., pp. 3–8.
- Kline, S. J., 1985a, "1983 Symposium on Uncertainty Analysis Closure," *ASME Journal of Fluids Engineering*, Vol. 107, pp. 181–182.
- Kline, S. J., 1985b, "The Purposes of Uncertainty Analysis," *ASME Journal of Fluids Engineering*, Vol. 107, pp. 153–160.
- Lassahn, G. D., 1985, "Uncertainty Definition," *ASME Journal of Fluids Engineering*, Vol. 107, p. 179.
- "Measurement Uncertainty," ANSI/ASME PTC 19.1—1985 Part I, 1986.
- Moffat, R. J., 1982, "Contributions to the Theory of Single-Sample Uncertainty Analysis," *ASME Journal of Fluids Engineering*, Vol. 104, pp. 250–260.
- Moffat, R. J., 1985, "Using Uncertainty Analysis in the Planning of an Experiment," *ASME Journal of Fluids Engineering*, Vol. 107, pp. 173–178.
- Moffat, R. J., 1988, "Describing the Uncertainties in Experimental Results," *Experimental Thermal and Fluid Science*, Vol. 1, pp. 3–17.
- Smith, R. E., Jr., and Wehofer, S., 1985, "From Measurement Uncertainty to Measurement Communications, Credibility, and Cost Control in Propulsion Ground Test Facilities," *ASME Journal of Fluids Engineering*, Vol. 107, pp. 165–172.

Microscale Heat Conduction in Dielectric Thin Films

A. Majumdar

Department of Mechanical and
Environmental Engineering,
University of California,
Santa Barbara, CA 93106

Heat conduction in dielectric thin films is a critical issue in the design of electronic devices and packages. Depending on the material properties, there exists a range of film thickness where the Fourier law, used for macroscale heat conduction, cannot be applied. This paper shows that in this microscale regime, heat transport by lattice vibrations or phonons can be analyzed as a radiative transfer problem. Based on Boltzmann transport theory, an equation of phonon radiative transfer (EPRT) is developed. In the acoustically thick limit, $\xi_L \gg 1$, or the macroscale regime, where the film thickness is much larger than the phonon-scattering mean free path, the EPRT reduces to the Fourier law. In the acoustically thin limit, $\xi_L \ll 1$, the EPRT yields the blackbody radiation law $q = \sigma(T_1^4 - T_2^4)$ at temperatures below the Debye temperature, where q is the heat flux and T_1 and T_2 are temperatures at the film boundaries. For transient heat conduction, the EPRT suggests that a heat pulse is transported as a wave, which becomes attenuated in the film due to phonon scattering. It is also shown that the hyperbolic heat equation can be derived from the EPRT only in the acoustically thick limit. The EPRT is then used to study heat transport in diamond thin films in wide range of acoustical thicknesses spanning the thin and the thick regimes. The heat flux follows the relation $q = 4\sigma T^3 \Delta T / (3\xi_L/4 + 1)$ as derived in the modified diffusion approximation for photon radiative transfer. The thermal conductivity, as currently predicted by kinetic theory, causes the Fourier law to overpredict the heat flux by 33 percent when $\xi_L \ll 1$, by 133 percent when $\xi_L = 1$, and by about 10 percent when ξ_L increases to 10. To use the Fourier law in both ballistic and diffusive transport regimes, a simple expression for an effective thermal conductivity is developed.

1 Introduction

Solid films of dielectric material of thicknesses between 100 Å and 100 μm are extensively used in semiconductor electronic devices. In electronic circuits, films of silicon dioxide (SiO₂) and silicon nitride (Si₃N₄) form barrier layers between electrically conducting regions (Mayer and Lau, 1990). To dissipate and spread the heat generated in electronic packages, dielectric films with high thermal conductivity such as those of aluminum nitride (AlN) and diamond (Guyer and Koshland, 1990; Ravi, 1991), are highly desirable. Since the temperature of solid state devices often determines their performance, heat transport in dielectric films is a critical issue in their design. With trends toward higher density chips and high heat generation, the thermal problem is becoming more acute.

Heat transport in dielectric crystalline materials is predominantly by atomic or crystal vibrations. These vibrations travel within a solid as waves. The energy of these waves is quantized and each quantum is called a phonon (Kittel, 1986). On a macroscopic scale, heat transport can be accurately modeled by the Fourier law as

$$q = -\lambda \nabla T, \quad (1)$$

where q is the heat flux, vector ∇T is the local temperature gradient, and λ is the thermal conductivity, which represents how easily phonons are transported within a material. Based on kinetic theory, the thermal conductivity can be related to other physical properties as (Ziman, 1960)

$$\lambda = \frac{1}{3} C v l, \quad (2)$$

where C is the specific heat per unit volume, v is the average speed of sound, and l is the mean free path between phonon

scattering events. Phonons in dielectric materials are scattered by boundaries, impurities, defects and other phonons.

Although the laws of macroscopic heat transport in dielectric media are well known, there exist regimes of size and temperature where such laws are no longer applicable. Flik et al. (1991) used simple arguments to show that the size effects on thermal conductivity will be present for diamond films thinner than 1 μm at room temperature. As the temperature decreases, even thicker films would fall in this *microscale* regime. Although the Fourier law may be valid for heat conduction in the plane of the thin film, it will break down for conduction across the film. The use of Eq. (1) in such cases can lead to significant errors.

The first question that one might ask is why the Fourier law breaks down at small scales. It is important to note that the definition of "thermal conductivity" depends solely on the existence of a temperature gradient within a material. Since temperature at a point can be defined only under *local* thermodynamic equilibrium (Bejan, 1988), a meaningful temperature can be defined only at points separated on an average by the mean free path l . This is because local thermodynamic equilibrium is restored by phonon scattering due to lattice imperfections and other phonons. Consider now the schematic diagram in Fig. 1 where heat is transported across a film of thickness L with temperatures T_1 and T_2 at the two boundaries. When the thickness of a film L is much larger than the mean free path, $L \gg l$, a macroscopic temperature gradient is established and the thermal conductivity is well defined. However, when the two length scales are comparable, $L \sim l$, a temperature gradient cannot be established and therefore the thermal conductivity cannot be defined. In the limiting case, with no phonon scattering within the film, the heat flux across the film is given as (Swartz and Pohl, 1989)

$$q = \sigma(T_1^4 - T_2^4), \quad (3)$$

where σ is the Stefan-Boltzmann constant for phonons (Ashcroft and Mermin, 1976). This is commonly known as the

Contributed by the Heat Transfer Division for publication in the JOURNAL OF HEAT TRANSFER. Manuscript received by the Heat Transfer Division March 1992; revision received September 1992. Keywords: Conduction, Radiation, Thermophysical Properties. Associate Technical Editor: R. O. Buckius.

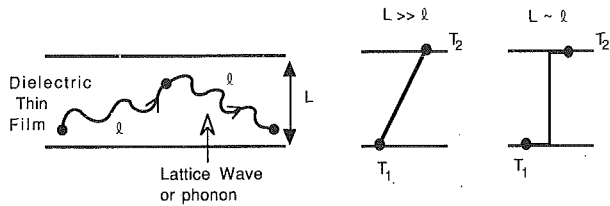


Fig. 1 Schematic diagram of temperature profiles in a thin dielectric film for two limiting cases: (i) $L \gg l$, (ii) $L \sim l$

Casimir (1938) limit for which the thermal conductivity cannot be defined. In this limit, phonons scatter only at boundaries, which restore local thermodynamic equilibrium. A boundary that thermalizes phonons can be considered black in the sense of photon radiation. It is apparent that as one goes from one limiting case to the other (see Fig. 1), heat conduction changes from a diffusive to a ballistic transport phenomenon. This is analogous to the change in transport laws while going from the optically thick to optically thin limiting cases in radiative transfer (Ozisik, 1973).

This study shows from fundamental principles that heat conduction by phonons can be analyzed as radiative transfer. A general theory of heat conduction is developed, showing that the Fourier law is a limiting case for steady-state macroscale heat transport. Two cases of heat transport across and along a thin film are considered. For the transient case, the theory shows that the hyperbolic heat equation, often used for microscale heat conduction, is valid only in the macroscale limit. Based on the Boltzmann transport theory, the equation of phonon radiative transfer (EPRT) is developed and solved. Finally, the EPRT is used to study heat transport in diamond thin films at different temperatures, film thicknesses, and impurity concentrations.

2 Phonon Transport—General Formulation

The physics of crystal vibrations in solids is well documented in several books (Kittel, 1986; Ziman, 1960; Ashcroft and Mermin, 1976). The energy of crystal vibrations is quantized in packets of $\hbar\omega$ where \hbar is Planck's constant divided by 2π and ω is the frequency of the crystal vibrations. Each quantum of energy is called a phonon. The statistics of phonons in thermodynamic equilibrium follows the Bose-Einstein distribution and is therefore similar to photons. When the phase of the crystal vibration wave is not important, phonons can be viewed as particles. The transport of phonons leads to the transport of heat in dielectric solids. A brief review of the physics of phonons is presented by Majumdar (1991).

In this study, phonon transport will be analyzed using the semiclassical Boltzmann equation often used to model transport of particles following an arbitrary distribution. In a general form, the equation can be written as (Ziman, 1960)

$$\frac{\partial f}{\partial t} + v \cdot \nabla f + a \cdot \frac{\partial f}{\partial v} = \left(\frac{\partial f}{\partial t} \right)_{\text{scatt}}, \quad (4)$$

where a is the particle acceleration and $f(r, v, t)$ is the distribution function, which depends on time t and particle position r and velocity v . Since phonons that are dominant in heat transport travel at the speed of sound, which does not change appreciably over a large frequency range, the third term containing $\partial f / \partial v$ can be neglected. The second term represents the drift or the advection of the distribution. The term on the right side of Eq. (4) provides the rate of change of f due to scattering.

To study any transport phenomenon, one needs to solve for the distribution function f as a function of position and time. For simplicity, consider f to vary only in the x direction. If phonon scattering is considered in a rigorous form, the scattering term becomes very complicated, making the Boltzmann equation difficult to solve (Ziman, 1960). However, the scat-

Nomenclature

A = nondimensional constant defined in Eq. (34)
 A_c = cross-sectional area, m^2
 a = atomic spacing in a lattice, m
 c = speed of light, ms^{-1}
 C = specific heat per unit volume, $Jm^{-3}K^{-1}$
 d = probability of diffuse phonon scattering at boundaries
 $\mathcal{D}(\omega)$ = density of states, $m^{-3}s$
 E_n = exponential integrals
 f = statistical distribution function
 F = nondimensional fourth power of temperature = $(T^4 - T_2^4) / (T_1^4 - T_2^4)$
 G = reciprocal lattice vector $|G| = 2\pi/a$, m^{-1}
 \hbar = Planck's constant divided by 2π , J_s
 I = directional-spectral phonon or photon intensity, $Wm^{-2}sr^{-1}s$
 J = nondimensional temperature = $(T - T_2) / (T_1 - T_2)$
 k = phonon wavevector, m^{-1}
 k_B = Boltzmann constant, JK^{-1}
 l = mean free path, m

L = film thickness, m
 \mathcal{L} = distance along the plane of thin film, m
 q = heat flux, Wm^{-2}
 R = radius of a lattice imperfection, m
 t = time, s
 T = temperature, K
 v = speed of sound, ms^{-1}
 x = coordinate direction and length, m
 y = distance along or in plane with a thin film
 α = constant of order unity
 η = number density of impurities, m^{-3}
 θ_D = Debye temperature, K
 κ = absorption coefficient, m^{-1}
 λ = thermal conductivity, $Wm^{-1}K^{-1}$
 Λ = phonon wavelength, m
 μ = cosine of an angle
 ξ = nondimensional x distance = x/l
 σ = Stefan-Boltzmann constant for phonons, $Wm^{-2}K^{-4}$
 τ = relaxation time, s
 φ = scattering cross section, m^2

Φ = phase function
 ψ = nondimensional y distance = y/l
 χ = distance perpendicular to thin film; also size parameter = $2\pi R/\Lambda$
 ω = angular frequency of phonons, s^{-1}
 Ω = solid angle, sr

Superscripts

o = equilibrium
 $+$ = forward direction ($\mu > 0$)
 $-$ = backward direction ($\mu < 0$)

Subscripts

a = absorption
 b = bulk
 dom = dominant in phonon energy
 D = Debye cutoff
 i = lattice imperfections
 L = film thickness
 N = normal phonon-phonon scattering
 r = residual
 s = scattering
 U = Umklapp phonon-phonon scattering
 ω = spectral quantity

tering term is often simplified by the relaxation-time approximation (Kittel, 1986), which reduces the Boltzmann equation to

$$\frac{\partial f_\omega}{\partial t} + v_x \frac{\partial f_\omega}{\partial x} = \frac{f_\omega^0 - f_\omega}{\tau}, \quad (5)$$

where f_ω is the distribution function as a function of phonon frequency ω , f_ω^0 is the equilibrium phonon distribution, which follows the Bose–Einstein distribution, v_x is the x component of the phonon velocity, and τ is the relaxation or the mean free time between scattering. Once f_ω is found by solving Eq. (5), the heat flux q_x in the x direction can be determined as (Ziman, 1960)

$$q_x(x, t) = \sum_{\mathbf{k}} v_x(\mathbf{k}) f_{\mathbf{k}}(x, t) \hbar \omega_{\mathbf{k}} = \int v_x f_\omega(x, t) \hbar \omega \mathfrak{D}(\omega) d\omega \quad (6)$$

which represents a net flux of phonon energy in the positive x direction. The summation in Eq. (6) is over all phonon wave vectors and can be transformed into an integral over frequency. Here $\mathfrak{D}(\omega)$ is the density of states such that the number of crystal vibrational modes between ω and $\omega + d\omega$ is $\mathfrak{D}(\omega)d\omega$. For a steady-state condition with $\partial f/\partial t = 0$, one of the simplifications often used in Eq. (5) is to assume that the advection term can be written as (Berman, 1976; Kittel, 1986)

$$\frac{df_\omega}{dx} = \frac{df_\omega^0}{dT} \frac{dT}{dx}, \quad (7)$$

where the phonon distribution at any point is assumed to be the equilibrium distribution. The chain rule then yields a spatial temperature gradient. Equation (5) can then be solved for f_ω

$$f_\omega(x) = f_\omega^0(x) - \tau v_x \frac{df_\omega^0}{dT} \frac{dT}{dx}. \quad (8)$$

If this solution is used in Eq. (6) to obtain q_x , the first term containing f_ω^0 will produce a zero heat flux because under equilibrium there is no net flux of phonons in any direction. Mathematically, since v_x is an odd function of direction, that is $v_x = -v_{-x}$, and f_ω^0 is an even function of direction, the integral of the product becomes zero. Therefore, the heat flux becomes

$$q_x = -\frac{dT}{dx} \int \tau v_x^2 \frac{df_\omega^0}{dT} \hbar \omega \mathfrak{D}(\omega) d\omega. \quad (9)$$

This is of course the Fourier law with the thermal conductivity λ as (Ziman, 1960)

$$\lambda = \frac{1}{3} \int \tau v^2 \frac{df_\omega^0}{dT} \hbar \omega \mathfrak{D}(\omega) d\omega, \quad (10)$$

where $v_x^2 = v^2/3$ has been used.² It is clear then that the simplification of Eq. (7), which yields the Fourier law, is not valid for the limiting case of $q = \sigma(T_1^4 - T_2^4)$. The assumption of Eq. (7) must therefore be abandoned for analyzing *microscale* heat transport. The development of a new approach is warranted and is now described.

Equation of Phonon Radiative Transfer. Using the analogy between photons and phonons as wave packets of energy, one can define an intensity of phonons I_ω as (Vincenti and Kruger, 1977)

$$I_\omega(\theta, \phi, x, t) = \sum_p \mathbf{v}(\theta, \phi) f_\omega(x, t) \hbar \omega \mathfrak{D}(\omega), \quad (11)$$

Here $\mathbf{v}(\theta, \phi)$ is the velocity vector in the direction of (θ, ϕ) within a unit solid angle and $\mathfrak{D}(\omega)$ is the density of states per unit volume. This makes the intensity the flux of energy per unit time, per unit area, per unit solid angle in the direction of phonon propagation and per unit frequency interval around ω . The summation in Eq. (11) is over the three phonon polarizations. Multiplying Eq. (5) by $\mathbf{v} \hbar \omega \mathfrak{D}(\omega)$, the Boltzmann equation can be transformed to

$$\frac{1}{v} \frac{\partial I_\omega}{\partial t} + \mu \frac{\partial I_\omega}{\partial x} = \frac{I_\omega^0(T(x)) - I_\omega}{v\tau(\omega, T)}, \quad (12)$$

where $v_x = v\mu$ and μ is the cosine of the angle between the phonon propagation direction and the x direction and I_ω^0 is the equilibrium intensity corresponding to a black body intensity at temperatures below the Debye temperature. Although Eq. (12) is for a one-dimensional case, it can be generalized to three dimensions where the second term will be replaced by three terms containing three directional cosines corresponding to the three orthogonal directions. It is evident that this equation has the same form as the equation of radiative transfer (ERT) used for one-dimensional systems (Ozisk, 1973; Siegel and Howell, 1982)

$$\frac{1}{c} \frac{\partial I_\omega}{\partial t} + \mu \frac{\partial I_\omega}{\partial x} = \kappa_a I_\omega^0 - (\kappa_a + \kappa_s) I_\omega + \frac{\kappa_s}{4\pi} \int_{4\pi} \Phi(\Omega' - \Omega) I_\omega' d\Omega', \quad (13)$$

where c is the speed of light, κ_a and κ_s are the absorption and scattering coefficients, respectively, Φ is the phase function, and Ω is the solid angle. Note that $v\tau$ in Eq. (12) is the mean free path, which is the reciprocal of the absorption coefficient used in ERT. The differences between Eq. (12) and ERT are: (i) The ERT contains an in-scattering term whereas Eq. (12) does not; and (ii) in the ERT the emission and absorption terms physically imply transfer of photon energy to other particles such as gas molecules, electrons or phonons. The right side of Eq. (12) represents restoration of thermodynamic equilibrium by interactions of phonons with electrons, holes, and other phonons. In that respect it is similar to the ERT since change of photon energy also restores equilibrium. In view of the similarities, it is appropriate to call Eq. (12) the *equation of phonon radiative transfer* (EPRT). Once the intensity is found by solving the EPRT, the heat flux can be determined as

$$q(x) = \int_{\Omega=4\pi} \int_0^{\omega_D} \mu I_\omega(x, \omega, \Omega) d\omega d\Omega. \quad (14)$$

The limitations of the analogy between photons and phonons appear in the phonon–phonon interactions, which are absent for photons. These phonon interactions are due to anharmonic forces between atoms and are vital in redistributing energy between different frequencies to restore thermodynamic equilibrium. The assumption of a relaxation time to represent such processes is a simplification, which linearizes the Boltzmann equation. In reality, the Boltzmann equation containing anharmonic interactions is nonlinear and very difficult to solve (Ziman, 1960). Another limitation in the EPRT is that the phase of the lattice waves is not considered. Therefore interference effects are neglected. This may not be a good assumption when phonons transport ballistically between two surfaces. However, if the surfaces bounding a region are diffuse, the phase information need not be important.

Steady-State Heat Conduction Across a Film. Consider the coordinate system of the dielectric film of thickness L in Fig. 2 in which the boundaries are rough enough to scatter phonons diffusely and thereby restore thermodynamic equilibrium. In a real solid state device with several layers of film, the film

²The total velocity v is related to its components as $v^2 = v_x^2 + v_y^2 + v_z^2$. To determine the statistical average velocity $\langle v \rangle$, one has to take the average of the three velocity components. In an isotropic medium the average speed in each direction will be the same such that $\langle v_x^2 \rangle = \langle v_y^2 \rangle = \langle v_z^2 \rangle$. Therefore, $\langle v^2 \rangle = \langle v^2 \rangle/3$.

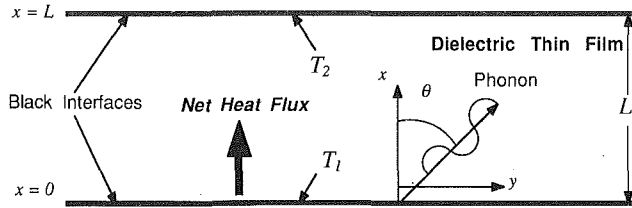


Fig. 2 Schematic diagram of heat transport across a dielectric film of thickness L with black interfaces at different temperatures

interfaces will either reflect or transmit phonons and in effect pose a resistance to heat flow (Swartz and Pohl, 1989). To simplify the situation, consider the Casimir limit where the boundaries are black with temperatures T_1 and T_2 . Such a situation is realized when a dielectric film is sandwiched between, say, two metallic films. Since the electron-phonon mean free path in the metals is much smaller than the phonon mean free path in the dielectric film, the two interfaces of the dielectric film can be assumed to be thermalizing black boundaries at fixed temperatures. This is analogous to the one-dimensional plane-parallel medium that is often considered in radiative heat transfer problems. The solution of the ERT under these conditions is well documented (Ozisik, 1973) and will be described only briefly here in the following sections.

Under steady state, the first term in the EPRT is zero. Consider a nondimensional distance ξ to be defined as $\xi = x/v\tau(\omega, T)$. This can be called the acoustic thickness of the medium, corresponding to the optical thickness for photon radiation. Since the relaxation time τ depends on frequency and temperature, as will be later shown, so will ξ for constant x . When the temperature dependence of τ is weak or when the temperature drop across the film is not very large, the spectral heat flux at any point ξ can be shown to be (Ozisik, 1973)

$$q_\omega(\xi) = 2\pi \left[I_\omega^+(0)E_3(\xi) + \int_0^\xi I_\omega^0(T(\xi'))E_2(\xi - \xi')d\xi' \right] - 2\pi \left[I_\omega^-(\xi_L)E_3(\xi_L - \xi) + \int_\xi^{\xi_L} I_\omega^0(T(\xi'))E_2(\xi' - \xi)d\xi' \right] \quad (15)$$

where $\xi_L = L/v\tau$ is the acoustical thickness of the medium, the superscripts + and - imply forward ($\mu > 0$) and backward ($\mu < 0$) directions, respectively, and $E_n(x)$ is the exponential integral (Siegel and Howell, 1982). The total heat flux is then obtained by integrating over all phonon frequencies. Now consider the limiting behaviors of acoustically thin and thick cases and the case of phonon radiative equilibrium.

Acoustically Thin Medium. In an acoustically thin medium, the phonon mean free path is much larger than the physical thickness of the medium such that $\xi_L \ll 1$. One might argue, however, that the mean free path can at the most be equal to L , that is, in the boundary scattering regime, and therefore the smallest value of $\xi = L/l$ is unity. It is important to note that the mean free path l is a statistical quantity and can be physically interpreted by the relation $p = \exp(-x/l)$ (Jeans, 1954). Here p is the probability that a particle would travel a distance x without undergoing a collision. Therefore it is possible to have $l \gg L$, which means that the probability of a phonon, emerging from one boundary and not being scattered until it reaches the other boundary is $\exp(-L/l)$.

In the acoustically thin case, the exponential integrals follow the limiting behavior $E_2(\xi) \rightarrow 1 - O(\xi)$ and $E_3(\xi) \rightarrow 1/2 - \xi + O(\xi^2)$. It can then be shown, that as in photon radiation (Viskanta, 1966)

$$q_\omega = \pi[I_\omega^+(0) - I_\omega^-(\xi_L)]. \quad (16)$$

If the temperatures T_1 and T_2 are much less than the Debye temperature, then the Planck blackbody distribution can be used for the surface intensities. Integrating over all frequencies, the total heat flux becomes equal to $\sigma(T_1^4 - T_2^4)$, which is the same as Eq. (3).

Acoustically Thick Medium. For an acoustically thick medium, the mean free path is much smaller than a geometric dimension of the medium. Using approximations for the exponential integrals and some manipulations, it can be shown that (Viskanta, 1966)

$$q_\omega(\xi) = -\frac{4\pi}{3} \frac{dI_\omega^0(T(\xi))}{d\xi}. \quad (17)$$

Integrating over all frequencies, the total heat flux can be written as

$$q(x) = -\frac{dT}{dx} \cdot \int_0^{\omega_D} \frac{4\pi}{3} v\tau(\omega, T) \frac{dI_\omega^0}{dT} d\omega. \quad (18)$$

This is the heat diffusion equation or the Fourier law with the integral being the thermal conductivity of the material and is the same as in Eq. (9).

Phonon Radiative Equilibrium. For steady state, the phonon radiative equilibrium is achieved when there is no source or sink of energy, that is $\nabla \cdot q = 0$. One must note that this is essentially the first law of thermodynamics. Integrating the one-dimensional EPRT over $-1 < \mu < 1$ and then over all the frequencies, the following equation is derived:

$$\frac{dq}{dx} = 2 \int_0^{\omega_D} \frac{I_\omega^0}{v\tau(\omega, T)} d\omega - \int_0^{\omega_D} \frac{d\omega}{v\tau(\omega, T)} \left(\int_{-1}^1 I_\omega d\mu \right). \quad (19)$$

Under phonon radiative equilibrium, $dq/dx = 0$, and therefore the two terms on the right side become equal. Although this suggests radiative equilibrium over all frequencies, it is possible to have a nonequilibrium condition at a particular frequency. In such a situation, however, the solution of the radiative transfer equation becomes complicated. Therefore, to obtain an easy approximate solution, one could assume a stringent condition of equilibrium at every frequency to get

$$I_\omega^0(T) = \frac{1}{2} \int_{-1}^1 I_\omega d\mu. \quad (20)$$

This guarantees that Eq. (19) is satisfied. The assumption is valid only when the medium is gray, that is, when the relaxation time is independent of the frequency. If Eq. (20) is integrated over all the frequencies and the temperature is much lower than the Debye temperature, then

$$\frac{\sigma T^4}{\pi} = \frac{1}{2} \int_0^{\omega_D} \left(\int_{-1}^1 I_\omega d\mu \right) d\omega. \quad (21)$$

To obtain the temperature at any location, it is necessary to know the intensity $I_\omega(x, \mu, \omega)$. The procedure to follow is to replace I_ω^0 in the EPRT by the integral in Eq. (20) to obtain

$$\frac{1}{v} \frac{\partial I_\omega}{\partial t} + \mu \frac{\partial I_\omega}{\partial x} = \frac{\left(\frac{1}{2} \int_{-1}^1 I_\omega d\mu \right) - I_\omega}{v\tau(\omega, T)} \quad (22)$$

Although Eq. (20) is derived for steady state, it will be shown later that it is valid for transient heat conduction.

Steady State Heat Conduction Along a Film. Consider now a temperature difference to exist in the plane of the film or in the y direction as shown in Fig. 3. To study heat transport over a distance L , one must note that the acoustical thickness

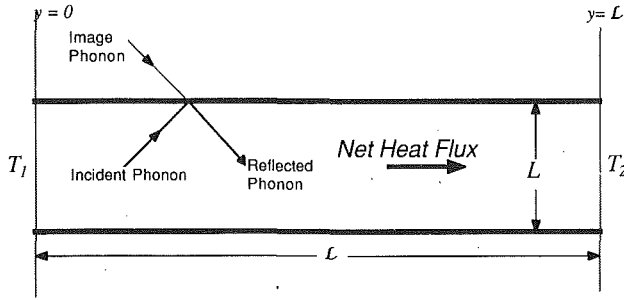


Fig. 3 Schematic diagram of heat transport along a dielectric thin film with phonon reflection at film surfaces

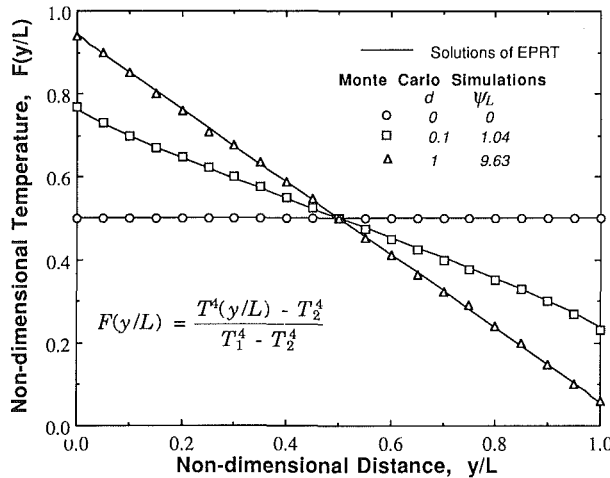


Fig. 4 Comparison of temperature profiles along a silicon crystal obtained by Monte Carlo simulations (Klitsner et al., 1988) and by solving the EPRT. Temperatures were much lower than the Debye temperature such that boundary scattering was dominant.

of the medium is $\psi_L = \mathcal{L}/l$ where l is the phonon mean free path and ψ is the nondimensional distance y/l . Since phonons propagating along the film are confined by the film thickness L , one must incorporate phonon scattering by the boundaries to evaluate the mean free path.

Specular reflection of phonons at the surface conserves phonon momentum and therefore does not pose any resistance to heat transport. When the boundary scattering is completely specular, the reflected phonon can be replaced by an image of the incident phonon as shown in Fig. 3. Therefore, the film boundaries can essentially be removed and heat transport by phonons along a film can be studied as a plane-parallel medium. Diffuse scattering poses resistance to phonon transport and must be included in mean free path calculations.

Using Monte Carlo simulations of phonon transport along a silicon crystal, Klitsner et al. (1988) obtained temperature profiles along the crystal length for different values of the diffuse scattering probability, d as shown in Fig. 4. The temperature profiles and the jumps at the wall are very similar to those observed under radiative equilibrium condition for photon radiative transfer in a plane-parallel medium. Note that as the probability of diffuse scattering increases, the temperature jumps at the walls decrease and a temperature gradient is established. Therefore, increase in the probability diffuse scattering essentially decreases the phonon mean free path.

To compare the results of Klitsner et al. (1988) with that of the present study, the EPRT was solved for a steady state using the discrete-ordinates method of Kumar et al. (1990). Since boundary scattering is dominant, the relaxation time was assumed to be frequency-independent making it a gray medium. The integral in Eq. (22) was approximated by Gaussian quadrature

$$\int_{-1}^1 I(\mu) d\mu = \sum_{j=1}^{2N} I(\mu_j) w_j \quad (23)$$

where μ_j are the discrete directions and w_j are the weights. In accordance with the results of Kumar et al. (1990) regarding accuracy, a quadrature of $N = 8$ was chosen. The results of the EPRT are shown as the solid lines in Fig. 4. The relation between the mean free path and the diffuse reflectivity was obtained from Klitsner et al. (1988). It is clear from Fig. 4 that the results are in excellent agreement with the Monte Carlo simulations, which essentially produces an accurate solution of the Boltzmann transport equation. The advantage of using the EPRT over Monte Carlo method is that the latter normally takes much more computer time to get any statistically reasonable answer. In the transient case, an ensemble Monte Carlo technique must be adopted, which makes it computer intensive (Jacoboni and Reggiani, 1983). However, the Monte Carlo technique has the advantage that realistic dispersion relation and scattering rates can be incorporated very easily making the stochastic calculations of minimum difficulty.

For phonon transport along an infinite rod, Ziman (1960) showed that the phonon mean free path limited by diffuse surface scattering is

$$l = \left(\frac{2-d}{d} \right) l_c \quad (24)$$

Here l_c is the mean free path for pure diffuse reflection and is given as $l_c = 1.12\sqrt{A_c}$ where A_c is the cross-sectional area of the rod. If transmission of phonons into the substrate is neglected, it can be inferred from Sondheimer's (1952) work that the phonon mean free path in thin films is

$$\frac{l}{L} = \frac{3}{4} \left(\frac{2-d}{d} \right) \ln \left(\frac{l_b}{L} \right) \quad \text{for } L \ll l_b$$

$$\frac{l}{L} = \frac{1}{L/l_b + 3d/8} \quad \text{for } l_b \ll L \quad (25)$$

where l_b is the phonon mean free path in a bulk medium, that is in the absence of boundary effects.

Unless the temperatures are much below the Debye temperature of a material, phonon scattering at most engineering surfaces are diffuse, rendering d close to unity. Therefore, if the bulk phonon mean free path is larger than the film thickness, that is $\xi_L = L/l_b < 1$, the effective phonon mean free path is of the order of the film thickness, $l \sim L$. Although L is typically of the order of or less than a micrometer, the distance \mathcal{L} in the y direction can be macroscopic spanning over several millimeters. Therefore, the acoustic thickness of the medium $\psi_L = \mathcal{L}/L$ can be very large. In this case, the Fourier law is valid and the thermal conductivity can be found by Eq. (2) or by a more rigorous analysis (Flik and Tien, 1990).

Transient Heat Conduction. To determine the transient thermal response of dielectric material in the microscale regime, one must solve the complete EPRT in Eq. (22). Before doing so, however, it is worth examining the nature of the transient EPRT. It is evident that the left-hand side of Eq. (22) represents a wave with characteristics $x - \mu vt = \text{const}$. Therefore, a phonon pulse should travel as a wave, undergoing attenuation due to scattering within the medium and eventually dying out. The question that arises is, could the EPRT in any way be related to the hyperbolic heat equation (Joseph and Preziosi, 1989; Bai and Lavine, 1991)?

Following Tavernier's (1962) work, the EPRT can be multiplied by μ and integrated over the range $-1 < \mu < 1$ and over all frequencies, finally arriving at

$$\frac{1}{v} \frac{\partial q}{\partial t} + \int_0^{\omega_D} \int_{-1}^1 \mu^2 \frac{\partial I_\omega}{\partial x} d\mu d\omega = - \int_0^{\omega_D} \frac{q_\omega}{v\tau(\omega, T)} d\omega \quad (26)$$

Now we make the following assumptions: (i) The relaxation time between scattering is independent of frequency and is a constant, (ii) for the second term on the left-hand side of Eq. (26), the expansion in Eq. (6), which yielded the Fourier law, can be employed. This reduces Eq. (26) to the Catteneo equation (Joseph and Preziosi, 1989)

$$\tau \frac{dq}{dt} + q = -\lambda \frac{dT}{dx} \quad (27)$$

The first law of thermodynamics states that

$$C \frac{\partial T}{\partial t} + \nabla \cdot q = 0 \quad (28)$$

where C is the specific heat per unit volume. When these two equations are combined to eliminate q , the hyperbolic heat equation can be derived to be

$$\tau \frac{\partial^2 T}{\partial t^2} + \frac{\partial T}{\partial t} = \frac{\lambda}{C} \frac{d^2 T}{dx^2} \quad (29)$$

It is important to note the assumptions involved in deriving the hyperbolic heat equation. Assumption (ii) yielded the Fourier law under steady state and the hyperbolic heat equation for the transient case. Since the Fourier law is not applicable in the *microscale* regime, the use of the hyperbolic heat equation in this regime is questionable. It is more logical to solve the transient EPRT of Eq. (22) for the phonon intensity and then determine the transient heat flux (Joshi and Majumdar, 1993). Equation (22) is based on the approximation made in Eq. (20) for the steady-state case where it was assumed that equilibrium was achieved at all phonon frequencies. This assumption is also valid for the transient case, since integration of Eq. (22) over all frequencies and direction gives

$$\frac{\partial U}{\partial t} + \nabla \cdot q = 2 \int_0^{\omega_D} \frac{I_\omega(T)}{v\tau} d\omega - \int_{-1}^1 \int_0^{\omega_D} \frac{I_\omega}{v\tau} d\omega d\mu \quad (30)$$

where U is the phonon energy density. The first law of thermodynamics suggests that the left-hand side of Eq. (30) is zero. Therefore Eq. (20) is valid for both steady and transient cases, making Eq. (22) a general equation for phonon transport.

The EPRT can be solved by existing techniques used in radiative transfer. However, it is necessary to determine the relaxation time $\tau(\omega, T)$ for the particular dielectric medium. This is discussed in the next section where ballistic and diffusive phonon transport are studied in diamond thin films.

3 Phonon Mean Free Paths in Diamond Thin Films

In addition to its mechanical and electrical properties, the high thermal conductivity of diamond makes it an ideal material for several applications of technological importance (Guyer and Koshland, 1990). One such application is in electronic devices and packages where extremely high heat fluxes are generated. Diamond thin films are the likely choice for dissipating such high heat fluxes. It is therefore important to study the mechanisms of heat conduction by phonons in thin films of diamond.

Phonon scattering in dielectric crystalline solids such as diamond can be divided into two categories: (i) elastic scattering by lattice imperfections, such as defects, dislocations, and boundaries, where the energy or the frequency of the incident lattice wave is unchanged; and (ii) inelastic scattering between three or more phonons where the frequency is modified. Recent experiments by Anthony et al. (1990) have shown that the room temperature thermal conductivities (see Table 1) of high purity type IIa ^{12}C diamond are strongly influenced by scattering at defects formed by the ^{13}C isotope. In order to isolate the contribution of the different scattering mechanisms and predict their influence at other temperatures, it is necessary to investigate in detail the phonon scattering mechanisms. In the fol-

Table 1 Thermal conductivities and mean free paths of type IIa diamond at room temperature for different concentrations of ^{13}C isotope

Concentration of ^{13}C in % ^a	Number density $\eta \times 10^{26}$ [m^{-3}]	Thermal Conductivity ^a , λ [W/m-K]	Effective mean free path, ℓ [μm]	Predicted impurity mfp, ℓ_i [μm]	U-process mean free path, ℓ_U [μm]
0.07	0.154	3320	0.447	9.57	0.468
0.50	1.100	2600	0.350	1.34	0.473
1.00	2.200	2230	0.273	0.67	0.461

^a Data from Anthony et al. (1990)

lowing discussion, elastic scattering by dislocations will not be considered in this study and can be found in more detail from Klemens (1958), Ziman (1960), and Berman (1976).

Phonon Scattering Mechanisms.

Scattering by Lattice Imperfections. Lattice imperfections include absence of a single or a group of atoms or presence of foreign atoms within a lattice. An incident lattice wave is scattered by such imperfections, thus resulting in resistance to heat transport. Experiments have shown that even a slight rise in impurity concentration can have a substantial effect on heat conduction (Worlock, 1966; Walton, 1967).

The relaxation time τ_i for imperfection scattering can be obtained from kinetic theory as (Vincenti and Kruger, 1977)

$$\tau_i = \frac{1}{\alpha\varphi\eta v} \quad (31)$$

where φ is the scattering cross section, η is the number of scattering sites per unit volume or defect density and α is a constant of the order of unity. It is convenient to divide the scattering cross section as a function of phonon wavelength into three regions where the wavelength is larger, roughly equal and smaller than the defect size. In the first regime the cross section φ follows the Rayleigh law (1896) and varies as the fourth power of phonon frequency. In the last regime, the effective cross section is equal to the projected area of the defect (Walton and Lee, 1967). In the second regime, Walton and Lee (1967) have shown that the cross section can have oscillations with the wavelength. However, when integrated over all the wavelengths to determine the total heat flux, these oscillations would average out. For simplicity in calculations, it is proposed in this study that the scattering cross section varies as

$$\varphi = \pi R^2 \left(\frac{\chi^4}{\chi^4 + 1} \right) \quad (32)$$

where R is the radius of the lattice imperfection and χ is the size parameter

$$\chi = \frac{2\pi R}{\Lambda} = \frac{\omega R}{v} \quad (33)$$

and Λ is the phonon wavelength. The proposed cross section has the correct limiting behaviors and involves a smooth transition between them.

It is interesting to note that the scattering cross section is not directly dependent on temperature. However, since the phonon frequency that is dominant in energy depends on the temperature, the cross section φ will be temperature dependent at low frequencies or low temperatures.

Inelastic Scattering (N and U Processes). Inelastic scattering between phonons occurs due to the anharmonic nature of interatomic potential energy. Consider a lattice wave propagating in a crystal. As it passes by atoms in a lattice, it moves them from their equilibrium positions, creating a local strain. When another lattice wave is incident on this strain field, it encounters a change in medium properties such as the speed of sound and is, hence, scattered. Such scattering processes

are often called intrinsic processes since they can occur even in a perfect crystal. Intrinsic scattering involves three or more phonons. Those involving four phonons or more are important only at temperatures much higher than θ_D (Joshi et al., 1970) and will not be considered in this study. A detailed description of inelastic scattering can be found from Ziman (1960).

There are two types of three-phonon inelastic scattering: the N process and the U process. Both these processes conserve phonon energy before and after the scattering. The N process conserves phonon momentum and therefore does not pose any resistance to heat flow (Ziman, 1960). If only N processes were to exist, a solid would have infinite conductivity. Therefore, one would be tempted to neglect them in finding an effective relaxation time. Although posing no direct resistance by themselves, N processes do play a role in resistance to heat flow. Since the frequency of incident phonons is changed in inelastic scattering, N processes are responsible for distributing the phonon energy over different frequencies. Since other scattering processes are frequency dependent, they feel the effect of phonons scattered by N processes. Therefore, N processes indirectly influence the resistance to heat flow. In contrast, U processes do not conserve momentum and therefore directly resist phonon transport. Although N processes have been shown to influence thermal conductivity (Callaway, 1959), neglecting N processes may not be totally inaccurate in some temperature ranges. At very low temperatures boundary scattering dominates. As the temperature increases, impurity scattering becomes important and a further increase in temperature makes U processes dominant and the N processes negligible. It is in the intermediate range between boundary scattering and U process that N processes play a role (Ziman, 1960). Although the EPRT allows the inclusion for N processes in the form of an effective relaxation time, they are neglected in this study for two reasons: (i) The calculations are carried in the regime where N processes are insignificant, and (ii) it is necessary to keep the calculations simple.

Several expressions for the relaxation times for U processes are used in the literature and the correct one is still a matter of discussion (Berman, 1976). An approximation commonly used for U process relaxation time is (Klemens, 1958)

$$\tau_U = A \frac{T}{\theta_D \omega} \exp\left(\frac{\theta_D}{\gamma T}\right) \quad (34)$$

where A is a nondimensional constant, which depends on the atomic mass, the lattice spacing, and the Gruineisen constant (Ashcroft and Mermin, 1976), and γ is a parameter representing the effect of crystal structure. This relation predicts the thermal conductivity to vary as $\lambda \sim T^3 \exp(\theta_D/\gamma T)$, which has been observed experimentally for several materials (Ziman, 1960). It provides a smooth transition from the T^3 behavior of the thermal conductivity at low temperatures to an exponential drop at higher temperatures.

Effective Relaxation Times and Contribution of Scattering Mechanisms. For solving the EPRT in Eq. (22), the effective relaxation time for phonon scattering is required. An assumption often used is to apply the Matthiessen rule, which adds up the scattering rates, or the reciprocal of the relaxation times for different scattering processes as (Ziman, 1960)

$$\frac{1}{\tau} = \frac{1}{\tau_i} + \frac{1}{\tau_U} \quad (35)$$

where τ is the effective relaxation time.³ Physically, this means adding up the resistances posed by each scattering process. The assumption is valid under the condition that the scattering processes do not interact with each other, which is clearly not

³If the denominator of Eq. (35) is multiplied by the speed of sound, one gets the Matthiessen rule for the mean free path, $1/l = 1/l_i + 1/l_U$.

Table 2 Physical properties of type IIa diamond

Lattice Constant, a	3.57 Å ^a
Specific Heat, C	517.05 [J/kg-K] ^b at 300 K 8.36 [J/kg-K] ^b at 77 K
Mass Density, ρ	3510 [kg/m ³] ^b
Debye Temperature, θ_D	1860 K ^a
Speed of Sound, v	12288 [m/s] ^c
Constant A in equation (34)	163.94 ^c
Stefan-Boltzmann constant, σ	50.47 [W/m ² -K ⁴] ^c

^aAshcroft and Mermin (1976); ^bTouloukian and Buyco (1970); ^csee explanation in text.

true for inelastic scattering. However, the error involved in applying the Matthiessen rule is usually quite small (Ziman, 1960) and therefore will be applied here.

The contribution of each scattering mechanism to the effective relaxation time can be found by isolating the relaxation times or mean free paths of each mechanism. Since the samples used by Anthony et al. (1990) were in the millimeter range, it can be safely assumed that the phonon transport was diffusive in their experiment. Therefore, using the kinetic theory expression for thermal conductivity of Eq. (2), $\lambda = Cv/3$, and using the specific heat and speed of sound from Table 2, the effective mean free path was calculated and listed in Table 1. It is evident that the mean free paths are less than a micrometer, thus justifying the assumption of diffusive transport in the experimental samples.

Based on the impurity concentration of ¹³C, the number density η per unit volume was calculated and also listed in Table 1. The wavelength of phonons dominant in phonon energy can be found by the relation $h\nu \sim \Lambda_{\text{dom}} k_B T$. For diamond at room temperature $\Lambda_{\text{dom}} = 2.16$ nm. Since the diameter of a ¹³C atom is assumed to be the lattice constant, the radius is $R = 1.785$ Å. This is used to find the size parameter $\chi = 0.51$. Therefore the value of the scattering cross section is $\varphi = 6.78 \times 10^{-21}$ m². Using this value and assuming α in Eq. (31) to be unity, the predicted impurity mean free paths $l_i = v\tau_i$ from Eq. (31) are determined and listed in Table 1. It is evident that since l_i is larger than the effective mean free path l , there must be another mechanism for resistance. Applying the Matthiessen rule for mean free paths, the mean free path for the U process, l_U , is determined and listed in Table 1. Note that all the values of l_U from the three experiments are within a maximum difference of only 2.6 percent, suggesting that Umklapp scattering is independent of impurity concentration. To calculate the constant A in Eq. (34), an average mean free path of $l_U = 0.46$ μm is chosen. From the thermal conductivity data of Berman et al. (1954) for diamond at different temperatures, the value of γ was found to be 1.58. Using $\omega = 2\pi\nu/\Lambda_{\text{dom}}$, $\gamma = 1.58$, $\tau_U = l_U/v$, $T = 300$ K, and $\theta_D = 1860$ K, the constant A is found to be 163.94.

Since the constants in the relaxation time expressions for impurity scattering and U processes are now known, the effective mean free path or relaxation time at other temperatures and impurity concentrations can be determined. For both impurity and U scattering, the frequency ω is replaced by $2\pi\nu/\Lambda_{\text{dom}}$ where Λ_{dom} is a function of temperature. Figure 5 shows the plot of the effective mean free path as a function of temperature for the three different impurity concentration used in the experiments of Anthony et al. (1990). Below 100 K, impurity scattering is dominant and the curves follow a power law of $L \sim T^{-4}$ where the exponent of 4 comes from Rayleigh scattering in Eq. (32). At temperatures higher than 100 K, U processes become dominant and therefore the exponential decay is evident. For higher concentrations it is clear that the mean free path decreases and the curves shift down. It is interesting to note that at liquid nitrogen temperatures of 77 K, the mean free path can be of the order of a millimeter and

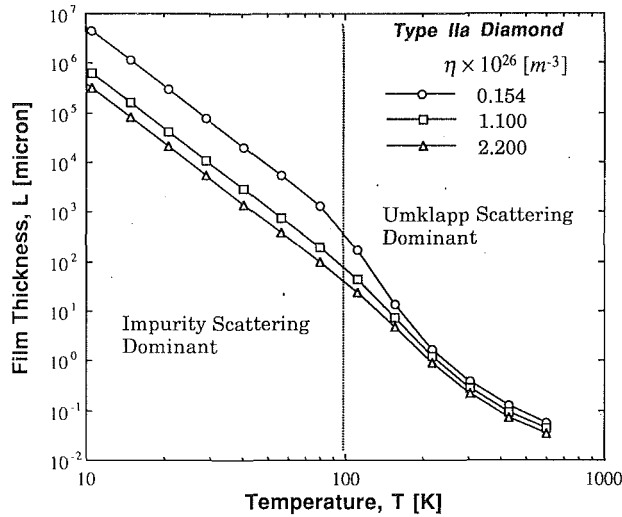


Fig. 5 Variation of phonon mean free path with temperature in type IIa diamond at different impurity concentrations. The predictions are based on room-temperature thermal conductivity measurements (Anthony et al., 1990).

therefore ballistic phonon transport can be observed in macroscopic samples.

4 Heat Transport Across Diamond Thin Films

In this section, the EPRT is solved to obtain the temperature distribution and heat flux across diamond thin films of the three different impurity concentrations listed in Table 1 and three different film thicknesses: (i) $L = 0.1 \mu\text{m}$, (ii) $L = 1.0 \mu\text{m}$, and (iii) $L = 10.0 \mu\text{m}$. To study the effect of temperature, the calculations are performed at two different temperatures: 77 K and 300 K. The room-temperature phonon mean free paths in diamond are listed in Table 1. The mean free paths at 77 K are obtained from Fig. 5 and are: $l = 2130 \mu\text{m}$, $314 \mu\text{m}$, and $158 \mu\text{m}$ for $\eta = 0.154$, 1.100 , and $2.200 \times 10^{26} \text{m}^{-3}$, respectively. The combination of three film thicknesses and six effective mean free paths at two different temperatures gives 18 values of the acoustic thickness, $\xi_L = L/l$, that range from 4.69×10^{-5} to 36.63 . This range is large enough to span the acoustically thin and thick regimes, respectively.

The EPRT was numerically solved by the same technique that was used to obtain the results in Fig. 4. The solution gives the intensity at any point and in the different directions of the discrete ordinates. The temperature is numerically obtained for the case of radiative equilibrium by the following expression:

$$\sigma T^4(\xi/\xi_L) = \frac{\pi}{2} \sum_{j=1}^{2N} I_j(\xi/\xi_L) w_j \quad (36)$$

The nondimensional temperature profiles in the diamond films are shown in Fig. 6. It is evident that phonon transport in the $0.1 \mu\text{m}$ film is purely ballistic at 77 K. In contrast, phonon transport in the $10 \mu\text{m}$ film is purely diffusive at 300 K. The other cases of different film thickness and temperatures fall between these two limiting cases. It is interesting to note that the change of impurity concentration by an order of magnitude does not have much effect on the temperature distribution for the film sizes and temperatures considered. When the transport is purely ballistic or purely diffusive, there is no effect of impurity concentration.

The heat flux is obtained by the following expression:

$$q(\xi/\xi_L) = 2\pi \sum_{j=1}^{2N} \mu_j I_j(\xi/\xi_L) w_j \quad (37)$$

Since the problem is solved for the case of radiative equilib-

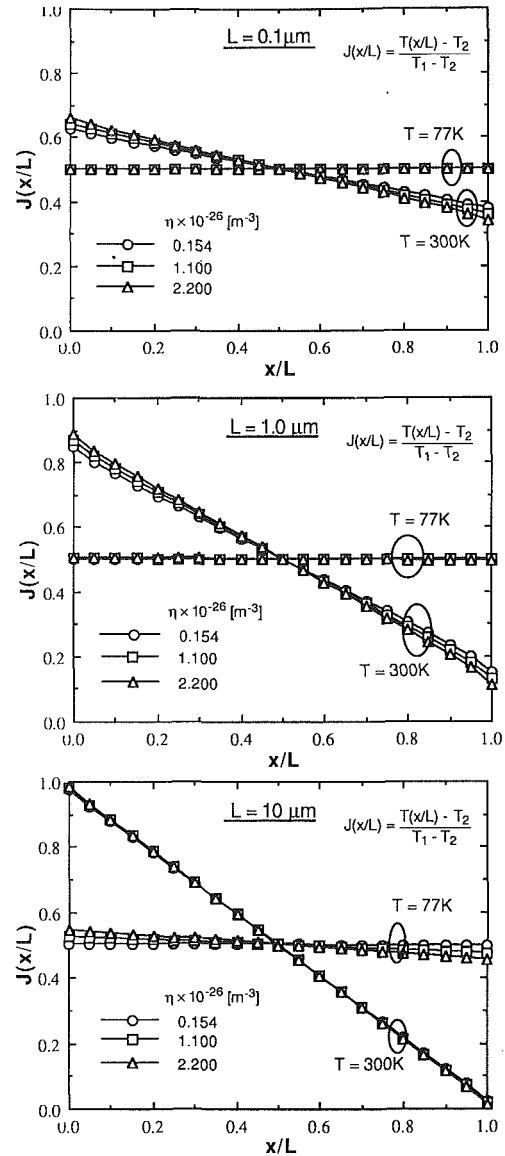


Fig. 6 The temperature profiles in diamond thin films of thickness (i) $L = 0.1 \mu\text{m}$, (ii) $L = 1.0 \mu\text{m}$, and (iii) $L = 10 \mu\text{m}$. The predictions are obtained at 77 K and 300 K and at the impurity concentrations used in the experiments of Anthony et al. (1990).

rium, it was found that the heat flux was constant along the film. This was a check to verify whether the solution was correct. The predictions for the heat flux are presented in nondimensional form as a function of acoustic thickness in Fig. 7. The solid line represents the nondimensional heat flux predicted by the modified diffusion approximation used in photon radiative heat transfer (Ozisik, 1973; Siegel and Howell, 1982). The excellent agreement suggests that the simple expression can be used to predict the heat flux.

The results for temperature profiles in Fig. 6 clearly suggest that unless the acoustic thickness is very large, phonon transport is not diffusive and temperature jumps do occur at the boundaries. Therefore, the Fourier law cannot be applied for such cases. However, it is common to find in the literature that even for very low temperatures where phonons transport ballistically, the value of thermal conductivity is quoted. It is commonly assumed that in this regime where boundary scattering is dominant, the mean free path is equal to the film thickness, that is $l = L$. The question that must now be addressed is how much error does one make when the thermal

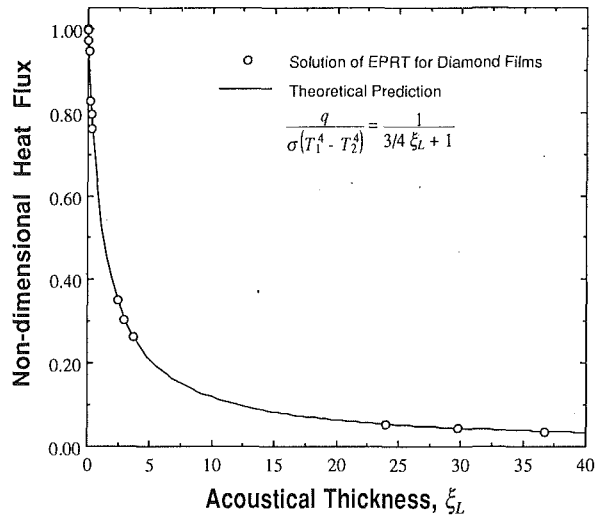


Fig. 7 Variation of the nondimensional heat flux as a function of the acoustical thickness. The comparison is made between the results obtained by solving the EPRT and those from the modified diffusion approximation.

conductivity in the boundary scattering regime is assumed to be $\lambda = Cv/3$. To quantitatively study this, a temperature difference $\Delta T = 0.1$ K was assumed to exist across a film. The heat flux, q_E , predicted by EPRT is

$$q_E = \frac{4\sigma T^3 \Delta T}{3 \left(\frac{L}{l} \right) + 1} \quad (38)$$

where the Stefan-Boltzmann constant σ for phonons was calculated as (Swartz and Pohl, 1989)

$$\sigma = \frac{\pi^2 k_B^4}{40 \hbar^3 v^2} \quad (39)$$

Using the speed of sound for diamond from Table 2, the value is found to be $\sigma = 50.47$ W/m²·K⁴. The expression for specific heat in terms of the physical constants is

$$C = \frac{4\pi^2 k_B^4 T^3}{10 \hbar^3 v^3} = \frac{16\sigma T^3}{v} \quad (40)$$

In conjunction with the mass density and the two values of C at 77 K and 300 K in Table 2, this expression was actually used to find the speed of sound to be $v = 12288$ m/s. This is comparable to the speed of sound of 13,500 m/s obtained by McSkimmin and Andreatch (1972).

The heat flux, q_F , predicted by the Fourier law is obtained by the expression

$$q_F = \frac{1}{3} Cv l \frac{\Delta T}{L} = \frac{16}{3} \sigma T^3 l \frac{\Delta T}{L} \quad (41)$$

Consider the limiting cases first. In the acoustically thick case, where $l \ll L$, Eq. (38) reduces to the same expression as that of the Fourier law in Eq. (41) thus resulting in no error. In the acoustically thin case the mean free path calculated from the Umklapp and impurity scattering is much larger than the film thickness. In this boundary scattering regime, the thermal conductivity is normally obtained by assuming $l = L$. In this case Eq. (41) reduces to $q_F = 16/3 \sigma T^3 \Delta T$ whereas the solution for the EPRT predicts $q_E = 4\sigma T^3 \Delta T$. Thus the Fourier law overpredicts by 33 percent. When $\xi_L = 1$, $q_E = 16/7 \sigma T^3 \Delta T$ whereas $q_F = 4\sigma T^3 \Delta T$. This gives a percentage error of 133 percent. The percentage errors between the prediction of the Fourier law and the EPRT for other values of acoustic thickness are shown in Fig. 8.

The Fourier law is overpredicted by 33 percent in the acoustically thin or ballistic regime because in determining the ther-

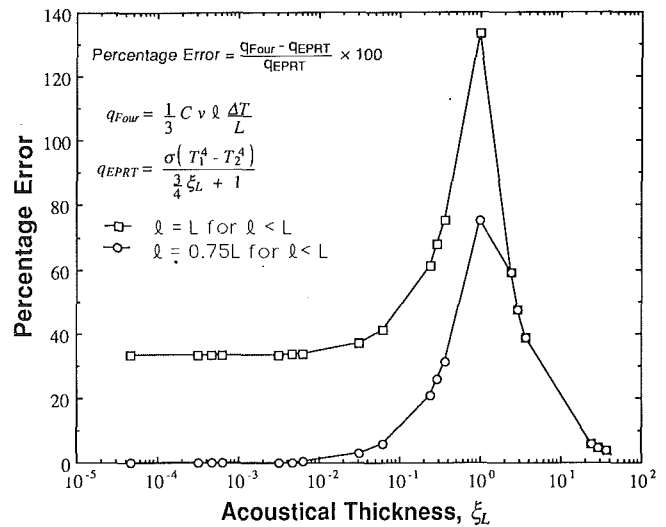


Fig. 8 Percentage error between the heat flux prediction by the Fourier law and by the EPRT.

mal conductivity, the mean free path is chosen to be equal to the film thickness, $l = L$. If the mean free path is chosen as $l = 3/4L$, this constant error can be eliminated in this regime, as shown in Fig. 8. However, a maximum error of about 75 percent is still encountered in the region $\xi_L = 1$. For $\xi_L > 1$, the error in both techniques coincides and decreases as ξ_L is increased. Although $\xi_L = 10$ can be considered to be acoustically thick, the error in the heat flux is still about 10 percent.

Although the heat flux in all regimes of acoustic thickness follows Eq. (38), the Fourier law and the concept of thermal conductivity are traditionally used more often. Therefore, it would be more convenient to recast Eq. (38) in the form of the Fourier law and develop an expression for an effective thermal conductivity that would be valid both in the ballistic and the diffusive regimes. Equation (38) can be rewritten as

$$q = \left[\frac{4\sigma T^3 L}{3 \left(\frac{L}{l} \right) + 1} \right] \frac{\Delta T}{L} \quad (42)$$

where the effective thermal conductivity is

$$\lambda = \frac{4\sigma T^3 L}{3 \left(\frac{L}{l} \right) + 1} = \frac{1}{3} Cv \left[\frac{l}{1 + \frac{4}{3} \left(\frac{l}{L} \right)} \right] \quad (43)$$

Therefore, the expression for thermal conductivity developed from kinetic theory (see Eq. (2)) can be used for all regimes provided the effective mean free path, expressed as

$$l_{\text{eff}} = \frac{l}{1 + \frac{4}{3} \left(\frac{l}{L} \right)} \quad (44)$$

is used.

5 Summary and Conclusions

This study shows that there exists a regime of temperature and thickness of dielectric thin films where the Fourier law cannot be applied to analyze heat conduction. In this regime, the study concludes that heat conduction by lattice vibrations or phonons behaves like radiative transfer. Based on the semiclassical Boltzmann transport theory, an equation of phonon radiative transfer (EPRT) is developed. The conclusions made about EPRT are as follows:

- 1 For steady-state heat conduction in the acoustically thick limit or the macroscale regime, where the film thickness is much larger than the phonon mean free path in a bulk material, the EPRT reduces to the Fourier law.
- 2 In the acoustically thin limit of heat conduction across a thin film, where the probability of phonon scattering within the film is very low, the EPRT yields the familiar blackbody radiation law $q = \sigma(T_1^4 - T_2^4)$ at temperatures much lower than the Debye temperature of the material.
- 3 For transient heat conduction, the EPRT behaves like a wave equation, suggesting that a heat pulse is transported as a wave, which gets attenuated within the medium by phonon scattering.
- 4 The hyperbolic heat equation can be derived from the transient EPRT only in the acoustically thick limit.

The EPRT was then used to study the steady-state heat transport in diamond thin films. Using recently published experimental data on room-temperature thermal conductivity of diamond, the contributions of impurity scattering and Umklapp scattering to the effective mean free path are determined. Using these data, the temperature field is obtained in diamond thin films of different thicknesses and at 77 K and 300 K. The results for heat flux are in excellent agreement with the simple expression of the modified diffusion approximation that is used in radiative transfer. It is demonstrated that if the thermal conductivity is predicted by the commonly used kinetic theory expression, the Fourier law overpredicts the heat flux by about 133 percent when the acoustic thickness is of order unity. This study presents a new method of predicting an effective thermal conductivity, which would allow the Fourier law to be used in both the ballistic and the diffusive transport regimes.

Acknowledgments

I would like to thank Aruna Joshi and Markus Flik for their critical comments and discussions. The support of National Science Foundation through Grant No. CTS-9114306 is greatly appreciated.

References

- Anthony, T. R., Banholzer, W. F., Fleischer, J. F., Wei, L., Kuo, P. K., Thomas, R. L., and Pryor, R. W., 1990, "Thermal Diffusivity of Isotopically Enriched ^{12}C Diamond," *Physical Review B*, Vol. 42, pp. 1104-1111.
- Ashcroft, N. W., and Mermin, N. D., 1976, *Solid State Physics*, W. B. Saunders, Philadelphia, PA.
- Bai, C., and Lavine, A. S., 1991, "Hyperbolic Heat Conduction in a Superconducting Film," presented at the ASME/JSME Thermal Engineering Joint Conference, Reno, NV, Mar. 17-22.
- Bejan, A., 1988, *Advanced Engineering Thermodynamics*, Wiley, New York, pp. 69-72.
- Berman, R., Foster, E. L., and Ziman, J. M., 1954, "The Thermal Conductivity of Dielectric Crystals: Effect of Isotopes," *Proceedings of the Royal Society of London*, Vol. A 237, pp. 344-354.
- Berman, R., 1976, *Thermal Conduction in Solids*, Oxford University Press, Oxford, United Kingdom.
- Callaway, J., 1959, "Model of Lattice Thermal Conductivity at Low Temperatures," *Physical Review*, Vol. 113, pp. 1046-1051.
- Casimir, H. B. G., 1938, "Note on the Conduction of Heat in Crystals," *Physica*, Vol. 5, pp. 495-500.
- Flik, M. I., and Tien, C. L., 1990, "Size Effect on the Thermal Conductivity of High- T_c Thin-Film Superconductors," *ASME JOURNAL OF HEAT TRANSFER*, Vol. 112, pp. 872-881.
- Flik, M. I., Choi, B. I., and Goodson, K. E., 1991, "Heat Transfer Regimes in Microstructures," presented at the ASME Winter Annual Meeting, Atlanta, GA, Dec. 1-6.
- Guyer, R. L., and Koshland, D. E., 1990, "Diamond: Glittering Prize for Materials Science," *Science*, Vol. 250, pp. 1640-1643.
- Herring, C., 1954, "Role of Low-Energy Phonons in Thermal Conduction," *Physical Review*, Vol. 95, pp. 954-965.
- Jacoboni, C., and Reggiani, L., 1983, "The Monte Carlo Method for the Solution of Charge Transport in Semiconductors With Applications to Covalent Materials," *Reviews of Modern Physics*, Vol. 55, pp. 645-705.
- Jeans, J. H., 1954, *The Dynamical Theory of Gases*, 4th ed., Dover, p. 257.
- Joseph, D. D., and Preziosi, L., 1989, "Heat Waves," *Reviews of Modern Physics*, Vol. 61, pp. 41-73.
- Joshi, A. A., and Majumdar, A., 1993, "Transient Ballistic and Diffusive Heat Transport by Phonons," submitted to *Journal of Applied Physics*.
- Joshi, Y. P., Tiwari, M. D., and Verma, G. S., 1970, "Role of Four-Phonon Process in the Lattice Thermal Conductivity of Silicon from 300 K to 1300 K," *Physical Review B*, Vol. 1, pp. 642-646.
- Kittel, C., 1986, *Introduction to Solid State Physics*, 6th ed., Wiley, New York.
- Klemens, P. G., 1958, "Thermal Conductivity and Lattice Vibrational Modes," in: *Solid State Physics*, Vol. 7, pp. 1-98, F. Seitz and D. Turnbull, eds., Academic Press, New York.
- Klitsner, T., VanCleve, J. E., Fischer, H. E., and Pohl, R. O., 1988, "Phonon Radiative Heat Transfer and Surface Scattering," *Physical Review B*, Vol. 38, pp. 7576-7594.
- Kumar, S., Majumdar, A., and Tien, C. L., 1990, "The Differential-Discrete-Ordinate Method for Solving the General Equation of Radiative Transfer," *ASME JOURNAL OF HEAT TRANSFER*, Vol. 112, pp. 424-429.
- Mayer, J. W., and Lau, S. S., 1990, *Electrical Materials Science*, Macmillan Publishing Co., New York.
- Majumdar, A., 1991, "Effect of Interfacial Roughness on Phonon Radiative Heat Conduction," *ASME JOURNAL OF HEAT TRANSFER*, Vol. 113, pp. 797-805.
- McSkimmin, H. J., and Andreatch, P., Jr., 1972, "Elastic Moduli of Diamond as a Function of Pressure and Temperature," *Journal of Applied Physics*, Vol. 43, pp. 2944-2948.
- Ozisik, M. N., 1973, *Radiative Transfer and Interactions With Conduction and Convection*, Wiley, New York.
- Ravi, K., 1991, "Technological Applications of CVD Diamond," *Synthetic Diamond: Emerging CVD Science and Technology*, K. E. Spear and J. P. Dismukes, eds., Wiley, New York.
- Rayleigh, Lord, 1896, *Theory of Sound*, Macmillan and Co., London.
- Siegel, R., and Howell, J. R., 1982, *Thermal Radiation Heat Transfer*, 2nd ed., Hemisphere Publishing Corp., New York.
- Sondheimer, E. H., 1952, "The Mean Free Path of Electrons in Metals," *Advances in Physics*, Vol. 1, pp. 1-42.
- Swartz, E. T., and Pohl, R. O., 1989, "Thermal Boundary Resistance," *Reviews of Modern Physics*, Vol. 61, pp. 605-668.
- Tavernier, J., 1962, "Sur l'equation de conduction de la chaleur," *Comptes Rendus Acad. Sci.*, Vol. 254, pp. 69-71.
- Touloukian, Y. S., and Buyco, E. H., 1970, "Specific Heats: Nonmetallic Solids," *Thermophysical Properties of Matter*, Vol. 5, IFI/Plenum, New York.
- Vincenti, W. G., and Kruger, C. H., 1977, *Introduction to Physical Gas Dynamics*, Robert Krieger Publ., New York.
- Viskanta, R., 1966, "Radiation Transfer and Interaction of Convection With Radiation Heat Transfer," in: *Advances in Heat Transfer*, Vol. 3, pp. 175-251, T. F. Irvine, Jr., and J. P. Hartnett, eds., Academic Press, New York.
- Walton, D., 1967, "Scattering of Phonons by a Square-Well Potential and the Effect of Colloids on the Thermal Conductivity. I. Experimental," *Physical Review*, Vol. 157, pp. 720-724.
- Walton, D., and Lee, E. J., 1967, "Scattering of Phonons by a Square-Well Potential and the Effect of Colloids on the Thermal Conductivity. II. Theoretical," *Physical Review*, Vol. 157, pp. 724-729.
- Worlock, J. M., 1966, "Thermal Conductivity in Sodium Chloride Crystals Containing Silver Chloride," *Physical Review*, Vol. 147, pp. 636-643.
- Ziman, J. M., 1960, *Electrons and Phonons*, Oxford University Press, London, United Kingdom.

Electron and Phonon Thermal Conduction in Epitaxial High- T_c Superconducting Films

K. E. Goodson

M. I. Flik

Department of Mechanical Engineering,
Massachusetts Institute of Technology,
Cambridge, MA 02139

Electrons and phonons are the carriers of heat in the a - b plane of the high- T_c superconductor $YBa_2Cu_3O_7$. In the absence of boundary scattering, the a - b plane thermal conductivity and the mean free path of each carrier type are calculated as functions of temperature using kinetic theory, the two-fluid model of the superconducting state, and experimental data for the thermal conductivity and electrical resistivity of a single crystal. The reduction by boundary scattering of the effective a - b plane thermal conductivity along an epitaxial $YBa_2Cu_3O_7$ film is predicted as a function of temperature and film thickness. The size effect on the phonon conductivity dominates over the size effect on the electron conductivity. The predicted electron mean free path is limited by scattering on defects and is in very good agreement with experimental data from infrared spectroscopy.

Introduction

In epitaxial high- T_c superconducting films with the crystallographic c axis normal to the plane of the film, conduction along the film occurs in the a - b plane. Electrons are responsible for 30–50 percent of thermal conduction in the a - b plane of single-crystal $YBa_2Cu_3O_7$ near its critical temperature, $T_c = 92$ K (Cohn et al., 1992b; Hagen et al., 1989), and 30–40 percent of thermal conduction in the a - b plane of single crystal $Bi_2Sr_2Ca_1Cu_2O_8$ near $T_c = 89$ K (Crommie and Zettil, 1990). Lattice vibrations, the energy quanta of which are phonons, account for the remaining fraction of the thermal conduction. Boundary scattering reduces the effective thermal conductivity along a film when the mean free path of a carrier is of the order of or larger than the film thickness. Determination of the effective conductivity along epitaxial high- T_c superconducting films must consider the mean free paths and contributions to the total conductivity of electrons and phonons in the absence of boundary scattering. At present, none of these quantities is known for temperatures lower than the critical temperature.

Epitaxial superconducting films possess great promise for application in electronic circuits (Van Duzer, 1988). The performance of superconducting devices, such as Josephson junctions, in hybrid electronic circuits is affected by temperature fields, the prediction of which requires the thermal conductivity (Flik and Hijikata, 1990; Lavine and Bai, 1990). The liquid-nitrogen bolometer is an infrared radiation detector that exploits the drastic change of electrical resistivity with temperature of a high- T_c superconducting film at the midpoint of its transition. The film and substrate thermal conductivities are required for the determination of the thermal behavior of this device (Flik et al., 1990; Kumar and Joshi, 1990). The thermal conductivity of superconducting films is required for the analysis of the thermal stability and the voltage response of thin-film microbridges irradiated by an electron-beam (Flik and Tien, 1990a, 1990b; Flik and Goodson, 1992).

Uher (1990) reviewed research on thermal conduction in high- T_c superconductors. Single crystals of high- T_c superconductors are assumed to possess equal thermal conductivities in the a and b directions, and a different conductivity in the

c direction. This assumption is a good approximation for $YBa_2Cu_3O_7$ because of its orthorhombic, nearly tetragonal crystal structure. As depicted in Fig. 1, the electron and phonon contributions to the conductivity are limited by scattering on defects in the lattice, such as point defects, stacking faults, and grain boundaries, as well as electron-phonon scattering. In thin films, the boundaries of the film can increase the rate of scattering.

Flik and Tien (1990c) determined the thermal conductivity as a function of temperature and film thickness of polycrystalline $YBa_2Cu_3O_7$ films, in which phonons dominate the thermal conduction. Their analysis did not consider electron transport and is not valid for the a - b plane of epitaxial films. Calculation of the size effect for this case requires knowledge of the contributions of electrons and phonons to the a - b plane thermal conductivity in the superconducting state. Geilikman and Kresin (1974) obtained theories for thermal conduction in superconductors that are in agreement with experimental data for low-temperature superconductors for the cases of electron conduction limited by defect scattering and phonon conduction limited by electron scattering. Tewordt and Wölkhausen (1989, 1990) modified the theory of Bardeen et al. (1959) for the phonon conductivity to account for the scattering of phonons on the defects in high- T_c superconductors. Measurements of the a - b plane thermal conductivity of single-crystal $YBa_2Cu_3O_7$ were reported by Hagen et al. (1989), Cohn et al. (1992a, 1992b), who calculated the phonon conductivity in the superconducting state using the theory of Tewordt and Wölkhausen (1990), and Peacor et al. (1991), who measured the influence of magnetic field strength on the thermal conductivity.

This work develops a new technique for calculating the a - b plane thermal conductivity of epitaxial high- T_c supercon-

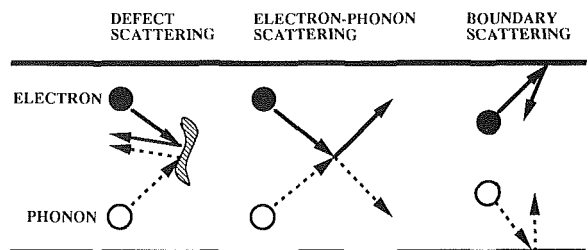


Fig. 1 Scattering mechanisms that limit thermal conduction in high- T_c superconducting films

Contributed by the Heat Transfer Division for publication in the JOURNAL OF HEAT TRANSFER. Manuscript received by the Heat Transfer Division June 1991; revision received April 1992. Keywords: Conduction, Cryogenics, Thermophysical Properties. Associate Technical Editor: L. S. Fletcher.

ducting films from measurements performed on a crystal in which boundary scattering is negligible. The technique is illustrated in the flowchart in Fig. 2. In the absence of boundary scattering, the mean free path of normal-state electrons below the critical temperature is calculated from normal-state electrical resistivity data. The electron thermal conductivity in the absence of boundary scattering in the superconducting state is calculated from the electron mean free path using kinetic theory and the two-fluid model for electrons in superconductors (Gorter and Casimir, 1934; Shoenberg, 1952). The phonon conductivity is obtained by subtracting the electron contribution from measured data in a large crystal, and the phonon mean free path is determined using kinetic theory. For a thin film, the effect of boundary scattering is analyzed separately for the electron and phonon contributions using the approximate relations of Flik and Tien (1990c). The technique is applied to epitaxial $\text{YBa}_2\text{Cu}_3\text{O}_7$ films using the a - b plane electrical resistivity and thermal conductivity data of Cohn et al. (1992b) for a single crystal. The effective thermal conductivity calculated in this work is not a material parameter. It is a geometry-dependent constant, the multiplication of which with the temperature gradient in the a - b plane of the film yields the thermal energy flux in the direction of this gradient.

Electron Thermal Conductivity

This section determines the electron mean free path and thermal conductivity in the absence of boundary scattering. The effect of boundary scattering is considered in the section entitled "Size Effect."

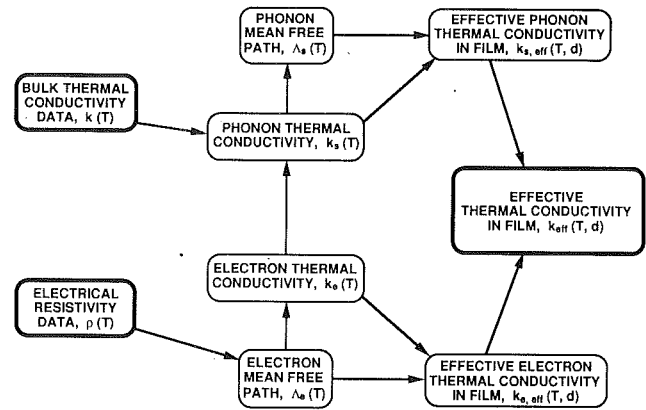


Fig. 2 Flowchart of the technique for determining the effective thermal conductivity along epitaxial high- T_c superconducting films

The mean free path of a carrier Λ is the average distance it travels between consecutive collisions. Matthiessen's rule (Ziman, 1960) relates the electron mean free path Λ_e to the electron mean free path limited by scattering on phonons, $\Lambda_{e,s}$, defects, $\Lambda_{e,d}$, electrons $\Lambda_{e,e}$, and boundaries, $\Lambda_{e,b}$,

$$\frac{1}{\Lambda_e} = \frac{1}{\Lambda_{e,s}} + \frac{1}{\Lambda_{e,d}} + \frac{1}{\Lambda_{e,e}} + \frac{1}{\Lambda_{e,b}} \quad (1)$$

The mean free paths for individual scattering mechanisms are unobservable. They describe the hypothetical situation where

Nomenclature

A = scattering cross section, m^2	S_n = normal metal electron entropy per unit volume, $\text{J m}^{-3} \text{K}^{-1}$	τ = scattering time, s
C = specific heat per unit volume, $\text{J m}^{-3} \text{K}^{-1}$	T = temperature, K	Φ = carrier flux through reference plane from one side, $\text{m}^{-2} \text{s}^{-1}$
d = film thickness, m	T_c = superconductor critical temperature, K	χ = function, defined in Eq. (8)
E_F = Fermi energy, J	T_R = reference temperature, Eq. (7), K	$d\Omega$ = differential solid angle
e = electron charge = $-1.602 \times 10^{-19} \text{ C}$	T_0 = temperature at $y = 0$, K	
h_p = Planck's constant = $6.626 \times 10^{-34} \text{ J s}$	v = velocity, m s^{-1}	
J_E = energy flux, W m^{-2}	X = fraction of free electrons in the normal state	
$J_p(q)$ = Debye integral, defined by Eq. (6)	x = coordinate normal to flow of thermal energy, m	
J_S = entropy flux, $\text{W m}^{-2} \text{K}^{-1}$	y = coordinate parallel to flow of thermal energy, m	
k = thermal conductivity, $\text{W m}^{-1} \text{K}^{-1}$	Z = parameter, Eq. (24)	
k_B = Boltzmann constant = $1.381 \times 10^{-23} \text{ J K}^{-1}$	z = coordinate normal to flow of thermal energy, m	
L = exchange length, m	γ = Sommerfeld parameter, $\text{J m}^{-3} \text{K}^{-2}$	
L_0 = Lorenz number = $2.45 \times 10^{-8} \text{ W } \Omega \text{ K}^{-2}$	δ = reduced film thickness = d/Λ	
m^* = effective electron mass, kg	ζ = function, defined in Eq. (5)	
m = electron rest mass = $9.110 \times 10^{-31} \text{ kg}$	η = coefficient, Eqs. (17) and (18)	
N_a = number density of atoms, m^{-3}	θ = Debye temperature, K	
n = free-electron number density, m^{-3}	Λ = mean free path for thermal conduction, m	
p = argument, Eqs. (6) and (12)	ξ = superconductor coherence length, m	
q, q' = arguments, Eq. (6)	ρ = electrical resistivity, $\Omega \text{ m}$	
r = distance from electron, m	ρ_0 = constant, Eqs. (5) and (8), $\Omega \text{ m}$	
r_B = Bohr radius = $5.292 \times 10^{-11} \text{ m}$		
r_s = material parameter, m		
S = electron entropy per unit volume, $\text{J m}^{-3} \text{K}^{-1}$		

Superscripts

- + = property of carriers traveling in positive y direction
- = property of carriers traveling in negative y direction

Subscripts

- a - b = property for transport in crystallographic a - b plane
- b = boundary
- c = property for transport parallel to crystallographic c axis
- d = defect
- e = electron
- e, b = electron property limited by boundary scattering
- e, d = electron property limited by defect scattering
- e, e = electron property limited by electron scattering
- e, s = electron property limited by phonon scattering
- eff = effective conductivity reduced by boundary scattering
- l = longitudinal
- s = phonon
- t = transverse

all other scattering mechanisms are inactive. In this section, thermal conduction is examined in the absence of boundary scattering, and the last term on the right is zero. Later in this section, it will be shown that the third term on the right is negligible compared to the second, leaving only the defect and phonon-limited terms.

The mean free path of electrons limited by defect scattering $\Lambda_{e,d}$ is independent of temperature. In a normal metal, this mean free path is related to the residual electrical resistivity ρ_d , the electrical resistivity in the limit of zero temperature, by (Ziman, 1960)

$$\Lambda_{e,d} = \frac{v_e m^*}{\rho_d n e^2}, \quad (2)$$

where v_e is the electron velocity, m^* is the effective electron mass, n is the free-electron number density per unit volume, and e is the electron charge.

Fiory et al. (1990) calculated m^* and n for transport in the a - b plane of $\text{YBa}_2\text{Cu}_3\text{O}_7$ from measurements of the effect of electrostatic charge density modulation on the inductance of an epitaxial $\text{YBa}_2\text{Cu}_3\text{O}_7$ film. This technique provides the most accurate measurements of these properties presently available and was applied to films with thicknesses from 300 to 1000 Å. These film thicknesses are much larger than the mean free path of electrons in $\text{YBa}_2\text{Cu}_3\text{O}_7$, which are calculated later in the present analysis. The data reported for the sample with the lowest normal-state electrical resistivity are employed in the present analysis, $m^* = 4.3 \times 10^{-30}$ kg and $n = 7.0 \times 10^{27}$ m⁻³.

A net flux of charge or energy through a plane is carried by electrons possessing energy very near the Fermi energy, E_F . In a Fermi free-electron gas, the Fermi energy is the chemical potential at zero temperature in the Fermi-Dirac energy distribution function (Kittel, 1986). The velocity of electrons possessing the Fermi energy is the Fermi velocity. The Fermi velocity is (Ziman, 1960)

$$v_e = \frac{\hbar_p (3\pi^2 n)^{1/3}}{2\pi m^*}, \quad (3)$$

where \hbar_p is Planck's constant. The Fermi velocity is $v_e = 1.5 \times 10^5$ m s⁻¹ for the a - b plane of $\text{YBa}_2\text{Cu}_3\text{O}_7$. The Fermi energy, $E_F = m^* v_e^2/2$, is 4.5×10^{-20} J.

The residual electrical resistivity in Eq. (2) cannot be measured directly in a superconductor because a superconductor is not electrically resistive below its critical temperature. The residual resistivity is deduced from the experimentally measured electrical resistivity at higher temperatures using Matthiessen's rule,

$$\rho = \rho_s + \rho_d, \quad (4)$$

where ρ_s is the electrical resistivity resulting from phonons. The electrical resistivity resulting from phonons is determined using the formula of Bloch (1930),

$$\rho_s = 4\rho_\theta \left(\frac{T}{\theta}\right)^5 J_5 \left(\frac{T}{\theta}\right) \equiv 4\rho_\theta \zeta \left(\frac{T}{\theta}\right), \quad (5)$$

where θ is the Debye temperature, ρ_θ is a constant that depends on the material, and ζ is a function defined here. The Debye temperature $\theta = 470$ K of $\text{YBa}_2\text{Cu}_3\text{O}_7$ is determined from experimental specific-heat data in the following section. The class of Debye integrals $J_p(q)$ is defined by

$$J_p(q) = \int_0^q \frac{(q')^p e^{q'}}{(e^{q'} - 1)^2} dq'. \quad (6)$$

Equation (5) was derived by neglecting electron-phonon umklapp processes and assuming that the distribution of phonons that scatter electrons is equal to the thermal equilibrium

distribution of phonons in the Debye model of lattice vibrations. Electron-phonon umklapp processes do not conserve the vectorial sum of the electron and phonon momenta. The Bloch formula is in excellent agreement with experimental data for normal metals. The normal-state a - b plane electrical resistivity of $\text{YBa}_2\text{Cu}_3\text{O}_7$ epitaxial films and single crystals varies almost linearly with temperature (Penney et al., 1988; Stormer et al., 1988), which is accommodated within a few percent by Eqs. (4) and (5). Equations (4) and (5) yield the residual resistivity from the total resistivity and its temperature derivative at a reference temperature T_R ,

$$\rho_d = \rho(T_R) - \left[\frac{\zeta \left(\frac{T}{\theta}\right)}{\frac{\partial}{\partial T} \left[\zeta \left(\frac{T}{\theta}\right) \right]} \right]_{T=T_R} \times \left[\frac{\partial \rho}{\partial T} \right]_{T=T_R}. \quad (7)$$

When evaluated with $\theta = 470$ K, the first quantity in brackets is equal to 44.0 K at $T_R = 110$ K, and 238.1 K at $T_R = 300$ K. Using the electrical resistivity measured by Cohn et al. (1992b) for specimen CR3, the residual electrical resistivity is $\rho_d = 0.57$ $\mu\Omega\text{m}$ and the electron mean free path limited by defect scattering given by Eq. (2) is $\Lambda_{e,d} = 63$ Å.

The electron mean free path limited by scattering on electrons, the inverse of the third term on the right of Eq. (1), is estimated by considering the decay of the electrostatic potential due to a single electron in an electron gas (Kittel, 1986). In a metal containing free electrons, the electrostatic potential due to a single electron is proportional to $\exp(-r/r_s)$, where r is the distance from the electron, $r_s = (r_B/4)^{1/2} n^{-1/6}$ is a length that depends on the material, and $r_B = 5.30 \times 10^{-11}$ m is the Bohr radius. The electron mean free path limited by scattering on electrons is approximately $\Lambda_{e,e} = (nA)^{-1}$, where A is the scattering cross section for electron-electron collisions. The scattering cross section is approximately the product of the area of a circle of radius r_s and the factor $(k_B T/E_F)^2$, $A \sim (k_B T/E_F)^2 \pi r_s^2$, where k_B is the Boltzmann constant. Combining these relations, $\Lambda_{e,e}$ is approximately $(E_F/k_B T)^2 (r_B n^{2/3})^{-1}$. At a temperature of 90 K, $\Lambda_{e,e}$ in the a - b plane of $\text{YBa}_2\text{Cu}_3\text{O}_7$ is almost three orders of magnitude larger than $\Lambda_{e,d}$ calculated from the electrical resistivity as described above, and contributes negligibly to the sum on the right of Eq. (1). Therefore, electron-electron collisions are neglected in the present analysis.

The electron thermal conductivity limited by phonon scattering in a normal metal is predicted by (Wilson, 1953)

$$\begin{aligned} \left(\frac{1}{k_{e,s}}\right)_{\text{normal}} &= \frac{4\rho_\theta}{L_0 T} \left[\left(\frac{T}{\theta}\right)^5 \left(J_5 \left(\frac{\theta}{T}\right) - \frac{1}{2\pi^2} J_7 \left(\frac{\theta}{T}\right) \right) \right] \\ &+ \frac{4\rho_\theta}{L_0 T} \left[\left(\frac{T}{\theta}\right)^3 \frac{3}{\pi^2} \left(\frac{n}{2N_a}\right)^{2/3} J_5 \left(\frac{\theta}{T}\right) \right] \\ &\equiv \frac{4\rho_\theta}{L_0 T} \chi \left(\frac{T}{\theta}, n, N_a\right), \quad (8) \end{aligned}$$

where L_0 is the Lorenz number, ρ_θ is the constant of Eq. (5), $N_a = 7.5 \times 10^{28}$ m⁻³ is the number density of atoms in $\text{YBa}_2\text{Cu}_3\text{O}_7$, and χ is a function defined here. Equation (8) is based on the same assumptions as Eq. (5). In the present analysis, Eq. (8) is approximated by omitting the first bracketed term. This simplification results in an error of less than 34 percent in the ratio $\Lambda_{e,s}(T)/\Lambda_{e,s}(T_c)$, which is employed in the present analysis. The error approaches 34 percent only at the lowest temperatures, where the importance of electron-phonon scattering is negligible compared to that of electron-defect scattering, limiting the effect of this error on the electron conductivity. Kinetic theory yields an expression for the electron thermal conductivity of a normal metal, $k_e = C_e v_e \Lambda_e/3$,

where C_e is the electron specific heat per unit volume (Ziman, 1960). The electron specific heat of a normal metal is $C_e = \gamma T$, where γ is the Sommerfeld parameter. Based on these relations and the simplified form of Eq. (8), the temperature dependence of the electron mean free path limited by phonon scattering is

$$\frac{\Lambda_{e,s}(T)}{\Lambda_{e,s}(T_c)} = \frac{T^3 J_5 \left(\frac{\theta}{T_c} \right)}{T^3 J_5 \left(\frac{\theta}{T} \right)} \quad (9)$$

The Sommerfeld parameter is given by (Ziman, 1960)

$$\gamma = \frac{\pi^2 k_B^2 n}{m^* v_e^2} \quad (10)$$

This expression yields $\gamma = 140 \text{ J m}^{-3} \text{ K}^{-2}$ for $\text{YBa}_2\text{Cu}_3\text{O}_7$.

In kinetic theory, transport of thermal energy by a single carrier type through a reference plane depends on the flux of carriers through that plane from one side, Φ , and their exchange length with respect to the plane, L (Rohsenow and Choi, 1961). The exchange length is the average distance carriers passing through the plane have traveled normal to the plane since their previous collisions. In an isotropic medium in equilibrium these parameters are $\Phi = Nv/4$, where N is the number density of carriers and v is their average velocity, and $L = 2\Lambda/3$. In the present analysis, electron conduction in the a - b plane of $\text{YBa}_2\text{Cu}_3\text{O}_7$ is determined based on these quantities.

The electrons in a superconductor are modeled as existing in two states, the superconducting state and the normal state. The electron entropy per unit volume, S , is assumed to be a function of the entropy per unit volume the electrons would possess if they were all normal, S_n , and the fraction of the electrons that are in the normal state, X . Although the parameters X and S_n are independent in nonequilibrium states, in stable equilibrium states they are related through temperature, $X = X(T)$ and $S_n = S_n(T)$. An electron passing through a plane is assumed to contribute to the quantity S_n as if it were part of an electron gas in equilibrium at the temperature of its previous collision. The superconductor coherence length ξ is the distance over which a disturbance in the number density of superconducting electrons propagates. In the a - b plane of $\text{YBa}_2\text{Cu}_3\text{O}_7$, the superconductor coherence length is approximately 1.2 nm (Salamon, 1989). It will be shown in the present analysis that the a - b plane electron mean free path varies between $\Lambda_e = 6.3 \text{ nm}$ at zero temperature and $\Lambda_e = 4.5 \text{ nm}$ at the critical temperature in this material. This indicates that the distance over which parameter X is free to vary, ξ , is somewhat smaller than the mean free path, Λ_e . To account for this, the electrons traveling in either direction through a reference plane are assumed to exhibit a parameter X characteristic of the local temperature at the reference plane.

To determine the electron thermal conductivity in the superconducting state, the flux of thermal energy through the x - z plane located by $y = 0$ is calculated based on a temperature field $T(y)$ with $T(y = 0) = T_0$. The entropy flux through the plane due to electrons traveling in the positive y direction is $J_S^+ = \Phi S^+ / n = v_e S^+ / 4$, where S^+ is the entropy per unit volume of these electrons as they reach the plane. Similarly, the entropy flux due to electrons traveling in the negative y direction is $J_S^- = v_e S^- / 4$, where S^- is the entropy per unit volume of those electrons as they reach the plane. The average of the y coordinates of the locations of the previous collisions of carriers traveling through the plane in the positive y location is $-L = -2\Lambda_e/3$. The average of the y coordinates of the locations of the previous collisions of carriers traveling through the plane in the negative y direction is $2\Lambda_e/3$.

The net flux of entropy resulting from electron transport is

$$J_S = \frac{v_e}{4} [S^+ - S^-] = \frac{v_e}{4} \left[S \left(S_n \left(T \left(y = -\frac{2\Lambda_e}{3} \right) \right) \right), X(T_0) \right] - S \left(S_n \left(T \left(y = \frac{2\Lambda_e}{3} \right) \right) \right), X(T_0) \right] \quad (11)$$

The temperature of the solid at points near the plane $y = 0$ is evaluated using Taylor's theorem for the function $T(y)$. Terms containing derivatives of second and higher order are neglected. Similarly, Taylor expansions yield the variation of $S = S(S_n, X)$ with respect to S_n and X about $S_n = S_n(T_0)$ and $X = X(T_0)$, and the variation of $S_n(T)$ and $X(T)$ with respect to T about $T = T_0$. Equation (11) becomes

$$J_S = \frac{v_e}{4} \left(-\frac{2}{3} \Lambda_e \right) \left(\frac{\partial S(S_n, X)}{\partial S_n} \right)_{y=0} \left(\frac{\partial S_n(T)}{\partial T} \right)_{y=0} \left(\frac{\partial T}{\partial y} \right)_{y=0} - \frac{v_e}{4} \left(\frac{2}{3} \Lambda_e \right) \left(\frac{\partial S(S_n, X)}{\partial S_n} \right)_{y=0} \left(\frac{\partial S_n(T)}{\partial T} \right)_{y=0} \left(\frac{\partial T}{\partial y} \right)_{y=0} = -\frac{v_e}{3} \Lambda_e \left(\frac{\partial S(S_n, X)}{\partial S_n} \right)_{y=0} \left(\frac{\partial S_n(T)}{\partial T} \right)_{y=0} \left(\frac{\partial T}{\partial y} \right)_{y=0} \quad (12)$$

The two-fluid model of electrons in the superconducting state (Gorter and Casimir, 1934; Shoenberg, 1952) provides the results $S(S_n, X) = S_n X^{1/2}$ and $X = (T/T_c)^4$ in equilibrium states at temperatures below T_c . In the present analysis the former relation is assumed to hold also in nonequilibrium states. Based on the Fermi free-electron model, the entropy of a normal electron gas is $S_n(T) = \gamma T$. The flux of thermal energy J_E is assumed to be the product of the temperature at the reference plane and the entropy flux,

$$J_E = T_0 J_S = -\frac{v_e}{3} \Lambda_e \gamma \frac{T_0^3}{T_c^2} \frac{\partial T}{\partial y} \quad (13)$$

The electron thermal conductivity at a temperature of $T = T_0$ is

$$k_e = \frac{J_E}{-\frac{\partial T}{\partial y}} = \frac{1}{3} \gamma \frac{T_0^3}{T_c^2} v_e \Lambda_e \quad (14)$$

Because the electron mean free path limited by defect scattering is independent of temperature, the normalized electron thermal conductivity limited by defect scattering is

$$\frac{k_{e,d}(T)}{k_{e,d}(T_c)} = \left(\frac{T}{T_c} \right)^3 \quad (15)$$

In Fig. 3, this simple result for the defect-limited electron thermal conductivity of superconductors is compared to that obtained by Geilikman and Kresin (1974) by solving the Boltz-

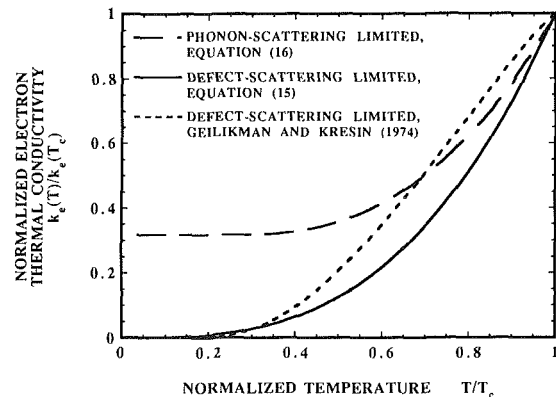


Fig. 3 Electron thermal conductivity in the superconducting state

mann equation. The two results agree within 35 percent. Equations (9) and (14) yield the electron thermal conductivity limited by phonon scattering,

$$\frac{k_{e,s}(T)}{k_{e,s}(T_c)} = \frac{J_5\left(\frac{\theta}{T_c}\right)}{J_5\left(\frac{\theta}{T}\right)} \quad (16)$$

This result is also shown in Fig. 3. The phonon-limited electron thermal conductivity drops more gradually with decreasing temperature than its defect-limited counterpart because the phonon number density decreases with decreasing temperature. The phonon-limited electron thermal conductivity is finite at low temperatures, due to the competing effects of a phonon number density and a normal-state electron number density, which both decrease with decreasing temperature. The low-temperature limit of $k_{e,s}$ cannot be observed experimentally because defect scattering limits the electron thermal conductivity.

The electron thermal conductivity above the critical temperature $k_e(T_c)$ is calculated from the a - b plane electrical resistivity ρ above the critical temperature using the Wiedemann-Franz law,

$$k_e = \eta \frac{L_0 T}{\rho}, \quad 0 < \eta \leq 1, \quad (17)$$

where η is predicted by (Wilson, 1953)

$$\eta = \frac{\frac{\rho_d}{4\rho\theta} + \zeta\left(\frac{T}{\theta}\right)}{\frac{\rho_d}{4\rho\theta} + \chi\left(\frac{T}{\theta}, n, N_a\right)} \quad (18)$$

The functions ζ and χ are defined in Eqs. (5) and (8), respectively. The coefficient η approaches unity at temperatures either large or small compared to the Debye temperature θ , and achieves a minimum value at a temperature less than θ . The larger the magnitude of the defect resistivity, indicated by the ratio $\rho_d/\rho\theta$, the closer is η to unity at temperatures comparable to θ . When scattering on defects dominates over scattering on phonons, Eq. (17) may be used with $\eta = 1$. The values of the parameters ρ_d , n , and N_a are given for $\text{YBa}_2\text{Cu}_3\text{O}_7$ in this section and $\theta = 470$ K is calculated in the following section. The parameter ρ_θ is determined to be $3.9 \mu\Omega\text{m}$ by fitting Eqs. (4) and (5) to the electrical resistivity data of Cohn et al. (1992b). The coefficient η is larger than 0.91 at all temperatures, and the deviation of η from unity is neglected in the present analysis. The electron mean free path Λ_e is calculated at temperatures greater than the critical temperature using Eq. (17) and the relations $k_e = C_e v_e \Lambda_e/3$ and $C_e = \gamma T$. At lower temperatures, it is determined using Eqs. (9), (2), and (1). The electron thermal conductivity in the superconducting state is calculated using Eq. (14).

Phonon Conductivity and Mean Free Path

The a - b plane thermal conductivity k is the sum of the electron component k_e and the phonon component k_s (Wilson, 1953)

$$k = k_e + k_s \quad (19)$$

The phonon thermal conductivity is obtained by subtracting the predicted electron contribution from the experimentally measured a - b plane thermal conductivity. The phonon mean free path Λ_s is calculated from the phonon thermal conductivity using the relation from kinetic theory for the phonon thermal conductivity (Ziman, 1960),

$$k_s = \frac{1}{3} C_s v_s \Lambda_s \quad (20)$$

where C_s is the specific heat per unit volume of phonons. The velocity v_s is the average speed of sound, which can be calculated from the measured velocity of longitudinal sound waves v_l and transverse sound waves v_t using $v_s^3 = 3/(2/v_l^3 + 1/v_t^3)$. It is likely that the average sound velocity is anisotropic in single-crystal $\text{YBa}_2\text{Cu}_3\text{O}_7$, i.e., that it has a value along the c axis different from that in the a - b plane. However, this anisotropy has not been experimentally demonstrated because the small size of available single crystals has prevented the accurate measurement of the absolute magnitude of the velocity of sound. Saint-Paul et al. (1988) showed that the transverse and longitudinal sound velocities vary with temperature by less than 5 percent of their absolute magnitude from 40 K to 160 K. The present analysis uses an average sound velocity, which is independent of temperature between 0 K and 120 K. The average sound velocity is obtained from measurements of the Debye temperature θ using (Kittel, 1986)

$$v_s = \frac{2\pi k_B \theta}{h_P (6\pi^2 N_a)^{1/3}}, \quad (21)$$

where $N_a = 7.5 \times 10^{28} \text{ m}^{-3}$ is the number density of atoms in $\text{YBa}_2\text{Cu}_3\text{O}_7$. The Debye temperature is determined from experimental data for the phonon specific heat using (Ziman, 1960)

$$C_s = 9N_a k_B \left(\frac{T}{\theta}\right)^3 J_4\left(\frac{\theta}{T}\right), \quad (22)$$

where the Debye integral $J_p(q)$ is defined in Eq. (6).

Beckman et al. (1987) showed that 97 percent of the specific heat of bulk $\text{YBa}_2\text{Cu}_3\text{O}_7$ is due to lattice vibrations. In the present analysis, the phonon specific heat of single-crystal $\text{YBa}_2\text{Cu}_3\text{O}_7$ is calculated from measurements of the total specific heat of polycrystalline bulk samples. The specific heat of the porous bulk samples is multiplied by the ratio of the mass density of a perfect single crystal to the measured mass density of the bulk samples. From 40 K to 120 K the data of Lang et al. (1988) are used, and from 10 K to 40 K the data of Ferreira et al. (1988) are used. Since the measurements at 40 K differed by 17 percent, the low-temperature data are multiplied by the ratio $C(40 \text{ K, Lang et al., 1988})/C(40 \text{ K, Ferreira et al., 1988})$ to provide a smooth transition. The specific heat C_s at 100 K is $1170 \text{ kJ m}^{-3} \text{ K}^{-1}$. The Debye temperature calculated using Eq. (22) varies from $\theta = 390$ K at a temperature of 10 K to $\theta = 520$ K at a temperature of 120 K. For the present analysis, the Debye temperature $\theta = 470$ K at a temperature of 90 K is employed, from which Eq. (21) yields an average sound velocity of $v_s = 3800 \text{ m s}^{-1}$. This compares well with the values of $v_l = 4000 \text{ m s}^{-1}$ and $v_t = 2500 \text{ m s}^{-1}$ measured by Lang et al. (1988) in sintered samples.

Size Effect

The reduction of the conductivity of a heat carrier along a film resulting from boundary scattering is calculated from the ratio of the film thickness to the bulk mean free path, $\delta = d/\Lambda$, using the approximate theory of Flik and Tien (1990c). Their result differs by less than 20 percent from the solution to the Boltzmann equation given by Sondheimer (1952) for electrons. For $\delta > 1$,

$$\frac{k_{\text{eff}}}{k} = 1 - \frac{2}{3\pi\delta}, \quad (23)$$

where k_{eff} is the thermal conductivity along the thin film and k is the bulk conductivity. For $\delta < 1$,

$$\frac{k_{\text{eff}}}{k} = 1 - \frac{2(1-Z^3)}{3\pi\delta} + \frac{2\delta}{\pi} \ln \frac{1+\delta+Z}{1+\delta-Z} - \frac{2}{\pi} \arccos \delta, \quad (24)$$

where $Z = (1 - \delta^2)^{1/2}$. Use of the bulk value of the thermal conductivity results in an error of less than 5 percent in the

predicted heat flux if the film thickness satisfies $d > 4.5\lambda$. Equations (23) and (24) are applied to the electron and phonon systems separately, yielding the effective conductivity of each carrier type from its bulk conductivity and mean free path, properties determined in the previous sections. The thermal conductivity of the film is equal to the sum of the reduced electron and phonon components.

The use of Eqs. (23) and (24) neglects the anisotropy of epitaxial $\text{YBa}_2\text{Cu}_3\text{O}_7$. These equations were derived for an isotropic material in which the ends of the free paths originating from a point fall on the surface of a sphere in the absence of boundary scattering. An estimate of the effect of phonon-boundary scattering on conduction in an anisotropic film indicates the error resulting from this simplification. The ratio of the phonon mean free path in the a - b plane to that along the c axis is approximately the square root of the ratio of the thermal conductivities, $\Lambda_{s,a-b}/\Lambda_{s,c} = (k_{a-b}/k_c)^{1/2}$ (Flik and Tien, 1990c). The conductivity ratio is $k_{a-b}/k_c \sim 5$ in $\text{YBa}_2\text{Cu}_3\text{O}_7$ (Hagen et al., 1989). The ends of the free paths originating from a point are assumed to fall on the surface of an ellipsoid whose axis of rotational symmetry is normal to the a - b plane, whose height normal to the a - b plane is $2\Lambda_{s,c}$, and whose cross section in the a - b plane containing the origination point is a circle of radius $\Lambda_{s,a-b}$. The effect of boundary scattering is calculated using the technique of Flik and Tien (1990c) with $\Lambda_{s,a-b} = \Lambda_{s,\text{isotropic}}$. Neglecting the anisotropy results in an overestimation of the size effect. The error is 36 percent for $\delta \ll 1$, 12 percent for $\delta = 1$, and approaches zero for $\delta \gg 1$.

The large anisotropy of the electrical resistivity, $\rho_e/\rho_{a-b} \sim 250$ above T_c in $\text{YBa}_2\text{Cu}_3\text{O}_7$ (Hagen et al., 1988) indicates that one or more of the quantities m^* , n , or the electron scattering time $\tau = \Lambda_e/v_e$ is less favorable for transport parallel to the c axis than for a - b plane transport. If either n or τ is responsible, the fraction of electron free paths that terminate at the film boundaries is smaller than that in an isotropic film, and the present analysis overpredicts the size effect on the electron thermal conduction. The electron contribution to the total conductivity is smaller than that of phonons, particularly at temperatures below the critical temperature, reducing the importance of this error. It will be shown that the size effect on the phonons dominates over the size effect on the electrons, further reducing the importance of this error.

Equations (23) and (24) are valid if phonons and electrons are reflected diffusely at the film surface. Diffuse reflection occurs if the carrier wavelength is of the order of or smaller than the standard deviation of the surface profile multiplied by 4π (Ziman, 1960). This is almost certainly satisfied by electrons in $\text{YBa}_2\text{Cu}_3\text{O}_7$, which have a wavelength of $2h_p/(v_e m^*) \sim 2$ nm. The average phonon wavelength is approximately $h_p v_s/k_B T$, which in $\text{YBa}_2\text{Cu}_3\text{O}_7$ at 25 K is 7 nm. In order for diffuse reflection to prevail at this temperature, roughness features of 6 Å must be present at the boundaries of the film. Majumdar and Tien (1990) analyzed the condition for diffuse reflection using a fractal description of the surface. If the fractal surface parameters can be determined from experiments, a limiting temperature can be determined above which most reflections are diffuse. Chen and Tien (1992) showed that the diffuse transmission of carriers through the boundaries does not influence the effect of boundary scattering on thermal conduction along a film. At low temperatures, where longer phonon wavelengths may decrease the fraction of phonons that are diffusely transmitted, the fraction of incident phonons transmitted through an interface is reduced by the acoustic mismatch of the two materials (Swartz and Pohl, 1989).

Summary of Technique

The technique developed in the present analysis for calculating the effective thermal conductivity in epitaxial high- T_c

superconducting films is appropriate for a superconductor in which both electrons and phonons contribute significantly to thermal conduction. Application of the Wiedemann-Franz law using normal-state electrical resistivity data has indicated that this is the case for the a - b plane of single crystal $\text{YB}_2\text{Cu}_3\text{O}_7$ and $\text{Bi}_2\text{Sr}_2\text{Ca}_1\text{Cu}_2\text{O}_8$, as well as for conduction in polycrystalline $\text{EuBa}_2\text{Cu}_3\text{O}_{7-x}$ (Izbizky et al., 1988) and $\text{La}_{2-x}\text{Sr}_x\text{CuO}_4$ with $x > 0.3$ (Sera et al., 1990).

Requirements

- 1 The electrical resistivity $\rho(T)$, $T_c < T < 300$ K, and the thermal conductivity $k(T)$, $20 \text{ K} < T < 300$ K of a large specimen.
- 2 The specific heat of the material, which is dominated by phonons, $C_s(T)$, $20 \text{ K} < T < 300$ K.
- 3 The effective mass m^* and number density n of electrons.

Procedure

- 1 Equations from the Sommerfeld free-electron model modified by an effective electron mass yield the properties of electrons. Calculate v_e using Eq. (3) and γ using Eq. (10).
- 2 Equations from the Debye model yield the properties of phonons. Calculate θ from the data $C_s(T)$ using Eq. (22), and calculate v_s using Eq. (21).
- 3 The Bloch formula for the phonon electrical resistivity and Matthiessen's rule yield the defect electrical resistivity. Choose as T_R the upper temperature of the superconducting to normal-state transition as deduced from $\rho(T)$. Calculate ρ_d from the data $\rho(T)$ using Eq. (7).
- 4 The kinetic-theory formulation of the electrical resistivity yields the electron mean free path limited by defect scattering. Calculate $\Lambda_{e,d}$, which is independent of temperature, from ρ_d using Eq. (2).
- 5 The Wiedemann-Franz law yields the electron thermal conductivity at the critical temperature. Calculate $k_e(T_c)$ from $\rho(T_R)$ and Eq. (17).
- 6 The kinetic-theory formulation of the thermal conductivity yields the electron mean free path at the critical temperature. Calculate $\Lambda_e(T_c)$ using the normal-state relation, $k_e(T_c) = C_e(T_c)v_e\Lambda_e(T_c)/3$, where $C_e(T_c) = \gamma T_c$.
- 7 Matthiessen's rule yields the electron mean free path limited by phonon scattering at the critical temperature. Calculate $\Lambda_{e,s}(T_c)$, from $\Lambda_e(T_c)$ and $\Lambda_{e,d}(T_c)$ using Eq. (1).
- 8 The Wilson formula for the electron thermal conductivity limited by phonon scattering yields the electron mean free path limited by phonon scattering in the superconducting state. Calculate $\Lambda_{e,s}(T)$, $0 < T < T_c$, from $\Lambda_{e,s}(T_c)$ using Eq. (9).
- 9 Matthiessen's rule yields the electron mean free path in the superconducting state. Calculate $\Lambda_e(T)$, $0 < T < T_c$, using $\Lambda_{e,s}(T)$ and $\Lambda_{e,d}$ in Eq. (1).
- 10 The kinetic method and the expression for the electron entropy given by the two-fluid model of electrons in superconductors yield the electron thermal conductivity in the superconducting state. Calculate $k_e(T)$, $0 < T < T_c$, from $\Lambda_e(T)$ using Eq. (14).
- 11 The assumption that the electron and phonon conductivities sum yields the phonon conductivity in the superconducting state. Calculate $k_s(T)$ from $k_e(T)$ and the data $k(T)$ using Eq. (19).
- 12 The kinetic-theory formulation of the thermal conductivity yields the phonon mean free path. Calculate $\Lambda_s(T)$ from $k_s(T)$ and the data $C_s(T)$ using Eq. (20).
- 13 Equations that account for the size effect in thin films yield the effective electron and phonon conductivities reduced by boundary scattering. Given a film of thickness d , calculate $k_{e,\text{eff}}(T)$ from $k_e(T)$ and $\Lambda_e(T)$ using Eqs. (23) and (24). Calculate $k_{s,\text{eff}}(T)$ from $k_s(T)$ and $\Lambda_s(T)$ using Eqs. (23) and (24).
- 14 Calculate $k_{\text{eff}}(T)$ by summing $k_{e,\text{eff}}(T)$ and $k_{s,\text{eff}}(T)$.

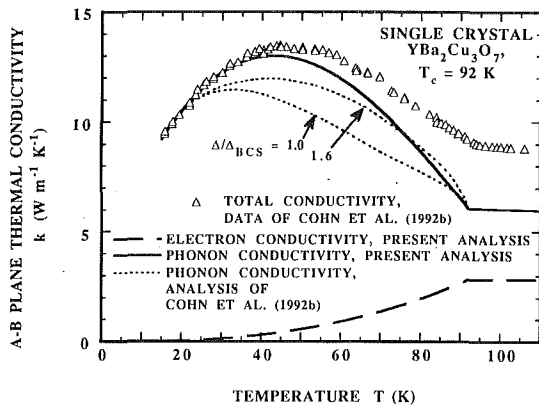


Fig. 4 Data for the a - b plane thermal conductivity of a $\text{YBa}_2\text{Cu}_3\text{O}_7$ crystal in the absence of boundary scattering, and predictions of the electron and phonon contributions

Results and Discussion

In this section, the technique developed in the previous sections for calculating the effective conductivity along high- T_c superconducting films is applied to the a - b plane of epitaxial $\text{YBa}_2\text{Cu}_3\text{O}_7$ films. The thermal conductivity and electrical resistivity data employed to calculate the electron and phonon conductivities and mean free paths in the absence of the size effect are those of crystal CR3 of Cohn et al. (1992b), the only single crystal for which both the electrical resistivity and the thermal conductivity have been reported as functions of temperature. The electron and phonon contributions to the a - b plane thermal conductivity of the crystal are shown in Fig. 4. The data exhibit the broad peak in the conductivity typical of high- T_c superconductors, which results from the phonon contribution to the conductivity. The phonon conductivity increases with decreasing temperature because of the decreasing number density of normal-state electrons, which are important scatterers of phonons. Superconducting electrons do not exchange energy or momentum with the lattice and do not scatter phonons. At temperatures below about 50 K, this enhancement of the phonon conductivity is offset by the decreasing number density of phonons with decreasing temperature. The electron contribution to the conductivity decreases with decreasing temperature because of the diminishing number density of normal-state electrons. Superconducting electrons carry no entropy and do not contribute to heat transport. The electron thermal conductivity is less than 10 percent of the total conductivity below 60 K.

Cohn et al. (1992b) fitted the phonon-conductivity formulation of Tewordt and Wölkhausen (1990) to the data at low temperatures, where the electron contribution is negligible, and to the phonon contribution determined using Eqs. (17) and (19) above the critical temperature. They employed different values of the superconductor energy gap compared to that of Bardeen et al. (1957), $\Delta/\Delta_{\text{BCS}}$, a ratio whose correct value is not known for $\text{YBa}_2\text{Cu}_3\text{O}_7$. The phonon conductivity predicted in the present analysis agrees within 10 percent with that of Cohn et al. (1992b) with $\Delta/\Delta_{\text{BCS}} = 1.6$. The present analysis determines that the electron conductivity is limited by defect scattering at temperatures up to the critical temperature, i.e., the second term on the right of Eq. (1) is always larger than the other terms. Each phonon conductivity prediction of Cohn et al. (1992b), when subtracted from the data, yields an electron conductivity that has a local maximum near 55 K. This is not consistent with the present analysis, nor with the electron conductivity limited by defect scattering of Geilikman and Kresin (1974).

Figure 5 shows the temperature dependence of the electron and phonon thermal conduction mean free paths in the absence of boundary scattering. The close similarity of the electron

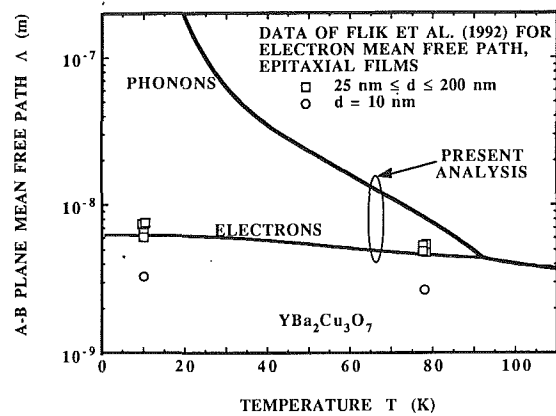


Fig. 5 Electron and phonon mean free paths in the a - b plane of $\text{YBa}_2\text{Cu}_3\text{O}_7$

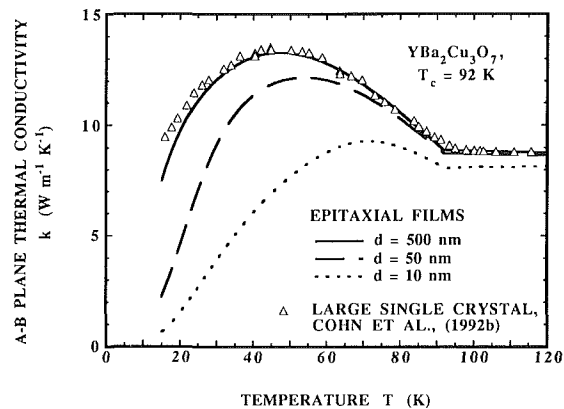


Fig. 6 Size effect on the a - b plane thermal conductivity of epitaxial $\text{YBa}_2\text{Cu}_3\text{O}_7$ films

and phonon mean free paths above the critical temperature is coincidental and is not reproduced by applying the technique of the present analysis to another crystal. The data are those of Flik et al. (1991), who developed a technique for fitting the experimentally measured infrared reflectance of $\text{YBa}_2\text{Cu}_3\text{O}_7$ films in the superconducting state, which yielded the electron mean free path Λ_e . The technique was applied to five films of thicknesses 10 nm, 25 nm, 50 nm, 100 nm, and 200 nm. At both 10 K and 78 K, the mean free path data are in excellent agreement with the predictions of the present analysis, with the exception of those for the 10 nm film, which indicate relatively small mean free paths. The different scattering rate in the 10 nm film may have resulted either from a different microstructure or from the increased importance of boundary scattering, since the thickness of the film was comparable to the electron mean free path (Flik et al., 1991).

The electron mean free path increases gradually with decreasing temperature because of the decreasing number density of phonons. The electron mean free path is limited by defect scattering, and therefore depends weakly on temperature and has a magnitude that depends on the microstructure of the sample. The phonon mean free path increases with decreasing temperature below the critical temperature because of the decreasing number density of normal-state electrons, which scatter phonons. The number density of normal-state electrons is constant above the critical temperature, resulting in a discontinuity in the temperature derivative of the phonon mean free path at the critical temperature. Phonons of wavelength large compared to the dimensions of point defects, dislocations, and impurities scatter less frequently on these defects than phonons of wavelength comparable to or smaller than the dimensions of these defects. The average phonon wavelength is inversely

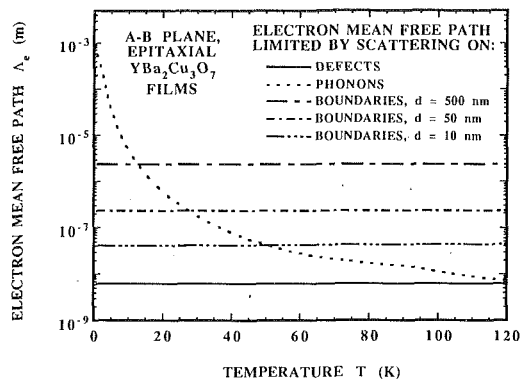


Fig. 7 Electron mean free paths for a - b plane thermal conduction in epitaxial $\text{YBa}_2\text{Cu}_3\text{O}_7$ films limited by scattering on defects, phonons, and the film boundaries

proportional to temperature, and the phonon mean free path increases quickly with decreasing temperature at low temperatures because of a decreasing rate of scattering on defects.

The predicted a - b plane thermal conductivities of epitaxial $\text{YBa}_2\text{Cu}_3\text{O}_7$ films of varying thickness d are shown in Fig. 6. The data are those for a large crystal and are included as the prediction for the limit of very thick films. Boundary scattering is negligible at temperatures above 20 K for a film thickness $d = 500$ nm. The thermal conductivity of the 50 nm film exhibits a significant size effect for temperatures below 55 K. Since the electron mean free path is much smaller than the film thickness in the entire temperature range, this size effect is due phonon-boundary scattering. The 10 nm film is of thickness comparable with the electron mean free path, which varies slowly with temperature, and boundary scattering is important in the entire temperature range shown. Because of the small relative magnitude of the electron thermal conductivity at low temperatures and the low electron mean free path, a significant size effect on the electron thermal conduction is confined to temperatures greater than 60 K and films of thickness less than 30 nm.

The components of the electron mean free path given in Eq. (1) are shown in Fig. 7. The electron mean free path limited by boundary scattering $\Lambda_{e,b}$ is calculated from Eq. (1) and the theoretical results for $\Lambda_{e,s}$ and $\Lambda_{e,d}$. The small relative magnitude of $\Lambda_{e,d}$ indicates that defect scattering is the dominant mechanism limiting electron conduction for each film thickness below 120 K.

Conclusions

The determination of the effective conductivity along epitaxial high- T_c superconducting films must consider the size effect on electrons and phonons separately only if the electron thermal conductivity is appreciable. This work shows that in the a - b plane of $\text{YBa}_2\text{Cu}_3\text{O}_7$ the phonon conductivity dominates over the electron conductivity at temperatures below 60 K, where the size effect in films is of the greatest importance. Below 60 K, the size effect may be calculated considering only phonon conduction.

This work calculates for the first time the mean free path of normal-state electrons in the superconducting state of $\text{YBa}_2\text{Cu}_3\text{O}_7$, and the result is in close agreement with data from infrared spectroscopy at 10 K and 78 K. This agreement is a strong endorsement of the simplifications that make the present analysis possible. The electron mean free path is limited by scattering on defects and increases gradually with decreasing temperature to 63 Å at 10 K.

The predictions of the present analysis should be compared to experimental data for the thermal conductivity along epitaxial high- T_c superconducting films. There is an urgent need

for experimental techniques that measure the thermal conductivity in epitaxial thin films such as those considered in this study.

Acknowledgments

K. E. G. acknowledges the support of the Office of Naval Research through an academic fellowship. Professor M. S. Dresselhaus provided valuable comments. The authors are indebted to Dr. S. A. Wolf for providing a preprint of his manuscript (Cohn et al., 1992b).

References

- Bardeen, J., Cooper, L. N., and Schrieffer, J. R., 1957, "Theory of Superconductivity," *Phys. Rev.*, Vol. 108, pp. 1175-1204.
- Bardeen, J., Rickayzen, G., and Tewordt, L., 1959, "Theory of the Thermal Conductivity of Superconductors," *Phys. Rev.*, Vol. 113, pp. 982-994.
- Beckman, O., Lundgren, P., Nordblad, P., Sandlund, L., Svendlinth, P., Lundström, T., and Rundqvist, S., 1987, "Specific Heat and Magnetic Susceptibility of Single-Phase $\text{YBa}_2\text{Cu}_3\text{O}_7$," *Phys. Lett. A*, Vol. 125, pp. 425-428.
- Bloch, F., 1930, "Zum Elektrischen Widerstandsgesetz bei tiefen Temperaturen," *Z. Phys.*, Vol. 59, pp. 209-214.
- Chen, G., and Tien, C. L., 1992, "Thermal Conductivity of Quantum Well Structures," AIAA Paper No. 92-0707.
- Cohn, J. L., Wolf, S. A., and Vanderah, T. A., 1992a, "Evidence for Strong Electron-Phonon Coupling in the Thermal Conductivity of $\text{YBa}_2\text{Cu}_3\text{O}_{7-\delta}$," *Phys. Rev. B*, Vol. 45, pp. 511-514.
- Cohn, J. L., Wolf, S. A., Vanderah, T. A., Selvamannickam, V., and Salama, K., 1992b, "Lattice Thermal Conductivity of $\text{YBa}_2\text{Cu}_3\text{O}_{7-\delta}$," *Physica C*, Vol. 192, pp. 435-442.
- Crommie, M. F., and Zettl, A., 1990, "Thermal Conductivity of Single-Crystal Bi-Sr-Ca-Cu-O," *Phys. Rev. B*, Vol. 41, pp. 10978-10982.
- Ferreira, J. M., Lee, B. W., Dalichaouchi, Y., Torikachvili, M. S., and Maple, M. B., 1988, "Low-Temperature Specific Heat of the High- T_c Superconductors $\text{La}_{1-x}\text{Sr}_x\text{CuO}_{4-\delta}$ and $\text{RBa}_2\text{Cu}_3\text{O}_{7-\delta}$ ($R = \text{Y, Eu, Ho, Tm, and Yb}$)," *Phys. Rev. B*, Vol. 37, pp. 1580-1586.
- Fiory, A. T., Hebard, A. F., Eick, R. H., Mankiewich, P. M., Howard, R. E., and O'Malley, M. L., 1990, "Metallic and Superconducting Surfaces of $\text{YBa}_2\text{Cu}_3\text{O}_7$ Probed by Electrostatic Charge Modulation of Epitaxial Films," *Phys. Rev. Lett.*, Vol. 65, pp. 3441-3444.
- Flik, M. I., and Hijikata, K., 1990, "Approximate Thermal Packaging Limit for Hybrid Superconductor-Semiconductor Electronic Circuits," *Heat Transfer 1990*, G. Hetsroni, ed., Hemisphere, New York, Vol. 2, pp. 319-324.
- Flik, M. I., Phelan, P. E., and Tien, C. L., 1990, "Thermal Model for the Bolometric Response of High- T_c Superconducting Films to Optical Pulses," *Cryogenics*, Vol. 30, pp. 1118-1128.
- Flik, M. I., and Tien, C. L., 1990a, "Intrinsic Thermal Stability of Anisotropic Thin-Film Superconductors," *ASME JOURNAL OF HEAT TRANSFER*, Vol. 112, pp. 10-15.
- Flik, M. I., and Tien, C. L., 1990b, "Intrinsic Thermal Stability for Scanning Electron Microscopy of Thin-Film Superconductors," *J. Appl. Phys.*, Vol. 67, pp. 362-370.
- Flik, M. I., and Tien, C. L., 1990c, "Size Effect on the Thermal Conductivity of High- T_c Thin-Film Superconductors," *ASME JOURNAL OF HEAT TRANSFER*, Vol. 112, pp. 872-881.
- Flik, M. I., Zhang, Z. Z., and Goodson, K. E., 1992, "The Electron Scattering Rate in Epitaxial $\text{YBa}_2\text{Cu}_3\text{O}_7$ Superconducting Films," *Phys. Rev. B*, Vol. 46, pp. 5606-5614.
- Flik, M. I., and Goodson, K. E., 1992, "Thermal Analysis of Electron-Beam Absorption in Low-Temperature Superconducting Films," *ASME JOURNAL OF HEAT TRANSFER*, Vol. 114, pp. 264-270.
- Gellikman, B. T., and Kresin, V. Z., 1974, *Kinetic and Nonsteady-State Effects in Superconductors*, Wiley, New York, pp. 5-7, 13-15.
- Gorter, C. J., and Casimir, H., 1934, "On Supraconductivity I," *Physica*, Vol. 1, pp. 306-320.
- Hagen, S. J., Jing, T. W., Wang, Z. Z., Horvath, J., and Ong, N. P., 1988, "Out-of-Plane Conductivity in Single-Crystal $\text{YBa}_2\text{Cu}_3\text{O}_7$," *Phys. Rev. B*, Vol. 37, pp. 7928-7931.
- Hagen, S. J., Wang, Z. Z., and Ong, N. P., 1989, "Anisotropy of the Thermal Conductivity of $\text{YBa}_2\text{Cu}_3\text{O}_{7-x}$," *Phys. Rev. B*, Vol. 40, pp. 9389-9392.
- Izbizky, M. A., Regueiro, M. N., Esquinazi, P., and Fainstein, C., 1988, "Thermal Conductivity and Superconductivity in $\text{EuBa}_2\text{Cu}_3\text{O}_{7-x}$," *Phys. Rev. B*, Vol. 38, pp. 9220-9223.
- Kittel, C., 1986, *Introduction to Solid State Physics*, Wiley, New York, pp. 106, 127-130, 135-140, 264-267.
- Kumar, S., and Joshi, A., 1990, "Thermal Analysis of a Transition-Edge High T_c Superconductor Infrared Detector," *Radiation Heat Transfer: Fundamentals and Applications*, T. F. Smith et al., eds., ASME HTD-Vol. 137, pp. 173-180.
- Lang, M., Lechner, T., Riegel, S., Steglich, F., Weber, G., Kim, T. J., Lüthi, B., Wolf, B., Rietschel, H., and Wilhelm, M., 1988, "Thermal Expansion, Sound Velocities, Specific Heat and Pressure Derivative of T_c in $\text{YBa}_2\text{Cu}_3\text{O}_7$," *Z. Phys. B*, pp. 459-463.
- Lavine, A. S., and Bai, C., 1990, "An Analysis of Heat Transfer in Josephson Junction Devices," *ASME JOURNAL OF HEAT TRANSFER*, Vol. 113, pp. 535-543.

- Majumdar, A., and Tien, C. L., 1990, "Reflection of Radiation by Rough Fractal Surfaces," presented at the ASME/AIAA Thermophysics and Heat Transfer Conference, Seattle, WA, June 13-20.
- Mannhart, J., Gross, R., Hipler, K., Huebener, R. P., Tsuei, C. C., Dimos, D., and Chaudari, P., 1989, "Spatially Resolved Observation of Supercurrents Across Grain Boundaries in YBaCuO Films," *Science*, Vol. 245, pp. 839-840.
- Peacor, S. D., Cohn, J. L., and Uher, C., 1991, "Effect of Magnetic Field on Thermal Conductivity of YBa₂Cu₃O_{7-δ} Single Crystals," *Phys. Rev. B*, Vol. 43, pp. 8721-8724.
- Penney, T., von Molnár, S., Kaiser, D., Holtzberg, F., and Kleinsasser, A. W., 1988, "Strongly Anisotropic Electrical Properties of Single-Crystal YBa₂Cu₃O_{7-x}," *Phys. Rev. B*, Vol. 38, pp. 2918-2921.
- Rohsenow, W. M., and Choi, H. Y., 1961, *Heat, Mass, and Momentum Transfer*, Prentice-Hall, Englewood Cliffs, NJ, pp. 486-501.
- Saint-Paul, M., Tholence, J. L., and Monceau, P., 1988, "Ultrasound Study of YBa₂Cu₃O_{7-δ} Single Crystals," *Solid State Comm.*, Vol. 66, pp. 641-643.
- Salamon, M. B., 1989, "Thermodynamic Properties, Fluctuations, and Anisotropy of High Temperature Superconductors," in: *Physical Properties of High Temperature Superconductors I*, D. M. Ginsberg, ed., World Scientific Publishing Co., Teaneck, NJ, pp. 39-70.
- Sera, M., Shamoto, S., Sato, M., Watanabe, I., Nakashima, S., and Kumagai, K., 1990, "Thermal Conductivity of High-T_c Oxides," *Solid State Comm.*, Vol. 74, pp. 951-956.
- Shoenberg, D., 1952, *Superconductivity*, Cambridge University Press, New York.
- Sondheimer, E. H., 1952, "The Mean Free Path of Electrons in Metals," *Advances in Physics*, Vol. 1, pp. 1-42.
- Stormer, H. L., Levi, A. F. J., Baldwin, K. W., Anzlowar, M., and Boebinger, G. S., 1988, "Normal-State Transport Parameters of Epitaxial Thin Films of YBa₂Cu₃O_{7-δ}," *Phys. Rev. B*, Vol. 38, pp. 2472-2476.
- Swartz, E. T., and Pohl, R. O., 1989, "Thermal Boundary Resistance," *Rev. Mod. Phys.*, Vol. 61, pp. 605-668.
- Tewordt, L., and Wölkhausen, T., 1989, "Theory of Thermal Conductivity of the Lattice for High-T_c Superconductors," *Solid State Comm.*, Vol. 70, pp. 839-844.
- Tewordt, L., and Wölkhausen, T., 1990, "Theory of Phonon Thermal Conductivity for Strong-Coupling s- and d-Wave Pairing in High T_c Superconductors," *Solid State Comm.*, Vol. 75, pp. 515-519.
- Uher, C., 1990, "Thermal Conductivity of High-T_c Superconductors," *Journal of Superconductivity*, Vol. 3, pp. 337-389.
- Van Duzer, T., 1988, "Superconductor-Semiconductor Hybrid Devices, Circuits and Systems," *Cryogenics*, Vol. 28, pp. 527-531.
- Wilson, A. H., 1953, *The Theory of Metals*, Cambridge University Press, New York, pp. 285, 290.
- Ziman, J. M., 1960, *Electrons and Phonons*, Oxford University Press, Oxford, United Kingdom, pp. 105-107, 259, 257-261, 285-287, 357-367, 456-460.

Multidimensional Inverse Heat Conduction Using the Monte Carlo Method

A. Haji-Sheikh

F. P. Buckingham

Department of Mechanical Engineering,
The University of Texas at Arlington,
Arlington, TX 76019-0023

The Monte Carlo method is used to solve inverse heat conduction problems when the surface temperature is spatial and time dependent. The standard random walk is modified to deal with curved boundaries. The proposed random walk has all the characteristics of the floating random walk, except its step size is small. This is a uniquely flexible method with excellent accuracy and it is computationally fast. The method is used to solve one- and three-dimensional heat conduction problems and the results are presented. A procedure is described to improve the accuracy of the solution, then used to calculate heat transfer from a cylindrical surface cooled by a stream of air.

Introduction

Inverse techniques refer to methods of indirectly determining local thermodynamical, thermophysical, and mechanical properties. The method of predicting surface temperature and heat flux using the time history of temperature at internal sites is known as inverse heat conduction. Inverse heat conduction evolved as a useful analytical tool following Stolz (1960). Among important early contributors to this temperature analysis technique are Sparrow et al. (1964) emphasizing the calculation of surface temperature, and Beck (1968) emphasizing the surface heat flux. The fundamentals of inverse conduction and an extensive survey are given by Beck et al. (1985). Inverse heat conduction can be used to calculate localized heat flux in multidimensional bodies; however, many methods of solution are numerical, e.g., Murio (1989) and Woodbury (1991). For simple geometries, it is possible to use a closed-form solution method to estimate the surface temperature and heat flux for three-dimensional heat conduction problems. However, despite the exact nature of the mathematical formulation, all solutions of this type are approximate and mathematical steps can be demanding (Jarny et al., 1991).

There are ongoing efforts by researchers to develop more powerful methods for solving inverse heat conduction problems when the temperature field depends on more than one spatial coordinate. The Monte Carlo method has some excellent features that can serve this need. It is an ideal technique for parallel processors because no communication between processors is needed until the Monte Carlo steps are complete. For the type of problem described in this paper, Monte Carlo is fast and efficient in comparison to other methods, since it provides a simple relation between the temperature at thermocouple sites and the surface temperature. It is particularly effective in solving inverse heat conduction problems in complex-shaped bodies. The descriptions of the Monte Carlo methods and random walk procedures are given by Haji-Sheikh (1988).

In this paper, the Monte Carlo method is employed to solve inverse heat conduction problems. To evaluate the suitability, accuracy, and existence of possible pitfalls, a series of numerical tests are conducted and the results are reported. It is shown that the Monte Carlo method has all the ingredients of simplicity and efficiency that one can expect from a numerical method. The accuracy of the Monte Carlo method is comparable to other techniques, while the programming effort and

computation time can be substantially less. In direct problems, the Monte Carlo method provides temperature values versus time only at specific sites, which can be an asset when applied to inverse heat conduction where temperatures are needed at a few discrete sites. Moreover, the Monte Carlo method provides a relation between temperature at the discrete sensor sites and the surface temperature, while no additional information concerning the temperature distribution throughout the material domain is required.

The solution using the Monte Carlo method can be emulated by other methods. The closed form or discrete numerical solutions can provide information given in this paper by the Monte Carlo method. A short discussion is included in a later section.

Description of the Monte Carlo Problem

Monte Carlo refers to a method of statistically determining the value of a physical variable. The random walk in heat conduction is a process to define a probabilistic relation between an interior point and points of the surface of a domain. The description of a random walk is well documented in the literature (Haji-Sheikh, 1988). However, in this paper, the standard random walk procedure is modified for application to inverse heat conduction problems; hence, a brief description is presented. For the diffusion equation, the temperature at a point within an isotropic region is related to the temperature of its neighboring points, Fig. 1, each Δx apart, by the relation (Haji-Sheikh, 1988)

$$T(x, y, z, \tau + \Delta\tau) = p_o T(x, y, z, \tau) + p_{x+} T(x + \Delta x, y, z, \tau) + p_{x-} T(x - \Delta x, y, z, \tau) + p_{y+} T(x, y + \Delta y, z, \tau) + p_{y-} T(x, y - \Delta y, z, \tau) + p_{z+} T(x, y, z + \Delta z, \tau) + p_{z-} T(x, y, z - \Delta z, \tau) \quad (1)$$

where

$$p_o = 1 - 6\alpha\Delta\tau/\Delta x^2 \quad (1a)$$

$$p_{x+} = p_{x-} = p_{y+} = p_{y-} = p_{z+} = p_{z-} = \alpha\Delta\tau/\Delta x^2 \quad (1b)$$

Because there is no negative probability, one must choose $p_o \geq 0$, which is the stability requirement in the explicit finite difference solution. If a region is composed of isotropic subregions, Eq. (1) applies to each subregion; however, minor modifications are needed when point (x, y, z) is located at the phase boundary (Haji-Sheikh, 1988). The thermophysical properties are assumed to be independent of temperature.

A Monte Carlo procedure begins by preselecting N_s random walks, referred to as the sample size. Theoretically, all random

Contributed by the Heat Transfer Division for publication in the JOURNAL OF HEAT TRANSFER. Manuscript received by the Heat Transfer Division April 30, 1992; revision received July 16, 1992. Keywords: Conduction, Measurement Techniques, Transient and Unsteady Heat Transfer. Technical Editor: R. Viskanta.

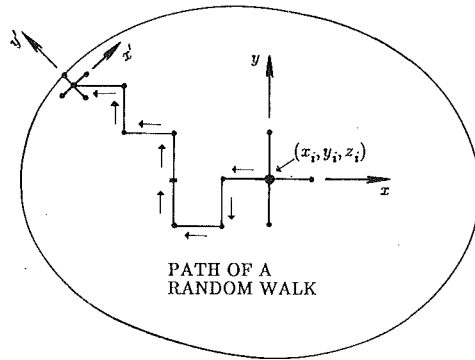


Fig. 1 Schematic of the material domain and the path of a random walk

walks depart from interior points whose coordinates are (x_i, y_i, z_i) at time t_i . According to Eq. (1), a fraction of the random walk equal to p_o remains at the same point, a fraction equal to p_{x+} goes to the point $(x_i + \Delta x, y_i, z_i)$, a fraction equal to p_{x-} goes to the point $(x_i - \Delta x, y_i, z_i)$, and so on. The same procedure should be repeated for the random walks at their new locations. For convenience of calculation, instead of following all random walks in groups, one can follow each random walk separately, one at a time, until each arrives at the boundary.

Usually, the random walk process begins by starting an N_s random walk from a site designated by the subscript "i"; that is, all N_s random walks are to depart from that site, one at a time. If one chooses $p_o = 0$, then a random walk starting from the site i whose coordinates are (x_i, y_i, z_i) has a probability of $1/6$ to move to any of the six neighboring points identified in Eq. (1). A random number drawn from a uniformly distributed set of random numbers dictates the next location of random walks. A random walk wanders in the region until it arrives at the proximity of the wall, Fig. 1. At this point, the standard random walk technique is modified to account for the curved boundaries while keeping the duration of each step small. The modified random walk procedure permits one to rotate the coordinates, if necessary, so that one point, e.g., point $(x', y' + \Delta x', z')$, on the right-hand side of Eq. (1) is located over the boundary. The new coordinate system is x', y', z' , see Fig. 1, whose y' coordinate is now perpendicular to the wall. If the wall is encountered following the next step, the random

walk is terminated, and the duration of that random walk in addition to the coordinates at the termination point will be stored in the computer memory for subsequent use. Otherwise, it is possible for the random walk to continue its journey within the body along a new set of grid points along the x, y, z coordinate axes. The coordinate axes can suffer a rotation any time a random walk arrives within a preselected distance from the wall. The modified random walk has the flexibility of the floating random walk (Haji-Sheikh, 1988) and, since the random walks are not required to remain along preselected grid points, it can deal with complex geometric boundaries with ease.

Another parameter to be recorded is the duration of each random walk; that is, the time for a random walk k to make its sojourn from the starting location to the boundary. When $p_o > 0$ a fraction of random walks may remain at the existing site during a period $\Delta\tau_k$. Statistically, the duration of a random walk will not change but the time for each step becomes smaller. It is analogous to requiring groups of travelers to reach their destination at an assigned time; they may take a rest during their trip if they walk a bit faster. This latter case may yield more accurate results. The time for each step (including the rest time) is $\Delta\tau_k$ and the duration of a random walk, τ_k , is the sum of all $\Delta\tau_k$'s. The sum of all surface temperatures at the point where the random walks arrive at the boundary divided by the sample size, N_s , is the temperature at the point (x_i, y_i, z_i) . The time of each step for the random walk k is $\Delta\tau_k = (1 - p_o)\Delta x^2/6\alpha$. The duration of that random walk, τ_k , is the sum of all $\Delta\tau_k$'s during the travel of that random walk. Therefore, if the random walk k begins at time t_i and the duration of the random walk is τ_k , the surface temperature at time $(t_i - \tau_k)$ must be recorded. The temperature at point i following completion of N_s random walks is

$$T_i(0, 0, 0, t_i) = \frac{1}{N_s} \sum_{k=1}^{N_s} T_s(x_k, y_k, z_k, t_i - \tau_k) \quad (2)$$

where $x_k, y_k,$ and z_k are the coordinates of the terminus point of the random walk k . Further details concerning the random walks with fixed step and the floating random walks are in Haji-Sheikh (1988).

The Monte Carlo procedure described above can be modified for prescribed surface heat flux instead of surface temperature. The computation of surface heat flux can be accomplished by a similar scheme, except a random walk will not terminate at

Nomenclature

\mathbf{A} = matrix with elements a_{ij}	M = number of time functions	\bar{t} = time, s
a_{ij} = elements of matrix \mathbf{A} , see Eq. (4)	N = number of time increments	x, y, z = Cartesian coordinates
c = array of coefficients	N_s = sample size or the number of random walks	Subscripts
c_j = unknown coefficients	Nu = Nusselt number = hD/k_a	e = time interval
D = diameter of cylinder, m	p = probability	$x+, x-$ = positive and negative directions along x axis
$f_j(t)$ = arbitrary selected time functions	q = heat flux, W/m^2	$y+, y-$ = positive and negative directions along y axis
i, j, k = indices	Re = Reynolds number = uD/ν	$z+, z-$ = positive and negative directions along z axis
h = heat transfer coefficient, $W/m^2 \cdot K$	r = dimensionless radial coordinate	α = thermal diffusivity, m^2/s
h_o = heat transfer coefficient at the stagnation point, $W/m^2 \cdot K$	r_o = radius, m	θ = angular coordinate
k = thermal conductivity of solid, $W/m \cdot K$	T_i = array of known values in Eq. (2)	ν = kinematic viscosity, m^2/s
k_a = thermal conductivity of air, $W/m \cdot K$	T = temperature, K	σ = standard deviation
	T_s = surface temperature, K	τ = duration of a random walk
	t = dimensionless time	$\Delta\tau_k$ = travel time for a step of a random walk

that wall; instead, it may go back into the material domain along the y' axis, Fig. 1. When a random walk is at a surface location with prescribed heat flux, the probability of returning inside the material domain is $2p_{y+}$ while the probability of moving along the x' or z' axes remains, as given by Eq. (1b). Whether the random walk moves to a different location or opts to remain at the same boundary point, the tally is the value of $2\alpha q_s/\Delta x^2$, where q_s is the surface heat flux at the instantaneous location of the random walk during its sojourn. Any time a random walk encounters a boundary point with prescribed heat flux, the heat flux at that point and at the time of arrival is the score. Clearly, this leads to continuation of the random walk process, until the initial temperature is the tally, $\tau_k = t_i$, or another surface with prescribed temperature is encountered. This increases the duration of a random walk, thereby increasing the computation time. In addition, instead of having a single tally, each random walk now requires several tallies. The only modification for prescribed surface heat flux is to replace the function $T_s(x_k, y_k, z_k, t_i - \tau_k)$ in Eq. (2) by several functions, each corresponding to a tally during the sojourn of random walk k .

Monte Carlo Method for Inverse Heat Conduction

In the inverse heat conduction, temperature sensors are embedded within a body and the surface temperature or heat flux is sought. Each sensor site is a location where N_s random walks should initiate. Because the number of sensor sites is finite, the Monte Carlo method is an ideal method of analysis. Prior to application of the Monte Carlo technique to a three-dimensional, inverse heat conduction problem, the following example is chosen to show the simplicity and efficiency of the Monte Carlo procedure.

Example 1. Consider a long, solid cylinder whose surface temperature changes with time, $T(t)$, independent of spatial coordinates and, since one sensor site is used, then $i=1$ in Eq. (2). The Monte Carlo method is used to calculate temperature at the center of the cylinder when the surface temperature is:

$$\begin{aligned} T_s &= 0 & \text{when } t < 0 \\ T_s &= t & \text{when } 0 < t < 0.5 \\ T_s &= 1 - t & \text{when } 0.5 < t \leq 1 \\ T_s &= 0 & \text{when } t > 1 \end{aligned}$$

It is assumed that $T=0$ when $t < 0$. The temperature values and standard deviation (STD) of error are plotted in Fig. 2. The input data obtained by the Monte Carlo method adequately simulate the experimental data. They have random errors and the probable error can be calculated (Haji-Sheikh, 1988, Section 16.8) using the standard deviation of data, see Fig. 2. The standard deviation shown in Fig. 2 is σ , where σ^2 is the variance of the Monte Carlo sampling.

Equation (2) is the direct Monte Carlo solution if $T_s(t)$ over the entire boundary is known. However, in inverse heat conduction problems, the temperature of the surface, $T_s(t)$, is unknown while the temperature at the site, $T(0, 0, 0, t_i)$, is known. The time-dependent surface temperature can be approximated by a linear combination of a set of M independent functions of time $f_1(t), f_2(t), \dots, f_M(t)$. The surface temperature is

$$T_s = \sum_{j=1}^M c_j f_j(t) \quad (3)$$

Now, one can devise a Monte Carlo procedure. Allow N_s random walks to leave from the center of the cylinder, one at a time. Store the duration of each random walk, $\tau_1, \tau_2, \dots, \tau_{N_s}$, in the computer memory as a computer file and use them

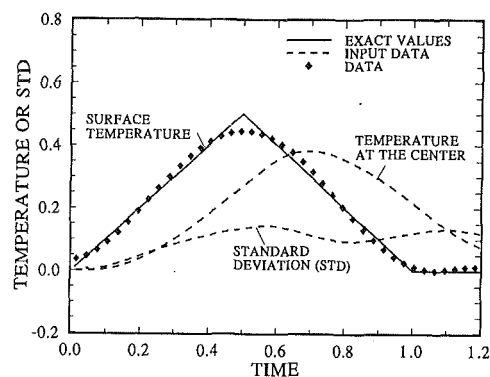


Fig. 2 Monte Carlo solution for the surface temperature of a solid cylinder using the entire time domain and seventh-degree polynomials

as needed. Using this scheme, one avoids unnecessary repetition of random walks throughout debugging of the computer program and subsequent computations. Next, subdivide the known temperature versus time trace at the sensor site into N time intervals so that t_i takes the values $t_{11}, t_{12}, \dots, t_{1N}$ at various time steps. At each time step, the elements of a matrix \mathbf{A} are computed from the relation

$$a_{ij} = \frac{1}{N_s} \sum_{k=1}^{N_s} f_j(t_{1i} - \tau_k); \quad \text{for } i = 1, 2, \dots, N \text{ and } j = 1, 2, \dots, M \quad (4)$$

When $\tau_k > t_{1i}$, the initial temperature, or zero for this example, is to be recorded. Any column j in matrix \mathbf{A} given by Eq. (4) can be viewed as the computed temperature at the sensor site subject to the surface temperature $f_j(t)$. For instance, Column 1 is the temperature at the center of the cylinder at times $t_{11}, t_{12}, \dots, t_{1N}$, assuming the surface temperature is $f_1(t)$. Similarly, Column 2 in matrix \mathbf{A} represents the central temperature if the surface temperature is $f_2(t)$, and so on. Substitution of Eq. (3) into Eq. (2) yields the following matrix relation:

$$\mathbf{A} \cdot \mathbf{c} = \mathbf{T}_i \quad (5)$$

The minimization principal (Hildebrand, 1956, Ch. 7) produces the following equation:

$$(\mathbf{A}^T \cdot \mathbf{A}) \mathbf{c} = \mathbf{A}^T \cdot \mathbf{T}_i \quad (6)$$

where \mathbf{A}^T is the transpose of matrix \mathbf{A} and \mathbf{T}_i is an array representing temperature at the sensor locations at time $t_{11}, t_{12}, \dots, t_{1N}$. Equation (6) represents M equations for M unknowns. The solution of coefficient c_j is readily available after inverting the matrix $(\mathbf{A}^T \cdot \mathbf{A})$; that is,

$$\mathbf{c} = (\mathbf{A}^T \cdot \mathbf{A})^{-1} \cdot (\mathbf{A}^T \cdot \mathbf{T}_i) \quad (7)$$

where array \mathbf{c} has elements c_1, c_2, \dots, c_M .

Now, the Monte Carlo procedure developed for inverse heat conduction can be used. The input data representing the surface temperature are in Fig. 2. It is assumed that Eq. (3) describes the surface temperature within the entire time domain and $f_1(t) = 1, f_2(t) = t, f_3(t) = t^2, \dots, f_M(t) = t^{M-1}$. The surface temperature is calculated using Eqs. (5)–(7) as described earlier and the data are plotted as discrete diamond symbols in Fig. 2. For comparison, the solid line in the figure is the exact value of the surface temperature. Polynomials of different degree were tested. The solution data in Fig. 2 were obtained using polynomials of degree 7. When the degree of the polynomial is large, some fluctuation in the computed data can be observed. For this reason, using polynomials of very high degrees may yield results of lower accuracy.

To improve the accuracy of the results plotted in Fig. 2, different strategies were examined. The time domain was divided into small subdomains and Eq. (3) was employed in each subdomain. For acceptable results, the value of Δt_e repre-

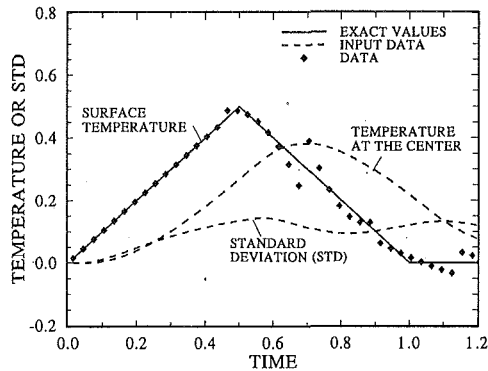


Fig. 3 Monte Carlo solution for the surface temperature of a solid cylinder using time intervals, $\Delta t_e = 0.225$, and polynomials of degree 3

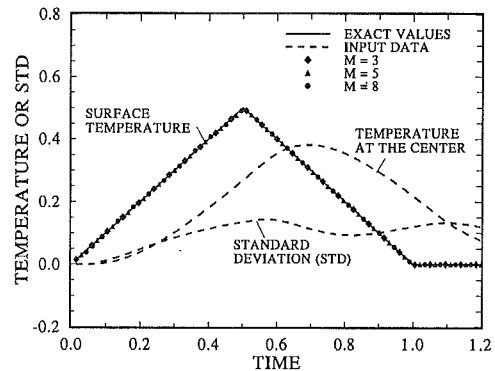


Fig. 5 Monte Carlo solution for the surface temperature of a solid cylinder using three time intervals with $M = 3, 5, \text{ and } 8$

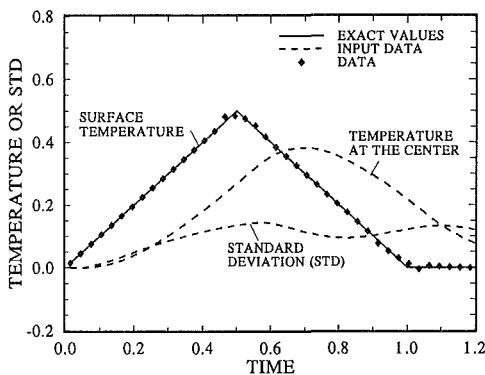


Fig. 4 Monte Carlo solution for the surface temperature of a solid cylinder using time intervals, $\Delta t_e = 0.15$, with overlap and polynomials of degree 3

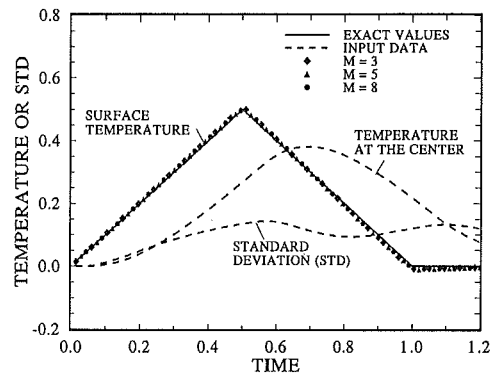


Fig. 6 Monte Carlo solution for the surface temperature of a solid cylinder using three time intervals with $M = 3, 5, \text{ and } 8$, and the second set of random walks

senting the span of each subregion should satisfy the following inequality:

$$\Delta t_e = \alpha \bar{\Delta t}_e / r_o^2 > \sim 0.2 \quad (8)$$

When $\Delta t_e < 0.2$, the error in the computed results may become excessive. When the temperature sensor is at r_i away from the center, the value of r_o in Eq. (8) can be replaced by $r_o - r_i$. Figure 3 uses the time intervals $\Delta t_e = 0.225$. The data show good agreement except at some isolated segments of the time domain. However, it was noticed that it is possible to improve the accuracy of the results even for smaller subdomains. A time domain $\Delta t_e = 0.15$ was selected; this time is extended by 0.075 so that the total time domain is 0.225 as used earlier. This extended time of 0.075 is referred to as the overlap time. The first step of the calculations begins for the time domain of $0 < t \leq 0.225$. After calculation of the surface temperature, the data beyond $t = 0.15$ were ignored. The second step of the calculation begins at $t = 0.15$ using $\Delta t_e = 0.15$ and an overlap of 0.075. The new time domain is $0.15 < t \leq 0.375$. Then, the computed temperature only for $0.15 < t < 0.3$ is retained, ignoring the overlap time. This procedure is continued through steps 3, 4, and so on, until the calculation of surface temperature is complete. The calculated surface temperature is in Fig. 4. Although the effective time domain is 0.225, the same as that for the data in Fig. 3, the accuracy of the data in Fig. 4 is superior to the data shown in Fig. 3. In the Monte Carlo method, the implementation of various multitime-domain schemes is a simple task. When the duration of a random walk is sufficiently large and the random walk terminates within a time interval with a previously computed surface temperature, one tallies the known surface temperature for that random walk for inclusion in Eq. (2). Then, the known tallies are moved to the left-hand side of Eq. (2) and included with the known temperature $T_i(0, 0, t_i)$.

Instead of subdividing the time domain into equally spaced small subdomains, a computationally faster procedure that can yield accurate surface temperature data is introduced. One can readily identify the time where there is a significant change of direction of temperature rate. Figure 2 shows that there is a substantial change at $t = 0.5$ and 1. Hence, the time domain is divided into three subdomains: 0 to 0.5, 0.5 to 1, and 1 to 1.5. The steps are identical to those described for data plotted in Fig. 4, except three large time subdomains are used. The computed surface temperature, Eq. (3), for $M = 3, 5, \text{ and } 8$ is shown in Fig. 5. The data show remarkable accuracy. The computed results shown in Fig. 5 are equally accurate for all values of M . As for the previous case, an overlap time of 0.075 is used.

In the Monte Carlo method, one uses a random number from a set of pseudo-random numbers to define the directions a random walk must choose. To show that the accuracy of the data in Fig. 5 is not peculiar to a particular set of random numbers, the computations were repeated using a second set of random numbers. The method of calculating data in Fig. 6 is identical to that used to produce data in Fig. 5, except a different set of random numbers was used. The accuracy of the plotted data in Fig. 6 is excellent; however, they show slightly larger errors than those in Fig. 5. The data in Fig. 6 are more representative of a Monte Carlo solution. According to Figs. 5 and 6, polynomials of high degree will not contribute significantly to the accuracy of computed data. Throughout this example, the time increment for data in matrix \mathbf{A} is 0.015; hence, only a fraction of the computed values is plotted in Figs. 2–6.

Following the successful completion of the studies of inverse heat conduction in a one-dimensional conduction model, a second study is directed toward the application of the Monte Carlo method to three-dimensional conduction. The same test cylinder is chosen as the test model, except now the temperature

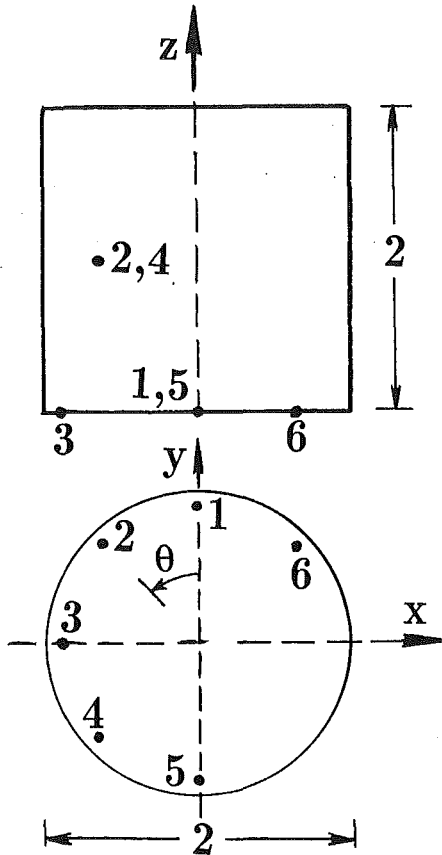


Fig. 7 Schematic of a cylinder with six embedded sensors

has angular and axial dependence. Details are presented in the next example.

Example 2. The data provided in this example are for a test specimen designed for an experimental study. A cylinder with dimensionless radius 1 is considered, Fig. 7. In the dimensionless space, the cylinder height is $L = 2$ and the thermal diffusivity is $\alpha = 1$. There are six embedded sensors, all with a radial coordinate of $r_i = 0.925$; the other coordinates are:

- 1 at $\theta = 0, z = 0$
- 2 at $\theta = \pi/4, z = 1$
- 3 at $\theta = \pi/2, z = 0$
- 4 at $\theta = 3\pi/4, z = 1$
- 5 at $\theta = \pi, z = 0$
- 6 at $\theta = 7\pi/4, z = 0$

where θ and z are the angular and axial coordinates. The numbers 1 through 6 are used to identify (θ, z) pairs listed above and shown in Fig. 7. Furthermore, it is assumed that the cylindrical surface is exposed to a variable temperature field over the cylindrical surface while $\partial T / \partial z = 0$ when $z = 0$ and $z = 2$.

The accuracy of an inverse thermal conduction procedure can best be studied if the exact value of a temperature function that produces the temperature traces at thermocouple sites is known. For this reason, a known surface temperature is imposed over the cylindrical surface, and the temperature at each of the six sensor sites is calculated. The calculated temperature values and the standard deviation of error in the temperature data are given in Fig. 8. These temperature traces will serve as input values to calculate the surface temperature by the

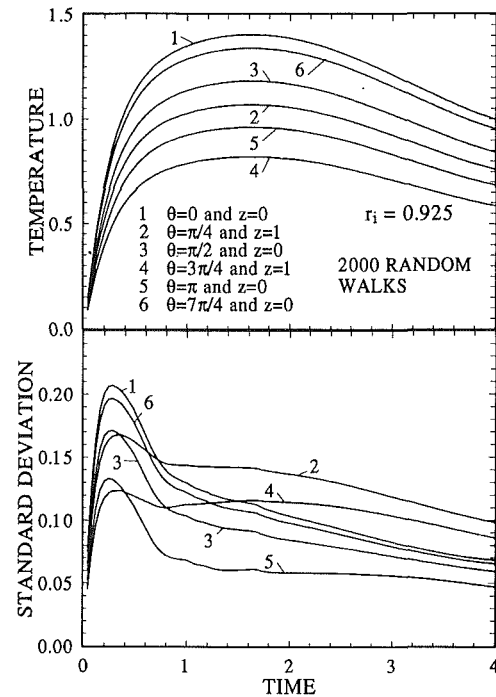


Fig. 8 Input temperatures and standard deviations at six sensor sites

Monte Carlo method. As described in the previous example, the standard deviations are useful for calculating errors in the input data.

The problem under consideration is three dimensional and the Monte Carlo procedure is quite similar to the one-dimensional case described earlier. There are two modifications: (1) As a random walk arrives at the surface, the coordinates of the termination point, as well as the duration of the random walk, must be recorded and stored in a computer file for subsequent use. (2) Functions that also describe the spatial dependence of the surface temperature must be added to Eq. (3).

Note that as $\Delta x \rightarrow 0$ and $N_s \rightarrow \infty$, Eq. (2) approaches the exact solution. Also, it is clear that in order to calculate an arbitrary exact surface temperature, one must have infinite temperature sensors. Since the number of sensor sites in a realistic application is usually small, only a small number of spatial functions can be accommodated. For this example, five different spatially dependent functions are selected for subsequent calculations.

The Monte Carlo procedure for this example begins by selecting a functional representation of the surface temperature as

$$T_s(\theta, z, t) = \sum_{j=1}^M c_{1j} t^{j-1} + \cos(\theta) \sum_{j=1}^M c_{2j} t^{j-1} + z^2 \sum_{j=1}^M c_{3j} t^{j-1} + \cos(2\theta) \sum_{j=1}^M c_{4j} t^{j-1} + z^2 \cos(\theta) \sum_{j=1}^M c_{5j} t^{j-1} \quad (9)$$

They represent $5M$ functions to describe the surface temperature. If the number of time increments in temperature traces is N , then the matrix \mathbf{A} has $5M$ columns and $6N$ rows. Because the radial coordinate for all sensor sites is the same and the surfaces at $z = 0$ and $z = 2$ are insulated, only one set of random walks is needed for all six sites. A proper programming technique can accomplish this but details are not essential to this presentation. The computation begins by using the random walks that have been stored previously, one at a time. Thus, the contribution of each random walk will be added to the elements of the matrix \mathbf{A} . For instance, when calculating the

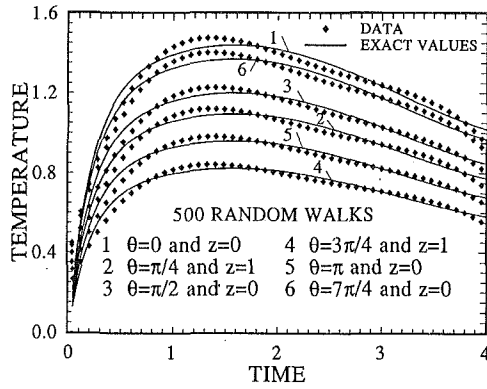


Fig. 9 Monte Carlo solution for the spatially dependent surface temperature of a solid cylinder using single time domain

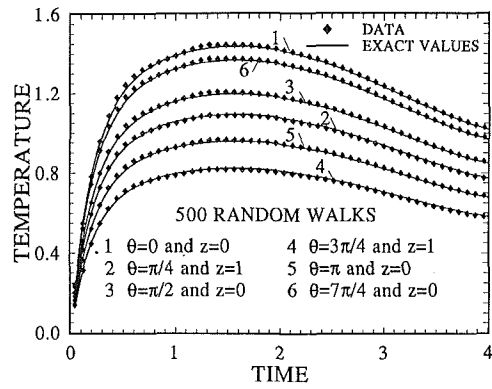


Fig. 11 Monte Carlo solution for the spatially dependent surface temperature of a solid cylinder using two time intervals and 500 random walks

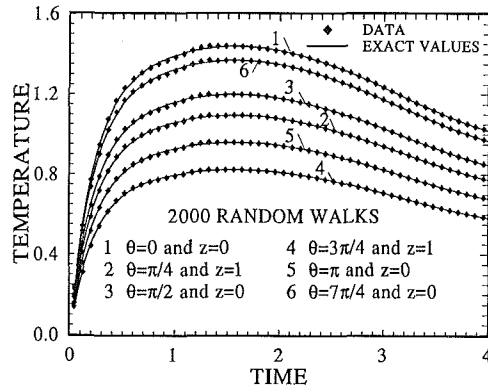


Fig. 10 Monte Carlo solution for the spatially dependent surface temperature of a solid cylinder using two time intervals and 2000 random walks

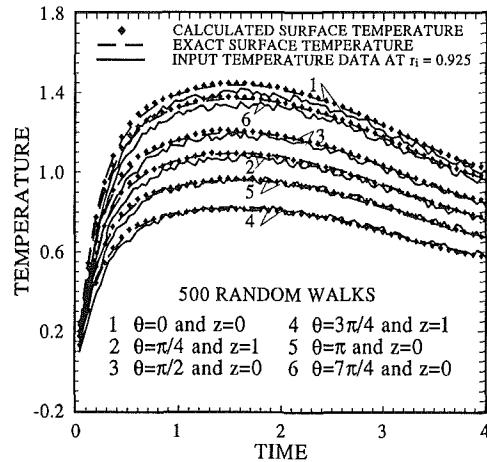


Fig. 12 Monte Carlo solution for the spatially dependent surface temperature of a solid cylinder using two time intervals and 500 random walks; input data with noise within ± 0.2

Column $M+3$, in the matrix \mathbf{A} , one assumes that the surface temperature is $t^2 \cos(\theta)$ and then proceeds to calculate the corresponding temperature at all six sites and N prescribed time increments to obtain $6N$ values for the Column $M+3$.

The methodology developed for the one-dimensional problem is employed in this example. First, using a single domain and $M=5$, the surface temperature is calculated using the input data in Fig. 8. The calculated surface temperatures are shown as discrete diamond-shaped data in Fig. 9. The surface temperature is plotted versus time for the same angular and axial coordinates as those for the six sensor sites, but for $r=1$. For comparison, the solid line indicates the exact surface temperature that is being sought. The data in Fig. 9 show that the slope of surface temperature changes when $t \sim 1.3$. Then, using the strategy observed in Example 1, the time domain is divided into two subdomains: one for $0 < t < 1.3$ and the other for $1.3 \leq t < 4$. The first domain is used with an overlap of 0.12 extending in the second domain, and then the c 's in Eq. (9) are calculated. After computation of the c 's, the overlap zone is ignored. During calculation of the surface temperature for the second subdomain, a random walk may arrive at the surface when $0 < t_i - \tau_k < 1.3$. Whenever the surface temperature at time $t_i - \tau_k$ is already known, then the known temperature is the tally for that random walk. Similar to the previous example, the known tallies will be included in vector \mathbf{T}_i . The computed temperature data for 2000 random walks are in Fig. 10. The results are exceptionally accurate, indicating that the Monte Carlo method is a viable method for solving inverse conduction problems. Indeed, a number of tests were run for smaller sample sizes. Good accuracy was observed even for a sample size as low as 50. In Fig. 11, a sample size of 500 random walks is used at each sensor site. The results show excellent accuracy despite the relatively small sample size. The agreement

between the discrete data and solid lines is good everywhere over the time domain. However, there is a very slight deviation at small time. This deviation is partially attributed to input data plotted in Fig. 8. An examination of the standard deviation of the input data, also plotted in Fig. 8, shows that the error in the input data is relatively large when $t \sim 0.3$.

Finally, a fixed amount of random noise was added to the input data to emulate amplifier noise. Random noise of ± 0.02 was added to the input data in Fig. 8. The calculations were carried out using the noisy input data displayed in Fig. 12. The solid lines in Fig. 12 are the input data at $r=0.925$ with superimposed noise. The computed surface temperature values for selected surface locations are also in Fig. 12. The exact surface temperature data are plotted using dashed lines for comparison. The accuracy of the calculated data is similar to those in Fig. 11 and the random noise in the input data has a small effect on the calculated surface temperature.

Example 3. It is of practical interest to calculate heat transfer from a cylindrical surface cooled by a stream of air. A cylinder selected for this example has the same dimensionless characteristics as the one used in Example 2. It is made of 316 stainless steel, 0.0508 m in diameter and 0.1016 m long. Type K thermocouples were embedded at dimensionless radial locations, as shown in Fig. 2, where all lengths are dimensionless using r_0 as the characteristic length. A coordinate system was established where $z=0$ is located at the midpoint of the specimen. Due to assumed symmetry, $\partial T / \partial z = 0$ at $z=0$. Ceramic insulations are attached to both ends so that $\partial T / \partial z = 0$ at

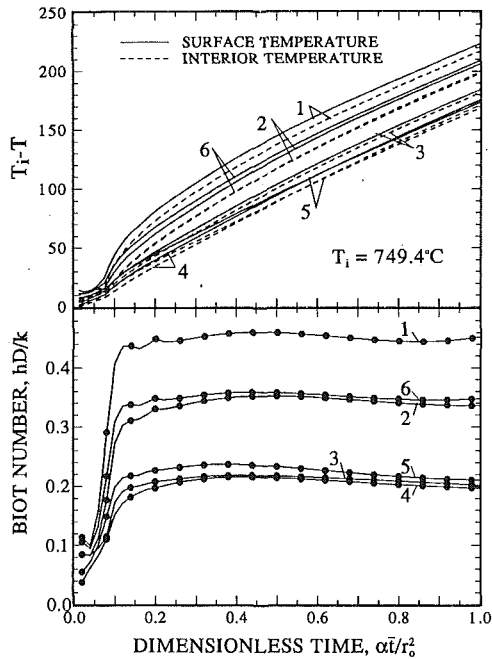


Fig. 13 Measured interior temperature, surface temperature, and heat transfer coefficient at selected locations when a jet of air impinges over a heated surface

$z = \pm 2$. The physical model was heated in a furnace and then cooled by an expanding jet of air. The jet impinges perpendicular to the axis of the cylinder so that the stagnation point of the jet at the cylinder surface is at $\theta = 0$ and $z = 0$. The nozzle was characterized by Lindemann (1991). A phase-Doppler analyzer was used to measure the velocity of the jet. During characterization, air was seeded with water particles; hence, the velocity of the water particles approximates the velocity of air. The nozzle exit was located 0.4 m from the stagnation point on the cylinder at $z = 0$. The flow rate of air is 0.47 kg/s and the maximum velocity of air at the center of the jet is ~ 15 m/s. The velocity reduces in a linear fashion to 5.5 m/s at 0.05 m from the center of the jet.

In this experiment, the cylinder was heated to an initial temperature of 750°C and then cooled using the nozzle with a jet stream temperature of $\sim 28^\circ\text{C}$ until thermocouples recorded $\sim 520^\circ\text{C}$. For this relatively narrow range of temperatures, the mean thermal diffusivity for 316 stainless steel is $4.73 \times 10^{-6} \text{ m}^2/\text{s}$ (Incropera and DeWitt, 1990). The temperatures at six thermocouple sites were recorded at a rate of 20 readings per second using a Hewlett Packard Model 3852A data acquisition system and computer controller. The data were stored on a magnetic cassette for subsequent data reduction. The dashed lines in Fig. 13 are the measured temperature data for all six thermocouple locations. The solid lines in the figure are the calculated surface temperature for the same θ and z coordinates as the thermocouples. Exactly the same method of analysis described in Example 2 is employed; that is, the c 's in Eq. (9) were calculated by the Monte Carlo method as described in Example 2. Once an equation for surface temperature is available, Eq. (9), the surface heat flux can be calculated using a direct method. An explicit finite difference technique is used to calculate the surface heat flux and, subsequently, the local heat transfer coefficient. For 10 divisions in the r direction, 12 divisions in the θ direction, and 10 divisions in the z direction, a dimensionless time increment equal to 0.000284 is used. The bottom portion of Fig. 13 shows the calculated dimensionless heat transfer coefficient, or the Biot number, at the same locations where surface temperature is reported in the upper portion of Fig. 13. Although the meas-

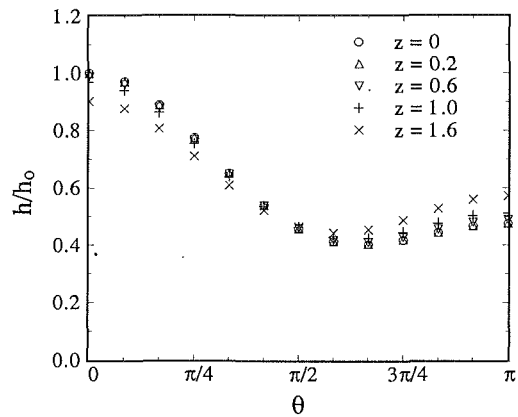


Fig. 14 Spatial variation of heat transfer coefficient based on the measured interior temperatures in Fig. 13

ured temperature traces, plotted in Fig. 13 show nearly smooth variations with time, the finite difference calculations show an early jump followed by low-frequency oscillations for the Biot number lines. The flow transients following the onset of spray and numerical calculation are responsible for the early jump in heat flux values. However, the cause for low-frequency oscillations is different. Thermocouples 3 and 4 show barely discernible temperature oscillations that have been amplified when heat flux is computed. During the experiment, air pressure before entering the nozzle fluctuates by 2 percent and the jet plume shows some oscillations. There are the major causes of fluctuations in the calculated surface heat flux.

This paper emphasizes and reports the computation of surface temperature by the Monte Carlo method and subsequent calculation of surface heat flux. For this reason and to maintain the integrity of the results, the heat transfer coefficient, reported in Fig. 13, is not corrected for the radiation effect. The emissivity of highly oxidized steel varies from 0.67 to 0.70 within the temperature range of 800 to 1000 K (Incropera and DeWitt, 1990). The contribution of radiation to the heat transfer data in Fig. 3 varies from 0.083 to 0.18 between surface temperatures of 530°C and 730°C . A sample calculation for the surface temperature of 650°C is selected to show the corrected heat transfer coefficient. All subsequent thermophysical properties are calculated at the mean film temperature. The results show a Biot number of 0.45, Fig. 13, reduced by a radiation effect of ~ 0.13 , and then multiplied by k/k_a ratio to yield $\text{Nu} = 124$. The average air velocity over a circular disk with a radius of $r_o = 0.0254 \text{ m}$ is equal to 11.8 m/s. Using the Reynolds number based on average velocity, $\text{Re} = 11,400$, the value of $\text{Nu}/\sqrt{\text{Re}}$ is 1.2; however, using the maximum velocity at the center yields $\text{Re} = 14,500$ and $\text{Nu}/\sqrt{\text{Re}} = 1.03$. The latter value $\text{Nu}/\sqrt{\text{Re}}$ is in excellent agreement with available data for crossflow over a heated cylinder (Eckert and Drake, 1972, Fig. 7-21).

Figure 14 is prepared to show the variation of h/h_o for different values of θ and z where h_o is the heat transfer coefficient at the stagnation point of the cylinder. It shows that the heat transfer coefficient is large at the stagnation point and gradually drops away from that point. The variation of h/h_o closely resembles the data of Eckert and Drake (1972, Fig. 7-21) for θ between 0 and $\pi/2$. Figure 14 shows that the h values are little affected by the z values between $z = 0$ to 1 but they are slightly lower when $z > 1$ and $0 < \theta < \pi/2$. However, in general, the values of h/h_o decrease as θ increases, pass through a minimum when θ is slightly larger than $\pi/2$, and then increase.

Discussion and Remarks

The method described is mathematically simple and com-

putationally fast. It has flexibilities that are unique to Monte Carlo. For instance, it is not required for the random walk to remain at preselected lattice points. Even with a small step size, it can be treated similarly to the floating random walk (Haji-Sheikh, 1988). This means that the random walk wanders everywhere in the domain, thereby accommodating complex boundary shapes. Also, heterogeneous bodies can be handled without a major change in the procedure.

One important feature of the Monte Carlo method transcends the statistical estimate of the unknown parameters. This feature enhances our ability to observe physical phenomena and often develop other analytical or numerical solution methods. The inverse problem is no exception as it introduces a procedure that can be used by various numerical and closed-form solution methods. Here, the Monte Carlo method is used to calculate the elements of matrix \mathbf{A} , Eq. (4). The computation of the elements of matrix \mathbf{A} is a direct conduction problem and can be done numerically or analytically. For example, one can use a function of time and space as the surface temperature and calculate column 1 of matrix \mathbf{A} . Then, use the second, third, and later functions as the individual surface temperature and calculate entries for columns 2, 3, and so on. If these chosen functions are independent and complete, the surface temperature is a linear combination of them. The remaining steps are standard matrix algebra, independent of the particular solution method, and Eq. (7) yields the coefficients. It is recommended to normalize the square matrix ($\mathbf{A}^T \cdot \mathbf{A}$) in order to avoid computer overflow.

The method of calculating the surface heat flux is similar to that for calculating the surface temperature. However, since a random walk will not terminate where surface heat flux is prescribed, the duration of a random walk can become excessively large. One way to improve the computation time is to subdivide the time domain into smaller subdomains and simultaneously calculate both temperature and heat flux. Consequently, the random walk will be terminated faster since the temperature is known initially and during earlier time intervals, while the heat flux remains unknown within a small time interval. Of course, one can always solve for the surface temperature and use a direct method such as finite difference to calculate the surface heat flux, as shown in Example 3.

Conclusion

The Monte Carlo method is a simple and accurate method

for solving various inverse heat conduction problems. The computation time for the one-dimensional problem was negligibly small. Using a personal DOS computer with a 486-25 processor, the computational time for data in Fig. 10 was the largest, less than 30 minutes. The programming effort for Monte Carlo is minimal yet it provides accurate surface temperature values. Another interesting feature of the Monte Carlo method presented in this paper is that the complexity of the material domain and the geometric shape of the region will not significantly alter the computer programming efforts or the computation time.

Acknowledgments

The authors acknowledge the financial support of Trinity Forge, Inc., of Mansfield, Texas, and technical support of S. Lindemann of Combustion Components Associates, Inc.

References

- Beck, J. V., 1968, "Surface Heat Flux Determination Using an Integral Method," *Nuclear Engineering and Design*, Vol. 7, pp. 170-178.
- Beck, J. V., Blackwell, B., and St. Clair, C. R., Jr., 1985, *Inverse Heat Conduction Ill-Posed Problems*, Wiley-Interscience Pub., New York.
- Eckert, E. R. G., and Drake, R. M., 1972, *Analysis of Heat and Mass Transfer*, McGraw-Hill, New York.
- Haji-Sheikh, A., 1988, "Monte Carlo Methods," *Handbook of Numerical Heat Transfer*, Chap. 16, W. J. Minkowycz et al., eds., Wiley, pp. 673-722.
- Hildebrand, F. B., 1956, *Introduction to Numerical Analysis*, McGraw-Hill, New York.
- Incropera, F. P., and DeWitt, D. P., 1990, *Fundamentals of Heat and Mass Transfer*, Wiley, New York.
- Jarny, Y., Ozisik, M. N., and Bardou, J. P., 1991, "A General Optimization Method Using Adjoint Equation for Solving Multidimensional Inverse Heat Conduction," *Int. J. Heat Mass Transfer*, Vol. 34, No. 11, pp. 2911-2919.
- Lindemann, S., 1991, "Laboratory Characterization of an Air Atomized, Low Flow Fog Nozzle," Combustion Components Associates, Inc. Report, Sept. 11.
- Murio, D. A., 1989, "The Mollification and the Numerical Solution of the Inverse Heat Conduction Problem by Finite Difference," *Comput. Math Applic.*, Vol. 17, No. 10, pp. 1385-1396.
- Sparrow, E. M., Haji-Sheikh, A., and Lundgren, T. S., 1964, "The Inverse Problem in Heat Conduction," *ASME Journal of Applied Mechanics*, Vol. 31, No. 3, pp. 369-375.
- Stolz, G., Jr., 1960, "Numerical Solutions to an Inverse Problem of Heat Conduction for Simple Shapes," *ASME JOURNAL OF HEAT TRANSFER*, Vol. 82, pp. 20-26.
- Woodbury, K. A., 1991, "Determination of Surface Heat Fluxes During Spray Quenching of Aluminum Using an Inverse Technique," ASME Paper No. 91-WA/HT-12.

Laser Beam Welding With Simultaneous Gaussian Laser Preheating

Y.-N. Liu
Graduate Student.

E. Kannatey-Asibu, Jr.
Associate Professor.

Department of Mechanical Engineering
and Applied Mechanics,
The University of Michigan,
Ann Arbor, MI 48109

An analytical solution of the dual laser beam welding process is presented. It is based on a Gaussian distributed leading heat source for preheating, followed by a line source for the actual welding process. The effect of beam distribution parameters as well as interbeam spacing and relative power intensities on the resulting temperature distribution and cooling rate are presented. For a preheating Gaussian source of power 1550 W, the depth of region above 500°C is 2.25 mm, and that above 250°C is 3.5 mm. The cooling rate at the weld centerline without preheating for a temperature of 650°C, input power 1800 W, and welding velocity 20 mm/s is found to be 1004°C/s. Under the same conditions, the cooling rate with a 1550 W preheating Gaussian distributed heat source (beam distribution parameter 1 mm, and interbeam spacing 10 mm) is reduced to 570°C/s.

Introduction

Laser beam welding (LBW) is a relatively new field in welding research that is not yet fully understood. Some of its characteristics give this high power intensity process great potential for the future. For example, the beam can be focused to a small radius that results in a smaller weld width, deeper penetration, and a smaller heat-affected zone size. It is also easy to control the irradiance by regulation of the current through the electric discharge. Other advantages include minimal contamination and the ability to manipulate the beam irradiance into ordinarily inaccessible areas by using mirrors or reflectors.

However, there are certain disadvantages associated with the laser beam welding process. In addition to the high capital cost of the equipment, the high energy intensity results in high cooling rates, which cause undesirable brittle microstructures in the workpiece, especially for high hardenability materials. To reduce the cooling rate, the workpieces are normally preheated before welding. This creates an additional step in the process, which reduces productivity. Furthermore, the traditional preheating is done on the entire workpiece, usually in a furnace, and is not limited to the welding area. This not only wastes energy, but may also affect other portions of the workpiece.

To improve this condition, the laser beam-splitting concept for welding is introduced. This is illustrated schematically in Fig. 1. The original laser beam is first split into two. One of the beams is used as a preheating energy source, the minor or leading heat source, which is then defocused and impinges on the workpiece. The other beam, the major or follower heat source, is the energy source for actual welding. This dual-beam laser welding solves the problems of conventional preheating, and because it combines preheating with the actual welding process, one step in the overall process is eliminated. It is also easy to control the preheating area by defocusing the minor heat source to heat up only the welding area, and thus not affect the rest of the workpiece.

In earlier work (Kannatey-Asibu, 1989, 1991), a preliminary analysis of the dual beam laser process was undertaken. Both the major and minor heat sources were modeled as point heat sources. This paper involves more realistic models for the heat sources with the major heat source (for actual welding) being

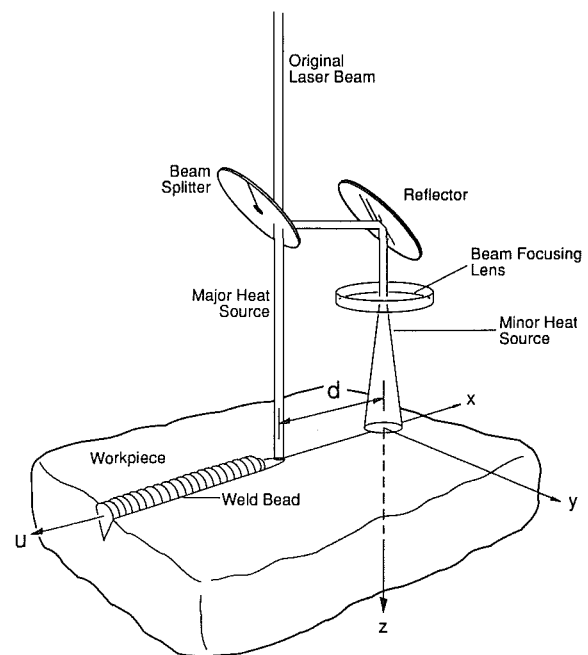


Fig. 1 Schematic of the split-beam laser welding system

assumed to be a line source, because of its deep penetration and keyhole effect. The minor heat source (for preheating) is modeled as a Gaussian distributed heat source, because it is to be defocused to cover a relatively wide area, and the material in this region is not expected to melt. At a certain point $x = -20$ mm, $y = z = 0$, the cooling rate is 2901°C/s in the point source model, but it is 1136.4°C/s in our new line-Gaussian model for the same conditions of the major and minor heat sources of 1800 W and 1550 W, respectively, and the material used is AISI 316. The effect of beam distribution parameters, interbeam spacing, and relative power intensity on temperature distribution and cooling rate are analyzed.

Background

The differential equation of conduction of heat in a body is given by (Arpaci, 1966):

$$\rho c \frac{dT}{dt} - \nabla \cdot (k \nabla T) - q = 0 \quad (1)$$

where ρ is the density of the material, c the specific heat, k

Contributed by the Heat Transfer Division and presented at the ASME Winter Annual Meeting, Anaheim, California, November 8-13, 1992. Manuscript received by the Heat Transfer Division May 1992; revision received August 1992. Keywords: Conduction, Laser Processing, Materials Processing and Manufacturing Processes. Associate Technical Editor: Y. Bayazitoglu.

the thermal conductivity, q the energy generation per unit volume within the medium, t is time, and T is the gage temperature.

For a moving medium of constant thermal conductivity, Eq. (1) reduces to the linear form:

$$\frac{\partial T}{\partial t} + \mathbf{V} \cdot \nabla T - \alpha \nabla^2 T - \frac{q}{\rho c} = 0 \quad (2)$$

where α is thermal diffusivity, and \mathbf{V} is the velocity vector of the moving medium. The temperature distribution for point and line sources in infinite media are available (Carslaw and Jaeger, 1959). Cline and Anthony (1977) found the temperature distribution due to a Gaussian laser beam on the surface of a solid. That produced by a scanning elliptical CW laser beam was obtained by Nissim et al. (1980). Transient temperature profiles in solids heated with a scanning Gaussian circular laser beam were also obtained by Chen and Lee (1983). The temperature rise produced by the absorption of a scanning Gaussian laser beam in a solid has been analyzed by Sanders (1984). An estimation of the effects of processing conditions and variable properties upon pool shape, cooling rates, and absorption coefficient in laser welding has been done by Chande and Mazumder (1984). An analysis of using two intersecting beams in laser machining was proposed by Chryssolouris et al. (1988). For dual heat source welding, the effect of two point heat sources has also been investigated (Kannatey-Asibu, 1989, 1991).

Analysis

This analysis is based on conduction in the workpiece only. The material properties are assumed to be temperature independent, and heat loss due to convection and radiation at the top of the workpiece is neglected. We also neglect the latent heat in this analysis. A steady-state temperature distribution is obtained, and cooling rate is calculated from this information.

We define a Cartesian coordinate system with origin at the center of the leading (minor) heat source on the surface of the

workpiece, Fig. 1. Positive x is in the welding direction, while the workpiece moves in the negative x direction with speed u , i.e., the velocity $\mathbf{V} = (u, 0, 0)$ in Eq. (2), where $u < 0$ in this case. Positive z is into the workpiece, and y is defined as the vector product of z and x to satisfy the right-hand rule. The workpiece is assumed to be semi-infinite, i.e., $-\infty < x, y < \infty$, and $0 \leq z < \infty$.

The initial conditions of the problem are then given by:

$$T(x, y, z, 0) = 0, \text{ everywhere in the domain.} \quad (3)$$

The boundary conditions are (for $t > 0$):

$$T(x, y, z, t) = 0 \text{ for } \begin{cases} x, y \rightarrow \pm \infty, \\ z \rightarrow \infty. \end{cases} \quad (4)$$

Since convection and radiation heat losses at the top surface of the workpiece are neglected, the boundary condition at the work surface, $z = 0$, is:

$$-k \frac{\partial T(x, y, z, t)}{\partial z} = 0 \text{ at } z = 0 \quad (5)$$

To satisfy this boundary condition, i.e., Eq. (5), we use the imaginary heat source technique. For any real point heat source in the region (x', y', z') , we assume that there is a corresponding imaginary heat source at $(x', y', -z')$ of the same strength as the real source. We also assume an infinite medium instead of a semi-infinite one. This makes the temperature field symmetric about the $z = 0$ plane, i.e., there is no heat transfer across the work surface ($z = 0$). Equation (4) then becomes:

$$T(x, y, z, t) = 0 \text{ for } x, y, z \rightarrow \pm \infty \quad (6)$$

The imaginary heat source technique simplifies the analysis. Suppose that at time $t = t'$, a unit heat pulse is emitted at (x', y', z') , and that an infinite medium moves uniformly past (x', y', z') with velocity $\mathbf{V} = (u, 0, 0)$, $u < 0$, parallel to the x axis. The gage temperature at the fixed point (x, y, z) and time t due to the unit heat pulse emitted at (x', y', z') and time t' is (Carslaw and Jaeger, 1959):

Nomenclature

c = specific heat	volume of the minor heat source	(x', y', z') = the location of a point in the heat source zone
d = interbeam spacing	q_2 = power supply per unit length of the major heat source	$\mathbf{V} = (u, 0, 0)$ = velocity vector of the moving medium
G = Green's function	R = reflectivity	α = thermal diffusivity of workpiece
g = gravitational acceleration	Ra = Rayleigh number	α_a = thermal diffusivity of air
h_{cv} = convection heat transfer coefficient	r = cooling rate (time rate of temperature drop)	β = beam power absorption coefficient
I = normal intensity	t = time	β_a = thermal expansion coefficient of air
k = thermal conductivity of the workpiece	t' = time that heat is applied	λ = keyhole depth
k_a = thermal conductivity of air	T = gage temperature (above ambient)	μ = n -dimensional mean vector
Nu = Nusselt number	T_{abs} = absolute temperature of the workpiece (in K)	ν_a = kinematic viscosity of air
P_1 = power supply of the minor heat source	T_1 = gage temperature due to the effect of the minor heat source	ρ = density of the workpiece
P_2 = power supply of the major heat source	T_2 = gage temperature due to the effect of the major heat source	σ = beam distribution parameter
P_{cv} = power loss due to convection	T_m = gage melting temperature	σ_{SB} = Stefan-Boltzmann constant
P_{ra} = power loss due to radiation	(x, y, z) = coordinate system at-	
q = power generation per unit volume within the medium		
q_1 = power supply per unit		

$$G(x, y, z, t) = \frac{1}{8\rho c[\pi\alpha(t-t')]^{3/2}} \times e^{-\left[\frac{[x-u(t-t')-x']^2 + (y-y')^2 + (z-z')^2}{4\alpha(t-t')}\right]} \quad (7)$$

Since Eq. (2) is linear, we obtain separate solutions for the individual heat sources and use superposition, provided a common coordinate system is used.

We neglect the latent heat in this analysis because the latent heat of melting is compensated by the latent heat of resolidification. Latent heat absorbed at the melting interface is liberated at the solidifying interface, which alters the temperature distribution somewhat but does not significantly affect the penetration depth (Cline and Anthony, 1977; Mazumder and Steen, 1980).

We first consider the leading Gaussian source. The general formulation for a multivariate normal intensity is given (Duda and Hart, 1973) by:

$$I(\mathbf{x}) = \frac{1}{(2\pi)^{n/2} |\Sigma|^{1/2}} \times e^{-1/2(\mathbf{x}-\mu)^T \Sigma^{-1} (\mathbf{x}-\mu)} \quad (8)$$

where \mathbf{x} is an n -dimensional column vector, μ is the n -dimensional mean vector, $|\Sigma|$ is the determinant of the $n \times n$ covariance matrix, and the superscripts T and -1 indicate transpose and inverse, respectively. For a bivariate Gaussian distribution centered at the origin, $\mathbf{x} = \begin{bmatrix} x' \\ y' \end{bmatrix}$, $\mu = \begin{bmatrix} 0 \\ 0 \end{bmatrix}$,

$n = 2$, $\Sigma = \begin{bmatrix} \sigma_x^2 & 0 \\ 0 & \sigma_y^2 \end{bmatrix}$, and Eq. (8) reduces to:

$$I \begin{bmatrix} x' \\ y' \end{bmatrix} = \frac{1}{2\pi \left| \begin{bmatrix} \sigma_x^2 & 0 \\ 0 & \sigma_y^2 \end{bmatrix} \right|^{1/2}} \times e^{-\frac{1}{2} [x' \ y'] \begin{bmatrix} \sigma_x^2 & 0 \\ 0 & \sigma_y^2 \end{bmatrix}^{-1} \begin{bmatrix} x' \\ y' \end{bmatrix}} \quad (9)$$

For a circular beam where the beam distribution parameters in the x and y directions are the same, i.e., $\sigma_x = \sigma_y = \sigma$, we have a planar heat distribution of:

$$I(x', y') = \frac{1}{2\pi\sigma^2} \times e^{-\frac{1}{2\sigma^2}(x'^2 + y'^2)} \quad (10)$$

Since the absorption in the z direction in a solid medium results in exponential attenuation (Wilson and Hawkes, 1987), the heat supply in the material per unit volume and unit time at a point (x', y', z') and time t' can then be expressed for a constant Gaussian power source P_1 as:

$$q_1(x', y', z') = \frac{\beta P_1(1-R)}{2\pi\sigma^2} \times e^{-\left[\frac{x'^2 + y'^2}{2\sigma^2} + \beta z'\right]} \quad \text{for } 0 \leq z < \infty \quad (11)$$

where β is the beam power absorption coefficient, which is a property of the base material, and is about 800 m^{-1} for mild steel (Mazumder and Steen, 1980), and 600 m^{-1} for AISI 316 steel (Kim, 1991). R is the reflectivity, the value of which is about 0.3 (Kim, 1991). If we consider the real and imaginary heat sources, q_1 becomes:

$$q_1(x', y', z') = \frac{\beta P_1(1-R)}{2\pi\sigma^2} \times e^{-\left[\frac{x'^2 + y'^2}{2\sigma^2} + \beta |z'| \right]} \quad \text{for } -\infty < z < \infty \quad (12)$$

where $|z'|$ is the absolute value of z' , so that q_1 is symmetric to the $z = 0$ plane. The amount of heat that is liberated in an

elemental volume at (x', y', z') and time interval dt' is $dQ_1 = q_1(x', y', z') dx' dy' dz' dt'$.

Thus for a Gaussian source of power P_1 , and a medium moving with velocity $\mathbf{V} = (u, 0, 0)$, the temperature rise over the period $t' = 0$ to t over the body is:

$$T_1(x, y, z, t) = \int_0^t \int_{-\infty}^{\infty} \int_{-\infty}^{\infty} \int_{-\infty}^{\infty} q_1(x', y', z') \times G(x', y', z', t' | x, y, z, t) dx' dy' dz' dt' \\ = \int_0^t \int_{-\infty}^{\infty} \int_{-\infty}^{\infty} \int_{-\infty}^{\infty} \frac{\beta P_1(1-R)}{2\pi\sigma^2} \times e^{-\left[\frac{x'^2 + y'^2}{2\sigma^2} + \beta |z'| \right]} \times \frac{1}{8\rho c[\pi\alpha(t-t')]^{3/2}} \times e^{-\left[\frac{[x-u(t-t')-x']^2 + (y-y')^2 + (z-z')^2}{4\alpha(t-t')}\right]} \times dx' dy' dz' dt' \quad (13)$$

which reduces to:

$$T_1(x, y, z, t) = \int_0^t \frac{\beta P_1(1-R)}{4\pi\rho c[\sigma^2 + 2\alpha(t-t')]^{1/2}} e^{\left[\alpha\beta^2(t-t') - \frac{[x-u(t-t')]^2 + y^2}{4\alpha(t-t') + 2\sigma^2}\right]} \times \left[e^{\beta z} \text{erfc}\left(\beta\sqrt{\alpha(t-t')} + \frac{z}{2\sqrt{\alpha(t-t')}}\right) + e^{-\beta z} \text{erfc}\left(\beta\sqrt{\alpha(t-t')} - \frac{z}{2\sqrt{\alpha(t-t')}}\right) \right] dt' \quad (14)$$

where $\text{erfc}(x)$ is the complementary error function, which is defined by:

$$\text{erfc}(x) = \frac{2}{\sqrt{\pi}} \int_x^{\infty} e^{-\xi^2} d\xi. \quad (15)$$

We now consider the line source. The laser beam is parallel to and directed in the positive z direction impinging on the surface $z = 0$ from time $t' = 0$. At high-power densities, the material melts, and a keyhole is formed that enables the laser beam to penetrate deeply into the interior of the material. As the laser power increases, the depth of penetration increases (Cline and Anthony, 1977). We again consider the imaginary heat source technique and assume uniform distribution of the heat source along the z direction. The center of the major heat source is at $x = -d$ and $y = 0$, behind the minor Gaussian source, with d as the distance between the centers of the two sources. If P_2 is the total power of this line source, the heat supply in the medium per unit length and unit time is:

$$q_2(x', y', z') = P_2 \frac{h(z')}{\lambda} \quad \text{for } \begin{cases} x' = -d \\ y' = 0 \\ -\infty < z' < \infty \end{cases} \quad (16)$$

where λ is the keyhole depth, and h is a function of z' :

$$h(z') = \begin{cases} 1 & \text{for } -\lambda \leq z' \leq \lambda \\ 0 & \text{for } |z'| > \lambda \end{cases} \quad (17)$$

Modeling the major heat source as a line source with uniform power distribution along the keyhole depth is an approximation for a thick material. However, since our current objective is to elucidate the theoretical viability of the general concept of dual beam welding, we use the simpler approach for now. However, the more realistic exponential function in the z direction will be incorporated into subsequent analyses. The keyhole depth is determined from the experimental results of

other researchers. For AISI 316 stainless steel, the keyhole depth is found to be 3 mm for a 1800 W laser power with 20 mm/s welding speed (Kim, 1991). The heat conduction is two dimensional close to the keyhole when z is less than the keyhole depth, but it becomes three dimensional at the bottom of the keyhole for a thick plate.

Thus, for the line source of power P_2 in a medium moving with velocity $\mathbf{V} = (u, 0, 0)$, the temperature rise over the period $t' = 0$ to t over the body is:

$$T_2 = \int_0^t \int_{-\lambda}^{\lambda} \frac{P_2(1-R)/\lambda}{8\rho c[\pi\alpha(t-t')]^{3/2}} \times e^{-\left[\frac{[x-u(t-t')+d]^2+y^2+(z-z')^2}{4\alpha(t-t')}\right]} dz' dt' \quad (18)$$

which reduces to:

$$T_2(x, y, z, t) = \int_0^t \frac{P_2(1-R)/\lambda}{8\rho c[\pi\alpha(t-t')]^{3/2}} e^{-\frac{[x-u(t-t')+d]^2+y^2}{4\alpha(t-t')}} \times \left[\operatorname{erfc}\left(\frac{z-\lambda}{2\sqrt{\alpha(t-t')}}\right) - \operatorname{erfc}\left(\frac{z+\lambda}{2\sqrt{\alpha(t-t')}}\right) \right] dt' \quad (19)$$

T_1 and T_2 are obtained by numerical integration. We first use Δt as a time step, which is about 10^{-10} s in the region close to the center of the heat sources and about 1 s in the region far away from the heat source. We use Simpson's rule in each time step, repeating until the steady-state temperature is obtained. A smaller time step $\Delta t/2$ is then used, again with Simpson's rule to obtain the steady-state solution for this smaller time step. The steady-state temperatures obtained from these two different time steps are then compared, and if the difference between them is less than 1°C , then steady state is considered to be achieved. Otherwise, even smaller time steps $\Delta t/4$, $\Delta t/8$, $\Delta t/16$. . . are used until the steady-state temperature converges (Burden and Faires, 1989). Since a common coordinate system is used, the total temperature rise is obtained by superposition. We only consider steady-state temperature distribution in this analysis because the system approaches steady state in seconds. The cooling rate (the time rate of temperature drop) is given by:

$$r = -\frac{dT}{dt} = -\frac{\partial T}{\partial t} - \frac{\partial T}{\partial x} \frac{dx}{dt} \quad (20)$$

When steady state is reached, the first term on the right-hand side of the above equation can be eliminated. The cooling rate then becomes:

$$r = -\frac{dT}{dt} = -\frac{\partial T}{\partial x} \frac{dx}{dt} = -u \frac{\partial T}{\partial x} \quad (21)$$

Results and Discussion

Since heat loss by convection and radiation was neglected in the analysis, we first provide justification for this. The heat loss at the top surface of the workpiece by natural convection, P_{cv} , can be calculated by:

$$P_{cv} = \int_A h_{cv} T dA \quad (22)$$

where A is the surface area, T is the temperature difference between the plate and ambient, and h_{cv} is the heat transfer coefficient, which can be determined from the Rayleigh number. The Rayleigh number Ra is given by:

$$Ra = \frac{g\beta_a TL^3}{\nu_a \alpha_a} \quad (23)$$

where g is the acceleration due to gravity, 9.8 m/s^2 , β_a is the coefficient of thermal expansion of air, $0.001/\text{K}$, T is gage temperature, L is a characteristic length (we use the width of the heat effected zone as L), ν_a is the kinematic viscosity of air, $121.9 \times 10^{-6} \text{ m}^2/\text{s}$, α_a is the thermal diffusivity of air, $168 \times 10^{-6} \text{ m}^2/\text{s}$, and the thermal conductivity of air, $k_a = 0.0667 \text{ W/m K}$ (Incropera and DeWitt, 1985).

The Nusselt number Nu is related to the Rayleigh number by:

$$Nu = \frac{h_{cv} L}{k_a} = 0.15 Ra^{1/3} = 0.15 \left(\frac{g\beta_a TL^3}{\nu_a \alpha_a} \right)^{1/3} \quad (24)$$

Thus, $h_{cv} = 0.31 T^{1/3}$, which gives $P_{cv} = \int_A h_{cv} T dA = 0.264 \text{ (W)}$ for the conditions used.

The radiation power loss P_{ra} can be obtained by the Stefan-Boltzmann law:

$$P_{ra} = \int_A \epsilon \sigma_{SB} (T_{abs}^4 - T_{\infty abs}^4) dA \quad (25)$$

where ϵ is the emissivity, which is 0.4 for oxidized stainless steel (Incropera and DeWitt, 1985), σ_{SB} is the Stefan-Boltzmann constant, $5.67 \times 10^{-8} \text{ W/m}^2\text{K}^4$, T_{abs} and $T_{\infty abs}$ are the absolute plate and ambient temperatures in degrees Kelvin, respectively. The radiation power loss obtained on this basis is $P_{ra} = 10.5 \text{ W}$.

Both the convection and radiation heat losses are small compared to the total power input (1550 W + 1800 W), so they can be neglected.

In determining T_2 from Eq. (19), we need to know the keyhole depth λ , which is a function of the power input P_2 , welding speed u , and material properties. It is determined by experimental results. For AISI 316 steel with $P_2 = 1800 \text{ W}$, $R = 0.3$, and $u = -20 \text{ mm/s}$, we found $\lambda = 3 \text{ mm}$ from the experimental data by Kim (1991). For this material, the thermal conductivity $k = 24 \text{ W/mK}$, the thermal diffusivity $\alpha = 4.5 \times 10^{-6} \text{ m}^2/\text{s}$, $\rho c = k/\alpha = 5.3 \times 10^3 \text{ J/m}^3\text{K}$ and melting temperature $T_m = 1500^\circ\text{C}$ (Kim, 1991). For a fixed laser power, λ decreases with increasing welding speed, because it takes time for the heat to penetrate the material, and the motion of the medium also carries energy away. For a given welding speed, higher power results in a deeper penetration depth, for example, for $u = -20 \text{ mm/s}$, $\lambda = 3 \text{ mm}$ for $P_2 = 1800 \text{ W}$, but $\lambda = 2 \text{ mm}$ for $P_2 = 900 \text{ W}$ for AISI 316 steel (Kim, 1991).

We use $P_2 = 1800 \text{ W}$ and $u = -20 \text{ mm/s}$ (the workpiece moves in the negative x direction) as an example, which results in an absorption depth of 3 mm. The interbeam spacing is 10 mm and the beam distribution parameter, σ , which determines the shape and size of the area covered by the Gaussian distributed laser beam (the minor heat source), is 1 mm. The power of the Gaussian minor heat source is 1550 W. Figure 2 is the gage temperature distribution at the work surface, $z = 0$, for these conditions. The peak temperature at the center of the major source is higher than the melting temperature. The gage temperature at the center of the minor source is 1226°C , which is lower than the melting temperature of the material, which is thus solid in this region.

Figures 3(a), 3(b), and 3(c) show the isothermal lines for the temperature effect due to the minor heat source in the $y = 0$ plane for $P_1 = 2000$, 1550, and 1000 W, respectively. A typical preheating temperature is 250°C (Kou, 1987). The depth of the isothermal line $T_1 = 250^\circ\text{C}$ directly beneath the minor heat source is about 4 mm for $P_1 = 2000 \text{ W}$, 3.5 mm for $P_1 = 1550 \text{ W}$, and 2.8 mm for $P_1 = 1000 \text{ W}$, and thus these are the respective depths to which the preheating would be effective. The higher the input power, the deeper the preheated depth, which is preferable for thick plates or deep penetration welding. For the major heat source conditions given, the first two of these preheating sources should be adequate. Also, because the preheated area is larger for high preheating power,

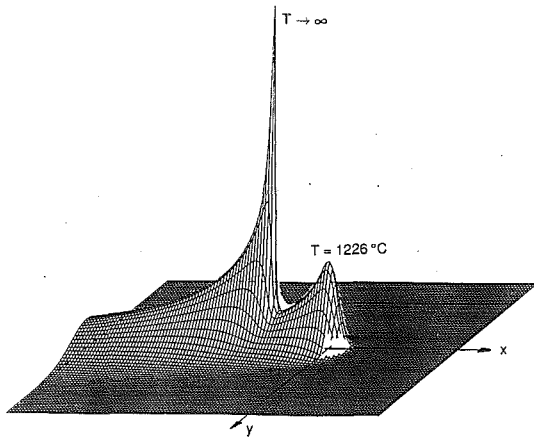


Fig. 2 Gage temperature distribution at the workpiece surface ($P_1 = 1550$ W, $P_2 = 1800$ W, $d = 10$ mm, $\sigma = 1$ mm, and welding velocity 20 mm/s)

a larger interbeam spacing can be used in this case. However, the high peak temperature of the high-power case may result in melting of the base metal, which is undesirable for preheating. From Fig. 3(b), the temperature at $z = 3.5$ mm is 250°C for $P_1 = 1550$ W, and the peak temperature is lower than the melting temperature. Thus, for illustration, we choose $P_1 = 1550$ W with $P_2 = 1800$ W, since it results in a penetration depth of 3 mm, which is covered by the preheating area.

Figure 4(a) shows the isothermal lines on the work surface. For the conditions used, the high-temperature region appears to be small, with the region above 250°C covering an area only about 8 mm wide. As expected, the temperature gradient in the x direction, which is linearly proportional to the cooling rate for a constant welding velocity, is highest along the weld center line. Figure 4(b) illustrates the isothermal lines along the weld center line, $y = 0$. We find that the radius of the region with temperature greater than the melting temperature of the material is rather small, about 1 mm wide, and that of the case without preheating is about 0.7 mm. The penetration is also shown, which is 3.0 mm. For a given temperature isotherm, the penetration of the minor heat source is smaller than that of the major heat source because the power density of the former is smaller. The keyhole is also shown in this figure. The temperature distribution around the keyhole is two dimensional (x and y dependence only), but in the regions deeper than the keyhole, it becomes three dimensional. Figure 4(c) shows the cooling rate with 1550 W preheating at the $x = -20$ mm cross section, 10 mm behind the major heat source. The cooling rate distribution is symmetric to the $y = 0$ plane, and the highest cooling rate occurs at the weld bead.

The metallurgical effects of thermal cycles depend not only on the cooling rate but also on the temperature at which that cooling rate is experienced. The solid-state phase transformation in steels normally occurs in the temperature range of 500 to 800°C . For a varying Gaussian leading heat source of power 1000, 1550, and 2000 W, together with a fixed major heat source of 1800 W, the corresponding cooling rates along the weld centerline for different temperatures are shown in Fig. 5. The higher the preheating power, the lower the cooling rate, a consequence of the preheating effect. At $T = 800^\circ\text{C}$ ($x = -16.9$ mm), the cooling rate is 1525°C/s without any preheating, but it reduces to 890°C/s for 1550 W preheating at $T = 800^\circ\text{C}$ ($x = -22$ mm). The difference in cooling rates is more significant at higher temperatures. This is because the higher temperature region is closer to the minor heat source, where the preheating effect is accentuated. At $x = -23.2$ mm, where $T = 500^\circ\text{C}$, the cooling rate is 600°C/s without preheating, but it becomes 340°C/s with 1550 W preheating at $x = -33$ mm, where again $T = 500^\circ\text{C}$.

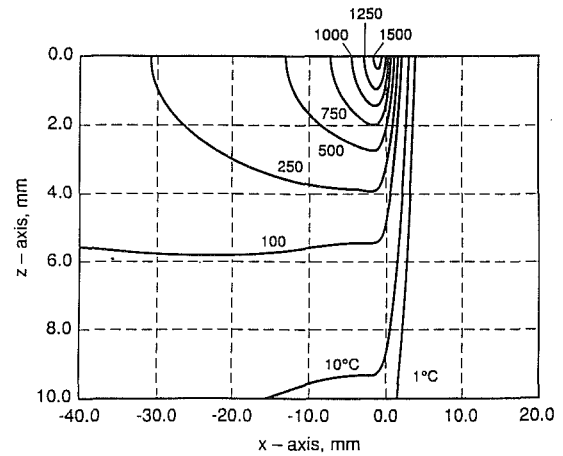


Fig. 3(a) $P_1 = 2000$ W

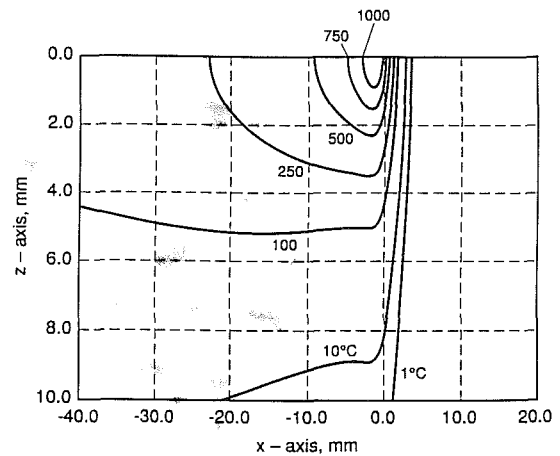


Fig. 3(b) $P_1 = 1550$ W

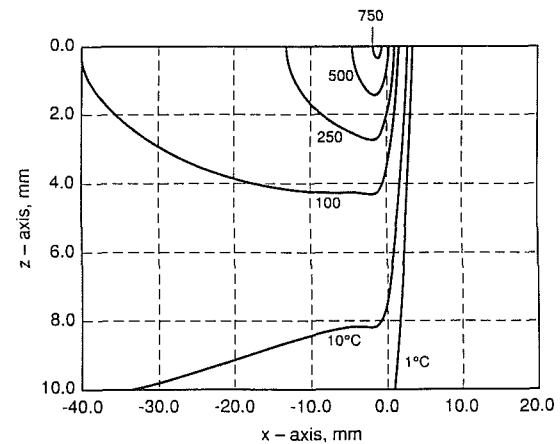


Fig. 3(c) $P_1 = 1000$ W

Fig. 3 Isothermal lines due to the minor heat source in the plane $y = 0$, and into the plate

The larger the beam distribution parameter σ , the larger the defocused area of the minor beam, and that implies a lower power density, i.e., power per unit area. That reduces the peak temperature and penetration, but broadens the preheated area. Figure 6 shows the Gaussian temperature distribution for three cases, $\sigma = 1$ mm, 2 mm, and 3 mm. With the same power input, 1550 W, the temperature distribution and cooling rate in the region far behind the heat source are almost the same for all three cases. Near the heat source, the temperature dis-

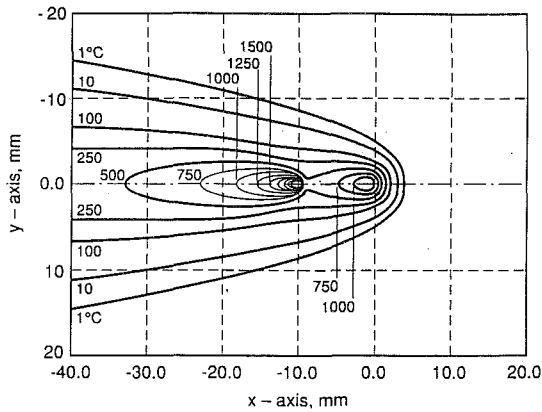


Fig. 4(a) Isothermal lines on the work surface ($P_1 = 1550$ W, $P_2 = 1800$ W, $d = 10$ mm, $\sigma = 1$ mm, and welding velocity 20 mm/s)

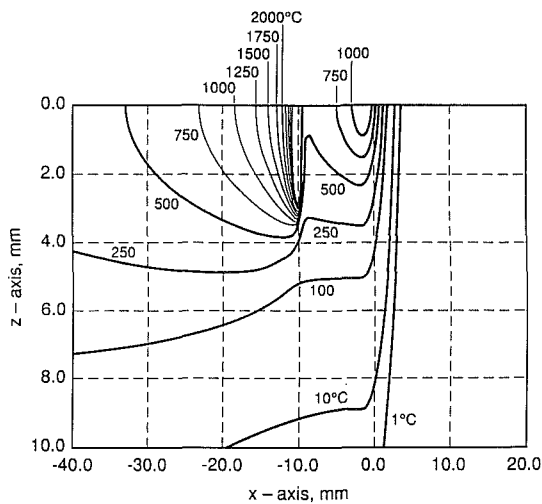


Fig. 4(b) Isothermal lines along the weld center line, $y = 0$, and into the plate ($P_1 = 1550$ W, $P_2 = 1800$ W, $d = 10$ mm, $\sigma = 1$ mm, and welding velocity 20 mm/s)

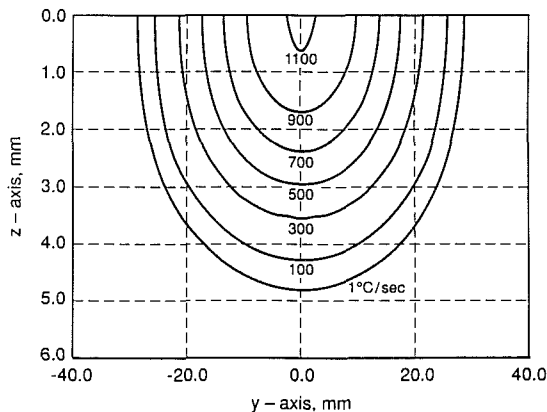


Fig. 4(c) Cooling rate distribution at the $x = -20$ mm cross section with $P_2 = 1800$ W and 1550 W preheating

tribution depends on the details of the heat source intensity. In particular, if a fixed amount of energy is deposited over a smaller area, it will initially heat a smaller volume of material, so the temperature rise will be greater. However, further away from the heat source, diffusion has caused the energy input to spread out into the entire workpiece. Therefore, for a fixed workpiece volume and a fixed power input, the temperature rise far from the heat source approaches a fixed value.

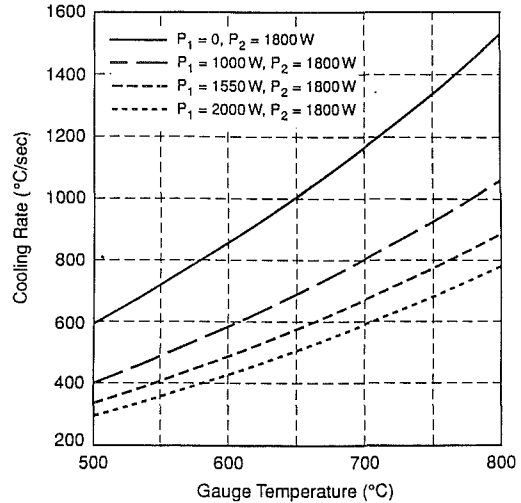


Fig. 5 Cooling rates for a major power input of 1800 W and various minor power inputs

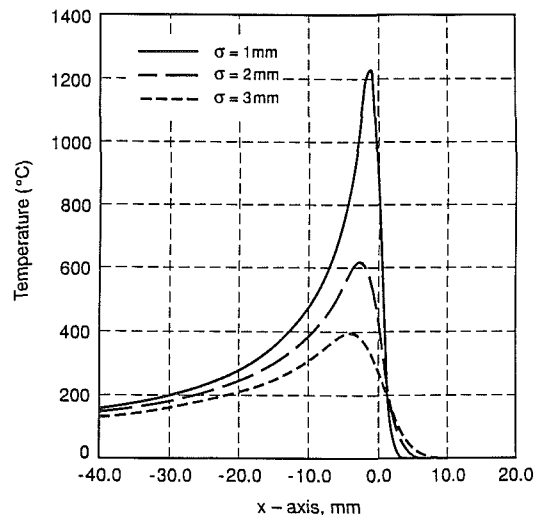


Fig. 6 Temperature distribution at the weld centerline due to various Gaussian distribution parameters of the minor heat sources

We increase the power of the minor heat source to 4940 W to make the peak temperature of $\sigma = 3$ mm equal to that of $\sigma = 1$ mm and preheating power of 1550 W. Figure 7(a) shows the temperature distribution of this condition. The peak temperatures of these two cases are the same, but the temperature at $x = -40$ mm is 156°C for $\sigma = 1$ mm, and $T = 406^\circ\text{C}$ for $\sigma = 3$ mm at the same location. It implies that if we have the same peak temperature for different σ , the larger σ requires more energy because of lower energy intensity, and the temperature will be higher than the smaller σ case for a given location, but then the cooling rate will be higher. On the other hand, if we look at the cooling rate at a certain temperature, the cooling rate for larger σ would be lower. The cooling rates of the resulting temperature field due to both the major and minor heat sources of various σ and P_1 (cases of Fig. 7(a)), for the temperature range between 500°C and 800°C are shown in Fig. 7(b) ($P_2 = 1800$ W). It shows that for the same power input, even though the difference in cooling rates is rather small, the smaller σ results in a lower cooling rate, but for the same peak temperature, $P_1 = 1550$ W for $\sigma = 1$ mm and $P_1 = 4940$ W for $\sigma = 3$ mm, the cooling rate is much lower for the latter.

Figure 8 shows the temperature distribution for a Gaussian distributed heat source in the plane $y = 0$, i.e., along the

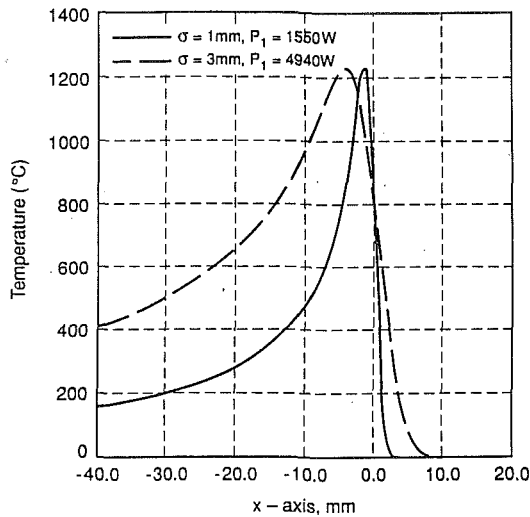


Fig. 7(a) Temperature distribution at the welding centerline due to the minor heat source, for $\sigma = 1$ mm, $P_1 = 1550$ W and $\sigma = 3$ mm, $P_1 = 4940$ W, which have the same peak temperature of 1226°C

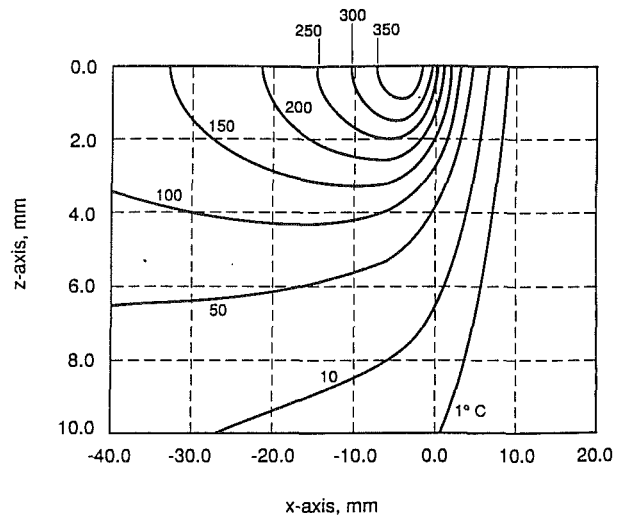


Fig. 8 Isothermal lines in the plane $y = 0$, and into the plate, for $\sigma = 3$ mm and same condition as Fig. 3(b)

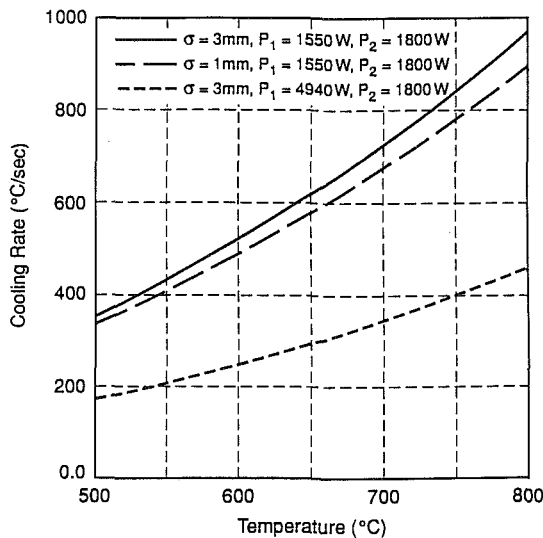


Fig. 7(b) Cooling rates due to both heat sources, for $\sigma = 3$ mm, $P_1 = 1550$ W; $\sigma = 1$ mm, $P_1 = 1550$ W and $\sigma = 3$ mm, $P_1 = 4940$ W. Major heat source is constant at 1800 W.

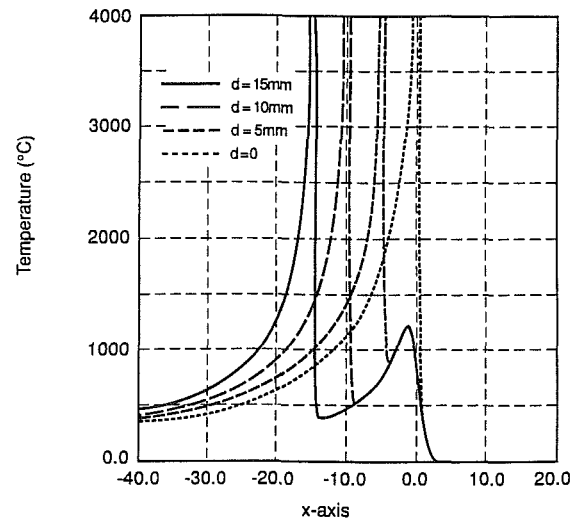


Fig. 9(a) Temperature distribution at the weld center line for different interbeam spacings with the same power inputs

welding center line, and into the plate, with $\sigma = 3$ mm. Compared with Fig. 3(b), for which $\sigma = 1$ mm, penetration is larger for smaller σ , because of the higher power density. For $T = 250^\circ\text{C}$, the isotherm line is 3.5 mm deep for $\sigma = 1$ mm. For $\sigma = 3$ mm, it is only 2 mm deep for the same temperature.

Figure 9(a) shows the temperature distribution for various interbeam spacings, $d = 0, 5, 10,$ and 15 mm. The center of the minor heat source is fixed at the origin, while the major source center is moved to $x = -d$ and $y = 0$. The input power of the major heat source is 1800 W, and the minor heat source 1550 W, $\sigma = 1$ mm, and welding velocity is 20 mm/s. The weld pool size is larger for the smaller interbeam spacing, which is about 6.25 mm long and 1.2 mm wide for $d = 0$, but 3.5 mm long and 0.8 mm wide for $d = 15$ mm. The penetration is also deeper for the smaller interbeam spacing, which is 3 mm for $d = 10$ mm, but 3.5 mm for $d = 0$. Figure 9(b) illustrates the cooling rates for various interbeam spacings in the temperature range of 500 to 800°C . For a certain temperature rise, the cooling rate of $d = 0$ is the smallest. However, the problem is one of producing a weld of a given penetration, say 3 mm in a plate of that thickness, while minimizing the

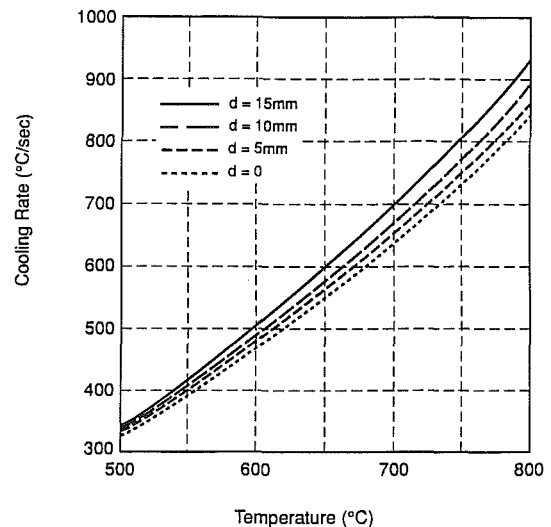


Fig. 9(b) Cooling rates due to both heat sources for different interbeam spacings with the same power inputs

cooling rate to prevent the formation of brittle microstructures, and also without burn-through. Thus we first need to determine the major heat source power that will produce the desired penetration, and then determine the appropriate minor heat source parameters that would minimize the cooling rate without increasing the penetration.

Summary

The results of the analysis indicate that:

- For the same power of the major heat source, a higher power preheating results in a lower cooling rate for a given temperature, and the higher the temperature, the larger the difference.
- The impact of the Gaussian distribution parameter σ on the temperature distribution and cooling rate is found to be generally small, even though the peak temperature is lower and the weld width larger for larger σ .
- The weld pool size increases as the interbeam spacing is decreased. The corresponding cooling rate, on the other hand, increases for a given location, but decreases at a given temperature with decreasing interbeam spacing.

Acknowledgments

Support of this work by the National Science Foundation under grant No. DDM-9114148 is gratefully acknowledged.

References

- Arpaci, V. S., 1966, "Equation of Conduction," in: *Conduction Heat Transfer*, Addison-Wesley, Reading, MA, pp. 44-46.
- Burden, R. L., and Faires, J. D., 1989, "Numerical Differentiation and Integration," *Numerical Analysis*, PWS-KENT Publishing Company, Boston, MA, pp. 145-217.
- Carslaw, H. S., and Jaeger, J. C., 1959, "The Use of Sources and Sinks in Cases of Variable Temperature," in: *Conduction of Heat in Solids*, 2nd ed., Oxford University Press, Oxford, United Kingdom, pp. 265-270.
- Chande, T., and Mazumder, J., 1984, "Estimating Effects of Processing Conditions and Variable Properties Upon Pool Shape, Cooling Rate, and Absorption Coefficient in Laser Welding," *J. Applied Physics*, Vol. 56, No. 7, pp. 1981-1986.
- Chen, I., and Lee, S., 1983, "Transient Temperature Profiles in Solids Heated With Scanning Laser," *J. Applied Physics*, Vol. 54, pp. 1062-1066.
- Chryssoulouris, G., Bredt, J., Kordas, S., and Wilson, E., 1988, "Theoretical Aspects of a Laser Machine Tool," *ASME Journal of Engineering for Industry*, Vol. 110, pp. 65-70.
- Cline, H. E., and Anthony, T. R., 1977, "Heat Treating and Melting Material With a Scanning Laser or Electron Beam," *J. Applied Physics*, Vol. 48, pp. 3895-3900.
- Duda, R. O., and Hart, P. E., 1973, "Bayes Decision Theory," *Pattern Classification and Scene Analysis*, Wiley, New York, pp. 10-43.
- Incropera, F. P., and DeWitt, D. P., 1985, "Free Convection," in: *Fundamentals of Heat and Mass Transfer*, Wiley, New York, pp. 418-455.
- Kannatey-Asibu, E., Jr., 1989, "Split-Beam Laser Welding," in: *Recent Trends in Welding Science and Technology*, S. A. David and J. M. Vitek, eds., ASM International, Materials Park, OH, pp. 443-451.
- Kannatey-Asibu, E., Jr., 1991, "Thermal Aspects of the Split-Beam Laser Welding Concept," *ASME Journal of Engineering Materials and Technology*, Vol. 113, pp. 215-221.
- Kim, J. D., 1991, "Parametric Evaluations of CO₂ Laser Beam Welding," *ASME Symposium on Welding and Joining Processes*, E. Kannatey-Asibu, Jr., H. S. Cho, and S. Fukuda, eds., ASME PED-Vol. 51, pp. 195-202.
- Kou, S., 1987, "Transformation-Hardening Materials: Carbon and Alloy Steels," *Welding Metallurgy*, Wiley, New York, pp. 334-347.
- Mazumder, J., and Steen, W. M., 1980, "Heat Transfer Model for CW Laser Material Processing," *J. Applied Physics*, Vol. 51, No. 2, pp. 941-947.
- Nissim, Y. I., Lietoila, A., Gold, R. B., and Gibbons, J. F., 1980, "Temperature Distributions Produced in Semiconductors by a Scanning Elliptical or Circular CW Laser Beam," *J. Applied Physics*, Vol. 51, No. 1, pp. 274-279.
- Sanders, D. J., 1984, "Temperature Distributions Produced by Scanning Gaussian Laser Beams," *Applied Optics*, Vol. 23, No. 1, pp. 30-35.
- Wilson, J., and Hawkes, J. F. B., 1987, "Industrial, Medical, and Military Applications," *Lasers, Principles and Applications*, Prentice Hall International, Englewood Cliffs, NJ, pp. 165-189.

Heat Transfer Within a Concrete Slab Applying the Microwave Decontamination Process

W. Li

M. A. Ebadian

Department of Mechanical Engineering,
Florida International University,
Miami, FL 33199

T. L. White

Fusion Energy Division.

R. G. Grubb

Chemical Technology Division.

Oak Ridge National Laboratory,
Oak Ridge, TN 37831

Decontamination of a radioactive contaminated concrete surface is a new technology for the treatment of radioactive waste. In this paper, concrete decontamination using microwave technology is investigated theoretically. A plane wave assumption of microwave propagation has been employed to estimate the microwave field and power dissipation within the concrete. A one-dimensional, unsteady heat conduction model with microwave heat dissipation resulting from microwave-material interaction has been used to evaluate frequency, steel reinforcement within the concrete, and thermal boundary conditions are also considered in the present model. Four commonly used microwave frequencies of 0.896, 2.45, 10.6, and 18.0 GHz have been utilized in the analysis. The results revealed that as the microwave frequency increases to, or higher than 10.6 GHz, the microwave power dissipation shifts toward the front surface of the concrete. Furthermore, it was observed that use of a higher frequency microwave could reduce power intensity requirements needed to raise the temperature difference or thermal stress to the same value in the same period of time. It was found that the presence of reinforcing steel mesh causes part of the microwave energy to be blocked and reflected. Thus, the temperature or thermal stress of the concrete increases before the reinforcement, and decreases after the reinforcement.

1 Introduction

Concrete has been used extensively for structural and radiation shielding purposes in nuclear installations. Over a period of time, as a consequence of irradiation or contamination, concrete may become radioactive on the exposed surface to a depth varying from millimeters to about ten centimeters, depending on the radiation history. At some stage, this radioactive contaminated concrete must be removed for disposal as low-level radioactive waste. The manner in which it is removed may have important implications for radioactive waste management. For example, waste treatment and disposal routes may be influenced by such factors as fragment size, quantity of dust, and the generation of secondary radioactive materials, such as water or gases from the demolition process. A range of demolition techniques often carried out by remote control exists that may be suitable for the removal of radioactive contaminated concrete. This includes sawing, stitch-drilling, impact breaking, high-pressure water cutting, thermic lancing, explosives, and expanding agents placed in drilling holes. All of the above processes generate dust or gases, or waste water, and most involve the application of force against the concrete surface requiring a robust and powerful manipulator.

Although millions of people use microwave ovens for daily cooking, applications of microwaves to industrial and scientific processing are still very limited. Some successful industrial applications of microwaves are thawing of frozen meat, vulcanization of rubber, commercial processing of bacon, and drying pasta, which have been described by Okress (1968) and Copson (1975). In the past decade, microwave technology has been applied to process many dielectric materials (Tinga and Nelson, 1973). More recently, microwave energy has been applied to remove contaminated concrete. Several groups, e.g., Yasunaka et al. (1987), in Japan, Hills (1989), in Europe, and White et al. (1992), in the United States, have begun developing

the new processes that use this technology in concrete decontamination. Presently, only a few publications (papers and/or reports) of this technology are available. This application is still in the early stages of research and the products of this technology have not been seen on the market yet.

The microwave heating process takes place inside the material, the depth of which governs how strongly the microwaves are absorbed, as one heats food in a microwave oven. The heat dissipated from the microwave energy depends on many conditions, such as the geometry and configuration of the concrete wall or block, the microwave field distribution, the microwave power level, and the dielectric and magnetic properties of the concrete material. Variation of the temperature distribution within the concrete depends on the thermal properties, heat dissipated from the microwave field, the geometry, and the thermal boundary conditions of the concrete wall or block. Finally, with constant ambient temperature, the microwave heating pattern will induce a nonuniform temperature distribution within the concrete, resulting in the highest temperature being located beneath the concrete surface. Therefore, the corresponding stress distribution will exceed the tensile strength of the concrete to spall off the contaminated concrete layer, as discussed by Hills (1989), White (1990), and White et al. (1992).

Decontamination of the concrete surface by microwave heating is a new technology in radioactive waste management. With respect to the advantages of microwave heating to remove the contaminated concrete layer, it is seen to have many positive aspects: (a) No secondary material is produced (e.g., gases, cutting or cooling liquids); (b) there is minimal or no contact between the concrete surface and the microwave applicator, thereby permitting the use of a lightweight manipulator; (c) dust generation is low; and (d) there is controlled, precise stripping of the concrete.

A theoretical investigation of heat transfer within a concrete slab under microwave heating has been carried out in the present paper. The objective of this paper is to investigate the variation of the temperature or thermal stress distribution

Contributed by the Heat Transfer Division for publication in the JOURNAL OF HEAT TRANSFER. Manuscript received by the Heat Transfer Division January 1992; revision received June 1992. Keywords: Conduction, Thermophysical Properties, Transient and Unsteady Heat Transfer. Associate Technical Editor: L. S. Fletcher.

within the concrete under certain circumstances. A plane microwave assumption and a one-dimensional unsteady heat conduction model with microwave heat dissipation are employed to investigate the variations of the microwave energy dissipation and the temperature distribution within the concrete. The major parameters affecting the concrete decontamination, such as microwave frequency, steel reinforcement, and thermal boundary conditions are considered in this model. The results of time-averaged microwave power dissipation ($P_{d,ave}L/P_{0,ave}$), and the variation of the dimensionless temperature distribution $(T - T_\infty)/(P_{0,ave}L/k)$, or dimensionless thermal stress $(-\sigma_{zz}k)/(\alpha EP_{0,ave}L)$, versus the dimensionless concrete thickness for different microwave frequencies (f) and microwave reflection (ρ_{sm}) are presented. The spatial average temperature before and after the steel reinforcement, θ_{sp} , versus microwave reflection (ρ_{sm}) for different microwave frequencies (f) are also illustrated. The effects of microwave frequency (f), microwave energy reflection from steel reinforcement (ρ_{sm}) and the thermal boundary condition (Biot number, Bi) on the front surface of the concrete and on variations of the temperature or thermal stress distributions are fully discussed in the present analysis.

2 Problem Formulation

A full model of concrete decontamination using microwave technology would require a vast number of parameters to be taken into consideration. Principally, an accurate evaluation of the microwave field, which determines heat dissipation within the concrete, is very important. After the microwave field is determined, the rate of heat dissipation can be calculated. This heat dissipation will determine the temperature distribution and its variation within the concrete. Usually, during the heating process, the difference between the maximum temperature and the lowest surface temperature could be in the range of 150–200°C. Since the relevant variations of dielectric and thermal properties of temperature for concrete are not yet available, a model for both the microwave field and the temperature field with constant magnetic, dielectric, and thermal properties is applied in order to understand the decontamination process further.

2.1 The Microwave Field. Microwaves are electromagnetic waves having frequencies from 300 MHz. to 300 GHz. Therefore, microwaves should satisfy Maxwell's equation, which describes electromagnetic fields, as illustrated by Wait (1985). For the plane wave propagating in the z direction, the electric and magnetic field vectors (\mathbf{e} and \mathbf{h}) can be assumed as:

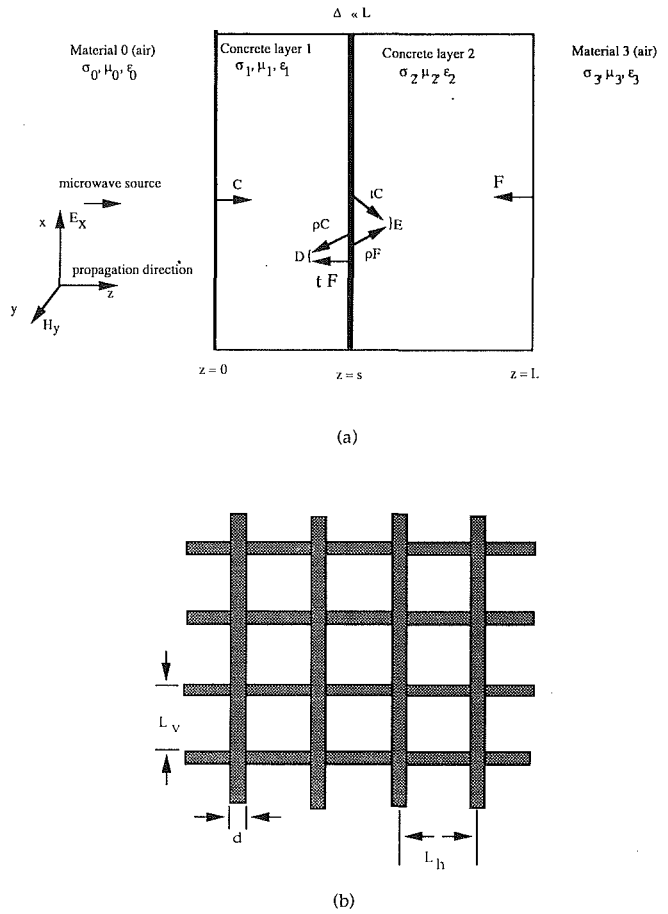


Fig. 1 Geometry of the concrete slab and the steel reinforcement mesh: (a) geometry of the concrete slab; (b) geometry of the steel reinforcement mesh within the concrete

$$\mathbf{e} = E_x e^{i\omega t} n_x, \text{ and } \mathbf{h} = H_y e^{i\omega t} n_y, \quad (1)$$

and the Maxwell equation for the plane wave propagating in the z direction can be simplified as:

$$\frac{dE_x}{dz} = i\mu\omega H_y \quad (2)$$

$$\frac{dH_y}{dz} = -(\sigma + i\omega\epsilon^*)E_x, \quad (3)$$

Nomenclature

A = complex constant
 B = complex constant
 Bi = Biot number = hL/k
 C = complex constant, Eq. (12)
 C_p = specific heat of the concrete, $J kg^{-1} K^{-1}$
 D = complex constant, Eq. (14)
 d = diameter of the steel reinforcement bar, m
 E = modulus of elasticity, Pa
 E_0 = amplitude of the initial electric field, $V m^{-1}$
 E_x = electric potential for the plane wave assumption, $V m^{-1}$
 \mathbf{e} = electric field vector, $V m^{-1}$
 F = complex constant, Eq. (15)
 f = microwave frequency, s^{-1} Hz
 f_n = constant, Eq. (30)

G = complex constant, Eq. (13)
 H_y = magnetic potential for the plane wave assumption, $A m^{-1}$
 h = heat transfer coefficient $W m^{-2} K^{-1}$
 \mathbf{h} = magnetic field vector, $A m^{-1}$
 Im = imaginary part of a complex number
 i = imaginary number = $\sqrt{-1}$
 k = thermal conductivity, $W K^{-1} m^{-1}$
 L = thickness of the concrete, m
 L_h = distance between the horizontal steel reinforcement bars, m
 L_v = distance between the vertical steel reinforcement bars, m
 N_n = constant, Eq. (32)

n = unit surface vector, m
 P_0 = power density, $W m^{-2}$
 P_d = power dissipation per unit volume, $W m^{-3}$
 q = dimensionless heat generation = $P_{d,ave}L/P_{0,ave}$
 Re = real part of a complex number
 r = complex constant determined by the dielectric properties, Eq. (7)
 s = distance at which the steel reinforcement is located, m
 T = temperature, K
 t = time, s
 t_{sm} = fraction of the microwave energy passed through the steel reinforcement = $1 - \rho_{sm}$
 v = arbitrary value, either θ or $P_{d,ave}$, Eq. (36)

with boundary conditions on the front and rear surfaces of the concrete slab:

$$E_{x0} = E_{x1}, \quad H_{y1}; \quad E_{x2} = E_{x3}, \quad H_{y2} = H_{y3} \quad (4)$$

where E_x and H_y are the amplitude of the electric and magnetic field vectors, respectively; μ is the magnetic permeability; ϵ^* is the complex dielectric permittivity; σ is the electric conductivity of the concrete, respectively; and n_x and n_y are the unit vectors in the x and y directions, respectively.

The general solution of these plane wave equations can be obtained in the following manner:

$$E_x = Ae^{-rz} + Be^{r'z} \quad (5)$$

$$H_y = \frac{1}{\eta} (Ae^{-rz} - Be^{r'z}), \quad (6)$$

Based on the above assumptions and boundary conditions, the electric and magnetic fields within the concrete can be solved as:

$$E_x = E_0(Ce^{-r_1z} + De^{r_1z}), \quad \text{for } 0 \leq z < s \quad (8)$$

$$H_y = \eta_1^{-1} E_0(Ce^{-r_1z} - De^{r_1z}), \quad \text{for } 0 \leq z < s \quad (9)$$

and

$$E_x = E_0(Fe^{-r_2z} + Ge^{r_2z}), \quad \text{for } s < z \leq L \quad (10)$$

$$H_y = \eta_2^{-1} E_0(Fe^{-r_2z} - Ge^{r_2z}), \quad \text{for } s < z \leq L \quad (11)$$

where E_0 is the wave amplitude determined by the incident power density. C , D , F , and G are constants determined by the magnetic and dielectric properties and the geometric configuration of the concrete slab:

$$C = \frac{2\eta_1[(\eta_3 + \eta_2) - \rho_{sm}(\eta_3 - \eta_2)e^{-2r_2L}]}{(\eta_3 + \eta_2)(\eta_1 + \eta_0)\rho_{sm}(\eta_3 + \eta_2)(\eta_1 - \eta_0) + (t_{sm}^2 - \rho_{sm}^2)(\eta_3 - \eta_2)(\eta_1 - \eta_0)e^{-2r_2L}} \quad (12)$$

in which

$$r = \sqrt{i\mu\omega(\sigma + i\omega\epsilon^*)} \quad \text{and} \quad \eta = \sqrt{i\mu\omega/(\sigma + i\omega\epsilon^*)}. \quad (7)$$

One can now consider a concrete slab consisting of two concrete layers that sandwich a reinforcement steel mesh at the location of $z = s$, as shown in Fig. 1(a). The front surface at $z = 0$ is exposed directly to the microwave source. Two concrete layers could have different magnetic and dielectric properties ($\mu_1, \epsilon_1, \sigma_1$ and $\mu_2, \epsilon_2, \sigma_2$), but the variations of these properties with the heating process (temperature) are assumed to be constant. As is generally known, concentration of ferromagnetic material in concrete is negligible. Therefore, the difference in the permeabilities of the concrete layers (μ_1 and μ_2) and the free-space (air) (μ_0) can also be neglected.

The steel reinforcement within the concrete is treated as a thin layer (Δ) of mixture of steel and concrete. The layer (Δ) is assumed as uniform reflection and transmission. The layer thickness (Δ) is very small and might be totally neglected, but it has certain magnetic, dielectric, and electric properties, which cause part of the microwave energy to be reflected. The fraction of the reflection (ρ_{sm}) is equal to the fraction of the cross-sectional area of the concrete slab taken up by the steel mesh (Hills, 1989). For example, the steel reinforcement, consisting of 2.5-cm-dia bars ($d = 2.5$ cm) on a 25 cm vertically and horizontally ($L_v = L_h = 25$ cm), is shown in Fig. 1(b). The reflection, $\rho_{sm} = [(L_v + L_h)d - d^2]/(L_v L_h) = 0.19$, and the steel mesh could pass a fraction of incident microwave energy ($t_{sm} = 0.81$).

$$G = \frac{t(\eta_3 - \eta_2)e^{-2r_2L}C}{(\eta_3 + \eta_2) - \rho_{sm}(\eta_3 - \eta_2)e^{-2r_2L}} \quad (13)$$

$$D = \rho_{sm}C + t_{sm}G \quad (14)$$

$$F = t_{sm}C + \rho_{sm}G. \quad (15)$$

The constants r and η are complex values, as well as the constants C , D , F , and G . Thus, the final solution of E_x and H_y is complex.

2.2 Incident Power and Power Dissipation. In electric and magnetic fields for the free-space (air) before interfacing with the concrete slab, the power density (P_0) carried by microwaves has the following relation with the wave amplitude (cf. Balanis, 1989):

$$P_0 = [\text{Re}(E_0 e^{i\omega t})]^2 / (120\pi). \quad (16)$$

According to Metaxas and Meredith (1983), the microwave power dissipation within the concrete (P_d) is related to the electric field (E_x) and effective dielectric loss (ϵ_{eff}), by

$$P_d = \omega\epsilon_{eff}[\text{Re}(E_x e^{i\omega t})]^2. \quad (17)$$

Since the frequencies of microwaves are very high (from 300 MHz to 300 GHz), the time scale of the variation of the microwave field is much smaller than that of the temperature variation in the concrete. Therefore, one can then separate the sinusoidal variation of the microwave with the unsteady heat

Nomenclature (cont.)

Y_n = n th eigenfunction, Eq. (31)

x, y = coordinates, m

z = coordinate of the wave propagation direction, m

α = thermal expansion coefficient, K^{-1}

α_T = thermal diffusivity, $m^2 s^{-1}$

Δ = thickness of layer of steel reinforcement, m

ϵ^* = complex dielectric permittivity = $\epsilon' - i\epsilon''$, $F m^{-1}$

ϵ' = real part of the complex dielectric permittivity $F m^{-1}$

ϵ'' = imaginary part of the complex dielectric permittivity $F m^{-1}$

ϵ_0 = permittivity of the free-space (air), $8.86 \times 10^{-12} F m^{-1}$

ϵ_{eff} = effective dielectric loss = $\epsilon'' + \sigma/\omega$, $F m^{-1}$

η = complex constant, Eq. (7)

θ = dimensional temperature = $(T - T_\infty)/(P_{0,ave}L/k)$

λ_n = n th eigenvalue, Eq. (33)

μ = magnetic permeability, Henries m^{-1}

μ_0 = permeability of the free-space (air), $4\pi \times 10^{-7}$, Henries m^{-1}

ξ = dimensionless coordinate = z/L

ρ = density, $kg m^{-3}$

ρ_{sm} = fraction of the energy reflected from the steel reinforcement = $1 - t_{sm}$

σ = electric conductivity, Ohm^{-1}

σ_c = compressive strength, Table 1

σ_{zz} = thermal stress in the z direction, Pa

τ = dimensionless time

ω = microwave angle frequency = $2\pi f$, $rad s^{-1}$

ΔT = temperature difference = $T - T_\infty$, [K]

Subscripts

ave = time average

sp = spatial average, Eq. (34)

x, y = components in the x or y direction

0 = material 0, free-space (air)

1 = material 1, concrete layer 1 ($0 \leq z \leq 0.1$ m)

2 = material 2, concrete layer 2 ($0.1 \text{ m} < z \leq 0.6$ m)

3 = material 3, free-space (air)

transport phenomena and use the time-averaged value of the incident power ($P_{0,ave}$) and power dissipation ($P_{d,ave}$):

$$P_{0,ave} = \frac{1}{120\pi} \frac{\omega}{2\pi} \int_0^{2\pi/\omega} [\text{Re}(E_0 e^{i\omega t})]^2 dt$$

$$= \frac{E_0^2}{120\pi} \frac{\omega}{2\pi} \int_0^{2\pi/\omega} \cos^2(\omega t) dt = \frac{E_0^2}{240\pi} \quad (18)$$

and

$$P_{d,ave} = \omega \epsilon_{eff} \frac{\omega}{2\pi} \int_0^{2\pi/\omega} [\text{Re}(E_x e^{i\omega t})]^2 dt$$

$$= \frac{\omega \epsilon_{eff}}{2} [\text{Re}^2(E_x) + \text{Im}^2(E_x)]. \quad (19)$$

2.3 Heat Transfer Within the Concrete. The temperature distribution and variation within the concrete, which determines the concrete spall off, is dependent on the thermal properties, microwave heat generation, and the thermal boundary conditions of the concrete. When the concrete is subjected to microwave attack, part of the microwave energy is dissipated as heat within the concrete.

A one-dimensional model of heat transport within the concrete is used to evaluate the unsteady temperature distribution along the propagation direction at different frequencies with and without the presence of reinforcing mesh. The thickness of the steel reinforcement mesh is also neglected in the concrete when the heat transport is considered. The thermal properties (k , thermal conductivity, and α_T , thermal diffusivity) are assumed to be constants. The governing equation for the heat transport can be written as:

$$\rho C_p \frac{\partial T}{\partial t} = k \frac{\partial^2 T}{\partial z^2} + p_{d,ave} \quad (20)$$

with the initial condition stated as being:

$$T = T_\infty \quad \text{at } t \leq 0, \quad (21)$$

in which $P_{d,ave}$ is the time-averaged microwave power dissipation.

When both sides of the concrete slab are maintained at the convective boundary condition, with the heat transfer coefficients (h_1 and h_2), the boundary conditions will have the following forms:

$$h_1(T - T_\infty) - k_1 \frac{\partial T}{\partial z} = 0, \quad \text{at } z = 0 \quad (22)$$

$$h_2(T - T_\infty) + k_2 \frac{\partial T}{\partial z} = 0, \quad \text{at } z = L, \quad (23)$$

where k_1 and k_2 are the concrete thermal conductivities for the front and back layers, respectively. The above boundary conditions reduce to the constant wall temperature condition when the heat transfer coefficients, h_1 and h_2 , approach infinity (∞).

By defining the following parameters:

$$\theta = \frac{T - T_\infty}{P_{0,ave} L / k}, \quad \xi = z/L, \quad \tau = \alpha_T t / L^2, \quad (24)$$

$$\text{Bi} = \frac{hL}{k}, \quad \text{and} \quad q = \frac{P_{d,ave} L}{P_{0,ave}}$$

the governing equation and the initial and boundary conditions can be obtained as:

$$\frac{\partial \theta}{\partial \tau} = \frac{\partial^2 \theta}{\partial \xi^2} + q \quad (25)$$

$$\theta = 0, \quad \text{at } \tau \leq 0 \quad (26)$$

$$\text{Bi}_1 \theta - \frac{\partial \theta}{\partial \xi} = 0, \quad \text{at } \xi = 0. \quad (27)$$

Table 1 Reference values of the properties of concrete

Properties	Description	Value
Composition	Composition, expressed as ratios to the cement content are:	
	20 mm crushed limestone aggregate	3.19
	sand	2.59
	cement (ordinary Portland)	1.00
	Water	0.60
	Density of cement content of concrete	300 kg m ⁻³
	Derivation: Komarovski (1961)	
Density of Concrete (ρ)	By inference from the cement content	
	Derivation: Komarovski (1961)	2,300 kg m ⁻³
Specific Heat (Cp)	Derivation: Ursu (1985)	650 J kg ⁻¹ K ⁻¹
Thermal Conductivity (k)	Derivation: Ursu (1985)	0.87 W m ⁻¹ K ⁻¹
Relative Permittivity, real part, (ϵ'/ϵ_0)	Derivation: Von Hippel (1954), Hasted and Shah (1964)	7.0
Relative Permittivity, imaginary part, (ϵ''/ϵ_0)	Derivation: Von Hippel (1954), Hasted and Shah (1964)	0.2
Thermal Expansion Coefficient (α)	Derivation: Mindess and Young (1981)	11.0 × 10 ⁻⁶ K ⁻¹
Compressive Strength (σ_c)	Derivation: Hills (1989)	50 MPa
Modulus of Elasticity (E)	Derivation: Mindess and Young (1981)	30 GPa

$$\text{Bi}_2 \theta + \frac{\partial \theta}{\partial \xi} = 0, \quad \text{at } \xi = 1 \quad (28)$$

The final temperature distribution can be solved and expressed as:

$$\theta(\xi, \tau) = \sum_{n=1}^{\infty} \frac{f_n}{\lambda_n^2} (1 - e^{-\lambda_n^2 \tau}) Y_n(\xi) \quad \text{for } \tau > 0, \quad 0 \leq \xi \leq 1, \quad (29)$$

where

$$f_n = \int_0^1 q(\xi) Y_n(\xi) d\xi, \quad (30)$$

$$Y_n(\xi) = \frac{1}{\sqrt{N_n}} \left[\frac{\lambda_n}{\text{Bi}_1} \cos(\lambda_n \xi) + \sin(\lambda_n \xi) \right], \quad n = 0, 1, 2, \dots, \infty, \quad (31)$$

$$N_n = \int_0^1 \left[\frac{\lambda_n}{\text{Bi}_1} \cos(\lambda_n \xi) + \sin(\lambda_n \xi) \right]^2 d\xi$$

$$= \frac{\lambda_n^2}{\text{Bi}_1^2} \left[\frac{1}{2} - \frac{1}{4\lambda_n} \sin(2\lambda_n) \right] + \frac{1}{\text{Bi}_1} \sin^2(\lambda_n)$$

$$+ \frac{1}{2} + \frac{1}{4\lambda_n} \sin(2\lambda_n), \quad n = 0, 1, 2, \dots, \infty, \quad (32)$$

in which the eigenvalue (λ_n) can be obtained by solving the following equation:

$$(\text{Bi}_1 - \text{Bi}_2) \lambda_n + (\lambda_n^2 + \text{Bi}_1 \text{Bi}_2) \tan \lambda_n = 0, \quad n = 0, 1, 2, \dots, \infty. \quad (33)$$

2.4 Thermal Stresses. The stress distribution depends on the thermal stress and the loading condition of the concrete. Without the external loadings, the stress is determined by thermal stress, which is dependent on the temperature distribution. The thermal stress distribution for the present one-dimensional problem can be related to the temperature distribution (cf. Johns, 1965):

$$\sigma_{zz} = -\alpha E \Delta T \quad (34)$$

where σ_{zz} is the thermal stress in the z direction; α is the thermal expansion coefficient of the concrete; E is the modulus of elasticity of the concrete, and ΔT is temperature difference ($T - T_\infty$). By definition, the compression stress is positive and the tension stress is negative.

By applying the dimensionless temperature, Eq. (24), the

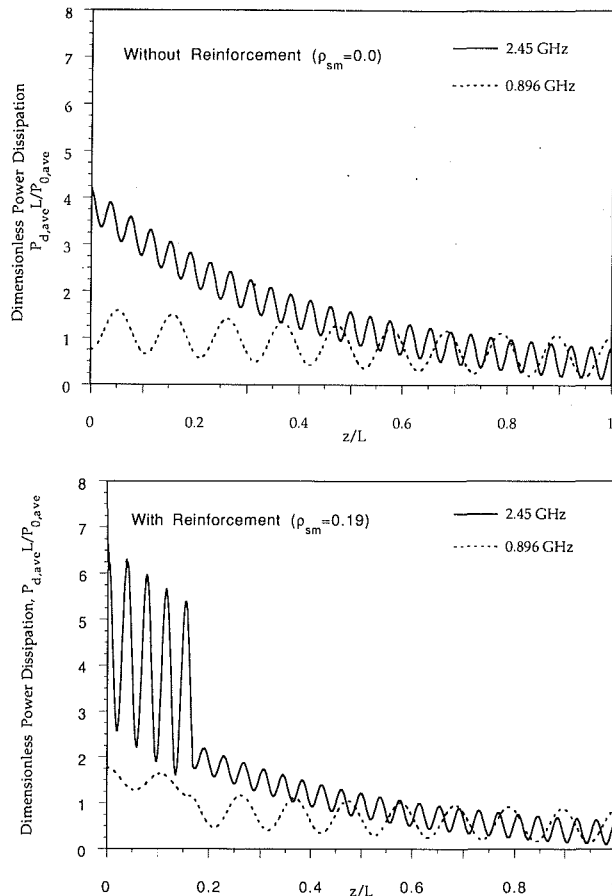


Fig. 2 Dimensionless power dissipation ($P_{d,ave}L/P_0$) within a 0.6 concrete slab for 0.896 and 2.45 GHz: (a) without steel reinforcement; (b) with steel reinforcement ($\rho_{sm} = 0.19$) at $z = 0.1$ m

relation between thermal stress and dimensionless temperature can be obtained as:

$$\sigma_{zz} = -\alpha E \frac{P_{0,ave}L}{k} \theta. \quad (35)$$

This indicates that the thermal stress (σ_{zz}) is proportional to the dimensionless temperature distribution (θ). Therefore, thermal stress will have the same behavior as the dimensionless temperature distribution.

3 Results and Discussion

In this section, a 0.6-m-thick concrete slab is considered based on the available concrete properties. The effects of microwave frequencies and the steel mesh reinforcement located at 0.1 m from the front surface on microwave power dissipation and the dimensionless temperature/thermal stress are discussed. The composition, and the magnetic, dielectric, and thermal properties of the concrete used in the analysis are listed in Table 1. In the microwave industry, only a few frequencies are available. Currently, four commonly used frequencies, 0.896, 2.45, 10.6, and 18.0 GHz are utilized.

3.1 Microwave Power Dissipation. It is known from Eq. (19) that the dimensionless microwave power dissipation ($P_{d,ave}L/P_{0,ave}$) depends on microwave field (E_x) and effective dielectric loss (ϵ_{eff}), where the microwave field (E_x) will be affected by the geometry (L) and configuration (s, ρ_{sm}). In Figs. 2(a) and 2(b), the microwave power dissipations ($P_{d,ave}L/P_{0,ave}$) for 0.896 GHz and 2.45 GHz frequencies, without and with steel reinforcement in the concrete, are presented. For higher frequencies, the oscillating period of the power dissi-

Table 2 Maximum dimensionless temperature and thermal stress at power intensity of $P_{0,ave} = 5 \times 10^4$ W/m² for different microwave frequencies without steel reinforcement ($\rho_{ms} = 0.0$)

Time (sec)	Microwave Frequency, f			
	$f = 0.896$ GHz	$f = 2.45$ GHz	$f = 10.6$ GHz	$f = 18.0$ GHz
	$\theta_{max} \setminus \sigma_{zz}$ (MPa)	$\theta_{max} \setminus \sigma_{zz}$ (MPa)	$\theta_{max} \setminus \sigma_{zz}$ (MPa)	$\theta_{max} \setminus \sigma_{zz}$ (MPa)
60	6.9 \ 0.79	18.2 \ 2.08	63.9 \ 7.27	94.4 \ 10.74
120	13.3 \ 1.52	34.0 \ 3.86	113.4 \ 12.90	163.0 \ 18.54
180	19.3 \ 2.19	49.3 \ 5.61	156.8 \ 17.83	220.0 \ 25.03
240	25.1 \ 2.86	65.1 \ 7.41	196.7 \ 22.39	269.8 \ 30.78
300	30.7 \ 3.50	80.6 \ 9.20	234.3 \ 26.66	315.0 \ 35.84

Table 3 Maximum dimensionless temperature and thermal stress at power intensity of $P_{0,ave} = 5 \times 10^4$ W/m² for different microwave frequencies with steel reinforcement ($\rho_{ms} = 0.19$)

Time (sec)	Microwave Frequency, f			
	$f = 0.896$ GHz	$f = 2.45$ GHz	$f = 10.6$ GHz	$f = 18.0$ GHz
	$\theta_{max} \setminus \sigma_{zz}$ (MPa)	$\theta_{max} \setminus \sigma_{zz}$ (MPa)	$\theta_{max} \setminus \sigma_{zz}$ (MPa)	$\theta_{max} \setminus \sigma_{zz}$ (MPa)
60	7.8 \ 0.89	21.2 \ 2.41	80.1 \ 9.08	121.3 \ 13.81
120	14.1 \ 1.60	41.0 \ 4.67	144.0 \ 16.38	212.1 \ 24.14
180	19.9 \ 2.26	60.7 \ 6.91	200.4 \ 22.80	289.8 \ 32.98
240	30.1 \ 3.42	80.2 \ 9.13	253.0 \ 28.79	400.0 \ 45.53
300	37.3 \ 4.24	99.9 \ 11.37	303.5 \ 34.54	425.0 \ 48.36

ation is too small to plot in the same scale. It is seen from Fig. 2(a) that the amplitude and maximum (or minimum) values of the power dissipation ($P_{d,ave}L/P_{0,ave}$) are almost uniform in the wave propagation direction for the frequency of 0.896 GHz. For the frequencies of 2.45 GHz, the amplitude of the power dissipation ($P_{d,ave}L/P_{0,ave}$) does not change too much, but its maximum (or minimum) values decay sharply in the wave propagation direction, which means more power is dissipated near the front surface. For the higher frequency, this shift of the microwave power dissipation toward the front surface is more obvious.

In Fig. 2(b), the power dissipation ($P_{d,ave}L/P_{0,ave}$) in the concrete at frequencies of 0.896 and 2.45 GHz with steel reinforcement bars of 2.5 cm diameter on a 25 cm center, vertically and horizontally ($\rho_{sm} = 0.19$ and $t_{sm} = 0.81$), is also presented. The power dissipation with reinforcement for the 0.896 GHz frequency evidently is not different from that without reinforcement at the same frequency. For the 2.45 GHz frequency, the effect of the reinforcement on the power dissipation is significant. More heat is dissipated from the front surface to the reinforcement ($z < 0.1$ m) than for the case without reinforcement, which could encourage a greater rise in temperature than beyond the reinforcement ($z > 0.1$ m). Usually, the distance of 0.1 m is the limit of the radioactive contamination, which implies that the proper use of either a higher microwave frequency, or steel reinforcement, could control the spall off distance of the radioactive contaminated concrete.

3.2 The Effect of Frequency (f) on Thermal Stress or Temperature Distribution. As shown in Eq. (35), thermal stress within the concrete is proportional to the dimensionless temperature. Therefore, both thermal stress (σ_{zz}) and dimensionless temperature (θ) will have the same behavior. For a 0.6-m-thick concrete slab in the absence of steel reinforcement, the dimensionless thermal stress or temperature distribution and its variation for four microwave frequencies (0.896, 2.45, 10.6, and 18.0 GHz) are plotted in Fig. 3.

It is shown in Fig. 3(a) that the shape of the dimensionless thermal stress/temperature distribution for the 0.896 GHz frequency is similar to the power dissipation ($P_{d,ave}L/P_{0,ave}$) at the same frequency. The peaks of thermal stress/temperature distribution decay slowly along the propagation direction (z). As time elapses, the thermal stress/temperature distribution

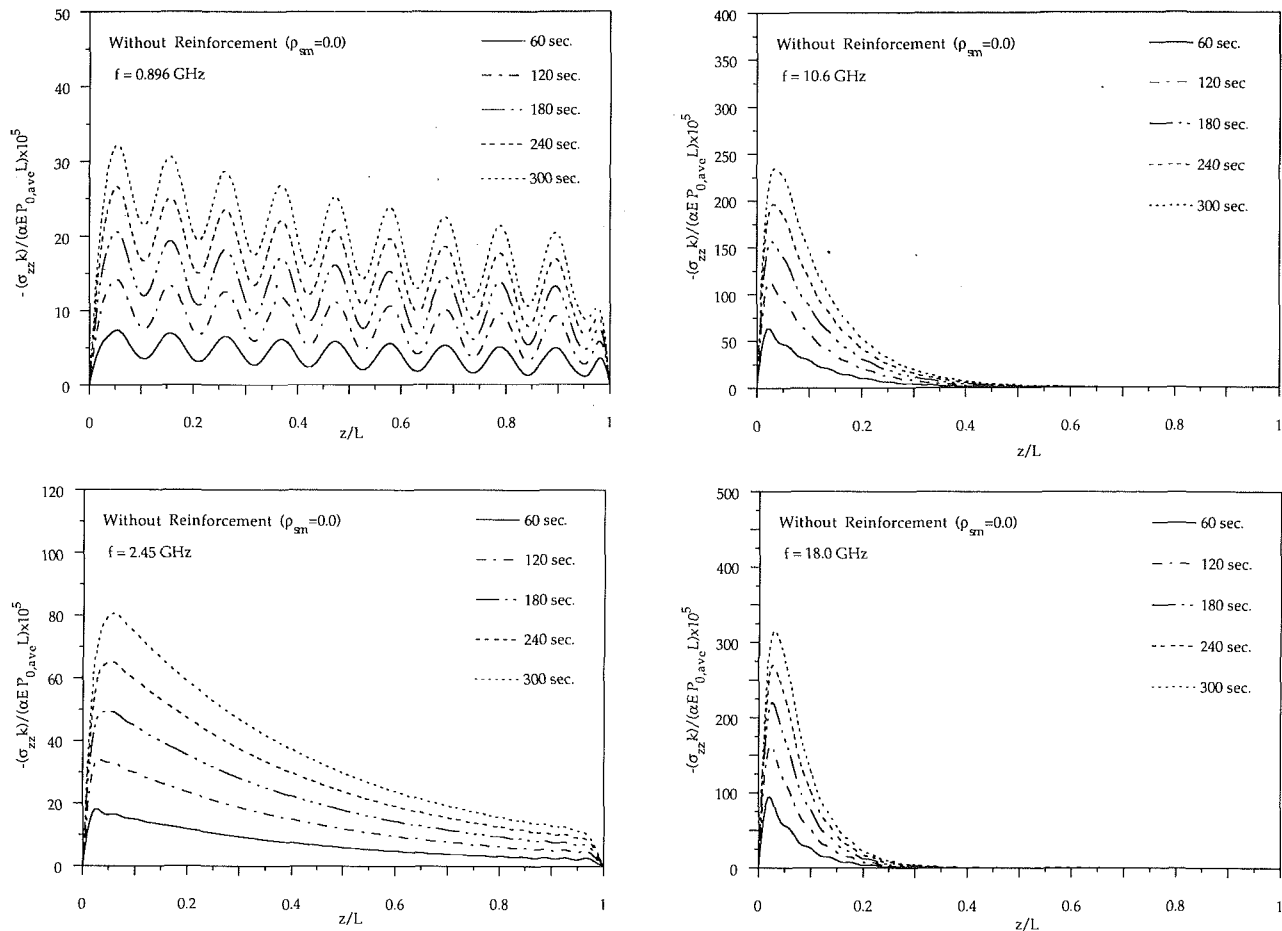


Fig. 3 Variation of the dimensionless thermal stress/temperature distribution within a 0.6 m concrete slab without steel reinforcement: (a) for microwave frequency 0.896 GHz; (b) for microwave frequency 2.45 GHz; (c) for microwave frequency 10.6 GHz; (d) for microwave frequency 18.0 GHz

retains the same shape. As frequency (f) increases, the shape of the thermal stress/temperature distribution changes, and is totally different from that of the power dissipation. As seen in Fig. 3(b), only one peak appears on the thermal stress/temperature distribution for the 2.45 GHz frequency. The power dissipation oscillation along the propagation direction does not appear on the thermal stress/temperature distribution and its variations since the temperature is affected by the spatial average power dissipation, as shown in Eq. (30). It is obvious that as the frequency increases, to 10.6 to 18.0 GHz in Figs. 3(c) and 3(d), the only temperature peak shifts toward the front surface, because the power dissipation and the thermal stress/temperature distribution near the front surface rise quicker than for the low frequencies, such as 0.896 and 2.45 GHz.

The maximum dimensionless temperature and thermal stress within the concrete in the absence of steel reinforcement for microwave power intensity of $P_{0,ave} = 5 \times 10^4 \text{ W/m}^2$ are tabulated and shown in Table 2. It is evident from this table that the maximum dimensionless temperature (θ) and thermal stress (σ_{zz}) increase as microwave frequency (f) increases. It is observed that at the same microwave power intensity ($P_{0,ave} = 5 \times 10^4 \text{ W/m}^2$), it takes 5 minutes (300 s) to raise the maximum dimensionless temperature (θ) to the value of 80×10^{-5} for the 2.45 GHz frequency. For the 10.6 and 18.0 GHz frequencies, this time reduces to less than 2 and 1 minutes (120 and 60 s), respectively. From this, it can be inferred that proper selection of the microwave frequency (f) could reduce the microwave power needed to raise the temperature difference

($T - T_\infty$) and thermal stress (σ_{zz}) to the same value in the same period of time.

As the maximum thermal stress/temperature distribution shifts toward the front surface, the thermal stress/temperature distribution at most locations in the concrete decreases to a lower level in the concrete, which indicates that during the microwave heating process, the stress will not cause any damage to the basic concrete construction, except in a small range near the front surface (approximately 15 percent of the concrete thickness for a frequency higher than 10.6 GHz).

3.3 The Effects of Reinforcement on Thermal Stress or Temperature Distribution. Reinforcement within the concrete is one of the major factors in concrete configuration. For a 0.6-m-thick concrete slab with reinforcement bars of 2.5 cm diameter with a 25 cm distance vertically and horizontally ($\rho_{ms} = 0.19$ and $t_{ms} = 0.81$), located at 0.1 m from the front surface, the maximum dimensionless temperature (θ) and thermal stress (σ_{zz}) within the concrete slab are calculated for microwave power intensity of $P_{0,ave} = 5 \times 10^4 \text{ W/m}^2$ and listed in Table 3. The dimensionless thermal stress or temperature and its variations for four different microwave frequencies (0.896, 2.45, 10.6, and 18.0 GHz) are presented in Fig. 4.

Comparing Table 3 with Table 2, it can be seen that the thermal stress/temperature distribution between the front surface and the steel reinforcement for the same frequency has been increased with the presence of steel reinforcement. The reason for this increase is that part of the microwave energy is forced back between the front surface and the reinforcement

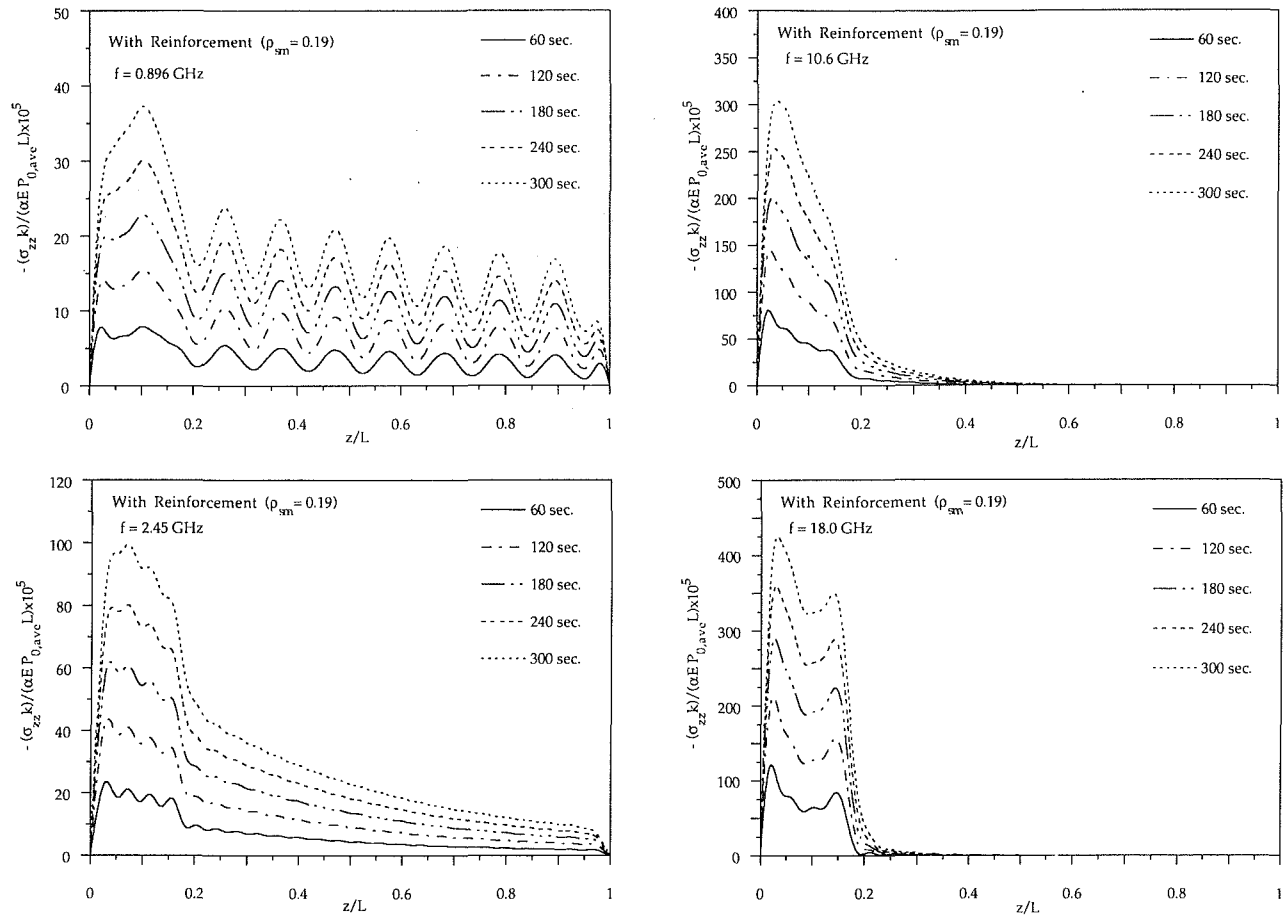


Fig. 4 Variation of the dimensionless thermal stress/temperature distribution within a 0.6 m concrete slab with steel reinforcement ($\rho_{sm} = 0.19$) at $z = 0.1$ m: (a) for microwave frequencies 0.896 GHz; (b) for microwave frequency 2.45 GHz; (c) for microwave frequencies 10.6 GHz; (d) for microwave frequency 18.0 GHz

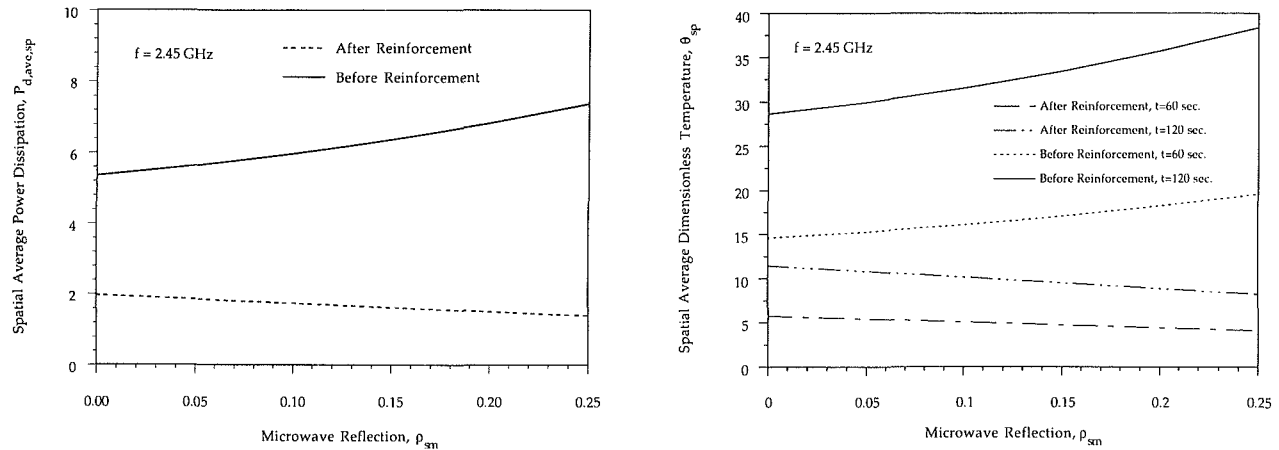


Fig. 5 Effect of reinforcement on the spatial average microwave power dissipation and the spatial average dimensionless temperature for $f = 2.45$ GHz; (a) spatial average microwave power dissipation, $P_{d,sp}$; (b) spatial average dimensionless temperature θ_{sp} , in a time period of 60 s and 120 s

due to the microwave reflection from the steel mesh, and more energy is dissipated in the area preceding the steel reinforcement. From Table 3, it can be estimated that the maximum thermal stress or dimensionless temperature between the front surface and the steel reinforcement is increased 13 percent in a time period of 60 seconds, and 21 percent in 300 seconds for the 0.896 GHz frequency. In a time period of 60 seconds, an

increase of the maximum dimensionless temperature and thermal stress with the steel reinforcement is 16 percent for the 2.45 GHz frequency, 25 percent for the 10.6 GHz frequency, and 28 percent for the 18.0 GHz frequency.

Comparing Fig. 4 with Fig. 3, it is seen that the shapes of dimensionless thermal stress/temperature distribution with steel reinforcement are roughly similar to that without steel rein-

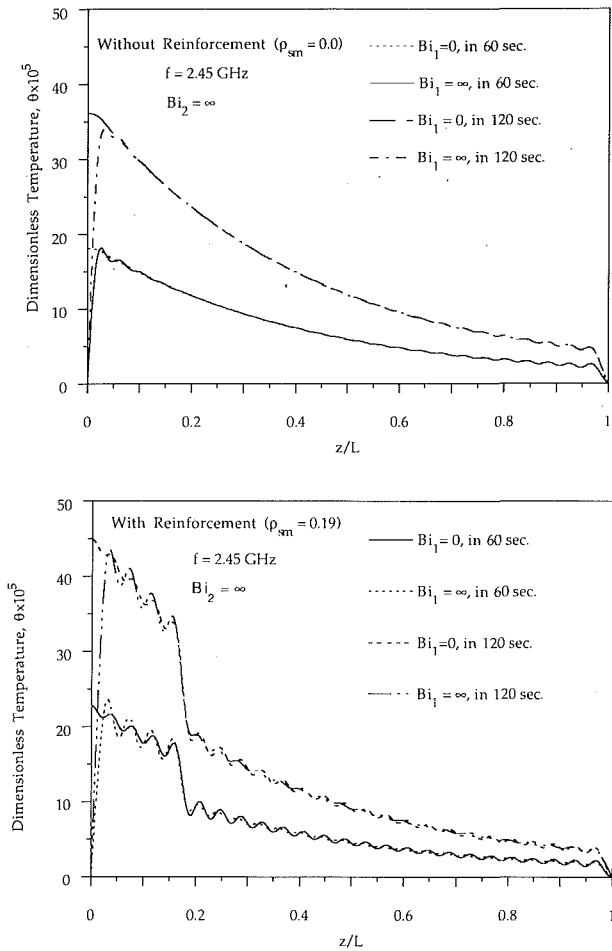


Fig. 6 Effect of the thermal boundary condition on the variation of dimensionless temperature in 60 s and 120 s for $f = 2.45$ GHz: (a) variation of the dimensionless temperature without steel reinforcement for different thermal boundary conditions; (b) variation of the dimensionless temperature with reinforcement ($\rho_{sm} = 0.19$) at $z = 0.1$ m for different thermal boundary conditions

forcement except that the maximum thermal stress/temperature value before the steel reinforcement increases, and the maximum dimensionless thermal stress/temperature distribution after the reinforcement decrease. As the microwave energy is partially reflected from the steel reinforcement, heat dissipation after the steel reinforcement is reduced. Therefore, the maximum temperature/thermal stress value after the steel reinforcement is decreased by comparing the case without steel reinforcement. For a more accurate explanation, a spatial average value, v , is defined as:

$$v_{sp} = \frac{1}{s_2 - s_1} \int_{s_1}^{s_2} v(\xi) d\xi, \quad (36)$$

where the average value before the reinforcement is represented as $v_{1,sp}$, and $s_1 = 0$ m and $s_2 = 0.1$ m, and the average value after the reinforcement is represented as $v_{2,sp}$, and $s_1 = 0.1$ m and $s_2 = 0.6$ m. Please note that the arbitrary value of v could be either $P_{d,ave}$ or θ .

The spatial average dimensionless power dissipations and dimensionless temperatures before and after the reinforcement ($P_{d,ave,1,sp}$, $P_{d,ave,2,sp}$ and $\theta_{1,sp}$, $\theta_{2,sp}$) for times of 60 and 120 seconds are presented in Figs. 5(a) and 5(b), respectively. It is shown from Fig. 5 that as the microwave reflection (ρ_{sm}) increases, the spatial average power dissipation and temperature before the steel reinforcement increase, and the spatial average power dissipation and temperature after the reinforcement decrease, as compared to the extreme case for microwave re-

flection, $\rho_{sm} = 0$ (or no reinforcement). Quantitatively, these increases and decreases of the spatial average power dissipation and temperature are almost proportional to the microwave reflection (ρ_{sm}) from the steel mesh. An increase of the average spatial temperature will correspond to an increase of the maximum temperature/thermal stress, which is very beneficial for spalling off the contaminated concrete layer before the reinforcement. On the other hand, a decrease of the spatial average temperature after the reinforcement will minimize the damage in the main concrete, which could protect the basic concrete construction.

3.4 Effects of the Thermal Boundary Conditions on the Temperature Distribution.

It is important to emphasize that the thermal boundary conditions on both sides of the concrete slab do not affect the microwave field. Based on an assumption of constant magnetic, dielectric, and thermal properties, the thermal boundary conditions affect only the heat transfer and temperature distribution within the concrete. In Fig. 6(a), the effect of the thermal boundary conditions on the temperature distribution at a 2.45 GHz frequency in 60 seconds and 120 seconds without steel reinforcement is presented. The same effect of thermal boundary conditions on the temperature distribution with steel reinforcement ($\rho_{sm} = 0.19$) is presented in Fig. 6(b). In Fig. 6, only the curves for two extreme cases of insulated boundary condition ($Bi_1 = 0$) and constant wall temperature condition ($Bi_1 = \infty$) are plotted. For all other values of Bi_1 , from 0 to ∞ , the corresponding temperature distribution will be between these two curves in the same time period. It is observed from Fig. 6 that when Biot number (Bi_1) at the front surface decreases from ∞ to 0, the front surface temperature rises from the ambient temperature for $Bi_1 = \infty$ to the highest value for $Bi_1 = 0$. The evident difference between these two extreme conditions occurs only in a narrow range ($z < 0.025$ m, 5 percent of the thickness). As is well known, concrete is a poor thermal conductor. It has a very poor ability to transport the heat dissipation within the concrete. Therefore, only the temperature near the front surface drops as the Biot number (Bi_1) increases, while the temperature in most parts of the concrete remains unchanged or changes slightly. The spatial average temperatures before and after the reinforcement position ($\theta_{1,sp}$ and $\theta_{2,sp}$) for the concrete with and without reinforcement are also calculated. Variations of these spatial average temperatures are very small. For example, the maximum difference of the spatial average temperature before the reinforcement ($\theta_{1,sp}$) for $\rho_{sm} = 0.19$ in a time period of 2 minutes (120 s) is less than 8 percent. Generally, it might be concluded that the effect of the Biot number (Bi_1) on the temperature/thermal stress distribution within the concrete might be negligible beyond 5 percent of the concrete thickness.

4 Concluding Remarks

Heat transfer and variations of the temperature/thermal stress distribution within a concrete slab exposed to a microwave source have been investigated. The effects of microwave frequency (f), microwave reflection from the steel reinforcement (ρ_{sm}) located at $z = 0.1$ m, and the front thermal boundary condition (Bi_1) on the temperature/thermal stress distribution within a 0.6 m concrete slab have been considered with a one-dimensional model in the present paper. Based on the available properties of the concrete, all effects of the above parameters have been studied.

As the microwave frequency increases to 10.6 GHz or 18.0 GHz, the maximum temperature/thermal stress distribution shifts toward the front surface of the concrete. Therefore, the temperature near the front surface rises quicker than for the low frequencies, such as 0.896 GHz and 2.45 GHz. At the same microwave power intensity ($P_{0,ave}$), it takes less time to

make the maximum temperature reach the same value of the temperature difference ($T - T_\infty$). Proper use of a higher microwave frequency could reduce the microwave power requirement needed to raise the temperature difference ($T - T_\infty$) to the same value in the same period of time.

With the presence of the reinforcing steel mesh, the maximum temperature/thermal stress distribution and spatial average temperature before the reinforcement increase, which is very helpful in spalling off the contaminated concrete layer before the reinforcement. As part of the microwave energy is blocked by the steel mesh reinforcement, the maximum temperature/thermal stress distribution and spatial average temperature after the reinforcement is reduced. This reduction of the spatial average temperature will lessen damage to the main concrete subjected to microwave heating, thus protecting the basic concrete construction.

As the Biot number (Bi_1) decreases, only the temperature distribution near the front surface increases. This evident change occurs in only a small distance (about $z < 0.025$ m, 5 percent of the thickness). Generally, the effects of the Biot number (Bi_1) might be negligible beyond that small distance (5 percent thickness).

Acknowledgments

The results presented in this paper were obtained in the course of research sponsored by the Department of Energy under Subcontract No. DE-AC05-84OR21400.

References

- Balanis, C. A., 1989, *Advanced Engineering Electromagnetics*, Wiley, NY.
- Copson, D. A., 1975, *Microwave Heating*, 2nd ed., AVI Publishing, Westport, CT.
- Hasted, J. B., and Shah, M. A., 1964, "Microwave Absorption by Water in Building Material," *Brit. J. Appl. Phys.*, Vol. 15, pp. 825-836.
- Hills, D. L., 1989, "The Removal of Concrete Layers From Biological Shields by Microwave," *EUR 12185, Nuclear Science and Technology*, Commission of the European Communities.
- Johns, D. J., 1965, *Thermal Stress Analyses*, Pergamon Press, New York.
- Komarowski, A. N., 1961, *Shielding Material for Nuclear Reactors*, Pergamon, New York.
- Metaxas, A. C., and Meredith, R. J., 1983, *Industrial Microwave Heating*, Peter Peregrinus, London.
- Mindess, S., and Young, J. F., 1981, *Concrete*, Prentice-Hall, New Jersey.
- Okress, E. C., 1968, *Microwave Power Engineering*, Vol. 2, Academic Press, New York.
- Tinga, W. R., and Nelson, S. O., 1973, "Dielectric Properties of Materials for Microwave Processing—Tabulated," *J. Microwave Power*, Vol. 8, No. 1, pp. 23-65.
- Ursu, I., 1985, *Physics and Technology of Nuclear Reactors*, Pergamon, New York.
- Von Hippel, A. R., 1954, *Dielectric Materials and Applications*, MIT Press, Cambridge, MA.
- Wait, J. R., 1985, *Electromagnetic Wave Theory*, Harper and Row Publisher, New York.
- White, T. L., 1990, "Microwave Solidification and Concrete Decontamination," *Oak Ridge National Laboratory Technical Task Plan*, Office of Technology Development, Oak Ridge National Laboratory, TN.
- White, T. L., Grubb, R. G., Pugh, L. P., Foster, D., Jr., and Box, W. D., 1992, "Removal of Contaminated Concrete Surfaces by Microwave Heating—Phase I Results," *Processing of 18th American Nuclear Society Symposium on Waste Management, Waste Management 92*, Tucson, AZ, Mar.
- Yasunaka, H., Shibamoto, M., and Sukagawa, T., 1987, "Microwave Decontaminator for Concrete Surface Decontamination in JPDR," *Proceedings of the Int. Decommissioning Symposium*, pp. 109-115.

Maximum Temperatures in Diamond Heat Spreaders Using the Surface Element Method

J. V. Beck

A. M. Osman

Heat Transfer Group,
Department of Mechanical Engineering and
Composite Materials and Structures Center,
Michigan State University,
East Lansing, MI 48824

G. Lu

Norton Company,
Northboro, MA 01532-1545

Diamond heat spreaders are very attractive for lowering the temperature of laser diodes and computer chip components. The use of diamonds as heat spreaders is very advantageous because its thermal conductivity is so large, about four times that of copper. The diamond heat spreader is mounted on a semi-infinite heat sink. The purposes of this paper are to present (a) a surface element method for the analysis of such composite systems, (b) a set of convenient algebraic equations for the maximum temperatures, (c) optimal geometry conditions and (d) some accurate numerical results. The analysis method is an adaptation of the unsteady surface element method but is different because the present problem is a steady-state one. The surface element method with one node gives a relatively simple algebraic solution, which contains all the important dimensionless groups. The one-node solution is simple, accurate, and has a form that can give deep insight into the effects of various parameters; for example, it permits derivation of the optimal geometry corresponding to the minimal temperature at the hot spot. The study shows that the optimal geometry of the thickness to radius aspect ratio of the diamond heat spreaders is about 0.4. In addition to the single-node analysis, a multinode analysis is developed and very accurate results are presented. These results show that the single-node analysis is generally within 2 percent.

Introduction

For the electronics industry, the move toward greater micro-miniaturization is a very important component of world market competitiveness. As a result, computer chips and other electronic devices will require cooling performance that far exceeds current practice. One way to lower the high local temperature in these devices is to use diamond as a heat spreader; for this application diamond is an excellent material from thermal aspects because its thermal conductivity is about 2000 W/m²°C, about four times that of copper. This paper presents an analysis and results for the diamond attached to a large heat sink. Related papers are by Garmire and Tavis (1984), Nakwaski (1986), and Doting and Molenaar (1988). The solution of this problem herein uses the surface element method (SEM) which is the steady-state version of the unsteady SEM (Keltner and Beck, 1981; Beck et al., 1992).

Many cases were solved using the finite element method (FEM) but a number of aspects were not completely satisfactory for several reasons, some of which are now given. (The same comments also apply to the finite difference method (FDM).) (1) The FEM does not take advantage of the relatively simple geometric elements of the problem, which has only two basic bodies, a finite cylinder and a semi-infinite body. In fact, the infinite dimensions of the latter present some difficulty for the FEM. (2) The FEM grid must be repeatedly changed to accommodate widely varying aspect ratios. (3) The FEM does not provide accurate simple algebraic expressions for the maximum temperature. The SEM, on the other hand, provides relatively simple algebraic equations; such analytical expressions contain the basic dimensionless groups and indicate their interactions.

The boundary element method (BEM) (Brebbia, 1978) provides another method that can be used to solve this problem and it has advantages over the FEM for this case. For example,

the semi-infinite body is more readily accommodate using the BEM than the FEM. But there can be a problem of the grid size adjacent to the heat source, a problem that does not exist in the SEM. Of even more importance is that the SEM can provide accurate analytical expressions. Neither the FEM nor the modern BEM methods do that. It should be noted, however, that the SEM and the BEM have some similarity in the sense that no interior discretization of the domain is required. The SEM uses surface elements only along the contact surface between the diamond spreader and the semi-infinite heat sink.

A related problem is the intrinsic thermocouple, which also involves a semi-infinite body and cylinder. It has been demonstrated that the unsteady single-node SEM analytical expressions are accurate over wide ranges of dimensionless groups and that the multinode SEM is extremely accurate (Keltner and Beck, 1981; Litkouhi and Beck, 1985). Again, the FEM, FDM, and BEM could all be used for the intrinsic thermocouple problem, but for the many cases and permutations of the basic geometries, it was much easier to use the single-node SEM and more accurate to use the multinode surface element method. This paper utilizes both the single and multinode versions of the SEM.

A brief outline of the remainder of the paper is now given. First, the mathematical model of a diamond heat spreader and heat sink chip is given and then followed by a development of the surface element method for a single node. Analytical solutions are discussed and optimal conditions are found. The next section discusses the multinode surface element method. This is followed by a discussion of graphic results and the conclusions.

Mathematical Model of the Diamond and Heat Sink Chip

Synthetic diamond heat spreaders are usually square or rectangular in cross section. When such a body is attached to a heat sink, the problem requires three Cartesian coordinates to describe it. It is shown by Negus et al. (1989) that square and

Contributed by the Heat Transfer Division for publication in the JOURNAL OF HEAT TRANSFER. Manuscript received by the Heat Transfer Division July 1991; revision received February 1992. Keywords: Conduction, Electronic Equipment, Numerical Methods. Associate Technical Editor: L. S. Fletcher.

circular heated areas on the surface of finite cylinders or semi-infinite bodies produce similar constriction or geometric resistance if the characteristic dimension is chosen to be the square root of the contact area, which is an insight first reported by Yovanovich et al. (1983). By capitalizing upon this observation (as also done by Doting and Molenaar, 1988), the present problem can be considerably simplified, at least for diamond shapes that do not deviate too much from a square, such as less than a factor of two in side lengths. Hence, the geometry to be analyzed is a circular diamond mounted on a semi-infinite body.

In this analysis the diamond (or other heat spreader material) is assumed to have isotropic and temperature-independent thermal conductivity. Furthermore the diamond thickness is considered to be sufficiently large so that macroscopic theory of heat conduction (Fourier's law) applies.

The thermal analysis of the problem using the SEM is considered in two parts, one for the diamond and one for the heat sink. Figure 1 shows the basic geometry of a circular diamond with a radius of a_2 and thickness of b_1 . A coordinate system is erected starting at the diamond centerline for the radial coordinate r and at the interface between the diamond and the heat sink for the y direction. The describing thermal model for the diamond heat spreader ($y > 0$) is

$$\frac{1}{r} \frac{\partial}{\partial r} \left[r \frac{\partial T_1}{\partial r} \right] + \frac{\partial^2 T_1}{\partial y^2} = 0, \quad 0 < r < a_2, \quad 0 < y < b_1 \quad (1a)$$

$$k_1 \frac{\partial T_1(r, b_1)}{\partial y} = \begin{cases} q_0 & 0 < r < a_1, \\ 0 & a_1 < r < a_2 \end{cases} \quad (1b)$$

$$\frac{\partial T_1(a_2, y)}{\partial r} = 0, \quad T_1 \text{ finite at } r = 0 \quad (1c, d)$$

At the upper surface of the diamond, at $y = b_1$ and from $r = 0$ to a_1 , there is a known heat flux, q_0 , which could be produced by a laser diode or an electronic chip. The boundary condition

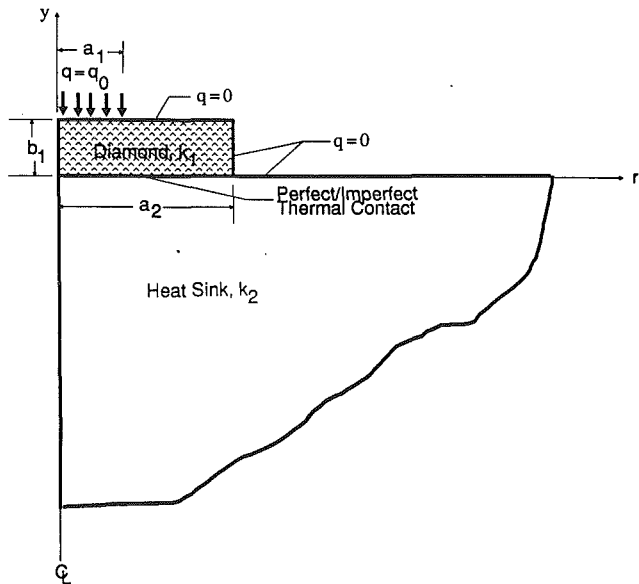


Fig. 1 Basic geometry of a diamond/heat sink model

at $y = 0$, the interface between the diamond and the heat sink, is given in Eqs. (3) and (4), below.

The model for the heat sink (assumed to be semi-infinite) is

$$\frac{1}{r} \frac{\partial}{\partial r} \left[r \frac{\partial T_2}{\partial r} \right] + \frac{\partial^2 T_2}{\partial y^2} = 0, \quad 0 < r < \infty, \quad y < 0 \quad (2a)$$

$$\frac{\partial T_2(r, 0)}{\partial y} = 0, \quad \text{for } r > a_2, \quad T_2 \text{ finite at } r = 0 \quad (2b, c)$$

$$T_2(r, y) = T_\infty \text{ as } r \rightarrow \infty \text{ or } y \rightarrow -\infty \quad (2d, e)$$

Nomenclature

a = heated radius of semi-infinite body (Appendix A)
 a_1 = heated region radius of heat spreader
 a_2 = diamond heat spreader radius
 $A^+ = a_1/a_2$
 b_1 = diamond thickness
 $B^+ = b_1/a_2 =$ diamond thickness to radius aspect ratio
 c = radius for average temperature from $r = 0$ to c
 $c^+ = c/a$
 $\bar{F}(A^+, C^+) =$ group defined by Eq. (B.6)
 $G =$ average dimensionless temperature at $y = 0$ in diamond
 $H(A^+, B^+) =$ group defined by Eq. (11b)
 $J_i =$ Bessel function of the first kind of order i ($i = 0, 1$)

$k_j =$ thermal conductivity of the j th body ($j = 1, 2$)
 $k_s =$ effective thermal conductivity for the interface resistance
 $K(u), E(u) =$ complete elliptic integral of the first and second kinds
 $n =$ number of interface nodes
 $q_a =$ average interface heat flux
 $q_0 =$ heat flux at the heated surface of the diamond
 $q_j^+ = q_j/q_0 =$ dimensionless heat flux element at the interface
 $r =$ radial coordinate
 $r^+ = r/a_2$ or r/a
 $S(A^+) =$ sum defined by Eq. (11a)
 $S_m(A^+) =$ term defined by Eq. (7a)

$T_i =$ temperature in diamond heat spreader ($i = 1$) or heat sink ($i = 2$)
 $T_\infty =$ ambient temperature
 $T_{\max} =$ maximum temperature in the diamond
 $T_2^+(r^+, 0) =$ dimensionless temperature = $(T_2(r^+, 0) - T_\infty)/(q_0 a/k_2)$
 $\bar{T}_2^+(r^+, 0) =$ average $T_2^+(r^+, 0)$ from $r^+ = 0$ to c^+
 $y =$ axial coordinate starting at interface (see Fig. 2)
 $\beta_m =$ eigenvalue of $J_1(\beta_m) = 0$
 $\delta =$ effective thickness of the interface resistance
 $\delta^+ =$ dimensionless interface thickness parameters, Eq. (17)
 $\Delta r =$ radial coordinate
 $\phi =$ dimensionless temperature

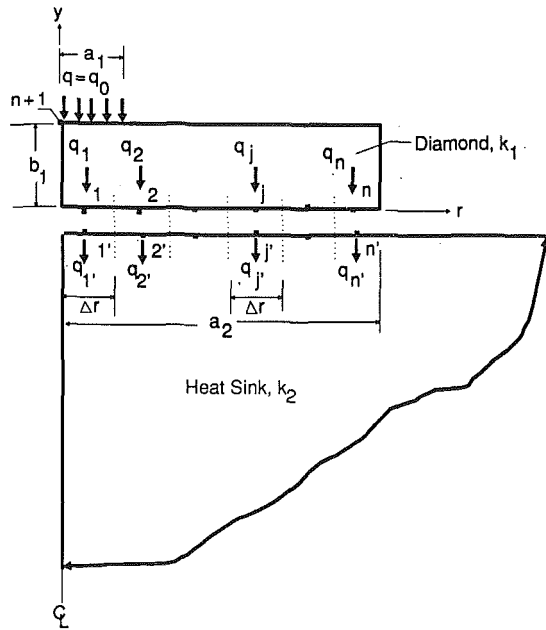


Fig. 2 Computational surface elements

The thermal interface between the diamond and the heat sink can be perfect or imperfect corresponding to (a) no interface thermal resistance, modeled as

$$T_1(r, 0) = T_2(r, 0),$$

$$k_1 \frac{\partial T_1(r, 0)}{\partial y} = k_2 \frac{\partial T_2(r, 0)}{\partial y}, \quad 0 < r < a_2 \quad (3, 4)$$

and (b) significant thermal resistance, modeled as

$$k_1 \frac{\partial T_1(r, 0)}{\partial y} = k_2 \frac{\partial T_2(r, 0)}{\partial y} = \frac{k_s}{\delta} [T_1(r, 0) - T_2(r, 0)],$$

$$0 < r < a_2 \quad (5)$$

where k_s is the effective thermal conductivity of the interface materials and δ is its effective thickness.

Using the heat conduction numbering system given by Beck et al. (1992), for perfect contact the number is R00Y0(C,2)B0+R02B0YC2B5 and for imperfect contact the number is R00Y0(C3,2)B0+R02B0Y(C3)2B5. The first part of each of these numbers is for the semi-infinite body (starting with the $y = -\infty$ "boundary"); R00 denotes the infinite radial region from $r = 0$ to ∞ and Y0 denotes the $y = -\infty$. The second parts starts with R02B0, which denotes a solid cylinder having an insulated boundary condition at the outer radius. The C denotes a perfect contacting interface and C3 denotes an imperfect contact. The YC2B5 denotes first a perfect contact by the C at the interface; then by the B5 it denotes a step radial change in the surface heat flux (denoted by the 2). The numbering system is important because it forces the user to consider carefully each part of the model and it also implies a simplified way of modeling the problem in two parts (Doting and Molenaar, 1988).

Simplified Single-Node SEM Solutions

The single-node SEM is used to illustrate the method and to provide some convenient equations. In addition to being relatively easy to evaluate, such expressions can yield deep insight into the dependence of the maximum temperature on the relevant dimensionless groups. Furthermore, they are easier to manipulate and use than the accurate (multinode) results, which are presented in graphic form. Moreover, the accurate results themselves are an approximation because the circular

geometry is used to model a square (or slightly rectangular) diamond shape.

There are at least two ways one can develop the single-node SEM. One matches a particular temperature at the interface. This could be done at the center ($r = 0$) or some other location. The other way uses the average temperature over the contact surface. It has been found that the average temperature at the interface produces more accurate results than matching at $r = 0$, for example. This analysis then uses the average interface expressions.

Perfect Thermal Contact. The temperature at the hot spot ($r = 0, y = b_1$) above the average temperature at $y = 0$ is obtained by using Eq. (B.2) in Appendix B to get

$$\Delta T_{\max} = \frac{q_0 a_1}{k_1} \left(B^+ A^+ + \sum_{m=1}^{\infty} S_m(A^+) \coth(\beta_m B^+) \right) \quad (6)$$

where $S_m(A^+)$, A^+ , and B^+ are defined as

$$S_m(A^+) = 2 \frac{J_1(\beta_m) A^+}{[\beta_m J_0(\beta_m)]^2}, \quad A^+ = \frac{a_1}{a_2}, \quad B^+ = \frac{b_1}{a_2} \quad (7a, b, c)$$

where $J_0(\cdot)$ and $J_1(\cdot)$ are Bessel functions. This equation for the temperature rise above that at $y = 0$ is found by simply setting G equal to zero in Eq. (B.2). The eigenvalues β_m are the zeros of $J_1(\beta_m) = 0$; the first two values are $\beta_1 = 3.83$ and $\beta_2 = 7.02$.

The average temperature of the region from $r = 0$ to a_2 at $y = 0$ of the semi-infinite body is found from Appendix A (or Negus et al.) to be

$$\bar{T}(y = 0) = [q_a a_2 / k_2] [8/3\pi] + T_{\infty} \quad (8)$$

where q_a is the average heat flux over the interface. This heat flux is related to the imposed heat flux q_0 by

$$q_a = q_0 / (A^+)^2 \quad (9)$$

The hot spot temperature is then obtained by simply adding Eqs. (6) and (8) to get after some re-arrangement and using Eq. (9)

$$T_{\max} - T_{\infty} = \frac{q_0 a_1}{k_1} \left(B^+ A^+ + S(A^+) + H(A^+, B^+) + \frac{8}{3\pi} A^+ \frac{k_1}{k_2} \right) \quad (10)$$

where

$$S(A^+) = \sum_{m=1}^{\infty} S_m(A^+), \quad H(A^+, B^+) = \sum_{m=1}^{\infty} S_m(A^+) [\coth(\beta_m B^+) - 1] \quad (11a, b)$$

The $H(A^+, B^+)$ function is nearly zero for $B^+ (= b_1/a_2)$ or diamond thickness to radius ratio) greater than 0.75, since $\beta_1 = 3.83$ and then $(\coth(\beta_1 B^+) - 1)$ is less than 0.01. The values for $m > 1$ are even smaller. Notice from Table 1 that the coefficient $S_m(A^+)$ is less than unity in absolute value and tends to decrease in value as m is increased. If the first term in Eq. (11b) is used and a series expansion for $\coth(\beta_m B^+)$ for large arguments is used, $H(A^+, B^+)$ is approximated by

$$H(A^+, B^+) \approx 2S_1(A^+) \exp(-2\beta_1 B^+) \quad (12)$$

This expression permits use of B^+ as small as 0.35 with errors less than 0.01 in the group $(\coth(\beta_1 B^+) - 1)$.

Although the number of terms to evaluate $S(A^+)$ can be large, the following simple and accurate expression can be used

$$S(A^+) \approx 1 - 1.106 A^+, \quad \text{for } A^+ < 0.5 \quad (13)$$

For $A^+ = 1/3$ the error is about -0.5 percent and is even less for smaller values of A^+ . Then for $B^+ > 0.35$, Eq. (10) can be approximated by the convenient expression

Table 1 Eigenvalues and details of $S_m(A^+)$ for $A^+ = 1/6$ and $1/3$

m	β_m	$S_m(A^+)$ for $A^+ = 1/6$	$S_m(A^+)$ for $A^+ = 1/3$
1	3.8317	0.25470	0.43411
2	7.0156	0.22118	0.24033
3	10.173	0.17898	0.05669
4	13.324	0.13065	-0.05075
5	16.471	0.08166	-0.06532

Table 2 Dimensionless temperature, $[T_{\max} - T_{\infty}]/(q_0 a_1/k_2)$, for $A^+ = 1/3$

b_1/a_1	$k_1/k_2 = 4$			Percent error in Eq. (14)
	Exact	Eq. (10)	Eq. (14)	
0.25	0.613	0.677		
0.5	0.524	0.536	0.516	-1.6
1.0	0.482	0.486	0.486	0.8
1.5	0.480	0.487	0.488	1.7
2.0	0.488	0.498	0.498	2.0
3.0	0.525	0.525	0.525	2.5

b_1/a_1	$k_1/k_2 = 1$			Percent error in Eq. (14)
	Exact	Eq. (10)	Eq. (14)	
0.5	1.022	1.16	1.21	18
1.0	1.054	1.069	1.093	3.7
1.5	1.095	1.095	1.10	0.5
2.0	1.142	1.143	1.142	0
3.0	1.246	1.251	1.248	0.2

$$T_{\max} - T_{\infty} \approx \frac{q_0 a_1}{k_2} \left[\frac{k_2}{k_1} [B^+ A^+ + 1 - 1.106 A^+ + 2S_1(A^+) \exp(-2\beta_1 B^+)] + \frac{8}{3\pi} A^+ \right] \quad (14)$$

This equation predicts that the maximum temperature is linear in B^+ (for fixed values of A^+) for sufficiently large values of B^+ (which are about $B^+ = 1$). The linear dependence upon the conductivity ratio is shown also. For B^+ values less than 1, the dependence on B^+ suggests that an optimal B^+ is possible; the optimal B^+ is said to exist for a minimum T_{\max} .

Equation (14) is surprisingly accurate for B^+ greater than 0.5, generally within 2 or 3 percent. Table 2 contains some values for the "exact solution" (which is obtained by the 10-node approximation using the multinode method), Eq. (10), and Eq. (14); the cases of $k_1/k_2 = 1$ and 4 are displayed for $A^+ = 1/3$. Notice that B^+ is related to b_1/a_1 by

$$b_1/a_1 = B^+ / A^+ \text{ or } B^+ = (b_1/a_1) A^+ \quad (15a, b)$$

Optimal Geometry for Diamond Heat Spreaders. For the exact and approximate values shown in Table 2, the k_1/k_2 value of 4 (heat spreader having a higher conductivity than the heat sink) there is a minimum value of the dimensionless temperature. This minimum indicates an optimal geometry. Notice that the minimum region is relatively large and is located for b_1/a_1 between 1 and 1.5 for both the exact and approximate values. This range corresponds to $B^+ = 1/3$ to $1/2$ for $A^+ = 1/3$.

One important benefit of analytical forms produced by the SEM is that they can be manipulated by differentiation and so on. Differentiating Eq. (14) with respect to B^+ , setting the expression equal to zero and using Eq. (15) yields the optimal value of b_1/a_1

$$(b_1/a_1) \Big|_{\text{opt}} = -\frac{1}{2A^+ \beta_1} \ln \left[\frac{A^+}{4S_1(A^+) \beta_1} \right] \quad (16)$$

which is equal to 1.17 and 2.47 for $A^+ = 1/3$ and $1/6$, respectively. These values are seen to agree very well with the more accurate values shown in Figs. 3 and 4, which are for the

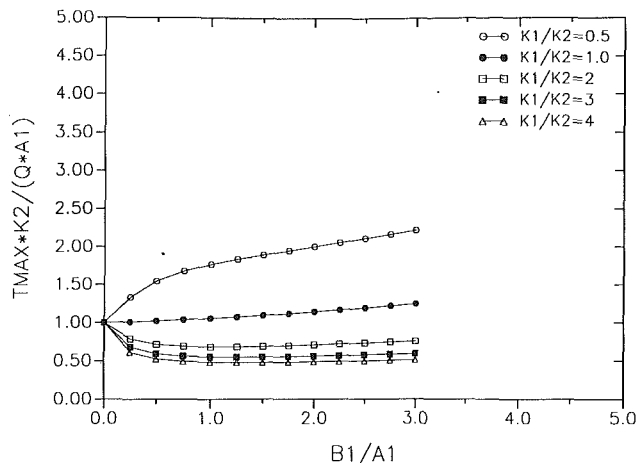


Fig. 3 Normalized maximum temperature for axisymmetric heat spreader, $A^+ = 1/3$ and perfect contact; $N = 10$ elements

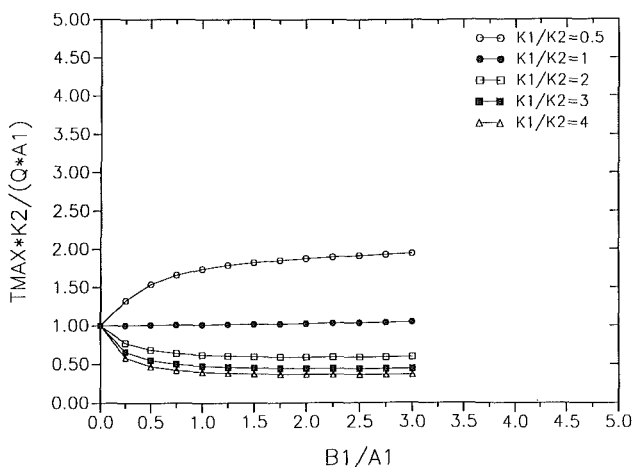


Fig. 4 Normalized maximum temperature for axisymmetric heat spreader, $A^+ = 1/6$ and perfect contact; $N = 10$ elements

multinode analysis. (The ordinate in these figures is labeled T_{\max} rather than $T_{\max} - T_{\infty}$.) It is interesting to observe that although the optimal b_1/a_1 is a strong function of A^+ , it is independent of the conductivity ratio. This conclusion is valid only if the conductivity ratio, k_1/k_2 , is larger than 1; see Table 2. The approximate analysis is not as accurate for b_1/a_1 less than about 1 when $k_1/k_2 \leq 1$. Hence the optimal location is not as accurately predicted for small conductivity ratios. However, this does not detract from the goal of the paper because heat spreaders have high thermal conductivity; diamond has the highest known value. Hence for diamond heat spreaders, $k_1/k_2 > 1$.

It is important to note the optimal shapes for the heat spreader given by Eq. (16). For the $A^+ = 1/3$, the optimal aspect ratio given by B^+ is about 0.39, and for $A^+ = 1/6$, it is about 0.41. (Two other optimal B^+ values for $A^+ = 0.267$ and 0.4 are 0.40 and 0.38, respectively.) Fortunately, the shape of the T_{\max} curves shown in Figs. 3 and 4 are quite flat so that other aspect ratios near $B^+ = 0.4$ can be used without significantly degrading the performance of the spreaders.

Doting and Molenaar (1988) also pointed out the existence of optimal geometric conditions but did not give any equation or condition analogous to Eq. (16). Their example, however, did yield an optimal geometry that agrees with Eq. (16).

Imperfect Thermal Contact. The above analysis can be readily extended to the case of imperfect contact both at the top $y = b_1$ where the laser diode or some device is being cooled

and at the interface ($y=0$). Equation (4) is used for the interface with the heat flux given in Eq. (9). A similar equation is used at $y=b_1$ and $r=0$ to a_1 with the heat flux of q_0 . The result is Eq. (14) with the additional,

$$\frac{q_0 a_1}{k_2} [\delta^+ \{1 + (A^+)^2\}]$$

where δ^+ is a group entering because of the imperfect thermal contact,

$$\delta^+ = k_2 \delta / (k_s a_1) \quad (17)$$

and where δ is the effective thickness of the layer causing the imperfect contact and k_s is its effective thermal conductivity. Notice that this term has the effect of increasing the maximum temperature. Furthermore, it has no effect on the value of the optimal aspect ratio.

This problem has been analyzed using finite element method as well as the multinode SEM. (The agreement is within a couple of percent, some of which can be explained by the difficulty in treatment of the semi-infinite boundary by the FEM.) It has been found that the multinode surface element method is very effective and efficient for this problem. It could be extended by using two or three nodes. In many cases that would be quite satisfactory. The algebra is more complicated but a symbolic algebra program could be employed to pursue that option if desired. Instead of doing that, the method is extended to n interface nodes and only numerical values are found, instead of algebraic expressions.

Development of Multinode Surface Element Method

Figure 2 shows n interface elements, both on the diamond and the heat sink. An arbitrary number of elements can be used. The surface elements on the diamond side of the interface are labeled $1, 2, 3, \dots, j, \dots, n-1, n$ and on the heat sink by $1', 2', \dots, n'-1, n'$. The elements are assumed to have equal radial distances of Δr so that

$$\Delta r = a_2 / n \quad (18)$$

where a_2 is the diamond radius. The heat flux across each element is assumed to be uniform and the average temperature across each element is used.

The maximum temperature is at the $r=0, y=b_1$ location for perfect contact. This location is labeled $n+1$. The basic equations for the heat sink and the diamond are now developed, followed by linking them together for perfect contact.

Heat Sink (Semi-infinite Body). The temperature at any location r_i is the sum of the components for the n interface heat fluxes; see Fig. 2. The dimensionless average surface temperature over the i th element (from $r=r_{i-1}$ to r_i) caused by a heat flux, q_j , from r_{i-1} to r_j is given by

$$\bar{T}_{2,i}^+ = \frac{g_j \Delta r}{k_2} \bar{\psi}_{ij} = \frac{q_0 a_1}{k_2} \frac{q_j^+}{A^+} \bar{\psi}_{ij} \quad (19)$$

where $\bar{\psi}_{ij}$ is called the influence coefficient and is given by

$$\bar{\psi} = \frac{1}{n} \frac{1}{2i-1} \left[j^2 \bar{\psi} \left(\frac{i}{j} \right) - j(i-1)^2 \bar{\psi} \left(\frac{i-1}{j} \right) - (j-1)^2 \bar{\psi} \left(\frac{i}{j-1} \right) + (j-1)(i-1)^2 \bar{\psi} \left(\frac{i-1}{j-1} \right) \right] \quad (20a)$$

where for example

$$\bar{\psi} \left(\frac{i}{j} \right) = \bar{T}_2^+ (r_i / r_j, 0) \quad (20b)$$

which can be evaluated using Eqs. (A.1, 2). (Notice that $\bar{\psi}_{ij}$ is not the same as $\bar{\psi}(i/j)$.) The following relations are used in Eqs. (19) and (20):

$$r_j = j \Delta r, \quad r_i^2 - r_{i-1}^2 = (2i-1) \Delta r^2, \quad q_j^+ = q_j / q_0 \quad (21a, b, c)$$

The average temperature over the i th element of the heat sink (that is, for $y=0^-$, $r_{i-1} < r < r_i$) is the sum of the temperature components for all the n heat flux elements, q_j^+ , at the interface or

$$\bar{T}_{2,i}^- = \frac{q_0 a_1}{k_2} \sum_{j'=1}^n \frac{q_{j'}^+}{A^+} \bar{\psi} \quad (22)$$

Diamond Heat Spreader (Finite Cylinder). The same procedure used for the heat sink can be used for the diamond. Equation (B.5) gives the diamond dimensionless surface temperature T_1 at $y=0$ averaged over surface element i caused by heating at element j . (The i th element is for $r_{i-1} < r < r_i$ and the j th element is similarly defined.) The average temperature rise at element i caused by the exiting heat fluxes, q_1, q_2, \dots, q_n at $y=0^+$ and the entering heat flux q_0 at $y=b_1$ is

$$\begin{aligned} \bar{T}_{1,i}^- &= - \sum_{j=1}^n \frac{q_j a_2}{k_1} \bar{\phi}_{ij} + \frac{q_0 a_1}{k_1} \bar{\phi}_{i,n+1} + \frac{q_0 a_1}{k_2} G \\ &= \frac{q_0 a_1}{k_2} \left(- \frac{k_2}{k_1} \left[\frac{1}{A^+} \sum_{j=1}^n q_j^+ \bar{\phi}_{ij} - \bar{\phi}_{i,n+1} \right] + G \right) \end{aligned} \quad (23)$$

where $\bar{\phi}_{ij}$ is obtained from Eq. (B.5); $n+1$ is for the upper heated surface location at $r=0$ (see Fig. 2); G is the average dimensionless temperature at $y=0^+$ from $r=0$ to a_2 ; and $\bar{\phi}_{i,n+1}$ is given by Eq. (B.4).

Coupling of Interface Equations. Equations for solving for the q_j components are found for perfect contact by using Eq. (3). Equating Eqs. (22) and (23) results in

$$\frac{1}{A^+} \sum_{j=1}^n q_j^+ \bar{\psi}_{ij} = - \sum_{j=1}^n q_j^+ \frac{k_2}{k_1} \frac{1}{A^+} \bar{\phi}_{ij} + \frac{k_2}{k_1} \bar{\phi}_{i,n+1} + G \quad (24)$$

Re-arranging Eq. (24) leads to

$$\sum_{j=1}^n q_j^+ \bar{X}_{ij} = \frac{k_2}{k_1} \bar{\phi}_{i,n+1} + G, \quad i=1, 2, 3, \dots, n \quad (25)$$

where

$$\bar{X}_{ij} = \frac{1}{A^+} \left[\bar{\psi}_{ij} + \frac{k_2}{k_1} \bar{\phi}_{ij} \right] \quad (26)$$

Equation (25) provides a set of n linear algebraic equations with $n+1$ unknowns, $q_1^+, q_2^+, \dots, q_n^+$ and G . Since G appears in each of these n equations, it can be simply removed by subtracting the $i=1$ equation from each to get

$$\begin{aligned} q_1^+ \bar{Z}_{i1} + q_2^+ \bar{Z}_{i2} + \dots \\ + q_n^+ \bar{Z}_{in} = \frac{k_2}{k_1} [\bar{\phi}_{i,n+1} - \bar{\phi}_{1,n+1}], \quad i=2, 3, \dots, n \end{aligned} \quad (27)$$

where \bar{Z} is defined by

$$\bar{Z}_{ij} = \bar{X}_{ij} - \bar{X}_{1j} = \frac{1}{A^+} \left[(\bar{\psi}_{ij} - \bar{\psi}_{1j}) + \frac{k_2}{k_1} (\bar{\phi}_{ij} - \bar{\phi}_{1j}) \right] \quad (28)$$

Another equation is needed because there are n unknowns q_j^+ in the $n-1$ equations given by Eq. (27). The n th equation is found from the condition of conservation of energy for the diamond; it is

$$q_1 \pi r_1^2 + q_2 \pi [r_2^2 - r_1^2] + \dots + q_n \pi [r_n^2 - r_{n-1}^2] = q_0 \pi a_1^2 \quad (29)$$

Divide this equation by q_0 and use Eq. (21c) to get

$$q_1^+ + 3q_2^+ + 5q_3^+ + 7q_4^+ + \dots + (2n-1)q_n^+ = (nA^+)^2 \quad (30)$$

The set of linear algebraic equations to be solved simultaneously is then Eq. (27) and Eq. (30).

The next task is to obtain the temperature at the hot spot; namely, at $r=0$ and $y=b_1$. This temperature is given by the temperature rise in the diamond at $r=0, y=b_1$ relative to that

at diamond interface node 1, ($\bar{T}_{1,1}$), plus the temperature at node 1 in the heat sink, ($\bar{T}_{2,1}$),

$$T(0, b_1) = \left[\phi_{n+1, n+1} - \sum_{j=1}^n \phi_{n+1, j} - \frac{q_0 a_1}{k_2} G \right] - \bar{T}_{1,1} + \bar{T}_{2,1} \quad (31a)$$

where $\phi_{n+1, n+1}$ is given by Eq. (B.3), $\phi_{n+1, j}$ is given by (B.7), $\bar{T}_{1,1}$ by Eq. (23) and $\bar{T}_{2,1}$ by Eq. (22). The first subscript ϕ is for the location of the temperature response and the second is for the location of heat flux source. The minus sign is used before the summation because the heat flux is leaving. Combining all these terms gives

$$T(0, b_1) = \frac{q_0 a_1}{k_2} \frac{k_2}{k_1} \left[\phi_{n+1, n+1} - \frac{1}{n A^+} \sum_{j=1}^n q_j^+ \phi_{n+1, j} + \frac{1}{A^+} \times \sum_{j=1}^n q_j^+ \bar{\phi}_{1, j} - \bar{\phi}_{1, n+1} + \frac{k_1}{k_2} \sum_{j=1}^n \frac{q_j^+}{A^+} \bar{\psi}_{1, j} \right] \quad (31b)$$

Equation (31b) is the desired maximum temperature for the case of perfect contact. Before it can be used, the q_j^+ components are obtained from a solution of the n simultaneous linear algebraic equations given by Eqs. (27) and (30).

The maximum temperatures can be now efficiently calculated for many ratios of the dimensionless groups (A^+ , B^+ , and k_2/k_1) even for extreme ratios of these quantities, conditions that could require much more computation for the finite element and finite difference methods. Notice, too, that the geometry does not require new mesh generations each time the geometric ratios are changed, as required by FDM, FEM, and BEM. Furthermore, the semi-infinite region of the heat sink causes no special problem.

The case of imperfect contact at the interface is treated similarly and is illustrated above for the case of a single node.

Results and Discussions

Figures 3 and 4 display some calculated multinode results for no interface resistance. The values of $T_{\max} k_2 / q_0 a_1$ are plotted versus b_1/a_1 , which is related to B^+ by $b_1/a_1 = B^+ / A^+$. Figure 3 is for the ratio of $a_1/a_2 = 1/3$ or the diamond radius to heated radius ratio of 3. The curves are nearly straight lines for $b_1/a_1 > 1.5$ ($B^+ > 0.5$) and are accurately approximated using Eq. (14). (Recall that $B^+ = A^+ b_1/a_1$.) For smaller values, particularly near $b_1/a_1 = 0$ the multinode method of this paper is needed; 10 nodes were used. For a small value of $b_1/a_1 = 0.25$, the diamond aspect ratio, B^+ , is equal to 0.043 for $A^+ = 1/6$. For such small values of aspect ratio, the FE and FD methods can be inaccurate because a large number of grid points are required. On the other hand the SEM gives the correct value of $T_{\max} = q_0 a_1 / k_2$ as b_1 goes to zero.

From a designer's point of view, the important conclusion that can be drawn from Figs. 3 and 4 is that the hot spot temperature can be reduced substantially through the use of diamond heat spreaders. Also there is an optimal configuration, indicated by the minimum temperatures, which is about $b_1/a_1 = 1.2$ for Fig. 3. (The $n = 1$ analysis given about the same value.) If the diamond heat spreader has three times the thermal conductivity of the heat sink, the maximum temperature rise is about 40 percent less in Fig. 3 and about 55 percent less in Fig. 4 compared to the case without the diamond heat spreader.

Figure 5 shows some results for a thermal resistance between both the diamond and heat sink and also between the upper surface of the diamond and the heat source. The results are plotted for the dimensionless number of $\delta^+ = 0.24$ (see Eq. (17)). The dimensionless temperatures are increased about $2\delta^+$ for b_1/a_1 near zero and about $\delta^+ [1 + (A^+)^2]$ for larger values. (Recall that thermal resistance is included not only at the interface ($y = 0$) but also above the heated region ($y = b_1$). The latter would be present even if the diamond were not used.)

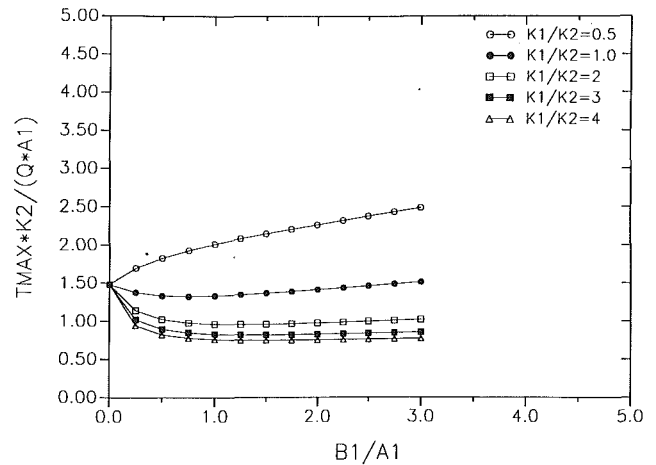


Fig. 5 Normalized maximum temperature for axisymmetric heat spreader, $A^+ = 1/3$ and imperfect contact with $\delta^+ = 0.24$; $N = 10$ elements

It is clear that the effect of a thermal contact resistance can be quite large for moderate values of δ^+ like 0.24.

Conclusions

An analysis is presented for diamond heat spreaders resting on semi-infinite heat sinks. The problem is first simplified by observing that square (or near square) heat spreaders can be approximated by using circular geometries; simplification results in reduction to two-dimensional analysis rather than three. The primary solution method is an extension of the unsteady surface element methods for finding the hot spot temperature when (a) many diamond thickness-to-radius aspect ratios are needed and (b) the aspect ratios are small. Even more important are the simple algebraic equations that are given, which are derived for a single interface node.

A wide range of conditions is covered. The effect of the interface thermal resistance is also included. An important result of this analysis is a relatively simple expression for the optimal geometry for heat spreaders. It has been found that the diamond optimal radius-to-thickness ratio B^+ is about 0.4. The error in the results is only a couple of percent and about the same as the approximation of the square cross section of the diamond heat spreader with the circular geometry.

Graphic results are given that show that diamond heat spreaders are very effective in reducing the hot spot temperature. The temperature rise at the hot spot can be reduced by over 50 percent for the thermal conductivity of the spreader, four times that of the heat sink.

References

- Beck, J. V., 1980, "Temperatures in Bodies Heated by a Constant Disk Heat Source," SAND80-1284, Sandia National Laboratories, Albuquerque, NM.
- Beck, J. V., Cole, K., Haji-Sheikh, A., and Litkouhi, B., 1992, *Heat Conduction Using Green's Functions*, Hemisphere Publishing Corp., Washington, DC.
- Brebbia, C. A., 1978, *The Boundary Element Method for Engineers*, Pentech Press, London.
- Doting, J., and Molenaar, J., 1988, "Isotherms in Diamond Heat Spreaders, Nonlinear Heat Transfer in an Excellent Conductor," presented at the Fourth Annual IEEE Semiconductor Thermal and Temperature Measurement Symposium, San Diego, CA, Feb. 10-12.
- Gamire, E. M., and Tavis, M. T., 1984, "Heat Sink Requirements for Coherent Operation of High-Power Semiconductor Laser Arrays," *IEEE Journal of Quantum Electronics*, Vol. QE-20, pp. 1277-1283.
- Keltner, N. R., and J. Beck, 1981, "Unsteady Surface Element Method," *ASME JOURNAL OF HEAT TRANSFER*, Vol. 103, pp. 759-769.
- Litkouhi, B., and Beck, J. V., 1985, "Intrinsic Thermocouple Analysis Using Multinode Unsteady Surface Element Method," *AIAA Journal*, Vol. 23, pp. 1609-1614.
- Nakwaski, W., 1986, "Thermal Model of Laser Diode Arrays," *Electronic Letters*, Vol. 22, pp. 1169-1170.

Negus, K. J., Yovanovich, M. M., and Beck, J. V., 1989, "On the Nondimensionalization of Constriction Resistance for Semi-infinite Heat Flux Tubes," *ASME JOURNAL OF HEAT TRANSFER*, Vol. 111, pp. 804-807.

Press, W. H., Flannery, B. P., Teukolsky, S. A., and Vetterling, W. T., 1986, *Numerical Recipes*, Cambridge University Press, NY.

Thomas, P. H., 1957, "Some Conduction Problems in the Heating of Small Areas of Large Bodies," *Quarterly J. Mech. and Appl. Math.*, Vol. X, Part 4, pp. 482-493.

Yovanovich, M. M., Thompson, J. C., and Negus, K. J., 1983, "Thermal Resistance of Arbitrarily Shaped Contacts," presented at the Third International Conference on Numerical Methods in Thermal Problems, Seattle, WA.

APPENDIX A

Temperatures in a Semi-infinite Heat Sink Heated by a Constant Heat Flux

The local surface temperature for a semi-infinite body heated by a circular heat source of radius a and constant heat flux q_0 and insulated elsewhere at the surface, $y=0$, was derived by Thomas (1957) and is given in Sect. 8.5.2 of Beck et al. (1992). The heat conduction numbering system for this case is R00Y02B5. The average dimensionless surface temperature for $r^+=0$ to c^+ (with c^+ defined by $c^+ \equiv c/a$) is given by

$$\bar{T}_2^+(c^+, 0) = \frac{4}{3\pi(c^+)^2} \left[[1 + (c^+)^2]E(c^+) - [1 - (c^+)^2]K(c^+) \right], \quad (A.1)$$

or

$$\bar{T}_2^+(c^+, 0) = \frac{4}{3\pi c^+} \left[[1 + (c^+)^2]E\{(c^+)^{-1}\} [1 - (c^+)^2]K\{(c^+)^{-1}\} \right] \quad (A.2)$$

where the first equation is for $0 < c^+$ and the latter for $1 < c^+$. See Press et al., p. 185 (1986) or Beck et al. (1992, Sect. 8.5.2) for definitions of the complete elliptic integrals of the first kind, $K(\cdot)$, and second kind, $E(\cdot)$.

A few values of $\bar{T}_2^+(c^+, 0)$ are 1, 0.96769, $8/3\pi = 0.84883$ and 0.48384 for $c^+ = 0, 0.5, 1$, and 2, respectively. See also Beck (1980), which contains extensive tables.

APPENDIX B

Temperature in a Finite Cylinder Diamond Heat Spreader

Two basic heat flux conditions are considered in this appendix. One is for heating at the upper surface ($y=b_1$) and the other is for the heating at $y=0$. The former represents the heat source into the diamond from the laser diode or chip and the latter is for the diamond-heat sink interface. In both cases, gradient boundary conditions are used. Consequently, steady-state conditions require that the same energy that enters leaves at some boundary.

The mathematical model is given by Eq. (1a, b) plus the average gradient condition at $y=0$ of

$$k_1 \frac{\partial \bar{T}_1(r, 0)}{\partial y} = q_a = q_0 a_1^2 / a_2^2 \quad (B.1)$$

The solution using separation of variables is

$$T_1(r^+, y^+) = \frac{q_0 a_1}{k_1} \times \left(y^+ B^+ A^+ + G + \sum_{m=1}^{\infty} S_m(A^+) J_0(\beta_m r^+) \frac{\cosh(\beta_m B^+ y^+)}{\sinh(\beta_m B^+)} \right) \quad (B.2)$$

where β_m is an eigenvalue found from $J_1(\beta_m) = 0$. The G value is the average dimensionless temperature at $y=0$; since gradient conditions are used, T can be determined only within an additive constant.

Heating at $y^+ = 1$. For this case, the heat conduction numbering system for this case is R02B0Y22B05; see Beck et al. (1992). Equation (B.2) can be used to obtain the dimensionless maximum temperature rise (at $r^+=0, y^+=1$),

$$\phi_{n+1, n+1} = B^+ A^+ + \sum_{m=1}^{\infty} S_m(A^+) \coth(\beta_m B^+) \quad (B.3)$$

The average dimensionless temperature between $(i-1)\Delta r$ and $i\Delta r$ at $y=0$ for heating at $y^+=1$ is (for $i=1, 2, \dots, n$),

$$\bar{\phi}_{i, n+1} = \frac{2}{(2j-1)\Delta r} \frac{a_2}{\Delta r} \times \sum_{m=1}^{\infty} S_m(A^+) \frac{jJ_1(\beta_m j \Delta r / a_2) - (j-1)J_1[\beta_m(j-1)\Delta r / a_2]}{\beta_m \sinh(\beta_m B^+)} \quad (B.4)$$

Heating at $y^+ = 0$. As before, the number for this case is R02B0Y22B50. The average dimensionless temperatures between $(i-1)\Delta r$ and $y=0$ for q_j between $(j-1)\Delta r$ and $j\Delta r$ at $y=0$ is

$$\bar{\phi}_{ij} = \frac{1}{2i-1} \left[ij\bar{F}\left(\frac{j\Delta r}{a_2}, \frac{i\Delta r}{a_2}\right) - (i-1)j\bar{F}\left(\frac{j\Delta r}{a_2}, \frac{(i-1)\Delta r}{a_2}\right) + i(j-1)\bar{F}\left(\frac{(j-1)\Delta r}{a_2}, \frac{i\Delta r}{a_2}\right) - (i-1)(j-1)\bar{F}\left(\frac{(j-1)\Delta r}{a_2}, \frac{(i-1)\Delta r}{a_2}\right) \right] \quad (B.5)$$

$$\bar{F}(A^+, C^+) \equiv 2 \sum_{m=1}^{\infty} S_m(A^+) \frac{J_1(\beta_m C^+)}{\beta_m \tanh(\beta_m B^+)} \quad (B.6)$$

The dimensionless temperature rise at $r^+=0, y^+=1$ caused by q_j is

$$\phi_{n+1, j} = \sum_{m=1}^{\infty} \left[jS_m\left(\frac{j\Delta r}{a_2}\right) - (j-1)S_m\left(\frac{(j-1)\Delta r}{a_2}\right) \right] H_m(B^+, 1) \quad (B.7)$$

$$H_m(B^+, y^+) = \frac{\cosh[\beta_m B^+(1-y^+)]}{\sinh(\beta_m B^+)} \quad (B.8)$$

Heat Transfer and Friction Factor Measurements in Ducts With Staggered and In-Line Ribs

Ying-Jong Hong
Graduate Student.

Shou-Shing Hsieh
Professor and Chairman.
Mem. ASME

Department of Mechanical Engineering,
National Sun Yat-Sen University,
Kaohsiung, Taiwan, 80424

The combined effects of rib alignment and channel aspect ratio on the distributions of the local heat transfer coefficient and on the friction factors for developing and fully developed flow in short square and rectangular channels ($L/D_H = 13.5-18$) with a pair of opposite rib-roughened walls were determined for Reynolds numbers ranging from 13,000 to 130,000. The channel aspect ratios are 1/2 and 1 and the rib alignment configurations are arranged as staggered and in-line types, respectively. The pitch to rib height ratio is 5.31 for all test channels. The local heat transfer distributions on the bottom rib-roughened wall from the channel entrance to the downstream region are presented and discussed. Semi-empirical heat transfer and friction correlations are developed, and the results are compared with those of previous investigations for similarly configured channels, which were roughened by regularly spaced transverse ribs.

Introduction

This paper is concerned with the effect of rib alignment on the friction and heat transfer characteristics of thermally developing, hydraulically fully developed turbulent flow in square and rectangular ducts. Two-dimensional repeated ribs were used on the top and bottom of the duct in staggered and in-line type alignments. Roughness is of great interest because it provides a substantial heat transfer coefficient increase (Hsieh and Christensen, 1984). The increased heat transfer can be used to reduce cooling requirements or to increase the turbine inlet gas temperature.

As the increase in heat transfer rate is accompanied by a friction factor increase (Webb et al., 1971), the preferred roughness geometry will yield the desired heat transfer augmentation with a minimum friction factor. Many studies (e.g., Nunner, 1958; Lewis, 1975; Gee and Webb, 1980) have been conducted on transverse-rib roughness (90 deg helical angle). Data for previous experimental investigations on repeated-rib roughness ducts as well as for the present study are listed in Table 1.

The internal passages can be approximately modeled as square or rectangular channels with two opposite rib-roughened walls. The heat transfer and friction characteristics in these channels are different from those of circular tubes, parallel plates, or annuli. One of the earliest experimental data was reported by Burggraf (1970), who studied the turbulent air flow in a square duct with two opposite ribbed walls with $\theta = 90$ deg, $p/e = 10$, and $e/D_H = 0.055$. Recently, most of the investigators have concentrated on Reynolds numbers from 10^4-10^5 and e/D_H up to 0.08, for fully developed turbulent flow. Several studies on developing flow have also been reported (e.g., Metzger et al., 1987; Han and Park, 1988).

The objective of the present study was to investigate the combined effects of channel aspect ratio and rib alignment on the local heat transfer distribution and friction in square and rectangular channels with two opposite rib-roughened walls in the thermally developing region for Reynolds number from 13,000 to 130,000. The channel width-to-height ratios were 1 and 1/2 (designated AR1 and AR2, respectively). The channel length-to-hydraulic diameter ratios (L/D_H) were 13.5 and 18.0.

The rib height-to-hydraulic diameter ratios (e/D_H) were 0.190 and 0.143. The rib pitch-to-height ratio (p/e) was 5.31. Table 2 shows briefly the rib geometries for each test channel. Air was the working fluid. Constant heat flux was the boundary condition for the ribbed walls. The side walls were adiabatic. Centerline friction factors and heat transfer coefficient distributions on the bottom ribbed wall were measured along the length of the test section.

Experimental Apparatus and Test Procedure

Measurements were carried out in an open-circuit suction type low-speed wind tunnel. A schematic of the experimental apparatus is shown in Fig. 1. A 3 hp blower forced air through the test channel. The Reynolds numbers based on the channel hydraulic diameter (D_H) ranged from 13,000 to 130,000. A 14-cm-dia pipe, equipped with a 9-cm-dia orifice plate, was used to measure mass flow rate.

The test channels were constructed by using commercial plexiglass (10 mm thick) and aluminum plates (5 mm thick). A 10.0 cm \times 10.0 cm square duct and a 20.0 cm (plexiglass) \times 10.0 cm (aluminum) rectangular duct were fabricated. Both are 180 cm long. For the cases of ribbed channel tests, aluminum ribs of square cross section were glued onto the top and bottom plates of the heated channels so that the rib turbulators on opposite walls were all parallel with a prescribed repeated distribution.

The top and bottom aluminum plates each had a woven heater. Each heater could be independently controlled by a variac transformer, which provided a controllable constant heat flux for the entire test plate. The time to reach steady state was less than 60 minutes. Further details of the apparatus are provided by Hsieh and Hong (1989). Over the range of test conditions, the wall-to-bulk fluid temperature difference was between 5°C and 46°C.

Since the turbulence generated by ribs tends to be dominant over secondary flow generated by buoyancy forces, the influence of free convection on the heat transfer in these experiments was believed to be negligible. In order to examine the influence of natural convection, the entire test section was inverted so that the temperature measurements were made along the top wall. A temperature asymmetry effect was not expected and, indeed, none was found in any of the tests. The measured wall-to-bulk fluid temperature differences were used to compute

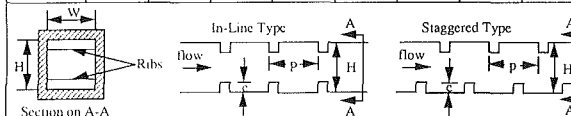
Contributed by the Heat Transfer Division for publication in the JOURNAL OF HEAT TRANSFER. Manuscript received by the Heat Transfer Division June 1991; revision received July 19, 1992. Keywords: Augmentation and Enhancement, Forced Convection, Turbines. Associate Technical Editor: R. J. Simoneau.

Table 1 Existing data for experimental investigations on repeated-rib roughness ducts

Previous Investigators	Physical Geometry	Boundary Condition	Contributions (Functional Relationship)	e^+ Range	e/D_H	p/c	Re_H	Applications
Webb & Eckert (1972)	Circular Tubes	Uniform Heat Flux	St, f, U_e^+ , g, η	$0 < e^+ < 25$	0.01 ~0.04	10	10,000 ~1000,000	Heat Exchanger
Han & Park (1988)	Square and Wide Rectangular Ducts	Uniform Heat Flux	Nu, f, η	$50 < e^+ < 1,000$	0.047, 0.078	10, 20	10,000 ~60,000	Gas Turbine
Han et al. (1989)	Narrow Rectangular Ducts	Uniform Heat Flux	Nu, f, U_e^+ , g, η	$50 < e^+ < 1,000$	0.047, 0.078	7.5, 10	10,000 ~60,000	Gas Turbine
Present Study	Square and Narrow Rectangular Ducts	Uniform Heat Flux	Nu, f, U_e^+ , g, η	$180 < e^+ < 4,000$	0.190, 0.143	5.31	13,000 ~130,000	Gas Turbine

Table 2 Rib geometries in each channel

CASE	H(cm)	W(cm)	e(cm)	D_H (cm)	p(cm)	e/D_H	e/H	p/c	Rib-Alignment	Test Range
AR1/STA	10.0	10.0	1.9	10.0	10.0	0.190	0.190	5.31	Staggered	13,000 < Re_H < 130,000
AR1/INL	10.0	10.0	1.9	10.0	10.0	0.190	0.190	5.31	In-Line	
AR2/STA	20.0	10.0	1.9	13.3	10.0	0.143	0.095	5.31	Staggered	
AR2/INL	20.0	10.0	1.9	13.3	10.0	0.143	0.095	5.31	In-Line	



With unheated and heated sections, each section has 36 ribs
 $D_H = 2WH/(H+W)$

the largest possible Rayleigh numbers (based on the duct hydraulic diameter) for each flow case. The extreme Rayleigh numbers were found to range from 8×10^8 to 1.1×10^9 . Reference to the maps of free, mixed, and forced convection regimes compiled by Metais and Eckert (1964) suggests that free convection should have little or no impact on the overall heat transfer for these Rayleigh numbers, even for low Reynolds number. It is only for $Re_H = 13,000$, where temperature differences were large, that the Rayleigh numbers indicate a proximity to the mixed regime where temperature asymmetries might be expected in the absence of ribs. For smooth ducts, the only distinct contribution due to free convection (about 12 percent) occurred at the last several downstream measurement stations for $Re_H = 13,000$. Therefore, heat transfer measurements were made only on the bottom ribbed wall of each test channels to represent both of the ribbed walls.

A total of 123 K-type thermocouples of 0.5 mm ϕ were measured. Ninety thermocouples were embedded in the cen-

terline of the bottom ribbed plate. Ten thermocouples, which were transversed vertically, were used to measure bulk mean air temperature entering the test channels. Ten thermocouples, which were transversed vertically, were used to measure bulk mean air temperature leaving the test channels. Seven thermocouples were used to measure the rib spanwise surface temperature at one downstream location in the test section for examining the temperature uniformity along the rib surface. Six were attached to the backside of the ribbed wall to measure the outer wall temperature of the test section for evaluation of heat loss. Detailed distributions of thermocouples are shown in Fig. 2. The thermocouple beads were carefully embedded into the wall and then ground flat to ensure that they were flush with the surface. Five pressure taps along the centerline of the bottom ribbed wall were used for static pressure drop measurement by Validyne Microtector with an accuracy of ± 0.01 cm of water. The pressure drop across the test channel was based on the isothermal conditions (test without heating).

Nomenclature

A = projected area
 AR = channel aspect ratio (ribs on side W) = W/H
 D_H = hydraulic diameter
 e = rib height
 e^+ = roughness Reynolds number = $(e/D_H) Re_H \sqrt{f/2}$
 f = isothermal friction factor
 G = mass flow rate
 g = gravity
 $g(e^+)$ = a function for heat-momentum analogy definition
 H = height of channel
 h = heat transfer coefficient
 k_f = thermal conductivity of air at film temperature
 L = test channel length

Nu = Nusselt number = hD_H/k_f
 p = pitch or pressure
 Pe = Peclet number = $Re_H Pr$
 Pr = Prandtl number = ν/α
 Δp = pressure drop
 Re_H = Reynolds number based on hydraulic diameter = UD_H/ν
 St = Stanton number = $Nu/(Re_H Pr)$
 T = local temperature
 T_{av} = bulk average temperature
 T_{bx} = local bulk temperature
 T_f = film temperature = $(T_w + T_{bx})/2$
 T_w = wall temperature
 T_∞ = ambient temperature

ΔT = temperature difference
 U = mean velocity of the working fluid
 u = mean axial velocity of the working fluid
 U_e^+ = momentum transfer roughness function = $\sqrt{2/f} + 2.5 \ln(2e/D_H) + 3.75$
 W = width of channel
 $\bar{\quad}$ = average
 α = thermal diffusivity = $k/\rho C_p$
 ϵ = emissivity
 η = efficiency index = $(\overline{Nu}/Nu(FD))/(f/f(FD))^{1/3}$
 ν = viscosity
 ρ = density of working fluid
 σ = Stefan-Boltzmann constant

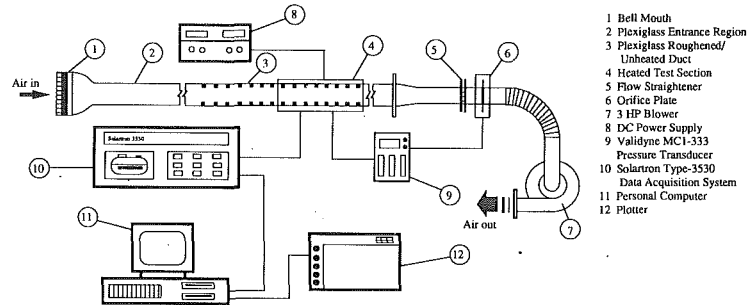


Fig. 1 Schematic of experimental apparatus and instruments (in-line type, staggered type could be switched)

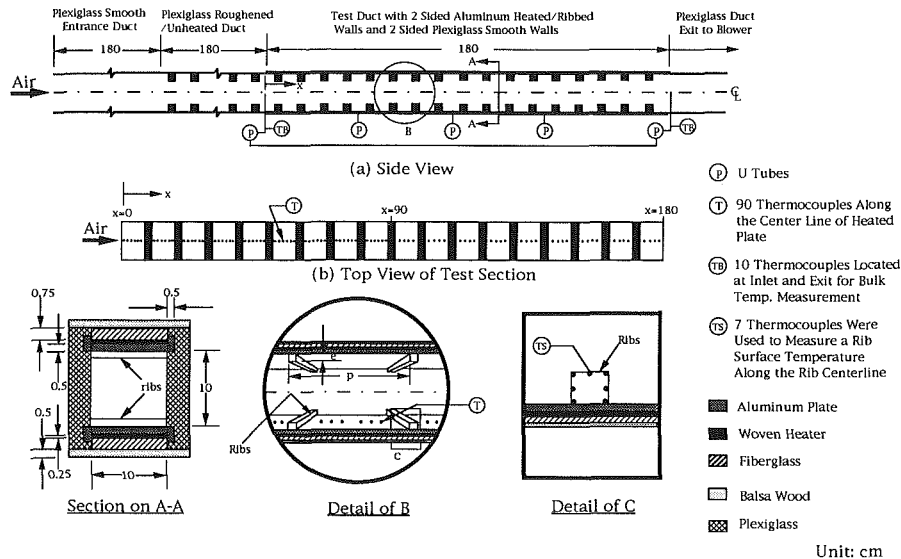


Fig. 2 Detailed thermocouple locations and dimensions of the test section (in-line type)

The location of the pressure tap with respect to the rib turbulator was also examined, and it was found that the relative positions of pressure taps with respect to the rib had no significant influence. A Schlumberger Solartron 3530 Data Logger was interfaced with an IBM AT PC for data acquisition.

Data Reduction

The friction factor was calculated from the pressure drop across the flow channel and the mass flow rate of the air as

$$f = \Delta p / \{4(L/D_H)[G^2/2\rho g]\} \quad (1)$$

The results were normalized by the friction factor for fully developed turbulent flow in smooth circular tubes ($10^4 < Re_H < 10^6$) as proposed by Blasius:

$$f/f(FD) = f/[0.046Re_H^{-0.2}] \quad (2)$$

The local heat transfer coefficient was calculated from the local heat transfer rate per unit surface area (Q_{net}/A) from the wall to the cooling air and divided by the difference of the local wall temperature (T_w), and the local bulk mean air temperature (T_{bx}). This means

$$h(x) = Q_{net}/[A(T_w - T_{bx})] \quad (3)$$

The heat transfer area used was always that of the smooth bottom wall (i.e., the projected area). The bulk mean air temperatures entering and leaving the test section each were measured with ten immersion thermocouples and then arithmetically averaged. The local bulk mean air temperature, T_{bx} , used in Eq. (3) was calculated by assuming a linear air temperature

rise along the flow channel. Over the range of test conditions, the inlet bulk mean air temperature (room temperature) was kept between 27 and 30°C.

The local heat fluxes were not strictly uniform due to both the temperature dependence of duct material properties, and axial heat conduction in the duct wall. The local heat fluxes were found by dividing the surface wall into 90 control volumes around each thermocouple. The local net heat transfer rate Q_{net} was the electrical power generated from the heater subtracted from the heat loss to the outside of the test channel and it is to be calculated based on the following energy balance equation:

$$Q_{net} = Q_t - Q_c - Q_r - Q_{axial} \quad (4)$$

where Q_t is the total power input to the test section, Q_c the conduction heat loss to the environment, Q_r the radiative heat loss from the roughened surface to its surroundings, and Q_{axial} the axial conduction heat loss through the duct wall. The value of Q_r was evaluated using a diffuse gray-surface network (Siegel and Howell, 1981). Heat loss from the outside of the duct wall through the fiberglass insulation ($k = 0.038 \text{ W/m}\cdot\text{K}$) that surrounded the test section was quite low (about 0.1 percent for the maximum). Also, the axial variation in heat transfer coefficients give rise to axial temperature gradients and conduction in the duct wall. Therefore, both circumferential and axial temperature gradients were examined and they were found to be small compared to those in transverse direction. The computation for the worst case of axial heat flux in the present results showed that, at most, the net heat conducted from a duct wall element to an adjacent element was 0.05

percent of the Joule heat generated in that element, even near the test section edge. For this study, the Peclet number ($RePr$) was typically greater than 9000. Therefore, heat transfer due to axial conduction through convection fluid (i.e., air) in the present study was neglected. The heat losses (Q_{axial}) due to conduction through upstream and downstream ends of aluminum plate were calculated to be no more than 3.2 percent, and due to radiation the loss was less than 1 percent of the total power input for all the cases studied. Therefore, the heater provided a nearly constant heat flux on each ribbed wall. In the present study, the total heat flux (Q_t/A) is kept at $1150 \pm 20 \text{ W/m}^2$. It was found that the local net heat transfer from the test channel to the cooling air agreed well (the deviation less than 8 percent) with the cooling air enthalpy rise along the test section.

The local values of the thermophysical properties of air were obtained at the local film temperature (T_f), $T_f = 0.5 (T_w(x) + T_{bx})$. The local Nusselt number was normalized by the equation proposed by Dittus and Boelter (1930) as

$$Nu/Nu(FD) = (h(x)D_H/k_f) / (0.023Re_H^{0.8}Pr^{0.4}) \quad (5)$$

Uncertainty Analysis

A conservative estimate of the accuracy of the temperature measurement is $\pm 0.2^\circ\text{C}$ (20/1 odds). The voltage was measured by a Hewlett Packard 3466A digital multimeter with a maximum uncertainty ± 1.2 percent (20/1 odds). Current was measured by an a-c ammeter with a maximum uncertainty of ± 1.5 percent (20/1 odds). This procedure resulted in a maximum uncertainty of ± 2.7 percent in the calculated power inputs. The maximum conductin heat loss through ribbed side wall and heat loss due to the radiation was estimated to be less than 3.2 and 0.9 percent, respectively, for Reynolds number larger than 13,000. The uncertainty for heat flux is found to be within 2.4 percent. The uncertainty associated with the length scale used in the data reduction was $\pm 1.0 \text{ mm}$ (20/1 odds). The thermophysical properties of the air were assigned an uncertainty of ± 3.0 percent, based on the observed variations in the reported values in the literature. These uncertainties would result in the maximum uncertainty of Nusselt number of about 6.0 percent using the uncertainties estimated procedure described by Kline and McClintock (1953) and modified by Moffat (1988). This occurs near the location of peak Nusselt number where wall-to-bulk temperature differences were smallest for Reynolds numbers greater than 13,000.

It was found that, for the minimum flow rate, which was the worst case, the uncertainties for Reynolds number and friction factor were about 6.2 and 5.4 percent, respectively.

Results and Discussion

Experimental Results for Smooth Channels. Before initiating experiments with the rib-roughened surfaces, the friction factor and heat transfer coefficient were determined for smooth ducts and compared with literature values. With the help of the pressure measurements, it was found that the developing length (i.e., the plexiglass entrance section plus plexiglass unheated section $\sim 36D_H$) for the smooth duct was long enough to guarantee the present smooth wall test duct reaching a hydrodynamically fully developed flow, as witnessed by the measured linearity of the axial pressure distribution. On the other hand, for a heated smooth test section, the heat transfer coefficient distributions measured/calculated exhibit a definite trend with the highest value at the beginning of the test section and decreasing monotonically with increasing downstream distance, eventually reaching a fully developed value. The fully developed heat transfer coefficient and friction factor values at $x/D_H \approx 10.0$ – 15.0 are correlated with Re_H , as shown in Fig. 3. The correlations of previous investigators are also in-

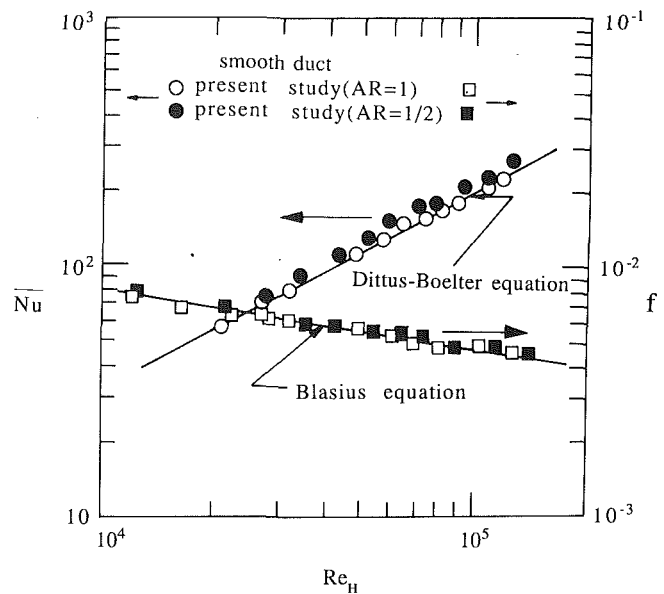


Fig. 3 Friction factor and heat transfer results for smooth ducts

cluded. It can be seen from this figure that there is good agreement between existing correlations and the experimental results for the present smooth ducts, except that the heat transfer results of the rectangular duct are slightly higher than those of the existing correlation. The discrepancy may be attributed to the boundary conditions. The accuracy of the temperature measurement was $\pm 0.2^\circ\text{C}$, which was reflected in the size of the data point. In the present study, the two-side wall adiabatic and two-side wall constant heat flux boundary conditions are different from those of Dittus and Boelter (1930). A circular tube with constant circumferential heat flux was reported in their paper. As can be seen from Fig. 3, the isothermal friction factors differ less than 7.8 and 9.2 percent from the Blasius equation for the present smooth square and rectangular ducts, respectively. The heat transfer coefficients differ less than 6.2 and 14.5 percent from the Dittus and Boelter (1930) equation for the present smooth square and rectangular ducts, respectively. This gives confidence that the present test procedure is accurate.

Experimental Results for Rib-Roughened Channels. A total of four cases were tested. Relevant dimensions of geometric parameters are listed in Table 2. The different rough ducts are described in a code for aspect ratio and rib alignment (see Table 2 for details). For example, duct AR1/STA refers to aspect ratio of 1 and staggered type, and duct AR2/INL refers to aspect ratio of 1/2 and in-line type.

Friction Factor. The roughened-duct friction factor versus Reynolds number data for different rib alignments in square and rectangular ducts are shown in Fig. 4. Although the turbulent flow friction factor in these ducts was found to be dependent on the rib alignment, it was independent of Reynolds number. This verifies that the present study is in the fully rough region for both aspect ratios. It can also be seen from Fig. 4 that the friction factor of the square duct is larger than that of the rectangular duct. In the present study, as shown in Fig. 4, the friction factors of AR1/STA, AR1/INL, AR2/STA, and AR2/INL were 8–13 times, 9–14 times, 3–4.7 times, and 2.5–4 times, respectively, higher than those of fully developed turbulent flow in smooth circular tubes.

It can be seen from Fig. 4 that in a square duct ($AR = 1$) the friction factor has a larger value in the in-line than in the staggered type rib alignment. This is perhaps due to the in-line type arrangement having higher effective blockage than

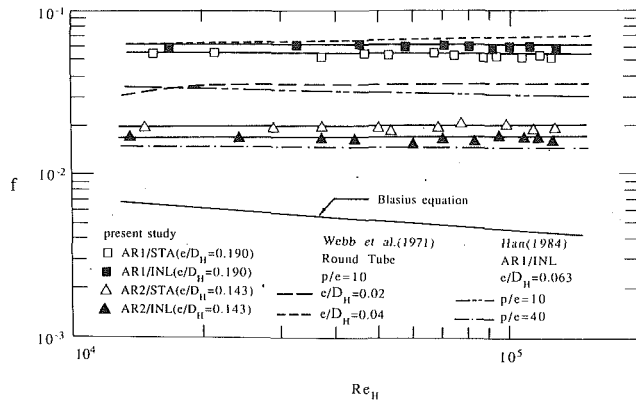


Fig. 4 Isothermal friction factor results for present study and compared with previous investigators

the staggered arrangement. When the main flow reaches the location of the rib, it would behave just like that in the forward facing step and backward facing step, i.e., a series of contractions and expansions as it passes through ribs. The reason for the large pressure drop is the significant blockage and distortion of the flow caused by the ribs. This phenomenon also prevails in the AR1/STA case, but its influence is less serious than in the AR1/INL case. Furthermore, as the flow passes through the region between two consecutive ribs, the existence of the rib at the opposite wall, at most, would cause the outer flow to turn its original path and to become a little bit concave. A heat transfer increase would be followed by the above flow distortion and impingement on the channel walls.

The rectangular duct shows a completely opposite trend. This is because the large mainflow distortion due to blockage that occurs in the AR1/INL case was not observed for the AR1/INL case. The obstruction encountered by the outer flow plays an important role and, eventually, it generates a big pressure drop as in the AR1 cases. Furthermore, from the results of the previous investigators (e.g., Webb et al., 1971; Hsieh and Hong, 1989), it is expected that, in the cases where pitch-to-rib height ratio is less than eight, the reattachment point will depend on Re_H and rib alignment. It is therefore concluded that the interrib space is completely occupied by the recirculating flow for $AR = 1/2$. The rib seems to have an influence only on the outer region of the flow. Perhaps the $p/e = 5.31$ of the present experiment is close to the reattachment/no reattachment boundary for the AR2/STA case. The spacing between two consecutive ribs may be on the edge of the recirculation range and the impingement breaks it up. In that case the staggered array would be more likely to reattach and yield higher pressure drop.

Heat Transfer Coefficients. The local Nusselt number ratios, normalized as in Eq. (5), are plotted as a function of the dimensionless axial coordinate x/D_H . Only typical results are shown here.

The distribution of heat transfer coefficient along the length of the duct is presented in Figs. 5 and 6 for square and rectangular ducts, respectively, for different Reynolds numbers and rib alignments. From an overall examination of these figures, a number of trends exist for these figures, and each duct has its own particular heat transfer characteristics (the shape of the $Nu/Nu(FD)$ versus the x/D_H distribution).

In staggered type ducts (i.e., AR1/STA and AR2/STA), as shown in Figs. 5 and 6, starting with a moderate value immediately adjacent to the inlet, the normalized Nusselt number rises rapidly and then decreases about as rapidly until the heat transfer coefficient levels off as that flow becomes thermally fully developed. It seems that the peak at inlet of staggered-type ducts was partly due to a step change in the wall tem-

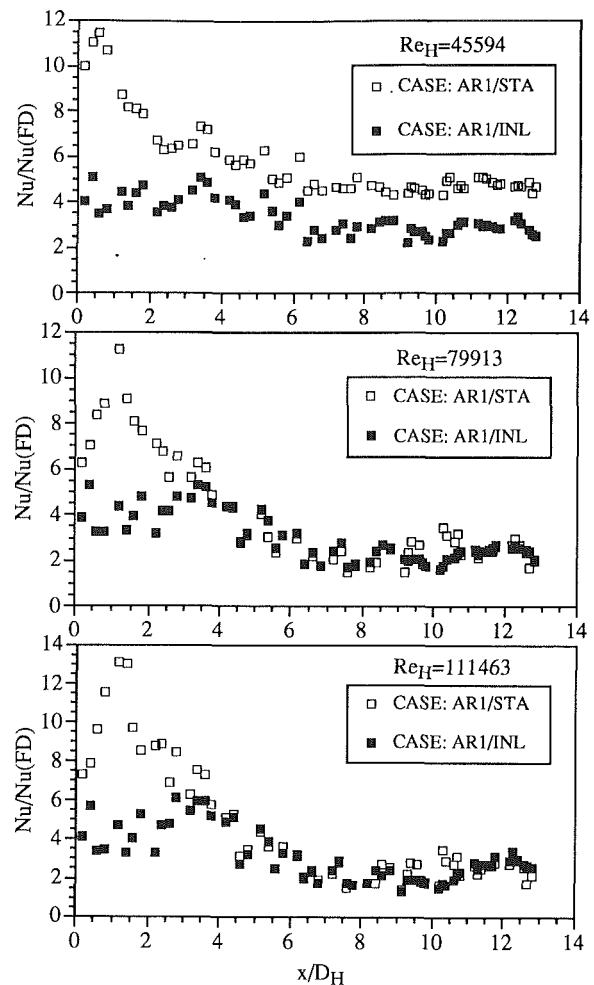


Fig. 5 Heat transfer results for square duct ($AR = 1$) with different rib alignment

perature at which a new thermal boundary layer is introduced and partly due to the abovementioned flow distortion and impingement. When the ribs are staggered, they appear to cause the flow to impinge upon the opposite walls more frequently, which results in a heat transfer increase. In contrast, from Figs. 5 and 6, the heat transfer distributions of the INLs were absolutely different from those of the STAs. The lack of an initial spike was noticeable. The distributions also did not agree with Han et al. (1989), in having a larger pitch-to-rib height ratio ($p/e = 7.5$) and a sudden entrance condition (entrance developing flow for both thermally and hydraulically). This may be partly because the present e/D_H is much higher, causing a vena-contracta effect and canceling out the usual inlet developing flow effect, and partly because the present heating boundary condition (only two ribbed walls were heated) as well as a step change in the wall temperature as stated in the STA case is quite different from Han et al. Figures 5 and 6 show that for both staggered geometries the peak of normalized Nusselt number ratio, $Nu/Nu(FD)$, increased as the Reynolds numbers increased. The shapes of the heat transfer coefficient distribution for both aspect ratios are very similar. The downstream asymptotic values of the normalized Nusselt numbers were about 2 for AR2/INL, 2.5 for AR2/STA, 3 for AR1/INL, and 4 for AR1/STA for low Reynolds numbers. However, as the Reynolds number increases, it indicates that the role of the rib alignment would no longer be as important as the Reynolds number is.

The mechanism of complex flow interaction results in different heat transfer characteristics in each rough channel. It

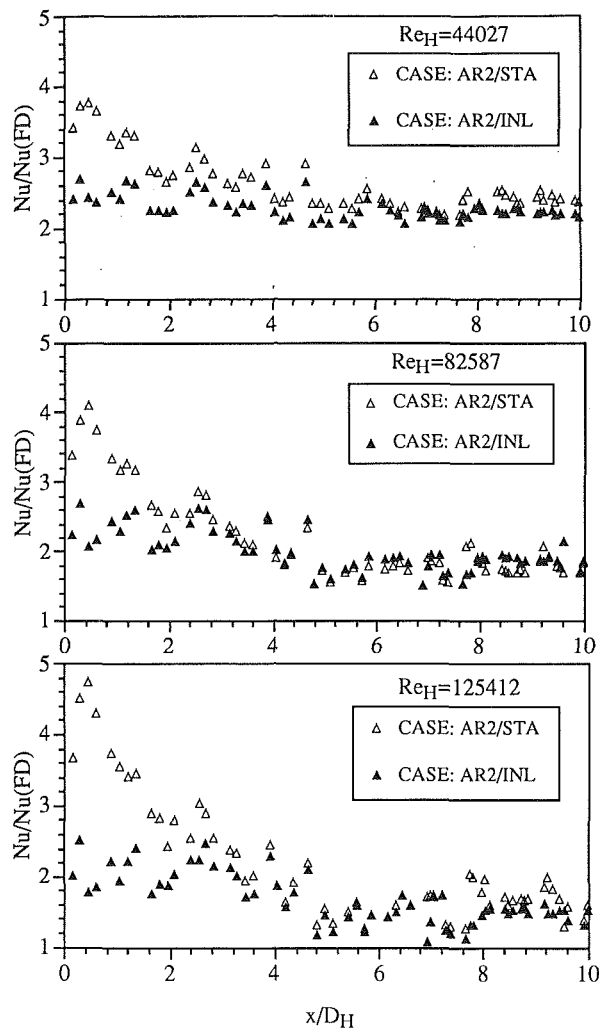


Fig. 6 Heat transfer results for rectangular duct ($AR = 1/2$) with different rib alignment

could be conjectured that the existence of a full recirculation cell at the interrib space for a channel with in-line ribs has a profound impact on the Nusselt number results. In such condition, the heat transported between the duct wall and the working fluid depends mainly on conduction through the ribs after convection to the ribs. On the other hand, in a channel with staggered ribs, the protruding ribs result in transverse changes in the flow pattern. This indicates that the flow is being deflected and impinging against the opposite wall even though the p/e value is less than eight. The strength of the flow deflection and impingement was greater in the square duct than that in the rectangular duct. This is also evidenced by the flow visualization studies reported by Hsieh and Hong (1989). Consequently, as can be seen from Figs. 5 and 6, the Nusselt number results were higher in staggered than in the in-line type alignment.

Centerline Average Heat Transfer and Friction Data. To develop the heat transfer and friction correlations, the average heat transfer coefficient and friction factor are required. Based on the local heat transfer and pressure distribution, it was found that the Nusselt number ratio has a periodically developed distribution in the downstream region and that the friction factor has a constant value in the range of Reynolds numbers studied. Therefore, all the pressure drop data were used for determining the average friction factor (f). However, only the data for $x/D_H = 10.0$ – 12.0 for the square duct and $x/D_H = 8.0$ – 10.0 for the rectangular duct were used for de-

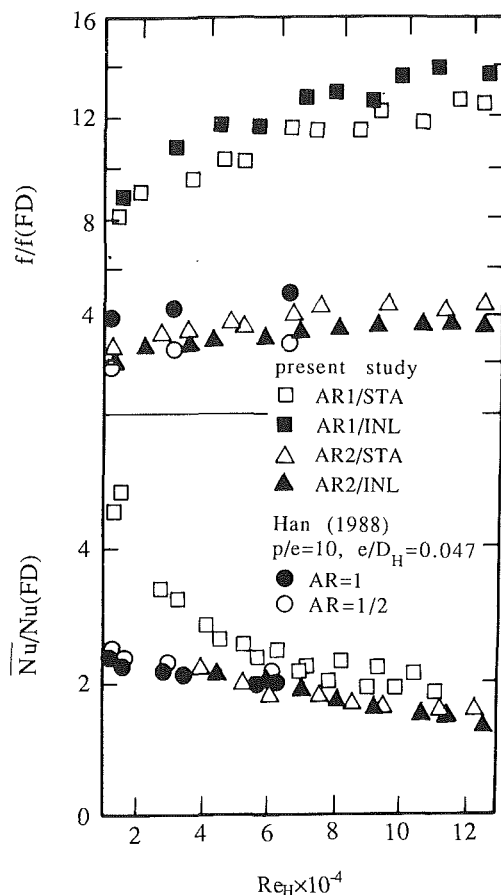


Fig. 7 Normalized friction factor and heat transfer versus Re_H for each test channel and compared with previous investigators

termining the average Nusselt number (\overline{Nu}). These centerline-average Nusselt (or Stanton) numbers were used for heat transfer performance comparison and for correlations discussed later in this section.

Figure 7 illustrates the combined effects of the Reynolds number and the rib alignment on the normalized Nusselt number and the normalized friction factor for all channels studied, respectively. The average heat transfer ratios on the ribbed-side wall decreases monotonically with the Reynolds number increase, whereas the average friction factor ratios increase monotonically with the Reynolds number increase, whereas the average friction factor ratios increase monotonically with the Reynolds number increase for all channels. These indicate that the increase of heat transfer in rib-roughened channels is more significant at low Reynolds number than that at high Reynolds number, but the trend of the friction factor is reversed for the whole range of Reynolds numbers. The results also show that, for a given Reynolds number, both the average heat transfer and the friction factor ratios decrease with an increase in channel aspect ratio.

Heat Transfer and Friction Correlations. Following the roughened channel analysis described by Dippery and Sabersky (1963), wall similarity laws were employed to correlate the friction and heat transfer data for fully developed turbulent flow in the square and rectangular channels with two opposite ribbed walls of the present study. The present friction similarity law could be considered a combination of smooth duct friction similarity law plus a correction term due to rough surface effect suggested by Dippery and Sabersky (1963). According to the friction similarity law, the measured overall friction factor (f), the rib height-to-hydraulic diameter ratio (e/D_H), and the Reynolds number could be correlated into a so-called friction

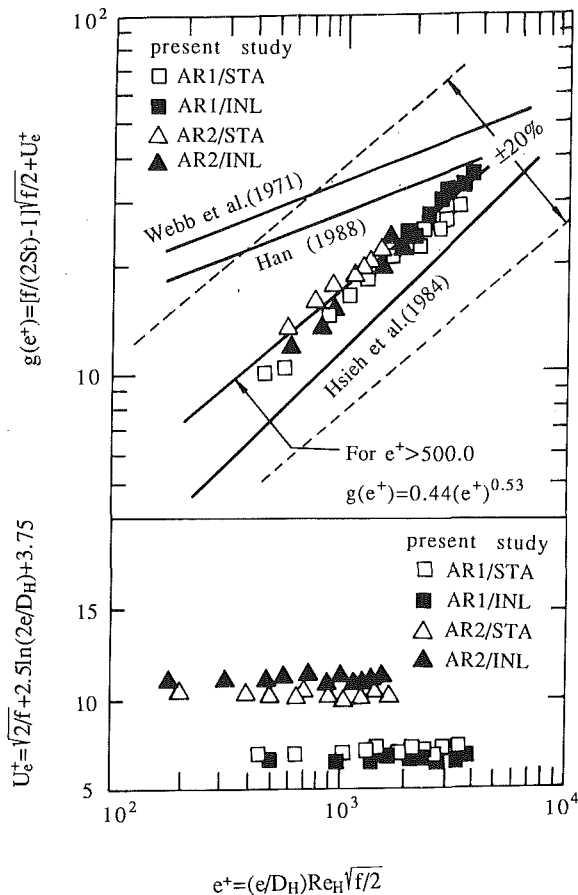


Fig. 8 U_e^+ and $g(e^+)$ versus e^+ for all ducts

roughness function ($U_e^+(e^+)$) for similar roughness geometry. However, U_e^+ is expected to have different values for different roughness types. A correlation of the present friction data is shown in Fig. 8, and it can be seen from this figure that the values of U_e^+ fall into two groups: AR1/STA and AR1/INL having an approximately constant value of $U_e^+ = 7$, and AR2/STA and AR2/INL having an approximately constant value of $U_e^+ = 11$ for the range of roughness Reynolds number studied. This again implies that the average friction factor depends on e/D_H and is independent of Reynolds number as also confirmed by earlier statements. This indicates that the present study is a fully rough regime as confirmed earlier in this section (cf. Fig. 4). The reason that makes the results fall into two groups was due to the influence of aspect ratio in the form of wall roughness. With the same rib height, as expected, there is a relatively larger roughness (e/D_H) in the channel with the smaller aspect ratio. In this study, the value of e^+ was as high as 4000 because of the larger rib height and Reynolds number being used.

The use of the present results to test the extension of the heat-momentum analogy equation to a rough surface for the current four cases is not easy. The flow patterns are different for these four different surface roughness arrangements due to their difference in dynamic similar sense. Nevertheless, such a correlation still seems promising in an overall sense. According to the heat transfer similarity law, the measured centerline-average Stanton number on the ribbed side wall (St), the average friction factor (f), and the friction roughness function $U_e^+(e^+)$ can be correlated into a so-called heat transfer roughness function $g(e^+, Pr)$ for the geometrically similar roughness. A plot of $g(e^+)$ versus e^+ is shown in Fig. 8. For a Prandtl number of 0.71 of the present study, the correlation of $g(e^+)$ shown in Fig. 8 can be represented by

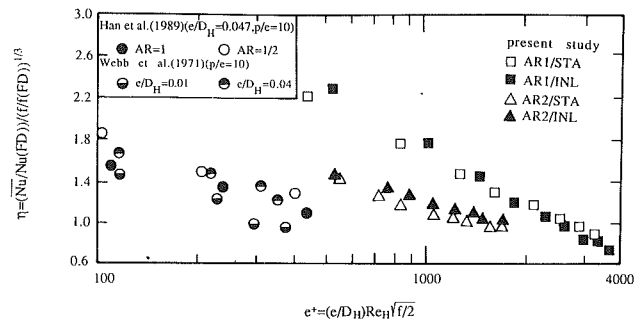


Fig. 9 Augmented heat transfer for a constant pumping power versus e^+ in each channel

$$g(e^+) = 0.44(e^+)^{0.53} \quad \text{for } e^+ \geq 500.0 \quad (6)$$

The deviation of Eq. (6) is ± 4.5 percent for 95 percent of the data shown in Fig. 8. Correlations of the square channel (four walls heated) with repeated ribs on opposite walls ($p/e = 10-20$) from Han (1988) as well as a circular tube (circumferentially heated) with transverse-rib roughness ($p/e = 10-40$) from Webb et al. (1971) and square duct (bottom finned-wall heated) with triangular fins ($p/e = 2-4.7$) on the floor from Hsieh and Christensen (1984) are also included in Fig. 8 for comparison. The values of the g function of present study are less than those of Han (1988) for rectangular channels with repeated ribs and those of Webb et al. (1971) for a circular duct over the present range of e^+ . On the other hand, the results of Hsieh and Christensen (1984) show that a square duct with one asymmetric roughened surface has lower g values than this study. Furthermore, as can be seen from Fig. 8, the slopes of the plots decrease as the values of p/e increase, and when p/e is larger than 10 the powers for the correlated equations seem to have the same value.

Heat Transfer Performance Comparison. One of the performance evaluation criteria was chosen to compare the enhanced heat transfer for the same surface area and friction factor as suggested by Webb and Eckert (1972). In view of the above discussion, an efficiency index, the equal friction factor performance criterion, can decide whether a given rough surface is potentially advantageous or not. This index was defined as

$$\eta = (\overline{Nu}/Nu(FD)) / (f/f(FD))^{1/3} \quad (7)$$

instead of the conventional one using Stanton number, from which η can be obtained for each of the four surface roughness configurations.

From Fig. 9, where η is plotted against e^+ , it can be seen that all rough channels do show the same trend; namely, there are higher values of η at lower roughness Reynolds number initially; the value of η then decreases monotonically at higher e^+ . This behavior was mainly caused by the friction factor for smooth duct ($f(FD)$), which is a function of Reynolds number. Most of the value of η were higher than 1, as shown in Fig. 9, which indicates that the roughened channels tested have better heat transfer performance when compared to a smooth duct. Upon closer examination of Fig. 9, it is found that the square channel with in-line ribs has better efficiency than the staggered ribs, but only in the range of $e^+ < 2000$. On the other hand, the rectangular duct with in-line ribs shows better results in all runs. One can also find the appropriate operating condition for these particular surface roughness configurations from this graph as far as the performance is concerned.

Concluding Remarks

The combined effects of rib alignment and channel aspect ratio on the distributions of the local heat transfer coefficient

and on the friction factors for developing flow in square and rectangular channels with a pair of opposite rib-roughened walls were investigated for Reynolds numbers ranging from 13,000 to 130,000. The following conclusions are drawn:

1 Although the turbulent flow friction factor in all test channels was found to be dependent on the rib alignment, it was independent of Reynolds number. This verifies that the present study is in the fully rough region for both aspect ratios. Moreover, in the present study, the friction factors of AR1/STA, AR1/INL, AR2/STA, and AR2/INL were 8–13 times, 9–14 times, 3–4.7 times, and 2.5–4 times, respectively, higher than those of fully developed turbulent flow in smooth circular tubes.

2 In staggered type ducts, starting with a moderate value immediately adjacent to the inlet, the normalized Nusselt number soars upward and reaches a sharp maximum, whereafter it begins to decrease at a rate that is about as rapid as that of the initial increase. Moreover, for AR1/STA and AR2/STA, the peak of normalized Nusselt number ratio, $\overline{Nu}/Nu(FD)$, increased with the Reynolds number increase. The rate of decrease slackens with the downstream distance increase, and finally levels off. The downstream regime value were asymptotic at about 3 times for AR1/STA and 2 times for AR2/STA higher than the fully developed values

3 The heat transfer results of in-line type roughened channels are very different from those of staggered type roughened channels, exhibiting a steady decreasing behavior. However, there are local oscillations at inlet regions in the distribution of heat transfer coefficients for both aspect ratios.

4 The average heat transfer ratios on the ribbed side wall decreases monotonically with increasing Reynolds number, whereas the average friction factor ratio increase monotonically with increasing Reynolds number for all channels. In addition, for a given Reynolds number, both the average heat transfer and the friction factor ratios decrease with increasing channel aspect ratio.

5 For all rough channels tested, there are higher values of η ($= 1.4$ – 2.4) at lower e^+ (say, $e^+ < 600$), which monotonically decrease to a lower rule of η ($= 0.8$ – 1.2) at higher e^+ (say, $e^+ > 1000$). Moreover, it is found that the square channel with in-line ribs has better efficiency than the staggered, but only in the range of $e^+ < 2000$. On the other hand, the rectangular duct with in-line ribs shows better results in all runs.

6 The heat transfer and friction correlations are developed to account for rib alignment, channel aspect ratio, and Reynolds number. The correlations are valid for $e^+ > 500$. These correlations can be used in the design of turbine airfoil cooling passages over the range of our experiment.

References

- Burggraf, F., 1970, "Experimental Heat Transfer and Pressure Drop With Two-Dimensional Turbulence Promoter Applied to Two Opposite Walls of a Square Tube," in: *Augmentation of Convective Heat and Mass Transfer*, E. E. Bergles, and R. L. Webb, eds., ASME, New York, pp. 70–79.
- Dippery, D. F., and Sabersky, R. H., 1963, "Heat and Momentum Transfer in Smooth and Rough Tubes at Various Prandtl Numbers," *Int. J. Heat Mass Transfer*, Vol. 6, pp. 329–353.
- Dittus, F. W., and Boelter, L. M. K., 1930, University of California, Berkeley, Publications on Engineering, Vol. 2, p. 443.
- Gee, D. L., and Webb, R. L., 1980, "Forced Convection Heat Transfer in Helically Rib-Roughened Tubes," *ASME JOURNAL OF HEAT TRANSFER*, Vol. 23, pp. 1127–1136.
- Han, J. C., 1984, "Heat Transfer and Friction in Channels With Two Opposite Rib-Roughened Walls," *ASME JOURNAL OF HEAT TRANSFER*, Vol. 106, pp. 774–781.
- Han, J. C., 1988, "Heat Transfer and Friction Characteristics in Rectangular Channels With Rib Turbulators," *ASME JOURNAL OF HEAT TRANSFER*, Vol. 110, pp. 321–328.
- Han, J. C., and Park, J. S., 1988, "Developing Heat Transfer in Rectangular Channels With Rib Turbulators," *ASME Int. J. Heat Mass Transfer*, Vol. 31, pp. 183–195.
- Han, J. C., Ou, S., Park, J. S., and Lei, C. K., 1989, "Augmented Heat Transfer in Rectangular Channels of Narrow Aspect Ratios With Rib Turbulators," *Int. J. Heat Mass Transfer*, Vol. 32, pp. 1619–1630.
- Hsieh, S. S., and Christensen, R. N., 1984, "Turbulent Heat Transfer on Rough Surface With Asymmetrical Heating," ASME Paper No. 84-HT-54.
- Hsieh, S. S., and Hong, Y. J., 1989, "Separating Flow Over Repeated Surface Mounted-Ribs in a Square Duct," *AIAA Journal*, Vol. 27, pp. 770–775.
- Kline, S. J., and McClintock, F. A., 1953, "Describing Uncertainties in Single-Sample Experiments," *Mechanical Engineering*, Vol. 75, Jan., pp. 3–8.
- Lewis, M. J., 1975, "An Elementary Analysis for Predicting the Momentum and Heat Transfer Characteristics of a Hydraulically Rough Surface," *ASME JOURNAL OF HEAT TRANSFER*, Vol. 97, pp. 249–254.
- Metais, B., and Eckert, E. R. G., 1964, "Forced, Mixed and Free Convection Regimes," *ASME JOURNAL OF HEAT TRANSFER*, Vol. 86, pp. 295–296.
- Metzger, D. E., Vedula, R. D., and Breen, D. D., 1987, "The Effect of Rib Angle and Length on Convection Heat Transfer in Rib-Roughened Triangular Ducts," *Proceedings of the 1987 ASME/JSME Thermal Engineering Joint Conference*, Vol. 3, pp. 327–333.
- Moffat, R. J., 1988, "Describing the Uncertainties in Experimental Results," *Exp. Thermal Fluid Science*, Vol. 1, pp. 3–17.
- Nikuradse, J., 1933, "Laws of Flow in Rough Pipes," *VDI Forsch.*, Vol. 361.
- Nummer, W., 1958, "Heat Transfer and Pressure Drop in Rough Tubes," *AERE lib/Trans.*, Vol. 786.
- Siegel, R., and Howell, J. R., 1981, *Thermal Radiation Heat Transfer*, 2nd ed., McGraw-Hill, New York.
- Suo, M., 1978, "Turbine Cooling," in: *The Aerothermodynamics of Aircraft Gas Turbine Engine*, G. Oates, ed., Air Force Aero Propulsion Lab. PFAPL TR 78-52.
- Taylor, J. R., 1980, "Heat Transfer Phenomena in Gas Turbines," ASME Paper No. 80-GT-172.
- Webb, R. L., Eckert, E. R. G., and Goldstein, R. J., 1971, "Heat Transfer and Friction in Tubes With Repeated-Ribs Roughness," *Int. J. Heat Mass Transfer*, Vol. 14, pp. 601–617.
- Webb, R. L., and Eckert, E. R. G., 1972, "Application of Rough Surfaces to Heat Exchanger Design," *Int. J. Heat Mass Transfer*, Vol. 15, pp. 1647–1658.

Local Heat Transfer Behavior and Its Impact on a Single-Row, Annularly Finned Tube Heat Exchanger

X. Hu

Graduate Research Assistant.

A. M. Jacobi

Assistant Professor of
Mechanical Engineering.
Assoc. Mem. ASME

Department of Mechanical and
Industrial Engineering,
The University of Illinois
at Urbana-Champaign,
Urbana, IL 61801

Experimental studies of the local mass transfer characteristics of annularly finned tubes in crossflow are presented. Variations due to boundary layer development, forward-edge separation, the tube wake, horseshoe vortices, and tip vortices are discussed. In addition, regularly located local maxima in mass transfer rates associated with the horseshoe vortex system are found, and conjecture as to their mechanism is offered. Inferring heat transfer behavior from the mass transfer results, we find that the true fin efficiency is always less than that obtained with an assumed constant convective heat transfer coefficient. The difference is 3–7 percent for high-conductivity materials such as aluminum alloys, and 9–17 percent for low-conductivity materials such as mild steels.

Introduction

The United States currently uses energy at a rate roughly equivalent to 39.8 million barrels of oil per day (Hedley, 1986). More than a third of this energy is used for residential and commercial space heating and air-conditioning, residential and commercial water heating, and industrial petrochemical processing (Krenz, 1984), and in these applications the finned-tube heat exchanger plays a major role. A 10 percent efficiency improvement in the cited applications would save about 1.5 million barrels of oil per day, and reduce atmospheric CO₂ emissions by about 400 million metric tons per year.

When evaluating or enhancing heat exchanger performance, the fin efficiency is an extremely important parameter. Several studies have been directed at optimizing the fin efficiency through geometric and material variations (see Eckert and Drake, 1987; Poulikakos, 1980), but due to the lack of information about local convective heat transfer characteristics, these studies adopted Gardner's assumption of a constant convective heat transfer coefficient over the entire fin (Gardner, 1945). A recent study by Huang and Shah (1991) explored all Gardner's assumptions for straight fins, and concluded that the uniform heat transfer coefficient assumption might lead to gross errors in analyzing fin heat transfer. In typical applications, the other Gardner assumptions lead to very small errors (see Huang and Shah, 1991).

The fin efficiency essentially compares the thermal performance of the fin to that of a perfect heat conductor, and from Eq. (1) the local effects are obvious.

$$\eta_f = \frac{\int_{A_f} h(r, \phi) \theta(r, \phi) dA}{\int_{A_f} h(r, \phi) dA} \quad (1)$$

If one assumes a constant heat transfer coefficient, Eq. (1) yields Gardner's fin efficiency, η_G .

Fin efficiency measurements are difficult to obtain, because temperature measurements within the fin or on its surface are inherently difficult to make without disrupting the heat transfer behavior. Thermocouples on the surface can significantly alter

the flow and heat transfer over the surface, and thermocouples within the fin alter its heat conduction behavior. Computational models of heat exchangers can predict certain aspects of the flow (e.g., see Mitra et al., 1991); however, accuracy in heat transfer prediction is limited, and experiments are still needed to verify the numerical results. Several experimental studies of local behavior have been undertaken, and the germane work is reviewed in the following paragraphs.

Literature Review

Neal and Hitchcock (1966) performed experiments with a fully heated model of a finned tube. A mild-steel model tube was placed in the second and sixth rows of a staggered tube bundle. Thermocouples were positioned at 30-deg intervals around the fin. They observed wide variations in local heat transfer behavior, with higher heat transfer over upstream portions of the fin. This behavior was explained as being due to the growing boundary layer and the tube wake. Neal and Hitchcock calculated fin efficiencies from several measured radial temperature distributions, and found true fin efficiencies about 16 percent lower than those obtained using Gardner's assumption. This work revealed some important aspects of the local finned-tube heat transfer characteristics. However, since thermocouples affect the nearby flow and heat transfer, Neal and Hitchcock used few sensors, and the resulting sacrifice in spatial resolution made the results inadequate for resolving detailed flow and heat transfer interactions (vortex structures, etc.).

Zukauskas et al. (1966) used a point heating method, which involved heating only a small portion of a fin and measuring the temperature of the heated portion. The position of the heated portion was changed to determine a spatial distribution of the heat transfer coefficient. Unfortunately, the point-heating method is subject to completely different thermal boundary layer development from that occurring in practice. In the experiment, the velocity boundary layer develops ahead of the thermal boundary layer because the leading edge of the fin may not coincide with the leading edge of the heated portion of the fin. In application the fin is almost always heated to its leading edge. Because of this artificial unheated starting length, the difference between experimental and actual behavior may be great.

Legkiy et al. (1974) studied local heat transfer on a single

tube with circular fins. They embedded six heat flux sensors on the fin surface, and used nearby thermocouples to infer local transfer coefficients. From their data one may infer that boundary layer development and root vortices play significant roles in the heat transfer; their data also suggest that leading-edge separation may be important. However, the spatial resolution was insufficient for a clear understanding of the local flow and heat transfer interactions, and the impact of the modifications needed to install flow and temperature transducers is unclear. Furthermore, the study was severely limited in its use of a single tube, as neighboring tubes may have a profound effect on both local and averaged behavior.

Kruckels and Kottke (1970) used a chemical reaction between a surface coating on a finned-tube heat exchanger and ammonia added to the air stream. The reaction caused a discoloration that was photometrically measured to yield mass transfer coefficients. The method relied on calibration to empirical results, and its accuracy is unclear. A direct comparison is difficult because of geometric differences, but the study of Kruckels and Kottke appears to yield transfer coefficients much lower than those of Legkiy et al. (1974) (discussed further with the results of this study). Qualitatively, the data of Kruckels and Kottke reflected the influence of the horseshoe vortex, tube wake, boundary-layer development, and leading-edge separation. The results were limited to two Reynolds numbers, and neither the heat transfer behavior nor the impact on fin efficiency were explored.

Another method relying on mass transfer results is that of naphthalene sublimation. Saboya and Sparrow (1974a, 1974b) and Goldstein and Sparrow (1976) have applied the technique to study local behavior on plate finned-tube heat exchangers. A more detailed review of the method, its applicability, and limitations may be found from Hu (1992) and Chen (1988).

Sparrow and Chastain (1986) studied angle-of-attack effects on a single annular fin on a single tube. They used a 30-deg section of the fin covered with a thin layer of naphthalene as

the "sensor," and put the sensor at varying locations. They concluded that the overall heat transfer performance of an annular fin was not significantly affected by small departures of the angle of attack from zero; however, they found local variations to be significant. The spatial resolution of their study was insufficient for determining local flow and heat transfer interactions, so they undertook a visual study, which showed the presence of forward-edge separation, boundary-layer development, horseshoe vortices, and a wake. The visual aspects of their study were significant, and improved our current understanding, but these studies were limited to angle-of-attack effects at a particular Reynolds number. The quantitative results from their naphthalene study are of limited use, because of the poor spatial resolution, and because the "sectional" use of naphthalene suffers a shortcoming analogous to the point-heating method. Furthermore, one must remember that these studies were conducted on a single tube with a single fin, not a finned tube in a heat exchanger.

The annularly finned tube heat exchanger finds wide application, and its performance remains an important issue. Correlations available in the literature rely on the assumption that the convective heat transfer coefficient is uniform on the finned surface. To understand and predict the performance of these devices, there must be a clear understanding of the local heat transfer behavior. This is especially true if one wishes to enhance or optimize the heat transfer performance. Previous studies on this topic have been limited in spatial resolution or applicability. The purpose of this report is to explore in detail the local heat transfer behavior in a one-row, finned-tube heat exchanger, to determine what flow structures play a role in this distribution, and how they impact the true fin efficiency.

Experimental Method

Experiments were conducted in a wind tunnel, shown schematically in Fig. 1, consisting of an inlet, a test section, an

Nomenclature

A_f = fin surface area, m^2	M^2 = dimensionless fin parameter = $D_F^2 h(r, \phi) / 2k_f \delta$	Δt = total elapsed time during wind-tunnel exposure, s
D_{AB} = the mass diffusivity of naphthalene ($C_{10}H_8$) in air, m^2/s	\bar{M}^2 = area-averaged dimensionless fin parameter = $D_F^2 \bar{h} / 2k_f \delta$	$\delta \tau$ = time interval between point measurements of the naphthalene contour, s
D_F = fin diameter, m	Nu = Nusselt number = hD_H/k	δ = fin thickness, m
D_H = hydraulic diameter of heat exchanger, m	Pr = Prandtl number	δ_{sb} = local naphthalene sublimation depth, m
D_T = tube outside diameter, m	R = dimensionless radius = $2r/D_F$	η_f = the true fin efficiency, Eq. 1
$h(r, \phi)$ = local heat transfer coefficient, W/m^2K	R_i = dimensionless radius at outside of tube = D_T/D_F	η_G = Gardner's fin efficiency, calculated assuming $h(r, \phi) = \bar{h}$
\bar{h} = heat transfer coefficient averaged over r and ϕ , W/m^2K	Re = Reynolds number = $U_{max} D_H / \nu$	θ = dimensionless temperature = $(T - T_\infty) / (T_o - T_\infty)$
$h_m(r, \phi)$ = local mass transfer coefficient, m/s	r = radial coordinate, m	θ_G = dimensionless temperature, θ , assuming $h(r, \phi) = \bar{h}$
$\bar{h}_m(r)$ = mass transfer coefficient averaged over ϕ , m/s	S_F = fin pitch, fins/m	ν = kinematic viscosity of the air, m^2/s
$\bar{h}_m(\phi)$ = mass transfer coefficient averaged over r , m/s	S_T = transverse tube pitch, m	Ξ = departure from Gardner's fin efficiency = $(\eta_G - \eta_f) / \eta_f$
$\bar{\bar{h}}_m$ = mass transfer coefficient averaged over r and ϕ , m/s	Sc = Schmidt number	ρ_s = mass density of solid naphthalene, kg/m^3
I_n, K_n = modified Bessel functions of the first and second kind, order n , respectively	Sh = Sherwood number = $h_m D_H / D_{AB}$	$\rho_{v,w}$ = mass density of naphthalene vapor at the fin surface, kg/m^3
k = thermal conductivity of the air, W/mK	T = temperature at a location (r, ϕ) on the fin, K	ϕ = angular coordinate, rad
k_f = thermal conductivity of the fin, W/mK	T_o = temperature at the fin base (i.e., at $R = R_i$), K	
	T_∞ = temperature in the free stream (i.e., the air temperature), K	
	U_{max} = maximum velocity (i.e., at minimum flow area), m/s	
	Δm = mass change during wind-tunnel exposure, kg	

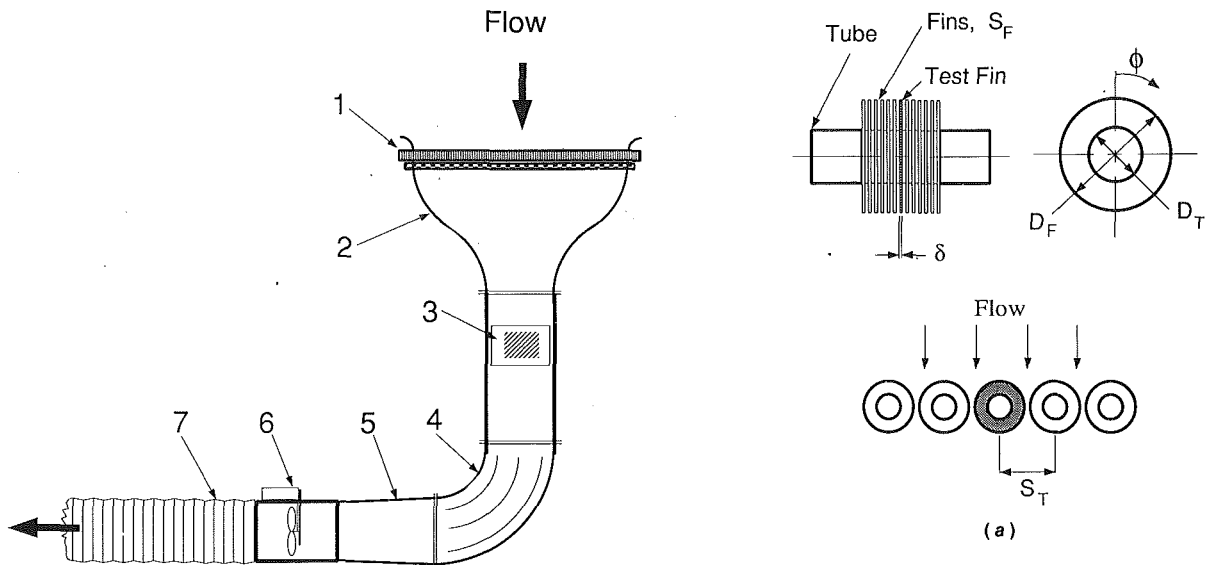


Fig. 1 Schematic of the induction wind tunnel used for the sublimation experiments: (1) inlet, (2) contraction, (3) test-section viewing window, (4) elbow, (5) transition, (6) blower, and (7) discharge

elbow/transition, a blower, and an open-loop discharge. The inlet was equipped with a 9:1 contraction, pull-out grids, and a honeycomb flow straightener. The velocity profile was measured with a Pitot tube and a hot-wire anemometer at the test-section inlet, and was found to be flat within 5.2 percent, with a free-stream turbulence on the order of 0.2 percent.

The test section ($40 \times 40 \times 135$ cm) provided visual access during experiments, and easy access to the heat exchanger for quick installation and removal of specimens. Downstream of the test section the flow encountered a 90-deg bend with turning vanes to avoid flow separation. The flow then entered a rectangular to circular transition.

The blower was located downstream of the test section to avoid heating the free-stream flow. The open-loop discharge vented air from the wind tunnel to the outside atmosphere, so that naphthalene did not contaminate the laboratory air. The air flow rate was modulated by varying the power input to the blower, and the maximum velocity at the test-section inlet was 9.0–10.0 m/s.

Five finned tubes were constructed and assembled as a single-row heat exchanger as shown in Fig. 2; its dimensions are given in Table 1. The center tube was made separable, so that a test fin could be installed. The test fin contained cast naphthalene, and all the other fins and tubes simply provided the proper flow conditions. The approach air flow was perpendicular to this single-row heat exchanger.

Casting of the Test Specimen. The mold and test fin were always cleaned carefully prior to casting a fin. To perform the casting, solid naphthalene was heated above its melting point of 80.2°C , and poured into a preheated mold. A vent hole allowed air to escape as the mold filled with liquid naphthalene. After solidification, it was often difficult to part the mold without breaking the naphthalene surface. Therefore, the mold was reheated to within a few degrees of the melting point of naphthalene, at which point it was parted. During this process, mold temperatures were monitored with type-T thermocouples installed within the mold. This procedure had a much higher success rate than parting the mold at room temperature, but successful castings still required a highly polished mold surface.

The heating and cooling rates during the casting process seemed to affect the appearance of the naphthalene surface, which was sometimes milky white, sometimes transparent, and sometimes semi-transparent. The transparent surface was

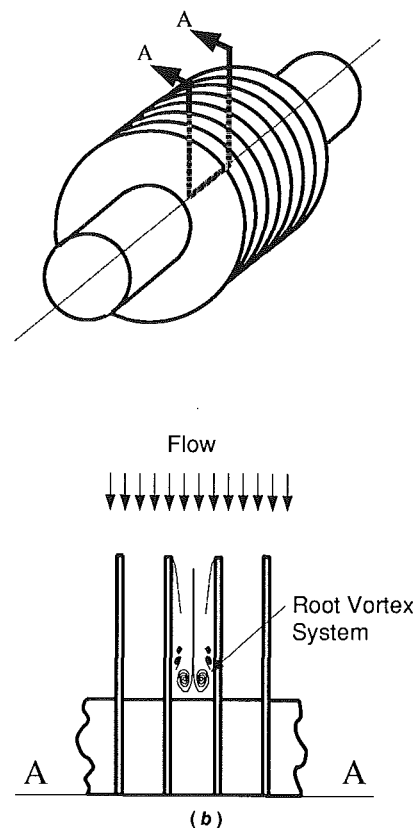


Fig. 2 Geometry and flow considerations: (a) geometry of the test fin and the single-row heat exchanger, (b) the general nature of the expected flow, showing horseshoe vortices between neighboring fins

hardest, and while no effect of this appearance has otherwise been noted in the literature, neither has it been discussed in detail.

After casting naphthalene on its surface, the test fin was geometrically identical to the other fins. To prevent sublimation by natural convection, the test fin was placed in a beaker covered with parafilm for storage. Solid naphthalene particles were put in the beaker in advance, to generate a condition close to saturation within the beaker.

Instrumentation. Temperature measurements were needed since the partial pressure of naphthalene is a function of the temperature. At room temperature, a 1°C change in temper-

Table 1 Heat exchanger dimensions

Fin diameter, D_F	Tube diameter, D_T	Fin pitch, S_F	Tube pitch, S_T	Fin thickness, δ
76.2 mm	38.1 mm	141 fins/m	76.2 mm	1.02 mm

ature will cause about a 10 percent change in the saturation pressure of naphthalene. Therefore, type-T thermocouples were placed on the heat exchanger surface near the test fin, and in the flow upstream and downstream of the exchanger. These thermocouples were used with a high-resolution A/D converter and signal amplifier to provide the needed temperature data ($\pm 0.25^\circ\text{C}$).

Pitot-static pressure differences at the inlet of the test section were measured with a Pitot-static tube and an electric manometer (± 0.12 Pa). Air density was inferred from laboratory temperature ($\pm 0.25^\circ\text{C}$), humidity ($\pm 2.5\%$ rh), and pressure (± 0.1 mmHg).

For the measurement of local naphthalene sublimation depths, a computer-controlled milling machine was used as a positioning device, with an ultraprecision depth gage, a signal conditioner, and a digital voltmeter used to measure surface contour. The depth gage had a published repeatability of ± 0.1 μm . The gage head was a 1-mm-dia sphere, which was adequate for resolving the observed spatial features. However, because of the gage head dimensions, surface irregularities, positioning uncertainty, and A/D conversion limitations, the sublimation depths were assigned an uncertainty of ± 0.58 μm . Typical sublimation depths were on the order of 25 μm .

The test fin was weighed before and after a wind tunnel exposure using a precision balance ($\pm 1(10^{-4})\text{g}$).

Experimental Procedure. The data acquisition system and wind tunnel apparatus were subjected to a warm-up period, and an initial reading of local naphthalene contour was recorded. Contour measurements were at 10-deg increments at 10 different radii, thus providing 360 points on the annular area of 34.2 cm^2 . Each surface contour map required about 20 minutes to complete. After the contour measurement, the fin was put into the storage beaker and moved to the wind tunnel room.

Barometric pressure and the other ambient conditions were recorded, and then the fin was weighted and installed in the wind tunnel. The wind tunnel speed was set, and during the test run the Pitot-static pressure and ambient conditions were recorded several times. Temperatures in the wind tunnel were recorded every two minutes by the computer-controlled data acquisition system. After 40 to 50 minutes in the wind tunnel, the blower was turned off, and the fin removed, weighed, and put back into the storage beaker. The barometric pressure and other ambient conditions were noted.

The fin was returned to the milling machine for the second naphthalene contour measurement. While conducting these experiments, it was found that the naphthalene sublimation depth caused by natural convection during contour measurement could be as high as 15 percent of that due to forced convection in the wind tunnel. To account for this contribution, a third measurement of the surface contour was taken immediately following the second, and as explained below, this afforded a correction for natural convection.

At the end of the first complete contour measurement, the first point sampled had a natural-convection exposure for a time period of τ , which was the total measuring time. The second point had a natural convection exposure corresponding to $\tau - \delta\tau$, where $\delta\tau$ was the time interval between two neighboring point measurements. The third point was exposed for $\tau - 2\delta\tau$, ... The n th point had no period of natural-convection exposure. When the second contour measurement started, the first point sampled had no added natural convection exposure; however, the second point had an added exposure of $\delta\tau$, the third $2\delta\tau$, and so on. The n th point was

exposed to natural convection for a period of τ during the second contour measurement. So, after recording the second surface contour measurement, every point sampled had been exposed to natural convection for the same period of time, τ . Assuming the natural-convection environment was constant during this period, which is a fairly good assumption because lab temperatures and naphthalene concentrations (solubility Grashof numbers) fluctuated very little, a third contour measurement taken immediately following the second would provide data on the local sublimation depths due to natural convection for a period of τ . This measurement was then used to correct the wind tunnel experiments for sublimation due to natural convection that occurred during contour measurement.

Reduction and Interpretation

The Reynolds number for flow through the heat exchanger followed the conventional usage

$$\text{Re} = \frac{U_{\max} D_H}{\nu} \tag{2}$$

where U_{\max} is the maximum flow velocity, and D_H is the hydraulic diameter of the heat exchanger. For this heat exchanger $D_H = 9.17\text{mm}$ (refer to Kays and London (1984) and Hu (1992) for definition and geometry details).

The local Sherwood number was determined from measurements of local sublimation depth and the appropriate thermophysical properties. It may be written as:

$$\text{Sh}(r, \phi) = \frac{h_m(r, \phi) D_H}{D_{AB}} \tag{3}$$

The diffusivity was obtained by correcting the data of Mack (1925) for the wind tunnel temperature and pressure per Chen and Othmer (1962). Assuming no free-stream concentration of naphthalene (care was taken to ensure this), the local mass transfer coefficients were determined from the sublimation depth measurements through

$$h_m(r, \phi) = \frac{\delta_{sb}(r, \phi) \rho_s}{\rho_{v,w} \Delta t} \tag{4}$$

Δt corresponds to the wind tunnel exposure time. The density of solid naphthalene was taken as 1162.0 kg/m^3 per Kudchadker et al. (1978), and $\rho_{v,w}$ was determined by assuming ideal gas behavior, with naphthalene vapor pressure determined using the correlation given by Ambrose et al. (1975). The sublimation depths were corrected for natural convection as discussed earlier. Average Sherwood numbers were determined by

$$\overline{\text{Sh}} = \frac{\overline{h_m} D_H}{D_{AB}} \tag{5}$$

where $\overline{h_m}$ was determined through direct integration:

$$\overline{h_m} = \frac{\rho_s}{\rho_{v,w} \Delta t} \frac{1}{A_f} \int_{A_f} \delta_{sb}(r, \phi) dA \tag{6}$$

or from the precision mass measurements

$$\overline{h_m} = \frac{\Delta m}{\rho_{v,w} \Delta t A_f} \tag{7}$$

which were used as a redundant measurement.

Other methods of averaging were useful for interpretation, namely, we defined:

$$\overline{\text{Sh}}(r) = \frac{\overline{h}_m(r) D_H}{D_{AB}} \quad (8)$$

where

$$\overline{h}_m(r) = \frac{1}{2\pi} \int_0^{2\pi} h_m(r, \phi) d\phi \quad (9)$$

and

$$\overline{\text{Sh}}(\phi) = \frac{\overline{h}_m(\phi) D_H}{D_{AB}} \quad (10)$$

where

$$\overline{h}_m(\phi) = \frac{8}{D_F^2 - D_T^2} \int_{D_T/2}^{D_F/2} h_m(r, \phi) r dr \quad (11)$$

The thermophysical properties of air were determined using correlations due to Kays and London (1984), and then invoking the heat and mass analogy (see Hu, 1992, for details) Nusselt numbers corresponding to the above Sherwood numbers were inferred through

$$\text{Nu} = \text{Sh} \left(\frac{\text{Pr}}{\text{Sc}} \right)^{1/3} \quad (12)$$

With this approach, the fin efficiency could be studied by modeling the annular fin as an isotropic homogeneous medium, and neglecting thermal gradients in the z direction (a thin-fin approximation¹):

$$\frac{\partial^2 \theta}{\partial R^2} + \frac{1}{R} \frac{\partial \theta}{\partial R} + \frac{1}{R^2} \frac{\partial^2 \theta}{\partial \phi^2} - M^2 \theta = 0 \quad (13)$$

with boundary conditions:

$$\theta(R = R_i, \phi) = 1 \quad \text{and} \quad \left(\frac{\partial \theta}{\partial R} \right)_{R=1} = 0 \quad (14)$$

and

$$\left(\frac{\partial \theta}{\partial \phi} \right)_{\phi=0} = \left(\frac{\partial \theta}{\partial \phi} \right)_{\phi=\pi} = 0$$

where

$$M^2 = D_F^2 h(r, \phi) / 2k_f \delta \quad (15)$$

The insulated fin tip boundary condition corresponds to the experimental conditions. Furthermore, since there are no published data available for the convective behavior from the fin tips, and since Huang and Shah (1991) demonstrate that the assumption has very little impact on the fin efficiency, it is a reasonable approach.

Using Eq. (12) and inferring local heat transfer results from the mass transfer experiments, Eqs. (13)–(15) were solved numerically using a finite difference technique. This temperature distribution was then used in Eq. (1), which was numerically integrated to yield the true fin efficiency, η_f . The numerical error in this procedure was estimated to be less than 1 percent.

If one assumes $h(r, \phi) = \overline{h}$, then Eqs. (13)–(15) have the well-known solution:

$$\theta_G = \frac{I_0(\overline{MR})K_1(\overline{M}) + K_0(\overline{MR})I_1(\overline{M})}{I_0(\overline{MR}_i)K_1(\overline{M}) + K_0(\overline{MR}_i)I_1(\overline{M})} \quad (16)$$

and,

$$\eta_G = \frac{2D_T D_F}{\overline{M}(D_F^2 - D_T^2)} \frac{I_1(\overline{M})K_1(\overline{MR}_i) - K_1(\overline{M})I_1(\overline{MR}_i)}{I_0(\overline{MR}_i)K_1(\overline{M}) + K_0(\overline{MR}_i)I_1(\overline{M})} \quad (17)$$

Applying the method of Kline and McClintock (1953), the uncertainties in Re were estimated to be 1 percent, and uncertainties in Sherwood numbers were estimated to be 5 percent

(Hu, 1992). However, these uncertainties were obtained assuming ρ_s as a known constant. Variations might occur through voids in the casting (refer also to the earlier note regarding the appearance of the naphthalene casting). When comparing the average Sherwood number obtained through integration of the local values, i.e., by Eq. (6), to that obtained from direct mass measurements, i.e., by Eq. (7), the differences were usually less than 10 percent. When the difference for a test exceeded 10 percent it was typically accompanied by a notably high local sublimation depth in a confined area on the fin, indicating that a small “flake” of naphthalene may have been broken from the surface during the experiment. Taking this possible source of error into account, we feel it is appropriate to assign an uncertainty of 5 percent to the local Sherwood numbers relative to each other (except for the cases discussed above), and an uncertainty of 10 percent to the averaged Sherwood number.

Results

Local Heat and Mass Transfer Behavior. The general nature of the flow is sketched in Fig. 2, and it may be useful to refer to the sketch throughout this discussion. Local Sherwood number distributions for Reynolds numbers between about 3300 and 12,000 are shown in Fig. 3. From the figure it may be noted that as Re increases, the distributions show a trend of generally increasing local Sh . At the lowest Re , the mass transfer was relatively high in two places: near the fin tip for $-90 \text{ deg} < \phi < 90 \text{ deg}$, due to boundary-layer development; and near the fin root for $-30 \text{ deg} < \phi < 30 \text{ deg}$, due to a weak or perhaps intermittent root vortex. At this Re , the mass transfer was lowest over all radii in $140 \text{ deg} < \phi < -140 \text{ deg}$, due to the tube wake.

For increasing Re , up to about 9000, the influence of boundary layer development and the horseshoe vortex become more prominent. The tube wake clearly plays a role; however, there appears to be backwash in the wake, as evidenced by higher mass transfer rates near the fin tip for $170 \text{ deg} < \phi < -170 \text{ deg}$.

For $Re \geq 9000$, it appears that the boundary layer may separate from the leading edge of the fin. This is suggested by the movement of the peak mass fluxes from the fin tip to a position farther back on the fin (a reattachment zone), and agrees with earlier observations by Kruckels and Kottke (1970). The horseshoe vortex and tube wake are still dominating features. With increasing Re above about 11,000, mass transfer over all r in $-90 \text{ deg} < \phi < 90 \text{ deg}$ is enhanced, but it is difficult to identify the flow features responsible.

An especially interesting interaction between the mass transfer and horseshoe vortex may be seen at almost all Re in Fig. 3, by examining the local Sh under the imagined core of the primary root vortex. Starting at $\phi \approx 0 \text{ deg}$ and following the vortex around the circumference of the tube, one notes almost periodic peaks in local Sh . These peaks are most obvious in the “legs” of the horseshoe vortex (see $Re = 4260, 6880, 8440, 9240$, and $10,800$), but we have also observed them in the “body” (i.e., $-90 \text{ deg} < \phi < 90 \text{ deg}$) (these features are identified in Fig. 4 for clarification). The high level of spatial resolution afforded by the sublimation technique allows this apparently unique observation.

We feel the peaks have two viable explanations. The first relies on the observed oscillatory behavior in the plane of symmetry of a root vortex system (Baker, 1979). In this case the geometry is complex, and the horseshoe vortex interacts with the vortex on the opposing fin, and with the fin surface (or the vortex image). As the two primary root vortices between a pair of fins interact, they induce a movement toward the tube. When the root vortex approaches the tube, it interacts with the tube surface, and is forced toward its fin. Interaction with the fin surfaces causes it to move back upstream until

¹The thin-fin approximation is appropriate for our study, as the maximum Biot number remains below 0.0011 (see Huang and Shah, 1991).

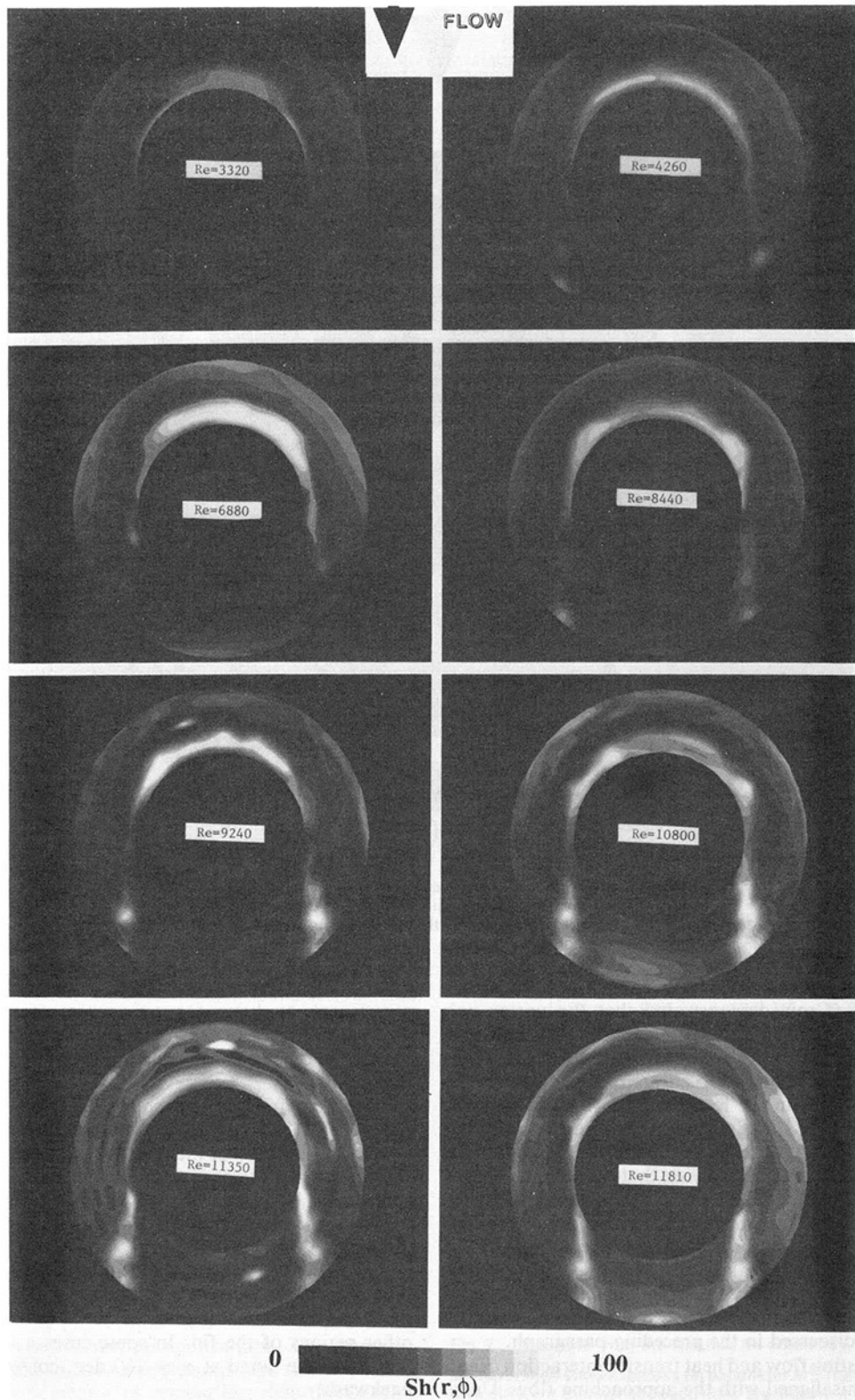


Fig. 3 Sample distributions of local Sherwood numbers on annular fins. From upper left, going right to left and down, distributions are shown for $Re = 3320, 4260, 6880, 8440, 9240, 10,800, 11,350,$ and $11,810$. Sherwood numbers range from 0 (black) to over 100 (white).

interaction with a secondary vortex lifts it from the fin toward the opposing primary vortex, thus restarting the cycle. If the frequency of this oscillatory behavior varied around the circumference of the cube, the horseshoe vortex system would be distorted in ϕ , and could produce the observed maxima.

The second conjectured mechanism relies on the manifestation of an instability similar to that occurring between the trailing vortices of an aircraft, i.e., a Crow (1970) instability. The idea of a Crow instability has appeal, as in the vortex "legs" one may observe little dependence of the location of

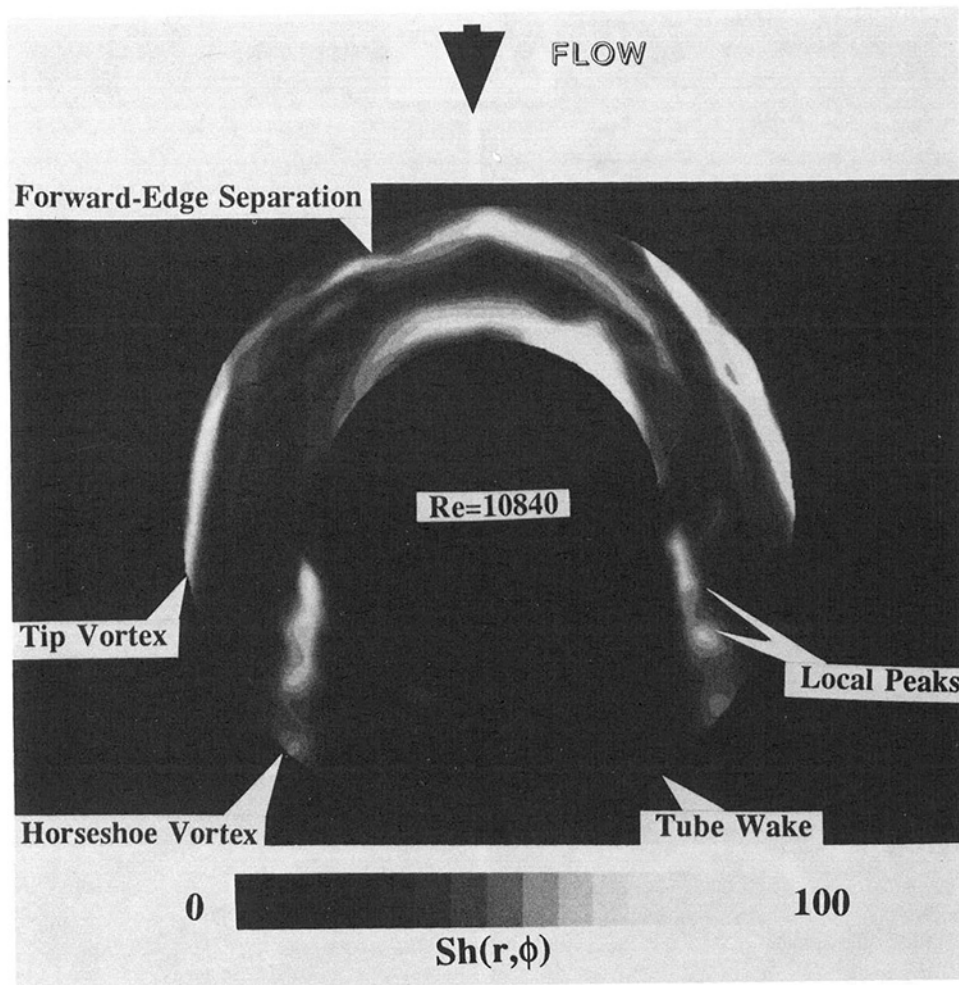


Fig. 4 Local Sherwood number distribution on the low-pressure side of an annular fin with a 2 deg angle of attack at a Reynolds number of 10,840, showing the influence of tip vortices, and local maxima in the legs of the horseshoe vortex

the peaks on Re . Crow demonstrated that the vortex pair generated by a moving aircraft would be symmetrically unstable at a wavelength of 8.6 times the distance between the vortices. From the sublimation measurements, one may determine that the peaks in the legs are fairly regularly spaced at 9 mm. Using Crow's analysis as a rough estimate of the behavior, this spacing of maxima would correspond to a wavelength of about 18 mm, thus implying that the vortices are 2.5 mm apart. The distance from fin surface to fin surface is about 6 mm, and thus one has an image of the primary vortices each about 1.75 mm from the fin surface, and separated by 2.5 mm. However, while the peaks in the legs appear insensitive to Re , the peaks appearing in the body appear to change location with Re , and might be due to a more complex interaction, like that discussed in the preceding paragraph.

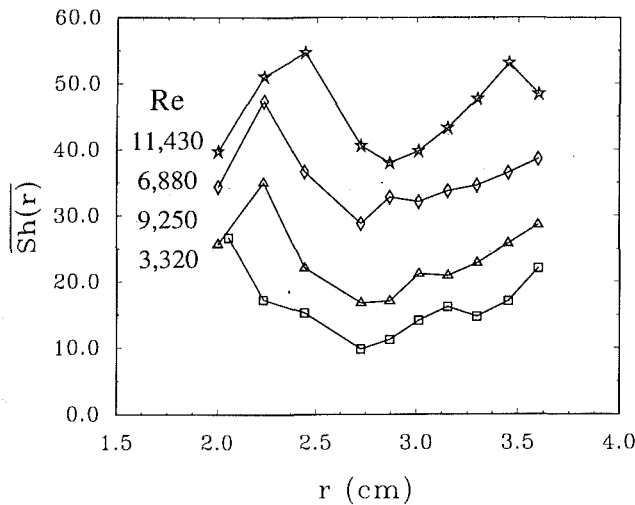
Another interesting flow and heat transfer interaction occurs when the fin is misaligned with the approaching flow. Under these conditions, tip vortices like those commonly pictured on delta wings form. An example of the resulting $Sh(r, \phi)$ distribution at $Re = 10,840$, for a fin at approximately a 2 deg angle of attack, is shown in Fig. 4. This is apparently the first time these structures have been reported in this context. Unfortunately, no mass transfer measurements were simultaneously available from the opposing side of the fin, and the impact of fin efficiency remains unclear.

Averaged Results. If the Sherwood number is averaged

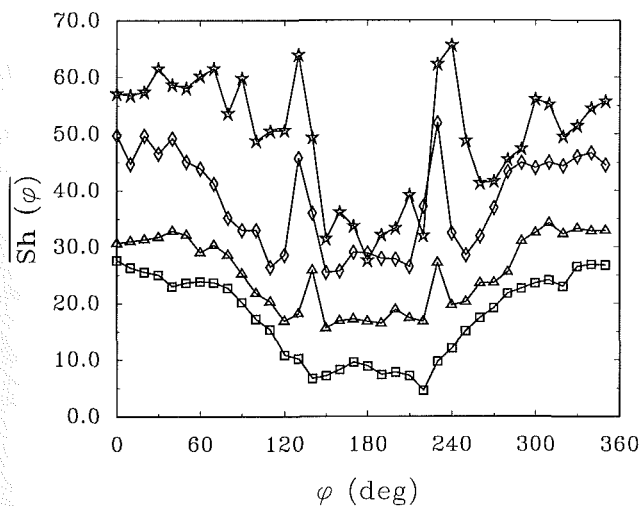
over r or ϕ , as shown for some representative data in Fig. 5, the data reinforce the earlier discussion, and provided a basis for further quantitative evaluation of the flow and heat transfer interactions.

The circumferentially averaged Sherwood numbers, $\overline{Sh}(r)$, have a jump from low to high as r increases into the root vortex system. With a further increase in r the transfer rates decrease, then eventually increase again as the fin tip is approached. In some cases, $\overline{Sh}(r)$ shows a drop near $r = D_F/2$, perhaps due to the separation bubble. The radially averaged Sherwood numbers, $\overline{Sh}(\phi)$, have higher values in the front of the tube, and usually have two peaks behind the tube due to the legs of the horseshoe vortex system. Between the legs of the vortex is the wake region, where $\overline{Sh}(\phi)$ is 25–40 percent lower than the other regions of the fin. In some cases a local maximum in $\overline{Sh}(\phi)$ may be noted at $\phi \approx 180$ deg, corresponding to wake backwash.

\overline{Sh} is shown as a function of Re in Fig. 6. A generalized correlation for finned tubes (Zukauskas, 1987) predicts averaged results about 20 percent higher than the data at low Reynolds numbers, and 30 percent higher at Reynolds numbers of 12,000. The data of Fig. 6 are for fin surfaces only (excluding the tube), and were not determined by tacitly assuming a constant heat transfer coefficient; while agreement between the correlation and the data may therefore not be expected, the general agreement is reassuring. By estimating averaged results from the local data presented by Kruckels and Kottke (1970),



(a)



(b)

Fig. 5 Partially averaged Sherwood number behavior: (a) circumferentially averaged, and (b) radially averaged. The Reynolds numbers are 3320, 9250, 6880, and 11,430, as noted in (a) for both the circumferentially and radially averaged results.

we find their results to be approximately 70 percent below our data.

Impact on Fin Efficiency. Applying the heat and mass analogy to the local distributions given above, and using the fin model discussed earlier, the impact of local variation in $Nu(r, \phi)$ on the fin efficiency, η_f , was studied. In this respect some attention to application is warranted, and two cases are presented in Table 2, one using k_f for common aluminum alloys, and one using k_f for mild steels. Mild steels are very commonly used in petrochemical applications. The representative data presented in the table demonstrate that the actual fin efficiency may be nearly 18 percent less than the Gardner fin efficiency, when local heat transfer behavior is properly included. For low-conductivity fins, the actual fin efficiency ranged from 55 to about 75 percent. The high-conductivity fins had actual efficiencies between 80 and 95 percent.

It is interesting to examine these results graphically, as shown in Fig. 7, where Ξ is plotted against \overline{M}^2 for the portion of the data presented in Table 2. These data appear to fall onto a single curve (as do the other data). This behavior strongly suggests that a given value of \overline{M}^2 would uniquely define Ξ , regardless of the Reynolds number. Although Ξ depends upon

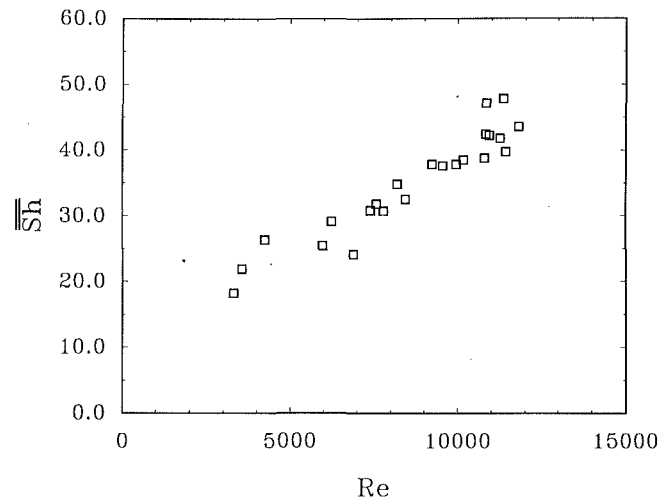


Fig. 6 Area-averaged Sherwood number behavior with Reynolds number for an annular fin surface (does not include the tube surface)

Table 2 Local effects on fin efficiency

Re	\overline{Sh}	\overline{h} (W/m ² K)	$\Xi = (\eta_G - \eta_f)/\eta_f$	
			$k_f = 171$ (W/mK)	$k_f = 46$ (W/mK)
3320	16.7	31.6	2.9%	8.6%
5980	26.1	49.5	4.2%	12.1%
6880	23.8	45.5	3.6%	10.5%
7580	26.6	50.5	4.6%	13.0%
8440	29.4	55.8	3.7%	10.3%
9560	33.8	64.2	4.7%	12.6%
10,180	39.5	75.1	4.6%	11.8%
10,800	43.5	82.7	6.4%	16.0%
10,840	40.9	77.7	5.5%	13.6%
11,350	45.2	86.3	6.0%	14.9%
11,430	46.2	88.4	7.0%	17.7%
11,810	43.5	92.9	6.5%	15.6%

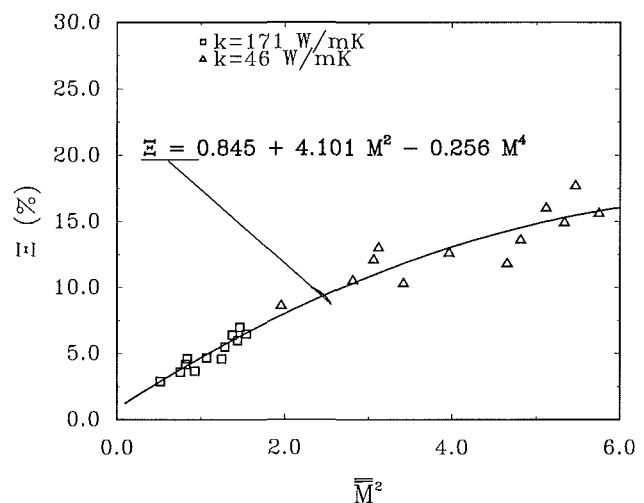


Fig. 7 Departure from the Gardner fin efficiency, Ξ (see Table 2), with area-averaged dimensionless fin parameter \overline{M}^2 . The results for two cases with different thermal conductivities are shown: $k = 46$ W/mK and $k = 171$ W/mK. A least-squares fit to the data is provided in the figure.

the Reynolds number, as is evident from Table 2, this dependence is evidently influenced by the overall levels of $h(r, \phi)$ (i.e., \overline{h}) more heavily than by changes in the details of the $h(r, \phi)$ distribution. Details on the flow are important; however, once the details are known, small changes are unimportant with respect to the difference between the true fin efficiency and the Gardner fin efficiency. In this case, a family of Ξ versus \overline{M}^2 curves for various geometric changes would be a

useful tool, allowing the engineer to apply existing heat exchanger correlations to slightly different geometries, with a high level of confidence that errors in fin efficiency have been properly taken into account. A fit to the data has been provided in Fig. 7.

Conclusions

Over the Reynolds number range of 3300 to 12,000, significant variations in local convective heat and mass transfer behavior occur. Boundary-layer development, forward-edge separation, the tube wake, and horseshoe vortices all play a role. Tip vortices may significantly influence local behavior for the annular fin, even if the angle of attack is very small (less than 3 deg); however, the overall effect on the fin efficiency remains unclear.

An instability in the horseshoe vortex system results in local maxima in the heat and mass transfer rates associated with that structure. These are significant, and our conjecture is that they are due to a Crow-like instability between the legs of opposing horseshoe vortices.

By inferring heat transfer behavior from the mass transfer results, the true fin efficiency was found to be nearly 18 percent below that predicted using Gardner's constant-heat-transfer-coefficient assumption for mild steel fins. The effect appears to be greatest at high Re. For high-conductivity materials (e.g., aluminum alloys), the effect is likely limited to 7 percent for $Re < 12,000$. Figure 7 and the provided curve fit are useful for assessing the impact of this effect for other materials.

For applications where a heat exchanger has been tested in a wind tunnel and is subsequently applied under conditions identical to the test conditions, the performance is known; notwithstanding, the local behavior is crucial to understanding finned-tube heat exchanger performance. Local flow structures play important roles, and it may be possible to enhance performance by manipulating these flow and heat transfer interactions. Local effects have a profound influence on the true fin efficiency, and should not be ignored. Correlations available in the literature are, strictly speaking, only applicable in convective environments identical to those under which they were developed. The parameter \bar{E} provides a convenient way to account for the local effects. Correlations available in the literature would be more widely applicable, and enhancement techniques more intelligently pursued, if the local behavior was understood and considered.

References

- Ambrose, D., Lawrenson, I. J., and Sprake, C. H. S., 1975, "The Vapor Pressure of Naphthalene," *Journal of Chemical Thermodynamics*, Vol. 7, pp. 1173-1176.
- Baker, C. J., 1979, "The Laminar Horseshoe Vortex," *Journal of Fluid Mechanics*, Vol. 95, pp. 347-367.
- Chen, N. H., and Othmer, D. F., 1962, "New Generalized Equation for Gas Diffusion Coefficient," *Journal of Chemical Engineering Data*, Vol. 7, No. 1, pp. 37-41.
- Chen, P. H., 1988, "Measurement of Local Mass Transfer From a Gas Turbine Blade," Ph.D. Dissertation, University of Minnesota, Minneapolis, MN.
- Crow, S. C., 1970, "Stability Theory for a Pair of Trailing Vortices," *AIAA Journal*, Vol. 8, pp. 2172-2179.
- Eckert, E. R. G., and Drake, R. M., 1987, *Heat and Mass Transfer*, Hemisphere Publishing, Washington, DC.
- Gardner, K. A., 1945, "Efficiency of Extended Surfaces," *ASME Transactions*, Vol. 67, pp. 621-631.
- Goldstein, L., Jr., and Sparrow, E. M., 1976, "Experiments on the Transfer Characteristics of a Corrugated Fin and Tube Heat Exchanger Configuration," *ASME JOURNAL OF HEAT TRANSFER*, Vol. 98, pp. 26-34.
- Hedley, D., 1986, *World Energy: The Facts and the Future*, 2nd ed., Facts on File Publications, New York.
- Hu, X., 1992, "Local Heat and Mass Transfer Characteristics of Circular-Finned Tubes," M.S. Thesis, Johns Hopkins University, Baltimore, MD.
- Huang, L. J., and Shah, R. K., 1991, "Assessment of Calculation Methods for Efficiency of Straight Fins of Rectangular Profile," *Advances in Heat Exchanger Design, Radiation, and Combustion*, ASME HTD-Vol. 182, pp. 19-30.
- Kays, W. M., and London, A. L., 1984, *Compact Heat Exchangers*, 3rd ed., McGraw-Hill, New York.
- Kline, S. J., and McClintock, F. A., 1953, "Describing Uncertainties in Single-Sample Experiments," *Mechanical Engineering*, Vol. 75, Jan., pp. 3-8.
- Krenz, J. H., 1984, *Energy Conversion and Utilization*, 2nd ed., Allyn and Beacon, Inc., Boston.
- Kruckels, W., and Kottke, V., 1970, "Untersuchung über die Verteilung des Wärmeübergangs an Rippen und Rippenrohr-Modellen," *Chemie. Ing. Tech.*, Vol. 42, pp. 355-362.
- Kudchadker, A. P., Kudchadker, S. A., and Wilhoit, R. C., 1978, *Naphthalene*, American Petroleum Institute, Washington, DC.
- Legkiy, V. M., Pavlenko, V. P., Makarov, A. S., and Zheludov, Y. S., 1974, "Investigation of Local Heat Transfer in a Tube With Annular Fins in Transverse Air Flow," *Heat Transfer—Soviet Research*, Vol. 6, No. 6, pp. 101-107.
- Mack, E., Jr., 1925, "Average Cross-Sectional Areas of Molecules by Gaseous Diffusion Methods," *Journal of American Chemistry Society*, Vol. 47, p. 2468.
- Mitra, N. K., Bastani, A., and Fiebig, M., 1991, "Numerical Simulation of 3D Periodically Fully Developed Flow Between Fins of a Compact Fin-Tube Heat Exchanger," *Advances in Heat Exchanger Design, Radiation, and Combustion*, ASME HTD-Vol. 182, pp. 37-41.
- Neal, S. B. H. C., and Hitchcock, J. A., 1966, "A Study of the Heat Transfer Processes in the Banks of Finned Tubes in Cross Flow, Using a Large Scale Model Technique," *Third International Heat Transfer Conference*, Chicago, IL, Vol. 3, pp. 290-298.
- Poulikakos, D., 1980, "Fin Geometry for Minimum Entropy Generation," M.S. Thesis, University of Colorado, Boulder, CO.
- Saboya, F. E. M., and Sparrow, E. M., 1974a, "Effect of Tube Relocation on the Transfer Capabilities of a Fin and Tube Heat Exchanger," *ASME JOURNAL OF HEAT TRANSFER*, Vol. 96, pp. 421-422.
- Saboya, F. E. M., and Sparrow, E. M., 1974b, "Local and Average Transfer Coefficients for One-Row Plate Fin and Tube Heat Exchanger Configurations," *ASME JOURNAL OF HEAT TRANSFER*, Vol. 96, pp. 265-272.
- Sparrow, E. M., and Chastain, S. R., 1986, "Effect of Angle of Attack on the Heat Transfer Coefficient for an Annular Fin," *International Journal of Heat and Mass Transfer*, Vol. 29, No. 8, pp. 1185-1191.
- Zukauskas, A., Stasiulevichius, J., and Skrinska, A., 1966, "Experimental Investigation of Efficiency of Heat Transfer of a Tube With Spiral Fins in Cross-flow," *Third International Heat Transfer Conference*, Chicago, IL, Vol. 3, pp. 299-305.
- Zukauskas, A., 1987, "Convective Heat Transfer in Cross Flow," in: *Handbook of Single-Phase Convective Heat Transfer*, S. Kakac, R. Shah, and W. Aung, eds., Wiley, New York, p. 6.41.

Optimal Arrays of Pin Fins and Plate Fins in Laminar Forced Convection

A. Bejan

J. A. Jones Professor of
Mechanical Engineering,
Fellow ASME

A. M. Morega

Student Member ASME.

Department of Mechanical Engineering
and Materials Science,
Duke University,
Durham, NC 27706

This paper reports the optimal geometry of an array of fins that minimizes the thermal resistance between the substrate and the flow forced through the fins. The flow regime is laminar. Two fin types are considered: round pin fins, and staggered parallel-plate fins. The optimization of each array proceeds in two steps: The optimal fin thickness is selected in the first step, and the optimal thickness of the fluid channel is selected in the second. The pin-fin array is modeled as a Darcy-flow porous medium. The flow past each plate fin is in the boundary layer regime. The optimal design of each array is described in terms of dimensionless groups. It is shown that the minimum thermal resistance of plate-fin arrays is approximately half of the minimum thermal resistance of heat sinks with continuous fins and fully developed laminar flow in the channels.

Introduction

The analyses and results reported in this paper were inspired by the recent work of Knight et al. (1991). These authors showed how to minimize the thermal resistance of a heat sink with closed finned channels and fully developed flow in each fin-to-fin channel. The individual fin was two-dimensional, i.e., continuous in the direction of flow, and with rectangular cross section (profile). The analysis of Knight et al. (1991) generalized and extended to turbulent flow the optimal finned heat sink analysis reported originally by Tuckerman and Pease (1981), and Tuckerman (1984).

Related studies conducted on electronic cooling in the 1980s, including experimental validations of the optimal designs, were reviewed by Phillips (1987) and Knight et al. (1991). More extensive reviews of the literature have been conducted by Incropera (1988) and Peterson and Ortega (1990). The optimization of two-dimensional plate fins continuous in the flow direction was treated also by Bar-Cohen and Jelinek (1985). Unlike Tuckerman and Pease (1981), Tuckerman (1984), Knight et al. (1991), and the present study, Bar-Cohen and Jelinek (1) did not consider the temperature rise that occurs in the flow direction, and (2) accounted for the heat transfer through the unfinned base area.

The intriguing aspect of this body of work was the conclusion that the fin geometry (fin thickness, channel spacing) can be chosen in a way that *minimizes* the thermal resistance between the base surface and the forced flow. This seemed to contradict Bejan's (1990) conclusion that the diameter of a pin fin (the hair strand) can be optimized so that the thermal resistance faced by the surface covered with hair is *maximum*. To the resolution of this apparent conflict we will return on the last page of the paper. One difference to note at this stage is that in the case of a surface covered with hair, the fin geometry has three dimensions (the fins are "short" in the flow direction), while in the existing work on finned heat sinks the fin geometry is two dimensional.

The fundamental question triggered by the above conflict is whether three-dimensional arrays of fins (e.g., pin fins) can be optimized for maximum heat transfer augmentation, i.e., in the manner of Tuckerman and Pease (1981). If they can be optimized, is their minimum thermal resistance smaller or greater than in the case of two-dimensional fins? A square array of pin fins with square fin cross-section was exhibited

by Tuckerman (1984, Fig. 3-4, p. 54), but was not optimized.

The present study focuses on the fundamental heat transfer problem of minimizing the overall thermal resistance of a three-dimensional array of fins, i.e., fins that are not continuous (short) in the flow direction. This is a fundamental heat transfer augmentation question with general implications in heat exchanger design. For this we consider two geometries, round pin fins (Fig. 1), and staggered parallel-plate fins (Fig. 4). The flow regime is laminar.

Pin Fins Model

Consider the flow forced through the array of pin fins shown in Fig. 1. Each pin fin has diameter d and length L . The area covered by the array is $B \times X$, in which B is the width of the entrance, and X the length measured in the downstream direction. The frontal area seen by the flow is therefore $B \times L$. The array type (staggered, square), i.e., the arrangement of the fins in the array, is not specified. The fluid space and the fin tips are capped with a cover plate made out of a relatively poor conductor. The material of the pin fin and substrate (silicon) has a relatively large thermal conductivity.

The object of the pin-fin heat sink is to augment the thermal contact between the substrate and the stream. When the heat

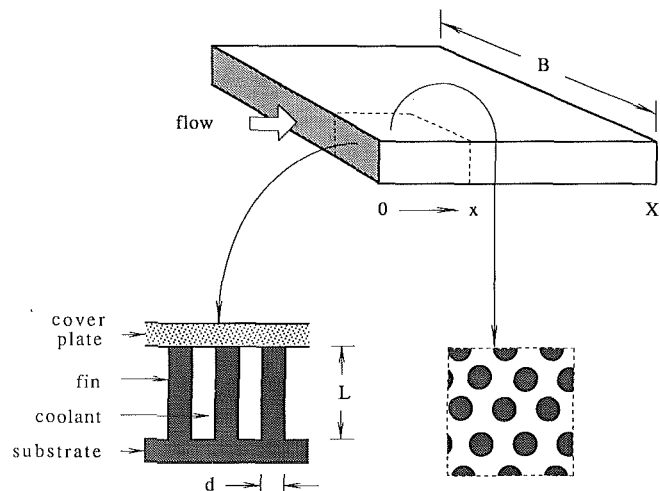


Fig. 1 Heat sink consisting of an array of pin fins cooled by forced convection

Contributed by the Heat Transfer Division for publication in the JOURNAL OF HEAT TRANSFER. Manuscript received by the Heat Transfer Division December 30, 1991; revision received June 26, 1992. Keywords: Electronic Equipment, Finned Surfaces, Heat Exchangers. Technical Editor: R. Viskanta.

flux generated by integrated circuit is prescribed, q'' , the augmentation of heat transfer translates into the decrease of the temperature difference between the substrate (the backing of the circuit), $T_w(x)$, and the local bulk temperature of the stream, $T_f(x)$. Both temperatures are functions of the streamwise position x : When q'' is uniform, T_w and T_f increase linearly with x .

The highest temperature is registered by the substrate at the downstream end of the heat sink, $T_h = T_w(X)$, while the lowest temperature is the inlet temperature of the stream, $T_c = T_f(0)$. The designer's objective is to maintain T_h below a certain (safe) level, or to minimize the ratio $(T_h - T_c)/q''$.

If we discount the array type, there remain two geometric parameters (degrees of freedom) in the optimization of the heat sink: the pin diameter d and the porosity ϕ of the porous structure formed by fins and coolant. An alternative parameter for porosity is the hydraulic diameter D_h of the fluid space, as we will see in Eq. (7). These two parameters can be selected by minimizing $(T_h - T_c)/q''$: this global operation requires an analysis of the entire heat sink volume $B \times L \times X$, as was done by Tuckerman and Pease (1981), Tuckerman (1984), and Knight et al. (1991) for the corresponding problem in which X -long plate fins of rectangular profile alternate with parallel-plate fluid channels.

The course followed by the present study consists of two distinct steps. In the first, the pin-fin diameter is selected based on a local heat transfer analysis, at a given x along the flow. In the second step, the porosity and hydraulic diameter are selected by taking into account also the temperature changes that occur in the downstream direction.

Pin-Fin Diameter

If we assume that the pin-fluid heat transfer coefficient h is uniform along L , the heat transfer rate through a single fin is

$$q_1 = h\pi dL(T_w - T_f)\eta \quad (1)$$

where $T_w(x)$ and $T_f(x)$ are the substrate and bulk fluid temperatures in the constant- x cross section. The efficiency of the fin with insulated tip is

$$\eta = \frac{\tanh(mL)}{mL} \quad (2)$$

in which

$$mL = \left(\frac{h\pi d}{k_w\pi d^2/4}\right)^{1/2} L = \left(\frac{4h}{k_w d}\right)^{1/2} L \quad (3)$$

Imagine next a small area of the substrate of size S , situated around the distance x downstream from the entrance to the channel. Let N be the number of pin fins that reside on S . The heat flux that is extracted by the coolant through the area S is $q'' = q_1 N/S$, which in view of Eq. (1) means

$$q'' = \frac{N}{S} h\pi dL(T_w - T_f)\eta \quad (4)$$

The ratio N/S is related to the fin diameter d and the porosity ϕ in the following manner. The area S is the sum of the roots of the fins, $N\pi d^2/4$, and the portion that is unfinned, ϕS . From this we conclude that

$$\frac{N}{S} = \frac{4(1-\phi)}{\pi d^2} \quad (5)$$

Assume that the fins are small, slender, and dense enough. The heat transfer coefficient is also independent of x when the flow is hydraulically and thermally fully developed. Scaling arguments can be used to anticipate that (Bejan, 1984,1990)

$$\frac{hD_h}{k_f} = \text{Nu}, \text{ constant} \quad (6)$$

in which the Nu constant is of order 1. We assume that the Nu constant is known (numerically, Nu falls in the range 3–8). The hydraulic diameter D_h is a representative length scale that is comparable with the transverse (average) dimension of the stream. For future reference, we note the relationship between D_h , ϕ , and d (Bejan, 1990)

$$D_h = \frac{\phi}{1-\phi} d \quad (7)$$

which can be derived from the definition of hydraulic diameter.

Nomenclature

b = dimensionless group, Eq. (9)
 B = width, m, Figs. 1 and 4
 c_p = specific heat at constant pressure, kJ/kg·K
 d = pin fin diameter, m
 D = plate to plate spacing, m
 D_h = hydraulic diameter, m
 F = function, Eq. (24)
 G = function, Eq. (10)
 h = heat transfer coefficient, W/m²K, Eq. (6)
 \bar{h} = heat transfer coefficient, W/m²K, Eq. (21)
 k_f = fluid thermal conductivity, W/m·K
 k_w = fin thermal conductivity, W/m·K
 k_z = constant of order 10²
 K = permeability, m², Eq. (13)
 L = fin length, m
 m = fin parameter, m⁻¹, Eqs. (3) and (22)
 \dot{m} = mass flow rate, kg/s
 n = plate fins in each row

N = number of pin fins on area S
Nu = Nusselt number, Eq. (6)
 p = number of rows
 \bar{P} = pressure drop group, Eq. (16)
 P_* = pressure drop group, Eq. (28)
 ΔP = overall pressure drop, N/m²
Pr = Prandtl number
 q_1 = heat transfer rate through one fin, W
 q'' = heat flux averaged over the area $B \times X$, W/m²
 S = sample area, m²
 t = plate fin thickness, m, Fig. 4
 T_c = fluid inlet temperature, K
 T_f = local bulk temperature of the fluid, K
 T_h = the highest temperature reached by the substrate, K
 T_w = local temperature of the substrate, K

T_∞ = local free-stream temperature of the fluid, K
 U = volume averaged velocity, m/s
 U_∞ = free-stream velocity, m/s
 X = length of substrate, m, Figs. 1 and 4
 α = thermal diffusivity, m²/s
 δ = dimensionless diameter, Eq. (9)
 η = fin efficiency
 μ = viscosity, kg/s·m
 ν = kinematic viscosity, m²/s
 ξ = plate fin swept length, m, Fig. 4
 ρ = fluid density, kg/m³
 τ = dimensionless thickness, Eq. (25)
 $\bar{\tau}$ = average shear stress, N/m², Eq. (19)
 ϕ = porosity
 Φ = dimensionless group, Eq. (26)
 $()_{\max}$ = maximum
 $()_{\min}$ = minimum
 $()_{\text{opt}}$ = optimal

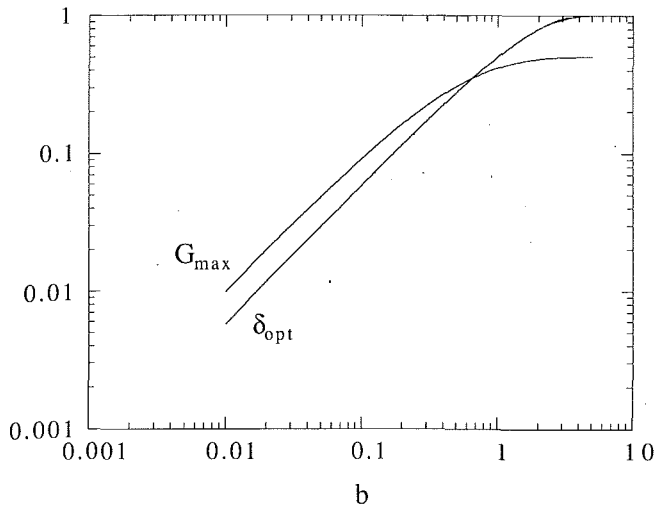


Fig. 2 Optimal pin fin diameter ($\delta_{\text{opt}} = d_{\text{opt}}/D_h$) and maximum local thermal conductance (G_{max})

For example, in the volume of the entire system BLX the volume occupied by fluid is $V_f = \phi BLX$, the total number of fins is $(N/S)BX$, and the total wetted surface (fins only) is $A_f = (N/S)BX \pi dL$. Equation (7) is the result of defining the hydraulic diameter as $D_h = 4V_f/A_f$.

By combining Eqs. (4)–(6), it is possible to express the local (S -averaged) thermal conductance in dimensionless form,

$$\frac{q''L}{k_w(T_w - T_f)} = \frac{b\delta^{1/2}}{\delta + 1} \tanh\left(\frac{b}{\delta^{1/2}}\right) \quad (8)$$

by defining

$$\delta = \frac{d}{D_h}, \quad b = \frac{L}{D_h} \left(4 \text{Nu} \frac{k_f}{k_w}\right)^{1/2} \quad (9)$$

Equation (8) is based on the assumption that the heat transfer through the base area $BX\phi$ is negligible. The problem of optimally selecting the fin diameter occurs only in the constant- x plane, in the context of increasing the local thermal conductance. If we assume that D_h has a certain, still unspecified value, then the only variable in the expression on the right-hand side of Eq. (8) is δ . That expression increases as $\delta^{1/2}$ when $\delta^{1/2}$ is smaller than b , and decreases monotonically as δ^{-1} when $\delta^{1/2}$ increases above b . This means that the δ -dependent group on the right-hand side of Eq. (8),

$$G(\delta, b) = \frac{\delta^{1/2}}{\delta + 1} \tanh\left(\frac{b}{\delta^{1/2}}\right) \quad (10)$$

has a maximum with respect to δ (or d) when b is fixed.

The optimal dimensionless fin diameter $\delta_{\text{opt}}(b)$ and the corresponding local maximum thermal conductance $G_{\text{max}}(b)$ have been determined numerically and reported in Fig. 2. Both quantities increase monotonically with b ; in fact δ_{opt} approaches 1 (i.e., $d_{\text{opt}} \rightarrow D_h$) when b exceeds approximately 5. In conclusion, in the limit of decreasing hydraulic diameter (large b) the optimal fin diameter matches the hydraulic diameter.

Porosity or Hydraulic Diameter

We now turn our attention to the changes that occur from one constant- x plane to the next. The temperature increase experienced by the coolant is

$$T_f(X) - T_c = \frac{q'' BX}{\dot{m} c_p} \quad (11)$$

where $q'' BX$ is the total heat transfer rate, and \dot{m} is the mass flow rate ($\dot{m} = \rho UBL$). The longitudinal velocity U has been

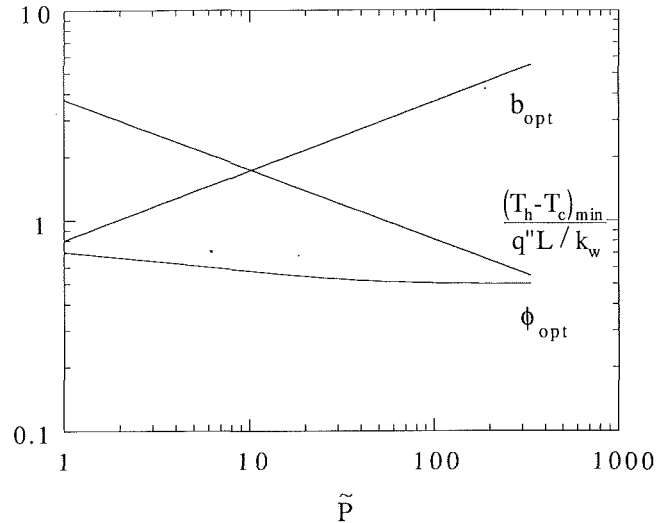


Fig. 3 Optimal inverse hydraulic diameter, b_{opt} , minimum overall temperature difference, and corresponding optimal porosity

averaged over the entire volume (fluid + fins). If the order of the pore Reynolds number $(U/\phi)D_h/\nu$ is smaller than approximately 10 [see also Eq. (17)], Darcy's law applies (Cheng, 1985), and the U velocity is proportional to the pressure drop ΔP maintained between inlet and outlet

$$U = \frac{K \Delta P}{\mu X} \quad (12)$$

Bejan (1990) surveyed the low-Reynolds-number friction data for flow across tube bundles (Eidsath et al., 1983; Happel, 1959; Mueller, 1985), and showed that the permeability K is adequately represented by the Carman-Kozeny model

$$K = \frac{\phi^3 d^2}{k_z(1 - \phi)^2} \quad (13)$$

in which k_z is a constant of order 10^2 (between 90 and 160) depending on the array type.

The highest substrate temperature occurs at $x = X$, where in the case $\delta = \delta_{\text{opt}}$ Eqs. (8) and (10) yield

$$T_h - T_f(X) \cong \frac{q''L}{k_w G_{\text{max}}(b)} \quad (14)$$

By eliminating the outlet temperature $T_f(X)$ between Eqs. (11) and (14), and after using Eqs. (7), (12), and (13), we can express the objective function $(T_h - T_c)/q''$ in the dimensionless form

$$\frac{T_h - T_c}{q''L/k_w} = \frac{1}{b G_{\text{max}}(b)} + \frac{b^2}{\bar{P}} [1 + \delta_{\text{opt}}(b)] \quad (15)$$

The number \bar{P} is the dimensionless pressure drop defined by

$$\bar{P} = 4 \frac{\text{Nu}}{k_z} \left(\frac{k_f}{k_w}\right)^2 \frac{\Delta P \cdot L^4}{\mu \alpha X^2} \quad (16)$$

Since G_{max} and δ_{opt} increase monotonically with b (see Fig. 2), the expression on the right-hand side of Eq. (15) has a minimum with respect to b . According to Eq. (9), the b number is the dimensionless counterpart of the inverse of the hydraulic diameter. Figure 3 shows the results of minimizing the expression Eq. (15) numerically, namely, the optimal inverse hydraulic diameter $b_{\text{opt}}(\bar{P})$, and the corresponding minimum of the objective function $(T_h - T_c)k_w/q''L$. The dimensionless pressure drop \bar{P} is the only number that can be varied at the end of this double minimization of the objective function.

Figure 3 shows also the optimal porosity that corresponds to the optimal hydraulic diameter information condensed in $b_{\text{opt}}(\bar{P})$. The curve $\phi_{\text{opt}}(\bar{P})$ was obtained by noting that ac-

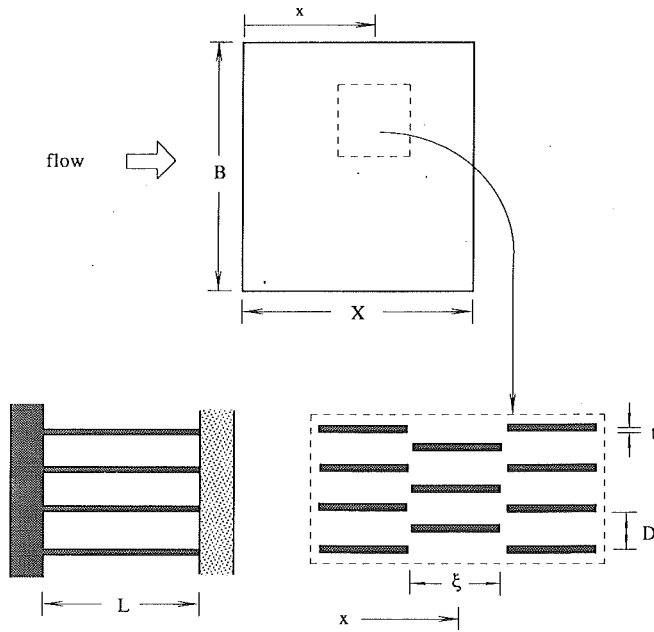


Fig. 4 Array of plate fins cooled by forced convection

According to Eq. (7) $\phi = 1/(1 + \delta)$, and that $\delta_{\text{opt}}(b)$ is furnished by Fig. 2, and $b_{\text{opt}}(\bar{P})$ is provided by Fig. 3. The optimal porosity decreases slowly as the pressure drop number \bar{P} increases.

The Darcy Flow Condition

The analysis and optimization of the array of pin fins were based on the Darcy-flow assumption, which is valid when the flow is sufficiently slow (or ΔP small) that the pore Reynolds number does not exceed the order of 10. The condition $(U/\phi)D_h/\nu \leq 10$ can be combined with Eqs. (7), (9), (12), (13), and (16), and the result is an upper limit for the imposed pressure difference,

$$\bar{P} \lesssim 10b^3 \frac{\text{Pr}}{(4 \text{Nu})^{1/2}} \left(\frac{k_f}{k_w} \right)^{1/2} \frac{L}{X} \quad (17)$$

If we consider an application in which the fluid is water near 40°C, the fin material is silicon, and $\text{Nu} \sim 6$, the right-hand side of the inequality (17) has the order of magnitude $b^3 L/X$. This inequality must be satisfied regardless of whether the array geometry (δ, b) has been selected optimally.

In the special cases in which the overall temperature difference has been minimized twice, with respect to δ and b , we can use the $b_{\text{opt}}(\bar{P})$ curve of Fig. 3 to write approximately $b_{\text{opt}} \cong 0.83 \bar{P}^{1/3}$. By substituting this expression into the inequality (17) for water and silicon, we arrive at the condition $L/X \geq 1$, which is not likely to happen in an actual design.

In conclusion, the curves of Fig. 3 for the pin fin array with optimal fin diameter (δ_{opt}) and optimal hydraulic diameter (b_{opt}) are not valid, because under those conditions the flow cannot be in the Darcy regime. On the other hand, the results of Fig. 2 are valid, provided b and \bar{P} satisfy the Darcy-flow condition (17). In other words, in the Darcy regime the pin fin array can be optimized only with respect to fin diameter. The once-minimized local and overall temperature differences are provided by Eqs. (14) and (15). The actual hydraulic diameter must be smaller than the optimal value indicated by b_{opt} of Fig. 3; in other words, b must be greater than b_{opt} . The porosity of the once-optimized array is smaller than the ϕ_{opt} value indicated in Fig. 3, especially in the small pressure drop limit.

Even though the twice-optimized array cannot function in Darcy flow, the curves of Fig. 3 can be expected to agree

qualitatively (in an order of magnitude sense) with the corresponding results that would hold for higher pore Reynolds numbers, i.e., when inertial effects become important at the pore (or fin length) level. This expectation is based on the fact that the transition from Darcy flow to non-Darcy (Forchheimer) flow is smooth and spread out over several orders of magnitude of pore Reynolds number. Furthermore, between these two limiting regimes the volume averaged velocity increases *monotonically* with the imposed pressure difference, as in Eq. (12) for Darcy flow.

To emphasize, Fig. 2 is correct, while Fig. 3 is valid only qualitatively (trends, orders of magnitude). The correctness of the trends revealed by Fig. 3 is demonstrated in the second part of our study, by analyzing a fin array in a flow regime where fluid inertia is not negligible: parallel plate fins coated with distinct boundary layers. An important conclusion derived from Fig. 3 is that the overall thermal conductance cannot be maximized *twice* in Darcy flow. This is important because thermal designers must know not only the success stories (i.e., the optimal results) but also where the most tempting conceptual traps are hidden.

Plate Fin Model

The heat sink with microchannels bordered by parallel-plate fins was the original design optimized by Tuckerman and Pease (1981). A key feature of that model was the fact that the channel was long and narrow in the direction of flow, i.e., that the flow was fully developed hydrodynamically and thermally. The effect of the thermally developing entrance region was included in subsequent studies (Tuckerman, 1984; Knight et al., 1991).

Beginning with this section of our study we focus on the limit in which the plate fins are so short and spaced so wide apart that the flow in between is of the boundary layer type (i.e., as at the start of the hydrodynamic entrance region). We consider this limit in the search for an array of fins with heat transfer coefficients higher than in fully developed flow. Phillips' (1987) review indicated that (1) the performance of interrupted fins should be at least as good as that of continuous fins, and (2) even in the vast heat exchanger literature the plate fin geometry has been avoided by theoreticians.

The model is shown in Fig. 4. Each plate fin has thickness t , height L , and swept length ξ . The spacing between two adjacent fin surfaces is D . We are assuming that the fin cross section $t \times \xi$ is sufficiently slender, the spacing D is wide enough, and the fin array type is such (e.g., staggered) that each swept face $\xi \times L$ is covered by a distinct laminar boundary layer. To the conditions that must be met for these assumptions to be valid we return in Eqs. (29) and (30). The heat transfer through the base area $BX\phi$ is assumed negligible.

Plate Fin Thickness

The fin array contains $p = X/\xi$ rows, and $n = B/(D + t)$ plate fins in each row. For the optimal selection of the fin thickness t we minimize the local thermal resistance in each row, that is the ratio $[T_w(x) - T_\infty(x)]/q''$, where x is the average longitudinal location of the row (Fig. 4), $T_w(x)$ is the temperature of the substrate of the row, $T_\infty(x)$ is the temperature of the coolant outside the boundary layer, and q'' is the uniform rate of heat rejection per unit area of substrate. The pressure drop ΔP over the total flow length X is

$$\Delta P = 2n \frac{X}{B} \bar{\tau} \quad (18)$$

where $\bar{\tau}$ is the fluid shear stress averaged over the swept length ξ of each plate (Incropera and DeWitt, 1990; Bejan, 1993),

$$\bar{\tau} = 1.328 \left(\frac{U_\infty \xi}{\nu} \right)^{-1/2} \frac{1}{2} \rho U_\infty^2 \quad (19)$$

In writing the force balance, Eq. (18), we have assumed that

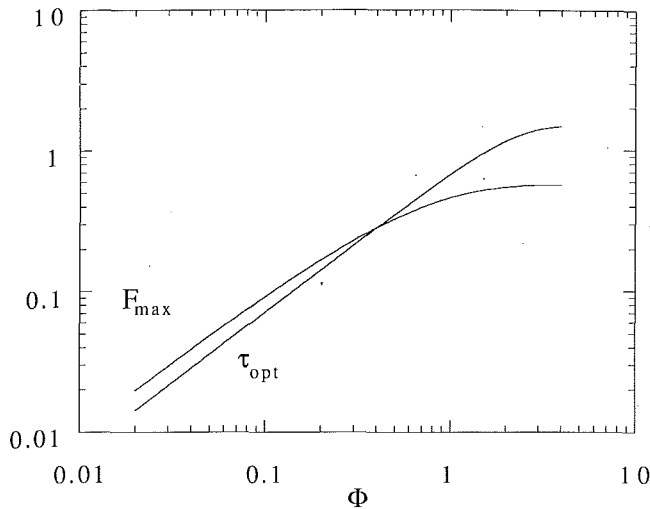


Fig. 5 Optimal plate fin thickness (τ_{opt}) and maximum local thermal conductance (F_{max})

the flow resistance contributed by the D -wide top and bottom surfaces of the channel is negligible, i.e., that $D \ll L$. Combined Eqs. (18) and (19) yield the fluid velocity outside the boundary layer, which occupies most of the D -wide channel,

$$U_{\infty} = \left(\frac{\Delta P \cdot B \xi^{1/2}}{1.328 n X \rho \nu^{1/2}} \right)^{2/3} \quad (20)$$

Under the same conditions the ξ -averaged heat transfer coefficient between the plate fin (assumed isothermal over ξ) and the free-stream fluid in the channel (U_{∞} , T_{∞}) is given by

$$\bar{h} = 0.664 \frac{k_f}{\xi} \text{Pr}^{1/3} \left(\frac{U_{\infty} \xi}{\nu} \right)^{1/2}, \quad \text{Pr} \geq 1 \quad (21)$$

In a manner that is analogous to the analysis of section 3, we calculate the heat transfer rate through one plate fin,

$$q_1 = 2L \xi \bar{h} (T_w - T_{\infty}) \frac{\tanh(mL)}{mL}, \quad mL = \left(\frac{2\bar{h}}{k_w t} \right)^{1/2} L \quad (22)$$

and the average heat flux extracted from the substrate, $q'' = nq_1/\xi B$. The local thermal conductance in one particular row, $q''/(T_w - T_{\infty})$, can be summarized as:

$$\frac{q'' L}{k_w (T_w - T_{\infty})} = \Phi \cdot F(\tau, \Phi) \quad (23)$$

where

$$F(\tau, \Phi) = \frac{\tau^{1/2}}{(1+\tau)^{5/6}} \tanh \left[\Phi \frac{(1+\tau)^{1/6}}{\tau^{1/2}} \right] \quad (24)$$

$$\tau = \frac{t}{D} \quad (25)$$

$$\Phi = 1.328^{1/3} \left(\frac{k_f}{k_w} \right)^{1/2} \frac{L/X}{(D/X)^{1/3}} \left(\frac{\rho \Delta P \cdot X^2}{\mu \alpha} \right)^{1/6} \quad (26)$$

The function F and the local thermal conductance have a maximum with respect to the plate thickness t (or τ). The optimal dimensionless thickness $\tau_{opt}(\Phi)$ and the corresponding maximum value $F_{max}(\Phi) = F[\tau_{opt}(\Phi), \Phi]$ have been obtained numerically and plotted in Fig. 5. Both quantities increase monotonically as the Φ group increases. By comparing Fig. 5 with Fig. 2 we note the analogy between the plate fin optimization (Φ , τ_{opt} , F_{max}) and the problem of pin fin optimization (respectively, b , δ_{opt} , G_{max}).

Plate-to-Plate Spacing

The optimal plate-to-plate spacing D can be determined by considering the tradeoff between the local thermal resistance

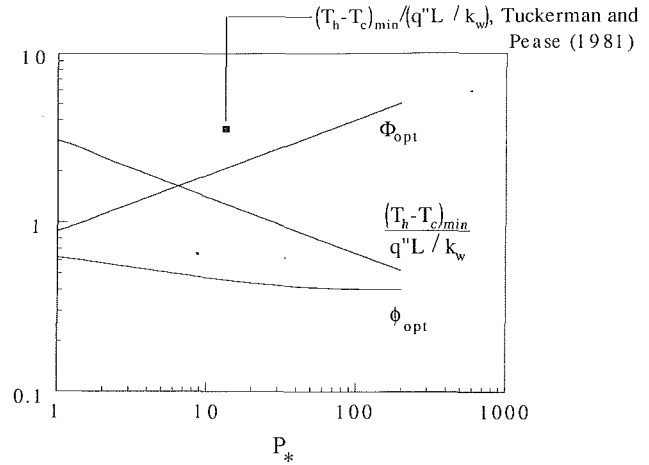


Fig. 6 Optimal plate-to-plate spacing (Φ_{opt}) and minimum overall temperature difference

analyzed until now, and the temperature rise experienced by the stream in the longitudinal direction, $T_{\infty}(x)$. The latter is given by Eq. (11) with $T_{\infty}(X)$ in place of $T_f(X)$, and $\dot{m} = n \rho L D U_{\infty}$. The local temperature difference in the last row, $T_h - T_{\infty}(X)$, is given by Eq. (23) with $\tau = \tau_{opt}(\Phi)$. By eliminating $T_{\infty}(X)$ between these modified Eqs. (11) and (23), we obtain the difference between the highest temperature on the substrate (T_h) and the lowest temperature of the coolant (T_c),

$$\frac{T_h - T_c}{q'' L / k_w} = \frac{1}{\Phi F_{max}(\Phi)} + \frac{\Phi^2}{P_*} [1 + \tau_{opt}(\Phi)]^{1/3} \quad (27)$$

where Φ is given by Eq. (26) and

$$P_* = \text{Pr}^{1/3} \left(\frac{k_f}{k_w} \right)^2 \frac{\Delta P \cdot L^4}{\mu \alpha X^2} \quad (28)$$

The effect of the plate-to-plate spacing D on the overall temperature difference, Eq. (27), is conveyed solely by the dimensionless group Φ , which varies inversely with $D^{1/3}$; cf. Eq. (26). The optimal spacing that minimizes the overall temperature difference is reported in Fig. 6 as $\Phi_{opt}(P_*)$ and $(T_h - T_c)_{min} k_w / q'' L$ versus P_* . The independent group P_* is proportional to the pressure drop across the entire array. The same figure shows the corresponding optimal porosity, $\phi_{opt} = [D/(D+t)]_{opt} = (1 + \tau_{opt})^{-1}$.

The results developed in the last three sections for plate fins are valid provided the boundary layers are distinct. This means that the boundary layer thickness scale for the swept length ξ , namely $\xi (U_{\infty} \xi / \nu)^{-1/2}$, must not exceed the scale of the plate-to-plate spacing D . In view of Eqs. (20) and (26), the requirement that $D > \xi (U_{\infty} \xi / \nu)^{-1/2}$ translates into a lower bound for the dimensionless group Φ ,

$$\Phi > \frac{L}{D} \left(\frac{k_f}{k_w} \right)^{1/2} \left(\frac{\text{Pr}}{1 + \tau_{opt}} \right)^{1/6} \quad (29)$$

In the case of water and silicon the conductivity ratio is such that the order of magnitude of $(k_f/k_w)^{1/2}$ is 0.1. Furthermore, if the scale of L/D is 10, and the scale of $[\text{Pr}/(1 + \tau_{opt})]^{1/6}$ is 1 (see Fig. 5), we conclude that the right-hand side of the inequality (29) is of order 1, i.e., that $\Phi > 1$. This condition for distinct boundary layers is compatible with the Φ_{opt} values plotted in Fig. 6: Φ_{opt} increases, and the boundary layers become more distinct as the pressure group P_* increases.

When the plate thickness and the plate-to-plate spacing are assigned their optimal values (τ_{opt} , Φ_{opt}), Eq. (30) and the curve $\Phi_{opt}(P_*)$ allows us to interpret the condition (29) as a lower bound for the number of rows in the flow direction (Fig. 4),

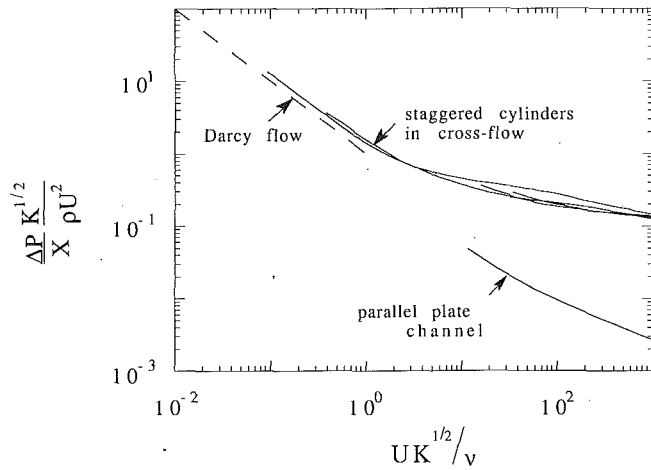


Fig. 7 Porous medium representation of the flow through staggered cylinders and parallel plate channels

$$p > \left(\frac{L}{D}\right)^4 \left(\frac{k_f}{k_w}\right)^2 \frac{\text{Pr}^{4/3}}{P_*(1 + \tau_{\text{opt}})} \quad (30)$$

By continuing the numerical example of the preceding paragraph, we find that the order of magnitude of the right-hand side of Eq. (30) is $1/P_*$. In other words, a least $1/P_*$ rows are needed for the boundary layers to be distinct. The P_* range covered by the abscissa of Fig. 6 is compatible with this requirement. In that P_* range, even a single row ($\xi = X$) would have plate fins covered by distinct boundary layers.

A second condition that must be satisfied by the number of rows p (or fin swept length ξ) is the condition that each boundary layer is laminar. By writing $U_\infty \xi / \nu \leq 5 \times 10^5$ for the range of laminar boundary layer flow, and by using Figs. 5 and 6 to approximate $\tau_{\text{opt}} \sim 2$ and $\Phi_{\text{opt}} \cong 0.9 P_*^{1/3}$ in the P_* range 1–200, we learn that each swept face must be short enough so that

$$p > 4 \times 10^{-6} \frac{P_*^{1/3} k_w}{\text{Pr} k_f} \left(\frac{X}{L}\right)^2 \quad (31)$$

In the water and silicon example mentioned already, the right-hand side of this last condition is of order $2 \times 10^{-4} P_*^{1/3} (X/L)^2$.

Discussion

The analyses of pin fins and plate fins have the same analytical structure. In the first step, the optimal fin thickness was determined by maximizing the local thermal conductance, that is, the conductance between substrate and coolant at a certain longitudinal position x . The optimal thickness of the fluid channel was determined in the second step, by minimizing the overall temperature difference ($T_h - T_c$), or, in practical terms, by minimizing the highest temperature of the substrate (T_h).

The common structure of the two analyses becomes evident as we compare Fig. 2 with Fig. 5, and Fig. 3 with Fig. 6. The role played by (b, δ, G, \bar{P}) for pin fins with Darcy flow, is played by (Φ, τ, F, P_*) for plate fins with inertial flow. In fact the pressure groups \bar{P} and P_* are both proportional to the overall pressure drop ΔP , so that

$$\frac{\bar{P}}{P_*} = \frac{4 \text{Nu}}{k_z \text{Pr}^{1/3}}, \quad (\text{constant}) \quad (32)$$

The rough value of the constant on the right-hand side is $1/10$, meaning that in an approximate sense $\bar{P} \cong P_*/10$. This estimate is based on the following values: $\text{Nu} \sim 6$, $k_z \sim 130$, and $\text{Pr} \sim 5$.

It is easy to verify (e.g., Fig. 7, next) that in the laminar boundary layer regime the pressure gradient along the plate-fin array $\Delta P/X$ is proportional to $U_\infty^{3/2}$. This regime then corresponds to the transition from Darcy flow ($\Delta P/X \sim U$) to non-Darcy flow ($\Delta P/X \sim U^2$) in the pin-fin array. In conclusion, the analogy between the two analyses shows that the trends and orders of magnitude indicated by the curves of Fig. 3 for pin-fin arrays are correct in a flow regime in which inertial effects are important to the fin-length level.

The analogy between the pin fin and plate fin analyses is illustrated further in Fig. 7, in which we used the pore Reynolds number on the abscissa ($UK^{1/2}/\nu$), and the dimensionless pressure gradient group ($\Delta P/X$) $K^{1/2}/\rho U^2$ on the ordinate. These coordinates are used routinely in convection in porous media (e.g., Nield and Bejan, 1992), so that the Darcy flow limit is represented by a straight line (dashed line in Fig. 7).

The bundle of four curves corresponds to flow across staggered cylinders (equilateral triangle array), with four transverse pitch/cylinder diameter ratios: 1.25, 1.5, and 2.5. The data for these four curves were taken from Zukauskas (1987), and the permeability K was modeled as in Eq. (13) with $k_z = 100$. The lower curve is for a parallel plate channel with aspect ratio $X/D = 10$. The permeability was derived from Poiseuille flow, $K = D^2/12$. The data are from Bodoia (Shah and London, 1978).

Figure 7 shows that the slope of the curve for the parallel-plate channel is nearly the same as that of the curve for the cylinder array in the "transition" regime, i.e., between Darcy flow (slope -1 in Fig. 7) and Forchheimer flow (slope 0). As an aside, it is worth noting that the "porous medium" presentation of the cylinder array leads to a much tighter collapse of the four curves than in Zukauskas' (1987) original graph. The later was constructed using heat exchanger terminology. Figure 7 is a new way of looking at some classical (handbook) information. This method of graphic presentation deserves to be extended to other heat exchanger geometries that can be viewed as saturated porous media.

As a numerical application, consider the following comparison with the optimal design for continuous fins reported by Tuckerman and Pease (1981). For the optimal design they used water and silicon, $B = X = 1$ cm, $\Delta P = 206.8$ kPa, $\text{Nu} = 6$, $L = 365$ μm , and the twice-minimized thermal resistance reached the value $(T_h - T_c)_{\text{min}}/(q'' BX) = 0.086$ $^\circ\text{C}/\text{W}$. These dimensions can be translated into the following dimensionless coordinates for Fig. 6,

$$P_* \cong 13.4, \quad \text{and} \quad \frac{(T_h - T_c)_{\text{min}}}{q'' L/k_w} \cong 3.53 \quad (33)$$

Figure 6 shows that the Tuckerman and Pease (1981) design point falls in the vicinity of the optimal plate-fin arrays determined in the present study. The minimum thermal resistance of Knight et al. (1991) falls by about 11 percent under Tuckerman and Pease's (1981) design point. In conclusion the minimum thermal resistance for arrays of plate fins is as small as approximately 40–50 percent of the minimum thermal resistance for continuous two-dimensional fins with fully developed laminar flow in the channels. Knight et al. (1991) showed that in turbulent flow the optimal design is significantly better than in laminar flow.

There is an entire family of optimized plate-fin arrays that are represented by a single P_* value in Fig. 6. For example, if we start with the same input data as in Tuckerman and Pease's design, we obtain $P_* \cong 13.4$ and, from Fig. 6, $\Phi_{\text{opt}} \cong 2.1$. Equation (26) delivers next the optimal spacing as a function of the unspecified number of rows, $D_{\text{opt}}/p^{1/2} = 9.4$ μm . Finally, from Fig. 5 we collect $\tau_{\text{opt}} \cong 1.2$, which means that the optimal plate thickness obeys the relation $t_{\text{opt}}/p^{1/2} \cong 11.3$ μm .

The number of rows p must be selected in a way that is consistent with the conditions (31) and (29). The laminar flow

condition (31) reduces to $p > 0.33$, while the distinct boundary layer criterion (29) becomes $L/D < 28$. We are free to select one parameter, p or D (or L/D), in a way that does not violate these two conditions. For example, if we select $L/D = 10$, the optimal design described in the preceding paragraph has the dimensions $D_{\text{opt}} = 37 \mu\text{m}$, $p = 15$, $\xi = 660 \mu\text{m}$, $t_{\text{opt}} = 44 \mu\text{m}$. The slenderness ratios D_{opt}/L and t_{opt}/ξ are small, i.e., in agreement with the assumptions made in the development of the analytical model (section 6). Since the ratio $t_{\text{opt}}/D_{\text{opt}}$ is slightly larger than 1, a longitudinal spacing of $2t_{\text{opt}}$ or $3t_{\text{opt}}$ must be left between two consecutive rows so that the flow that exits from one parallel plate channel can get around the next plate fin, which stands in the way. This additional spacing is small with respect to the fin swept length ξ (because $t_{\text{opt}} \ll \xi$), therefore the results of Figs. 5 and 6 should apply (approximately) even when τ_{opt} is slightly greater than 1 (the thermal conductance will be slightly lower than in Figs. 5 and 6).

We return now to the observation made in the Introduction, namely the apparent conflict between fin arrays that can be optimized to augment heat transfer (the present study), and fins that can be optimized to maximize the thermal insulation effect (Bejan, 1990). The latter was demonstrated in the analysis of hair strands acting as pin fins on a flat surface swept by a developing boundary layer flow. The explanation lies in the fact that in the case of surfaces covered with hair the porosity is very high (0.97–0.99), and a significant fraction of the total heat transfer is contributed by direct contact between the bare surface (the unfinned portions) and the fluid (air). That contribution was negligible in the present study. The optimal hair strand diameter resulted from a tradeoff between the heat transfer contributions made by the finned and unfinned portions of the skin. Such a tradeoff is not encountered when the unfinned surface does not contribute a significant fraction to the overall heat transfer rate.

In conclusion, the new fundamental ideas that are advanced by this paper are:

(a) The existence of an optimal pin fin array for maximum thermal conductance, when the streamwise temperature increase is significant. Before this paper, we knew only of optimal pin fin arrays for minimum thermal conductance (Bejan, 1990).

(b) The analogy between the pin fin array and the plate fin array as flows through saturated porous media at successively higher pore Reynolds numbers (Fig. 7). The traditional treatment (e.g., heat exchanger terminology) of such geometries is based on "duct" fluid mechanics, not porous medium fluid mechanics.

(c) The analogy between (or common structure of) the geo-

metric optimization of the pin fin array and the optimization of the plate fin array.

(d) The most appropriate (the fewest) dimensionless groups for the pin fin array geometry are δ and b in Eq. (9). The corresponding groups for the plate fin array geometry are τ and Φ , which are proposed now in Eqs. (25),(26).

Acknowledgments

This work was sponsored by the IBM Corporation, Research Triangle Park, NC. The technical advice and encouragement received from Dr. Sang W. Lee are very much appreciated.

References

- Bar-Cohen, A., and Jelinek, M., 1985, "Optimum Arrays of Longitudinal, Rectangular Fins in Convective Heat Transfer," *Heat Transfer Engineering*, Vol. 6, No. 3, pp. 68–78.
- Bejan, A., 1984, *Convection Heat Transfer*, Wiley, New York, p. 85.
- Bejan, A., 1990, "Theory of Heat Transfer From a Surface Covered With Hair," *ASME JOURNAL OF HEAT TRANSFER*, Vol. 112, pp. 662–667.
- Bejan, A., 1993, *Heat Transfer*, Wiley, New York, pp. 237, 244.
- Cheng, P., 1985, "Geothermal Heat Transfer," in: *Handbook of Heat Transfer Applications*, 2nd ed., W. M. Rohsenow, J. P. Hartnett, and E. N. Ganic, eds., McGraw-Hill, New York, Chap. 11.
- Eidsath, A., Carbonell, R. G., Whitaker, S., and Herrmann, L. R., 1983, "Dispersion in Pulsed Systems III—Comparison Between Theory and Experiments for Packed Beds," *Chem. Eng. Sci.*, Vol. 38, pp. 1803–1816.
- Happel, J., 1959, "Viscous Flow Relative to Arrays of Cylinders," *AICHE J.*, Vol. 5, pp. 174–177.
- Incropera, F. P., 1988, "Convection Heat Transfer in Electronic Equipment Cooling," *ASME JOURNAL OF HEAT TRANSFER*, Vol. 110, pp. 1097–1111.
- Incropera, F. P., and DeWitt, D. P., 1990, *Fundamentals of Heat and Mass Transfer*, 3rd ed., Wiley, New York, p. 395.
- Knight, R. W., Goodling, J. S., and Hall, D. J., 1991, "Optimal Thermal Design of Forced Convection Heat Sinks—Analytical," *ASME Journal of Electronic Packaging*, Vol. 113, pp. 313–321.
- Mueller, A. C., 1985, "Process Heat Exchangers," in: *Handbook of Heat Transfer Applications*, 2nd ed., W. M. Rohsenow, J. P. Hartnett, and E. N. Ganic, eds., McGraw-Hill, New York, Chap. 4, part 2.
- Nield, D. A., and Bejan, A., 1992, *Convection in Porous Media*, Springer-Verlag, New York, p. 11.
- Peterson, G. P., and Ortega, A., 1990, "Thermal Control of Electronic Equipment and Devices," *Advances in Heat Transfer*, Vol. 20, pp. 181–314.
- Phillips, R. J., 1987, "Forced-Convection, Liquid-Cooled Microchannel Heat Sinks," M.S. Thesis, Massachusetts Institute of Technology, Cambridge, MA.
- Shah, R. K., and London, A. L., 1978, *Laminar Flow Forced Convection in Ducts*, Academic Press, New York, p. 163.
- Tuckerman, D. B., and Pease, R. F. W., 1981, "High-Performance Heat Sinking for VLSI," *IEEE Electron Device Letters*, Vol. EDL-2, No. 5, pp. 126–129.
- Tuckerman, D. B., 1984, "Heat Transfer Microstructures for Integrated Circuits," Ph.D. Thesis, Stanford University, Stanford, CA.
- Zukauskas, A., 1987, "Convective Heat Transfer in Cross Flow," in: *Handbook of Single-Phase Convective Heat Transfer*, S. Kakac, R. K. Shah, and W. Aung, eds., Wiley, New York, Chap. 6.

Effects of Sodium and Potassium Chlorides on Silica Fouling

S. H. Chan

Wisconsin Distinguished Professor.

Z. J. Chen

Graduate Research Assistant.

P. He

Graduate Research Assistant.

Department of Mechanical Engineering,
University of Wisconsin—Milwaukee,
Milwaukee, WI 53201

The effects of NaCl and KCl salts in aqueous solutions on silica fouling of heat exchangers under turbulent flow conditions were examined experimentally over a range of pH, velocity, and salt concentration levels. The fundamental attachment process of silica fouling from those aqueous solutions was described. The silica fouling rate in NaCl solutions was found to be greater than that in KCl solutions. In all cases, the fouling rate increased with the salt concentration. When both salts were present simultaneously, the fouling rate found to be closer to that of the KCl system than that of the NaCl system. Effects of salinity on equilibrium solubility of silica at 165°C were also reported. Finally, the plausible theory of polymerization and the fundamental ion-cloud theory were used to describe the silica scale attachment process and the possible causes of salt effects on silica fouling of heat transfer surfaces.

Introduction

Scale deposition on heat transfer surfaces adds an additional thermal resistance, which may often exceed the convective resistance in the thermal boundary layer. When the fouling layer builds up, heat transfer is reduced, the pressure drop is increased, and in some cases the layer can simply incapacitate the entire system due to blockage of the flow passage or severe reduction in thermal efficiency. The importance of the fouling problem in heat transfer has long been recognized (Taborek et al., 1972), but progress has been slow in the fundamental understanding and modeling of fouling phenomena because of the complexity of the physical and chemical fouling processes involved and the coupling with heat, mass and momentum transport processes (Taborek et al., 1972; Sutor et al., 1977; Somerscales and Knudsen, 1981; Bryers, 1982; Melo et al., 1988; Chan and Ghassemi, 1991).

Silica is one of the important contributors to scaling when underground water (brine) is used, since silica is one of the primary components of the earth's crust. It can form on heated or unheated surfaces in contact with the brine. Silica scale is a major concern in the petroleum oil recovery and geothermal energy utilization industries (Wahl, 1977).

A number of studies have been made on kinetics, solubility, and polymerization of dissolved silica (Iler, 1979; Fournier and Rave, 1977; Bohlman et al., 1980; Weres et al., 1979, 1980, 1981, 1982; Rothbaum and Rohde, 1979; Barnes, 1979; Marshall, 1980; Marshall and Warakowski, 1980; Chen and Marshall, 1982; Chan, 1989). However, the mechanism of polymerization, for example, still is not well understood. Others reported a few silica fouling data taken at geothermal fields (Lombard, 1978; Gudmundsson and Bott, 1979) and at laboratories under controlled environments (Bohlman et al., 1981; Chan et al., 1988). Those studies are far from complete since silica fouling is affected by many factors, including temperature, pH, solubility, polymerization kinetics, the concentrations and the kinds of salt present in the solution, thermal-hydraulic conditions, and so forth.

A survey of geothermal brines throughout the world indicates that there are more than ten different types of salt present in brines. The dominant salt is sodium chloride (NaCl), followed by potassium chloride (KCl). These two dominant salts were selected for the present study. Their individual and compound effects on silica fouling under various concentrations, pH, and flow rate conditions were investigated experimentally.

Experimental Results and Discussion

Experimental Facility and Procedure. The experimental facility used is a high-pressure (1.58 MPa), high temperature (190°C), corrosion-resistant loop in the UWM Fouling Heat Transfer Laboratory. It was designed to investigate the effects of silica supersaturation, brine pH, Reynolds number, and corrosive salts and other ions on the formation of silica scale. The scale was formed on the inner surface of a titanium tube (2.82 m long, 2.54 cm diameter, and 0.165 cm tube wall thickness) of a cocurrent, double-tube heat exchanger with the brine on the tube side and distilled deionized water on the shell side.

Originally the test heat exchanger was designed as a counterflow heat exchanger. However, during the boiler installation-redesign period, it was decided to change the design so that the hot saturated brine passed through the instrumentation branches before entering the heat exchanger, thus minimizing the scaling potential. This new design also minimized the distance between the end of the heat exchanger where the brine is supersaturated and the point of reheating at the boiler. Due to the large coolant mass flow rate, the temperature drop of the coolant flowing through the heat exchanger was only 2°C (see Table 1). Thus, the cocurrent arrangement presents no significant disadvantage as compared to the counterflow design. The details of the design were given previously (Chan et al., 1982) and the experimental procedure can be found from Chan et al. (1988).

The only major modification to the loop design was the change of the saturator location and the installation of a magnetic pump (March MFG TE-7H-MD) to form a saturator loop separated from the primary loop so that the brine in the titanium brine tank can be brought to saturation with dissolving chemicals before the start of the fouling experiment. A schematic diagram of the modified loop is shown in Fig. 1. Run No. T3-KM2 (see Tables 1-3) was conducted using this design while run Nos. TT1-C, TT1-D, TT1-D02, and TT2-B were obtained under the original design using a single brine mechanical pump to drive both the saturator and the primary brine loops. Later the brine mechanical pump in the brine loop was also replaced by another magnetic pump (the same model but different pumping power) to conduct the rest of the experiments.

A high-grade silica gel (Fisher Scientific Co.) without aluminum and sodium was placed in the columns of the saturators with 100 mesh size screens at both ends of the saturators. The silica was dissolved in the brine circulating through the saturators until the solubility equilibrium was reached. During experiment T3-Na4, 30 milliliters of the hot brine sample taken from the brine tank were quenched to room temperature and mixed with 5 milliliters of NaOH to prevent the supersaturated

Contributed by the Heat Transfer Division for publication in the JOURNAL OF HEAT TRANSFER. Manuscript received by the Heat Transfer Division April 1991; revision received September 1992. Keywords: Augmentation and Enhancement, Fouling, Heat Exchangers. Associate Technical Editor: W. A. Fiveland.

Table 1 Thermal-hydraulic conditions in fouling experiments

Run No.	Re_b	T_{b1} in (°C)	T_{b2} in (°C)	T_{b1} out (°C)	T_{b2} out (°C)	T_{c1} in (°C)	T_{c2} in (°C)	T_{c1} out (°C)	\dot{m}_{b1} (kg/s)	V_{b1} (m/s)	\dot{m}_{c1} (kg/s)	U_{oc1} ($W/m^2 \text{ } ^\circ C$)	Run Time (h)
T3-Na4	73413	163.3	164.2	123.3	118.8	73.1	74.2	75.0	0.265	0.691	9.46	3075	500
TT2-B2	73412	164.1	165.5	122.8	124.4	72.2	73.3	73.4	0.265	0.691	9.46	3155	295
TT2-B	69453	151.1	162.2	116.6	120.9	73.3	74.3	74.3	0.265	0.691	9.46	3084	123
TT1-C	75790	165.2	-----	124.4	-----	71.3	72.3	72.1	0.265	0.691	9.46	2615	185
T4-KM1	73322	162.1	163.2	121.6	118.5	71.8	72.9	72.9	0.265	0.691	9.48	3071	560
T4-KM3	74105	166.5	166.5	123.6	122.5	69.3	70.4	70.4	0.265	0.691	9.44	3052	566
T3-KM2	73413	164.1	164.5	122.5	119.8	71.1	72.3	72.3	0.265	0.691	9.44	3110	152
T4-KM2	34953	164.0	165.1	109.9	107.2	73.7	74.4	72.9	0.126	0.329	9.45	2292	600
TT1-D	76150	164.8	-----	124.8	-----	71.9	72.9	72.9	0.265	0.691	9.47	2608	150
TT2-002	52225	167.2	166.9	120.5	118.8	71.9	73.2	73.2	0.189	0.494	6.93	2505	160
T5-NK1	74335	165.5	165.5	124.4	120.1	71.6	73.2	73.2	0.265	0.691	9.38	3049	400
T5-NK2	73717	164.9	166.1	124.8	123.3	71.1	72.2	72.2	0.265	0.691	9.51	2924	800

T_b - brine temperature, \dot{m}_b , V_b - brine mass flow rate and brine velocity,

T_c - coolant temperature, \dot{m}_c - coolant mass flow rate, U_{oc1} - heat transfer coefficient at starting time, subscript 1 - starting time value, subscript 2 - after induction time.

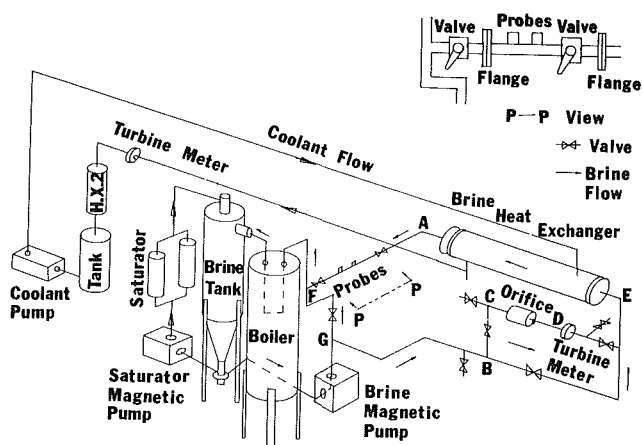


Fig. 1 The high-pressure, high-temperature, corrosion-resistant loop sample from polymerizing. The sample was immediately filtered through two membranes, the one with 8 μm pore size laid on the top of the one with 0.22 μm pore size. The de-

hydrated membranes were placed under an electron microscope and two particles were found on the 8 μm membrane but none on the 0.22 μm membrane. The two particles were identified to be rust. Thus it was assumed that the silica gel was dissolved in the brine and no silica particles larger than 0.22 μm in diameter existed in the brine loop.

A calibration was performed on the brine tube prior to scaling runs with distilled water in the brine loop and a special bulk fluid temperature probe was inserted in the center of the titanium tube. Its purpose was to obtain the thermal resistance R_{oi} between each of the eight thermocouples in the tube wall and the outer tube surface on the coolant side. From the results for a clean tube, it is possible to calculate the local overall heat transfer coefficients for a fouled heat exchanger. The method is that of Wilson as modified by Fischer et al. (1975).

The loop is instrumented to yield both overall and local transient fouling resistances for all experiments. The overall thermal fouling resistance (over the entire length of a heat exchange) was reduced from

$$R_f = \frac{1}{U_{of}} - \frac{1}{U_{oc1}} \quad (1)$$

Nomenclature

A_o = outer tube of surface area
 C = concentration in molarity or ppm
 e_o = electrostatic unit charge
 \dot{m} = mass flow rate, kg/s
 M = molarity, kg mole per liter of solution
 N_{av} = Avogadro's number
 Re_b = Reynolds number of brine
 R = thermal fouling resistance, $m^2 \text{ } ^\circ C/W$
 r = radius of ion, m
 $\equiv SiOH, \equiv SiO^-$ = representation of surface silicon atom with three bonds to solid silica and one to neutral or ionized hydroxy group
 t = time period, h
 T = temperature, $^\circ C$
 U = overall heat transfer coefficient, $W/m^2 \text{ } ^\circ C$

V = fluid velocity, m/s
 Z_i = valency of the reference ion
 γ_i = radius of the reference ion
 $\Delta\mu_{i-1}$ = chemical-potential change
 ψ_i = electrostatic potential at a surface of the reference ion

Subscripts

b = brine
 c = coolant
 cl = clean
 f = fouling film or fouling condition
 in = inlet of heat exchanger
 out = outlet of heat exchanger
 1 = at starting time
 2 = at the minimum thermal resistance time

where

$$U_o = \frac{\dot{Q}}{A_o \text{LMTD}} \quad (2)$$

$$\text{LMTD} = \frac{(T_{b2} - T_{c2}) - (T_{b1} - T_{c1})}{\ln\left(\frac{T_{b2} - T_{c2}}{T_{b1} - T_{c1}}\right)} \quad (3)$$

The log mean temperature difference and \dot{Q} ($= m_b C_{pb} \Delta T_b$) were calculated from the experimental brine mass flow rate, and the mixed mean inlet and outlet temperatures of brine and coolant. C_{pb} and ρ_b of the brine were calculated from Wahl (1977). The U_{oc1} values are listed in Table 1. The R_f so obtained is the thermal resistance due to the scale deposited on the inner surface of the titanium tube.

The accuracy of the thermocouple was $\pm 0.5^\circ\text{C}$. A Kaye's multichannel recorder was used to convert the analog thermocouple voltages to digital signals. Its standard accuracy is listed as $\pm [(0.003 \text{ percent of reading}) + 0.3^\circ\text{C}]$. The combined uncertainty of the temperature measuring system was therefore estimated to be $\pm 0.8^\circ\text{C}$. Also, the accuracy of the turbine meter was ± 1 percent over the range of the flow rate measurement. An error analysis yields the following:

$$\frac{\Delta \dot{Q}_b}{\dot{Q}_b} = \left[\frac{\partial \dot{Q}_b}{\partial \dot{m}_b} \Delta \dot{m}_b + \frac{\partial \dot{Q}_b}{\partial (\Delta T_b)} \Delta (\Delta T_b) \right] / \dot{Q}_b = \pm 5 \text{ percent}$$

$$\frac{\Delta(\text{LMTD})}{\text{LMTD}} = \frac{\partial(\text{LMTD})}{\partial [(T_{b2} - T_{c2}) - (T_{b1} - T_{c1})]} \Delta [(T_{b2} - T_{c2})$$

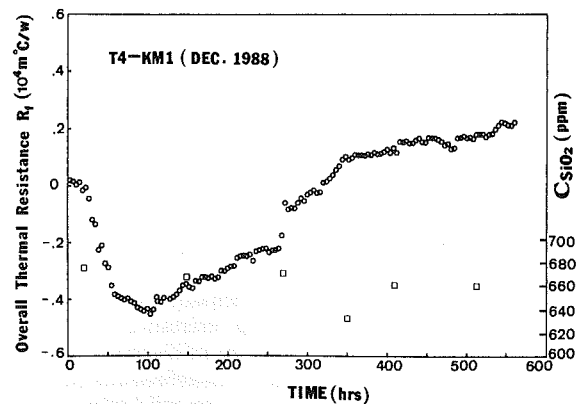
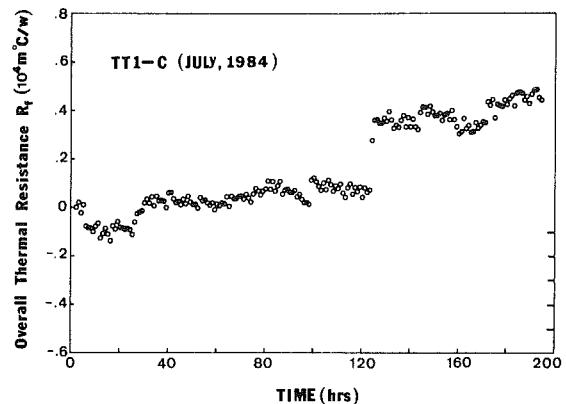
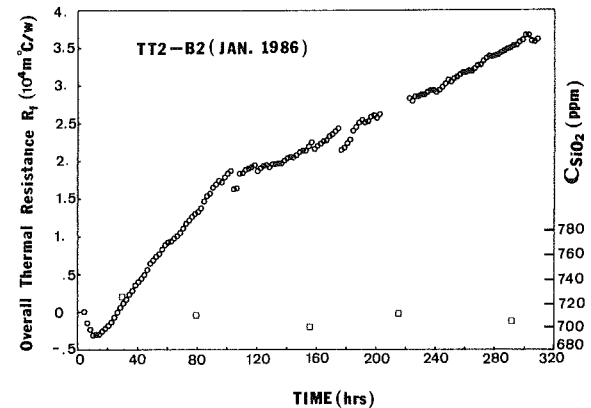
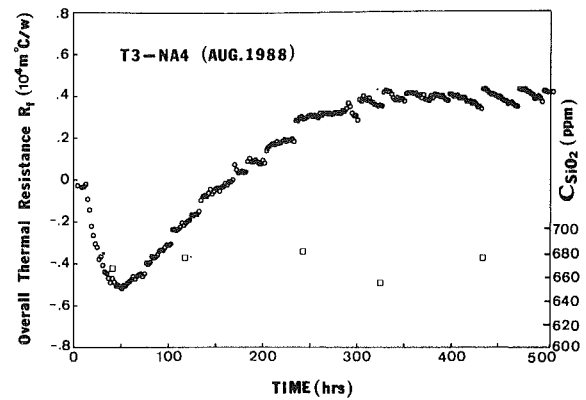
$$- (T_{b1} - T_{c1})] + \frac{\partial(\text{LMTD})}{\partial \left[\ln\left(\frac{T_{b2} - T_{c2}}{T_{b1} - T_{c1}}\right) \right]} \Delta \left[\ln\left(\frac{T_{b2} - T_{c2}}{T_{b1} - T_{c1}}\right) \right]$$

$$\text{LMTD} = 15.8 \text{ percent}$$

$$\frac{\Delta U_o}{U_o} = \frac{\Delta \dot{Q}_b}{\dot{Q}_b} + \frac{\Delta(\text{LMTD})}{\text{LMTD}} = 20.8 \text{ percent} \quad (4)$$

Thus, the uncertainty of the fouling resistance R_f was estimated to be ± 20.8 percent or less in the fouling data to be presented next.

Fouling Data. Twelve sets of experimental results using synthetic brines were obtained and are presented in Fig. 2 under turbulent flow conditions. They provide the transient thermal resistances (over the length of heat exchanger) of the silica scale. Three of them (TT1-C, TT1-D, and TT2-B), taken from the previous study (Chan et al., 1988), are included here to facilitate the discussion on the effects of NaCl versus KCl salts on silica scale formation. All 12 fouling thermal resistance curves exhibit an "induction period" and an initial drop in resistance. The "induction period" is herein referred to as the time it takes to reach the minimum resistance. It does not signify the conventional nucleation time, which is much shorter. The initial drop in resistance was also reported by Gudmundsson and Bott (1979), Bohlman et al. (1981), and Chan et al. (1988). It was explained as an enhancement in heat transfer induced by a small amount of scale deposit in the initial period. The deposit increased the surface roughness (as confirmed by the increase in the pressure drop across the heat exchanger shown in Table 3) and promoted a turbulence motion. A simple calculation, for example, indicated that the convective heat transfer is increased by 25 percent when the roughness/tube diameter ratio of a smooth tube is increased to 2×10^{-3} . For a given heat flux, the increase in the heat transfer coefficient should reduce the difference between the hot brine and the tube surface temperature. Consequently, the surface temperature is expected to be higher, the silica supersaturation near



the surface to be lower, and the deposition rate to be less. In addition, the initial, sparse scale deposits acted as heat transfer fins to further enhance heat transfer. The heat transfer enhancement, however, was eventually counterbalanced and

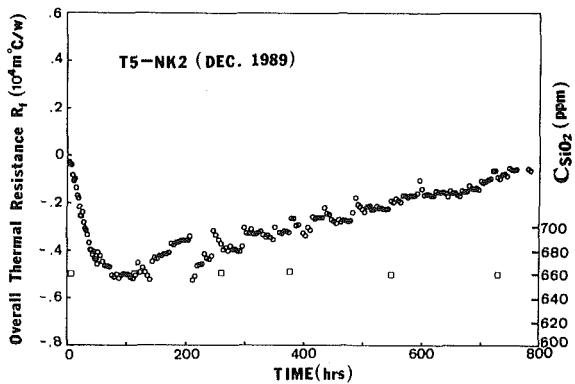
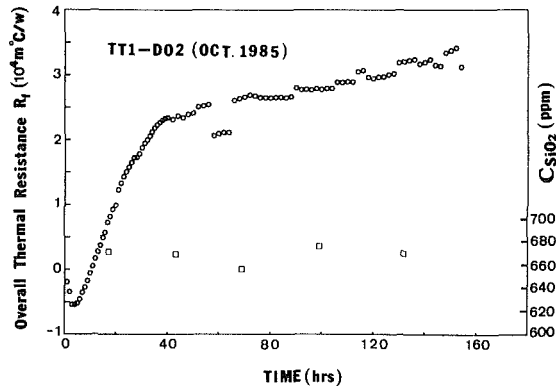
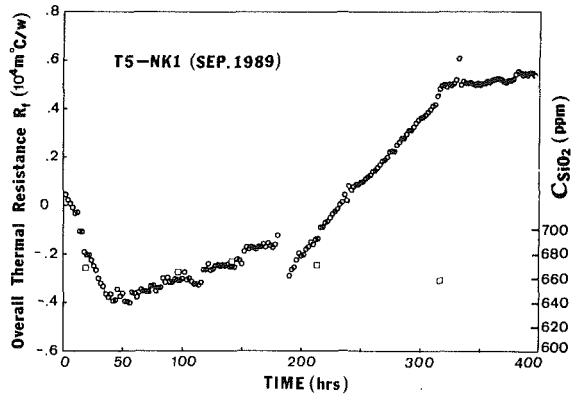
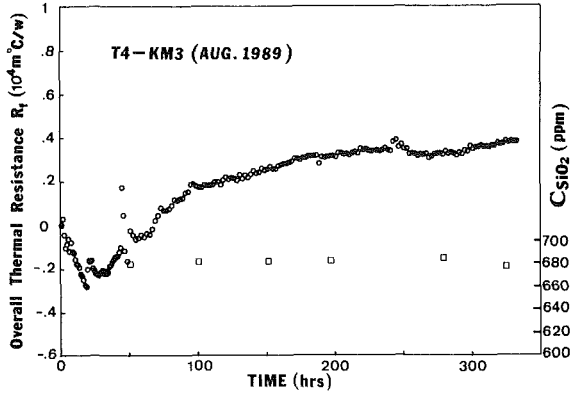
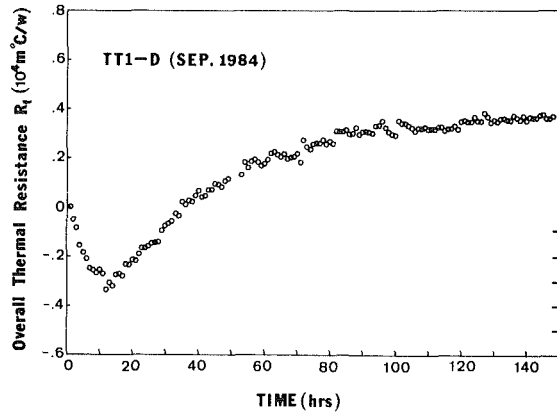
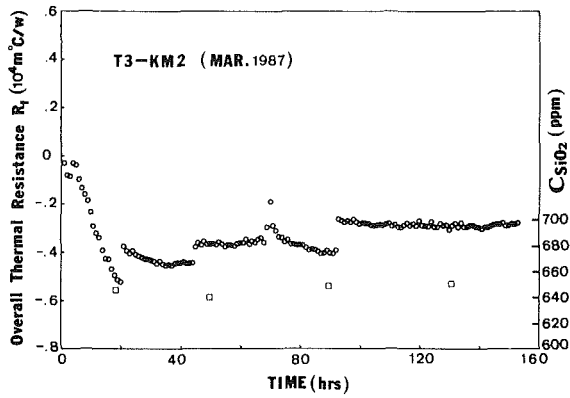
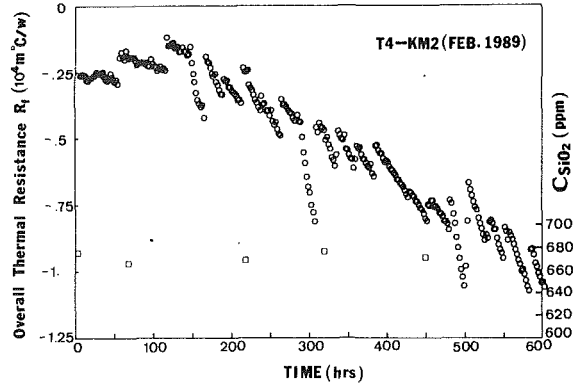
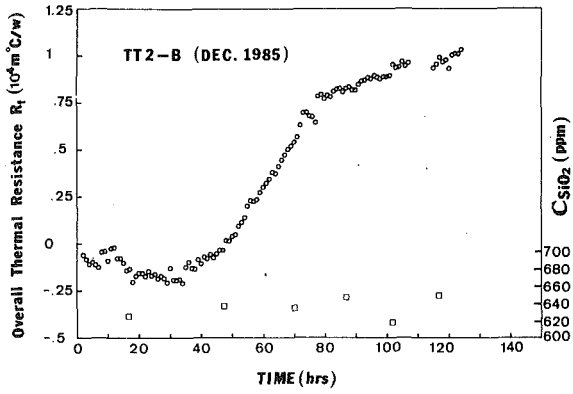


Fig. 2(A-L) Transient silica overall fouling thermal resistance profiles under various chemical and thermal-hydraulic conditions listed in Tables 1 and 2

Table 2 Chemical composition in fouling experiments

Run No.	$C_{SiO_2}^1$	C_{NaCl}^2	C_{NaAc}^4	C_{KCl}	pH	TDS ³
T3-Na4	0.0012 (675)	0.05 (2925)	0	0	7.26	3600
TT2-B2	0.0120 (720)	0.1 (5850)	0	0	8.74	6529
TT2-B	0.0106 (636)	0.1 (5850)	0	0	7.40	6478
TT1-C	0.0095 (570)	1.0 (58500)	0	0	5.80	59070
T4-KM1	0.0112 (679)	0	0	0.005 (373)	7.42	1052
T4-KM3	0.0113 (682)	0	0	0.05 (3730)	7.20	4412
T3-KM2	0.0107 (646)	0	0	0.1 (7460)	7.42	8106
T4-KM2	0.0111 (674)	0	0	0.05 (3730)	7.20	4412
TT1-D	0.0109 (660)	0	0.1 (13610)	0	7.3	14250
TT1-D02	0.0111 (666)	0	0.1 (13610)	0	7.5	14276
T5-NK1	0.0111 (667)	0.1	0	0.005 (373)	7.4	1060
T5-NK2	0.0109 (660)	0.1	0	0.05 (3730)	7.4	4410

1) saturation concentration, 2) units of SiO₂, NaCl, NaAc and KCl concentration in molarity and (PPM),

3) total dissolved solids in (PPM), and 4) NaAc is NaC₂H₃O₂ · 3H₂O

Table 3 Comparison of fouling behavior

Run No.	$\frac{dR_f}{dt}$ (m ² °C/W h) × 10 ⁷	$\frac{dR_f}{dt}$ (m ² °C/W h) × 10 ⁷	Asymptotic value of R_f (m ² °C/W) × 10 ⁵	Percent increase in ΔP across heat exchanger
T3-Na4	4.72 (50 - 230 h)		4.2	163
TT2-B2	24.17 (11 - 102 h)	9.34 (102 - 300 h)		398
TT2-B	23.67 (44 - 78 h)	5.55 (78 - 123 h)		245
TT1-C	4.31 (25 - 185 h)			64
T4-KM1	1.29 (115 - 270 h)	2.37 (270 - 350 h)	2.0	76
T4-KM3	5.33 (25 - 100 h)	1.35 (100 - 240 h)	3.7	151
T3-KM2	1.83 (24 - 95 h)		-2.8	36
T4-KM2	< 0			
TT1-D	12.6 (12 - 54 h)		4.0	193
TT1-D02	83.0 (5 - 38 h)		31.7	412
T5-NK1	1.69 (50 - 180 h)	5.93 (185 - 320 h)	5.5	196
T5-NK2	2.0 (105 - 205 h)	0.65 (220 - 760 h)		81

overtaken by the increasing thermal resistance as the deposit built up with time. Since the fouling resistance R_f is defined as the difference between the later and the initial total resistances, $R_f=0$ initially. Then, with the heat transfer enhancement, the total resistance at later times decreased afterward, resulting in negative R_f values as shown in all 12 experimental runs. It is clear that, by inspecting Figs. 2(A-L), the runs (T4-KM1, T4-KM3, T3-KM2, T4-KM2, T5-NK1, and T5-NK2) with the dissolved KCl salt required a longer time to recover to the initial state ($R_f=0$) than those with the dissolved NaCl salt (T3-Na4, TT2-B2, TT2-B, and TT1-C) because of a slower rate of scale deposition.

Table 1 lists the thermal-hydraulic conditions of the fouling experiments, which includes the Reynolds number (Re_b), the brine temperature at the inlet (T_{bin}) and at the outlet (T_{bout}) of the heat exchanger. Two sets of brine temperatures are given, one at the time the measurements began (T_{b1}) and the other at the induction time (T_{b2}). Similarly, the coolant temperatures (T_c) and the initial, reference overall heat transfer coefficient

(U_{oc1}) under clean tube condition, etc., are also given. Chemical compositions are listed in Table 2, while the comparisons of fouling behaviors are summarized in Table 3. In the latter, the time rate of change of thermal resistance curve (the slope, dR_f/dt) immediately after the induction time is given. If there is an obvious subsequent change in the slope, another value is also listed for reference. For consistency, the subsequent discussion and comparison are based on the first value. Finally, if the curves exhibit asymptotic behavior, the asymptotic values are listed as well.

In all experiments the scale layer on the tube surface near the heat exchanger inlet was observed to be fairly smooth and the surface was covered evenly by scale. However, at the outlet section, much rougher scale in the form of ridges, normal to the flow direction, was observed and the tube surface between ridges was found to be relatively free of scale deposition. This behavior may be attributed to the coagulation between silica particles in the brine due to the bulk supersaturation. Coagulation of silica reduces the number of silica particles, increases

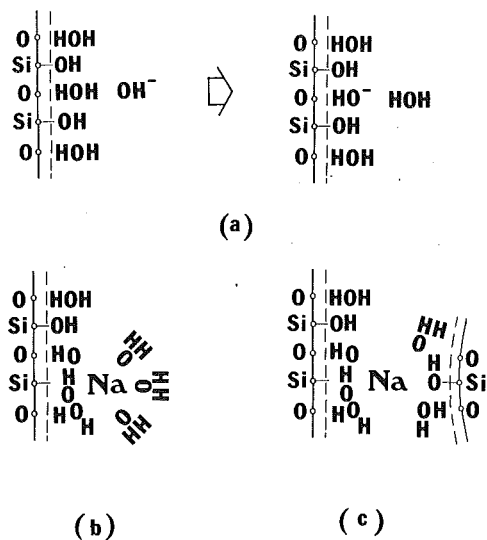


Fig. 3 Possible bonding between silica particles through coordination with flocculating metal cations (Iler, 1979)

the particle size, and hence, presumably, leads to the rougher scale at the outlet.

NaCl Concentration Effect. In comparing run No. T3-Na4 with TT2-B2 and TT2-B, the fouling resistance slope increases from 4.7×10^{-7} to $24 \times 10^{-7} \text{ m}^2 \text{ }^\circ\text{C/W h}$ (dR_f/dt in Table 3) when the NaCl concentration increases from 0.05 to 0.1 M (molarity, see Table 2). An explanation of this effect of NaCl on silica fouling is possible if reference is made to the hypothesis of aggregation of particles proposed by Iler (1979). In Fig. 3(a), a silica particle is in contact with a brine solution. The Si atom is bonded to an OH molecule to achieve an outer shell having eight electrons (Octet rule). This silanol group (SiOH) is exposed to the brine. Between the silanol groups, the space is filled with water molecules, HOH. As an OH^- ion approaches a HOH molecule, the electron of OH^- is transferred to HOH, forming a negatively charged HO^- on the surface and a free HOH molecule in the bulk. The adsorbed hydroxyl ion is responsible for the negative surface charge. The positively charged Na^+ ion in the solution is surrounded by the oxygen atoms of six water molecules of hydration. The oxygen of one of the six adjacent water molecules can be replaced by the oxygen of the (SiOH) group as shown in Fig. 3(b). Thus the sodium ion is adsorbed on the silica surface. The positive charge of the sodium ion also neutralizes the negative charge of the adjacent HO^- as illustrated in Fig. 3(b). Similarly, one or more of the water molecules still attached to the outwardly disposed side of the sodium can be displaced by silanol groups on the surface of another silica particle. The sodium ion may thus act as a bridge between two silica particles.

It is believed that the surfaces of nonnoble metals are covered by hydroxyl groups, as are the surfaces of the various forms of silica (Weres et al., 1980). The above bridging hypothesis, termed the "bridging theory," is thus applicable to the present silica scale on a heat transfer surface.

Applying this bridging theory to the present fouling experiments, the greater the NaCl salt content in the brine, the greater the number of bridging Na^+ ions and therefore the faster the fouling rate as a consequence of a reduction in the repulsive force between negatively charged colloidal particles and the negatively charged deposition surface. However, it was suggested that around each silica particle there is a boundary layer containing a preponderance of Na^+ ions (Iler, 1979). Ultimately, the surface of each silica colloidal particle becomes saturated with the salt ions, and the further addition of salt

may result in both the particles and deposition surface bearing a positive charge such that the further addition of salt ions becomes a stabilizing agent and decreases the tendency of fouling. This may explain why the fouling rate is reduced (TT1-C versus TT2-B) even though the NaCl concentration is increased by an order of magnitude (0.1 M to 1 M NaCl). Furthermore, it is noted that salt concentration is not the sole factor in determining the fouling rate. When the pH value of the brine is reduced from 8.7 (TT2-B2) to 5.8 (TT1-C), the solubility of the dissolved silica in the brine is reduced and the subsequent supersaturation ratio of the brine is decreased. Thus the combined effect of pH and salt concentration yields a reduction of the fouling rate of three runs (in decreasing order): TT2-B2, TT2-B, and TT1-C.

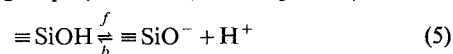
KCl Concentration Effect. In runs T4-KM1 and T4-KM3 all experimental conditions were kept the same except the KCl salt concentrations, which were varied, respectively, from 0.005 M to 0.05 M. Similar to the NaCl effect, the fouling rate increases as the KCl concentration increases, possibly because K^+ ions, just like Na^+ ions, can act as a bridging agent to promote polymerization on the silica layer on the heat exchanger surface. However, the fouling rate decreases when the KCl salt concentration is increased to 0.1 M in T3-KM2 and, in fact, the fouling resistance remains below the initial value even after 150 hours of operation. Confirmation was made by examining the fouling surface of the tube after the experiment was completed. It was observed that only sparse scales were found on the surface. The reason may be attributed to the reduction in solubility (682 ppm in T4-KM3 down to 646 ppm in T3-KM2) due to an increasing amount of KCl salt in the solution, and the KCl stabilizing effect at high salinity similar to that of NaCl.

It is noted that the fouling curve of T4-KM1 suffers a discontinuity (see Fig. 2) at the 270th hour of experimentation, since the rupture disk of the boiler was broken and the immersion heaters in the boiler were turned off automatically. Brine was, however, continuously circulated through the heat exchanger for 8 hours with greater supersaturation due to a lower brine temperature during this period. The brine was drained, the rupture disk replaced, and the brine refilled. A jump in the fouling curve was thus expected when the experiment was restarted 20 days later, possibly due to aging effects.

Comparison Between NaCl and KCl Effects. The experimental results showed that NaCl and KCl salts have a markedly different effect on fouling surface appearance and thermal resistance. For those runs with sodium chloride, the silica fouling rate is higher and the silica scale formation on the tube surface appears relatively smooth and even. By contrast, the fouling rate is smaller, the scale looks much rougher, and some surface area remains uncovered by scales in those experiments with potassium chloride solutions. To explain these marked differences completely presents no easy task, since the effects of salts on silica polymerization have been investigated for a long time but the mechanism is not yet fully understood (Iler, 1979; Chan, 1989). An attempt is made here, however, to clarify the behavior by invoking the free energy difference between sodium and potassium ions and by drawing on the work of Iler (1979).

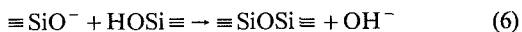
According to Iler's bridging proposal discussed above, the positively charged sodium acts as a bridge between two particles (or between the fouled surface and a silica particle). However, the X-ray spectrometry analysis of scale composition found no significant traces of sodium. This implies that after particles are bridged together, Na^+ ions somehow manage to escape from the bonding. One can conceive of a situation in which silica colloidal particles are initially in solubility equilibrium with dissolved silica, and the sodium in the solution acts to neutralize the negative charges on the surfaces of silica colloidal

particles at their points of contact. The formation of the negative charges on silica particle surfaces is due to the ionization of surface silanol groups (Iler, 1979; Fleming, 1981):



It is noted that the negative charge on the surface of amorphous silica can be represented in a number of ways (Iler, 1979, p. 355). The above is one form of surface charge representation.

When the brine becomes supersaturated with silica, there exists a driving force for the reaction of an $\equiv\text{SiO}^-$ ion on a silica surface with a nonionized silanol group, $\text{HOSi}\equiv$, on another silica surface to proceed as follows (Iler, 1979):



Such a silica condensation results in an increase of the silica scale ($\equiv\text{SiOSi}\equiv$) layer on the heat transfer surface.

Since both sodium chloride and potassium chloride are strong electrolytes, they are completely dissociated in aqueous solutions. Both sodium ions and potassium ions are monovalent and should act as a bridging ion in the same way. In most of the experiments, the salinity of the brines ranged from 0.005 M to 0.1 M. The concentrations of silicic acid were usually less than 0.1 M, while the pH values were around 7. It is possible to compare two sets of experimental systems (like TT2-B and T3-KM2) under essentially the same experimental conditions, except that one set uses NaCl and the other uses KCl as the salt. The difference in the fouling factor is then caused only by the presence of cations, Na^+ versus K^+ . The reduction in the Gibbs free energy when an ion (Na^+ or K^+) is placed in a cloud of ions in an ionic aqueous solution is described by the Debye-Hückel theory for ion-cloud interactions (Bockris and Reddy, 1970):

$$\Delta\mu_{i-l} = \frac{N_{av} Z_i e_0}{2} \psi_i \quad (7)$$

Physically, $\Delta\mu_{i-l}$ represents the chemical-potential change when one mole of ions is placed in a cloud of ions in an ionic solution. When an ion is placed in an ionic solution, as shown in Fig. 3(b), it is exposed to a local electric field ψ_i induced by the surrounding ions, including polarized water molecules. The smaller the radius of the ion, the closer the ion to the surrounding ions or to the polarized water molecules, and therefore the greater ψ_i . Consequently, by Eq. (7), $(\Delta\mu_{i-l})_{\text{H}^+} > (\Delta\mu_{i-l})_{\text{Na}^+} > (\Delta\mu_{i-l})_{\text{K}^+}$ since the radii of ions are in reverse order, namely, $r_{\text{H}^+} < r_{\text{Na}^+} < r_{\text{K}^+}$. Since the reduction in the Gibbs free energy of ion-ion interaction in a Na^+ system is larger than that of a K^+ system, it appears that the potential (or the driving force) is greater to form silicon scale in the system containing Na^+ ions than the system containing K^+ ions. This may explain the experimental results (see Fig. 2 and Table 3) that more scale was found in the experimental series containing NaCl than the series containing KCl salt. In the system with Na^+ ions, a silica monomer (or a silica colloidal particle) is bridged to a silica scale by Na^+ ions (see Fig. 3c). The Na^+ ions then escape to allow the monomer (or the silica particle) to "collapse" on the silica scale surface. This polymerization process results in a growth of silica scale. Na^+ ions thus act like a catalyst, which speeds up the reaction process. Since the Na^+ ionic radius is smaller than the K^+ ionic radius as mentioned above, the monomer (or the silica particle) is brought closer to the silica surface by Na^+ ions (than by K^+ ions) and they are, presumably, easier to collapse together due to a stronger surface charge interaction. This may thus explain why the fouling rate of NaCl solution is greater than that of the KCl solution and why more surface area is covered by scales from NaCl than from KCl solutions. Finally, because the salt ions (Na^+ or K^+) only serve to bridge a silica particle to a silica scale surface and are desorbed from the surface, it

is expected that no significant salt impurities will be found in the silica scale, which is in agreement with the results of chemical composition analysis of the silica scale as reported earlier (Chan et al., 1988).

In summary, the fundamental silica scale attachment process and the subsequent growth of silica scale by polymerization have been described. Also, the fouling characteristics due to the presence of NaCl or KCl salt in silica solutions have been explained. The combined effects of NaCl and KCl are to be studied next.

Combined NaCl and KCl Effects. With the understanding of the individual effects of NaCl and KCl salts, the combined effects of NaCl and KCl salts were then examined when both were present in the solution. The T5-NK1 and T5-NK2 experiments contained the same NaCl but different KCl concentrations. As shown in Table 3, the fouling rate increases with KCl concentration (0.005 M in T5-NK1 versus 0.05 M in T5-NK2).

It is noted that the T5-NK1 fouling curve jumps at the 180th hour (see Fig. 2) due to an excessive loss of brine through a cracked gasket. The experiment was necessarily halted to replace the gasket, the brine was refilled, and the experiment was restarted 5 days later. The aging effect may be attributed to the change in the fouling rate after the test was restarted. It should be mentioned that the silica fouling data reported here were obtained with considerable effort. Due to the inherent experimental difficulties associated with the high-pressure and high-temperature nature of the entire loop system, compounded by the corrosiveness of the salt solution, some experimental runs were inevitably interrupted (like T5-NK1) in spite of the great care taken in the design and operation of the experimental system.

Comparison is now made between T5-NK1 and TT2-B or between T5-NK1 and T4-KM1. In the T5-NK1 run, the brine solution contained both NaCl (0.1 M) and KCl (0.005 M). In the TT2-B and T4-KM1 runs, the solution contained only NaCl (0.1 M) and KCl (0.005 M), respectively. One would expect that the fouling rate of T5-NK1 with two salts present would be greater than either one of the two (TT2-B and T4-KM1) that contained only a single salt. However, the experimental results indicated otherwise. As shown in Table 3, the fouling rate of the combined salt solution is less than that of TT2-B and is, instead, closer to the slower one (T4-KM1). A repeated experiment, T5-NK2, with even more KCl salt added reveals the same conclusion. The latter can be seen if comparison is made between T5-NK2 and TT2-B, as well as between T5-NK2 and T4-KM3 (0 M NaCl, 0.05 M KCl). The fouling thermal resistance rate of T5-NK2 was less than T4-KM3 because the initial silica concentration of T5-NK2 was less than that of T4-KM3 (see Table 2), resulting in a lower supersaturation in the test section.

A possible explanation is given here. It is noted that the ionic mobility of the K^+ ion is 50 percent greater than that of the Na^+ ion (Eucken, 1951). This means that K^+ ions, as the same finite equivalent concentration and the same electric potential gradient, move at a speed 50 percent faster in an ionic solution than Na^+ ions. Thus, when both NaCl and KCl salts are present, K^+ ions are more likely to move to a position to bridge silica particles (or monomers) together. Consequently, K^+ ions may dominate over Na^+ ions as the bridging agent, and the silica fouling in the combined NaCl-KCl system may therefore be more similar to the fouling in KCl than in the NaCl system.

Velocity Effects. The mass flow rate is an important variable, which affects both the convective transport of silica toward the deposition surface and the shear stresses to which deposits are subjected. It is evident that in the NaCl solution series the fouling rate decreases with the increased mass flow

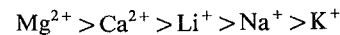
rate when comparison is made between TT1-DO2 and TT1-D. By assuming that the surface reaction is controlled, it is expected that higher velocity induces larger wall shear stress, which in turn reduces the fouling rate. It was suggested (Weres et al., 1980) that the deposits by the molecular deposition process are almost indestructible once formed as a hard surface layer and hence are independent of the hydrodynamic conditions (such as velocity, etc.) of fluid. However, the colloidal silica does not form a hard scale and its deposits are affected by the fluid hydrodynamic conditions (Weres et al., 1980; Gudmundsson and Bott, 1979). There appears to be a good reason to assert that silica colloidal particle deposition is the dominant fouling process in the present experimental circumstances (at least in the section near the outlet of the heat exchanger tube) if one makes reference to the much higher asymptotic value of R in TT1-DO2 than that in TT1-D.

The asymptotic trend observed above can be explained as follows. In the present experiments, the brine mass flow rates were held constant during the course of the experiments. Since the flow passage area of the heat exchanger tube decreases as the scale layer is building up in the tube, the brine velocity increases with time and so is the shear stress on the scale layer. If the shear stress is considered to be the dominant scale removal factor (Taborek et al., 1972), the scale removal rate should increase and be equal to the scale deposition rate, resulting in an asymptotic scale layer thickness as observed here.

It is interesting to note that in T4-KM2, the scale deposit was found to be too thin to retard the heat transfer enhancement caused by scale-induced turbulence, so that the thermal resistance never recovers to the clean condition value even after 600 hours of operation. A repeated experiment revealed the same. It should be pointed out, however, that T4-KM2 was conducted at the lowest velocity design limit. Constant adjustment of the flow rate was found necessary due to flow instability, which may affect the scale formation to some extent.

pH Effects. It is known that the solubility of silica increases with pH in the alkaline range and the pH value has no effect on the solubility of silica at low pH values. Very little attention, however, has been paid to the other effect of pH, namely, that the absorption of OH^- ions on the silica surface increases with pH in the range of pH 3.5 to 10.5 (Bolt, 1957; Bowen and Epstein, 1979). Increasing the absorption of OH^- ions increases the repulsive interactions between a silica particle and a silica deposition surface. Hence it reduces the deposition rate. Runs TT2-B and TT2-B2 were compared since they are at the same salt concentration and differ only in pH. One might thus expect the fouling rate of TT2-B2 to be lower than that of TT2-B since the former had a higher pH value and a stronger repulsive interaction. However, a higher pH value raised the silica solubility in the brine of TT2-B2 (see Table 2). It produced a higher silica supersaturation ratio and, therefore, a higher fouling rate in the test section. Hence, it is not surprising that the fouling rates of both runs were nearly the same since the competing effect of the higher silica supersaturation ratios was compensated for by the effect of the increasing absorption of OH^- ions on silica surfaces.

Salinity Effect on Amorphous Silica Solubility. Since the present brine tank maintained the working brines at solubility equilibrium during the course of this study, the silica concentration C_{SiO_2} listed in Table 2 provides solubility data at T_{b1} (see Table 1, around 165°C). It is seen that the solubility in NaCl solution (675 ppm in T3-Na4 with 0.05 M NaCl) is smaller than in KCl solution (682 ppm in T4-KM3 with 0.05 M KCl). This is in agreement with the recent works of Marshall and Warakowski (1980) and Chan et al. (1987), who reported that the effect of cations on decreasing the silica solubility follows the order of



The present data further show that the silica solubility decreases with increasing salt concentrations. For KCl salt, for example, the solubility is reduced from 682 ppm in T4-KM3 to 646 ppm in T3-KM2 when the KCl concentration is increased from 0.05 to 0.1 M. This is also in agreement with the trend reported in their works.

Conclusions

The present investigation can be summarized as follows:

1 Thermal resistance data for silica scale taken under turbulent flow conditions have been presented over a range of pH, velocity, and NaCl and KCl concentrations.

2 At 165°C, the equilibrium silica solubilities in NaCl and KCl aqueous solutions have been presented. The solubility was found to decrease with increasing salt concentration, and NaCl has a greater solubility effect than KCl.

3 At a given molarity of salt, the silica fouling rate in the NaCl aqueous solution is greater than the rate in the KCl system. Furthermore, the fouling rate increases with salt concentration, at a fixed pH.

4 When both NaCl and KCl were present in the solution, the fouling rate was found to be closer to that of the KCl solution.

5 More surface area was found to be covered by scales from NaCl than from KCl solutions.

6 The inherent competing effect of pH on silica scale deposition has been described.

7 The physical appearance of silica scale was smoother and more even in the NaCl system than in the KCl system. The scale was also smoother at the inlet section of the heat exchanger tube than at the outlet.

8 The use of the polymerization theory and the concept of the Gibbs free energy of ions seems to explain most of the silica scale behavior reported in this study.

Acknowledgments

This research was sponsored by the National Science Foundation under grants No. CBT-8807406 and CTS-9117230. Special thanks are due to Drs. W. Kao and J. Neumann for their advice.

References

- Barnes, H. L., 1979, *Geochemistry of Hydrothermal Ore Deposits*, 2nd ed., Wiley, New York.
- Bockris, J. O. M., and Reddy, A. K. N., 1970, *Modern Electrochemistry*, Plenum Press, New York, Vol. 1, pp. 180-202; Vol. 2, p. 743.
- Bohlmann, E. G., Mesmer, R. E., and Berlinski, P., 1980, "Kinetics of Silica Deposition From Simulated Geothermal Brines," *Society of Petroleum Engineers Journal*, pp. 239-248.
- Bohlmann, E. G., Shore, A. J., Berlinski, P., and Mesmer, R. E., 1981, "Silica Scaling in Simulated Geothermal Brines," Oak Ridge National Laboratory Report No. ORNL/TM-7681.
- Bolt, G. H., 1957, "Determination of the Charge Density of Silica Sols," *J. Phys. Chem.*, Vol. 61, p. 1166.
- Bowen, B. D., and Epstein, N., 1979, "Fine Particle Deposition in Smooth Parallel-Plate Channels," *J. Colloid and Interface Sci.*, Vol. 72, No. 1, pp. 81-97.
- Bryers, R. W., ed., 1982, *Fouling of Heat Exchanger Surface*, Proceedings of the Engineering Foundation Conference, White Haven, PA, Oct. 31-Nov. 5.
- Chan, S. H., Neusen, K. F., Shadid, J. Chou, S. F., and Lin, C. C., 1982, "Geothermal Transient Fouling Heat Transfer Measurements," *Fouling of Heat Exchanger Surfaces*, R. W. Bryers, ed., Engineering Foundation, New York.
- Chan, S. H., Neusen, K. F., and Chang, C. T., 1987, "The Solubility and Polymerization of Amorphous Silica in Geothermal Energy Applications," *Proceedings of 1987 ASME-JSME Thermal Engineering Joint Conference*, Vol. 3, pp. 103-108.

- Chan, S. H., Rau, H., DeBellis, C., and Neusen, K. F., 1988, "Silica Fouling of Heat Transfer—Experiments and Model," *ASME JOURNAL OF HEAT TRANSFER*, Vol. 110, pp. 841–849.
- Chan, S. H., 1989, "A Review on Solubility and Polymerization of Silica," *Geothermics*, Vol. 18, No. 12, pp. 49–56.
- Chan, S. H., and Ghassemi, K. F., 1991, "Analytical Modeling of Calcium Carbonate Deposition for Laminar Falling Films and Turbulent Flow in Annuli: Part I—Formulation and Single-Species Model; Part II—Multi-species Model," *ASME JOURNAL OF HEAT TRANSFER* (in press).
- Chen, C. T. A., and Marshall, W., 1982, "Amorphous Silica Solubilities IV. Behavior in Pure Water and Aqueous Sodium Chloride, Sodium Sulfate, Magnesium Chloride, and Magnesium Sulfate Solutions up to 350°C," *Geochimica et Cosmochimica Acta*, Vol. 46, pp. 279–287.
- Eucken, A., 1951, *Grundriss der Physikalischen Chemie*, 7th ed., Akademische Verlagsgesellschaft, Leipzig, Germany, p. 557.
- Fischer, P., Sutor, J. W., and Ritter, R. E., 1975, "Fouling Measurement Techniques," *Chem. Eng. Prog. Symp. Ser.*, Vol. 17, No. 7, pp. 62–72.
- Fleming, B. A., 1981, "Polymerization Kinetics and Ionization Equilibria in Aqueous Silica Solutions," Ph.D. Dissertation, Princeton University, Princeton, NJ.
- Fournier, R. O., 1970, "Silica in Thermal Waters: Laboratory and Field Investigations," in: *Proc. Int. Symp. on Hydrogeochemistry and Biogeochemistry*, Tokyo, Sept. 7–9, pp. 122–139.
- Fournier, R. O., and Rave, J. J., 1977, "The Solubility of Amorphous Silica in Water at High Temperatures and Pressure," *American Mineralogist*, Vol. 62, pp. 1052–1056.
- Goto, K., 1956, "Effect of pH on Polymerization of Silicic Acid," *J. Phys. Chem.*, Vol. 60, pp. 1007–1008.
- Gudmundsson, J. S., and Bott, T. R., 1979, "Deposition of Silica From Geothermal Waters on Heat Transfer Surfaces," *Desalination*, Vol. 28, pp. 125–145.
- Iler, R. K., 1979, *The Chemistry of Silica—Solubility, Polymerization, Colloid and Surface Properties, and Biochemistry*, Wiley, New York, p. 214, 341–342, 355, 375–378.
- Lombard, G. L., 1978, "Heat Exchanger Tests With Moderately Scaling Geothermal Brine," *AIChE Symp. Series No. 174*, Vol. 74, pp. 281–287.
- Marshall, W. L., 1980, "Amorphous Silica Solubilities—I. Behavior in Aqueous Sodium Nitrate Solutions: 20–300°C, 0–6 Molal," *Geochimica et Cosmochimica Acta*, Vol. 44, pp. 907–913.
- Marshall, W. L., and Warakowski, J. M., 1980, "Amorphous Silica Solubilities—II, Effect of Aqueous Salt Solutions at 25°C," *Geochimica et Cosmochimica Acta*, Vol. 44, pp. 915–924.
- Melo, L. F., Bott, T. R., and Bernardo, C. A., eds., 1988, *Fouling Science and Technology*, NATO ASI Series E, Applied Sciences, Vol. 145, Kluwer Academic Pub., Boston, MA.
- Rothbaum, H. P., and Rohde, A. G., 1979, "Kinetics of Silica Polymerization and Deposition From Dilute Solutions Between 5 and 180°C," *J. of Colloid and Interface Sci.*, Vol. 71, No. 3, pp. 533–559.
- Somerscales, E. F. C., and Knudsen, J. G., eds., 1981, *Fouling of Heat Transfer Equipment*, Hemisphere Pub. Corp., Washington, DC.
- Sutor, J. W., Marnier, W. J., and Ritter, R. B., 1977, "The History and Status of Research in Fouling of Heat Exchangers in Cooling Water Service," *The Canadian Journal of Chemical Engineering*, Vol. 55, pp. 374–380.
- Taborek, J., Aoki, T., Ritter, R. B., Palen, J. W., and Knudsen, J. G., 1972, 1972a, "Fouling: The Major Unresolved Problem in Heat Transfer (Parts I and II)," *Chemical Engineering Program*, Vol. 68, No. 2, pp. 59–67; Vol. 68, No. 7, pp. 69–78.
- Taborek, J., Aoki, T., Ritter, R. B., Palen, J. W., and Knudsen, J. G., 1972b, "Predictive Methods for Fouling Behavior," *Chemical Engineering Progress*, Vol. 68, No. 7, pp. 69–78.
- Wahl, E. F., 1977, *Geothermal Energy Utilization*, Wiley, New York.
- Weres, O., Yee, A. W., and Tsao, L., 1979, "Kinetic Equations and Type Curves for Predicting the Precipitation of Amorphous Silica From Geothermal Brines," presented at the SPE of AIME International Symposium on Oilfield and Geothermal Chemistry, Houston, TX, Jan. 22–24, Paper No. SPE 7888.
- Weres, O., Yee, A., and Tsao, L., 1980, "Kinetics of Silica Polymerization," Lawrence Berkeley Laboratory, Report LBL-7033.
- Weres, O., Yee, A., and Tsao, L., 1981, "Kinetics of Silica Polymerization," *J. of Colloid and Interface Science*, Vol. 84, No. 2, pp. 379–402.
- Weres, O., Yee, A., and Tsao, L., 1982, "Equations and Type Curves for Predicting the Polymerization of Amorphous Silica in Geothermal Brines," *Society of Petroleum Engineers J.*, Feb., pp. 9–16.

Convective Heat Transfer Enhancement Due to Intermittency in an Impinging Jet

D. A. Zumbrunnen

M. Aziz¹

Thermal Sciences Research Laboratory,
Department of Mechanical Engineering,
Clemson University,
Clemson, SC 29634-0921

An experimental investigation has been performed to study the effect of flow intermittency on convective heat transfer to a planar water jet impinging on a constant heat flux surface. Enhanced heat transfer was achieved by periodically restarting an impinging flow and thereby forcing renewal of the hydrodynamic and thermal boundary layers. Although convective heat transfer was less effective during a short period when flow was interrupted, high heat transfer rates, which immediately follow initial wetting, prevailed above a threshold frequency, and a net enhancement occurred. Experiments with intermittent flows yielded enhancements in convective heat transfer coefficients of nearly a factor of two, and theoretical considerations suggest that higher enhancements can be achieved by increasing the frequency of the intermittency. Enhancements need not result in an increased pressure drop within a flow system, since flow interruptions can be induced beyond a nozzle exit. Experimental results are presented for both the steady and intermittent impinging jets at distances up to seven jet widths from the stagnation line. A theoretical model of the transient boundary layer response is used to reveal parameters that govern the measured enhancements. A useful correlation is also provided of local heat transfer results for steadily impinging jets.

Introduction

Although impinging jets are frequently utilized for cooling, heating, and drying, relatively little consideration has been given to enhancing convective heat and mass transfer processes in these flows. Most prior research with impinging jets has focused on the heat transfer and fluid mechanics that result when jets, without modification, impinge on surfaces. This emphasis is in contrast to the robust research that has ensued in achieving enhancements in duct flows by active modification of the flow or the heat transfer surface. Designers are presently improving heat exchanger performance by incorporating stagnation flows by means of baffles or flow nozzles. However, this practice relies on the high convective heat transfer coefficients associated with all stagnation flows and does not exploit other techniques that might enhance heat transfer processes in the impinging flow itself. Implementation of jet arrays in engineering systems is sometimes forestalled by excessive fluid consumption. Although high convective heat and mass transfer coefficients can be generated, only a small portion of the fluid in an impinging jet actually participates, while most of the fluid is confined to a relatively thick overriding layer. Means to enhance heat and mass transfer processes in impinging jet flows can therefore be of significant interest and practical benefit.

As a jet approaches the impingement surface, a stagnation region about a stagnation point or line is formed in which a decrease in flow velocities gives rise to an increase in static pressure. The stagnation region for a cylinder in a crossflow is similar geometrically to the stagnation region arising beneath a planar impinging jet, since stagnation lines arise in both cases; in contrast, stagnation regions for circular jets and spheres are symmetric about a stagnation point. Thus, research with cylinders and spheres in crossflows can provide important insights with regard to impinging jets. Smith and Kuethe (1966) formulated a phenomenological theory to relate turbulence in-

tensity Tu in air to convective heat transfer at the stagnation line for a cylinder in a cross flow. Their work was later applied to circular air jets of diameter D and relationships were proposed of the form $Nu_D Re_D^{0.5} = a + bTuRe_D^{0.5} - c [TuRe_D^{0.5}]^2$, where a , b , and c are positive constants (Hoogendoorn, 1977). This relationship demonstrates that enhancements due to turbulence attain maximum values as the turbulence intensity increases for a specific Reynolds number. Lowery and Vachon (1975) induced turbulence in an air stream with screens and grids and found that heat transfer coefficients in the stagnation region of a cylinder in crossflow were larger than laminar values with a maximum factor of about 1.6. Results were consistent with the relationship given above.

Sutera et al. (1963) obtained approximate solutions to the Navier-Stokes equations for two-dimensional, steady, stagnation flow in which a unidirectional vorticity was steadily transported. Their results showed that the scale and orientation of the vortex was an important factor in determining whether the hydrodynamic and thermal boundary layers were affected by the simulated turbulence in the incident flow. A neutral scale existed at which amplification by stretching was exactly balanced by viscous losses and the vorticity approached the boundary layers with constant intensity. For vortices larger than this neutral scale, the turbulent intensity increased, or was amplified, upon passage of vortices through the stagnation region. Resulting enhancements in convective heat transfer were found to be higher at larger Prandtl numbers. Convective heat transfer coefficients have been reported in studies with turbulent planar water jets (Miyasaka and Inada, 1980; Zumbrunnen et al., 1989; Vader et al., 1991), which exceed those predicted from laminar flow theory by factors ranging from 1.3 to 1.9 for similar Reynolds and Prandtl numbers. The diversity in reported data is likely due to differences in turbulence levels and the characteristics of incident vortices. Relying on turbulence effects to obtain specified enhancements in engineering systems is therefore presently uncertain.

Heat transfer in the stagnation region of a jet can be affected by the velocity profile at the nozzle exit. Scholtz and Trass (1970) measured local mass transfer rates between an axisymmetric, laminar air jet and a naphthalene surface. The jet issued from a pipe with a fully developed laminar profile (i.e., a

¹Currently with Camp, Dresser, and McKee, Inc., Houston, TX.

Contributed by the Heat Transfer Division and presented at the National Heat Transfer Conference, San Diego, California, August 9-12, 1992. Manuscript received by the Heat Transfer Division March 30, 1992; revision received July 7, 1992. Keywords: Augmentation and Enhancement, Jets, Transient and Unsteady Heat Transfer. Associate Technical Editor: F. P. Incropera.

parabolic profile). At the same Reynolds numbers based on nozzle diameter and average nozzle discharge velocity, mass transfer rates for jets with parabolic profiles were more than twice as large as those for jets with uniform profiles. A related study was later performed by Sparrow and Lee (1975) to determine theoretically the effect of a fully developed laminar velocity profile on heat and mass transfer due to a planar jet. Their results showed increases of almost a factor of two in heat and mass transfer rates near the stagnation line when the jet velocity is parabolic. However, neither study considered the effect of gravity on a liquid jet, which can flatten the velocity profile and significantly reduce the enhancements. Enhancements have also been shown to diminish rapidly and lead to smaller heat transfer coefficients beyond about one jet width from the stagnation point (Zumbrunnen et al., 1992).

In this study, a novel technique of enhancing heat transfer in impinging jet flows is investigated that is effective in both laminar and turbulent flows. Enhancement is achieved by briefly and repetitively interrupting the jet flow and thereby halting the development of the hydrodynamic and thermal boundary layers. Such a flow will be referred to subsequently as an *intermittent flow*. Although little or no cooling is available during a brief interval when the flow is interrupted, the thermal resistance due to the newly forming thermal boundary layers is extremely small each time the flow is resumed and a net enhancement can thereby arise.

Flow intermittency can be regarded as a type of pulsatile flow. Convective heat transfer to a pulsating, circular air jet impinging on a heated copper plate was studied for pulse frequencies up to 18 Hz (Nevins and Ball, 1961). Pulse amplitudes in some experiments were sufficiently large to achieve flow intermittency. Spatially averaged Nusselt numbers were found to be independent of the amplitude and frequency of the pulsations and were in satisfactory agreement with correlations for steady, impinging jets. However, as will be shown, enhancements were not obtained since the pulsation frequencies in the intermittent flow were too low.

Enhancements due to intermittency will only occur if the frequency of the intermittency is sufficiently high to maintain time-averaged thermal boundary layer thicknesses much thinner than steady-state values and thereby offset reduced heat transfer during the brief period when flow is absent. In order to discern the frequencies for which enhancements can be expected in the vicinity of the stagnation line, the transient response of the thermal boundary layer must be understood. In planar jet impingement, the velocity component u_∞ at the edge of the hydrodynamic boundary layer is related to the distance x_j from the stagnation line (i.e., a line of symmetry along the impingement surface in the jet plane) by

$$u_\infty = Cx_j \quad (1)$$

where C is a constant (Schlichting, 1979). A theoretical model of the thermal boundary layer response in a steady, planar, stagnation flow to temporal variations in surface heat flux or temperature has shown that responses are more rapid at lower Prandtl numbers for $0.7 < Pr < 15.0$, but are chiefly governed by the value of C (Zumbrunnen, 1992). The model-predicted, unforced response of the thermal boundary layer referenced to its steady-state value is shown in Fig. 1 for a constant surface temperature in terms of the variable $\Psi_*^{1/2}$. The unforced response corresponds to the dynamic behavior with no external stimulus or forcing when the boundary layer thickness is initially zero. This case approximates the thermal boundary layer growth in an intermittent flow. Close inspection of Fig. 1 indicates that thermal boundary layer thicknesses are within 1 percent of their steady values at about dimensionless times τ ($\tau = Ct$) of 4 and 6 for Prandtl numbers of 0.7 and 15, respectively.

The ratio of the instantaneous Nusselt number to the steady-state Nusselt number, Nu_* is also presented in Fig. 1. Small thermal boundary layer thicknesses that prevail early in the transient correspond to Nu_* greater than unity. In the intermittent flows of this study, Nusselt numbers are very high in the early stages of the continuous flow period in each inter-

Nomenclature

C = free-stream velocity gradient [Eq. (1)]	number to steady-state Nusselt number at the stagnation line ($x = 0$)	T_s = local surface temperature along test strip
C_* = dimensionless free-stream velocity gradient = $Cw/v_j = \pi/4$	Pr = Prandtl number evaluated at local film temperature	T_∞ = temperature of jet free stream
D = diameter of a cylinder	Pr_0 = Prandtl number at stagnation line ($x = 0$)	Tu = turbulence intensity
f = intermittency frequency	R = electrical resistance of exposed length of strip	u_∞ = local velocity component parallel to strip surface in the free stream
$g(x)$ = function given by Eq. (4)	Re_w = Reynolds number evaluated at local film temperature = $v_j w / \nu$	v_j = incident jet impingement velocity
H = thickness of test strip	Re_{w0} = Reynolds number at stagnation line ($x = 0$) = $v_j w / \nu$	w = incident jet width
I = electrical current passing through test strip	S_w = Strouhal number = $f w / v_j$	W = spanwise dimension of test strip
J = nozzle width	S_{wt} = threshold Strouhal number [Eq. (2)]	x = dimensionless distance = x_j / w
k = thermal conductivity of fluid	t = time	x_j = distance along impingement surface from stagnation line
k_s = thermal conductivity of test strip	t_{bl} = time period for boundary layer growth in intermittent flow cycle	y = vertical position within test strip
L = length of test strip	T = temperature in strip	Δ = instantaneous thermal boundary layer thickness
N = number of blades (3 or 6) mounted on the wheel (Fig. 4)	T_b = local temperature at bottom side of test strip (Fig. 2)	Δ_{ss} = steady-state thermal boundary layer thickness
Nu_w = Nusselt number based on jet width = hw/k	T_f = local film temperature = $[T_s(x_j) + T_\infty]/2$	Γ = dimensionless time for boundary layer growth = Ct_{bl}
Nu_D = Nusselt number based on cylinder diameter = hD/k		τ = dimensionless time = Ct
Nu_* = ratio of instantaneous Nusselt number to steady-state Nusselt number		Ψ_* = square of thermal boundary layer thickness ratio = $(\Delta/\Delta_{ss})^2$
Nu_{w0}^* = ratio of time-averaged Nusselt		

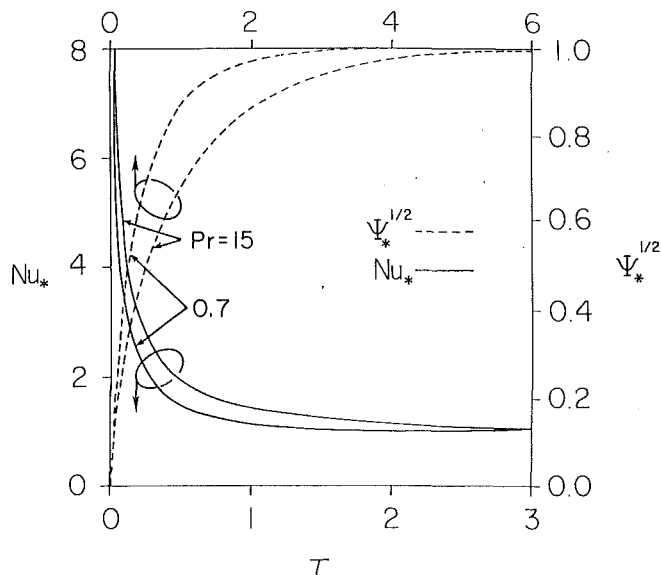


Fig. 1 Theoretical, unforced transient response of the thermal boundary layer and Nusselt number in a planar stagnation flow with Ψ_* ($\tau = 0$) = 0 (Zumbrunnen, 1992)

mittency cycle and repetitively approach steady values in a comparative manner. Enhancements to convective heat transfer on a time-averaged basis will therefore be higher for shorter continuous flow periods. In order to gage frequencies at which the intermittencies can give rise to enhancements in the vicinity of the stagnation line, it is useful to designate Γ as the dimensionless time τ for the continuous flow period in each cycle of the intermittent flow. Figure 1 indicates that little enhancement can be expected when Γ is larger than about 3. An approximate criterion for the dimensionless threshold frequency in terms of the Strouhal number $S_w (= fw/v_j)$ above which enhancement is expected ($0.7 \leq Pr \leq 15$) is therefore given by

$$S_{wr} \approx \frac{C_*}{3} \quad (2)$$

where C_* ($= Cw/v_j$) is the dimensionless velocity gradient at the stagnation line. For planar jets with a uniform velocity profile across the jet width, $C_* = \pi/4$ (Inada et al., 1981). Enhancements near the stagnation line are therefore expected when $S_{wr} \geq 0.26$. In the aforementioned study by Nevins and Ball (1961), dimensionless frequencies were less than 0.01. This value is far below the threshold frequency and steady-state Nusselt numbers thereby prevailed over most of the pulse cycle, yielding little enhancement, as reported.

In light of the theoretical motivation provided in Fig. 1 and given the practical importance of stagnation flows, the effect of flow intermittency on convective heat transfer to a planar water jet impinging on a constant heat flux surface has been investigated. An apparatus was developed to produce intermittency frequencies up to 142 Hz. A maximum Strouhal number of 0.365 was achieved and enhancements of nearly a factor of two resulted. Required threshold frequencies are consistent with Eq. (2). In order to achieve comparable improvements in heat transfer by simply increasing the flow rate supplied to a nozzle, elementary calculations show that fluid supply pressures would need to be raised by a factor of about 5.7 for turbulent flow conditions. However, enhancements by intermittency need not require increases in pressure drop within a flow system and may therefore have practical importance. For example, intermittency may be induced by briefly and repetitively obstructing the flow emerging from a nozzle or by sequencing flow interruptions to individual nozzles within a jet array such that a continuous flow is maintained in a supply system.

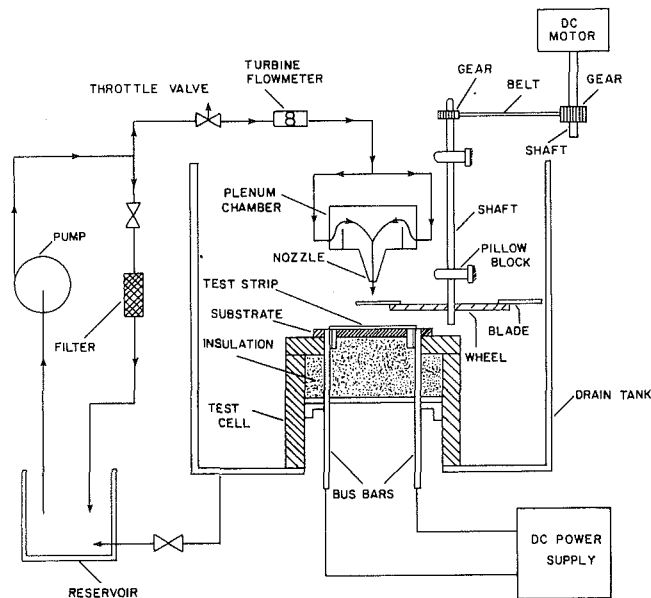


Fig. 2 Schematic representation of the experimental apparatus (not to scale)

Experimental Apparatus and Methods

The apparatus is shown schematically in Fig. 2. The test cell was that part of the experimental apparatus that housed electrical and thermocouple wires and contained the necessary components needed to make heat transfer measurements. The test cell was a sealed unit to prevent water infiltration and was constructed from an electrically and thermally insulating, phenolic-canvas composite. An electrically heated nickel-chromium alloy test strip (0.0102 cm thick) was mounted on a thin substrate of the same composite material. Thermocouples were inlaid in the substrate at several positions for local temperature measurements of the bottom side of the strip. The test cell was filled with fiberglass insulation to minimize heat losses. Heat was generated by passing an electrical current through the test strip via heavy copper bus bars. A planar jet was formed by a convergent nozzle attached to a plenum chamber, which incorporated baffle plates and a flow element to reduce turbulence entering the nozzle opening. Filtered water was supplied by an electrically driven centrifugal pump and a turbine flow meter was used to measure flow rates supplied to the nozzle. Blades mounted along the circumference of a wheel deflected the jet away from the test strip to achieve the flow intermittency. A shaft and gear-belt arrangement was employed to transmit the torque from a direct current, variable speed motor to the wheel. It is important to note that alternate techniques can also be employed to induce intermittency; but the blade/wheel arrangement was selected since it provided positive control of the flow over wide ranges in jet velocity and frequency.

Two transparent plastic blocks were machined to precise specifications with a numerically controlled milling machine and were fastened together to form the nozzle. A straight convergent section (7.62 cm long) was incorporated to provide a uniform velocity profile at the nozzle exit. A short transition section (0.2 cm long) straightened the flow prior to discharge. The inlet opening was 5.08 cm by 25.4 cm while the discharge opening was 5.08 cm by 0.508 cm. A flow element was placed in the plenum chamber just above the nozzle opening. The flow element was constructed from a stainless steel honeycomb flash arrestor with 0.079 cm hexagonal cells. The overall thickness of the flow element was 6.2 cm. Experiments were performed with the flow element removed to ascertain its effect on the results and no appreciable difference was observed for experiments with steady or intermittent flow. For the condi-

tions considered, local flow velocities across the nozzle width and length were found by hot film probe measurements to be within 1 percent of the average value determined by readings from the turbine flow meter and the dimensions of the nozzle opening. The jet temperature was measured with a copper-constantan thermocouple probe placed above the flow element. Corrections to the jet discharge velocity and width were made to account for thinning due to gravitational acceleration (Zumbrennen et al., 1989). Jet Reynolds numbers (Re_{j0}) were calculated from the corrected velocity and width for both the steady and intermittent jet flows. Thus, comparisons are presented with respect to the fluid expenditure at the nozzle opening and no attempt is made to decrease the Reynolds number for the intermittent flows to account for effluent deflected away from the strip by the rotating blades.

A detailed view of the substrate shown schematically in Fig. 2 is given in Fig. 3. Thermocouple wires were inlaid in spanwise grooves and junctions were located at the midpoint. The thermocouple wires passed through holes provided at the ends of each groove for connection to lead wires. The spanwise orientation of the grooves corresponded to an isotherm on the strip due to the planar symmetry of the impinging jet flow. Conductive heat losses from the junctions along the lead wires, as confirmed by calculation, were therefore negligible. All grooves were machined with a high-precision milling machine to locate the thermocouples accurately beneath the test strip. The spacing between neighboring grooves was smaller near the centerline in order to discern more accurately from convective heat transfer distributions the precise location of the stagnation line in the planar jet flow. The bare thermocouple wire was coated with lacquer to isolate it electrically from the electrical current in the test strip. A small bead of thermally conductive grease was applied to each junction to ensure good thermal contact with the test strip.

The thermocouples were fabricated from 0.0127-cm-dia copper and constantan (ANSI Type T) wires. Junctions were formed from a pancakelike weld. Excess weld material was carefully removed, yielding a nearly cylindrical junction with

a diameter only slightly larger than that of the thermocouple wire. The time response of the thermocouples was estimated by idealizing the thermocouple bead as a slab with one adiabatic surface and solving the transient, one-dimensional heat conduction equation for the response due to a step change in temperature imposed at the opposite surface. The time required for the slab to attain uniformly the imposed temperature to within 1 percent was 0.004 s, which corresponded to a frequency response of 250 Hz.

Although the frequency response of the thermocouple junctions reported above exceeds the highest imposed intermittency frequency (142 Hz) in the experiments, the time response of the test strip itself must also be considered in order to infer surface temperatures for convective heat transfer calculations. A scaling analysis with the heat conduction equation showed that heat transfer along the length of the thin test strip was negligible and heat losses from the bottom side of the test strip were estimated to be less than 0.5 percent of the heat transferred to the jet. A one-dimensional, transient numerical model was therefore developed to simulate the thermal response of an electrically heated test strip with an adiabatic lower surface. Convective cooling, with a periodic heat transfer coefficient resembling the transient shown in Fig. 1, was imposed at the upper surface. Results indicated that time-averaged temperatures at the bottom side of the test strip and a steady-state thermal analysis can be used to infer the corresponding surface temperatures and time-averaged convective heat transfer coefficients to within 0.2 percent for the range of frequencies investigated. Thus, in the steady-state analysis, the bottom side was modeled as an adiabatic surface ($dT/dy=0$) and the heat flux to the jet was calculated from the strip resistance, electrical current, and exposed strip surface area. Surface temperatures corresponding to the measured, time-averaged temperatures at the bottom side of the test strip were calculated from the solution to the one-dimensional heat conduction equation with uniform volumetric heat generation due to ohmic heating (McMurray et al., 1966). The resulting expression [$T_s = T_b - QH^2/2k_s$, where $Q = \dot{P}R/LWH$] and the measured

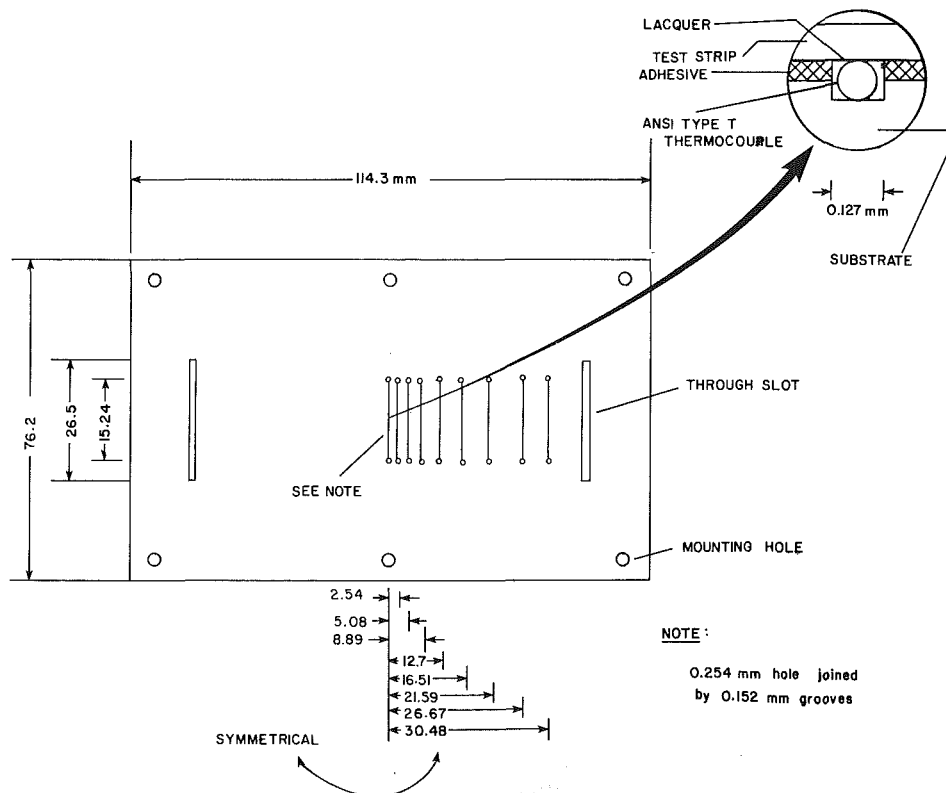


Fig. 3 Detailed view of substrate plate and locations of thermocouples

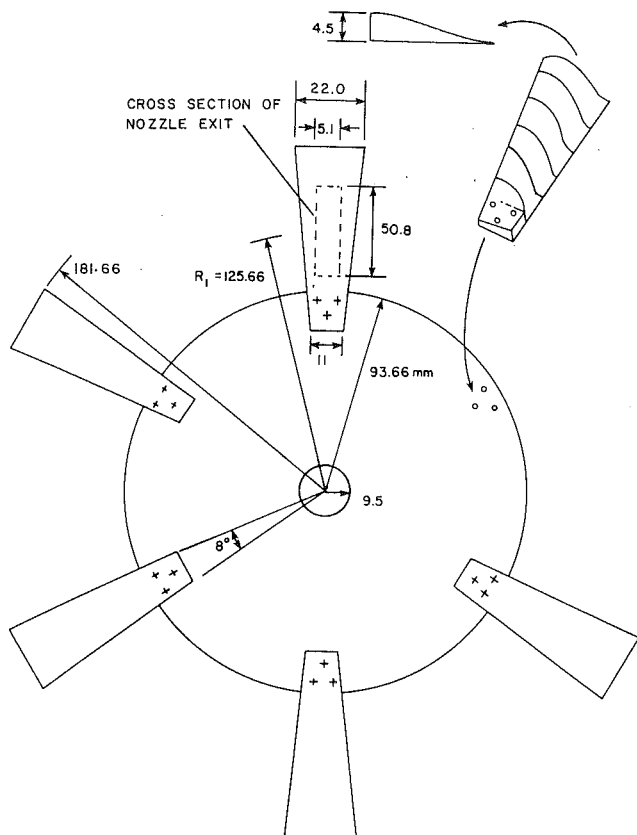


Fig. 4 Wheel-blade assembly used to induce intermittency in the impinging jet flow

jet temperature were used with Newton's law of cooling to determine local convective heat transfer coefficients. All thermophysical properties were evaluated at the local film temperature $T_f = [(T_s(x_j) + T_\infty)/2]$.

Temperatures at the bottom side of the test strip were measured sequentially at each thermocouple location (Fig. 3) with a single integrating voltmeter and digital multiplexer. The voltmeter provided an initial average temperature over an integration period of about 270 ms. Measurements were repeated and an improved time-averaged temperature was found for each thermocouple by summing all readings and dividing by the total number of readings. The number of readings was increased until deviations in calculated averages were less than 0.5 percent. Typically, 20 readings were sufficient to meet this criterion.

The wheel-blade assembly is shown in Fig. 4. The assembly consisted of a maximum of six removable stainless steel blades mounted on a thin stainless steel wheel. The assembly was rotated in the clockwise direction with the thin edge of the blades penetrating the free surface of the planar jet. The blade width was larger than the nozzle width to completely deflect the jet from the test strip and thereby induce the intermittency in the impinging flow. Experiments were performed with either three blades (separated by 120 deg to maintain balance) or six blades. When three blades were used, higher rotational speeds were required to obtain the same intermittency frequency. The higher speeds resulted in decreased time intervals for flow deflection since the blade resided beneath the nozzle opening for shorter periods.

A detailed uncertainty analysis (Aziz, 1991) with the method of sequential perturbations (Moffat, 1988) was performed to account for all possible error sources. Relative uncertainties in Nusselt numbers were found to vary from 7 to 9 percent for jet Reynolds numbers (Re_{w0}) ranging from 3100 to 20,750,

respectively. Slightly higher uncertainties occurred at the larger Reynolds numbers since temperature differences between the strip surface and jet were smaller.

Results and Discussion

Baseline Experiments With Steady Jets. Convective heat transfer distributions were determined for steady-flow conditions in order to establish a baseline against which results for the intermittent jets can be compared. Experiments were performed for $3100 < Re_{w0} < 20,750$ and $Pr_0 \approx 5.8$. Results were correlated in accordance with the method described by Zumbrennen et al. (1989). This method is based on theoretical distributions, which can be expressed as

$$Nu_w(x) = g(x) Re_w^m Pr^n \quad (3)$$

where $g(x)$ is a function of x and m and n are constants. Thermophysical properties in Eq. (3) are evaluated at the local film temperature T_f . Experimental values of Nu_w , Re_w , and Pr_0 were utilized in a least-squares analysis to find optimal stagnation line values for m and $g(0)$. A value of 0.4 was specified for n to provide consistency with other studies (Downs and James, 1987; Zumbrennen et al., 1989; Vader et al., 1991) and since the influence of Prandtl number variations was not discernible over the small Prandtl number range in the experiments. The resulting correlation is given by Eq. (4):

$$Nu_w(x) Re_w^{-0.589} Pr^{-0.4} = g(x) \quad (4a)$$

where for $0 < x < 1.6$

$$g(x) = 0.230 - 0.01547x^2 \quad (4b)$$

and for $1.6 < x < 6.0$

$$g(x) = 0.293 - x(0.08058 - 0.01124x + 0.0006x^2). \quad (4c)$$

Convective heat transfer distributions in accordance with Eq. (4) are shown in Fig. 5. For each Reynolds number, distributions are symmetric and the largest heat transfer coefficient occurs at the stagnation line. Equation (4) is accurate to within 2.1 percent of the average of all local values. Stagnation Nusselt numbers (Nu_{w0}) are compared to results obtained from previous studies of water jets in Fig. 6. Because fluid temperatures differed between the studies, all Nusselt numbers were normalized to $Pr = 0.4$ with $n = 0.4$ in Eq. (3). Stagnation Nusselt numbers differ from laminar flow theory by -4 and $+12$ percent for Reynolds numbers of 3000 and 25,000, respectively. Values are lower in comparison to the results reported by Miyasaka and Inada (1980) and Zumbrennen et al. (1989). However, in both of these studies, stagnation Nusselt numbers exceeded those predicted from laminar theory by 60 to 80 percent and the high Nusselt numbers were attributed to turbulence in the jet and vorticity amplification effects. Experimental results are in good agreement with those reported recently by Vader et al. (1991) for a planar water jet and test cell similar to the one employed in this study. Deviations between reported results may demonstrate the influence of vorticity in a jet on convective heat transfer. The convergent nozzle geometry, plenum chamber with baffle plates, and flow element, which were previously described, were therefore incorporated in this study to reduce ambiguity in the jet condition. In the intermittent impinging jet, flow conditions in the jet remained largely unchanged since intermittency was induced by briefly deflecting flow external to the nozzle away from the test cell. However, some brief disruption of the jet was unavoidable upon initial wetting of the strip surface and may have contributed to a portion of the observed enhancement discussed below. Since hot-film probes in anemometry systems must be immersed in a continuous liquid flow to avoid burn-out, turbulence intensity measurements in the intermittent jet flow were not possible. Given this situation, theoretical con-

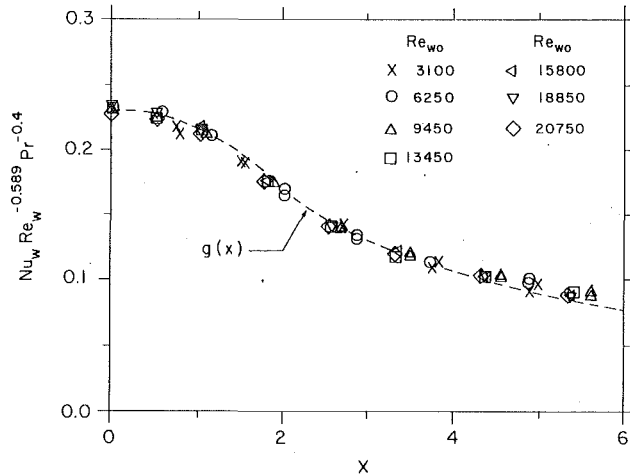


Fig. 5 Convective heat transfer distributions for the steady jets with $Pr_0 = 5.8$

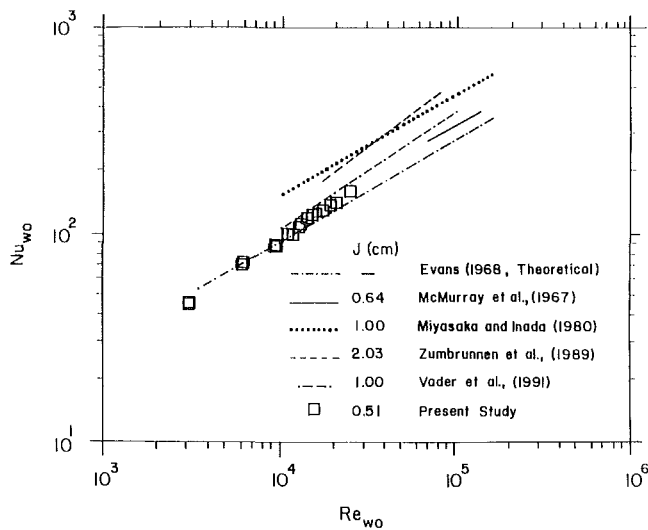


Fig. 6 Comparison of stagnation line Nusselt numbers at $Pr_0 = 4.0$

siderations and selective alterations to the apparatus were employed to confirm that enhancements were largely due to intermittency.

Experiments With Intermittent Jets. The intermittent flow was observed with a digital stroboscope in order to elucidate the interaction between the blade and the jet and to assess jet uniformity upon rewetting the strip. Observations are summarized in Fig. 7. Upon entry of the thin edge of the blade (Fig. 4) into the free surface of the jet (Fig. 7a), flow on the entry side was immediately deflected away from the test strip while flow adjacent to the unaffected jet surface continued downward without noticeable disruption. The downward jet flow steadily diminished as the blade continued its path through the jet until the test strip was completely shielded from the jet by the blade (Fig. 7b). Since the blade speed greatly exceeded the jet velocity, a nearly uniform slug of liquid descended toward the plate and a gap in the jet flow occurred beneath the blade and the liquid slug to produce the intermittency. As the blade exited the jet (Fig. 7c), liquid was deflected by the blade and generated a backwash (Fig. 7d). The unobstructed jet penetrated the backwash, which diminished rapidly as the blade moved further from the jet, and rewetted the surface. The backwash involved a greater portion of the jet fluid at low jet velocities and high intermittency frequencies. Consequently, additional cooling was provided in some cases to the

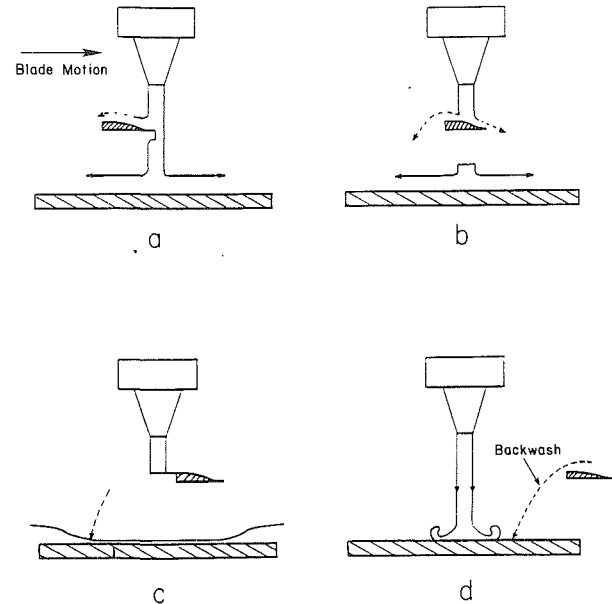


Fig. 7 Summary of stroboscopic observations of the intermittent jets

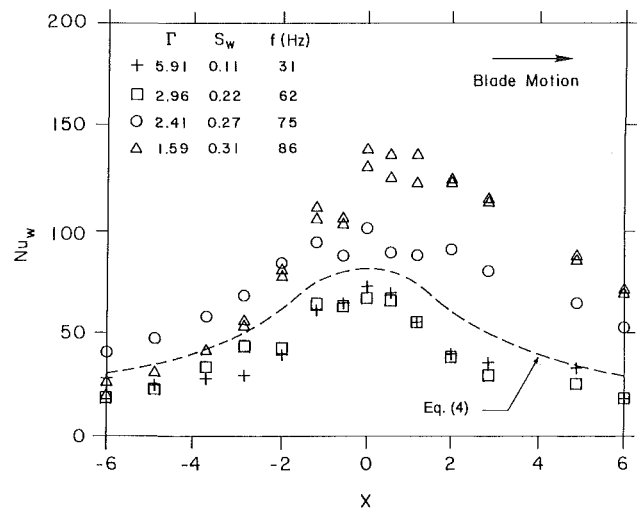


Fig. 8 Local time-averaged Nusselt numbers for intermittent jets with $Re_{w0} = 6500$ and $Pr_0 = 5.6$

side of the strip in the direction of blade motion while cooling was reduced on the opposite side. This phenomenon will be referred to as *jet distortion* in subsequent discussions.

Local time-averaged Nusselt numbers for the intermittent flow with $Re_{w0} \approx 6500$ are shown in Fig. 8 at the positions corresponding to the thermocouple locations in Fig. 3. Although all results in the figure correspond to the same jet velocity, small variations in the Reynolds and Prandtl numbers were due to the dependence of thermophysical properties on the film temperature T_f , which differed slightly in the experiments. Jet Reynolds numbers for both the steady flow and intermittent flows were calculated with jet velocities determined from the turbine flow meter (Fig. 2) and nozzle geometry. Thus, no attempt was made to modify the Reynolds number to account for flow intermittency. (Had a modification been performed, larger enhancements would have been reported for a given Reynolds number since less fluid is involved in heat transfer to an intermittent flow.) The heat transfer distribution for the steadily impinging jets [Eq. (4)] is shown for comparison. At low intermittency frequencies ($f = 31$ Hz and $f = 62$ Hz), local Nusselt numbers are below those for the

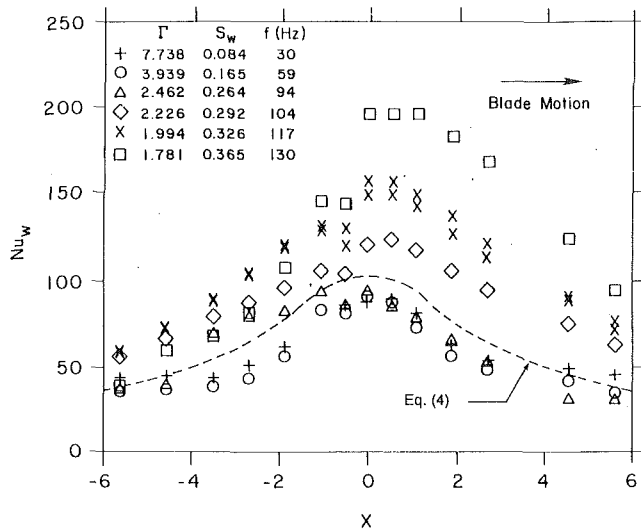


Fig. 9 Local time-averaged Nusselt numbers for intermittent jets with $Re_{w0} = 9450$ and $Pr_0 = 5.6$

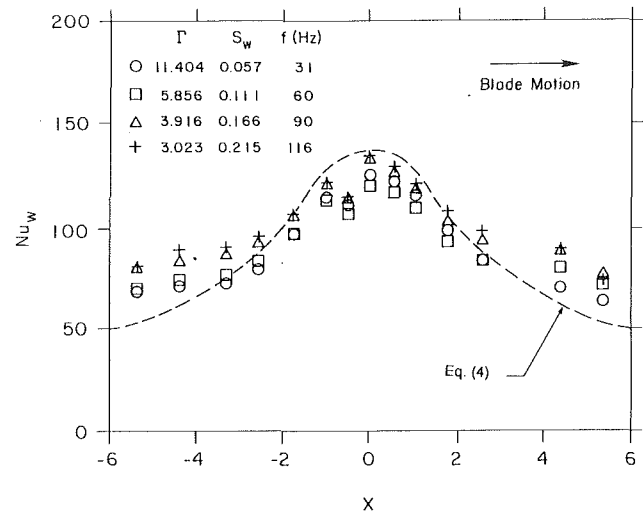


Fig. 11 Local time-averaged Nusselt numbers for intermittent jets with $Re_{w0} = 16,000$ and $Pr_0 = 5.8$

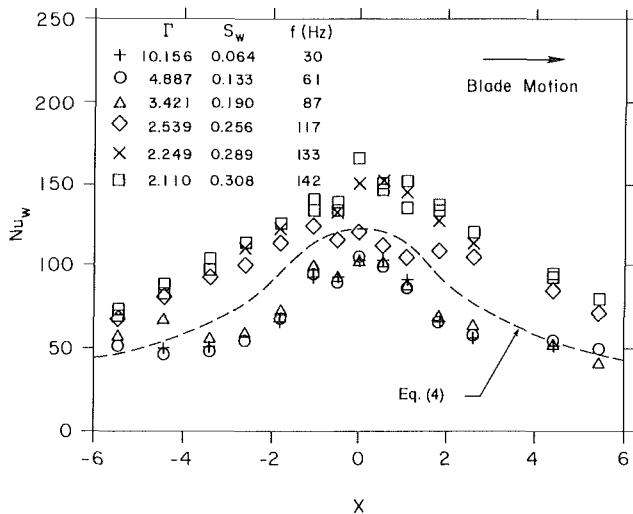


Fig. 10 Local time-averaged Nusselt numbers for intermittent jets with $Re_{w0} = 12,500$ and $Pr_0 = 5.8$

steady jet. This diminution occurs since the enhanced cooling during boundary layer development is insufficient to offset the reduced cooling during the brief period when the jet does not impinge on the strip surface during each intermittency cycle. The relatively long periods for boundary layer development are indicated by the value of Γ and the Strouhal number S_w is far below the threshold value $S_{wf} (\approx 0.26)$ calculated from Eq. (2). However, as the intermittency frequency is increased, enhancements become apparent both at the stagnation line ($x=0$) and away from the stagnation line. Jet distortion is evident at the highest frequency ($f = 86$ Hz) since the corresponding blade speed is greatest and the distribution is skewed in the direction of blade motion. Lower velocity jets were more readily influenced by the rotating blades and far greater jet distortion was thereby observed at lower jet Reynolds numbers. Such distortion at high frequencies can be avoided by employing alternate means to achieve the flow intermittency.

Greater enhancements were attained at larger Reynolds numbers ($Re_{w0} = 9450$) in Fig. 9, where higher intermittency frequencies were possible due to less jet distortion. As in Fig. 8, local Nusselt numbers were smaller than those for a steady jet at the lowest frequencies. Symmetric distributions indicate that jet distortion was not significant for $f < 130$ Hz as the inter-

mittency frequency was raised and enhancements were evident both at the stagnation line ($x = 0$) and away from the stagnation line. Local Nusselt numbers at the highest intermittency frequency exceed values for steady jets by a factor of two at the stagnation line. Similar enhancements were achieved for $f = 117$ Hz away from the stagnation line, suggesting that the boundary layer response may be slower beyond the stagnation region. Enhancements were also observed for $Re_{w0} \approx 12,500$ (Fig. 10); however, the smaller Strouhal numbers S_w lead to lower enhancements. At still a higher Reynolds number (Fig. 11), enhancement occurs only beyond the stagnation region ($|x| \geq 2$), where results again suggest that the boundary layer forms more slowly. Although Eq. (2) pertains to regions close to the stagnation line, a slower response (i.e., a smaller value of S_w) is suggested by this relationship at positions farther from the stagnation line where local velocity gradients in the free stream are smaller.

Smaller values of Γ correspond to briefer periods for boundary layer development during each subsequent cycle in the intermittent flow. Nusselt numbers should therefore become larger as Γ decreases in a manner resembling the theoretical result in Fig. 1. The ratio of the Nusselt number for an intermittent flow to the Nusselt number for a steady flow of the same Reynolds and Prandtl numbers at the stagnation line (Nu_{w0}^*) is shown versus Γ in Fig. 12. As expected, values of Nu_{w0}^* increase rapidly as Γ decreases. For large Γ , Nu_{w0}^* is less than unity since the time for boundary layer development is too lengthy and the related higher heat transfer coefficients are insufficient to offset the poor cooling conditions when flow ceases in the intermittency cycle. The similarity between Figs. 1 and 12 suggests strongly that enhancements are predominantly due to boundary layer renewal and not to the turbulence effects previously described.

Experiments were performed with three blades separated by 120 deg on the wheel (Fig. 4) to maintain rotational balance, in lieu of six blades used to obtain the results above, and a comparison is provided in Fig. 13. Since the wheel with three blades was rotated at twice the rotational speed to obtain the same intermittency frequency as when six blades were used, the period when the flow ceased (i.e., the *no-flow period*) to impinge on the strip and the associated elapsed time for reduced cooling conditions, were shorter. Thus, Nusselt numbers for $f = 31$ Hz and $N = 3$ blades are in good agreement with the steady jet correlation [Eq. (4)], although enhancement is not observed since the intermittency frequency is too low. (Small enhancements for $|x| \geq 5$ were attributed in stroboscopic ob-

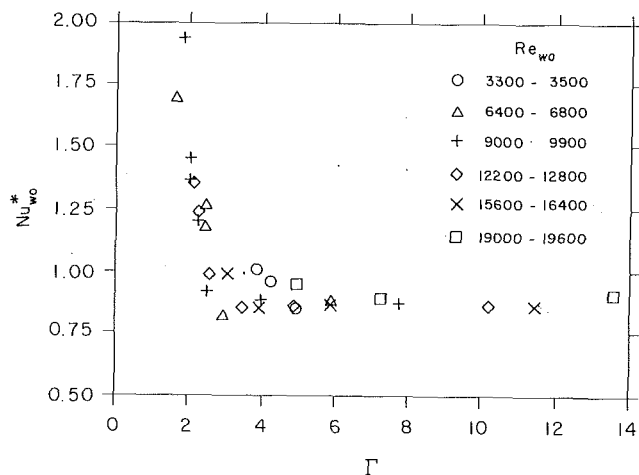


Fig. 12 Dependence of time-averaged Nusselt numbers for the intermittent flows on the dimensionless time for boundary layer growth at the stagnation line ($x = 0$) [note similarity to Fig. 1]

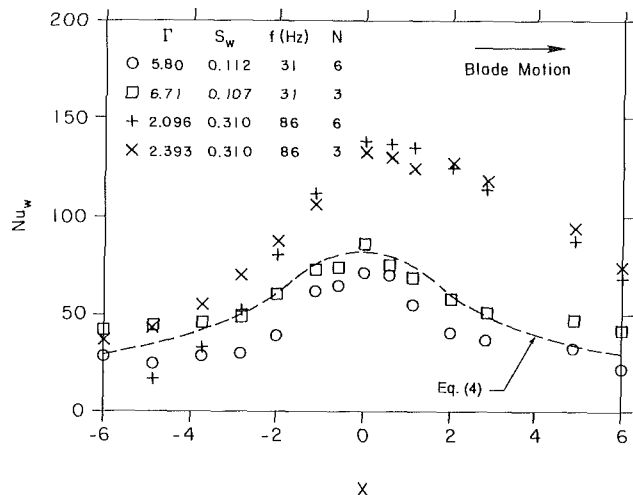


Fig. 13 Effect of the number of blades on local time-averaged Nusselt numbers for intermittent jets with $Re_{w0} = 6500$ and $Pr_0 = 5.7$

servations to blade backwash effects.) For $N = 6$ and $f = 31$ Hz, the no-flow period is longer and local Nusselt numbers are less than steady-state values. Similar enhancements occurred at the higher frequency ($f = 86$ Hz) for both $N = 3$ and $N = 6$ since time-averaged Nusselt numbers depended predominantly on the high instantaneous Nusselt numbers arising during boundary layer development. Since the impact speed of the blades on the jet was greater with three blades installed, the good agreement at the higher frequency also demonstrates that enhancements were due to boundary layer renewal and not to turbulence effects. To confirm that turbulence effects were negligible, experiments were also performed with the blunt edge of the blade entering the jet achieved by rotating the wheel (Fig. 4) in the counterclockwise direction. No discernible effect on Nusselt numbers near the stagnation line was observed with this orientation, although greater jet distortion caused reductions in Nusselt numbers near the extreme edges of the strip.

Conclusion

Intermittency in an impinging jet flow can enhance convective heat transfer if the frequency of the intermittency is suf-

ficiently high. Enhancements occur both beneath the jet and at locations several jet widths from the jet axis. This characteristic differs from enhancements due to nonuniformity in the velocity profile across the nozzle width, which are confined to the stagnation region and cannot be increased beyond a specific level. Moreover, unlike enhancement due to turbulence effects where maximum enhancements are attained as turbulence levels are increased, measured enhancements due to intermittency increased monotonically with intermittency frequency. Further study is required to determine whether enhancements can also be achieved with submerged jets, such as gas jets, to accelerate drying and heating processes. Enhancements can be expected if the boundary layer development is chiefly governed by the incident flow and not by fluids resident on the surface.

Acknowledgments

Support for this work was provided by the National Science Foundation of the United States under Grant No. CTS-8918154 and is gratefully acknowledged.

References

- Aziz, M., 1991, "The Effect of Intermittent Flow on Convective Heat Transfer to a Planar Impinging Water Jet," M.S. Thesis, Clemson University, Clemson, SC.
- Downs, S. J., and James, E. H., 1987, "Jet Impingement Heat Transfer—A Literature Review," ASME Paper No. 87-HT-35.
- Evans, H. L., 1962, "Mass Transfer Through Laminar Boundary Layers. 7 Further Similar Solutions to the B -Equation for the Case $B = 0$," *International Journal of Heat and Mass Transfer*, Vol. 5, pp. 35-57.
- Hoogendoorn, C. J., 1977, "The Effect of Turbulence on Heat Transfer at a Stagnation Point," *International Journal of Heat and Mass Transfer*, Vol. 20, pp. 1333-1338.
- Inada, S., Miyasaka, Y., and Izumi, R., 1981, "A Study of the Laminar Flow Heat Transfer Between a Two-Dimensional Water Jet and a Flat Surface With Constant Heat Flux," *Bulletin of the JSME*, Vol. 24, pp. 1803-1810.
- Lowery, G. W., and Vachon, R. I., 1975, "The Effect of Turbulence on Heat Transfer From Heated Cylinders," *International Journal of Heat and Mass Transfer*, Vol. 18, pp. 1229-1242.
- McMurray, D. C., Myers, P. S., and Uyehara, O. A., 1966, "Influence of Impinging Jet Variables on Local Heat Transfer Coefficients Along a Flat Surface With Constant Heat Flux," *Proceedings of the Third International Heat Transfer Conference*, Vol. II, pp. 292-299.
- Miyasaka, Y., and Inada, S., 1980, "The Effect of Pure Forced Convection on the Boiling Heat Transfer Between a Two-Dimensional Subcooled Water Jet and a Heated Surface," *Journal of Chemical Engineering of Japan*, Vol. 13, pp. 22-28.
- Moffat, R. J., 1988, "Describing Uncertainties in Experimental Results," *Experimental Thermal and Fluid Science*, Vol. 1, pp. 3-17.
- Nevins, R. G., and Ball, H. D., 1961, "Heat Transfer Between a Flat Plate and a Pulsating Impinging Jet," *Proceedings of the National Heat Transfer Conference*, Boulder, CO, Vol. 60, pp. 510-516.
- Schlichting, H., 1979, *Boundary-Layer Theory*, 7th ed., McGraw-Hill, New York, pp. 95-96.
- Scholtz, M. T., and Trass, O., 1970, "Mass Transfer in a Nonuniform Impinging Jet," *American Institute of Chemical Engineering Journal*, Vol. 16, pp. 82-96.
- Smith, M. C., and Kuethe, A. M., 1966, "Effects of Turbulence on Laminar Skin Friction and Heat Transfer," *The Physics of Fluids*, Vol. 9, pp. 2337-2344.
- Sparrow, E. M., and Lee, L., 1975, "Analysis of Flow Field and Impingement Heat/Mass Transfer Due to a Nonuniform Slot Jet," *ASME JOURNAL OF HEAT TRANSFER*, Vol. 97, pp. 191-197.
- Sutera, S. P., Maeder, P. F., and Kestin, J., 1963, "On the Sensitivity of Heat Transfer in the Stagnation Point Boundary Layer to Free Stream Vorticity," *Journal of Fluid Mechanics*, Vol. 16, pp. 497-520.
- Vader, D. T., Incropera, F. P., and Viskanta, R., 1991, "Local Convective Heat Transfer From a Heated Surface to an Impinging, Planar Jet of Water," *International Journal of Heat and Mass Transfer*, Vol. 34, pp. 611-623.
- Zumbrunnen, D. A., Incropera, F. P., and Viskanta, R., 1989, "Convective Heat Transfer Distributions on a Plate Cooled by Planar Water Jets," *ASME JOURNAL OF HEAT TRANSFER*, Vol. 111, pp. 889-896.
- Zumbrunnen, D. A., 1992, "Transient Convective Heat Transfer in Planar Stagnation Flows With Time-Varying Surface Heat Flux and Temperature," *ASME JOURNAL OF HEAT TRANSFER*, Vol. 114, pp. 85-93.
- Zumbrunnen, D. A., Incropera, F. P., and Viskanta, R., 1992, "A Laminar Boundary Layer Model of Heat Transfer Due to a Nonuniform Planar Jet Impinging on a Moving Plate," *Wärme- und Stoffübertragung*, Vol. 27, pp. 311-319.

Stagnation-Point Heat Transfer During Impingement of Laminar Liquid Jets: Analysis Including Surface Tension

Xin Liu¹

L. A. Gabour
Graduate Student.

J. H. Lienhard V
Associate Professor.

Department of Mechanical Engineering,
Massachusetts Institute of Technology,
Cambridge, MA 02139

The stagnation-zone characteristics of an impinging liquid jet are of great interest because the maximum heat transfer coefficient occurs in that region. This paper is an analytical study of the fluid flow and heat transfer in the stagnation zone of an unsubmerged liquid jet. The role of surface tension is emphasized. Stagnation-zone transport is strongly dependent on the potential flow above the boundary layer. Only a few studies have examined the potential flow of an unsubmerged jet, each using approximate potential flow theory and neglecting surface tension. In this paper, numerical solutions for a laminar unsubmerged jet are obtained, using a simulation method for steady, inviscid, incompressible flow with surface tension. A series solution that satisfies the boundary conditions in an approximate manner is constructed in terms of Legendre functions. Numerical solution of the momentum equation shows that surface tension has an effect on the stagnation-point flow field when the Weber number is small. Solutions of the associated boundary layer problem are used to obtain predictions of the influence of Weber number on the stagnation-zone heat transfer. The results are validated by comparison to measurements at high Weber number.

1 Introduction

The stagnation zone of an impinging jet is characterized by an extremely thin thermal boundary layer. This results in a very large heat transfer coefficient, but it also sensitizes the stagnation-zone cooling efficiency to various parametric influences that would be less important for a thicker thermal boundary layer. Such effects include minor variations in the free-stream flow field, wall roughness, wall conduction, and so on. In this paper, we examine the role of surface tension, which can change the shape of the jet's free surface and alter the radial velocity gradient over the stagnation-zone boundary layer.

The stagnation-point flow field has been studied extensively for submerged jets. The theory is based on an infinite flow field assumption under which the partial differential equations of the boundary layer admit a similarity transformation (Schlichting, 1979; White, 1991). The free-stream flow is determined from a separate potential-flow calculation. For an unsubmerged jet, the free surface between the liquid and gas phases imposes an additional boundary condition, which greatly complicates the calculation of the inviscid flow above the wall boundary layer; a numerical solution is required. The influence of the free surface on the near-wall flow field is even more complex for small Weber numbers, when surface tension effects are strong. This may be of particular concern for small-diameter jets.

Numerical methods for free-surface problems generally fall into one of two classes (Crank, 1984). In the first class, the problem is solved as originally formulated in the physical plane. After computation of approximate trial solutions, the free boundary is adjusted numerically to an improved free boundary. In the second class, the problem is recast by some suitable change of coordinates, and the transformed problem is solved numerically as a fixed-boundary problem.

To avoid solving the full Navier-Stokes equations, the stagnation flow can be divided into an inviscid flow and a boundary layer. The inviscid flow, which provides the free-stream condition needed for the near-wall viscous flow, represents the primary computational problem. Schach (1935) employed an integral-equation method, which was developed from Green's theorem. Shen (1962) expanded the velocity potential in a series using Legendre polynomials. The free-streamline boundary condition was satisfied in an average manner. Shen suggested an iteration scheme, but it lacked a method for successively correcting the approximated free-streamline position and it was not actually carried out. Strand (1964) expanded the velocity potential in Bessel functions. The free-streamline boundary condition was satisfied by discrete points. None of those solutions included the surface tension.

In the following, a series solution that includes surface tension is constructed. An iteration scheme for the free surface is conducted using a correction function. The solution is given by Legendre functions and satisfies the free-surface boundary conditions in an approximate manner, with accuracy improving as more terms are retained. The solution is validated by comparison to experimental data for high Weber number, laminar jets, which have both uniform velocity profiles and large Reynolds numbers.

2 Analysis

The flow field is separated into an outer, inviscid, irrotational flow and a near-wall viscous boundary layer. The inviscid flow is determined using potential-flow theory with surface tension along the free streamline. The resulting radial velocity distribution along the wall is used as the free-stream flow in the subsequent boundary-layer calculation. Gravitational effects are neglected.

Inviscid Impinging Jet Flow. For an inviscid, axisymmetric, and irrotational jet (Fig. 1), the velocity potential is given by

$$\nabla^2 \phi = 0 \quad (1)$$

¹Present address: Carrier Corporation, Syracuse, NY.

Contributed by the Heat Transfer Division for publication in the JOURNAL OF HEAT TRANSFER. Manuscript received by the Heat Transfer Division April 3, 1992; revision received June 26, 1992. Keywords: Forced Convection, Jets. Associate Technical Editor: F. P. Incropera.

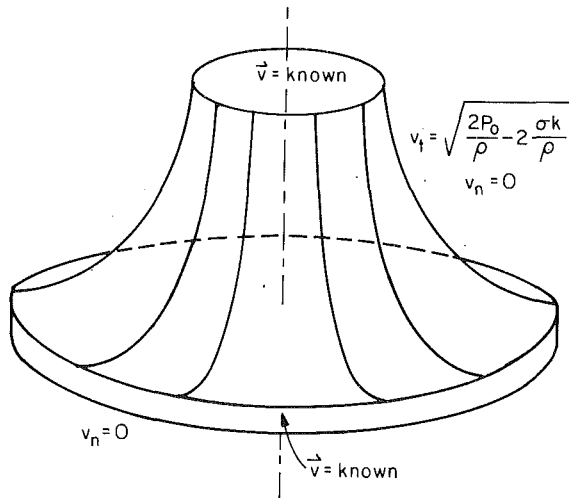


Fig. 1 Computational domain and boundary conditions

The boundary condition along the inlet to the computational domain is

$$\mathbf{v} = \text{known} = \mathbf{u}_f \quad (2)$$

In the present computation, the inlet velocity is assumed to be uniform (and thus irrotational) and purely downward. The inlet is located at a distance of one diameter above the wall; the orifice producing the jet is presumably somewhat farther above the wall. For a jet issuing from a plenum, the influence of surface tension on the inlet velocity must be taken into account as

$$u_f = C_v \sqrt{\frac{2P_0}{\rho}} = \sqrt{1 - \frac{4}{We_d}} \sqrt{\frac{2P_0}{\rho}} \quad (3)$$

for sharp-edged orifices, with C_v the velocity coefficient, P_0 the plenum gage pressure, ρ the liquid density, and We_d the Weber number.² The Weber number characterizes the magnitude of the surface tension pressure relative to the dynamic pressure:

$$We_d = \frac{\rho u_f^2 d}{\sigma} \quad (4)$$

where σ is the surface tension and d is the jet diameter.

Along the free streamline, the velocity normal to the surface is obtained from the condition of no flow through the liquid surface:

$$v_n = 0 \quad (5)$$

The velocity tangent to the streamline is obtained from Bernoulli's equation:

$$v_t = \sqrt{\frac{2P_0}{\rho} - 2\frac{\sigma\kappa}{\rho}} \quad (6)$$

where κ is the curvature of the free surface. The Bernoulli constant is evaluated at the inlet and has the same value for all streamlines. Along the target plate and the axis of symmetry

$$v_n = 0 \quad (7)$$

²Lienhard and Lienhard (1984) showed viscous losses to have a negligible effect on C_v for a sharp-edged orifice. Equation (3) above corrects an error in their handling of surface tension for a circular jet's C_v . The correct expression for C_v is $\sqrt{1 - K_2 C_D^{3/2} / \sqrt{Re_d} - 4/We_d}$ for $K_2 = 0.242738$ and C_D the discharge coefficient (≈ 0.611). Equation (3) is correct to ~ 0.1 percent for $We_d \geq 10$ and $Re_d \geq 10000$.

Nomenclature

A_0, A_1, A_2 = consts in Eq. (25)	Pr = Prandtl number of liquid	streamline coordinates, m/s
A_{2n} = consts in Eq. (20)	Q = volume flow rate of jet, m^3/s	We_d = Weber number = $\rho u_f^2 d / \sigma$
B = dimensionless velocity gradient = $2(d/u_f)(\partial U/\partial r)$	q_w = wall heat flux, W/m^2	y = axial coordinate in cylindrical coordinates, m
B_n = consts in Eq. (25)	r = radius coordinate in spherical coordinates, or radius coordinate in cylindrical coordinates, m	α = thermal diffusivity of liquid, m^2/s
C_n = consts in Eq. (25)	$R(\theta)$ = spherical radius-coordinate of free surface, m	β = numerical relaxation factor
C_v = velocity coefficient for liquid jets	Re_d = Reynolds number of the jet = $u_f d / \nu$	θ = polar angle of spherical coordinates
d = jet diameter, fully contracted, m	T_w, T_f = temperature of wall, incoming liquid jet, K	κ = free surface curvature, m^{-1}
d_o = orifice diameter, m	u, v = liquid velocity components in radial, axial direction of cylindrical coordinates, m/s	μ = dynamic viscosity of liquid, $kg/m \cdot s$
$f_n(\theta)$ = any continuous function of θ	u_f = incoming jet velocity = $C_v \sqrt{2P_0/\rho}$, m/s	ν = kinematic viscosity of liquid, m^2/s
h = heat transfer coefficient = $q_w / (T_w - T_f)$, $W/m^2 \cdot K$	$U(r)$ = radial velocity just outside boundary layer, m/s	ρ = density of liquid, kg/m^3
$G(Pr)$ = function of Prandtl number given by Eq. (31)	\mathbf{v} = liquid velocity vector = $\nabla \phi$, m/s	σ = surface tension, N/m
k = thermal conductivity of liquid, $W/m \cdot K$	v_n = normal velocity in streamline coordinates, m/s	ϕ = velocity potential, m^2/s
Nu_d = Nusselt number based on jet diameter = $q_w d / k(T_w - T_f)$	v_t = tangent velocity in streamline coordinates, m/s	$\partial/\partial n$ = derivative normal to the solution domain boundary
p = local gage pressure in liquid, Pa		$\partial/\partial t$ = derivative tangent to the solution domain boundary
P_0 = gage pressure in plenum, Pa		
P_{2n} = Legendre function of $2n$ order		

Superscripts

- (n) = result from the n th iteration
 * = dimensionless variable

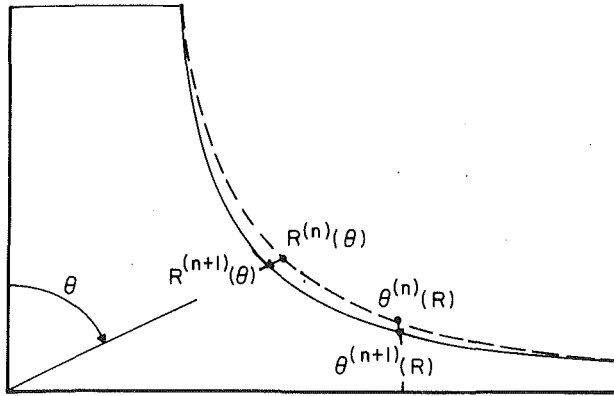


Fig. 2 Free-surface iteration

Schach's results (1935) show that the velocity is essentially uniform and parallel to the target plate for a radius larger than 1.25 diameter. In the present computation, the outlet is placed at $r/d=1.25$ and the outlet velocity is assumed uniform and parallel to the target. From Bernoulli's equation, the outlet speed is then

$$v_t = \sqrt{\frac{2P_0}{\rho}} \quad (8)$$

neglecting the free surface curvature.

Inlet Velocity Profile Boundary Condition. Our calculations assume a uniform velocity distribution for the incoming jet. This distribution occurs, for example, at a few diameters distance from a sharp-edged orifice. Often, the velocity profiles of jets issuing from nozzles are not uniform. A jet flowing from a long pipe, in which the flow is fully developed, has a parabolic velocity profile if it is laminar or a one-seventh power law profile if it is turbulent. Other cases may lie between these nonuniform distributions. However, for long jets, viscosity (or turbulent mixing) will produce a uniform profile at large distances from the nozzle.

Previous investigations have shown that a nonuniform velocity profile can produce larger stagnation-point velocity gradients and higher Nusselt numbers than for a uniform profile. For example, prediction and experiments by Scholtz and Trass (1970) showed that an axisymmetric, parabolic profile jet has 2.27 times the heat transfer of a uniform-profile jet. Sparrow and Lee (1975) found similar results for planar jets. Previous studies also show that velocity profile effects become more pronounced as the nozzle is moved very close to the target ($l/d < 1$). Furthermore, many experimental and numerical studies show that the distance at which the surface velocity approaches the mean velocity depends strongly on both the nozzle type and Reynolds number (Scriven and Pigford, 1959; Duda and Vrentas, 1967; Davies and Makepeace, 1978).

The Physical Coordinates and Nondimensional Equations. If Eqs. (1)–(8) are to be solved, a choice of a physical coordinate system is required. Cylindrical coordinates (Strand, 1964) have the advantage that the boundary conditions at the inlet and outlet are simplified, since the inlet and outlet coincide with one of the coordinate planes. However, concurrent difficulties occur because the free-surface derivatives in these coordinates become either infinite or zero at the inlet and outlet. While those derivatives are irrelevant for the zero-surface-tension case, they are essential when surface tension is included. Spherical coordinates (Shen, 1962) avoid the above problems while preserving the simplicity of the mathematical expressions. We adopt spherical coordinates with radius r and polar angle θ . The origin is placed at the stagnation point with the pole along the vertical axis of symmetry; the free-surface radius is $R(\theta)$ (Fig. 2).

Dimensionless velocity is defined relative to the ideal-jet velocity:

$$\mathbf{v}^* = \frac{\mathbf{v}}{u_j} \quad (9)$$

The coordinates r and R are nondimensionalized as

$$r^* = \frac{r}{2d} \quad (10)$$

$$R^* = \frac{R}{2d} \quad (11)$$

The factor of 2 is included to make the dimensionless radius less than unity in the computational domain so as to guarantee the convergence of the series expansion (Eq. (20)). In addition, we scale the velocity potential and the surface curvature as

$$\phi^* = \frac{\phi}{2du_j} \quad (12)$$

$$\kappa^* = 2d\kappa \quad (13)$$

In terms of the velocity potential, the dimensionless equation of motion is

$$\nabla^2 \phi^* = \left[\frac{1}{r^{*2}} \frac{\partial}{\partial r^*} \left(r^{*2} \frac{\partial}{\partial r^*} \right) + \frac{1}{r^{*2} \sin \theta} \left(\frac{\partial}{\partial \theta} \sin \theta \frac{\partial}{\partial \theta} \right) \right] \phi^* = 0 \quad (14)$$

The boundary condition along the inlet (Eqs. (2)–(3)) is

$$\left(\frac{\partial \phi^*}{\partial n^*} \right)_{\text{inlet}} = \frac{\partial \phi^*}{\partial r^*} \cos \theta - \frac{1}{r^*} \frac{\partial \phi^*}{\partial \theta} \sin \theta = -1 \quad (15)$$

The boundary condition along the outlet (Eq. (8)) is

$$\left(\frac{\partial \phi^*}{\partial n^*} \right)_{\text{outlet}} = \frac{\partial \phi^*}{\partial r^*} \sin \theta + \frac{1}{r^*} \frac{\partial \phi^*}{\partial \theta} \cos \theta = \sqrt{1 + 4/We_d} \quad (16)$$

Along the free surface, the boundary conditions (Eqs. (5)–(6)) are

$$\begin{aligned} \left(\frac{\partial \phi^*}{\partial n^*} \right) &= \frac{1}{\sqrt{\left(\frac{1}{R^*} \frac{dR^*}{d\theta} \right)^2 + 1}} \left(\frac{\partial \phi^*}{\partial r^*} - \frac{1}{r^{*2}} \frac{\partial \phi^*}{\partial \theta} \frac{dR^*}{d\theta} \right) = 0 \quad (17) \\ \left(\frac{\partial \phi^*}{\partial t^*} \right) &= \frac{1}{\sqrt{\left(\frac{1}{R^*} \frac{dR^*}{d\theta} \right)^2 + 1}} \left(\frac{1}{r^*} \frac{\partial \phi^*}{\partial r^*} \frac{dR^*}{d\theta} + \frac{1}{r^*} \frac{\partial \phi^*}{\partial \theta} \right) \\ &= \sqrt{1 - \kappa^*/We_d + 4/We_d} \quad (18) \end{aligned}$$

The dimensionless curvature of the free surface, κ^* , is given by:

$$\kappa^* = \frac{R^* \left(\frac{d^2 R^*}{d\theta^2} - R^* \right) - 2 \left(\frac{dR^*}{d\theta} \right)^2}{\left[R^{*2} + \left(\frac{dR^*}{d\theta} \right)^2 \right]^{3/2}} + \frac{\frac{\cot \theta}{r^*} \frac{dR^*}{d\theta} - 1}{\left[R^{*2} + \left(\frac{dR^*}{d\theta} \right)^2 \right]^{1/2}} \quad (19)$$

Inviscid-Flow Solution Procedure. The solution of Laplace's equation in spherical coordinates is

$$\phi^*(r^*, \theta) = \sum_{n=0}^{\infty} A_{2n} r^{*2n} P_{2n}(\cos \theta) \quad (20)$$

where $P_{2n}(\cos \theta)$ is the Legendre function of $2n$ order. The Legendre function automatically satisfies the boundary condition (Eq. (7)) along the target and the axis of symmetry.

The coefficients A_{2n} cannot be determined by conventional

orthogonal-function methods. If the jet boundary can be located, we may pursue the problem using a modification of an alternative method due to Shen (1962), as follows.

Assume $f_n(\theta)$ is an arbitrary continuous function of θ , and multiply both sides of the boundary conditions by f_n . Substitute ϕ^* into the equations and integrate along the boundaries to obtain a set of nonlinear algebraic equations. By solving the set of algebraic equations, the coefficients A_{2n} can be calculated. Initially, the location of the jet's free boundary is both unknown and unlikely to coincide with a coordinate line. To proceed, we may assume a jet free boundary and integrate the equations along this assumed boundary; then we may correct the previous boundary and repeat the computation until the solution converges, satisfying both Eq. (14) and the boundary conditions (Eqs. (15)–(19)). Shen (1962) also suggested an iteration scheme for use with this method, but he did not carry it out.

The principal difficulty with Shen's iteration scheme was the lack of a method of successively correcting the free-boundary shape. We suggest an alternative method to locate the free boundary, as represented by the function $R^* = R^*(\theta)$. The constraint on the free surface is a flux condition that the total flow rate over every jet cross section must be the same. Specifically, for any θ ,

$$\int_0^{R^*(\theta)} 2\pi \frac{d\phi^*}{d\theta} dr^* = Q^* \quad (21)$$

or, equivalently, for any R^* ,

$$\int_0^{\theta(R^*)} 2\pi \frac{d\phi^*}{dr^*} R^* d\theta = Q^* \quad (22)$$

We integrate the total flow rate over a cross section. If the flow rate is larger than Q^* , we pull in the free boundary (Fig. 2). If the flow rate is smaller than Q^* , we push out the free boundary. Then, the correction function for Eq. (21) is

$$R^{*(n+1)}(\theta) = R^{*(n)}(\theta) \left[1 + \beta \left(Q^* - \int_0^{R^{*(n)}(\theta)} 2\pi \frac{d\phi^*}{d\theta} dr^* \right) \frac{1}{Q^*} \right] \quad (23)$$

where β is a relaxation factor. The convergence of the iteration strongly depends on the value of β . In the present computation, β was chosen between 0.03 to 0.2. Similarly, for Eq. (22)

$$\theta^{(n+1)}(R^*) = \theta^{(n)}(R^*) \left[1 + \beta \left(Q^* - \int_0^{\theta^{(n)}(R^*)} 2\pi R^* \frac{d\phi^*}{dr^*} d\theta \right) \frac{1}{Q^*} \right] \quad (24)$$

In the computation, discrete points on the free surface are chosen to be corrected by the above two equations. For points near the inlet and the outlet Eq. (24) is used; for the other points Eq. (23) is used, to achieve better convergence. The points that represent the shape of the free surface then are fitted to the following equation:

$$R^*(\theta) = A_0 + \sum_{n=1}^3 \frac{B_n}{(\theta - A_1)^n} + \sum_{n=1}^3 \frac{C_n}{(A_2 - \theta)^n} \quad (25)$$

where A_0, A_1, A_2, B_n, C_n are adjustable constants. The accuracy of the curve fit is within ± 0.2 percent. This fitted equation is substituted back into the original equations to calculate a new set of coefficients of A_{2n} . In principle, it is not necessary to curve fit the points; the equation could be discretized instead. However, curve fitting simplifies the calculation significantly.

Boundary Layer Solution. For the boundary layer, cylindrical coordinates are more convenient than spherical coordinates, since the boundary layer is very thin and no singularity arises as for the free surface. The basic equations for axisymmetric flow are

$$\frac{\partial(ur)}{\partial r} + \frac{\partial(vr)}{\partial y} = 0 \quad (26)$$

$$u \frac{\partial v}{\partial r} + v \frac{\partial v}{\partial y} = -\frac{1}{\rho} \nabla p + \nu \nabla^2 v \quad (27)$$

with the energy equation

$$u \frac{\partial T}{\partial r} + v \frac{\partial T}{\partial y} = \alpha \nabla^2 T \quad (28)$$

In these equations, r represents the radial distance from the stagnation point and y the vertical distance from the target plane (White, 1991).

The velocity just outside the boundary layer can be obtained from Eq. (20)

$$U(r) = \sum_{n=0}^{\infty} 2nA_{2n}r^{2n-1}P_{2n}(\cos(\theta = \pi/4)) \quad (29)$$

Very close to the stagnation point only the first term in the above equation need be considered. The solution of the boundary layer equations can be obtained using a standard similarity transformation, from which the Nusselt number at the stagnation point is obtained as:

$$Nu_d = G(\text{Pr}) \text{Re}_d^{1/2} \sqrt{2 \frac{d}{u_f} \frac{\partial U}{\partial r}} \quad (30)$$

where (White, 1974)

$$G(\text{Pr}) \approx \begin{cases} \frac{\sqrt{2 \text{Pr}/\pi}}{1 + 0.804552\sqrt{2 \text{Pr}/\pi}} & \text{Pr} \leq 0.15 \\ 0.53898 \text{Pr}^{0.4} & 0.15 < \text{Pr} < 3.0 \\ 0.60105 \text{Pr}^{1/3} - 0.050848 & \text{Pr} \geq 3.0 \end{cases} \quad (31)$$

The boundary condition can be either uniform wall temperature or uniform wall heat flux, since the stagnation-point boundary layer thickness is independent of r . The effect of the Weber number, or surface tension, on Nusselt number is implicit in the above equation through its effect on the dimensionless velocity gradient.

4 Results

Validation of the flow-field solution is based on a comparison to existing results for infinite Weber number (Schach, 1935). The essential contribution of the flow field solution to the subsequent stagnation-point heat transfer analysis is the streamwise velocity gradient that enters the Nusselt number

$$B = 2 \frac{d}{u_f} \frac{dU}{dr} \quad (32)$$

For the present solutions, B is 1.832 for infinite Weber number. This value differs from Schach's value of 1.76 by only 4 percent, corresponding to a difference of about 2 percent in Nusselt number. While both the present solution and Schach's result are approximate, the good agreement between the two results lends a measure of confidence to the present procedure. An experimental comparison is described below.

Calculated Inviscid Flow Field and Velocity Profiles. Figure 3 shows the free-surface shape and nondimensional inviscid velocity distribution, v/u_f , for infinite Weber number. In the plane of the axis of symmetry, the radius of curvature of the free surface is smaller than the jet radius. For an axisymmetric jet, the free surface begins to deflect much closer to the target than for a planar jet.

Free-surface deflection is caused by the increased pressure near the stagnation point. The above characteristics are also seen in Fig. 4, which shows the calculated nondimensional pressure distribution, p/P_0 . The pressure is a maximum at the

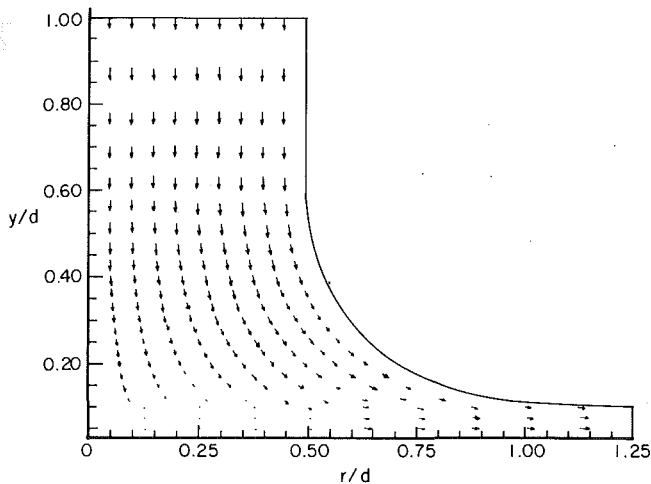


Fig. 3 The inviscid velocity field, v^* , for $We_d \rightarrow \infty$ from the potential-flow solution

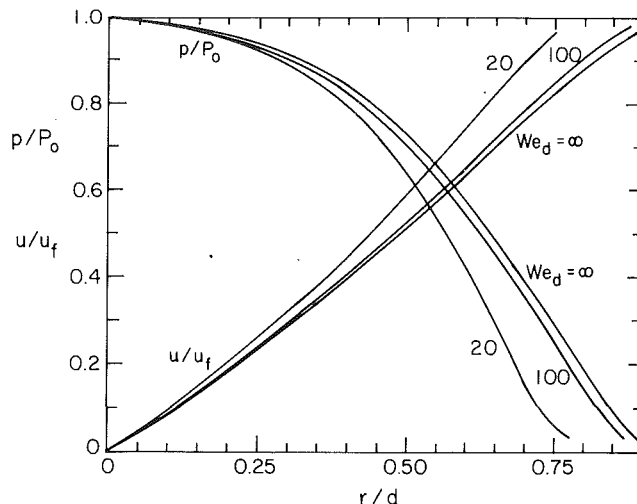


Fig. 6 Velocity and pressure variation along the target plate ($y/d=0$) for several values of Weber number and inviscid flow

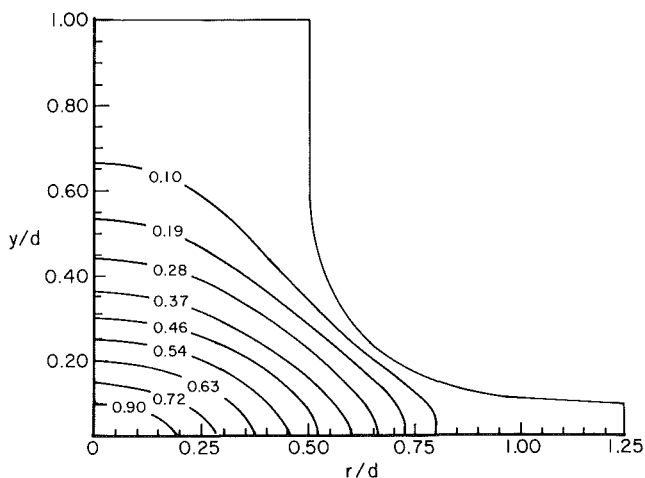


Fig. 4 The inviscid pressure distribution, p/P_0 , as $We_d \rightarrow \infty$

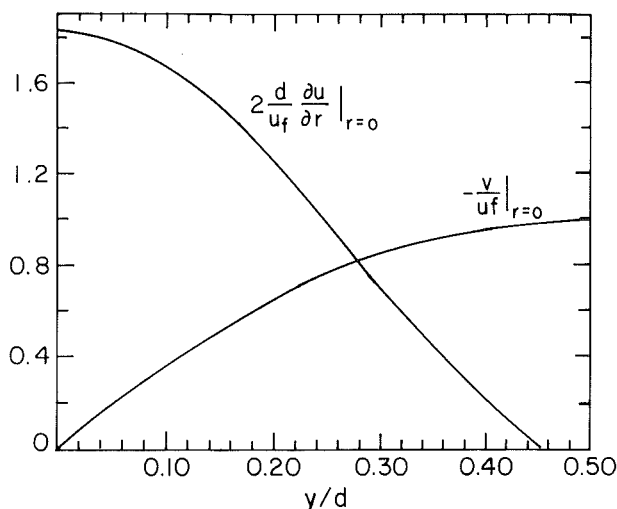


Fig. 7 Vertical profiles of downward velocity and radial velocity-gradient along jet centerline for inviscid flow ($We_d \rightarrow \infty$)

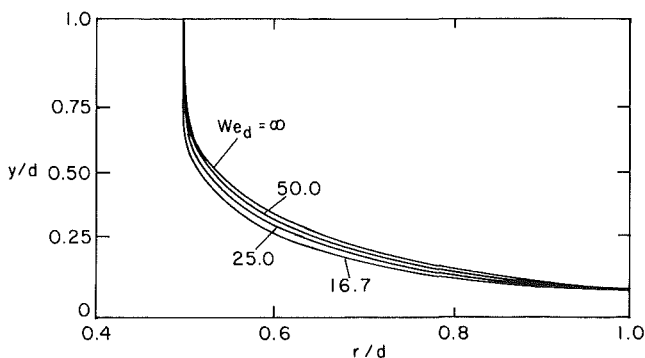


Fig. 5 The free-surface shape for several values of Weber number and inviscid flow

stagnation point and decreases steadily with increasing radius. In the region $r < 0.25d$, the nondimensional pressure is larger than 0.75; beyond $r/d = 0.8$, the pressure is less than 10 percent of the stagnation pressure.

The Role of Weber Number. Figure 5 shows the calculated free-surface shape as a function of Weber number. The free-surface deflection is progressively reduced as Weber number decreases. This happens because surface tension provides an

additional restoring force, which balances the higher pressure near the stagnation region.

A lower bound on the Weber number is set by surface-tension choking of the nozzle. Lienhard and Lienhard (1984) showed that flow from a circular orifice will choke when

$$We_{d_o} = \frac{\rho u_f^2 d_o}{\sigma} \approx 8 \quad (33)$$

where the orifice diameter is d_o . Under these conditions, the surface-tension force prevents a steady flow from the upstream plenum.

Figure 6 shows the velocity and pressure variation along the target plate at different Weber numbers. The smaller the Weber number, the faster the velocity grows with radius and the quicker the pressure drops along the plate. Because the surface curvature changes from concave (along the incoming jet) to almost flat (in the far field), surface tension pressure decreases radially and produces a net increase in the momentum of the outflowing liquid. Thus, the downstream velocity tends toward the ideal-jet velocity, $\sqrt{2P_0/\rho}$, which is greater than the incoming velocity u_f . The vertical velocity distribution is shown in Fig. 7.

A previous paper (Liu et al., 1991) estimated from boundary layer growth ideas that the stagnation zone is confined to the

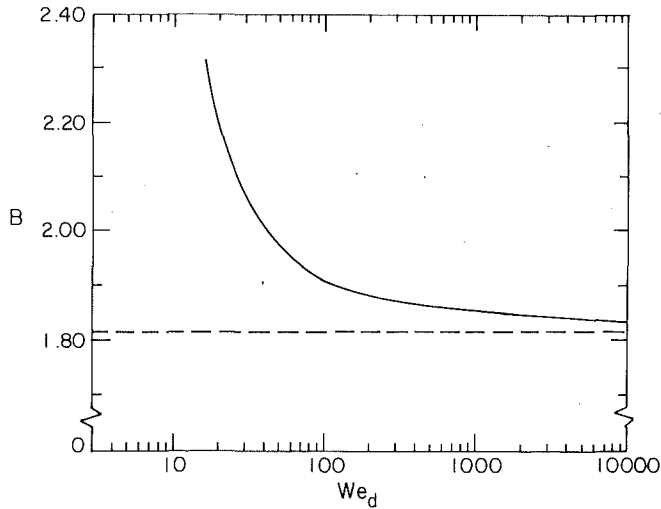


Fig. 8 Effect of Weber number on the free-stream (inviscid) stagnation-point velocity gradient, $B = 2(d/u_s)(\partial U/\partial r)$

region $r/d \leq 0.787$. Figure 6 shows that the linear rise of velocity expected for true stagnation-point flow occurs only for $r/d < 0.35$, although it may provide a useful approximation to r/d as large as 0.75.

Figure 8 and Table 1 show the effect of Weber number on the velocity gradient at the stagnation point. The dimensionless gradient, B , at the stagnation point is higher for smaller values of Weber number. The increase is related to both the decrease in free-surface deflection (Fig. 5) and the increase of the downstream speed above the incoming liquid speed (Fig. 6). As the Weber number decreases from infinity to 16.7, the dimensionless velocity gradient increases by 26 percent. Since the Nusselt number is proportional to the square root of the velocity gradient, the Nusselt number goes up by about 13 percent. For common cooling applications with water, the Weber number is usually more than several hundred, and Weber number effects will be negligible. For low-velocity small-diameter jets, however, such effects may have some importance.

Table 2 shows the Nusselt number formulae obtained from Eq. (30) when the values of B from this or other investigations are employed or when different expressions for $G(\text{Pr})$ are used. The theoretical results may be compared to experimental data available for high Weber numbers. Experiments with uniform velocity profile, laminar jets for $2100 < \text{We}_d < 34,000$ and high Reynolds numbers are represented by

$$\text{Nu}_d = 0.745 \text{Re}_d^{1/2} \text{Pr}^{1/3} \quad (34)$$

to an accuracy of about ± 5 percent (for details, see Liu, 1992; Liu et al., 1991, present some related data). In general, the predictions are in good agreement with the data.

Two comments should be made in regard to turbulent liquid jets. First, because the Reynolds number is greater than 2400 for most turbulent jets, the Weber number is usually large, as is seen from the following:

$$\text{We}_d = \left(\frac{\rho u_j d}{\mu} \right)^2 \frac{\mu^2}{\rho \sigma d} = \text{Re}_d^2 \frac{\mu^2}{\rho \sigma d} \quad (35)$$

Thus, unless jet diameter is very small, direct stagnation-point surface-tension effects can be neglected for turbulent jets.

Second, turbulence may increase the Nusselt number at the stagnation point by disrupting the already thin boundary layer there. This effect has been experimentally observed by comparing nearly-uniform-profile turbulent and laminar liquid jets (Lienhard et al., 1992), and is well documented in submerged flows and submerged jets (Kestin, 1966; Mehendale et al., 1991; Simmons et al., 1990). The laminar formulae developed above are not recommended for turbulent jets.

Table 1 Velocity gradients at the stagnation point during laminar jet impingement: $B/2 = (d/u_s)(\partial U/\partial r)$; l is either the height of the inviscid-flow computational-domain or the experimental jet's length

Investigators	$B/2$	jet type	inlet velocity profile	l/d	We_d
Miyazaki and Silberman (1972)	0.951	planar	uniform	0.5	∞
	0.457	planar	uniform	1.5	∞
Sparrow and Lee (1975)	0.964	planar	uniform	0.5	∞
	0.445	planar	uniform	1.5	∞
	0.393	planar	uniform	∞	∞
	1.74	planar	parabolic	0.25	∞
	1.51	planar	parabolic	1.5	∞
Scholtz and Trass (1970)	3.76	circular	parabolic	1.0	∞
	0.731	circular	uniform	1.0	∞
Schach (1935)	0.88	circular	uniform	1.5	∞
Shen (1962)	0.743	circular	uniform	1.5	∞
Strand (1964)	0.958	circular	uniform	1.0	∞
Present computations	0.916	circular	uniform	1.0	∞
	0.981	circular	uniform	1.0	50
	1.06	circular	uniform	1.0	25
	1.16	circular	uniform	1.0	16.7
Present data	0.77	circular	uniform	> 6	> 2100

Table 2 Axisymmetric stagnation-point Nusselt number expressions for various investigations

Investigators	Nu_d	Velocity gradient & initial distribution
Scholtz and Trass (1970)	$0.727 \text{Re}_d^{1/2} \text{Pr}^{0.361}$ $1 < \text{Pr} < 10, l/d = 1.0$	Strand (1964) uniform laminar
Scholtz and Trass (1970)	$1.648 \text{Re}_d^{1/2} \text{Pr}^{0.361}$ $1 < \text{Pr} < 10, l/d = 0.5$	Inviscid vortex eqn., parabolic
Nakoryakov et al. (1978)	$0.753 \text{Re}_d^{1/2} \text{Pr}^{1/3}$	Schach (1935) uniform laminar
Liu et al. (1991) Eqn. 30	$0.797 \text{Re}_d^{1/2} \text{Pr}^{1/3}$ $\text{Pr} > 3, l/d > 1.5$	Schach (1935) uniform laminar
Eqn. 30	$0.813 \text{Re}_d^{1/2} \text{Pr}^{1/3}$ $\text{Pr} > 3, l/d = 1$	Present ($\text{We}_d \rightarrow \infty$)
Eqn. 30	$0.832 \text{Re}_d^{1/2} \text{Pr}^{1/3}$ $\text{Pr} > 3, l/d = 1.5$	Strand (1964) ($\text{We}_d \rightarrow \infty$)
Eqn. 30	$0.733 \text{Re}_d^{1/2} \text{Pr}^{1/3}$ $\text{Pr} > 3, l/d = 1.5$	Shen (1962) ($\text{We}_d \rightarrow \infty$)
Lienhard et al. (1991)	$1.24 \text{Re}_d^{1/2} \text{Pr}^{1/3}$ $\text{Pr} > 3, l/d > 1.5$	Correlation, turbulent/splattering
Stevens and Webb (1991)	$2.67 \text{Re}_d^{0.567} \text{Pr}^{0.4} (l/d)^{-0.0336} (u_j/d)^{-0.237}$	Correlation, turbulent

5 Conclusions

The influence of surface tension on stagnation-point heat transfer beneath an impinging liquid jet has been analytically studied. The results include the zero-surface-tension (high Weber number) case as a limit. Various past results for the stagnation-point Nusselt number are also summarized.

- Surface tension affects the stagnation-point velocity gradient and Nusselt number for We_d less than about 100. The increase in Nusselt number is about 13 percent at a Weber number of 16.7. For most industrial cooling applications, however, We_d is too large for this effect to be of significance.

- The dimensionless stagnation-point velocity gradient obtained for $\text{We}_d \rightarrow \infty$ is $B = 1.832$, in good agreement with the results of Schach (1935) and others.

- Stagnation-point Nusselt number formulae for this and previous investigations are summarized in Table 2. Those results include both laminar and turbulent jets with both uniform and nonuniform velocity profiles; most have experimental validation. For laminar jets, the results differ principally in the method of correlating Prandtl number effects; more data are needed at very high and very low Prandtl number. For high Weber number, uniform, laminar jets, and experimental data are well represented by $\text{Nu}_d = 0.745 \text{Re}_d^{1/2} \text{Pr}^{1/3}$, which is within the range of the various predictions.

Acknowledgments

This work was supported by the A. P. Sloan Foundation and by the National Science Foundation under grant No. CBT-8858288.

References

- Crank, J., 1984, *Free and Moving Boundary Problems*, Clarendon Press, Oxford, United Kingdom.
- Davies, J. T., and Makepeace, 1978, "Measurement of the Surface Ages of Water Jets," *AIChE Journal*, Vol. 24, No. 3, pp. 524-530.
- Duda, J. L., and Vrentas, J. S., 1967, "Fluid Mechanics in Laminar Liquid Jets," *Chem. Eng. Sci.*, Vol. 22, p. 866.
- Kestin, J., 1966, "The Effect of Free-Stream Turbulence on Heat Transfer Rates," *Adv. Heat Transfer*, Vol. 3, pp. 1-32.
- Lienhard, J. H., V, and Lienhard, J. H., 1984, "Velocity Coefficients for Free Jets From Sharp-Edged Orifices," *ASME Journal of Fluid Engineering*, Vol. 106, pp. 13-17.
- Lienhard, J. H., V, Liu, X., and Gabour, L. A., 1992, "Splattering and Heat Transfer During Impingement of a Turbulent Liquid Jet," *ASME JOURNAL OF HEAT TRANSFER*, Vol. 114, pp. 362-372.
- Liu, X., Lienhard, J. H., V, and Lombara, J. S., 1991, "Convective Heat Transfer by Impingement of Circular Liquid Jets," *ASME JOURNAL OF HEAT TRANSFER*, Vol. 113, pp. 571-582.
- Liu, X., 1992, "Liquid Jet Impingement Heat Transfer and Its Potential Applications at Extremely High Heat Fluxes," Doctoral Thesis in Mechanical Engineering, MIT, Cambridge, MA.
- Mehendale, A. B., Han, J. C., and Ou, S., 1991, "Influence of High Mainstream Turbulence on Leading Edge Heat Transfer," *ASME JOURNAL OF HEAT TRANSFER*, Vol. 113, pp. 843-850.
- Miyazaki, H., and Silberman, E., 1972, "Flow and Heat Transfer on a Flat Plate Normal to a Two-Dimensional Laminar Jet Issuing From a Nozzle of Finite Height," *Int. J. Heat Mass Transfer*, Vol. 15, pp. 2097-2107.
- Nakaryakov, V. E., Pokusaev, B. G., and Troyan, E. N., 1978, "Impingement of an Axisymmetric Liquid Jet on a Barrier," *Int. J. Heat Mass Transfer*, Vol. 21, No. 9, pp. 1175-1184.
- Schach, W., 1935, "Umlenkung eines kreisförmigen Flüssigkeitsstrahles an einer ebenen Platte senkrecht zur Strömungsrichtung," *Ing.-Arch.*, Vol. 6, pp. 51-59.
- Schlichting, H., 1979, *Boundary Layer Theory*, 7th ed., McGraw-Hill, New York.
- Scholtz, M. T., and Trass, O., 1970, "Mass Transfer in a Nonuniform Impinging Jet," *AIChE Journal*, pp. 82-96.
- Scriven, L. E., and Pigford, R. L., 1959, "Fluid Dynamics and Diffusion Calculations for Laminar Liquid Jets," *AIChE Journal*, Vol. 5, p. 397.
- Shen, Y. C., 1962, "Theoretical Analysis of Jet-Ground Plane Interaction," IAS Paper No. 62-144.
- Simmons, S. G., Hager, J. M., and Diller, T. E., 1990, "Simultaneous Measurements of Time-Resolved Surface Heat Flux and Freestream Turbulence at a Stagnation Point," *Heat Transfer 1990*, Proc. Ninth Intl. Heat Transfer Conf., Jerusalem, Vol. 2, pp. 375-380.
- Sparrow, E. M., and Lee, L., 1975, "Analysis of Flow Field and Impingement Heat/Mass Transfer Due to a Nonuniform Slot Jet," *ASME JOURNAL OF HEAT TRANSFER*, Vol. 97, pp. 191-197.
- Stevens, J., and Webb, B. W., 1991, "Local Heat Transfer Coefficients Under an Axisymmetric Single-Phase Liquid Jet," *ASME JOURNAL OF HEAT TRANSFER*, Vol. 113, pp. 71-78.
- Strand, T., 1964, "On the Theory of Normal Ground Impingement of Axisymmetric Jets in Inviscid Incompressible Flow," AIAA Paper No. 64-424.
- White, F. M., 1974, *Viscous Fluid Flow*, McGraw-Hill, New York, p. 183.
- White, F. M., 1991, *Viscous Fluid Flow*, 2nd ed., McGraw-Hill, New York, pp. 159-162.

Correlating Equations for Impingement Cooling of Small Heat Sources With Single Circular Liquid Jets

D. J. Womac

S. Ramadhyani

F. P. Incropera

Heat Transfer Laboratory,
School of Mechanical Engineering,
Purdue University,
West Lafayette, IN 47907

Experimental data have been obtained for liquid jet impingement cooling of small square heat sources resembling electronic integrated circuit chips. Both free-surface and submerged jet configurations have been studied for a range of velocities, nozzle diameters, and nozzle-to-heater separation distances, with water and a fluorocarbon liquid (3M FC-77) as coolants. Major trends in the data have been explained in terms of the underlying hydrodynamic and thermal phenomena. The data, obtained over parameter ranges applicable to the cooling of microelectronic chips, have been compared with the predictions of previously developed correlations for jet impingement heat transfer and substantial discrepancies between the data and the predictions have been noted. Based on the present data, two new correlating equations, one for free-surface and the other for submerged jet impingement, have been developed and presented.

Introduction

An attractive means of obtaining large heat transfer coefficients at a surface involves impingement of a high-speed fluid jet on the surface. The practicality of this arrangement has resulted in its being employed in several industrial applications including annealing of metals, tempering of glass, cooling of gas turbine blades, and drying of paper and textiles. While the use of air jets, as in the foregoing applications, is common, liquid jet impingement, which is associated with extremely high heat transfer coefficients, has seldom been needed in the past. With the recent development of very large scale integrated circuit (VLSI) electronic chips, a need has arisen for cooling techniques capable of absorbing heat fluxes as high as 200 W/cm^2 , while maintaining modest temperature differences between the coolant and the chip (Ramadhyani and Incropera, 1988). Liquid jet impingement appears to be a natural choice for the task (Kiper, 1984) and has, in fact, been employed for thermal management in a commercial computer (Yamamoto et al., 1987).

The cooling of VLSI chips is a difficult undertaking but is essential for reliability and efficiency of operation. Chip surface temperatures are commonly maintained between 50°C and 100°C to avoid deterioration of system performance or logic errors (Chu and Simons, 1984; Bergles, 1986). The stringency of the cooling requirements precludes conventional forced air cooling, and mandates the use of liquid coolants. Although most of the liquid cooling schemes in current use involve indirect cooling through an intermediate "cold plate," in the future, direct liquid immersion techniques may be used, with the coolant applied to the chip surface by jet impingement. The development of such a cooling scheme will require knowledge of the effects of the jet velocity, the thermophysical properties of the fluid, the jet diameter, the nozzle-to-chip spacing, and the size of the chip.

The existing literature on jet impingement heat transfer may be grouped into two categories: free-surface jet impingement and submerged jet impingement. Free-surface jet impingement involves a jet of liquid discharging into an ambient gas and impinging normally on the target surface (Fig. 1a). With the

submerged jet, the fluid is discharged into stagnant fluid of the same type (Fig. 1b). As described by Womac et al. (1990), the flow phenomena in the two cases differ, and there are corresponding differences in the heat transfer characteristics of the two configurations.

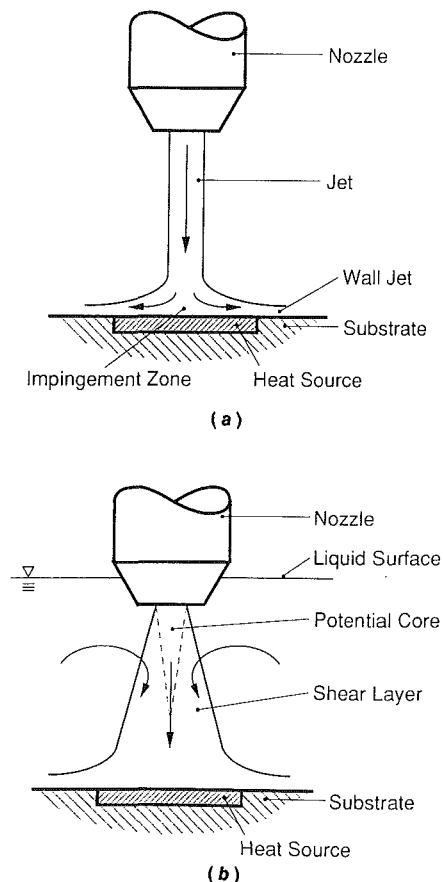


Fig. 1 Free-surface (a) and submerged (b) jet configurations

Contributed by the Heat Transfer Division for publication in the JOURNAL OF HEAT TRANSFER. Manuscript received by the Heat Transfer Division February 1991; revision received September 1992. Keywords: Electronic Equipment, Forced Convection, Jets. Associate Technical Editor: H. R. Jacobs.

A distinguishing feature of a free-surface liquid jet is the negligibly small shear stress at the jet/gas interface. Consequently, in the absence of significant gravitational acceleration, the nozzle exit velocity is preserved, virtually unchanged, until impingement on the target. Heat transfer from the surface is, therefore, usually not greatly affected by changes in the nozzle-to-surface separation distance. An additional characteristic feature of free-surface jet impingement is that, with liquids of low surface tension, some of the liquid may splash from the surface after impingement, thus reducing the cooling capacity of the jet.

The submerged jet configuration is characterized by a shear layer between the jet and the ambient fluid. For jet Reynolds numbers, Re_d , exceeding 1000, the shear layer is turbulent. With increasing distance from the nozzle, the shear layer thickens by entraining ambient fluid, while the potential core, in which the fluid velocity is unaffected by the shear layer, shrinks and eventually disappears. Beyond the tip of the potential core, the centerline velocity of the jet diminishes while the turbulence increases substantially. The length of the potential core varies with Re_d , achieving a value of 20 nozzle diameters at $Re_d = 1000$ and diminishing sharply thereafter to a minimum of approximately five nozzle diameters for Reynolds numbers in the range $3500 \leq Re_d \leq 5500$ (Hrycak et al., 1970). With further increases in Reynolds number, the length of the potential core gradually increases to a maximum of approximately seven nozzle diameters. In comparison to free-surface jets, submerged jet impingement heat transfer is more sensitive to the nozzle-to-surface separation distance, especially if the target surface is beyond the end of the potential core.

With both free-surface jet and submerged jet impingement, an impingement zone may be identified wherein the liquid is decelerated as it approaches the surface and is deflected to flow parallel to the surface. This region is characterized by a strong favorable pressure gradient parallel to the surface that tends to laminarize the flow. Downstream of the impingement zone, in the wall jet region, the favorable pressure gradient disappears, and the flow may undergo a transition to turbulence. For submerged jet impingement and $S/d < 6$, the transition to turbulence is manifested by a secondary peak in the local heat transfer coefficient around $r/d \approx 1.9$ (Martin, 1977). In the case of free-surface jet impingement, the flow may undergo a hydraulic jump at some distance from the impingement zone, leading to local augmentation of the heat transfer coefficient.

For single-phase, axisymmetric, free-surface jet impingement, Metzger et al. (1974) experimentally determined the effects of Reynolds number, Prandtl number, and the ratio of

the heated surface diameter to the nozzle diameter on the average Stanton number at an isothermal impingement surface. Several nozzles and impingement surfaces of various diameters were used, and water and an oil were employed as coolants. Their data were represented to within 25 percent by the following correlation:

$$\overline{St} = 2.74 Re_d^{-0.652} Pr^{-0.513} \left[\frac{D}{d} \right]^{-0.774} \left[\frac{\mu_s}{\mu_{aw}} \right]^{-0.37} \quad (1)$$

over the ranges $2.2 \times 10^3 \leq Re_d \leq 138.2 \times 10^3$, $3 \leq Pr \leq 151$, and $1.75 \leq D/d \leq 25.1$. The term involving the ratio (D/d) represents an attempt to incorporate the heater diameter into the correlation in a simple way, but little theoretical justification can be provided for the functional form of that term. Jiji and Dagan (1988) conducted an experimental investigation of free-surface jet impingement using a 12.7-mm-square heated surface as the target and nozzles of diameter 0.5 mm and 1 mm. Water and FC-77 (a fluorocarbon liquid manufactured by 3M Co.) were used as coolants. Their results were found to be well correlated by

$$\frac{\overline{Nu}_l}{Pr^{0.33}} = 3.84 \left[0.008 \left(\frac{l}{d} \right) + 1 \right] Re_d^{0.5} \quad (2)$$

Local convection coefficients were measured by Nakoryakov et al. (1978), Faggiani and Grassi (1990), and Stevens and Webb (1991), and analytical representations of the measured local convection coefficients were developed. Based on their measurements, Stevens and Webb also presented a correlating equation for the local Nusselt number at the stagnation point of the impinging jet. Since their data displayed some sensitivity to the diameter of the jet, they found it necessary to include a dimensional multiplier (involving the ratio U_e/d) in an otherwise dimensionless equation:

$$Nu_o = 2.67 Re_d^{0.567} Pr^{0.4} \left(\frac{S}{d} \right)^{-0.0336} \left(\frac{U_e}{d} \right)^{-0.237} \quad (3)$$

Chaudhury (1964) presented a purely theoretical solution to the problem of heat transfer under a laminar jet impinging on an isothermal surface and derived local convection coefficients on the basis of that solution. Liu and Lienhard (1989) used an integral solution technique to determine local Nusselt numbers for a laminar jet impinging on a uniform heat flux surface and compared their theoretical predictions to a limited set of experimental data. A more exhaustive discussion, along with recommended equations for calculating local Nusselt numbers, was provided in a subsequent study by Liu et al. (1991). However, formulas for the average Nusselt number were not provided. Theoretical predictions of local Nusselt number

Nomenclature

A = surface area of heat source
 c_p = specific heat at constant pressure
 D = diameter of circular impingement surface
 d_i = diameter of the free surface jet in the impingement plane, given by Eq. (12)
 d = nozzle diameter
 \bar{h} = surface average heat transfer coefficient
 k = thermal conductivity of the fluid
 L = characteristic length given by Eq. (14) or Eq. (18)

l = length of the side of the square heat source
 \overline{Nu} = heater average Nusselt number
 Pr = Prandtl number
 q = heater power dissipation
 Re_d = nozzle Reynolds number = $U_e d / \nu$
 r = radial coordinate
 S = nozzle-to-heater separation distance
 \overline{St} = heater average Stanton number = $\bar{h} / \rho U_e c_p$
 \overline{T}_s = heater average surface temperature

T_{up} = fluid temperature at the nozzle exit
 U_e = mean fluid velocity at nozzle exit
 U_i = mean fluid velocity in the impingement plane
 μ = dynamic viscosity
 ν = kinematic viscosity
 ρ = fluid density

Subscripts

aw = evaluated at the adiabatic wall temperature
 o = stagnation point
 s = evaluated at the surface average temperature

distributions under laminar impinging jets have also been presented by Wang et al. (1989a, 1989b, 1989c).

Submerged jet impingement has been studied much more extensively. Comprehensive reviews of the literature have been presented by Martin (1977) and Womac (1989). Noteworthy contributions include those by Brdlik and Savin (1965) and Sitharamayya and Raju (1969), who studied the effects of the Reynolds number, nozzle diameter, separation distance, and the ratio of heater diameter to nozzle diameter on the average heat transfer coefficient. Several different correlations for the average Nusselt number have been proposed by the aforementioned investigators. For $S/d \leq 6.2$, $1.67 \leq D/d \leq 18.75$, and $2000 \leq Re_d \leq 20,000$, Brdlik and Savin proposed the equation

$$\overline{Nu}_D = 1.54 Re_D^{0.5} Pr^{0.33} \quad (4)$$

For $S/d < 7$, $8 \leq D/d \leq 58$, and $2000 \leq Re_d \leq 40,000$, Sitharamayya and Raju proposed the correlation

$$\overline{Nu}_d = \left[32.49 Re_d^{0.523} + 0.266 \left(\frac{D}{d} - 8 \right) Re_d^{0.828} \right] \left(\frac{d}{D} \right)^2 Pr^{0.33} \quad (5)$$

which was obtained by superposing contributions associated with the impingement and wall jet regions. The foregoing correlations suggest that the average Nusselt number is approximately independent of the separation distance for $S/d < 7$. For a wider range of this parameter, Martin recommended the correlation

$$\overline{Nu}_d = \frac{d}{D} \frac{\left[2 - 4.4 \frac{d}{D} \right]}{\left[1 + 0.2 \left(\frac{S}{d} - 6 \right) \left(\frac{d}{D} \right) \right]} F(Re_d) Pr^{0.42} \quad (6a)$$

where

$$F(Re_d) = 2 Re_d^{0.5} \left[1 + \frac{Re_d^{0.55}}{200} \right]^{0.5} \quad (6b)$$

The correlation is applicable to the parameter ranges $2 \leq S/d \leq 12$, $5 \leq D/d \leq 15$, and $2000 \leq Re_d \leq 400,000$. As will later be demonstrated, serious errors may arise if this correlation is used outside its ranges of applicability.

Local convection coefficients were measured by Rao and Trass (1964), Dawson and Trass (1966), Gardon and Cobonpue (1961), Vlachopoulos and Tomich (1971), and Vickers (1959), and various correlating equations for the local Nusselt number have been presented by these investigators. In general, these studies reveal that radial variations of the local Nusselt number are strongly dependent on S/d , with a secondary peak being observed around $r/d \approx 1.9$ for $S/d < 6$. For $S/d < 4$, the maximum in the local Nusselt number distribution at the stagnation point gives way to a local minimum.

The diversity in the forms of the various correlations proposed for both free-surface and submerged jet impingement is indicative of the inherent difficulty in choosing the most appropriate scales and dimensionless groups to use in the correlations. For instance, with a round jet impinging on a circular heat source, the nozzle diameter, d , and the heater diameter, D , are both possible choices for use as the length scale in the Reynolds number. For small D/d , heat transfer would be dominated by the impingement region, suggesting that d would be the superior choice, while for large D/d , heat transfer would be dominated by the wall-jet region, and D would be the more appropriate length scale. For applications involving jet impingement cooling of electronic chips, the ratio of chip size to nozzle diameter may lie in the range where heat transfer is not dominated by either the impingement region or the wall jet region. Consequently, previously developed correlations may not be suitable for extrapolation to this range.

The objective of the present work is to examine the effect of the pertinent dimensionless parameters, in ranges relevant to the cooling of electronic chips, for both free-surface and submerged jet impingement. Experimental data obtained for both configurations are presented in dimensionless form, and explanations for the observed trends, in terms of the pertinent physical phenomena, are provided. The measured data for both configurations are compared with the predictions of previously developed correlations, and discrepancies between the measurements and predictions are highlighted. These discrepancies provide the motivation for the presentation of new correlating equations based on the experimental data obtained in this study.

The information presented in this paper is relevant to single circular jets. A practical electronic chip cooling scheme may, possibly, entail the use of multiple small jets to cool each chip, with attendant hydrodynamic interactions between adjacent jets. The results of the present study provide a starting point for an examination of the more complicated multiple-jet situation.

Experimental Apparatus and Procedures

The experimental apparatus consisted of a flow loop, heater module, power supply, and data acquisition unit. The flow loop consisted of a gear pump, a heat exchanger, regulating valves, turbine flowmeters, a degassing facility, and a test chamber. Conditions within the test chamber could be varied to obtain either free-surface or submerged jet impingement. A traversing mechanism mounted to the top of the test chamber allowed variation of the nozzle-to-heater separation distance from 0 to 25 mm with a resolution of 0.05 mm.

Several nozzles (Fig. 2a) were fabricated to provide discharge diameters of $d = 0.978, 1.65, 3.11,$ and 6.55 mm. The inlet diameter of each nozzle was 9.52 mm, resulting in area contraction ratios of 95 and 2.11 for the smallest and largest diameter nozzles, respectively. Although velocity profile measurements were not made, it is expected that the large contraction ratios for all but the 6.55 mm nozzle produced jets with uniform velocity profiles and low turbulence levels.

The heater module consisted of a 12.7-mm-square, 3-mm-thick copper block, which was flush mounted into a fiberglass heater support. A 12.7-mm-square electrical resistance heater, consisting of a nichrome resistance element sputtered on a beryllium oxide substrate, was pressed into firm contact with the back surface of the copper block. The block was instrumented with seven copper-constantan thermocouples of 0.0762-mm-dia wire. Straight holes of 0.457 mm diameter were drilled through the block at the locations shown in Fig. 2(b), and each thermocouple was silver soldered to the block at its surface. An automatic data acquisition and control system was used to monitor and record the fluid temperature upstream of the nozzle, copper block temperatures, flow rate, and heater power dissipation. A d-c power supply was used to power the resistance heater.

During the experiments the flow rate and power were varied. For each increase in the flow rate the heater power was adjusted to maintain a temperature difference between the copper block and the upstream fluid of approximately 10°C . A few experiments were conducted holding flow rate constant, while S/d and power were varied. Again heater power was adjusted to maintain a temperature difference of approximately 10°C .

The average heat transfer coefficient over the heated surface was determined from

$$\bar{h} = \frac{q}{A(\bar{T}_s - T_{up})} \quad (7)$$

where A is the area of the heated surface (12.7 mm \times 12.7 mm), \bar{T}_s the area-weighted average of the seven surface temperatures, T_{up} the fluid temperature upstream of the nozzle,

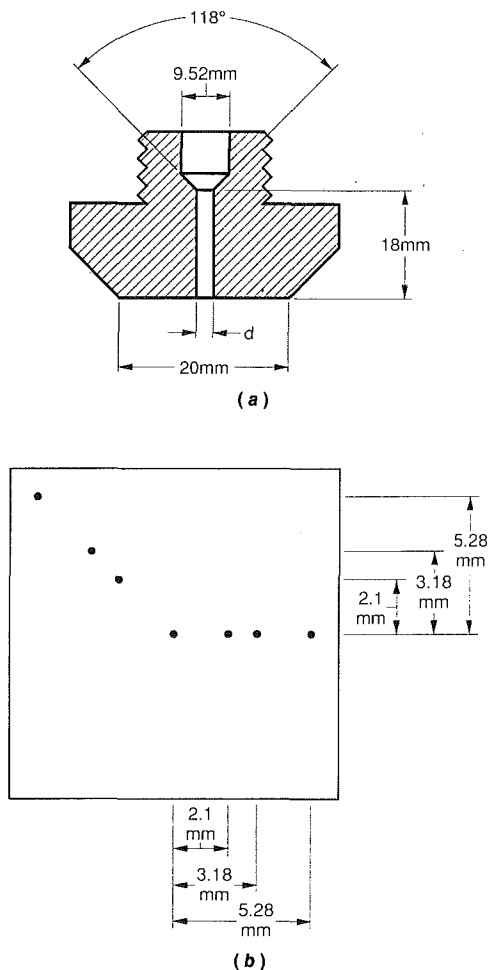


Fig. 2 Nozzle and heater characteristics: (a) nozzle geometry and (b) placement of thermocouples on the heat source (dimensions are in mm)

and q the power supplied to the heater. Surface temperature nonuniformities averaged about 0.5°C for the water experiments and about 0.1°C for the FC-77 studies for a surface-to-fluid temperature difference of 10°C . The maximum non-uniformities were 1.5°C and 0.2°C for water and FC-77, respectively. A two-dimensional numerical model was used to calculate heat losses by conduction through the fiberglass heater support. Since worst-case losses were predicted to be only 2 percent, all of the power supplied to the heater was assumed to be dissipated through the front surface of the copper block.

In order to present the data in dimensionless form and to effect comparisons with previously developed correlations, Reynolds numbers and heater-average Nusselt numbers were defined in various ways. While the general forms of the definitions were

$$\overline{\text{Nu}}_{L_c} = \frac{\bar{h}L_c}{k} \quad (8a)$$

and

$$\text{Re}_{L_c} = \frac{U_c L_c}{\nu} \quad (8b)$$

the choice of the characteristic length L_c and the characteristic velocity U_c varied, depending on the particular situation. In presenting and discussing the results, the chosen characteristic lengths and velocities will, in each case, be specified. The fluid thermophysical properties employed in Eq. (8) were evaluated at a film temperature defined as

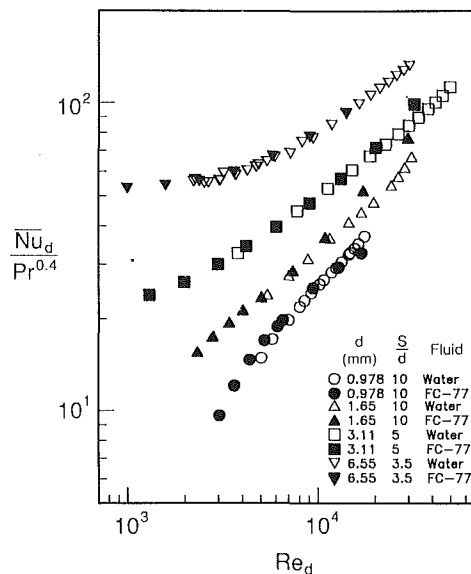


Fig. 3 Variation of the heater-average Nusselt number with Reynolds number for various nozzle diameters and nozzle-to-heater separations (free-surface jet)

$$T_{\text{film}} = 0.5(\bar{T}_s + T_{up}) \quad (9)$$

A detailed analysis of the various experimental uncertainties is provided by Womac (1989). The maximum overall uncertainties in the Nusselt number, calculated using the heater length as the characteristic length, were determined to be ± 2.6 percent and ± 5.7 percent for water and FC-77, respectively. For Reynolds numbers calculated on the basis of the nozzle diameter, uncertainties varied with the size of the nozzle. With the 6.55 mm nozzle, the uncertainties associated with water and FC-77 were ± 3.2 percent and ± 12.7 percent, respectively. With the 0.978 mm nozzle, the corresponding uncertainties were ± 11.8 percent and ± 17.2 percent.

Results and Discussion

Free-Surface Jet Results. For free-surface jets of water and FC-77, Fig. 3 shows the dependence of the average Nusselt number on the Reynolds number for various nozzle diameters. For all the data shown, the hydraulic jump occurred beyond the edge of the heater. The characteristic length employed in the Nusselt and Reynolds numbers is the nozzle diameter, d , and the characteristic velocity is the jet exit velocity, U_e . The open symbols correspond to water ($\text{Pr} \approx 7$), while the solid symbols correspond to FC-77 ($\text{Pr} \approx 25$). The good agreement between the data for the two fluids is due to the use of the ordinate variable $\overline{\text{Nu}}_d/\text{Pr}^{0.4}$, which successfully accounts for the difference in Prandtl number. Although the dimensionless separation distance S/d is different for the different nozzles, the data for the various nozzles can still be compared, because the Nusselt number is only weakly dependent on the separation distance for the free-surface jet conditions of this study.

For a fixed Re_d , the Nusselt number increases with increasing nozzle diameter. This trend is due to the use of the nozzle diameter, d , as the length scale in the Nusselt number. Although for a fixed Re_d , increases in the nozzle diameter are associated with reductions in velocity and corresponding reductions in the heat transfer coefficient, the presence of d in the Nusselt number more than compensates for the reduction of the heat transfer coefficient. When plotted on logarithmic coordinates, as shown in Fig. 3, the data generally fall along straight lines. However, deviations are observed in the FC-77 data for nozzle diameters of 0.978 mm and 6.55 mm, and in

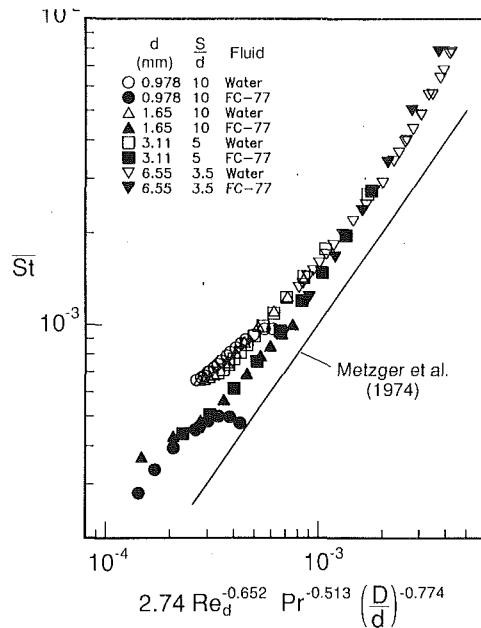


Fig. 4 Comparison of free-surface jet data with correlation developed by Metzger et al. (1974)

the water data for the 6.55 mm nozzle. The FC-77 data obtained with the 0.978 mm nozzle exhibit a slope that is initially large but diminishes with increasing Reynolds number. In contrast, the data obtained with the 6.55 mm nozzle exhibit slopes that are initially small but increase with increasing flow rate. These contradictory trends are the result of separate physical phenomena, which are discussed in the ensuing paragraphs.

At very low flow rates with small diameter jets, the thickness of the thermal boundary layer forming on the heater surface is comparable to the thickness of the thin sheet of fluid flowing away from the stagnation point. If the developing thermal boundary layer reaches the free surface, significant attenuation of heat transfer may be expected downstream of that point due to bulk warming of the fluid. Hence, the Nusselt number diminishes rapidly with decreasing Reynolds number for small diameter jets at low flow rates. Rough estimates of the thermal boundary layer thickness at low Reynolds numbers suggest that the 0.978-mm-dia data for both water and FC-77 are affected by this phenomena, although the reduction in Nusselt number in the water data is not immediately apparent from an examination of the data trend.

At high flow rates with small diameter jets of FC-77, visual observation of the jet showed that the fluid splashed away from the free surface in the vicinity of the impingement region. Splashing has the effect of removing fluid from the radial flow, resulting in a reduction of the thickness of the fluid sheet. In some cases, the radially flowing liquid layer is thin enough to allow the thermal boundary layer to reach the free surface, resulting in the heat transfer reduction. The effect is noticeable with the 0.978 mm jet of FC-77 at high Reynolds numbers, where the data show a tendency to level off.

The data for the 6.55-mm-dia nozzle deviate from linearity at low Reynolds numbers due to the acceleration of the jet by gravity. At low Reynolds numbers, the jet discharge velocity is small enough for gravitational acceleration to have an appreciable effect as the liquid descends towards the heater surface. To assess the gravitational acceleration of the jet, an impingement velocity U_i was calculated and compared to the average jet discharge velocity U_e . The impingement velocity, given by

$$U_i = (U_e^2 + 2gS)^{0.5} \quad (10)$$

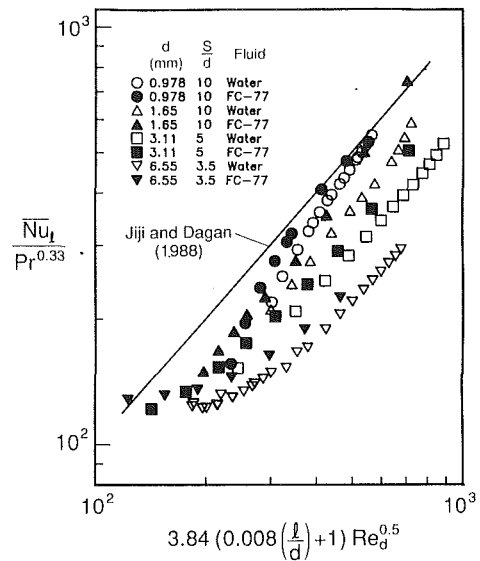


Fig. 5 Comparison of free-surface jet data with correlation developed by Jiji and Dagan (1988)

is the average velocity that the jet would have in the impingement plane, if the impingement surface were not present. The impingement velocity for this nozzle at $S/d = 3.5$ was calculated to be greater than the jet exit velocity by a factor of 4.6 at a Reynolds number of 1000, and a factor of 1.28 at a Reynolds number of 3000. As shown by Womac et al. (1990), if the Nusselt number for the 6.55 mm nozzle is replotted against a Reynolds number based on the impingement velocity, the data points no longer deviate from linearity at low flow rates.

Figure 4 compares the present data with the free-surface jet correlation of Metzger et al. (1974). Since the correlation was developed for circular heat sources, while the present data were obtained with square heat sources, an approximately equivalent heat source diameter $D = (\sqrt{2}l + l)/2$ was computed for use in the correlation. For the 0.978 mm and 1.65 mm nozzles, sizable differences are observed between the FC-77 and water data. The data for the two fluids obtained with the 3.11 mm and 6.55 mm nozzles are observed to be in better agreement with each other. Although the correlation variables are moderately successful in collapsing the data for the various nozzles and the two fluids, all the data exceed the solid line corresponding to the correlation, with deviations ranging from 40 to 70 percent. Since the parameter ranges associated with the correlation encompass the values corresponding to the present data, the systematic deviation between the data and the correlation is unexpected.

It is especially difficult to reconcile the difference between the present data and their correlation when the experimental conditions of the study by Metzger et al. are considered. In their study, the liquid jet issued from a long tube under fully developed turbulent flow conditions for the water experiments and fully developed laminar flow conditions for some of the oil experiments. As discussed recently by Wolf et al. (1990), turbulence in the jet can cause substantial heat transfer enhancement. It is also known (Sparrow and Lee, 1975) that a fully developed laminar flow profile produces a higher heat transfer coefficient at the stagnation point than a uniform velocity profile of equivalent flow rate. It would therefore be reasonable to expect that the correlation resulting from their experimental data would predict higher heat transfer coefficients than those measured in the present work.

In Fig. 5, the present data are compared with the correlation for small square heat sources presented by Jiji and Dagan

Table 1 Range of pertinent parameters for single free-surface jet correlation, Eq. (13)

d (mm)	L/d	Re _d Range	Re _l Range
1.65	4.14	2300-31,000	9500-128,000
3.11	1.96	1250-51,000	2450-100,000
6.55	0.670	1000-33,000	670-22,000

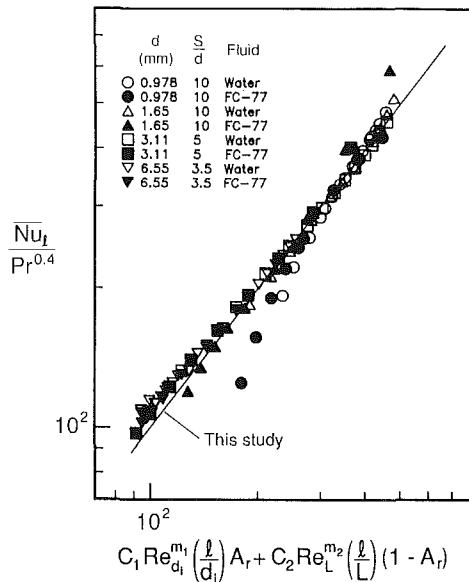


Fig. 6 Comparison of free-surface jet data with correlation of this study

(1988). This correlation does not collapse the data for the different nozzles as well as the Metzger correlation and, in addition, is not completely successful in bringing the water and FC-77 data together. It appears that the Prandtl number exponent of 0.33 employed in this correlation is too low, as evidenced by the better results obtained in collapsing the water and FC-77 data with an exponent of 0.40 (Fig. 3). The correlation overpredicts the data obtained with the 6.55 mm nozzle by as much as 130 percent and the data from the 0.978 mm nozzle by up to 50 percent. The better agreement obtained with the smaller nozzle is because the correlation was developed from data obtained with nozzle diameters of 0.5 and 1.0 mm.

In view of the foregoing deviations, an attempt was made to develop a correlating equation for the present data. This equation was constructed by separately considering the impingement region and the wall jet. Separate correlating equations were utilized for the two regions, and the average Nusselt number for the whole heat source was obtained as an area-weighted combination of the two equations. As noted earlier, a similar approach was used by Sitharamayya and Raju (1969) to correlate their submerged jet impingement data. The impingement region correlation was of the form

$$\frac{\overline{Nu}_{d_i}}{Pr^{0.4}} = C_1 Re_{d_i}^m \quad (11)$$

the Reynolds number being based on the impingement velocity, U_i , and the impingement diameter, d_i . The latter is given by

$$d_i = (U_e/U_i)^{0.5} / d \quad (12)$$

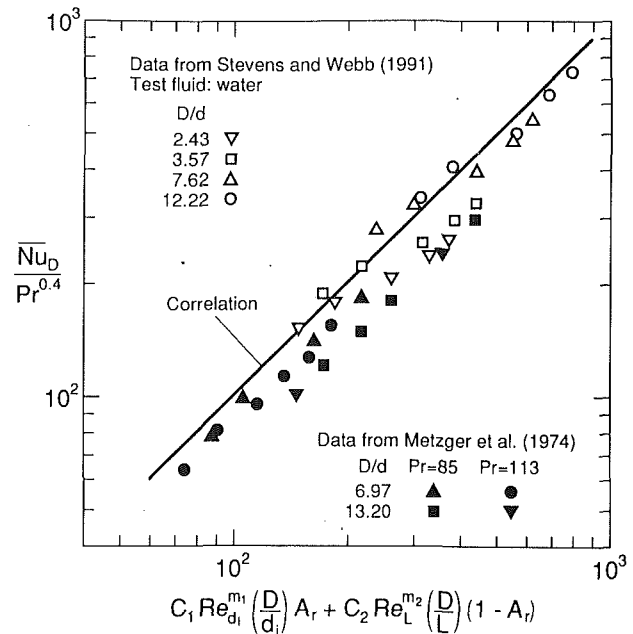


Fig. 7 Comparison of the present correlation with the free-surface jet data of other investigators

Both analytical predictions and previous experimental results indicate that the exponent m should be 0.5 (Burmeister, 1983; Ma et al., 1988). The wall jet region correlation was of the form

$$\frac{\overline{Nu}_L}{Pr^{0.4}} = C_2 Re_L^n \quad (13)$$

the Reynolds number being based on the impingement velocity and the average length of the wall jet region, L . The latter is given by

$$L = \frac{0.5(\sqrt{2}l - d_i) + 0.5(l - d_i)}{2} \quad (14a)$$

$$= 0.5(D - d_i) \quad (14b)$$

An area-weighted combination of the foregoing correlations yields

$$\frac{\overline{Nu}_l}{Pr^{0.4}} = C_1 Re_{d_i}^m \frac{l}{d_i} A_r + C_2 Re_L^n \frac{l}{L} (1 - A_r) \quad (15)$$

where

$$A_r = \frac{\pi d_i^2}{4l^2} \quad (16)$$

With m set equal to 0.5, optimal values of C_1 , C_2 , and n were determined using a least-squares technique to match water and FC-77 data obtained with the three larger nozzles. The data from the 0.978 mm nozzle were affected by bulk warming and were, therefore, not utilized in developing the correlation. The values were determined to be $C_1 = 0.516$, $C_2 = 0.491$, and $n = 0.532$. The correlation was determined for both water ($Pr \approx 7$) and FC-77 ($Pr \approx 25$) over the range of parameters given in Table 1.

Figure 6 displays a comparison of the correlation with all the free-surface jet data generated in this study. While the agreement between the data and the proposed correlation is, in general, quite good, a few data points obtained with the 0.978 mm nozzle at low Reynolds numbers fall below the correlation due to bulk warming effects. The correlation is within ± 15 percent of all the data not affected by bulk warming. The average error is 2.5 percent, and the standard deviation of the data points from the correlation is 3.8 percent. If the

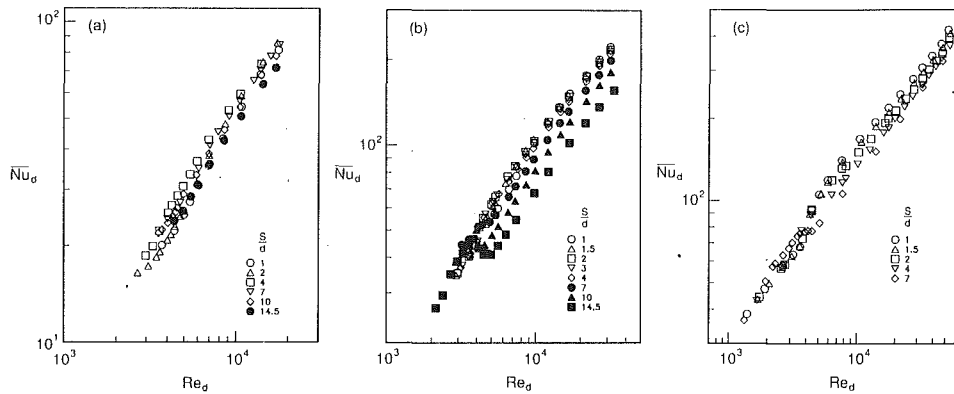


Fig. 8 Effect of separation distance on heater-average Nusselt number for submerged jet impingement: (a) $d = 0.978$ mm, (b) $d = 1.65$ mm, (c) $d = 3.11$ mm

low Reynolds number data for the 0.978 mm nozzle are included, the correlation is within ± 45 percent, the average error is 3.6 percent, and the standard deviation is 6.3 percent.

To test the accuracy of the correlation against independently obtained data, heater-average Nusselt numbers were extracted from the papers by Metzger et al. (1974) and Stevens and Webb (1991). The former paper provided data obtained with oils ($Pr = 85$, $Pr = 113$), and the latter paper provided data obtained with water. The Prandtl number associated with the water data, although not specified in the paper, would be in the range of five to 10. The proposed correlation is compared with these independent data in Fig. 7. In general, the high Prandtl number data of Metzger et al. fall below the correlation. The average and maximum deviations of these data from the correlation are -20 percent and -33 percent, respectively. The water data straddle the correlation more closely, the average and maximum deviations being -6 percent and -30 percent, respectively. It appears, therefore, that the correlation provides predictions of reasonable accuracy for intermediate Prandtl numbers but somewhat overpredicts the high Prandtl number data.

An effort was also made to construct an equation for the heater-average Nusselt number by integrating the formulas for the local Nusselt number recommended by Liu et al. (1991). The resulting equation could be cast into a form resembling Eq. (15), with separate terms representing the contributions of the impingement, transition, and wall-jet regions. The Nusselt numbers predicted by the equation are, on the average, 20 percent below the present data. The largest differences (up to 80 percent) arise with the data from the 6.55 mm nozzle. Although the agreement with the experimental data is not entirely satisfactory, it is appropriate to recognize that the development of a heater-average Nusselt number formula by superposition of the individual Nusselt numbers for the various zones along the heater represents a fundamentally sound approach. As was done in the development of Eq. (15), better agreement with the data can be obtained by adjustment of some of the constants in the formula for the heater-average Nusselt number resulting from integrating the local Nusselt number expressions by Liu et al.

Submerged Jet Results. Figures 8(a, b, c) display the variations of the heater-average Nusselt number with Reynolds number under submerged jet conditions, for the 0.978, 1.65, and 3.11 mm nozzles, respectively. The different data symbols on each figure correspond to different values of the parameter S/d , and all the displayed data were obtained with water.

In comparison to the free-surface jet data, the submerged jet data for these three nozzles display a greater sensitivity to S/d . With the 0.978 mm nozzle (Fig. 8a), the average Nusselt number increases slightly as S/d increases from a value of one

to a value of four. Data for the larger separation distances lie below those obtained at $S/d = 4$. With the 1.65 mm nozzle (Fig. 8b), and $Re_d \leq 4000$, S/d has a small effect on the Nusselt number in the range $1 \leq S/d \leq 14.5$. For $Re_d \geq 4000$, Nu_d decreases with increasing S/d in the range $4 \leq S/d \leq 14.5$, while being relatively invariant in the range $1 \leq S/d \leq 4$. An interesting feature of the data corresponding to large separation distances ($7 \leq S/d \leq 14.5$) is the sharp decrease in Nu_d with increasing Re_d at $Re_d \approx 4000$. With the 3.11 mm nozzle (Fig. 8c), Nu_d is relatively insensitive to S/d for $Re_d \leq 5000$, but diminishes with increasing S/d for $Re_d \geq 5000$. Once again, the variations are not large in the range $1 \leq S/d \leq 4$.

The relative invariance of Nu_d with S/d for $1 \leq S/d \leq 4$, especially for $Re_d \leq 4000$, is attributed to the fact that the heat source is situated within the length of the potential core of the jet, and is, therefore, washed primarily by fluid from within the potential core. Since the velocity in the potential core corresponds closely to the jet exit conditions, for a fixed jet exit velocity U_e , the average Nusselt number would be expected to be virtually invariant with changes in separation distance. The reduction in Nusselt number with increasing S/d , for large separation distances ($S/d \geq 7$), occurs because the heater is situated beyond the potential core and the fluid velocity diminishes with increasing separation distance in this region.

The sharp decrease in Nu_d with increasing Re_d observed at $Re_d \approx 4000$ in the 1.65 mm nozzle data is attributed to a rapid shortening of the potential core to a point where impingement occurs beyond the tip of the potential core. The associated reduction of impingement velocity decreases the Nusselt number until the minimum potential core length is reached at $Re_d \approx 5000$.

The foregoing discussion highlights the fact that, in submerged jet impingement, the highest heat transfer coefficients are obtained at small separation distances ($S/d \leq 4$). This behavior is a fortunate circumstance from the point of view of electronic packaging, where compactness of the cooling scheme is an important requirement. Figure 9 presents results obtained with water and FC-77, for $3 \leq S/d \leq 4$, using four different nozzles. As in the case of free-surface jets, the Prandtl number exponent of 0.4 is successful in collapsing the data for the two fluids. Unlike the free-surface jet results, splashing and gravitational acceleration effects play no part in the submerged jet situation. The data for the two smaller nozzles display a noticeable change in slope around $Re_d \approx 4000$ that may be attributed to the completion of the hydrodynamic transition to turbulence.

A comparison of free-surface and submerged jet results obtained with the 1.65 mm diameter nozzle is provided in Fig. 10. Although the comparison is made between submerged jet

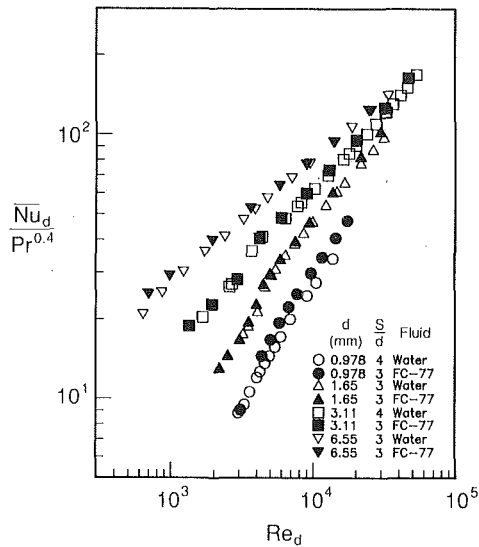


Fig. 9 Variations of the heater-average Nusselt number with Reynolds number and jet diameter under submerged jet conditions

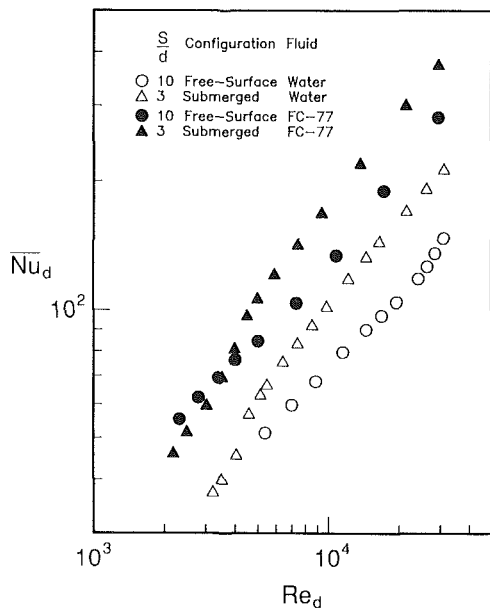


Fig. 10 Comparison of heater-average Nusselt number under free-surface and submerged jet impingement conditions ($d = 3.11$ mm)

results obtained at $S/d = 3$ and free-surface jet results obtained at $S/d = 10$, the value of S/d has a negligible influence on the free-surface jet results and, therefore, the difference in the values has no bearing on the comparison. Results obtained with both water and FC-77 show that Nusselt numbers are higher under submerged jet conditions for $Re_d \geq 4000$. Although no data were collected with water for $Re_d < 4000$, the FC-77 results indicate that the free-surface jet Nusselt numbers are slightly higher for $Re_d \leq 4000$. The higher Nusselt numbers obtained with the submerged jet for $Re_d \geq 4000$ are attributed to heat transfer enhancement by turbulence generated in the free shear layer of the jet.

The data presented in Fig. 9 are replotted in Fig. 11 using the variables employed in the correlation proposed by Martin (Eq. (6)). Since the abscissa variable involves the diameter (D) of a circular impingement surface, an approximately equivalent diameter was calculated for the present results using the formula $D = 0.5(l + \sqrt{2}l)$. It is observed that the correlation variables collapse the water and FC-77 data and successfully

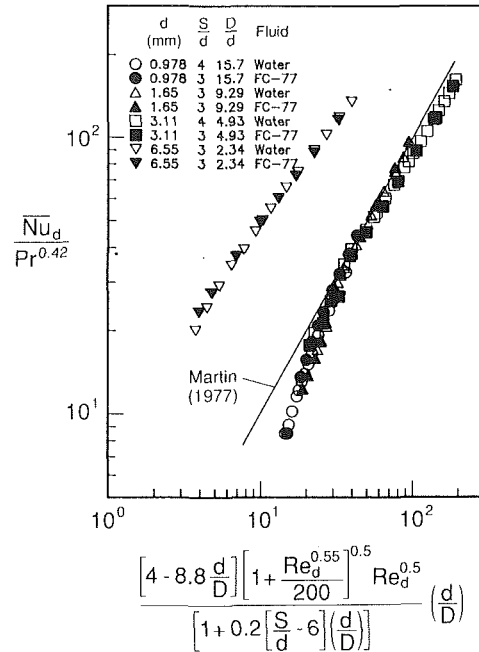


Fig. 11 Comparison of submerged jet data with correlation recommended by Martin (1977)

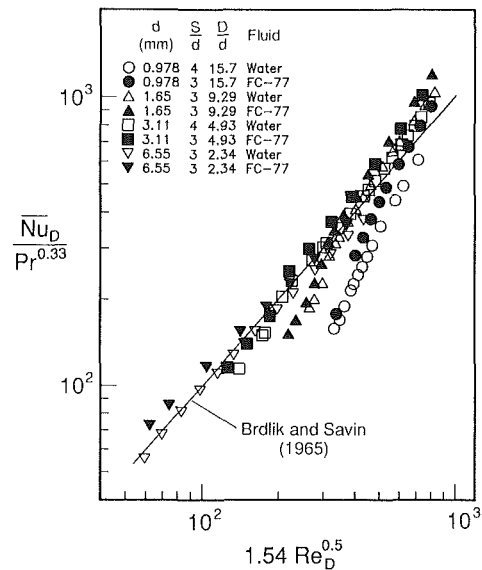


Fig. 12 Comparison of submerged jet data with correlation developed by Brdlik and Savin (1965)

bring together the data obtained with the three smaller nozzles. However, the data obtained with the largest nozzle (6.55 mm) deviate considerably from the other data when plotted in this form. In addition, the correlation lies significantly above the data at low values of the abscissa variable. The deviation of the 6.55 mm nozzle data from the correlation is understandable, since the correlation was developed for the range $5 \leq D/d \leq 15$, while the 6.55 mm nozzle corresponds to $D/d = 2.34$. Clearly, the use of Martin's correlation beyond its ranges of applicability can result in large errors. This feature of the correlation is a consequence of its complicated functional form, as shown in Eq. (6). The other nozzles do, however, lie within the aforementioned range of D/d , and the reason for the disagreement at low values of the abscissa variable is not apparent. The deviations occur in the range of Reynolds numbers cor-

Table 2 Range of pertinent parameters for single submerged jet correlation, Eq. (15)

d (mm)	L/d	Re _d Range	Re _L Range
1.65	4.53	2000-32,000	9100-145,000
3.11	1.76	1300-54,000	2300-95,000
6.55	-	600-34,000	-

responding to hydrodynamic transition to turbulence where different data sets may differ depending on the initial velocity profiles and turbulence levels of the nozzles.

Figure 12 presents a comparison with the correlation developed by Brdlik and Savin (1965) (Eq. (4)). This correlation is not as successful in collapsing the water and FC-77 results as the Martin correlation, and, in addition, the data for the different nozzles do not come together as well. The greatest deviations from the correlation occur with the smallest nozzle (0.978 mm). Thus, as with the Martin correlation, the Brdlik and Savin equation enjoys limited success in correlating the present data. The data for the 0.978 mm and 1.65 mm nozzles were also compared with the correlation by Sitharamayya and Raju (1969). Since the form of the correlation precludes its use for $D/d < 8$, the data for the two larger nozzles were not included in the comparison. The correlation is fairly successful at collapsing the water and FC-77 data for a given nozzle, but fails to collapse the data for the two nozzles.

As with the free-surface jet results, an attempt was made to correlate the present data by considering the impingement and wall jet regions separately. Based on local heat transfer coefficient data cited by Martin, the impingement region was assumed to extend up to $r = 1.9d$, followed by a sharp transition to a turbulent wall jet. An area-weighted combination of correlations for the two regions yields

$$\frac{\overline{Nu}_L}{Pr^{0.4}} = C_1 Re_d^m \frac{l}{d} A_r + C_2 Re_L^n \frac{l}{L} (1 - A_r) \quad (17)$$

where $A_r = \pi(1.9d)^2/l^2$, and the average length of the wall jet region is given by

$$L = \frac{(0.5\sqrt{2}l - 1.9d) + (0.5l - 1.9d)}{2} \quad (18)$$

If the calculated values of A_r and L are such that either $A_r > 1$ or $L < 0$, values of 1 and 0 are assigned to A_r and C_2 , respectively. The values of m and n were set equal to 0.5 and 0.8, respectively, and optimal values of C_1 and C_2 were obtained by a least-squares technique using only the data obtained for separation distances in the range $1.5 < S/d \leq 4$. The values were determined to be $C_1 = 0.785$ and $C_2 = 0.0257$. The correlation was determined for both water ($Pr \approx 7$) and FC-77 ($Pr \approx 25$) over the range of parameters shown in Table 2. Data obtained with the 0.978 mm nozzle, and with the 1.65 mm and 3.11 mm diameter nozzles for $Re_d < 4500$, deviated substantially from the other data and were not included in developing the correlation. The correlation is within ± 16 percent of the data for which it was determined, with an average error of ± 7.2 percent and a standard deviation of 8.4 percent. When the 0.978 mm nozzle data and the low Re_d data for the 1.65 mm and 3.11 mm nozzles are included, the correlation is within ± 47 percent of all the data, the average error is ± 11 percent, and the standard deviation is 14 percent. The correlation is compared with the entire data set in Fig. 13, and in general, the agreement is observed to be quite good.

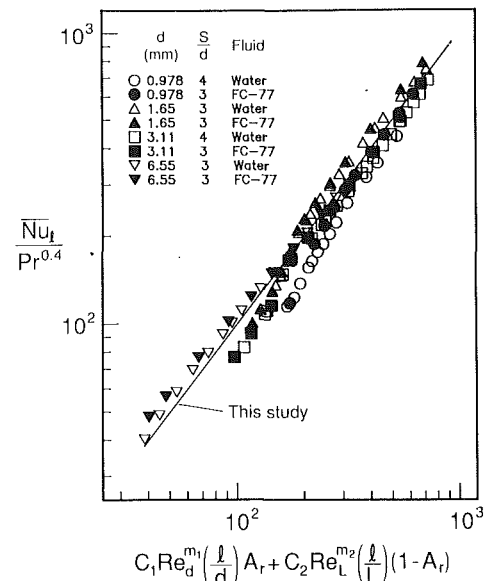


Fig. 13 Comparison of submerged jet data with correlation of this study

Conclusions

Experimental data have been presented for heat transfer from small square heat sources cooled by circular impinging liquid jets, under both free-surface and submerged jet conditions. The data trends suggest that several different effects, both hydrodynamic and thermal, combine to influence the heat transfer coefficient. Under free-surface jet conditions, the heat transfer coefficient can be attenuated by bulk warming of the thin fluid sheet flowing over the surface, if the nozzle diameter is small and the flow velocity is low. Conversely, with large nozzles and very low nozzle exit velocities, the impingement velocity and heat transfer coefficient can be enhanced by gravitational acceleration of the jet. Under submerged jet conditions, the heat transfer coefficient is influenced by the location of the heater relative to the potential core of the jet. While for $S/d \leq 4$ the heat transfer coefficient varies weakly with the separation distance, much stronger variations exist for greater values of S/d . For $Re_d \geq 4000$, the heat transfer coefficient is greater under submerged jet conditions than under free-surface jet conditions, due to turbulence generated in the shear layer of the submerged jet.

Prior studies of both free-surface and submerged jet impingement heat transfer have resulted in the development of several correlating equations for the heater-average Nusselt number. In view of the complexity of the hydrodynamic and thermal phenomena involved, it is not surprising that each of these correlations is applicable over somewhat restricted ranges of the pertinent dimensionless groups. The present data have been obtained over parameter ranges applicable to the cooling of microelectronic chips. Since some of the data deviate substantially from the predictions of previously developed correlations, new correlating equations have been developed based on the present data. Each of the two correlations, one applicable to free-surface jet impingement and the other to submerged jet impingement, is an area-weighted combination of separate correlations for the impingement and wall jet regions. These correlations may be useful in the development of liquid jet impingement cooling schemes for future high-heat flux electronic chips.

References

- Bergles, A. E., 1986, "The Evolution of Cooling Technology for Electrical,

- Electronic, and Microelectronic Equipment," *Heat Transfer in Electronic Equipment 1986*, ASME HTD-Vol. 57, pp. 1-9.
- Brdlik, P. M., and Savin, V. K., 1965, "Heat Transfer Between an Axisymmetric Jet and a Plate Normal to the Flow," *Journal of Engineering Physics*, Vol. 8, pp. 91-98.
- Burmeister, L. C., 1983, *Convective Heat Transfer*, Wiley, New York, pp. 312-319, 384-393.
- Chaudhury, Z. H., 1964, "Heat Transfer in a Radial Liquid Jet," *Journal of Fluid Mechanics*, Vol. 20, Part 3, pp. 501-511.
- Chu, R. C., and Simons, R. E., 1984, "Thermal Management of Large Scale Digital Computers," *The International Society for Hybrid Microelectronics*, Vol. 7, No. 3, pp. 35-43.
- Dawson, D. A., and Trass, O., 1966, "Mass Transfer in a Turbulent Radial Wall Jet," *The Canadian Journal of Chemical Engineering*, Vol. 44, pp. 121-129.
- Faggioli, S., and Grassi, W., 1990, "Round Liquid Jet Impingement Heat Transfer: Local Nusselt Numbers in the Region With Non-zero Pressure Gradient," *Proceedings of the Ninth International Heat Transfer Conference*, Vol. 4, pp. 197-202.
- Gardon, R., and Cobonpue, J., 1961, "Heat Transfer Between a Flat Plate and Jets of Air Impinging on It," *Proceedings of the Second International Heat Transfer Conference*, pp. 454-460.
- Hrycak, P., Lee, D. T., Gauntner, J. W., and Livengood, J. N. B., 1970, "Experimental Flow Characteristics of a Single Turbulent Jet Impinging on a Flat Plate," NASA TN D-5690.
- Jiji, L. M., and Dagan, Z., 1988, "Experimental Investigation of Single Phase Multi-jet Impingement Cooling of an Array of Microelectronic Heat Sources," *Cooling Technology for Electronic Equipment*, W. Aung, ed., Hemisphere Publishing Corporation, pp. 333-351.
- Kiper, A. M., 1984, "Impinging Water Jet Cooling of VLSI Circuits," *International Communications in Heat and Mass Transfer*, Vol. 11, pp. 517-526.
- Liu, X., and Lienhard, J. H., V., 1989, "Liquid Jet Impingement Heat Transfer on a Uniform Flux Surface," *Heat Transfer Phenomena in Radiation, Combustion, and Fires*, ASME HTD-Vol. 106, pp. 523-530.
- Liu, X., Lienhard, J. H., V., and Lombarda, J. S., 1991, "Convective Heat Transfer by Impingement of Circular Liquid Jets," *ASME JOURNAL OF HEAT TRANSFER*, Vol. 113, pp. 571-582.
- Ma, C. F., Tian, Y. Q., Sun, H., Lei, D. H., and Bergles, A. E., 1988, "Local Characteristics of Heat Transfer From a Small Heater to an Impinging Round Jet of Liquid of Larger Pr Number," presented at the International Symposium on Heat Transfer Enhancement and Energy Conservation, Canton, People's Republic of China.
- Martin, H., 1977, "Heat and Mass Transfer Between Impinging Gas Jets and Solid Surfaces," *Advances in Heat Transfer*, Vol. 13, pp. 1-60.
- Metzger, D. E., Cummings, K. N., and Ruby, W. A., 1974, "Effects of Prandtl Number on Heat Transfer Characteristics of Impinging Liquid Jets," *Proceedings of the Fifth International Heat Transfer Conference*, Vol. II, pp. 20-24.
- Nakoryakov, V. E., Pokusaev, B. G., and Troyan, E. N., 1978, "Impingement of an Axisymmetric Liquid Jet on a Barrier," *International Journal of Heat and Mass Transfer*, Vol. 21, pp. 1175-1184.
- Rao, V. V., and Trass, O., 1964, "Mass Transfer From a Flat Surface to an Impinging Turbulent Jet," *The Canadian Journal of Chemical Engineering*, Vol. 42, pp. 95-99.
- Ramadhani, S., and Incropera, F. P., 1988, "Forced Convection Cooling of Discrete Heat Sources With and Without Surface Enhancement," *Cooling Technology for Electronic Equipment*, W. Aung, ed., Hemisphere Publishing Corporation, pp. 317-332.
- Sitharamayya, S., and Raju, K. S., 1969, "Heat Transfer Between an Axisymmetric Jet and a Plate Held Normal to the Flow," *The Canadian Journal of Chemical Engineering*, Vol. 47, pp. 365-368.
- Sparrow, E. M., and Lee, L., 1975, "Analysis of Flow Field and Impingement Heat/Mass Transfer Due to a Nonuniform Slot Jet," *ASME JOURNAL OF HEAT TRANSFER*, Vol. 97, pp. 191-197.
- Stevens, J., and Webb, B. W., 1991, "Local Heat Transfer Coefficients Under an Axisymmetric, Single-Phase Liquid Jet," *ASME JOURNAL OF HEAT TRANSFER*, Vol. 113, pp. 71-78.
- Vickers, J. M. F., 1959, "Heat Transfer Coefficients Between Fluid Jets and Normal Surfaces," *Industrial and Engineering Chemistry*, Vol. 51, No. 8, pp. 967-972.
- Vlachopoulos, J., and Tomich, J. F., 1971, "Heat Transfer From a Turbulent Hot Air Jet Impinging Normally on a Flat Plate," *The Canadian Journal of Chemical Engineering*, Vol. 49, pp. 462-466.
- Wang, X. S., Dagan, Z., and Jiji, L. M., 1989a, "Heat Transfer Between a Circular Free Impinging Jet and a Solid Surface With Nonuniform Wall Temperature or Wall Heat Flux—1. Solution for the Stagnation Region," *International Journal of Heat and Mass Transfer*, Vol. 32, No. 7, pp. 1351-1360.
- Wang, X. S., Dagan, Z., and Jiji, L. M., 1989b, "Heat Transfer Between a Circular Free Impinging Jet and a Solid Surface With Nonuniform Wall Temperature or Wall Heat Flux—2. Solution for the Boundary Layer Region," *International Journal of Heat and Mass Transfer*, Vol. 32, No. 7, pp. 1361-1371.
- Wang, X. S., Dagan, Z., and Jiji, L. M., 1989c, "Conjugate Heat Transfer Between a Laminar Impinging Liquid Jet and a Solid Disk," *International Journal of Heat and Mass Transfer*, Vol. 32, No. 11, pp. 2189-2197.
- Wolf, D. H., Viskanta, R., and Incropera, F. P., 1990, "Local Convective Heat Transfer From a Heated Surface to a Planar Jet of Water With a Non-uniform Velocity Profile," *ASME JOURNAL OF HEAT TRANSFER*, Vol. 112, pp. 899-905.
- Womac, D. J., 1989, "Single Phase Axisymmetric Liquid Jet Impingement Cooling of Discrete Heat Sources," M.S. Thesis, Purdue University.
- Womac, D. J., Aharoni, G., Ramadhani, S., and Incropera, F. P., 1990, "Single Phase Liquid Jet Impingement Cooling of Small Heat Sources," *Heat Transfer—1990, Proceedings of the Ninth International Heat Transfer Conference*, Vol. 4, pp. 149-154.
- Yamamoto, H., Udagawa, Y., and Suzuki, M., 1987, "Cooling System for FACOM M-780 Large-Scale Computer," *Cooling Technology for Electronic Equipment*, W. Aung, ed., Hemisphere Publishing Corporation, pp. 701-714.

Conjugate Heat Transfer From a Heated Disk to a Thin Liquid Film Formed by a Controlled Impinging Jet

A. Faghri

S. Thomas

M. M. Rahman¹

Department of Mechanical and
Materials Engineering,
Wright State University,
Dayton, OH 45435

An experimental and numerical study of the heat transfer from a heated horizontal disk to a thin film of liquid is described. The liquid was delivered to the disk by a collar arrangement such that the film thickness and radial velocity were known at the outer radius of the collar. This method of delivery is termed as a controlled impinging jet. Flow visualization tests were performed and heat transfer data were collected along the radius of the disk for different volumetric flow rates and inlet temperatures in the supercritical and subcritical regions. The heat transfer coefficient was found to increase with flow rate when both supercritical and subcritical regions were present on the heated surface. A numerical simulation of this free surface problem was performed, which included the effects of conjugate heat transfer within the heated disk and the liquid. The numerical predictions agree with the experimental results and show that conjugate heat transfer has a significant effect on the local wall temperature and heat transfer coefficient.

Introduction

The heat transfer from heated plates or disks due to impinging jets has received attention recently because of the high heat transfer rates that can be achieved. The types of impinging jet most useful in engineering applications are the submerged and the free liquid jets. A jet is submerged if it flows into a stagnant fluid of similar hydrodynamic properties, such as a gas jet flowing into a gaseous environment. Submerged impinging jets of air are employed to dry paper and textile products, to cool heated components of gas turbine engines, and to de-ice aircraft systems. A free liquid jet issues from a pressurized nozzle into a gas such that the liquid and gas do not interact appreciably. Therefore, the free liquid jet impinges on the heated surface with little change in its hydrodynamic characteristics, whereas the submerged jet spreads into the surrounding medium due to viscous diffusion. Free liquid jet impingement cooling is used in the production of sheets of glass and metal products. Both submerged air jets and free liquid jets have been investigated with respect to cooling electronic components.

When a free liquid jet impinges normally onto a horizontal surface, the liquid spreads out into a thin film flowing radially away from the stagnation point. At some radial distance, the liquid film thickness increases dramatically and the velocity of the film decreases due to continuity. This phenomenon is called a circular hydraulic jump and is an exchange between the momentum of the thin, fast-moving film (supercritical region) and the hydrostatic pressure of the thick, slow-moving liquid downstream from the jump (subcritical region).

The flow of a free liquid jet impinging normally on a surface was first studied by Watson (1964). The thin film from the stagnation point to the hydraulic jump was analyzed by using inviscid theory, boundary-layer theory, and a similarity solution using the Pohlhausen integral technique for different

regions of the flow. The heat transfer from a constant-temperature plate to the thin film in the same regions studied by Watson was analyzed in a similar fashion by Chaudhury (1964).

Azuma and Hoshino (1984) presented experimental measurements of fluid flow in a radially spreading thin film discharging from a cylindrical gap formed between a circular nozzle and a flat glass plate. In different parts of their paper, the criteria for laminar-turbulent transition, the film thickness, the velocity profile across the film, stability criteria, and wall pressure fluctuations were presented. Ishigai et al. (1977) experimentally measured the liquid film thickness and heat transfer from a thin film generated by an impinging liquid jet onto a perpendicular surface. Craik et al. (1981) studied the circular hydraulic jump formed by an impinging jet of liquid on a horizontal plate. The film thickness in the region near the hydraulic jump was measured using a light absorption technique with a laser and a strong dye. Their flow visualization studies showed the presence of an eddy just downstream of the jump.

More recently, Stevens and Webb (1991) measured local heat transfer coefficients from an electrically heated plate to a round impinging free jet of water. Correlations were developed for the stagnation point, local, and average Nusselt numbers. The controlled parameters were the jet Reynolds number, the nozzle-to-plate spacing, and the jet diameter. While the hydraulic jump was seen in the experiment and a correlation for the radius of the jump was given in terms of jet diameter and Reynolds number, the heat transfer coefficient was measured only in the supercritical region; that is, from the stagnation point to the hydraulic jump.

Vader et al. (1991) measured local heat transfer coefficients from a heated plate to a planar impinging free jet of water. The jet velocity and temperature were controlled parameters. The authors gave correlations for the local and stagnation point Nusselt numbers. It was found that the free-stream turbulence intensity, Prandtl number, and velocity gradient in the stagnation region can influence the heat transfer enhancement factor, which is the ratio of the measured Nusselt number to the Nusselt number for a flow with zero free-stream turbulence.

The conjugate heat transfer between a laminar impinging free liquid jet and a solid disk was studied by Wang et al.

¹Present address: Mainstream Engineering Corp., 200 Yellow Place, Rockledge, FL 32955.

Contributed by the Heat Transfer Division and presented at the National Heat Transfer Conference, Minneapolis, Minnesota, July 28-31, 1991. Manuscript received by the Heat Transfer Division July 29, 1991; revision received May 27, 1992. Keywords: Conjugate Heat Transfer, Jets, Rotating Flows. Associate Technical Editor: F. P. Incropera.

(1989). The heat transfer was calculated in the solid and liquid regions independently and matched at the interface. For the liquid film, the radial conduction was neglected except for the stagnation region, where the jet actually impinged on the surface. The analysis was limited to the supercritical region before the hydraulic jump.

Many researchers in the past have examined the heat transfer from a disk due to the presence of a normally impinging free liquid jet. In the present study, however, it was desired to determine the heat transfer due to a thin film that issues from a narrow pressurized cylindrical opening near the center of the disk, which is termed a controlled impinging liquid jet. With a controlled impinging jet, the liquid film is first formed between the horizontal plate and a coaxial disk (collar) near the center of the plate. The collar is set to some specified distance above the plate, which is the inlet height of the thin film. The liquid film then emerges onto the horizontal plate from between the collar and the plate, at which point it is a free surface flow. There is a development length from the outer radius of the collar where the thin film develops from a Poiseuille-type flow to a free surface flow. Depending on the Froude number at the inlet (outer radius of the collar), a circular hydraulic jump may or may not occur on the horizontal plate. The difference between the free and the controlled liquid impinging jets is that there is no stagnation point in a controlled jet. Also, due to the collar above the disk, the flow is contained between two circular, coaxial disks before being ejected onto the surface of the heated disk. This makes comparison between the free and controlled impinging jets difficult not only due to the different flow structures, but also due to the different length scales involved. The motivation for the present fundamental study is directed toward physical modeling of a controlled liquid impinging jet, related to a vapor-absorption refrigeration cycle, which is an attractive option for use in a microgravity environment due to the elimination of the vapor compressor and due to the availability of waste heat. The controlled liquid impinging jet is also of significant interest in many heat pump, heat exchanger, and space electronic cooling applications.

Thomas et al. (1990) numerically studied the free surface flow generated by a controlled impinging liquid jet using the one-dimensional MacCormack predictor-corrector technique. This approach was chosen due to the similarity between the flow of liquid through a hydraulic jump and the flow of gas through a shock wave. The liquid film height was found for plane and radial flows under zero and normal gravity. The

hydraulic jump height and location was predicted under normal gravity for plane and radial flows. The film thickness increased monotonically for plane flow under zero gravity, while the film could either increase monotonically, or first decrease and then increase for radial flow under zero gravity.

Rahman et al. (1990) numerically evaluated the heat transfer coefficient from an isothermally heated plate and a plate with a uniform heat flux to a thin film generated by a controlled impinging liquid jet. A boundary-fitted curvilinear coordinate system was employed to solve the transport equations and boundary conditions, since the free surface was irregular and could not be handled with cartesian or cylindrical systems. Rahman et al. (1991) analytically solved the mass, momentum, and energy conservation equations using uniform and parabolic velocity profiles for plane and radially spreading flows under zero and normal gravity. Closed-form solutions of the liquid film thickness and Nusselt number were derived in some cases, whereas numerical integration of ordinary differential equations were necessary in other cases. These studies developed numerically computed distributions as well as simplified equations for the film thickness and heat transfer coefficient, which considered transport only in the liquid region with prescribed boundary conditions at the solid-fluid interface.

Thomas et al. (1991) measured the film thickness across a stationary and rotating horizontal disk using the capacitance technique, where the liquid was delivered to the disk by a controlled impinging jet. The aim was to provide an understanding of the fundamental hydrodynamic processes which occur in the flow. The film thickness upstream from the hydraulic jump was affected mainly by the inertial and frictional forces on the fluid, and the radial spreading of the film.

In all previous numerical simulation studies concerning the controlled impinging jet, the effects of conjugate heat transfer within the heated disk were not considered. It may also be mentioned here that the previous analytical study by Wang et al. (1989) was for free jet impingement, and the results were valid only for the supercritical region before the jump. In addition, no attempts were made in the previous numerical investigations for comparison with experimental heat transfer studies due to the lack of experimental data. The purpose of the present study is to measure local heat transfer coefficients from a heated disk to a controlled impinging liquid jet of distilled water. The controlled parameters in this study are the volumetric flow rate and the inlet temperature of the water. The ranges of flow rate, inlet temperature, total heat rate, inlet

Nomenclature

A = heated area, m^2	r_e = exit radius of liquid, m	\mathbf{V}_{in} = velocity vector at $r = r_{in}$, $m s^{-1}$
b = thickness of disk, m	r_{hin} = inner radius of heater (outer radius of collar), m	\mathbf{V}_{out} = velocity vector at $y = 0$, $r_{out} < r < r_e$, $m s^{-1}$
d = distance from thermocouple bead to disk-fluid interface, m	r_{hout} = outer radius of heater, m	w = component of velocity in the radial direction, $m s^{-1}$
Fr_{in} = inlet Froude number = $W_{in}/\sqrt{g\delta_{in}}$	r_{in} = inner radius of collar, m	W_{in} = average radial fluid velocity at $r = r_{hin}$, $m s^{-1}$
g = gravitational acceleration, $m s^{-2}$	r_{out} = outer radius of disk, m	α = thermal diffusivity, $m^2 s^{-1}$
h = local convective heat transfer coefficient = $(Q/A)/(T_s - T_{in})$, $W m^{-2} K^{-1}$	Re_{in} = inlet Reynolds number = $W_{in}\delta_{in}/\nu = V/(2\pi r_{hin}\nu)$	δ = liquid film thickness, m
k = thermal conductivity, $W m^{-1} K^{-1}$	t = time, s	δ_{in} = vertical distance between the disk and the collar, m
\mathbf{n} = unit vector normal to the free surface	\mathbf{t} = unit vector tangential to the free surface	ν = kinematic viscosity, $m^2 s^{-1}$
Nu = Nusselt number = $2 r_{hin}h/k_f$	T_{in} = inlet water temperature at $r = r_{in}$, K	ρ = density, $kg m^{-3}$
p = pressure, $N m^{-2}$	T_m = measured wall temperature, K	σ = surface tension, $N m^{-1}$
Pr = Prandtl number = ν/α	T_s = temperature at disk-fluid interface, K	$\boldsymbol{\tau}$ = stress tensor, $N m^{-2}$
Q = total heat input, W	v = component of velocity in the normal direction, $m s^{-1}$	
r = radial location, m	V = volumetric flow rate, $m^3 s^{-1}$	
	\mathbf{V} = velocity vector, $m s^{-1}$	

Subscripts

f = fluid
 w = wall

Table 1 Experimental parameters

Case No.	V (lpm)	T _{in} (°C)	Q (W)	Re _{in}	Pr	Fr _{in}
1	2.0	20.6	1513	102.	7.18	8.24
2	2.0	25.1	1515	114.	6.32	8.24
3	2.0	30.3	1526	129.	5.47	8.24
4	2.0	35.2	2017	145.	4.78	8.24
5	2.0	39.8	1990	162.	4.22	8.24
6	3.0	20.2	2014	151.	7.29	12.36
7	3.0	24.8	1999	169.	6.38	12.36
8	3.0	29.9	2027	192.	5.53	12.36
9	3.0	35.0	2035	217.	4.81	12.36
10	3.0	40.1	2000	244.	4.19	12.36
11	4.0	19.5	1973	198.	7.41	16.48
12	4.0	25.0	2005	227.	6.34	16.48
13	4.0	30.0	2017	256.	5.51	16.48
14	4.0	34.9	2027	288.	4.82	16.48
15	4.0	39.9	1995	324.	4.21	16.48
16	5.0	20.3	2258	253.	7.25	20.60
17	5.0	25.2	3058	285.	6.31	20.60
18	5.0	29.8	3113	319.	5.55	20.60
19	5.0	35.0	3004	361.	4.81	20.60
20	5.0	40.0	2982	406.	4.20	20.60
21	6.0	19.7	1752	299.	7.37	24.72
22	6.0	25.1	3020	341.	6.32	24.72
23	6.0	30.1	2982	385.	5.50	24.72
24	6.0	35.0	3010	433.	4.81	24.72
25	6.0	40.1	2991	488.	4.19	24.72
26	7.0	20.0	2215	351.	7.31	28.84
27	7.0	25.0	3157	397.	6.34	28.84
28	7.0	29.9	3157	447.	5.53	28.84
29	7.0	35.1	3209	507.	4.79	28.84
30	7.0	40.0	3125	568.	4.20	28.84
31	8.0	24.6	3079	449.	6.41	32.96
32	8.0	30.0	3095	513.	5.51	32.96
33	8.0	35.1	3092	579.	4.79	32.96
34	8.0	40.1	3092	651.	4.19	32.96

Reynolds number, Prandtl number, and inlet Froude number are given in Table 1. Furthermore, a complete numerical simulation of this free surface problem including the effects of conjugate heat transfer in the supercritical, jump, and subcritical regions is carried out for comparison with the experimental data.

Experimental Setup

The purpose of the experiment was to determine the basic phenomena associated with heat transfer from a stationary disk to a thin liquid film of distilled, deionized water. The thin film was generated on the disk by a controlled impinging liquid jet, where the liquid emanates from a pressurized vessel in the center of the stationary disk.

The schematic of the experimental setup is shown in Fig. 1. The 406.4-mm-dia, 6.35-mm-thick disk was mounted onto a hollow high-precision stainless steel spindle. The stainless steel collar was 101.6 mm in diameter. The disk was made of 6061 aluminum with a surface finish of 3.8×10^{-4} mm, flatness 2×10^{-3} mm, and thermal conductivity $k_w = 155 \pm 7 \text{ W m}^{-1} \text{ K}^{-1}$ (Miner and Seastone, 1955). The working fluid flowed from the circulating pump to the hollow spindle. The liquid then passed up above the disk and through eight 3.17-mm-dia radial holes in the hollow spindle, which were covered by the collar. The collar directed the eight liquid streams down and outward so that the fluid flowed onto the top side of the disk with a velocity only in the radial direction. The collar also made sure that the height of the liquid at the collar did not change with respect to the azimuthal direction. Uniformity of the fluid flow in the azimuthal direction was checked by noting the variation in the radial location of the hydraulic jump. At the points where the eight radial liquid jets exited through the vertical shaft, the radius of the hydraulic jump was increased

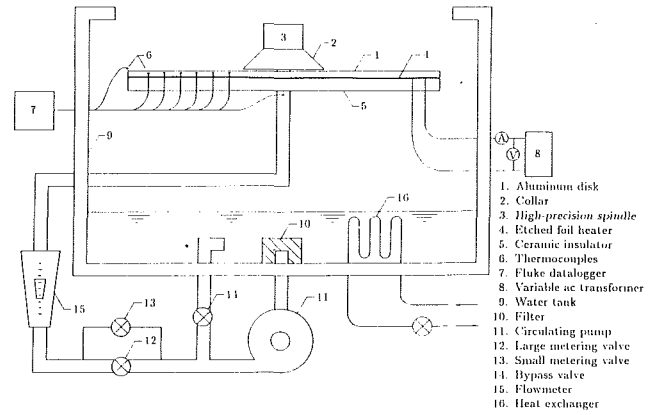


Fig. 1 Experimental setup for the controlled liquid impinging jet

by less than 5 mm for the maximum flow rate. This uniformity is due to the small gap height and the relatively long radial extent of the collar. The vertical distance between the disk and the collar ($\delta_{in} = 0.254 \text{ mm}$) was set by a stainless steel shim. After the fluid flowed over the disk, it was collected by the water tank to be recirculated. The flow rate of the liquid, ranging from 2.0 to 8.0 lpm in steps of 1.0 lpm, was varied by the large and small metering valves, which provided the gross and fine adjustments. The volumetric flow rate was determined by the in-line flowmeter, which had an uncertainty of ± 5 percent of the reading.

A flat etched foil heater (Minco Products, Inc., Minneapolis, MN) between the underside of the disk and the ceramic insulator was used to heat the aluminum disk. The ceramic insulator was disk-shaped with an outside diameter of 371.4 mm, thickness 16.27 mm, and thermal conductivity $0.15 \text{ W m}^{-1} \text{ K}^{-1}$. The heater was held between the disk and the insulation by screws through the ceramic insulator, which were threaded into the disk. A piece of flexible backing insulation was placed between the heater and the ceramic insulator so that the heater was evenly compressed against the disk. The heater was 0.635 mm thick with an outside diameter of 356 mm and inside diameter 101.6 mm, which was the same as the outside diameter of the collar. A variable a-c transformer was used to power the heater, and two Fluke multimeters were used to measure the voltage and amperage, which resulted in a combined uncertainty of ± 2 percent of the power reading. Six type T thermocouples with uncertainties of $\pm 0.5^\circ \text{C}$ were mounted in evenly spaced 1.5-mm-dia holes in the underside of the disk to monitor the temperature of the disk. An epoxy with a high thermal conductivity was used to secure the thermocouples in place and to fill the thermocouple wells, so that the effects of removing the material from the disk were minimized. The distance from the thermocouple beads to the surface of the disk was measured to be $d = 1.52 \pm 0.1 \text{ mm}$. A type T thermocouple probe with an uncertainty of $\pm 0.5^\circ \text{C}$ was placed inside the hollow spindle just before the collar to measure the inlet water temperature. A similar probe measured the water temperature just before the fluid exited the disk. The total heat input ranged from 1500 W at 2.0 lpm to 3000 W at 8.0 lpm to obtain temperature differences ($T_s - T_{in}$) large enough for accurate measurements of the heat transfer coefficient. The uncertainty of the reported heat transfer coefficient data was calculated by the method given by Miller (1989) to be within ± 12 percent. A heat exchanger was placed in the water tank to vary the inlet water temperature from 20 to 40°C in steps of 5°C . A bypass valve was used to circulate the water over the heat exchanger to achieve the maximum heat transfer possible from the system.

A Fluke Datalogger was used to collect and temporally average the temperature measurements. Data were taken every

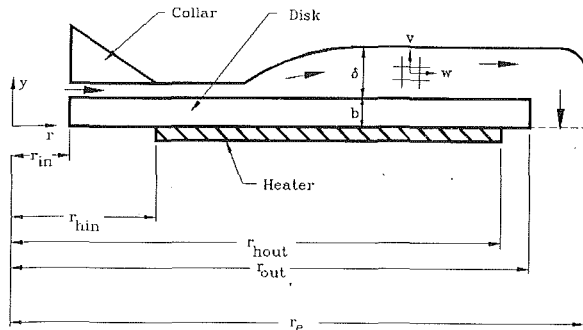


Fig. 2 Schematic of the heated disk

ten minutes until a steady condition was reached, at which time the steady-state temperatures were recorded. The disk surface temperatures were estimated by the one-dimensional Fourier law of heat conduction to be $T_s = T_m - (Q/A)(d/k_w)$. The validity of this assumption is discussed later in the paper. The heat loss through the insulation was estimated to be less than 1 percent, so no correction was made in the reduced data. The properties of water were evaluated at the inlet temperature. Duplicate tests were periodically run in order to check the repeatability of the data, which was always within ± 5 percent. The overall uncertainty of the measured Nusselt number values was estimated to be ± 13 percent, and that of the dimensionless radial distance was ± 2 percent.

Numerical Simulation

The fluid is discharged axisymmetrically through a slot at the center of the disk and flows radially to the edge where it encounters a free fall due to gravity. Depending on the flow rate, the flow may encounter a hydraulic jump where the incoming supercritical flow transforms to a subcritical flow downstream from the jump. Part of the disk is electrically heated from the bottom, producing a uniform heat flux. Heat is transferred via conduction through the disk wall and by convection from the top surface to the liquid film. The coordinate system used for the numerical model is shown in Fig. 2. The computation domain consists of the solid disk of thickness b and liquid film of thickness δ , extending over the radial distance $r_e - r_{in}$. The flow was assumed to be laminar and incompressible. The fluid was assumed to be Newtonian in nature. The temperature changes in the system were assumed to be small enough to produce insignificant changes in the solid or fluid properties. The equations governing the conservation of mass, momentum, and energy in the fluid region for constant properties are:

$$\nabla \cdot \mathbf{V} = 0 \quad (1)$$

$$\frac{D\mathbf{V}}{Dt} = -\frac{1}{\rho} \nabla p + \nu \nabla^2 \mathbf{V} + \mathbf{g} \quad (2)$$

$$\frac{DT_f}{Dt} = \alpha \nabla^2 T_f \quad (3)$$

In the solid region, $\mathbf{V} = 0$. The energy equation can be written as

$$\nabla^2 T_w = 0 \quad (4)$$

The boundary conditions are as follows:

at the entrance ($r = r_{in}$):

$$0 < y < b: \frac{\partial T_w}{\partial r} = 0 \quad (5a)$$

$$b < y < b + \delta_{in}: \mathbf{V} = \mathbf{V}_{in}, T_f = T_{in} \quad (5b)$$

at the exit ($y = 0, r_{out} < r < r_e$):

$$\mathbf{V} = \mathbf{V}_{out}, \frac{\partial T_f}{\partial y} = 0 \quad (6)$$

at the bottom wall ($y = 0$):

$$r_{in} < r < r_{hin}: \frac{\partial T_w}{\partial y} = 0 \quad (7a)$$

$$r_{hin} < r < r_{hout}: -k_w \frac{\partial T_w}{\partial y} = q_w \quad (7b)$$

$$r_{hout} < r < r_{out}: \frac{\partial T_w}{\partial y} = 0 \quad (7c)$$

at the free surface ($y = b + \delta, r_{hin} < r < r_{out}$):

$$\underline{\tau} \cdot \mathbf{n} = 0, \underline{\tau} \cdot \mathbf{t} = 0, \frac{d\delta}{dr} = \frac{v}{w}, \frac{\partial T_f}{\partial n} = 0 \quad (8a)$$

$$\delta = \delta_{out}(\text{at } r = r_{out}) \quad (8b)$$

at the bottom face of the collar ($y = b + \delta_{in}, r_{in} < r < r_{hin}$):

$$\mathbf{V} = 0, \frac{\partial T_f}{\partial y} = 0 \quad (9)$$

at the disk-fluid interface:

$$\mathbf{V} = 0, T_w = T_f \quad (10a)$$

$$k_w \frac{\partial T_w}{\partial y} = k_f \frac{\partial T_f}{\partial y} \quad (y = b, r_{in} < r < r_{out}) \quad (10b)$$

$$k_w \frac{\partial T_w}{\partial r} = k_f \frac{\partial T_f}{\partial r} \quad (0 < y < b, r = r_{out}) \quad (10c)$$

Here b is the thickness of the disk, δ_{in} is the vertical distance between the disk and the collar, $r_{hin} - r_{in}$ is the radial extent of the collar, $r_{hout} - r_{hin}$ is the radial extent of the heater, and n is the coordinate directed normal to the free surface. The free surface of the film does not encounter a strong surface tension in most regions except very close to the exit. Therefore, from a scaling argument, it can be proven that for a thin film, the $\underline{\tau} \cdot \mathbf{n}$ condition can be written as $p = 0$, where p is the difference between the static pressure of the fluid and that of the surrounding medium. The film height at the outer radius of the disk was determined by taking into account the gravity-driven discharge of the fluid and the surface tension in that region (Rahman et al., 1992).

$$\delta_{out} = \frac{\left(\frac{V}{2\pi r_{out} \sqrt{g}}\right)^{2/3} + \sqrt{\left(\frac{V}{2\pi r_{out} \sqrt{g}}\right)^{4/3} + \frac{8\sigma}{\rho g}}}{2} \quad (11)$$

The radial location of the free surface at the exit is given by

$$r_e = r_{out} + 0.5\delta_{out} \quad (12)$$

The location of the free surface between the outer radius of the disk ($r = r_{out}$) and the actual exit ($r = r_e$) was approximated by a quarter circular arc and a vertical straight line. The velocities \mathbf{V}_{in} and \mathbf{V}_{out} were assumed to be uniform over the cross section and their magnitudes were obtained from the given flow rate. The free surface height between the radial locations $r_{hin} < r < r_{out}$ was determined by an iterative procedure, where the mass and momentum conservation equations in the fluid region were solved. The procedure, the pressure optimization method, was originally developed by Rahman et al. (1990) and later improved by Rahman et al. (1992). In this procedure, the supercritical and subcritical flows were solved separately and the location of the jump was ascertained from a basic momentum balance. In each region, the free surface was approximated by an algebraic equation with a number of arbitrary constants. These constants were optimized by an exhaustive search technique, which minimized the error in the pressure distribution on the free surface. Once the location of the free

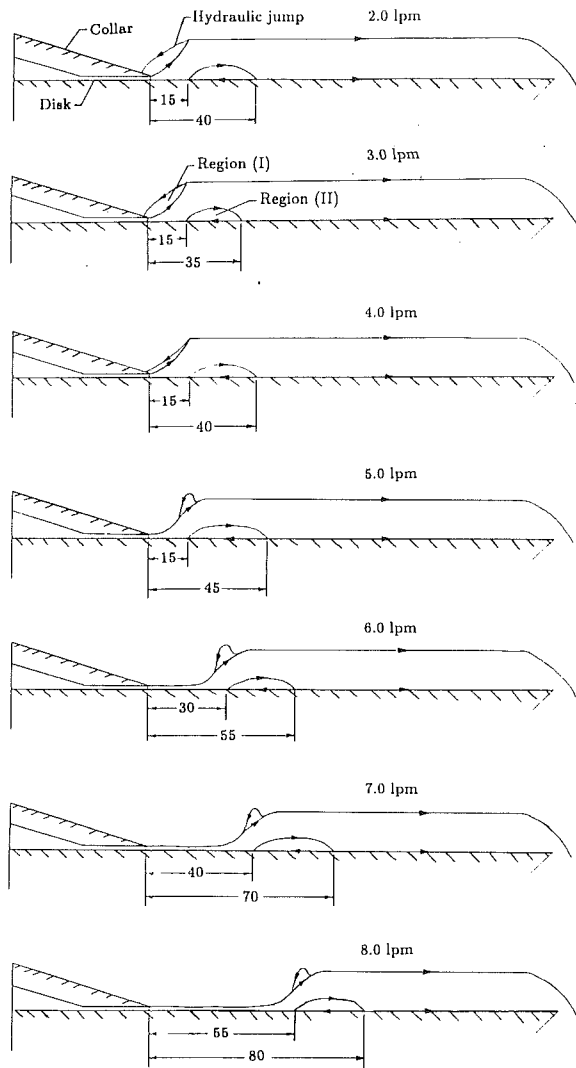


Fig. 3 Locations of hydraulic jump and recirculation regions (lengths in mm, vertical axis exaggerated for clarity)

surface in the supercritical and subcritical regions and the location and slope of the jump were completely determined, the energy equations in the solid and fluid regions were solved as a conjugate problem.

For the calculations of fluid flow and conjugate heat transfer, a boundary-fitted curvilinear coordinate system was used. The irregular free surface conformed to one of the boundaries of the computation domain. In the solid region, 20 cells across the thickness of the disk and 50 cells in the radial direction were used. In the fluid region, 30 cells were used across the thickness of the film and 50 cells were used in the radial direction between r_{in} and r_{out} . Between r_{out} and r_e , 5 cells in the radial direction and 50 cells normal to that were used to complete the computation domain. The distributions of cells were uniform in each of the solid and fluid regions between r_{in} and r_{out} . Between r_{out} and r_e , a uniform distribution was used in the radial direction, whereas in the y direction, a thickness of $b/20$ was used for the first 20 cells to match with the adjacent solid cells, and the remaining cells were uniformly distributed. The solution was checked for grid independence by comparing the computed results with different numbers of grids in the solid and fluid regions. With a gradual increase in the number of grid cells in both the solid and fluid regions, it was found that the computed heat transfer coefficient distribution converged to a single solution. No significant changes were seen beyond the number of cells used here for the computations.

Comparing results for 30×50 cells in the fluid region over the disk with results for 20×45 cells, the difference in the heat transfer coefficient was within 2 percent. Similarly, in the solid region, the results corresponding to 25×50 cells and 20×50 cells showed a maximum difference of 0.1 percent. The governing equations were discretized using the control-volume approach preserving the primary physical variables and solved using the SIMPLEST algorithm.

Results and Discussion

Flow Visualization. Before discussing the results of the heat transfer experiment, some comments concerning the general hydrodynamics of this particular flow are in order. Figure 3 shows the general flow structure of the liquid film for the full range of flow rates considered. Dye was injected into the flow with a small diameter hypodermic needle near the free surface and near the disk to determine the radial extent of the recirculation regions around the hydraulic jump. The film thickness in the subcritical region is depicted to be constant, which is valid away from the hydraulic jump and the edge of the disk (Thomas et al., 1991). Near the edge of the disk, the film thickness decreases as the liquid accelerates and falls off the disk. The direction of the flow is denoted by arrows in the figures. The exact radial locations of the recirculation regions and the hydraulic jump were difficult to measure due to the fluctuating nature of the flow. Therefore, uncertainties in the radial measurements were conservatively estimated to be on the order of ± 5 mm.

In all cases, two regions of recirculation were present. The first region (I) rode on top of the hydraulic jump, and the second region (II) was adjacent to the disk immediately downstream from the jump. Even though the first recirculation region could not be traced numerically, due to the approximate nature of the film height distribution in the vicinity of the hydraulic jump, the second region was found to be present in the numerical computation (Rahman et al., 1992). At low flow rates (2.0 to 4.0 lpm), region I was attached to the collar where the flow was introduced to the disk. In this case, a supercritical region was not present. As the flow rate increased from 2.0 to 4.0 lpm, the length of region I was nearly constant. However, the thickness of the liquid film adjacent to the collar decreased and the cross-sectional shape of region I narrowed, as shown in Fig. 3. At higher flow rates (> 4.0 lpm), region I detached from the collar and became a "roller" residing on top of the hydraulic jump. The length and location of region II was nearly the same for flow rates from 2.0 to 5.0 lpm. For higher flow rates, region II traveled downstream with the hydraulic jump. The length of region II was nearly constant at approximately 25 mm for all flow rates considered.

Heat Transfer Results. A typical experimental measurement of the disk surface temperature distribution for a flow rate of $V = 4.0$ lpm, heat input of $Q = 2000$ W, and different inlet temperatures is shown in Fig. 4. The disk temperature was lowest near the inlet since the mean fluid temperature was lowest, and the velocity gradient, which directly contributes to the heat transfer rate, was highest at this location. The disk temperature steadily increased along the radius due to convective heating. Downstream, however, the temperature of the disk decreased. This temperature decrease is due to the intersection of two thermal boundary layers forming on the disk. The first boundary layer develops from the jump location and grows downstream. The second boundary layer develops from the end of the recirculating region and grows upstream due to the direction of the recirculating flow. As the thermal boundary layer thickness increases, T_s increases. The maximum temperature corresponds to the location where the thermal boundary layers for the forward-moving flow and that for the recircu-

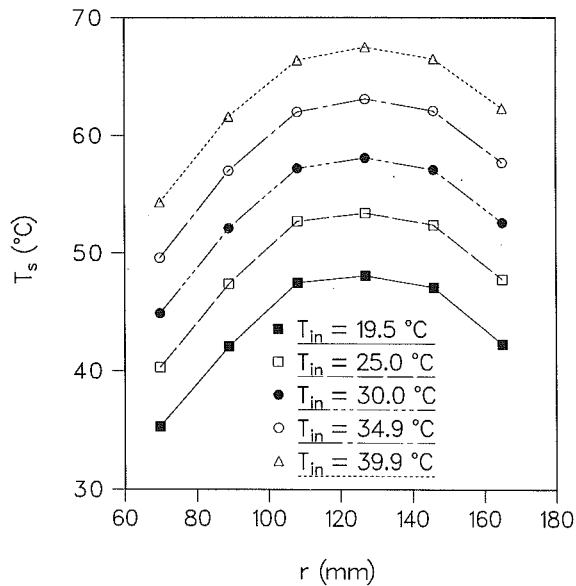


Fig. 4 Experimental surface temperature measurements along the radius for various inlet temperatures with $V = 4.0$ lpm and $Q = 2000$ W

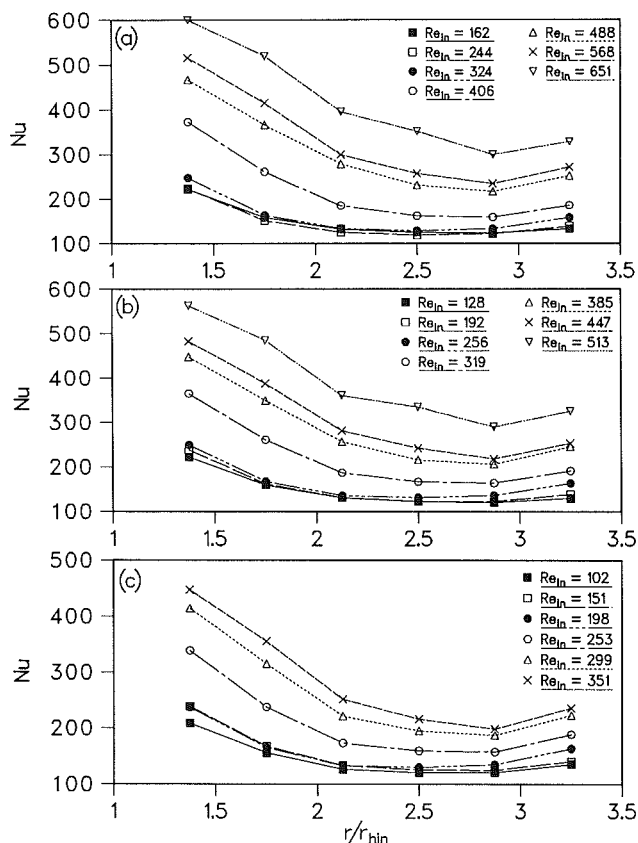


Fig. 5 Radial distribution of Nusselt number for various inlet Reynolds numbers: (a) $Pr = 4.2$, (b) $Pr = 5.5$, (c) $Pr = 7.3$

lating flow intersect each other. As the inlet temperature increased, the wall temperatures along the disk for the same heat rate increased accordingly.

The Nusselt number Nu versus the dimensionless radial distance r/r_{hin} is presented in Fig. 5 for Prandtl numbers of $Pr = 4.2, 5.5,$ and 7.3 and different values of the inlet Reynolds number Re_{in} . In all three cases, Nu decreased across the disk and then increased due to the interaction of the thermal boundary layers in the subcritical region as discussed above. At the

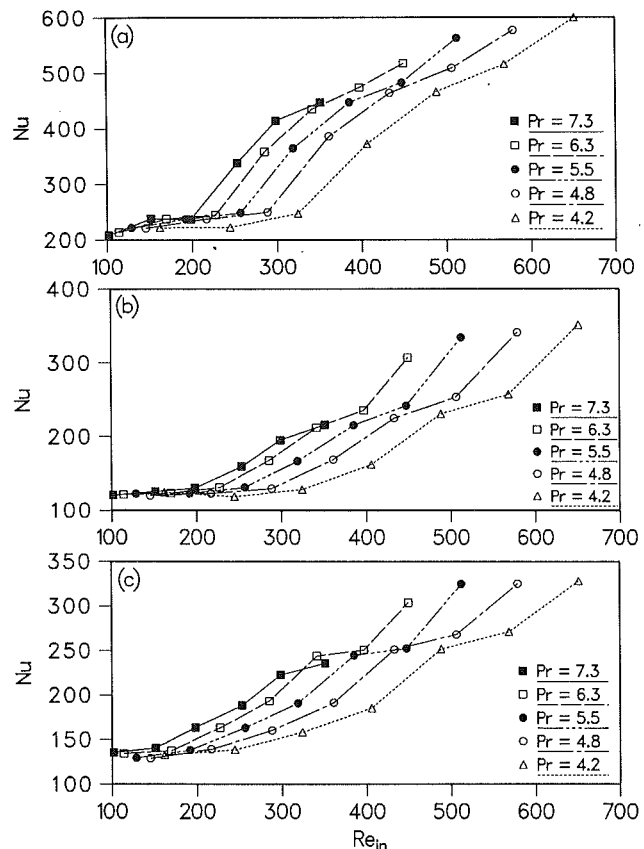


Fig. 6 Nusselt number versus Reynolds number for various Prandtl numbers: (a) $r/r_{hin} = 1.375$, (b) $r/r_{hin} = 2.500$, (c) $r/r_{hin} = 3.250$

three lowest Reynolds number values in each graph, the profile of Nu remained nearly the same. For the higher values of Re_{in} , however, Nu increased dramatically. The Reynolds numbers at this sudden increase correspond to $V = 5.0$ lpm, where the hydraulic jump was first pushed away from the collar. At this flow rate, the flow became supercritical over part of the heated surface. In the supercritical region, the liquid film is thinner and fluid velocity is higher than that in the subcritical region. Therefore, a larger heat transfer coefficient is expected. As the flow rate increased, the fluid velocity near the wall and the extent of the supercritical region increased, both of which contribute to the enhancement of heat transfer from the disk surface to the fluid stream.

The sudden increase in Nu at a particular flow rate is also shown in Fig. 6, where the Nusselt number is plotted versus Re_{in} at $r/r_{hin} = 1.375, 2.5,$ and 3.25 and different Pr . In all cases, the transition occurred at lower Re_{in} for higher values of Pr due to the change in the kinematic viscosity over the temperature range. However, the general trend is that Nu was nearly constant until it suddenly increased as Re_{in} increased through a critical value.

Figure 7(a) shows the distribution of the measured temperatures at the thermocouple locations, and the corresponding computed temperature at that location for a flow rate of 2.0 lpm. The measured and computed temperatures both show the same trend: The temperature increased with radial distance, attained a peak and decreased farther downstream. Comparing the magnitudes of temperature at different locations, it was found that the numerical prediction was within 10 percent of the measured value. This difference may be attributed to the uncertainties in the experimental measurements as well as approximations associated with theoretical modeling and finite-difference computation. The temperatures at thermocouple locations corresponding to flow rates of 4.0 lpm and 7.0 lpm

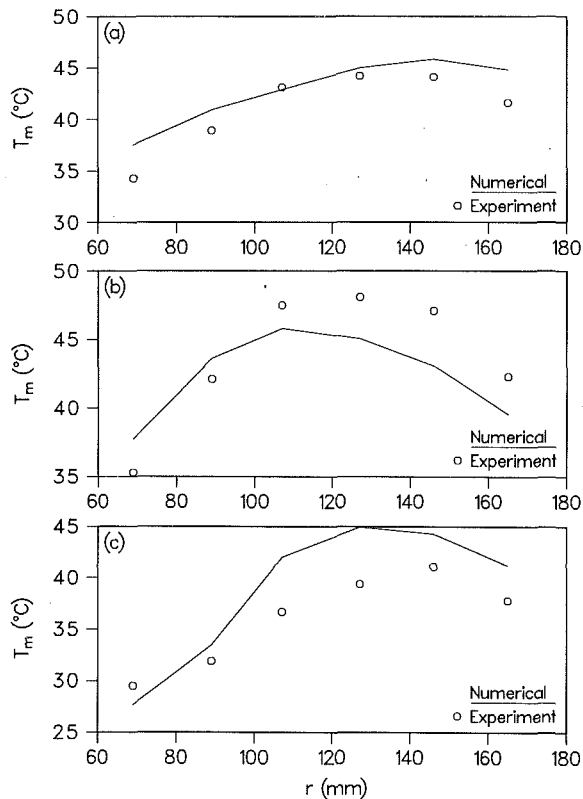


Fig. 7 Comparison of the measured and computed radial temperature distribution for $T_{in} = 20^\circ\text{C}$: (a) 2.0 lpm, $Q = 1500\text{ W}$, (b) 4.0 lpm, $Q = 2000\text{ W}$, (c) 7.0 lpm, $Q = 2200\text{ W}$

are shown in Figs. 7(b) and 7(c), respectively. In both plots, the measured and computed results showed the same trend, and the values were within 15 percent.

The validity of using the one-dimensional Fourier heat conduction approximation in determining the disk surface temperature can be seen in Fig. 8, where the experimental heat transfer coefficient is compared to the numerical results. The experimental data points are all within 20 percent of the numerical data for the case that includes the effect of conjugate heat transfer. The heat transfer coefficient distribution at a flow rate of 2.0 lpm is plotted in Fig. 8(a). The results corresponding to conjugate heat transfer using the actual disk thickness show a good comparison with the experimental measurements. The decrease of the heat transfer coefficient at smaller radii was due to the development of a thermal boundary layer. The heat transfer coefficient attained a minimum and then increased farther downstream due to the thickening and subsequent thinning of the thermal boundary layer in the downstream direction. It can be seen in Fig. 8 that the numerical results both with and without conjugate effects predict this increase in the downstream region. Figure 8(a) also shows the heat transfer coefficient distribution corresponding to a disk of zero thickness, where the conjugate effect was absent. The heat transfer coefficient increased downstream monotonically, except at very small radii where the heating was started. In the absence of any conduction in the disk wall, the heat flux remained constant across the heated area and zero at locations where heating was absent. In this case, the heat transfer coefficient was dependent only on the fluid motion. In the presence of conduction at the wall, however, the heat was transmitted to the areas where heating was not provided, and the heat flux at the disk-fluid interface depended on the rate at which heat could be carried out by convection and that which could be supplied by the wall via conduction. It may also be mentioned here that the heat transfer coefficient in the present work was defined in terms of the input heat flux ($Q/$

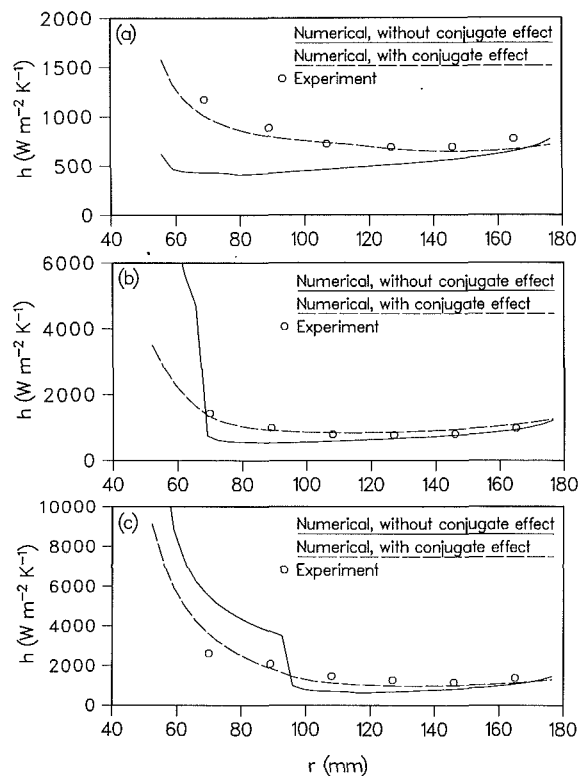


Fig. 8 Effect of conjugate heat transfer on the radial heat transfer coefficient distribution for $T_{in} = 20^\circ\text{C}$: (a) 2.0 lpm, $Q = 1500\text{ W}$, (b) 4.0 lpm, $Q = 2000\text{ W}$, (c) 7.0 lpm, $Q = 2200\text{ W}$

A), in contrast to the actual interfacial heat flux commonly used in the analysis of conjugate heat transfer (Faghri et al., 1989). Since the input heat flux was constant over the entire heated area, the disk surface temperature was the only variable in the definition of the heat transfer coefficient. This new definition, however, was essential to facilitate a comparison of the numerical results with the experimental data, since the interfacial heat flux was unknown in the experiment.

The distribution of the heat transfer coefficient for a flow rate of 4.0 lpm is plotted in Fig. 8(b). The results of the numerical simulation with the actual disk thickness again show a reasonably good comparison with the experimental measurements. The figure also shows results corresponding to zero thickness where the conjugate effect was absent. In the case of 4.0 lpm, the numerical prediction showed that there was a small supercritical region after the fluid was discharged from the slot, and the jump occurred approximately 20 mm from the outer radius of the collar. Computations were also made for a disk of different thickness, keeping the flow rate and heat flux at its prescribed experimental value. The distribution of the heat transfer coefficient for different thicknesses were found to fall in between the cases of zero and the actual thickness in a monotonic fashion. For a disk of zero thickness, there was a sudden drop in the heat transfer coefficient at the location of the jump, and the heat transfer coefficient was large in the supercritical region and small in the subcritical region. With an increase in disk thickness, the heat transfer coefficient decreased in the supercritical region and increased in the subcritical region. This was a result of conduction through the disk wall, which supplied more heat in the subcritical region and decreased it somewhat in the supercritical region. The decrease of the heat transfer coefficient with the increase of the disk thickness in the supercritical region was also seen in the analytical results of Wang et al. (1989) for conjugate heat transfer to an impinging free liquid jet. Calculations were also performed for a steel disk, which has a smaller thermal con-

ductivity than the aluminum disk considered in the present experiment. It was found that with a decrease in the thermal conductivity of the solid, the radial conduction effects that decreased the heat transfer coefficient in the supercritical region and increased it in the subcritical region were also minimized. The heat transfer coefficient distribution for the steel disk was between that of the aluminum disk and a disk of zero thickness, as expected.

The heat transfer coefficient at a flow rate of 7.0 lpm is shown in Fig. 8(c). For a disk of zero thickness, the heat transfer coefficient decreased slowly in the supercritical region, encountered a sudden drop at the hydraulic jump, and then increased downstream in the subcritical region. The sudden drop at the jump disappeared and the distribution was smoothed out when conduction in the wall was present, as seen in the plot corresponding to the actual disk thickness. The decrease in the heat transfer coefficient at smaller radii was due to the development of the thermal boundary layer and the increase at larger radii was due to the increase in the fluid velocity. Again, a better comparison with the experimental measurements was obtained when heat conduction in the disk wall was taken into account.

From the above results, it may be concluded that in the design of heat transfer devices involving liquid jet impingement or thin film flows, both conduction in the wall and convection in the fluid need to be considered to predict the overall performance. Due to larger heat transfer coefficients, one may like to have a larger extent of the supercritical region. For a circular disk, it may be easily achieved by increasing the inlet Reynolds number, or by rotating the disk about its axis.

Conclusions

The local heat transfer coefficients from a heated disk to a controlled impinging jet have been measured for flow rates of $V = 2.0$ to 8.0 lpm and inlet temperatures of $T_{in} = 20$ to 40°C . The Nusselt number increased with flow rate all across the disk when the hydraulic jump moved away from the collar due to the increase in the extent of the supercritical region and the greater fluid velocity in the supercritical and subcritical regions. The above results also show that the effects of conjugate heat transfer are important in real engineering applications. An error as large as 100 percent was seen in the present system if radial heat conduction in the disk wall was neglected.

Acknowledgment

Funding for this work was provided by the NASA Goddard Space Flight Center, Greenbelt, MD, under contract No. NAG5-956.

References

- Azuma, T., and Hoshino, T., 1984, "The Radial Flow of a Thin Liquid Film," *Bulletin of JSME*, Vol. 27, No. 234, pp. 2739-2770.
- Chaudhury, Z. H., 1964, "Heat Transfer in a Radial Liquid Jet," *J. Fluid Mech.*, Vol. 20, Part 3, pp. 501-511.
- Craik, A. D. D., Latham, R. C., Fawkes, M. J., and Gribbon, P. W. F., 1981, "The Circular Hydraulic Jump," *J. Fluid Mechanics*, Vol. 112, pp. 347-362.
- Faghri, A., Chen, M. M., and Mahefkey, E. T., 1989, "Simultaneous Axial Conduction in the Fluid and Pipe Wall for Forced Convective Laminar Flow With Blowing and Suction at the Wall," *Int. J. Heat Mass Transfer*, Vol. 32, pp. 281-288.
- Ishigai, S., Nakanishi, S., Mizuno, M., and Imamura, T., 1977, "Heat Transfer of the Impinging Round Water Jet in the Interference Zone of Film Flow Along the Wall," *Bulletin of JSME*, Vol. 20, pp. 85-92.
- Miller, R. W., 1989, *Flow Measurement Engineering Handbook*, 2nd ed., McGraw-Hill, New York.
- Miner, D., and Seastone, J., eds., 1955, *Handbook of Engineering Materials*, Wiley, New York.
- Rahman, M. M., Faghri, A., Hankey, W. L., and Swanson, T. D., 1990, "Prediction of Heat Transfer to a Thin Liquid Film in Plane and Radial Flows," *ASME JOURNAL OF HEAT TRANSFER*, Vol. 112, No. 3, pp. 822-825.
- Rahman, M. M., Hankey, W. L., and Faghri, A., 1991, "Analysis of the Fluid Flow and Heat Transfer in a Thin Liquid Film in the Presence and Absence of Gravity," *Int. J. Heat Mass Transfer*, Vol. 34, No. 1, pp. 103-114.
- Rahman, M. M., Faghri, A., and Hankey, W. L., 1992, "Fluid Flow and Heat Transfer in a Radially Spreading Thin Liquid Film," *Numerical Heat Transfer*, Part A, Vol. 21, pp. 71-90.
- Stevens, J., and Webb, B. W., 1991, "Local Heat Transfer Coefficients Under an Axisymmetric, Single-Phase Liquid Jet," *ASME JOURNAL OF HEAT TRANSFER*, Vol. 113, pp. 71-78.
- Thomas, S., Hankey, W., Faghri, A., and Swanson, T., 1990, "One-Dimensional Analysis of the Hydrodynamic and Thermal Characteristics of Thin Film Flows Including the Hydraulic Jump and Rotation," *ASME JOURNAL OF HEAT TRANSFER*, Vol. 112, No. 3, pp. 728-735.
- Thomas, S., Faghri, A., and Hankey, W., 1991, "Experimental Analysis and Flow Visualization of a Thin Liquid Film on a Stationary and Rotating Disk," *ASME Journal of Fluids Engineering*, Vol. 113, No. 1, pp. 73-80.
- Vader, D. T., Incropera, F. P., and Viskanta, R., 1991, "Local Convective Heat Transfer From a Heated Surface to an Impinging, Planar Jet of Water," *Int. J. Heat Mass Transfer*, Vol. 34, No. 3, pp. 611-623.
- Wang, X. S., Dagan, Z., and Jiji, M., 1989, "Conjugate Heat Transfer Between a Laminar Impinging Liquid Jet and a Solid Disk," *Int. J. Heat Mass Transfer*, Vol. 32, No. 11, pp. 2189-2197.
- Watson, E. J., 1964, "The Radial Spread of a Liquid Jet Over a Horizontal Plane," *J. Fluid Mech.*, Vol. 20, Part 3, pp. 481-499.

Zeng-Yuan Guo
Professor.
Mem. ASME

Xiao-Bo Wu
Graduate Student.

Department of Engineering Mechanics,
Tsinghua University,
Beijing 100084,
People's Republic of China

Thermal Drag and Critical Heat Flux for Natural Convection of Air in Vertical Parallel Plates

Variable property effects on vertical channel natural convection in air are studied systematically. Numerical solutions of the governing equations show that both the mass flow rate and heat transfer in the channel are not only lower than the constant property results, but also show a nonmonotonic variation with increasing wall temperature or wall heat flux. This phenomenon, which seemingly conflicts with the conventional knowledge, has also been identified by experiments. For a vertical channel with a uniform heat flux boundary condition, the wall may experience a sharp rise in temperature up to damage of the channel if the wall heat flux is greater than the critical heat flux. This implies that the crisis phenomenon (or burnout) may occur in channel natural convection in gas as well as in the boiling process.

Introduction

Vertical two-dimensional channels formed by parallel plates are a frequently encountered configuration in thermal engineering equipment: for example, the finned exchanger, the collector of solar energy, the core of nuclear reactors, and the electronic and microelectronic equipment in recent years. Since Elenbas (1942) first proposed the problem of natural convection, extensive analytical and experimental results have been obtained on this problem. The constant property approximation (Boussinesq approximation) was commonly adopted in previous works (Bodoia and Osterle, 1962; Aung, 1972; Bruch et al., 1986; Guo et al., 1987) in order to simplify the analyses, while only a little attention has been paid to variable property effects. When the characteristic temperature difference is not very small compared with the absolute temperature, changes in fluid physical properties for the problem studied cannot be ignored and the variable property effects on flow properties or heat transfer used to taken into consideration by means of the reference temperature method and property ratio method. Sparrow and Gregg (1958) discussed how to choose the reference temperature for evaluating the fluid properties in the case of vertical plate or cylinder. Clausing (1982, 1985) studied the variable property effects and obtained new correlations for natural convective heat transfer from vertical isothermal surfaces in gases by use of the property ratio method. Based on a numerical analysis of laminar natural convection of air and oil in vertical parallel plates and circular tubes with uniform wall temperature, including the temperature dependence of all physical properties of the fluids, Aihara et al. (1986) suggested that the natural convection characteristics can be normalized to agree with those with constant fluid properties if the wall temperature is taken as the reference for evaluating the fluid properties.

Unlike the previous works, the emphasis here is put on the mechanism of variable property effects on mass flow and heat transfer rate in channel natural convection. Consequently, some new phenomena, such as a critical heat flux, have been revealed, by numerical analysis and experiments, that would not be otherwise observed, even when the variable property effects are taken into account through choice of the reference temperature or using the property ratio method.

Contributed by the Heat Transfer Division for publication in the JOURNAL OF HEAT TRANSFER. Manuscript received by the Heat Transfer Division July 1991; revision received April 1992. Keywords: Mixed Convection, Natural Convection, Rotating Flows. Associate Technical Editor: J. R. Lloyd.

2 Governing Equations

The representative vertical channel formed by two parallel plates of height l and infinite length, separated by a distance $2b$, is shown in Fig. 1. For this two-dimensional, steady, laminar natural convection, the governing equations with variable properties are as follows:

$$\frac{\partial}{\partial x}(\rho u) + \frac{\partial}{\partial y}(\rho v) = 0 \quad (1)$$

$$\rho u \frac{\partial u}{\partial x} + \rho v \frac{\partial u}{\partial y} = \frac{\partial}{\partial y} \left(\mu \frac{\partial u}{\partial y} \right) + \rho \beta g (T - T_\infty) - \frac{dp'}{dx} \quad (2)$$

$$C_p \rho u \frac{\partial T}{\partial x} + C_p \rho v \frac{\partial T}{\partial y} = \frac{\partial}{\partial y} \left(k \frac{\partial T}{\partial y} \right) \quad (3)$$

with boundary conditions

$$\text{For } x=0, 0 \leq y < b; u = u_0, v = 0, T = T_\infty, p' = -u_0^2/2$$

$$\text{For } x \geq 0, y = 0; \partial u / \partial y = 0, v = 0, \partial T / \partial y = 0$$

$$\text{For } x \geq 0, y = b; u = 0, v = 0, T = T_w \text{ or } q = q_w$$

$$\text{For } x = 1, p' = 0 \quad (4)$$

where $p' = p - p_\infty$, $dp_\infty/dx = -\rho_\infty g$.

Applying the following transformation for nondimensionalization (Bodoia and Osterle, 1962)

$$U = b^2 u / (l \nu_\infty \text{Gr}_\infty), \quad V = b v / \nu_\infty$$

$$X = x / (l \text{Gr}_\infty), \quad Y = y / b$$

$$P = b^4 p' / (\rho_\infty l^2 \nu_\infty^2 \text{Gr}_\infty^2),$$

$$\theta = (T - T_\infty) / (T_w - T_\infty), \quad \text{Gr}_\infty = \beta g (T_w - T_\infty) b^4 / (l \nu_\infty^2)$$

for isothermal cases

$$\theta = (T - T_\infty) k_\infty / (b q_w), \quad \text{Gr}_\infty = \beta g q_w b^5 / (l k_\infty \nu_\infty^2)$$

for isoflux cases, (5)

Eqs. (1)-(4) can then be reduced to

$$\frac{\partial}{\partial X} \left(\frac{\rho}{\rho_\infty} U \right) + \frac{\partial}{\partial Y} \left(\frac{\rho}{\rho_\infty} V \right) = 0 \quad (6)$$

$$U \frac{\partial U}{\partial X} + V \frac{\partial U}{\partial Y} = \frac{\rho_\infty}{\rho} \frac{\partial}{\partial Y} \left(\frac{\rho_\infty}{\rho} C_1(\theta) \frac{\partial U}{\partial Y} \right) + \theta - \frac{\rho_\infty}{\rho} \frac{dP}{dX} \quad (7)$$

$$U \frac{\partial \theta}{\partial X} + V \frac{\partial \theta}{\partial Y} = \frac{\rho_\infty}{\rho} \frac{1}{\text{Pr}_\infty} \frac{\partial}{\partial Y} \left(\frac{\rho_\infty}{\rho} C_2(\theta) \frac{\partial \theta}{\partial Y} \right) \quad (8)$$

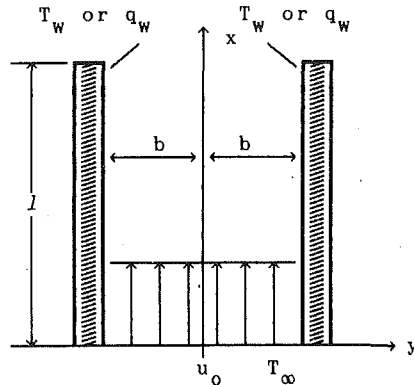


Fig. 1 Geometry of vertical parallel channel

with boundary conditions:

$$\text{For } X=0, 0 \leq Y < 1; U = U_0, V = 0, \theta = 0, P = -U_0^2/2$$

$$\text{For } X \geq 0, Y = 0; \quad \partial U / \partial Y = 0, V = 0, \partial \theta / \partial Y = 0$$

$$\text{For } X \geq 0, Y = 1; \quad U = 0, V = 0, \theta = 1 \text{ or } C_2(\theta) \partial \theta / \partial Y = 1$$

$$\text{For } X = L; \quad P = 0 \quad (9)$$

where $L = 1/Gr$, $C_p = \text{const}$, $C_1(\theta) = \rho\mu/\rho_\infty\mu_\infty$, $C_2(\theta) = \rho k/\rho_\infty k_\infty$.

It can be found that an additional factor, ρ_∞/ρ , appears in several terms of governing equations of variable properties compared with those of constant property ones. This implies that the density variation plays a very important role in variable property effects. In view of the fact that the influence of pressure variation on the air density is very much smaller than that of temperature variation (in the present case, $\Delta T/T_\infty$ is of the order of 10^{-1} and $\Delta p/p_\infty$ is of the order of 10^{-4}) the following expression holds with good approximation:

$$\rho_\infty/\rho = T/T_\infty = Hv\theta + 1 \quad (10)$$

where

$$Hv = \begin{cases} (T_w - T_\infty)/T_\infty & \text{for isothermal cases} \\ q_w b / (k_\infty T_\infty) & \text{for isoflux cases} \end{cases} \quad (11)$$

The use of the following temperature dependence of the viscosity and the conductivity of air, which were proposed by Sparrow and Gregg (1958),

$$\frac{\mu}{\mu_\infty} = \frac{(T/T_\infty)^{3/2}}{(T + 107.9)/(T_\infty + 107.9)}, \quad \frac{k}{k_\infty} = \frac{(T/T_\infty)^{3/2}}{(T + 202.2)/(T_\infty + 202.2)} \quad (12)$$

Nomenclature

b = channel half-spacing, m
 C_p = specific heat capacity, J/(k·kg)
 g = gravitational acceleration, m/s²
 k = thermal conductivity, W/(m·K)
 l = channel height, m
 \dot{m} = mass flow rate in the half-channel, kg/(s·m)
 \dot{M} = dimensionless mass flow rate in the half-channel
 p = air pressure, N/m²
 P = dimensionless air pressure
 q = heat flux, W/m²

Q = heat transfer rate in the half channel, W/m
 T = thermodynamic temperature, K
 u, v = velocity components in x, y coordinates, m/s
 U, V = dimensionless velocity in dimensionless X, Y coordinates
 X_t = thermal entrance length, m
 β = volumetric expansion coefficient, 1/K
 θ = dimensionless temperature
 μ = dynamic viscosity, kg/(s·m)
 ν = kinetic viscosity, m²/s
 ρ = air density, kg/m³

Subscripts

∞ = ambient fluid
 c = constant property
 cr = critical
 w = wall

Dimensionless Groups

Gr = Grashof number = $g\beta(T_w - T_\infty)b^4/(\nu_\infty^2)$ or $g\beta q_w b^5/(lk_\infty \nu_\infty^2)$
 Hv = heating intensity = $(T_w - T_\infty)/T_\infty$ or $g_w b/(k_\infty T_\infty)$
 Nu = Nusselt number = $Qb/[k_\infty(T_w - T_\infty)]$
 Pr = Prandtl number = ν_∞/a_∞
 Ra = Rayleigh number = $Gr \cdot Pr$

leads to

$$C_1(\theta) = \frac{(\theta Hv + 1)^{1/2}}{(0.375\theta Hv + 1)}, \quad C_2(\theta) = \frac{(\theta Hv + 1)^{1/2}}{(0.597\theta Hv + 1)} \quad (13)$$

Consequently, it is convenient to predict the variable property effects, taking the dimensionless heating intensity Hv as a parameter, in numerical solutions of Eqs. (6)–(9).

3 Results and Discussion

The governing equations, Eqs. (6)–(9), were solved numerically by the SIMPLE algorithm. The grid system of 40×80 was used for calculations and the change in results amounts to 1 percent if the grid size was reduced by a factor of 2. The local criterion for numerical convergence (the maximum relative difference between two consecutive iterations for any local variable) was 10^{-4} .

With the guessed values of the entrance velocity u_0 , the corresponding exit pressures $p(l)$ can be obtained by the solutions of governing equations. The values of u_0 were sought under the condition $p - p_\infty = 0$ at the channel exit. The correction of Δu_0 's may be determined by use of a linear interpolation (or extrapolation) method. The procedure was repeated until the criterion $(p - p_\infty)/(0.5\rho_\infty u_0^2) < 10^{-4}$ was satisfied.

The numerical results are so arranged as to show the effects of the fluid property variations, in particular the density variation, on the mass flow and heat transfer in the vertical channel.

3.1 Constant Wall Temperature Channel. In the case of the constant wall temperature, natural convection in the vertical channel is independent of radiative heat transfer between the channel and the ambient, since the air can be regarded as a nonabsorbing medium for low temperature.

Figure 2 shows the illustrative curves of the dimensionless mass flow rate, \dot{M} , in the parallel isothermal plates versus the dimensionless channel height, L , with the heating intensity, Hv , as parameter. The definition of the dimensionless mass flow rate is

$$\dot{M} = \frac{b\dot{m}}{\rho_\infty \nu_\infty Gr_\infty} = \int_0^1 \frac{\rho}{\rho_\infty} U dY \quad (14)$$

where the dimensional mass flow rate in the half-channel is

$$\dot{m} = \rho_\infty u_0 b = \int_0^b \rho u dy \quad (15)$$

Curve No. 1 in Fig. 2 represents the constant property results (obtained with Boussinesq approximation), which are in good agreement with the existing data (Bodoia and Osterle, 1962;

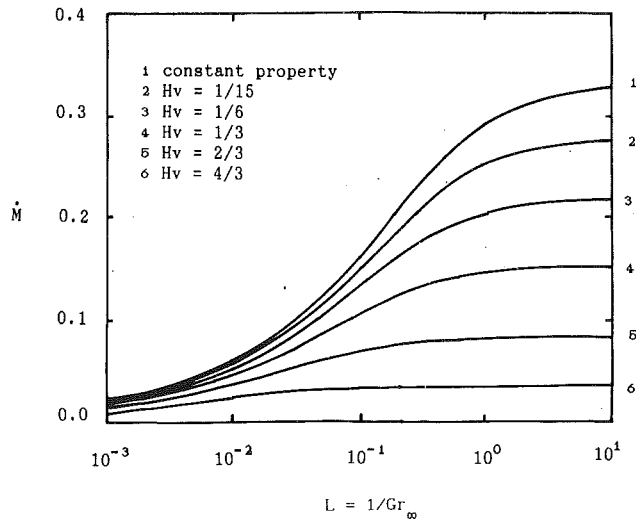


Fig. 2 Dimensionless mass flow rate versus dimensionless channel height

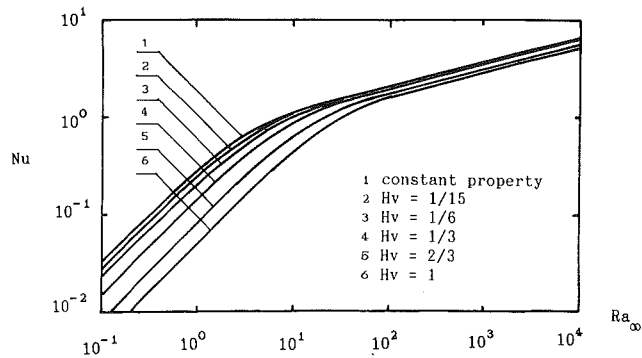


Fig. 3 Nu as a function of Ra_∞ with Hv as parameter

Aung, 1972). The other curves show the results when the variable property effects are taken into account. It is clearly found that the dimensionless mass flow rates, unlike the constant property results, are dependent on the heating intensity and decrease as the heating intensity increases. The overestimation of the constant property results of the dimensional mass flow rate becomes marked for large L , which correspond to the cases of the fully developed channel flow. Gui (1988) and Guo et al. (1989) obtained an analytical relation of the dimensionless mass flow rate with and without Boussinesq approximation for the fully developed channel flow:

$$\dot{M} = \frac{\dot{M}_c}{[1.36(Hv + 1)^{7/2}/(Hv + 1.36)]} \quad (16a)$$

For the cases of small Hv , we have the following simpler approximations than Eqs. (12) and (13) for the fluid property variations:

$$C_1(\theta) = \rho\mu/\rho_\infty\mu_\infty = 1, \quad C_2(\theta) = \rho k/\rho_\infty k_\infty = 1 \quad (17)$$

Hence, Eq. (16a) can be reduced to

$$\dot{M} = \dot{M}_c / (Hv + 1)^3 \quad (16b)$$

where the subscript c indicates the constant property result.

This implies that a temperature difference of 30 K ($Hv = 0.1$ as $T_\infty = 300$ K) will lead to an overestimation of 33 percent in mass flow rate in the vertical channel. Consequently, one should be careful not to neglect the variable property effects even for the small temperature difference between the wall and the ambient in some cases.

The Nusselt numbers $Nu (= Qb/lk_\infty(T_w - T_\infty))$ for the vertical channel are displayed in Fig. 3. The total heat transfer

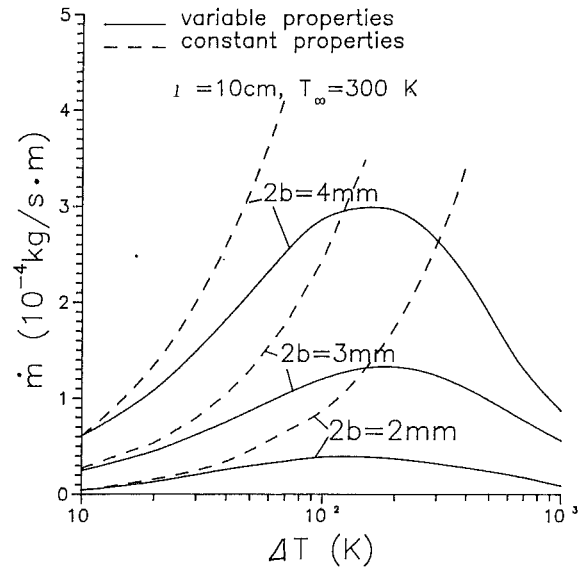


Fig. 4 Mass flow rate in the isothermal channel as a function of temperature difference between the wall and the ambient

from one wall to air can be evaluated in terms of the enthalpy increase of air through the half-channel as follows:

$$Q = \int_0^b \rho C_p u (T - T_\infty) dy \quad (18)$$

where u and T are the velocity and temperature, respectively, at the exit cross section of the channel.

As for the dimensionless mass flow rate case, the constant property results (curve No. 1) overestimate the Nusselt number, and the difference in Nusselt number between the constant property case and the variable property case rises with increasing heating intensity and decreasing Rayleigh number. For the fully developed channel flow, we have in correspondence with Eqs. (16a) and (16b)

$$Nu = \frac{Nu_c}{[1.36(Hv + 1)^{7/2}/(Hv + 1.36)]} \quad (19a)$$

and

$$Nu = Nu_c / (Hv + 1)^3 \quad (19b)$$

It is well known that the pumping flow through the vertical channel is due to the presence of the buoyancy. Consequently, it is conventionally considered that the pumping flow rate will go up if the wall temperature and the consequent buoyancy increase. This view has been verified by some experiments and numerical calculations with constant property approximation. However, variable property results given by the solutions of Eqs. (1)–(4), as shown in Fig. 4, indicate that the mass flow rate in the vertical channel goes down, rather than up, with increasing wall temperature if the wall temperature is above a certain value. The physical reason for this phenomenon (called thermal clogging), which seemingly conflicts with the conventional knowledge, is that even though the buoyancy goes up, the viscous drag and thermal drag (thermally induced pressure drop) (Guo, 1991) also go up as the temperature difference increases; the mass flow rate will decrease with rising temperature difference if the drags (mainly the thermal drag) increase more rapidly than the driving force (Gui et al., 1988), because the buoyancy will approach a limit rather than go up indefinitely as the wall temperature rises continuously.

This phenomenon has also been verified qualitatively through the measurement of the thermal entry length of vertical channel by means of laser speckle photography. Details of the experimental apparatus and procedure are found from Guo et al.

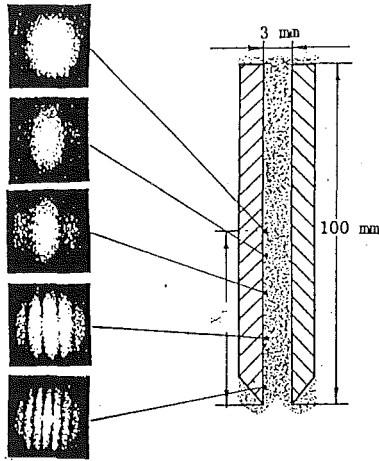


Fig. 5(a) Laser specklegram for air at different elevations of channel

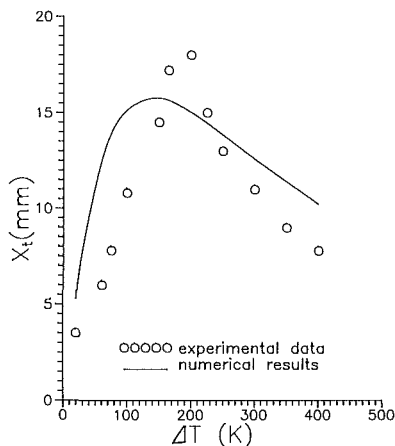


Fig. 5(b) Thermal entrance length variation with the temperature difference between the wall and the ambient

(1991), and therefore only a brief description is provided here. The test channel consists of two vertical parallel copper plates, with 215 mm height and 3 mm spacing. The copper plates were heated by electric heaters embedded in them. Six thermocouples were used for measuring the plate temperature. The results show that the nonuniformity of the plate is less than 0.5 K. The channel natural convection may be defined as fully developed when the temperature gradient and the consequent density gradient in the cross section of the channel disappear. The spacing between fringes in laser speckle diagrams for points at different elevation, as shown in Fig. 5, is inversely proportional to the density gradient at corresponding points. As a result, the thermal entrance length X_t can then be determined from the channel entrance to the point where the Young's fringes in speckle diagram (that is, the temperature gradient in the cross section at that elevation) disappear. In the case of constant property results, raising the wall temperature leads to the monotonic increase of the mass flow rate, which thins the thickness of the boundary layer and extends the hydrodynamic and thermal entrance region. If the variable property effects are taken into consideration, it can be expected that the thermal entrance length X_t will first increase and then decrease due to the nonmonotonic variation of mass flow rate in the channel with continuous rise of temperature difference from zero. In the present cases, the plate-to-ambient temperature difference varied all the way from 15 to 530 K. The experiments indicate indeed the nonmonotonic variation of the thermal entrance length X_t with the temperature difference, as plotted in Fig. 5(b), and the maximum X_t occurs at about

$\Delta T = 185$ K. The numerical results in the thermal entrance length X_t and the flow rate \dot{m} for the same channel geometry are also given in Fig. 5(b) for comparison. In calculations, the thermal entrance length X_t was determined from the channel entrance to the location where the density gradient of air at the plate surface decreases to a value of $0.2 \times 10^{-2} (\text{kg}/\text{m}^3 \cdot \text{mm})$ which corresponds to the resolution of density gradient for present laser speckle photography. Qualitative agreement has been found between the experimental and computational results in the variation of X_t with the temperature difference. The nonmonotonic variation of the thermal entrance length X_t must be attributed to the nonmonotonic variation of the mass flow rate in the channel with the temperature difference. Here, the experimental error depends mainly on the accuracy of measuring the spacings of Young's fringes. The resulting error in X_t is less than 1 mm for the present experiments. Assumptions of two dimensionality of channel flow, the origin of the boundary layer being at the channel entrance, and constant heat capacity in the theoretical model, may also be responsible for the discrepancy between computational and experimental results.

3.2 Constant Wall Heat Flux Channel. Heat transfer by natural convection from vertical plates with given heat flux is commonly encountered in the electronic communication and nuclear reactor industry, for example, in convectively cooled rack-mounted printed circuit boards containing heat dissipating integrated circuits or nuclear reactor cores containing the plate-form fuel elements whose decay heat should be able to be taken away by natural convection as pumps stop working.

For the case of the constant wall heat flux, the channel natural convection is coupled with radiative heat transfer between two plates and between the channel and the ambient. For symmetric heating with an aspect ratio less than 0.01, radiation was found to have little effect (Carpenter et al., 1976). As the aspect ratio was increased to 0.03–0.06, radiative end loss (radiation to the inlet-exit of channel) could amount to 5–15 percent of total heat transfer for the plate temperature range of 300 K to 380 K, depending on the surface emissivity. In order to reveal the variable property effects on the channel flow and heat transfer, the channel natural convection in the absence of radiation was studied and the numerical results for the channel natural convection with constant heat flux are given in Figs. 6–9. Like the case of constant wall temperature, a maximum for the mass flow rate in the channel does exist as the wall heat flux increases continuously, as shown in Fig. 6. What does differ is that the mass flow rate drops steeply with increasing wall heat flux after the mass flow rate reaches its maximum. Furthermore, there is no longer a solution (see later) when the heat flux is beyond some value, q_{cri} , which is here called critical heat flux. It can be also found in Fig. 6 that the critical heat flux decreases considerably as the channel spacing shrinks. Figure 7 shows the variation of the mass flow rate with the channel height, taking the given wall heat flux as parameter. It is clear that the critical heat flux is also strongly dependent on the channel height. In order to explore the physical meaning of the critical heat flux at which there is no solution for the vertical channel convection, Figure 8 was plotted. It shows the wall temperature as a function of heat flux for given channel geometry. As anticipated, the wall temperature at different elevations starts by going up gradually with increasing wall heat flux. However, when the wall heat flux reaches a certain value, the wall temperatures at different elevations each exhibit an abrupt and endless increase. This phenomenon is similar to the “burnout” in the boiling process and clarifies why there is no solution for channel natural convection if the heat flux is above its critical value. These results imply that the crisis phenomenon exists also in gaseous single-phase, channel natural convection as well as in the boiling process, where it can cause damage to the system.

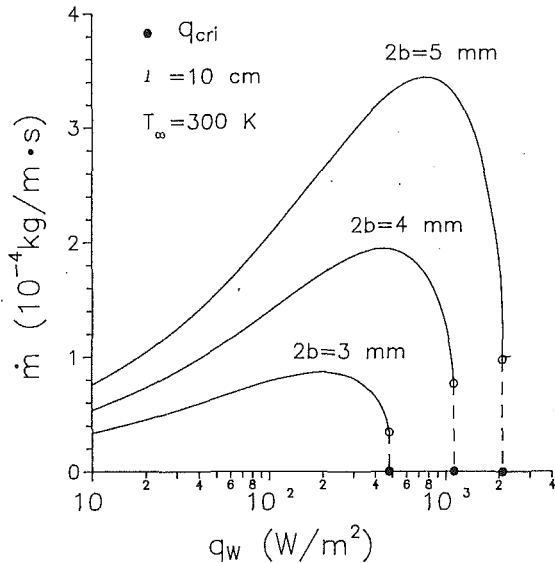


Fig. 6 Mass flow rate in the isoflux channel as a function of wall heat flux with the channel spacing as parameter

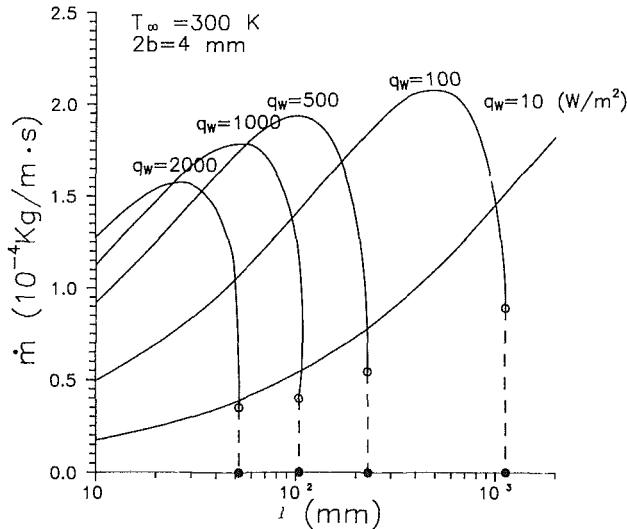


Fig. 7 Mass flow rate in the isoflux channel as a function of channel height with wall heat flux as parameter.

This crisis phenomenon is undoubtedly attributed to the variable property effects, in particular, effects induced by density variation (i.e., effects of thermal drag), which leads to the reduction in the mass flow rate in the channel and the consequent reduction in the ability to take the heat away from the channel. The heat transfer ability by natural convection for a given geometry of the vertical channel has been proved to be limited by (Guo et al., 1989)

$$Q_{lim} = C(\rho_{\infty} g C_p T_{\infty} b^3) / (3\nu_{\infty}) \quad (19)$$

where C is a constant.

It can be seen that the heat transfer limit is very sensitive to channel spacing and independent of the channel height. As a result, if the imposed heat flux is beyond this heat transfer limit for channel, the wall temperature goes up indefinitely and finally leads to the damage of the channel.

The specific numerical result in Fig. 9 reveals the effects of individual property variation on the mass flow rate in the channel. The curve of mass flow rate versus the wall heat flux, including the influence of all property variations except density change, is similar to but below the curve with constant property

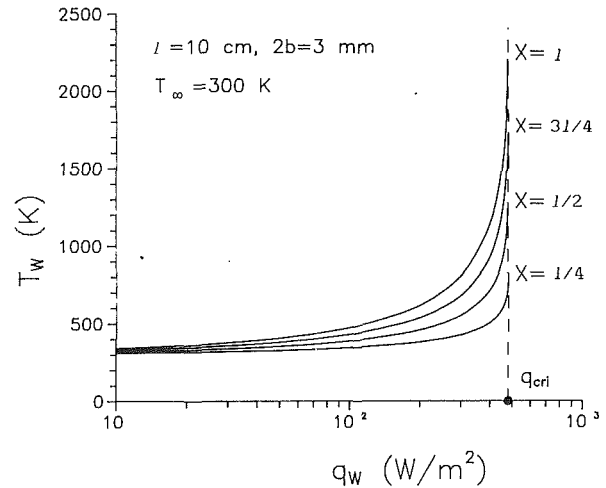


Fig. 8 Wall temperature at different elevations as a function of wall heat flux

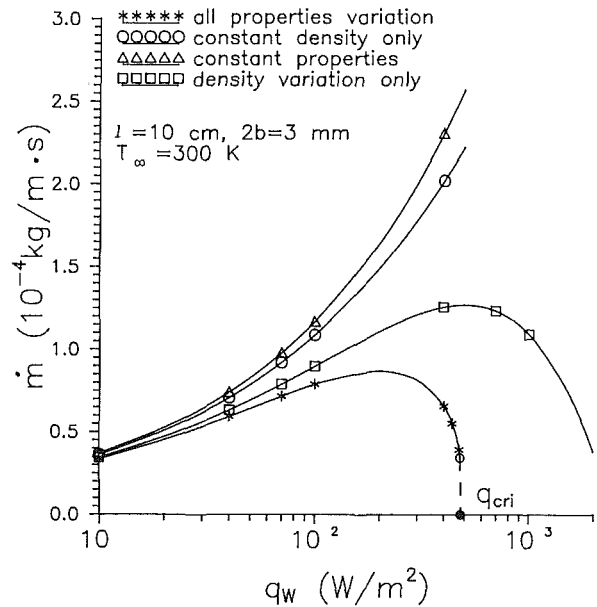


Fig. 9 Effect of individual property variation on the mass flow rate in channel

approximation. However, the mass flow rate in the channel, if only density variation is taken into consideration, is not only lower than the constant property results, but also exhibits a nonmonotonic variation with the wall heat flux. This suggests that the effect of density variation is responsible for the crisis phenomena in the channel natural convection in air.

After rearranging and fitting the numerical results, a correlation between the critical heating intensity (dimensionless critical heat flux) and the Rayleigh number is given:

$$(H\nu_{\infty}^2 / Ra_{\infty})_{cri} = 0.06 \quad (20)$$

where $Ra_{\infty} = Gr_{\infty} Pr_{\infty}$. The dimensional expression of the critical heat flux is given:

$$q_{w, cri} = 0.06 (\rho_{\infty} C_p g b^3 T_{\infty}) / (\nu_{\infty} l) \quad (21)$$

For example, the critical heat flux is equal to 1055 W/m^2 for the vertical plate channel of 10 cm in height and 4 mm in spacing ($2b = 4 \text{ mm}$). Correlation (20) provides a new criterion for the thermal analysis and design of the plate-type fuel elements in the nuclear reactor core and the rank-mounted printed circuit boards, etc., that is, the working parameters there should

be so chosen that the heat load is lower than their critical heat flux in order to keep the system efficiently cooled and safe.

When the wall temperature becomes so high that the radiative heat transfer cannot be neglected compared with natural convection, the radiation between plates will reduce the wall temperature gradient and maximum wall temperature, and the radiative end loss will lower the speed of increase of the wall temperature with the wall heat flux. It can be expected that the presence of radiation does not change the nonmonotonic variation of mass flow rate and the critical phenomenon of channel natural convection, except that the wall temperature goes up abruptly, but not indefinitely, when the "burnout" conditions are approached.

4 Concluding Remarks

1 Property variations due to heating will lead to the reduction of both dimensionless mass flow rate and Nusselt number for the vertical channel natural convection compared with the constant property results. For the fully developed case of constant wall temperature channel, analytical relations on the mass flow rate and heat transfer between the constant property and variable property results have been obtained.

2 Unlike the conventional knowledge, both numerical and experimental results show that the mass flow rate in the channel exhibits the nonmonotonic change, that is, first goes up then goes down after reaching a maximum with a continuous increase in the temperature difference or wall heat flux if the variable property effects are taken into account.

3 The crisis phenomenon (or burnout) may occur in the channel natural convection in air with the heat flux given as well as in the boiling process, because the heat transfer ability for given channel geometry is limited. Correlation (21), which can predict the critical heat flux, provides a new criterion for thermal analysis and design of devices with narrow space.

4 Specific numerical results show that the effect of the density variation, that is, the effect of thermal drag, is responsible for the nonmonotonic change of the mass flow rate and the consequent burnout phenomenon in channel natural convection in the cases of wall heat flux given.

References

- Aihara, T., Maruyana, S., and Choi, J. S., 1986, "Laminar Free Convection With Variable Fluid Properties in Vertical Ducts of Different Cross-Sectional Shapes," *Heat Transfer*, C. L. Tien, V. P. Carey, and J. K. Ferrel, eds., Hemisphere Publishing Corporation, Vol. 4, pp. 1581-1586.
- Aung, W., 1972, "Fully Developed Laminar Free Convection Between Vertical Plates Heated Asymmetrically," *International Journal of Heat and Mass Transfer*, Vol. 15, pp. 1577-1580.
- Aung, W., and Worku, G., 1986, "Developing Flow and Flow Reversal in a Vertical Channel With Asymmetric Wall Temperatures," *ASME JOURNAL OF HEAT TRANSFER*, Vol. 108, No. 2, pp. 299-304.
- Bodoia, J. R., and Osterle, J. F., 1962, "The Development of Free Convection Between Heated Vertical Plates," *ASME JOURNAL OF HEAT TRANSFER*, Vol. 84, pp. 40-44.
- Bruch, T., Rhodes, T., and Acharya, S., 1986, "Laminar Natural Convection Between Finitely Conducting Vertical Plates," *International Journal of Heat and Mass Transfer*, Vol. 29, No. 6, pp. 819-830.
- Carpenter, J. K., Briggs, D. G., and Sernas, V., 1976, "Combined Radiation and Developing Laminar Free Convection Between Vertical Flat Plates With Asymmetric Heating," *ASME JOURNAL OF HEAT TRANSFER*, Vol. 98, No. 1, pp. 95-100.
- Cebeci, T., and Bradshaw, P., 1984, *Physical and Computational Aspects of Convective Heat Transfer*, Springer-Verlag, New York, pp. 302-312.
- Clausing, A. M., and Kempka, S. N., 1981, "The Influence of Property Variation on Natural Convection From Vertical Surfaces," *ASME JOURNAL OF HEAT TRANSFER*, Vol. 103, No. 4, pp. 609-612.
- Clausing, A. M., 1985, "Natural Convection Correlations of Heat Transfer," *ASME JOURNAL OF HEAT TRANSFER*, Vol. 107, No. 1, pp. 133-138.
- Elenbas, W., 1942, "Heat Dissipation of Parallel Plates by Free Convection," *Physica*, Vol. 9, No. 1, pp. 1-28.
- Gui, Y. W., Li, Z. X., and Guo, Z. Y., 1988, "Thermal Drag in Channel Natural Convection," *Heat Transfer Science and Technology*, B. X. Wang, ed., Hemisphere Publishing Corp., pp. 91-96.
- Gui, Y. W., 1988, "Natural Convection of Air in Vertical Parallel Plates," Ph.D. dissertation, Department of Engineering Mechanics, Tsinghua University, People's Republic of China.
- Guo, Z. Y., Li, Z. X., and Gui, Y. W., 1987, "Analytical and Experimental Study on Natural Convection Between Isothermal Vertical Plates," *Cooling Techniques for Electronic Equipment*, W. Aung, ed., Hemisphere Publishing Corp., pp. 15-25.
- Guo, Z. Y., Li, Z. X., and Gui, Y. W., 1989, "Variable Property Effect and Thermal Drag During Natural Convection in Vertical Channels," *Chinese Journal of Engineering Thermophysics*, Vol. 1, No. 1, pp. 103-109.
- Guo, Z. Y., 1991, "Thermal Drag in Forced Duct Flow," *International Journal of Heat and Mass Transfer*, Vol. 34, No. 1, pp. 229-235.
- Guo, Z. Y., Song, Y. Z., and Zhao, X. W., 1991, "Experimental Investigation on Natural Convection in Channel by Laser Speckle Photography," *Experimental Thermal and Fluid Science*, Vol. 4, No. 5, pp. 594-600.
- Sparrow, E. M., and Gregg, J. L., 1958, "The Variable Fluid Property Problem in Free Convection," *ASME JOURNAL OF HEAT TRANSFER*, Vol. 80, No. 2, pp. 879-886.

R. K. Tripathi

G. Nath

Department of Mathematics,
Indian Institute of Science,
Bangalore 560 012, India

Unsteady Boundary Layer Free Convection Flow Over Horizontal Cylinder and Sphere Embedded in a Stratified Medium

Introduction

Free convection flows in a thermally stratified medium over cylinder and sphere occur in many engineering and natural system of practical interest. The steady free convection flow over horizontal cylinder and sphere embedded in isothermal as well as nonisothermal media has been studied by several investigators, for example, Eichhorn et al. (1974), Lin and Chao (1974), Chen and Eichhorn (1979), Hasan and Mujumdar (1985), and Kumari and Nath (1989).

In many convection processes the time-dependent variations of surface temperature arise. In technology, transients are common during start-up and shut-down. Unsteady free convection flows over horizontal wires and horizontal cylinders with time-dependent surface temperature have been studied by Vest and Lawson (1972), and Parsons and Mulligan (1980). A literature survey reveals that very limited work has been done on free convection flows over cylinders and spheres with time-dependent surface temperature and that also deals with the sudden step change in surface temperature, which may be unrealistic with respect to actual physical circumstances.

In the present work the unsteady laminar free convection flow over a two-dimensional body (horizontal cylinder) and an axisymmetric body (sphere) immersed in a linearly stratified medium has been studied. The unsteadiness in the flow field is due to the wall temperature, which varies continuously with time, unlike the previous studies of sudden step change. In regard to the present analysis, it must be mentioned that near the upper stagnation point, the boundary layer thickens, and the curvature, streamwise effects, and motion pressure neglected in the boundary layer analysis are no longer valid. The situation worsens as the stratification increases.

Analysis

The physical model and coordinate system for a two-dimensional body (horizontal cylinder) and an axisymmetric body (sphere) are the same as used by Lin and Chao (1974). The temperature of the fluid far from the body surface increases linearly with vertical distance, i.e., $T_\infty(\bar{x}) = T_{\infty 0} + a\bar{x}$, where \bar{x} is measured from the forward stagnation point of the body and is parallel to the direction of the gravity and $a = dT_\infty/d\bar{x} \geq 0$. The time-dependent surface temperature of the body is $T_w(t)$ and we assume that $T_{w0} > T_{\infty 0}$, where T_{w0} is the surface temperature of the body at $t = 0$. The effect of stratification on natural convection heat transfer can be expressed in terms of a stratification parameter S , which has been defined as $S = aL/\Delta T_m$, where L is the height of the body and ΔT_m is the temperature difference, $T_{w0} - T_{\infty 0}$, at the midheight of the body. With the Boussinesq assumption, the boundary layer equations governing the unsteady free convection flow over two-dimensional and axisymmetric bodies can be expressed as:

$$(ru)_x + (rv)_y = 0 \quad (1)$$

$$u_t + uu_x + vv_y = \nu u_{yy} + g\beta(T - T_\infty) \sin(2x/L) \quad (2)$$

$$T_t + uT_x + vT_y = \alpha T_{yy} \quad (3)$$

Table 1 Local heat transfer results ($Nu/Gr_L^{1/4}$) for horizontal cylinder evaluated by various investigators when $t^* = S = 0$, $Pr = 0.7$

θ deg.	Lin and Chao (1974)	Hasan and Mujumdar (1985)	Present results
0	0.4402	0.44021	0.44017
60	0.4186	0.41926	0.41919
120	0.3508	0.35407	0.35318
150	0.2923	0.31661	0.29891

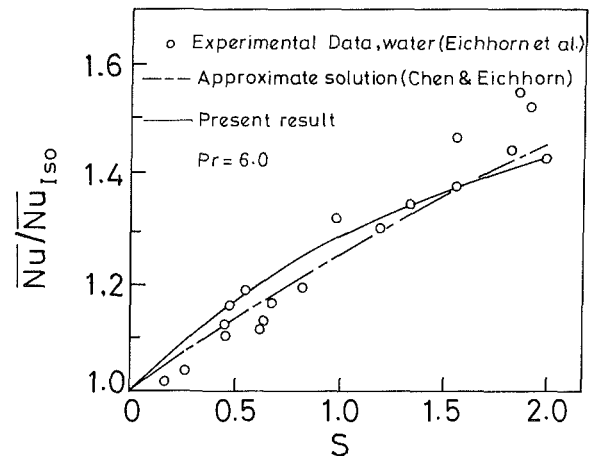


Fig. 1 Effect of stratification on mean Nusselt number (cylinder) for $t^* = 0$

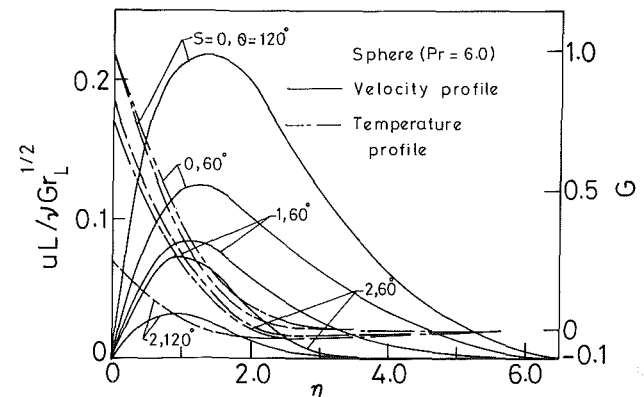


Fig. 2 Velocity and temperature profiles (sphere) for various values of the stratification parameter S at $t^* = 0$

Contributed by the Heat Transfer Division for publication in the JOURNAL OF HEAT TRANSFER. Manuscript received by the Heat Transfer Division June 1991; revision received April 1992. Keywords: Natural Convection, Stratified Flows. Associate Technical Editor: W. A. Sirignano.

The initial and boundary conditions are expressed as
 $u(x, y, 0) = u_i(x, y); v(x, y, 0)$

$$= v_i(x, y); T(x, y, 0) = T_i(x, y) \quad (4)$$

$$\left. \begin{aligned} u(x, 0, t) = v(x, 0, t) = 0; T(x, 0, t) = T_w(t) \\ u(x, \infty, t) = 0; T(x, \infty, t) = T_\infty(x) \end{aligned} \right\} \quad (5)$$

The above equations can be recast into dimensionless form by applying the following transformations:

$$\left. \begin{aligned} X = x/L, R = r/L, Y = yGr_L^{1/4}/L, t^* = \nu Gr_L^{1/2} t/L^2, U = uL/\nu Gr_L^{1/2}, \\ Pr = \nu/\alpha, Gr_L = g\beta(T_{w0} - T_{\infty0})L^3/\nu^2, (T - T_\infty)/(T_w - T_{\infty0}) = G, \\ (T_w - T_{\infty0})/(T_{w0} - T_{\infty0}) = \phi(t^*), T_\infty = T_{\infty0} + a(L/2)[1 - \cos(2X)] \\ V = \nu L/\nu Gr_L^{1/4} \end{aligned} \right\} \quad (6)$$

The surface temperature of the body $T_w(t)$ can be written as $T_{\infty0} + (T_{w0} + T_{\infty0})\phi(t^*)$. It consists of a basic steady distribution T_{w0} with a weak superimposed time-varying distribution governed by the unsteady function $\phi(t^*)$. In the resulting nondimensional equations, which are not given here to conserve space, we use the approach of Lin and Chao (1974) and apply the following transformations:

$$\left. \begin{aligned} \xi = \int_0^X R^2 U^* dX, \eta = (2\xi)^{-1/2} R U^* Y, \psi(X, Y) = (2\xi)^{1/2} F(\xi, \eta), \\ RU = \partial\psi/\partial Y, RV = -\partial\psi/\partial X, U = U^* F', \\ V = -(2\xi)^{-1/2} R U^* [F + 2\xi F_\xi + 2\xi (R^2 U^*)^{-1} F' (\partial\eta/\partial X)], \\ U^* = \bar{U}L/(\nu Gr_L^{1/2}), g\beta(T_{w0} - T_{\infty0}) \sin(2X) = \bar{U} d\bar{U}/dx \\ \sin(2X) = U^* (dU^*/dX), U^* = \left(2 \int_0^X \sin(2X) dx \right)^{1/2} \end{aligned} \right\} \quad (7)$$

We find that the equation of continuity is identically satisfied and the momentum equation, Eq. (2) and the energy equation, Eq. (3), become, respectively

$$F'' + FF'' + \lambda(\phi G - F'^2) - PF'_\xi = 2\xi(F'F'_\xi - F_\xi F'') \quad (8)$$

$$\left. \begin{aligned} Pr^{-1}G'' + FG' - P\phi^{-1}\phi'_t G - PG'_t \\ - 2S(2+S)^{-1}\phi^{-1}F'Q \sin(2X) = 2\xi(F'G_\xi - F_\xi G') \end{aligned} \right\} \quad (9)$$

where

$$\left. \begin{aligned} \lambda = 2(\xi/U^*) (dU^*/d\xi) = 2\xi \sin(2X)/(R^2 U^{*3}) \\ P = 2\xi/(R^2 U^{*2}), Q = 2\xi/(R^2 U^*) \end{aligned} \right\} \quad (10)$$

and the prime denotes $\partial/\partial\eta$.

The boundary conditions are given by

$$\left. \begin{aligned} F = F' = 0, G = 1 - S(S+2)^{-1}\phi^{-1}(1 - \cos 2X) \text{ at } \eta = 0 \\ F' = 0, G = 0 \text{ as } \eta = \infty \end{aligned} \right\} \quad (11)$$

The initial conditions at $t^* = 0$ are given by the steady-state equations obtained from Eqs. (8) and (9) by inserting $t^* = 0$; $\phi = 1$; $\phi'_t = F'_t = G'_t = 0$ into them.

Nomenclature

F = dimensionless stream function
 g = gravitational acceleration
 G = dimensionless temperature
 Gr_L = Grashof number
 $= g\beta\Delta T_0 L^3/\nu^2$
 k = thermal conductivity
 Pr = Prandtl number
 q_w = local heat transfer rate
 r, R = radial distance and dimensionless radial distance, respectively

t, t^* = dimensional and dimensionless times, respectively
 T = temperature
 u, v = velocity components
 U, V = dimensionless velocity components
 \bar{U} = hypothetical outer stream velocity function
 x, y = streamwise and normal coordinates, respectively
 X, Y = dimensionless coordinates
 α = thermal diffusivity

β = coefficient of thermal expansion
 ξ, η = transformed coordinates
 ν = kinematic viscosity
 ψ = dimensional stream function

Subscripts

x, y, t = derivatives with respect to x, y, t, ξ , and t^* , respectively
 i, iso = initial and isothermal conditions, respectively

The quantity of physical interest is the heat transfer coefficient (Nusselt number), which can be expressed as:

$$Nu = q_w L/k\Delta T_m = -(1 + S/2)(2\xi)^{-1/2} R U^* \times Gr_L^{1/4} \phi(t^*) G'(\xi, 0, t^*) \quad (12)$$

where

$$q_w = -k(\partial T/\partial y)_{y=0} \quad (13)$$

As has been done by Chen and Eichhorn (1979), the gross heat transfer rate from the body surface is used to calculate Nu , the mean Nusselt number. To compute the results at various angular distances θ from the forward stagnation point, the relations giving values of $\xi, \eta, \lambda, U, P, Q, R$, etc. in terms of θ for the cases of circular cylinder and sphere given by Kumari and Nath (1989) have been used.

Results and Discussion

The governing equations, Eqs. (8) and (9), under boundary conditions (11) and initial conditions obtained from Eqs. (8) and (9) by putting $t^* = 0$ have been solved numerically using an implicit finite difference scheme in combination with the quasilinearization technique described in detail by Inouye and Tate (1974). To fix the step sizes for computation, they have been optimized using the Richardson extrapolation formula. Finally, the computation has been carried out with $\delta\eta = \delta t^* = 0.05$, $\delta\theta = 4$ deg and $6 \leq \eta_\infty \leq 10$. For $\theta \geq 120$ deg, $\delta\theta = 1$ deg is used. All computations were carried out on a VAX-8810 digital computer.

In order to assess the accuracy of the present method, we have compared our heat transfer results for horizontal cylinder when $t^* = S = 0$ and $Pr = 0.7$, with the results of Lin and Chao (1974) and nonsimilarity solution of Hasan and Mujumdar (1985) in Table 1. The results have been found to be in close agreement. In Fig. 1 the effect of stratification is shown on the mean Nusselt number (\bar{Nu}) for the geometry of the horizontal cylinder. For comparison the experimental data of Eich-

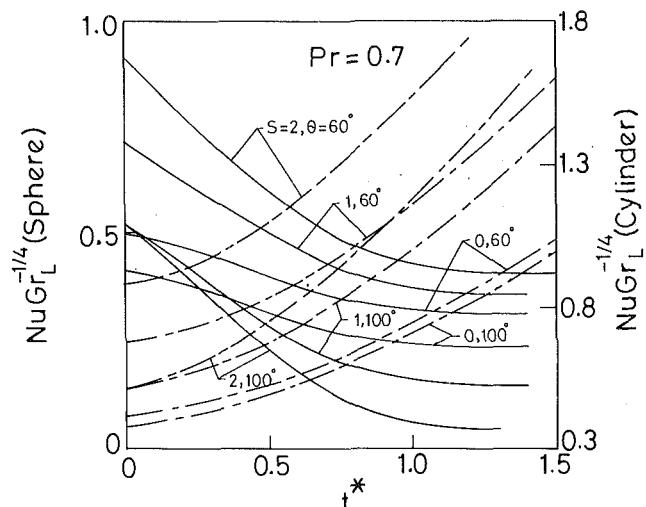


Fig. 3 Effect of wall temperature on local heat transfer coefficient: — sphere when $\phi(t^*) = 1 - a(1 - e^{-ct^{*2}})$, $a = 0.25$, $c = 1.0$; - - - cylinder when $\phi(t^*) = 1 + \epsilon t^{*2}$, $\epsilon = 0.25$

horn et al. 1974) and the results of approximate solution of Chen and Eichhorn (1979) have been also shown in Fig. 1. The results for the case of a sphere, for which the related figure is not given here to save space, have some deviation from the results of previous investigators. This is because in the rear half of the sphere, the boundary layer becomes thick, and therefore in that region we cannot expect accurate results for heat transfer and hence for the average heat transfer from the whole body.

In Fig. 2 steady-state velocity and temperature profiles are shown at two different θ locations for the cases of a sphere ($Pr = 6.0$). From the figure it is clear that the reduction in velocity due to the stratification is more at higher θ locations. For instance, at $\theta = 120$ deg the reduction in peak velocity is about 82 percent, when the stratification parameter increases from 0 to 2 whereas at $\theta = 60$ deg it is about 43 percent for the same change in stratification. Figure 2 also shows that the presence of high thermal stratification can cause a slight negative nondimensional temperature. It is also seen that the dip in the temperature profile is more in the case of $Pr = 6.0$ (water) than in the case of $Pr = 0.7$ (air). To conserve space, the figures showing the velocity and temperature profiles for the cases of

horizontal cylinder and sphere ($Pr = 0.7$) and cylinder ($Pr = 6.0$) are not given here because they do not give any new information.

Figure 3 shows that effects of quadratically increasing wall temperature ($\phi(t^*) = 1 + \epsilon t^{*2}$, $\epsilon > 0$) and exponentially decaying wall temperature ($\phi(t^*) = 1 - a(1 - e^{-ct^{*2}})$, $a > 0$, $c > 0$) for the cases of a cylinder and a sphere ($Pr = 0.7$), respectively. It is found that heat transfer increases rapidly with time when $\phi(t^*) = 1 + \epsilon t^{*2}$, $\epsilon > 0$, whereas for exponential decay in wall temperature it decreases and attains a steady state after a certain time. It is observed that for large linear stratification the change in heat transfer with the change of wall temperature is more pronounced.

Conclusions

The average heat transfer is found to increase with the increase of ambient thermal stratification. The reduction in maximum velocity due to stratification is more at higher θ locations. A slight reversal in temperature profiles is observed. The effect of variation of wall temperature on heat transfer is more pronounced for large stratification.

References

- Chen, C. C., and Eichhorn, R., 1979, "Natural Convection From Spheres and Cylinders Immersed in a Thermally Stratified Fluid," *ASME JOURNAL OF HEAT TRANSFER*, Vol. 101, pp. 566-569.
- Eichhorn, R., Lienhard, J. H., and Chen, C. C., 1974, "Natural Convection From Isothermal Spheres and Horizontal Cylinders Immersed in a Stratified Fluid," *Proceedings of the Fifth International Heat Transfer Conference*, Tokyo, Japan, Vol. 3, pp. 10-14.
- Hasan, M., and Mujumdar, A. S., 1985, "Simultaneous Heat and Mass Transfer in Free Convection From a Horizontal Cylinder," *AIAA J.*, Vol. 23, pp. 1602-1608.
- Inouye, K., and Tate, A., 1974, "Finite-Difference Version of Quasi-linearization Applied to Boundary Layer Equations," *AIAA J.*, Vol. 12, pp. 558-560.
- Kumari, M., and Nath, G., 1989, "Double Diffusive Unsteady Free Convection on Two-Dimensional and Axisymmetric Bodies in a Porous Medium," *Int. J. Energy Research*, Vol. 13, pp. 379-391.
- Lin, F. N., and Chao, B. T., 1974, "Laminar Free Convection Over Two-Dimensional and Axisymmetric Bodies of Arbitrary Contour," *ASME JOURNAL OF HEAT TRANSFER*, Vol. 94, pp. 435-442.
- Parsons, J. R., Jr., and Mulligan, J. C., 1980, "Onset of Natural Convection From a Suddenly Heated Horizontal Cylinder," *ASME JOURNAL OF HEAT TRANSFER*, Vol. 102, pp. 636-639.
- Vest, C. M., and Lawson, M. L., 1972, "Onset of Convection Near a Suddenly Heated Horizontal Wire," *Int. J. Heat Mass Transfer*, Vol. 15, pp. 1281-1283.

Natural Convection in a Partial Sector-Shaped Enclosure: Experimental Results

N. Al-ani
Graduate Student.

M. W. Nansteel
Associate Professor.

Department of Mechanical and
Aerospace Engineering,
Florida Institute of Technology,
Melbourne, FL 32901

An experimental study of the buoyancy-induced motion and heat transfer in a differentially heated partial sector-shaped enclosure is carried out. Radial surfaces of the sector are heated and cooled isothermally while the circumferential surfaces are insulated. Water is used as the working fluid in experiments with sector angles $\alpha = 30, 45, \text{ and } 90 \text{ deg}$ for Rayleigh number in the range $4 \times 10^8 \leq Ra \leq 3 \times 10^9$. Laser illumination/streak photography is used to visualize the flow. Steady laminar motion is observed, with flow structure qualitatively independent of sector angle except for the case $\alpha = 90 \text{ deg}$. Circulation intensity is found to increase modestly with sector angle. Convection energy transfer across the sector increases rapidly with respect to transport by conduction for increasing α . Total energy transport across the sector is a nonmonotonic function of sector angle due to the competing mechanisms of conduction and convective transport. The existence of a sector angle α^ , which minimizes the cross-sector heat transfer rate, is discussed.*

1 Introduction

Natural convection processes play an important role in the environmental control of residential and commercial buildings. Of special importance, with respect to energy utilization, are the processes occurring during the summer months in the air space between the roof and the ceiling of single homes. Energy transfer rates across the attic space and subsequent cooling loads can be substantial in warm, solar-rich climates. The mechanism of interest presently is the buoyancy-induced convection heat transfer that occurs in a wedge-shaped attic space, during the daytime, from the roof surface of the house to the attic floor, i.e., the ceiling of the living space. Thermal radiation transfer will certainly play a major role in the process overall; however, the focus here will be on the convective transfer. A thorough understanding of the convective transport may lead to procedures for decreasing the heat transfer rates in attic geometries, which in turn may lead to reduced energy consumption and cooling costs.

Some aspects of the buoyancy-induced fluid motion and heat transfer in attic-shaped enclosures have been considered in the past. Flack et al. (1979) carried out experiments for air-filled triangular (isosceles) enclosures with adiabatic bases and the remaining surfaces heated and cooled isothermally. Experiments were carried out for aspect ratios between 0.29 and 0.87 and Grashof numbers, based on enclosure side wall length, of order 10^6 . Flack et al. observed steady laminar motion in the triangular space and overall heat transfer rates from the heated to the cooled surface that were similar to those previously reported for differentially heated rectangular enclosures. Flack (1980) also experimentally studied convection in isosceles triangles. In this work either the base was cooled and both the inclined surfaces were heated or the base was heated and the inclined surfaces were cooled. Grashof numbers ranged from 10^5 – 10^6 and enclosure aspect ratio occupied the same range as in the study of Flack et al. (1979). For cases of cooling from below, Flack (1980) observed steady laminar flow with heat transfer rates exceeding the rate due to pure conduction by only 30 percent while heating from below resulted in transi-

tional and turbulent flow with heat transfer rates exceeding the pure conduction rate by 500 percent. Akinsete and Coleman (1982) numerically studied convection of air in right triangular-shaped enclosures due to isothermal heating and cooling of the base and inclined surfaces. Calculations were also made for constant heat flux conditions on these surfaces. The length of the adiabatic vertical surface of the enclosure was varied between 6 and 100 percent of the base length while Grashof number ranged between 800 and 64,000. For the case of isothermal boundaries (hot and cold) the boundary temperature is discontinuous at the vertex where the hot and cold surfaces meet. Akinsete and Coleman (1982) used a limiting numerical procedure to obtain a finite value for local heat flux at the singular vertex as well as a finite global heat transfer rate. A similar singularity exists for the boundary conditions that Flack et al. (1979) and Flack (1980) attempted experimentally to reproduce. The heat transfer behavior in the vicinity of such singular points is discussed fully by Nansteel et al. (1986). Poulidakos and Bejan (1983a) carried out experiments in air- and water-filled enclosures of right triangular shape. In this study the enclosure was composed of one vertical, one horizontal, and one sloping surface with a height-to-length ratio of 0.207. The lower horizontal and upper sloped walls were isothermally heated and cooled, respectively, while the vertical surface was insulated. Poulidakos and Bejan used a "truncated-tip" design in their experiments so that the heated and cooled surfaces would not be in direct contact and hence avoided the singularity discussed above. This design resulted in a minimum separation distance between the two surfaces that was approximately 7 percent of the vertical dimension of the enclosure. Near the upper end of the range of the investigated Rayleigh numbers (10^5 – 10^9) the flow was reported to be turbulent with an approximately isothermal core and thin boundary layers near the enclosure walls. Poulidakos and Bejan (1983b) also investigated convection in an attic space by asymptotic and numerical means. They developed closed-form expressions for the fluid motion and temperature for the case of very shallow enclosures. In the numerical simulation a short transition length, δ , was used near the vertex at which the heated and cooled surfaces meet in order to avoid the discontinuous boundary temperature singularity. The length of this section was taken to be one-tenth of the enclosure length.

Contributed by the Heat Transfer Division for publication in the JOURNAL OF HEAT TRANSFER. Manuscript received by the Heat Transfer Division February 12, 1992; revision received July 22, 1992. Keywords: Building Heat Transfer, Enclosure Flows, Natural Convection. Associate Technical Editor: J. R. Lloyd.

Poulikakos and Bejan investigated the effect of aspect ratio and Prandtl number on the motion and heat transfer rate. Their numerical simulations indicate that the asymptotic theory (for shallow spaces) predicts the flow and temperature fields accurately, provided that the space is at least 100 times longer than it is high. Martin del Campo et al. (1988) made calculations for the buoyancy-induced convection in air-filled isosceles triangles for a range of thermal boundary conditions including heating-from-below, cooling-from-below, and heating and cooling on opposite inclined surfaces. Grashof number ranged from 10^3 to 10^6 while aspect ratio ranged from 0.1 to 10. For the case of cooling from below it was shown that convective heat transfer rates (singular conduction heat transfer was subtracted from the Nusselt number) were greatest for triangles with aspect ratio between one and three. Karyakin et al. (1988) numerically studied transient, buoyancy-induced convection in isosceles-triangular-shaped enclosures. Either the base of the triangle was insulated and the inclined surfaces were heated and cooled isothermally or the base was cooled and the inclined surfaces were both heated isothermally. Transient calculations began with the fluid initially isothermal at the average temperature of the hot and cold surfaces. Results were obtained for Grashof number in the range of 10^3 – 10^8 , aspect ratios between 0.25 and 2, and $Pr = 1$. Only local values of the heat transfer rate were reported by Karyakin et al. in recognition of the unbounded heat transfer behavior at the singular vertices of the enclosure. Karyakin et al. reported damped oscillatory behavior for stream function and Nusselt number in cases of large Grashof number. These oscillations exhibited increased damping for the case of cooling-from-below, probably as a consequence of the more stable density stratification present in this configuration. Yu and Nansteel (1990) studied the buoyancy-induced fluid motion in a sectorial region of opening angle α in which the angle bisector was parallel to the gravity vector (opening upward). They demonstrated the existence of an infinite cascade of counterrotating eddies of rapidly diminishing strength as the corner vertex is approached in the wedge angle range $126 \text{ deg} \leq \alpha \leq 142 \text{ deg}$. These eddies are similar to those first predicted by Moffatt (1964).

In the present study the triangular-attic geometry is replaced by the fluid-filled partial circular sector of opening angle α shown in Fig. 1. The radial surfaces $\theta = \alpha, 0$ are heated and cooled isothermally while the remaining circumferential surfaces $\bar{r} = \bar{r}_i, \bar{r}_o$ are insulated. The partial sector geometry shown

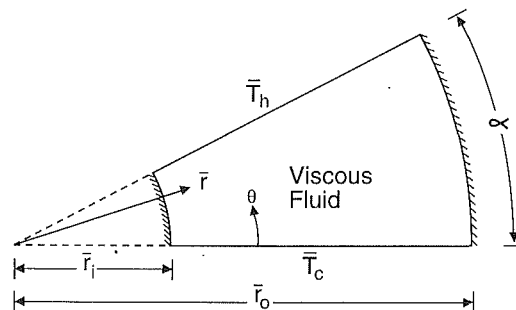


Fig. 1 Partial sector geometry

in Fig. 1 is a convenient means of avoiding the discontinuous boundary temperature singularity. Furthermore, the inner circumferential surface $\bar{r} = \bar{r}_i$ is appropriate for simulating convection in actual attic spaces since there is, typically, a short vertical section separating the roof and the ceiling surfaces and this section is often shaded from solar input by a short roof overhang. The present study focuses on the steady, buoyancy-induced flow structure that develops in the enclosure and the rate of energy transfer across the sector. Of particular interest here is the dependence of the flow structure and heat transfer rate on the sector angle α and the heating intensity.

2 Dimensionless Parameters

Nondimensionalization of the equations governing mass, momentum, and energy conservation for the fluid-filled partial sector yields the functional dependence

$$\chi = \chi(r, \theta; Ra, Pr, r_i, \alpha) \quad (1)$$

in which χ represents any of the dimensionless quantities p' (pressure), T (temperature), or \mathbf{u} (velocity). The geometric parameters $r_i = \bar{r}_i/\bar{r}_o$ and α fix the shape of the enclosure while

$$Ra = \frac{g\beta\bar{r}_o^3(\bar{T}_h - \bar{T}_c)}{\nu\kappa} \quad (2)$$

$$Pr = \nu/\kappa \quad (3)$$

are the Rayleigh and Prandtl numbers. Equation (1) follows from the assumption of steady, laminar, constant property flow of a Boussinesq fluid with negligible viscous dissipation and pressure work effects, cf. Al-ani (1991). The average heat flux on the heated surface

Nomenclature

c_p = constant pressure specific heat, J/kg-K	Q^* = dimensionless heat transfer, Eq. (5)	\bar{T}_h = heated surface temperature, K
g = gravitational acceleration, m/s^2	Q_c = cold wall heat transfer rate, W	\bar{T}_o = reference temperature = $(\bar{T}_h + \bar{T}_c)/2$, K
k = fluid thermal conductivity, W/m-K	Q_h = hot wall heat transfer rate, W	\mathbf{u} = dimensionless fluid velocity vector = $\bar{\mathbf{u}}\bar{r}_o/\nu$
Nu = Nusselt number, Eq. (8)	r = dimensionless radial coordinate = \bar{r}/\bar{r}_o	$\bar{\mathbf{u}}$ = fluid velocity vector, m/s
p' = dimensionless pressure = $\bar{p}'\bar{r}_o^2/\rho_o\nu^2$	\bar{r} = radial coordinate, m	α = sector opening angle, rad
\bar{p} = pressure, Pa	r_i = radius ratio = \bar{r}_i/\bar{r}_o	α^* = value of α that results in minimum heat transfer, rad
\bar{p}' = modified pressure = $\bar{p} + \rho_o g \bar{r} \sin \theta$, Pa	\bar{r}_i = sector inner radius, m	β = thermal expansion coefficient, K^{-1}
Pr = Prandtl number, Eq. (3)	\bar{r}_o = sector outer radius, m	θ = circumferential coordinate, rad
q = average heat flux, W/m^2 , Eq. (4)	Ra = Rayleigh number, Eq. (2)	κ = thermal diffusivity = $k/\rho_o c_p$, m^2/s
q_{cond} = average heat flux due to conduction, W/m^2 , Eq. (7)	T = dimensionless temperature = $(\bar{T} - \bar{T}_o)/(\bar{T}_h - \bar{T}_c)$	μ = dynamic viscosity, N-s/ m^2
q_{conv} = average heat flux due to convection, W/m^2 , Eq. (9)	\bar{T} = temperature, K	ν = kinematic viscosity, m^2/s
	\bar{T}_c = cold surface temperature, K	ρ = density, kg/m^3
	T_{cond} = dimensionless fluid temperature corresponding to pure conduction, Eq. (6)	ρ_o = reference density, kg/m^3

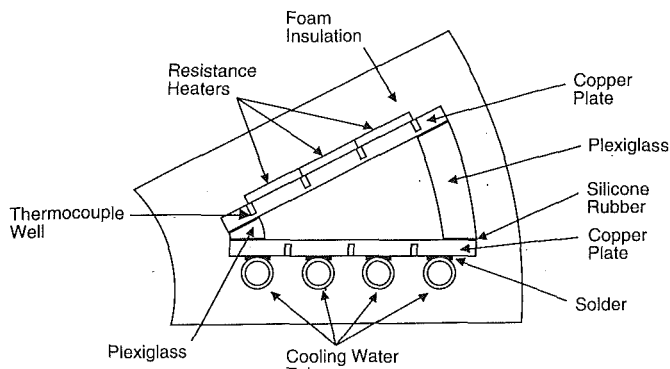


Fig. 2 Test section

$$q = \frac{1}{\bar{r}_o - \bar{r}_i} \int_{\bar{r}_i}^{\bar{r}_o} k \frac{\partial \bar{T}}{\partial \theta} (\bar{r}, \alpha) d\bar{r} \quad (4)$$

is used to define the dimensionless heat transfer rate across the enclosure, Q^* :

$$Q^* = \frac{q(\bar{r}_o - \bar{r}_i)}{k(\bar{T}_h - \bar{T}_c)} \quad (5)$$

The fluid temperature field corresponding to pure conduction ($\mathbf{u} = 0$) is

$$T_{\text{cond}} = \frac{\theta}{\alpha} - \frac{1}{2} \quad (6)$$

and the corresponding average heat flux on the hot surface is

$$q_{\text{cond}} = \frac{k(\bar{T}_h - \bar{T}_c)}{\alpha(\bar{r}_o - \bar{r}_i)} \ln \frac{\bar{r}_o}{\bar{r}_i} \quad (7)$$

As a measure of the importance of convective effects with respect to conduction, the Nusselt number Nu is defined as the ratio of the actual (average) heat flux across the enclosure to the heat flux that would prevail in the absence of convection,

$$Nu = \frac{q}{q_{\text{cond}}} = \frac{\alpha Q^*}{\ln \bar{r}_o / \bar{r}_i} \quad (8)$$

3 Experimental Apparatus

Figure 2 shows a schematic of the test section for the case $\alpha = 30$ deg while Fig. 3 depicts the experimental test system. The test section consists of a water-filled partial circular sector with adiabatic circumferential boundaries at $\bar{r} = \bar{r}_i = 2.54$ cm and $\bar{r} = \bar{r}_o = 10.2$ cm, i.e., the radius ratio $\bar{r}_i/\bar{r}_o = 1/4$. The circumferential surfaces of the test section are machined from 5.08 cm o.d. and 20.3 cm i.d., 1.27 cm wall thickness plexiglass tubes, respectively. The radial, isothermal surfaces are made of copper plates 10.2 cm wide, 30.5 cm in depth (normal to the plane of Fig. 2), and 6.3 mm in thickness. The two end plates (parallel to the plane of Fig. 2) are made of 1.27-cm-thick plexiglass and 0.95-cm-thick optical glass. The entire test section is insulated with 5-cm-thick polyurethane foam insulation. The surface of the upper (hot) plate is heated by three thermofoil resistance heaters. The energy dissipation rates of the three heaters are controlled independently through three variable transformers in order to produce a nearly uniform temperature on the heated surface, $\theta = \alpha$. The lower (cold) plate is cooled by water passing through four copper tubes (6.3 mm i.d.), which are soldered to the lower surface of the cold plate. The cooling water flow through these tubes is arranged in counterflow fashion and is controlled by four valves, which may be adjusted independently. Cooling water bath temperature is maintained constant by a chiller and a temperature controller. The temperature stability of the system is on the order of $\pm 0.1^\circ\text{C}$. This is less than 1 percent of the overall

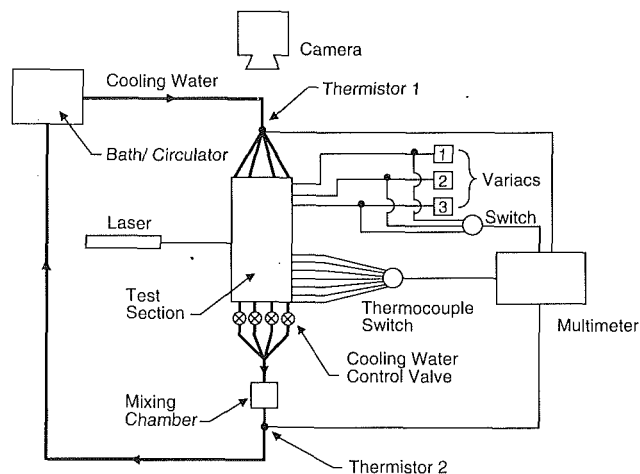


Fig. 3 Experimental test system

temperature difference $\bar{T}_h - \bar{T}_c$ observed in the experiments. Temperature of the heated and cooled plates is monitored with 24 gage copper-constantan thermocouples located in holes that are drilled to within 1 mm of the inner (wet) surface of the plates. Four thermocouples are installed on the upper plate and three on the lower surface. The thermocouples are distributed evenly in the radial direction near the center span of the enclosure. Cooling water temperature measurement upstream and downstream of the test section is accomplished by two 2.54 mm glass-probe thermistors, cf. Fig. 3. These thermistors are calibrated to within 0.05°C with a precision mercury-in-glass thermometer. This uncertainty is less than 2 percent of the smallest cooling water temperature differential measured. In this way the rate of energy absorption by the cooling water may be calculated and compared with the heat transfer rate at the heated surface.

4 Experimental Procedure and Data Reduction

Experiments are carried out with distilled, degassed water as the working fluid. Basic measurements required are the thermocouple millivoltages for the heated and cooled surfaces, thermistor resistances, resistance heater voltages, and the cooling water volumetric flow rate. The hot surface heat transfer rate is obtained from resistance and voltage measurements for each of the resistance heaters while the cool surface heat transfer is calculated from the cooling water temperature change and volumetric flow rate. The surface temperatures \bar{T}_h and \bar{T}_c are taken as the mean of the measured temperatures on the hot and cold plates, respectively. It is found that spatial deviations of surface temperature from \bar{T}_h and \bar{T}_c on the heated and cooled plates can usually be maintained below 1 percent of the overall temperature difference $\bar{T}_h - \bar{T}_c$. Before data collection, steady conditions are verified by periodically monitoring hot and cold surface thermocouple output and also by monitoring resistance of the thermistor downstream of the test section in the cooling water stream. This is an especially sensitive measure since the thermistor sensitivity is on the order of $3 \text{ k}\Omega/^\circ\text{C}$. Final confirmation of steady-state conditions is made by comparison of the heat transfer rates at the heated and cooled surfaces after reduction of the data. It is found that these two rates do not differ by more than 19 percent and on the average differ by only 10–15 percent. The difference in these rates is thought to reflect heat losses from the enclosure rather than transient conditions because the difference is found to be independent of the experimental run time. Heat loss rates from the enclosure of 10–20 percent are notable in view of the fact that cross-sector heat transfer rates are on the order of only 50 W or less. Note that the heat transfer rates measured on the heated and cooled surfaces include the energy transfer

by conduction through the plexiglass circumferential walls of the test section. Hence, a small correction is made to these rates so they reflect only the rate of transfer across the fluid space. This correction, which is made with the assumption of one-dimensional conduction in the plexiglass, is found to be less than 10 percent of the hot to cold surface heat transfer. The resulting heat transfer rates are used to compute the spatial average heat flux, q , in Eq. (4). In computing the parameters Ra and Nu the physical properties of water are evaluated at the mean temperature of the radial surfaces, $(\bar{T}_h + \bar{T}_c)/2$. Analysis of the uncertainties in physical properties and in measuring temperature and heat transfer rate indicate that the corresponding uncertainties in Rayleigh and Nusselt numbers are approximately ± 5 and ± 11 percent, respectively.

Laser illumination-streak photography is used to visualize the flow. During experimental trials the flow is seeded with small particles, which are composed of a vinyl toluene/butadiene copolymer. The mean diameter of particles remaining in suspension at the time of the flow visualization study is less than $50 \mu\text{m}$. These particles are chosen because they have a density similar to the density of water (specific gravity ≈ 1.026) and are highly reflective. During visualization of the flow the insulation on the optical glass end plate is removed. The flow is visualized by passing a 10 mW He-Ne laser beam through a 2-mm-dia cylindrical lens to form a thin sheet of laser light normal to the axis of the test section and in the plane of the buoyancy-induced flow. The sheet of light is passed through the plexiglass surface $\bar{r} = \bar{r}_o$ at approximately midspan. Laser light is side-scattered from the particles (normal to the plane of Fig. 2) and is recorded through time lapse photography by a 35 mm Nikon FM2N camera positioned just outside the optical glass endwall. The camera is fitted with a 105 mm macro lens so that the entire flow field may be visualized. Local fluid velocity is estimated by dividing particle streak length by the exposure time of the photograph. Particle streak lengths were measured from 5×7 in. black and white prints using a magnification loupe with a 20 mm reticle scale graduated in increments of 0.1 mm. Measurement of particle streak length was difficult, especially in the vicinity of enclosure boundaries, due to light reflection from the boundary resulting in decreased contrast. Also, uncertainty was introduced due to difficulty in distinguishing the end of a streak due to one particle from the beginning of another streak. As a result, local velocity measurements are considered accurate to only about 40 percent.

5 Results and Discussion

Experimental results for buoyancy-induced flow in the partial sector with $r_i = \bar{r}_i/\bar{r}_o = 1/4$ and $\alpha = 30, 45,$ and 90 deg are discussed below. Flow visualization photographs are presented for the sector angles $\alpha = 30$ and 90 deg as well as heat transfer results for the parameter ranges $4.24 \times 10^8 \leq Ra \leq 3.07 \times 10^9$, $3.5 \leq Pr \leq 5.3$.

Flow Visualization. Particle visualization experiments for the cases $\alpha = 30, 45,$ and 90 deg indicated, from visual as well as photographic observation, that the buoyancy-induced flow in the partial sector is both steady and laminar. Visualization of the flow at various transverse positions (that is, in the coordinate direction normal to the \bar{r}, θ plane) showed little dependence of the flow on this transverse coordinate, at least in a qualitative sense. That is, flow features are similar but slight variations in shape and location of some structures were noted. Also, the observed flow structure was qualitatively similar for each of the three slope angles, with some minor exceptions for the case $\alpha = 90$ deg. In each case the flow is composed of a large sector-shaped convection cell with opening angle approximately equal to α , exhibiting circulation in the clockwise sense, and a relatively quiescent horizontal layer

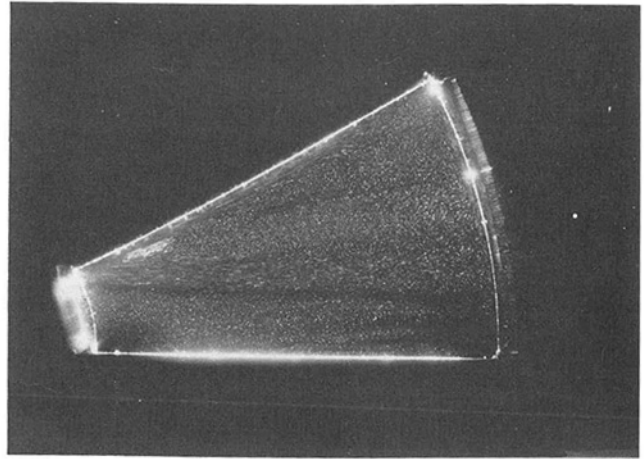


Fig. 4 Flow visualization photograph: $\alpha = 30$ deg, $Ra = 9.78 \times 10^8$, 4 second time exposure

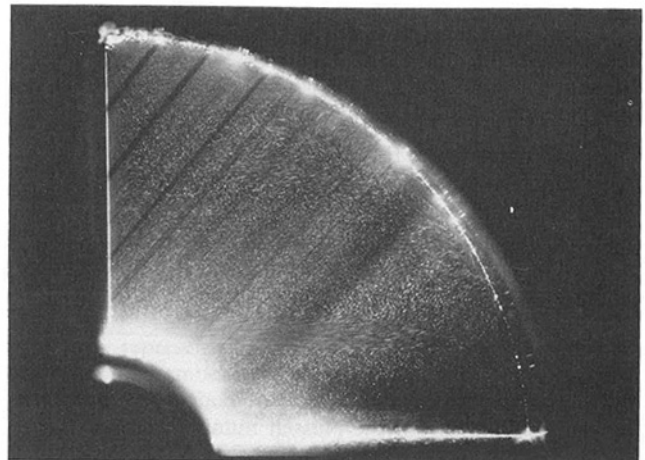


Fig. 5 Flow visualization photograph: $\alpha = 90$ deg, $Ra = 2.26 \times 10^9$, 16 second time exposure

adjacent to the cooled lower surface. The sector-shaped cell consists of a low-velocity core region surrounded by boundary layers adjacent to the surfaces $\theta = \alpha$ and $\bar{r} = \bar{r}_o$ and a nearly horizontal free jet structure located at a vertical distance of $\bar{r}_i \sin \alpha$, approximately, from the cooled lower surface. The failure of this sector-shaped cell to fill the entire enclosure, although surprising, is not without precedent for high-Rayleigh number enclosure convection. Similar qualitative behavior was observed for partially divided rectangular enclosures heated and cooled on the vertical surfaces by Nansteel and Grief (1981) experimentally for $Ra = 0(10^{11})$ and also numerically by Winters (1983) for $Ra = 0(10^7-10^9)$.

Flow visualization photographs are shown in Figs. 4 and 5 for the cases $\alpha = 30$ and 90 deg, respectively. Note, for the case $\alpha = 30$ deg, Fig. 4, that the center of the main cell is located very near the meeting location of the heated surface boundary layer and the horizontal jet, i.e., near $\bar{r} = \bar{r}_i$, $\theta = \alpha$. This behavior is similar to the numerical results reported by Kimura and Bejan (1985) for convection in a rectangular enclosure with the lower surface cooled (isothermally) and one vertical surface heated (isothermally) for Rayleigh numbers in the range 10^3-10^7 and $0.7 < Pr < 7$. The center of the convective cell in that study moved closer to the differentially heated corner with increasing Rayleigh number. Since the cell center in the present case is near the upstream end of the heated surface, $\alpha = 30$ deg, fluid is discharged or de-entrained from the boundary layer over most of the downstream portion of this surface, cf. Fig. 4. The discharge is especially intense in the approximate vicinity of $\bar{r} = \bar{r}_i + 3(\bar{r}_o - \bar{r}_i)/4$ where a

substantial portion of the layer appears to separate from the heated surface. A similar structure was observed for the case $\alpha = 45$ deg. However, note that in the case $\alpha = 90$ deg, Fig. 5, the region of intense circulation observed near the base of the heated surface for $\alpha = 30$ and 45 deg is absent. A far weaker and less distinct eddying motion is observed nearer the downstream end of the heated surface. The location of this eddy is best discovered by observing the strong entrainment of core fluid into the vertical boundary layer at locations upstream of the cell center and fluid discharge from the layer just downstream. Perhaps the region of intense circulation adjacent to the heated surface for small sector angles is a consequence of the driving shear caused by the close proximity of the heated surface layer to the horizontal jet flow for small α . For the case of $\alpha = 90$ deg, fluid from the vertical boundary layer is turned through an angle of 90 deg near the upper end of the surface $\theta = \alpha$ and empties into the layer adjacent to the unheated surface, $\bar{r} = \bar{r}_o$. This fluid, c.f. Fig. 5, follows a meandering path along the upstream end of the unheated surface. Careful observation of several photographs, however, indicates that the flow in this region is steady. For the sector angles $\alpha = 30$ and 45 deg this sinuous flow pattern was not observed. Also, a secondary zone of recirculation is observed for each of the sector angles adjacent to the unheated circumferential surface $\bar{r} = \bar{r}_o$. However, the strength of the recirculation appears to increase with increasing α . Just downstream of this zone of recirculation, boundary layer fluid is discharged into the core. The horizontal jet structure, which in each case is substantially thicker than the wall-bounded layers, appears to decrease slightly in thickness and intensify in the streamwise direction. This thinning of the jet is somewhat more pronounced for the case $\alpha = 30$ deg, cf. Fig. 4. The same effect is observed in the calculations of Winters (1983) for buoyancy-driven flow in a partially divided rectangular enclosure. In the case of Winters, streamline convergence in the streamwise direction indicated a two- or threefold velocity increase. For the larger sector angles, $\alpha = 45$ and 90 deg, it seems that the jet velocity increases as the fluid progresses toward the base of the heated surface but the jet thickness changes little. This may be a consequence of the stronger entrainment of core fluid into the jet layer along the majority of its span for the larger sector angles, compare Figs. 4 and 5.

Approximate velocity magnitudes in the heated surface boundary layer, the unheated surface layer, $\bar{r} = \bar{r}_o$, and the horizontal jet are given in Table 1 for the cases $\alpha = 30, 45,$ and 90 deg. Table 1 indicates the greatest velocities measured in each region of the flow. These results indicate a substantially greater velocity in the heated surface boundary layer for larger slope angles, i.e., $\alpha = 45$ and 90 deg. This effect is probably due, for the most part, to the greater influence of buoyancy when the surface is more closely aligned with the gravity vector. An additional factor that contributes to this trend is the decreased viscous resistance to circulation for larger sector angles. The slightly greater value of Ra prevailing for the 45 and 90 deg cases as compared to the 30 deg case also plays a role. Velocities in the unheated surface boundary layer appear to be roughly the same for the two cases, $\alpha = 30$ and 45 deg. The rather modest variation in circulation intensity with α , cf. Table 1, is expected on the following grounds. On a vertical heated surface in a quiescent fluid, boundary layer velocity is roughly proportional to \sqrt{g} , cf. Sherman (1990). When the surface is inclined at an angle α from the horizontal, the component of the gravitational force along the surface is diminished by the factor $\sin \alpha$ and therefore boundary layer velocity adjacent to the surface should be diminished by the factor $\sqrt{\sin \alpha}$ from the vertical surface case ($\alpha = 90$ deg). The corresponding factors for $\alpha = 30$ and 45 deg are approximately 71 and 84 percent, respectively, which are not inconsistent with the measured velocities in Table 1 considering the limited precision of the measurements. Velocities in the quiescent hori-

Table 1 Approximate boundary layer velocity magnitudes, mm/s; dimensionless magnitudes, $|\mathbf{u}| = \bar{u}/\bar{r}_o/\nu$, are given in parentheses

α	30°	45°	90°
Ra	$9.78 \cdot 10^8$	$1.41 \cdot 10^9$	$2.26 \cdot 10^9$
Heated surface	0.8 (124)	1.2 (179)	1.2 (194)
Unheated surface	0.6 (93)	0.6 (93)	1.0 (168)
Jet	0.7 (96)	0.5 (78)	0.8 (123)

zonal layer adjacent to the cooled surface, $\theta = 0$, are quite insignificant compared with those in the sector-shaped cell and can only be detected in the longest exposure photographs. Velocity magnitudes in this region are on the order of one millimeter per minute or $|\mathbf{u}| = 0(2)$.

The flow structure observed in the partial sector geometry is quite distinct from the motion numerically computed by Poulikakos and Bejan (1983b) and experimentally observed by Flack (1980) for triangular enclosures. In each of these studies the convection cell was observed to fill virtually the entire volume of the enclosure. Such a flow structure was also predicted by Akinsete and Coleman (1982) for air-filled triangular spaces. The present structure, in which a quiescent layer isolates the main convective cell from the cool surface, probably will only appear in a partial sector geometry (or in a triangular geometry with truncated vertex) and then only for large values of Rayleigh number as suggested by Winters (1983) in the context of rectangular cavities with partial divisions. The flow field observed presently may in fact result in increased convective transport compared with full sector or complete triangular enclosures because the cell contour is somewhat shorter in length.

Heat Transfer. Heat transfer data for the case $\alpha = 30$ deg are shown in Table 2. Note that the rate of heat loss from the test section for $\alpha = 30$ deg was less than 19 percent of the hot surface heat transfer rate and averaged, in most runs, between 10 and 15 percent. For the case $\alpha = 45$ deg heat loss rates were less than for $\alpha = 30$ deg, averaging between 6 and 9 percent, and for $\alpha = 90$ deg they were less than 15 percent.

The results for Nusselt number are plotted versus Rayleigh number in Fig. 6 for $\alpha = 30, 45,$ and 90 deg. The solid lines through the data in Fig. 6 for $\alpha = 45$ and 90 deg represent the least-square curve fit to the data while the solid line through the data for $\alpha = 30$ deg represents the average value, $Nu = 1.92$, for this value of α . Recall that Nu, as defined in Eq. (8), represents the ratio of the heat flux across the sector (due to conduction and convection) to the heat flux that would exist in the complete absence of convection. It is anticipated that an increase in Ra should correspond to a monotonic increase in convective transfer and therefore an increase in Nu. Such a trend, however, is not observed in Fig. 6 for the case of $\alpha = 30$ deg. The absence of a distinct positive slope for the data for $\alpha = 30$ deg is explained as follows. The value $Nu \approx 2$ indicates that convective effects are relatively weak for $\alpha = 30$ deg, even for $Ra = 0(10^9)$, and since Nusselt number must asymptotically approach unity for decreasing Ra, the rate of change of Nu with Ra should be correspondingly small. Even a small variation of Nu with Ra is not detected in Fig. 6, for $\alpha = 30$ deg, because heat losses from the test section are substantially greater for the high Rayleigh number experimental runs than for the ones at lower values of Ra. Note from Table 2 that the fractional heat losses, $(Q_h - Q_c)/Q_h$, average greater than 15 percent for the six runs with $Ra > 9 \times 10^8$ and only about 9.5 percent for runs with $Ra < 9 \times 10^8$. Since Nu is based upon the average of Q_h and Q_c , the effect is to shift high Rayleigh number data toward smaller values of Nu. The expected increase in Nu with increasing Ra

Table 2 Heat transfer data, $\alpha = 30$ deg

Run	Ra	Pr	Q^*	Nu	Q_h	Q_c	$\frac{Q_h - Q_c}{Q_h}$	\bar{T}_h	\bar{T}_c	$(\bar{T}_h - \bar{T}_c)$
					(W)	(W)	%	(°C)	(°C)	(°C)
1	$2.81 \cdot 10^9$	3.5	4.92	1.86	58.1	49.6	14	78.5	27.4	51.1
2	$2.09 \cdot 10^9$	3.8	4.92	1.86	49.0	42.4	14	70.6	27.0	43.6
3	$1.64 \cdot 10^9$	4.1	4.82	1.82	41.6	36.5	12	64.8	26.7	38.1
4	$1.37 \cdot 10^9$	4.2	4.98	1.88	39.5	32.1	19	61.0	27.0	34.0
5	$9.36 \cdot 10^8$	4.6	5.16	1.95	31.6	26.3	17	53.6	26.9	26.8
6	$7.15 \cdot 10^8$	4.9	4.99	1.88	25.5	22.2	13	48.8	26.0	22.9
7	$6.00 \cdot 10^8$	5.0	5.13	1.94	22.6	20.2	11	46.3	26.3	20.0
8	$5.64 \cdot 10^8$	5.0	5.33	2.01	21.1	20.4	3	45.8	27.0	18.8
9	$4.75 \cdot 10^8$	5.1	5.10	1.93	18.8	16.4	13	43.5	26.8	16.7
10	$5.18 \cdot 10^8$	5.1	5.36	2.03	20.5	19.2	6	44.5	26.6	17.9
11	$4.24 \cdot 10^8$	5.3	4.96	1.87	17.3	15.3	11	41.6	25.7	15.8
12	$9.78 \cdot 10^8$	4.5	5.27	1.99	32.4	27.7	14	54.6	27.4	27.2

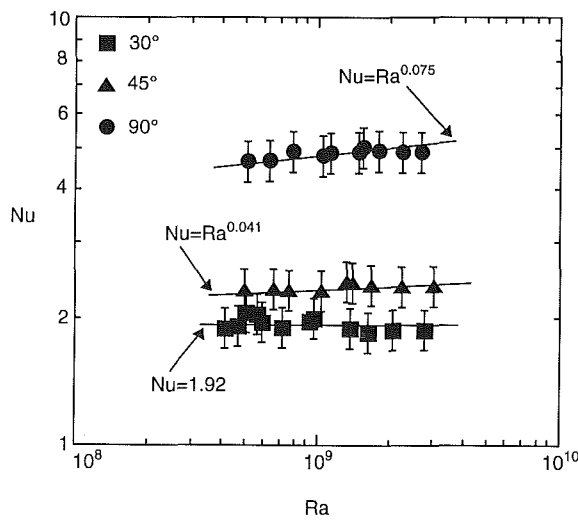


Fig. 6 Nusselt number versus Rayleigh number: $\alpha = 30, 45, 90$ deg

is observed, however, for the cases $\alpha = 45$ and 90 deg. Heat losses are again higher for the experimental runs at higher Rayleigh number; however, the effect is not great enough to mask the dependence of Nu on Ra. Note, Fig. 6, that Nu increases rapidly with sector angle α , in the range $30 \text{ deg} < \alpha < 90$ deg. For example, the magnitude of Nu is approximately 20–25 percent greater for a sector angle of 45 deg than for $\alpha = 30$ deg for the same value of Ra. Hence a greater proportion of the energy transfer across the sector is occurring via convection for larger sector angles. The present data also suggest that the convective energy flux itself increases with increasing sector angle for sufficiently large values of Ra. Convective heat flux is given by

$$q_{\text{conv}} = (\text{Nu} - 1)q_{\text{cond}} \quad (9)$$

Using Eq. (7) in Eq. (9) and holding \bar{r}_o , \bar{r}_i , and $(\bar{T}_h - \bar{T}_c)$ fixed leads to the proportionality

$$q_{\text{conv}} \propto \frac{(\text{Nu} - 1)}{\alpha}$$

The present data yield $(\text{Nu} - 1)/\alpha = 1.75, 1.85,$ and 2.6 for $\alpha = 30, 45,$ and 90 deg, respectively, for $\text{Ra} = 3 \times 10^9$ and therefore q_{conv} is a weakly increasing function of sector angle. It is interesting to note as well, however, that the overall heat transfer rate for fixed Rayleigh number *decreases* with in-

creasing α for $30 \text{ deg} \leq \alpha \leq 45$ deg. This can be clearly seen from the data of Fig. 6 along with the definition of the dimensionless heat transfer rate Q^* , Eq. (5). With $\bar{r}_o/\bar{r}_i = 4$ the data yield $Q^* \approx 5, 4.3,$ and 4.5 for $\alpha = 30, 45,$ and 90 deg, respectively, at $\text{Ra} = 3 \times 10^9$. This behavior occurs as a result of decreasing conduction heat transfer [cf. Eq. (7)] with increasing α . That is, even though convective transfer increases as a proportion of the total heat transfer and convection itself increases with increasing α , overall heat transfer decreases due to the decrease of conduction. The downward trend in Q^* with increasing α may not persist at high values of Ra or larger α and in fact may be reversed, since under these circumstances convective effects may be dominant enough to overshadow the trend in conduction. This is apparently the case for sector angles near 90 deg for the present data. For $\alpha = 90$ deg conduction heat transfer is only half as great as in the case $\alpha = 45$ deg; however, convective transport is nearly four times the magnitude of conduction ($\text{Nu} \approx 5$) so that the total heat transfer rate is slightly greater than for the case of $\alpha = 45$ deg. Hence the present data suggest that a sector angle $\alpha = \alpha^*$ exists at which the rate of heat transfer across the sector is a minimum. This minimum arises due to the competing mechanisms of conduction and convective heat transport that decrease and increase, respectively, for increasing values of α . The sector angle α^* that minimizes heat transfer may not exist, however, for all values of Ra and \bar{r}_i/\bar{r}_o . Consider, for example, the cases of very small Rayleigh number and very small \bar{r}_i/\bar{r}_o . In each instance energy transport by conduction will dominate uniformly for all α in the range $0 < \alpha < 90$ deg and heat transfer rate Q^* will decrease monotonically with increasing α . On the other hand, a minimum in the heat transfer, with respect to α , will always exist for arbitrarily large values of Ra, since the sector angle can always be made sufficiently small such that transport by conduction will dominate due to the throttling or choking effect on the circulation.

6 Conclusions

The buoyancy-induced motion and heat transfer in a differentially heated partial sector-shaped enclosure have been studied experimentally. Flow visualization indicates that the basic flow structure is similar for sector angles $\alpha = 30$ and 45 deg with some minor variations for the case of $\alpha = 90$ deg. Although Nusselt number increases monotonically with increasing sector angle, heat transfer decreases and then increases with increasing α due to the competing mechanisms of conduction and convective transport. This finding implies the existence of a sector angle that minimizes the heat transfer across the sector.

Acknowledgments

The authors appreciate the support of the Florida Solar Energy Center during the course of this work.

References

- Akinsete, V. A., and Coleman, T. A., 1982, "Heat Transfer by Steady Laminar Free Convection in Triangular Enclosures," *Int. J. Heat Mass Transfer*, Vol. 25, No. 7, pp. 991-998.
- Al-Ani, N., 1991, "Buoyancy-Induced Flow in a Sector-Shaped Enclosure," M.S. thesis, Florida Institute of Technology, Melbourne, FL.
- Flack, R. D., Konopnicki, T. T., and Rooke, J. H., 1979, "The Measurement of Natural Convective Heat Transfer in Triangular Enclosures," *ASME JOURNAL OF HEAT TRANSFER*, Vol. 101, pp. 648-654.
- Flack, R. D., 1980, "The Experimental Measurement of Natural Convection Heat Transfer in Triangular Enclosures Heated or Cooled From Below," *ASME JOURNAL OF HEAT TRANSFER*, Vol. 102, pp. 770-772.
- Karyakin, Yu. E., Sokovishin, Yu. A., and Martynenko, O. G., 1988, "Transient Natural Convection in Triangular Enclosures," *Int. J. Heat Mass Transfer*, Vol. 31, No. 9, pp. 1759-1766.
- Kimura, S., and Bejan, A., 1985, "Natural Convection in a Differentially Heated Corner Region," *Physics Fluids*, Vol. 28, pp. 2980-2989.
- Martin del Campo, Ernesto, Sen, Mihir, and Ramos, Eduardo, 1988, "Analysis of Laminar Natural Convection in a Triangular Enclosure," *Numerical Heat Transfer*, Vol. 13, pp. 353-372.
- Moffatt, H. K., 1964, "Viscous and Resistive Eddies Near a Sharp Corner," *J. Fluid Mech.*, Vol. 18, pp. 1-18.
- Nansteel, M. W., and Greif, R., 1981, "Natural Convection in Undivided and Partially Divided Rectangular Enclosures," *ASME JOURNAL OF HEAT TRANSFER*, Vol. 103, pp. 623-629.
- Nansteel, M. W., Sadhal, S. S., and Ayyaswamy, P. S., 1986, *Significant Questions in Buoyancy-Affected Enclosure or Cavity Flows*, ASME Winter Annual Meeting, Vol. 60, p. 123.
- Poulikakos, D., and Bejan, A., 1983a, "Natural Convection Experiments in a Triangular Enclosure," *ASME JOURNAL OF HEAT TRANSFER*, Vol. 105, pp. 652-655.
- Poulikakos, D., and Bejan, A., 1983b, "Fluid Dynamics of an Attic Space," *J. Fluid Mech.*, Vol. 131, pp. 251-269.
- Sherman, F. S., 1990, *Viscous Flow*, McGraw-Hill, p. 79.
- Winters, K. H., 1983, "Laminar Natural Convection in a Partially-Divided Cavity," *Third Int. Conf. on Numerical Methods in Thermal Problems*, Seattle, WA.
- Yu, K. M., and Nansteel, M. W., 1990, "Buoyancy-Induced Stokes Flow in a Wedge-Shaped Enclosure," *J. Fluid Mech.*, Vol. 221, pp. 437-451.

Investigation of Natural Convection Heat Transfer in Converging Channel Flows Using a Specklegram Technique

K. D. Kihm
Assistant Professor.
Mem. ASME

J. H. Kim
Graduate Research Assistant.

L. S. Fletcher
Thomas A. Dietz Professor.
Fellow ASME

Department of Mechanical Engineering,
Texas A&M University,
College Station, TX 77843

Natural convection heat transfer characteristics in converging vertical channel flows were studied by nonintrusively measuring the wall temperature gradients using a laser specklegram technique. Local and average heat transfer coefficients were obtained for forty different configurations, including five different inclination angles from the vertical, $\gamma=0, 15, 30, 45$ and 60 deg, with eight different channel exit openings for each inclination angle. Correlations for both local and average Nusselt numbers, based on the channel length L , were determined as functions of Grashof number, where the local Grashof number, based on the channel length L , ranged up to 7.16×10^6 and the overall Grashof number varied from 3.58×10^5 ($\gamma=60$ deg) to 7.16×10^6 ($\gamma=0$), depending upon the inclination angle. As the top opening was decreased, both local and average Nusselt numbers deviated from the single inclined plate theory and significant reductions in heat transfer resulted. The minimum opening ratio, at which the average Nusselt number started decreasing from that for the single plate, was determined as $(b/L)_{\min}=0.07, 0.1, 0.3, 0.35,$ and 0.4 for inclination angles of $0, 15, 30, 45$ and 60 deg, respectively. For Ra^ larger than 10^5 , average Nusselt numbers, based on the channel opening b , approached the single-plate limit of the vertical channel flow theory, which was modified to incorporate the reduced gravity due to the inclination. When Ra^* was smaller than 10^5 , however, neither the single-plate limit nor the fully developed limit properly described the heat transfer characteristics in the converging channel.*

Introduction

Converging air channels that form a triangular enclosure are commonly used in a wide range of buildings, not only for structural strength but also for enhanced insulation of the air-filled space between a ceiling and a roof. Partial openings at both the top and bottom corners of the enclosure will induce converging air flow because of the natural convection boundary layers growing along the inclined roof surfaces (Fig. 1). These openings will reduce the heat transfer from the inclined roof surfaces to the air inside with increase in the convective heat transfer to the outside air through the thermal boundary layers. This enables the ceiling (the bottom plate) to be effectively insulated against the heat penetration from the inclined roof surfaces. When the top opening is too small, however, the boundary layers on the two inclined surfaces will merge and the heat transfer to the outside air will be significantly reduced. The reduction in heat transfer occurred as result of the retardation of the convective air stream because of the narrowed passages, and the phenomenon can be referred as a "choked" state. If the top opening were completely closed, no convective thermal boundary layers would develop. Instead, stratified fluid layers of different densities would be stacked vertically and the heat transfer would occur predominantly by thermal conduction, which results a significant reduction in heat transfer. The choking condition accompanying a heat transfer reduction must be identified and should be avoided to ensure the optimal cooling of inclined surfaces.

Since the pioneering study of heat convection in vertical parallel channel flow by Elenbaas (1942), a number of early

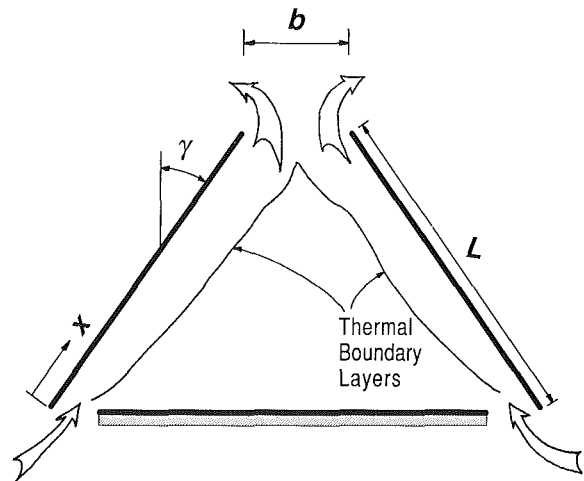


Fig. 1 A schematic illustration of thermal boundary layers in a triangular enclosure

investigators, e.g., Eckert and Carlson (1961), Levy (1972), Wirtz and Stutzman (1982), Bar-Cohen and Rohsenow (1984), and Anand et al. (1992), have indicated that there exists an optimum plate spacing with the highest average Nusselt number occurring when the natural convective heat transfer along the plates reaches its maximum. Naylor et al. (1991) studied the entrance flow effects numerically using the full elliptic equations with extended inlet boundary conditions. They concluded that a full elliptic solution is necessary to determine accurate local quantities near the channel entrance. Martin et al. (1991) investigated a similar problem numerically, specifically for the case of very low Rayleigh number flows. They found that the well-accepted asymptotic behavior for the fully developed solution was valid only under limited conditions.

Contributed by the Heat Transfer Division and presented at the ASME Winter Annual Meeting, Atlanta, Georgia, December 1-6, 1991. Manuscript received by the Heat Transfer Division December 16, 1991; revision received July 2, 1992. Keywords: Flow Visualization, Natural Convection. Technical Editor: R. Viswanta.

Flack et al. (1979) and Flack (1980) studied heat transfer rates inside a closed triangular enclosure with no openings. The two inclined side walls were heated and cooled, respectively, and the bottom surface was maintained adiabatic. The heat transfer characteristics were seen to be somewhat different from that of a single heated or cooled inclined plate, because of the interference of the thermal boundary layers near the upper corners.

When the upper and lower corners are partially opened, the development of thermal boundary layers will be different and a converging convective flow will result. The heat transfer characteristics, therefore, will be different from the results of the closed system, and also will be different from that of a parallel channel system since the thermal boundary layers develop in a different manner. As a consequence, heat transfer characteristics inside converging channel flow should be investigated because they have not been previously examined.

Heat transfer characteristics in a converging channel configuration, with partial openings on top and bottom corners, were experimentally studied in the present investigation. A nonintrusive specklegram technique (Merzkirch, 1989), with a digital fringe processing system, was employed to measure the wall temperature gradients directly along inclined isothermal surfaces. Both local and average heat transfer coefficients were determined from the measured values of the wall temperature gradients. The effect of the openings on the heat transfer rate was investigated to determine the minimum opening ratio corresponding to the maximum heat transfer from the inclined plates through the convective thermal boundary layers. Differences were identified between the data presented in this paper and data previously obtained for a single inclined plate, and for parallel channel flows formed with double vertical heated plates. The Grashof number was modified to account for the reduced gravitational effect due to the inclination of the isothermal walls, i.e., $Gr_x = Gr_x \cos \gamma$ (Kierkus, 1968; Hasan and Eichhorn, 1979). Local Nusselt numbers are presented in terms of local Grashof numbers. Results for average Nusselt numbers, based on the channel opening b , are also presented as function of Ra^* as suggested by Elenbaas (1942). The characteristics of the thermal layers were visualized qualitatively using a Schlieren technique.

Experimental Apparatus and Data Processing

The experimental apparatus encompasses the converging channel facility, which provides two inclined isothermal plates and a bottom adiabatic plate, and the support assembly for adjustment of both the inclination angle and the opening ratios. The diagnostic system includes a He-Ne laser specklegram system for direct and nonintrusive measurements of the wall temperature gradients. A computerized evaluation of the specklegram fringe spacings is also briefly described for the data reduction process.

Converging Channel. Each of the two isothermal walls was made with 12.7-mm-thick copper plate with dimensions of 125 mm (L) by 200 mm (H), which was grooved from the back surface to provide a passage for the circulating water, as shown in Fig. 2. The plate was machined to a 45-deg knife edge on the lower side to reduce the leading edge disturbance on the thermal layer downstream (Yang and Jerger, 1964, and others thereafter). Both plates were heated by a single constant-temperature bath to maintain a uniform wall temperature. A water jacket was installed on the back of each plate using 10-mm-thick Lexan. A total of six K-type thermocouple probes were embedded to within 1 mm from the front surface of each plate to monitor the uniformity and consistency of the wall temperature. The typical variance between the readings of the six thermocouples was $\pm 0.2^\circ\text{C}$ for the case of 60°C wall temperature, with a measurement uncertainty of ± 0.3 percent. The range of ambient temperature varied from 24.5 to 28°C on a daily basis during the experimental study, and the wall temperature ranged from 56 to 62°C so that the temperature differential, $T_w - T_e$, remained within $32.7 \pm 1.2^\circ\text{C}$ throughout the geometric variations. The ambient temperature was also measured with a thermocouple probe and showed negligible variance over a several hour period.

The bottom plate was fabricated from 12.7-mm-thick balsa wood to simulate an adiabatic wall condition. The opening of the two lower corners was adjusted to be one half of the top opening for all the variations of the top opening so that the air inlet and outlet cross-sectional areas were identical. The main role of the bottom adiabatic plate placed herein was to prevent the possible upstream hydrodynamic and/or thermal

Nomenclature

b = opening at the top of the channel	L = inclined plate dimension perpendicular to the optical path = 125 mm	z = coordinate parallel to the optical path
c = distance between the ground glass and the focal plane of a camera (Fig. 3)	m = magnification of a physical object to a speckle image on the ground glass	β = volumetric coefficient of expansion = $1/T_e = 1/300 \text{ K} = 3.333 \times 10^{-3} \text{ K}^{-1}$
c_p = specific heat at constant pressure, $\text{kJ/kg}\cdot^\circ\text{C}$ or $\text{J/kg}\cdot^\circ\text{C}$	m' = magnification of the speckle image to a camera recording image	γ = inclination angle of the inclined plate measured from the vertical, deg
d = distance between the specklegram slide and the screen (Fig. 4)	n = index of refraction of air	λ = wave length of He-Ne laser = 632.8 nm
Gr_x = local Grashof number = $g\beta \cos \gamma (T_w - T_e)x^3/\nu^2$	Nu_x = local Nusselt number = hx/k	μ = dynamic viscosity, $\text{kg/m}\cdot\text{s}$
Gr_L = overall Grashof number = $g\beta \cos \gamma (T_w - T_e)L^3/\nu^2$	Nu_b = average Nusselt number = $\bar{h}b/k$	ν = kinematic viscosity of air, m^2/s
g = gravitational constant = 9.8 m/s^2	Nu_L = average Nusselt number = $\bar{h}L/k$	ρ = air density, kg/m^3
H = inclined plate dimension parallel to the optical path = 200 mm	Ra^* = Rayleigh number as defined by Elenbaas (1942) = $\frac{g\beta \cos \gamma (T_w - T_e)b^3}{\nu^2} \cdot \frac{\nu}{\alpha} \cdot \frac{b}{L}$	Subscripts
h = thermal convection coefficient, $\text{W/m}^2\cdot^\circ\text{C}$	s = fringe spacing	e = properties evaluated at the ambient temperature
\bar{h} = average thermal convection coefficient, $\text{W/m}^2\cdot^\circ\text{C}$	T = temperature, $^\circ\text{C}$	r = properties evaluated at the reference temperature, $T_r = T_w - 0.38(T_w - T_e)$, suggested by Sparrow and Gregg (1958)
k = thermal conductivity, $\text{W/m}\cdot^\circ\text{C}$	x = coordinate parallel to the inclined plate	w = properties evaluated at the wall temperature of the inclined plate
	y = coordinate normal to the inclined plate	

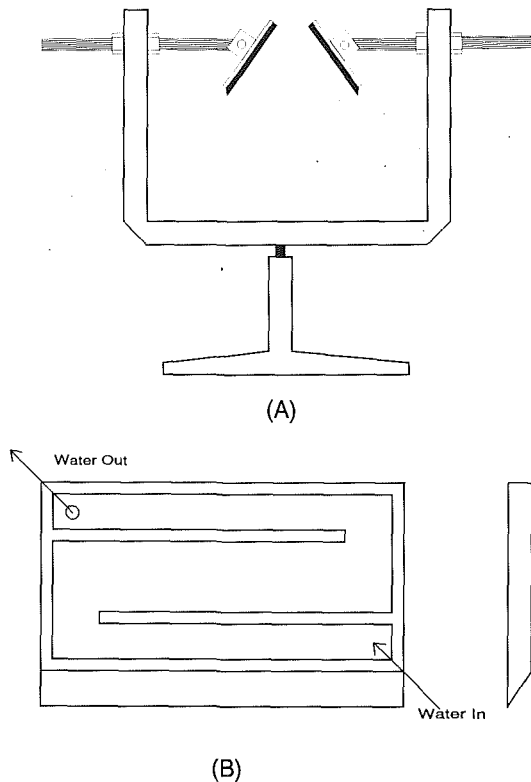


Fig. 2 Schematic diagrams of the experimental setup: (A) support and positioning assembly, and (B) water jacket for the isothermal inclined plate

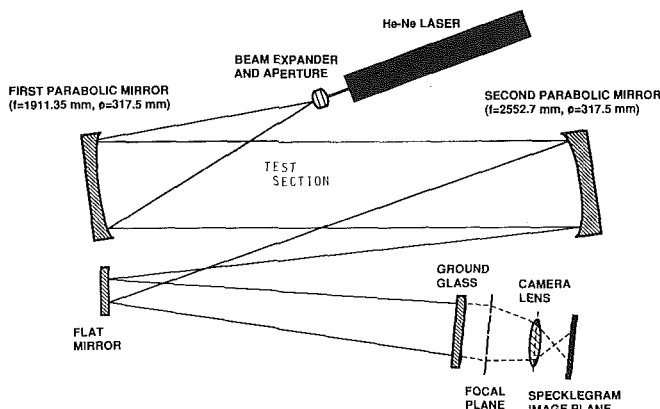


Fig. 3 Optical configuration of the specklegram recording system

fluctuations from entering the channel. Preliminary Schlieren visualization showed that as long as the total inlet area A_i of the two lower corners was kept the same as the upper exit area A_o , the thermal boundary layers near the leading edge of the inclined plate were not affected by the presence of the bottom plate. For the ratio A_i/A_o smaller than unity, the overall heat transfer may decrease since the bottom plate would act to restrict the incoming air flow and also could interfere with the boundary layers near the leading edge of the inclined plate.

A special feature of the support assembly is its versatility in providing a variable spacing between the plates and an adjustable inclination angle for both plates, with 15-deg increments. The end planes of the triangular enclosure were covered with optically flat glass, 3.2 mm thickness, to eliminate, insofar as possible, the three-dimensional ambiguity that otherwise would occur near the ends (Sparrow and Bahrami, 1980; Azevedo and Sparrow, 1985).

Specklegram System. Figure 3 presents the optical layout of the specklegram system that was used to measure the wall

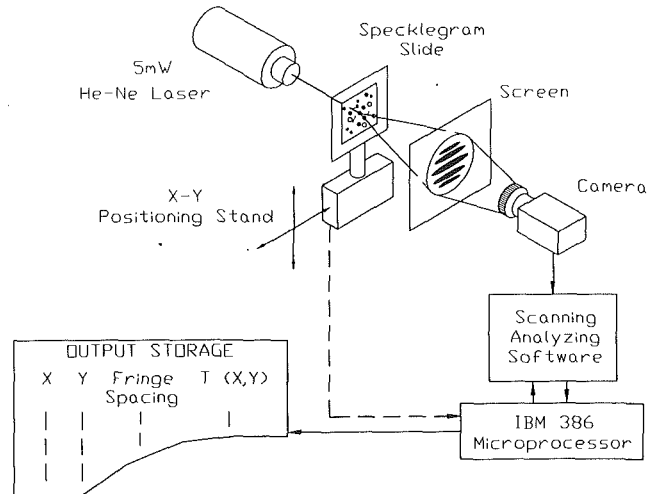


Fig. 4 Schematic illustration of the data reduction process for specklegram

temperature gradients nonintrusively. A 35 mW He-Ne laser of 632.8 nm wavelength was used as the coherent and monochromatic light source. The laser beam was expanded to 120 mm diameter using a microscope objective lens. The expanded beam was collimated by a parabolic mirror to form parallel light rays throughout the test section. After passing the test section, the light rays were focused by the second parabolic mirror onto a ground glass on which the image of the test section was constructed. Speckles are formed spatially behind the ground glass because of the interference of randomly diffracting rays from the granular surface of the ground glass. Speckles are, therefore, formed regardless of the presence of a test field. When a test field is present in the parallel beam passage, the light rays will be refracted because of the index-of-refraction variations in the test field and the resulting speckles will have different spatial locations with respect to speckles recorded without the test field. Each pair of speckles, with and without the test field, shares the same origination point in the test field.

The specklegram, a superimposed image of speckles with and then without the presence of the test field, was recorded using a 4 by 5 inch format bellows camera with high resolution and medium sensitivity ILFORD pan F50 ASA film. The amount of translocation of individual speckles has a precise relationship to the density or temperature gradient in the test section. A simple consideration of the optical geometry with an assumption of the Gladstone-Dale relationship (Eckert and Goldstein, 1976) derives an expression for the temperature gradient (Kihm et al., 1991):

$$\frac{\partial T}{\partial y} = \frac{\lambda \cdot d}{H \cdot c \cdot s} \cdot \left(\frac{dn}{dT} \right)^{-1} \cdot \frac{m}{m'} \quad (1)$$

where the geometric constants H , c , and d represent the width of the inclined plate, the distance from the ground glass to the focal plane (Fig. 3), and the distance between the specklegram slide and the screen (Fig. 4), respectively. The magnification of the second parabolic mirror is denoted by m , and m' denotes the magnification of the recording system. The relationship for the refractive index of air at the 632.8 nm wavelength of He-Ne laser gives an expression for the constant, dn/dT (Vest, 1979):

$$\frac{dn}{dT} = - \frac{1.075 \times 10^{-6}}{(1 + 0.00368184 T)^2} \quad (2)$$

where T is in degrees Celsius. T was taken as being equal to the wall temperature since the air temperature adjacent to the wall should be closely equal to the wall temperature. The wall temperature variations were negligibly small (± 0.3 percent)

and the measurement uncertainty due to the temperature dependence of dn/dT is also expected to be negligibly small.

The temperature gradient, $\partial T/\partial y$, can now be determined from the measurement of the fringe spacing, s , of Young's fringes, which are constructed by illuminating the specklegram with a small He-Ne laser (Fig. 4). The fringe spacings were measured using a software called FRINGE that scans and identifies locations with the maximum and minimum light intensities on a digitized fringes imaged by a video camera. This digitized measurement of fringe spacing must be very accurate and the measurement uncertainty is estimated to be within ± 1 percent. The constituent equation for the specklegram technique, Eq. (1), should be accurate with ± 1 to 2 percent error at most, since those physical lengths, magnifications, and other optical parameters in the equation were provided from straightforward measurements or from well-established theories.

Additional measurement uncertainties for the wall temperature gradient, $(\partial T/\partial y)_w$, can result from the defocusing of the test section on the specklegram recording plane. The image of the test object on a specklegram must be slightly defocused and this is an essential consequence in recording speckles with a measurable distinctiveness between speckle dislocations. The uncertainty due to the image biasing can be estimated with an image blur ratio (Kihm, 1992), which is defined as a ratio of the defocusing distance measured from the ground glass to the focal length of the Schlieren head, or the second parabolic mirror (Fig. 3). As the measurement location is placed farther away from the optical axis, the uncertainty because of the defocusing will be higher since the light ray diffraction increases with increase in the traverse distance from the optical axis. The maximum uncertainties associated with the image defocusing combined with the measurement location effect were calculated to be within ± 0.3 mm for the case of an object distance of 62.5 mm (equivalent to $L/2$) from the optical axis. In the gray zone, which resulted from the image uncertainties, the signal-to-noise ratios of the data were somewhat reduced, but the fringes were still distinguishable. The speckle dislocation data were obtained at the nearest location to the wall to evaluate wall temperature gradients. The calculations also showed that the maximum value of the image blur ratio was up to 0.8 percent for the worst case. The overall measurement uncertainties for the wall temperature gradient because of the defocusing, therefore, should be within 1 percent for a very conservative estimation.

Data Reduction. Considering an energy balance between an isothermal wall at T_w and the ambient air at temperature T_e , the correlation of the local heat transfer coefficient is expressed as:

$$\frac{h(x)}{k} = -\frac{(\partial T/\partial y)_w}{(T_w - T_e)} \quad (3)$$

where the thermal conductivity k can be evaluated at the wall temperature since the heat conduction occurs at the wall. The actual evaluation of the thermal conductivity, however, was not necessary in determining the heat transfer correlations since the local Nusselt number, $Nu_x = h(x)x/k$, was directly determined from the right-hand side of Eq. (3):

$$Nu_x = \frac{h(x)}{k} x = -\frac{(\partial T/\partial y)_w}{(T_w - T_e)} x \quad (4)$$

and the local Grashof number is defined:

$$Gr_x = g\beta \cos \gamma (T_w - T_e) x^3 / \nu_r^2 \quad (5)$$

where the volumetric expansion coefficient for ideal gases

$$\beta = 1/T_e \quad (6)$$

Assuming that the air density variations were small across the thermal boundary layers for the range of temperatures considered, the reciprocal of the ambient temperature was set equal

to β (Holman, 1981). The kinematic viscosity of air, ν_r , was obtained at the reference temperature, T_r ,

$$T_r = T_w - 0.38(T_w - T_e) \quad (7)$$

This reference temperature, which was suggested for improved fitting by Sparrow and Gregg (1958), results in a slightly higher temperature than the arithmetic mean of the wall and ambient temperatures. If the volumetric expansion coefficient were to be evaluated at the same reference temperature as in Eq. (7), the resultant Grashof number would be reduced by up to 5 percent.

The average convection heat transfer coefficient is then determined by integrating Eq. (3) along the inclined plate length, L :

$$\bar{h} = \frac{1}{L} \int_0^L h(x) dx = -\frac{k}{L} \int_0^L \frac{(\partial T/\partial y)_w}{(T_w - T_e)} dx \quad (8)$$

and the average Nusselt number based on the plate length is

$$\bar{Nu}_L = \bar{h}L/k = -\int_0^L \frac{(\partial T/\partial y)_w}{(T_w - T_e)} dx \quad (9)$$

and the Grashof number based on plate length is

$$Gr_L = g\beta \cos \gamma (T_w - T_e) L^3 / \nu_r^2 \quad (10)$$

where β and ν_r are specified similarly to the case of the local correlations.

The experimental study of heat transfer using conventional techniques necessitates several requirements since the electric power of the surface (foil) heater is usually measured. The most stringent requirements among these include: (1) the whole experimental apparatus must be extensively insulated to minimize the heat loss through other than the primary surface and (2) the radiation loss from the surface must be subtracted from the measured heater power. The measurement accuracy will be limited because of the heat loss from nonperfect insulation as well as the radiation loss. In determining the heat convection coefficients, both Nu_x and \bar{Nu}_L , using the specklegram technique, neither the radiation heat loss nor the heat loss other than the surface needs to be determined. This is because the specklegram technique exclusively ascertains only the convective heat transfer rate from the surface by directly measuring the wall temperature gradients. The radiation heat transfer from the heated surface is not associated with the measurements and can be considered as a completely separate phenomenon. The bulky insulation material wrapped around the experimental configuration is no longer necessary when the specklegram technique is employed. This simplicity with enhanced accuracy is the primary advantage of the laser specklegram technique and the technique can significantly alleviate the difficulties that would occur in heat transfer experiments with the conventional methods, particularly for the case of natural convection problems where the amount of heat transfer is in general very minute and the heat losses can significantly affect the measurement accuracy.

Results and Discussion

Local and average heat transfer characteristics for converging channel flows along inclined isothermal plates were determined for five different inclination angles, $\gamma = 0, 15, 30, 45,$ and 60 deg from the vertical, and for up to eight different opening ratios, $b/L = 0.02, 0.05, 0.1, 0.2, 0.3, 0.4, 1,$ and 2 for each inclination angle. Local and average Nusselt number correlations were determined where overall Grashof number ranged from 3.58×10^6 ($\gamma = 60$ deg) to 7.16×10^6 ($\gamma = 0$).

Figure 5 presents Young's fringe patterns constructed at different locations on a specklegram taken for $\gamma = 30$ deg and $b/L = 0.2$. The very steep temperature gradient near the inclined wall created distinctive fringes with narrow spacing (inset photos A and B) and the gradual temperature gradient near

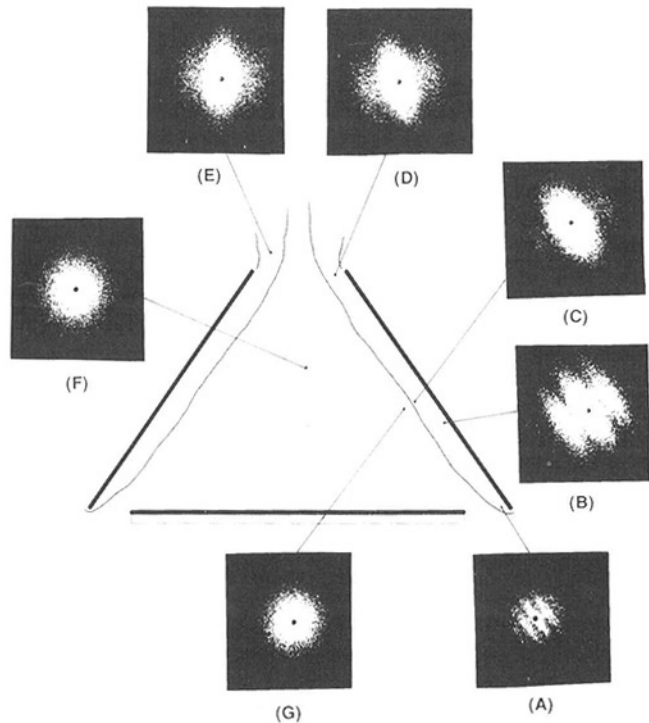


Fig. 5 Local patterns of the speckle fringes in converging flows with inclined isothermal plates

the boundary resulted in less distinctive fringes with wide spacing (inset photo C). At the top opening (inset photos D and E), where thermal boundary layers developed because of the temperature gradient between the heated air from inside and the cooler ambient air, the fringe patterns were observed. Outside the thermal layer (inset photos F and G) no fringe patterns were constructed, indicating zero or extremely low temperature gradients. The fringe orientation, which is perpendicular to a local temperature gradient, indicates the primary direction of heat transfer. The fringe patterns, therefore, provide qualitative information on the temperature gradient as well as the primary direction of heat transfer.

Figure 6 presents the correlations of local heat transfer coefficients for vertical parallel channel flows with several different spacings. The solid line represents the theory of Ostrach (1952) for a vertical isothermal single plate:

$$Nu_x = 0.5046 (Gr_x/4)^{0.25} \quad (11)$$

Good agreement between the experimental data and the theory was shown for opening ratios down to 0.1, which indicated that each wall acts as an independently inclined plate without affecting each other, when b/L was equal to or greater than 0.1. The good agreement also demonstrated the measurement accuracy of the specklegram technique. For $b/L=0.05$, the local Nusselt number started to deviate from the theory when the local Grashof number was larger than 5×10^4 . The deviation from the single plate theory implied that the two thermal boundary layers started interfering with each other, which resulted in a decrease in the wall temperature gradients for $Gr_x > 5 \times 10^4$. When the local Grashof number exceeded 10^5 , for the case of $b/L=0.05$, the fringes were not clearly constructed since the fully developed thermal boundary layers resulted in horizontally uniform temperature field and the overall heat transfer rate was further decreased. The speckle dislocations were very small and the fringe spacing approached infinity because of the extremely low wall temperature gradients. The minimum opening, at which the thermal layers started interfering with each other and the amount of heat transfer started decreasing from that of a single plate limit, was estimated to be close to b/L of 0.05.

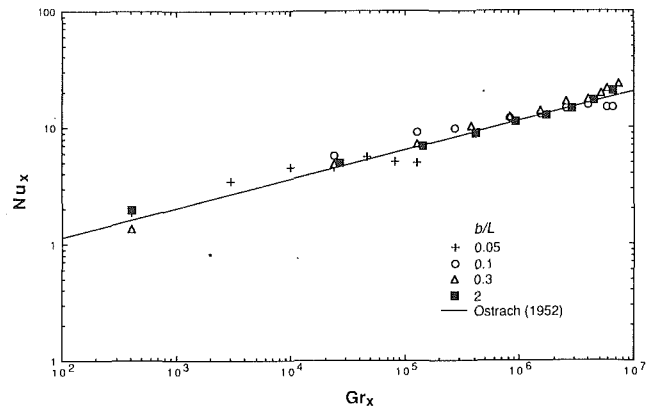


Fig. 6 Local Nusselt number versus local Grashof number for a vertical isothermal channel flow

Bar-Cohen and Rohsenow (1984) proposed the following experimentally extrapolated relationship of the minimum opening ratio for the case of a vertical isothermal channel flow:

$$\left(\frac{b}{L}\right)_{\min} = \frac{2.714}{\left(\frac{c_p \rho^2 g \beta L^3 (T_w - T_e)}{\mu k}\right)^{1/4}} \quad (12)$$

For the conditions in Fig. 6, $c_p = 1007 \text{ J/kg} \cdot ^\circ\text{C}$, $\rho = 1.10564 \text{ kg/m}^3$, $g = 9.8 \text{ m/s}^2$, $\beta = 3.333 \times 10^{-3} \text{ K}^{-1}$, $L = 0.125 \text{ m}$, $T_w - T_e = 32^\circ\text{C}$, $\mu = 1.9377 \times 10^{-3} \text{ kg/m} \cdot \text{s}$, and $k = 0.02776 \text{ W/m} \cdot ^\circ\text{C}$, $(b/L)_{\min}$ was calculated to be equal to 0.0584. This calculation agrees fairly well with the value of 0.05, which was estimated from the measurement of the local heat transfer coefficient in Fig. 6.

Figure 7 presents Schlieren pictures of thermal boundary layers along the vertical channel for three different opening ratios of $b/L = 0.2, 0.1$, and 0.05 . Convective thermal boundary layers appear darker on the Schlieren photographs since the light intensity change is proportional to the temperature (or density) gradient, and regions outside the thermal boundary layers are viewed as relatively bright images indicating very low temperature gradients. For $b/L = 0.2$, separate thermal boundary layers developed with no interference with each other (Fig. 7A). The bright region between the thermal layers indicated horizontally uniform temperature distributions and the incoming air was induced to flow upward due to the vertically driven buoyancy force, i.e., a so-called chimney effect. When the opening ratio was reduced to 0.1 (Fig. 7B), thermal layers still grew independently and the vertically induced flow region was developed. The distinctiveness of the thermal boundary layers near the top exit was slightly diminished as the thermal layers started interfering with each other. When the opening ratio was further decreased to 0.05 (Fig. 7C), the two layers merged to be fully developed well before the top opening, and a horizontally uniform temperature field occurred thereafter. The developing thermal layers (dark regions) existed only near the entrance where the most of heat transfer occurred, and in the fully developed region thereafter heat transfer rate would be very small with nearly zero values of wall temperature gradients. From the visualization, $(b/L)_{\min}$ was also estimated to be approximately equal to 0.05.

A rough indication of the start of transition from laminar to turbulent flow in a vertical configuration was suggested by Cebeci and Bradshaw (1988) to be in the range of the local Grashof number, based on the plate length L , from 6.25×10^{10} to 1.3×10^{11} . The transition condition for the air flow developing along a single vertical plate, however, has been studied by several investigators experimentally as well as analytically: Tritton (1962) used a fiber anemometer to survey the region of intermittent turbulence and suggested a critical value of $Gr_x = 8.57 \times 10^6$. Lloyd and Sparrow (1970) employed an elec-

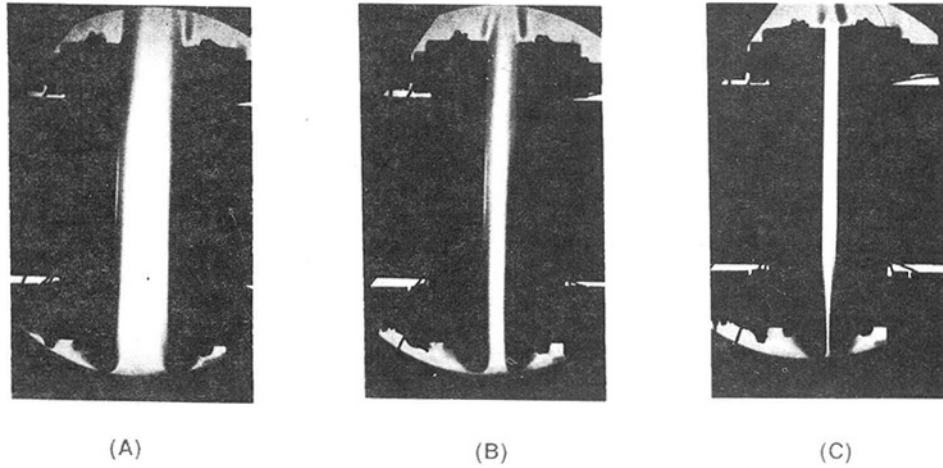


Fig. 7 Schlieren visualization of the development and merging of thermal layers inside the parallel channel with $b/L = 0.2$ (A), 0.1 (B), and 0.05 (C)

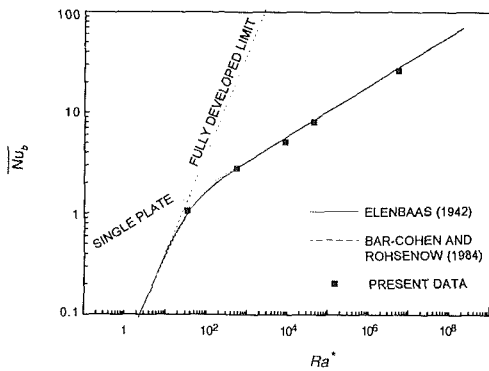


Fig. 8 Average Nusselt number based on the top opening, $\overline{Nu}_b = \overline{hb}/k$, versus Rayleigh number, $Ra^* \equiv \frac{g\beta \cos \gamma (T_w - T_o) b^3}{\nu_r^2} \cdot \frac{\nu_r}{\alpha} \cdot \frac{b}{L}$ (Elenbaas, 1942)

trochemical flow visualization technique and determined the onset for fluid disturbances as $Gr_x = 1.24 \times 10^9$. Study of theoretical predictions for the critical Grashof number can be further divided into two categories depending on the approaching methods: (1) the traditional wave instability approximation and (2) the vortex instability simulation. Haaland and Sparrow (1973a) studied the problem using a perturbation equation with the wave instability concept and predicted a critical value of $Gr_x = 1.17 \times 10^6$. They also investigated the vortex stability for the natural convection along a vertical plate (Haaland and Sparrow, 1973b). Chen and Tzuoo (1982) made an analysis of vortex instability and their calculation resulted in a value of $Gr_x = 1.2 \times 10^6$, very close to that of Haaland and Sparrow (1973a). Tzuoo et al. (1985) later improved the theory by employing the wave instability theory and predicted a somewhat larger value of critical Grashof number, $Gr_x = 6.2 \times 10^6$. The Grashof numbers for the present study ranged up to 7.16×10^6 , which was close to the lower limit of the existing data and predictions. The thermal boundary layers therefore remained stable in most regions along the plate as far as there exist no interferences between the layers, i.e., as long as b/L was kept larger than $(b/L)_{min}$.

The local heat convection coefficients were integrated along the plate length following Eq. (8) to determine the average values and the results are presented in Fig. 8. The Nusselt number has been defined based on the channel width, $\overline{Nu}_b \equiv \overline{hb}/k$, and the abscissa represents the modified Rayleigh number as defined by Elenbaas (1942):

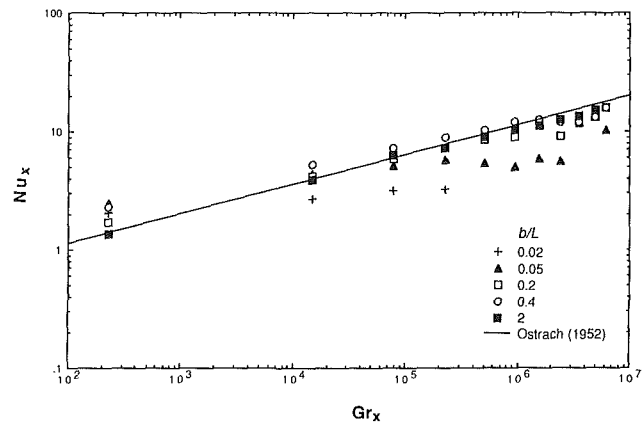


Fig. 9 Local Nusselt number versus local Grashof number for the converging flow with an inclination angle $\gamma = 30$ deg

$$Ra^* = \frac{g\beta \cos \gamma (T_w - T_o) b^3}{\nu_r^2} \cdot \frac{\nu_r}{\alpha} \cdot \frac{b}{L} \quad (13)$$

where γ is equal to zero for the vertical channel and the subscript r denotes an evaluation of the property at the reference temperature given by Sparrow and Gregg (1958). Also presented in Fig. 8 are the experimentally extrapolated correlations for the case of vertical channel flow by Elenbaas (1942) and by Bar-Cohen and Rohsenow (1984). The data showed very good agreement with the previous correlations ensuring the measurement accuracy of the specklegram technique. As discussed earlier with Fig. 6, the data obtained for $b/L = 0.05$ ($Ra^* \approx 30$) approached the fully developed limit having a lower Nusselt number than the single plate limit because of the merging of thermal layers, which significantly reduces the heat transfer rate. In integrating and averaging the data for the case of $b/L = 0.05$, a logarithmic extrapolation was made for the region of $Gr_x > 10^5$ where the speckle measurements were not available because of overly low wall temperature gradients after the merging of the thermal boundary layers. An interesting thing to note is that a selection of different functional forms for the extrapolation, such as polynomial functions, does not noticeably alter the resultant \overline{Nu}_b since h rapidly decays to zero in the extrapolated region ranging from $Gr_x > 10^5$ to $Gr_L = 7.16 \times 10^6$.

Figure 9 presents results of the local Nusselt number versus Grashof number for $\gamma = 30$ deg. The solid line again represents Ostrach's theory with a modified Grashof number (Eq. (5)),

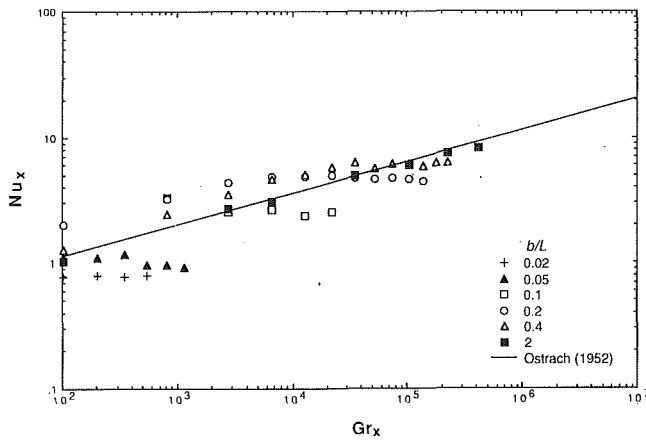


Fig. 10 Local Nusselt number versus local Grashof number for the converging flow with an inclination angle $\gamma = 60$ deg

which accounted for the decreased gravitational effect due to the inclination of the plate. The good agreement of the data for the single inclined plate, represented by the case of $b/L = 2$, with the theory implies that the convective heat transfer along a single inclined plate can be predicted accurately by the modified theory by Ostrach (1952). The merging of the thermal boundary layers in the previous vertical channel flow occurred primarily as a result of the growth of the two boundary layers under parallel free-stream air flow. For the case of the inclined isothermal walls, the boundary layers were more unstable and thicker partly because of the reduced buoyancy and partly because of the entrainment of the recirculating flow driven in the converging air flows. When the top opening was large, the flow recirculation disappeared since the converging channel effect was weak, and the thermal layers developed individually without affecting each other. For this case, the heat transfer rate approached that of the inclined single plate results. As the top opening decreased, however, the thermal boundary layers started interfering with each other and the convection heat transfer decreased from the case of the single inclined plate. The Nusselt number variations were nearly flat, indicating that the local heat convection coefficient, h , decreased dramatically with x . With decrease in b/L , the discrepancy of the data from the theory started at smaller Grashof number because the merging of thermal boundary layers occurred nearer the leading edge. For the case of b/L of 0.02, the measured Nusselt numbers were below the theory for most regions of the plate except near the entrance and, therefore, the most region of the channel flow must have been fully developed with merged thermal layers. The local Nusselt number showed a slight increase near the top opening after relatively flat values in the merging region. At the top opening, the thermal layers redeveloped and the heat transfer was enhanced gradually because of the heat transfer between the emerging flow stream and the cooler ambient air above.

As the inclination angle, γ , was increased from 30 to 60 deg, the discrepancies between the data and the single plate theory have been increased (Fig. 10). The data measured for a single plate, $b/L = 2$, agreed fairly well with theory, demonstrating that the thermal boundary layer development along the inclined plate with large b/L was similar to the case of the single plate. As the top opening was decreased, however, the thermal boundary layer development was different. The Schlieren visualization indicated that the thermal layers started merging as early as at $b/L = 0.4$. When the inclination angle increased from 30 to 60 deg keeping the top opening ratio the same, the convergence of the inclined channel, which was defined as the ratio of the bottom width to the top opening, had been doubled. This stronger restrictions to the air flow resulted that the thermal boundary layers merged for larger value of b/L for $\gamma = 60$

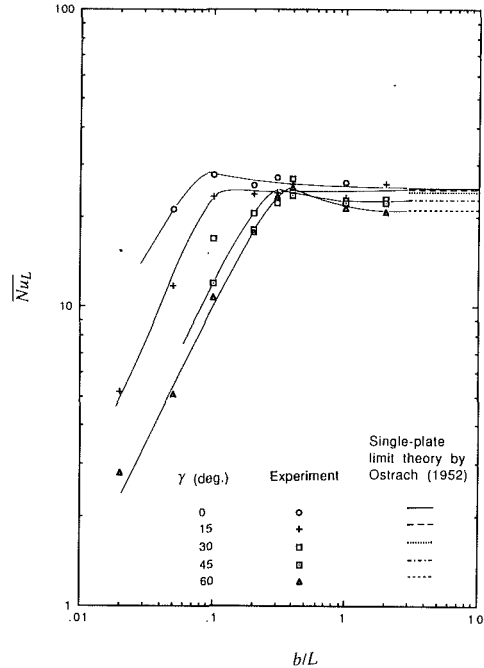


Fig. 11 Average Nusselt number based on the plate length, $\overline{Nu}_L = \overline{hL}/k$, versus the opening ratio b/L for five different inclination angles: $\gamma = 0, 15, 30, 45,$ and 60 deg [$Gr_L (= g\beta \cos \gamma (T_w - T_\infty)L^3/\nu^2)$ ranged from 3.58×10^6 ($\gamma = 60$ deg) to 7.16×10^6 ($\gamma = 0$)]

deg than for the case of $\gamma = 30$ deg. In converging channel flows the flow recirculations act to disturb the thermal layers, whereas the gravitational contribution tends to stabilize the thermal layers. The buoyancy driving of the thermal layers decreased for $\gamma = 60$ deg compared with the case for $\gamma = 30$ deg because of the stronger flow recirculations and the reduced gravity.

Further decrease of the top opening reduced the dependence of the local Nusselt number on the local Grashof number. For b/L values of 0.02 and 0.05, the local Nusselt numbers were nearly independent of the Grashof number, indicating that the rate of heat transfer dramatically decreased along the inclined plate. For the cases of these extremely narrow top openings, the thermal boundary layers were distinctive only near the channel entrance and the two layers merged and mixed thereafter. When the top opening is reduced below $(b/L)_{min}$, the convective heat transfer characteristics for converging channel flows could not be properly described with the theory for a single inclined plate.

Average Nusselt and Grashof numbers were calculated using Eqs. (8)–(10) and are presented for five different inclination angles from 0 to 60 deg as functions of the top opening ratio, b/L , in Fig. 11. The overall Grashof number, Gr_L , ranged from 3.58×10^6 ($\gamma = 60$ deg) to 7.16×10^6 ($\gamma = 0$). When the top opening was large, \overline{Nu}_L approached the single plate limit of Ostrach (1952) regardless of the inclination angles. As b/L decreased, a slight increase in \overline{Nu}_L was observed until the maximum peak was reached. When the top opening decreased further, the average Nusselt number started decreasing and eventually became far smaller than the corresponding single plate limit. The minimum top opening ratios for the maximum average Nusselt numbers were determined from Fig. 11 and are summarized in Table 1. Table 1 also tabulates the data presented in Fig. 11. The minimum opening ratio increased with increase in the inclination angle with approximately a linear relationship.

Figure 12 presents a rearrangement of the data in terms of \overline{Nu}_b versus Ra^* and the results are compared with the parallel plate correlations obtained by Elenbaas (1942). For relatively large values of b/L with Ra^* larger than 10^5 , the average

Table 1 Average Nusselt number, $\overline{Nu}_L = \overline{h}L/k$ for $Pr=0.71$; Gr_L ($\equiv g\beta \cos \gamma(T_w - T_a)L^3/\nu^2$) ranged from 3.58×10^6 ($\gamma = 60$ deg) to 7.16×10^6 ($\gamma = 0$)

b/L	γ (degrees)	0	15	30	45	60
0.02		--	5.17	9.72	--	2.78
0.05		21.21	11.798	16.876	--	5.08
0.1		27.867	23.554	16.926	12.06	10.8
0.2		25.65	24.028	20.667	18.187	17.75
0.3		27.122	24.168	22.309	--	23.37
0.4		--	25.816	26.857	23.64	25.25
1.0		26.258	23.35	22.791	22.28	21.53
2.0		--	25.933	23.029	22.44	20.91
∞ : single-plate limit (Ostrach, 1952)		24.952	24.736	24.07	22.88	20.98
$(b/L)_{min}$		0.07	0.1	0.3	0.35	0.4

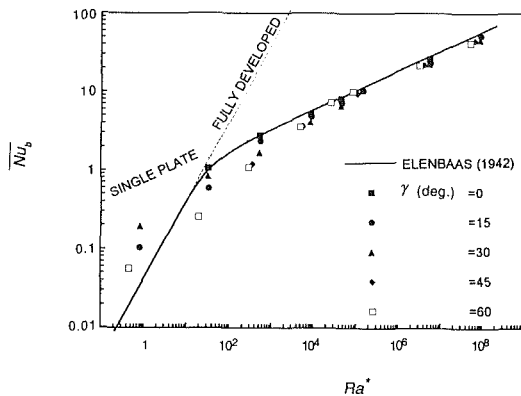


Fig. 12 Average Nusselt number based on the top opening, $\overline{Nu}_b = \overline{h}b/k$, versus Rayleigh number, $Ra^* = \frac{g\beta \cos \gamma(T_w - T_a)b^3}{\nu^2} \frac{\nu_r b}{\alpha L}$ (Elenbaas, 1942)

Nusselt number for the converging channel configurations approached the single-plate limit of parallel channel flow. The Rayleigh number was weighted by the factor $\cos \gamma$ to incorporate the reduced gravity due to the plate inclination. As b/L decreased for Ra^* less than 10^5 , however, the data obtained for converging flow agreed neither with the single-plate limit nor with the fully developed limit. The data in general showed lower values of \overline{Nu}_b than those for the case of parallel channel flow. It is believed that the merging of thermal boundary layers nearer the leading edge than for the parallel channel flow primarily contributed to the reduction in heat transfer. The convergence or inclination of the channel plates appeared to induce a premature choking and resulted in a reduction in heat transfer from the case of the vertical channel flows. This observation seemed valid only when Ra^* was larger than unity.

For Ra^* smaller than unity, the average Nusselt numbers for converging channel flows showed higher values than the fully developed limit of the parallel channel flow. The Schlieren visualization study showed some evidence that when the plates were inclined and have an extremely narrow top opening, $b/L=0.02$, somewhat longer thermal boundary layers developed before they merged or diffused than when the plates were parallel. The overall amount of heat transfer should have been predominantly determined by the region where the thermal boundary layers developed, because after the layers merged or diffused the amount of heat transfer would be significantly diminished. Although it would be necessary to pursue the study

for more extensive investigations, it is presently conjectured that the rather higher \overline{Nu}_b than the fully developed limit for the case of Ra^* smaller than unity may be attributed to the apparently longer development of thermal boundary layers along the inclined channel plates than for the case of parallel channel with the same opening at the top.

Summary and Conclusions

Both local and average correlations of heat transfer coefficients have been obtained for laminar natural convection heat transfer occurring inside converging flows. Measurements were made for wall temperature gradients using a nonintrusive specklegram technique for eight different opening ratios ranging from 0.02 to 2 and five different inclination angles from the vertical, down to 60 deg, corresponding to the local Grashof number, Gr_x , ranging up to 7.16×10^6 and the average Grashof number, Gr_L , ranging from 3.58×10^6 to 7.16×10^6 depending on the inclination angle. Results were compared with theoretical predictions for a single isothermal plate by Ostrach (1952) with various inclinations. The data were also rearranged for \overline{Nu}_b versus Ra^* and the results were compared with the correlation for vertical channel flows given by Elenbaas (1942).

Conclusions of the present investigation include:

- 1 The minimum opening ratio has been experimentally determined to be $(b/L)_{min} = 0.07, 0.1, 0.3, 0.35,$ and 0.4 for $\gamma = 0, 15, 30, 45,$ and 60 deg, respectively.
- 2 For $b/L < (b/L)_{min}$, the merging of thermal boundary layers for converging channel flows occurs nearer the leading edge than for the case of parallel channel flow and significant reductions in Nu_x and Nu_L from the single plate limit result.
- 3 For $b/L > (b/L)_{min}$, Nu_x and \overline{Nu}_L approaches the theoretical predictions for the single plate limit regardless of the inclination angles as far as the reduced gravity is properly considered.
- 4 For Ra^* larger than 10^5 , \overline{Nu}_b approaches the single-plate limit of parallel channel flow regardless of the inclination angles as far as the reduced gravity is properly considered. This, together with conclusion (3), ensures the measurement accuracy of the specklegram technique.
- 5 For Ra^* larger than 1.0, \overline{Nu}_b for the converging channel flows is in general smaller than the case of vertical channel flow even after the reduced gravity was considered. This may be attributed to the fact that the thermal boundary layers merge nearer the leading edge when the heated plates are inclined.
- 6 For Ra^* smaller than 1.0, \overline{Nu}_b exceeds that of the fully developed limit of parallel channel flow. It is believed that this may be due to the longer development of thermal boundary layers along the inclined plates than along the vertical plates.

References

- Anand, N. K., Kim, S. H., and Fletcher, L. S., 1992, "The Effect of Plate Spacing on Free Convection Between Heated Parallel Plates," *ASME JOURNAL OF HEAT TRANSFER*, Vol. 114, No. 2, pp. 515-518.
- Azevedo, L. F. A., and Sparrow, E. M., 1985, "Natural Convection in Open-Ended Inclined Channels," *ASME JOURNAL OF HEAT TRANSFER*, Vol. 107, pp. 893-901.
- Bar-Cohen, A., and Rohsenow, W. M., 1984, "Thermally Optimum Spacing of Vertical, Natural Convection Cooled, Parallel Plates," *ASME JOURNAL OF HEAT TRANSFER*, Vol. 106, pp. 116-123.
- Cebeci, T., and Bradshaw, P., 1988, *Physical and Computational Aspects of Convective Heat Transfer*, Springer-Verlag, New York, p. 274.
- Chen, T. S., and Tzuoo, K. L., 1982, "Vortex Instability of Free Convection Flow Over Horizontal and Inclined Surfaces," *ASME JOURNAL OF HEAT TRANSFER*, Vol. 104, pp. 637-643.
- Eckert, E. R., and Carlson, W. O., 1961, "Natural Convection in an Air Layer Enclosed Between Two Vertical Plates With Different Temperatures," *Int. J. Heat Mass Transfer*, Vol. 2, pp. 106-120.
- Eckert, E. R. G., and Goldstein, R. J., eds., 1976, *Measurements in Heat Transfer*, McGraw-Hill, New York, pp. 241-244.
- Elenbaas, W., 1942, "Heat Dissipation of Parallel Plates by Free Convection," *Physica*, Vol. 9, No. 1, pp. 1-28.
- Flack, R. D., Konopnicki, T. T., and Rooke, J. H., 1979, "The Measurement

- of Natural Convective Heat Transfer in Triangular Enclosures," *ASME JOURNAL OF HEAT TRANSFER*, Vol. 101, pp. 648-654.
- Flack, R. D., 1980, "The Experimental Measurement of Natural Convection Heat Transfer in Triangular Enclosures Heated or Cooled From Below," *ASME JOURNAL OF HEAT TRANSFER*, Vol. 102, pp. 770-772.
- Haaland, S. E., and Sparrow, E. M., 1973a, "Wave Instability of Natural Convection Flow on Inclined Surfaces Accounting for Nonparallelism of the Basic Flow," *ASME JOURNAL OF HEAT TRANSFER*, Vol. 96, pp. 405-407.
- Haaland, S. E., and Sparrow, E. M., 1973b, "Vortex Instability of Natural Convection Flow on Inclined Surfaces," *Int. J. Heat Mass Transfer*, Vol. 16, pp. 2355-2367.
- Hasan, M. M., and Eichhorn, R., 1979, "Local Nonsimilarity Solution of Free Convection Flow and Heat Transfer From an Inclined Isothermal Plate," *ASME JOURNAL OF HEAT TRANSFER*, Vol. 101, pp. 642-647.
- Holman, J. P., 1981, *Heat Transfer*, 5th ed., McGraw-Hill, New York, p. 267.
- Kierkus, W. T., 1968, "An Analysis of Laminar Free Convection Flow and Heat Transfer About an Inclined Isothermal Plate," *Int. J. Heat Mass Transfer*, Vol. 11, pp. 241-253.
- Kihm, K. D., Kastell, D., and Fletcher, L. S., 1991, "Study of Thermal Boundary Layers Occurring Around the Leading Edge of a Vertical Isothermal Wall Using Speckle Photography," *Proceedings ASME/JSME Thermal Engineering Conference*, J. R. Lloyd and Y. Kurosaki, eds., Vol. 1, pp. 25-33.
- Kihm, K. D., 1992, "Image Blurring of Test Section Boundary in a Laser Specklegram Technique Measuring Temperature Gradients of Compressible Medium," *Applied Optics*, Vol. 31, No. 28, pp. 5907-5910.
- Levy, E. K., 1972, "Optimum Plate Spacing for Laminar Natural Convection Heat Transfer From Parallel Vertical Isothermal Flat Plates," *ASME JOURNAL OF HEAT TRANSFER*, Vol. 93, pp. 463-465.
- Lloyd, J. R., and Sparrow, E. M., 1970, "On the Instability of Natural Convection Flow on Inclined Plates," *Journal of Fluid Mechanics*, Vol. 42, pp. 465-470.
- Martin, L., Raithby, G. D., and Yovanovich, M. M., 1991, "On the Low Rayleigh Number Asymptote for Natural Convection Through an Isothermal, Parallel-Plate Channel," *ASME JOURNAL OF HEAT TRANSFER*, Vol. 113, pp. 899-905.
- Merzkirch, W., 1989, "Speckle Photography," in: *Handbook of Flow Visualization*, W. J. Yang, ed., Hemisphere Publishing Corp., New York, Ch. 11.
- Naylor, D., Floryan, J. M., and Tarasuk, J. D., 1991, "A Numerical Study of Developing Free Convection Between Isothermal Vertical Plates," *ASME JOURNAL OF HEAT TRANSFER*, Vol. 113, pp. 620-626.
- Ostrach, S., 1952, "An Analysis of Laminar Free Convection Heat Transfer About a Flat Plate Parallel to the Direction of the Generating Body Force," NACA TN-2635.
- Sparrow, E. M., and Gregg, J. L., 1958, "The Variable Fluid Property Problem of Free Convection," *ASME JOURNAL OF HEAT TRANSFER*, Vol. 80, pp. 879-886.
- Sparrow, E. M., and Bahrami, P. A., 1980, "Experiments on Natural Convection From Vertical Parallel Plates With Either Open or Closed Edges," *ASME JOURNAL OF HEAT TRANSFER*, Vol. 102, pp. 221-227.
- Sparrow, E. M., and Azevedo, L. F. A., 1985, "Vertical-Channel Natural Convection Spanning the Fully-Developed Limit and the Single-Plate Boundary-Layer Limit," *Int. J. Heat Mass Transfer*, Vol. 28, No. 10, pp. 1847-1857.
- Tritton, D. J., 1962, "Transition to Turbulence in the Free Convection Boundary Layers on an Inclined Heated Plate," *Journal of Fluid Mechanics*, Vol. 16, pp. 417-435.
- Tzuoo, K. L., Chen, T. S., and Armaly, B. F., 1985, "Wave Instability of Natural Convection Flow on Inclined Surfaces," *ASME JOURNAL OF HEAT TRANSFER*, Vol. 107, pp. 107-111.
- Vest, C. M., 1979, *Holographic Interferometry*, Wiley, New York, pp. 363-365.
- Yang, K. T., and Jerger, E. W., 1964, "First-Order Perturbations of Laminar Free-Convection Boundary Layers on a Vertical Plate," *ASME JOURNAL OF HEAT TRANSFER*, Vol. 86, pp. 107-115.
- Wirtz, R. A., and Stutzman, R. J., 1982, "Experiments on Free Convection Between Vertical Plates With Symmetric Heating," *ASME JOURNAL OF HEAT TRANSFER*, Vol. 104, pp. 501-507.

Natural Convection From L-Shaped Corners With Adiabatic and Cold Isothermal Horizontal Walls

D. Angirasa

Assoc. Mem. ASME

R. L. Mahajan

Mem. ASME

Department of Mechanical Engineering,
University of Colorado,
Boulder, CO 80309-0427

A numerical study of two-dimensional fluid flow and heat transfer by natural convection from L-shaped corners is reported. The vertical side is hot isothermal, and the horizontal side is either adiabatic or cold isothermal at the ambient temperature. The effect of changing the aspect ratio (length of the horizontal side/height of the vertical side) on the transport from the vertical side is studied in detail. It is shown that when the length of the horizontal wall is of the order of the boundary layer thickness on the vertical side, the entrainment flow as well as the boundary layer flow are influenced significantly by a change in the length of the horizontal surface. The heat transfer rate from the vertical side also decreases with increasing length. For values of the aspect ratio > 0.3 ($Pr = 0.7$), the Nusselt number for the vertical plate is about 10 percent less than that for the vertical plate. As the length of the horizontal plate increases further, the flow in the outer region undergoes a significant change, but the heat transfer from the vertical heated leg remains unaffected. As the aspect ratio approaches ≈ 2.0 , increasing the length of the horizontal side ceases to have any further influence on the entire flow field. Comparison of Nusselt number with past experimental data for air shows good agreement. Finally, Nusselt number correlations in the range of Rayleigh number from 10^5 to 10^9 are presented.

Introduction

Natural convection from an isothermal vertical surface in an extensive fluid medium is one of the most widely studied problems in heat transfer. Besides its fundamental importance in the understanding of the heat transfer phenomenon in buoyancy-induced flows, it finds many applications of common occurrence. A comparative problem of natural convection from corners has not received much attention despite its equal importance. Natural convection heat transfer from corners with different wall and ambient boundary conditions has many applications in cooling of electronic components, packages, and equipment.

It is possible to construct various types of corners depending on the geometric dimensions, and orientation. Natural convection flows are extremely sensitive to these factors, and hence it is not possible to generalize results obtained in one context, and apply them to another. It is useful to categorize corners into three types: (i) horizontal, (ii) vertical, and (iii) inclined. In Fig. 1, examples of the three types of corner are shown. A horizontal corner is formed by joining a flat plate to a vertical surface, either at its leading or trailing edge. In case of rectangular corners, the former results in an L-shaped body (Fig. 1a), and the latter in a T (Fig. 1b). A vertical corner is formed by vertically joining two flat plates (Fig. 1e). Two-dimensional flows are possible for L- and T-shaped corners (Figs. 1a-d) if the third side (H) is much larger, while for vertical and inclined corners (Figs. 1e and 1f), the flow is essentially three dimensional. The two plates may have different wall conditions; for instance, one hot isothermal, and the other adiabatic, and so on.

Natural convection flows adjacent to the various corners discussed above are quite complex to model numerically, and are almost impossible to solve purely by analysis. Very few

theoretical and numerical studies are reported, and experimental studies are even scarcer. Luchini (1986) studied the horizontal corner depicted in Fig. 1(a) analytically and numerically, with different values of θ (vertical plate—hot isothermal, and the other plate—cold isothermal), and tried to identify different regions of flow behavior. The method of

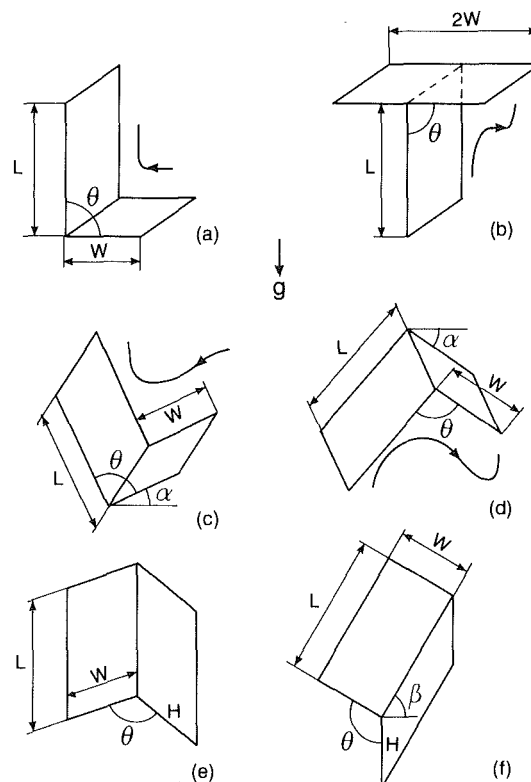


Fig. 1 Various types of corners

Contributed by the Heat Transfer Division and presented at the ASME Winter Annual Meeting, Atlanta, GA, December 1-6, 1991. Manuscript received by the Heat Transfer Division December 1991; revision received June 1992. Keywords: Natural Convection, Numerical Methods. Associate Technical Editor: J. R. Lloyd.

matched asymptotic expansions was used, and the numerical solutions were obtained by a finite-difference method. There was a wide disagreement between analytical and numerical prediction of skin friction. No heat transfer results, however, were given. Rodighiero and de Socio (1983) performed experiments in air for the case of the adiabatic horizontal wall (Fig. 1a, $\theta = 90$ deg). Their experimental heat transfer data were correlated as $Nu = 0.465 Ra^{0.253}$ (for $Pr = 0.7$). This correlation is valid only if the length of the horizontal wall (W) is far greater than the thickness of the boundary layer on the vertical side. Comparatively, the recommended correlation for an isothermal vertical plate, without the horizontal extension at the leading edge, is $\bar{Nu} = 0.59 Ra^{0.25}$ (McAdams, 1954).

Jaluria (1985) numerically studied the interaction of natural convection wakes arising from two line thermal sources mounted on a vertical adiabatic surface with a cold isothermal horizontal wall joined at the leading edge. One of the heat sources is placed at the corner, and hence the horizontal wall absorbs heat from it. The buoyancy is reduced because of this heat removal. In addition, the horizontal plate blocks entrainment from the bottom side. Merkin and Smith (1982) considered the geometry in Fig. 1(b) with obtuse θ , and the one in Fig. 1(d) with the outer sides of the plates heated, and the plane of symmetry vertical.

Two papers, Riley and Poots (1972), and later Kim and Kim (1988) considered the rectangular vertical corner shown in Fig. 1(e). For this geometry, the flow is three dimensional. Both the works cited above used the method of matched asymptotic expansions to discuss the velocity and thermal fields in the corner layer region, and in the three-dimensional boundary layer regions on either wall. The crossflow governed primarily by a potential flow region far away from the corner was also discussed. Riley and Poots (1972) compared the calculated vertical velocity, horizontal velocity into the corner, and the wall heat transfer coefficients with the experimental measurements of van Leeuwen et al. (1971), and found the agreement to be good. The numerical results of Riley and Poots (1972) also confirmed the experimentally observed "chimney effect" in the vertical corner region, in which the vertical velocity is larger than that for a single vertical plate.

Recently Kim et al. (1991) extended the work of Riley and Poots (1972), and Kim and Kim (1988) to include both acute and obtuse angles for θ (Fig. 1e). In a related work, Liu and Guerra (1985) considered various angles for θ for the vertical corner in a saturated porous medium.

The foregoing survey of literature on natural convection from corners shows that a considerable amount of work needs to be done to understand the complexity of natural convection flows, and transport processes in all types of corner. Fortunately, numerical methods available now allow us to perform

detailed calculations of these flows, and predict flow and heat transfer phenomena with accuracy. In this paper, we report the results of a comprehensive numerical study of the horizontal corner, or the L-shaped body (Fig. 1a, $\theta = 90$ deg), with the vertical side hot isothermal, and the horizontal, adiabatic and cold isothermal. The problem also has fundamental relevance, since it clarifies the influence of the fluid entrained from the bottom on the flow and heat transfer characteristics of the vertical natural convection boundary layer. We consider the entire range of the aspect ratio (length of the horizontal side/height of the vertical plate) between the two asymptotic limits of no horizontal wall and a very long wall.

Analysis

Referring to Fig. 1(a), the height of the vertical side is L , and the length of the horizontal side, W . The vertical and horizontal sides are, respectively, aligned with the x and y axes. The vertical side is isothermal at t_w , and the horizontal side is either adiabatic, or isothermal at t_∞ , which is the temperature of the ambient fluid. Using the Boussinesq approximation, the governing equations in nondimensional form for laminar, two-dimensional incompressible buoyancy-driven flows with constant fluid properties are

$$\frac{\partial U}{\partial X} + \frac{\partial V}{\partial Y} = 0 \quad (1)$$

$$\frac{\partial U}{\partial \tau^*} + U \frac{\partial U}{\partial X} + V \frac{\partial U}{\partial Y} = -\frac{\partial P}{\partial X} + \frac{1}{\sqrt{Gr}} \left(\frac{\partial^2 U}{\partial X^2} + \frac{\partial^2 U}{\partial Y^2} \right) + T \quad (2)$$

$$\frac{\partial V}{\partial \tau^*} + U \frac{\partial V}{\partial X} + V \frac{\partial V}{\partial Y} = -\frac{\partial P}{\partial Y} + \frac{1}{\sqrt{Gr}} \left(\frac{\partial^2 V}{\partial X^2} + \frac{\partial^2 V}{\partial Y^2} \right) \quad (3)$$

$$\frac{\partial T}{\partial \tau^*} + U \frac{\partial T}{\partial X} + V \frac{\partial T}{\partial Y} = \frac{1}{\sqrt{GrPr}} \left(\frac{\partial^2 T}{\partial X^2} + \frac{\partial^2 T}{\partial Y^2} \right) \quad (4)$$

In the above equations, $P = p/\rho U_c^2$, $Gr = [g\beta(t_w - t_\infty)L^3/\nu^2]$ is the Grashof number, and $Pr = \nu/\alpha$, the Prandtl number. Although we are interested only in the steady-state solutions, the transient terms are retained in Eqs. (2)–(4) for marching the discretized equations to the asymptotic steady-state solution.

In arriving at Eqs. (1)–(4) from the dimensional form (see, for instance, Gebhart et al., 1988), the following nondimensional variables were defined:

$$X = x/L, \quad Y = y/L, \quad \tau^* = \tau U_c/L$$

$$U = u/U_c, \quad V = v/U_c, \quad T = (t - t_\infty)/(t_w - t_\infty) \quad (5)$$

where $U_c = [g\beta(t_w - t_\infty)L]^{1/2}$ is the reference convective velocity. By defining vorticity ω as

Nomenclature

g = gravitational acceleration	W = length of the horizontal side	β = coefficient of thermal expansion
k = thermal conductivity of the fluid	W^* = nondimensional length of the horizontal side = W/L	θ = angle between the horizontal and the corner
L = height of the vertical side	x, y = space coordinates in vertical and horizontal directions	θ = angle between the plates
p = pressure	X, Y = nondimensional space coordinates	ν = kinematic viscosity
P = nondimensional pressure = $p/\rho U_c^2$	Gr = Grashof number = $g\beta(t_w - t_\infty)L^3/\nu^2$	ρ = density
t = temperature	\bar{Nu} = average Nusselt number	τ = time
T = nondimensional temperature	\bar{Nu}_o = average Nusselt number for a vertical plate	τ^* = nondimensional time
u, v = velocity components in x and y directions, respectively	Pr = Prandtl number = ν/α	ψ = stream function
U, V = nondimensional velocity components	α = thermal diffusivity	ω = vorticity
U_c = reference convective velocity = $\sqrt{g\beta(t_w - t_\infty)L}$	θ = angle between the horizontal plane and a side	
		Subscripts
		w = wall
		∞ = indicating reference (ambient) temperature

$$\omega = \frac{\partial U}{\partial Y} - \frac{\partial V}{\partial X} \quad (6)$$

we reduce the governing Eqs. (1)–(3) to the following vorticity-transport equation

$$\frac{\partial \omega}{\partial \tau^*} + U \frac{\partial \omega}{\partial X} + V \frac{\partial \omega}{\partial Y} = \frac{\partial T}{\partial Y} + \frac{1}{\sqrt{\text{Gr}}} \left(\frac{\partial^2 \omega}{\partial X^2} + \frac{\partial^2 \omega}{\partial Y^2} \right) \quad (7)$$

We define a stream function ψ such that

$$U = \frac{\partial \psi}{\partial Y} \quad \text{and} \quad V = -\frac{\partial \psi}{\partial X} \quad (8)$$

From Eqs. (6) and (8), it follows that

$$\omega = \nabla^2 \psi \quad (9)$$

Boundary Conditions. The physical boundary conditions of the L-shaped body are

$$y = 0 \quad t = t_w, \quad u = 0, \quad v = 0$$

$$y \rightarrow \infty \quad t = t_\infty, \quad u = 0$$

$$x = 0 \quad 0 \leq y \leq W \quad u = 0, \quad v = 0$$

For the case of adiabatic horizontal wall,

$$x = 0 \quad 0 < y \leq W \quad \frac{\partial T}{\partial x} = 0$$

and for isothermal horizontal wall,

$$x = 0 \quad 0 < y \leq W \quad T = t_\infty \quad (10)$$

In nondimensional form, the boundary conditions are given as

$$Y = 0 \quad T = 1, \quad U = 0, \quad V = 0$$

$$Y \rightarrow \infty \quad T = 0, \quad U = 0$$

$$X = 0 \quad 0 \leq Y \leq W^* \quad U = 0, \quad V = 0$$

where $W^* = W/L$.

The temperature boundary conditions on the horizontal wall are

$$X = 0 \quad 0 < Y \leq W^* \quad \frac{\partial T}{\partial X} = 0 \quad (\text{adiabatic}) \quad (11)$$

$$X = 0 \quad 0 < Y \leq W^* \quad T = 0 \quad (\text{isothermal})$$

The numerical boundary conditions for ψ and ω will be discussed in the next section.

Evaluation of Nusselt Number. The average Nusselt number for the vertical heated surface of the L-shaped body with the horizontal side either adiabatic or isothermal at the ambient temperature is given by

$$\overline{\text{Nu}} = \int_0^1 \left(-\frac{\partial T}{\partial Y} \right)_{Y=0} dX \quad (12)$$

Numerical Procedures

The energy and vorticity-transport equations (Eqs. (4) and (7)) are solved by the Alternating Direction Implicit (ADI) method of Peaceman and Rachford, described in the textbook by Roache (1982). The discretized transient equations are marched in time to an asymptotic steady-state solution. Upwind-differencing is employed for convective terms for numerical stability because of the higher values of the Grashof number considered. The diffusive terms and the buoyancy term are discretized by central differencing. The Successive Over Relaxation (SOR) method is utilized for solving the stream function equation, Eq. (9). Iteration convergence is obtained for stream function solution at each time-step.

Uniform grid-spacings are employed in both the directions. Since greater resolution is required in the Y direction in the

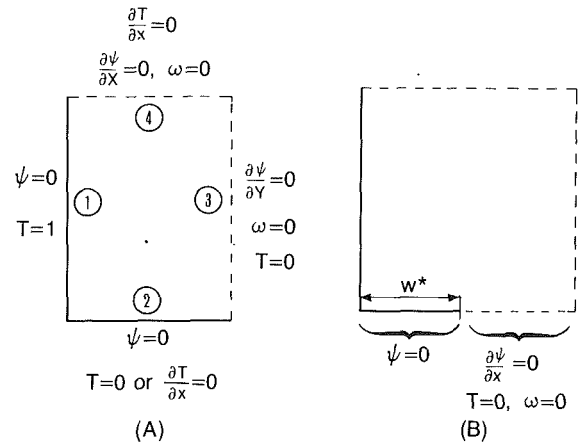


Fig. 2 Numerical boundary conditions (A) without extended domain and (B) with extended domain

Table 1 Comparison of $\overline{\text{Nu}}$ for the two methods of computations for $W^* = 0.5$, $\text{Pr} = 0.7$, and $\text{Gr} = 10^6$

Method A	Method B
14.80	14.88

wall region, the number of grid points required in the Y direction for this depends on the value of W^* . Typically 41 grid points were needed for $W^* = 0.5$. For $W^* = 2.67$, 241 points were used.

Two criteria are employed to check for steady state:

$$|\xi_{ij}^{n+1} - \xi_{ij}^n|_{\max} \leq \epsilon, \quad \text{and} \quad \left| \frac{\xi_{ij}^{n+1} - \xi_{ij}^n}{\xi_{ij}^n} \right|_{\max} \leq \epsilon$$

where ξ is T , and ω . In the above criteria n refers to time, and i and j to space. The value of ϵ is prescribed to be 10^{-5} . We have found that the temperature field converges faster than the flow field. Hence the convergence test was done on both T and ω . The same type of iterative convergence test was carried out for ψ at each time step. The nondimensional time step chosen is of the order of 0.01.

The average Nusselt number (Eq. (12)) is evaluated using Simpson's rule. To account for the effect of the end points, an open-ended formula has been employed (Press et al., 1986).

The computational domain is formed as a rectangle with the two sides of the L . The numerical boundary conditions employed are shown in Fig. 2(A). The boundary conditions on sides 3 and 4 are obtained after careful numerical experimentation. The stream function ψ on walls 1 and 2 is constant, and is taken to be zero. On sides 3 and 4 the gradients of ψ are prescribed to be zero. For a discussion on the outflow boundary conditions on side 4, see Roache (1982). On side 3, $\partial \psi / \partial Y = 0$ gives $U = 0$. Physically it means that fluid is horizontally entrained into the computational flow domain. This boundary condition is valid so long as the length W^* is much larger than the boundary layer thickness on the heated vertical plate (side 1). When the width W^* is comparable to the boundary layer thickness, the computational domain in the Y direction should be extended beyond the horizontal leg W^* .

The boundary layer thickness on the vertical side may be roughly assessed by either an integral method, or similarity analysis of the boundary layer on a flat vertical plate (Gebhart, 1971). Using either of the two methods, the boundary layer thickness at the top of the plate is ≈ 0.2 . Conservatively, we have chosen a value of $W^* = 0.5$ as the length below which the computational domain in the Y direction has to be extended. The extended domain and the boundary conditions

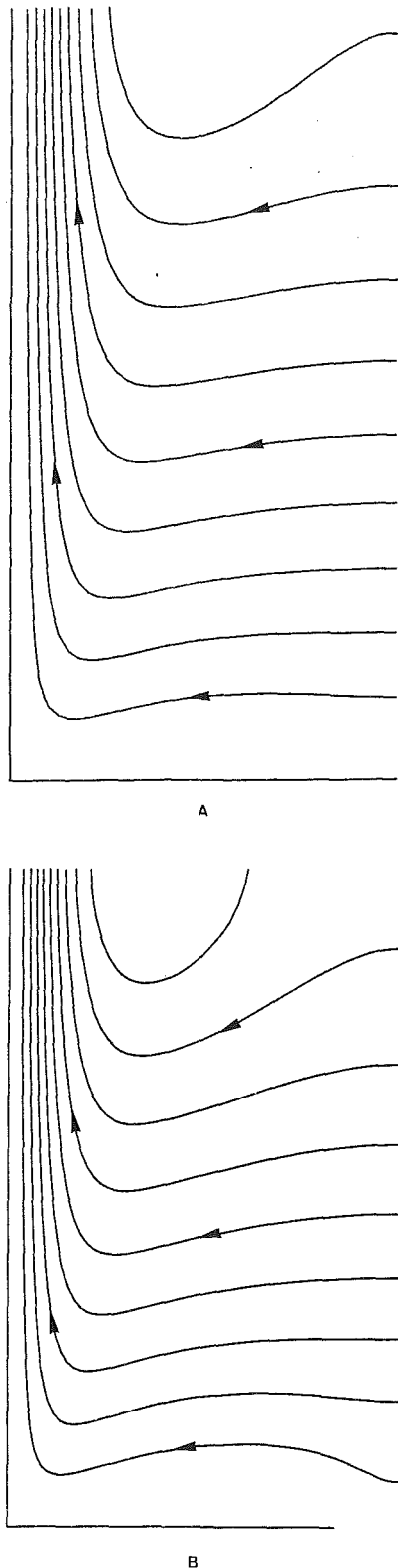


Fig. 3 Stream function contours for methods A and B; $Gr = 10^6$, $Pr = 0.7$, and $W^* = 0.5$

are shown in Fig. 2(B). Hereafter, we refer to these two systems of computation as method A ($W^* > 0.5$), and method B ($W^* < 0.5$), respectively.

We first compare the results obtained with both methods for the same value of W^* ($=0.5$) to verify that they yield the same results. In this case, for method B, the computational domain in the Y direction is extended to 0.6. In Table 1, values

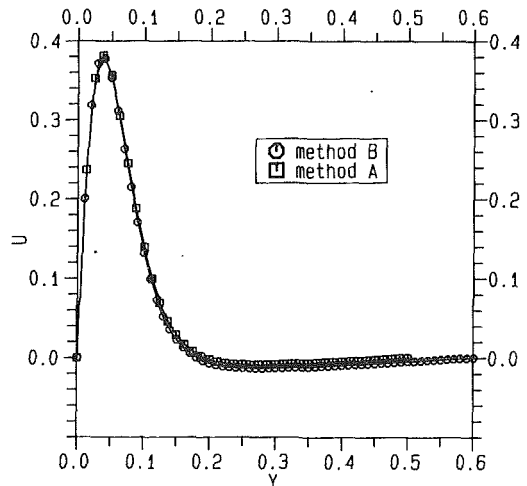


Fig. 4 Comparison of vertical velocity profiles for methods A and B; $X = 0.5$, $Gr = 10^6$, and $Pr = 0.7$

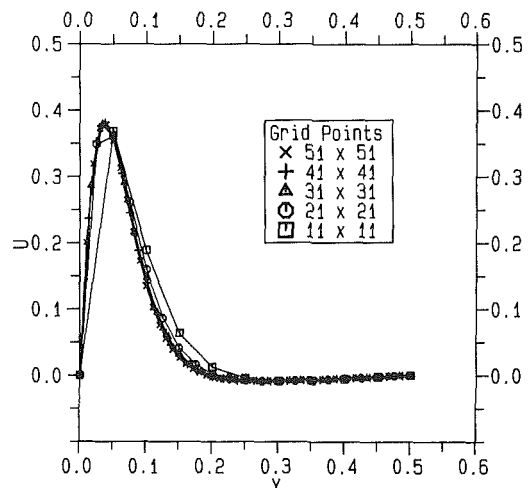


Fig. 5 Grid-independence demonstration: U -velocity profiles at $X = 0.5$ for $Gr = 10^6$, $Pr = 0.7$, and $W^* = 0.5$ for method A

of \overline{Nu} are compared, and we note that the agreement is good. Figures 3 and 4, respectively, give the stream function contours and typical vertical velocity profiles for the two methods A and B. The stream function contours show that the flow patterns are the same for both methods, except in the regions far away from the heated vertical wall. Even here, the differences are small. The velocity profiles also concur with this behavior. Therefore, we conclude that if W^* is much larger than the vertical boundary layer thickness, method A gives accurate numerical solutions.

Grid-Independence Study. To study the effect of the grid size on the solutions, a series of calculations were first performed by varying the number of grid points in each direction for the case $W^* = 0.5$. The parameters for this study are $Gr = 10^6$ and $Pr = 0.7$. In Fig. 5 vertical velocity profiles at $X = 0.5$ are shown for different number of grid points. We have found that for method A, 41×41 grid points are adequate to ensure a maximum error of 1 percent in temperature, stream function, and vorticity. The maximum error in the average Nusselt number due to the grid size is estimated as 1.5 percent. To obtain a Nusselt number correlation with method A, the number of grid points used for $Gr = 10^7$ and 10^8 are, respectively, 51×51 and 61×61 .

When W^* is varied, the grid points in the Y direction are

dependent on the value of W^* for accuracy. Table 2 lists the number of grid points employed for different values of W^* for method *A*. The maximum deviation of \overline{Nu} from the average is 0.8 percent. As we will explain in the next section, \overline{Nu} is constant for larger values of W^* . Hence, the number of grid points given in the table give accurate solutions.

Results and Discussion

Effect of W^* for Adiabatic Horizontal Walls. To study the effect of the length W^* on the flow and heat transfer, we

Table 2 $Pr = 0.7$ and $Gr = 10^6$

W^*	No. of grid points	\overline{Nu}
0.5	41 × 41	14.80
0.6	41 × 61	14.91
0.75	51 × 81	14.98
1.0	51 × 81	14.81
1.5	41 × 121	14.79
2.0	41 × 161	14.78
2.67	41 × 241	14.85

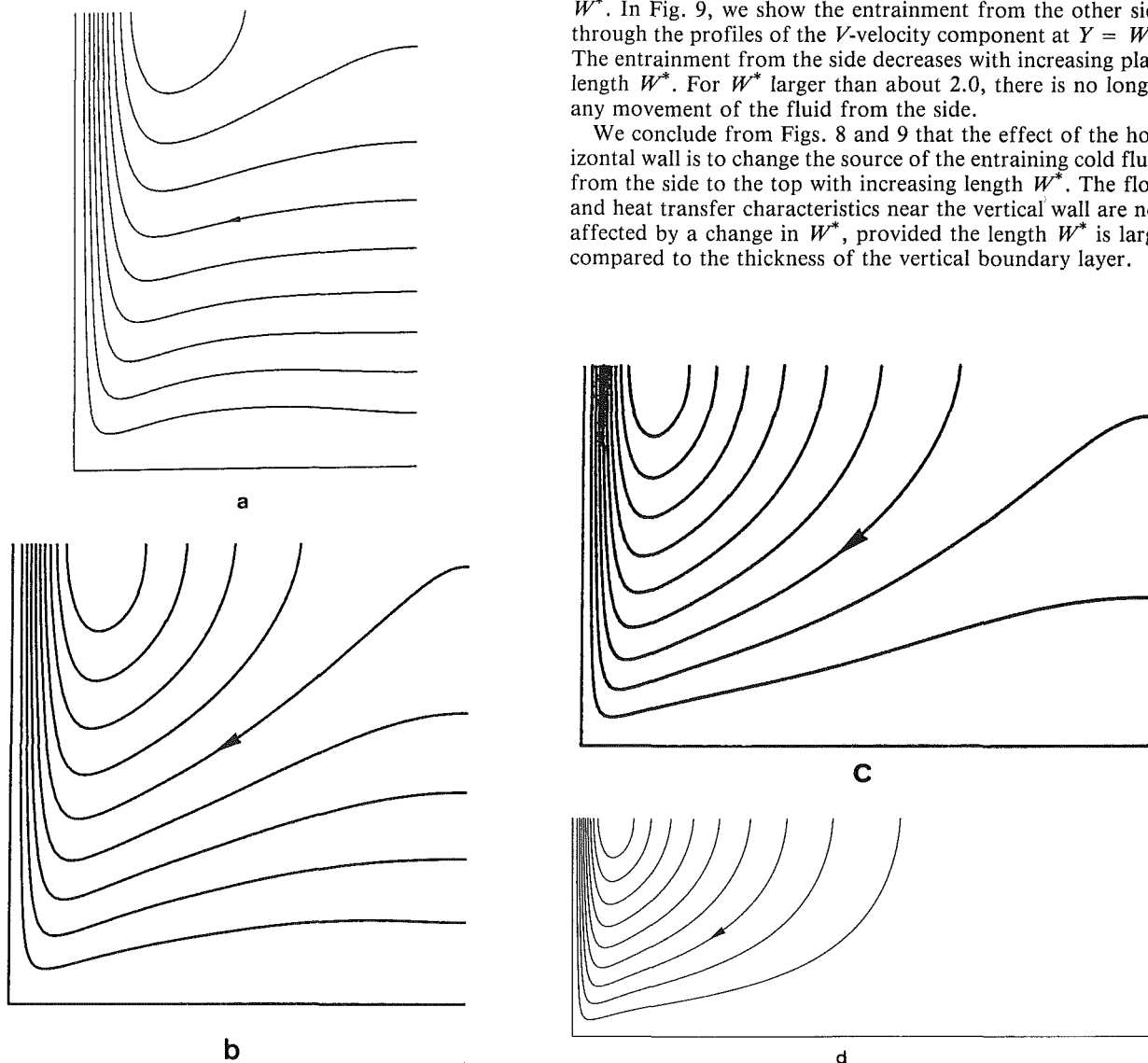


Fig. 6 Stream function contours for $Gr = 10^6$, $Pr = 0.7$ for $W^* = (a)$ 0.75, (b) 1.0, (c) 1.5, (d) 2.67

carried out computations for W^* ranging from 0.0 to 2.67, the latter value corresponding to the one in the experiments of Rodighiero and de Socio (1983). For $W^* \geq 0.5$, the values of \overline{Nu} are shown in Table 2. The effect of increasing W^* on \overline{Nu} is rather insignificant. The concomitant changes in the entrainment of fluid, however, are large.

Figure 6 presents the stream function contours for different values of the length of the horizontal adiabatic wall. For the values of W^* up to 0.75, we do not observe much entrainment from the top. As the length is increased further, most of the cold fluid is drawn from the top. For $W^* = 2.67$, almost all cold fluid is entrained only from the top, and at the free edge of the adiabatic plate there is no fluid movement. The change in the direction of the entraining cold fluid, however, did not at all affect the thermal character of the boundary layer. Figure 7(a) shows a typical isotherm contour plot, which is the same for all values of W^* larger than 0.5. This behavior is consistent with the near-constant values of \overline{Nu} shown in Table 2.

The vertical velocity profiles at $X = 1$, for the case of the adiabatic bottom wall, are shown in Fig. 8. U -velocity components change in the "wings" of the profiles, while the boundary layer characteristics are undisturbed. The negative values of the velocity component increase in the wings with increasing values of W^* , indicating that there is more entrainment of cold fluid from the top for larger values of the plate length W^* . In Fig. 9, we show the entrainment from the other side through the profiles of the V -velocity component at $Y = W^*$. The entrainment from the side decreases with increasing plate length W^* . For W^* larger than about 2.0, there is no longer any movement of the fluid from the side.

We conclude from Figs. 8 and 9 that the effect of the horizontal wall is to change the source of the entraining cold fluid from the side to the top with increasing length W^* . The flow and heat transfer characteristics near the vertical wall are not affected by a change in W^* , provided the length W^* is large compared to the thickness of the vertical boundary layer.

Effect of Short Adiabatic Extensions at the Leading Edge. In the discussions so far, we considered the effect of a long horizontal adiabatic plate at the leading edge of a hot vertical plate. In this section, we study the influence of short adiabatic extensions at the leading edge with lengths comparable to the thickness of the boundary layer.

First we consider the average Nusselt number for the vertical plate without horizontal extension. The computed value of the average Nusselt number for this case is 16.21. The similarity solution of Gebhart et al. (1988) for $Pr = 0.72$ is 15.04, and the correlation of Churchill and Chu (1975) gives 15.53. McAdams' experimental (1954) correlation yields a Nusselt number of 17.1.

Figure 10 shows the stream function contours for W^* varying from 0 to 0.3. Figure 10(a) corresponds to the vertical plate ($W^* = 0$) with no extension. Expectedly, cold fluid is entrained into the boundary layer from both the side and the bottom. With increasing length of the protrusion at the leading edge, there will be less entrainment from the bottom as reflected in Fig. 10. Because of this, the local heat transfer rates fall with

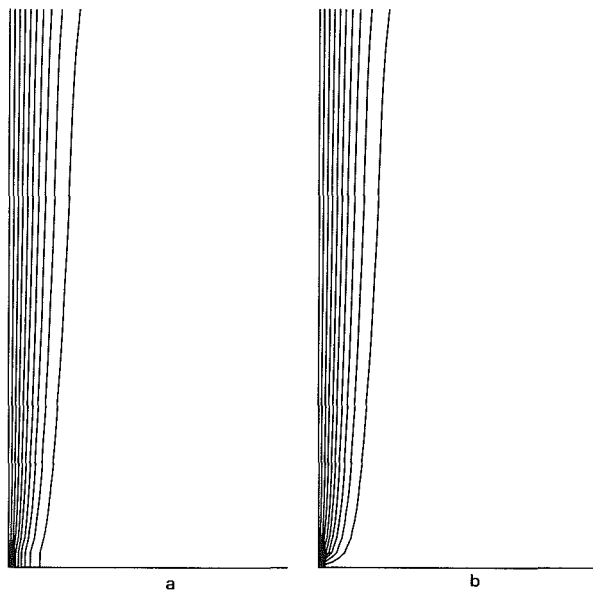


Fig. 7 Typical isotherms for (a) adiabatic horizontal wall, (b) isothermal horizontal wall; $Gr = 10^6$, $Pr = 0.7$, and $W^* = 0.5$; T_w (vertical) = 1.0 and $\Delta T = 0.1$

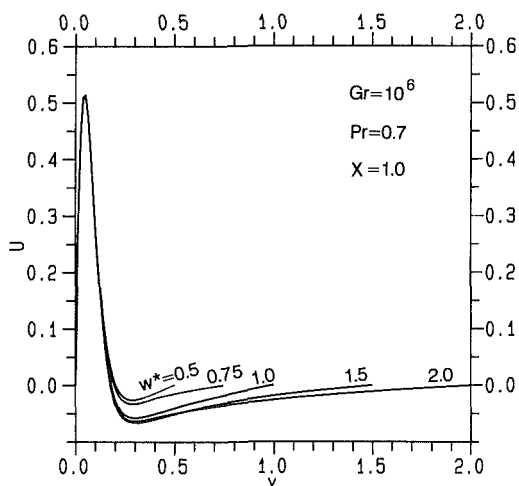


Fig. 8 U -velocity components at $X = 1.0$ for various values of W^* ; $Gr = 10^6$ and $Pr = 0.7$

increasing W^* in the bottom half of the vertical plate. Figure 11 shows the local Nusselt number (based on the height of the vertical plate L) for increasing W^* , beginning with $W^* = 0$. The height X is plotted on the ordinate to reflect the physical situation of the vertical plate. For $W^* >$ about 0.3, there is little change in the local Nusselt number. This is in agreement with the earlier result of constant Nu for $W^* \geq 0.5$. Figure 12 shows the variation of \bar{Nu} with W^* . \bar{Nu} decreases with increasing length of the side W^* , and at about $W^* = 0.3$ the decrease is about 9 percent compared to that of the pure vertical plate (\bar{Nu}_0). A further increase in W^* has no effect on \bar{Nu} .

The above behavior is what one would expect from considerations of entrainment flow. In the absence of the horizontal plate, there is entrainment flow from the region below $X = 0$. Near the leading edge of the vertical wall this acts as an externally imposed flow on the buoyancy-induced flow adjacent to the vertical wall. The effect of the side plate is to block this entrainment flow and thus reduce the heat transfer rate from the vertical wall. For $W^* > 0.3$, the additional flow blocked has an insignificant influence on the thermal character of the boundary layer, and does not affect the heat transfer rate from the wall.

Comparison With Experimental Data. For comparison, we used the experimental correlation of Rodighiero and de Socio (1983), who made measurements for three plates of heights 0.127 m, 0.21 m, and 0.3 m for a fixed horizontal adiabatic surface of length 0.8 m. All of these correspond to $W^* \gg 1.0$. They found that in the range of W^* investigated, the aspect ratio has no influence on the heat transfer rates. This is in agreement with numerical results, which show very little dependence on W^* for $W^* >$ about 0.3. In Table 3 we present our results for different values of Gr for $W^* = 0.5$, and compare these with their experimental data for the tallest of their plates for which $W^* = 0.8/0.3 = 2.67$. Since $W^* > 0.3$, the aspect ratio has an insignificant effect on \bar{Nu} (see Table 2 and Fig. 12), and our \bar{Nu} results for $W^* = 0.5$ might be taken

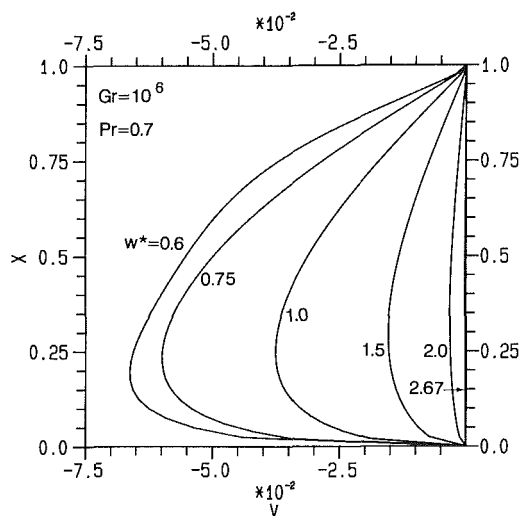


Fig. 9 V -velocity components at W^* for different values of W^* ; $Gr = 10^6$ and $Pr = 0.7$

Table 3 Comparison of Nu for $Pr = 0.7$

Gr	Present		Rodighiero and de Socio (1983)
	Adiabatic	Isothermal	Adiabatic
10^6	14.80	15.20	14.00
10^7	25.52	25.90	25.08
10^8	43.26	43.52	44.90

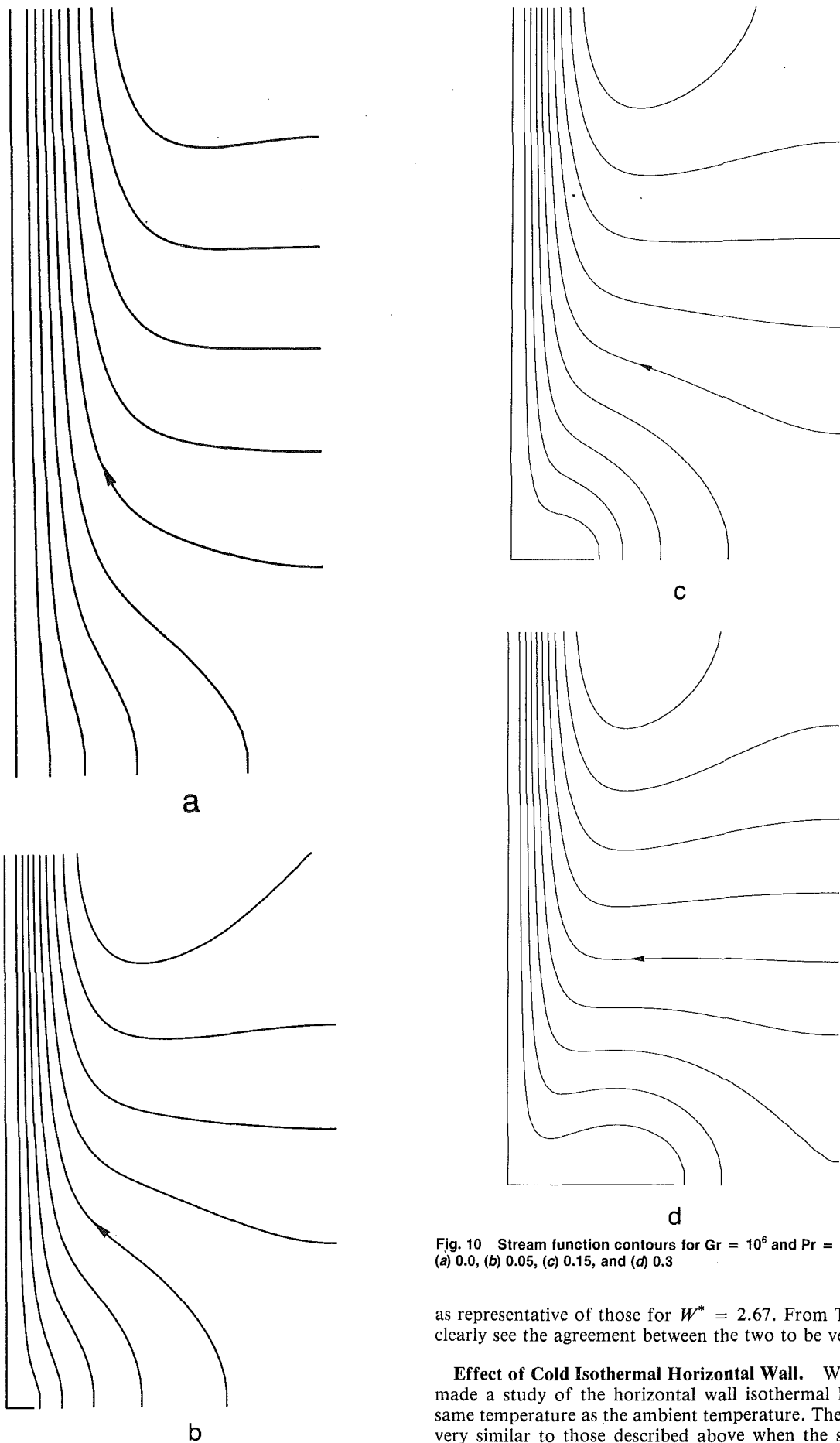


Fig. 10 Stream function contours for $Gr = 10^6$ and $Pr = 0.7$ for $W^* =$ (a) 0.0, (b) 0.05, (c) 0.15, and (d) 0.3

as representative of those for $W^* = 2.67$. From Table 3, we clearly see the agreement between the two to be very good.

Effect of Cold Isothermal Horizontal Wall. We have also made a study of the horizontal wall isothermal held at the same temperature as the ambient temperature. The results are very similar to those described above when the side wall is

Table 4 Correlation of \overline{Nu} data

	m	n	Ra	Pr	Average Deviation from Data
Corner with adiabatic horizontal wall Present (numerical)	0.666	0.232	10^5-10^9	0.1-100	± 7 percent
Corner with isothermal horizontal wall Present (numerical)	0.833	0.221	10^5-10^9	0.7-7.0	± 6 percent
Corner with adiabatic horizontal wall Rodighiero and de Socio (1983) (experimental)	0.465	0.253	10^6-10^8	0.7	
Vertical plate Recommended experimental (McAdams, 1954)	0.59	0.25	10^4-10^9		

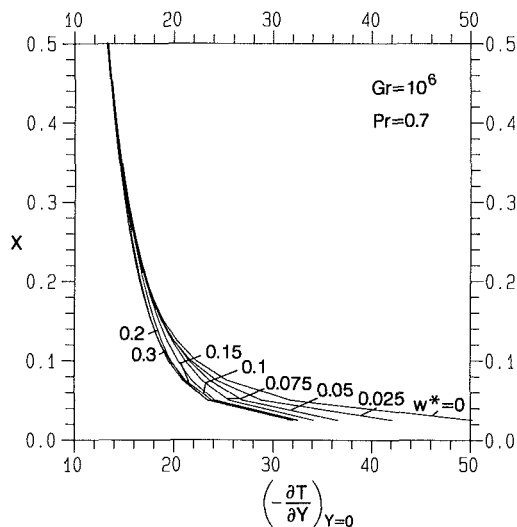


Fig. 11 Effect of short protrusions on the local Nusselt number

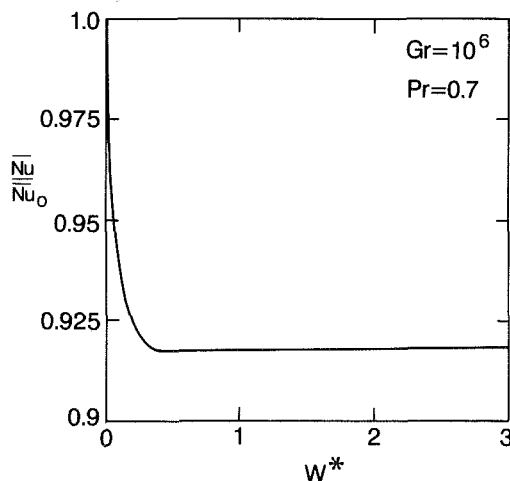


Fig. 12 Effect of the length of the horizontal side on the average Nusselt number; maximum deviation of data points from the curve = ± 0.5 percent

adiabatic. We note however that \overline{Nu} for this case is slightly higher, as shown in Table 3. This can be attributed to sharper wall temperature gradients in the corner regions due to heat loss from the bottom plate in that region (see Fig. 7b).

In Fig 7(b), we show typical isotherm contours for the iso-

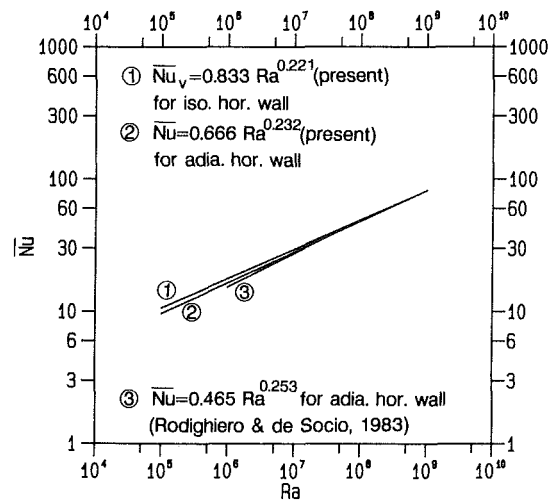


Fig. 13 Correlations of \overline{Nu}

thermal horizontal wall. We observe that there is a large difference in the corner region between the two cases of adiabatic and cold isothermal horizontal walls. In the isothermal case, the horizontal plate absorbs thermal energy in the corner region, leading to sharper temperature gradients.

Correlation of \overline{Nu} Data. Computed \overline{Nu} data for corners with large horizontal plates are correlated using a least-square fit (see, for instance, Press et al., 1986) in the form

$$\overline{Nu} = m Ra^n$$

The results are summarized in Table 4 along with the experimental correlation of Rodighiero and de Socio (1983) for a corner with adiabatic horizontal wall, and the recommended correlation for the vertical flat plate (McAdams, 1954).

In Fig. 13 the experimental and the present numerical correlations are compared. In the experimental range of Pr and Ra, the correlations agree very well.

Conclusions

We have reported a numerical study of natural convection from L-shaped corners with adiabatic and isothermal horizontal walls at the ambient temperature. The main conclusions of this study are:

- 1 When short protrusions of lengths comparable to the thickness of the boundary layer are joined at the leading edge of the vertical plate, the heat transfer rate decreases with increasing length of the protrusion. This is because of the blocking of the entrainment from the bottom by the protrusion.

2 If the length of the horizontal side is larger than the boundary layer thickness, then the heat transfer rate from the vertical plate does not vary with the length. For air ($Pr = 0.7$), the Nusselt number is about 10 percent less than the \overline{Nu} of the vertical plate with no extension. The effect on the entrainment is significant; it changes from the bottom and side to essentially from the top.

3 The calculated Nusselt numbers agree well with the measured data for air.

References

- Churchill, S. W., and Chu, H. H. S., 1975, "Correlating Equations for Laminar and Turbulent Free Convection From a Vertical Plate," *Int. J. Heat Mass Transfer*, Vol. 18, pp. 1323-1329.
- Gebhart, B., 1971, *Heat Transfer 2e*, McGraw-Hill, New York, Chap. 8.
- Gebhart, B., Jaluria, Y., Mahajan, R. L., and Sammakia, B., 1988, *Buoyancy-Induced Flows and Transport*, Hemisphere, Washington, DC.
- Jaluria, Y., 1985, "Interaction of Natural Convection Wakes Arising From Thermal Sources on a Vertical Surface," *ASME JOURNAL OF HEAT TRANSFER*, Vol. 107, pp. 883-892.
- Kim, M. H., and Kim, M.-U., 1988, "Natural Convection Near a Rectangular Corner," *Int. J. Heat Mass Transfer*, Vol. 31, pp. 1357-1364.
- Kim, M. H., Kim, M.-U., and Choi, D. H., 1991, "Natural Convection Near a Vertical Corner of an Arbitrary Angle," *Int. J. Heat Mass Transfer*, Vol. 34, pp. 1327-1336.
- Liu, C. Y., and Guerra, A. C., 1985, "Free Convection in a Porous Medium Near the Corner of Arbitrary Angle Formed by Two Vertical Flat Plates," *Int. Comm. Heat Mass Transfer*, Vol. 12, pp. 431-440.
- Luchini, P., 1986, "Analytical and Numerical Solutions of Natural Convection in a Corner," *AIAA J.*, Vol. 24, pp. 841-848.
- McAdams, W. J., 1954, *Heat Transmission 3e*, McGraw-Hill, New York.
- Merkin, J. M., and Smith, F. T., 1982, "Free Convection Boundary Layer Near Corner and Sharp Trailing Edges," *ZAMP*, Vol. 33, pp. 36-52.
- Press, W. H., Flannery, B. P., Teukolsky, S. A., and Vetterling, W. T., 1986, *Numerical Recipes*, Cambridge University Press, New York.
- Riley, D. S., and Poots, G., 1972, "Thermal Convection in a Heated Vertical Corner," *Quarterly J. Mechanics and Applied Mathematics*, Vol. 25, pp. 401-421.
- Roache, P. J., 1982, *Computational Fluid Dynamics*, Hermosa, Albuquerque, NM.
- Rodighiero, C., and de Socio, L. M., 1983, "Some Aspects of Natural Convection in a Corner," *ASME JOURNAL OF HEAT TRANSFER*, Vol. 105, pp. 212-214.
- van Leeuwen, J. H., Looman, C. M., and Schenk, J., 1971, "Experimental Study of Velocity and Temperature Distribution for Free Convection in a Corner," *Int. J. Heat Mass Transfer*, Vol. 14, pp. 561-564.

Natural Convection Between Two Horizontal Cylinders in an Adiabatic Circular Enclosure

C. J. Ho
Professor.
Mem. ASME

W. S. Chang
Former Graduate Student.

C. C. Wang
Former Graduate Student.

Department of Mechanical Engineering,
National Cheng Kung University,
Tainan, Taiwan 701

A numerical study of natural convection flow structure and heat transfer has been undertaken for air around two horizontal, differentially heated cylinders confined to an adiabatic circular enclosure. Parametric simulations were performed to assess the effects of gap width between cylinders as well as the inclination angle of the enclosure with respect to gravity. Results clearly indicate that the fluid flow complexity and heat transfer characteristics of air amid the cylinders and enclosure wall are strongly affected by the Rayleigh number, the inclination angle, and the gap width between the cylinders. With the exception of the vertical orientation, heat exchange between the differentially heated cylinders is predominantly controlled by a counterclockwise recirculating flow enclosing them. In addition, flow visualization experiments were conducted for the physical configuration under consideration, and a generally good agreement for the flow pattern was observed between the predictions and the experiments, further validating the present numerical simulation.

Introduction

This paper is concerned with the buoyancy-driven fluid flow and heat transfer between two horizontal, differentially heated circular cylinders enclosed in an adiabatic circular enclosure as depicted schematically in Fig. 1. In the physical configuration under consideration here, the heat exchange process between the two cylinders may involve the interaction of buoyant streams individually induced by heating or cooling around them inside the adiabatic enclosure. Such natural convection configuration is primarily of fundamental relevance to the heat tracing system (Kohli, 1979) commonly used to minimize heat exchange of a piping system with the ambient in order to prevent the fluids contained in the pipelines from freezing or condensing.

A number of studies have been undertaken for natural convection heat transfer between an array of horizontal heating elements (wires or tubes) (Razelos, 1985; Parsons and Arey, 1987; Choi and Cha, 1989). The citations listed in these representative studies provide further references for this problem. It has been established that the natural convection heat transfer from arrays of heating elements is significantly affected by the plume-rise effect, which strongly depends on the geometrical configuration of the heating elements array. However, it appears that most of this literature dealt with arrays of heating elements situated in an infinite fluid medium. In practical situations, the heating element array may be confined in a finite fluid space by solid boundaries. The presence of enclosing solid boundaries can significantly alter the natural convection heat transfer characteristics between the heating elements. Therefore, it is practically important to address the natural convection heat transfer problem between heating elements in a confined space. Crupper and Warrington (1981) studied natural convection heat transfer experimentally from a set of four horizontal hot cylinders to a cooled cubical enclosure. Further experiments were reported considering the effects of different geometric arrangements of the cylinder array in a rectangular enclosure (Warrington and Weaver, 1990). More recently, Lacroix (1992) performed a numerical study of natural convection heat transfer from two vertically separated heated cylinders to a rectangular cavity cooled from above.

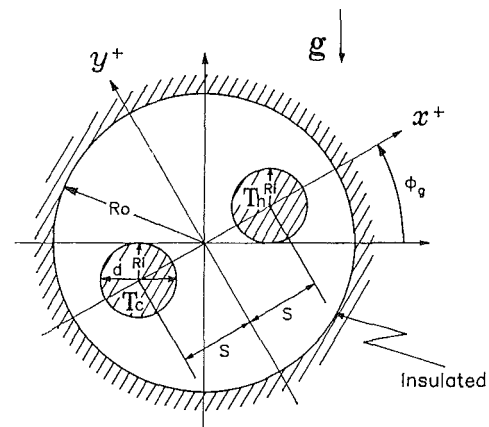


Fig. 1 Schematic diagram of the physical configuration investigated

The objective of the present study was to provide physical insight to the nature of buoyancy-driven fluid flow and heat transfer pertinent to the physical configuration considered for which little or no information is available. In so doing, numerical simulations via a finite difference method have been performed for the steady two-dimensional laminar natural convection phenomenon induced between the differentially heated horizontal cylinders inside the circular enclosure. Complementary to the numerical simulations, flow visualization experiments were also conducted for the physical configuration under consideration. Of particular emphasis in this study was the influence of the gravitational orientation of the enclosure as well as the center-to-center gap width between the cylinders on the natural convection fluid flow and heat transfer between the thermally active cylinders in the enclosure.

Mathematical Formulation

As illustrated in Fig. 1, an adiabatic circular enclosure of radius R_0 contains two horizontal circular cylinders having identical diameters, d . The two cylinders are located symmetrically with respect to the center of the circular enclosure, separated by a center-to-center distance $2s$. Moreover, the two cylinders are isothermally heated at different temperature, T_h and T_c , respectively. The buoyancy-driven fluid flow resulting from the temperature difference between the cylinders is assumed to be steady, two-dimensional, and laminar. Further,

Contributed by the Heat Transfer Division for publication in the JOURNAL OF HEAT TRANSFER. Manuscript received by the Heat Transfer Division June 1992; revision received September 1992. Keywords: Enclosure Flows, Flow Visualization, Natural Convection. Associate Technical Editor: J. R. Lloyd.

the thermophysical properties of the fluid are temperature independent, except for the density, for which the Oberbeck-Boussinesq approximation is valid. Viscous dissipation and compressibility effects are also neglected.

With the foregoing assumptions, the governing partial differential equations in dimensionless form for the conservation of mass, momentum, and energy are cast in terms of vorticity, stream function, and temperature. Moreover, to deal effectively with the geometrically complicated solution domain of the present problem, a composite overlapping grid system as exemplified in Fig. 2 is applied here so as to embed a general curvilinear coordinate system for the interior among three cylindrical grids around the circular solid boundaries, namely the surfaces of the two horizontal cylinders and the circular enclosure. The cylindrical grids constructed independently around these circular boundaries not only allow the resolution of any steep temperature gradients arising in the regions, but also provide an easier and more accurate evaluation of the Nusselt number on the cylinder surfaces. Furthermore, to ensure that the composite grids remain both continuous and smooth across the internal subgrid boundaries, an overlap between the internal boundaries of cylindrical and curvilinear grids is introduced so that the interaction among the different subgrids can be done by updating (transferring) the Dirichlet conditions on the internal subgrid boundaries. Based on this composite grid system, the dimensionless governing differential equations are cast in cylindrical polar coordinates and a general curvilinear coordinate, respectively. In cylindrical polar coordinates:

$$\frac{1}{r} \frac{\partial \psi}{\partial \phi} \frac{\partial \omega}{\partial r} - \frac{1}{r} \frac{\partial \psi}{\partial r} \frac{\partial \omega}{\partial \phi} = \text{Pr} \left[\text{Ra} \left(\cos \phi \frac{\partial \theta}{\partial r} - \frac{\sin \phi}{r} \frac{\partial \theta}{\partial \phi} \right) + \nabla^2 \omega \right] \quad (1)$$

$$\nabla^2 \psi = -\omega \quad (2)$$

$$\frac{1}{r} \frac{\partial \psi}{\partial \phi} \frac{\partial \theta}{\partial r} - \frac{1}{r} \frac{\partial \psi}{\partial r} \frac{\partial \theta}{\partial \phi} = \nabla^2 \theta \quad (3)$$

where

$$\nabla^2 \equiv \frac{\partial^2}{\partial r^2} + \frac{1}{r} \frac{\partial}{\partial r} + \frac{1}{r^2} \frac{\partial^2}{\partial \phi^2}$$

In the curvilinear coordinates (Thompson et al., 1974):

$$\frac{1}{J} \left(U \frac{\partial \omega}{\partial \xi} + V \frac{\partial \omega}{\partial \eta} \right) = \text{Pr} \left\{ \frac{\text{Ra}}{J} \left[\cos \phi_g \left(\frac{\partial y}{\partial \eta} \frac{\partial \theta}{\partial \xi} - \frac{\partial x}{\partial \xi} \frac{\partial \theta}{\partial \eta} \right) - \sin \phi_g \left(\frac{\partial x}{\partial \xi} \frac{\partial \theta}{\partial \eta} - \frac{\partial y}{\partial \eta} \frac{\partial \theta}{\partial \xi} \right) \right] + \bar{\nabla}^2 \omega \right\} \quad (4)$$

$$\bar{\nabla}^2 = -\omega \quad (5)$$

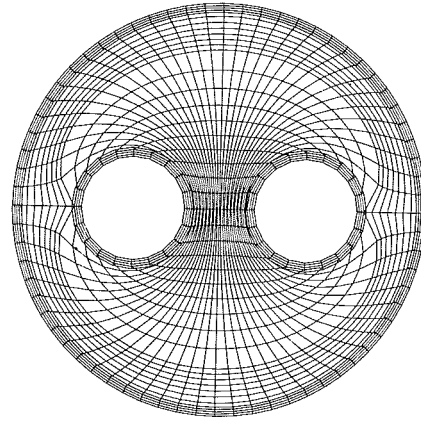


Fig. 2 A typical composite overlapping grid system

$$\frac{1}{J} \left(U \frac{\partial \theta}{\partial \xi} + V \frac{\partial \theta}{\partial \eta} \right) = \bar{\nabla}^2 \theta \quad (6)$$

where U and V are the contravariant velocity components along the ξ and η directions, defined as

$$U = \frac{\partial \psi}{\partial \eta}; \quad V = -\frac{\partial \psi}{\partial \xi} \quad (7)$$

and

$$\bar{\nabla}^2 \equiv \frac{1}{J^2} \left(a_1 \frac{\partial^2}{\partial \xi^2} - 2a_2 \frac{\partial^2}{\partial \xi \partial \eta} + a_3 \frac{\partial^2}{\partial \eta^2} \right) + P \frac{\partial}{\partial \xi} + Q \frac{\partial}{\partial \eta} \quad (8a)$$

$$a_1 \equiv \left(\frac{\partial x}{\partial \eta} \right)^2 + \left(\frac{\partial y}{\partial \eta} \right)^2 \quad (8b)$$

$$a_2 \equiv \frac{\partial x}{\partial \xi} \frac{\partial x}{\partial \eta} + \frac{\partial y}{\partial \xi} \frac{\partial y}{\partial \eta} \quad (8c)$$

$$a_3 \equiv \left(\frac{\partial x}{\partial \xi} \right)^2 + \left(\frac{\partial y}{\partial \xi} \right)^2 \quad (8d)$$

Here the coordinate control functions P and Q are based on the forms devised by Thomas and Middlecoff (1980).

The dimensionless boundary conditions of the problem considered are:

$$\frac{\partial \psi}{\partial r} = \frac{\partial \psi}{\partial \phi} = 0, \quad \psi = \psi_h \text{ (constant)}, \quad \theta = 0.5 \quad (9a)$$

$$\frac{\partial \psi}{\partial r} = \frac{\partial \psi}{\partial \phi} = 0, \quad \psi = \psi_c \text{ (constant)}, \quad \theta = -0.5 \quad (9b)$$

Nomenclature

a_1, a_2, a_3 = geometric coefficients
 d = diameter of cylinder
 g = gravitational acceleration
 h = heat transfer coefficient
 J = Jacobian
 Nu = Nusselt number
 P = coordinate control function
 Pr = Prandtl number = ν/α
 r^+ = radial coordinate
 r = dimensionless radial coordinate = r^+/d
 Ra = Rayleigh number = $g\beta(T_h - T_c)d^3/(\nu\alpha)$
 R_i = radius of cylinder

R_o = radius of circular enclosure
 s = half center spacing between cylinders
 T = temperature
 T_m = mean temperature = $(T_h + T_c)/2$
 U, V = contravariant velocity components
 α = thermal diffusivity
 β = thermal expansion coefficient
 η = transformed coordinate
 θ = dimensionless temperature = $(T - T_m)/(T_h - T_c)$

ν = kinematic viscosity
 ξ = transformed coordinate
 ϕ = angular coordinate
 Φ = angular location on cylinder surface
 ϕ_g = inclination angle
 ψ = dimensionless stream function
 ω = dimensionless vorticity

Subscripts

c = cold cylinder
 h = hot cylinder
 m = mean value
 max = maximum value
 o = circular enclosure

on the surfaces of the two isothermally heated cylinders, respectively, and

$$\psi = 0, \quad \frac{\partial \theta}{\partial r} = 0 \quad (9c)$$

on the surface of the circular adiabatic enclosure.

The governing differential equations in either cylindrical or curvilinear coordinates, Eqs. (1)–(6), as well as the boundary conditions, Eq. (9), possess a symmetry that obeys the following transformation:

$$\begin{aligned} \theta^*(r, \phi) &= -\theta(r, \phi + \pi), & \omega^*(r, \phi) &= \omega(r, \phi + \pi), \\ \psi^*(r, \phi) &= \psi(r, \phi + \pi) \\ \theta^*(x, y) &= -\theta(-x, -y), & \omega^*(x, y) &= \omega(-x, -y), \\ \psi^*(x, y) &= \psi(-x, y) \end{aligned} \quad (10)$$

where the $()^*$ denotes the transformed fields. From this symmetry, it follows that the boundary stream functions on the two horizontal cylinders, ψ_h and ψ_c , should be identical, but remain to be determined. This unknown value of the boundary stream function is determined from the requirement of single valuedness of pressure, which in turn leads to evaluation of a line integral in terms of vorticity and temperature around the horizontal cylinder surface (Adlam, 1986).

Numerical Method

Numerical simulations of the physical problem under consideration have been performed via a finite difference method for solving the set of governing differential equations, Eqs. (1)–(6), subjected to the boundary conditions, Eq. (9). The partial differential equations were discretized using a second-order central differencing formula on both the cylindrical and curvilinear grids, respectively. By means of a line-by-line relaxation scheme, the resulting systems of finite difference equations were solved independently on the four subgrid domains. The calculations in each subgrid domain were linked by using Dirichlet conditions on the interior border of the overlapping grid region through an interpolation based on the solutions calculated in the adjoining subgrid domain. For interpolation, a bivariable linear interpolation scheme (Part and Chang, 1988) was adopted.

In the iterative calculation procedure for the steady-state solution to the present problem, the unknown boundary stream functions on the thermally active cylinders were updated based on the newly obtained vorticity and temperature fields. The iterative calculation was continued until a prescribed relative convergence of 10^{-5} was satisfied for all the field variables of the problem. Moreover, an energy balance between the horizontal cylinders within 0.1 percent was achieved for all the converged calculations obtained.

The accuracy of the present calculation has been investigated by performing a grid independence test for each subgrid domain. For instance, differences between the results of the average heat transfer rate and the stream function extreme for $Ra = 10^6$, $s/d = 0.8333$, $\phi_g = 90$ deg using a composite grid mesh consisting of 15 (radial) \times 31 (angular) cylindrical mesh around the thermally active cylinders; 5 (radial) \times 81 (angular) mesh around the surface of the circular enclosure, 41 \times 45 curvilinear grids for the interior region amid the solid circular boundaries and that of 17 \times 49, 7 \times 121, and 61 \times 69 meshes in the respective subgrid domain was found to be less than 2 percent. Depending on the gap width between the cylinders, three composite grid systems were employed for the present calculations: (15 \times 41, 5 \times 89, 45 \times 57), (15 \times 41, 5 \times 89, 45 \times 55), (15 \times 41, 5 \times 101, 51 \times 55) for $s/d = 0.7, 0.8333$, and 1.0, respectively.

Flow Visualization Experiment

In order to reveal the pattern of buoyancy-driven flow be-

tween the horizontal cylinders inside the circular enclosure, flow visualization experiments were performed in an air-filled test cell that mimics the physical configuration depicted in Fig. 1. The circular cylindrical enclosure was a 8-cm-id. plastic tube 20 cm long with an outer insulation blanket of 5 cm thick; and the two thermally active horizontal cylinders were constructed of brass tubes of outer radius 1 cm. To facilitate flow passage for a thermally regulated fluid, an annular counterflow channel is constructed inside each of the brass tubes. The condition of differentially heated isothermal surface temperature on the two brass tubes was achieved by circulating a thermally regulated fluid (a mixture of ethanol in water) from two constant temperature baths, respectively. For visual investigation of the flow structure, double-pane Plexiglas windows were used as the front and rear walls of the test cell.

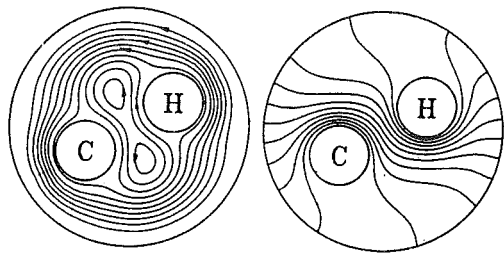
The surface temperature measurements at each cylinder were made by four copper-constantan thermocouples installed circumferentially at 90 deg intervals at the middle plane of the test cell and by another two thermocouples positioned axially along the surface of the cylinders. The surface temperature variations on the cylinders were found to be less than 0.2°C both axially and around the cylinder.

Smoke for the flow visualization experiment was generated by burning an incense stick inside a plastic smoke generation tube. The smoke was then injected slowly through two small holes drilled on the circular container of the test cell. The transverse cross-sectional view of the buoyancy-driven flow field in the midlength of the test cell was made visible by a sheet of light provided by two halogen slit light sources located symmetrically around the test cell. The cross-sectional views of the flow pattern developed inside the test cell were produced photographically by a Nikon F-4 camera.

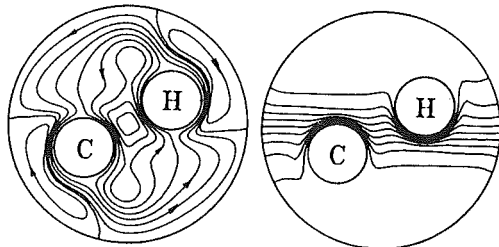
Numerical Results

Numerical simulations have been undertaken for the steady-state buoyancy-driven fluid flow and heat transfer of air ($Pr = 0.71$) arising between the thermally active horizontal cylinders inside an adiabatic circular enclosure of $R_o/R_i = 4$ with the relevant dimensionless parameters in the following ranges: $Ra = 10^3$ to 10^7 ; s/d (center-to-center spacing between cylinders) = 0.7 to 1.0; and $0 \text{ deg} \leq \phi_g$ (inclination angle of the enclosure) ≤ 90 deg. It should be noted that the calculations for $\phi_g = 0$ deg with high Ra ($> 10^5$) encountered great difficulty in obtaining converged solutions, for which the fluid flow under this orientation may be periodic in time due to the stronger buoyant plume activities. A truly transient simulation is therefore necessary in future work. The numerical results will therefore be presented with primary focus on the influences of Ra , s/d , and ϕ_g in the abovementioned ranges on the steady-state natural convection fluid flow structure and heat transfer characteristics between the horizontal cylinders inside the circular enclosure.

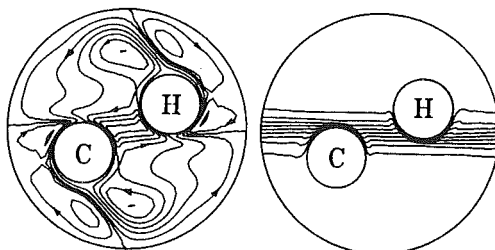
Flow and Temperature Fields. First of all, the flow structure and temperature distribution developed between the horizontal cylinders in the circular enclosure are presented by means of contour maps of streamlines and isotherms. Figure 3 exemplifies the streamline patterns (left) and isotherm distributions (right) at three values of Rayleigh number with $s/d = 0.8333$ and $\phi_g = 30$ deg. The capital letters "H" and "C" centered at two cylinders in the contour plots are used to denote the hot and cold horizontal cylinders, respectively. The increment between adjacent isotherms is 0.1. At $Ra = 10^3$, as is expected, the isotherms in Fig. 3(a) display a conduction-dominated distribution in the presence of weak flow field featuring an outer counterclockwise recirculating motion, channeling through the narrow gap between the thermally active cylinders and the adiabatic circular enclosure wall, together with an inner corotating recirculation pinched between the cylinders. Further, there exists, respectively, a thermal bound-



(a) $Ra=10^3$ ($\psi_{\min}=-0.3364$, $\psi_{\max}=3.6587$)



(b) $Ra=10^5$ ($\psi_{\min}=-1.9907$, $\psi_{\max}=10.3502$)

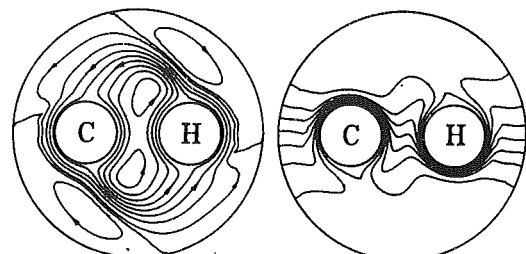


(c) $Ra=5 \times 10^6$ ($\psi_{\min}=-6.7056$, $\psi_{\max}=21.7029$)

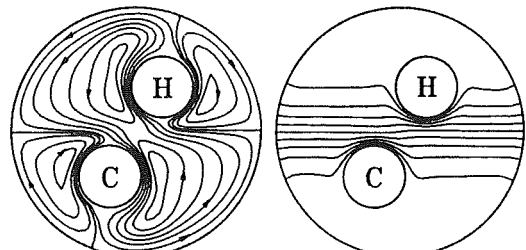
Fig. 3 Contours of streamlines (left) and isotherms (right) for different Rayleigh number with $s/d=0.8333$, $\phi_g=30$ deg in a circular enclosure of $R_o/R_i=4$

ary layer around lower/upper portion of the hot/cold cylinder. With increased buoyancy force at higher Ra ($=10^5$), Fig. 3(b), the isotherms tend to become stratified and the thermal boundary layers around the cylinders become thinner. The air bulk above the hot cylinder and below the cold cylinder appears to be isothermal, respectively, at temperatures close to those of the cylinders. Moreover, the streamlines for $Ra=10^5$ feature a pair of corotating clockwise secondary cells developed, respectively, in the narrow gap between the cylinder and the enclosure wall, in addition to the intensified counterclockwise recirculating flow enclosing the cold and hot cylinders. With further higher Ra , the aforementioned features of the flow structure and temperature distribution become more pronounced as illustrated in Fig. 3(c) for $Ra=5 \times 10^6$. Another important fact that can be observed in Fig. 3 is that the heat exchange between the hot and cold cylinders under such orientation is predominantly conveyed by the counterclockwise recirculating flow enclosing them.

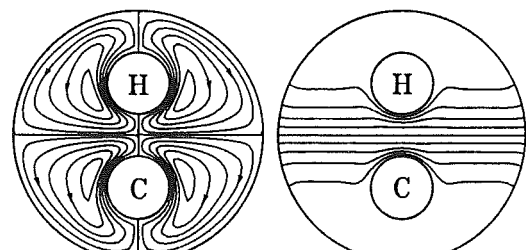
Figure 4 illustrates the typical influence of the inclination of the circular enclosure with respect to gravity on the flow and temperature fields for $Ra=10^5$ and $s/d=0.8333$. In comparison with Fig. 3(b) for $\phi_g=30$ deg, it is evident from Fig. 4 that lowering of the orientation from $\phi_g=30$ deg to the horizontal orientation ($\phi_g=0$ deg) results in stronger flow field as indicated by the higher stream function extreme shown in the figure; and thermal plume activities can readily be detected originating, respectively, from the top of the hot cylinder (hot plume) and the bottom of the cold (cold plume). Furthermore, the isotherms reveal that either plume tends to slant toward the neighboring cylinder in conformity with the outer coun-



(a) $\phi_g=0^\circ$ ($\psi_{\min}=-4.1872$, $\psi_{\max}=22.7489$)



(b) $\phi_g=60^\circ$ ($\psi_{\min}=-2.6318$, $\psi_{\max}=4.2958$)

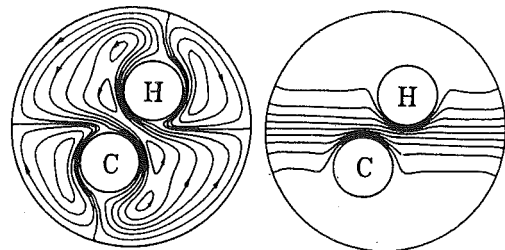


(c) $\phi_g=90^\circ$ ($\psi_{\min}=-3.3108$, $\psi_{\max}=3.3102$)

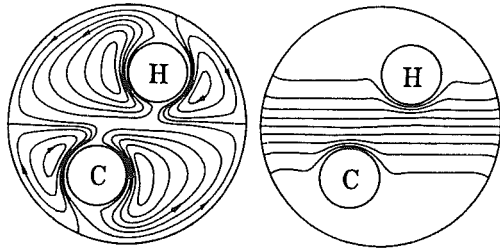
Fig. 4 Influence of inclination angle on flow patterns and temperature distributions for $Ra=10^5$ and $s/d=0.8333$

terclockwise recirculating flow structure shown in the streamline plot. On the other hand, increasing the tilt angle toward the vertical orientation ($\phi_g=90$ deg), as shown in Fig. 4(c), affects the clockwise and the counterclockwise recirculating flows in the enclosure differently. The pair of clockwise secondary recirculations can be seen to grow and intensify progressively while the counterclockwise recirculating flow enclosing the cylinders becomes substantially impeded. Accordingly, a flow structure characterized by two pairs of counterrotating recirculations around the hot and cold cylinders, respectively, is formed in a vertically orientated enclosure. Furthermore, both the flow structure and the temperature field shown in Fig. 4(c) clearly display a symmetry with respect to both the vertical and the horizontal axis of the circular enclosure. Further examination of the isotherms in Fig. 4 reveals that the thermal boundary layers on the thermally active cylinders are greatly degraded with increasing ϕ_g up to the vertical orientation, indicative of a reduced heat transfer rate.

As the gap width between the thermally active cylinders, s/d , is decreased, the inner counterclockwise recirculation between the cylinders becomes markedly intensified and further squeezed resulting in vortex splitting, as shown in Fig. 5(a) for $s/d=0.7$. It follows that the thermal boundary layers on the cylinders become more distinct, hence yielding higher convective heat transfer rate. Meanwhile, the decrease of s/d leads to intensification of the clockwise secondary recirculations in the narrow gap between the cylinders and the enclosure wall. Conversely, an opposite effect arises from the enlargement of the gap width between the cylinders, as displayed in Fig. 5(b)



(a) $S=0.7$ ($\psi_{\min}=-2.7570$, $\psi_{\max}=4.8347$)



(b) $S=1.0$ ($\psi_{\min}=-2.1966$, $\psi_{\max}=3.2680$)

Fig. 5 Flow structures and temperature fields at two different gap width between cylinders for $Ra = 10^5$ and $\phi_g = 60$ deg

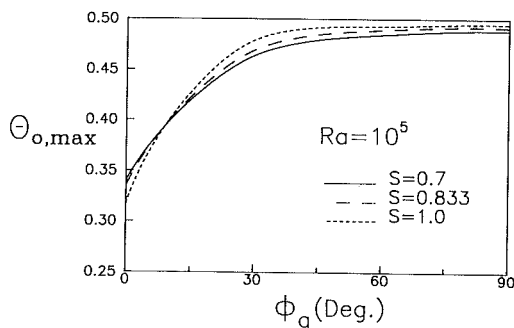
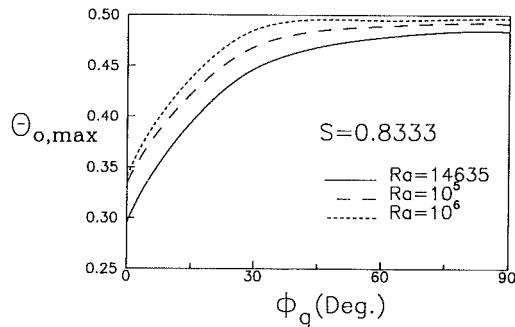


Fig. 6 Dependence of the maximum surface temperature at the circular enclosure on the inclination angle

for $s/d = 1$. Moreover, the thermal boundary layers on the hot and cold cylinders are seen to degrade markedly with the enlargement of s/d , hence resulting in decreased heat transfer rate from the cylinders.

Another quantity of practical interest is the maximum surface temperature on the adiabatic circular enclosure, $\theta_{o,\max}$, which is plotted versus the inclination angle as exemplified in Fig. 6. An overview of the figure reveals that the maximum

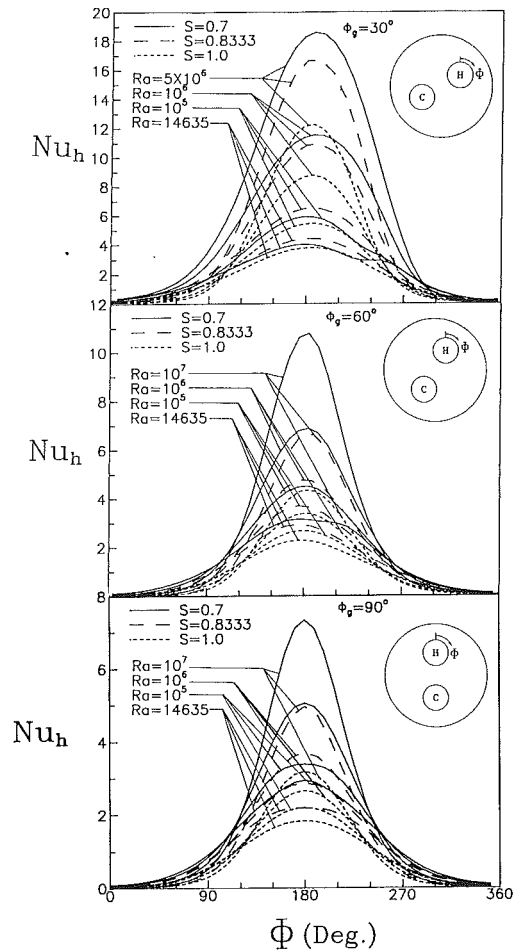


Fig. 7 Variations of local Nusselt number along the hot cylinder at different inclination angles

surface temperature on the enclosure wall exhibits a rapid rise as the enclosure is tilted from the horizontal and then asymptotically reaches a flat maximum value near the vertical orientation. The magnitude of the maximum surface temperature also shows a significant dependence on the Rayleigh number; the increase of Ra results in higher surface temperature. Moreover, the variation of the gap width between cylinders, as conveyed in Fig. 6(b), appears to exert a rather mild influence on the maximum surface temperature, depending on the inclination angle of the enclosure. For $\phi_g > 15$ deg, the shifting of the hot cylinder toward the circular enclosure wall as a result of increasing s/d gives rise to a somewhat higher maximum surface temperature on the enclosure.

Heat Transfer Results. Next, attention will be focused on the results of local heat transfer rate on the thermally active cylinders, which are presented by means of local Nusselt numbers defined as:

$$Nu_h = \frac{h_h d}{k} = -\frac{\partial \theta}{\partial n} \quad (11a)$$

and

$$Nu_c = \frac{h_c d}{k} = \frac{\partial \theta}{\partial n} \quad (11b)$$

where n denotes a normal coordinate to the surfaces of the thermally active cylinders.

Figure 7 elucidates the angular profile of the local heat flux along the hot cylinder enclosed in circular enclosure of three orientations for three values of s/d at various Ra . The angular

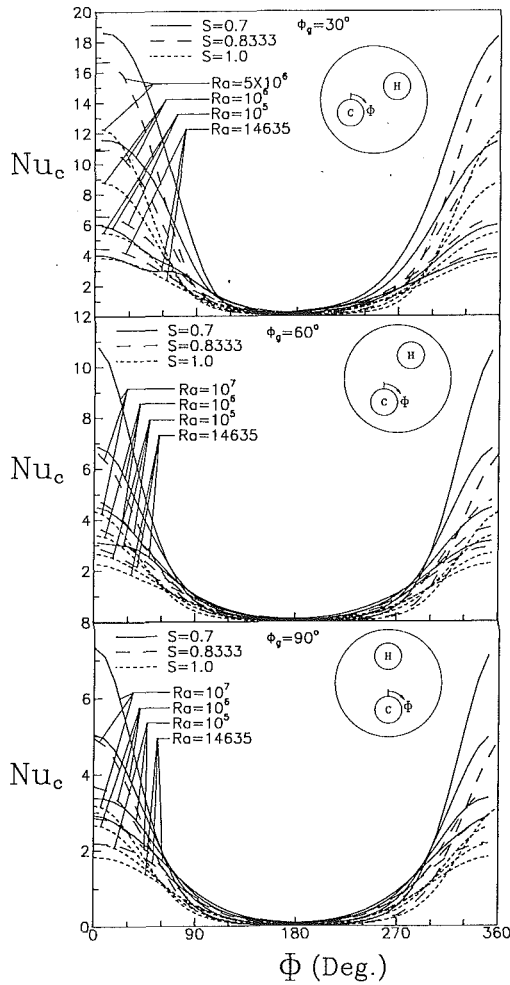


Fig. 8 Variations of local Nusselt number along the cold cylinder at different inclination angles

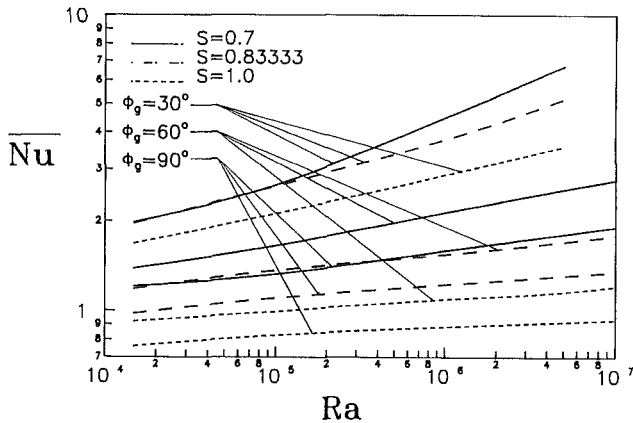


Fig. 9 Relation of the average Nusselt number with the Rayleigh number

location, Φ , shown in the figure is measured clockwise from the top of the cylinder. Scrutiny of the figure reveals that the local heat flux, in general, tends to increase from the top to the bottom of the hot cylinder and then displays a decreasing trend angularly from the bottom returning to the top. With the exception of the vertical orientation, $\phi_g = 90$ deg, it can be noticed that the distributions of the local Nusselt number exhibit a slight asymmetry with respect to the vertical axis of the hot cylinder, reflecting the effect of counterclockwise recirculating flow enclosing the cylinders displayed in Fig. 4. More-

Table 1 Constants C and m for Eq. (12)

s/d	ϕ_g	Ra	C	m	Average Deviation
0.7	30°	10^4 — 5×10^6	0.2466	0.2116	4.34 %
	60°	10^4 — 10^7	0.4864	0.1072	1.84 %
	90°	10^4 — 10^7	0.5972	0.0713	1.55 %
0.8333	30°	10^4 — 5×10^6	0.3947	0.1653	1.84 %
	60°	10^4 — 10^7	0.6606	0.0613	0.82 %
	90°	10^4 — 10^7	0.6186	0.0488	1.03 %
1.0	30°	10^4 — 5×10^6	0.4749	0.1303	0.59 %
	60°	10^4 — 10^7	0.6140	0.0413	0.31 %
	90°	10^4 — 10^7	0.5735	0.0301	1.09 %

over, with increasing either Ra or ϕ_g , the angular profile of the local Nusselt number becomes more distinct such that the heat transfer is highly concentrated in the lower half of the hot cylinder directly facing the cold cylinder. The heat transfer at the upper portion of the hot cylinder can be seen to be negligible as a result of isothermal air bulk in the region. Furthermore, the enlargement of s/d tends to produce an effect opposite to that of increasing Ra ; lower local Nusselt number in the lower half of the hot cylinder can be observed for larger s/d .

For the cold cylinder, as displayed in Fig. 8, the angular variations of the local Nusselt number appears to be opposite to those observed on the hot cylinder; the heat transfer takes place mainly on the upper half of the cold cylinder directly facing the hot cylinder.

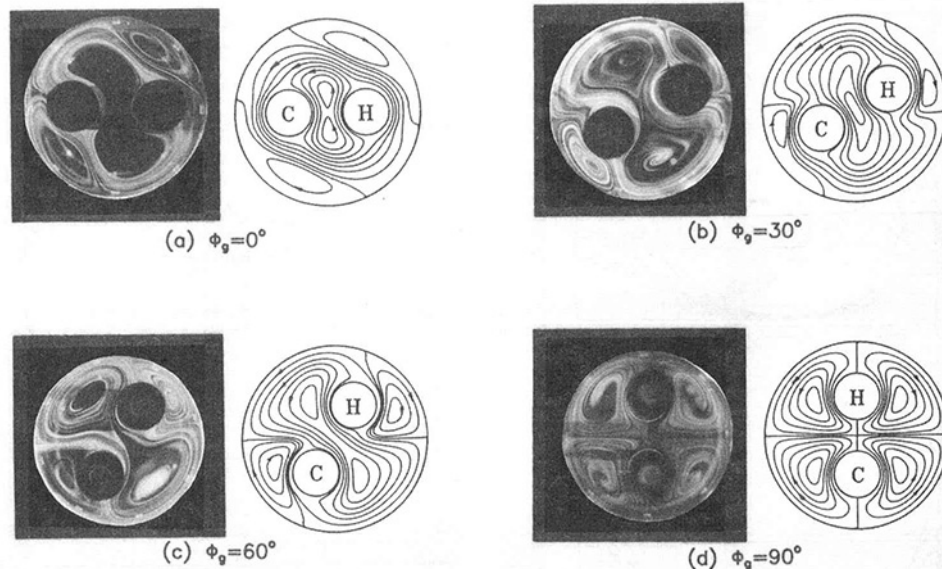
In Fig. 9, the circumferentially averaged Nusselt number on the hot cylinder is plotted versus the Rayleigh number for different values of s/d and ϕ_g . As demonstrated in Fig. 9, the average heat transfer rate from the cylinder is a function of Ra , s/d , and ϕ_g . As generally expected, the overall heat transfer rate increases with the increase of Ra . The inclination angle and the gap width between cylinders appear to have similar effects on the average Nusselt number. The increase of ϕ_g or s/d can give rise to substantial decreases of the average heat transfer rate from the hot cylinder. Furthermore, the present results of the average Nusselt number can be correlated via a least-square regression analysis in the form

$$Nu = CRa^m \quad (12)$$

where the coefficients C and m are listed in Table 1 for different values of ϕ_g and s/d . The decreasing values of the exponent m with the increase of either ϕ_g or s/d as indicated in the table further reflect the aforementioned effects of these geometric parameters on the natural convection heat transfer between the cylinders.

Comparison With Flow Visualization Experiments

Finally, to validate further the accuracy of the numerical simulations undertaken, the predicted flow structures are compared with results of the flow visualization experiments. Figure 10 exemplifies the comparison of the computed streamline patterns with the flow visualization photographs for $Ra = 14,635$, $s/d = 0.8333$, at four different inclination angles of the enclosure; and a generally good qualitative agreement can be readily observed. A closer examination of Fig. 10 can, nevertheless, detect, excluding the vertical orientation $\phi_g = 90$ deg, the discrepancy between the prediction and the experiment



$Ra=14635$, $S=0.833$

Fig. 10 Comparison of the predicted flow structures under various inclination angles with photographs of the flow visualization experiments for $Ra=14635$, $s/d=0.8333$

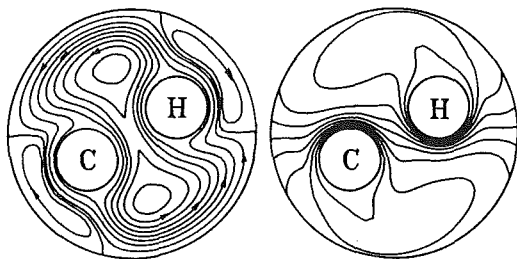


Fig. 11 Predicted flow structure and isotherm distribution at $\phi_g=30$ deg for $Ra=14,635$ and $s/d=0.8333$ in the circular enclosure with a convective boundary condition with the ambient

on the inner counterclockwise rotating vortex structure pinched between the thermally active cylinders. This may be partly caused by the inevitable heat exchange of the air inside the enclosure with the ambient during the flow visualization tests as a result of the practical difficulty in achieving perfectly insulated enclosure wall experimentally. To further explore this point, numerical simulations for the circular enclosure having a convective boundary condition with the ambient are currently under way. From some preliminary results obtained, we found that the inner vortex structure between the cylinders can be strongly affected by the imperfectly insulated condition on the enclosure wall; and as exemplified in Fig. 11 for $\phi_g=30$ deg with $Ra=14,635$ and $s/d=0.8333$ in the circular enclosure with convective boundary condition, the predicted inner vortex flow structure is apparently in much better agreement with the flow visualization results shown in Fig. 10. Furthermore, it can be seen from isotherms in Fig. 11 that in the presence of heat exchange with the ambient, the slanted thermal plume activities on the cylinders become more pronounced.

Concluding Remarks

In the present article, the problem of natural convection flow and heat transfer of air between two horizontal, differently heated circular cylinders confined to an adiabatic circular enclosure has been studied numerically by means of a finite difference method. Results from the numerical simulations undertaken indicate that the fluid flow complexity and the heat

transfer characteristics of air amid the thermally active cylinders and the circular enclosure wall are strongly affected by the Rayleigh number, the gap width between the cylinders, and the inclination angle of the circular enclosure with respect to gravity. Except for the vertical orientation, the heat transfer mechanism between the hot and cold cylinders is predominantly controlled by the counterclockwise recirculating flow structure enclosing them. Increasing either the gap width between the cylinders or the inclination angle of the circular enclosure leads to lower heat exchange between the cylinders. To verify the present simulations, flow visualization experiments mimicking the physical configuration considered have been conducted and a generally good agreement between the prediction and the experiment was observed for the patterns of buoyancy-driven air flow around the horizontal cylinders except the counterclockwise inner vortex structure. Such discrepancy may be in part due to heat exchange of air in the test cell with the ambient as a result of practical difficulty in achieving perfectly insulated boundary in the flow visualization experiments.

The present study is by no means complete. A wider range of parametric simulations as well as experimental data of the heat transfer rate are needed in future work. Investigations are under way to explore the effect of heat exchange of air inside the enclosure with the ambient on natural convection flow structure and heat transfer between the differentially heated cylinders.

Acknowledgments

Support from the National Science Council of ROC through grant No. NSC 81-0401-E006-03 in this study is gratefully acknowledged. Also, the assistance of Mr. Y.T. Cheng in performing the calculations as well as in preparation of the data is greatly appreciated.

References

- Adlam, J. H., 1986, "Computation of Two-Dimensional Time-Dependent Natural Convection in a Cavity Where There Are Internal Bodies," *Computers & Fluids*, Vol. 14, No. 2, pp. 141-157.
- Choi, Kyung-Jin, and Cha, Soyong, 1989, "Plume-Rise Effect on Natural Convection Heat Transfer in Staggered Arrays of Circular Heating Elements," *AIAA J. Thermophysics and Heat Transfer*, Vol. 4, pp. 228-232.

Crupper, G., and Warrington, R. O., 1981, "Natural Convection Heat Transfer Between Tube Bundles and a Cubical Enclosure," *ASME JOURNAL OF HEAT TRANSFER*, Vol. 103, No. 1, pp. 103-107.

Kohli, I. P., 1979, "Steam Tracing of Pipelines," *Chemical Engineering*, Mar. pp. 156-163.

Lacroix, M., 1992, "Natural Convection Heat Transfer Around Two Horizontal Cylinders Inside a Rectangular Cavity Cooled From Above," *Numerical Heat Transfer*, Part A, Vol. 21, pp. 37-54.

Park, Seong-Keun, and Chang, Keun-Shik, 1988, "Numerical Study on Interactive Laminar Natural Convection From a Pair of Vertically Separated Horizontal Cylinders," *Numerical Heat Transfer*, Vol. 14, pp. 61-74.

Parsons, J. R., Jr., and Arey, M. L., Jr., 1987, "Development of Convective Heat Transfer Near Suddenly Heated Vertically Aligned Horizontal Wires," *ASME JOURNAL OF HEAT TRANSFER*, Vol. 109, pp. 912-918.

Razelos, P., 1985, "An Interferometric Investigation of the Effect of Separation Distance and Temperature Imbalance on Natural Convection for Two Horizontal Cylinders at Moderate Rayleigh Number," *Wärme- und Stoffübertragung*, Vol. 19, pp. 255-262.

Thomas, P. D., and Middlecoff, J. F., 1980, "Direct Control of the Grid Point Distribution in Meshes Generated by Elliptic Equations," *AIAA Journal*, Vol. 18, pp. 562-656.

Thompson, J. F., Thames, F. C., and Mastin, C. F., 1974, "Automatic Numerical Generation of Body-Fitted Curvilinear Coordinates System for Fluid Containing Any Number of Arbitrary Two-Dimensional Bodies," *Journal of Computational Physics*, Vol. 15, pp. 299-319.

Warrington, R. O., and Weaver, R. A., 1990, "Natural Convection Heat Transfer Between Arrays of Horizontal Cylinders and Their Enclosure," *Heat Transfer—1990*, Vol. 2, pp. 205-209.

Natural Convection in the Inclined, Cranked Thermosyphon

G. S. H. Lock

J. Fu

Department of Mechanical Engineering,
University of Alberta,
Edmonton, Alberta, Canada T6G 2G8

Consideration is given to natural convection in a cranked, tubular thermosyphon oriented in various ways with respect to the vertical. Experiments on a small-bore, water-filled tube are used to investigate three orientational effects: by tilting in a vertical plane containing the tubes; by incremental rotation about the axis of the horizontal connecting tube; and by incremental rotation about a horizontal axis parallel to the thermosyphon tube axes. The results reveal similarities between the cranked and linear thermosyphons. In general, horizontal alignments are found to produce higher heat transfer rates.

Introduction

The tubular thermosyphon is a well-known device admirably suited to the transmission of large heat fluxes. In its simplest form it consists of a straight, fluid-filled tube connecting a heat source to a heat sink. Under the influence of thermally induced buoyancy forces, circulation within the tube is capable of transferring large amounts of thermal energy from the hot end to the cold end. In addition to its thermal effectiveness, which does not require an external power supply, its dependence on a body force field creates a one-way valve effect whereby heat is transferred much more effectively against the field direction than with it. Thus a stationary vertical thermosyphon tube convects upward, but only conducts downward, the former process being much superior to the latter.

Ever since its forerunner, the Perkins tube, appeared over a century ago (King, 1931), the tubular thermosyphon has found many applications, in some of which the internal circulation is driven by simple thermal buoyancy; in others, evaporation and condensation accompany a circulation driven by Archimedean buoyancy forces (Lock, 1992). In the geotechnical context of northern development, it has been used extensively to maintain soil in a frozen condition and may also be used to create an underwater ice blockage in northern rivers (Cheng and Zarleng, 1990; Lock, 1986). Under these circumstances, when the heated section (which is buried or submerged) lies vertically beneath the cooled section (which is cooled by the wind), the heat valve effect ensures a seasonal alteration in performance. Very large heat fluxes during the winter freezing period are succeeded by very low heat fluxes during the summer thawing period; the overall effect of the device thus increases each successive year.

In an industrial context, the tubular thermosyphon has been used extensively in heat exchanger design (Lee and Bedrossian, 1978; Larkin, 1983; Vasiliev, 1987; Dobran, 1989; Groll, 1989; Ma and Hou, 1989). For the most part, these designs incorporate boiling and condensation and are thus not concerned with single-phase behavior which, in defining the lower range of effective operation, may be a superior alternative when the thermal resistances on either side of the device are large enough to control overall performance. Typically, the designs employ straight tubes. Here again, the designer is restricted to simple, though common, circumstances in which a stationary heat source lies immediately adjacent to, and largely beneath, a heat sink.

To some extent, the linear, inclined thermosyphon provides the designer with increased flexibility, especially if the heated and cooled sections may be separated by an adiabatic section

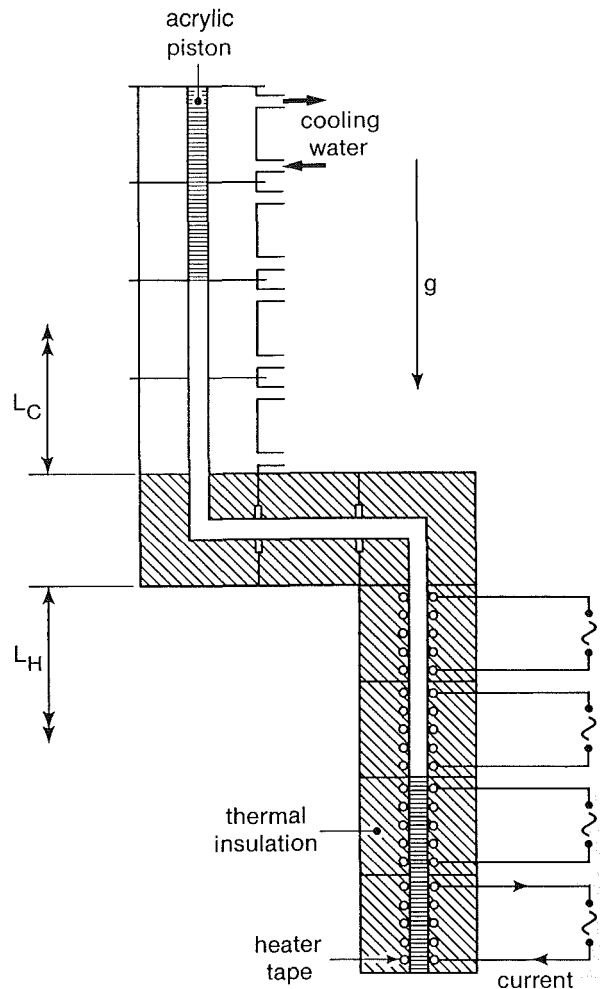


Fig. 1 Schematic of apparatus

but, in general, the need for additional configurations continues as new applications arise. The cranked, or offset, tubular thermosyphon is one example that has already appeared. It is shown schematically in Fig. 1 with the main tubes, aligned vertically, being connected by an adiabatic offset length aligned horizontally. In this configuration, the device is suited to cooling and freezing in and around construction piles (Waters, 1974). With the main tubes aligned more or less horizontally, it has been used to prevent thermal erosion beneath roads and airstrips (Long, 1984).

In an earlier paper (Lock and Ladoon, 1991), an exploratory study of the vertical configuration was undertaken experimentally under single-phase conditions. While this offers be-

Contributed by the Heat Transfer Division for publication in the JOURNAL OF HEAT TRANSFER. Manuscript received by the Heat Transfer Division January 13, 1992; revision received June 19, 1992. Keywords: Heat Exchangers, Heat Pipes and Thermosyphons, Natural Convection. Associate Technical Editor: J. R. Lloyd.

havioral insights, it provides no information on the effects of orientation. Accordingly, the present work was undertaken, again under single-phase conditions. This paper is therefore an extension of the previous work. To facilitate comparisons, the same fluid (water) has been used and the system geometry has also been fixed: The main length-diameter ratios $L_H/D = L_C/D$ have the representative value of 20:1, while the offset length-diameter ratio is fixed at 4:1, the value at, or above, which the offset effect may not be neglected in the vertical configuration (Lock and Ladoon, 1991).

The Experiments

Apparatus. The experiments were conducted on the small-bore apparatus shown schematically in Fig. 1. It consisted of 1.98-cm-dia copper tubes joined in a cranked configuration. The overall length of each of the heated and cooled sections was 80 cm, but this length could be varied by means of the acrylic pistons inserted as shown. In fact, the length of these sections was fixed at 40 cm, while that of the adiabatic offset was fixed at 8 cm measured between the axes of the main tubes.

The heated section was divided into four equal lengths of 20 cm, each being supplied with its own heater; only two of these sections were used in the present work. As indicated, the heaters were formed from electrically resistive tape sheathed in asbestos and wound over the section length. This was done after thermocouples had been installed. The heater tapes were connected in parallel, thus providing an adjustment of the local heat flux density and tube wall temperature. A thick layer of fiberglass insulation was wrapped around the heater so as to limit any heat lost to the atmosphere.

The cooled section was also divided into four equal lengths, each being provided with its own cooling jacket as indicated; again, only the two innermost sections were employed here. Coolant flow rate was used to reduce local wall temperatures in the vicinity of a chosen isotherm; no attempt was made to control the local heat flux density.

The main tubes were joined with a length of the same bore tube, the connection being a short, right-angled bend at each end extending 6 cm beyond the mouth of the main tube. As indicated, this offset length was also wrapped in a thick layer of fiberglass insulation.

Instrumentation. No attempt was made to measure the heat removed by the cooling water because, under the steady conditions studied, it is equal to the net heat supplied in the heated section. The latter was calculated by subtracting the heat leakage from the gross supply rate. The electrical power was supplied from the building mains and measured in the usual way with an ammeter and voltmeter. The heat leakage was determined from a calibration test undertaken before the experiments proper began. This test consisted of plotting the power supplied against the difference in temperature between the tube wall and the room air when the tube was filled with styrofoam insulation. Typically, the leakage was about 10 percent of the gross supply rate.

Temperatures were measured throughout using copper-constantan thermocouples. These were installed in the room air and around the tube walls at 4-cm intervals along the tube

length in both the heated and cooled sections, though not in the adiabatic section. Thermocouple signals were fed through a switching box and read on a digital voltmeter. Average wall temperatures in each of the diatomic tubes were calculated from at least ten thermocouples; typically, the variation over the wall was ± 2 K. Fluid properties were evaluated at a temperature midway between the average tube wall temperatures.

Inclinations were measured with a simple protractor and a level.

A formal error analysis of the data was also undertaken using the definitions of Nusselt number and Rayleigh number given below. Assuming external errors to be small, as later confirmed, the mean square errors in these variables were calculated from the uncertainties in the measured quantities. Representative uncertainty bars thus determined are shown in Figs. 3, 5, and 7. They are consistent with the scatter observed, except for three "wild" points (in the low Nu data in Fig. 3) for which we have no explanation.

Test Procedure and Schedule. The test procedure was as follows. Having chosen a particular configuration, the apparatus was cleaned and filled with tap water. The cooling water was then turned on and the power to the heater tapes set at some convenient value in the anticipated range. After about one hour, adjustments in the power levels to individual heaters were made in order to achieve a better approximation to an isothermal heated wall; for the same reasons, minor adjustments were also made to the cooling water flow rates. Further refinements were made periodically over a subsequent period of about two hours at the end of which steady conditions had been reached.

At this point, readings were taken of the gross power to individual heaters, local wall temperatures, and the room air temperature. From these readings to the net heat supply rate was calculated along with the average wall temperatures T_H and T_C in the heated and cooled sections, respectively. The heat flux density \dot{q} , based on the heated surface area (πDL_H), was then used to determine the diameter-based Nusselt number defined by

$$Nu = \dot{q}D/k (T_H - T_C)$$

The diameter-based Rayleigh number defined by

$$Ra = \beta g (T_H - T_C) D^3 / \nu \kappa$$

was also calculated.

The gross power was then altered slightly and the procedure repeated until the Rayleigh number range of the apparatus had been covered. A curve of Nu versus Ra was then plotted. The entire process was then repeated for another configuration. Table 1 lists the range of conditions covered and specifies the geometry. The definitions of the tilt, skew, and roll angles are given in the next section.

Discussion of Results

Thus far, the term "inclination" has been studiously avoided so as to make a clear distinction between the three degrees of rotational freedom indicated in Fig. 2. In this paper, *tilt* α refers to a cranked thermosyphon inclined in a vertical plane

Nomenclature

D = tube diameter
 k = fluid thermal conductivity
 L = tube length
 Nu = Nusselt number
 \dot{q} = heat flux density
 Ra = Rayleigh number

T = absolute temperature
 α = tilt angle
 β = thermal expansion coefficient
 γ = skew angle
 δ = roll angle
 κ = thermal diffusivity

ν = momentum diffusivity

Subscripts

C = cooled section
 H = heated section
 A = adiabatic section

Table 1 Summary of experimental conditions

Variable	Range
Rayleigh number	$10^{5.9} < Ra < 10^{7.6}$
Tilt angle	$-22^\circ < \alpha < +90^\circ$
Skew angle	$0 < \gamma < 90^\circ$
Roll angle	$0 < \delta < 90^\circ$

$L_H = 40$ cm
 $L_C = 40$ cm
 $L_A = 8.0$ cm
 $D = 1.98$ cm
 fluid: water

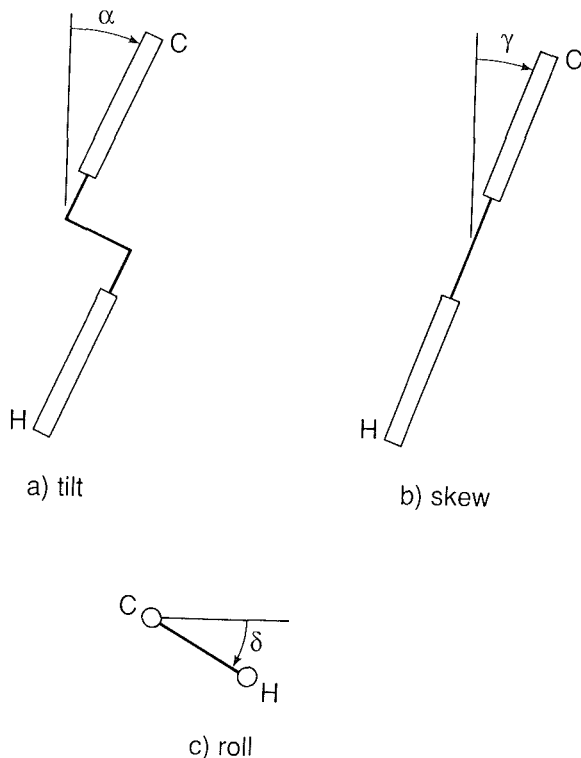


Fig. 2 Tilt, skew, and roll definitions

containing the tube axes; positive tilt angles are defined as shown. *Skew* γ refers to inclination (with respect to the vertical) about the horizontal axis of the offset length. *Roll* δ , on the other hand, refers to inclination of the heated section beneath the cooled section when their axes are both horizontal; positive roll is defined in the figure. It is clear from these definitions that a tilt of 90 deg is equivalent to a roll of 90 deg, while a roll of 0 deg corresponds to a skew of 90 deg.

The Effect of Tilt. In the vertical position ($\alpha = 0$ deg), the deep flow in the heated and cooled sections is essentially an annular reflux pattern in which fluid near the tube wall moves away from the closed end while a central, replenishing core moves in the opposite direction. On the other hand, reflux in the offset length is essentially bifilamental and stably stratified; hot fluid moves over cold fluid moving in the opposite

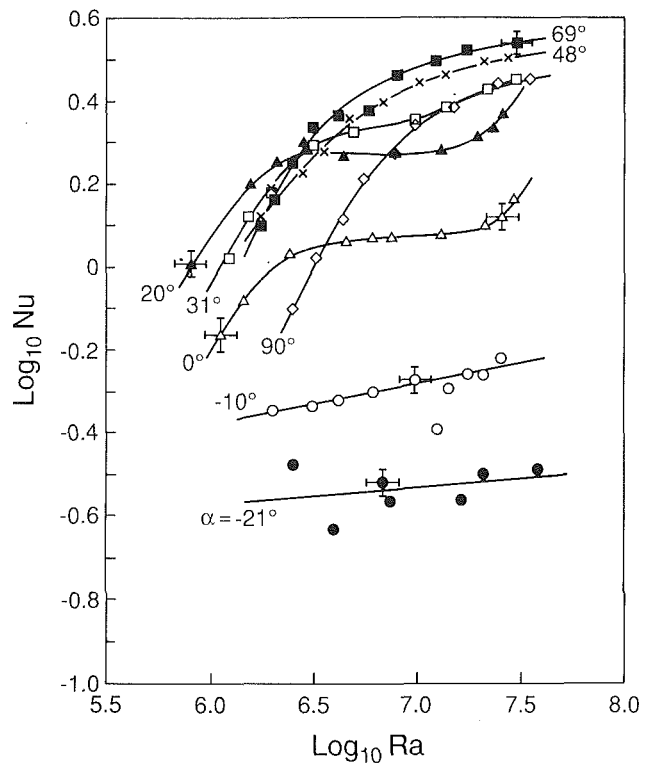


Fig. 3 Effect of Rayleigh number on heat transfer during tilting

direction. In general, these differing patterns are reconciled near the open ends of the heated and cooled sections (Lock and Ladoon, 1991). A filament leaving the offset length tends to remain close to the inner corner and becomes the core of the deep flow, while the exiting annular flow tends to collect near the outer corner to become the filament entering the offset length. Under the influence of tilt, this pattern may be expected to retain its symmetry about the plane of tilt.

Figure 3 shows the effect of varying the Rayleigh number for each of a series of tilt angles, positive and negative. It is immediately obvious that the vertical results separate very different behavior between positive and negative tilt angles. As Fig. 2 indicates, the effect of a negative tilt is to lower the cooled section relative to the heated section with the eventual result, at $\alpha = -90$ deg, the system is stably stratified and natural convection ceases. Figure 3 reveals how rapid this deterioration is. When the heat flux becomes very small, the system performance is not much better than pure conduction ($\log_{10} Nu \approx -1.4$) once the tilt falls below -20 deg. The copper wall raises the actual conduction limit, the precise value having little practical significance.

Positive tilts evidently improve performance, in general, but the effect is not monotonic. For lower Rayleigh numbers, e.g., $Ra < 10^{6.5}$, the $\log Nu \sim \log Ra$ data exhibit a steep slope. Extrapolation downward suggests that slopes in the range $10^{5.5} < Ra < 10^{6.5}$ may be expected to be of the order 1.0. This in turn indicates a laminar impeded flow régime (Lighthill, 1953; Bayley and Lock, 1965), as previously observed in the linear thermosyphon.

For higher Rayleigh numbers, the high positive tilt data reveal a smooth transition to another flow régime in which the annular-core structure of the flow deep within the heated and cooled sections has been partly replaced by a bifilamental structure extending either side of the offset length and eventually filling the entire system. When $\alpha = 90$ deg, the primary flow pattern consists of a single loop.

The behavior of the system changes yet again when the tilt angle is small but positive. The high Rayleigh number data

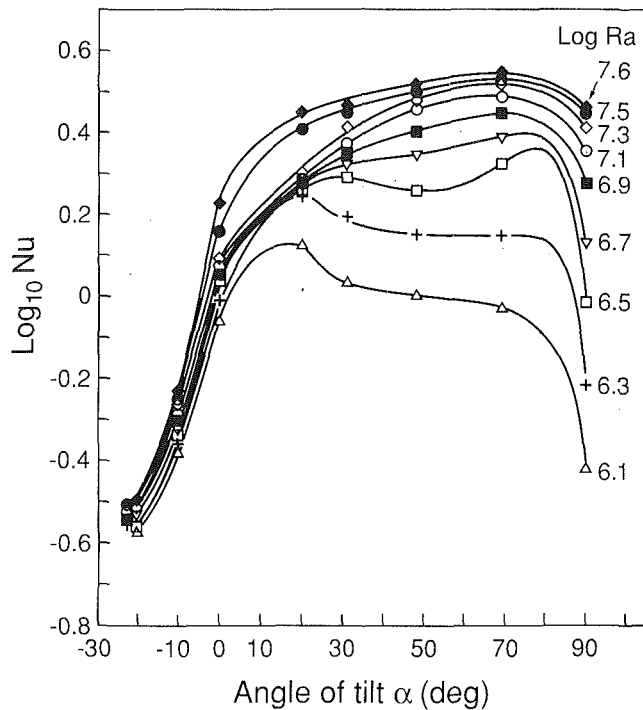


Fig. 4 Effect of tilt angle on heat transfer

under these conditions were found to be much steeper, suggesting a turbulent boundary layer flow, at least beyond $Ra = 10^{7.3}$ (Lock and Ladoon, 1991). However, as Fig. 3 reveals, the transition from a laminar impeded régime to a turbulent boundary layer may extend over a considerable range of Rayleigh number during which the Nusselt number remains almost constant. This is evidently a fully mixed turbulent régime in which the scale of turbulence is not small in relation to the tube diameter. Increases in tilt were found to reduce and eventually eliminate this transitional régime.

The effect of tilt may be seen in Fig. 4, which is a cross plot of Fig. 3. The simple but dramatic effect of negative tilts is clearly evident, as is the more complex effect of positive tilts. For low Rayleigh numbers corresponding to laminar impeded flow, e.g., $Ra = 10^{6.1}$, the existence of a single maximum is seen at low tilt angles. However, the data also exhibit an inflection point, which, as the Rayleigh number is increased, develops into a local minimum in the vicinity of $\alpha = 45$ deg.

The resulting bimodal curve may be explained by examining the overall effect of tilt on the main (diabatic) tubes and the offset (adiabatic) tube under laminar conditions. A tube tilted with respect to the vertical develops a less vigorous primary flow and a more vigorous secondary flow. The opposite is true for a tube tilted with respect to the horizontal, at least in the range $0 \text{ deg} < \alpha < 90 \text{ deg}$ (Lock and Han, 1989; Lock and Kirchner, 1992). The attendant rises in Nusselt number are evident in Fig. 4. However, when $\alpha \approx 0$ deg, the hot filament leaving the heated section occupies the upper surface of the offset length (nearer the cooled section) but when $\alpha \approx 90$ deg it occupies the opposite surface (further from the cooled section). Similarly, the hot filament moving over the upper surface of the heated and cooled sections when $\alpha \approx 90$ deg becomes a core-annular flow when $\alpha \approx 10$ deg. In the intermediate tilt angle range, the flow in all three tubes must somehow turn over in conditions that introduce an ambiguity similar to that found in the elbow thermosyphon under laminar impeded conditions (Lock and Park, 1991). The resulting transitional régime occupies a substantial tilt range.

For turbulent conditions, e.g., $Ra > 10^{7.3}$, the situation changes. When the tilt is small, a turbulent boundary layer

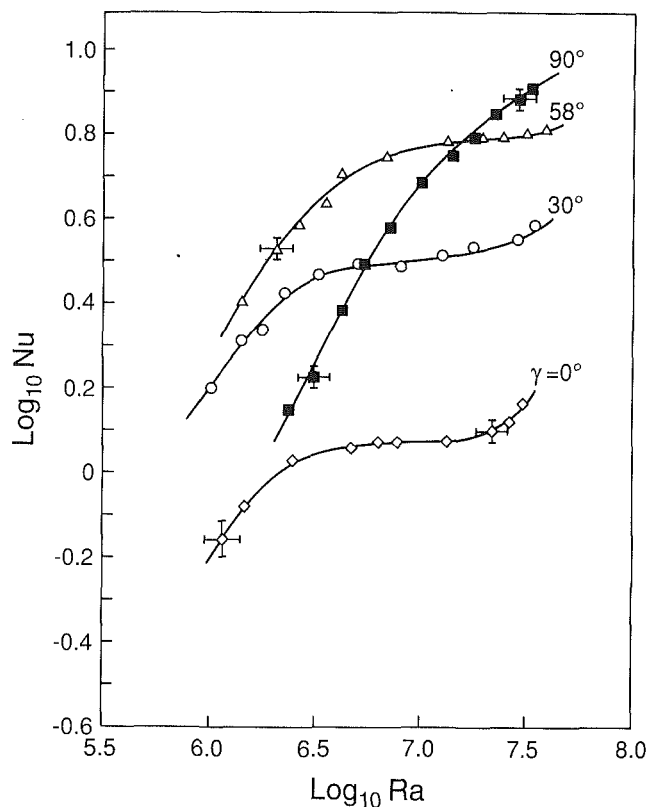


Fig. 5 Effect of Rayleigh number on heat transfer during skewing

controlled by stratification in the offset length has been suggested (Lock and Ladoon, 1991). As the tilt increases, however, this turbulent loop must also turn over. In the process, the flow in the offset length evidently becomes fully mixed with the result that a vigorous turbulent boundary layer cannot be established in the main tubes; only a weak loop may form. Consequently, the Nusselt number then varies little with Rayleigh number, as seen in Fig. 3. Under these conditions, the initial effect of decreasing α beneath 90 deg is to improve performance slightly through increases in direct buoyancy in the main tubes. As α decreases further, however, the natural tendency for the main tube flow to turn over eventually leads to a fully mixed flow throughout. The heat transfer rate then falls off rapidly with decreasing α unless the Rayleigh number is high enough to establish a stratified turbulent boundary layer. From Figs. 3 and 4 it appears that this latter régime is restricted to large Rayleigh numbers and small tilt angles. By contrast, the fully mixed régime appears to exist under two sets of conditions: for small tilt angles when $10^{6.3} < Ra < 10^{7.3}$ and for large tilt angles when $Ra > 10^{7.3}$.

The Effect of Skew. From Fig. 2 it is clear that the effect of skew is to destroy the planar symmetry noted during the tilt experiments. The effect of Rayleigh number under skewed conditions is shown in Fig. 5. For low Rayleigh numbers, e.g., $Ra < 10^{6.5}$, the presence of a laminar impeded régime is again evident, regardless of the skew angle γ . However, the high Rayleigh number data reveal that skew has a significant influence. The turbulent boundary layer behavior at $\gamma = 0$ deg is first replaced by flatter, fully mixed flow data as the skew angle increases but as γ approaches 90 deg, the slope of the data is restored, an interesting contrast with the effect of tilt, where the offset length does not remain horizontal. Under skewed conditions, the offset length tends to maintain a stratified flow, and hence the gradual disappearance of the skew influence in the main tubes as γ approaches 90 deg makes possible the eventual restoration of a turbulent boundary layer

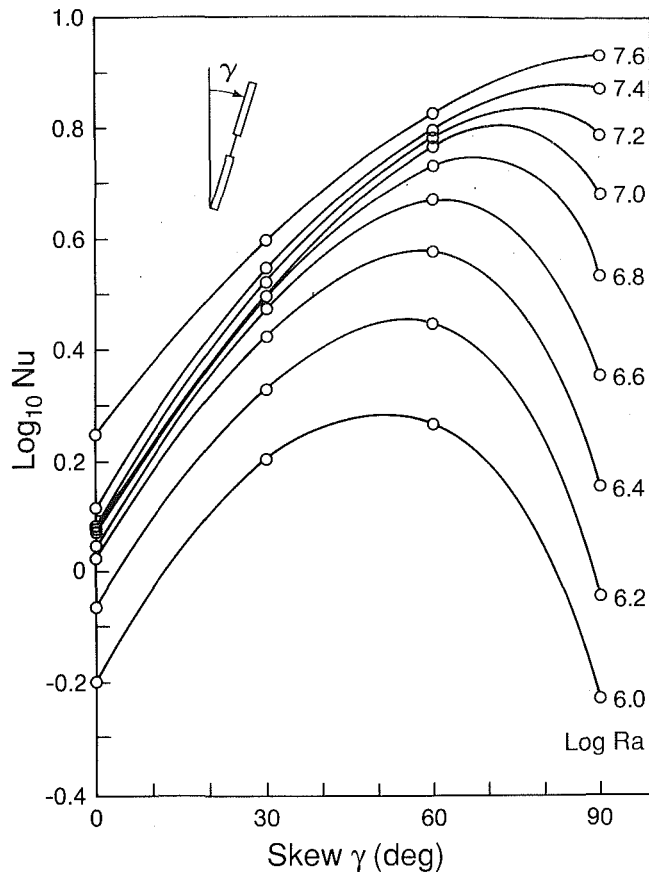


Fig. 6 Effect of skew angle on heat transfer

flow; unfortunately, the data are not extensive enough to rule out the existence of an intermediate laminar boundary layer régime. Skew also influences the fully mixed flow régime, the almost horizontal region of the data for $\gamma=0$ deg gradually shifting and extending to higher Rayleigh numbers as the skew angle increases. Along with it, the upper limit of the laminar impeded régime also shifts to higher Rayleigh numbers.

A crossplot of these data is shown in Fig. 6, from which it is evident that a simple maximum with respect to skew exists under laminar impeded conditions. Given the previously discussed reconciliation of the flow patterns in the offset and main tubes, this behavior is not unexpected. It stems from two superimposed tendencies. First, the bifilamental flow in the offset length must rotate slowly so as to keep the hot filament above the cold filament, which is moving in the opposite direction. Secondly, the bifilamental flow must extend farther and farther into the heated and cooled sections as the skew increases. Previous work on inclined linear tubes has revealed that the deep annular flow gradually recedes in favor of a bifilamental flow as the horizontal position is approached (Lock and Zhao, 1990; Lock and Kirchner, 1992). The overall result of increasing γ is therefore gradually to decrease the direct primary buoyancy in the main tubes while increasing the direct secondary effects. The offset length acts merely as a connector. Initially, the secondary effects increase more rapidly than the primary effects decrease, but as γ approaches 90 deg, the reverse is true. A maximum skew angle is thus created.

For higher Rayleigh numbers the situation again changes. When the skew angle is small, a laminar impeded régime is separated from a turbulent boundary layer régime by a fully mixed turbulent régime. Figure 5 not only shows that the upper limit of this intermediate régime shifts upward with skew but suggests that the extent of the régime reduces slightly; the high Rayleigh number data for $\gamma=30$ and 58 deg indicate a steep-

ening curve and thus signal entrance to a turbulent boundary layer régime. This leads to the suggestion that the transition from laminar to turbulent flow shifts from $Ra=0(10^{6.5})$ for small skews, which engender fully mixed flow, to $Ra=0(10^{7.3})$ for large skews, which engender boundary layer flow. It therefore appears that the $Ra=10^{7.6}$ data in Fig. 6 are all in the turbulent boundary layer régime; the flow is always turbulent and always stratified.

This explanation accounts for the monotonic form of the large Rayleigh number curves. Flow conditions are then essentially controlled by the horizontal offset length, which exchanges hot and cold fluid filaments between two "reservoirs." The closer the "reservoir" tubes are to the horizontal, the easier will be the penetration of the filaments along their lengths; without skew, the filaments do not penetrate far into the main tubes (Lock and Ladoon, 1991).

It is to be expected that the behavior of the skewed system would be symmetric about $\gamma=0$ deg, regardless of whether the flow is laminar or turbulent. However, symmetry would not be expected about $\gamma=90$ deg. It is more likely that the performance would deteriorate with skew angles exceeding 90 deg, at least up to $\gamma=180$ deg, another point of symmetry. This deterioration is clearly evident in the laminar data shown in Fig. 6. Under turbulent conditions, the gradual rise in Nusselt number with γ in the range $0 \text{ deg} < \gamma < 90 \text{ deg}$, coupled with the expected decline for $\gamma > 90 \text{ deg}$, implies a simple maximum. The figure indicates that optimal performance occurs at $\gamma=90$ deg for very large Rayleigh numbers, but occurs at progressively smaller skew angles as the Rayleigh number is decreased; in particular, the optimum skew angle is about 50 deg under laminar impeded conditions when the performance is often better than under turbulent conditions without skew. These are important lessons for the designer.

The Effect of Roll. The potential benefits of large tilt and skew angles, especially at high Rayleigh numbers, lead quite naturally to a consideration of roll, when the heated and cooled sections both remain horizontal. Figure 2 provides a reminder that the offset length is now inclined at the roll angle δ to the horizontal, and its ability to maintain a stratified flow thus varies. Figure 2 also indicates that symmetry about $\delta=90$ deg (and -90 deg) may be expected but not, in general, about $\delta=0$ deg.

Figure 7 shows the effect of Rayleigh number for each of four roll angles in the range $0 \text{ deg} < \gamma < 90 \text{ deg}$. Once more the existence of laminar impeded behavior is clearly evident. In distinction to the corresponding tilt and skew curves, Figs. 3 and 5, the data consist of a family of monotonic curves; the $\delta=60$ deg data may be the exception. In view of the earlier discussion, this suggests a smooth transition from laminar impeded flow to turbulent flow with the nature of the turbulence varying with the roll angle. As noted above, the high Rayleigh data in the absence of roll ($\gamma=0$ deg) probably belong to the turbulent boundary layer régime whereas at $\gamma=90$ deg, they belong to a fully mixed régime in which the heat transfer rate is understandably lower. The vestiges of a fully mixed régime appear to be present in the data for $\gamma=60$ deg but are not evident at $\gamma=30$ deg.

In the crossplot presented in Fig. 8, the effect of roll is seen more clearly. In the laminar impeded range, which now extends almost up to $Ra=10^{7.0}$, optimal behavior is again evident. Since the heated and cooled sections remain horizontal, this is evidently caused by the adiabatic offset length for the same reasons discussed earlier. Once the flow is turbulent, however, the maximum is transferred to the zero roll angle where it presumably remains for higher Rayleigh numbers, not because of symmetry, but because negative roll angles may be expected to create a deterioration in performance. The monotonicity of the high Rayleigh curves in Fig. 8 is caused by a gradual change from fully mixed flow to boundary layer flow; the explanation

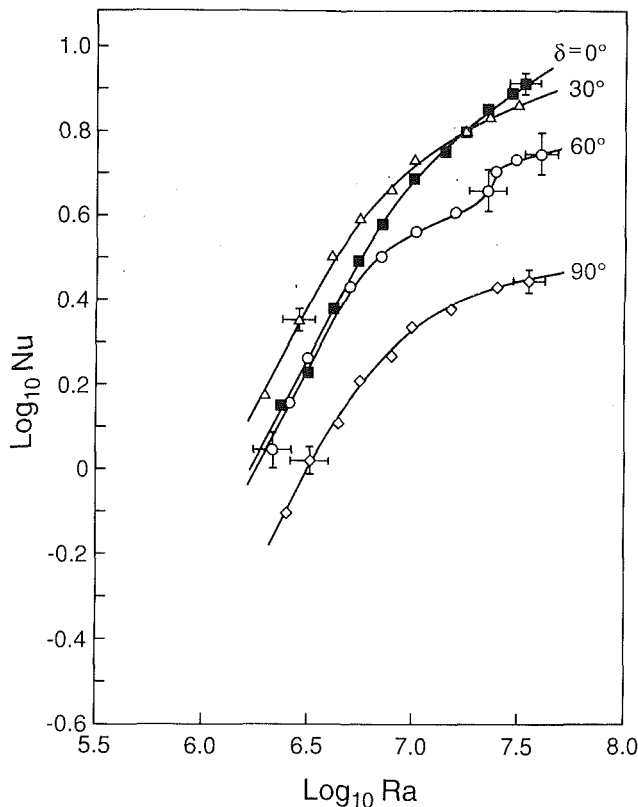


Fig. 7 Effect of Rayleigh number on heat transfer during rolling

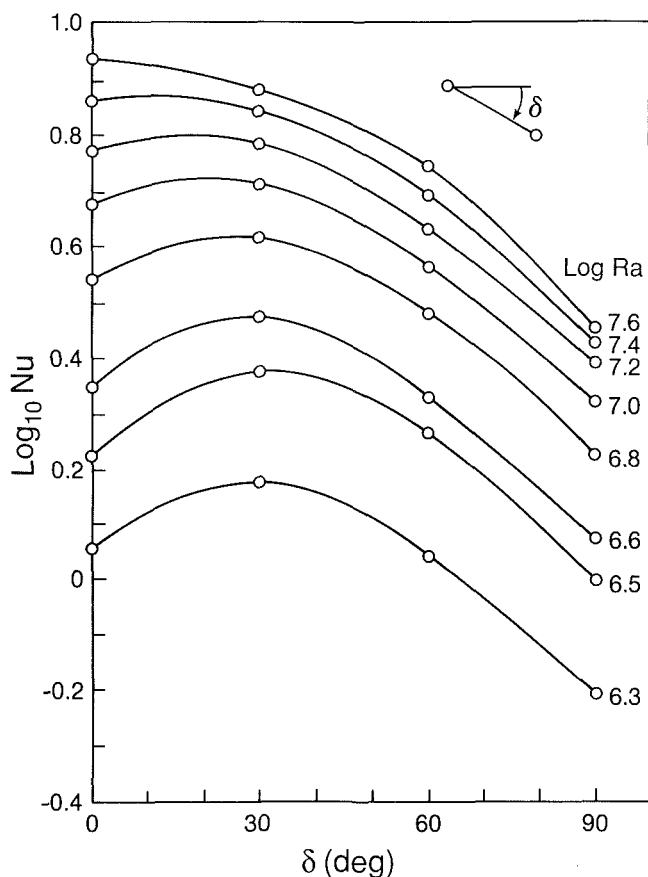


Fig. 8 Effect of roll angle on heat transfer

thus differs from that given for the corresponding curves in Fig. 6 where the flow, being controlled by the horizontal offset, never appears to exhibit fully mixed behavior.

Conclusions

In these experiments, tilting the thermosyphon created the greatest range of behavior. Negative tilts were found to produce a very rapid deterioration in performance while positive tilts created complex improvements. For low Rayleigh numbers, flow behavior was typically in the laminar impeded régime in which positive tilts with respect to either the vertical or the horizontal increased the heat transfer rate, but only over a narrow range of tilt angles.

For high Rayleigh numbers, the flow was turbulent. With small tilt angles, the transition to turbulence first created a fully mixed flow with its characteristically constant Nusselt number, but further increases in Rayleigh number converted this into a turbulent boundary layer flow. With large tilt angles, the boundary layer flow régime was evidently suppressed. It is concluded that this change of behavior reflects the changing ability of the offset length to maintain a stratified flow under tilted conditions.

The same régimes were observed under skewed conditions, but, with the offset length remaining horizontal, the complexity of the régime map was reduced. Small skew angles produced a boundary layer flow, which appeared to be restored at high skew angles. It is concluded that this restoration reflects the re-establishment of a single loop penetrating farther into the heated and cooled sections than when the skew is small.

Since the heated and cooled sections both remained horizontal during roll changes, the maximal form of the data under laminar impeded conditions has been attributed to the role of the offset length. Likewise, it is suggested that under high Rayleigh number conditions the offset length is largely responsible for the shift from turbulent boundary layer flow to fully mixed flow as the roll increases over the first 90 deg.

From a designer's point of view, the results reveal that various orientations are accompanied by a wide range of penalties and benefits. It is clear that rotation of the device about any given axis may be used to vary the heat transfer rate substantially under given temperature conditions. This feature raises some interesting possibilities in thermoregulation. The highest Nusselt number recorded was well over an order of magnitude greater than the lowest. If the design is limited to a fixed configuration, a choice of various maxima is available, depending upon the desired general layout and upon whether operating conditions are laminar or turbulent.

Acknowledgment

We wish to thank the Natural Sciences and Engineering Research Council, who made this work possible, and to express our gratitude for the assistance obtained from Messrs. A. Muir and B. Ceilin of the Department of Mechanical Engineering, University of Alberta.

References

- Bayley, F. J., and Lock, G. S. H., 1965, "Heat Transfer Characteristics of the Closed Thermosyphon," *ASME JOURNAL OF HEAT TRANSFER*, Vol. 87, pp. 30-40.
- Cheng, K. C., and Zarling, J. P., 1990, "Applications of Heat Pipes and Thermosyphons in Cold Regions," *Proc. 7th Int. Heat Pipe Conf.*, Minsk.
- Dobran, F., 1989, "Heat Pipe Research and Development in the Americas," *Heat Recovery Systems and CHP*, Vol. 9, No. 1, pp. 67-100.
- Groll, M., 1989, "Heat Pipe Research and Development in Western Europe," *Heat Recovery Systems and CHP*, Vol. 9, No. 1, pp. 19-66.
- King, C. R., 1931, "Perkins' Hermetic Tube Boilers," *The Engineer*, Vol. 152, pp. 405-406.

- Larkin, B. S., 1983, "A Thermosyphon Heat Exchanger for Use in Animal Shelters," *Can. Soc. Agric. Engineers*, Paper #74-210.
- Lee, Y., and Bedrossian, A., 1978, "The Characteristics of Heat Exchangers Using Heat Pipes or Thermosyphons," *Int. J. Heat Mass Transfer*, Vol. 21, No. 2, pp. 221-229.
- Lighthill, M. J., 1953, "Theoretical Considerations on Free Convection in Tubes," *Quart. J. Mech. and Appl. Math.*, Vol. VI, No. 4, pp. 398-439.
- Lock, G. S. H., 1986, "Control of Spring Run-Off in Northern Rivers: The Ice Veil Concept," *Polar Record*, Vol. 23, No. 145, pp. 451-457.
- Lock, G. S. H., and Han, J.-C., 1989, "Buoyant Laminar Flow of Air in Long, Square-Section Cavity Aligned With the Temperature Gradient," *J. Fluid Mech.*, Vol. 207, pp. 489-504.
- Lock, G. S. H., and Zhao, Litong, 1990, "The Effect of Inclination on an Air-Filled, Open Thermosyphon at Low Rayleigh Numbers," *Proc. ASME/AIChE/AIAA Conf.*, Seattle, WA.
- Lock, G. S. H., and Ladoon, D., 1991, "Heat Transfer Characteristics of a Cranked Thermosyphon," *Proc. 3rd Int. Symp. on Cold Regions*, pp. 417-428.
- Lock, G. S. H., and Park, S., 1991, "A Numerical Study of the Right-Angled Thermosyphon," *Proc. 10th Int. Conf. on Offshore Mech. and Arctic Eng.*, Vol. IV, pp. 113-118.
- Lock, G. S. H., 1992, *The Tubular Thermosyphon*, Oxford University Press.
- Lock, G. S. H., and Kirchner, J. D., 1992, "Some Characteristics of the Inclined, Closed Tube Thermosyphon Under Low Rayleigh Number Conditions," *Int. J. Heat Mass Trans.*, Vol. 35, No. 1, pp. 165-173.
- Long, E., 1984, *Frozen Assets*, Arctic Foundations Inc.
- Ma, T., and Hou, Z., 1989, "Heat Pipe Research and Development in China," *Heat Recovery Systems and CHP*, Vol. 9, No. 6, pp. 499-512.
- Vasiliev, L. L., 1987, *Heat Pipe Heat Exchangers*, Nauka i Tekhnica, Minsk.
- Waters, E. D., 1974, "Heat Pipes to Stabilize Piling on Elevated Alaska Pipeline Sections," *Pipeline and Gas Journal*, Vol. 201, No. 10, pp. 46-58.

Heat Transfer Characteristics of the Single-Phase, Elbow Thermosyphon

G. S. H. Lock

D. Ladoon

Department of Mechanical Engineering,
University of Alberta,
Edmonton, Alberta, Canada T6G 2G8

This paper describes the results of single-phase experiments on a right-angled, or elbow, thermosyphon with the cooled section upright and the heated section horizontal. For diameter-based Rayleigh numbers less than $10^{7.6}$, the data indicate the existence of two flow regimes: fully mixed and impeded. A flow model is used to suggest how the cooled section and heated section flow patterns are coupled together. This model satisfactorily explains the effect of geometry on heat transfer, as revealed in the usual plots of Nusselt number versus Rayleigh number. Thermal performance was found to be comparable to that of the linear thermosyphon.

Introduction

For many years, the tubular thermosyphon has provided a simple and inexpensive means for the transmission of heat from a high-temperature source to a low-temperature sink (Lock, 1992). In an industrial context, the purpose varies enormously: from the supply of heat in a baker's oven (Reay, 1982) to the removal of heat from a gas turbine blade (Majcen and Šarunac, 1984); and more recently it has been used to transfer heat as a key element in heat exchangers (Larkin, 1983).

Thermosyphons have also found extensive use in the development of northern regions. Frequently, the applications of these devices are aimed at the stabilization of soil beneath building foundations and in the vicinity of the supports of other engineering structures (Cheng and Zarling, 1990). In addition to these, there are many other more specialized applications; for example, in the control of spring runoff (Lock, 1986) or the control of ice on bridge decks (Wilson, 1973). Most commonly, the device has been installed in linear form, but as experience grows so does the designer's ingenuity. Consequently, nonlinear configurations may be expected to appear more frequently.

The right-angled, or elbow, thermosyphon is a device that has already seen service in a northern engineering context (Zarling and Haynes, 1987). As with the linear configuration, it may be used in either of two basic modes: single phase and two-phase. Thus far, applications have been restricted to the latter mode, and have not been accompanied by any theoretical analysis aimed at prediction or understanding of the *modus operandi*. To our knowledge, no experimental work on the single-phase elbow thermosyphon has reached the open literature. There is evidently a need to establish the physics of the device and, from the flow model thus developed, to inform the discussion of past and future performance data. It is also important to establish useful heat transfer correlations.

To this end, work at the University of Alberta has been concentrated into fundamental studies of the elbow thermosyphon in its most conservative form, namely, the single-phase mode operating under low Rayleigh number conditions. The work has been divided into two complementary parts: numerical analysis of flow and heat transfer in a short, elbow thermosyphon; and experimental analysis of the thermal performance of tubes with a variable geometry. In both instances

the fluid considered has been water; conditions have ranged from the lower conduction limit up to fully mixed turbulence. In this paper, emphasis will be placed on the experimental data obtained using the small-diameter rig described below. Specifically, these data will be used to display the heat transfer rate measured for various geometrical configurations. The curves presented will also be discussed from a fundamental point of view, using a suggested flow model, and from the standpoint of an empirical correlation developed for design purposes.

Experimental Considerations

The Rig. A schematic of the experimental rig is given in Fig. 1, from which it is evident that the orientation chosen corresponds to a horizontal, heated section joined at 90 deg to the bottom of a vertical, cooled section. Symmetry dictates that this orientation will possess exactly the same heat transfer characteristics as that in which the heated section is vertical and located beneath a horizontal, cooled section. This becomes evident when it is recognized that the flow pattern in the horizontal section would then be inverted but is otherwise unchanged; the same holds true for the vertical section and for the region joining the two sections. The whole pattern is thus inverted, a fact that does not alter the heat transfer rate. The arrangement studied is thus suited to the exploration of behavior under conditions that apply to a variety of practical circumstances, e.g., for heat exchangers, the maintenance of permafrost, anti-icing of bridge decks, etc.

As indicated in Fig. 1, the rig consisted of two tubes, both of which were made of copper; each had an inner diameter of 1.98 mm and a wall thickness of 2 mm. The horizontal section was heated electrically using resistive tape wound over a wrapping of electrically insulating fibreglass tape; this was put in place after thermocouples had first been installed, as described later. The section was divided into four equal lengths of 20 cm, each of which was equipped with its own electrical winding. With these independent windings connected in parallel, the heat supply rate could be varied over the total tube length, thus permitting control over the tube wall temperature, nominally set at a constant value. Electrical power was supplied from the building main via Variac transformers, and was measured in the usual way using an ammeter and voltmeter. Thermal insulation was wrapped over the heaters, as indicated in Fig. 1.

The vertical section, also 80 cm in overall length, was cooled with a water jacket divided into four equal lengths. The independent flow rates in these four lengths again enabled control to be exercised over the tube wall temperature. Neither the

Contributed by the Heat Transfer Division for publication in the JOURNAL OF HEAT TRANSFER. Manuscript received by the Heat Transfer Division May 1991; revision received June 1992. Keywords: Geophysical Heat Transfer, Heat Pipes and Thermosyphons, Natural Convection. Associate Technical Editor: J. H. Kim.

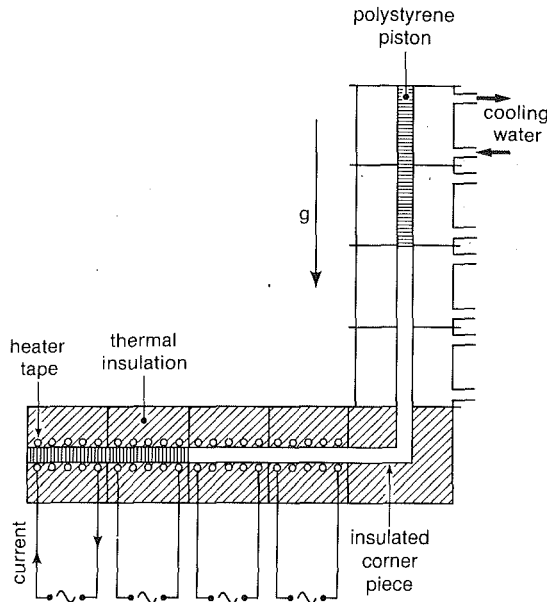


Fig. 1 Schematic of elbow thermosyphon apparatus

cooled section nor the heated section exhibited precisely isothermal wall conditions; the nonuniformity, axially and circumferentially, was small enough to be ignored for the purposes of generating empirical performance data, as evidenced by an error analysis. These observations are similar to those made elsewhere (Lock and Simpson, 1987). Between the heated and cooled sections was a junction piece consisting of a right-angled blend. In contrast to the main tubes, this section was neither heated nor cooled; instead it was wrapped in a thick layer of thermal insulation to approximate an adiabatic boundary condition.

Instrumentation and Calibration. Temperatures were measured using copper-constantan thermocouples connected via a set of switching boxes to a digital thermometer. Thermocouples were located every 2 cm in four rows along 20 cm long heated and cooled sections; these rows were positioned equidistant from each other around the tube circumference. The thermocouple junctions were laid in shallow axial grooves, 1 mm deep and about 0.5 cm long, cut into the outer wall of the copper tube. The wires were then laid out axially for several centimeters so that end conduction errors would be minimized. The 40 thermocouples thus installed in each section were bundled together before being led out to the switching box through a specially sealed boss on each cooling jacket, or between insulation layers on the heated sections. A thermocouple was also used to measure the ambient air temperature.

Before the tests proper were begun, the heated section was calibrated to determine the heat leakage under test conditions. This was done with the corner piece in place and the entire heated section filled with a styrofoam cylinder. A plot of power supply versus the difference in temperature between the tube wall and the room air was then constructed. Not surprisingly, the plot was linear. It was subsequently used to subtract the heat leakage from the gross power supplied, thereby providing

Table 1 Test schedule

Test Series	L_H (cm)	L_C (cm)
1	20	20
2	40	40
3	60	60
4	80	80
5	40	20
6	40	40
7	40	60
8	40	80

$$D = 1.98 \text{ cm}$$

$$3.1 < Pr < 7.1$$

$$-0.35 < \log_{10} Nu < 0.66$$

$$6.0 < \log_{10} Ra < 7.6$$

the rate of heat transfer into the fluid within the thermosyphon. Under the steady-state conditions of the tests, this net heat transfer rate must be equal to that leaving the cooled section. Therefore, no attempt was made to measure the heat lost in the cooled section.

Test Procedure and Schedule. Tube geometry was altered using a variety of polystyrene pistons, which, when inserted through the tube ends distance from the junction, simply shut down the length of tube over which they extended; the remaining length, which was fully operational, could thus be varied between 20 cm and 80 cm, thereby permitting a wide range of values for the heated length-diameter ratio (L_H/D) and the heated-cooled length ratio (L_H/L_C). For any given geometry, a performance curve was obtained in the form Nu versus Ra, where

$$Nu = \frac{\dot{Q}}{\pi k L_H (T_H - T_C)}$$

and

$$Ra = \frac{\beta g (T_H - T_C) D^3}{\nu \kappa}$$

both based on tube diameter D and overall temperature difference ($T_H - T_C$). These are commonly used definitions and thus facilitate comparison with other work; the Nusselt number is based on the heated surface area, which is usually of greater interest. The range of nondimensional variables covered is shown in Table 1.

Each test was conducted as follows: With the heated and cooled lengths chosen and the corresponding polystyrene piston in place, the tube was filled with water. The water supplying the cooling jackets was then turned on, followed by the electrical power supplying the heated lengths. After about one hour, the thermocouples were monitored and adjustments made to both the cooling water and the electrical power supply so that a better approximation to isothermal wall conditions could be obtained. This procedure was repeated later with the result that, after an initial period of six to eight hours had elapsed,

Nomenclature

D = tube diameter
 k = thermal conductivity
 L = tube length
 m, n = exponents
 Nu = Nusselt number

\dot{Q} = heat flux
 Ra = Rayleigh number
 T = temperature
 β = thermal expansion coefficient
 δ = boundary layer thickness

κ = thermal diffusivity
 ν = momentum diffusivity

Subscripts

C = cooled
 H = heated

the system had reached a steady state. Subsequently, the elapsed time for steady state was found to be 3–4 hours.

Readings of at least 10 thermocouples were used to determine the average wall temperatures in each of the heated and cooled sections. The heat leakage was then calculated using the ambient temperature and subtracted from the measured supply rate. Following common procedure, fluid properties were evaluated at the mean temperature $(T_H + T_C)/2$ and used to calculate the principal nondimensional groups: Pr, Nu, and Ra.

A formal error analysis of the data was also undertaken using the definitions of Nu and Ra given above. Assuming external errors to be small, as later confirmed, the mean square errors in these variables were calculated from the uncertainties in the measured quantities. The uncertainty bars thus determined (and illustrated in Figs. 3 and 4) were consistent with the scatter observed.

Discussion of Results

Hydrodynamic and Thermal Characteristics. It is not immediately obvious how the thermal performance of the elbow thermosyphon will compare with that of the linear thermosyphon; nor is it clear how the flow should be modeled. In the vertical cooled section, it is reasonable to suppose that the flow pattern will resemble that found in the vertical thermosyphon; that is, an annulus of cooled, descending fluid will surround a relatively warm core of ascending fluid (Bayley and Lock, 1965). Likewise, it is to be expected that the horizontal linear thermosyphon would provide a flow model of the heated section considered in this paper: a simple, bifilamental reflux flow (Lock and Han, 1989). These individual flow patterns are very different from each other and must somehow be reconciled in the junction region.

The behavior of the tilted, linear thermosyphon provides some useful background information. When such a tube is vertical, an annular reflux flow prevails; with the tube horizontal, the pattern of the reflux primary flow is bifilamental. For tilt angles between these limits, it has been found that the deep flow near the closed tube ends retains an annular structure while the midtube flow, extending both sides of the junction region, possesses the bifilamental form (Lock and Kirchner, 1992). Under these conditions, each midtube filament becomes, or has come from, one of the two parts of the annular structure; the core in the deep flow is thus formed from the filament moving toward it, while secondary motion in the annulus converts it to a filament moving away from the closed end.

This behavior suggests that reconciliation of the horizontal, bifilamental flow and the vertical, annular flow in the elbow thermosyphon may be effected in a similar way; that is, the hot tongue of fluid moving along the upper surface of the heated section will become the ascending core in the cooled section, while fluid in the descending annulus will regroup near the corner to form the cold return flow moving over the lower surface of the heated section. This combined flow is shown schematically in Fig. 2. The results of a recent numerical study on an elbow thermosyphon under laminar conditions confirms this flow model (Lock and Park, 1991). Under turbulent conditions, similar arguments apply, although the corner region may eventually become a “reservoir” of fully mixed fluid supplying both sections.

The thermal behavior of this system should reflect some of the characteristics of vertical and horizontal thermosyphons or, more generally, of the tilted thermosyphon. The plots of Nusselt number provided by Figs. 3, 4, and 5 confirm this expectation, but require some explanation. For low Rayleigh numbers, e.g., $Ra < 10^{6.5}$, the curves in Figs. 3 and 4 are seen to steepen, a feature usually associated with laminar, impeded flow. Under these conditions, boundary layers cannot exist because their thickness is comparable with the tube radius.

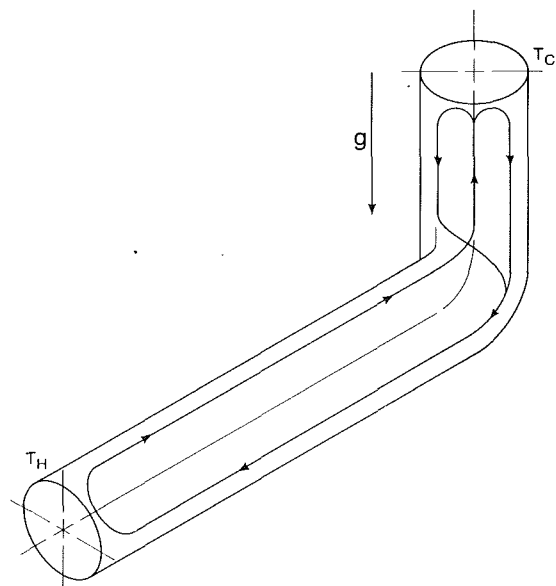


Fig. 2 Flow model of the elbow thermosyphon

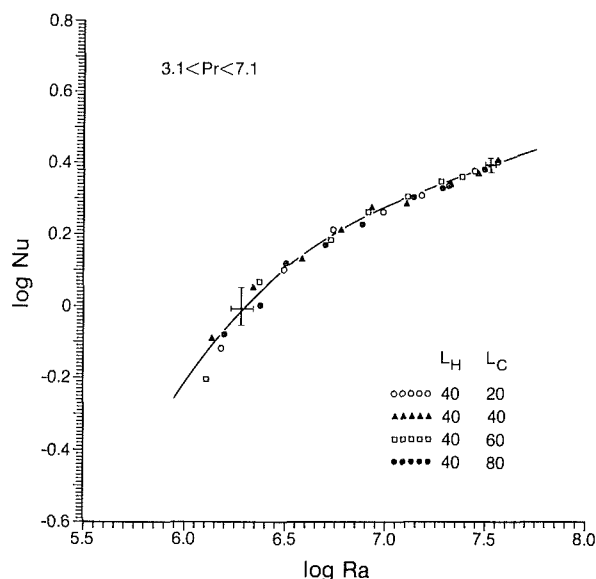


Fig. 3 Effect of heated-cooled length ratio on heat transfer

Theoretically, the slope of the $Nu \sim Ra$ curve is then 1.0, very close to the suggested asymptotes indicated. However, the data are not accurate enough or extensive enough to confirm this trend quantitatively and therefore it is only possible to state that the results are consistent with the expectation that entry to the laminar, impeded regime would occur if the Rayleigh numbers were lowered further.

For higher Rayleigh numbers, the data are much more accurate, as indicated by the error bars, but conditions within the thermosyphon are by no means obvious. At first glance, it appears that laminar, impeded flow has given way to laminar, boundary layer flow. A scaling analysis for laminar boundary layer conditions indicates that the boundary layer thickness δ is given by

$$\frac{\delta}{D} = 0 \left[\frac{(L_H/D)}{Ra} \right]^{1/4} \quad (1)$$

for a vertical tube and

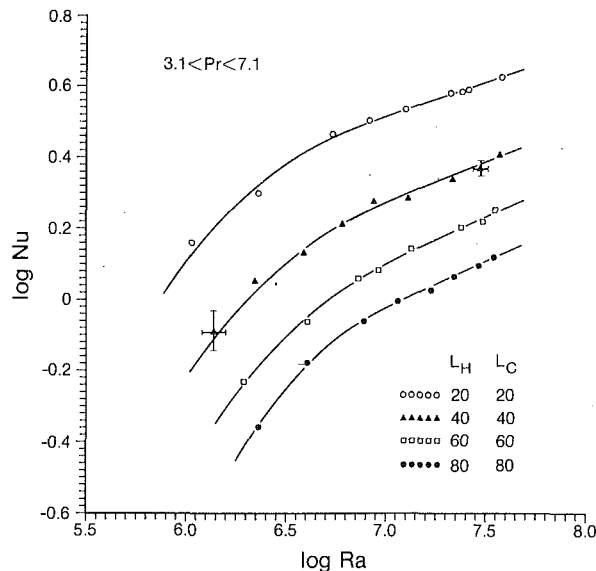


Fig. 4 Effect of heated length-diameter ratio on heat transfer

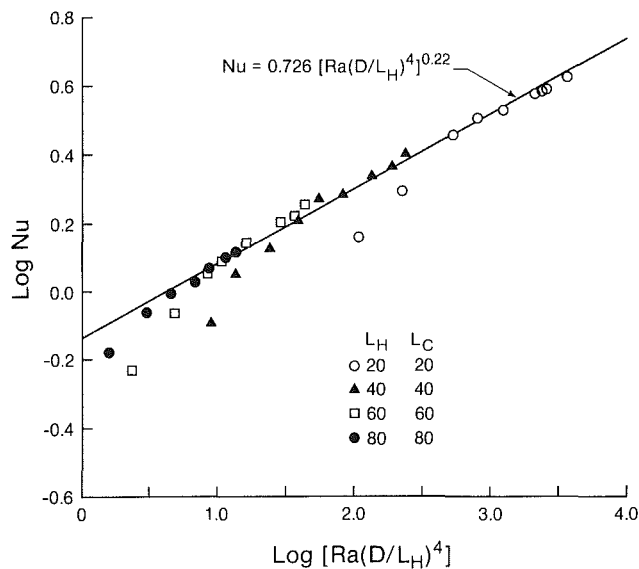


Fig. 5 Empirical correlation

$$\frac{\delta}{D} = 0 \left[\frac{(L_H/D)^2}{Ra} \right]^{1/5}$$

for a horizontal tube. Together, these equations suggest that for $Ra > 10^7$, a laminar boundary layer would occupy only a small fraction of the tube width. But the existence of laminar flow is in doubt. It was noted by Martin (1955), for example, that the transition to turbulence in a water-filled, open thermosyphon took place at the upper limit of the laminar, impeded regime. The higher Rayleigh number data obtained here are therefore more likely to represent turbulent conditions: specifically, fully mixed turbulence, about which more will be said later.

For a Rayleigh number of 10^7 , the Nusselt number indicated in Fig. 4 is seen to be about 3.2 when $L_H/D = 10:1$. This may be compared to values obtained with a linear, water-filled, closed thermosyphon having the same length-diameter ratio and heated-cooled length ratio. Lock and Kirchner (1992) found that at this Rayleigh number the Nusselt number was 2.5 for a vertical tube and 5.0 for one tilted at 45 deg. This

suggests that at least for Rayleigh numbers above the laminar impeded limit, the performance of an elbow thermosyphon is comparable to that of a tilted linear thermosyphon under otherwise identical conditions.

Finally, it should be mentioned that no attempt has been made here to investigate the effect of Prandtl number. The principal reason for this stems from the general observation that Prandtl number has little effect on thermosyphon heat transfer efficiency in the established regimes unless it is much smaller than unity, e.g., in liquid metals. However, it is worth noting that the Prandtl number may influence the transition from laminar to turbulent flow, and may perhaps alter the range of the regimes discussed above.

The Effect of Geometry. Having identified two regimes, the study was next directed to the effect of geometry on the heat transfer rate. This enquiry divides naturally into two major parts: the effect of heated-cooled length ratio, and the effect of the length-diameter ratio; the corner geometry, as a minor variable, was held fixed. The first of these is described by the data of Fig. 3. With the heated length fixed at 40 cm ($L_H/D = 20:1$), the cooled length was varied from 20 cm to 80 cm. It is immediately evident that all of the data lie within the uncertainty bands and hence it must be concluded that the heated-cooled length ratio had no effect.

To explain this, it is useful to turn to the flow model suggested earlier. This contains a coupling mechanism, which is strongly influenced by Rayleigh number but is essentially unchanged by geometry. Under laminar (impeded) conditions, the advective nature of the coupling will be retained regardless of geometry. Thus the effect of varying the cooled length is to simply change the dimensions of the "reservoir" that supplies cold fluid to the mouth of the heated section; it evidently does not significantly affect the temperature or velocity of this cold entry fluid.

The transition to turbulence in an elbow thermosyphon has not been studied but it is likely to be triggered by the tongue of hot fluid leaving the heated section. Since this ultimately enters the ascending core it is capable of creating a fully mixed flow in which a laminar boundary layer no longer exists. Such mixing creates a "reservoir" of isothermal fluid from which the heated and cooled sections are both supplied. Under these conditions, variations in the cooled length evidently produce no effect on the temperature of this "reservoir." While the data shown in Fig. 3 were obtained with the heated length fixed, it is suggested that a similar set of data, based on the cooled section, would be obtained by varying the heated length.

By way of contrast, the effect of the length-diameter ratio was found to be very substantial, as may be judged from Fig. 4 in which the heated-cooled length ratio was fixed at $L_H/L_C = 1.0$. The explanation of the trend relies on the flow model and, in particular, on the earlier suggestion that the coupling mechanism remains unchanged by geometry. In this situation, each section behaves more or less like an open thermosyphon for which the mouth conditions remain unaltered. Any deterioration in performance may then be attributed to the increasing length of the tube. It is therefore not surprising to find from Fig. 4 that the Nusselt number is an inverse function of the length-diameter ratio. More significant, perhaps, is the strength of the effect in both regimes. The knee in the curve, which roughly marks the division between laminar-impeded flow and fully mixed turbulent flow, does not appear to be significantly affected by geometry in the range covered; only a slight shift to higher Rayleigh numbers is noticeable as the length-diameter ratio is increased. This is consistent with the damping effect to be expected in longer tubes.

Empirical Correlation. These findings lead quite naturally to the possibility that the effect of tube geometry may be represented completely by the length-diameter ratio incorporated directly into the Rayleigh number; that is,

$$\text{Nu} = A \left[\left(\frac{D}{L_H} \right)^n \text{Ra} \right]^m \quad (3)$$

in which $m = 1.0$ in the laminar impeded regime but $0.20 < m < 0.33$ for higher Rayleigh numbers. Given the mean slope $m = 0.22$ of the upper data in Fig. 4 it was found that $n = 4.0$. In view of the fact that $n = 1$ or 2 for a linear thermosyphon under laminar conditions, depending upon whether it is vertical or horizontal, this empirical finding was unexpected. All of the data obtained have been replotted according to Eq. (3) in Fig. 5, from which it is evident that the correlation is acceptable in the fully mixed regime but less so in the impeded regime where the trend is obscured by a greater error.

Two observations may be made on the correlation attempt in Fig. 5. Firstly, it is clear that the variable $\text{Ra} (D/L)^4$ works well but is at variance with laminar flow characteristics. This adds weight to the earlier suggestion that the flow was turbulent. To substantiate the suggestion further another finding may be noted. Lock and Simpson (1987) discovered that their turbulent data for methanol in a linear, closed thermosyphon incorporated the effect of length-diameter ratio through the same variable, $\text{Ra}(D/L)^4$. Lock and Simpson also found that this variable did not correlate their data in the impeded regime, and this leads naturally to the second observation on Fig. 5. At the lower end of the Rayleigh number range studied it is clear that the data points falls well below the correlation, and do so in a systematic way. Despite the larger error in these data, they appear to require a different correlating variable, possibly $\text{Ra} (D/L)$ if turbulence is absent.

Without the impeded data point, the correlation shown in Fig. 5 follows Eq. (3) with $A = 0.726$, $n = 4.0$, and $m = 0.22$. The scatter is then well within the uncertainty band. This result compares favorably with the correlation of Lock and Simpson, who found that $A = 1.19$, $n = 4.0$, and $m = 0.29$ for a vertical tube.

Conclusions

In this paper an attempt has been made to describe the heat transfer characteristics of the elbow thermosyphon. Focusing on fundamental behavior, a systematic series of experiments has been undertaken using a small, inexpensive rig in which a cooled vertical section, positioned upright, was connected to a horizontal, heated section. The laboratory data thus obtained have been used to reveal the effects of the principal parameters on heat transfer performance; specifically, the role of geometry and Rayleigh number have been explored under steady conditions.

A flow model has been suggested to reconcile the very different flow patterns found in vertical and horizontal thermosyphons. Based on observations of the behavior of tilted, linear thermosyphons, this model consists of preserving the well-known characteristic of vertical and horizontal tubes through a coupling mechanism in which annular and bifilamental reflux flow patterns were mutually convertible. The model is supported by a previous numerical study of laminar flow.

The data, plotted in the form of Nu versus Ra , exhibited two regimes found in linear thermosyphons; namely, laminar impeded flow at low Rayleigh numbers and fully mixed turbulent flow at higher Rayleigh numbers. This is consistent with the proposed coupling mechanism, which effectively converts the heated and cooled sections to interdependent, open ther-

mosyphons. The coupling mechanism also helps explain why the effect of heated-cooled length ratio was found to be negligible while the effect of length-diameter ratio was not. As with linear thermosyphons, it was found that the effect of length-diameter ratio could be absorbed in a single variable consisting of the Rayleigh number multiplied by a power of the length-diameter ratio. This permitted an overall correlation of the turbulent data to be made in the form

$$\text{Nu} = f \left[\text{Ra} \left(\frac{D}{L} \right)^n \right]$$

where $n \approx 4.0$. The correlation may not be extrapolated to lower Rayleigh numbers where the flow enters the laminar, impeded regime. On the other hand, it may be confidently extrapolated to higher Rayleigh numbers more appropriate to current applications.

In general terms, the heat transfer performance of the elbow thermosyphon was found to be comparable to that of the linear thermosyphon, at least in this Rayleigh number range. This is an important finding because it frees the thermosyphon designer from the constraint of linearity and thus widens the range of application of the device.

Acknowledgments

This work was undertaken with a grant from the Natural Sciences and Engineering Research Council of Canada to whom we are indebted. We would also like to thank the technicians and machinists of the Department of Mechanical Engineering, Messrs. A. Muir, T. Nord, and B. Cielin in particular. Mr. Litong Zhao assisted with the empirical correlation.

References

- Bayley, F. J., and Lock, G. S. H., 1965, "Heat Transfer Characteristics of the Closed Thermosyphon," *ASME JOURNAL OF HEAT TRANSFER*, Vol. 87, pp. 30-40.
- Cheng, K. C., and Zarling, J. P., 1990, "Applications of Heat Pipes and Thermosyphons in Cold Regions," *Proc. 7th Int. Heat Pipe Conf.*, Minsk.
- Larkin, B. S., 1983, "A Thermosyphon Heat Exchanger for Use in Animal Shelters," Paper #74,210, Canadian Society of Agricultural Engineers.
- Lock, G. S. H., 1986, "The BIVA Project," *Proc. I.A.H.R. Symp. on Ice*, Iowa, Vol. II, pp. 269-280.
- Lock, G. S. H., and Simpson, G. A., 1987, "Performance of a Closed Tube Thermosyphon With Large Length-Diameter Ratios," *Proc. 6th Int. Offshore Mech. and Arctic Eng. Symp.*, Vol. IV, pp. 69-77.
- Lock, G. S. H., and Han, J.-C., 1989, "Buoyant Laminar Flow of Air in a Long, Square-Section Cavity Aligned With the Ambient Temperature Gradient," *J. Fluid Mech.*, Vol. 207, pp. 489-504.
- Lock, G. S. H., and Park, S., 1991, "A Numerical Study of the Right-Angled-Thermosyphon," *Proc. 10th Int. Offshore Mech. and Arctic Eng. Symp.*, Vol. IV, pp. 113-117.
- Lock, G. S. H., 1992, *The Tubular Thermosyphon*, Oxford University Press, United Kingdom.
- Lock, G. S. H., and Kirchner, J. D., 1992, "Some Characteristics of the Inclined, Closed Tube Thermosyphon Under Low Rayleigh Number Conditions," *Int. J. Heat Mass Transf.*, Vol. 35(1), pp. 165-173.
- Majcen, M., and Šarunac, N., 1984, "Heat Pipe Cooled Twin Aerofoil Blade as an Element for Higher Efficiency of Long Life Gas Turbines," in: *Heat and Mass Transfer in Rotating Machinery*, D. E. Metzger and N. H. Afgan, eds., Hemisphere Publishing Co., pp. 689-700.
- Martin, B. W., 1955, "Free Convection in an Open Thermosyphon With Special Reference to Turbulent Flow," *Proc. Roy. Soc.*, Vol. A230, pp. 502-530.
- Reay, D. A., 1982, "The Perkins-Tube—A Noteworthy Contribution to Heat Exchanger Technology," *Heat Recovery Systems*, Vol. 2, pp. 173-187.
- Wilson, C. H., 1973, "A Demonstration Project for De-Icing of Bridge Decks," *Bridge Engineering*, Vol. 1, pp. 189-197.
- Zarling, J. P., and Haynes, F. D., 1987, "Heat Transfer Characteristics of a Commercial Thermosyphon With an Inclined Evaporator Section," *Proc. 6th Int. Offshore Mech. and Arctic Eng. Symp.*, Vol. IV, pp. 79-84.

H. K. Park

X. Xu

C. P. Grigoropoulos

Department of Mechanical Engineering,
University of California,
Berkeley, CA 94720

N. Do¹

L. Klees²

P. T. Leung³

A. C. Tam

IBM Research Division,
Almaden Research Center,
San Jose, CA 95120-6099

Transient Optical Transmission Measurement in Excimer-Laser Irradiation of Amorphous Silicon Films

The transient temperature field development during heating of an amorphous silicon (a-Si) film, deposited on a fused quartz substrate, by pulsed excimer laser irradiation is studied. Static reflectivity and transmissivity measurements are used to obtain the thin film optical properties at elevated temperatures. Experimental in-situ, transient, optical transmission data are compared with heat transfer modeling results. The variation with temperature of the material complex refractive index across the thin film thickness is taken into account. The effects of the film thickness and thermal diffusivity, as well as of the laser pulse shape, are discussed.

I Introduction

Pulsed laser irradiation is employed over a wide spectrum of materials processing applications, including surface hardening, alloying, curing, synthesis of compounds, and deposition of thin films. In semiconductor systems (Wood et al., 1984), it is used to anneal ion-implantation surface damage, recrystallize amorphous and polycrystalline films, and enhance dopant diffusion. Recent studies (Zapka et al., 1991) have shown that one of the most effective ways of removing sub-micron-sized particles from solid surfaces is by deposition of a liquid film on a substrate surface and application of a UV excimer laser pulse on the surface. One of the main issues in improving such processes is the control of the induced transient temperature field. Time-resolved optical transmission and reflection measurements have been reported for the investigation of the irradiation of c-Si silicon on sapphire structures at picosecond (Lompere et al., 1983) and nanosecond (Lowndes, 1982; Lowndes and Jellison, 1984) time scales.

The complex melting and solidification behavior observed in pulsed laser irradiated materials, including nonequilibrium effects, has been studied numerically by Wood and Geist (1986a, 1986b). Time-resolved reflectivity measurements on bulk silicon and germanium using a pulsed excimer KrF laser heating beam were combined with melting-model calculations to explain the mechanism of inhomogeneous melting nucleation (Jellison et al., 1986a). The initial formation and subsequent explosive propagation of buried molten layers in amorphous silicon irradiated by excimer lasers was studied by time-resolved visible and infrared reflectivity and transmissivity measurements (Lowndes et al., 1987). A variety of experimental tech-

niques, including time-resolved transmission, x-ray diffraction, and electrical conductivity measurements, have been used in conjunction with numerical simulations to show that the pulsed laser irradiation of semiconductors is a thermal phenomenon (Jellison et al., 1986b).

The optical transient reflectivity and transmissivity measurements are based on the variation of the material complex refractive index with temperature. The temperature variation of the normal incidence surface reflectivity for bulk samples is generally small (for crystalline silicon (c-Si) $dR/dT \sim 10^{-5} K^{-1}$). Interference effects significantly enhance the variation of the thin film reflectivity with temperature. This effect was demonstrated by Grigoropoulos et al. (1991) in their measurements of the thin polysilicon film reflectivity during continuous wave (CW) laser annealing. The thin film reflectivity is expected to be a strong function of the film thickness for semitransparent films. This work presents an optical transmission probing technique for the transient, in-situ monitoring of the temperature field in pulsed excimer laser irradiation of thin amorphous silicon (a-Si) films. A numerical conductive heat transfer model for the transient temperature field in the thin film structure and the substrate is applied. Static measurements of the thin film complex refractive index at elevated temperatures are used to obtain the transient thin film transmissivity from the temperature profile across the thin film. The predicted and experimental transmissivities are in excellent agreement, thus validating the use of this technique for non-intrusive experimental temperature measurement.

II.1 Static Measurements. Amorphous silicon films of 0.2 and 1.0 μm thickness were deposited by e-beam evaporation of crystalline silicon in vacuum onto 250- μm -thick fused quartz substrates. The substrate temperature was kept to 140°C and the deposition rate at 10 Å/s. The uniformity and accuracy of the thickness of the a-Si layer were confirmed using a Tencor Alpha-Step 200 surface profilometer. The samples were then annealed at a temperature of 380°C, in a nitrogen chamber for about 5 hours until optical measurements (reflectivity and transmissivity) were reproducible. The annealing process does

¹Present address: Physics Department, University of California, Irvine, CA 92717.

²Permanent address: Institut für Angewandte Physik, Technische Hochschule Darmstadt, Hochschulstr. 6, D-6100 Darmstadt, Germany.

³Permanent address: Department of Physics, Portland State University, Portland, OR 97207-0751.

Contributed by the Heat Transfer Division for publication in the JOURNAL OF HEAT TRANSFER. Manuscript received by the Heat Transfer Division April 1992; revision received August 1992. Keywords: Laser Processing, Materials and Manufacturing Processes, Radiation Interactions. Associate Technical Editor: R. O. Buckius.

not cause nitridation, for which much higher temperatures (above 1200°C) would be needed (Nakamura et al., 1983).

It has been reported (Siregar et al., 1979) that the optical properties of submicron-thick, a-Si films do not vary significantly with temperature at the Nd:YAG, $\lambda = 1.064 \mu\text{m}$ laser light wavelength. Recent studies (Do et al., 1992) have revealed a significant variation of the optical properties of amorphous silicon films with temperature at the $\lambda = 0.752 \mu\text{m}$ diode laser light wavelength.

The standard static reflectivity, \mathcal{R} , and transmissivity, \mathcal{T} , measurement procedure was used to determine the temperature dependence of the components of the thin film complex refractive index. An infrared diode laser beam ($\lambda = 0.752 \mu\text{m}$) was directed onto the sample at normal incidence. The sample was mounted on a heated aluminum block. The heater-thermocouple system varied the sample temperature from room temperature to about 400°C. The reflectivity and transmissivity signals are detected by photodiodes, which are connected to an oscilloscope. The components of the complex refractive index, $n(T)$, and $k(T)$, are then obtained from these measurements iteratively, by applying thin film optics, Fresnel-type relations. A thermal expansion rate of $3 \times 10^{-6} \text{C}^{-1}$ is assumed for the a-Si film. For the 0.2- μm -thick a-Si films used in this work, at the $\lambda = 0.752 \mu\text{m}$ wavelength, and in the temperature range of 293–650 K, the following linear expressions are obtained:

$$n = n(T) = 4.0 + 1.30 \times 10^{-4} (T - 293) \quad (1a)$$

$$k = k(T) = 0.055 + 2.30 \times 10^{-4} (T - 293) \quad (1b)$$

Figures 1 (a, b) compare these expressions to measured complex refractive index components of 1.0- μm -thick amorphous silicon films, and to high-temperature optical data of bulk crystalline silicon (c-Si) samples (Jellison and Burke, 1986). Figure 2 shows the computed thin film reflectivity, \mathcal{R} , transmissivity, \mathcal{T} , and absorptivity, $\mathcal{A} = 1 - \mathcal{R} - \mathcal{T}$, for the 0.2- μm -thick film, as functions of temperature, at the $\lambda = 0.752 \mu\text{m}$ wavelength. The results reproduce the steady-state measurements well. The estimated fractional uncertainty in the measurement of the components of the complex refractive index is ± 2 percent for n and ± 3 percent for k .

II.2 Transient Measurements. The layer is illuminated by a KrF ($\lambda = 0.248 \mu\text{m}$) excimer laser beam (Fig. 3). The probing diode laser beam ($\lambda = 0.752 \mu\text{m}$) is approximately normal onto the sample surface. The transmitted signal is captured by a fast photodiode and a digitizing oscilloscope. The photodiode has a rise time of 1 ns, and the oscilloscope sampling speed is 1 Gsample/s. Care is taken in the experiment to (a) minimize electrical noise interference by shielding the connecting cables to the oscilloscope and (b) collect all the transmitted light to

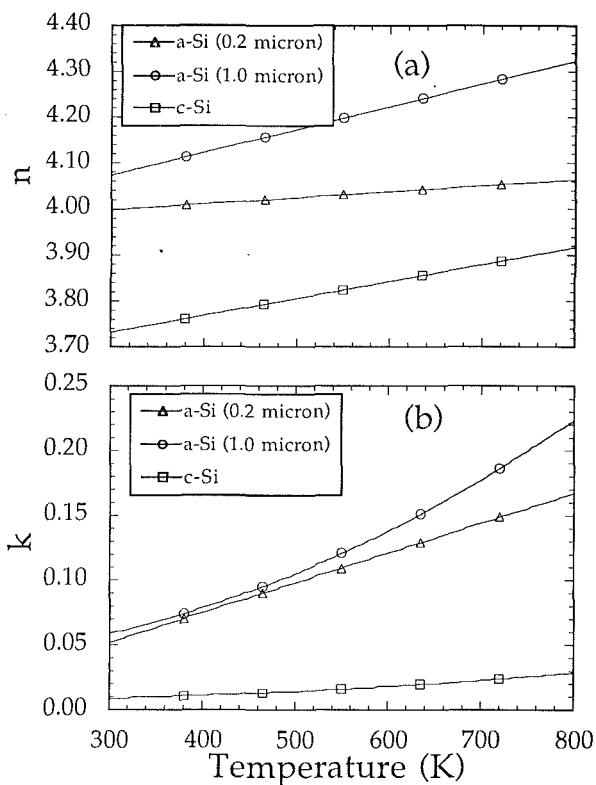


Fig. 1 Temperature dependence of the complex refractive index of 0.2 and 1.0- μm -thick amorphous silicon (a-Si) films and bulk crystalline silicon (c-Si) at $\lambda = 0.752 \mu\text{m}$: (a) real part; (b) imaginary part

the detector by using appropriate focusing lenses before the detector. The laser beam fluence, F , is determined by measuring the pulse energy using an energy meter. The estimated fractional uncertainty in the measurement of the laser pulse fluence is ± 5 percent. The laser beam spot area on the sample surface, is measured to be about 0.5cm^2 .

II.3 Heat Transfer Modeling. The temperature profile penetration in the glass substrate is of the order of $1 \mu\text{m}$. Thus, it may be assumed that the heat transfer at the center of the laser beam is essentially one dimensional. For the nanosecond time scales considered in this work, nonequilibrium and non-Fourier, thermal wave effects are negligible. For temperatures below the melting temperature, the conductive heat transfer in the solid silicon layer is given by:

$$\rho C_p \frac{\partial T}{\partial t} = \frac{\partial}{\partial x} \left(K \frac{\partial T}{\partial x} \right) + Q_{ab}(x, t) \quad (2)$$

Nomenclature

\mathcal{A} = absorptivity
 C_p = specific heat
 d = layer thickness
 d_p = absorption penetration depth
 d_{si} = semiconductor layer thickness
 d_s = substrate thickness
 E_g = optical energy gap
 F = laser beam fluence
 h = Planck's constant
 i = imaginary unit
 I = incident laser light intensity
 K = thermal conductivity
 k = extinction coefficient
 \mathcal{M} = transmission matrix

n = real part of refractive index
 \hat{n} = complex refractive index
 N = number of layers in the thin film
 Q_{ab} = power absorbed by the thin silicon layer
 \mathcal{R} = reflectivity
 r = Fresnel reflection coefficient
 t = time
 t_l = length of laser pulse
 t_p = time of occurrence of peak laser intensity
 t_r = Fresnel transmission coefficient
 T = temperature

\mathcal{T} = transmissivity
 T_∞ = ambient temperature
 x = coordinate in the direction normal to the sample surface
 α = thermal diffusivity
 γ = absorption coefficient
 λ = laser light wavelength
 ν = light frequency
 ρ = density

Subscripts

si = silicon
 s = substrate

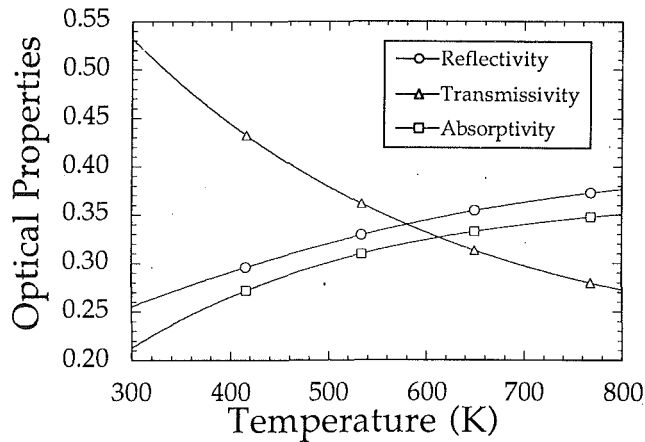


Fig. 2 Temperature dependence of the reflectivity, transmissivity, and absorptivity for the 0.2- μm -thick amorphous silicon film, at a wavelength $\lambda = 0.752 \mu\text{m}$

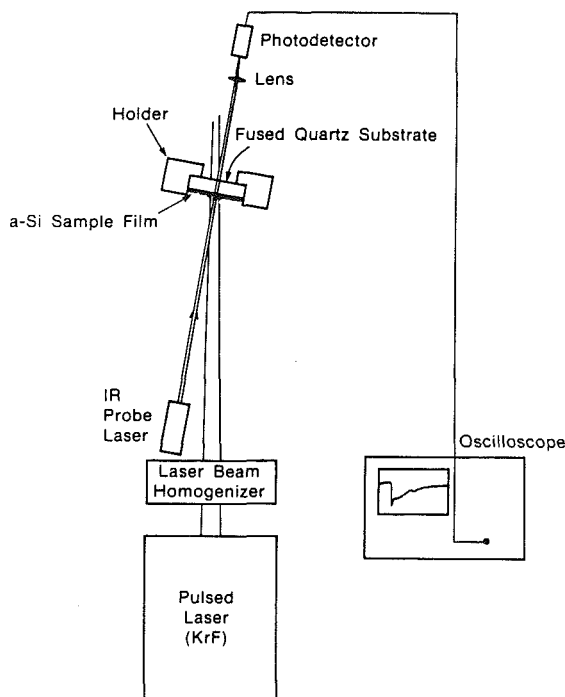


Fig. 3 Schematic of the experimental apparatus

In the above equation, x is the coordinate normal to the sample surface ($x = 0$), ρ is the density, T is the temperature, C_p is the specific heat for constant pressure, K is the thermal conductivity. The variation of the material thermal properties (Ong et al., 1986) is considered. The amorphous silicon complex refractive index at the KrF excimer laser light wavelength ($\lambda = 0.248 \mu\text{m}$) is taken as $\hat{n} = n - ik = 1.69 - i 2.76$ (Palik, 1985). These optical constants yield an absorption coefficient, $\gamma = 1.40 \times 10^6 \text{ cm}^{-1}$. The corresponding absorption penetration depth in the thin film, $d_p = 1/\gamma$, is of the order of seven nanometers, thus prohibiting any radiation absorption in the quartz substrate. The radiation photon energy for the KrF excimer laser light, $h\nu$, is much larger than the semiconductor optical energy gap, E_g , and the absorption coefficient, γ , is so high, that the temperature dependence of the material optical properties at $\lambda = 248 \text{ nm}$ is expected to be small (Wood and Jellison, 1984). The optical property data for crystalline silicon (c-Si), at elevated temperatures (Jellison and Modine, 1982) show little dependence of the optical properties on tem-

perature in the UV range, but to the authors' knowledge, no detailed data for a-Si exist. It is thus reasonable to assume that no interference and internal refraction-reflection effects modify the local energy absorption in the thin film. Such effects have been shown to be important in pulsed ruby ($\lambda = 0.694 \mu\text{m}$), and frequency doubled Nd:YAG ($\lambda = 0.532 \mu\text{m}$) laser irradiation of silicon layers (Grigoropoulos et al., 1992), and also in absorption detection of defects in hydrogenated, amorphous silicon, (a-Si:H) films (Asano and Stutzmann, 1991). The laser energy is transferred to the lattice in times of the order of 10^{-12} - 10^{-11} s, for both nanosecond and picosecond laser pulses. It is not expected that carrier diffusion and recombination effects play a significant role in nanosecond laser processing of semiconductor materials (Wood and Jellison, 1984). The energy absorption $Q_{ab}(x, t)$, follows an exponential decay in the material:

$$Q_{ab}(x, t) = (1 - \mathcal{R})I(t)\gamma e^{-\gamma x} \quad (3)$$

In the substrate there is no energy absorption, and Eq. (2) is valid, with $Q_{ab} = 0$. Measurements of the laser pulse temporal profile, $I(t)$, have shown that the pulse fluence, F , is distributed in a triangular shape, with the pulse length, $t_l = 26 \text{ ns}$, and the peak intensity occurring at $t_p = 6 \text{ ns}$.

$$I(t) = \frac{2Ft}{t_l t_p} \quad 0 < t < t_p$$

$$I(t) = \frac{2F(t_l - t)}{t_l(t_l - t_p)} \quad t_p < t < t_l \quad (4)$$

$$I(t) = 0 \quad t_l < t$$

Convection and radiation losses are negligible, due to the high incident laser intensities (of the order of 10^{11} W/m^2) and the short time scales considered in this problem. The temperature penetration in the structure is small, so that the bottom substrate surface remains at the ambient temperature, T_∞ .

$$\left. \frac{\partial T}{\partial x} \right|_{x=0} = 0 \quad (5a)$$

$$T(x = d_{si} + d_s, t) = T_\infty \quad (5b)$$

Initially the structure is isothermal, at the ambient temperature:

$$T(x, 0) = T_\infty \quad (6)$$

Continuity of both temperature and heat flux is applied at the film/substrate interface.

The heat conduction was solved numerically by an implicit finite difference algorithm. A depth of $x = 5 \mu\text{m}$ is sufficient to contain the temperature field penetration. The temperature field in the semiconductor film induces changes in the a-Si film complex refractive index at the $\lambda = 0.752 \mu\text{m}$ wavelength. These changes were accounted for in the picosecond irradiation of thin c-Si films (Lompre et al., 1983) by assuming an average temperature for the fitting of the measured optical properties. In this study, the semiconductor film is treated as a stratified multilayer structure (Jacobsson, 1965; Born and Wolf, 1980; Knittl, 1976) composed of N layers of varying complex refractive index. Wave optics effects are also considered in the substrate, which is represented by the $m = N + 1$ layer, and is transparent at the probing laser light wavelength, $\lambda = 0.752 \mu\text{m}$. Utilizing the formalism of the characteristic transmission matrix, the lumped structure reflectivity and transmissivity can be obtained. The m th layer of thickness d_m , which may be absorbing, having a complex refractive index $\hat{n}_m = n_m - ik_m$, is represented by the 2×2 matrix \mathfrak{M}_m , whose elements are complex:

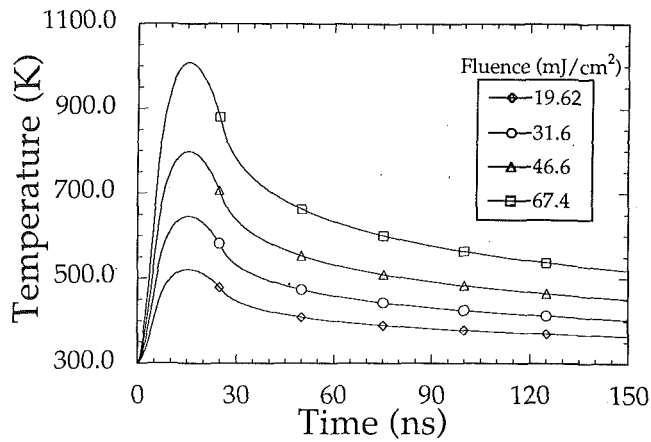


Fig. 4 Surface temperature histories for a 0.2- μm -thick amorphous silicon layer, irradiated with a KrF excimer laser ($\lambda = 0.248 \mu\text{m}$) for laser fluences $F = 19.62, 31.6, 46.6 \text{ mJ/cm}^2, 67.4 \text{ mJ/cm}^2$; the laser pulse length $t_l = 26 \text{ ns}$

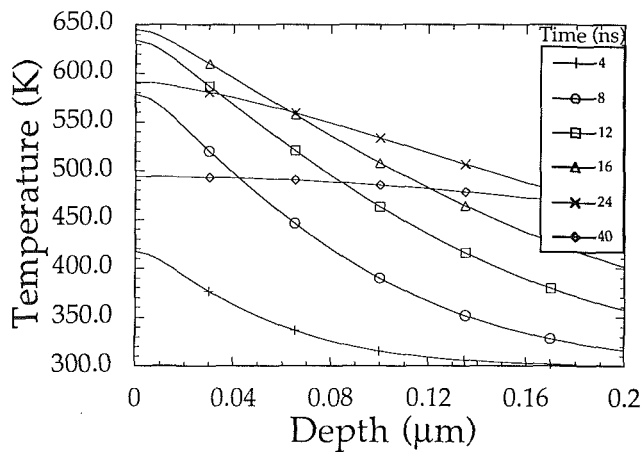


Fig. 5 Computed temperature profiles in a 0.2- μm -thick amorphous silicon layer, irradiated with a KrF excimer laser; the laser fluence $F = 31.6 \text{ mJ/cm}^2$ and the pulse length $t_l = 26 \text{ ns}$

$$\mathfrak{M}_m = \begin{pmatrix} \cos\left(\frac{2\pi}{\lambda} \hat{n}_m d_m\right) & \frac{i}{\hat{n}_m} \sin\left(\frac{2\pi}{\lambda} \hat{n}_m d_m\right) \\ i \hat{n}_m \sin\left(\frac{2\pi}{\lambda} \hat{n}_m d_m\right) & \cos\left(\frac{2\pi}{\lambda} \hat{n}_m d_m\right) \end{pmatrix} \quad (7)$$

The multilayer transmission matrix, \mathfrak{M} , is:

$$\mathfrak{M} = \prod_{m=1}^{N+1} \mathfrak{M}_m \quad (8)$$

The reflection and transmission Fresnel coefficients, r and t_r , are:

$$r = \frac{(\mathfrak{M}(1, 1) + \mathfrak{M}(1, 2)) - (\mathfrak{M}(2, 1) + \mathfrak{M}(2, 2))}{(\mathfrak{M}(1, 1) + \mathfrak{M}(1, 2)) + (\mathfrak{M}(2, 1) + \mathfrak{M}(2, 2))} \quad (9a)$$

$$t_r = \frac{2}{(\mathfrak{M}(1, 1) + \mathfrak{M}(1, 2)) + (\mathfrak{M}(2, 1) + \mathfrak{M}(2, 2))} \quad (9b)$$

The structure reflectivity and transmissivity in terms of r and t_r follow

$$\mathfrak{R} = |r|^2 \quad (10a)$$

$$\mathfrak{T} = |t_r|^2 \quad (10b)$$

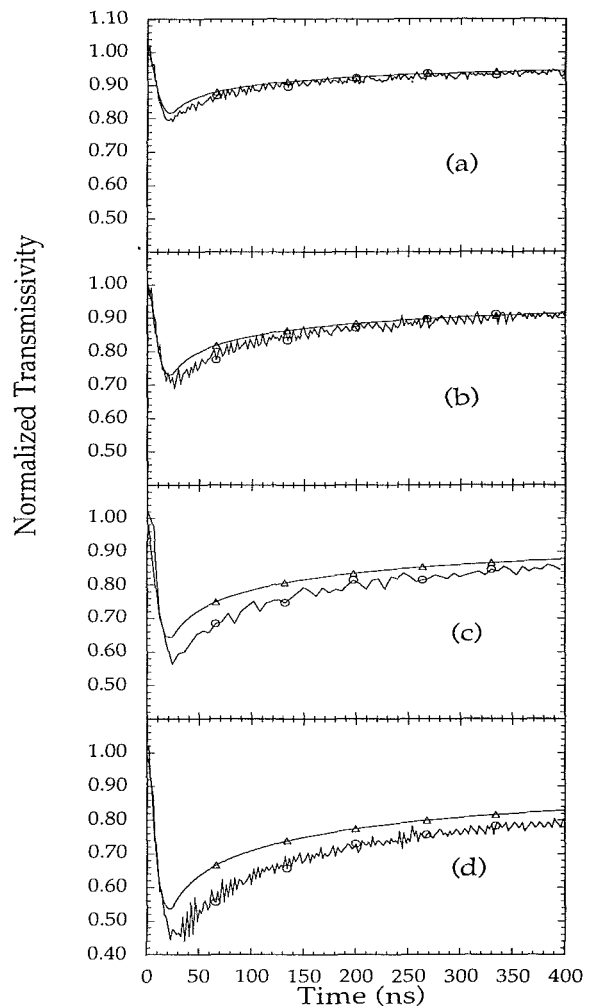


Fig. 6 Comparison between the numerical predictions (smooth solid line) and the experimental transient transmissivity measurement (noisy signal) for a 0.2- μm -thick amorphous silicon layer, irradiated with a KrF excimer laser ($\lambda = 0.248 \mu\text{m}$); results are shown as laser beam fluences, F : (a) 19.62 mJ/cm^2 ; (b) 31.6 mJ/cm^2 ; (c) 46.6 mJ/cm^2 ; (d) 67.4 mJ/cm^2 ; the pulse length, $t_l = 26 \text{ ns}$

III Results

The amorphous silicon layer was irradiated by laser pulse fluences, $F = 19.62, 31.6, \text{ and } 46.6, \text{ and } 67.4 \text{ mJ/cm}^2$. Some results obtained during these experiments have been reported by Park et al. (1992). Figure 4 shows predicted surface temperature histories for these fluences. The peak temperature occurs approximately at a time of 15 ns. The calculated temperature profiles across the thickness of the silicon layer are shown in Fig. 5 for a laser fluence, $F = 31.6 \text{ mJ/cm}^2$. The experimental transmissivity signal was normalized by the steady-state value before heating. The predicted transmissivity was also normalized by the transmissivity at a temperature $T_\infty = 300 \text{ K}$. This normalization is consistent with the measurement of the complex refractive index of the layer from reflectivity and transmissivity data. The comparison between experiment and model for the laser beam fluences, $F = 19.62 \text{ and } 31.6 \text{ mJ/cm}^2$, is shown in Figs. 6(a) and 6(b). It can be stated that the model accurately captures the experimental trend. The calculated peak temperature for the fluence, $F = 31.6 \text{ mJ/cm}^2$, is approximately 650 K (Fig. 4). It is recalled that the thin film optical properties have been measured up to this temperature range. At higher fluences, the agreement is not as close (Figs. 6c, d), though both the time occurrence of the peak temperature and the cooling trend are predicted quite well.

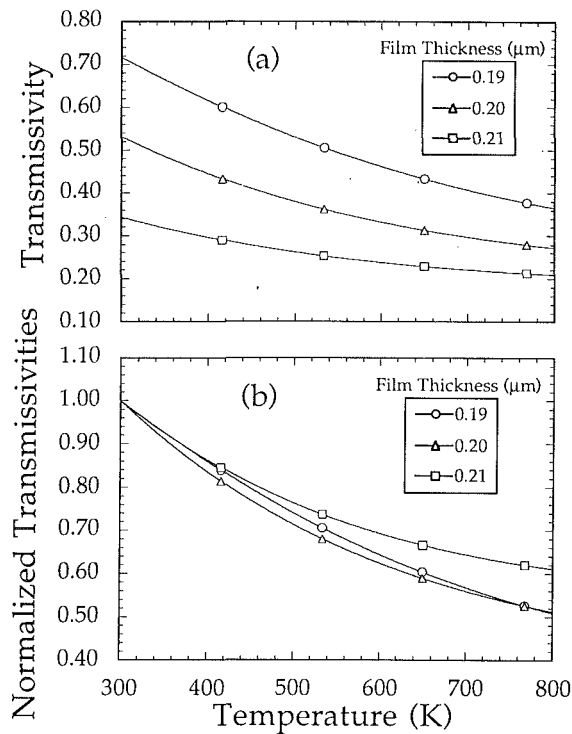


Fig. 7 Thickness dependence of the thin film transmissivity: (a) absolute values; (b) normalized values

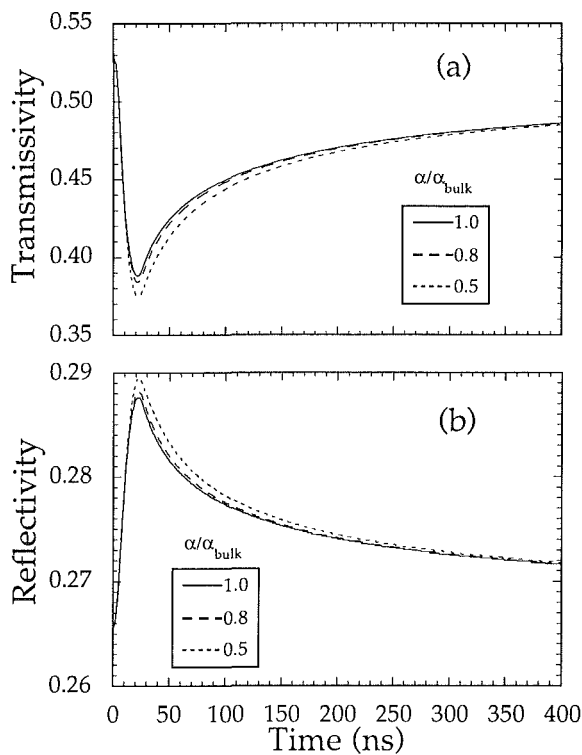


Fig. 8 Effect of variations of the thin film thermal diffusivity on the predicted: (a) reflectivity; (b) transmissivity; the excimer laser beam ($\lambda = 0.248 \mu\text{m}$) fluence, $F = 31.6 \text{ mJ/cm}^2$, the pulse length, $t_l = 26 \text{ ns}$

Variations of the thin film thickness by $\pm 0.01 \mu\text{m}$, cause absolute transmissivity departures of about 40 percent from the values that correspond to the nominal $0.2 \mu\text{m}$ amorphous silicon layer thickness used in this work (Fig. 7a). The use of the normalized transmissivity measurements significantly re-

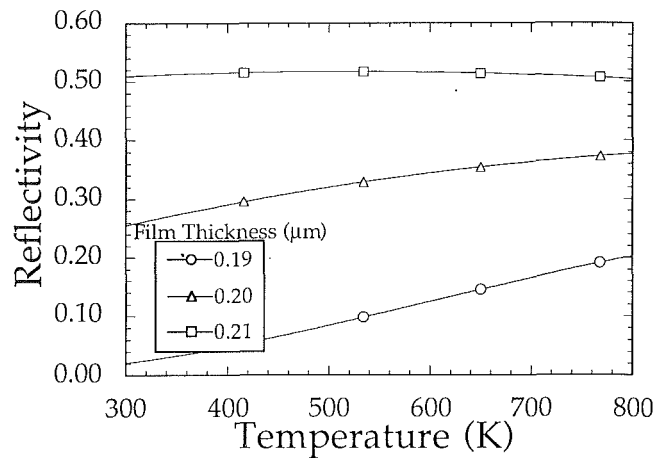


Fig. 9 Thickness dependence of the film reflectivity for the $\lambda = 0.752 \mu\text{m}$ wavelength

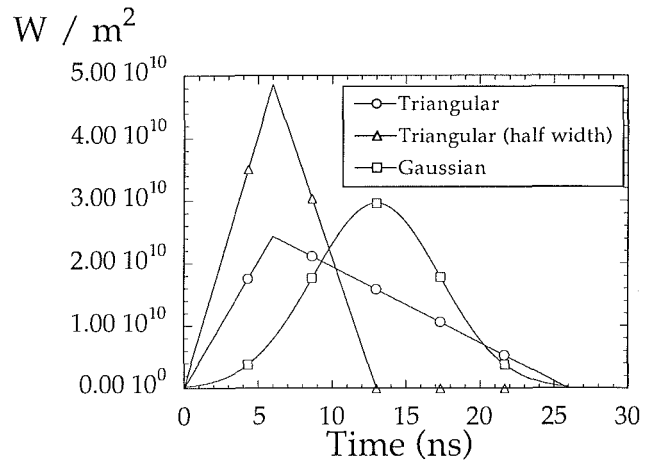


Fig. 10 Different laser pulse intensity distributions for a total fluence, $F = 31.6 \text{ mJ/cm}^2$; the laser wavelength $\lambda = 0.248 \mu\text{m}$

duces this deviation to about 10 percent at a temperature $T = 650 \text{ K}$ (Fig. 7b). The uncertainty in the normalized transmissivity measurement is estimated to be ± 0.04 . Numerical computations have shown that the magnitudes of the transient reflectivity and transmissivity are not very sensitive to reduction of the thin film thermal diffusivity by 50 percent (Figs. 8a, b). On the contrary, the thin film steady-state reflectivity measurement is quite sensitive to film thickness variations. Figure 9 shows that the reflectivity for a $0.21 \mu\text{m}$ film thickness slowly decays with temperature, whereas it increases almost linearly for the $0.20 \mu\text{m}$ and $0.19 \mu\text{m}$ film thicknesses. On the contrary, the decay of the transmissivity signal with temperature is monotonically behaved, with decreasing values for increasing thicknesses. The long-term temperature field depends mainly on the substrate thermal properties. The pulse intensity temporal profile used in these calculations (Eq. (4)) was fitted to experimentally acquired data. This profile may vary from pulse to pulse. Numerical experiments with different laser intensity temporal profiles (Fig. 10) corresponding to a laser beam fluence of 31.6 J/cm^2 were conducted to estimate the effect of the related experimental uncertainty. Whereas much shorter pulses ($t_l = 13 \text{ ns}$) raise the temperature faster, intensity distributions over the measured pulse length, $t_l = 26 \text{ ns}$, produce little change to the calculated reflectivity and transmissivity signals (Figs. 11a, b).

IV Conclusions

A method for monitoring the transient temperature field in

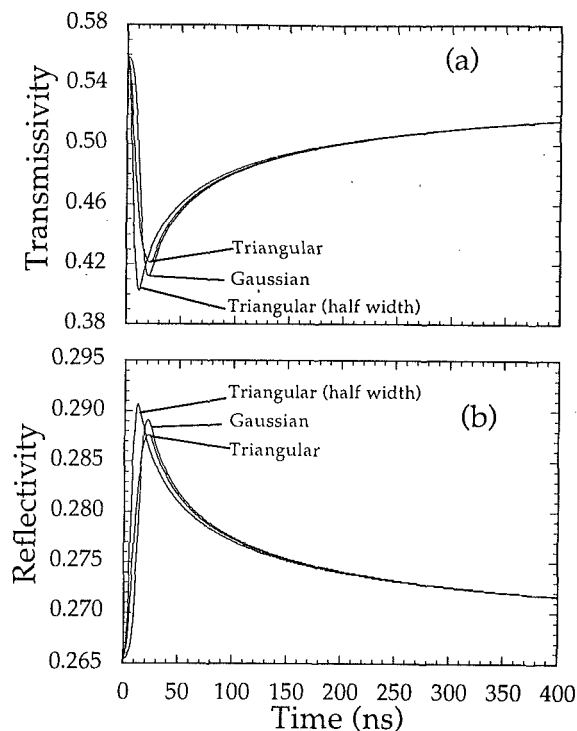


Fig. 11 Calculated probing laser ($\lambda = 0.752 \mu\text{m}$) (a) transmissivity and (b) reflectivity signals for the laser beam intensity profiles given in Fig. 10

pulsed excimer laser irradiation of thin a-Si films has been presented. An infrared ($\lambda = 0.752 \mu\text{m}$) diode laser has been used as a probe for in-situ optical transmission measurements. The temperature dependence of the components of the complex refractive index of the a-Si films has been determined at this wavelength in the temperature range from room temperature to about 400°C using static reflectivity and transmissivity measurements. The heat transfer in the excimer laser irradiated a-Si film has been calculated numerically. The transient transmissivity for the probe laser light has been calculated by assuming a variation of the a-Si material complex refractive index according to the statically measured optical property data. The predicted and experimental transmissivity signals were in excellent agreement for the excimer laser fluences that produce temperatures within the range of the static optical property measurement. The optical transmission measurements presented in this work accurately capture the transient temperature field in excimer laser irradiated amorphous silicon films.

Acknowledgments

Support of this work by the National Science Foundation, under Grant No. CTS-9096253, and in part by the Computer Mechanics Laboratory of the University of California at Berkeley, is gratefully acknowledged. The experimental work presented at this paper was conducted at the IBM Almaden Research Center.

References

- Asano, A., and Stutzmann, 1991, "Depth Profiling of Nonuniform Optical Absorption in Thin Films: Application to Hydrogenated Amorphous Silicon," *J. Appl. Phys.*, Vol. 70, No. 9, pp. 5025-5034.
- Born, M., and Wolf, E., 1980, *Principles of Optics*, 6th ed., Pergamon, Exeter, United Kingdom, pp. 51-70, pp. 611-633.
- Do, N., Klees, L., Leung, P. T., Tong, F., Leung, W. P., and Tam, A. C., 1992, "Temperature Dependence of Optical Constants for Amorphous Silicon," *Appl. Phys. Lett.*, Vol. 60, No. 18, pp. 2186-2188.
- Grigoropoulos, C. P., Dutcher, W. E., and Barclay, K. E., 1991, "Radiative Phenomena in CW Laser Annealing," *ASME JOURNAL OF HEAT TRANSFER*, Vol. 113, pp. 657-662.
- Grigoropoulos, C. P., Park, H. K., and Xu, X., 1992, "Modeling of Pulsed Laser Irradiation of Thin Silicon Films," *Int. J. Heat Mass Transfer*, in press.
- Jacobsson, R., 1965, "Light Reflection From Films of Continuously Varying Refractive Index," in: *Progress in Optics*, Vol. 5, E. Wolf, ed., North-Holland, Amsterdam, pp. 247-286.
- Jellison, G. E., Jr., and Burke, H. H., 1986, "The Temperature Dependence of the Refractive Index of Silicon at Elevated Temperatures at Several Laser Wavelengths," *J. Appl. Phys.*, Vol. 60, No. 2, pp. 841-843.
- Jellison, G. E., Jr., Lowndes, D. H., Mashburn, D. N., and Wood, R. F., 1986a, "Time-Resolved Reflectivity Measurements of Silicon and Germanium Using a Pulsed Excimer KrF Laser Heating Beam," *Phys. Rev. B*, Vol. 34, No. 4, pp. 2407-2415.
- Jellison, G. E., Jr., Lowndes, D. H., and Wood, R. F., 1986b, "Fundamental Aspects of Pulsed-Laser Irradiation of Semiconductors," *SPIE*, Vol. 710, pp. 24-34.
- Jellison, G. E., Jr., and Modine, F. A., 1983, "Optical Functions of Silicon Between 1.7 and 4.7 eV at Elevated Temperatures," *Phys. Rev. B*, Vol. 27, No. 12, pp. 7466-7472.
- Knittl, Z., 1976, *Optics of Thin Films*, Wiley, Prague, Czechoslovakia, pp. 182-282.
- Lompre, L. A., Liu, J. M., Kurz, H., and Bloembergen, N., 1983, "Time-Resolved Temperature Measurement of Picosecond Laser Irradiated Silicon," *Appl. Phys. Lett.*, Vol. 43, No. 2, pp. 168-170.
- Lowndes, D. H., 1982, "Time-Resolved Optical Transmission and Reflectivity of Pulsed-Ruby-Laser Irradiated Crystalline Silicon," *Phys. Rev. Lett.*, Vol. 48, No. 4, pp. 267-271.
- Lowndes, D. H., and Jellison, G. E., Jr., 1984, "Time Resolved Measurements During Pulsed Laser Irradiation of Silicon," in: *Semiconductors and Semimetals*, Vol. 23, R. F. Wood, C. W. White, and R. T. Young, eds., Academic, Orlando, FL, pp. 313-404.
- Lowndes, D. H., Penycook, S. J., Jellison, G. E. Jr., Withrow, S. P., and Mashburn, D. N., 1987, "Solidification of Highly Undercooled Liquid Silicon Produced by Pulsed Laser Melting of Ion-Implanted Amorphous Silicon: Time-Resolved and Microstructural Studies," *J. Mater. Res.*, Vol. 2, No. 5, pp. 648-680.
- Nakamura, H., Kaneko, M., Matsumoto, S., Fujita, S., and Sasaki, A., 1983, "Thermal Nitridation of Silicon in Nitrogen Plasma," *Appl. Phys. Lett.*, Vol. 43, No. 7, pp. 691-693.
- Ong, C. K., Tan, S. H., and Sin, E. H., 1986, "Calculations of Melting Threshold Energies of Crystalline and Amorphous Materials Due to Pulsed-Laser Irradiation," *Mater. Sci. Engng.*, Vol. 79, pp. 79-85, and references therein.
- Palik, E. D., 1985, *Handbook of Optical Constants of Solids, I*, Academic Press, New York, p. 571.
- Park, H. K., Xu, X., Grigoropoulos, C. P., Do, N., Klees, L., Leung, P. T., and Tam, A. C., 1992, "Temporal Profile of Optical Transmission Probe in Pulsed Laser Heating of Amorphous Silicon Films," *Appl. Phys. Lett.*, Vol. 61, No. 7, pp. 749-751.
- Siregar, M. R. T., Von Allmen, M., and Luthy, W., 1979, "Temperature Dependence of Optical Absorption at $\lambda = 1.06 \mu\text{m}$ in Amorphous and Crystalline Silicon," *Helv. Phys. Acta*, Vol. 52, No. 45, pp. 45-48.
- Wood, R. F., and Jellison, G. E., Jr., 1984, "Melting Model of Pulsed Laser Processing," in: *Semiconductors and Semimetals*, R. F. Wood et al., eds., Vol. 23, Academic Press, Orlando, FL, pp. 165-250.
- Wood, R. F., and Geist, G. A., 1986a, "Theoretical Analysis of Explosively Propagating Molten Layers in Pulsed-Laser-Irradiated a-Si," *Phys. Rev. Lett.*, Vol. 57, No. 7, pp. 873-876.
- Wood, R. F., and Geist, G. A., 1986b, "Modeling of Nonequilibrium Melting and Solidification in Laser-Irradiated Materials," *Phys. Rev. B*, Vol. 34, No. 4, pp. 2606-2620.
- Wood, R. F., White, C. W., and Young, R. T., eds., 1984, "Pulsed Laser Processing of Semiconductors," *Semiconductors and Semimetals*, Vol. 23, Academic Press, Orlando, FL.
- Zapka, W., Ziemlich, W., and Tam, A. C., 1991, "Efficient Pulsed Laser Removal of $0.2 \mu\text{m}$ Sized Particles From a Solid Surface," *Appl. Phys. Lett.*, Vol. 58, No. 20, pp. 2217-2219.

Discrete Ordinates Solutions of Nongray Radiative Transfer With Diffusely Reflecting Walls

J. A. Menart

Department of Mechanical Engineering,
University of Minnesota,
Minneapolis, MN 55455

HaeOk Skarda Lee

NASA Lewis Research Center,
Cleveland, OH 44135

Tae-Kuk Kim

Department of Mechanical Engineering,
Chung-Ang University,
Seoul, South Korea

Nongray gas radiation in a plane parallel slab bounded by gray, diffusely reflecting walls is studied using the discrete ordinates method. The spectral equation of transfer is averaged over a narrow wavenumber interval preserving the spectral correlation effect. The governing equations are derived by considering the history of multiple reflections between two reflecting walls. A closure approximation is applied so that only a finite number of reflections have to be explicitly included. The closure solutions express the physics of the problem to a very high degree and show relatively little error. Numerical solutions are obtained by applying a statistical narrow-band model for gas properties and a discrete ordinates code. The net radiative wall heat fluxes and the radiative source distributions are obtained for different temperature profiles. A zeroth-degree formulation, where no wall reflection is handled explicitly, is sufficient to predict the radiative transfer accurately for most cases considered, when compared with increasingly accurate solutions based on explicitly tracing a larger number of wall reflections without any closure approximation applied.

I Introduction

Accurate analyses of radiative transfer in high-temperature environments are important for deriving the design parameters for many applications such as furnaces, combustors, nuclear reactors, gas turbines, fire safety, and solar energy systems. The radiative transfer by hot molecular gases such as H₂O and CO₂ involves transfer mechanisms that are difficult to model even in simple systems. The primary difficulty in modeling the gas radiation is due to the strong wavenumber-dependent properties of the gases.

For accurate solutions, the spectral correlation between the gas radiative properties and the intensity field must be taken into account when the radiative transfer equation is averaged over a finite wavenumber interval. Information on the fine structure of the gas radiative properties must be considered. Although simple gas models like the gray gas and the gray-band approximations can give fairly accurate wall flux predictions, internal radiative source distributions cannot be predicted with the same accuracy (Kim et al., 1991a; Edwards and Matavosian, 1984).

Accurate, nongray solutions for plane parallel media bounded by black or nearly nonreflecting walls have been obtained using the discrete ordinates method and a statistical narrow-band model (Kim et al., 1991a). In the present paper, the work of Kim et al. (1991a) is extended to model accurately the radiative transfer in gas media bounded by diffusely reflecting walls that account for correlation effects between the gas properties and the wall reflected intensity. A numerical analysis is performed for gray emitting and reflecting walls, and solutions are obtained to illustrate the effect of handling reflecting walls in a correct manner.

Reflecting wall problems have been treated by Edwards (1962), Edwards and Matavosian (1984), and Nelson (1979a, 1979b, 1984, 1986) to obtain the net radiative wall fluxes for enclosures containing isothermal gases. Exact formulations for two-zone enclosures were presented by Nelson (1979a). An accurate approximate solution technique was given by Nelson (1979b, 1984, 1986), who writes the band-averaged wall radiosity expressions in the context of the zonal method. His closure approximation assumes that the band transmittances

corresponding to higher orders than that handled explicitly are set equal to the highest order band transmittance handled explicitly. Nelson shows a clear error analysis for the cases he has considered. Edwards (1962) presented approximate expressions using the band-energy approximation, adjusting the widths of wide-band absorptances for better accuracy. He also presented an exact series solution for handling a simple enclosure with specularly reflecting walls. Edwards and Matavosian (1984) presented approximate expressions using total radiation properties.

The publications listed above do not present results for the radiative source distributions and do not consider the case of nonisothermal media, although the work of Nelson (1979b, 1984, 1986) appears as though it could be extended to handle nonisothermal gases. The current formulations are more general and can be used to obtain both the wall fluxes and radiative source distributions for nonisothermal media needed for heat transfer analyses. In this work nonisothermal media are treated using the Curtis-Godson method (Godson, 1953; Young, 1977). No results are presented for inhomogeneous media, but inhomogeneous media can be handled in the same manner as nonisothermal media.

The discrete ordinates method (Carlson and Lathrop, 1968) is applied to this spectrally dependent gas radiation problem (Kim, 1990). The spectral average of the equation of transfer is considered, and formulations suitable for narrow-band models are developed. The statistical narrow-band model (Goody, 1964; Ludwig et al., 1973) with an exponential-tailed-inverse line-strength distribution (Malkmus, 1967) is used in this work. The required narrow-band parameters, based on line-by-line calculations, are from Hartmann et al. (1984) and Soufiani et al. (1985).

A simple one-dimensional slab of pure H₂O is considered to study the effect of reflecting walls. Three different types of temperature profiles are prescribed for a one-dimensional slab: a boundary-layer type, a parabolic type, and a uniform profile. The total gas pressure is always kept at one atmosphere, and the concentration of the gas species is assumed uniform. The slab thickness is varied from 0.1 to 1.0 m.

II Spectrally Averaged Equation of Transfer

The spectral equation of transfer is averaged over a small wavenumber interval $\Delta\nu$, where $\Delta\nu$ is the interval used for a

Contributed by the Heat Transfer Division and presented at the National Heat Transfer Conference, Minneapolis, Minnesota, July 28-31, 1991. Manuscript received by the Heat Transfer Division November 20, 1991; revision received June 8, 1992. Keywords: Radiation. Associate Technical Editor: R. O. Buckius.

narrow-band model. Even in a narrow wavenumber interval a radiating gas may have hundreds of major absorption lines. The intensity field resulting from emission and absorption by the gas medium also has a similar number of peaks. These spectral dependencies cause strong spectral correlations between the radiating gas properties and intensity (Edwards, 1962). When the correlations between the transmittance and intensity are neglected, the solution generally gives results quite different from the correlated solution (Zhang et al., 1988).

The wavenumber-averaged equation of transfer for an absorbing-emitting medium is written as

$$\frac{\overline{\partial I_\nu(s, \Omega)}}{\partial s} + a_\nu(s) \overline{I_\nu(s, \Omega)} = a_\nu(s) \overline{I_{b\nu}(s)} \quad (1)$$

The overbar symbol indicates that the quantity is averaged over a finite wavenumber interval $\Delta\nu$. The terms under the same overbar must be averaged as a unit for an accurate non-gray solution. Since the blackbody intensity is a smooth function of the wavenumber, a constant value can be assumed for a small $\Delta\nu$.

Evaluating $\overline{a_\nu(s)I_\nu(s, \Omega)}$ by following the narrow-band formulation presented by Kim et al. (1991a) results in the equation of transfer written as

$$\frac{\partial \overline{I_\nu(s, \Omega)}}{\partial s} = \frac{\partial \overline{\tau_\nu(s^* \rightarrow s)}}{\partial s^*} \Big|_{s^*=s} \overline{I_{b\nu}(s)} + \overline{C_\nu(s, \Omega)} \quad (2)$$

where $\overline{\tau_\nu(s^* \rightarrow s)}$ is defined as the spectrally averaged transmittance from the location s^* to s :

$$\overline{\tau_\nu(s^* \rightarrow s)} \equiv \exp \left\{ - \int_{s^*}^s a_\nu(s^{**}) ds^{**} \right\} \quad (3a)$$

The derivatives of the averaged transmittance are used to define $\overline{a_\nu(s)}$ and combinations of the absorption coefficient and transmittance as

$$\frac{\partial \overline{\tau_\nu(s^* \rightarrow s)}}{\partial s^*} \Big|_{s^*=s} = \overline{a_\nu(s)} \quad (3b)$$

and

$$\frac{\partial \overline{\tau_\nu(s^* \rightarrow s)}}{\partial s} = a_\nu(s^*) \overline{\tau_\nu(s^* \rightarrow s)} \quad (3c)$$

The spectral absorption term $\overline{C_\nu(s, \Omega)}$ is defined in a general form as

$$\overline{C_\nu(s, \Omega)} = \frac{\partial}{\partial s} \left\{ \overline{I_{w\nu}(s_w, \Omega) \tau_\nu(s_w \rightarrow s)} \right\} + \int_{s_w}^s \overline{I_{b\nu}(s^*)} \frac{\partial}{\partial s} \left\{ \frac{\partial \overline{\tau_\nu(s^* \rightarrow s)}}{\partial s^*} \right\} ds^* \quad (4)$$

and represents the absorbed intensity in the wavenumber interval $\Delta\nu$ by the gas element ds . Equations (2) and (4) together are similar to Eq. (6) of Kim et al. (1991a) for nonreflecting walls, except that $\overline{I_{w\nu}(s_w, \Omega) \tau_\nu(s_w \rightarrow s)}$ is now kept as a unit so that reflecting walls may be treated in a correlated manner. In these equations s_w is a point at a wall, and s is a point within the absorbing-emitting medium.

III Preparation for Solution of Spectrally Averaged Equations

In order to solve Eqs. (2) and (4) properly for reflecting walls, the term $\overline{I_{w\nu}(s_w, \Omega) \tau_\nu(s_w \rightarrow s)}$ is expanded into an infinite series, which physically represents the tracking of the radiant energy through all of its reflections. This is required because the spectrally integrated band-transmittance is history dependent. The spectral transmittance is not history dependent, but it is not practical to do line-by-line calculations in solving engineering radiative transfer problems. Note also that the gray-band transmittance is not history dependent. Since it is not possible to account for an infinite number of terms, only a finite number of terms or reflections are treated explicitly and the rest are handled in an approximate manner, i.e., a closure approximation is made.

In this section of the paper the spectral absorption term in Eq. (4) is written out in a nonspectrally averaged form to different degrees of expansion. On such a spectral basis all the equations presented in this section are exact and equivalent to each other. They differ only to the extent to which the reflected radiation is tracked in an explicit manner.

Formulations for $C_\nu^\pm(s, \Omega)$ in $\mu > 0$ directions are presented below using series representations of the boundary intensity $I_{0\nu}^\pm(s_0, \Omega)$. Expressions used for the calculation of the negatively directed boundary intensity $I_{L\nu}^-(s_L, \Omega)$ for $\mu < 0$ directions are

Nomenclature

a_ν = spectral absorption coefficient, cm^{-1}
 C_ν = spectral absorption term, $\text{kW}/(\text{m}^3 \cdot \text{sr} \cdot \text{cm}^{-1})$
 $-dq/dx$ = total radiative source term, kW/m^3
 I_ν = spectral radiative intensity, $\text{kW}/(\text{m}^2 \cdot \text{sr} \cdot \text{cm}^{-1})$
 \overline{k}_ν = mean line-intensity to spacing ratio, $\text{cm}^{-1} \text{atm}^{-1}$
 L = thickness of the slab, m
 M = number of grid points in x direction
 \hat{n} = inward normal vector to enclosure walls
 N = order of the discrete ordinate approximation, or the total number of ordinate directions
 q_i = total net radiative heat flux in x direction, kW/m^2
 s = position variable along a path, cm

$s^* \rightarrow s$ = path length from s^* to s , cm
 u = pressure-path length parameter, $\text{atm} \cdot \text{cm}$
 x = x coordinate, cm
 Δx = thickness of a control volume, cm
 w_n = angular weight for the n th ordinate direction
 $\overline{\beta}_\nu$ = mean line-width to spacing ratio
 ϵ = wall emissivity
 θ = polar angle
 μ = direction cosine in x direction ($= \cos \theta$)
 $\Delta\nu$ = wavenumber interval, cm^{-1}
 ρ = wall reflectivity
 $\tau_\nu(s^* \rightarrow s)$ = spectral transmittance between points s^* and s
 Ω = ordinate direction
 $d\Omega$ = differential solid angle

Superscripts

*or** = integration variable or position superscript
 $(\overline{\quad})$ = spectral average
 $'$ or $''$ or $'''$ = indicator of μ directions (see Fig. 1)
 $+$ = in the positive x direction
 $-$ = in the negative x direction

Subscripts

0 or 1 = wall at $x=0$ (wall 1)
 b = blackbody
 i = spatial index in x direction ($i=1, M$)
 k = dummy spatial index
 L or 2 = wall at $x=L$ (wall 2)
 n = angular index for discrete ordinate directions ($n=1, N$)
 w = wall
 ν = spectral

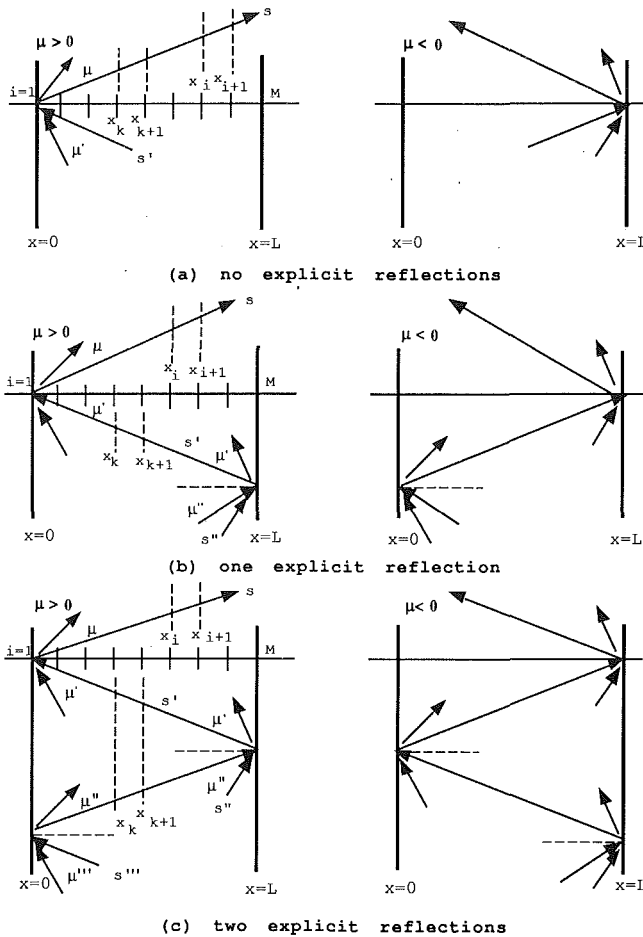


Fig. 1 Schematic diagrams of multiple reflections in the slab

similar and are thus not presented here. Only where it is necessary in the formulation of the positive directed intensities ($\mu > 0$) will the negative directed intensities ($\mu < 0$) be mentioned.

Figure 1 is a schematic diagram used to trace the reflection history of the boundary intensity for the absorption term. For $I_{0\nu}^+(s_0, \Omega)$, the no explicit reflection formulation (Fig. 1a) considers the $\mu > 0$ direction explicitly, while including the remaining reflections from the $\mu' < 0$ and all other directions implicitly. The one explicit reflection formulation (Fig. 1b) considers the $\mu > 0$ and $\mu' < 0$ directions explicitly, while the reflections from the $\mu'' > 0$ and all other directions are included implicitly. The two explicit reflections formulation (Fig. 1c) considers the $\mu > 0$, $\mu' < 0$, and $\mu'' > 0$ directions

explicitly for $I_{0\nu}^+(s_0, \Omega)$, and the reflections from the $\mu''' < 0$ and all other directions are included implicitly. The left side of Fig. 1 gives the directions for the positive directed intensity,

$$I_{0\nu}^+(s_0, \Omega) = \epsilon_{0\nu} I_{b0\nu}(s_0) + \frac{1 - \epsilon_{0\nu}}{\pi} \int_{\hat{n}_0 \cdot \Omega' < 0} |\hat{n}_0 \cdot \Omega'| \left[\begin{aligned} & I_{L\nu}^-(s'_L, \Omega') \tau_\nu(s'_L \rightarrow s'_0) \\ & + \int_{s'_L}^{s'_0} a_\nu(s'^*) I_{b\nu}(s'^*) \tau_\nu(s'^* \rightarrow s'_0) ds'^* \end{aligned} \right] d\Omega'. \quad (8)$$

and the right side gives the directions for the negative directed intensity.

In the following equations the number of primes on Ω and s indicates the corresponding μ direction. The ranges of the direction cosines for the positive directed intensity, $I_{0\nu}^+(s_0, \Omega)$, are $0 < \mu < 1$, $-1 < \mu' < 0$, $0 < \mu'' < 1$, and $-1 < \mu''' < 0$, and for the negative directed wall intensity, $I_{L\nu}^-(s_L, \Omega)$, they are $-1 < \mu < 0$, $0 < \mu' < 1$, $-1 < \mu'' < 0$, and $0 < \mu''' < 1$. In the expressions below, the wall emissivities are assumed to be slow varying functions of wavenumber. The actual, angularly dependent total paths are used to compute the transmittances.

(a) No Explicit Reflection Formulation. If no wall reflection for the spectral absorption term is handled in an explicit manner, then the equation for the absorption term on a spectral basis is Eq. (4) with the overbar symbols removed and subscripts adjusted for the wall at $x = 0$,

$$C_\nu^+(s, \Omega) = \frac{\partial}{\partial s} \{ I_{0\nu}^+(s_0, \Omega) \tau_\nu(s_0 \rightarrow s) \} + \int_{s_0}^s I_{b\nu}(s^*) \frac{\partial}{\partial s} \left\{ \frac{\partial \tau_\nu(s^* \rightarrow s)}{\partial s^*} \right\} ds^*. \quad (5)$$

This equation includes all wall reflections implicitly, as can be seen by considering the wall intensity expression for wall 1 ($x=0$) of the slab (see Fig. 1a, $\mu > 0$);

$$I_{0\nu}^+(s_0, \Omega) = \epsilon_{0\nu} I_{b0\nu}(s_0) + \frac{1 - \epsilon_{0\nu}}{\pi} \int_{\hat{n}_0 \cdot \Omega < 0} |\hat{n}_0 \cdot \Omega| I_{L\nu}^-(s_0, \Omega) d\Omega \quad (6)$$

where $I_{L\nu}^-(s_0, \Omega)$ is the negative directed intensity impinging on wall 1 and $I_{b0\nu}(s_0)$ is the blackbody emission by wall 1. The subscripts 0 indicate that the variables are related to the wall at $x = 0$, e.g., \hat{n}_0 is the enclosure inward normal vector from wall 1, and $|\hat{n}_0 \cdot \Omega|$ is the corresponding vector dot product. The reflected component of Eq. (6), the second term on the right-hand side, results from radiant intensity that has undergone multiple reflections with the boundary walls.

This reflected intensity is strongly dependent upon the wavenumber, since it also depends on the intensity from the gas medium. For reflecting walls in general, the spectral dependency of the wall reflected intensity is strong and shows a similar complexity in its spectral distribution as the gas transmittance. Thus on a spectral basis this equation is correct, but errors may be introduced unless care is taken when averaging this equation over a finite wavenumber interval.

(b) One Explicit Reflection Formulation. The one explicit reflection expression for $C_\nu^+(s, \Omega)$ is written as

$$C_\nu^+(s, \Omega) = \epsilon_{0\nu} I_{b0\nu}(s_0) \frac{\partial}{\partial s} \{ \tau_\nu(s_0 \rightarrow s) \} + \int_{s_0}^s I_{b\nu}(s^*) \frac{\partial}{\partial s} \left\{ \frac{\partial \tau_\nu(s^* \rightarrow s)}{\partial s^*} \right\} ds^* + \frac{1 - \epsilon_{0\nu}}{\pi} \int_{\hat{n}_0 \cdot \Omega' < 0} |\hat{n}_0 \cdot \Omega'| \left[\begin{aligned} & \frac{\partial}{\partial s} \{ I_{L\nu}^-(s'_L, \Omega') \tau_\nu(s'_L \rightarrow s'_0) \tau_\nu(s_0 \rightarrow s) \} \\ & + \int_{s'_L}^{s'_0} I_{b\nu}(s'^*) \frac{\partial}{\partial s} \frac{\partial}{\partial s'^*} \{ \tau_\nu(s'^* \rightarrow s'_0) \tau_\nu(s_0 \rightarrow s) \} ds'^* \end{aligned} \right] d\Omega'. \quad (7)$$

The wall intensity expression for $I_{0\nu}^+(s_0, \Omega)$ with one explicit reflection (see Fig. 1b, $\mu > 0$) was substituted into Eq. (5) to write the above equation;

The following expression, derived from the definitions given in Eqs. (3a)–(3c) written on a spectral basis, has also been used in obtaining Eq. (7);

$$\frac{\partial}{\partial s} \frac{\partial}{\partial s'^*} \{ \tau_\nu(s'^* \rightarrow s'_0) \tau_\nu(s_0 \rightarrow s) \} = \frac{\partial}{\partial s} \{ a_\nu(s'^*) \tau_\nu(s'^* \rightarrow s'_0) \tau_\nu(s_0 \rightarrow s) \}. \quad (9)$$

(c) Two Explicit Reflections Formulation. The two explicit reflections expression for $C_\nu^+(s, \Omega)$ is written as

$$C_\nu^+(s, \Omega) = \epsilon_{0\nu} I_{b0\nu}(s_0) \frac{\partial}{\partial s} \{ \tau_\nu(s_0 \rightarrow s) \} + \int_{s_0}^s I_{b\nu}(s^*) \frac{\partial}{\partial s} \left\{ \frac{\partial \tau_\nu(s^* \rightarrow s)}{\partial s^*} \right\} ds^* + \frac{1 - \epsilon_{0\nu}}{\pi} \int_{\hat{n}_0 \cdot \Omega' < 0} |\hat{n}_0 \cdot \Omega'| \left[\epsilon_{L\nu} I_{bL\nu}(s'_L) \frac{\partial}{\partial s} \{ \tau_\nu(s'_L \rightarrow s'_0) \tau_\nu(s_0 \rightarrow s) \} + \int_{s'_L}^{s'_0} \left[I_{b\nu}(s'^*) \frac{\partial}{\partial s} \frac{\partial}{\partial s'^*} \{ \tau_\nu(s'^* \rightarrow s'_0) \tau_\nu(s_0 \rightarrow s) \} \right] ds'^* \right] d\Omega' + \frac{1 - \epsilon_{0\nu}}{\pi} \frac{1 - \epsilon_{L\nu}}{\pi} \int_{\hat{n}_0 \cdot \Omega' < 0} |\hat{n}_0 \cdot \Omega'| \int_{\hat{n}_L \cdot \Omega'' < 0} |\hat{n}_L \cdot \Omega''| \left[\frac{\partial}{\partial s} \{ I_{0\nu}^+(s_0'', \Omega'') \tau_\nu(s_0'' \rightarrow s'_L) \tau_\nu(s'_L \rightarrow s'_0) \tau_\nu(s_0 \rightarrow s) \} + \int_{s_0''}^{s'_L} \left[I_{b\nu}(s''^*) \frac{\partial}{\partial s} \frac{\partial}{\partial s''^*} \{ \tau_\nu(s''^* \rightarrow s'_L) \tau_\nu(s'_L \rightarrow s'_0) \tau_\nu(s_0 \rightarrow s) \} \right] ds''^* \right] d\Omega'' d\Omega'. \quad (10)$$

The wall intensity expression at $x = 0$ including two explicit reflections (see Fig. 1c, $\mu > 0$),

$$I_{0\nu}^+(s_0, \Omega) = \epsilon_{0\nu} I_{b0\nu}(s_0) + \frac{1 - \epsilon_{0\nu}}{\pi} \int_{\hat{n}_0 \cdot \Omega' < 0} |\hat{n}_0 \cdot \Omega'| \left[\epsilon_{L\nu} I_{bL\nu}(s'_L) \tau_\nu(s'_L \rightarrow s'_0) + \int_{s'_L}^{s'_0} a_\nu(s'^*) I_{b\nu}(s'^*) \tau_\nu(s'^* \rightarrow s'_0) ds'^* \right] d\Omega' + \frac{1 - \epsilon_{0\nu}}{\pi} \frac{1 - \epsilon_{L\nu}}{\pi} \int_{\hat{n}_0 \cdot \Omega' < 0} |\hat{n}_0 \cdot \Omega'| \int_{\hat{n}_L \cdot \Omega'' < 0} |\hat{n}_L \cdot \Omega''| \left[I_{0\nu}^+(s_0'', \Omega'') \tau_\nu(s_0'' \rightarrow s'_L) \tau_\nu(s'_L \rightarrow s'_0) + \int_{s_0''}^{s'_L} a_\nu(s''^*) I_{b\nu}(s''^*) \tau_\nu(s''^* \rightarrow s'_L) \tau_\nu(s'_L \rightarrow s'_0) ds''^* \right] d\Omega'' d\Omega', \quad (11)$$

was substituted into Eq. (5) to obtain the above equation. The following expression, in addition to Eq. (9), has been used in obtaining Eq. (10);

$$\frac{\partial}{\partial s} \frac{\partial}{\partial s''^*} \{ \tau_\nu(s''^* \rightarrow s'_L) \tau_\nu(s'_L \rightarrow s'_0) \tau_\nu(s_0 \rightarrow s) \} = \frac{\partial}{\partial s} \{ a_\nu(s''^*) \tau_\nu(s''^* \rightarrow s'_L) \tau_\nu(s'_L \rightarrow s'_0) \tau_\nu(s_0 \rightarrow s) \}. \quad (12)$$

IV Closure Approximation

The spectral absorption expressions of Eqs. (5), (7), and (10) are all exact and equivalent to each other. Equations (7) and (10) are simply expanded forms of Eq. (5). When these equations are averaged over a $\Delta\nu$ interval, the wall or gas emission terms, like $I_{b0\nu}^+(s_0, \Omega)$, $I_{bL\nu}^-(s'_L, \Omega)$ and $I_{b\nu}(s^*)$, can be averaged separately over a narrow band with the introduction of negligibly small error. This is because Planck's blackbody function is a relatively slow varying function of wavenumber. The wall intensities, however, have strong spectral dependencies, and errors are introduced in separately averaging the terms involving wall intensities, which include reflected components like $I_{0\nu}^+(s_0'', \Omega'')$ and $I_{L\nu}^-(s'_L, \Omega')$.

A closure approximation is described below that assumes that a "gray", or separately averaged wall intensity value can be utilized in calculating the spectral absorption term. This allows for an approximate averaging of the remaining reflections in Eqs. (5), (7), and (10) over a small wavenumber interval. An additional approximation is necessary to complete the analyses, because the separately averaged wall intensities appearing in these equations are unknown.

The closure approximation suggested here is slightly different from those suggested by other researchers. This should not be surprising because there are many ways in which a closure

approximation can be devised. The main drawback of the current closure approximation is that a general error analysis

is not very meaningful, since the errors are dependent on the particular spectral characteristics of the wall intensity in a given wavenumber interval. The spectral characteristics of a particular problem will be influenced by such factors as the composition of the gases in the medium and the pressures and temperatures of the problem. The reason for using the closure method given below is the ease in incorporating it into an existing discrete ordinates code (Kim, 1991a). To show the type of error introduced by this closure approximation, the closure results will be compared with the no-closure approximation solutions, which show a more systematic decay toward the exact solutions.

(a) Zeroth-Degree Closure. A widely applied approximation assumes that the intensity incident onto the wall, $I_\nu^-(s_0, \Omega)$ in Eq. (6), is independent of wavenumber over a narrow band. This assumption, along with the fact that the wall emitted intensity is accurately approximated by a constant value in a narrow wavenumber interval, leads to the approximation $\bar{I}_{0\nu}^+(s_0, \Omega) \tau_\nu(s_0 \rightarrow s) \cong \bar{I}_{0\nu}^+(s_0, \Omega) \bar{\tau}_\nu(s_0 \rightarrow s)$. The spectral absorption term (Eq. (5)) with this zeroth-degree closure for the wall reflection (no correlation for the wall reflected intensity) is then written as:

$$\bar{C}_v^+(s, \Omega) = \bar{I}_{0v}^+(s_0, \Omega) \frac{\partial}{\partial s} \{ \bar{\tau}_v(s_0 \rightarrow s) \} + \int_{s_0}^s \bar{I}_{bv}(s^*) \frac{\partial}{\partial s} \left\{ \frac{\partial \bar{\tau}_v(s^* \rightarrow s)}{\partial s^*} \right\} ds^* \quad (13)$$

No further approximation is necessary for this order of closure approximation, since the wall intensity shown above is the wall intensity given by the solution of the equation of transfer (Eq. (2)) and the associated boundary conditions:

$$\bar{I}_{0v}^+(s_0, \Omega) = \bar{\epsilon}_{0v} \bar{I}_{b0v}(s_0) + \frac{1 - \bar{\epsilon}_{0v}}{\pi} \int_{\hat{n}_0 \cdot \Omega < 0} |\hat{n}_0 \cdot \Omega| \bar{I}_v^-(s_0, \Omega) d\Omega \quad (14a)$$

and

$$\begin{aligned} \bar{C}_v^+(s, \Omega) = & \bar{\epsilon}_{0v} \bar{I}_{b0v}(s_0) \frac{\partial}{\partial s} \{ \bar{\tau}_v(s_0 \rightarrow s) \} + \int_{s_0}^s \bar{I}_{bv}(s^*) \frac{\partial}{\partial s} \left\{ \frac{\partial \bar{\tau}_v(s^* \rightarrow s)}{\partial s^*} \right\} ds^* \\ & + \frac{1 - \bar{\epsilon}_{0v}}{\pi} \int_{\hat{n}_0 \cdot \Omega' < 0} |\hat{n}_0 \cdot \Omega'| \left[\bar{\epsilon}_{L\nu} \bar{I}_{bL\nu}(s'_L) \frac{\partial}{\partial s} \{ \tau_v(s'_L \rightarrow s'_0) \tau_v(s_0 \rightarrow s) \} \right. \\ & \left. + \int_{s'_L}^{s'_0} \left[\bar{I}_{bv}(s'^*) \frac{\partial}{\partial s} \frac{\partial}{\partial s'^*} \{ \tau_v(s'^* \rightarrow s'_0) \tau_v(s_0 \rightarrow s) \} \right] ds'^* \right] d\Omega' \\ & + \frac{1 - \bar{\epsilon}_{0v}}{\pi} \frac{1 - \bar{\epsilon}_{L\nu}}{\pi} \int_{\hat{n}_0 \cdot \Omega' < 0} |\hat{n}_0 \cdot \Omega'| \int_{\hat{n}_L \cdot \Omega'' < 0} |\hat{n}_L \cdot \Omega''| \cdot \\ & \cdot \left[\bar{I}_{0v}^+(s''_0, \Omega'') \frac{\partial}{\partial s} \{ \tau_v(s''_0 \rightarrow s''_L) \tau_v(s'_L \rightarrow s'_0) \tau_v(s_0 \rightarrow s) \} \right. \\ & \left. + \int_{s''_0}^{s''_L} \left[\bar{I}_{bv}(s''^*) \frac{\partial}{\partial s} \frac{\partial}{\partial s''^*} \{ \tau_v(s''^* \rightarrow s''_L) \tau_v(s'_L \rightarrow s'_0) \tau_v(s_0 \rightarrow s) \} \right] ds''^* \right] d\Omega'' d\Omega'. \quad (16a) \end{aligned}$$

$$\bar{I}_{L\nu}^-(s_L, \Omega) = \bar{\epsilon}_{L\nu} \bar{I}_{bL\nu}(s_L) + \frac{1 - \bar{\epsilon}_{L\nu}}{\pi} \int_{\hat{n}_L \cdot \Omega < 0} |\hat{n}_L \cdot \Omega| \bar{I}_v^+(s_L, \Omega) d\Omega \quad (14b)$$

Equations (2), (13), (14a), and (14b) and the associated negative intensity expression for $\bar{C}_v^-(s, \Omega)$ are solved simultaneously to obtain the intensity field. Equation (13) substituted into Eq. (2) gives the equation used by Kim et al. (1991a) for nonreflecting or weakly reflecting walls. The zeroth-degree closure leads to exact solutions for nonreflecting walls.

(b) First-Degree Closure. For a first-degree closure approximation $\bar{I}_{L\nu}^-(s'_L, \Omega')$ out of wall 2 is assumed to be independent of the wavenumber over a narrow band, i.e., the approximation $\frac{\bar{I}_{L\nu}^-(s'_L, \Omega') \tau_v(s'_L \rightarrow s'_0) \tau_v(s_0 \rightarrow s)}{\tau_v(s'_L \rightarrow s'_0) \tau_v(s_0 \rightarrow s)} \cong \bar{I}_{L\nu}^-(s'_L, \Omega') \cdot \frac{\tau_v(s'_L \rightarrow s'_0) \tau_v(s_0 \rightarrow s)}{\tau_v(s'_L \rightarrow s'_0) \tau_v(s_0 \rightarrow s)}$ is made. The resulting expression for $\bar{C}_v^+(s, \Omega)$, which comes from averaging Eq. (7) with the above approximation, is written as

$$\begin{aligned} \bar{C}_v^+(s, \Omega) = & \bar{\epsilon}_{0v} \bar{I}_{b0v}(s_0) \frac{\partial}{\partial s} \{ \bar{\tau}_v(s_0 \rightarrow s) \} + \int_{s_0}^s \bar{I}_{bv}(s^*) \frac{\partial}{\partial s} \left\{ \frac{\partial \bar{\tau}_v(s^* \rightarrow s)}{\partial s^*} \right\} ds^* \\ & + \frac{1 - \bar{\epsilon}_{0v}}{\pi} \int_{\hat{n}_0 \cdot \Omega' < 0} |\hat{n}_0 \cdot \Omega'| \left[\bar{I}_{L\nu}^-(s'_L, \Omega') \frac{\partial}{\partial s} \{ \tau_v(s'_L \rightarrow s'_0) \tau_v(s_0 \rightarrow s) \} \right. \\ & \left. + \int_{s'_L}^{s'_0} \left[\bar{I}_{bv}(s'^*) \frac{\partial}{\partial s} \frac{\partial}{\partial s'^*} \{ \tau_v(s'^* \rightarrow s'_0) \tau_v(s_0 \rightarrow s) \} \right] ds'^* \right] d\Omega'. \quad (15a) \end{aligned}$$

Since the wall intensity $\bar{I}_{L\nu}^-(s'_L, \Omega')$ is unknown, it is taken to be equivalent to

$$\bar{I}_{L\nu}^-(s'_L, \Omega') = \bar{\epsilon}_{0v} \bar{I}_{b0v}(s'_L) + \frac{1 - \bar{\epsilon}_{L\nu}}{\pi} \int_{\hat{n}_L \cdot \Omega < 0} |\hat{n}_L \cdot \Omega| \bar{I}_v^+(s_L, \Omega) d\Omega \quad (15b)$$

to complete the closure approximation. The quantity $\bar{I}_v^+(s_L, \Omega)$ comes from the solution of Eq. (2), the boundary conditions, Eqs. (14a) and (14b), Eqs. (15a) and (15b), and the associated equations to obtain the negative directed intensities. Thus, all the quantities on the right-hand side of Eq. (15a) are obtainable using an iterative solution procedure.

(c) Second-Degree Closure. For the second-degree closure, the following approximation is made:

$$\begin{aligned} \bar{I}_{0v}^+(s''_0, \Omega'') \tau_v(s''_0 \rightarrow s''_L) \tau_v(s'_L \rightarrow s'_0) \tau_v(s_0 \rightarrow s) \\ \cong \bar{I}_{0v}^+(s''_0, \Omega'') \tau_v(s''_0 \rightarrow s''_L) \tau_v(s'_L \rightarrow s'_0) \tau_v(s_0 \rightarrow s). \end{aligned}$$

That is, $\bar{I}_{0v}^+(s''_0, \Omega'')$ of Eq. (11) is taken to be independent of wavenumber over a narrow band. Using this approximation in the averaging process of Eq. (10) gives

The approximation

$$\bar{I}_{0v}^+(s''_0, \Omega'') = \bar{\epsilon}_{0v} \bar{I}_{b0v}(s''_0) + \frac{1 - \bar{\epsilon}_{0v}}{\pi} \int_{\hat{n}_0 \cdot \Omega < 0} |\hat{n}_0 \cdot \Omega| \bar{I}_v^-(s_0, \Omega) d\Omega \quad (16b)$$

is made to close off the solution, $\bar{I}_v^-(s_0, \Omega)$ is obtained from the solution of the equation of transfer. The simultaneous solution of Eqs. (2), (14a), (14b), (16a), and (16b) and the associated negative intensity expressions is required to obtain the intensity field.

Higher order spectral absorption terms can be easily written but are not presented, since the present numerical study considers only up to a second degree closure. In general the approximations made in higher order solutions are less severe than those in the lower order solutions, because the reflected

component of radiant energy becomes smaller with each succeeding reflection.

(d) The No-Closure Approximations. The errors in the closure approximation can be avoided by tracking only the emitted wall intensity through all possible reflections. There

is then no error in separately averaging the wall intensities. Thus the accuracy of the no-closure approximation is only dependent on the number of reflections explicitly included in the formulation.

The no-reflection, no-closure approximation for $\bar{C}_\nu^+(s, \Omega)$ is then written as

$$\bar{C}_\nu^+(s, \Omega) = \bar{\epsilon}_{0\nu} \bar{I}_{b0\nu}(s_0, \Omega) \frac{\partial}{\partial s} \{ \bar{\tau}_\nu(s_0 \rightarrow s) \} + \int_{s_0}^s \frac{\partial}{\partial s} \left\{ \frac{\partial \bar{\tau}_\nu(s^* \rightarrow s)}{\partial s^*} \right\} \bar{I}_{b\nu}(s^*) ds^* \quad (17)$$

The one-reflection, no-closure approximation for $\bar{C}_\nu^+(s, \Omega)$ is

$$\bar{C}_\nu^+(s, \Omega) = \bar{\epsilon}_{0\nu} \bar{I}_{b0\nu}(s_0) \frac{\partial}{\partial s} \{ \bar{\tau}_\nu(s_0 \rightarrow s) \} + \int_{s_0}^s \bar{I}_{b\nu}(s^*) \frac{\partial}{\partial s} \left\{ \frac{\partial \bar{\tau}_\nu(s^* \rightarrow s)}{\partial s^*} \right\} ds^* + \frac{1 - \bar{\epsilon}_{0\nu}}{\pi} \int_{\hat{n}_0 \cdot \Omega' < 0} |\hat{n}_0 \cdot \Omega'| \left[\bar{\epsilon}_{L\nu} \bar{I}_{bL\nu}(s'_L) \frac{\partial}{\partial s} \overline{\tau_\nu(s'_L \rightarrow s'_0) \tau_\nu(s_0 \rightarrow s)} + \int_{s'_L}^{s'_0} \left[\bar{I}_{b\nu}(s'^*) \frac{\partial}{\partial s} \frac{\partial}{\partial s'^*} \overline{\tau_\nu(s'^* \rightarrow s'_0) \tau_\nu(s_0 \rightarrow s)} \right] ds'^* \right] d\Omega' \quad (18)$$

The two-reflection, no-closure approximation for $\bar{C}_\nu^+(s, \Omega)$ is written as

$$\bar{C}_\nu^+(s, \Omega) = \bar{\epsilon}_{0\nu} \bar{I}_{b0\nu}(s_0) \frac{\partial}{\partial s} \{ \bar{\tau}_\nu(s_0 \rightarrow s) \} + \int_{s_0}^s \bar{I}_{b\nu}(s^*) \frac{\partial}{\partial s} \left\{ \frac{\partial \bar{\tau}_\nu(s^* \rightarrow s)}{\partial s^*} \right\} ds^* + \frac{1 - \bar{\epsilon}_{0\nu}}{\pi} \int_{\hat{n}_0 \cdot \Omega' < 0} |\hat{n}_0 \cdot \Omega'| \left[\bar{\epsilon}_{L\nu} \bar{I}_{bL\nu}(s'_L) \frac{\partial}{\partial s} \overline{\tau_\nu(s'_L \rightarrow s'_0) \tau_\nu(s_0 \rightarrow s)} + \int_{s'_L}^{s'_0} \left[\bar{I}_{b\nu}(s'^*) \frac{\partial}{\partial s} \frac{\partial}{\partial s'^*} \overline{\tau_\nu(s'^* \rightarrow s'_0) \tau_\nu(s_0 \rightarrow s)} \right] ds'^* \right] d\Omega' + \frac{1 - \bar{\epsilon}_{0\nu}}{\pi} \frac{1 - \bar{\epsilon}_{L\nu}}{\pi} \int_{\hat{n}_0 \cdot \Omega' < 0} |\hat{n}_0 \cdot \Omega'| \int_{\hat{n}_L \cdot \Omega'' < 0} |\hat{n}_L \cdot \Omega''| \left[\bar{\epsilon}_{0\nu} \bar{I}_{b0\nu}(s''_0) \frac{\partial}{\partial s} \overline{\tau_\nu(s''_0 \rightarrow s''_L) \tau_\nu(s'_L \rightarrow s'_0) \tau_\nu(s_0 \rightarrow s)} + \int_{s''_0}^{s''_L} \left[\bar{I}_{b\nu}(s''^*) \frac{\partial}{\partial s} \frac{\partial}{\partial s''^*} \overline{\tau_\nu(s''^* \rightarrow s''_L) \tau_\nu(s'_L \rightarrow s'_0) \tau_\nu(s_0 \rightarrow s)} \right] ds''^* \right] d\Omega'' d\Omega' \quad (19)$$

The no-reflection, no-closure approximation is not expected to be accurate for reflecting walls, since the intensities reflected at the walls are not included in any manner. As the number of included reflections increases, however, the wall reflected components, which are not included in the no-closure approximation, have a longer path through the medium and become smaller in magnitude. Therefore, considering a finite number of reflections can yield very accurate results. An exact formulation must consider an infinite number of reflections with no closure approximation (Nelson, 1979a; Edwards, 1962).

V Discretized Equation of Transfer

To solve the averaged equation of transfer numerically, an angular discretization (indicated by the subscript $n = 1, N$ where the positive μ directions used to obtain the positive directed intensities are indicated by $n = N/2 + 1, N$ and the negative μ directions for obtaining the negative directed intensities are indicated by $n = 1, N/2$) and a spatial discretization (indicated by the subscript $i = 1, M$) are applied using the grid scheme shown in Figs. 1(a-c). Equation (2) is discretized as

$$\{ \bar{I}_{\nu, n, i+1/2} - \bar{I}_{\nu, n, i} \} = (1 - \bar{\tau}_{\nu, n, i-i+1}) \bar{I}_{b\nu, i+1/2} + (\Delta x_i / |\mu_n|) \bar{C}_{\nu, n, i+1/2} \quad (20)$$

where the subscripts with $i+1/2$ denote quantities at the control volume centers. The following boundary conditions are used for all orders of solution:

at $x=0$, and $n=N/2+1, N$

$$\bar{I}_{\nu, n, 1} = \bar{\epsilon}_{0\nu} \bar{I}_{b0\nu} + \frac{(1 - \bar{\epsilon}_{0\nu})}{\pi} \sum_{n=1}^{N/2} |\mu_n| w_n \bar{I}_{\nu, n, 1} \quad (21)$$

at $x=L$, and $n=1, N/2$

$$\bar{I}_{\nu, n, M} = \bar{\epsilon}_{L\nu} \bar{I}_{bL\nu} + \frac{(1 - \bar{\epsilon}_{L\nu})}{\pi} \sum_{n=N/2+1}^N |\mu_n| w_n \bar{I}_{\nu, n, M} \quad (22)$$

Note that $\bar{I}_{\nu, n, 1}$ in the summation of Eq. (21) and $\bar{I}_{\nu, n, M}$ on the left side of Eq. (22) are negative directed intensities. $\bar{I}_{\nu, n, 1}$ on

the left-hand side of Eq. (21) and $\bar{I}_{\nu, n, M}$ in the summation of Eq. (22) are positive directed intensities. The spectral absorp-

tion term $\bar{C}_{\nu, n, i+1/2}$ is evaluated from the particular order of closure approximation applied. For the zeroth-degree closure approximation shown in Eq. (13), this is discretized as (for $\mu_n > 0$, or $n = N/2 + 1, \dots, N$)

$$(\Delta x_i / |\mu_n|) \bar{C}_{\nu, n, i+1/2} = \bar{I}_{\nu, n, 1} \{ \bar{\tau}_{\nu, n, 1-i+1} - \bar{\tau}_{\nu, n, 1-i} \} + \sum_{k=1}^{i-1} [\{ \bar{\tau}_{\nu, n, k+1-i+1} - \bar{\tau}_{\nu, n, k+1-i} \} - \{ \bar{\tau}_{\nu, n, k-i+1} - \bar{\tau}_{\nu, n, k-i} \}] \bar{I}_{b\nu, k+1/2} \quad (23)$$

where the subscripts used for the transmittance $\bar{\tau}_{\nu, n, k-i+1}$ indicate that $\bar{\tau}$ is based on the length $(x_{i+1} - x_k) / |\mu_n|$ (see Fig. 1a).

The discretized form of the spectral absorption terms for first- and second-degree closure approximations can be written in a similar fashion. The first-degree closure approximation involves calculating the transmittances of length scales up to $2L/\mu$, e.g., the transmittance $\bar{\tau}_{\nu, n', k-1, n, 1-i+1}$ is determined along the path $x_k / |\mu_{n'}| + x_{i+1} / |\mu_n|$ (see Fig. 1b). The second-degree closure approximation involves calculating the transmittances with length scales up to $3L/\mu$, e.g., the transmittance $\bar{\tau}_{\nu, n'', k-M, n', M-1, n, 1-i+1}$ used for obtaining the positive directed intensity is evaluated along the angular path $|x_k - L| / |\mu_{n''}| + L / |\mu_{n'}| + x_{i+1} / |\mu_n|$ for $(n = N/2 + 1, \dots, N)$, $(n' = 1, \dots, N/2)$, and $(n'' = N/2 + 1, \dots, N)$.

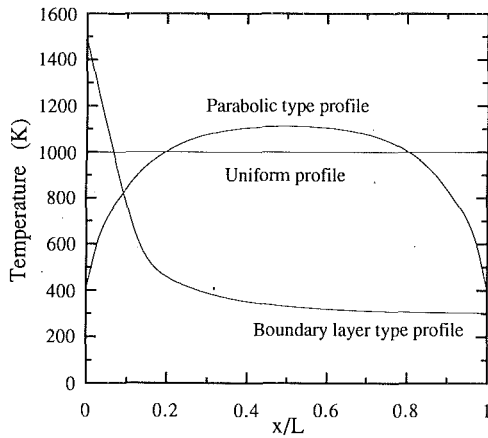


Fig. 2 Temperature profiles

The solutions of Eqs. (20), (21), and (22) with the proper spectral absorption term inserted for the desired order of solution is obtained by iteration. This iteration procedure for one narrow band is exactly the same as that for a gray gas. The difference occurs in the formulation of the spectral absorption term, which takes the spectral correlation of terms into account.

The integration over the wavenumber spectrum is accomplished by using band blackbody fractions. These discretized equations are solved by modifying the one-dimensional, non-gray discrete ordinates code developed for nonreflecting walls (Kim et al., 1991a). The resulting band intensities are summed to give the total intensity distribution. Once the total intensities, $\bar{I}_{n,i}$, are calculated, the total net radiative flux is found from

$$q_i = \sum_{n=1}^N \mu_n w_n \bar{I}_{n,i} \quad (24)$$

The total radiative source term, $-dq/dx$, is obtained by finite differencing the total net fluxes.

VI Results and Discussions

Solutions for nongray absorbing and emitting slabs of gas media are obtained by using the accurate discrete ordinates method, and taking the spectral correlation effects into account for gray, diffusely reflecting walls. As in the first paper (Kim et al., 1991a), the statistical narrow-band model with exponential-tailed-inverse line-strength distribution (Malkmus, 1967) is used to calculate the transmittances through the gas medium,

$$\bar{\tau}_\nu(s^* \rightarrow s) = \exp \left[-\frac{\bar{\beta}_\nu}{\pi} \left(\sqrt{1 + \frac{2\pi u \bar{k}_\nu}{\bar{\beta}_\nu}} - 1 \right) \right] \quad (25)$$

The required narrow-band parameters are obtained from those published by Hartmann et al. (1984) and Soufiani et al. (1985). Nonisothermal media are treated by using the Curtis-Godson method (Godson, 1953; Young, 1977; Zhang et al., 1988).

The same temperature profiles used by Kim et al. (1991a) are used here to examine the effects of the spectral correlation for different wall reflectivities. The first profile has a uniform medium temperature of 1000 K with both walls at 0 K, indicated as "Uniform profile" in Fig. 2. The second temperature profile indicated as "Parabolic type profile" in Fig. 2 is taken from Zhang et al. (1988) and has a nearly parabolic shape. The third profile indicated as "Boundary layer type profile" is taken from a combined radiation-convection boundary layer solution for a gray gas (Lee et al., 1990).

A 20-direction Gaussian quadrature set is selected for accurate calculations for all of the cases. The overall slab thickness is divided into 20 uniform sublayers ($M = 22$) for the

numerical calculations. The one-dimensional discrete ordinates code has been shown to yield excellent comparisons with exact and numerical gray media solutions available in the literature (Kim, 1990).

Gray wall emissivities of $\epsilon = (1 - \rho) = 0.9, 0.5, 0.1$ are considered for this study. The gas medium consists of pure H₂O vapor at 1 atm for all the cases considered. All of the important bands in the wavenumber spectrum from 0 to ∞ are included in this analysis. The narrow band parameters from Hartmann et al. (1984) and Soufiani et al. (1985) are given within the following limits: 150–2375 cm⁻¹, 2875–4250 cm⁻¹, and 4500–8000 cm⁻¹. The nongray reflecting wall solutions are obtained by using zeroth-, first-, and second-degree closure approximations and by the no-closure approximations using up to two reflections. Since the no-closure approximation solutions systematically approach the exact solutions, they will be used to evaluate the closure approximations.

The closure approximations given in Section IV are the same as the correlation approximations presented in a conference paper (Kim et al., 1991b), although the conference paper omits the description of the approximations shown in Eqs. (15b) and (16b) for the first-degree and second-degree correlations. Also, a programming error, which gave false results for all but the zeroth-degree solutions in the conference paper, has been corrected for the results presented here.

The situation with one reflecting wall and one black wall is considered first. For this case, the no-closure analysis with one reflection is the exact solution. Figures 3(a)–3(c) show the comparisons between the exact one-reflection solutions and those of the zeroth- and first-degree closure solutions for the three temperature profiles shown in Fig. 2. The no-reflection solutions without a closure approximation are also included in these figures.

The first-degree closure solutions of the volumetric radiative source distributions, $-dq/dx$, are identical to the exact solution as indicated in the legends. As expected, significant differences are shown between the exact and the no-reflection, no-closure solutions. The zeroth-degree closure solution is seen to give quite accurate results. For the uniform temperature profile (Fig. 3a), the largest error of 26 percent from the exact solutions is observed in the zeroth-degree closure solutions next to the reflecting wall at $x = 0$. For the parabolic-type temperature case (Fig. 3b) the error next to the reflecting wall is only 7 percent between the exact and the zeroth-degree closure solutions. The boundary layer type temperature profile case (Fig. 3c) also shows only small errors in the zeroth-degree closure approximation. The error next to the reflecting wall is 7 percent.

The analysis for reflecting walls with identical diffuse reflectivities, $\rho = \rho_1 = \rho_2$, are considered next for the parabolic type temperature profile. Figures 4(a), 4(b), and 4(c) show the nongray results using up to a second-degree closure approximation for diffuse wall reflectivities of $\rho = 0.1, 0.5$, and 0.9 respectively, with the same slab thickness of $L = 0.5$ m. Figures 4(d) and 4(e) consider slab thicknesses of $L = 0.1$ m and 1.0 m, respectively, with $\rho = 0.9$. The no-closure solutions using up to a two-reflection approximation are also included in these figures.

For weakly reflecting walls of $\rho = 0.1$ and $L = 0.5$ m (Fig. 4a), the radiative source distributions obtained from the zeroth-, first-, and second-degree closure formulations result in nearly the same solutions and are hidden underneath the one- and two-reflection, no-closure solutions. There are also very little differences between the no-closure solutions. Only the no-reflection solution shows any visible error. This is because the multiply reflected terms in the formulations shown in Eqs. (7) and (10) become negligible for small ρ .

As ρ is increased, the multiply reflected terms become more important. For $\rho = 0.5$ and $L = 0.5$ m (Fig. 4b), the no-closure solutions converge to the exact solution. The two-

reflection approximation is therefore taken to be the exact solution. Only the no-reflection, no-closure solution shows large errors. The zeroth-degree closure results are already hidden under the one- and two-reflection solutions, with an error of 6 percent next to the walls and 1.6 percent at the center of of

the slab compared to the exact solution. The first-degree closure solution nearly overlaps the second-degree closure solution. The second-degree solution is 0.25 percent in error next to the wall and -0.5 percent in error at the center of the slab. As ρ is further increased to 0.9 for $L = 0.5$ m (Fig. 4c),

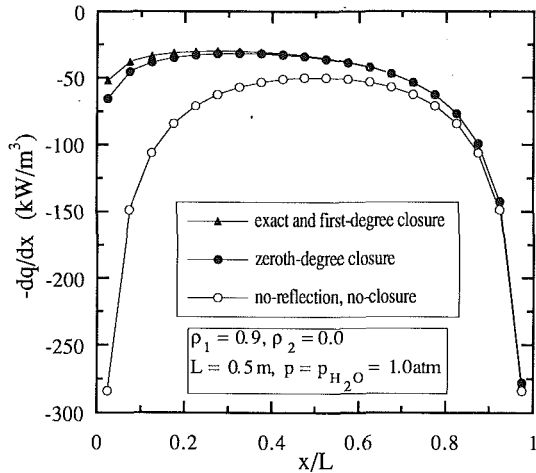


Fig. 3(a) Radiation source distributions for the uniform temperature profile (one reflecting wall)

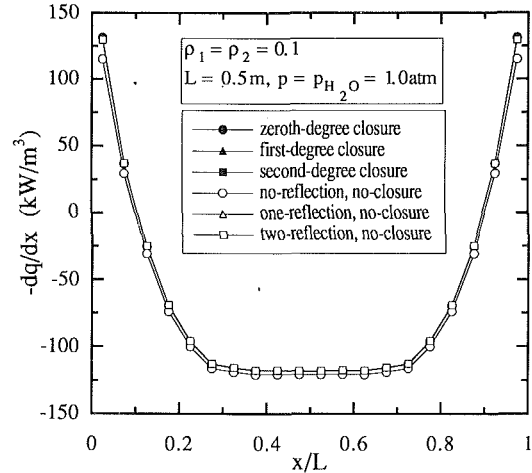


Fig. 4(a) Radiation source distributions for $\rho = 0.1$ and $L = 0.5$ m (two reflecting walls, parabolic-type temperature profile)

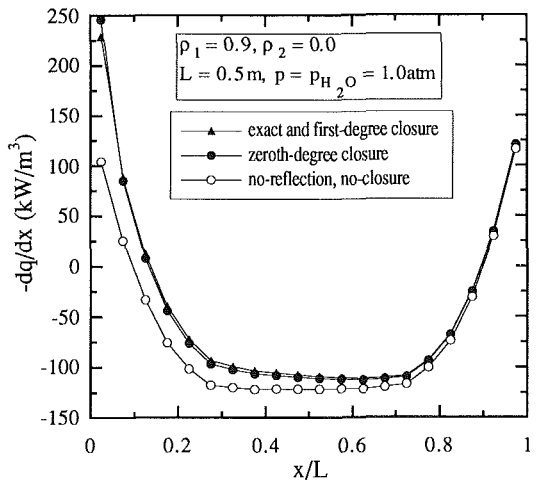


Fig. 3(b) Radiation source distributions for the parabolic-type temperature profile (one reflecting wall)

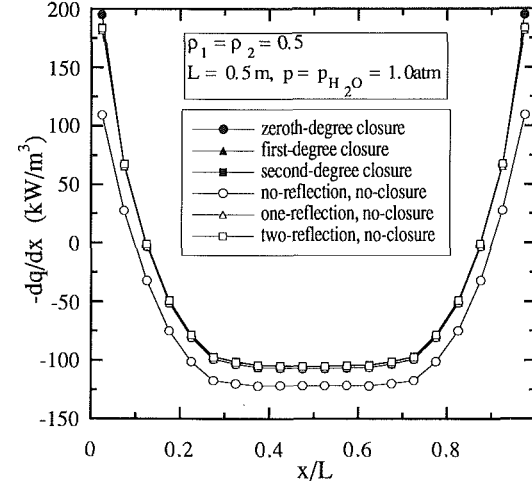


Fig. 4(b) Radiation source distributions for $\rho = 0.5$ and $L = 0.5$ m (two reflecting walls, parabolic-type temperature profile)

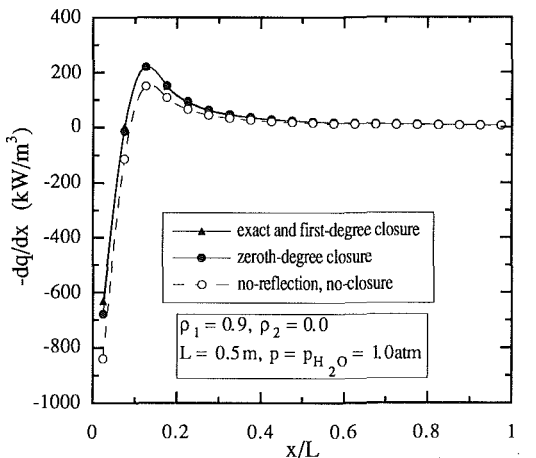


Fig. 3(c) Radiation source distributions for the boundary-layer type temperature profile (one reflecting wall)

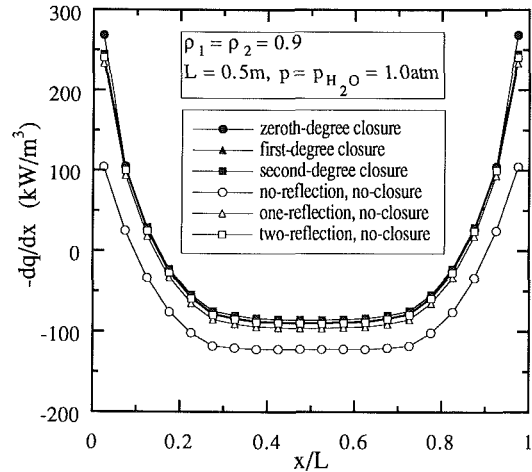


Fig. 4(c) Radiation source distributions for $\rho = 0.9$ and $L = 0.5$ m (two reflecting walls, parabolic-type temperature profile)

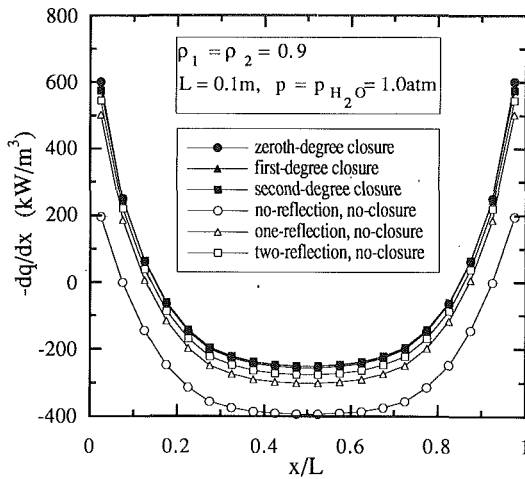


Fig. 4(d) Radiation source distributions for $\rho = 0.9$ and $L = 0.1$ m (two reflecting walls, parabolic-type temperature profile)

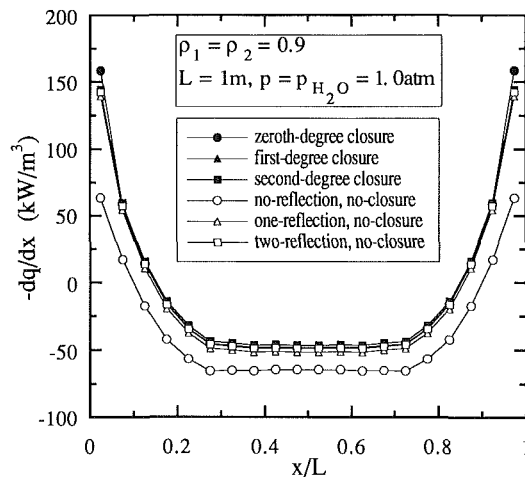


Fig. 4(e) Radiation source distributions for $\rho = 0.9$ and $L = 1.0$ m (two reflecting walls, parabolic-type temperature profile)

the highly reflecting walls give large reflected components of the wall intensity. The no-reflection, no-closure analysis shows large errors as expected, but the no-closure approximations are converging toward an exact solution. If the two-reflection approximation is taken as the exact solution, the zeroth-degree closure approximation is 12 percent in error next to the walls and 2 percent at the center. The first-degree closure analysis is 1 percent in error at the walls and -5 percent at the center. The second-degree closure solution is 2 percent in error next to the walls and -5 percent at the center.

Even though the walls are highly reflecting, if the absorption by the gas medium is large, the multiple reflection effect is significantly reduced. Either the total gas pressure or the slab thickness can be increased to obtain large optical depths. Figures 4(c), 4(d), and 4(e) show the effect of the slab thickness on the accuracy of the solutions. In these figures, the radiative source distributions for $\rho = 0.9$ are presented for three different slab thicknesses, $L = 0.5, 0.1$, and 1.0 m, respectively, using different scales for $-dq/dx$.

For the smallest optical depth, $L = 0.1$ m (Fig. 4d), the largest discrepancies are shown between the no-closure solutions. Although approaching the exact solutions, the two-reflection approximation is clearly not the final solution. The zeroth-, first-, and second-degree closure solutions are all close to the two-reflection approximation. As the plate spacing is

Table 1 Net radiative wall fluxes for $\rho_1 = 0.9, \rho_2 = 0.0$, and $L = 0.5$ m (kW/m^2)

		no reflection	one reflection
Boundary Layer	wall 1	11.74 (-56.6%)	27.07 (exact)
	wall 2	21.74 (-8.4%)	23.74 (exact)
Parabolic	wall 1	-17.68 (998%)	-1.61 (exact)
	wall 2	15.89 (-20.9%)	20.08 (exact)
Uniform	wall 1	-24.23 (918%)	-2.38 (exact)
	wall 2	24.23 (-13.7%)	28.07 (exact)

(b) With Closure Approximation

		zeroth degree	first degree
Boundary Layer	wall 1	27.07 (0%)	27.07 (0%)
	wall 2	24.60 (3.6%)	23.74 (0%)
Parabolic	wall 1	-1.61 (0%)	-1.61 (0%)
	wall 2	20.74 (3.3%)	20.08 (0%)
Uniform	wall 1	-2.38 (0%)	-2.38 (0%)
	wall 2	29.12 (3.7%)	28.07 (0%)

Table 2 Net radiative wall fluxes with two reflecting walls (kW/m^2)

		no reflection	one reflection	two reflection
$\rho=0.1$	0.5	± 16.46 (8.9%)	± 15.14 (0.1%)	± 15.12 (0%)
	0.5	± 16.83 (71.9%)	± 10.26 (4.8%)	± 9.79 (0%)
$\rho=0.9$	0.1	± 12.09 (229%)	± 5.17 (40.9%)	± 3.67 (0%)
	0.5	± 17.20 (341%)	± 5.41 (38.7%)	± 3.90 (0%)
	1.0	± 18.06 (370%)	± 5.29 (37.8%)	± 3.84 (0%)

(b) With Closure Approximation

		zeroth degree	first degree	second degree
$\rho=0.1$	0.5	± 15.19 (0.5%)	± 15.12 (0%)	± 15.12 (0%)
	0.5	± 9.91 (2.6%)	± 9.72 (0.6%)	± 9.66 (0%)
$\rho=0.9$	0.1	± 2.41 (3.0%)	± 2.40 (2.6%)	± 2.34 (0%)
	0.5	± 2.76 (2.2%)	± 2.80 (3.7%)	± 2.70 (0%)
	1.0	± 2.73 (2.2%)	± 2.77 (3.7%)	± 2.67 (0%)

increased to $L = 1.0$ m (Fig. 4e), the solutions by the one-reflection and two-reflection approximations show only small differences, and the two-reflection, no-closure analysis for this case could be considered to be the exact solution. For the $L = 0.1$ m case, the radiative source next to the reflecting walls is 11 percent in error using the zeroth-degree closure analysis, 1 percent using a first-degree closure analysis, and 1 percent using a second-degree closure analysis as compared to the two-reflection, no-closure results.

Table 1 shows the net radiative wall fluxes for one diffuse reflecting wall and one black wall. The no-closure solutions are given in Table 1(a), while the closure solutions are in Table 1(b). The analysis considering one reflection without the closure approximation gives the exact solutions for all the temperature profiles considered. The first-degree closure solutions

are identical to the exact solutions. The fluxes at the reflecting wall (wall 1) using the zeroth-degree closure analysis are accurate, while there are errors in the fluxes at the nonreflecting wall (wall 2). The small errors come from the approximations made in treating the reflected radiation from wall 1, which affects the flux at the opposite nonreflecting wall. The largest error in the fluxes at the nonreflecting wall is found for the uniform temperature profile, which shows a 3.7 percent error.

When both boundary walls are reflecting, exact solution is possible only by including an infinite number of reflections explicitly in the analysis. However, the multiply reflected components become small with an increasing number of reflections for small ρ and large optical depths. Table 2 shows some results for $\rho = \rho_1 = \rho_2 = 0.1, 0.5,$ and 0.9 with the parabolic-type temperature profile. The error comparisons for the no-closure approximation results are with respect to the two-reflection, no-closure solutions. The error comparisons for the closure approximation results are with respect to the second-degree closure solutions, since some of the two-reflection, no-closure solutions have not yet converged. The no-closure solutions are given in Table 2(a), and the closure solutions are given in Table 2(b).

For $\rho = 0.1$ and 0.5 , with $L = 0.5$ m, the two-reflection, no-closure results are nearly the exact solutions as shown in Figs. 4(a) and 4(b). For these cases, the closure approximations are quite close to the two-reflection, no-closure results. For the $\rho = 0.9$ cases, the two-reflection, no-closure solutions have not yet converged to the exact solution. Still, the closure solutions are very close to each other and appear to anticipate the magnitudes of higher order no-closure solutions.

VII Conclusions

The wavenumber-averaged equation of transfer suitable for a discrete ordinates analysis is derived for a one-dimensional, nongray, absorbing-emitting slab including multiple reflection effects. Solutions are obtained for infinite, parallel, gray, diffusely reflecting walls enclosing a nongray, pure H₂O vapor.

The effect of multiple reflections is significant for highly reflecting walls. For the parabolic-type temperature profile considered, the no-closure solutions require more than two reflections to approach exact solutions for ρ equal to 0.9. The multiple reflection effect is reduced as the wall reflectivity ρ is reduced and as the optical depth of the slab is increased. If the medium is optically thin, more reflections must be explicitly included.

For the specific conditions tested in this study, using the zeroth-degree closure approximation gives quite accurate results compared to the two-reflection, no-closure results. Higher order solutions are so close to the zeroth-degree solutions for these cases that they may not be desirable for engineering applications due to the large amounts of computer time required to obtain them.

Acknowledgments

This work was supported, in part, by the National Science Foundation Grant NSF/CTS-8451076. A grant from the Minnesota Supercomputer Institute is also gratefully acknowledged.

References

- Carlson, B. G., and Lathrop, K. D., 1968, "Transport Theory—The Method of Discrete-Ordinates," in: *Computing Methods in Reactor Physics*, H. Greenspan, C. N. Kelber, and D. Okrent, eds., Gordon & Breach, New York, pp. 166–266.
- Edwards, D. K., 1962, "Radiation Interchange in a Nongray Enclosure Containing an Isothermal Carbon-Dioxide-Nitrogen Gas Mixture," *ASME JOURNAL OF HEAT TRANSFER*, Vol. 84, pp. 1–11.
- Edwards, D. K., and Matavosian, R., 1984, "Scaling Rules for Total Absorptivity and Emissivity of Gases," *ASME JOURNAL OF HEAT TRANSFER*, Vol. 106, pp. 684–689.
- Godson, W. L., 1953, "The Evaluation of Infrared Radiation Fluxes Due to Atmospheric Water Vapor," *Quarterly Journal of Royal Meteorological Society*, Vol. 79, pp. 367–379.
- Goody, R. M., 1964, *Atmospheric Radiation*, Clarendon Press, Oxford, pp. 122–170.
- Hartmann, J. M., Levi Di Leon, R., and Taine, J., 1984, "Line-by-Line and Narrow-Band Statistical Model Calculations for H₂O," *Journal of Quantitative Spectroscopy and Radiative Transfer*, Vol. 32, No. 2, pp. 119–127.
- Kim, T.-K., 1990, "Radiation and Combined Mode Heat Transfer Analyses in Absorbing, Emitting, and Mie-Anisotropically Scattering Media Using the S-N Discrete Ordinates Method," Ph.D. dissertation, University of Minnesota, Minneapolis, MN.
- Kim, T.-K., Menart, J. A., and Lee, H. S., 1991a, "Nongray Radiative Gas Analyses Using the S-N Discrete Ordinates Method," *ASME JOURNAL OF HEAT TRANSFER*, Vol. 113, pp. 946–952.
- Kim, T.-K., Menart, J. A., and Lee, H. S., 1991b, "S-N Discrete Ordinates Solutions of Nongray Radiative Transfer With Diffusely Reflecting Walls," *Fundamentals of Radiation Heat Transfer*, ASME HTD-Vol. 160, pp. 79–87.
- Lee, H. S., Menart, J. A., and Fakheri, A., 1990, "A Multilayer Radiation Solution for Boundary Layer Flow of Gray Gases," *Journal of Thermophysics and Heat Transfer*, Vol. 4, pp. 180–185.
- Ludwig, C. B., Malkmus, W., Reardon, J. E., and Thomson, J. A. L., 1973, *Handbook of Infrared Radiation From Combustion Gases*, NASA SP-3080, Scientific and Technical Information Office, Washington, DC.
- Malkmus, W., 1967, "Random Lorentz Band Model With Exponential-Tailed S⁻¹ Line-Intensity Distribution Function," *Journal of the Optical Society of America*, Vol. 57, No. 3, pp. 323–329.
- Nelson, D. A., 1979a, "Band Radiation Within Diffuse-Walled Enclosures, Part I: Exact Solutions for Simple Enclosures," *ASME JOURNAL OF HEAT TRANSFER*, Vol. 101, pp. 81–84.
- Nelson, D. A., 1979b, "Band Radiation Within Diffuse-Walled Enclosures, Part II: An Approximate Method Applied to Simple Enclosures," *ASME JOURNAL OF HEAT TRANSFER*, Vol. 101, pp. 85–89.
- Nelson, D. A., 1984, "Band Radiation of Isothermal Gases Within Diffuse-Walled Enclosures," *International Journal of Heat and Mass Transfer*, Vol. 27, No. 10, pp. 1759–1769.
- Nelson, D. A., 1986, "Nongray Total Radiation Within an Enclosure," *ASME Paper No. 86-HT-29*.
- Soufiani, A., Hartmann, J. M., and Taine, J., 1985, "Validity of Band-Model Calculations for CO₂ and H₂O Applied to Radiative Properties and Conductive-Radiative Transfer," *Journal of Quantitative Spectroscopy and Radiative Transfer*, Vol. 33, No. 3, pp. 243–257.
- Young, S. J., 1977, "Nonisothermal Band Model Theory," *Journal of Quantitative Spectroscopy and Radiative Transfer*, Vol. 18, pp. 1–28.
- Zhang, L., Soufiani, A., and Taine, J., 1988, "Spectral Correlated and Non-correlated Radiative Transfer in a Finite Axisymmetric System Containing an Absorbing and Emitting Real Gas-Particle Mixture," *International Journal of Heat and Mass Transfer*, Vol. 18, pp. 2261–2272.

Refractive Index Effects on Radiation in an Absorbing, Emitting, and Scattering Laminated Layer

R. Siegel

Research Scientist,
Fellow ASME

C. M. Spuckler

Research Scientist,
Assoc. Mem. ASME

NASA Lewis Research Center,
Cleveland, OH 44135

A simple set of equations is derived for predicting temperature distributions and radiative energy flow in a two-region semitransparent laminated layer in the limit of zero heat conduction. The composite is heated on its two sides by unequal amounts of incident radiation. The two layers of the composite have different refractive indices, and each material absorbs, emits, and isotropically scatters radiation. The interfaces are diffuse, and all interface reflections are included. To illustrate the thermal behavior that is readily calculated from the equations, typical results are given for various optical thicknesses and refractive indices of the layers. Internal reflections have a substantial effect on the temperature distribution and radiative heat flow.

Introduction

The use of ceramic materials for parts or coatings is of interest for high-temperature applications. Some of these materials have reinforcing fibers or are laminated so it is necessary to consider heat transfer in composite regions. The surrounding temperatures are high, which provides substantial radiative heating. Since some of the materials are semitransparent, their temperature distributions depend on the internal radiative heat flow. The refractive index of a semitransparent material can have a considerable effect on its temperature distribution. The refractive index governs the amount of transmission into the interior of the material and affects the internal reflections that occur. Of more significance, the emission within a material depends on the *square* of its refractive index; hence internal emission can be many times that for a blackbody radiating into a vacuum. Since radiation exiting through an interface into a vacuum cannot exceed that of a blackbody, the amount of internal reflection can be substantial. It redistributes energy within the layer and tends to make the temperature distribution more uniform than for a material with refractive index close to one.

To obtain the general solution for the temperature distribution in a composite semitransparent layer requires solving the integral equations of energy transfer in each region, including heat conduction, and matching temperatures and heat flows at the internal interface. A spectral calculation can be carried out in each significant wavelength band and the total energy flow found by summing over the bands. A numerical solution by computer is required. A simple limiting solution is obtained here that is helpful and informative. The purpose of this paper is to show that in the limit with no heat conduction and for gray layers with refractive indices greater than one, the solution for a composite region can be obtained from information that is already known and results calculated very easily. The effects of surface reflections and isotropic scattering are included. The solution of integral equations is not required. The limiting result can be helpful in initiating iterative computer solutions for a more general analysis and for checking the validity of numerical solutions.

The development here builds on the analysis of Siegel and Spuckler (1992) where it was shown that for radiative equilib-

rium in a gray layer with diffuse interfaces, the temperature distribution and radiative heat flux for any index of refraction is obtained very simply from available results for an index of refraction of one. The present paper applies these ideas to a two-layer laminate subjected to external heating on its outer surfaces. Each of the layers emits, absorbs, and isotropically scatters radiation. For simplicity the medium surrounding the laminate has a refractive index of one.

The outer surfaces of the laminate, and the interface between the two layers, are each assumed diffuse. This is probably a reasonable approximation for unpolished materials that are bonded together. Transmitted radiation, or radiation emitted from the interior, is assumed to be diffuse when it reaches the inner surface of an interface. If the index of refraction of the material is greater than that of the surrounding medium, some of the internal radiation is in angular directions for which there is total internal reflection. This retains energy within the layer and tends to equalize its temperature distribution.

Some of the important early work on calculating heat transfer behavior in semitransparent layers was done by Gardon (1958) who developed an analysis for temperature distributions during heat treating and cooling of glass plates including index of refraction effects. The interfaces were optically smooth, and the specular reflections at the interfaces were computed from the Fresnel reflection relations. A similar application (Fowle et al., 1969), predicted heating in a window of a re-entry vehicle. Recent papers by Rokhsaz and Dougherty (1989), Ping and Lallemand (1989), and Crosbie and Shieh (1990) further examined the effects of Fresnel boundary reflections and having a refractive index larger than one. Many analyses of both steady and transient heat transfer in single or multiple plane layers such as Amlin and Korpela (1979), and Tarshis et al. (1969), have used diffuse conditions at the interfaces as in the present study. Thomas (1992) set up a solution procedure to include a ceramic interface that is partially specular and diffuse. Ho and Ozisik (1987) carried out a numerical analysis of radiation and conduction in a two-region laminate without including refractive index effects and hence without internal interface reflections.

Analysis

A laminated plane layer is made of two different materials that have thicknesses D_1 and D_2 as shown in Fig. 1. Both sublayers absorb, emit, and isotropically scatter radiation. The

Contributed by the Heat Transfer Division for publication in the JOURNAL OF HEAT TRANSFER. Manuscript received by the Heat Transfer Division April 13, 1992; revision received July 23, 1992. Keywords: Radiation. Associate Technical Editor: R. O. Buckius.

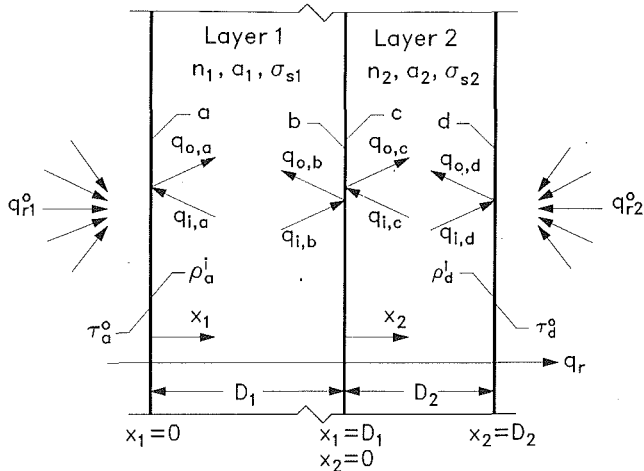


Fig. 1 Laminated two-layer geometry, coordinate system, and nomenclature for heat fluxes at interfaces

limiting case is considered here where the temperature distribution within the composite is dominated by radiation so heat conduction is neglected. Each material has a constant refractive index; it is the effect of the two different n values that is investigated here along with having different optical thicknesses for the layers. The materials provide significant scattering, so the interfaces between the two layers and between each layer and the surrounding air or vacuum (with $n = 1$) are assumed diffuse. The laminated layer is subjected to diffuse radiation from the surroundings of q_{r1}^o and q_{r2}^o on the two outer boundaries $x_1 = 0$ and $x_2 = D_2$; for convenience here $q_{r1}^o > q_{r2}^o$. Inside each layer there are outgoing and incoming fluxes, q_o and q_i , at each interior interface. Since scattering is included, the local optical depth in each layer is related to its x coordinate by $\kappa = (a + \sigma_s)x$. Using an individual coordinate in each of the two layers facilitates the formulation and solution that follows.

The temperature distribution in each layer is governed by an integral equation given by Siegel and Howell (1981), modified with index of refraction factors as,

$$n_1^2 \sigma T_1^4(\kappa_1) = \frac{1}{2} [q_{o,a} E_2(\kappa_1) + q_{o,b} E_2(\kappa_{D1} - \kappa_1)] + \frac{n_1^2}{2} \int_0^{\kappa_{D1}} \sigma T_1^4(\kappa_1^*) E_1(|\kappa_1 - \kappa_1^*|) d\kappa_1^* \quad (1a)$$

$$n_2^2 \sigma T_2^4(\kappa_2) = \frac{1}{2} [q_{o,c} E_2(\kappa_2) + q_{o,d} E_2(\kappa_{D2} - \kappa_2)] + \frac{n_2^2}{2} \int_0^{\kappa_{D2}} \sigma T_2^4(\kappa_2^*) E_1(|\kappa_2 - \kappa_2^*|) d\kappa_2^* \quad (1b)$$

The radiative flux is a *constant* through the entire laminated layer for the present conditions of radiative equilibrium. The relation of flux to temperature distribution in each of the two layers is obtained by evaluating the equation for q_r for a plane layer from Siegel and Howell (1981) at $x_1 = 0$ and $x_2 = 0$,

$$q_r = q_{o,a} - 2q_{o,b} E_3(\kappa_{D1}) - 2n_1^2 \int_0^{\kappa_{D1}} \sigma T_1^4(\kappa_1) E_2(\kappa_1) d\kappa_1 \quad (2a)$$

$$q_r = q_{o,c} - 2q_{o,d} E_3(\kappa_{D2}) - 2n_2^2 \int_0^{\kappa_{D2}} \sigma T_2^4(\kappa_2) E_2(\kappa_2) d\kappa_2 \quad (2b)$$

The following dimensionless groups are now defined:

$$\Phi_1(\kappa_1) = \frac{n_1^2 \sigma T_1^4(\kappa_1) - q_{o,b}}{q_{o,a} - q_{o,b}}; \quad \Phi_2(\kappa_2) = \frac{n_2^2 \sigma T_2^4(\kappa_2) - q_{o,d}}{q_{o,c} - q_{o,d}} \quad (3a, b)$$

$$\Psi_1 = \frac{q_r}{q_{o,a} - q_{o,b}}; \quad \Psi_2 = \frac{q_r}{q_{o,c} - q_{o,d}} \quad (4a, b)$$

Equations (1) and (2) then transform to (note that within each layer $X_j = x_j/D_j = \kappa_j/\kappa_{Dj}$ where $j = 1$ or 2)

$$\Phi_j(X_j, \kappa_{Dj}) = \frac{1}{2} E_2(\kappa_{Dj} X_j) + \frac{1}{2} \kappa_{Dj} \int_0^1 \Phi_j(X_j^*, \kappa_{Dj}) E_1(\kappa_{Dj} |X_j - X_j^*|) dX_j^* \quad (j=1, 2) \quad (5)$$

$$\Psi_j(\kappa_{Dj}) = 1 - 2\kappa_{Dj} \int_0^1 \Phi_j(X_j, \kappa_{Dj}) E_2(\kappa_{Dj} X_j) dX_j \quad (j=1, 2) \quad (6)$$

It is noted that Eqs. (5) and (6) are the same for each layer,

Nomenclature

a = absorption coefficient of layer, m^{-1}
 a, b, c, d = the four internal sides of the interfaces in the two-layer laminate
 D = thickness of plane layer, m
 E_1, E_2, E_3 = exponential integral functions,
 $E_m(x) = \int_0^1 \mu^{m-2} \exp(-x/\mu) d\mu$
 $F(n)$ = function of refractive index defined in Eq. (15a)
 n = index of refraction
 q = heat flux, W/m^2
 q_r^o = externally incident radiation flux, W/m^2
 T = absolute temperature, K
 T_{s1}, T_{s2} = temperatures of surrounding radiating regions, K
 x_1, x_2 = coordinates normal to

boundaries of individual plane layers, m; $X_1 = x_1/D_1, X_2 = x_2/D_2$
 X = coordinate through two-layer laminate, $X = X_1$ in first layer, $X = X_2$ in second layer
 κ = optical depth = $(a + \sigma_s)x$; κ_D = optical thickness = $(a + \sigma_s)D$
 κ_e = extinction coefficient in the complex index of refraction; $\bar{n} = n - i\kappa_e$
 σ = Stefan-Boltzmann constant, $W/m^2 \cdot K^4$
 σ_s = scattering coefficient of layer, m^{-1}
 ρ^i = reflectivity of interface for internally incident radiation
 τ^o = transmissivity of surface for externally incident radiation

Φ = dimensionless temperature distribution, Eq. (3)
 Ψ = dimensionless radiative heat flux, Eq. (4)

Subscripts

i, o = incoming and outgoing radiation
 j = index 1 or 2 for each of the two sublayers in composite
 r = radiative quantity
 $1, 2$ = layers adjacent to the hotter and cooler surroundings; hotter and cooler surroundings

Superscripts

i = at inside surface of an interface
 o = at outside surface of an interface
 $*$ = dummy variable of integration

and that $\Phi(X, \kappa_D)$ and $\Psi(\kappa_D)$ are not functions of n . Hence to obtain Φ and Ψ for all $n \geq 1$ it is necessary to solve Eq. (5) only once for each κ_D and use each result to determine Ψ from Eq. (6). Tabulated results for some $\Phi(X, \kappa_D)$ and $\Psi(\kappa_D)$ are available from references such as Heaslet and Warming (1965) and Siegel and Spuckler (1992).

Although solutions for Φ and Ψ are available, the present analysis has not yet provided $T(\kappa_1)$, $T(\kappa_2)$, and q_r since Eqs. (3) and (4) contain the outgoing boundary fluxes $q_{o,a}$, $q_{o,b}$, $q_{o,c}$, and $q_{o,d}$ that are unknown. These fluxes must be expressed in terms of known quantities; this is accomplished by looking at the boundary and interface conditions in detail.

At the two outer boundaries the internal fluxes are related to the transmission of external flux and the reflection of internal flux by

$$q_{o,a} = q_{r1}^o \tau_a^o + q_{i,a} \rho_a^i; \quad q_{o,d} = q_{r2}^o \tau_d^o + q_{i,d} \rho_d^i \quad (7a, b)$$

At the inside surfaces of the outer boundaries there are the following relations between the radiative flux and the outgoing and incoming fluxes:

$$q_r = q_{o,a} - q_{i,a}; \quad q_r = -q_{o,d} + q_{i,d} \quad (8a, b)$$

Equations (7a) and (8a) are combined to eliminate $q_{i,a}$ and similarly Eqs. (7b) and (8b) to eliminate $q_{i,d}$. This yields

$$q_{o,a} = \frac{1}{1 - \rho_a^i} (q_{r1}^o \tau_a^o - q_r \rho_a^i) \quad (9a)$$

$$q_{o,d} = \frac{1}{1 - \rho_d^i} (q_{r2}^o \tau_d^o + q_r \rho_d^i) \quad (9b)$$

By using similar relations at interfaces b and c on either side of the internal interface, the following relations are found between the outgoing fluxes and the radiant flux q_r being transferred:

$$q_{o,b} = \frac{1}{1 - \rho_b^i} [q_{o,c} \tau_b^o + q_r (\rho_b^i - \tau_b^o)] \quad (10a)$$

$$q_{o,c} = \frac{1}{1 - \rho_c^i} [q_{o,b} \tau_c^o - q_r (\rho_c^i - \tau_c^o)] \quad (10b)$$

The radiant flux q_r can now be obtained. The $q_{o,a}$ from Eq. (9a) and $q_{o,b}$ from Eq. (10a) are substituted into Eq. (4a). The $q_{o,c}$ is then eliminated by using Eq. (4b), and the $q_{o,d}$ is eliminated by using Eq. (9b). The resulting expression is solved for q_r to yield

$$q_r = \frac{\frac{\tau_a^o}{1 - \rho_a^i} q_{r1}^o - \frac{\tau_b^o}{1 - \rho_b^i} \frac{\tau_d^o}{1 - \rho_d^i} q_{r2}^o}{\frac{1}{\Psi_1} + \frac{\rho_a^i}{1 - \rho_a^i} + \frac{\rho_b^i}{1 - \rho_b^i} + \frac{\tau_b^o}{1 - \rho_b^i} \left(\frac{\rho_d^i}{1 - \rho_d^i} - 1 + \frac{1}{\Psi_2} \right)} \quad (11)$$

As a result of total internal reflections at interfaces when radiation passes into a medium with a lower refractive index, there are the following relations at the four surfaces of the interfaces:

$$\tau_a^o = (1 - \rho_a^i) n_1^2; \quad \tau_b^o = (1 - \rho_b^i) \left(\frac{n_1}{n_2} \right)^2 \quad (12a-d)$$

$$\tau_c^o = (1 - \rho_c^i) \left(\frac{n_2}{n_1} \right)^2; \quad \tau_d^o = (1 - \rho_d^i) n_2^2$$

Equation (12) is used to eliminate the τ 's from Eq. (11) and the final result for q_r becomes:

$$\frac{q_r}{q_{r1}^o - q_{r2}^o} = \frac{n_1^2}{\frac{1}{\Psi_1} + \frac{\rho_a^i}{1 - \rho_a^i} + \frac{\rho_b^i}{1 - \rho_b^i} + \left(\frac{n_1}{n_2} \right)^2 \left(\frac{\rho_d^i}{1 - \rho_d^i} - 1 + \frac{1}{\Psi_2} \right)} \quad (13a)$$

By starting the previous algebra with Eq. (4b) rather than Eq. (4a) an alternative expression for q_r is found as:

$$\frac{q_r}{q_{r1}^o - q_{r2}^o} = \frac{n_2^2}{\frac{1}{\Psi_2} + \frac{\rho_c^i}{1 - \rho_c^i} + \frac{\rho_d^i}{1 - \rho_d^i} + \left(\frac{n_2}{n_1} \right)^2 \left(\frac{\rho_a^i}{1 - \rho_a^i} - 1 + \frac{1}{\Psi_1} \right)} \quad (13b)$$

The q_r is the same from expressions (13a) and (13b); evaluating both relations is a check on the solution.

The temperature distributions in the two layers are now obtained. Starting with Eq. (3b), $T_2(\kappa_2)$ can be obtained from $n_2^2 \sigma T_2^4(\kappa_2) = q_{o,d} + (q_{o,c} - q_{o,d}) \Phi_2(\kappa_2)$. The $q_{o,c} - q_{o,d}$ is eliminated by using Eq. (4b) to give $n_2^2 \sigma T_2^4(\kappa_2) = q_{o,d} + (q_r / \Psi_2) \Phi_2(\kappa_2)$. The $q_{o,d}$ is now eliminated by using Eq. (9b), and τ_d^o is eliminated by using Eq. (12d). The final result for $T_2(\kappa_2)$ is placed into the dimensionless form

$$\frac{\sigma T_2^4(\kappa_2) - q_{r2}^o}{q_{r1}^o - q_{r2}^o} = \frac{q_r}{q_{r1}^o - q_{r2}^o} \left[\frac{\rho_d^i}{1 - \rho_d^i} + \frac{\Phi_2(\kappa_2)}{\Psi_2} \right] \frac{1}{n_2^2} \quad (14a)$$

In a similar fashion the dimensionless $T_1(\kappa_1)$ distribution is obtained. Starting with Eq. (3a) and eliminating $q_{o,b}$ using Eq. (4a) gives $n_1^2 \sigma T_1^4(\kappa_1) = q_{o,a} + (q_r / \Psi_1) [\Phi_1(\kappa_1) - 1]$. The $q_{o,a}$ is eliminated using Eq. (9a), and τ_a^o is eliminated using Eq. (12a). Then $-n_1^2 q_{r2}^o$ is added to both sides of the equation. The final dimensionless result for $T_1(\kappa_1)$ is,

$$\frac{\sigma T_1^4(\kappa_1) - q_{r2}^o}{q_{r1}^o - q_{r2}^o} = 1 - \frac{q_r}{q_{r1}^o - q_{r2}^o} \left[\frac{\rho_a^i}{1 - \rho_a^i} - \frac{\Phi_1(\kappa_1) - 1}{\Psi_1} \right] \frac{1}{n_1^2} \quad (14b)$$

To use these relations, values of ρ^i are needed for various refractive indices. The externally incident radiation is diffuse. Although the interfaces are not optically smooth, it is assumed that each bit of roughness acts as a smooth facet so that the reflectivity can be obtained from the Fresnel interface relations for a nonabsorbing dielectric medium. By integrating the reflected energy over all incident directions the relation for $\rho^i(n)$ is (Siegel and Howell, 1981),

$$\rho^i(n) \equiv F(n) = \frac{1}{2} + \frac{(3n+1)(n-1)}{6(n+1)^2} + \frac{n^2(n^2-1)^2}{(n^2+1)^3} \ln \left(\frac{n-1}{n+1} \right) - \frac{2n^3(n^2+2n-1)}{(n^2+1)(n^4-1)} + \frac{8n^4(n^4+1)}{(n^2+1)(n^4-1)^2} \ln(n) \quad (15a)$$

This is for radiation passing into a material of higher refractive index where $n = n_h/n_s$ (n_h and n_s are the "higher" and "smaller" n values). When going in the reverse direction from a higher to a smaller n value, the ρ^i is given by (Richmond, 1963)

$$\rho^i(n) = 1 - \frac{1}{n^2} [1 - F(n)] \quad (n = n_h/n_s) \quad (15b)$$

The relations in Eq. (15) are for perfect dielectrics, that is, for materials that do not attenuate radiation internally. As discussed by Cox (1965), in the spectral regions where ceramic materials are semitransparent to radiation the extinction coefficient, κ_e , in the complex index of refraction is usually not large enough to significantly affect the surface reflectivity. The absorption coefficient, a , in a material is related to κ_e by $a = 4\pi\kappa_e/\lambda_0$. Since wavelengths λ_0 for thermal radiation are in the micrometer range, only a small value of κ_e is required for this relation to yield a large value for a . If the extinction coefficient κ_e is large enough to influence the interface reflectivity relations, the absorption coefficient will be so large that the radiating layer is essentially opaque unless its thickness is much smaller than the ceramic layers considered here.

The required relations have now been provided to evaluate Eqs. (13) and (14) for the heat flux and temperature distribution in a laminated two-layer region. The equations contain the functions $\Phi(X, \kappa_D)$ and $\Psi(\kappa_D)$ that are available in the literature as tabulated results for a single layer with $n = 1$. For a laminated layer, these functions are inserted corresponding to the optical thickness of each sublayer of the composite. It is not

necessary to solve any integral equations to evaluate the present solution.

A convenient alternative to using the exact numerical solutions for the functions Φ and Ψ in Eqs. (13) and (14) is to use Φ and Ψ available from the diffusion approximation. The accuracy of this approximation is discussed in the next section. The diffusion relations for a plane layer are (Siegel and Howell, 1981)

$$\Psi(\kappa_D) = \frac{1}{\frac{3}{4}\kappa_D + 1} \quad (16a)$$

$$\Phi(X, \kappa_D) = \Psi(\kappa_D) \left[\frac{3}{4}\kappa_D(1-X) + \frac{1}{2} \right] \quad (16b)$$

When used with Eqs. (13) and (14), Eqs. (16) provide rapid predictions of heat flux and temperature distributions for any optical thicknesses and refractive indices of the sublayers in the laminate.

Results and Discussion

For a plane layer in radiative equilibrium with absorption and isotropic scattering and for $n = 1$, the $\Phi(X, \kappa_D)$ and $\Psi(\kappa_D)$ are known functions or can be calculated from Eqs. (5) and (6). These functions are the building blocks required to evaluate the present solution for a two-layer region including refractive index effects and interface reflections. The exact solutions for $\Phi(X, \kappa_D)$ and $\Psi(\kappa_D)$ obtained by solving Eqs. (5) and (6) were examined in detail by Heaslet and Warming (1965). The numerical results used here for $\Phi(X, \kappa_D)$ and $\Psi(\kappa_D)$ (Siegel and Spuckler, 1992) are in excellent agreement with previous work and were carried out to obtain values for a large range of optical thicknesses, $0.1 \leq \kappa_D \leq 100$.

An alternative set of basic functions for $\Phi(X, \kappa_D)$ and $\Psi(\kappa_D)$, which was found to be accurate for the present conditions and is very simple to implement, is to use the diffusion results in Eqs. (16a, b). A comparison of exact and diffusion functions is given in Table 1 for various optical thicknesses. The diffusion results are reasonably accurate, but there are some differences when the optical thickness is small. Results for two-layer laminated regions were calculated from the present analysis using both exact and diffusion functions for the required $\Phi(X, \kappa_D)$ and $\Psi(\kappa_D)$. There was little difference in the results for the laminate, so for convenience the diffusion functions were used for evaluating the illustrative results presented here. For simplicity and sufficient accuracy the diffusion functions are recommended for temperature distribution and heat flux calculations using the analytical Eqs. (13) and (14).

The diffusion functions also have an advantage in the theory used for developing the present equations for two layers where the interfaces are assumed diffuse. Since in the diffusion approximation the radiation is everywhere diffuse, there is no discontinuity in radiative behavior when energy crosses a diffuse interface. In the exact solution for a single plane layer the diffuse energy leaving an internal boundary is no longer diffuse after it travels across the layer. The radiative energy passing across from one layer into another thus undergoes a change in its angular distribution when crossing a diffuse interface between the two regions. This can have a small effect on the temperatures adjacent to the internal interface. This effect is not present when using the diffusion functions for Φ and Ψ .

For the graphic results shown here, $\Phi(X, \kappa_D)$ and $\Psi(\kappa_D)$ were obtained from Eqs. (16), but exact results such as those in Table 1 could have been used. The Ψ_1 and Ψ_2 were substituted into Eq. (13a) to obtain the dimensionless radiative flux through the two layers; the heat flux was checked by evaluating the alternative Eq. (13b). The dimensionless flux was substituted into Eqs. (14a, b) to obtain dimensionless temperature dis-

Table 1 Comparison of results from exact (E) and diffusion (D) solutions
(a) Dimensionless temperature distribution, Φ

x	Optical Thickness							
	$\kappa_D = 0.1$		$\kappa_D = 1$		$\kappa_D = 10$		$\kappa_D = 100$	
	E	D	E	D	E	D	E	D
0	.5710	.5349	.7582	.7143	.9495	.9412	.9948	.9934
0.1	.5541	.5279	.6946	.6714	.8511	.8529	.8974	.8947
0.2	.5397	.5209	.6429	.6286	.7627	.7647	.7994	.7961
0.3	.5262	.5140	.5942	.5857	.6750	.6765	.6998	.6974
0.4	.5130	.5070	.5468	.5429	.5874	.5882	.6000	.5987
0.5	.5000	.5000	.5000	.5000	.5000	.5000	.5000	.5000
0.6	.4870	.4930	.4532	.4571	.4125	.4118	.4000	.4013
0.7	.4738	.4861	.4058	.4143	.3249	.3235	.3002	.3026
0.8	.4603	.4791	.3571	.3714	.2372	.2353	.2007	.2040
0.9	.4459	.4721	.3054	.3286	.1488	.1471	.1026	.1053
1.0	.4290	.4651	.2419	.2857	.0505	.0588	.0052	.0066

(b) Dimensionless heat flux, Ψ

Optical Thickness κ_D	Ψ	
	E	D
0.1	.9157	.9302
1	.5534	.5714
10	.1168	.1177
100	.0122	.0132

Table 2 Interface reflectivities

n_1	n_2	ρ_a^i	ρ_b^i	ρ_c^i	ρ_d^i
1	1	0	0	0	0
1	1.5	0	.0918	.5964	.5964
1	2	0	.1606	.7902	.7902
1	3	0	.2762	.9196	.9196
1.5	3	.5964	.1606	.7902	.9196
2	1	.7902	.7902	.1606	0
2	4	.7902	.1606	.7902	.9604
3	1.5	.9196	.7902	.1606	.5964
4	2	.9604	.7902	.1606	.7902

tributions in each layer. The values of the interface reflectivities were evaluated from Eqs. (15a) and (15b) depending on whether radiation is passing into a region of higher or lower refractive index. The reflectivity values at the four surfaces in Fig. 1 are given in Table 2 for the combinations of n_1 and n_2 values used in Figs. 2-5. In the results that follow, the temperature distributions are plotted against a continuous X coordinate where $X = X_1$ in layer 1 and $X = 1 + X_2$ in layer 2; thus $0 \leq X \leq 2$.

Reciprocal Behavior of Dimensionless Temperatures. Figure 2 illustrates a reciprocal behavior for the temperature results. Compared to Fig. 2(a), both the n values and the optical thicknesses of the two layers have been interchanged in Fig. 2(b). It is noted that rotating Fig. 2(a) 180 deg gives dimensionless temperature distributions that are the same as in Fig. 2(b). It was also found that the radiative heat flux through the laminate does not depend on the order of placement of the two layers relative to the side with larger incident radiation.

Effect of Optical Thickness. Figure 2(a) also illustrates the effect of the optical thicknesses of the two layers. The solid and dashed profiles are respectively for optical thicknesses of the first layer of $\kappa_{D1} = 1$ and 10. The families of curves correspond to optical thicknesses in the second layer of $\kappa_{D2} = 0.1, 1, 3, 10, 30$, and 100. As optical thickness increases, the

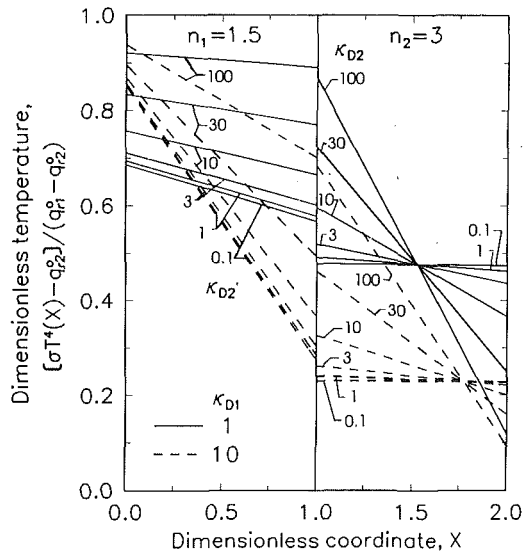


Fig. 2(a) Layer with lower index of refraction adjacent to higher source of radiant energy

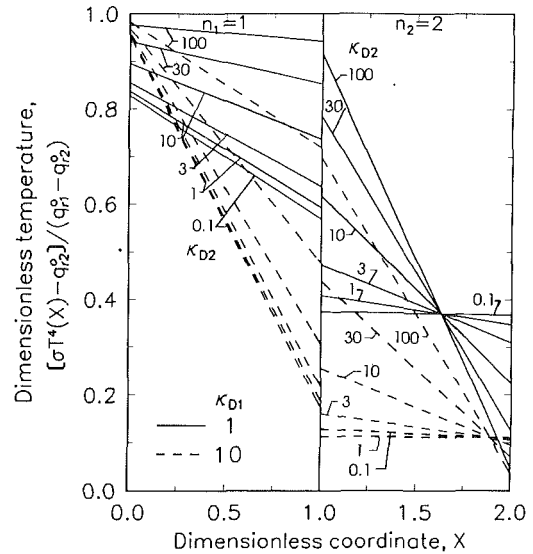


Fig. 3(a) Indices of refraction: $n_1 = 1$ and $n_2 = 2$

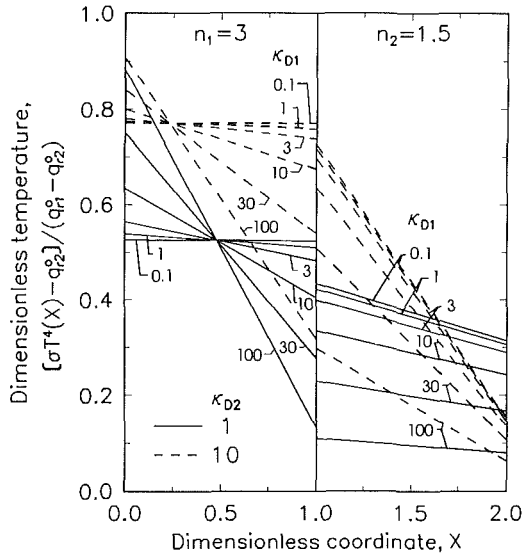


Fig. 2(b) Demonstration of reciprocity by interchanging n and κ_D values

Fig. 2 Dimensionless temperature distributions for indices of refraction $n_1 = 1.5$ and $n_2 = 3$, two optical thicknesses in layer 1, and six optical thicknesses in layer 2 (values reversed in Fig. 2(b))

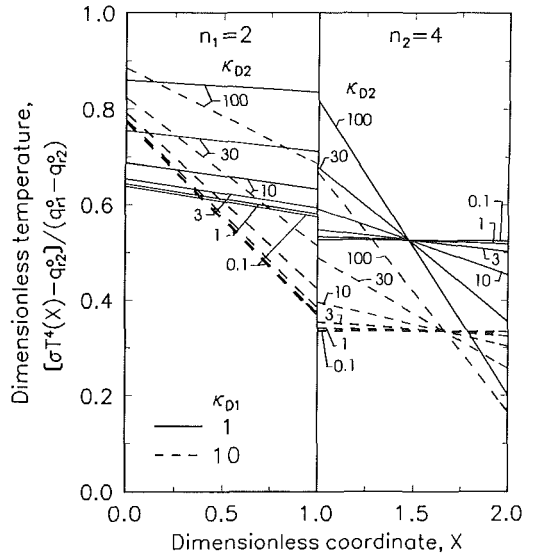


Fig. 3(b) Indices of refraction: $n_1 = 2$ and $n_2 = 4$

Fig. 3 Effect of magnitude of index of refraction on dimensionless temperature distributions in layers as a function of optical thicknesses; ratio $n_2/n_1 = 2$

resistance to radiative heat flow increases so the temperature gradients in the second layer increase. For $\kappa_{D2} = 0.1$ the second layer is optically thin and its temperature distribution is essentially uniform. For $\kappa_{D2} = 100$, however, there is a steep gradient in the second layer. When $\kappa_{D1} = 10$ the large temperature changes in the first layer cause the temperatures in the second layer to be lower than those for $\kappa_{D1} = 1$. The dimensionless radiative heat fluxes are given in Table 3 and they illustrate how the heat flux decreases with increasing optical thickness.

Effect of Magnitude of Refractive Index. The effect of the size of the refractive indices n_1 and n_2 is illustrated in Figs. 2(a), 3(a, b), which form a set of three arrays of temperature distributions. The optical thicknesses are as described in the previous section. The ratio of n_2/n_1 is kept equal to 2 for these three sets of profiles, but the refractive indices increase by factors of 1:1.5:2 in the order of Figs. 3(a), 2(a), and 3(b). Larger refractive indices increase the amount of internal re-

flexion at the two outer interfaces as a result of total reflection when radiation is leaving a material with a higher refractive index. This tends to equalize the temperature distributions within the layers as the n values increase. The reflections at the interface between the layers remain the same because n_2/n_1 is constant.

For $\kappa_{D1} = 1$, increasing the refractive index provides decreased temperatures in the first layer. An increased amount of the incident radiant energy is reflected away at the first interface and does not heat the laminate. Internal reflections increase energy absorption within the laminated region, thereby increasing the average temperature level in the second layer.

Effect of Order of Refractive Indices in Heat Flow Direction. In Fig. 4 the κ_D values are the same as in Fig. 3. The n values, however, are interchanged so the largest refractive index is now adjacent to the environment that provides the largest incident radiation. This changes the amount of totally reflected energy within the layers as compared with Fig. 3. Since total internal reflection is increased in the first layer and

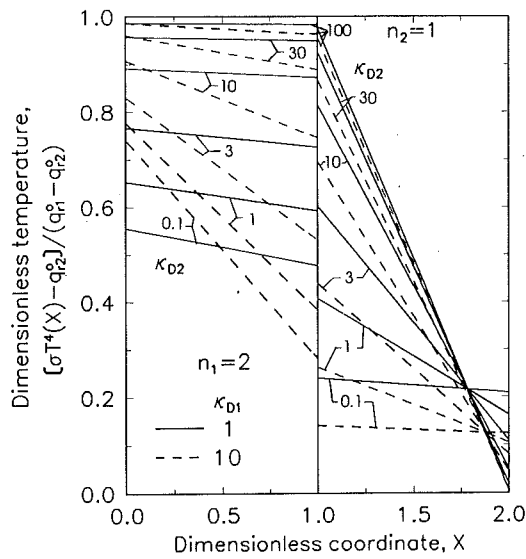


Fig. 4(a) Indices of refraction: $n_1 = 2$ and $n_2 = 1$

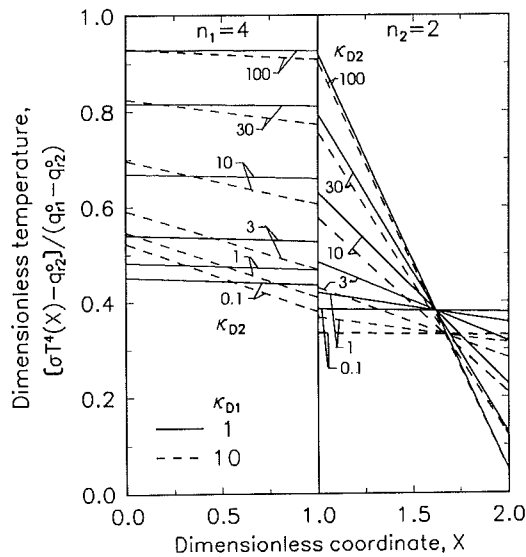


Fig. 4(b) Indices of refraction: $n_1 = 4$ and $n_2 = 2$

Fig. 4 Effect of inverting the indices of refraction as compared with Fig. 3; ratio $n_2/n_1 = 1/2$

decreased in the second, the temperatures become more uniform in the first layer and have steeper gradients in the second. The temperature profiles in the first layer are not as close together as on Fig. 3.

Effect of Changing Refractive Index in One Layer. For all the distributions in Fig. 5 the refractive index in the first layer is retained at $n_1 = 1$. In the second layer the values are: $n_2 = 1, 1.5, 2,$ and 3 . The optical thicknesses in the two layers are equal. Three families of curves are shown for $\kappa_{D1} = \kappa_{D2} = 0.2, 2, 20$. Hence the solid curves for each layer are optically thin, the dashed curves are for an intermediate optical thickness, and the short dashed curves are for a rather thick region.

Consider the solid profiles for $\kappa_{D1} = \kappa_{D2} = 0.2$. When $n = 1$ there are no interface reflections and a continuous temperature profile is obtained through the laminated region. For $n_2 > 1$ the profiles become discontinuous at the internal interface, and as n_2 becomes larger the discontinuity increases. For $\kappa_{D1} = \kappa_{D2} = 0.2$, an increased n_2 raises the temperatures in the first layer and makes the temperatures more uniform in the second layer. For the short dashed curves with $\kappa_{D1} = \kappa_{D2} = 20$, there is a different effect. As n_2 increases, the temperatures

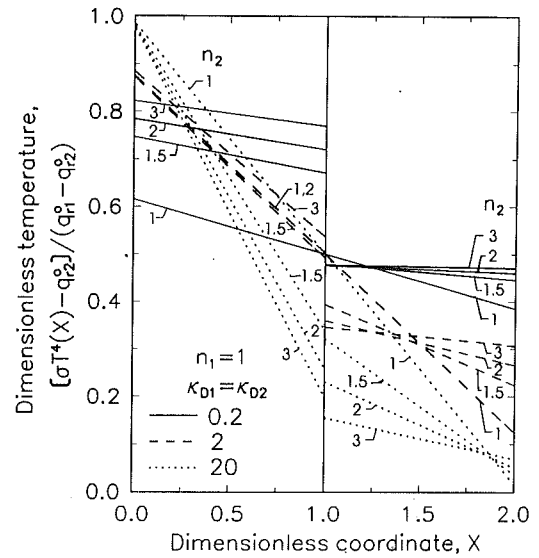


Fig. 5 Effect of index of refraction ratio n_2/n_1 on dimensionless temperature distributions for optical thickness varying from thin to thick

Table 3 Dimensionless radiative heat flux, $q/(q_0^* - q_2^*)$

κ_{D2}	$\kappa_{D1} = 1$					
	$n_1 = 1, n_2 = 2$	$n_1 = 1.5, n_2 = 3$	$n_1 = 2, n_2 = 4$	$n_1 = 2, n_2 = 1$	$n_1 = 2, n_2 = 4$	$n_1 = 4, n_2 = 2$
0.1	0.3447	0.3574	0.3393	0.4175	0.3545	0.3545
1	0.3257	0.3480	0.3345	0.3257	0.3345	0.3345
3	0.2903	0.3290	0.3243	0.2188	0.2972	0.2972
10	0.2102	0.2760	0.2931	0.1018	0.2138	0.2138
30	0.1175	0.1890	0.2299	0.0403	0.1187	0.1187
100	0.0462	0.0899	0.1311	0.0129	0.0464	0.0464

κ_{D2}	$\kappa_{D1} = 10$					
	$n_1 = 1, n_2 = 2$	$n_1 = 1.5, n_2 = 3$	$n_1 = 2, n_2 = 4$	$n_1 = 2, n_2 = 1$	$n_1 = 2, n_2 = 4$	$n_1 = 4, n_2 = 2$
0.1	0.1036	0.1725	0.2158	0.2449	0.3084	0.3084
1	0.1018	0.1703	0.2138	0.2102	0.2931	0.2931
3	0.0981	0.1656	0.2096	0.1598	0.2641	0.2641
10	0.0869	0.1510	0.1961	0.0869	0.1961	0.1961
30	0.0655	0.1206	0.1657	0.0377	0.1130	0.1130
100	0.0352	0.0708	0.1073	0.0127	0.0455	0.0455

n_2	$n_1 = 1$		
	$\kappa_{D1} = \kappa_{D2} = 0.2$	$\kappa_{D1} = \kappa_{D2} = 2$	$\kappa_{D1} = \kappa_{D2} = 20$
1	0.7692	0.2500	0.0323
1.5	0.5065	0.2548	0.0427
2	0.4310	0.2495	0.0479
3	0.3548	0.2316	0.0518

in the first layer are reduced, while the temperatures in the second layer become more uniform as before. For an intermediate optical thickness, $\kappa_{D1} = \kappa_{D2} = 2$, there is a small decrease in temperatures in the first layer as n_2 is increased, and then with a further increase in n_2 the temperatures increase. The radiative heat fluxes in Table 3 show a similar reversal in trend when going from an optically thin to an optically thick layer.

Conclusions

A convenient solution was obtained for temperature distributions and radiative heat fluxes in a laminated two-layer region with radiative energy incident on each outer boundary. The interfaces are assumed diffuse with the intent of modeling interface reflections of a ceramic material. The limiting case

considered here is for a two-layer laminate in radiative equilibrium (no heat conduction) that emits, absorbs, and isotropically scatters radiation. The solution yields results for two laminated layers by using known dimensionless temperature and heat flux functions for a single semitransparent radiating layer with $n = 1$. These functions are combined through the coupling at the interfaces to yield the solution for a two-layer laminated region with $n > 1$. The coupling relations include transmission through the interfaces and all internal reflections within the layers. The result is a set of simple algebraic expressions for the temperature distribution in each of the layers, and for the radiative heat flux through the laminated region. Results were evaluated using the basic functions for a single layer obtained by both exact and diffusion methods. Unless the optical thickness is much smaller than one, the diffusion results are within engineering accuracy, and they provide an especially simple way to compute results for two layers.

Illustrative results are given for a variety of refractive indices and optical thicknesses of the layers. A reciprocity relation was found for the temperature distributions. If the order of the refractive indices of the layers is reversed as well as their optical thicknesses, the temperature distributions become inverted mirror images. It was found that increasing the refractive index in each layer, while keeping their ratio constant, generally makes the temperature profiles more uniform as the result of increased internal reflections. When the refractive index of the second layer is increased, and the first is kept unchanged, the temperatures in the layers can either increase or decrease depending on the layer optical thicknesses.

References

Amlin, D. W., and Korpela, S. A., 1979, "Influence of Thermal Radiation on the Temperature Distribution in a Semi-transparent Solid," *ASME JOURNAL OF HEAT TRANSFER*, Vol. 101, pp. 76-80.

Cox, R. L., 1965, "Fundamentals of Thermal Radiation in Ceramic Materials," in: *Thermal Radiation in Solids*, S. Katzoff, ed., NASA SP-55, pp. 83-101.

Crosbie, A. L., and Shieh, S. M., 1990, "Three-Dimensional Radiative Transfer for Anisotropic Scattering Medium With Refractive Index Greater Than Unity," *Journal of Quantitative Spectroscopy and Radiative Transfer*, Vol. 44, No. 2, pp. 299-312.

Fowle, A. A., Strong, P. F., Comstock, D. F., and Sox, C., 1969, "Computer Program to Predict Heat Transfer Through Glass," *AIAA Journal*, Vol. 7, No. 3, pp. 478-483.

Gardon, R., 1958, "Calculation of Temperature Distributions in Glass Plates Undergoing Heat-Treatment," *Journal of the American Ceramic Society*, Vol. 41, No. 6, pp. 200-209.

Heaslet, M. A., and Warming, R. F., 1965, "Radiative Transport and Wall Temperature Slip in an Absorbing Planar Medium," *International Journal of Heat and Mass Transfer*, Vol. 8, No. 7, pp. 979-994.

Ho, C.-H., and Ozisik, M. N., 1987, "Combined Conduction and Radiation in a Two-Layer Planar Medium With Heat Flux Boundary Conditions," *Numerical Heat Transfer*, Vol. 11, pp. 321-340.

Ping, T. H., and Lallemand, M., 1989, "Transient Radiative-Conductive Heat Transfer in Flat Glasses Submitted to Temperature, Flux, and Mixed Boundary Conditions," *International Journal of Heat and Mass Transfer*, Vol. 32, No. 5, pp. 795-810.

Richmond, J. C., 1963, "Relation of Emittance to Other Optical Properties," *Journal of Research of the National Bureau of Standards*, Vol. 67C, No. 3, pp. 217-226.

Rokhsaz, F., and Dougherty, R. L., 1989, "Radiative Transfer Within a Finite Plane-Parallel Medium Exhibiting Fresnel Reflection at a Boundary," *Heat Transfer Phenomena in Radiation, Combustion and Fires*, ASME HTD-Vol. 106, pp. 1-8.

Siegel, R., and Howell, J. R., 1981, *Thermal Radiation Heat Transfer*, 2nd ed., Hemisphere, Washington, DC.

Siegel, R., and Spuckler, C. M., 1992, "Effect of Index of Refraction on Radiation Characteristics in a Heated Absorbing, Emitting and Scattering Layer," *ASME JOURNAL OF HEAT TRANSFER*, Vol. 114, pp. 781-784.

Tarshis, L. A., O'Hara, S., and Viskanta, R., 1969, "Heat Transfer by Simultaneous Conduction and Radiation for Two Absorbing Media in Intimate Contact," *International Journal of Heat and Mass Transfer*, Vol. 12, pp. 333-347.

Thomas, J. R., Jr., 1992, "Coupled Radiation/Conduction Heat Transfer in Ceramic Liners for Diesel Engines," *Numerical Heat Transfer*, Part A, Vol. 21, pp. 109-120.

Investigation of an Evaporating Extended Meniscus Based on the Augmented Young-Laplace Equation

S. DasGupta

J. A. Schonberg

P. C. Wayner, Jr.

The Isermann Department of
Chemical Engineering,
Rensselaer Polytechnic Institute,
Troy, NY 12180-3590

The microscopic details of fluid flow and heat transfer near the contact line of an evaporating extended meniscus of heptane formed between a horizontal substrate and a "washer" were studied at low heat fluxes. The film profile in the contact line region was measured using ellipsometry and microcomputer-enhanced video microscopy, which demonstrated the details of the transition between a nonevaporating superheated flat thin film and an evaporating curved film. Using the augmented Young-Laplace equation, the interfacial properties of the system were initially evaluated in situ and then used to describe the transport processes. New analytical procedures demonstrated the importance of two dimensionless parameters. Both fluid flow and evaporation depend on the intermolecular force field, which is a function of the film profile. The thickness and curvature profiles agreed with the predictions based on interfacial transport phenomena models. The heat flux distribution and the pressure field were obtained. Since there are significant resistances to heat transfer in this small system due to interfacial forces, viscous stresses, and thermal conduction, the "ideal constant heat flux" cannot be attained. The description of the pressure field gives the details of the coupling between the disjoining and capillary pressures.

Introduction

The augmented Young-Laplace equation has been used to model the "pressure jump," $P_l - P_v$, at the evaporating liquid-vapor interface in the contact line region (Potash and Wayner, 1972; Renk et al., 1978; Moosman and Homsy, 1980; Cook et al., 1981; Wayner, 1991):

$$P_l - P_v = \frac{B}{\delta^n} - \sigma K \quad (1)$$

$$\frac{B}{\delta^n} = \frac{B}{\delta^4} = -\Pi, \quad \delta \geq 40 \text{ nm} \quad (2)$$

$$\frac{B}{\delta^n} = \frac{A}{\delta^3} = -\Pi, \quad \delta \leq 20 \text{ nm} \quad (3)$$

where P_l is the liquid pressure, P_v is the vapor pressure, $6\pi A$ is the Hamaker constant (negative for a completely wetting liquid), B is the retarded dispersion constant for thicker films, $\delta(x)$ is the film thickness, K is the curvature, and σ is the surface tension. The first term on the right-hand side of Eq. (1) is called the disjoining pressure, $-\Pi$, and it represents the change in body force within the liquid due to long-range van der Waals forces between the liquid and solid over a narrow range of thickness (Derjaguin and Churaev, 1976). The second term is the classical equation of capillarity. Here, we use a "pressure jump" model to account for both the disjoining and capillary pressures while keeping in mind that the disjoining pressure is really a model of the film thickness dependent intermolecular force field. The shape-dependent intermolecular force field can be used to control fluid flow and heat transfer. Conversely, transport processes are studied by measuring the temperature field and the liquid film shape. Truong and Wayner (1987) discussed the restrictions on the use of these simple expressions for the disjoining pressure. Potash

and Wayner (1972) initially used Eq. (1) to model evaporation from an extended meniscus, which consisted of the intrinsic meniscus described by the classical equation of capillarity, σK , and a thin adsorbed film extending beyond the intrinsic meniscus described by the disjoining pressure, $-\Pi$. These concepts are of generic importance in such diverse fields as spreading, drying, lubrication, condensation, boiling, heat pipes, and thermosyphons.

To place this work in perspective we first discuss four related publications, which have different emphases. Wu and Peterson (1991) studied a wickless micro-heat pipe with dimensions of $1 \times 1 \times 10$ -100 mm. Since the fluid had a finite contact angle, they successfully used the classical equation of capillarity to describe the internal fluid dynamics of this integral device. Xu and Carey (1990) used a completely wetting fluid to study film evaporation from a microgrooved surface with grooves 64 μm wide and 190 μm deep. The classical equation of capillarity was used in the apex region of the groove and the disjoining pressure equation was used in the thin film region on the side walls to describe fluid flow. Although these two studies did not completely validate the models, the models appeared to provide a realistic treatment of the integral data. In order to study the microscopic details of the augmented Young-Laplace model, Cook et al. (1981) used a scanning microphotometer to determine the heat transfer characteristics of the evaporating contact line region of a film on an inclined flat plate partially immersed in a liquid pool. A completely wetting fluid was studied by measuring the film thickness profile in the thickness range $10^{-7} < \delta(x) < 10^{-5}$ m. The results supported the hypothesis that fluid flow and evaporation in the contact line region of a thin film results from a change in the thin film thickness profile. Truong and Wayner (1987) used a photo-scanning ellipsometer with an attached interferometer to measure simultaneously both regions of an equilibrium extended meniscus down to a thickness of 25 nm. The accuracy of the augmented Young-Laplace equation for describing the isothermal equilibrium meniscus was confirmed. Herein, new an-

Contributed by the Heat Transfer Division for publication in the JOURNAL OF HEAT TRANSFER. Manuscript received by the Heat Transfer Division December 1991; revision received June 1992. Keywords: Evaporation, Flow Visualization, Thin Film Flow. Associate Technical Editor: L. C. Witte.

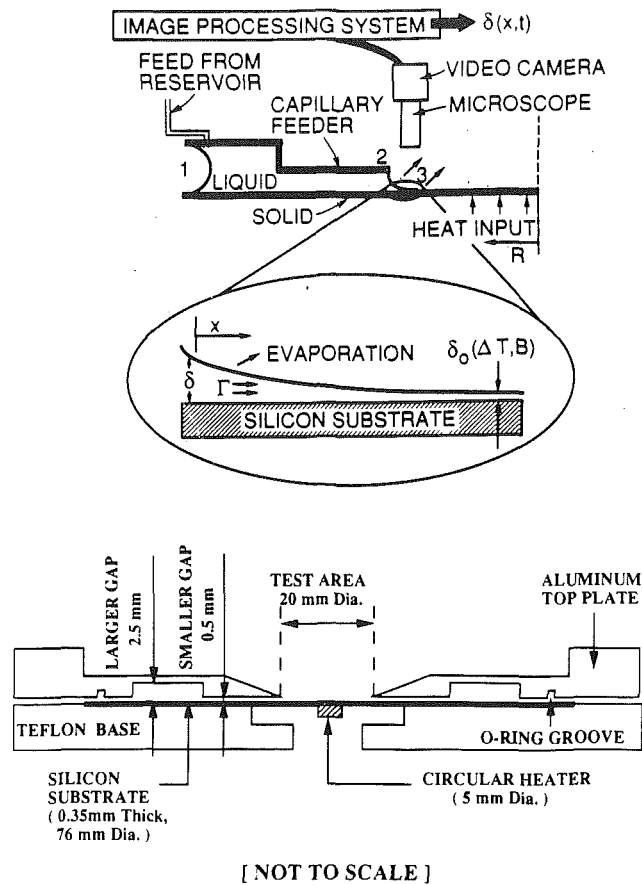


Fig. 1 Cross-sectional view of capillary feeder

alytical techniques are used to analyze more detailed data obtained using improved experimental equipment.

Different experimental techniques have been used to study the equilibrium disjoining pressure of a simple system like an alkane on a wetting substrate. Derjaguin and Zorin (1957) and Gee et al. (1989) studied the adsorption of alkanes on substrates at high disjoining pressures. Blake (1975) measured low dis-

joining pressures of alkanes on α -alumina and Ingram (1974) studied very low disjoining pressures of alkane films on a silica plate. Truong and Wayner (1987) and Sujanani and Wayner (1990) measured the profile in both the low disjoining pressure region just above the transition region and the capillary pressure region. These results demonstrate that the DLP theory (Dzyaloshinskii et al., 1961) correctly predicts the value of the Hamaker constant but the value is very sensitive to contamination, temperature gradients, etc.

The isothermal and the evaporating meniscus thickness profiles in the region controlled by capillarity have been measured as a function of heat flux using interferometry (e.g., Mirzamoqhadam and Catton, 1988; Voutsinos and Judd, 1985; Renk and Wayner, 1979; Cook et al., 1981; Kayser et al., 1985; Truong and Wayner, 1986). The profile of a wetting liquid near the transition region, where both capillary and van der Waals dispersion forces are equally important, has been measured using interferometry and ellipsometry (Bascom et al., 1964; Truong and Wayner, 1987; Sujanani and Wayner, 1990, 1991; DasGupta et al., 1991).

In the current research using an ellipsometer and a micro-computer-enhanced interferometer based on video microscopy (Fig. 1), the advantages of previously developed optical techniques are significantly enhanced. In this case, each pixel acts as a photometer for ease of data recording and analysis. The new procedures allow the critical interfacial properties of the system to be initially evaluated in situ and then used to obtain additional details concerning the evaporation process. The resulting details qualitatively confirm the use of the augmented Young-Laplace equation model to describe transport processes in the contact line region. The smallness of the emphasized subregion (thickness $\delta < 3 \mu\text{m}$ with a length of approximately $200 \mu\text{m}$) still precludes the use of a heat balance to obtain a quantitative confirmation. However, a macroscopic heat balance for the whole system was obtained and described in a preliminary presentation of the data by DasGupta et al. (1991). *The new analytical procedures presented herein significantly enhance the use of the data to describe the microscopic transport processes.* Using the new procedure, two dimensionless groups are found to be important: one represents the ratio of capillarity to disjoining effects; the other represents the resistance to thermal conduction. The heat flux distribution and the details of the pressure field are obtained. We find that,

Nomenclature

$A = 6\pi\bar{A}$ = Hamaker constant	Q = power input setting	η = dimensionless film thickness = δ/δ_o
a = coefficient defined by Eq. (7)	R = universal gas constant; radial distance	κ = dimensionless parameter
b = coefficient defined by Eq. (7)	t = time	λ = dimensionless length
B = modified Hamaker constant	ΔT = characteristic temperature difference between solid and vapor	ν = kinematic viscosity
C = evaporation coefficient	T_{lv} = temperature of the liquid-vapor interface	ξ = dimensionless distance
Δh_m = heat of vaporization per unit mass	T_s = substrate temperature, constant	Π = disjoining pressure
Δh = heat of vaporization per unit volume	T_v = temperature of the vapor, constant	Π_o = characteristic pressure
K = curvature	V_l = molar volume of the liquid	ρ = density
k = thermal conductivity of the liquid film	x = coordinate distance along the substrate	σ = surface tension
l = characteristic length (Eq. (15))	β = constant; see Eqs. (23) and (24)	ϕ = dimensionless pressure difference
\dot{m} = evaporative mass flux	Γ = theoretical mass flow rate	
$\dot{m}^{id} = \alpha(T_s - T_v)$ = ideal evaporative mass flux	δ_o = reference film thickness	
M = molecular weight	δ = thickness of the liquid film	
\bar{M} = dimensionless interfacial heat or mass flux	Δ = difference	
P_v = reference vapor pressure	ϵ = dimensionless parameter	
P_l = liquid pressure		
P_{lv} = vapor pressure at liquid-vapor interface		

Subscripts

l = liquid
lv = liquid-vapor
v = vapor
s = solid

Superscripts

id = ideal, based on kinetic theory
' = derivatives

since there are significant resistances to heat transfer due to interfacial forces, viscous stresses, and thermal conduction in this small system, the "ideal constant heat flux" based on kinetic theory cannot be obtained. The resulting description of the pressure field gives the details of the coupling between the disjoining and capillary pressures.

Experimental

Herein, only a few comments concerning the experimental details are presented so that the analytical procedures can be emphasized. The experimental details are given by DasGupta et al. (1991) and Wayner et al. (1991). A cross-sectional diagram of the circular capillary feeder system is shown in Fig. 1. Liquid flowed from a reservoir (maintained at a constant level) as a result of a difference in capillary and disjoining pressure (caused by intermolecular forces) and formed a meniscus at the edge of the thinner gap at position 2. The contact line region, area 3, governed the critical initial condition for the stability and behavior of the evaporating meniscus and hence the performance of the capillary feeder system. In the thinnest portion of the meniscus represented by δ_p , evaporation did not occur. The distance between the edge of the heater (of 5 mm diameter) and the location of the first destructive fringe ($\delta \sim 0.1 \mu\text{m}$) was 6 mm.

An aluminum trapezoidal cell chamber was fabricated to enclose the circular capillary feeder system, which allowed for measurable continuous liquid feed with simultaneous interferometric and ellipsometric measurements of film thicknesses. Two wide circular grooves with different channel depths as shown in Fig. 1 were made by a milled aluminum washer pressing against a smooth silicon wafer with a Teflon encapsulated O-ring in between. The difference in groove depths maintained a steady flow of liquid toward the center of the silicon plate by capillary pumping to replenish the amount evaporated. The circular test area and a circular heat source, made by baking a platinum compound, naturally eliminated edge effects that were present in the previous rectangular design. Small (0.3 mm) chromel-alumel thermocouples (not shown) were attached 1.5 mm apart at the bottom of the silicon substrate to measure the absolute temperature level with an accuracy of $\pm 0.1^\circ\text{C}$. Special optical windows were made at 70 deg angles with the base for maximum ellipsometric sensitivity. The capillary feeder was connected to an outside reservoir (a graduated cylinder that contained pure test liquid) by means of a very thin capillary tube, which supplied fresh liquid by capillary suction to replenish the liquid evaporated in the test area. The liquid levels were manually kept the same in the reservoir and the feeder. The total rate of evaporation was calculated by measuring the amount of liquid added to the outside reservoir.

A schematic diagram of the experimental setup is shown in Fig. 2. A conventional null ellipsometer with the configuration of light source, polarizer, fixed compensator, sample, analyzer, microscope objective lenses, and a photodetector was used to determine the film thickness of the flat adsorbed film that formed ahead of the meniscus. Interference phenomena were used to determine the profile of the capillary meniscus in the thickness range $\delta \geq 0.1 \mu\text{m}$. The index of refraction of the fluid was assumed to be that of a bulk liquid and equal to 1.387. The sensitivity and accuracy of the ellipsometer were confirmed by measuring the optical constants of standard substrates (e.g., measured optical constants for RCA cleaned silicon wafer were $n_s = 3.87 \pm 0.01$, $k_s = 0.04 \pm 0.01$, whereas literature values are $n_s = 3.882$, $k_s = 0.019$). The errors due to the optical imperfections present in the windows were also measured. The final estimate was an error of about $\pm 4 \text{ \AA}$ for the adsorbed thin film region. The maximum error in the capillary meniscus region was less than $0.01 \mu\text{m}$ based on repeated measurements and the absolute value of the error

SYMBOLS

A: Analyzer	M: Microscope
C: Compensator	MUL: Monochromatic Unipolarized Light
CPL: Circularly Polarized Light	P: Polarizer
D: Detector	PM: Photomultiplier
F: Filter	PPL: Plane Polarized Light
FCG: Frame Code Generator	VA: Variable Aperture
HRV: Image Resolution VCR	SS: Scanning Stage
IPM: Image Processing Microcomputer	VC: CCD Video Camera
L: Helium-Neon Laser	

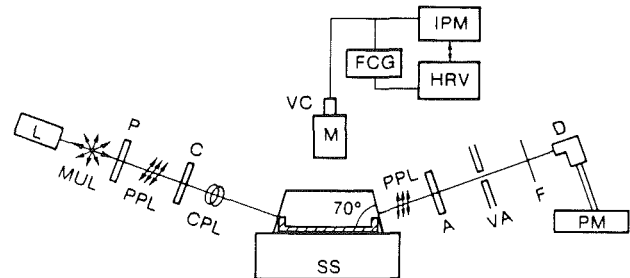


Fig. 2 Schematic diagram of experimental setup

decreased (always within 5 percent) as the thin film was approached. The estimated errors in film thicknesses in these two regions were included in the captions of the experimentally obtained film thickness profile figures. We used a high-power, long working distance microscope (Wild Model M420) with coherent light ($\lambda = 525 \text{ nm}$) at normal incidence and the reflected interference patterns were captured using a CCD camera (Sony HVM200).

To automate data acquisition, improve data resolution, and enhance data analysis, we analyzed the interferometric images using an image processing system. Briefly, the system consisted of a 16 MHz IBM-PC286 clone computer equipped with real time frame grabber and frame processor boards (DT-2851 and DT-2858 from Data Translation Inc.). The image captured from the microscope through a CCD camera was digitized into 490 (vertical) \times 512 (horizontal) space pixels and assigned one of 256 possible grey values representing an intensity from 0 (black) to 255 (white). Thus the image area, already magnified considerably by the microscope, was divided into microscopic pixels, which acted as individual, simultaneous light sensors. Each picture provided data on one frame, i.e., 1/30th of a second in real time. The interferometric fringes formed were parallel because the radial distance from the center [$\sim 8.8 \text{ mm}$] was large compared to the meniscus width [$\sim 0.2 \text{ mm}$]. When viewed at high magnification [area viewed $\sim 0.3 \text{ mm} \times 0.3 \text{ mm}$], the fringes were almost invariant in a direction perpendicular to the radius and could therefore be averaged spatially to improve the signal/noise ratio. The light level was optimized to prevent pixel saturation (excessive light) and to ensure linearity of the analog to digital conversion. Light below a certain level drastically increased the signal/noise ratio. For our system the best combination of resolution, light level, signal/noise ratio, and magnification was found by adding a $4.0 \times$ effective magnification in the tube. Each pixel represented a diameter of $0.625 \mu\text{m}$. Transient data was captured by continuously recording on a high quality U-Matic Sony VO-9600 VCR. The VCR had a B/W resolution of more than 300 lines. A Sony FCG-700 Frame Counter superimposed each frame with a permanent identification number.

Silicon was used as the substrate because of its reflective, polished, smooth, easily available, and reproducible surface. We note that a native oxide about 3–5 nm thick was always present on the surface. All cleaning procedures were done inside a class-100 clean hood. The cell was first immersed in pure ethanol (absolute—200 proof) for 6 to 7 hours. The cell

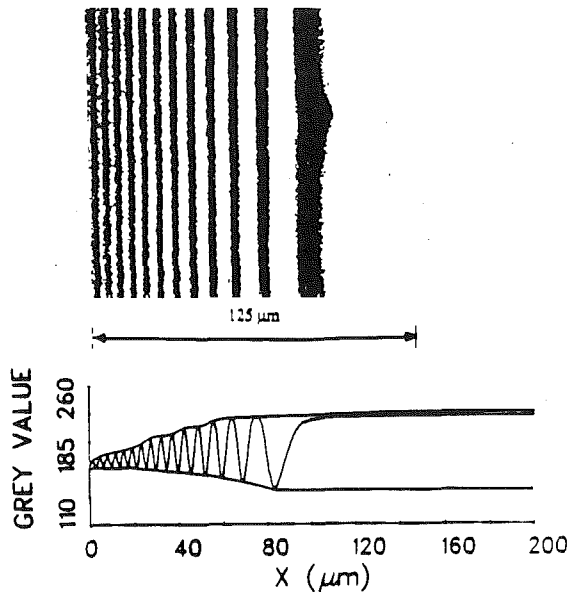


Fig. 3 Interface bands and reflectivity profile

parts were again rinsed with fresh alcohol and then dried in an oven at 180°C. Extreme care was taken to ensure that no dust particles or impurities could come in contact with the silicon wafer. After drying, the cell parts were rinsed with pure test fluid and blow dried with extra-dry grade nitrogen. Heptane was used as received from Aldrich (Gold label, 99+ percent). The system was left to equilibrate with the surroundings for 3 hours before taking data. An optical interference pattern representing the thickness profile was readily observed (Fig. 3). From that a plot of the pixel grey value versus distance was extracted. The grey value at each pixel was a measure of the reflectivity. As is evident from Fig. 3, the reflectivity underwent a cyclic change with increase in film thickness. The computer program scanned the peaks and valleys and filtered the noise from the real peaks/valleys. It then interpolated peak/valley envelopes and by analyzing the relative reflectivity of any pixel with respect to these (dark and light pixel envelopes), determined a film thickness at every pixel (DasGupta et al., 1991).

Experimental Results

Two examples of the measured thickness profiles (with estimated errors in caption) are shown in Fig. 4. The profiles were shifted on the x axis to the same relative position at a fixed thickness. The adsorbed film thicknesses in the flat region were $\delta_0 = 7.5$ nm and $\delta_0 = 15$ nm. The profile for $\delta_0 = 15$ nm can be termed as a "very near-equilibrium case with very small evaporation," whereas $\delta_0 = 7.5$ nm is a "near-equilibrium case with small evaporation." Subsequent analysis and discussion in this paper will clarify these terminologies. The next figure (Fig. 5) shows $\delta^{1/2}$ versus distance plots obtained during evaporation with controlled rates of energy input, Q . These two figures clearly show that the isothermal profiles were more spread out and that the thickness of the adsorbed film, δ_0 , decreased with an increase in power input (surface temperature). In an isothermal horizontal system of spreading liquid on a solid substrate at the exit of a capillary, the curvature should remain constant in the region where dispersion forces can be neglected. So the film profile in this range approximates a parabola and a plot of $\delta^{1/2}$ versus x is a straight line. If the curvature is constant, it is related to the slope of this line as $K_c = 2(\delta^{1/2}/dx)^2$. The experimental values of $\delta^{1/2}$ are given in Figs. 4 and 5. For the case where $\delta_0 = 15$ nm, $\delta^{1/2}$ versus x is nearly a straight line, which means the system was very close to isothermality, but for $\delta_0 = 7.5$ nm the line

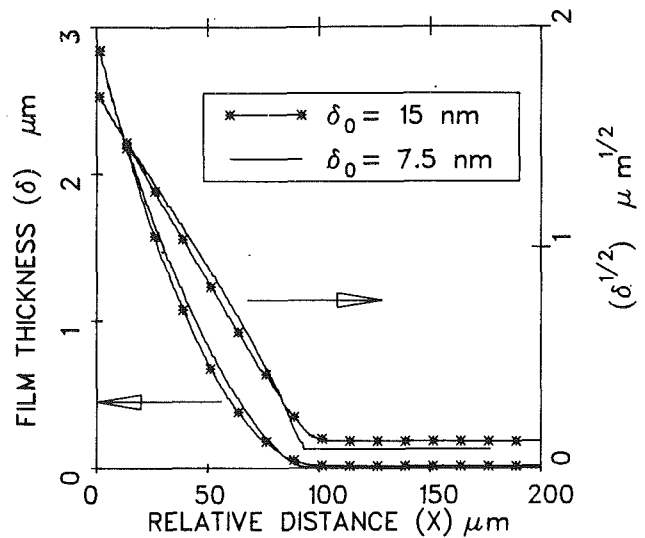


Fig. 4 Film thickness profile for heptane on silicon with a native surface oxide (very near equilibrium with very small evaporation, $Q = 0.0$ W, $\delta_0 = 15 \pm 0.4$ nm, and near equilibrium with small evaporation, $Q = 0.0$ W, $\delta_0 = 7.5 \pm 0.4$ nm). The data are essentially continuous for the capillary region since a pixel measures a region with a diameter of 0.625 μm . The maximum error in δ in the capillary region is 0.01 μm and the absolute value of the error decreases with decrease in film thickness (always with 5 percent).

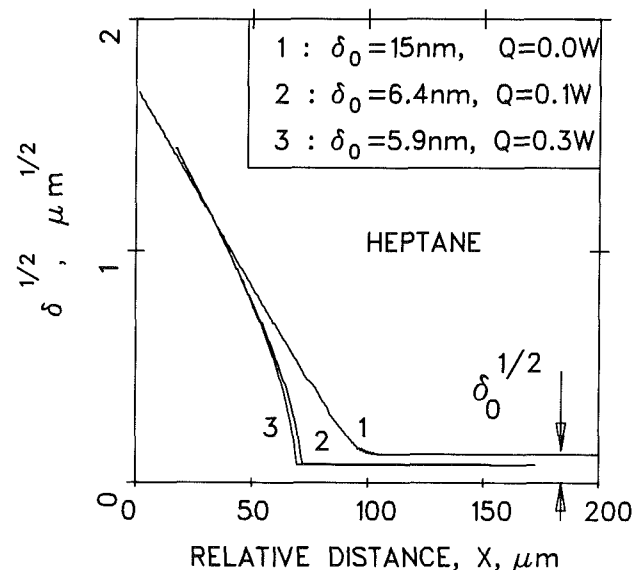


Fig. 5 $\delta^{1/2}$ versus X (very near equilibrium with very small evaporation, $\delta_0 = 15 \pm 0.4$ nm and evaporation with controlled rate of heat inputs, $\delta_0 = 6.4 \pm 0.4$ nm and 5.9 ± 0.4 nm). The data are essentially continuous for the capillary region since a pixel measures a region with a diameter of 0.625 μm . The maximum error in δ in the capillary region is 0.01 μm and the absolute value of the error decreases with decrease in film thickness (always within 5 percent).

bends downward, showing the presence of a curvature gradient and hence some evaporation. Although the heater was off, $Q = 0$, a small amount of heat conduction from the surroundings might have caused the phase change. Figure 6 is another example of $\delta^{1/2}$ versus x profile. The data clearly show the presence of a curvature gradient, a transition region, and an adsorbed film.

Theoretical

The immediate theoretical precursors to this work are the studies of Wayner et al. (1976), Moosman and Homsy (1980),

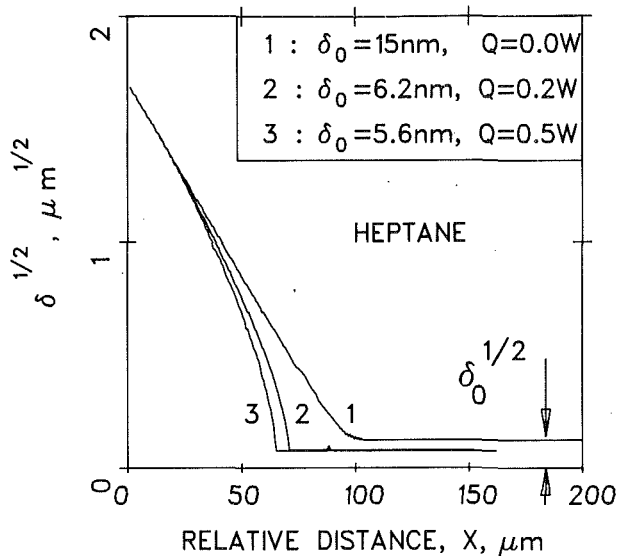


Fig. 6 $\delta^{1/2}$ versus X (very near equilibrium with very small evaporation, $\delta_0 = 15 \pm 0.4$ nm and evaporation with controlled rate of heat inputs, $\delta_0 = 6.2 \pm 0.4$ nm and 5.6 ± 0.4 nm). The data are essentially continuous for the capillary region since a pixel measures a region with a diameter of $0.625 \mu\text{m}$. The maximum error in δ in the capillary region is $0.01 \mu\text{m}$ and the absolute value of the error decreases with decrease in film thickness (always within 5 percent).

Table 1 Characteristics of the evaporating thin film

Power Input (W)	δ_0 (nm)	ϵ	\bar{A} (Joules)	ΔT ($^{\circ}\text{K}$)	\dot{m}^{id} ($\text{kg}/\text{m}^2 \cdot \text{sec}$)	q^{id} (W/m^2)
0.0	15.0 ± 0.4	2.50	1.27×10^{-22}	4.51×10^{-5}	6.83×10^{-5}	2.48×10^1
0.1	6.4 ± 0.4	1.10	1.23×10^{-22}	5.61×10^{-4}	8.50×10^{-4}	3.08×10^2
0.2	6.2 ± 0.4	1.13	1.15×10^{-22}	5.79×10^{-4}	8.76×10^{-4}	3.18×10^2
0.3	5.9 ± 0.4	1.10	1.13×10^{-22}	6.60×10^{-4}	9.99×10^{-4}	3.62×10^2
0.5	5.6 ± 0.4	1.05	1.14×10^{-22}	7.60×10^{-4}	1.15×10^{-3}	4.17×10^2
2.0	4.8 ± 0.4	1.60	0.88×10^{-22}	1.08×10^{-3}	2.44×10^{-3}	8.86×10^2

and Wayner (1991). At steady state, liquid flows in the film because of evaporation, which is a function of local superheat and pressure. The tendency of the liquid to evaporate is reduced by adsorption (spreading system) and a negative capillary pressure. The local superheat is the temperature difference between the liquid-vapor interface, T_{lv} , and the vapor phase, T_v , which is presumed to be isothermal and pure. In this study the adsorption forces are restricted to the London-van der Waals dispersion force and the film is assumed to be fairly flat. Because of the heat conduction resistance of the film the liquid-vapor interface of the thicker portions of the film will be less superheated than the thinner portions. In the ultrathin region, due to the strong liquid-solid intermolecular force field, the film does not evaporate even though it is superheated. Therefore, we expect the evaporation rate to be highest where the film thickness is moderate. The variation of surface tension with temperature is neglected. Marangoni flow is expected to be relatively small because of the purity of the fluid and small temperature variation along the interface. This and the constant ΔT assumptions used below are justified by the following experimental observation. The temperature gradient in the ra-

dial direction in the silicon substrate for the $Q = 0.5$ W case was approximately $10^{-2} \text{ }^{\circ}\text{C}/\text{m}$. The length of the region studied with a nonuniform temperature where evaporation occurred was approximately 10^{-4} m. Therefore the average temperature change along the plate in this region where evaporation occurred was $10^{-2} \text{ }^{\circ}\text{C}$. The average temperature difference across the liquid film and interface, ΔT , reported in Table 1 was of the order of $10^{-4} \text{ }^{\circ}\text{C}$. Therefore, we feel that the constant substrate temperature assumption was justified.

The liquid pressure, P_l , and the vapor phase pressure, P_v , are related by the following form of Eq. (1):

$$P_l - P_v = \frac{\bar{A}}{\delta^3} - \sigma \frac{d^2 \delta}{dx^2} [1 + (\delta')^2]^{3/2} \quad (4)$$

Hereafter, the simplified form of curvature in which $\delta' \ll 1$ is valid and used for the fairly flat film experimentally studied. Lubrication theory relates the mass flow rate in a slightly tapered thin film to the pressure gradient in the flow direction:

$$\Gamma(x) = \frac{-1}{3\nu} \delta^3 \frac{d}{dx} [P_l] \quad (5)$$

where $\Gamma(x)$ is the mass flow rate and ν is the kinematic viscosity. Following Wayner et al. (1976, 1991), the evaporative flux is modeled as a function of the temperature and pressure jumps at the interface according to the expression

$$\dot{m} = a(T_{lv} - T_v) + b(P_l - P_v) \quad (6)$$

where \dot{m} is the evaporative flux, T_{lv} is the temperature of the liquid-vapor interface, and T_v is the temperature of the vapor. The coefficients a and b are defined as

$$a = C \left(\frac{M}{2\pi R T_{lv}} \right)^{1/2} \left(\frac{P_v M \Delta h_m}{R T_v T_{lv}} \right), \quad b = C \left(\frac{M}{2\pi R T_{lv}} \right)^{1/2} \left(\frac{V_l P_v}{R T_{lv}} \right) \quad (7)$$

C is the accommodation coefficient taken to be 2.0, M is the molecular weight, P_v is the vapor pressure at temperature, T_v , V_l is the molar volume of the liquid. Δh_m is the enthalpy of vaporization per unit mass, at temperature T_{lv} . In practice the temperature T_{lv} is unknown. However, the liquid-vapor interface temperature and the substrate temperature are related by the one-dimensional conduction heat transfer equation:

$$\frac{k}{\delta} (T_s - T_{lv}) = \dot{m} \Delta h_m \quad (8)$$

where k is the thermal conductivity of the liquid film. Following Moosman and Homsy (1980), Eqs. (6) and (8) may be combined to eliminate T_{lv} in favor of T_s :

$$\dot{m} = \frac{1}{1 + \frac{a \Delta h_m}{k} \delta} [a(T_s - T_v) + b(P_l - P_v)] \quad (9)$$

This equation and Eq. (4) clearly demonstrate the direct effect of film thickness, curvature, and intermolecular forces on the evaporation rate. The temperature difference $\Delta T = T_s - T_v$ is taken to be a constant. This model implies that the vapor and solid phases do not present significant resistances to evaporation. We note that the thermal conductivity of silicon is very large. The local evaporation rate is linked to the flow rate in the film through a material balance:

$$\frac{d\Gamma}{dx} = -\dot{m} \quad (10)$$

The coupled differential equations are thus Eq. (4) and

$$\frac{1}{3\nu} \frac{d}{dx} \left(\delta^3 \frac{dP_l}{dx} \right) = \frac{1}{1 + \frac{a \Delta h_m}{k} \delta} [a \Delta T + b(P_l - P_v)] \quad (11)$$

Next the variables are nondimensionalized. Consider a strictly flat film, for which $\delta(x, t) = \delta_0$. There is no pressure gradient in such a film. Therefore the right-hand side of Eq. (11) must be zero. Hence,

$$b(P_l - P_v) = -a\Delta T; \quad \frac{\bar{A}}{\delta_0^3} = -\frac{a}{b} \Delta T \quad (12)$$

If δ_0 is so chosen, the flat film is a solution to the governing equations, Eqs. (4) and (11). The reference thickness is thus fixed and the reference pressure is the magnitude of the pressure of such a film. This pressure is given by Eq. (12) as

$$\Pi_0 = \left(\frac{a}{b}\right) \Delta T \quad (13)$$

The dimensionless pressure difference is defined as

$$\phi = (P_l - P_v) / \Pi_0 \quad (14)$$

The scaling of x is now stipulated by Eq. (11) as:

$$l = \sqrt{\frac{-\bar{A}}{\nu a \Delta T}}; \quad \bar{A} < 0 \quad (15)$$

\bar{A} is negative for a spreading film and $\dot{m}^{id} = a(T_s - T_v) = a\Delta T$ is the characteristic ideal evaporative mass flux at the interface based on kinetic theory with $T_{lv} = T_s$ and $P_l = P_v$. The dimensionless position and thickness are defined as $\xi = x/l$ and $\eta = \delta/\delta_0$. The dimensionless forms of Eqs. (11) and (4) are

$$\frac{1}{3} \frac{d}{d\xi} \left(\eta^3 \frac{d\phi}{d\xi} \right) = \frac{1}{1 + \kappa\eta} (1 + \phi) \quad (16)$$

$$\phi = -\frac{1}{\eta^3} - \epsilon \frac{d^2\eta}{d\xi^2} \quad (17)$$

where the parameters κ and ϵ are

$$\kappa = \frac{a\Delta h_m \delta_0}{k}; \quad \epsilon = \frac{\sigma \delta_0 b \nu}{-\bar{A}} \quad (18)$$

The parameter κ is a measure of the importance of the resistance of the film to thermal conduction. The second term in the right-hand side of Eq. (17) is the dimensionless curvature. The parameter ϵ is a measure of the importance of capillary pressure effects relative to disjoining pressure effects.

Two far-field conditions are imposed on the solution. The first condition is

$$\text{for } \xi \rightarrow \infty: \eta \rightarrow 1; \quad \phi \rightarrow -1 \quad (19)$$

The film thickness is assumed to approach asymptotically the nonevaporating thin film thickness mentioned previously. The second condition is

$$\text{for } \xi \rightarrow -\infty: \eta \rightarrow \infty; \quad \phi \rightarrow \phi_m \quad (20)$$

Numerical Solution

The governing equations, Eqs. (16) and (17), are transformed with the substitution $\lambda = \xi/(\epsilon)^{1/2}$ to yield,

$$\frac{1}{3} \frac{d}{d\lambda} \left(\eta^3 \frac{d\phi}{d\lambda} \right) = \frac{1 + \phi}{1 + \kappa\eta} \quad (21)$$

$$\phi = -\frac{1}{\eta^3} - \frac{d^2\eta}{d\lambda^2} \quad (22)$$

The farfield behavior described by Eq. (19) may be further described by analysis of Eqs. (21) and (22), using a Taylor series for η near 1 and ϕ near -1 . The result from Schonberg et al. (1992) is (as $\lambda \rightarrow \infty$)

$$\eta \rightarrow 1 + \beta_0 \exp\left(-\lambda \sqrt{\frac{3\epsilon}{\kappa+1}}\right) + \beta_1 \exp(-\lambda\sqrt{3}) \quad (23)$$

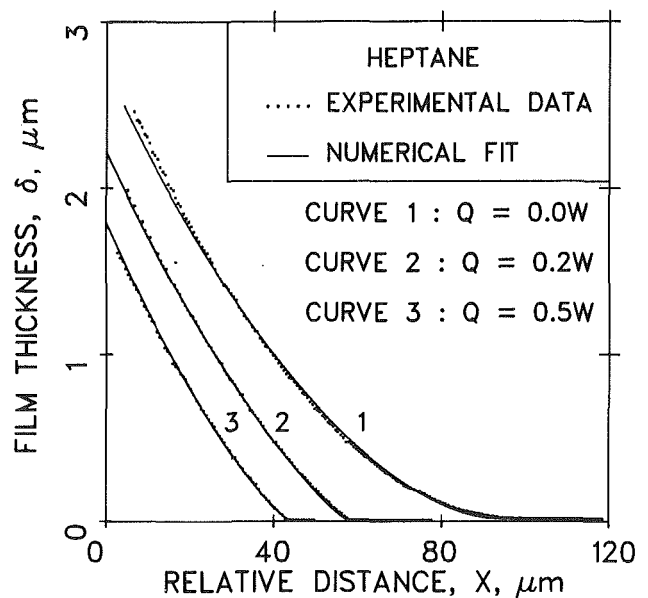


Fig. 7 Comparison of theory and experiments: curve 1: $Q = 0.0$ W, $\delta_0 = 15 \pm 0.4$ nm, $\kappa = 6.48 \times 10^{-2}$, $\epsilon = 2.5$, $\beta_0 = -1.870 \times 10^{-4}$, $\beta_1 = 1.0 \times 10^{-2}$, Curve 2: $Q = 0.2$ W, $\delta_0 = 6.2 \pm 0.4$ nm, $\kappa = 2.67 \times 10^{-2}$, $\epsilon = 1.13$, $\beta_0 = -6.059 \times 10^{-3}$, $\beta_1 = 1.0 \times 10^{-2}$, Curve 3: $Q = 0.5$ W, $\delta_0 = 5.6 \pm 0.4$ nm, $\kappa = 2.44 \times 10^{-2}$, $\epsilon = 1.05$, $\beta_0 = -8.645 \times 10^{-3}$, $\beta_1 = 1.0 \times 10^{-2}$

$$\phi \rightarrow -1 + 3\beta_0 \left(1 - \frac{\epsilon}{\kappa+1}\right) \exp\left(-\lambda \sqrt{\frac{3\epsilon}{\kappa+1}}\right) \quad (24)$$

This result provides four initial conditions to the Adams method NAG routine DO2CBF. As written these are more like "final conditions" than initial conditions, however, the independent variable in the code is actually $-\lambda$ and so Eqs. (23) and (24) provide initial conditions. A value of $-\lambda$ is chosen (typically -2.8), η , $-d\eta/d\lambda$, ϕ , and $-d\phi/d\lambda$ are calculated, and the routine is called. The value of $-\lambda$ must be sufficiently negative so that η is close enough to 1 and ϕ to -1 that the expressions (23) and (24) are a valid approximation of η and ϕ . The analytical expressions for $d\eta/d\lambda$ and $d\phi/d\lambda$ are simply the derivatives of η and ϕ . Therefore, the solutions η and ϕ are functions of ϵ , κ , β_0 , and β_1 .

The numerical solution is compared to the experimental results in the following way. After calculating κ using Eq. (18) a value of ϵ is selected and then the ratio of β_0 to β_1 is varied while one of them (typically β_1) is held constant. This ratio β_0/β_1 is varied until the two end points of the data are matched by the numerical result. If the value of ϵ is too large, the numerical solution curves too much relative to the data (the points between the end points), lagging below. If the value of ϵ is too small the numerical solution is too straight and the data between the end points lagged below the solution. In this way the "best" value of ϵ is selected. Some examples of the comparison between data and model are pictured in Fig. 7. Here δ_0 is the measured value, κ depends on δ_0 and ϵ is the unknown being determined. The complete result for all the power input settings is presented in Table 1.

The numerical solution scheme was carefully examined for its stability and accuracy. The built-in tolerance parameter of the nag routine was adjusted until the final solution of the differential equations did not depend on the tolerance level selected. The solutions were assumed to be sufficiently accurate when the numerical meniscus shape (dimensionless slope) change was less than 1 percent for an order of magnitude change in the tolerance level.

In Table 1 values of δ_0 , ϵ , \bar{A} , \dot{m}^{id} , q^{id} , $(T_s - T_v)$, and T_s are given for the data. The values of δ_0 and T_s are measured. The

Table 2 Theoretical values of \bar{A} from Truong and Wagner (1987)

Film Thickness (nm)	\bar{A} (Octane/Si) (Joules)	\bar{A} (Octane/SiO ₂) (Joules)
5	3.07×10^{-21}	3.95×10^{-22}
10	2.76×10^{-21}	3.29×10^{-22}
20	2.21×10^{-21}	2.01×10^{-22}
50	1.26×10^{-21}	1.16×10^{-22}
100	6.95×10^{-22}	6.47×10^{-23}

values of \bar{A} are obtained using Eq. (18). The values of $\Delta T = (T_s - T_v)$ are obtained using Eq. (12). To set the absolute temperature level, the absolute value of T_s is used for the absolute value of T_v to calculate the ratio b/a and b . The effect of this difference in temperature is negligible. The values of \dot{m}^{id} and q^{id} are thus obtained using

$$\dot{m}^{id} = a\Delta T; \quad q^{id} = a\Delta T\Delta h_m \quad (25)$$

As can be seen from Table 1, the values of ΔT are extremely small, too small to be experimentally measured. Furthermore as the power input increases, δ_o decreases and q^{id} increases. We note that, at the highest power studied, the contact line thickness, δ_o , is still substantially greater than a monolayer.

The right-hand side of Eq. (16) is also the dimensionless mass flux at the liquid-vapor interface, \dot{M} :

$$\dot{M} \equiv \frac{\dot{m}}{\dot{m}^{id}} = \frac{1}{1 + \kappa\eta} (1 + \phi) \quad (26)$$

Discussion

This work demonstrates that by the proper selection of ϵ , β_0 , and β_1 , a fair and meaningful agreement can be obtained between the theoretical [model Eq. (16)] and experimental profiles. We find that the values of the modified Hamaker constant, \bar{A} , are not a function of the evaporation rate. The modified Hamaker constants characterize the interface conditions. Therefore, we have measured \bar{A} in situ and used it to describe the characteristics of an evaporating meniscus.

Truong and Wayner (1987) computed the theoretical values of \bar{A} for a flat film of octane on silicon and silicon dioxide (considering the difference between ideal and real surfaces, this is a good approximation for heptane on silicon or silicon dioxide) as a function of film thickness. The values they calculated for \bar{A} are given in Table 2.

The theoretical results in Table 2 show that the value of \bar{A} decreases with an increase in the film thickness. In our present study the substrate (silicon) always had a native oxide present on it with an approximate thickness of 3~5 nm and the \bar{A} obtained from the model is basically averaged over varying thicknesses, starting from the adsorbed film to the thickness at which dispersion force effect becomes negligible. So the measured \bar{A} is an average \bar{A} for the whole ultrathin region. In addition, the theoretical values of \bar{A} are for ideal surfaces. However, due to the presence of adsorbed water layers, etc., on the surface of the substrate, the surface energy of a real surface would have a lower value than the ideal and hence a lower value of \bar{A} will result. This clearly indicates that the measured \bar{A} values in this study are justified and in close agreement with the theory. We note that the ideal value was calculated using the quantum field theory of statistical physics.

In Fig. 8 the dimensionless pressure, ϕ , and curvature, η'' , profiles are presented for two power settings. The interfacial pressure difference can be obtained by multiplying the dimensionless pressure by the reference disjoining pressure, Π_o , which

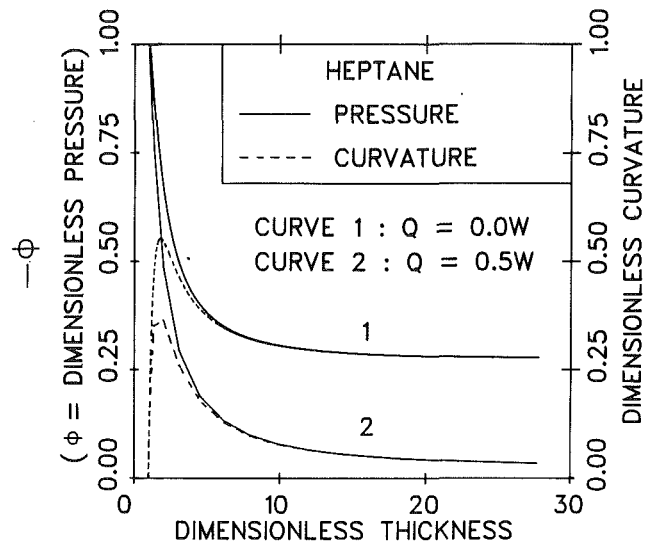


Fig. 8 Plot of dimensionless pressure and curvature versus dimensionless film thickness: curve 1: $Q = 0.0$ W, $\delta_o = 15 \pm 0.4$ nm, $\pi_o = 3.76 \times 10^1$ N/m², Curve 2: $Q = 0.5$ W, $\delta_o = 5.6 \pm 0.4$ nm, $\pi_o = 6.32 \times 10^2$ N/m²

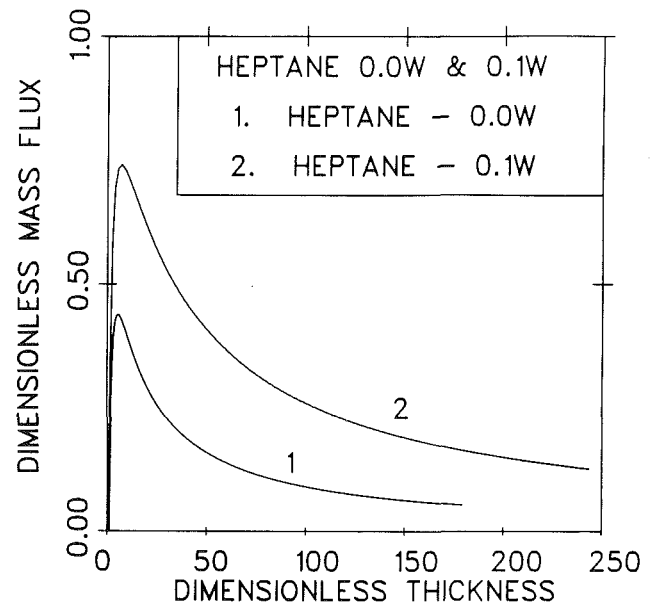


Fig. 9 Dimensionless mass flux \dot{M} versus dimensionless film thickness: Case 1: $Q = 0.0$ W, $\delta_o = 15 \pm 0.4$ nm, $\dot{m}^{id} = 6.83 \times 10^{-5}$ kg/m² · s, Case 2: $Q = 0.1$ W, $\delta_o = 6.4 \pm 0.4$ nm, $\dot{m}^{id} = 8.50 \times 10^{-4}$ kg/m² · s

is given in the caption. These results clearly demonstrate that, initially, fluid flow results from a disjoining pressure gradient. In this region the curvature builds up to a maximum value at a relatively small thickness. Then, curvature gradient causes flow in the thicker region. In general this curvature buildup increases the pumping capacity of a meniscus. The thickness can be obtained by multiplying the dimensionless thickness by the reference thickness, δ_o , which is also given in the caption.

The dimensionless interfacial heat or mass evaporative flux, \dot{M} , profiles are presented in Figs. 9 and 10. The dimensionless evaporative mass flux can be obtained by multiplying these values by the reference ideal mass flux, \dot{m}^{id} . To obtain the heat fluxes, the reference ideal heat fluxes are also given in Table 1. The right-hand side of Eq. (16), which is equal to $\dot{M} = \dot{m}/\dot{m}^{id} = q/q^{id}$, can be used to describe the characteristics of the profile. At the interline, δ_o , the dimensionless pressure, ϕ ,

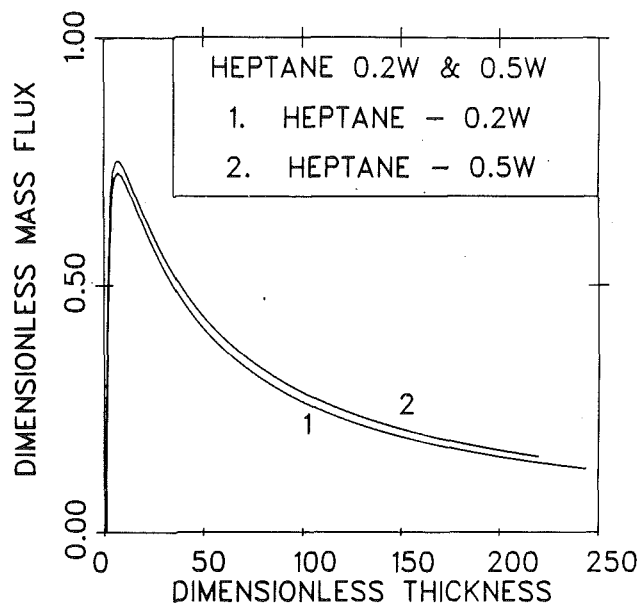


Fig. 10 Dimensionless mass flux \dot{M} , versus dimensionless film thickness: Case 1: $Q = 0.2$ W, $\delta_0 = 6.2 \pm 0.4$ nm, $\dot{m}^{id} = 8.76 \times 10^{-4}$ kg/m²·s, Case 2: $Q = 0.5$ W, $\delta_0 = 5.6 \pm 0.4$ nm, $\dot{m}^{id} = 1.15 \times 10^{-3}$ kg/m²·s)

is given by $\phi = -1$. Therefore, the flux is equal to zero. The variation of ϕ with thickness is given in Fig. 8. These figures show that the absolute value of ϕ decreases as the thickness increases. Therefore, the interfacial flux increases because the effect of interfacial forces decreases. This increase does not continue to the ideal value because of conductive resistance in the liquid film, which is represented by $\kappa\eta$ in Eq. (16). Therefore, we obtain a maximum in the flux profile and note that the resistances are substantial. A recent numerical study by Stephan and Busse (1992) also predicted substantial resistances in the contact line region.

Conclusions

Ellipsometry and microcomputer-enhanced interferometry can be used to measure the thin film profile accurately as a function of the evaporation rate.

The augmented Young-Laplace equation with the Kelvin-Clapeyron equation and kinetic theory can be used to model fluid flow and evaporative heat transfer in the contact line region.

Since there are significant resistances to heat transfer in this small system due to interfacial forces, viscous stresses, and thermal conduction, the "ideal constant heat flux" based on kinetic theory cannot be obtained.

Acknowledgments

This material is based on work supported by the Aero Propulsion Laboratory, Air Force Wright Aeronautical Laboratory, Aeronautical Systems Division (AFSC), United States Air Force, Wright Patterson AFB, Ohio 45433-6533 under contract F33615-88-C-2821. The U.S. Government is authorized to reproduce and distribute reprints for governmental purposes notwithstanding any copyright notation. Any opinions, findings and conclusions or recommendations expressed in this publication are those of the authors and do not necessarily reflect the view of the U.S. Air Force.

References

- Bascom, W. D., Cottingham, R. L., and Singletary, C. R., 1964, "Dynamic Surface Phenomena in the Spontaneous Spreading of Oils on Solids," *Contact Angle, Wettability and Adhesion*, R. E. Gould, ed., Adv. Chem. Ser. Vol. 43, Am. Chem. Soc., Washington, DC, pp. 355-379.
- Blake, T. D., 1975, "Investigation of Equilibrium Wetting Films of *n*-Alkanes on α -Alumina," *J. Chem. Soc., Faraday Trans. I*, Vol. 71, pp. 192-208.
- Cook, R., Tung, C. Y., and Wayner, P. C., Jr., 1981, "Use of Scanning Microphotometer to Determine the Evaporative Heat Transfer Characteristics of the Contact Line Region," *ASME JOURNAL OF HEAT TRANSFER*, Vol. 103, pp. 325-330.
- DasGupta, S., Sujanani, M., and Wayner, P. C., Jr., 1991, "Microcomputer Enhanced Optical Investigation of an Evaporating Liquid Film Controlled by a Capillary Feeder," *Proceedings of the Second World Conference on Experimental Heat Transfer, Fluid Mechanics and Thermodynamics*, J. F. Keffer, et al., eds., Elsevier Science Publishing Co. Inc., New York, pp. 361-368.
- Derjaguin, B. V., and Zorin, Z. M., 1957, "Optical Study of the Adsorption and Surface Condensation of Vapors in the Vicinity of Saturation on a Smooth Surface," *Proc. 2nd Int. Conf. Surface Activity*, J. H. Schulman, ed., Butterworths, London, Vol. 2, pp. 145-152.
- Derjaguin, B. V., Nerpin, S. V., and Churaev, N. V., 1965, "Effect of Film Transfer Upon Evaporation of Liquids From Capillaries," *Bull. Rilem*, Vol. 29, pp. 93-98.
- Derjaguin, B. V., and Churaev, N. V., 1976, "The Definition of Disjoining Pressure and Its Importance in the Equilibrium and Flow of Thin Films," *Colloid J. USSR*, Vol. 38, pp. 438-448.
- Dzyaloshinskii, I. E., Lifshitz, E. M., and Pitaevskii, L. P., 1961, "The General Theory of Van der Waals Forces," *Ad. Phys.*, Vol. 10, pp. 165-209.
- Gee, M. L., Healy, T. W., and White, L. R., 1989, "Ellipsometric Studies of Alkane Adsorption on Quartz," *J. Colloid Interface Sci.*, Vol. 131, No. 1, pp. 18-23.
- Ingram, B. J., 1974, "Wetting of Silica by *n*-Alkanes," *J. Chem. Soc., Faraday Trans. I*, Vol. 70, pp. 868-876.
- Kayser, R. F., Schmidt, J. W., and Moldover, M. R., 1985, "Wetting Layers and Dispersion Forces for a Fluid in Contact With a Vertical Wall," *Phys. Rev. Lett.*, Vol. 54, pp. 707-710.
- Mirzamaoghadam, A. Y., and Catton, I., 1988, "Holographic Interferometry Investigation of Enhanced Tube Meniscus Behavior," *ASME JOURNAL OF HEAT TRANSFER*, Vol. 110, pp. 208-213.
- Moosman, S., and Homsy, S. M., 1980, "Evaporating Menisci of Wetting Fluids," *J. of Colloid and Interface Sci.*, Vol. 73, pp. 212-223.
- Potash, M., Jr., and Wayner, P. C., Jr., 1972, "Evaporation From a Two-Dimensional Extended Meniscus," *Int. J. Heat Mass Transfer*, Vol. 15, pp. 1851-1863.
- Renk, F., Wayner, P. C., Jr., and Homsy, G. M., 1978, "On the Transition Between a Wetting Film and a Capillary Meniscus," *J. of Colloid and Interface Sci.*, Vol. 67, pp. 408-414.
- Renk, F. J., and Wayner, P. C., Jr., 1979, "An Evaporating Ethanol Meniscus, Part I: Experimental Studies," *ASME JOURNAL OF HEAT TRANSFER*, Vol. 101, pp. 55-62.
- Schonberg, J., DasGupta, S., and Wayner, P. C., 1992, to be published.
- Stephan, P. C., and Busse, C. A. 1992, "Analysis of the Heat Transfer Coefficient of Grooved Heat Pipe Evaporator Walls," *Int. J. Heat Mass Transfer*, Vol. 35, pp. 383-391.
- Sujanani, M., and Wayner, P. C., Jr., 1990, "Spreading and Evaporative Processes in Thin Films," *Hydrodynamics of Dispersed Media*, J. P. Hulin et al., eds., Elsevier, North Holland, pp. 55-62.
- Sujanani, M., and Wayner, P. C., Jr., 1991, "Microcomputer-Enhanced Optical Investigation of Transport Processes With Phase Change in Near-Equilibrium Thin Liquid Films," *J. Colloid and Interface Science*, Vol. 143, No. 2, pp. 472-488.
- Truong, J. G., and Wayner, P. C., Jr., 1986, "A Study of Transport Phenomena in the Interline Region of an Evaporating Thin Liquid Film Using a Scanning Ellipsometer," *Proceedings of the 8th International Heat Transfer Conference*, C. L. Tien et al., eds., Hemisphere Publishing Corp., Washington, Vol. 2, pp. 507-512.
- Truong, J. G., and Wayner, P. C., Jr., 1987, "Effect of Capillary and Van der Waals Dispersion Forces on the Equilibrium Profile of a Wetting Liquid: Theory and Experiment," *J. Chem. Phys.*, Vol. 87, pp. 4180-4188.
- Voutsinos, C. M., and Judd, R. L., 1975, "Laser Interferometric Investigation of the Microlayer Evaporation Phenomena," *ASME JOURNAL OF HEAT TRANSFER*, Vol. 97, pp. 88-92.
- Wayner, P. C., Jr., Kao, Y. K., and LaCroix, L. V., 1976, "The Interline Heat Transfer Coefficient of an Evaporating Wetting Film," *Int. J. Heat Mass Transfer*, Vol. 19, pp. 487-492.
- Wayner, P. C., Jr., 1991, "The Effect of Interfacial Mass Transport on Flow in Thin Liquid Films," *Colloids and Surfaces*, Vol. 52, pp. 71-84.
- Wayner, P. C., Jr., DasGupta, S., and Schonberg, J., 1991, "Effect of Interfacial Forces on Evaporative Heat Transfer in a Meniscus," U.S. Air Force Report, No. WL-TR-91-2061.
- Wu, D., and Peterson, G. P., 1991, "Investigation of the Transient Characteristics of a Micro Heat Pipe," *J. Thermophysics*, Vol. 5, pp. 129-134.
- Xu, X., and Carey, V. P., 1990, "Evaporation From a Micro-grooved Surface—An Approximate Heat Transfer Model and Its Comparison With Experimental Data," *J. Thermophysics*, Vol. 4, pp. 512-520.

T. D. Tang
Post-Doctoral Fellow.

M. T. Pauken
Graduate Research Assistant.

S. M. Jeter
Associate Professor.

S. I. Abdel-Khalik
Professor.

The George W. Woodruff School of
Mechanical Engineering,
Georgia Institute of Technology,
Atlanta, GA 30332-0405

On the Use of Monolayers to Reduce Evaporation From Stationary Water Pools

An experimental investigation has been conducted to quantify the extent by which monolayers of fatty alcohols can reduce evaporation from a deep stationary water pool within a controlled environment. Octadecanol (stearyl alcohol), $C_{17}H_{35}-CH_2-OH$, was chosen as the surface film and ethanol was selected to be the spreading agent. Evaporation suppression of 60 percent was achieved at a water temperature of $25^\circ C$ with an air temperature of $20^\circ C$ and a relative humidity of 70 percent. The experimental techniques and data have been validated by comparing the measured evaporation rates for film-free water with earlier data published by other investigators. Data for the evaporation rates of water covered by octadecanol films were correlated as a function of vapor concentration differences between the water surface and air.

Introduction

The fundamental law of evaporation is credited to Dalton (1834); his generalized formula of evaporation into calm air is given by:

$$J = C(P_w - P_a) \quad (1)$$

where J is the rate of evaporation, C is a coefficient dependent upon experimental conditions, P_w is the vapor pressure of the water surface, and P_a is the partial pressure of the water vapor at the ambient air temperature. Since then, many investigators have contributed to understanding the phenomenon of water evaporation into still and moving air and have found that the coefficient C is somewhat dependent on the vapor pressure differential. This dependence creates a nonlinearity that is often represented by a nonunity exponent on the vapor pressure difference term.

Most of the research on evaporation of water into still air has been empirical in nature. Sharpley and Boelter (1938) and Boelter et al. (1946) measured the evaporation rate from a 30-cm-dia pan of water into quiet air in a humidity and temperature-controlled chamber with water temperatures ranging from 20° to $90^\circ C$. The evaporation rate was determined by measuring the change in height of the water level in a standpipe connected to the evaporation pan. To measure the change in water level, an optical interference pattern was set up by an etched glass grating that pivoted on a float resting in the standpipe. This apparatus provided rapid determination of the evaporation rate by the movement of the interference bands. The results of Boelter et al. for the evaporation rates of clean water surfaces into still air are given by:

$$J = 0.074(P_w - P_a)^{1.22} \quad (2)$$

where the evaporation rate, J , has units of $kg/m^2/h$ while the vapor pressure difference $P_w - P_a$ is in kPa. Hickox (1944) duplicated Boelter's work with a 30-cm-dia pan and measured evaporation rates with a floating optical interferometer over a temperature range of 20° to $35^\circ C$ and achieved virtually the same results. Hickox presented a linear regression of his data that nearly matches Boelter's regression over similar evaporation conditions.

Investigations of the effect of oil films on reducing water

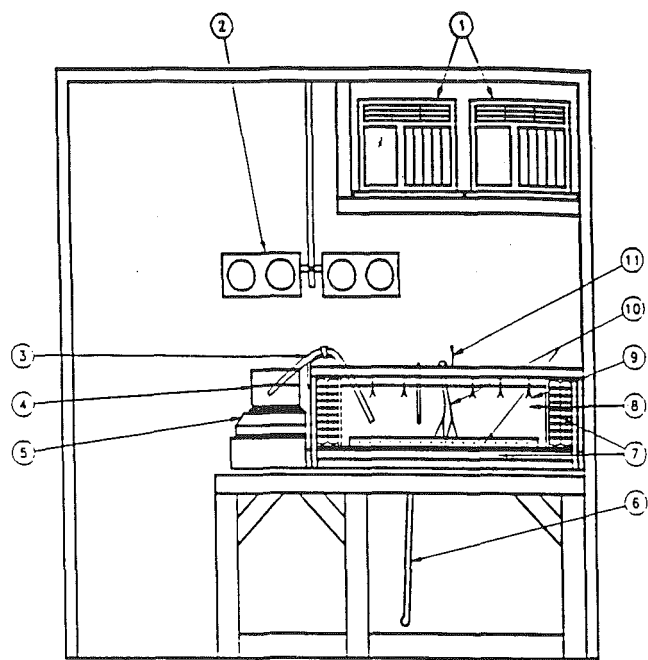
evaporation began in the early twentieth century (Devaux, 1965). Oil films can form either a monolayer or a multilayer. In the 1940s, much attention was given to the use of multilayer films of oil mixture for natural evaporation control (Frenkiel, 1965). Despite the ability of multilayer films to suppress evaporation, work with such films declined because they tended to collapse or were damaged easily by the action of dust and wind. Unlike multilayer films, monolayer films have better resistance to conditions encountered in the field (Mansfield, 1953).

Monolayers interact with the surface water molecules to form a new surface, which has a lower surface tension than a film-free surface. This lowering of surface tension results from the insertion of monomolecules among the surface water molecules, and the long chain monomolecules resist each other, resulting in a force that is opposite to the surface tension. Surface pressure, which is defined as the difference between the surface tension without a monolayer and the surface tension with a monolayer, has the dimensions of force per unit length.

Numerous laboratory studies have identified the characteristics of monolayers in terms of evaporation suppression. Among the monolayer compounds examined, long chain fatty alcohols, especially hexadecanol ($C_{15}H_{31}-CH_2-OH$) and octadecanol ($C_{17}H_{35}-CH_2-OH$), exhibit excellent evaporation resistances (Barnes and La Mer, 1962). The evaporation resistance depends on many factors such as water and ambient temperatures, film surface pressure, chain length of monolayer, and film purity. The evaporation resistance of most monolayers increases when the surface pressure increases (Barnes and Hunter, 1990). Increasing the water temperature tends to degrade the ability of the film to reduce evaporation (Deo et al., 1960). This temperature effect on evaporation reduction decreases as the chain length increases. The evaporation resistance increases significantly with the chain length (La Mer et al., 1964). Impurities suppress evaporation resistance; the effect of impurities is especially significant at low surface pressure (Costin and Barnes, 1967). Spreading solvents are needed to enhance spreading of the film on the water surface because the long chain alcohols are waxy solids in the natural state. Solvents used in spreading films are reported to include benzene, ethanol, kerosene, mineral turpentine, petroleum ether, and others (Frenkiel, 1965).

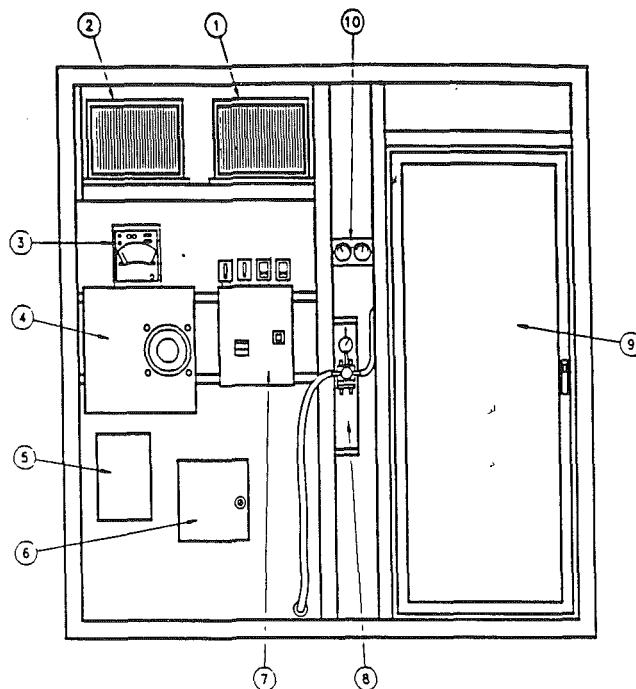
For field investigations such as water reservoirs, lakes, and ponds, experimental results showed that it is practical to reduce water evaporation by covering the water surface with thin

Contributed by the Heat Transfer Division for publication in the JOURNAL OF HEAT TRANSFER. Manuscript received by the Heat Transfer Division March 1992; revision received June 1992. Keywords: Evaporation, Mass Transfer. Associate Technical Editor: L. C. Witte.



1 Air Conditioners	7 Bubble & Styrofoam Insulation
2 1000 Watt Heat Lamps	8 Water Tank
3 Scale Siphon tube	9 Water Temp. Thermocouples
4 Glass Water Container	10 Water Heaters
5 Digital Scale	11 Air Temp. Thermocouple
6 Water Level Indicator Siphon	

Fig. 1(A) Interior equipment layout of evaporation experiment station



1 5000 Blu Air-Conditioner	6 A.C. & Heat Lamp Relay Box
2 7500 Blu Air-Conditioner	7 Water Heater Control Box
3 Weston Wall-meter	8 Water Level Indicator
4 Variac	9 Door
5 Metabyte EXP-16 Sub-Multiplexer	10 Temp. & Humidity Gauges

Fig. 1(B) Exterior equipment layout of evaporation experiment station

films, which act as evaporation barriers. However, the results have been mixed because of the difficulty in controlling experimental conditions. Vines (1962) used hexadecanol on a large water storage tank and suppressed evaporation by 20 to 50 percent depending on weather conditions. Extensive experiments were initiated by the Bureau of Reclamation in 1955 (Timblin et al., 1957) to study the evaporation reduction of hexadecanol and other monolayers. In those tests, a 64 percent evaporation reduction was obtained with hexadecanol. The effectiveness of surface films in the field depends on experimental conditions such as air and water temperatures, water surface conditions, surface film selected, spreading method, spreading rate, film maintenance, wind, dust, and rain (Frenkiel, 1965). No field investigations on evaporation suppression have been reported since 1970.

To develop a better understanding of evaporation retardation for industrial usage such as waste water management, this research has been concentrated on water evaporation suppression utilizing octadecanol films under controlled temperature and humidity conditions. Based on the data obtained here, an empirical equation to quantify the effectiveness of octadecanol films has been developed. The water was held at temperatures ranging from 25°C to 50°C while the conditions of the air were set to 20°C ± 1°C and a relative humidity of 50 or 70 percent.

Experimental Methods

The evaporation tank was patterned after the specifications for a Class-A evaporation pan commonly used in meteorology (U.S. Dept. of Commerce, 1955). As shown in Fig. 1(A) and 1(B), a Class-A pan measures 1.2 m (47 in.) i.d. and 25.4 cm (10 in.) deep. The water evaporation tank was constructed from 6.35 mm (0.25 in.) high-density polyethylene sheet, which was chosen for its resistance to corrosion and good thermal and electrical insulation capability. Use of this material resulted in a nearly inert container for evaporation studies. To elevate the water temperature to the desired conditions, two immersion heaters were installed near the bottom of the tank. These were designed with a low heat flux to provide safe and uniform heating throughout the tank with up to 2000 W of total power. The heaters were made from nichrome wire encased in PTFE spaghetti tubing. The heater wires were coiled into a spiral near the bottom of the tank and supported by a polyethylene frame. The heaters were controlled by a PID temperature controller that sensed the water temperature through six T-type thermocouples connected in parallel to provide an average water temperature reading for the controller. These thermocouples were evenly spaced across the diameter of the tank at a depth of 5 to 8 cm below the water surface.

Referring to Fig. 1(A), the evaporation rate from the tank was determined by monitoring the weight of water in a small glass pan (item 4) connected to the evaporation pan (item 8)

Nomenclature

C = evaporation coefficient
 C_a = concentration of water vapor in the atmosphere

C_w = concentration of water vapor at the saturated liquid state
 J = rate of evaporation
 P_a = partial pressure of the water va-

por at the ambient air temperature
 P_w = vapor pressure of the water surface

via a 1.9 cm (3/4 in.) i.d. siphon tube (item 3). The weight of the small pan was determined by an electronic balance (item 5) with an RS-232 serial port for digital output to a computer. The mass loss from the evaporation tank produced a proportional decrease in weight on the balance. This proportionality constant was determined by calculation and experiment and yielded a measurement uncertainty of ± 1.6 percent. During the experiment, the evaporation rate was calculated from the difference in balance readings taken over 15-min time intervals.

To control the environment in which evaporation takes place, an enclosure with transparent acrylic panels around the water tank was constructed so that the experiment could be viewed without disturbing the conditions. The interior and exterior layout of the enclosure and experiment station are shown in Figs. 1(A) and 1(B), respectively. Since evaporation of the water at elevated temperatures humidified and heated the air within the enclosure, it was necessary to remove the excess moisture and heat with two small air conditioners capable of providing 12,500 Btu of cooling. The air conditioners were staged to provide better control of the humidity. The air-conditioner staging strategy could be changed at any time through the computer program that controlled and monitored the experiment.

During the dehumidification process, the latent cooling load constituted a major portion (e.g., 50–80 percent) of the total cooling load. Consequently, overcooling of the space could often occur. To prevent overcooling, radiant heat lamps were used to provide space heat when the air temperature dropped below 20°C. The radiant heat of the lamps provided an even heating of the enclosure.

The air speed above the water surface was measured with two instruments. A commercial thermal anemometer mounted 0.2 m above the surface measured a speed of 6 to 9 m/min (20 to 30 ft/min) with occasional excursions to 15 m/min (50 ft/min) due to wandering eddies. A commercial vane anemometer, of the type commonly used to monitor fume hoods, measured the horizontal component of the velocity to be approximately ± 6 m/min (20 ft/min) with occasional excursions to 9 m/min (30 ft/min). These two disparate instruments were consistent and indicated that the air speed above the water (6 to 9 m/min) was within the range of typical indoor conditions.

To monitor the surface pressure continuously, it was necessary to measure the change of surface tension after a monolayer was spread. A precision balance of 1 mg resolution was used to suspend a glass Wilhelmy plate into the water surface. The plates used were 0.15 mm in thickness, 60 mm in height, and 20 mm wide. The Wilhelmy plate balance was mounted on a bridge 0.5 m above the 1.2-m-dia tank as shown in Fig. 2. A weighing hook was installed at the bottom of the Wilhelmy plate balance pan and passed through a hole in the bridge. An extension chain was used as the connector between the hook and a clip that affixed the Wilhelmy plate. Before each experiment, water was added to the tank until the Wilhelmy plate was 90 percent immersed into water.

At high water temperatures, it was necessary to prevent water vapor from condensing on the Wilhelmy plate in order to assure the accuracy of the surface pressure data. A fixed acrylic tube (~7.5 cm o.d.) and a thin acrylic skirt (~8.0 cm i.d.) mounted on a floating polystyrene block were placed between the bridge and the water surface to encompass the chain, clip, and Wilhelmy plate. The acrylic skirt floated on the water surface as the water level fell. The distance between the bottom of the skirt and water surface was maintained at 0.3 cm by the foam block. Dry air provided by two air pumps flowed through two long plastic tubes to the acrylic tube. These long plastic tubes were submerged in the tank and served as a heat exchanger so that the air coming out of the tubes was warmer than the ambient air since the water temperature was always higher than the air temperature. Warm, dry air then flowed through the acrylic tube and skirt, thus preventing water condensation

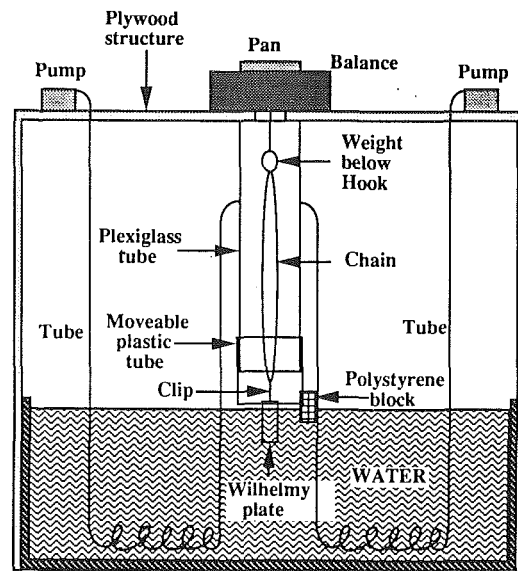


Fig. 2 Apparatus for measuring surface pressure

on the plate. At low temperatures, moisture condensation was not a problem. However, the apparatus was still used for experimental consistency.

As water evaporated from the tank, the water level dropped and reduced the buoyancy force on the plate. The reduced buoyancy force will slightly increase the load on the balance; this increase would be erroneously interpreted as an increase in surface tension or decrease in surface pressure unless corrected. The change in the submerged volume of the plate can be computed from the change in water level times the cross-sectional area of the plate. The change in the buoyancy force is the product of the change in submerged volume times the specific weight of the water. The resulting change in the buoyancy force can be subtracted from the total change in the load on the balance to yield the residual change due only to a change in the surface pressure. This correction was verified by measuring the change in the buoyancy force on the Wilhelmy plate when no film was present; for these experiments, the indicated surface pressure should remain zero throughout the experiment.

Before applying the octadecanol films, the Wilhelmy plate balance was first zeroed. After spreading the surface film with cotton swabs using ethanol as the solvent, the Wilhelmy plate balance would show a negative reading, which indicated the lowering of surface tension. The absolute value of this reading divided by the perimeter of the plate (40.3 mm) is the surface pressure of the film. Octadecanol was applied continuously as long as the surface pressure increased. If an excessive amount of octadecanol was applied, the surface pressure would decrease. The compactness of the octadecanol film, the evaporation barrier, could further decrease if octadecanol was continuously applied. The maximum achievable surface pressure, the equilibrium surface pressure, depends upon the water temperature, air temperature, and water surface conditions.

The experiment was controlled and monitored by a personal computer that used two internal bus data acquisition and control systems; one to collect data and the other to send output signals to the environmental control system. The computer collected relative humidity and air temperature data every 60 seconds and sent the appropriate control signals to relays that operated the air conditioners and heat lamps to control the environmental conditions. Relative humidity was measured by a thin-film capacitive sensor that was calibrated over saturated salt solutions of sodium chloride, potassium carbonate, and lithium chloride. The air temperature was measured by a T-type thermocouple located 25 cm above the water surface.

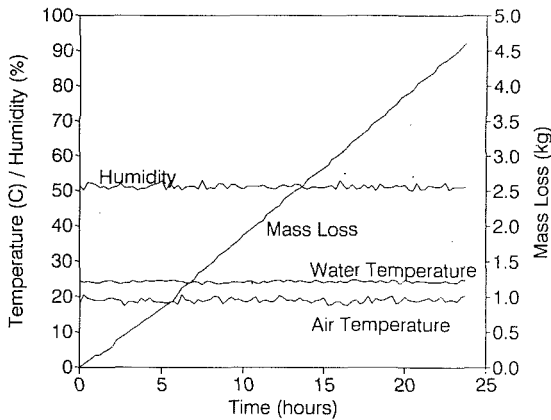


Fig. 3 Experimental conditions and results (25°C, 50 percent, RH, no film)

Every 15 minutes the computer collected the water temperature data from six T-type thermocouples (separate from those used by the PID controller) and two electronic balance readings. The program averaged the air temperature and humidity readings taken over the previous 15 minute period and recorded these to a data file on floppy disk with the water temperature and balance data. The evaporation rate was calculated from the difference in balance readings taken over 15 minute time intervals. The surface pressure was computed from the difference in precision balance readings including the effect of buoyancy force. For fresh water, each experiment was operated for 24 hours while experiments using film-covered water were operated for 48 hours. A sample of the data collected over a 24-hour period is shown in Fig. 3, which illustrates the general stability of the experimental conditions.

Experimental Results

Comparison With Literature Data for Film-Free Water. In order to validate the experimental procedures and techniques, evaporation data for film-free water pools have been obtained and compared with earlier data published by other investigators. A total of eight different conditions were examined in the present study. These conditions correspond to water temperatures of 25, 30, 40 and 50°C and relative humidities of 50 and 70 percent. The ambient air temperature was 20°C for each run. The evaporation rate, temperature, and humidity data for each run (of 24 hour duration) were consolidated to produce average values for the entire test. The results are shown in Fig. 4 where the evaporation rate is plotted versus the concentration differences. Regression analysis on the data shows that the evaporation rate can be predicted by the following relation:

$$J = 35.0 (C_w - C_a)^{1.237} \quad (3)$$

where J has units of $\text{kg}/\text{h}/\text{m}^2$, C_w is the concentration of water vapor at the saturated liquid state in units of kg/m^3 , and C_a is the concentration of water vapor in the atmosphere.

Equation (3) is in close agreement with Boelter's equation for evaporation in terms of concentration differences over the same range:

$$J = 38.3 (C_w - C_a)^{1.25} \quad (4)$$

Equation (3) yields evaporation rates that are 3 to 5.5 percent lower than Boelter's over the range of concentration differences indicated in Fig. 4. Rohwer (1931, 1934) studied the effects of evaporation pan size on evaporation. He compared evaporation from a 0.91 m (3 ft) square pan and a 1.22 m (4 ft) circular pan, which is about the same size of the current investigation with that from a 7,284,000 m^2 (1800 acre) res-

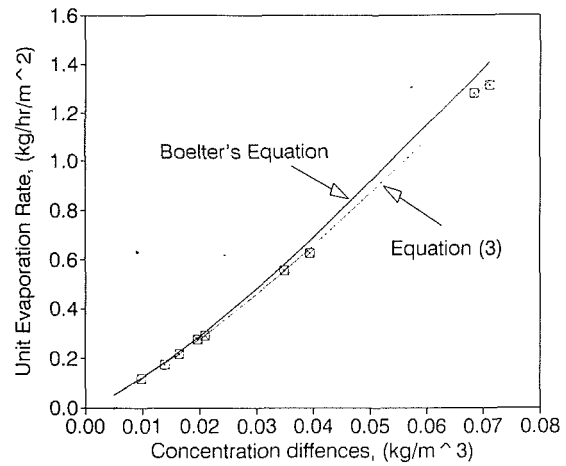


Fig. 4 Comparison with literature data for fresh water

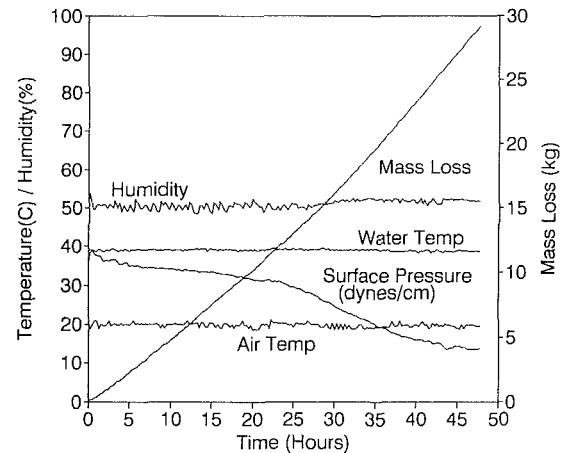


Fig. 5 Experimental conditions and results (40°C, 50 percent RH, deionized water, film)

ervoir. Rohwer and other experimenters (Sleight, 1927; Hickox, 1944) have noted that the measured evaporation rates per unit area decrease as the size of the evaporation pan increases. It was suggested that the effect of convection currents induced by concentration differences near the edges of the water decreases if the water surface area increases. No optimal pan size for evaporation was identified. For the present study, the rate reduction appears to be in agreement with their conclusions.

Hickox (1944) also studied the vapor transfer by utilizing dimensionless moduli in a manner similar to that for heat transfer by convection. Following the analog between heat transfer, mass transfer, and experimental data on evaporation, he concluded that among all the variables such as temperature, viscosity, vapor concentration difference, and the characteristic dimension of the surface, the most important variable affecting the rate of evaporation is the vapor concentration difference raised to the 1.25 power because of its effect on convection.

Evaporation Data for Monolayer-Covered Water. For water covered with octadecanol films, the air temperature was held at 20°C for each trial. The influence of humidity was investigated by running one set of tests at 50 percent and the other at 70 percent RH for various water temperatures. The water temperatures were set to 25°, 30°, 35°, 40°, and 50°C. An extra data set with a relative humidity of 40 percent was run with the 30°C water to investigate effects at lower humidity conditions. In all, there were 11 data sets for water covered with octadecanol films.

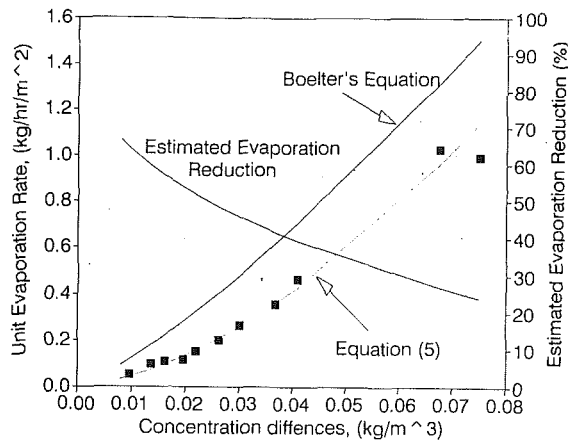


Fig. 6 Effects of films on the rates of water evaporation

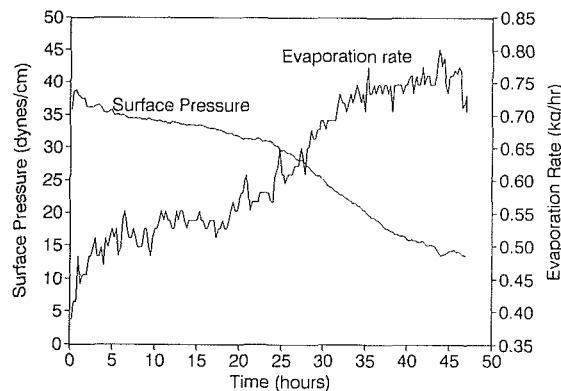


Fig. 7 Evaporation rate versus surface pressure

In addition to the measured parameters described in fresh water experiments, the surface pressure, which indicates the compactness of the monolayer film, was also monitored. The composite graph presented in Fig. 5 includes water temperatures, air temperature, relative humidity, surface pressure, and mass loss by the evaporation tank over a 48 hour period. The results for the first 24 h (where no significant deterioration in the surface pressure was observed) were used to calculate the average evaporation rate as a function of the vapor concentration driving potential (Fig. 6). Each data point in Fig. 6 represents the average evaporation rate and the corresponding average vapor concentration driving potential during the first 24 h of the test. The evaporation rate increases as the concentration difference increases. These discrete data points show a clear trend whereby the evaporation reduction percentage decreases as the concentration difference increases. At a water temperature of 50°C, film spreading was difficult. For these two tests, it was difficult to know when the surface pressure exactly reached the equilibrium value because of the rapid evaporation of the spreading solvent during spreading.

The data shown in Fig. 6 have been used to develop an empirical equation for the evaporation rate of water covered with an octadecanol film, the same format as Boelter's equation (Boelter et al., 1946):

$$J = 76.0(C_w - C_a)^{1.62} \quad (5)$$

The data indicates that the evaporation rate is suppressed by about 60 percent at 25°C and approximately 25 percent at 50°C. The declivity in evaporation reduction percentage as the water temperature increases may be attributed to two primary factors. At high water temperatures (high concentration differences), more water molecules have higher kinetic energy and have a better chance to penetrate the films and then escape to

the air. Furthermore, at high water temperatures, the evaporation rate of the octadecanol film becomes significant and may deteriorate the film quality.

The relationship between surface pressure and evaporation reduction at 40°C and 50 percent RH can be seen in Fig. 7. In this figure, water evaporation rates as well as surface pressures are plotted as functions of time. Initially, when the surface pressure is high, the evaporation rate is low. The evaporation rate increases as surface pressure decreases. This phenomenon clearly illustrates the importance of surface pressure to evaporation reduction and the practical possibility of using surface pressure as a continuous indicator of the film effectiveness. The reduction in surface pressure with time is attributed to factors such as contaminants and dust in the air, evaporation or solution of the monolayer, and other film damage. Maintenance of an adequate surface pressure over a long period of time is critical for evaporation suppression. Due to the difficulties of having a completely dust-free water surface, a measurement uncertainty of ± 1.6 percent in the evaporation rate, a $\pm 1^\circ\text{C}$ uncertainty in the temperature measurement, and a ± 2 percent variation in humidity, a ± 5 percent variation of water evaporation suppression at various water temperatures may be expected.

Discussion and Conclusions

For most laboratory studies, the evaporimeter and Langmuir trough developed by Langmuir and Schafer (1943) were used as standard apparatus to measure the rate of water evaporation. A movable barrier placed within the trough was used to compress the monolayer film in order to obtain a maximum surface pressure. The evaporation from a water surface with or without a monolayer film was measured by the amount of water absorbed by a desiccant placed a few millimeters above the water surface. Because the desiccant can only absorb a small amount of water, these laboratory experiments could not be conducted for more than a few minutes. Spreading of the monolayer with highly volatile solvent such as petroleum ether worked effectively primarily because the water surface area of the trough was very limited. Consequently, spreading the monolayer before the solvent evaporated was not difficult. Langmuir and Schafer found that the rate of evaporation was decreased by an astonishing factor of 10^4 by a compressed monolayer film of hexadecanol. A 90 percent evaporation reduction was observed by using alkoxy ethanols as evaporation retardants (Deo et al., 1960). These laboratory results are useful for elucidating the fundamental properties of various monolayers. But since these experimental conditions were optimally controlled, the results are significantly different from those expected in the field.

Unlike laboratory experiments, results of field tests carried out on ponds or reservoirs are dependent on numerous factors such as rain, wind, dust, ambient temperature, film pressure, film evaporation, spreading method, spreading rate, water surface area, purity of the monolayer, etc. Due to the influence of these factors, the data reported in the literature can only represent the effectiveness of the film under those specific experimental conditions. Among experiments conducted in the past, fatty alcohols have been successfully used on large water reservoirs, reducing water losses to 25–70 percent (Timblin et al., 1957; Vines, 1962).

In the current investigation, water evaporation reduction by utilizing octadecanol films was confirmed. Results show reductions as high as 60 percent. Proper methods of spreading the monolayer film and maintaining the film could be crucial to the results. It is vital to maintain a compressed and effective monolayer film on the water surface for extended periods of time because the molecules of the monolayer film evaporate slowly to the air. It is, therefore, essential to supply the molecules of the retardant to the water surface continuously in

order to maintain the equilibrium surface pressure. Also, due to the fact that the evaporation resistance induced by monolayer films is extremely sensitive to impurities that could be introduced during the spreading, it is desirable to minimize the possibility of introducing impurities to the water surface by maintaining a dust-free experimental environment. Natural convection in the water could possibly have an impact on film degradation at the higher water temperatures (40 and 50°C) in this study, but it has been shown that the major contributor to film degradation is evaporation of the film itself (Frenkiel, 1965). The film material, octadecanol, is not very soluble in water; thus natural convection currents could not pull film material into the bulk of the water. At lower water temperatures (25°, 30°, and 35°C), natural convection currents in the water are minimal.

Considerable difficulty is normally encountered in large-scale tests; the difficulty is manifested through the inconsistency of initial surface pressure reading, which is considered as the indicator of the initial effectiveness of the evaporation barrier. The difficulty results from a failure to provide a clean and dust-free water surface. Any impurity, foreign agent, or even residual films will significantly decrease film effectiveness. Hence, it is nearly impossible to specify the equilibrium surface pressure at any specific water temperature; only a range of equilibrium surface pressure can be identified. For example, our experimental equilibrium surface pressure for water at 25°C ranges from 30 to 38 dynes/cm. Another phenomenon of interest is that the patterns of film degradation vary for different runs even when the experimental conditions are apparently identical. Because the importance of the relationship between the surface pressure and evaporation reduction is shown in Fig. 7, the results point to the practical possibility of using the surface pressure as a continuous means for monitoring the film effectiveness. Since surface pressure indicates the compactness of a film, it also indicates the effectiveness of the film as an evaporation barrier. When the surface pressure is low the film is sparse and water can easily evaporate through it. Nevertheless, the mechanism of film degradation needs further investigation.

References

- Barnes, G. T., and La Mer, V. K., 1962, *Retardation of Evaporation by Monolayers: Transport Process*, V. K. La Mer, ed., Academic Press, New York, pp. 9-33.
- Barnes, G. T., and Hunter, D. S., 1990, "The Evaporation Resistance of Octadecanol Monolayers as a Function of Temperature," *J. Colloid Interface Science*, Vol. 136, No. 1, pp. 198-212.
- Boelter, L. M. K., Gordon, H. S., and Griffin, J. R., 1946, "Free Evaporation Into Air of Water From a Free Horizontal Quiet Surface," *Industrial and Engineering Chemistry*, Vol. 38, No. 6, pp. 596-600.
- Costin, I. S., and Barnes, G. T., 1967, "The Purification of Long Chain Alcohols for Monolayer Studies," *J. Colloid Interface Science*, Vol. 25, pp. 584-585.
- Dalton, J., 1834, *Meteorological Observations and Essays*, 2nd ed.
- Deo, A. V., Sanjana, N. R., Kulkarni, S. B., Gharpurey, M. K., and Biswas, A. B., 1960, "Compressibility and Specific Evaporation Resistance of Monolayers of Long Chain Alcohols and Glycol Mono-alkyl Ethers," *Nature*, Vol. 187, pp. 870-871.
- Devaux, H., 1965, "Oil Films on Water and on Mercury: Summary of 1903-1913 Researches on Oil Films," *Ann. Rep. Smithsonian Inst.*, pp. 261-273.
- Frenkiel, J., 1965, *Arid Zone Res.*, XXVII, *Evaporation Reduction*, UNESCO, Paris.
- Hickox, I., 1944, "Evaporation From a Free Water Surface," *Am. Soc. Civil Eng. Proc.*, Vol. 70, pp. 1297-1327.
- Langmuir, I., and Schaefer, V. J., 1943, "Rates of Evaporation of Water Through Compressed Monolayers on Water," *J. Franklin Institute*, Vol. 235, pp. 119-162.
- La Mer, V. K., Healy, T. W., and Aylmore, L. A., 1964, "The Transport of Water Through Compressed Monolayers of Long Chain *n*-Paraffine Alcohols," *J. Colloid Science*, Vol. 19, pp. 673-684.
- Mansfield, W. W., 1953, "The Effect of Surface Films on the Evaporation of Water," *Nature*, Vol. 172, No. 4389, pp. 1101-1103.
- Rohwer, C., 1931, "Evaporation From Free Water Surfaces," *Bulletin*, No. 271, U.S.D.A.
- Rohwer, C., 1934, "Evaporation From Different Types of Pans," *Transactions ASCE*, Vol. 99, pp. 673-703.
- Sharpley, B. F., and Boelter, L. M. K., 1938, "Evaporation of Water Into Quiet Air From a One-Foot-Diameter Surface," *Industrial and Engineering Chemistry*, Vol. 30, No. 10, pp. 1125-1131.
- Sleight, R. B., 1927, *Transactions ASCE*, Vol. 90, pp. 303-316.
- Timblin, L., Moran, W., and Garstka, W., 1957, "Use of Monomolecular Layers for Reservoir Evaporation Reduction," *J. Amer. Water Works Assoc.*, Vol. 49, pp. 841-848.
- US Dept. of Commerce, 1955, *Instructions for Climatological Observers*, Circular B, U.S.G.P.O.
- Vines, R. G., 1962, "Evaporation Control: a Method of Treating Large Surfaces," *Retardation of Evaporation by Monolayers*, V. K. La Mer, ed., Academic Press, New York, pp. 137-160.

L. Z. Zeng
Graduate Research Assistant.

J. F. Klausner
Assistant Professor.

Department of Mechanical Engineering,
University of Florida,
Gainesville, FL 32611

Nucleation Site Density in Forced Convection Boiling

Measurements of nucleation site density, n/A , have been obtained for forced convection boiling of refrigerant R113 in a horizontal 25 × 25 mm i.d. square transparent test section with a nichrome heating strip. It has been found that the behavior of the nucleation site density is significantly different from that found in pool boiling. The mean vapor velocity, heat flux, and system pressure appear to exert a strong parametric influence. It is demonstrated that although the nucleation site density is dependent on the critical cavity radius, r_c , it is not sufficient for correlating n/A .

Introduction

The heat transfer associated with forced convection boiling is typically treated as resulting from two distinct and additive contributions as suggested by Rohsenow (1952): that due to bulk turbulence and that due to the ebullition process. Chen (1966) coined the term macroconvection to designate the transport of heat from the heating surface due to the bulk turbulent motion of the two-phase mixture and the term microconvection to designate that portion of heat transport associated with the incipience, growth, and departure of vapor bubbles. Chen (1966) subsequently proposed the following flow boiling heat transfer relation:

$$h_{2\phi} = Eh_l + Sh_b \quad (1)$$

where $h_{2\phi}$ is the flow boiling heat transfer coefficient, h_l is the single-phase heat transfer coefficient due to the liquid fraction flowing, h_b is the heat transfer coefficient appropriate for nucleate pool boiling, E is an amplification factor to account for increasing bulk turbulence with increasing vapor quality, and S is a suppression factor to account for the effective superheat seen by growing vapor bubbles during flow boiling. Here, Eh_l is the heat transfer contribution due to macroconvection while Sh_b is that due to microconvection. Numerous flow boiling heat transfer correlations have since been proposed that follow the same basic form as Eq. (1), many of which have been tested by Gungor and Winterton (1986). None of these correlations can satisfactorily correlate all of the flow boiling heat transfer data available in the literature. Klausner et al. (1992a) have demonstrated that the bubble departure mechanism for pool and flow boiling can be significantly different, depending on flow conditions, thus casting doubt on Chen's (1966) formulation of the microconvective component of heat transfer. In order to model the microconvection component of heat transfer in flow boiling reliably, detailed information on the incipience, growth, and departure of vapor bubbles is required. This work is specifically concerned with nucleation site density in forced convection boiling.

Due to its governing influence on heat transfer, the nucleation site density has been the focus of numerous investigations for pool boiling (Clark et al., 1959; Griffith and Wallis, 1960; Kurihara and Meyers, 1960; Gaertner and Westwater, 1960; Hsu, 1962; Gaertner, 1963, 1965; Nishikawa et al., 1967; Singh et al., 1976). The general consensus from these investigations is that the formation of nucleation sites is highly dependent on surface roughness, geometry of microscopic scratches and pits on the heating surface, the wettability of the fluid, the amount of foreign contaminants on the surface, as well as the

material from which the surface was fabricated. Due to the large number of variables that are difficult to control, none of these investigators were successful in developing a general correlation for nucleation site density. Griffith and Wallis (1960) suggested that for a given surface the critical cavity radius, r_c , is the only length scale pertinent to incipience provided the wall superheat is uniform. Although they recognized the wall superheat is nonuniform in pool boiling, they used r_c to correlate the nucleation site density as follows:

$$\frac{n}{A} = C_1 \left(\frac{1}{r_c} \right)^m \quad (2)$$

where n/A is the nucleation site density, C_1 and m are empirically determined constants, and when $\rho_l \gg \rho_v$

$$r_c = \frac{2\sigma T_{\text{sat}}}{\rho_v h_{fg} \Delta T_{\text{sat}}} \quad (3)$$

where T_{sat} is the saturation temperature, σ is the surface tension, h_{fg} is the latent heat of vaporization, and $\Delta T_{\text{sat}} = T_w - T_{\text{sat}}$ is the wall superheat.

Nucleation site density data of Griffith and Wallis (1960) for pool boiling of water on a copper surface are shown in Fig. 1 as a function of ΔT_{sat} . For $n/A < 4 \text{ cm}^{-2}$ the nucleation site density increases smoothly with increasing ΔT_{sat} . However, for $n/A > 4 \text{ cm}^{-2}$ no correlation exists between n/A and ΔT_{sat} . Moore and Mesler (1961) used a fast response thermocouple to demonstrate that the heating surface temperature directly beneath a nucleation site in pool boiling experiences rapid fluctuations. Recently Kenning (1991) used thermochromic liquid crystals to measure the spatial variation of wall superheat with pool boiling of water on a 0.13-mm-thick stainless steel heater. It was demonstrated that the wall superheat was very nonuniform and $|\Delta T'_{\text{sat}}|/\Delta T_{\text{sat}}$ varied from 0.25 to 1.5 over a distance of a few mm, where an overbar implies an ensemble spatial average and a prime denotes a spatial variation from the mean. Using a conduction analysis, it was also shown that in the presence of ebullition, spatial nonuniformities of wall superheat on the surface of "thick plates" may also be significant depending on geometry and thermal conductivity of the plate. Kenning's (1991) result suggests that a microlength scale, which is related to the spatial temperature field, may also be important in characterizing incipience of vapor bubbles. According to the suggestion of Eddington et al. (1977) and the experimental findings of Calka and Judd (1985), at low n/A where nucleation sites are sparsely distributed, neighboring nucleation sites do not interact thermally. However, at large n/A where nucleation sites are closely packed, thermal interference among neighboring sites exists. Since it has been demonstrated that ΔT_{sat} is highly nonuniform in the presence of nucleation sites, a question arises as to whether at large n/A the average wall superheat is sufficient for characterizing the

Contributed by the Heat Transfer Division for publication in the JOURNAL OF HEAT TRANSFER. Manuscript received by the Heat Transfer Division March 1992; revision received August 1992. Keywords: Boiling, Forced Convection. Associate Technical Editor: L. C. Witte.

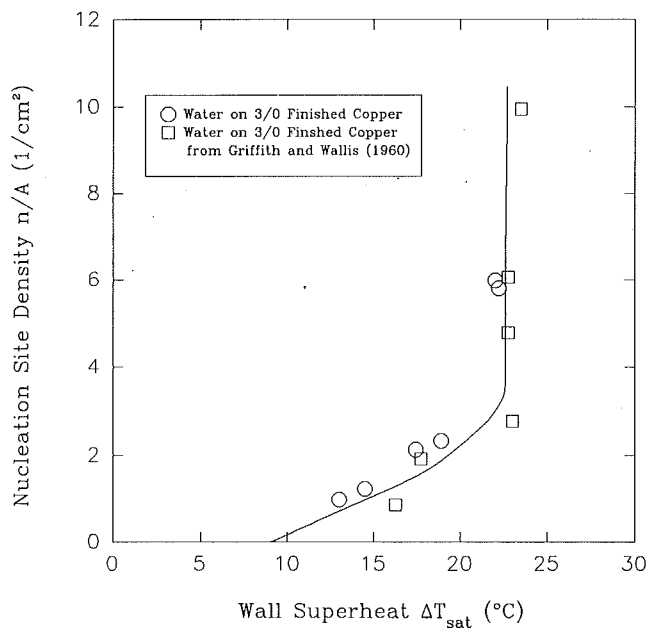


Fig. 1 Pool boiling nucleation site density data from Griffith and Wallis (1960)

local wall superheat experienced by individual nucleation sites. The data displayed in Fig. 1 suggest that it is not.

Few similar studies on nucleation site density in flow boiling have been reported. In one such investigation Eddington and Kenning (1978) measured the nucleation site density with subcooled flow boiling of water for a narrow range of flow conditions. It was suggested that n/A is related to r_c . The objectives of the present work are twofold: (1) to study the influence of flow and thermal conditions on the nucleation site density in saturated forced convection boiling, and (2) determine whether or not the nucleation site density in flow boiling is solely a function of the critical radius, r_c , as has been suggested for pool boiling. Measurements of nucleation site density have been obtained for flow boiling of refrigerant R113 in a 25×25 mm i.d. square transparent tube. These measurements have been obtained for the isolated bubble regime with stratified flow. In general, the liquid/vapor interface was wavy and periodic slugs of liquid were observed passing through the test section. No flow regime transitions were observed. The liquid phase Reynolds number based on the mean velocity ranged from 12,000 to 27,000 and that for the vapor phase ranged from 24,000 to 80,000. The flow conditions are characterized by the mass flux, G , liquid film thickness, δ , vapor quality, x , mean liquid velocity u_l , and mean vapor velocity, u_v . Thermal conditions are characterized by the heat flux, q_w , the wall superheat, ΔT_{sat} , and saturation conditions (saturation temperature, T_{sat} , or saturation pressure, P_{sat}). The controllable inputs of the flow boiling facility are: G , x , P_{sat} (or T_{sat}), and q_w . Of the flow parameters considered, only two are independent since the mean liquid and vapor velocities were respectively calculated from

$$u_l = \frac{G(1-x)D}{\rho_l \delta} \quad (4)$$

and

$$u_v = \frac{GxD}{\rho_v(D-\delta)} \quad (5)$$

where D is the inside dimension of the horizontal square test section for which only the lower surface is covered with a liquid film. Therefore, when investigating the influence of one of the flow parameters on nucleation site density at constant saturation conditions, only one other flow parameter could be held constant, which introduced complexities in interpreting the data. The range of flow and thermal parameters covered in this work, which to a large extent were governed by the ability to visualize nucleation sites, are as follows: $G = 125$ – 290 kg/m²-s, $u_v = 1.6$ – 4.7 m/s, $u_l = 0.35$ – 0.68 m/s, $\delta = 3.5$ – 9.5 mm, $q_w = 14.0$ – 23.0 kW/m², $\Delta T_{sat} = 13.0$ – 18.0 °C, and $T_{sat} = 55.0$ – 75.0 °C.

Experimental Facility

The experimental facility in which flow boiling measurements of nucleation site density were obtained is shown schematically in Fig. 2. The refrigerant R113 forced convection boiling facility has been designed specifically to allow for flow visualization. A variable speed model 221 Micropump is used to pump R113 through the facility. The volumetric flow rate of refrigerant through the facility is monitored with an Erdco Model 2521 vane type flow meter equipped with a 4–20 mA analog output. Calibration of the flow meter demonstrates that it is accurate to within ± 0.5 percent of full scale, which is the repeatability claimed by the manufacturer. At the outlet of the flow meter, five preheaters, each of which has a maximum heat rate of 5 kW, have been installed. Each preheater consists of a 25.4 mm i.d., 1.2-m-long hard copper pipe around which 18 gage nichrome wire has been circumferentially wrapped. The nichrome wire is electrically insulated from the copper pipe with ceramic beads. The heaters are thermally insulated with 25.4-mm-thick fiberglass insulation. The voltage inputs to the preheaters are controlled with five 240 volt a-c autotransformers. The heat loss from the preheaters as a function of temperature difference between the insulation outer surface and ambient air has been predetermined from calibration.

A horizontal flow boiling visual test section is located downstream of the preheaters. A capacitance based liquid film thickness sensor, described in detail by Klausner et al. (1992b) has been installed on either side of the test section. The main body of the test section is comprised of a 25×25 mm inner dimension square pyrex tube that is 4 mm thick and 0.457 m long. A 0.13-mm-thick and 22-mm-wide nichrome strip, used for heating, has been attached to the lower inside surface of the square tube with epoxy. Six equally spaced 36 gage type E thermocouples have been attached to the back side of the nichrome strip using high thermal conductivity epoxy. In order to avoid biased temperature readings caused by a "fin effect," the thermocouple leads were also attached to the back of the heating strip over a length of at least 7 cm before being exposed

Nomenclature

D = square test section inner dimension, m
 G = mass flux, kg/m²-s
 h_{fg} = latent heat of vaporization, J/kg-K
 n/A = nucleation site density, 1/cm²
 r_c = critical cavity radius, m

T_{sat} = saturation temperature, °C or K
 ΔT_{sat} = wall superheat = $T_w - T_{sat}$, °C
 u = mean velocity, m/s
 x = vapor quality

δ = liquid film thickness, m or mm
 ρ = density, kg/m³
 σ = surface tension, N/m

Subscripts

l = liquid
 v = vapor

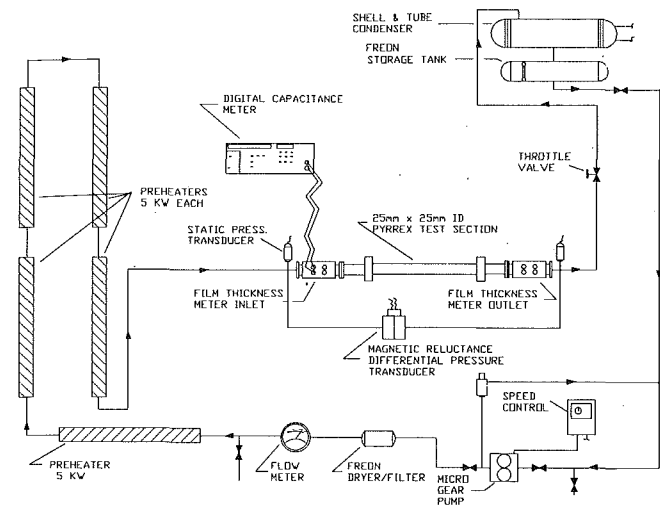


Fig. 2 Schematic diagram of flow boiling facility

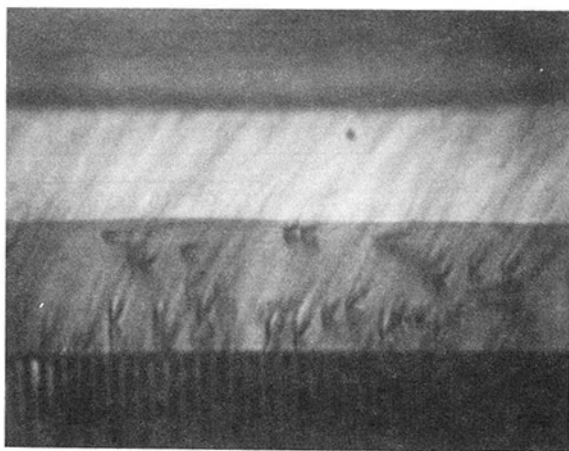


Fig. 3 Typical photograph of nucleation site density

to ambient air. The thermocouples are accurate to within $\pm 0.5^\circ\text{C}$ and measurements are repeatable to within $\pm 0.1^\circ\text{C}$. A conduction analysis showed that the temperature difference between the upper and lower surface of the heating strip is within 0.1°C for the maximum heat flux investigated and is within the repeatability of the thermocouples. A similar test section was fabricated in which the underside of the nichrome strip was coated with cholesteric liquid crystals. In order to heat the strip, a 36 volt, 120 amp d-c power supply has been electrically connected across the brass blocks with 2 gage cable.

Viatran model 2416 static pressure transducers have been installed at the inlet and outlet of the test section to measure the saturation pressure. They have an accuracy of ± 0.5 percent of full scale (30 psig). All bulk temperature and exterior temperature measurements are made with type E thermocouples. All analog signals have been input to an Access 12 bit digital data acquisition system, which consists of two 16-channel multiplexer cards with programmable gain from 1 to 1000. The multiplexer cards are interfaced with an 8-channel, 12-bit analog to digital (A/D) converter, which was mounted in an AT style personal computer.

The nucleation site density was measured optically with a digital imaging facility. The facility consists of a Videk Megaplus CCD camera with 1320×1035 pixel resolution. The CCD camera is equipped with a Vivitar 50 mm macro lens with high resolution and low optical distortion. The output of the CCD camera is input to an Epix 4 megabyte framegrabber. The framegrabber allows for either high resolution (1320×1035) or low resolution (640×480) imaging. Due to

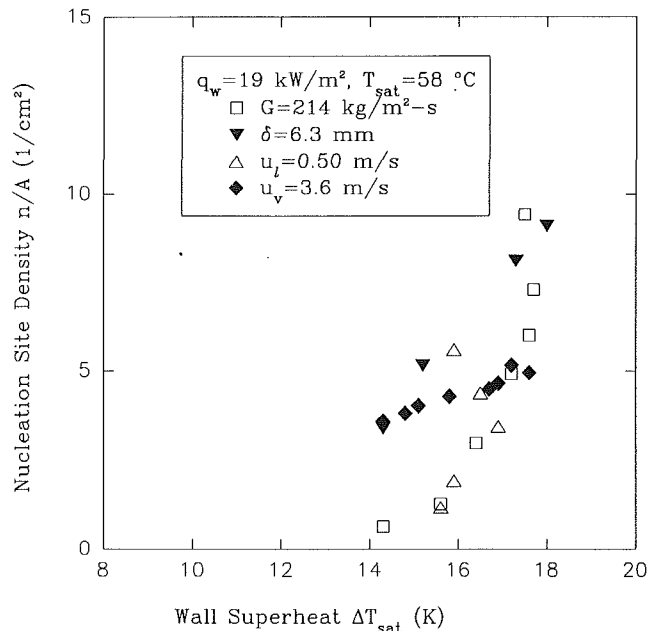


Fig. 4 Nucleation site density as a function of wall superheat for constant heat flux and saturation temperature

the wavy interface of the two-phase mixture it is not possible to observe the nucleation sites clearly from a view normal to the heating surface. Therefore, the nucleation sites must be viewed through the side wall of the test section through the liquid film. A typical image of nucleation sites is displayed in Fig. 3. Images are displayed on a Sony analog monitor with 1000 lines per inch resolution, and may also be printed on a Hewlett Packard Laser Jet III laser printer. Only nucleation sites within a 1.4-cm-wide by 2.2-cm-long area located at the center of the strip were counted. The nucleation site density measured from an ensemble average of 50 images was compared against that based on an average of ten images; identical results were obtained. Therefore, all nucleation site density measurements reported herein are based on an ensemble average of ten images. Presumably intermittent sites are accounted for. The problem of hysteresis was avoided by measuring nucleation site density only for increasing heat flux and increasing vapor velocity.

Experimental Results

Nucleation site density measurements have been obtained for a constant heat flux, $q_w = 19 \text{ kW/m}^2$, and saturation temperature, $T_{\text{sat}} = 58^\circ\text{C}$, over a range of flow conditions in which either the mass flux, G , liquid film thickness, δ , liquid velocity, u_l , or vapor velocity, u_v , was maintained constant. The nucleation site density, n/A , is shown as a function of wall superheat, ΔT_{sat} , in Fig. 4. The n/A data are not well correlated with ΔT_{sat} . In light of Fig. 1 and Eqs. (2) and (3), the behavior of n/A with ΔT_{sat} is considered to be anomalous. In order to demonstrate that the observed behavior is not simply due to experimental error, pool boiling nucleation site density data were obtained using the current facility by filling the test section with liquid and heating the nichrome surface while the circulation pump was off. Therefore the only net flow was induced by natural convection currents. The data are displayed in Fig. 5 as a function of both ΔT_{sat} and q_w . It is seen that n/A increases smoothly with both ΔT_{sat} and q_w in a similar fashion to the data shown in Fig. 1. As seen from Fig. 4, parameters other than ΔT_{sat} alone appear to exert an influence on n/A .

In order to examine the influence of the flow parameters on n/A , the nucleation site density is first plotted against vapor

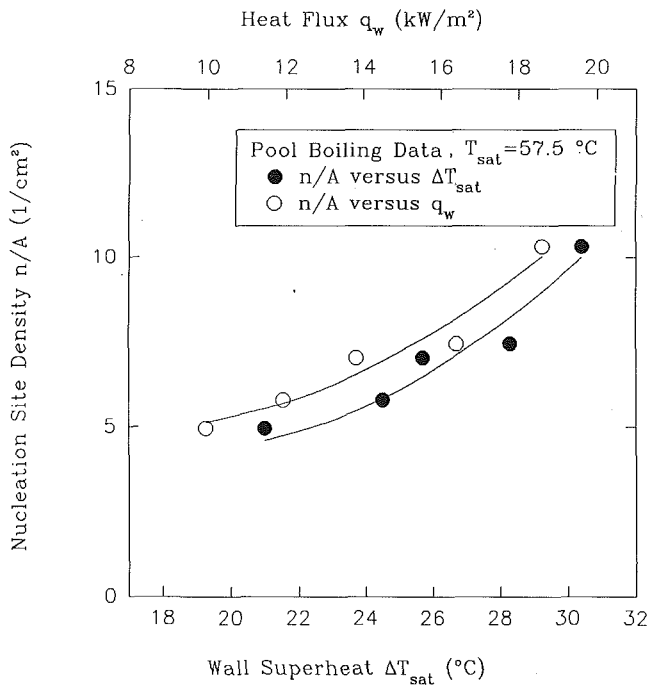


Fig. 5 Pool boiling nucleation site density as a function of wall superheat

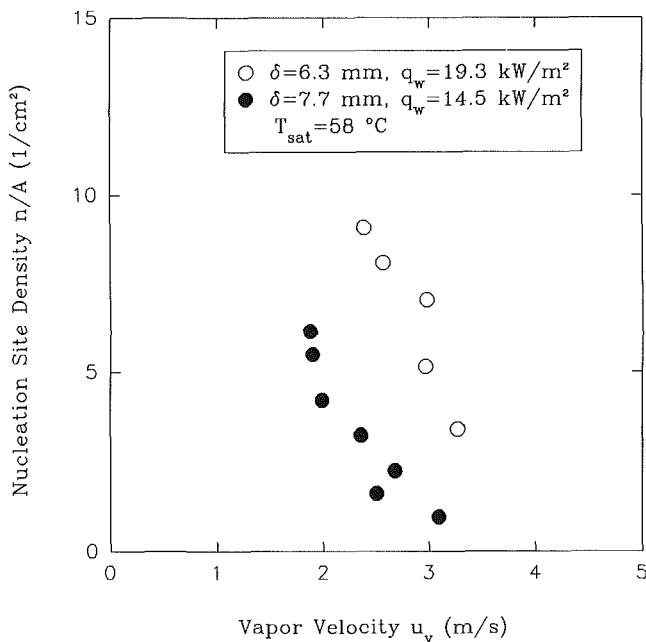


Fig. 6 Nucleation site density as a function of vapor velocity for constant heat flux and liquid film thickness

velocity at a fixed heat flux, q_w , and fixed liquid film thickness, δ , as shown in Fig. 6. It is seen that n/A decreases markedly with increasing vapor velocity, u_v . At a fixed heat flux, liquid film thickness, and saturation conditions, the data appear to fall on a single curve. As the heat flux is increased the curve shifts toward higher nucleation site density. Therefore, when investigating the influence of the flow parameters on n/A the heat flux will be maintained constant. Upon examination of Eqs. (4) and (5) it is possible that the trend shown in Fig. 6 is due to either increasing G or u_l instead of increasing u_v . To sort out whether G , u_v , or u_l has a controlling influence on n/A , Figs. 7 and 8 have been prepared. In Fig. 7, n/A is shown to increase with increasing G when u_l when q_w are fixed, but

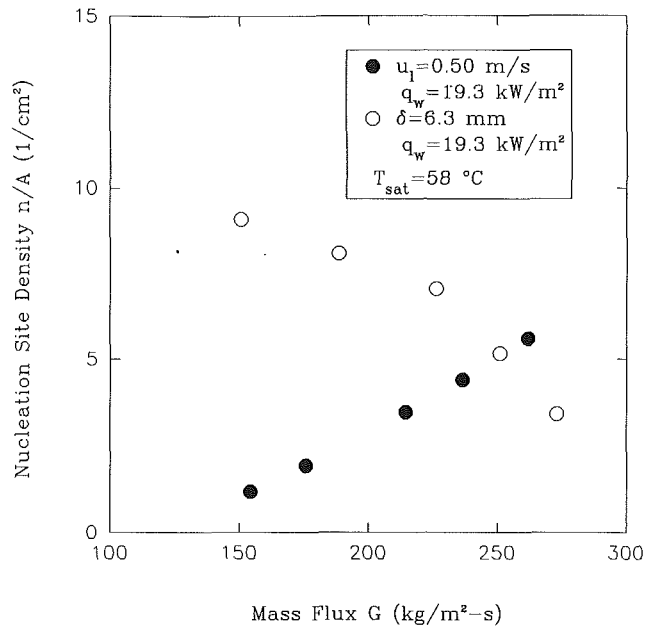


Fig. 7 Nucleation site density as a function of mass flux

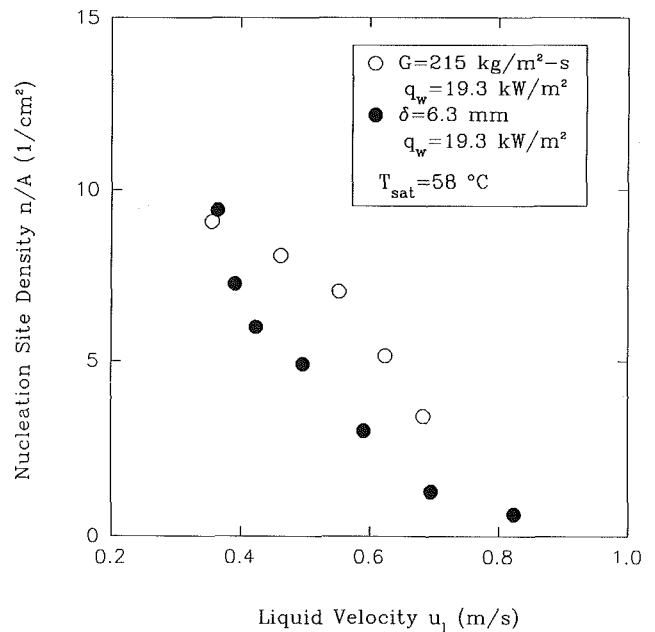


Fig. 8 Nucleation site density as a function of liquid velocity

decreases with increasing G when δ and q_w are fixed, and thus it appears that parameters other than G are controlling n/A . In Fig. 8 n/A is shown to decrease with increasing u_l for fixed G and q_w . When δ and q_w are fixed, n/A also decreases with increasing u_l , but the curve shape is significantly different. When comparing Figs. 6 and 8 it appears that n/A is better behaved when displayed as a function of u_v . Further evidence of this supposition is provided in Fig. 9 where n/A is displayed as a function of u_v for $q_w = 19.5 \text{ kW/m}^2$, $T_{\text{sat}} = 58^\circ\text{C}$, $G = 215 \text{ kg/m}^2\text{-s}$, and $u_l = 0.58$ and 0.49 m/s . It is seen that all of the data approximately fall on a single curve, thus demonstrating the governing influence of the mean vapor velocity on nucleation site density. The liquid film thickness δ is also shown as a function of u_v . Thus, the effect of liquid film thickness on n/A is also included in Fig. 9. Therefore, it is necessary to investigate the influence of δ on n/A .

In pool boiling, Nishikawa et al. (1967) demonstrated that

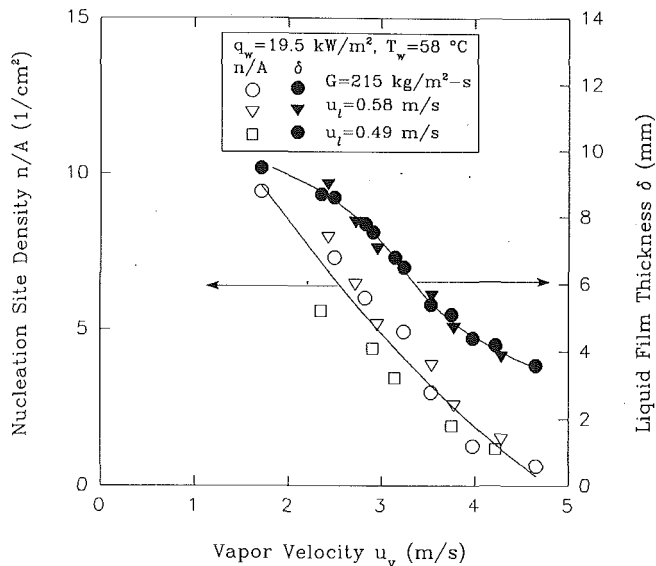


Fig. 9 Nucleation site density and liquid film thickness as a function of vapor velocity for constant heat flux and either constant mass flux or constant liquid velocity

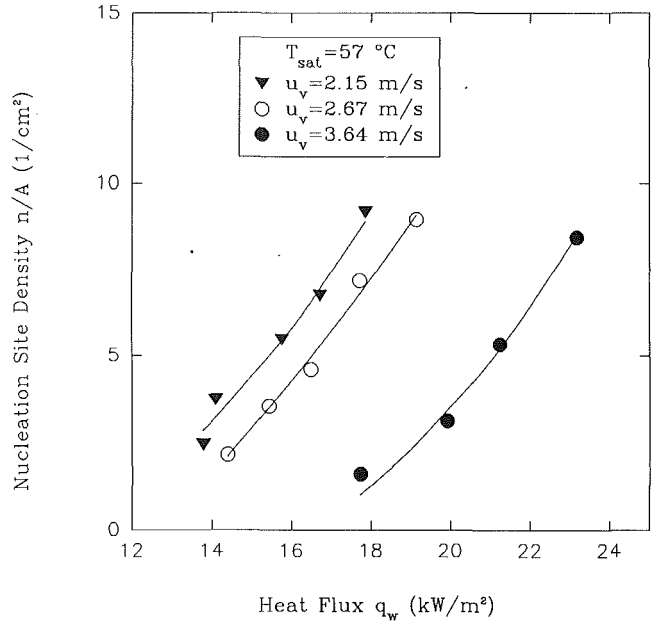


Fig. 11 Nucleation site density as a function of heat flux

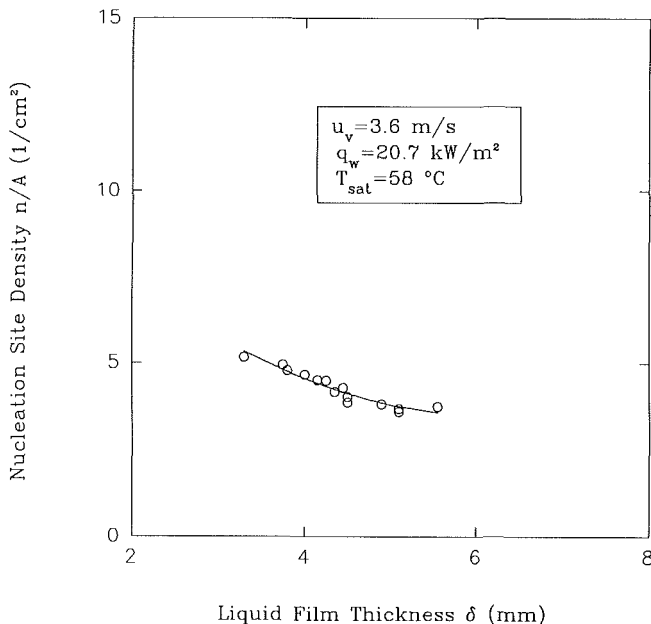


Fig. 10 Nucleation site density as a function of liquid film thickness

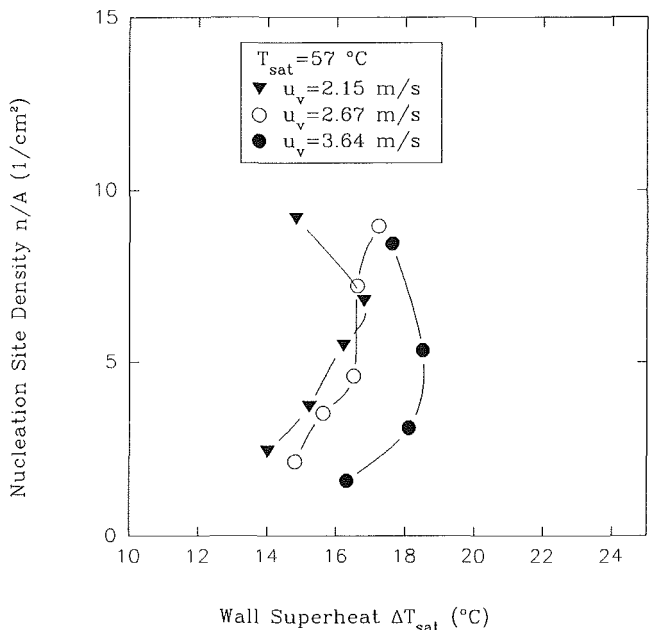


Fig. 12 Nucleation site density as a function of wall superheat

the nucleation site density increases with declining liquid film thickness. Mesler (1976) postulated that the same behavior should follow for flow boiling and used it to explain the measured increase in flow boiling heat transfer coefficient with declining liquid film thickness for stratified or annular flow. To the best of the authors' knowledge direct evidence supporting or refuting Mesler's claim has yet to be presented. To sort out the direct influence of liquid film thickness on nucleation site density, Fig. 9 suggests that it is necessary to maintain a fixed u_v , q_w , and T_{sat} . Figure 10 shows n/A as a function of liquid film thickness at $u_v = 3.58$ m/s, $q_w = 20.7$ kW/m², and $T_{sat} = 58$ °C. It is seen that indeed n/A increases with declining film thickness, which tends to support Mesler's claim regarding n/A as a function of film thickness, provided that u_v , q_w , and T_{sat} are fixed. However, over the range of film thickness investigated (3–6 mm) the increase in n/A is only marginal. Because n/A was obtained using a visualization technique,

it was not possible to obtain data for $\delta < 3$ mm. As $\delta \rightarrow 0$ the behavior of n/A is uncertain. To determine whether u_v or δ has a stronger influence on n/A , Fig. 9 is re-examined where it is seen that n/A decreases with decreasing δ , which is due primarily to increasing u_v . Therefore, it appears that u_v has a governing influence on the nucleation site density. An explanation and significance of this finding will be discussed later.

When testing the influence of thermal conditions on n/A , it is necessary to control u_v . In Fig. 11, n/A is shown as a function of q_w for three different values of u_v at $T_{sat} = 57$ °C. It is seen that at a fixed u_v , n/A increases smoothly with increasing q_w . As u_v increases, the curves shift toward decreasing n/A . The trends are consistent with those in Fig. 6. The n/A data from Fig. 11 are shown as a function of ΔT_{sat} in Fig. 12. The data display an anomalous behavior similar to that in Fig. 4.

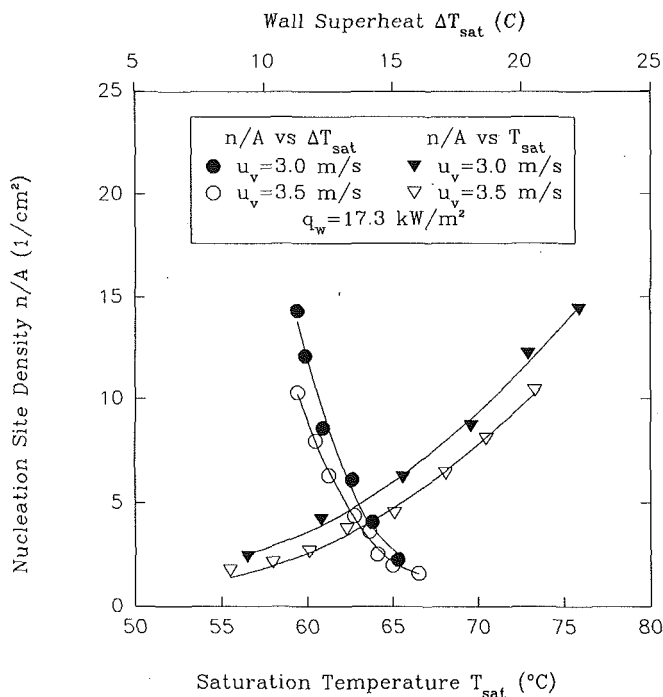


Fig. 13 Nucleation site density as a function of saturation temperature

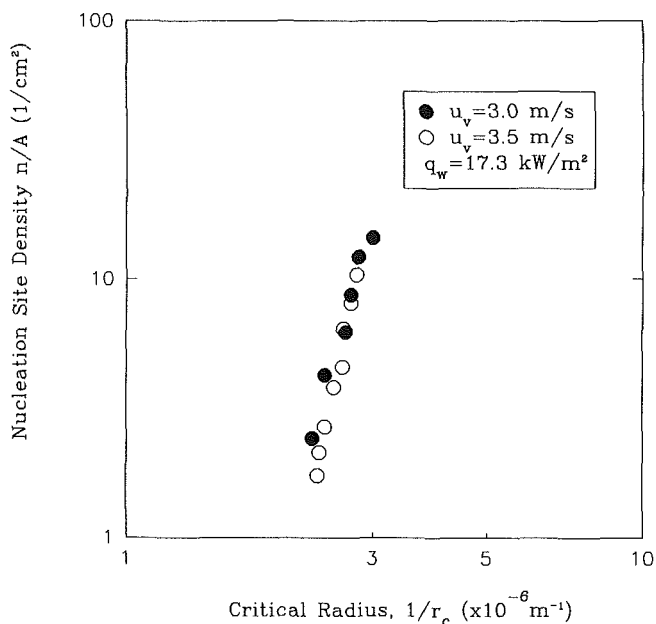


Fig. 14 Nucleation site density as a function of critical radius for constant heat flux and vapor velocity

To examine the dependence of n/A on the critical radius, it was decided that a constant heat flux would be maintained, and r_c would be controlled by raising the system pressure. Doubling the system pressure has the effect of essentially doubling the vapor density and increasing T_{sat} by several percent. The nucleation site density was measured for fixed u_v and q_w in which T_{sat} increased by 20°C by raising the system pressure from 1.3 to 2.3 bars. From these data Figs. 13 and 14 have been prepared. It is seen from Fig. 13 that ΔT_{sat} decreases with increasing T_{sat} . Nevertheless, n/A increases due to a decrease in r_c . This can be seen from Fig. 14, which shows increasing n/A with increasing $1/r_c$. Because the only physically sound explanation for the increase in n/A with increasing T_{sat} is due to a decrease in r_c , these data suggest that r_c is an important

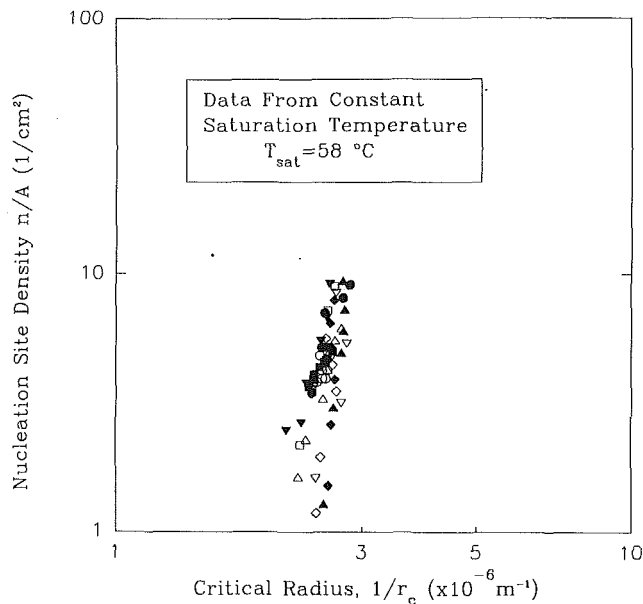


Fig. 15 Nucleation site density as a function of critical radius for all the flow boiling data

parameter in characterizing flow boiling nucleation site density.

Discussion of Results

Although the data in Fig. 14, as well as theoretical considerations, suggest that r_c is an important correlating parameter for flow boiling nucleation site density, it is by itself insufficient for correlating n/A . In Fig. 15, all the nucleation site density measurements obtained in this study, for $T_{sat} = 58^\circ\text{C}$, are displayed as a function of r_c . Although the data appear to be collapsed, a correlation in the form of Eq. (2) would not be useful due to the steepness of the slope. The pool boiling nucleation site density data of Griffith and Wallis (1960) display a similar behavior for large n/A .

In an attempt to understand this behavior, consideration is first given to the pool boiling analysis of Hsu (1962) in which it was demonstrated that the nonuniform liquid temperature field seen by a vapor embryo attempting to grow is important when considering incipience criteria. If a linear temperature profile is assumed for the liquid layer, a minimum cavity radius required for incipience may be expressed solely as a function of either ΔT_{sat} or q_w , provided properties are maintained constant. The data displayed in Fig. 4 show that ΔT_{sat} or q_w alone are insufficient for correlating flow boiling n/A data. Bergles and Rohsenow (1964) attempted a similar analysis for flow boiling, and the assumption of a linear temperature profile can also lead to the definition of a critical cavity radius that is solely dependent on ΔT_{sat} or q_w , provided properties are maintained constant. One shortcoming in these analyses is the assumption of a linear temperature profile in the liquid thermal layer. Certainly, the strength of the heat flux as well as that of the bulk turbulence will have a strong influence on the shape of the thermal layer. Nevertheless, these analyses suggest that in addition to the critical cavity radius based on Eq. (3), a length scale related to the thermal layer thickness may also be important in characterizing n/A .

In addition, it is emphasized that r_c has been calculated using Eq. (3) taking the wall superheat to be the average value, $\overline{\Delta T_{sat}}$. As mentioned earlier, Kenning (1991) used liquid crystal thermography to show that $|\Delta T'_{sat}|/\overline{\Delta T_{sat}}$ could be as large as 1.5 for pool boiling. In this study the liquid crystal boiling test section was used in conjunction with a Panasonic video recorder to record the flow boiling temperature field of the

heating surface for the following flow and thermal conditions: $u_v = 3.0$ m/s, $q_w = 18.1$ kW/m², and $T_{\text{sat}} = 58.3^\circ\text{C}$. It was found the temperature field was very nonuniform in both space and time and $|\Delta T'_{\text{sat}}|/\Delta T_{\text{sat}}$ was as large as 0.5. Therefore, it appears that the average wall superheat is insufficient for characterizing the local wall superheat experienced by individual nucleation sites.

The data presented thus far satisfy the objectives of this work: (1) Of the flow and thermal parameters investigated, u_v , q_w , and T_{sat} appear to have a governing influence on n/A . (2) By itself, r_c is not sufficient for correlating n/A . Pool boiling n/A correlations based on r_c are not applicable to flow boiling.

The above results raise a fundamental question: What is the physical basis for the apparently strong influence of u_v and q_w on n/A ? Unfortunately, with the experimental technique employed in this investigation, a conclusive answer to this question is out of reach. Some insight is gained by considering that bulk turbulence in stratified two-phase flow is largely dependent on interfacial waves. The interfacial shear stress is the means by which wave information is communicated to the liquid film. Andritsos and Hanratty (1987) have provided extensive experimental evidence that the mean vapor velocity is a controlling parameter on the interfacial shear stress. Increasing u_v results in enhanced bulk turbulence, and therefore a variation in u_v or q_w should have a significant impact on the heating surface temperature field as well as the thermal layer temperature profile, which are both believed to control the incipience process. Future investigations should focus on measuring the probability density function of the wall superheat, pdf (ΔT_{sat}) as well as the thermal layer temperature profile. The pdf (ΔT_{sat}) and the thermal layer temperature profile may be useful in assessing the influence of spatial nonuniformities of ΔT_{sat} on n/A and in providing insight into possible interactions of micro- and macroconvection.

Acknowledgments

This material is based on work supported by the National Science Foundation under Grant No. CTS-9008269. The many useful suggestions provided by Professors B. T. Chao and R. Mei during the course of this work are greatly appreciated.

References

Andritsos, N., and Hanratty, T. J., 1987, "Influence of Interfacial Waves in Stratified Gas-Liquid Flows," *AIChE J.*, Vol. 33, No. 3, pp. 444-454.

Bergles, A. E., and Rohsenow, W. M., 1964, "The Determination of Forced-Convection Surface-Boiling Heat Transfer," *ASME JOURNAL OF HEAT TRANSFER*, Vol. 86, pp. 365-372.

Calka, A., and Judd, R. L., 1985, "Some Aspects of the Interaction Among Nucleation Sites During Saturated Nucleate Boiling," *Int. J. Heat Mass Transfer*, Vol. 28, No. 12, pp. 2331-2341.

Chen, J. C., 1966, "Correlation for Boiling Heat Transfer to Saturated Fluids in Convective Flow," *I&EC Process Design and Development*, Vol. 5, No. 3, pp. 322-329.

Clark, H. B., Strenge, P. S., and Westwater, J. W., 1959, "Active Sites for Nucleate Boiling," *Chem. Eng. Progress Symp. Series*, Vol. 55, No. 29, pp. 103-110.

Eddington, R. I., Kenning, D. B. R., and Korneichev, A. I., 1977, "Comparison of Gas and Vapor Bubble Nucleation on a Brass Surface in Water," *Int. J. Heat Mass Transfer*, Vol. 21, pp. 855-862.

Eddington, R. I., and Kenning, D. B. R., 1978, "The Prediction of Flow Boiling Bubble Populations From Gas Bubble Nucleation Experiments," *Proc. 6th Int. Heat Transfer Conf.*, Vol. 1, pp. 275-280.

Gaertner, R. F., and Westwater, J. W., 1960, "Population of Active Sites in Nucleate Boiling Heat Transfer," *Chem. Eng. Progress Symp. Series*, Vol. 56, No. 30, pp. 39-48.

Gaertner, R. F., 1963, "Distribution of Active Sites in the Nucleate Boiling of Liquids," *Chem. Eng. Progress Symp. Series*, Vol. 59, No. 41, pp. 52-61.

Gaertner, R. F., 1965, "Photographic Study of Nucleate Pool Boiling on a Horizontal Surface," *ASME JOURNAL OF HEAT TRANSFER*, Vol. 87, pp. 17-29.

Griffith, P., and Wallis, J. D., 1960, "The Role of Surface Conditions in Nucleate Boiling," *Chem. Eng. Progress Symp. Series*, No. 30, Vol. 56, pp. 49-63.

Gungor, K. E., and Winterton, R. H. S., 1986, "A General Correlation for Flow Boiling in Tubes and Annuli," *Int. J. Heat Mass Transfer*, Vol. 29, No. 3, pp. 351-358.

Hsu, Y. Y., 1962, "On the Size Range of Active Nucleation Cavities on a Heating Surface," *ASME JOURNAL OF HEAT TRANSFER*, Vol. 98C, pp. 207-216.

Kenning, D. B. R., 1991, "Wall Temperature Patterns in Nucleate Boiling," Technical Report OUEL 1867/91, University of Oxford, Oxford, United Kingdom.

Klausner, J. F., Mei, R., Bernhard, D. M., and Zeng, L. Z., 1992a, "Vapor Bubble Departure in Forced Convection Boiling," *Int. J. Heat Mass Transfer*, in press.

Klausner, J. F., Zeng, L. Z., and Bernhard, D. M., 1992b, "Development of a Film Thickness Probe Using Capacitance for Asymmetrical Two-Phase Flow With Heat Addition," *Rev. Sci. Instrum.*, Vol. 63, No. 5, pp. 3147-3152.

Kurihara, H. M., and Meyers, J. E., 1960, "The Effects of Superheat and Surface Roughness on Boiling Coefficients," *AIChE J.*, Vol. 6, No. 1, pp. 83-91.

Mesler, R. B., 1976, "A Mechanism Supported by Extensive Experimental Evidence to Explain High Heat Fluxes Observed During Nucleate Boiling," *AIChE J.*, Vol. 22, No. 2, pp. 246-252.

Moore, F. M., and Mesler, R. B., 1961, "The Measurement of Rapid Surface Temperature Fluctuations During Nucleate Boiling of Water," *AIChE J.*, Vol. 7, No. 4, pp. 620-624.

Nishikawa, K., Kusuda, H., Yamasaki, K., and Tanaka, K., 1967, "Nucleate Boiling at Low Liquid Levels," *Bulletin of JSME*, Vol. 10, No. 38, pp. 328-338.

Rohsenow, W. M., 1952, "Heat Transfer Symposium," Engineering Research Institute, University of Michigan, Ann Arbor, MI.

Singh, A., Mikic, B. B., and Rohsenow, W. M., 1976, "Active Sites in Boiling," *ASME JOURNAL OF HEAT TRANSFER*, Vol. 98C, pp. 401-406.

Effects of Heating Surface Materials on a Liquid-Solid Contact State in a Sessile Drop-Boiling System

S. Inada¹

W.-J. Yang

Department of Mechanical Engineering and
Applied Mechanics,
University of Michigan,
Ann Arbor, MI 48109

Three experimental investigations are performed on the liquid-solid contact state at the instant when a liquid comes in contact with a heating surface in the transition-boiling regime between the maximum evaporation rate point and the spheroidal state: (1) measuring the piezoelectric potential by means of a quartz oscillator being placed on the heating surface, (2) monitoring the boiling sound generated at the instant of liquid-solid contact using a condenser microphone, and (3) observation of drop behavior, by means of high-speed photography. The information obtained from these three investigations is synthesized to quantify the liquid-solid contact state. The study has disclosed the roles of thermal properties and heating surface temperatures on the endurance time of the instantaneous liquid-solid contact state and the relationship between the critical bubble radius and the measured vapor-liquid interfacial pressure difference.

Introduction

The phenomenon of the evaporation of a liquid drop in contact with a heating surface was investigated by Tamura and Tanasawa (1958). Its basic characteristics are exhibited by the lifetime curve, which has the maximum evaporation rate point and the Leidenfrost point corresponding to the minimum and maximum drop evaporation times, respectively. Most literature is concerned with drop evaporation on the heating surfaces in a temperature range of either around or higher than the Leidenfrost point or at and lower than the maximum evaporation rate point. The studies of heating surface materials in these temperature ranges include Baumeister and Simon (1973) and Nishio and Hirata (1978), who treated the effects of thermal properties of heating surface materials on the drop behavior and the Leidenfrost point. Temple-Pediani (1969) investigated the effects of heating surface materials in the temperature range surrounding the maximum evaporation rate point, which diminished with an increase in the thermal conductivity of a heating material. In contrast, Takano and Kobayashi (1991) found that the temperature range expanded toward a higher value in testing a ceramic surface of low thermal conductivity. For water drops on a heating surface with a temperature ranging from the nucleate-boiling state to the transition-boiling state, Makino and Michiyoshi (1984) obtained an empirical formula that correlated the liquid-solid contact time with the heating surface temperature, thermal properties, and drop diameter.

It is revealed from the literature survey that research work on the effects of heating surface materials is limited to the temperature in the vicinity of either the maximum evaporation rate point or the Leidenfrost point. Little attention has been focused on the effects of heating surface materials on the liquid-solid contact state in the transition boiling regime between the maximum evaporation rate point and the Leidenfrost point. The main reasons are that (i) the drop lifetime undergoes

an abrupt change in this range, and (ii) the drop exhibits complex behavior in its short-time stay on the heating surface, such as break-up, splashing, film boiling, and rebound. These factors cause difficulty in a quantitative treatment. When a drop evaporates during a direct contact with a heating surface, the surface temperature at the liquid-solid interface falls instantaneously upon its contact. On the other hand, the interfacial temperature rises if the film-boiling state occurs instantaneously. When bubbles are formed inside the drop, it produces boiling sounds, and some changes may take place at the liquid-solid interface depending upon the bubble size. The references cited above investigated the liquid-solid contact state using high-speed photography. The photographic observation alone is insufficient to unveil the liquid-solid contact state in the transition boiling regime. Other methods should be employed in parallel to quantify an instantaneous liquid-solid contact.

On a drop lifetime curve, the transition regime is generally considered the region where the average drop lifetime is enhanced with an increase in the heating surface temperature. However, in a certain temperature range within the transition-boiling regime, drops exhibited a violent miniaturization phenomenon, resulting in an augmentation in the heat transfer performance. The phenomenon is similar to that of a vapor explosion at the liquid-liquid contact and its miniaturization mechanism is disclosed by Inada and Yang (1991). Such a phenomenon is of interest in the safety problem of nuclear reactors, performance improvements of liquid fuel, internal combustion engines, etc.

The present study is to determine when such a phenomenon will occur and its mechanisms. In order to achieve the objectives: (i) The instantaneous, liquid-solid contact state is determined by measuring the piezoelectric potential using a quartz oscillator placed on the heating surface; (ii) a condenser microphone is employed to monitor the boiling sound, which is generated simultaneously with the liquid-solid contact; and (iii) the dynamic behavior of drops is observed with the aid of high-speed photography. The results obtained from these three experiments are synthesized to quantify the phenomenon, through which the effects of heating surface materials on the liquid-solid contact state are determined.

¹Visiting scholar on leave from the Department of Mechanical Engineering, Gunma University, Kiryu, Japan.

Contributed by the Heat Transfer Division for publication in the JOURNAL OF HEAT TRANSFER. Manuscript received by the Heat Transfer Division July 1991; revision received January 1992. Keywords: Boiling, Direct-Contact Heat Transfer, Sprays-Droplets.

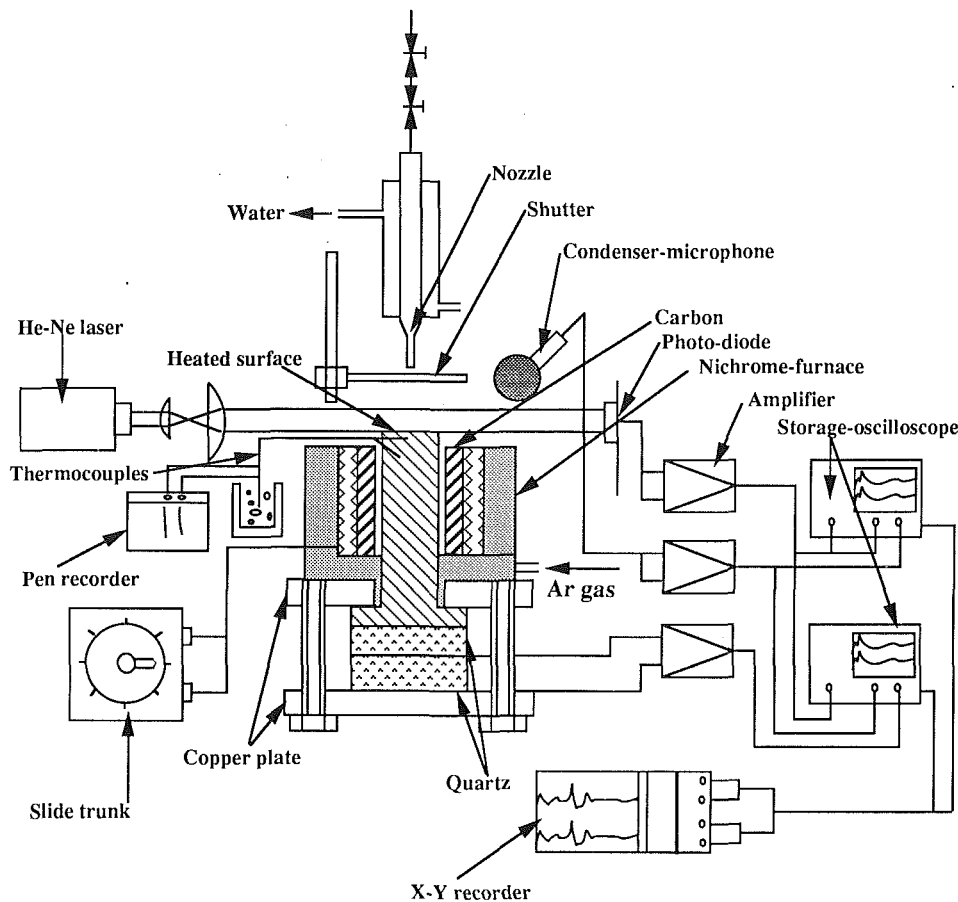


Fig. 1 Schematic of experimental apparatus

Experimental Apparatus and Procedure

Figure 1 is a schematic diagram of the experimental apparatus used in this study. Prior to each test, the distilled water to be used as drops was boiled for over 30 min for degassing. The initial temperature of the falling drops was maintained at a desired subcooling of 85 K by circulating water at a constant temperature around a supply tube, which was connected to the drop nozzle. In order to obtain drops of uniform size (with a 4 mm diameter), two needle valves regulated the flow rate inside the supply tube and maintained the dropping period constant. The oil immersion method was employed to ascertain the uniformity of the drop diameter. Next, 50 drops were collected and measured by means of a direct reading balance

to evaluate the diameter of each drop. Drops were released from a height of 40 mm, equivalent to a Weber number of 43. Upon an impact at this value of the Weber number, drops would not break up due to the impact energy. The drops were continually released from the nozzle and were intercepted by the shutter, which could be suddenly removed to allow only one drop to fall on the center of the heating surface. The falling drops were at ambient conditions of room temperature and one atmospheric pressure.

The heating surface was composed of a cylinder with a 15-mm diameter and a 150-mm length. Its materials were brass, SUS 304, and SUS 304, having its top and side surfaces being plasma-sprayed with 0.5-mm-thick ceramics (Al_2O_3). In the case of the copper cylinder, the tip surface (i.e., impact surface)

Nomenclature

C_p = specific heat of heating surface, kJ/kgK	ΔP = pressure difference across bubble surface, Pa	Y = amplitude of piezoelectric potential, mm
k = drop diameter, mm	ΔP_g = pressure change converted from oscillation acceleration, Pa	β = maximum acoustic pressure, Pa, dB
D_q = diameter of quartz oscillator, mm	ΔP_m = vapor-liquid interfacial pressure difference, Pa	ρ = density of heating surface, kg/m ³
E = amplitude of piezoelectric potential, mV	r = bubble radius, m	ρ_f = drop density, kg/m ³
f = frequency of microbubble formation, Hz	r_0 = critical bubble radius, m	ρ_v = vapor density, kg/m ³
g = oscillation acceleration, m/s ²	t = time, s	σ = surface tension coefficient, N/m
k = thermal conductivity of heating surface, W/mK	T_s = saturated temperature, K	τ = time, ms
L = latent heat of evaporation, kJ/kg	T_v = vapor temperature, K	τ_b = bubble departure time, ms
m = mass of piezoelectric acceleration pickup, g	T_{wi} = initial temperature of heating surface, °C	τ_c = liquid-solid contact time, ms
	ΔT_{sat} = superheat of surrounding liquid = $T_v - T_s$, K	τ_r = residence time of a drop on heating surface, ms

was diffusion-bonded with 0.03-mm-thick platinum plate to prevent its oxidation. Except for the ceramic surface, all surfaces were polished by an emery paper 5/0 (maximum roughness of 0.5 μm after polishing). The maximum roughness on the ceramic surface was 12 μm . The roughness of each surface was measured using a SE-30H Surfcoorder manufactured by the Kosaka Works, Japan. The heat was supplied to the heating surface through the side surface of the cylinder from a nichrome furnace via a carbon hollow cylinder. The temperature regulation was performed by means of a slide trunk.

For monitoring the heating surface temperature, 0.05-mm-dia copper-constantan thermocouples in case of the platinum surface, and 0.05-mm-dia chromel-alumel thermocouples in the case of the SUS 304 surface, were spot-welded on the side surface near the impact surface. In the case of the brass surface, chromel-alumel sheath thermocouples were inserted into holes drilled from the side surface to the cylindrical center. For measuring the ceramic surface temperature, one of each 0.05-mm-dia chromel-alumel thermocouples was attached to the surface and the side using a ceramic adhesive. Argon gas was sent in through a duct underneath the electrical furnace to prevent the oxidation of the cylinder, diffusion-bonded part and thermocouples. The measured temperatures were recorded in a pen recorder.

The lower end of the cylinder was flange-shaped and sat on top of two R-T cut quartzes with a diameter $D_g = 20$ mm and thickness of 10 mm. The flanged end together with the two quartzes was sandwiched between a pair of copper plates and were firmly fixed by bolts. Both end surfaces of each quartz were gold-plated by the vacuum deposition method so that they would function as electrodes. The two quartzes were arranged parallel with one electrode being grounded and the other as lead for the power output.

An acoustic-field-type condenser microphone (frequency characteristics 30 kHz) was employed to detect the boiling sound that was generated at the instant of liquid-solid contact during the initial stage of drop impact. Simultaneous with the boiling sound, elastic-longitudinal waves were generated inside the heating body. The signals were transmitted to the quartzes through the heating body, with the calculated acoustic transmission time of 0.05 ms. By means of quartz oscillator, the waves were measured as piezoelectric potential. The natural frequency of the quartzes was approximately 170 kHz.

The next step is to determine when the boiling sounds were produced after drop impact and when the piezoelectric potentials took place. The drop behavior on the heating surface was detected as the output signal of a photodiode. This signal was superimposed as a time reference on those of both the boiling sounds and the piezoelectric potentials. The expanded beam from a 5 mW He-Ne laser irradiated the heating surface in parallel. The incident light was intercepted by the photodiode with a response time of 2.5 μs and light-receiving area of 6.6 mm^2 . Then, a change in the behavior of the drop on the heating surface would appear as a change in the amount of light obstruction. The output voltages of the photodiode, boiling sounds, and quartz oscillators were simultaneously amplified, stored in storage oscilloscopes, and then delineated on an X-Y recorder in the wave form. The characteristic frequency of the amplifiers had a constant sensitivity up to 30 kHz. The characteristic frequency of the storage-oscilloscope was 60 MHz. The output from the photodiode was also used as a trigger of the storage oscilloscope.

A quartz oscillator can measure the pressure change on its surface as a piezoelectric potential. The results presented in the previous study (Inada and Yang, 1991) indicate the following:

Over the entire range of measurements of the initial heating surface temperature, the boiling sound was detected but the output signal that can be monitored by a quartz oscillator was limited to a certain temperature range. It was within this range

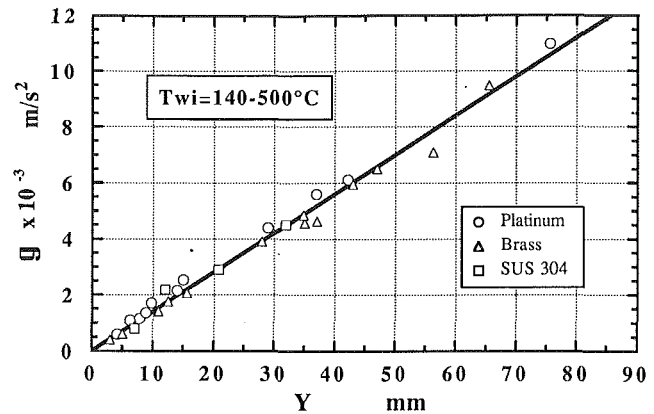


Fig. 2 Calibration curve for conversion between piezoelectric potential and pressure

that one observed liquid-solid contact accompanied by a rapid generation and departure of microbubbles. The output from the quartz oscillator was considered to be due to a pressure difference at the gas-liquid interface, which occurred at a rapid generation of bubbles on the heating surface. For the sake of investigating its propriety, the oscillator output was calibrated and then converted into the pressure change ΔP_g as follows: Under conditions identical to the actual experiment, the apparatus depicted in Fig. 1 was employed. Instead of a drop as a falling body onto the heating surface, a piezoelectric acceleration pickup of mass $m = 1.6$ g, was released. The gravitational acceleration g was measured by an accelerometer with the frequency characteristics of 30 kHz. Its output, together with the piezoelectric potential E from the quartzes, was simultaneously recorded on the storage oscilloscope. The pressure change is

$$\Delta P_g = mg / (\pi D_q^2 / 4) \quad (1)$$

Here, m denotes the mass of the piezoelectric acceleration pickup; g , the oscillation acceleration resulting from the impact; and D_q , the diameter of the quartz oscillator. The measurement of pressure changes on the heating surface by means of the quartz oscillator was based on the calibration curve, E versus ΔP_g .

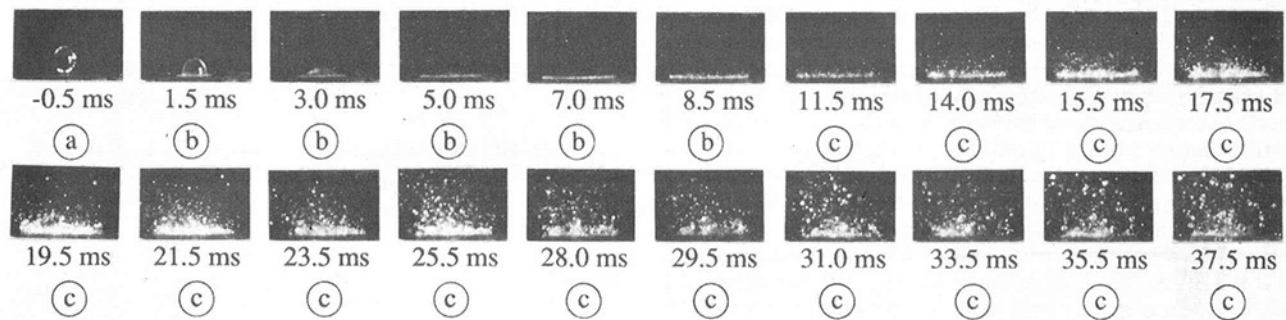
Figure 2 is the calibration curve. The ordinate is the acceleration g measured by the accelerometer, which is equivalent to ΔP_g calculated from Eq. (1). The abscissa is the amplitude Y (mm) of the piezoelectric potential recorded on the X-Y recorder and is equivalent to E (mV). It is disclosed from Fig. 2 that the ΔP_g - E relationship is linear and independent of the heating surface material as well as the temperature.

Results and Discussion

The results are classified into five categories:

1. Process of Drop Deformation and Output Signals From Photodiode. It is disclosed in the present study that under the liquid-solid contact condition, the drop ejected a great number of liquid micro globules splashing into the surroundings. The globule splashing during the process of drop deformation following the impact was exhibited in two forms, Cases I and II, as shown in Fig. 3 for drops on a heated platinum surface. The number under each photograph indicates the elapsed time after the impact. In Case I, the globule splashing occurred at a substantial time after the residence time. This phenomenon resembled that that had been observed at the maximum evaporation rate point. At a certain surface temperature, a spherical drop became a disk shape upon its impact on the surface. It then gradually returned to a spherical shape, followed by rebounding from the surface. The change of drop shape during this period resembles the deformation of a free

Case I Platinum surface at $T_{wi}=160\text{ }^{\circ}\text{C}$



Case II Platinum surface at $T_{wi}=300\text{ }^{\circ}\text{C}$

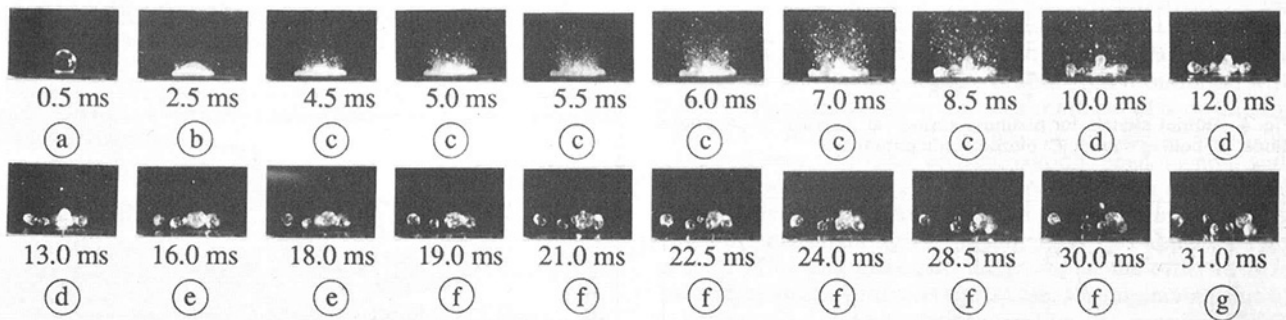


Fig. 3 Miniaturization phenomena (splashing of liquid microglobules)

falling drop due to vibration. The deformation period of the former is practically equal to the vibrational period of the latter. Based on the experimental observation, the residence time τ_r is defined as the time corresponding to the first period in the free vibration of a drop: $\tau_r = (\pi/4)(\rho_f d^3 / \sigma)^{1/2}$. Here ρ_f , d , and σ are, respectively, the density, diameter, and surface tension of the drop. $\tau_r = 23$ ms in the present study. Case II had the drop splashing occurring within the residence time and its pre-impact temperature of the heating surface T_{wi} was higher than that in Case I. In the photographs of Fig. 3, the entire duration of drop deformation is divided into various processes, as characterized by the current drop morphology. The names of these processes are represented by the symbols (a) through (g). (a) denoted the impact process; (b), liquid-film migrating process; (c), splashing process; (d), film boiling process; (e), rebounding process; (f), floating process; and (g), re-impact process. Since the drop morphology changed or the drop position changed in the upward or downward direction, a variation corresponding to this change would appear in the photodiode output signal. Accordingly, it is possible to determine, at each instant, which of the processes (a) through (g) shown in Fig. 3 is taking place by examining the wave shape of the photodiode output signals.

The recording A in Fig. 4 is a photodiode output signal, corresponding to Case II in Fig. 3. During process (a) when the drop was falling toward the heating surface, it was obstructing the light-receiving surface of the photo-sensor, causing a steep fall in the output signal. Upon its impact, the drop spread into a liquid film over the heating surface in process (b). The laser light irradiated the light-receiving surface of the photo sensor again, resulting in a rapid upturn of the output signal. In process (c), the drop was in a violent ejection of liquid micro globules, which locally obstructed the laser light. Consequently, the output signal fluctuated in accordance with

the extent of splashing strength. At the postprocess (c), the drop remained on the heating surface in the form of a disk with a huge crater (in Case II of Fig. 3, the globule splashing flew off from the heating surface). The cratered disk drop gradually became supported by a vapor film. This corresponds to process (d) in the state of partially obstructing the laser beam, causing the output signal to fall. Should the film boiling state be sustained, the laser beam would be obstructed and the output signal would be at a low location. Process (e) had this disk drop rebounding from the heating surface, with the output signal rising upward. The rebounded drop began floating in the air, with the maximum height from the heating surface of up to 3 mm. This was process (f). During processes (d) through (f), several drops broke away from the parent drop. Each individual drop formed a sphere due to the surface tension force. These drops in floating might coalesce, fall back, and re-impact with the heating surface. This was process (g). During re-impact, the laser light was obstructed, causing the output signal to fall, but not a linear rapid fall as in process (a). The reasons included the fact that the drop morphology was not a single sphere and that the falling speed was low, about the same magnitude as the rebounding speed in process (e).

2 Output Signals of Boiling Sounds and Duration Time of Liquid-Solid Contact. Figures 4-7 are typical output signals obtained from platinum, brass, SUS 304, and ceramic surfaces, respectively. A is an output signal from the photodiode; B, the boiling sound detected by means of the condenser microphone with the amplitude corresponding to the acoustic pressure; and C, piezoelectric potential monitored using the quartz oscillators. In the case of piezoelectric potential, the peak-to-peak amplitude corresponds to the pressure difference at the gas-liquid interface (difference between the pressure inside the microbubbles and the atmospheric pressure surrounding the

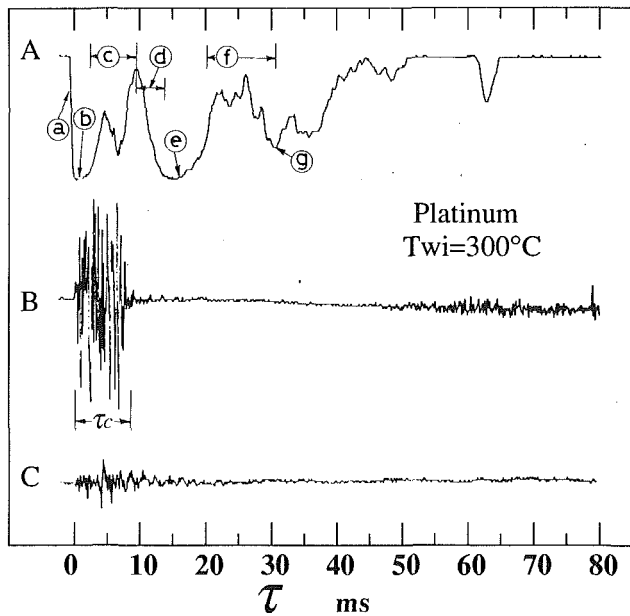


Fig. 4 Output signals for platinum surface at $T_{wi} = 300^\circ\text{C}$: (A) photodiode; (B) boiling sound; (C) piezoelectric potential

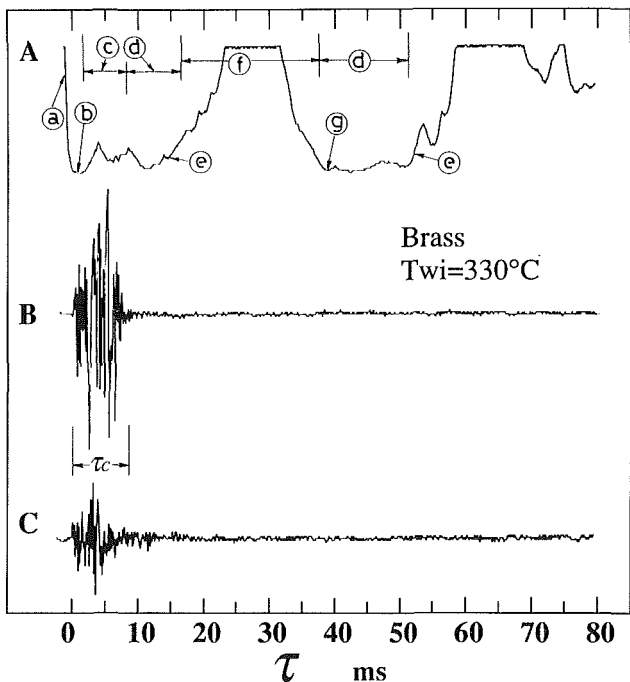


Fig. 5 Output signals for brass surface at $T_{wi} = 330^\circ\text{C}$: (A) photodiode; (B) boiling sound; (C) piezoelectric potential

bubbles). Its period corresponds to the formulation period of these microbubbles. One can determine the liquid-solid contact state of a drop on each material by simultaneously correlating these signals A, B, and C. The names of the deformation processes defined in Fig. 3 are noted on the signal A.

As mentioned previously, in the case of the platinum heating surface ($T_{wi} = 300^\circ\text{C}$) in Fig. 4, the miniaturization phenomenon (i.e., splashing of liquid microglobules) took place following drop impact. The splashing ended at a time of about $\tau_r/3$. During this time, both signals B and C exhibited large amplitudes, which lasted about $\tau_r/3$. It implies the occurrence of a high-frequency liquid-solid contact accompanied by the formation of microbubbles, which triggered the miniaturization phenomenon. The observation serves as evidence to sup-

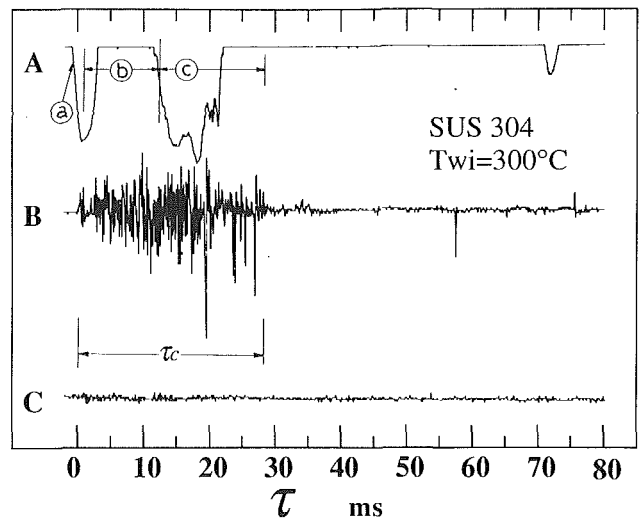


Fig. 6 Output signals for SUS 304 surface at $T_{wi} = 300^\circ\text{C}$: (A) photodiode; (B) boiling sound; (C) piezoelectric potential

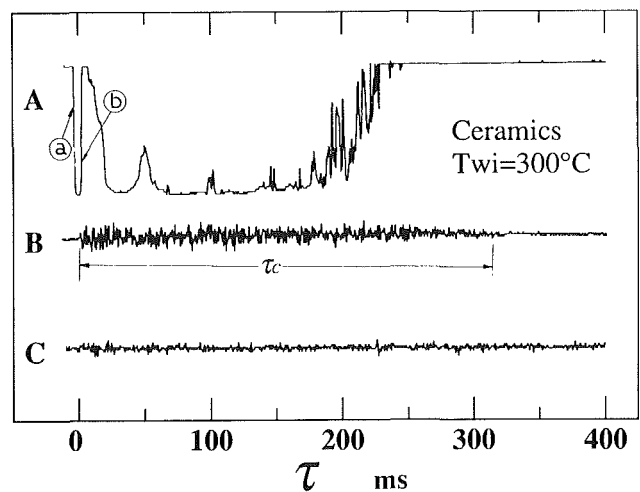


Fig. 7 Output signals for ceramic surface at $T_{wi} = 300^\circ\text{C}$: (A) photodiode; (B) boiling sound; (C) piezoelectric potential

port the mechanisms of miniaturization (Inada and Yang, 1991).

Figure 5 is an example for the brass heating surface at $T_{wi} = 330^\circ\text{C}$. The surface was freshly polished for the test and the surface temperature was within the temperature range for the near maximum amplitudes of both signals B and C. Judging from signal A varying, and large amplitudes of signals B and C, similar to the platinum surface case in Fig. 4, it is obvious that liquid-solid contact took place accompanied by a violent splashing of microbubbles. No variation appeared in signals B and C at the re-impact (g) and the film boiling state (d) prevailed without liquid-solid contact. This means that drop subcooling had fallen substantially during the initial impact and the subsequent liquid-solid contact, although the initial drop temperature was maintained at a relatively high degree of subcooling, 85 K.

Figure 6 shows the output signals for the fresh SUS 304 surface at $T_{wi} = 300^\circ\text{C}$. An oscillation of signal B (boiling sound) began at the moment of drop impact with its duration time τ_c much exceeding τ_r . The fluctuation of signal C was too weak to recognize. A much larger oscillation of signal B was observed in the second half of the duration time. Since it was accompanied by a variation of signal A, the liquid-solid contact state was, as in Case I of Fig. 3, under a violent nucleate boiling condition.

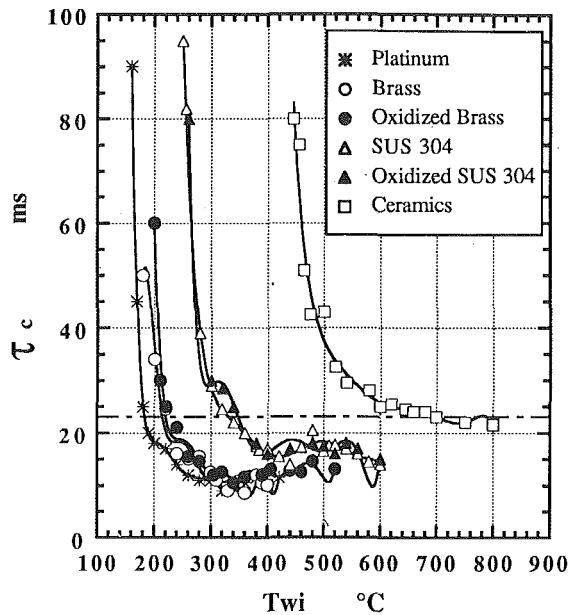


Fig. 8 Effects of initial temperature of heating surface on duration time of liquid-solid contact

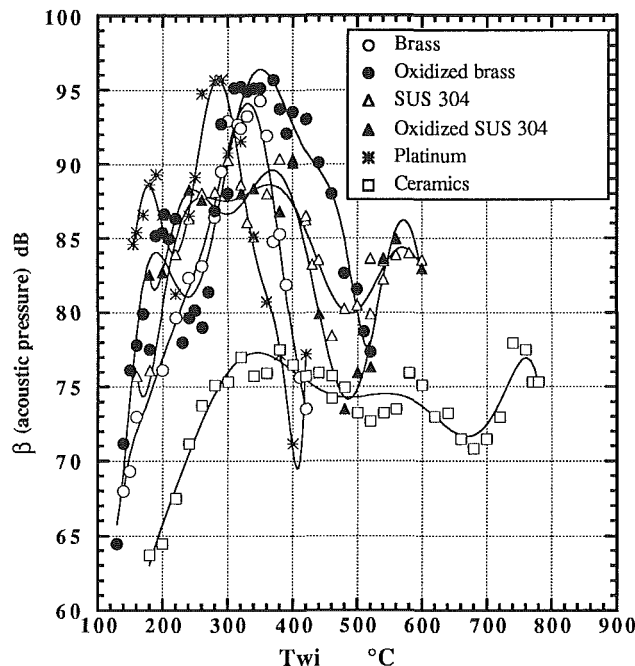


Fig. 9 Effects of heating surface temperature on boiling sound

In Fig. 7 showing the output signals for the ceramic surface at 300°C, one observes that the boiling sound began at the drop impact with rather moderate amplitudes and a long duration time. The variation in signal C was practically indiscernible. Accordingly, the liquid-solid contact was under a nucleate-boiling state. However, signal A has a minor fluctuation after the liquid-film migrating process (b), but otherwise remained at the low position. Such a liquid-solid contact condition was also observed on a metal surface, which was covered with a porous scale (Inada et al., 1988). The drop base had a thin liquid film in contact with the heating surface to undergo evaporation. In the case of a ceramic surface, such a condition prevailed up to $T_{wi} \approx 700^\circ\text{C}$. As a result, a short-lifetime region extended into a high-temperature domain in the drop lifetime curve, serving as evidence in support of the

experimental result (Takano and Kobayashi, 1991). It is of importance to note that the signals for the platinum surface at 160°C resembled those of the ceramic surface at 300°C (Fig. 7), because both surfaces at the corresponding temperatures were sufficiently wetted and in the nucleate boiling state.

In summary, the liquid-solid contact state accompanied by the splashing of liquid microglobules can be classified in Cases I and II, both with the generation of boiling sounds during the liquid-solid contact. Defining the duration time of boiling sounds as the liquid-solid contact time τ_c , the position of τ_c was indicated with signal B in Figs. 4-7. Figure 8 plots τ_c against T_{wi} for all heating surface materials tested. It is seen that τ_c diminishes rapidly with an increase in T_{wi} . The dotted line corresponds to the drop residence time τ_r . The heating surface temperature at which τ_c is lower than τ_r varies with the surface material; roughly, $T_{wi} \geq 200^\circ\text{C}$ for platinum, $T_{wi} \geq 230^\circ\text{C}$ for brass, $T_{wi} \geq 350^\circ\text{C}$ for SUS 304, and $T_{wi} \geq 700^\circ\text{C}$ for ceramics. Furthermore, the nucleate-boiling state is observed in the heating-surface temperature range for $\tau_c \geq \tau_r$. In the range with $\tau_c < \tau_r$, the vapor-liquid interfacial pressure difference (signal C) became detectable, with the duration time of amplitude fluctuations coinciding with τ_c . In the latter regime, microbubbles were formed inside the drop in synchronization with liquid-solid contact, beginning at the moment of drop impact. The drop rebounded from the heating surface at about the residence time, τ_r . The miniaturization phenomenon with splashing prior to the rebounding took place in the range of heating surface temperatures where τ_c is minimum in Fig. 8. The order of magnitude of the minimum τ_c is approximately $\tau_r/3$ for brass and platinum, increasing in the order of SUS 304 and ceramics. In the ceramics case, the minimum value of τ_c is close to τ_r and the corresponding T_{wi} exceeds 700°C, indicating a smooth transition from a nucleate-boiling state (with a liquid film coexisting at the drop base) to a film-boiling state. In conclusion, the order of magnitude of the minimum τ_c is greatly affected by the thermal properties of heating surface materials, as will be discussed in the succeeding section.

3 Effects of Heating Surface Materials on Acoustic Pressure.

Figure 9 is a plot of β versus T_{wi} , where β is the effective value of the maximum boiling pressure during liquid-solid contact monitored by means of a condenser microphone. The influence of surface conditions, due to oxidation of the heating surface, on the acoustic pressure is most prominent in the brass case. It is due to an increase in the wettability between the brass surface and the drop in the presence of an oxidized film on the surface, resulting in an intermittent liquid-solid contact even in the spheroidal state. As the data of confirmation, signals A, B, and C for a brass surface at $T_{wi} = 200^\circ\text{C}$ are presented in Fig. 10. In the clean surface case, Fig. 10(a), the boiling sound was generated at the drop impact and during the liquid-film migrating process. It was followed by a spheroidal state during which the phenomena of film boiling-drop rebound-re-impact were repeated. In the oxidized surface case, Fig. 10(b), an intermittent liquid-solid contact occurred, as evidenced by the recording of large-amplitude boiling sounds.

It is observed in Fig. 9 that a change in the heat surface conditions does not significantly affect the maximum value of boiling sounds. The maximum value is largest in brass and platinum, and decreases in the order of SUS 304 and ceramics. The value of $\sqrt{\rho C_p k}$ is also lined up in the order of brass, platinum, SUS 304, and ceramics (ρ , C_p , and k , are, respectively, the density, specific heat, and heat conductivity of heating surface material). The property $\sqrt{\rho C_p k}$ is an important parameter related to the interfacial temperature at the moment of contact between two bodies of different temperatures. In the case of a quartz heating surface (Inada and Yang, 1991), the $\sqrt{\rho C_p k}$ parameter is smaller than that of ceramics and is 0.145×10^4 [$\text{W s}^{1/2}/\text{m}^2\text{-K}$]. The boiling sound produced by the impact of a water drop on a quartz heating surface was dull

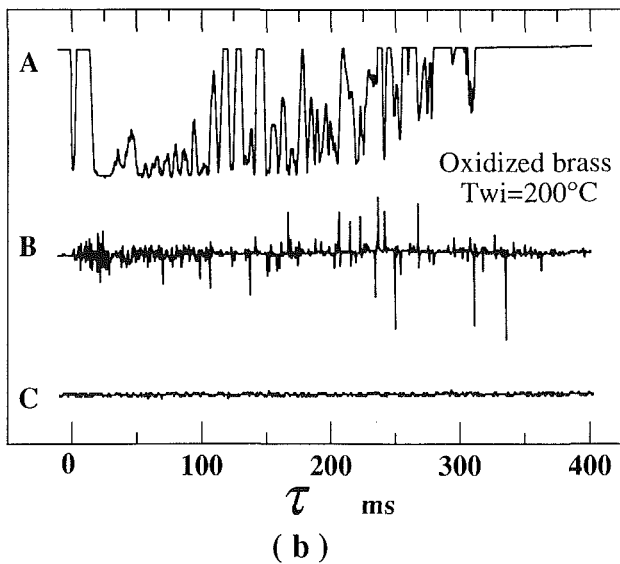
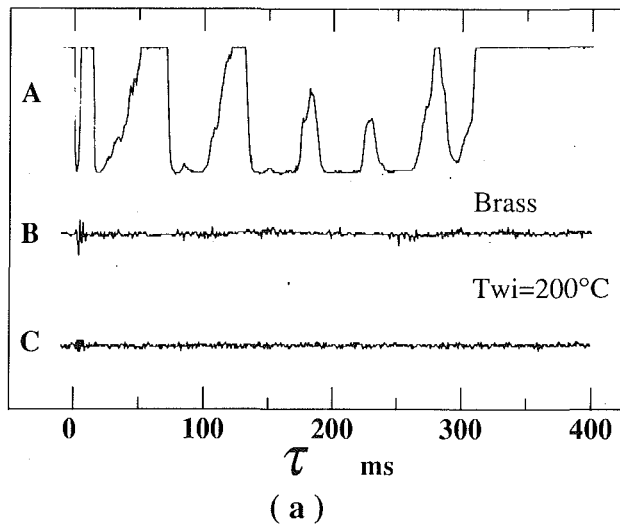


Fig. 10 Effects of heating surface condition on liquid-solid contact state; (a) clean brass surface and (b) oxidized brass surface

even at a high heat-surface temperature of 560°C , while the drop splashing was in the state of Case I as illustrated in Fig. 3. The holographic interferometric interference fringes of the liquid-solid contact state on the quartz surface was photographed from the opposite side of the surface. Results indicated the formation of a liquid-solid contact surface to wet the quartz surface and the generation of two to three relatively large bubbles of approximately 0.5 to 1.5 mm in diameter, causing the splashing phenomenon. The latter observation confirmed the drop to be under a nucleation-boiling state.

In reference to Fig. 8 and the maximum value of the acoustic pressure in Fig. 9, one may conclude that as the acoustic pressure increases, τ_c is reduced. This means the acoustic pressure is large in the case of an instantaneous liquid-solid contact.

4 Frequency of Microbubble Formation and Pressure Difference at Vapor-Liquid Interface. Figure 11 illustrates the relationship between the vapor-liquid interfacial pressure difference ΔP_m and the heating surface temperature prior to the placement of a drop T_{wi} . ΔP_m denotes the difference between the saturated vapor pressure inside the bubble and the liquid pressure surrounding the bubble. It is the driving force for the growth of a vapor microbubble within the drop. ΔP_m for both the clean and oxidized brass surfaces is high, with the maximum

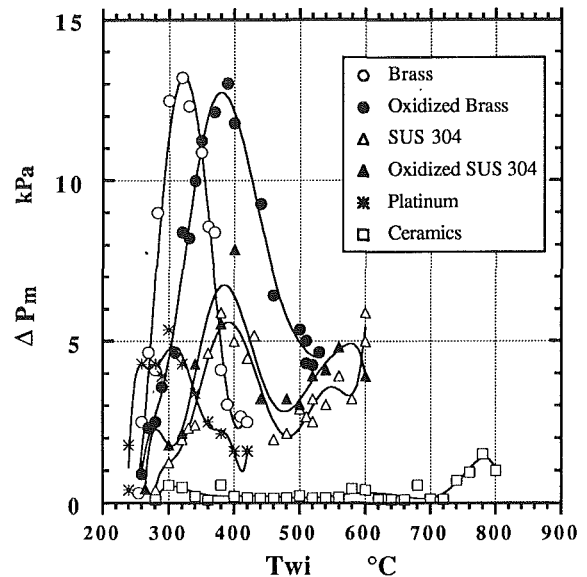


Fig. 11 Effects of heating surface material on vapor-liquid interfacial pressure difference

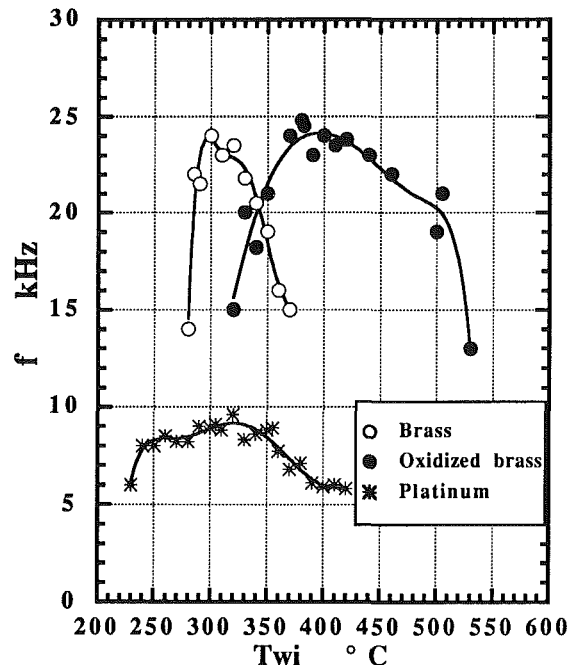


Fig. 12 Effects of initial temperature of heating surface on frequency of microbubble formation

value reaching 13 kPa. The value of T_{wi} corresponding to the maximum ΔP_m is higher for the oxidized brass surface than the clean one. In the platinum case, which has a higher acoustic pressure as seen in Fig. 9, ΔP_m is low, with the maximum value below one half of that for brass. The difference in ΔP_m 's is related to the difference in f 's, the frequencies of microbubble formation on the heating surface. In order to prove this thought, the frequencies of bubble formation on brass and platinum are plotted against T_{wi} in Fig. 12 for comparison. It is seen that the f value for platinum is less than one half that of brass. In other words, ΔP_m is high for a high f . This means that a more frequent liquid-solid contact and its resulting rapid bubble generation will cause a high vapor-liquid interfacial pressure difference. Like the acoustic pressure, β in Fig. 9 has a close relationship with the duration time τ_c in Fig. 8, and ΔP_m in Fig. 11 and f in Fig. 12 are closely related.

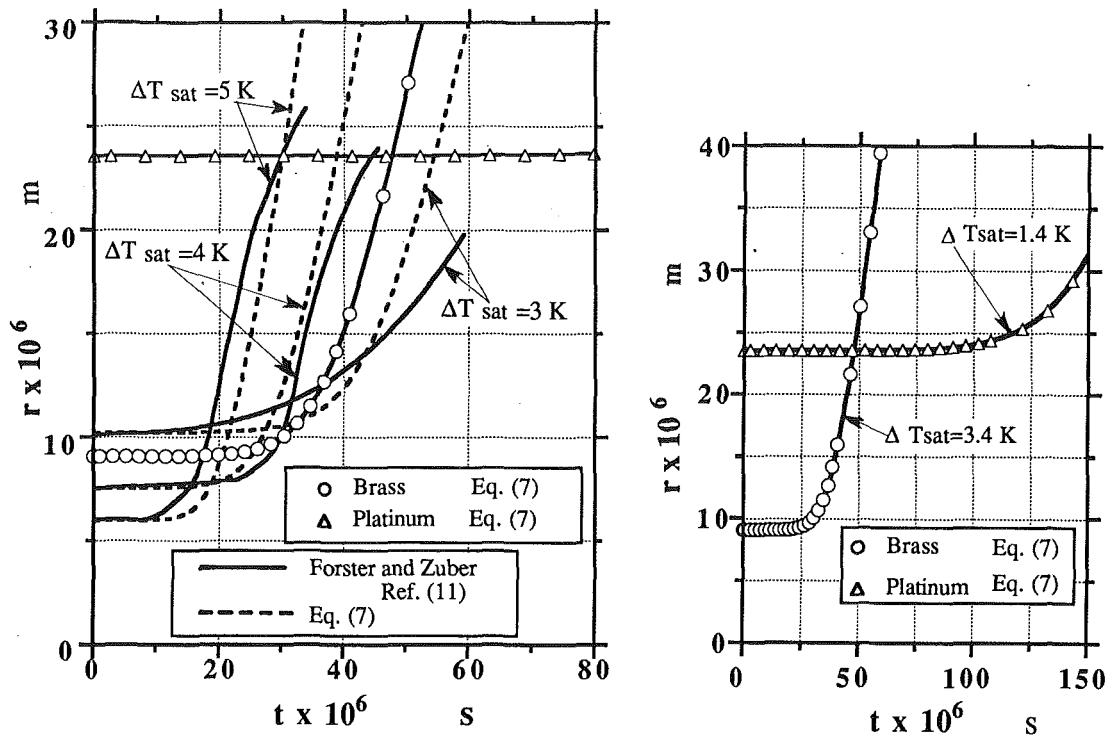


Fig. 13 Radius-time history of bubble at initial growth stage

5 Mechanics of the Initial Stage of Microbubble Growth. In order to explain the mechanics of microbubble growth using the results in the preceding section, it is necessary to solve the equation of motion, which equates the inertia force of the virtual mass, i.e., the liquid mass surrounding a bubble in a rapid growth, to the force exerted by the vapor pressure inside the bubble. The vapor pressure must be higher than the surrounding liquid pressure (atmospheric pressure in this case) by ΔP . Since the vapor temperature within the microbubble is in thermal equilibrium with the surrounding liquid, the liquid surrounding the bubble is superheated by the amount equivalent to ΔP . For simplicity, a bubble is situated in a quiescent, superheated liquid layer and maintains a spherical shape during its growth. The force-balance equation, on a unit surface area of the bubble, is obtained as

$$\rho_f r [d^2 r / dt^2] + (3/2)(dr/dt)^2 = \Delta P - 2\sigma/r \quad (2)$$

Here, ρ_f denotes the liquid density; r , the bubble radius; t , time; σ , surface tension of the liquid; and ΔP , pressure difference across the bubble surface. The left-side terms of Eq. (2) corresponds to the liquid inertia force, which acts to suppress the drop downward. The second term on the right side is the surface tension force through which the liquid constricts the bubble. These forces are balanced by an upward one, which is induced by the vapor pressure inside the bubble, ΔP (force per unit surface area). When Eq. (2) is applied to a bubble in an infinite liquid, it is called Plesset's bubble dynamic equation.

It is observed in Fig. 12 that microbubbles are generated at a very high frequency. In other words, these bubbles depart very rapidly from the heating surface. The mechanism of bubble departure inside a heated sessile drop is described by Inada and Yang (1991): A bubble is generated on the heating surface at the instant when an ever-oscillating vapor liquid interface comes in contact with the heating surface. It departs from the heating surface at the moment when the interface detaches from the heating surface, due to an unbalance of the forces acting on the bubble. Hence, a bubble would continue to grow following Eq. (2), until the force balance in Eq. (2) is compelled

to break. The present study defines the initial stage of bubble growth as the time interval from the formation, $t=0$, to the time of departure $\tau_b = 1/f$.

In solving Eq. (2) for the growth of a bubble in a superheated liquid of infinite dimension, both Plesset and Zwick (1952) and Forster and Zuber (1954) employed the Clausius-Clapeyron equation for the ΔP term. Equation (2) becomes an integro-differential form, which needs a computer for the solution. Here, the evaluation of ΔP is simplified as follows: At the initial state of $t=0$, the bubble is at static equilibrium with

$$r = r_0, \quad dr/dt = 0 \quad (3)$$

and

$$\Delta P_m = 2\sigma/r_0 \quad (4)$$

where r_0 is the critical bubble radius. Since the measured ΔP_m in Fig. 11 is the maximum, peak-to-peak change in the output signals of the piezoelectric potential, its average value during the detachment time ($t=0$ to τ_b) is taken to be $2/5 \Delta P_m$. Taking into consideration Eq. (2) at the initial state, i.e., zero on the right side, one postulates

$$\Delta P = (2/5)\Delta P_m + (3/5)(2\sigma/r) \quad (5)$$

The relationship between the critical bubble radius and the degree of superheating in the surrounding liquid, ΔT_{sat} , is given by

$$r_0 = \frac{2\sigma T_v}{L\rho_v \Delta T_{sat}} \quad (6)$$

Here, σ , L , and ρ_v are the surface tension, latent heat of evaporation, and vapor density at the saturated temperature T_s , respectively. T_v is the vapor temperature corresponding to the liquid pressure. $\Delta T_{sat} = T_v - T_s$. The substitution of Eqs. (4) and (5) into Eq. (2) yields

$$\rho_f r [d^2 r / dt^2] + (3/2)(dr/dt)^2 = (4\sigma/5)(1/r_0 - 1/r) \quad (7)$$

The equation is subject to the initial conditions, Eq. (3), and can be solved numerically using the Runge-Kutta method.

Figure 13 is the radius-time history during the initial stage of the bubble growth. The solid lines are the results of Forster and Zuber (1954) for $\Delta T_{\text{sat}} = 3, 4, \text{ and } 5 \text{ K}$, while the broken lines represent the results obtained from Eq. (7). The maximum values of ΔP_m in Fig. 11 are found to be $0.13 \times 10^5 \text{ Pa}$ and $0.05 \times 10^5 \text{ Pa}$ for brass and platinum, respectively. They are used in Eq. (7) to determine the $r-t$ relationships for brass and platinum represented in Fig. 13 by a circle and a triangle, respectively. In the present case, the values of ΔT_{sat} are 3.4 K and 1.4 K for brass and platinum, respectively. The values of τ_b are evaluated from Fig. 12 to be 0.042 ms and 0.110 ms for brass and platinum, respectively. At $t = 0.042 \text{ ms}$ and 0.110 ms, Fig. 13 gives the bubble radius r to be $17.0 \mu\text{m}$ and $24.5 \mu\text{m}$ for brass and platinum, respectively. The bubbles of these sizes are on the same order of magnitude as the microbubble being photographed by a drum camera.

The next step is to consider the generation of vapor bubbles. The results in Fig. 13 are obtained under the assumption that at zero time, a vapor bubble at a initial radius of r_0 is in a uniformly superheated liquid. An estimate of conductive heat transfer from the heating surface to form such a superheated liquid would take an order of magnitude longer than one period of bubble formation. Hence, bubble formation and liquid-solid contact occur simultaneously. At low surface temperatures, the heating surface was sufficiently wetted by the liquid and thus the microbubbles were generated in the same way as nucleate boiling. However, at high surface temperatures, a boiling phenomenon resembling the transition boiling in pool boiling took place, with the formulation and collapse of vapor films repeated instantaneously. It was the instant of vapor film collapse when direct contact between the solid and liquid phases occurred with simultaneous formation of vapor bubbles. The site of microbubble formation is where an ever-oscillating vapor liquid interface comes in contact with the heating surface (Inada and Yang, 1991). The mechanism for the formation of microbubbles is considered as follows: At a rapid period of liquid-solid contact, the heating surface temperature is always maintained at a desired level, which is sufficient to cause a rapid change in the liquid density upon a liquid-solid contact. Such a rapid change in the density causes the liquid to become oscillatory. The liquid oscillation then induces the formation of a bubble nucleus with the critical bubble radius. No detailed data are available on the oscillatory phenomenon resulting from a rapid change in the liquid density. However, evidence has been obtained from the photographic results of a drum camera (Inada and Yang, 1991). It indicates a high-frequency oscillation of the free surface at the drop base, which occurs simultaneously with the liquid-solid contact at the moment of drop impact upon the heating surface. The growth of the bubble nucleus is attributed to a supply of vapor from a thin superheated liquid layer at the drop base. It progresses by maintaining both thermal and mechanical balance. The bubble growth is limited because the superheated liquid layer is very thin. The bubble departure radius at $t = \tau_b$, which is determined by equation, is about the same order of magnitude as the critical bubble radius. In conclusion, this study deals with the formulation and departure of microbubbles that are about the size of the critical bubble radius. Hence, the validity of Eq. (5) is confirmed. In other words, the postulation is justified that the measured vapor-liquid interfacial pressure difference, ΔP_m is balanced with the surface tension force of the liquid to constrict a bubble of the critical radius r_0 .

Conclusions

The study has directed its effort to the transition regime from the vicinity of the maximum evaporation rate point to the spheroidal state. The effects of the heating surface material and temperature on the liquid-solid contact state has been determined. The piezoelectric potential method has been employed to monitor the microbubble formation at the moment of liquid-solid contact as the vapor-liquid interfacial pressure difference and the bubble generation frequency. It is concluded from the study that:

- 1 The miniaturization phenomenon (splashing of liquid microglobules) that occurs under liquid-solid contact condition is exhibited in two ways. One is the nucleate-boiling type splashing as observed at the maximum evaporation rate point. The other type is the splashing under the vapor-liquid interfacial pressure difference following the formation of microbubbles inside the drop. The former takes place for the contact duration time τ_c equal to or greater than the drop residence time τ_r , while the latter occurs when $\tau_c < \tau_r$.
- 2 The heating surface temperature T_{wi} to cause $\tau_c < \tau_r$ differs depending upon the surface material. Its value increases with a decrease in the thermal property $\sqrt{\rho C_p k}$.
- 3 The maximum value of boiling acoustic pressure increases with an increase in $\sqrt{\rho C_p k}$ or a decrease in τ_c .
- 4 The vapor-liquid pressure difference increases with an increase in the frequency of microbubble generation, or equivalently, a rapid period of liquid-solid contact.
- 5 The measured, vapor-liquid interfacial pressure difference, ΔP_m , is related to the critical bubble radius r_0 and the liquid surface tension σ by $\Delta P_m = 2\sigma/r_0$.

References

- Baumeister, K. J., and Simon, F. F., 1973, "Leidenfrost Temperature—Its Correlation for Liquid Melts, Cryogenics, Hydrocarbons, and Water," ASME JOURNAL OF HEAT TRANSFER, Vol. 95, pp. 166–173.
- Forster, H. K., and Zuber, N., 1954, "Growth of a Vapor Bubble in a Superheated Liquid," *J. of Appl. Phys.*, Vol. 25, pp. 474–478.
- Inada, S., Miyasaka, Y., Sakumoto, M., and Mogi, I., 1988, "Evaporation Behaviors of a Water Droplet and Heat Transfer on the Heated Surface Contaminated by Scale Adherence," *Trans. JSME*, Vol. 54, pp. 2121–2127.
- Inada, S., and Yang, W.-J., 1991, "Visualization of Liquid-Solid Contact Process of Drop Impinging on a Hot Quartz Plate by Laser Holographic Interferometry," *Proceedings, the ASME-JSME Thermal Engineering Joint Conference*, Vol. 3, pp. 361–364.
- Inada, S., and Yang, W.-J., 1992, "Mechanisms of Miniaturization of Sessile Drops on a Heated Surface," to appear in *International Journal of Heat and Mass Transfer*.
- Makino, K., and Michiyoshi, I., 1984, "The Behavior of a Water Droplet on Heated Surface," *International Journal of Heat and Mass Transfer*, Vol. 27, pp. 781–791.
- Nishio, S., and Hirata, M., 1978, "Study on the Leidenfrost Temperature (2nd Report, Behavior of Liquid-Solid Contact Surface and Leidenfrost Temperature)," *Trans. JSME*, Vol. 44, pp. 1335–1346.
- Plesset, M. S., and Zwick, S. A., 1952, "A Nonsteady Heat Diffusion Problem With Spherical Symmetry," *J. Appl. Phys.*, Vol. 23, pp. 95–98.
- Takano, T., and Kobayashi, K., 1991, "Vaporization Behavior of a Single Droplet Impinging on a Heated Surface With a Flame-Sprayed Ceramic Coating," *Heat Transfer—Japanese Research*, Vol. 20, pp. 1–17.
- Tamura, Z., and Tanasawa, Y., 1958, "Evaporation and Combustion of a Drop Contacting With a Hot Surface," *Proceedings, 7th Symp. on Combustion*, pp. 509–522.
- Temple-Pediani, R. W., 1969, "Fuel Drop Vaporization Under Pressure on a Hot Surface," *Proc. IMechE*, Vol. 184, pp. 677–690.

Flashing Inception in Water During Rapid Decompression

E. Elias

Department of Mechanical Engineering,
Technion,
Haifa 32000, Israel

P. L. Chambré

Department of Nuclear Engineering,
University of California,
Berkeley, CA 94720

A phenomenological model is presented for predicting the thermodynamic conditions at the onset of flashing in liquid undergoing a static or flow depressurization transient. It is shown that at extremely high rates of decompression (pulse expansion), a liquid may reach the homogeneous nucleation limit of superheat before appreciable phase transition occurs. A criterion for pulse expansion is derived by an asymptotic solution of the mass and energy equations in conjunction with the equation for spontaneous bubble nucleation and growth near the flashing inception point. The effect of impurities and dissolved gases is considered by an empirically defined heterogeneous nucleation coefficient. The model predicts the minimum pressure at the flashing point with a probable error of less than 11 percent, using 83 experimental data points.

1 Introduction

In the event of rapid decompression of an initially subcooled liquid, the liquid may penetrate into a domain of metastable states in which the pressure drops below the saturation pressure corresponding to the initial liquid temperature. At a certain lower pressure, a limit is eventually reached at which vapor starts to generate explosively. If the rate of decompression is fast enough (pulse expansion) the liquid may reach the kinetic limit of superheat before phase transition occurs (Skripov, 1974; Frenkel, 1955; Avedisian, 1986; Van Stralen and Cole, 1979). At slower depressurization rates, the presence of impurities and dissolved gases in the liquid's volume and at the container walls induces flashing at higher pressures, or lower liquid superheats, than would be sustained in a liquid free of impurities.

Knowing the conditions at the onset of phase transition is important for understanding the physical processes leading to explosive flashing of liquids, as well as for the design of boilers, steam generators, and refrigeration, distillation, and desalination equipment. The subject of flashing is also important in the containment of liquified gases and in the analysis of hypothetical loss of coolant accidents (LOCA) in nuclear reactors.

Explosive boiling of liquids under rapid heating conditions has been discussed by Skripov (1974) for two typical processes: bulk and surface heating. The first consists of heating the liquid by intense infrared or laser radiation, while the second refers to quick heating of dissolved electrolytes or immersed metal wires by an electric current. Impact conditions were defined as the minimum heating rate necessary to induce in the liquid the kinetic limit of superheat. Criteria for impact conditions were derived for each of the above processes by assuming that the rate of heat imparted to the liquid considerably exceeds the rate of heat consumed by evaporation at the existing vapor-bubble nucleation centers. It is argued that for sufficiently high heating rates, the roles of evaporation as a temperature regulator becomes ineffective, so that the liquid reaches its kinetic limit of superheat before appreciable amount of vapor is generated. At lower heating rates some of the existing nucleation centers may be activated, resulting in flashing at a lower degree of superheat. At atmospheric pressure the kinetic limit of superheat in water ($\sim 205^\circ\text{C}$) is shown to be reached at surface heating rates of at least $1.3 \times 10^8 \text{C/s}$ (Skripov, 1974, p. 95).

Phase transition during isothermal decompression of liquids

is discussed by Avedisian (1985), Skripov et al. (1988), and in several theoretical and experimental studies in relation to the safety analysis of light water nuclear reactors (Fritz et al., 1976; Edwards and O'Brien, 1970; Reocreux, 1974; Miyatake et al., 1973; Hooper and Abdulmessih, 1966; Abuaf et al., 1983; Miller, 1985; Kenning and Thirunavukarasu, 1970). Examination of the reported degree of liquid superheat at the flashing point reveals that it strongly depends on the initial liquid temperature and the imposed rate of depressurization. In slow depressurization transients the pressure at the onset of flashing may be considerably higher than the kinetic limit. On the other hand, at higher decompression rates the existing nucleation sites in the liquid remain inactive, and the liquid superheat approaches the maximum limit determined by random density fluctuations that lead to homogeneous nucleation. Alamgir et al. (1980, 1981) conducted a series of decompression experiments in water, which, in a few cases, reached $1.83 \times 10^5 \text{MPa/s}$, bringing the liquid close to its theoretical kinetic limit of superheat. The effect of nucleation in existing centers (heterogeneous nucleation) was later modeled empirically by Alamgir and Lienhard (1981) based on the arbitrary assumption that the minimum pressure (maximum liquid superheat) is reached when the tube's wall is entirely covered by small vapor nuclei. Alamgir and Lienhard's correlation is applicable in the reduced temperature range of 0.62 to 0.935 (reduced pressure 0.012 to 0.6) and for high rates of depressurization in the range of 400 to $1.83 \times 10^5 \text{MPa/s}$. The correlation yields the pressure undershoot within ± 10.4 percent (one standard deviation) within the specified range of application. Larger errors are expected at lower rates of depressurization, typical to flow in pipes or nozzles.

Several attempts have been made to extend the Alamgir and Lienhard model to low depressurization rates characteristic of flow systems. For instance, Levy and Abdollahian (1982) modified the correlation by fitting the data measured in the Marviken test section (EPRI, 1982). Jones (1979) has introduced an empirical parameter to account for the effect of turbulence in the flow channel. The role of that effect was later shown by Abuaf et al. (1983) to be insignificant when flow in converging-diverging nozzles is considered. Careful examination of the available models and empirical correlations for predicting the pressure undershoot at the flashing point leads to the conclusion that no single model is applicable over the large range of depressurization rates encountered experimentally.

This paper presents a theoretical model for the maximum liquid superheat at the flashing inception point, which is applicable for low and high rates of depressurization. First a relationship is derived between the imposed decompression rate and the resulting degree of superheat. The analysis is based

Contributed by the Heat Transfer Division for publication in the JOURNAL OF HEAT TRANSFER. Manuscript received by the Heat Transfer Division July 1991; revision received June 1992. Keywords: Evaporation, Multiphase Flows, Non-equilibrium Flows. Associate Technical Editor: J. H. Kim.

on an asymptotic solution of the mass and energy equations in conjunction with the equation for spontaneous bubble nucleation and growth near the flashing inception point. The model enables the determination of the rate of decompression necessary to induce the kinetic limit of superheat at the onset of flashing. An empirical correlation is then developed to account for heterogeneous nucleation on dissolved gases and impurities in the liquid's volume. The model is shown to predict the minimum pressure at the flashing point with a probable error of less than 11 percent, using 83 experimental data points.

2 The Model

The model considers the decompression of an initially subcooled bulk of liquid either by a controlled expansion of the liquid volume, or by acceleration and frictional pressure losses. The first process, termed here "static depressurization," refers to a nonflowing liquid, while the second is applicable to flow depressurization.

During decompression, vapor bubbles may form on nucleation sites in the liquid volume produced by fluctuations in the thermal motion of the liquid's molecules and on impurities and dissolved gases in the liquid's volume and on the container walls (Skripov, 1974; Hirth and Pound, 1963). The process of bubble formation and growth during depressurization continuously increases the vapor content of the system. At a certain pressure below saturation, known as the flashing inception pressure, the rate of pressure recovery due to vapor formation eventually balances and exceeds the imposed rate of decompression. Thus, in a static depressurization transient, the flashing inception point may be characterized by a minimum point on a pressure versus time curve. In a flow system, the imposed rate of depressurization prior to flashing is caused mainly by wall friction and fluid acceleration. Since the formation of a two-phase mixture typically enhances the frictional and acceleration pressure drop along the flow channel, the imposed rate of decompression increases downstream of the

flashing point. In order to arrive at a unique criterion for flashing in both static and flow depressurization processes, the point of flashing inception is identified, in this work, as the point at which the rate of pressure recovery due to phase change equals the initial imposed rate of depressurization prior to flashing.

Derivation of a mathematical relationship between the imposed expansion rate and the maximum degree of liquid superheat at the flashing inception point requires solution of the conservation equations for the fluid in conjunction with a constitutive relation for the rate of vapor generation. In the following, the mass and energy conservation equations are formulated for an expanding volume of fluid. An asymptotic solution is then outlined in the next section for predicting the homogeneous rate of vapor generation at the onset of flashing. Heterogeneous effects are then considered empirically using the experimental results reported to date in both static and flow systems.

For an adiabatic system, the mass and energy conservation equations, in a Lagrangian frame of reference, are (Lahey and Moody, 1979)

Mixture mass:

$$\frac{d}{dt} (\bar{\rho} V) = 0 \quad (1)$$

Vapor mass:

$$\frac{d}{dt} (\rho_g V_g) = \Gamma'_g \quad (2)$$

Mixture energy:

$$\frac{d}{dt} (V \bar{\rho} \bar{u}) = - \left(P_g \frac{dV_g}{dt} + P_l \frac{dV_l}{dt} \right) \quad (3)$$

where Γ'_g is the rate of vapor generation, V is the system's volume, and V_l and V_g are the volumes occupied by the liquid and gas phase, respectively.

Nomenclature

$A[\theta(t)]$ = function defined in Eq. (20)	P_s = saturation pressure at the initial liquid temperature, T	Γ = vapor generation rate per unit volume, Eq. (7)
a_h = partial derivatives of liquid density with respect to enthalpy	ΔP = pressure undershoot at the flashing inception point = $P_s - P_m$	γ = coefficient in Eq. (9)
a_p = partial derivatives of liquid density with respect to pressure	r = bubble radius	ϵ = parameter defined in Eq. (26a)
B = coefficient in Eq. (21a)	r_c = critical radius of an unstable nucleus	η = parameter defined in Eq. (27)
c = coefficient in Eq. (21b)	S = dimensionless depressurization rate, Eq. (34)	θ = normalized pressure, Eq. (9)
C_o = coefficient in Eq. (31)	T = initial liquid temperature	ρ = density at the initial conditions
$G_b[\theta(t)]$ = Gibbs function	T_r = reduced temperature	$\bar{\rho}$ = average mixture density
g = number of molecules in bubble	t = time	Σ = rate of depressurization
h = specific enthalpy	t_o = time at which pressure reaches P_s	σ = surface tension of liquid in contact with its own vapor at the initial temperature T
h_{ig} = heat of vaporization	t_m = time at which pressure reaches P_m	τ = parameter defined in Eq. (25)
I_o = coefficient in Eq. (21)	U = flow velocity	ψ = heterogeneity coefficient, Eq. (31)
$I(\theta)$ = frequency of homogeneous nucleation events per molecular collision	u = specific internal energy	
k = Boltzmann's constant	\bar{u} = average specific internal energy of the mixture	
M = molecular mass	V = mixture volume	Subscripts
m = mass of a molecule	v_b = volume of a gas molecule	c = critical conditions
N = number density of the liquid	α = volumetric void fraction	g = gas phase
N_A = Avogadro's number	β = coefficient in Eq. (9)	l = liquid phase
P = pressure	Γ' = vapor generation rate, Eq. (2)	m = flashing inception point
P_m = static pressure at the flashing inception point		o = initial conditions
		r = reduced
		s = saturation

The mixture properties can be defined in terms of the volumetric void fraction, α , and the vapor and liquid properties as follows:

$$\begin{aligned}\bar{u} &\equiv \frac{\alpha\rho_g u_g + (1-\alpha)\rho_l u_l}{\bar{\rho}} \\ \bar{\rho} &\equiv \alpha\rho_g + (1-\alpha)\rho_l \\ V &\equiv V_g + V_l\end{aligned}\quad (4)$$

In terms of the specific enthalpy, h , the internal energies of the two phases are

$$\begin{aligned}u_g &= h_g - \frac{P_g}{\rho_g} \\ u_l &= h_l - \frac{P_l}{\rho_l}\end{aligned}\quad (5)$$

Substituting Eqs. (4) and (5) into Eqs. (1)–(3) and realizing that $\alpha \ll 1$ prior to flashing results in

$$\frac{\rho_l}{V} \frac{dV}{dt} - (\rho_l - \rho_g) \frac{d\alpha}{dt} + a_h \frac{dh_l}{dt} + a_p \frac{dP_l}{dt} = 0 \quad (6)$$

$$\rho_g \frac{d\alpha}{dt} = \Gamma_g \quad (7)$$

$$\rho_g h_{lg} \frac{d\alpha}{dt} + \rho_l \frac{dh_l}{dt} - \frac{dP_l}{dt} = 0 \quad (8)$$

where $\Gamma_g \equiv \Gamma'_g/V$ is the specific rate of vapor generation and

$$a_h \equiv \left(\frac{\partial \rho_l}{\partial h_l} \right)_{P_l}, \quad a_p \equiv \left(\frac{\partial \rho_l}{\partial P_l} \right)_{h_l}$$

Eliminating dh_l/dt between Eqs. (6) and (8) and using Eq. (7) yields an explicit expression for the pressure rate, $d\theta/dt$, as a function of the imposed expansion rate, $(1/V)(dV/dt)$, and Γ_g

$$\frac{d\theta}{dt} = \frac{\gamma}{V} \frac{dV}{dt} - \beta \frac{\Gamma_g}{\rho_g} \quad (9)$$

where

$$\theta \equiv \frac{P_s - P_l}{P_s} \quad (9a)$$

$$\gamma \equiv \frac{\rho_l^2}{P_s(a_h + \rho_l a_p)} \quad (9b)$$

$$\beta \equiv \frac{a_h \rho_g h_{lg} + \rho_l(\rho_l - \rho_g)}{P_s(a_h + \rho_l a_p)} \quad (9c)$$

and P_s is the saturation pressure corresponding to the initial liquid temperature. The first term on the left-hand side of Eq. (9) is the imposed rate of expansion, which is related to the rate of decompression. The second term is the rate of pressure recovery due to vapor formation. At the onset of flashing ($t = t_m$), these two terms balance each other, yielding

$$\frac{\rho_g \gamma}{\beta V} \frac{dV}{dt} = \Gamma_g \quad \text{at } t = t_m \quad (10)$$

Equation (10) relates the imposed rate of expansion to the specific rate of vapor generation at the flashing point. Since in many experimental systems the initial decompression rate is reported rather than the imposed expansion rate, Eq. (10) is restated in terms of the initial pressure rate by defining $t = t_o$ as the time at which the system pressure first reaches P_s . At $t = t_o$ the rate of vapor generation is negligibly small; therefore, Eqs. (9) and (9a) yield (with $P_s = \text{const}$)

$$\frac{1}{V} \frac{dV}{dt} \Big|_{t_o} = - \frac{1}{\gamma P_s} \frac{dP_l}{dt} \Big|_{t_o} \equiv \frac{\Sigma}{\gamma P_s} \quad (11)$$

where Σ is the initial decompression rate. Since both the decompression rate, Σ , and the imposed expansion rate, $(1/V)(dV/dt)$, are nearly constant prior to the flashing inception point ($t < t_m$) (Alamgir et al., 1980, 1981; Alamgir and Lienhard, 1981), Eq. (11) may be substituted into eq. (10) to yield a criterion for the impact vapor generation rate in a depressurization transient

$$\frac{\rho_g \Sigma}{\beta P_s} = \Gamma_g \quad \text{at } t = t_m \quad (12)$$

We note that in a static decompression, Σ is an independent parameter, which can be measured directly. On the other hand, in a steady flow depressurization, such as flow in pipes or converging diverging nozzles, the initial pressure rate is typically determined by the measured static pressure drop along the flow channel as suggested by Abuaf et al. (1983):

$$\Sigma = U \frac{dP}{dz} \quad (13)$$

where U is the flow velocity and z is the distance along the flow path.

Equations (10) and (12) relate the expansion or decompression rate, respectively, to the rate of vapor generation at the flashing point. The utilization of Eqs. (10) or (12) for predicting the flashing pressure requires the specification of Γ_g at the flashing point, as a function of the system pressure and temperature at that point. A vapor generation model applicable near the flashing inception point is developed in the next section.

3 Vapor Generation Model

In order to arrive at a constitutive relation for the rate of vapor formation as a function of the prevailing temperature and pressure, a kernel function, $g(t, t')$, is defined as the bubble size, measured by the number of molecules, at time t in a vapor bubble created as a critical nucleus at time t' . The specific rate of vapor generation is

$$\Gamma_g = \int_{t_o}^t m I[\theta(t')] \frac{dg(t, t')}{dt} dt' \quad (14)$$

where m is the mass of a molecule and $I[\theta(t')]$ is the rate of nucleation events at t' per unit volume of the mixture. The bubble size, $g(t, t')$, is governed by the rates of vaporization and condensation of molecules at the vapor-liquid interface as given by Skripov (1974, p. 33)

$$\frac{dg(t, t')}{dt} = \frac{4\pi r^2}{\sqrt{2\pi m k T}} (P_s - P_g) \quad (15)$$

where r is the bubble's radius, T is the liquid temperature, and k is Boltzmann's constant.

Equation (15) is more conveniently expressed in terms of the dimensionless pressure difference, θ , rather than $P_s - P_g$. We note that in a critical bubble the vapor pressure, P_g , differs only slightly from the saturation vapor pressure, P_s , near a flat interface at the same temperature. The vapor can, therefore, be regarded as incompressible during its expansion from P_s to P_g . Considering the conditions of mechanical and chemical equilibrium one obtains (Glaser, 1984; Skripov, 1974, p. 22)

$$(P_s - P_l)\rho_g = (P_s - P_g)\rho_l \quad (16)$$

Substituting $(P_s - P_g)$ from Eq. (16) into Eq. (15) yields

$$\frac{dg(t, t')}{dt} = \frac{\rho_g}{\rho_l} \frac{4\pi r^2}{\sqrt{2\pi m k T}} P_s \theta(t) \quad (17)$$

In addition the bubble radius is related to $g(t, t')$ by

$$g(t, t') = \frac{4\pi r^3}{3v_b} \quad (18)$$

and the vapor molecular mass, m , is defined by

$$m = \frac{M}{N_A} \quad (19)$$

where M is the liquid molecular weight and N_A is the Avogadro number.

Combining Eqs. (18) and (19) with Eq. (17), we obtain after integration with $g(t, t) \approx 0$ (i.e., neglecting the initial size of the nucleus)

$$g(t, t') = \left(\frac{A[\theta(t)]}{3} (t-t') \right)^3 \quad (20)$$

where

$$A[\theta(t)] \equiv \left(\frac{3v_b}{4\pi} \right)^{2/3} \frac{4\pi\rho_g P_s \theta(t)}{\rho_l \sqrt{2\pi m k T}}$$

In ordinary liquids, the rate of embryo formation, $I[\theta(t')]$ in Eq. (14), depends on the nature and concentration of impurities and noncondensable gases in the liquid. Since typically the impurity characteristics are unknown, a model for the specific vapor generation rate is developed here first for the better-defined case of homogeneous nucleation. The final result is then extended empirically to account for heterogeneous nucleation in practical boiling systems.

The rate of spontaneous nucleation per unit volume in a liquid free of impurities is given by (Blander and Katz, 1975)

$$I[\theta(t')] = I_o \exp\left(-\frac{c}{[\theta(t')]^2}\right) \quad (21)$$

where

$$I_o = N \sqrt{\frac{2\sigma}{\pi m B}} \quad (21a)$$

$$c = \frac{16\pi\sigma^3}{3kTP_s^2(1-\rho_g/\rho_l)^2} \quad (21b)$$

and N is the number density of the liquid ($N = N_A \rho_l / M$). In deriving Eq. (21) use has been made again of Eq. (16) to introduce the relative pressure difference $\theta(t')$ in lieu of $(P_g - P_l)$. The factor B in Eq. (21) is 2/3 except for cavitation, in which case $B \approx 1$ (Blander, 1979). The exponent $c/[\theta(t')]^2 \equiv Gb(t')$ in Eq. (21) is the Gibbs function, which defines the minimum work needed to create a bubble of critical size.

At the onset of flashing ($t = t_m$), we have $\theta(t_m) \equiv \theta_m$ and from Eq. (14)

$$\Gamma_g = \int_{t_o}^{t_m} m I[\theta(t')] \frac{dg(t_m, t')}{dt} dt' \quad (22)$$

Substituting Eqs. (20) and (21) into Eq. (22) yields

$$\frac{9\Gamma_g}{m I_o [A(\theta_m)]^3} = \int_{t_o}^{t_m} \exp\left(-\frac{c}{[\theta(t')]^2}\right) (t_m - t')^2 dt' \quad (23)$$

To evaluate the integral on the right-hand side of Eq. (23), we expand the Gibbs function about θ_m as follows:

$$Gb(\theta) \approx Gb(\theta_m) + \left(\frac{dGb}{d\theta}\right)_{\theta_m} [\theta(t') - \theta_m] \quad (24)$$

which is valid near θ_m . Furthermore, we express the dynamics of $\theta(t)$ about θ_m by

$$\theta_m - \theta(t') = \tau(t_m - t')^2 \quad (25)$$

which is also valid near θ_m . The rate coefficient, τ , is determined in the appendix using the balance equation, Eq. (9).

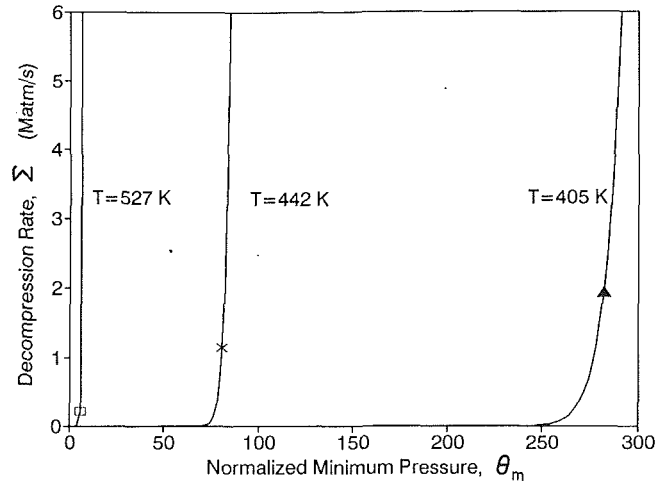


Fig. 1 Decompression rates required to induce maximum superheat in water at various initial temperatures, based on Eq. (30)

Using the approximate expression of $Gb(\theta)$, the integral term in Eq. (23) (denoted here as I_1) becomes

$$I_1 = \int_{t_o}^{t_m} \exp\left\{-Gb(\theta_m) + \tau \left(\frac{dGb}{d\theta}\right)_{\theta_m} (t_m - t')^2\right\} (t_m - t')^2 dt' \\ \equiv e^{-Gb(\theta_m)} \int_{t_o}^{t_m} e^{-\epsilon(t_m - t')^2} (t_m - t')^2 dt' \quad (26)$$

where

$$\epsilon \equiv -\tau \left(\frac{dGb}{d\theta}\right)_{\theta_m} = \tau \frac{2c}{\theta_m^3} \quad (26a)$$

Let $\sqrt{\epsilon}(t_m - t') = \eta$, then

$$I_1 = \frac{e^{-Gb(\theta_m)}}{\epsilon^{3/2}} \int_0^{\sqrt{\epsilon}(t_m - t_o)} e^{-\eta^2} \eta^2 d\eta \equiv \frac{e^{-Gb(\theta_m)}}{\epsilon^{3/2}} \phi_2[\sqrt{\epsilon}(t_m - t_o)] \quad (27)$$

where $\phi_2(\infty) = \sqrt{\pi}/4$ (see appendix).

Substituting Eq. (27) into Eq. (23) and considering Eqs. (10) and (11) yields after some rearrangements

$$\frac{9\Sigma}{\beta v_b I_o [A(\theta_m)]^3 P_s} = \frac{e^{-Gb(\theta_m)}}{\epsilon^{3/2}} \phi_2[\sqrt{\epsilon}(t_m - t_o)] \quad (28)$$

where v_b is the volume of a vapor molecule ($v_b = m/\rho_g$).

Equation (28) is developed into its final form by substituting $\epsilon^{3/2}$ from the appendix (Eq. (46))

$$\frac{9\Sigma}{\beta v_b I_o [A(\theta_m)]^3 P_s} = \frac{\sqrt{\pi}}{4} e^{-c/\theta_m^2} \frac{\theta_m^2}{[(\Sigma/P_s)(4/\sqrt{\pi})c]^3} \quad (29)$$

or

$$\left(\frac{4\Sigma}{\sqrt{\pi} P_s}\right)^4 \frac{1}{3\beta v_b I_o} \left(\frac{3c}{A(\theta_m)\theta_m^3}\right)^3 = e^{-c/\theta_m^2} \quad (30)$$

where the dependence of the normalized maximum pressure undershoot, θ_m , on Σ should be noted.

Given the initial decompression rate, Σ , in pure liquid at temperature T , Eq. (30) yields the normalized pressure undershoot at the flashing point, θ_m . To gain a better understanding of the parameters influencing the flashing process, typical results calculated by Eq. (30) are plotted in Fig. 1 for pure water at different initial temperatures in the Σ range of 0 to 6×10^6 atm/s. It is shown that for a given liquid temperature, θ_m reaches an asymptotic value that is almost independent of the imposed rate of depressurization.

It is commonly accepted that the limit of superheat can be predicted from Eq. (21) by appropriately setting the value of

Table 1 Pulse decompression conditions for water at an initial pressure P_s and initial temperature T

P_s (atm)	T (K)	θ_m	Σ (atm/s)
2.85	405.37	282.02	1.930×10^6
7.53	441.62	80.71	1.141×10^6
18.25	481.63	22.92	5.782×10^5
41.56	526.61	5.81	2.148×10^5
61.77	551.54	2.62	1.058×10^5
75.13	564.75	1.66	6.730×10^4
87.81	575.71	1.11	4.359×10^4
91.66	578.80	0.99	3.813×10^4
94.93	581.34	0.89	3.410×10^4
100.64	585.63	0.75	2.778×10^4
109.66	592.02	0.57	2.004×10^4
151.92	617.42	0.14	3.295×10^3
193.50	637.28	0.02	1.540×10^2

$I[\theta(t_m)]$. To demonstrate the utility of this assumption, it was used to calculate θ_m at different initial temperatures, using $I[\theta(t_m)] = 10^{12} \text{ m}^{-3} \cdot \text{s}^{-1}$ (Van Stralen and Cole, 1979). Results are listed in Table 1 and indicated by data points in Fig. 1. It is seen that the corresponding values of the decompression rates do not always lie on the vertical asymptote (as seen in Fig. 1 for $T=405 \text{ K}$). Hence, values of θ_m calculated using this assumption, when compared to Eq. (30), would indicate a dependence on Σ . Also, by Eq. (21), if θ_m is dependent on Σ in the knee portion of the curves in Fig. 1, then so is I . In the asymptotic portion, I becomes independent of Σ .

In the above formulation, the vapor and liquid properties were calculated at the initial liquid temperature and the corresponding saturation pressure. Since the time to reach the flashing inception point is typically very short (in the range of microseconds to a few milliseconds), the assumption of constant liquid temperature may be considered realistic. Properties of steam and water were calculated using the thermodynamic relations listed by Haar et al. (1984) for stable and metastable water.

4 Nonhomogeneous Nucleation

Under most conditions in which boiling occurs, bubbles nucleate on certain contaminants of the system: dissolved gas in the liquid, gas-saturated solid particles, poorly wettable inclusions and container walls, cracks, etc. Heterogeneous nucleation reduces the maximum attainable degree of superheat at the flashing point. Since, generally, there is no a priori information on the nature of the heterogeneous nucleating centers in the liquid, an empirical approach is used in this study in order to extend the utility of Eq. (30) for predicting θ_m in practical boiling systems.

In several idealized cases the kinetics of heterogeneous nucleation is amenable to theoretical evaluation. For instance, the effect on the homogeneous nucleation pressure of dissolved gases is predicted by Forest and Ward (1977, 1978). Heterogeneous nucleation at a smooth solid surface or at a liquid-liquid interface is considered by Hirth and Pound (1963) and by Blander and Katz (1975). In this latter case, the rate of surface heterogeneous nucleation was calculated by a relation similar to Eq. (21) with a correction factor applied to the work of formation of a critical bubble, and by modifying the pre-

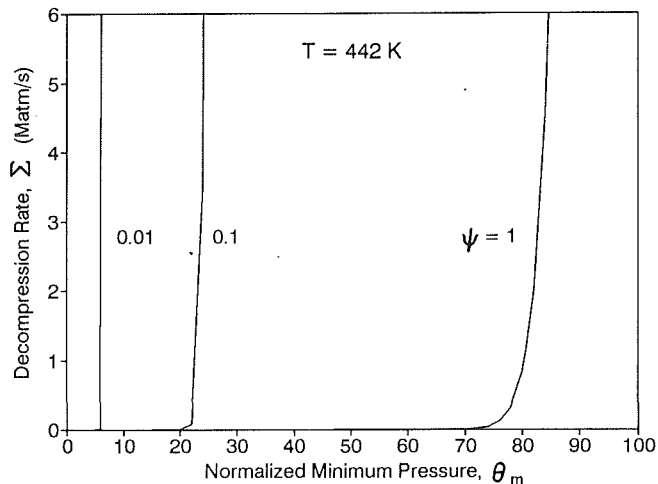


Fig. 2 Effect of the heterogeneity coefficient ψ on θ_m at $T = 442 \text{ K}$, based on Eq. (32)

exponent term, I_o . A similar approach is used here to account for heterogeneous nucleation on the surface of suspended solid impurities in the liquid's volume. It is assumed that the heterogeneous-nucleation rate in the liquid's volume can be described by

$$I[\theta(t')] = C_o \exp\left(-\frac{c\psi}{[\theta(t')]^2}\right) \quad (31)$$

where ψ is a heterogeneity function, which depends on the wetting angle. The pre-exponent term, C_o , is not completely determined and may also depend on the angle of contact with which the liquid wets the solid impurities. For simplicity, in the present study C_o is assumed not to depend on the wetting angle, and its effect is included implicitly in the term ψ . Replacing Eq. (21) by Eq. (31) and replacing thus in Eq. (30) c by $c\psi$ yields an expression for pressure undershoot that is applicable for both homogeneous and heterogeneous nucleation:

$$\left(\frac{4\Sigma}{\sqrt{\pi}P_s}\right)^4 \frac{1}{3\beta v_b C_o} \left(\frac{3c}{A(\theta_m)\theta_m^3}\right)^3 = \frac{e^{-c\psi/\theta_m^2}}{\psi^3} \quad (32)$$

In a single-component liquid with no impurities, ψ is unity and Eq. (32) reduces to Eq. (30) with $C_o = I_o$. However, in ordinary liquids ψ may lie in the range of $0 < \psi < 1$, depending on the number density of the impurities and on the contact angle between the liquid and the surface on which nucleation takes place. Since the value of ψ is not a priori known, Eq. (32) may be regarded as an expression of θ_m as a function of three independent variables, T , Σ , and ψ . The functional dependence between θ_m and ψ and Σ is illustrated in Fig. 2, which shows typical results calculated by Eq. (32) for water at initial temperature of 442 K. In Fig. 2, C_o was taken equal to I_o . It is shown in the asymptotic portion of the curve, that for a given water temperature, θ_m is strongly dependent on the value of ψ . Reducing ψ lowers θ_m , the degree of liquid superheat at the flashing point.

To utilize Eq. (32) for predicting θ_m , it was first used together with experimental data to determine ψ for various liquid temperatures and decompression rates. We note that the left-hand side of Eq. (32) depends only on T , Σ , and θ_m , which is either known a priori or measurable in a typical depressurization flashing experiment. Equation (32) forms a transcendental relation for ψ and was solved by Newton's iteration procedure over a wide range of T , θ_m , and Σ covering the range of existing experimental data. The resulting values of the heterogeneity factor, ψ , were found to satisfy a correlation in terms of the reduced initial temperature of the liquid, T_r , and a normalized depressurization rate, S . S is defined by the ratio of the initial

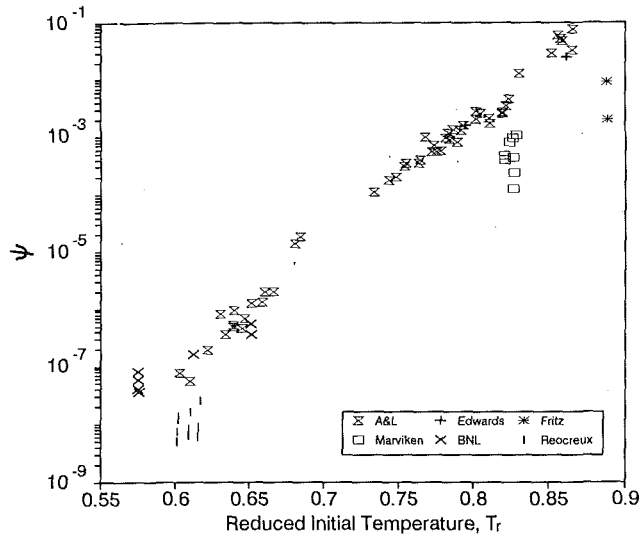


Fig. 3 Heterogeneity coefficient, ψ , versus initial reduced liquid temperature

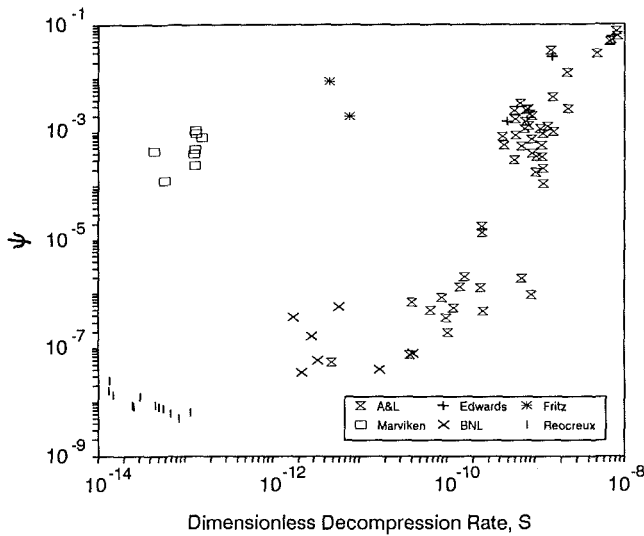


Fig. 4 Heterogeneity coefficient, ψ , versus dimensionless rate of depressurization, S

rate of depressurization, Σ , and the net rate of molecules impinging on the surface of a bubble having a critical radius, r_c (cf. Eq. (17)).

$$S \equiv \frac{\Sigma / (\theta_m P_s)}{4\pi\rho_g r_c^2 P_s \theta_m / \rho_l \sqrt{2\pi m k T}} \quad (33)$$

Since $r_c = 2\sigma / (\theta_m P_s)$ (Frenkel, 1955, p. 371), the dimensionless rate of depressurization becomes

$$S = \frac{\Sigma \rho_l \sqrt{2\pi m k T}}{16\pi\rho_g \sigma^2} \quad (34)$$

Figure 3 displays the calculated heterogeneity factors plotted against the initial reduced temperature of the liquid. Figure 4 is a plot of ψ versus the dimensionless rate of depressurization, S . The higher values of ψ correspond to data taken at high rates of depressurization and high initial temperatures typical to static decompression experiments. The lower values of ψ correspond to flow experiments in which depressurization results mainly from friction and acceleration losses in the flow channel.

The calculated set of ψ was empirically correlated as a function of T_r and S by

$$\psi = c_1 T_r^2 S^{c_3} \quad (35)$$

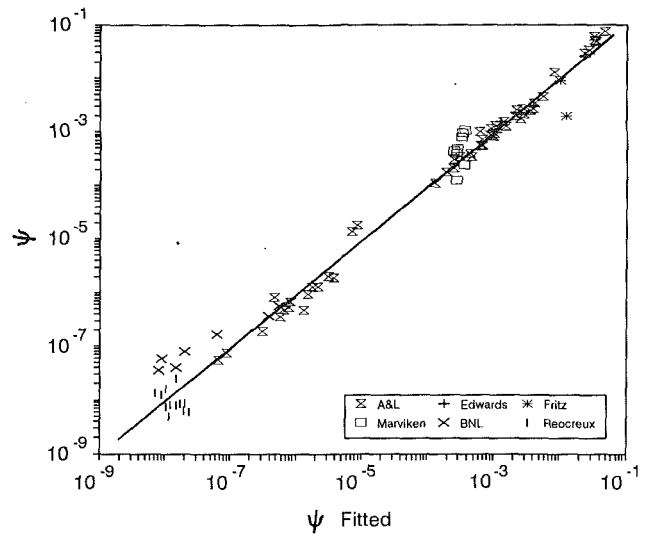


Fig. 5 Calculated versus fitted ψ

where the coefficients c_1 to c_3 , estimated by a least-squares fit to the data, are: $c_1 = 1.5061 \times 10^3$, $c_2 = 31.906$, and $c_3 = 0.3103$. Note that Eq. (35) is nondimensional. It exhibits the physically correct trend of parameters in that ψ approaches zero at very low rates of depressurization (since $c_3 > 0$), which implies that the pressure undershoot (or the attainable degree of superheat) decreases with decreasing S . On the other hand, ψ increases with S as displayed in Fig. 4. At extremely high rates of decompression (not reached in any of the reported experiments), ψ may reach unity, and Eq. (32) reduces to the homogeneous case of Eq. (30).

Figure 5 depicts the heterogeneity factor calculated from Eq. (32) against the predictions of Eq. (35) over the studied range of experimental data, which includes the static depressurization data of Alamgir et al. (1980, 1981), Edwards and O'Brien (1970), Friz et al. (1976), and the large-scale data measured at the Marviken test facility in Sweden (EPRI, 1982). In the Marviken data only the pressure undershoot measured at the top of the pressure vessel is considered. Flow decompression data include the pipe flow experiments of Reocreux (1974) and the converging diverging nozzle data of Zimmer et al. (1979) at BNL. In analyzing the Reocreux (1974) data the pressure undershoot was taken at the reported point of first bubble appearance. For the nozzle flow experiments, the minimum pressure was taken as the measured throat pressure.

Equation (35) brings together the data of many investigators in the range of conditions bounded by

$$0.57 < Tr < 0.935$$

$$0.13 < \Sigma < 1.85 \times 10^6 \text{ atm/s (or } 1.4 \times 10^{-14} < S < 8.4 \times 10^{-9})$$

(35a)

Equations (32) and (35) form the final flashing inception model. By eliminating ψ between the two equations, one can solve for the flashing inception point, θ_m , in terms of T_r and S . Numerical studies have shown that the calculated values of ψ are relatively insensitive to the value of C_o . However, since C_o was taken as I_o in this study, it is necessary to use the same value when using the model.

The accuracy of the model is demonstrated in Fig. 6, which plots the predicted versus measured pressure undershoot, $\Delta P \equiv P_s - P_m$. Generally good agreement is obtained over the studied range of initial conditions, although some specific tests are predicted with larger errors. For instance, in the Marviken data the measured pressure undershoots vary from about 2 to 6 atm, whereas the predicted values are close to 3.7 atm for all runs. Also one experiment of Friz et al. is overpredicted

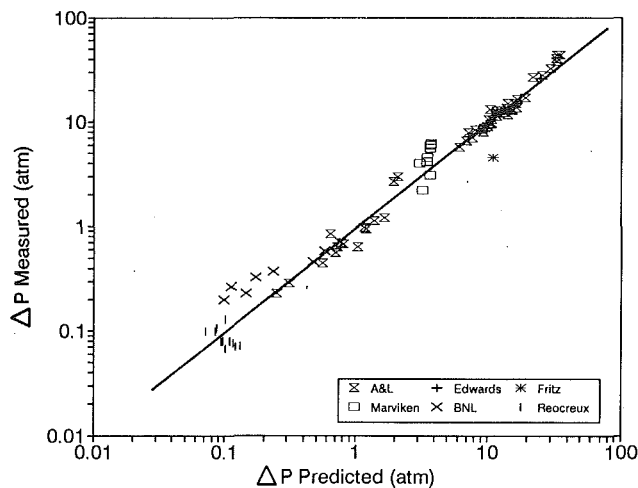


Fig. 6 Comparison of pressure undershoot measurements with the solution of Eqs. (32) and (35)

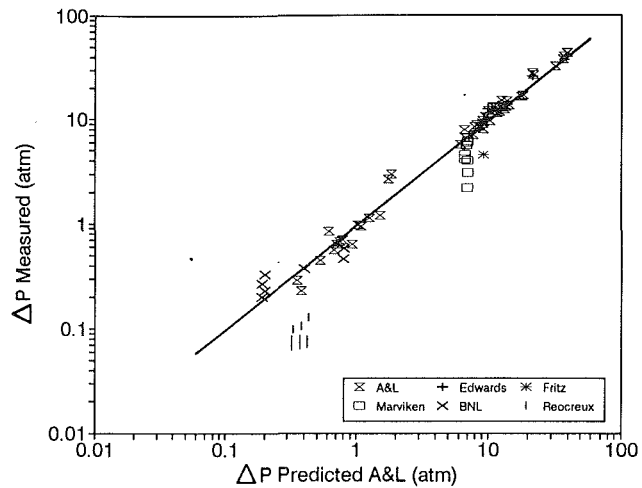


Fig. 8 Comparison of pressure undershoot measurements with the Alamgir and Lienhard (1981) correlation

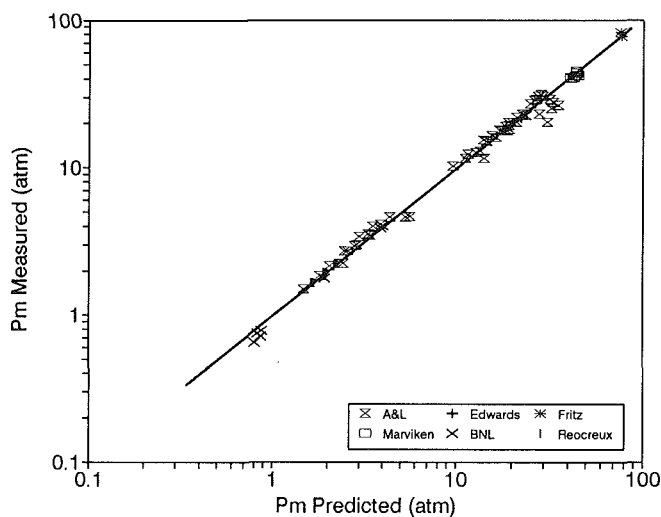


Fig. 7 Predicted versus measured pressures at the point of flashing inception

by almost a factor of two. The large errors in predicting the Marviken data are believed to be due to the inherent limitation of the present model, which is based on a lumped parameter approach assuming uniform pressure and temperature throughout the system. Neglect of pressure and heat transport time is not fully justified in large systems such as the Marviken test facilities. Large prediction errors are noted in some of the BNL and Reocreux flow data. In these tests, the pressure undershoot is typically small. The relative measurement errors are expected to be large and to contribute to the observed disagreement with the model. Better agreement is obtained in the high-pressure undershoot range.

Figure 7 shows the measured versus predicted minimum pressure, P_m . Again, satisfactory agreement is demonstrated in most of the static and flow transients. For the 83 data points presented in Fig. 7 the average deviation between the measured and predicted minimum pressure is 10.8 percent. The maximum error is about 25 percent.

For completeness, we present in Fig. 8 the measured pressure undershoot data against the predictions by the Alamgir and Lienhard (1981) correlation. While good agreement is obtained for the data taken at high initial temperature and high rates of depressurization such as (Alamgir et al., 1980, 1981; Edwards and O'Brien, 1970; Friz et al., 1976), the Alamgir and Lienhard correlation in its original form fails to predict the EPRI (1982) data and the flow data of Reocreux (1974), which

are characterized by slow depressurization. These limitations of the Alamgir and Lienhard correlation have been noticed previously by Alamgir and Lienhard (1982) and Abuaf et al. (1983).

5 Conclusions

When a hot liquid is suddenly transferred from a high to low-pressure environment, its pressure drops rapidly with time below the saturation pressure corresponding to the initial liquid temperature. This pressure undershoot plays an important role in the subsequent vapor generation and pressure recovery processes. In certain cases the minimum pressure is also important in defining the dynamic loads imposed on the system structure.

To understand the transient response of a liquid to a sudden change in pressure, a mathematical relationship has been derived between the initial rate of decompression and the resulting liquid superheat. The model is based on an asymptotic estimation of the mass and energy equations of the fluid at the flashing inception point. In pure liquids, heterogeneous nucleation in the liquid due to activation of ready nucleation centers in the bulk can be neglected. In this case the model yields the rate of decompression required to transfer the liquid into its homogeneous limit of metastable state. A heterogeneity factor has been empirically defined in order to extend the utility of the model for ordinary boiling systems. It is noted that at high decompression rates, the heterogeneity effect is reduced and the model results approach those obtained for the homogeneous nucleation case.

The model has been validated against experimental data covering a wide range of initial temperatures and depressurization rates. It is shown to be applicable for both static and flow transients.

Acknowledgments

The authors are indebted to Professor Donald Olander of UC Berkeley for his useful suggestions and discussions.

References

- Abuaf, N., Jones, O. C., Jr., and Wu, B. J. C., 1983, "Critical Flashing Flows in Nozzles With Subcooled Inlet Conditions," *ASME JOURNAL OF HEAT TRANSFER*, Vol. 105, pp. 379-383.
- Alamgir, Md., Kan, C. Y., and Lienhard, J. H., 1980, "An Experimental Study of the Rapid Depressurization of Hot Water," *ASME JOURNAL OF HEAT TRANSFER*, Vol. 102, pp. 433-438.
- Alamgir, Md., Kan, C. Y., and Lienhard, J. H., 1981, "Early Response of Pressurized of Hot Water in a Pipe to a Sudden Break," EPRI Report NP-1867.
- Alamgir, Md., and Lienhard, J. H., 1981, "Correlation of Pressure Under-

shoot During Hot Water Depressurization," ASME JOURNAL OF HEAT TRANSFER, Vol. 103, pp. 52-55.

Avedisian, C. T., 1985, "The Homogeneous Nucleation Limits of Liquids," *J. Phys. Chem. Ref. Data*, Vol. 14, No. 3, pp. 695-729.

Avedisian, C. T., 1986, "Bubble Growth in Superheated Liquid Droplets," in: *Encyclopedia of Fluid Mechanics*, N. P. Chermisinoff, ed., Vol. 3, pp. 131-190.

Blander, M., and Katz, T. L., 1975, "Bubble Nucleation in Liquids," *AIChE Journal*, Vol. 21, pp. 833-848.

Blander, M., 1979, "Bubble Nucleation in Liquids," *Advances in Colloid and Interface Science*, Vol. 10, pp. 1-32.

Edwards, A. R., and O'Brien, T. P., 1970, "Studies of Phenomena Connected With Depressurization of Water Reactors," *Journal British Nuclear Energy Society*, Vol. 9, pp. 125-135.

EPRI, 1982, "The Marviken Full Scale Critical Flow Tests," Report No. NP-2370.

Forest, T. W., and Ward, C. A., 1977, "Effect of Dissolved Gas on the Homogeneous Nucleation Pressure of a Liquid," *J. Chem. Phys.*, Vol. 66, No. 6, pp. 2322-2330.

Forest, T. W., and Ward, C. A., 1978, "Homogeneous Nucleation of Bubbles in Solution at Pressures Above the Vapor Pressure of the Pure Liquid," *J. Chem. Phys.*, Vol. 69, No. 5, pp. 2221-2226.

Frenkel, J., 1955, *The Kinetic Theory of Liquids*, Dover Publ. Inc., New York.

Friz, G., Reibold, W., and Schulze, W., 1976, "Studies on Thermodynamic Non-equilibrium in Flashing Water," *Transient Two-Phase Flow*, Proc. CSNI Specialists Meeting, Toronto, AEC of Canada Ltd., Aug. 3-4, pp. 511-523.

Glaser, H., 1984, "Equilibrium Radii of Small Vapor Bubbles and Liquid Droplets," *Int. J. Heat Mass Transfer*, Vol. 27, No. 9, pp. 1439-1443.

Haar, L., Gallagher, J. S., and Kell, G. S., 1984, *NBS/NRC Steam Tables*, Hemisphere Publishing Corp., Washington, DC.

Hirth, J. P., and Pound, G. M., 1963, *Condensation and Evaporation: Nucleation and Growth Kinetics*, Pergamon Press, Oxford, United Kingdom.

Hooper, C. F., and Abdelmessih, A. H., 1966, "The Flashing of Fluids at Higher Superheats," *Proc. 3rd Int. Heat Transfer Conf.*, Vol. 4, No. 117, p. 44.

Jones, O. C., Jr., 1979, "Flashing Inception in Flowing Liquids in Non-equilibrium Two-Phase Flows," *ASME 18th National Heat Transfer Conf.*, San Diego, CA, Aug. 6-8, pp. 29-34.

Kenning, D. B. R., and Thirunavukarasu, K., 1970, "Bubble Nucleation Following a Sudden Pressure Reduction in Water," *Proc. Fourth International Heat Transfer Conference*, Paris-Versailles, Vol. 5, Paper No. B 2.9.

Lahey, R. T., and Moody, F. J., 1979, "The Thermal Hydraulic of a Boiling Water Reactor," ANS Monogram, IL, Chap. 5.

Levy, S., and Abdollahian, D., 1982, "Homogeneous Non-equilibrium Critical Flow Model," *International Journal of Heat and Mass Transfer*, Vol. 25, pp. 759-770.

Miller, R. S., 1985, "Photographic Observations of Bubble Formation in Flashing Nozzle Flow," *ASME JOURNAL OF HEAT TRANSFER*, Vol. 107, pp. 751-755.

Miyatake, O., Murakami, K., Kawata, K., and Fujii, F., 1973, "Fundamental Experiments With Flash Evaporation," *Heat Transfer—Jap. Res.*, Vol. 2, No. 4, p. 89.

Reocreux, M., 1974, "Contribution a l'Etude des Debits Critiques en Ecoulement Diphasique Eau-Vapeur," Ph.D. Dissertation, Universite Scientifique et Medicale de Grenoble, France.

Skrupov, V. P., 1974, *Metastable Liquids*, Wiley, New York (English translation).

Skrupov, V. P., et al., 1988, "Thermophysical Properties of Liquids in the Metastable (Superheated) State," Gordon and Breach Science Publishers, New York (English translation).

Van Stralen, S., and Cole, R., 1979, *Boiling Phenomena*, Hemisphere Publishing Corp., Washington, DC.

Zimmer, G. A., Wu, B. C. J., Leonhardt, W. J., Abuaf, N., and Jones, O. C., Jr., 1979, "Pressure and Void Distribution in a Converging-Diverging Nozzle With Non-equilibrium Water Vapor Generation," BNL-NUREG-26003.

$$\frac{d^2\theta}{dt^2} = -\beta \frac{d^2\alpha}{dt^2} \quad (36)$$

But from Eq. (25), which we assume valid near θ_m ,

$$\frac{d^2\theta}{dt^2} = -2\tau \quad (37)$$

so that

$$\tau = \frac{\beta}{2} \frac{d^2\alpha}{dt^2} \quad (38)$$

One can compute $d^2\alpha/dt^2$ from Eq. (14) and since by Eq. (20)

$$g(t, t) = \frac{dg(t, t)}{dt} = 0$$

we obtain

$$\frac{d^2\alpha}{dt^2} = v_b \int_{t_0}^{t'} I[\theta(t')] \frac{d^2g(t, t')}{dt^2} dt' \quad (39)$$

Hence at $t = t_m$ we have from Eqs. (38) and (39)

$$\tau = \frac{\beta v_b}{2} \int_{t_0}^{t_m} I[\theta(t')] \frac{d^2g(t_m, t')}{dt^2} dt' \quad (40)$$

But from Eq. (20)

$$\frac{d^2g}{dt^2} = \frac{2[A(\theta_m)]^3}{9} (t_m - t'), \quad t' \leq t_m \quad (41)$$

Repeating the integration steps that lead to Eq. (27), Eqs. (40) and (41) yield

$$\begin{aligned} \tau &= \frac{\beta v_b [A(\theta_m)]^3}{9\epsilon} I_0 e^{-G_b(\theta_m)} \int_0^{\sqrt{\epsilon}(t_m - t_0)} e^{-\eta^2} \eta d\eta \\ &= \frac{\beta v_b [A(\theta_m)]^3}{9\epsilon} I_0 e^{-G_b(\theta_m)} \phi_1 [\sqrt{\epsilon}(t_m - t_0)] \end{aligned} \quad (42)$$

But from Eq. (28)

$$\frac{\beta v_b [A(\theta_m)]^3}{9\epsilon} I_0 e^{-G_b(\theta_m)} = \frac{\Sigma \sqrt{\epsilon}}{P_s \phi_2 [\sqrt{\epsilon}(t_m - t_0)]} \quad (43)$$

Substituting Eq. (43) into Eq. (42) yields

$$\tau = \sqrt{\epsilon} \frac{\Sigma \phi_1}{P_s \phi_2} \quad (44)$$

The dependence of τ on the rate of decompression, Σ , in Eq. (44) is noteworthy. Since we require ϵ rather than τ in Eq. (28), one obtains with the help of Eq. (26a)

$$\sqrt{\epsilon} = -\frac{\Sigma}{P_s} \left(\frac{dGb}{d\theta} \right)_{\theta_m} \frac{\phi_1 [\sqrt{\epsilon}(t_m - t_0)]}{\phi_2 [\sqrt{\epsilon}(t_m - t_0)]} \quad (45)$$

Now since typically $\sqrt{\epsilon}(t_m - t_0) > 10$ due to ϵ being very large, $\phi_2 = \pi/4$, and $\phi_1 = 1/2$, so that Eq. (45) yields

$$\sqrt{\epsilon} = \frac{4c}{\sqrt{\pi} \theta_m^3} \frac{\Sigma}{P_s} \quad \text{and} \quad \epsilon^{3/2} = \frac{1}{\theta_m^9} \left(\frac{4c\Sigma}{\sqrt{\pi} P_s} \right)^3 \quad (46)$$

APPENDIX

To determine τ and thus ϵ , we differentiate Eq. (9) with respect to t :

Simulation of the Early Startup Period of High-Temperature Heat Pipes From the Frozen State by a Rarefied Vapor Self-Diffusion Model

Y. Cao

A. Faghri

Dept. of Mechanical
and Materials Engineering,
Wright State University,
Dayton, OH 45435

The heat pipe startup process is described physically and is divided into five periods for convenience of analysis. The literature survey revealed that none of the previous attempts to simulate the heat pipe startup process numerically were successful, since the rarefied vapor flow in the heat pipe was not considered. Therefore, a rarefied vapor self-diffusion model is proposed, and the early startup periods, in which the rarefied vapor flow is dominant within the heat pipe, are first simulated numerically. The numerical results show that large vapor density gradients existed along the heat pipe length, and the vapor flow reaches supersonic velocities when the density is extremely low. The numerical results are compared with the experimental data of the early startup period with good agreement.

Introduction

The study of high-temperature heat pipe startup from the frozen state is important in many areas, such as the design and operation of satellite radiators, cooling the leading edges of re-entry vehicles and hypersonic aircraft, and the cooling of nuclear and isotope reactors.

Cotter (1967) was one of the first to study the dynamics of heat pipe startup. Different transient modes of heat pipe startup were described, and the various mechanisms that may inhibit successful startup were discussed qualitatively. For the analysis, the frontal startup mode was selected in conjunction with a lumped one-dimensional effective conductivity model.

The heat pipe is a complex system that involves many heat transfer modes, such as heat conduction in the wall and wick, melting of the working fluid in the wick, evaporation and condensation at the liquid-vapor interface, liquid flow in the porous wick, and compressible vapor flow in the core. Therefore, it is very difficult to obtain a generalized analytical solution for heat pipe dynamics. In this case, numerical analyses are needed for the study of heat pipe startup from the frozen state. Previous studies include those of Chang and Colwell (1985), Costello et al. (1987), Seo and El-Genk (1988), Bowman and Hitchcock (1988), Hall and Doster (1990), Jang et al. (1990), and Cao and Faghri (1990a). The numerical models involve different assumptions and are at different stages of development. However, most of these models assumed that the working fluid in the wick is completely thawed, and only involved the transient response of the heat pipe to a power load with the continuum flow assumption. Exceptions are the studies of Costello et al. (1987), Hall and Doster (1990), and Jang et al. (1990).

The numerical model developed by Jang et al. (1990) may be one of the most comprehensive mathematical models of heat pipe startup from the frozen state to date. Different startup periods were described and the general mathematical formulation for each period was given. In an attempt to solve the

governing equations, the liquid flow in the porous medium was neglected, and the vapor flow was simplified to a one-dimensional model. The numerical simulation was conducted in two separate stages, i.e., the initial stage and the transient continuum stage. In the initial stage, the liquid-vapor interface was assumed to be adiabatic, and only the heat conduction in the wall and the melting in the wick were considered. For the second stage, the vapor was assumed to be in a continuum flow state. An effort to couple the continuum vapor flow with the wick and wall was made, but the coupling was apparently not completed and the linkage between the two stages was not considered.

During the early stage of startup when the melting interface has reached the vapor-wick interface, the vapor-wick interface cannot be considered to be adiabatic. Otherwise, there would be no molecular vapor accumulation in the heat pipe core, and the vapor flow would never reach the continuum state. Also, during the early startup period, the vapor density in the heat pipe core is very low and partly loses its continuum characteristics. The vapor flow in this condition is usually referred to as rarefied vapor flow. In all of the above models, the rarefied vapor diffusion and heat transfer were not taken into account, although this is one of the key factors in the heat pipe startup process, and no comparison of the numerical results with the available experimental data for the early startup period was made. In general, the conventional continuum vapor flow theory is not applicable to rarefied vapor flow, and special treatment of the vapor flow in this region is needed.

In this paper, a rarefied vapor self-diffusion model is proposed to simulate the early stage of heat pipe startup from the frozen state. The numerical results are compared with experimental data by Faghri et al. (1991a, 1991b) to validate the numerical modeling, and some heat pipe startup mechanisms are discussed.

Description and Mathematical Formulation of Heat Pipe Startup

The startup process of a liquid metal heat pipe from the frozen state may be divided into several periods for convenience of analysis:

Contributed by the Heat Transfer Division and presented at the National Heat Transfer Conference, San Diego, California, August 9-12, 1992. Manuscript received by the Heat Transfer Division July 26, 1991; revision received July 1992. Keywords: Heat Pipes and Thermosyphons, Liquid Metals, Transient and Unsteady Heat Transfer. Associate Technical Editor: H. R. Jacobs.

1 The heat pipe wick is initially in the frozen state. The heat pipe core can be considered to be completely evacuated before startup. The heat pipe in its initial state is illustrated in Fig. 1 (period 1).

2 Power is applied to the evaporator section of the heat pipe. Heat conduction through the wall and melting of the working fluid in the porous wick take place. However, the liquid-solid melting interface has not yet reached the wick-vapor boundary, and the heat pipe core is still evacuated because no evaporation has taken place in the evaporator section (Fig. 1, period 2).

3 In the evaporator section, the working fluid in the wick is completely melted, and evaporation takes place at the liquid-vapor interface. The vapor pressure is so low that the vapor flow is in a rarefied or free molecular condition. Also, some working fluid in the wick is still in the solid state in the adiabatic and condenser sections of the heat pipe (Fig. 1, period 3).

4 As evaporation continues, the amount of vapor accumulated in the core is large enough in the evaporator that a continuum flow is established there. Near the condenser end of the heat pipe, however, the vapor flow is still in the rarefied or free molecular regime. This period may be called the intermediate period (Fig. 1, period 4).

5 The working fluid in the wick is completely melted and continuum flow is established over the entire heat pipe length. The heat pipe continues to operate and gradually reaches steady state (Fig. 1, period 5).

This paper primarily deals with the early stage of the heat pipe startup, i.e., periods 1-3. Cao and Faghri (1990a) have successfully simulated the heat pipe dynamics with transient continuum vapor flow (period 5) by a conjugate compressible two-dimensional analysis. The study of the intermediate period

4, as well as the coupling of all periods together, is beyond the scope of the present effort.

The governing equations for each section (wall, wick, and vapor) are described below.

Governing Equation for the Heat Pipe Wall. The heat transfer through the heat pipe wall is by conduction. The corresponding governing equation is

$$\rho_w c_w \frac{\partial T}{\partial t} = k_w \left[\frac{1}{r} \frac{\partial}{\partial r} \left(r \frac{\partial T}{\partial r} \right) + \frac{\partial^2 T}{\partial z^2} \right] \quad (1)$$

The equation above is applicable to periods 1-5.

Governing Equation for the Porous Wick Structure. For the porous wick structure, the change of phase of the frozen working fluid must be considered. The wick structure is assumed to be isotropic and homogeneous. The phase change model of Cao and Faghri (1990b) is employed in this study, which is a fixed-grid formulation having the advantage of eliminating time step and grid size limitations. The governing equation below is also applicable for periods 1-5:

$$\frac{\partial(\rho_{\text{eff}}CT)}{\partial t} = \frac{\partial}{\partial z} \left(k_{\text{eff}} \frac{\partial T}{\partial z} \right) + \frac{1}{r} \frac{\partial}{\partial r} \left(k_{\text{eff}} r \frac{\partial T}{\partial r} \right) - \frac{\partial(\rho_{\text{eff}}S)}{\partial t} \quad (2)$$

The coefficients $C = C(T)$, $S = S(T)$, and $k_{\text{eff}} = k_{\text{eff}}(T)$ in Eq. (2) are given by Eqs. (3)-(5), respectively.

$$C(T) = \begin{cases} c_{se} & (T < T_m - \delta T) & \text{(solid phase)} \\ c_{me} + \frac{H}{2\delta T} & (T_m - \delta T \leq T \leq \delta T + T_m) & \text{(mushy phase)} \\ c_{le} & (T > T_m + \delta T) & \text{(liquid phase)} \end{cases} \quad (3)$$

$$S(T) = \begin{cases} c_{se}(\delta T - T_m) & (T < T_m - \delta T) & \text{(solid phase)} \\ c_{me}\delta T + \frac{H}{2} - \left(c_{me} + \frac{H}{2\delta T} \right) T_m & (T_m - \delta T \leq T \leq \delta T + T_m) & \text{(mushy phase)} \\ c_{se}\delta T + H - c_{le}T_m & (T > T_m + \delta T) & \text{(liquid phase)} \end{cases} \quad (4)$$

Nomenclature

C = coefficient in Eq. (2), J/(kg-K)
 c = specific heat, J/(kg-K)
 D = vapor core diameter, m
 D_v = self-diffusion coefficient, m²/s
 G = mass flux, kg/(m²·s)
 h = convective heat transfer coefficient, W/(m²-K)
 H = latent heat, J/kg
 k = thermal conductivity, W/(m-K)
 Kn = Knudsen number
 L = total length of the heat pipe, m, or latent heat, J/kg
 MW = molecular weight, kg/kmol
 \dot{m}_i = mass flux at the liquid-vapor interface, kg/(m²-s)
 M = Mach number = $w / \sqrt{\gamma p / \rho_v}$
 p = pressure, N/m²
 q = heat flux, W/m²
 Q = heat input at active evaporators, W
 R = gas constant, J/(kg-K)
 R_u = universal gas constant, kJ/(kmol-K)
 R_v = vapor space radius, m

R_w = wick-wall interface radius, m
 R_o = outer pipe wall radius, m
 r = radial coordinate, m
 S = coefficient in Eq. (2), J/kg
 t = time, s
 T = temperature, K
 T_m = melting temperature, K
 v = radial velocity, m/s
 w = axial velocity, m/s
 z = axial coordinate, m
 α = condensation or evaporation coefficient
 δ = wall or liquid-wick thickness, m
 $2\delta T$ = phase-change temperature range, K
 ϵ = maximum energy of attraction between a pair of molecules, or radiation emissivity
 κ = Boltzmann constant, J/K
 λ = vapor mean free path, m
 μ = dynamic viscosity of the vapor, kg/(m-s)
 ρ = density, kg/m³
 σ = collision diameter, Å, or Stefan-Boltzmann constant, W/(m²-K⁴)

ϕ = porosity
 Ω_D = collision integral for mass diffusion

Subscripts

a = adiabatic
 am = ambient
 c = condenser
 e = evaporator
 eff = effective
 f = working fluid
 l = liquid or working fluid in the liquid state in the wick
 le = wick region where the working fluid is in the liquid state
 m = mushy phase
 me = wick region where the working fluid is in the mushy phase range
 s = saturation, or working fluid in the solid state in the wick
 se = wick region where the working fluid is in the solid state
 v = vapor
 w = wall
 ws = wick structure material

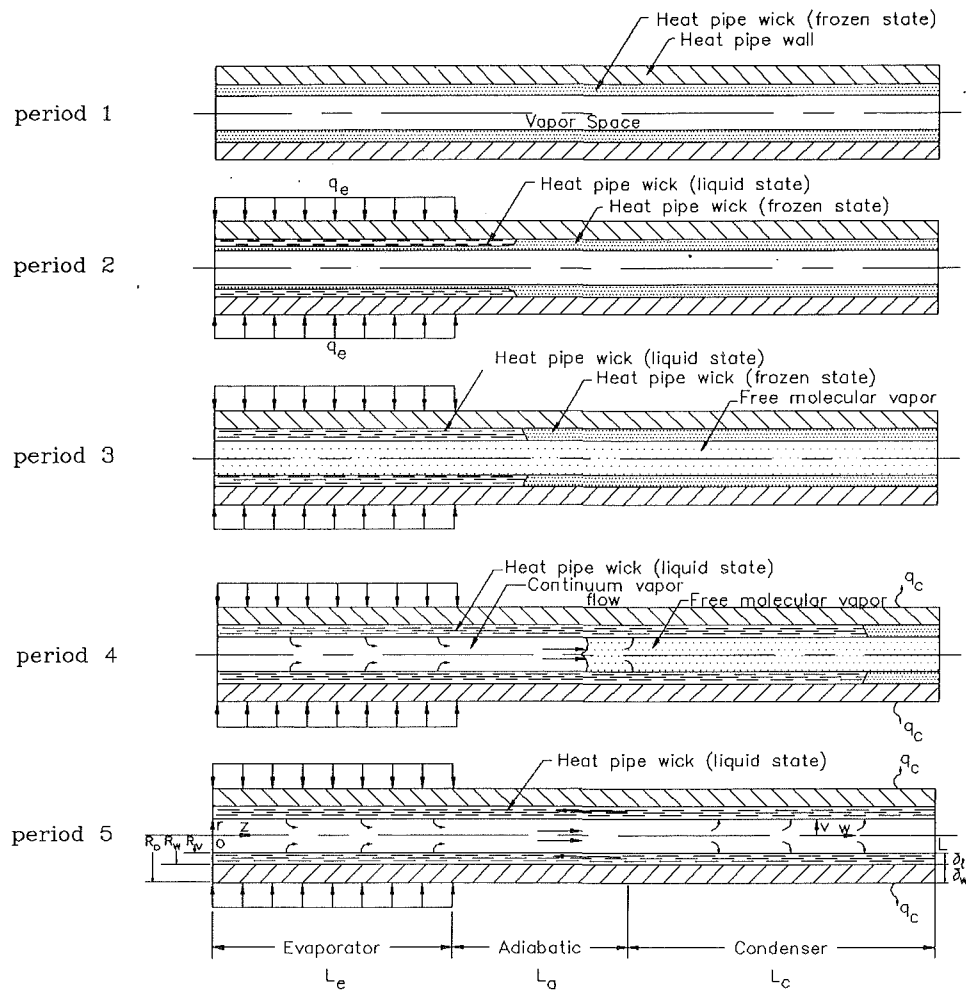


Fig. 1 Evolution of heat pipe startup process from the frozen state (not to scale)

$$k_{\text{eff}} = \begin{cases} k_{se} & (T < T_m - \delta T) & \text{(solid phase)} \\ k_{se} + (k_{le} - k_{se}) (T - T_m + \delta T) / 2\delta T & (T_m - \delta T \leq T \leq \delta T + T_m) & \text{(mushy phase)} \\ k_{le} & (T > T_m + \delta T) & \text{(liquid phase)} \end{cases} \quad (5)$$

where

$$\rho_{\text{eff}} = \varphi \rho_l + (1 - \varphi) \rho_{ws}$$

$$c_{se} = \varphi c_s + (1 - \varphi) c_{ws}$$

$$c_{le} = \varphi c_l + (1 - \varphi) c_{ws}$$

$$c_{me} = 0.5 (c_{se} + c_{le})$$

The values of k_{se} and k_{le} depend on the particular heat pipe wick structure. For a wrapped screen wick, k_{se} and k_{le} are calculated using the equation given by Chi (1976).

$$k_{se} = k_s [(k_s + k_{ws}) - (1 - \varphi)(k_s - k_{ws})] / [(k_s + k_{ws}) + (1 - \varphi)(k_s - k_{ws})]$$

$$k_{le} = k_l [(k_l + k_{ws}) - (1 - \varphi)(k_l - k_{ws})] / [(k_l + k_{ws}) + (1 - \varphi)(k_l - k_{ws})]$$

It should be pointed out that the effect of the liquid flow in the wick on the temperature distribution has been neglected. The analysis of Cao and Faghri (1990a) showed that for high-temperature heat pipes with liquid metal working fluids, this

assumption is reasonable. The reason is that the porous wick is very thin, the thermal conductivity of the liquid metal is very high, and heat conduction dominates in the wick of the liquid metal heat pipe. The validity of this conduction model in the wick was also documented by other authors such as Ivanovskii et al. (1982) and Dunn and Reay (1982).

Governing Equations for the Rarefied Vapor Flow. In the early stage of the heat pipe startup from the frozen state, the vapor pressure and density are very small in the heat pipe core. Because of the low density, the vapor in the rarefied state is somewhat different from the conventional continuum state. Also, the vapor density gradient is very large along the axial direction of the heat pipe. The vapor flow along the axial direction is mainly caused by the density gradient via vapor molecular diffusion. Upon neglecting the presence of noncondensable gases, the rarefied vapor flow can be simulated by a self-diffusion model. The term self-diffusion here means the interdiffusion of particles of the same mass due to a gradient in density (Hirschfelder et al., 1966). The governing equations were derived by applying the principles of the conservation of mass and energy in a differential cylindrical control volume

in conjunction with the definition of mass flux (Hirschfelder et al., 1966).

Mass self-diffusion:

$$\frac{\partial \rho}{\partial t} - \frac{\partial}{\partial z} \left(D_v \frac{\partial \rho}{\partial z} \right) - \frac{1}{r} \frac{\partial}{\partial r} \left(r D_v \frac{\partial \rho}{\partial r} \right) = 0 \quad (6)$$

Energy equation:

$$\begin{aligned} \frac{\partial}{\partial t} (\rho c_v T) + \frac{1}{r} \frac{\partial}{\partial r} (G_r c_p r T) + \frac{\partial}{\partial z} (G_z c_p T) \\ = \frac{1}{r} \frac{\partial}{\partial r} \left(r k_v \frac{\partial T}{\partial r} \right) + \frac{\partial}{\partial z} \left(k_v \frac{\partial T}{\partial z} \right) \end{aligned} \quad (7)$$

where the mass fluxes G_r and G_z are

$$G_r = \rho v = -D_v \frac{\partial \rho}{\partial r}, \quad G_z = \rho w = -D_v \frac{\partial \rho}{\partial z}, \quad (8)$$

D_v is the self-diffusion coefficient, and k_v is the vapor molecular conductivity.

Equation of state:

$$p = \rho RT \quad (9)$$

The evaluation of the low-density properties such as D_v is carried out using the kinetic theory of gases (Eckert and Drake, 1959; Edwards et al., 1979; Hirschfelder et al., 1966). The coefficient of self-diffusion is obtained from the relation based on the Chapman-Enskog kinetic theory (Hirschfelder et al., 1966):

$$D_v = 2.628 \times 10^{-7} \frac{\sqrt{T^3/MW}}{p \sigma^2 \Omega_D (\kappa T/\epsilon)} \quad (10)$$

where p is the pressure in atmospheres, σ is the collision diameter in Å, ϵ is the maximum energy of attraction between a pair of molecules, κ is the Boltzmann constant, and Ω_D is the collision integral for mass diffusion. For sodium, both σ and ϵ/κ can be found from the table for constants of the Lennard-Jones potential model (Edwards et al., 1979), which gives

$$\sigma = 3.567 \text{ Å}, \quad \epsilon/\kappa = 1375 \text{ K}$$

The value of the collision integral Ω_D can also be found from the same reference, which is listed as a function of $\kappa T/\epsilon$.

It must be mentioned that the term rarefied vapor here is used to refer to the low-density vapor state that has partly lost its continuum characteristics. In some references, such as those of Eckert and Drake (1959) and Ivanovskii et al. (1982), the rarefied gases were subdivided into intermediate and free molecular regions. In this study, we intend to neglect these sub-differences for simplicity.

Boundary Conditions. At both ends of the heat pipe, $z=0$ and L :

$$\frac{\partial \rho}{\partial z} = 0, \quad \frac{\partial T}{\partial z} = 0 \quad (11)$$

At the centerline, $r=0$, the symmetry condition implies:

$$\frac{\partial T}{\partial r} = 0, \quad \frac{\partial \rho}{\partial r} = 0 \quad (12)$$

For the outer pipe wall surface:

evaporator:

$$k_w \frac{\partial T}{\partial r} \Big|_{r=R_o} = q_e \quad (13)$$

adiabatic:

$$\frac{\partial T}{\partial r} \Big|_{r=R_o} = 0 \quad (14)$$

condenser:

$$-k_w \frac{\partial T}{\partial r} \Big|_{r=R_o} = \begin{cases} h (T_w - T_{am}) & \text{(convection)} \\ \sigma \epsilon (T_w^4 - T_{am}^4) & \text{(radiation)} \end{cases} \quad (15)$$

where h is the convective heat transfer coefficient, T_w and T_{am} are the outer wall surface temperature and the environment temperature, respectively, ϵ is the emissivity, and σ is the Stefan-Boltzmann constant.

After the melting interface in the wick reaches the wick-vapor interface, $r=R_v$, evaporation or condensation takes place. The relation for the interface mass flux applied here is that of Silver and Simpson (1961):

$$\dot{m}_i = \left(\frac{2\alpha}{2-\alpha} \right) \sqrt{\frac{MW}{2\pi R_u}} \left(\frac{p_i^*}{\sqrt{T_i}} - \frac{p_v}{\sqrt{T_v}} \right) = \begin{cases} > 0 & \text{evaporation} \\ < 0 & \text{condensation} \end{cases} \quad (16)$$

where α is the condensation or evaporation coefficient, and p_i^* is the equilibrium pressure corresponding to the liquid surface temperature T_i , and can be calculated using the Clausius-Clapeyron equation:

$$p_i^* = p_{rf} \exp \left[-\frac{h_{fg}}{R} \left(\frac{1}{T_i} - \frac{1}{T_{rf}} \right) \right]$$

where p_{rf} and T_{rf} are the reference pressure and temperature. There are other relations for the interfacial mass flux \dot{m}_i such as that of Wayner and Schonberg (1990), which includes the effect of surface curvature. However, Eq. (16) is well established and widely used. Sukhatme and Rohsenow (1966) showed that α may change from 0.1 to 1 according to the surface condition with $\alpha=1$ being the upper limit.

Numerical Procedure

The governing equations were discretized by employing the control-volume finite-difference approach described by Patankar (1980, 1988). A combination of the direct method (TDMA) and the Gauss-Siedel method was employed to solve the discretization equations. The two regions, wall/wick and vapor, were solved separately and coupled via the interface mass fluxes. At $t=0$, the heat pipe is in the frozen state, and the heat pipe core is virtually evacuated. In order to simulate this condition, a very small value of vapor density, such as 10^{-8} kg/m^3 , was assigned to the vapor space as the initial vapor density. The sequence of numerical steps was as follows:

1 Initialize the temperature in the heat pipe wall and wick regions. The heat pipe was initially in a frozen state, and the vapor density in the vapor space was taken to be a very small value such as 10^{-8} kg/m^3 .

2 Heat input was applied at the outer wall surface of the evaporator. Before the melting front of the working fluid in the wick reached the vapor-wick interface, an adiabatic boundary condition was specified at the interface, and Eqs. (1) and (2) were solved to obtain the temperature distribution in the wall and wick regions. (The vapor region does not need to be considered in this step.)

3 After the melting front reached the vapor-wick interface, the interface mass flux was calculated using Eq. (16).

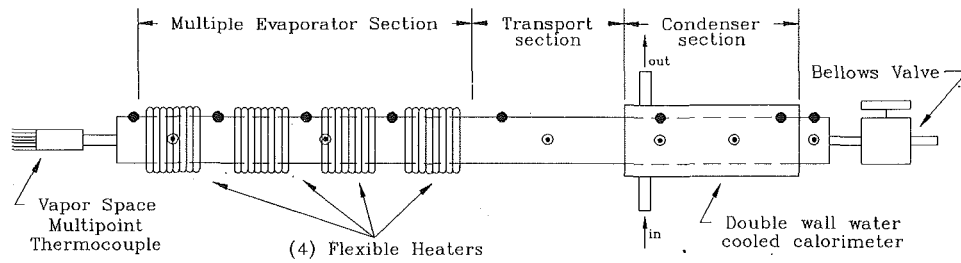
4 Solve Eq. (6) in conjunction with Eq. (16) to obtain the density distribution in the heat pipe core.

5 Calculate mass fluxes ρw and ρv in the heat pipe core using Eq. (8).

6 Solve Eq. (7) to obtain the temperature distribution in the heat pipe core and update D_v using the newly obtained temperature and density.

7 Solve Eqs. (1) and (2) in conjunction with Eq. (16) to obtain the temperature in the wall and wick.

8 Steps (3)–(7) are repeated until convergence is reached for each time step. The converged solution was assumed to be



Evaporator section length --- (4) 53 mm evaporators with 90 mm separation = 502 mm total
 Transport length --- 188 mm
 Condenser length --- 292 mm

● Wall thermocouple
 ○ Vapor-space thermocouple

Fig. 2 High-temperature heat pipe configuration and thermocouple locations

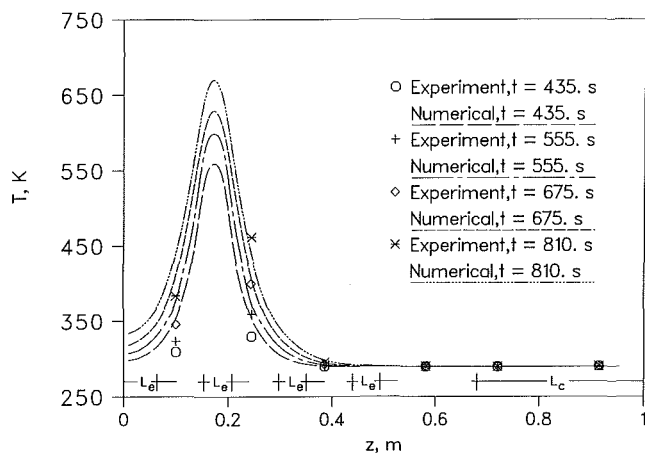


Fig. 3 The outer wall temperature compared with the experimental data for case 24a (evaporator 2 active, $Q = 60$ W)

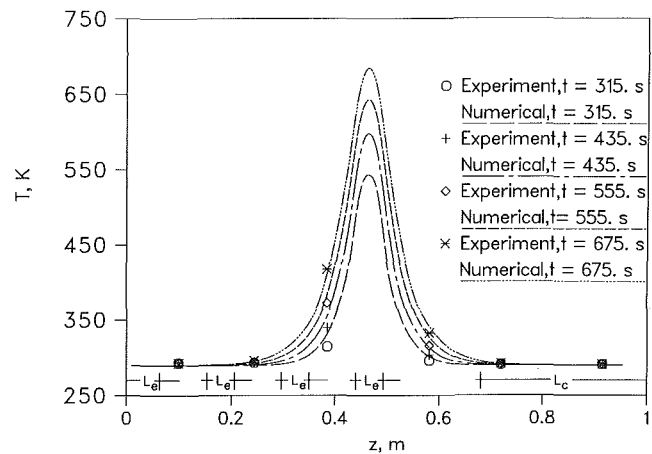


Fig. 5 The outer wall temperature compared with the experimental data for case 28a (evaporator 4 active, $Q = 69$ W)

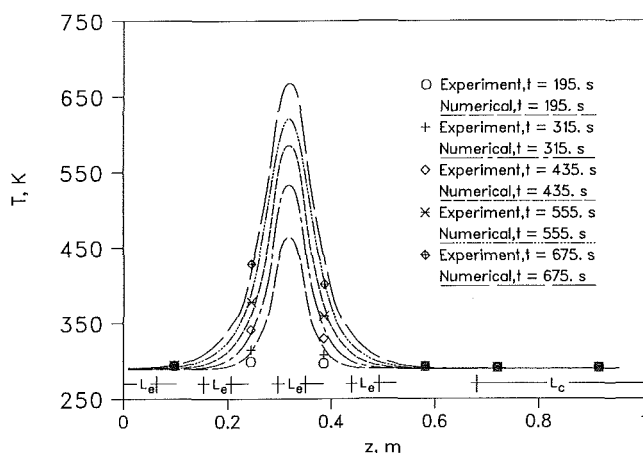


Fig. 4 The outer wall temperature compared with the experimental data for case 26a (evaporator 3 active, $Q = 66$ W)

reached when the relative change of temperature was less than 10^{-4} .

Results and Discussion

In order to validate the numerical modeling, numerical results were first compared with experimental data by Faghri et al. (1991a, 1991b). The heat pipe studied by Faghri et al. is a

multiple heat source sodium/stainless steel heat pipe with a vapor core radius $R_v = 10.75$ mm, a wrapped screen wick of thickness $\delta_w = 0.456$ mm, and stainless steel wall of thickness $\delta_w = 2.15$ mm. The configuration of the heat pipe and the heater locations are schematically shown in Fig. 2. The whole heat pipe system was initially at the ambient temperature, and the working fluid in the heat pipe wick was in the frozen state. Experimental data were taken for the heat pipe startup processes with different heat inputs at different heaters. Figures 3–5 compare the numerical and experimental outer wall temperatures for cases 24a, 26a, and 28a from Faghri et al. (1991a), respectively. Since the objective of this paper is to study the early stage of heat pipe startup, the comparisons also focussed on this range. As can be seen, the agreement between the numerical results and the experimental data is generally good. A grid size of 22×56 and a time step of $\Delta t = 15$ s were used in the numerical calculations. The condensation coefficient α in Eq. (16) was taken to be 0.3 in all three cases, and the phase-change temperature range $2\delta T$, which is defined as the transition temperature range of phase-change materials from the pure solid to the pure liquid, was taken to be 1.0 K to simulate phase change at a single temperature. It has been shown by Cao and Faghri (1990b) that a moderately small δT is sufficient to simulate the phase-change problem occurring at a single temperature. In all three cases, the melting fronts reached the vapor-liquid interface in the active evaporator regions very quickly (about 40 s). This means that startup period 2 in Fig. 1 is very short. The numerical solutions were essentially independent of the grid size used. A change from a grid size of

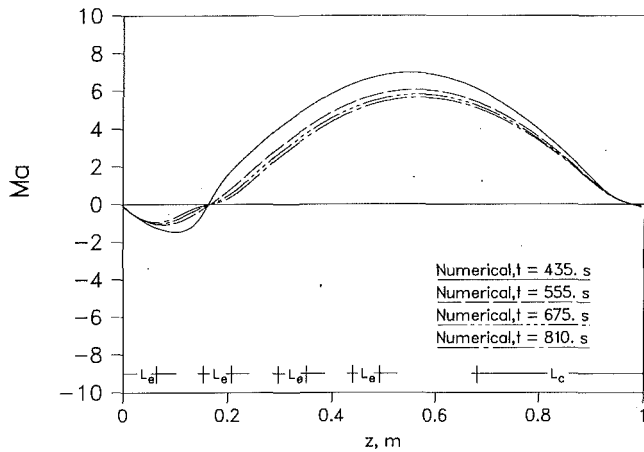


Fig. 6 The vapor Mach number along the axial direction at different times for case 24a (evaporator 2 active, $Q = 60$ W)

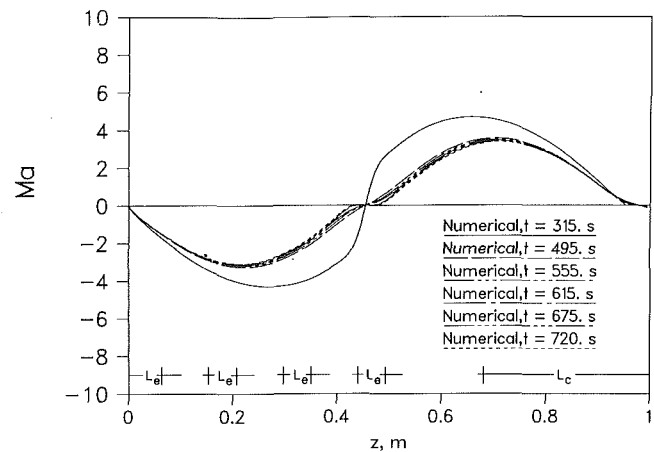


Fig. 8 The vapor Mach number along the axial direction at different times for case 28a (evaporator 4 active, $Q = 69$ W)

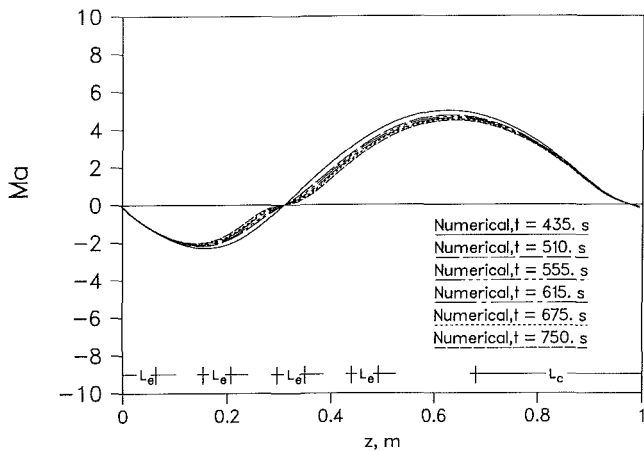


Fig. 7 The vapor Mach number along the axial direction at different times for case 26a (evaporator 3 active, $Q = 66$ W)

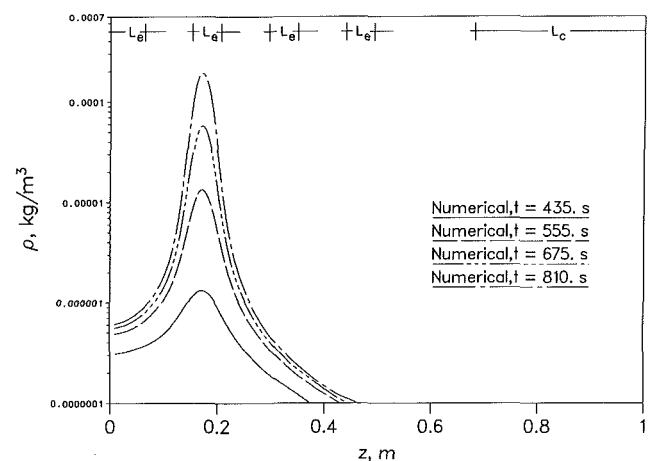


Fig. 9 The vapor density along the axial direction at different times for case 24a (evaporator 2 active, $Q = 60$ W)

20×54 to 40×108 , for example, resulted in a maximum change in wall temperature of less than 1.8 percent.

Figures 6–8 show the corresponding vapor Mach numbers at the centerline along the axial direction. For the three cases, the active heaters (the heaters to which power was applied) are located somewhat apart from the evaporator end cap, and the vapor flows toward both the condenser and the evaporator end caps. For case 24a in Fig. 6, the effect of the evaporator end cap existence is obvious due to the proximity of the active heater to the evaporator end cap. For case 28a in Fig. 8, however, the vapor flows in both directions almost symmetrically since the active evaporator is located near the middle of the heat pipe. In the earlier time periods, the vapor density was very low, and the corresponding Mach numbers were high. As the vapor was being accumulated in the active heater section due to the evaporation at the vapor–liquid interface, the vapor velocities decreased to the subsonic state ($M < 1$), due to the larger vapor density in this region. Still, away from the active heater region, the vapor density was very low, and the vapor velocities reached the supersonic state in both directions, and gradually decreased to zero due to the vapor condensation to the vapor–wick interface within the condenser portion of the heat pipe. It should be emphasized that the supersonic flow is solely due to the extremely low vapor density in the heat pipe core. Although the vapor velocity is very high, the mass flux $G_z = \rho_v w$ in the axial direction is still very low. This can be further explained by examining the vapor density distributions. Figures 9–11 show the corresponding vapor density distribu-

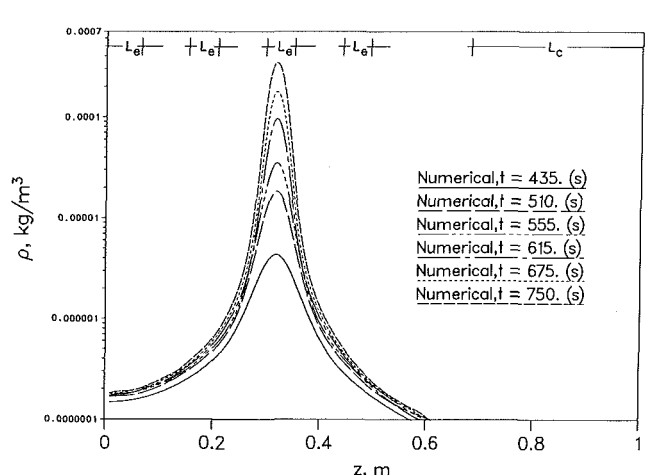


Fig. 10 The vapor density along the axial direction at different times for case 26a (evaporator 3 active, $Q = 66$ W)

tions along the axial direction at different times. Although the vapor density in the active heater regions increases significantly with time, very large density gradients exist in both directions, and the vapor density remains very low outside the active evaporator regions. The continuum flow in the vapor core is considered to be established when the vapor mean free path,

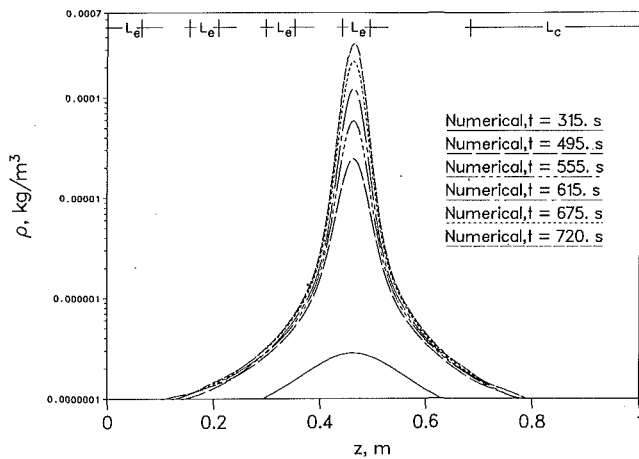


Fig. 11 The vapor density along the axial direction at different times for case 28a (evaporator 4 active, $Q = 69$ W)

λ , is substantially less than the minimum dimension, D , of the vapor flow passage. This criterion is usually expressed by the Knudsen number

$$\text{Kn} = \frac{\lambda}{D} \leq 0.01 \quad (17)$$

The mean free path given by Tien and Lienhard (1979) is

$$\lambda = \frac{1.051 \kappa T}{\sqrt{2} \pi \sigma^2 p} = \frac{1.051 \kappa}{\sqrt{2} \pi \sigma^2 R \rho_v} \quad (18)$$

For sodium vapor and a vapor core diameter of $D = 2.15$ cm, Eq. (17) gives

$$\rho_v \geq 3.3 \times 10^{-4} \text{ kg/m}^3$$

It can be seen from Figs. 10 and 11 that when $t > 750$ s and $t \geq 720$ s, respectively, the vapor flows in the active heater regions have already reached the continuum flow state, while the vapor flows in the rest of the heat pipe regions are still in the rarefied vapor flow or free molecular states.

As mentioned before, the evaporation/condensation coefficient α may change significantly depending on the surface condition, and there is little information available concerning the value of α for the vapor-wick surface in a heat pipe. In the numerical calculations for the above three cases, the evaporation/condensation coefficient α in Eq. (16) was taken to be 0.3. The influence of the condensation coefficient on the numerical simulation was examined by running case 24a again with different values of the condensation coefficient α . Figure 12 presents the outer wall temperature distributions in the axial direction for different values of α . The numerical results are insensitive to the evaporation/condensation coefficient α . Since the numerical solutions depend on the interfacial mass flux \dot{m}_i , which in turn depends on both the evaporation/condensation coefficient α and the pressure difference between the wick-vapor interface and the vapor flow, a larger value of α resulted in a higher vapor pressure and reduced the pressure difference between the wick-vapor interface and the vapor flow. As a result, the two factors offset each other, the interfacial mass flux \dot{m}_i remained relatively constant, and the numerical solutions were insensitive to the evaporation/condensation coefficient α .

Conclusions and Remarks

The early startup period of high-temperature heat pipes from the frozen state has been studied numerically by applying the rarefied vapor self-diffusion model. The numerical results have been compared with the corresponding experimental data with good agreement, indicating that the self-diffusion model is

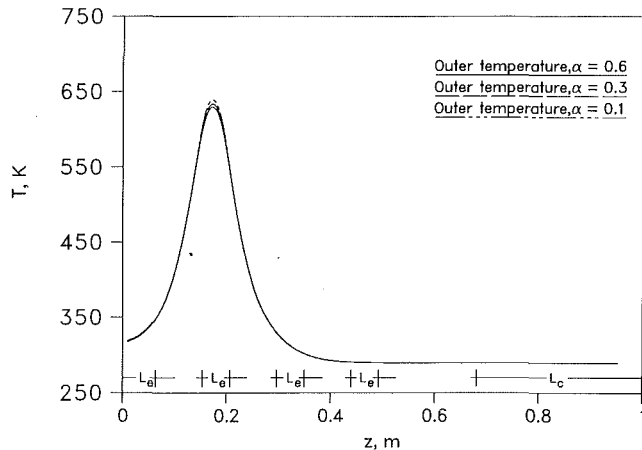


Fig. 12 The outer wall temperatures with different condensation coefficients at $t = 675$ s for case 24a (evaporator 2 active, $Q = 60$ W)

appropriate to simulate the early frozen state startup period of the heat pipe. The numerical results revealed that the startup period 2 is very short, and large vapor density gradients exist along the heat pipe length during the startup process. The continuum criterion (Eq. (17)) indicated that by the end of the early startup period, continuum vapor flow has been established in the active evaporator region. After this time, a continuum vapor flow model should be applied to this region. It is suggested that in future studies, a continuum vapor flow model be coupled with the rarefied vapor self-diffusion model, and all of the heat pipe startup periods be linked.

Acknowledgments

Funding for this work was provided by a joint effort of the NASA Lewis Research Center and the Thermal Energy Group of the Aero Propulsion Laboratory of the U.S. Air Force under contract No. F33615-89-C-2820.

References

- Bowman, J., and Hitchcock, J., 1988, "Transient, Compressible Heat-Pipe Vapor Dynamics," *Proc. 25th ASME National Heat Transfer Conf.*, Houston, TX, pp. 329-337.
- Cao, Y., and Faghri, A., 1990a, "A Transient Two-Dimensional Compressible Analysis for High Temperature Heat Pipes With a Pulsed Heat Input," *Numer. Heat Transfer, Part A*, Vol. 18, pp. 483-502.
- Cao, Y., and Faghri, A., 1990b, "A Numerical Analysis of Phase-Change Problems Including Natural Convection," *ASME JOURNAL OF HEAT TRANSFER*, Vol. 112, pp. 812-816.
- Chang, W. S., and Colwell, G. T. 1985, "Mathematical Modeling of the Transient Operating Characteristics of a Low-Temperature Heat Pipe," *Numer. Heat Transfer*, Vol. 8, pp. 169-186.
- Chi, S. W., 1976, *Heat Pipe Theory and Practice*, Hemisphere, Washington, D.C.
- Costello, F. A., et al., 1987, "Detailed Transient Model of a Liquid-Metal Heat Pipe," *Trans. 4th Symposium on Space Nuclear Power Systems*, CONF-870102-Summs, Albuquerque, NM, pp. 393-402.
- Cotter, T. P., 1967, "Heat Pipe Start-Up Dynamics," *Proc. Thermionics Conversion Specialist Conf.*, Palo Alto, CA, Oct. 30-Nov. 1.
- Dunn, P. D., and Reay, D. A., 1982, *Heat Pipes*, 3rd ed., Pergamon Press, Oxford, United Kingdom.
- Eckert, E. R. G., and Drake, R. M., 1959, *Heat and Mass Transfer*, McGraw-Hill, New York.
- Edwards, D. K., Denny, V. E., and Mills, A. F., 1979, *Transfer Processes*, Hemisphere Publishing Corp., New York.
- Faghri, A., Buchko, M., and Cao, Y., 1991a, "A Study of High Temperature Heat Pipes With Multiple Heat Sources and Sinks, Part I: Experimental Methodology and Frozen Startup Profiles," *ASME JOURNAL OF HEAT TRANSFER*, Vol. 113, pp. 1003-1009.
- Faghri, A., Buchko, M., and Cao, Y., 1991b, "A Study of High Temperature Heat Pipes With Multiple Heat Sources and Sinks, Part II: Analysis of Continuum Transient and Steady State Experimental Data With Numerical Predictions," *ASME JOURNAL OF HEAT TRANSFER*, Vol. 113, pp. 1010-1016.
- Hall, M. L., and Doster, J.M., 1990, "A Sensitivity Study of the Effects of

Evaporation/Condensation Accommodation Coefficients on Transient Heat Pipe Modeling," *Int. J. Heat Mass Transfer*, Vol. 33, pp. 465-481.

Hirschfelder, J. O., Curtiss, C. F., and Bird, R. B., 1966, *Molecular Theory of Gases and Liquids*, Wiley, New York.

Ivanovskii, M. N., Sorokin, V. P., and Yagodka, I. V., 1982, *The Physical Principles of Heat Pipes*, Clarendon Press, Oxford, United Kingdom.

Jang, J. H., Faghri, A., Chang, W. S., and Mahefkey, E. T., 1990, "Mathematical Modeling and Analysis of Heat Pipe Start-Up From the Frozen State," *ASME JOURNAL OF HEAT TRANSFER*, Vol. 112, pp. 586-594.

Merrigan, M. A., Keddy, E. S., and Sena, J. T., 1986, "Transient Performance Investigation of a Space Power System Heat Pipe," *Proc. AIAA/ASME 4th Joint Thermophysics and Heat Transfer Conf.*, Paper No. AIAA-86-1237, Boston, MA, June 2-4.

Patankar, S. V., 1980, *Numerical Heat Transfer and Fluid Flow*, McGraw-Hill, New York.

Patankar, S. V., 1988, "Elliptic Systems: Finite-Difference Method I," in:

Handbook of Numerical Heat Transfer, W. J. Minkowycz et al., eds., Wiley, New York.

Seo, J. T., and El-Genk, M. S., 1988, "A Transient Model for Liquid Metal Heat Pipes," *Proc. Fifth Symposium on Space Nuclear Power Systems*, Albuquerque, NM, Jan. 11-14.

Silver, R. S., and Simpson, H. C., 1961, "The Condensation of Super-Heated Steam," *Proceedings of a Conference held at the National Engineering Laboratory*, Glasgow, Scotland.

Sukhatme, S. P., and Rohsenow, W. M., 1966, "Heat Transfer During Film Condensation of a Liquid Metal Vapor," *ASME JOURNAL OF HEAT TRANSFER*, Vol. 88, pp. 19-28.

Tien, C. L., and Lienhard, J. H., 1979, *Statistical Thermodynamics*, Hemisphere Publishing Corp., New York.

Wayner, P. C., and Schonberg, J., 1990, "Heat Transfer and Fluid Flow in an Evaporating Extended Meniscus," *Proc. 9th Int. Heat Transfer Conf.*, Jerusalem, Israel, Vol. 4, pp. 229-234.

E R R A T A

To the paper "Direct Numerical Simulation of Passive Scalar Field in Turbulent Channel Flow," by N. Kasagi, Y. Tomita, and A. Kuroda, published in the ASME JOURNAL OF HEAT TRANSFER, Vol. 114, No. 3, August 1992, pp. 598-606.

Error:

$$\begin{aligned}
 0 = & - \frac{2}{\text{Pr}} \frac{\overline{\partial\theta'^+ \partial u_j'^+ + \partial\bar{\theta}^+}}{\partial x_i'^+ \partial x_i'^+ \partial x_j'^+} - \frac{2}{\text{Pr}} \frac{\overline{\partial\theta'^+ \partial\theta'^+ \partial\bar{u}_j^+}}{\partial x_i'^+ \partial x_j'^+ \partial x_i'^+} - \frac{2}{\text{Pr}} \frac{\overline{\partial\theta'^+ \partial u_j'^+ \partial\theta'^+}}{\partial x_i'^+ \partial x_i'^+ \partial x_j'^+} \\
 & \text{Mean gradient production} \qquad \text{Turbulent production} \\
 & - \frac{2}{\text{Pr}} \frac{\overline{u_j'^+ \frac{\partial\theta'^+}{\partial x_i'^+} \frac{\partial^2\bar{\theta}^+}{\partial x_j'^+ \partial x_i'^+}}}{\partial x_i'^+ \partial x_j'^+ \partial x_i'^+} - \frac{2}{\text{Pr}^2} \overline{\left(\frac{\partial^2\theta'^+}{\partial x_i'^+ \partial x_j'^+} \right)^2} \\
 & \text{Gradient production} \qquad \text{Dissipation} \\
 & - \frac{1}{\text{Pr}} \frac{\partial}{\partial x_j'^+} \overline{\left(\frac{\partial\theta'^+}{\partial x_i'^+} \frac{\partial\theta'^+}{\partial x_i'^+} u_j'^+ \right)} + \frac{1}{\text{Pr}^2} \frac{\partial^2}{\partial x_j'^+{}^2} \overline{\left(\frac{\partial\theta'^+}{\partial x_i'^+} \frac{\partial\theta'^+}{\partial x_i'^+} \right)}. \qquad (9) \\
 & \text{Turbulent diffusion} \qquad \text{Molecular diffusion}
 \end{aligned}$$

Correction:

$$\begin{aligned}
 0 = & - \frac{2}{\text{Pr}} \frac{\overline{\partial\theta'^+ \partial u_j'^+ \partial\bar{\theta}^+}}{\partial x_i'^+ \partial x_i'^+ \partial x_j'^+} - \frac{2}{\text{Pr}} \frac{\overline{\partial\theta'^+ \partial\theta'^+ \partial\bar{u}_j^+}}{\partial x_i'^+ \partial x_j'^+ \partial x_i'^+} - \frac{2}{\text{Pr}} \frac{\overline{\partial\theta'^+ \partial u_j'^+ \partial\theta'^+}}{\partial x_i'^+ \partial x_i'^+ \partial x_j'^+} \\
 & \text{Mean gradient production} \qquad \text{Turbulent production} \\
 & - \frac{2}{\text{Pr}} \frac{\overline{u_j'^+ \frac{\partial\theta'^+}{\partial x_i'^+} \frac{\partial^2\bar{\theta}^+}{\partial x_j'^+ \partial x_i'^+}}}{\partial x_i'^+ \partial x_j'^+ \partial x_i'^+} - \frac{2}{\text{Pr}^2} \overline{\left(\frac{\partial^2\theta'^+}{\partial x_i'^+ \partial x_j'^+} \right)^2} \\
 & \text{Gradient production} \qquad \text{Dissipation} \\
 & - \frac{1}{\text{Pr}} \frac{\partial}{\partial x_j'^+} \overline{\left(\frac{\partial\theta'^+}{\partial x_i'^+} \frac{\partial\theta'^+}{\partial x_i'^+} u_j'^+ \right)} + \frac{1}{\text{Pr}^2} \frac{\partial^2}{\partial x_j'^+{}^2} \overline{\left(\frac{\partial\theta'^+}{\partial x_i'^+} \frac{\partial\theta'^+}{\partial x_i'^+} \right)}. \qquad (9) \\
 & \text{Turbulent diffusion} \qquad \text{Molecular diffusion}
 \end{aligned}$$

A Numerical Analysis of High-Temperature Heat Pipe Startup From the Frozen State

Y. Cao

A. Faghri

Department of Mechanical and
Materials Engineering,
Wright State University,
Dayton, OH 45435

Continuum and rarefied vapor flows co-exist along the heat pipe length for most of the startup period. A two-region model is proposed in which the vapor flow in the continuum region is modeled by the compressible Navier-Stokes equations, and the vapor flow in the rarefied region is simulated by a self-diffusion model. The two vapor regions are linked with appropriate boundary conditions, and heat pipe wall, wick, and vapor flow are solved as a conjugate problem. The numerical solutions for the entire heat pipe startup process from the frozen state are compared with the corresponding experimental data with good agreement.

Introduction

The study of the entire heat pipe startup process from the frozen state has practical engineering importance. During the high-temperature startup process from the frozen state, large temperature gradients exist along the heat pipe length. These large temperature gradients generate significant thermal stresses in the heat pipe container wall, which may severely affect the life of the heat pipe. In order to analyze these thermal stresses, information about the temperature distribution along the heat pipe container is needed. Also, it is desirable to know the location of the hot zone front at a specific time during startup, and the time needed to start a heat pipe fully under specific boundary conditions. The objective of this paper is to develop a numerical model that can simulate the entire heat pipe startup process and provide information for the practical needs mentioned above.

Since the heat pipe is a complex system that involves many heat transfer modes, numerical analyses are often needed for the detailed study of heat pipe startup from the frozen state. These studies include Chang and Colwell (1985), Costello et al. (1987), Seo and El-Genk (1988), Bowman and Hitchcock (1988), Hall and Doster (1990), Jang et al. (1990), and Cao and Faghri (1990a). Most of these models assumed that the working fluid in the wick was completely thawed, and only involved the transient response of the heat pipe to a power load with the continuum flow assumption in the heat pipe vapor space, except those by Costello et al. (1987), Hall and Doster (1990), and Jang et al. (1990). A literature survey revealed that none of the previous numerical investigations covered the entire heat pipe startup process from the early free-molecular vapor condition to the final steady-state operation, and a systematic verification of the models using experimental data was not done.

Since most heat pipes have a long, slender configuration, and the heat pipe wall temperature drops sharply from the hot zone to the cold zone in the axial direction during startup, the heat pipe startup process is actually the movement of the hot temperature front from the evaporator region to the condenser cap. Therefore, most of the startup time is during the intermediate period. In addition, when the heat input at the evaporator is high enough, after the hot zone reaches the condenser end cap and the continuum vapor flow is established over the entire heat pipe length, the heat pipe working temperature will continue to rise until a steady-state condition is reached. During

startup, continuum and rarefied vapor flows co-exist in different portions of the heat pipe, so these two different flows should be considered simultaneously and be coupled to simulate the entire startup process. In this paper, a two-region model is proposed to link the continuum and rarefied vapor flows in the heat pipe. In the continuum flow region, the continuum momentum and energy equations are solved; in the rarefied flow region, the self-diffusion model proposed by Cao and Faghri (1993) is applied. Appropriate boundary conditions and modifications are used to couple these two regions and to model the entire heat pipe as a conjugate problem. In summary, the model presented in this paper predicts the dynamics of the heat pipe from the frozen state to steady-state operation.

Mathematical Formulation

Conservation Equations for the Continuum Vapor Flow Region. The early experimental study conducted by Wageman and Guevara (1960), which simulated an evaporator by injecting air through a porous pipe, showed that the experimental results closely matched the laminar flow theory by Yuan and Finkelstein (1956) even for axial Reynolds number up to 10^5 , where turbulence should have been well established. The recent detailed experimental study by Bowman and Hitchcock (1988) for a simulated heat pipe showed that the vapor flow was always laminar in the evaporator, while it could become turbulent in the condenser when the axial Reynolds number was relatively high. The experiments by Bowman and Hitchcock indicated that the axial Reynolds number at which the condenser flow would remain laminar was about 1.2×10^4 . During the high-temperature heat pipe startup process, the axial vapor velocity can be very high, and the flow can be supersonic. However, the axial Reynolds number is relatively small. The numerical study by Faghri et al. (1991b) showed that, even after continuum vapor flow was established along the entire heat pipe length, the axial Reynolds number was less than 500, which is far less than the transition Reynolds numbers mentioned above. The reason is that the vapor densities of liquid metal working fluids are very low compared with those of working fluids for low or medium temperature heat pipes. Therefore, the continuum vapor flow in the heat pipe can be assumed to be laminar along the entire heat pipe length.

The conservation equations for transient, compressible, laminar vapor flow with constant viscosity are given as follows (Ganic et al., 1985):

Continuity equation:

$$\frac{\partial \rho}{\partial t} + \frac{1}{r} \frac{\partial}{\partial r} (\rho r v) + \frac{\partial}{\partial z} (\rho w) = 0 \quad (1)$$

Contributed by the Heat Transfer Division and presented at the ASME National Heat Transfer Conference, San Diego, California, August 9-12, 1992. Manuscript received by the Heat Transfer Division January 1992; revision received May 1992. Keywords: Heat Pipes and Thermosyphons, Transient and Unsteady Heat Transfer. Associate Technical Editor: T. W. Simon.

Radial momentum equation:

$$\frac{\partial}{\partial t}(\rho v) + \frac{1}{r} \frac{\partial}{\partial r}(\rho r v^2) + \frac{\partial}{\partial z}(\rho v w) = -\frac{\partial p}{\partial r} + \frac{4}{3} \mu \frac{1}{r} \frac{\partial}{\partial r} \left(r \frac{\partial v}{\partial r} \right) + \mu \frac{\partial^2 v}{\partial z^2} + \mu \left(\frac{1}{3} \frac{\partial^2 w}{\partial z \partial r} - \frac{4}{3} \frac{v}{r^2} \right) \quad (2)$$

Axial momentum equation:

$$\frac{\partial}{\partial t}(\rho w) + \frac{1}{r} \frac{\partial}{\partial r}(\rho r v w) + \frac{\partial}{\partial z}(\rho w^2) = -\frac{\partial p}{\partial z} + \frac{\mu}{r} \frac{\partial}{\partial r} \left(r \frac{\partial w}{\partial r} \right) + \frac{4}{3} \mu \frac{\partial^2 w}{\partial z^2} + \frac{1}{3} \mu \left(\frac{1}{r} \frac{\partial v}{\partial z} + \frac{\partial^2 v}{\partial z \partial r} \right) \quad (3)$$

Energy equation:

$$\rho c_p \left(\frac{\partial T}{\partial t} + v \frac{\partial T}{\partial r} + w \frac{\partial T}{\partial z} \right) = k \left[\frac{1}{r} \frac{\partial}{\partial r} \left(r \frac{\partial T}{\partial r} \right) + \frac{\partial^2 T}{\partial z^2} \right] + \frac{Dp}{Dt} + \mu \Phi \quad (4)$$

where

$$\Phi = 2 \left[\left(\frac{\partial v}{\partial r} \right)^2 + \left(\frac{v}{r} \right)^2 + \left(\frac{\partial w}{\partial z} \right)^2 \right] + \left(\frac{\partial v}{\partial z} + \frac{\partial w}{\partial r} \right)^2 - \frac{2}{3} \left[\frac{1}{r} \frac{\partial}{\partial r} (r v) + \frac{\partial w}{\partial z} \right]^2$$

The equation of state for both rarefied and continuum vapor flows is given by

$$p = \rho RT \quad (5)$$

Conservation Equations for the Rarefied Vapor Flow Region.

In the early stage of the heat pipe startup from the frozen state, the vapor pressure and density are very small in the heat pipe core. Because of the low density, the vapor in the rarefied state is somewhat different from that in the continuum state. Also, the vapor density gradient is very large along the axial direction of the heat pipe. The vapor flow in the axial direction is mainly caused by the density gradient via vapor molecular diffusion. Upon neglecting the presence of noncondensable gases, the rarefied vapor flow can be simulated by a self-diffusion model (Cao and Faghri, 1993). The term self-diffusion here means the interdiffusion of particles of the same mass due to a gradient in density (Hirschfelder et al., 1966). The mass and energy conservation equations were derived for a differential cylindrical control volume in conjunction with the definition of mass flux (Hirschfelder et al., 1966).

Mass self-diffusion:

$$\frac{\partial \rho}{\partial t} - \frac{\partial}{\partial z} \left(D_v \frac{\partial \rho}{\partial z} \right) - \frac{1}{r} \frac{\partial}{\partial r} \left(r D_v \frac{\partial \rho}{\partial r} \right) = 0 \quad (6)$$

Nomenclature

C = coefficient in Eq. (11), J/(kg-K)	Q = heat input at active evaporators, W	κ = Boltzmann constant, J/K
c = specific heat, J/(kg-K)	Q_o = heat output at condenser, W	λ = vapor mean free path, m
c_{me} = average effective specific heat of the wick over the liquid wick and the solid wick, J/(kg-K)	q = heat flux, W/m ²	μ = dynamic viscosity of the vapor, kg/(m-s)
c_p = specific heat at constant pressure, J/(kg-K)	R = gas constant, J/(kg-K)	ρ = density, kg/m ³
c_v = specific heat at constant volume, J/(kg-K)	R_o = outer pipe wall radius, m	$\rho_{i,c}$ = interfacial density on the continuum vapor flow side, kg/m ³
D = vapor core diameter, m	R_u = universal gas constant, kJ/(kmol-K)	σ = collision diameter, Å, or Stefan-Boltzmann constant, W/(m ² -K ⁴)
D_v = self-diffusion coefficient, m ² /s	R_v = vapor space radius, m	φ = heat pipe wick porosity
G = vapor mass flux, kg/(m ² -s)	R_w = wick-wall interface radius, m	Ω_D = collision integral for mass diffusion
H = latent heat due to melting or freezing, J/kg	r = radial coordinate, m	
h = convective heat transfer coefficient, W/(m ² -K)	S = coefficient in Eq. (11), J/kg	
h_{fg} = latent heat of vaporization, J/kg	T = temperature, K	
k = thermal conductivity, W/(m-K)	T_a = ambient temperature, or the initial temperature of the frozen heat pipe, K	
Kn = Knudsen number	$T_{i,c}$ = interfacial temperature on the continuum vapor flow side, K	
L = total length of the heat pipe, m	$T_{i,r}$ = interfacial temperature on the rarefied vapor flow side, K	
L_a = length of the adiabatic section, m	T_m = melting temperature, K	
L_c = length of the condenser section, m	T_{tr} = transition temperature, K	
L_e = length of the evaporator section, m	t = time, s	
MW = molecular weight, kg/kmol	v = radial velocity, m/s	
\dot{m}_i = mass flux at the liquid-vapor interface, kg/(m ² -s)	w = axial velocity, m/s	
M = Mach number = $w/\sqrt{\gamma p/\rho_v}$	$w_{i,r}$ = interfacial axial velocity on the rarefied vapor flow side, m/s	
p = pressure, N/m ²	z = axial coordinate, m	
	α = condensation or evaporation coefficient	
	γ = ratio of specific heats	
	$2\delta T$ = phase-change temperature range, K	
	ϵ = maximum energy of attraction between a pair of molecules, or radiation emissivity	
		Subscripts
		a = adiabatic or ambient
		c = condenser
		e = evaporator
		eff = effective
		i = interface
		l = liquid or working fluid in the liquid state in the wick
		le = wick region where the working fluid is in the liquid state
		m = mushy phase
		me = wick region where the working fluid is in the mushy state
		rf = reference
		s = saturation, or working fluid in the solid state in the wick
		se = wick region where the working fluid is in the solid state
		tr = transition from rarefied to continuum
		v = vapor
		w = wall or wick
		ws = wick structure material

Energy equation:

$$\frac{\partial}{\partial t} (\rho c_v T) + \frac{1}{r} \frac{\partial}{\partial r} (G_r c_p r T) + \frac{\partial}{\partial z} (G_z c_p T) = \frac{1}{r} \frac{\partial}{\partial r} \left(r k_v \frac{\partial T}{\partial r} \right) + \frac{\partial}{\partial z} \left(k_v \frac{\partial T}{\partial z} \right) \quad (7)$$

where the mass fluxes G_r and G_z are

$$G_r = \rho v = -D_v \frac{\partial \rho}{\partial r}, \quad G_z = \rho w = -D_v \frac{\partial \rho}{\partial z} \quad (8)$$

D_v is the coefficient of self-diffusion, which is given by the relation based on the Chapman-Enskog kinetic theory (Hirschfelder et al., 1966; Cao and Faghri, 1991).

$$D_v = 2.628 \times 10^{-7} \frac{\sqrt{T^3/MW}}{\rho \sigma^2 \Omega_D (\kappa T/\epsilon)} \quad (9)$$

p is the pressure in atmospheres, σ is the collision diameter in Å, ϵ is the maximum energy of attraction between a pair of molecules, κ is the Boltzmann constant, and Ω_D is the collision integral for mass diffusion. The heat dissipation has been neglected due to the low vapor temperature and small vapor viscosity during the heat pipe startup from the frozen state.

Conservation Equation for the Heat Pipe Wall. The heat transfer through the heat pipe wall is by conduction. The corresponding conservation equation is

$$\rho_w c_w \frac{\partial T}{\partial t} = k_w \left[\frac{1}{r} \frac{\partial}{\partial r} \left(r \frac{\partial T}{\partial r} \right) + \frac{\partial^2 T}{\partial z^2} \right] \quad (10)$$

The above equation is applicable to the entire heat pipe startup process.

Conservation Equation for the Porous Wick Structure. For the porous wick structure, the change of phase of the frozen working fluid must be considered. The wick structure is assumed to be isotropic and homogeneous. The phase change model (Cao and Faghri, 1990b) employed in this study is a fixed-grid formulation, which has the advantage of eliminating time step and grid size limitations. The conservation equation below is also applicable for the entire heat pipe startup process:

$$\frac{\partial}{\partial t} (\rho_{\text{eff}} C T) = \frac{\partial}{\partial z} \left(k_{\text{eff}} \frac{\partial T}{\partial z} \right) + \frac{1}{r} \frac{\partial}{\partial r} \left(k_{\text{eff}} r \frac{\partial T}{\partial r} \right) - \frac{\partial}{\partial t} (\rho_{\text{eff}} S) \quad (11)$$

The coefficients $C = C(T)$, $S = S(T)$, and $k_{\text{eff}} = k_{\text{eff}}(T)$ in Eq. (11) are given by Eqs. (12)–(14), respectively.

$$C(T) = \begin{cases} c_{se} & (T < T_m - \delta T) & \text{(solid phase)} \\ c_{me} + \frac{H}{2\delta T} & (T_m - \delta T \leq T \leq \delta T + T_m) & \text{(mushy phase)} \\ c_{le} & (T > T_m + \delta T) & \text{(liquid phase)} \end{cases} \quad (12)$$

$$S(T) = \begin{cases} c_{se} (\delta T - T_m) & (T < T_m - \delta T) & \text{(solid phase)} \\ c_{me} \delta T + \frac{H}{2} - \left(c_{me} + \frac{H}{2\delta T} \right) T_m & (T_m - \delta T \leq T \leq \delta T + T_m) & \text{(mushy phase)} \\ c_{se} \delta T + H - c_{le} T_m & (T > T_m + \delta T) & \text{(liquid phase)} \end{cases} \quad (13)$$

$$k_{\text{eff}} = \begin{cases} k_{se} & (T < T_m - \delta T) & \text{(solid phase)} \\ k_{se} + (k_{le} - k_{se}) (T - T_m + \delta T) / 2\delta T & (T_m - \delta T \leq T \leq \delta T + T_m) & \text{(mushy phase)} \\ k_{le} & (T > T_m + \delta T) & \text{(liquid phase)} \end{cases} \quad (14)$$

where

$$\begin{aligned} \rho_{\text{eff}} &= \varphi \rho_l + (1 - \varphi) \rho_{ws} \\ c_{se} &= \varphi c_s + (1 - \varphi) c_{ws} \\ c_{le} &= \varphi c_l + (1 - \varphi) c_{ws} \\ c_{me} &= 0.5(c_{se} + c_{le}) \end{aligned}$$

The values of k_{se} and k_{le} depend on the particular heat pipe wick structure, and can be calculated using the equation given by Chi (1976).

Boundary Conditions. At both ends of the heat pipe, $z = 0$ and L :

$$\frac{\partial \rho}{\partial z} = 0, \quad \frac{\partial T}{\partial z} = 0, \quad v = w = 0 \quad (15)$$

At the centerline, $r = 0$, the symmetry condition implies:

$$\frac{\partial T}{\partial r} = 0, \quad \frac{\partial \rho}{\partial r} = 0, \quad \frac{\partial w}{\partial r} = 0, \quad v = 0 \quad (16)$$

For the outer pipe wall surface:

Evaporator:

$$k_w \frac{\partial T}{\partial r} \Big|_{r=R_0} = q_e \quad (17)$$

Adiabatic:

$$\frac{\partial T}{\partial r} \Big|_{r=R_0} = 0 \quad (18)$$

Condenser:

$$-k_w \frac{\partial T}{\partial r} \Big|_{r=R_0} = \begin{cases} h(T_w - T_a) & \text{(convection)} & (19a) \\ \sigma \epsilon (T_w^4 - T_a^4) & \text{(radiation)} & (19b) \end{cases}$$

where h is the convective heat transfer coefficient, T_w and T_a are the outer wall surface temperature and the environmental temperature, ϵ is the emissivity, and σ is the Stefan-Boltzmann constant.

At the wick-vapor interface, $r = R_v$, evaporation or condensation takes place after the melting interface in the wick reaches the wick-vapor interface. The relation for the interface mass flux applied here is that due to Silver and Simpson (1961):

$$\dot{m}_i = -\rho_i v_i =$$

$$\left(\frac{2\alpha}{2-\alpha} \right) \sqrt{\frac{MW}{2\pi R_u}} \left(\frac{p_l^*}{\sqrt{T_l}} - \frac{p_v}{\sqrt{T_v}} \right) \begin{cases} > 0 & \text{evaporation} & (20a) \\ < 0 & \text{condensation} & (20b) \end{cases}$$

where α is the condensation/evaporation coefficient. p_l^* is the equilibrium saturation pressure corresponding to the liquid

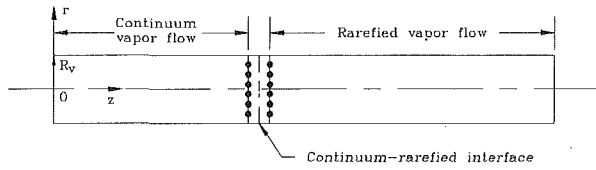


Fig. 1 Schematic of continuum and rarefied vapor regions as well as the interfacial grids

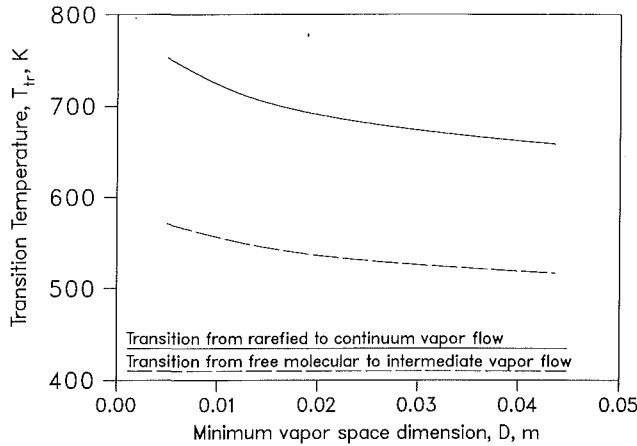


Fig. 2 Transition temperatures for sodium as heat pipe working fluid

temperature T_l , and can be calculated using the Clausius-Clapeyron equation:

$$p_l^* = p_{rf} \exp \left[-\frac{h_{fg}}{R} \left(\frac{1}{T_l} - \frac{1}{T_{rf}} \right) \right] \quad (21)$$

where p_{rf} and T_{rf} are the reference pressure and temperature. Sukhatme and Rohsenow (1966) showed that α may change from 0.1 to 1 according to the surface condition, with $\alpha = 1$ being the upper limit. Cao and Faghri (1993) showed that the numerical results were insensitive to the evaporation/condensation coefficient since the pressure difference and α in Eq. (20) offset each other when the vapor flow and heat pipe wick were solved as a conjugate problem.

As was mentioned before, a two-region model for the vapor flow in the heat pipe was employed. These two regions, namely, the continuum vapor and rarefied vapor regions, are coupled at the continuum-rarefied interface, which is assumed to be planar. The two regions as well as the interfacial grids are schematically shown in Fig. 1. It is essential to maintain the mass balance across the interface at each time step. The boundary condition at the continuum-rarefied interface is

$$w = w_{i,r}, \quad \frac{\partial v}{\partial z} = 0, \quad T = T_{i,r} \quad (\text{for the continuum vapor flow}) \quad (22a)$$

$$\rho = \rho_{i,c}, \quad T = T_{i,c} \quad (\text{for the rarefied vapor flow}) \quad (22b)$$

where $w_{i,r}$ and $T_{i,r}$ are the interfacial axial velocity and temperature on the rarefied vapor flow side, and are obtained from the rarefied vapor flow solution. $\rho_{i,c}$ and $T_{i,c}$ are the interfacial vapor density and temperature on the continuum vapor flow side, and are obtained from the continuum vapor flow solution.

Numerical Procedure

The conservation equations and boundary conditions for the heat pipe wall, wick, and vapor, including the continuum and rarefied vapor regions, are described by Eqs. (1)–(22). Since a two-region model for the vapor flow is employed in

this study, the interfacial temperature between the continuum and rarefied vapor flows should be close to the corresponding transition temperature from the rarefied to the continuum vapor flow. Continuum flow is considered to be established when the mean free path of the vapor, λ , is substantially less than the minimum dimension, D , of the vapor flow passage. This criterion is usually expressed by the Knudsen number:

$$Kn = \frac{\lambda}{D} \leq 0.01 \quad (23)$$

The mean free path given by Tien and Lienhard (1979) is

$$\lambda = \frac{1.051 \kappa T}{\sqrt{2} \pi \sigma^2 p} = \frac{1.051 \kappa}{\sqrt{2} \pi \sigma^2 R \rho_v} \quad (24)$$

By assuming that the vapor is in the saturated state, the transition vapor temperature T_{tr} can be easily obtained by using Eqs. (23) and (24), combined with the equation of state, Eq. (5) and the Clausius-Clapeyron equation, Eq. (21):

$$\ln(T_{tr} \rho_v R / p_{rf}) + \frac{h_{fg}}{R} \left(\frac{1}{T_{tr}} - \frac{1}{T_{rf}} \right) = 0 \quad (25)$$

where

$$\rho_v = \frac{1.051 \kappa}{\sqrt{2} \pi \sigma^2 R D Kn} \quad (26)$$

p_{rf} and T_{rf} are the reference (saturation) pressure and temperature. Equation (25) can easily be solved for T_{tr} iteratively using the Newton-Raphson/Secant method (Pletcher et al., 1988).

The transition vapor temperature from rarefied to continuum vapor flow thus obtained is given in Fig. 2 as a function of the minimum vapor space dimension with $Kn = 0.01$. For a circular heat pipe, the minimum dimension should be interpreted to be the vapor space diameter of the heat pipe, D , which appears in Eq. (26). Rarefied vapor flow ($Kn > 0.01$) is also conventionally subdivided into free molecular vapor flow ($Kn \geq 1$), and intermediate vapor flow ($0.01 < Kn < 1$) (Ivanovskii et al., 1982). The corresponding transition vapor temperature from free molecular to intermediate vapor flow is also given in Fig. 2 with $Kn = 1$.

As mentioned before, the heat pipe startup process is actually a process in which the hot zone (continuum vapor region) moves from the evaporator region to the condenser end cap. The location of the continuum-rarefied interface moves with time during the startup process. In order to handle the moving interface numerically, the interface was considered to be temporarily stationary during the iterations within a time step. By the end of the time step, the rarefied vapor temperature at the centerline grid next to the interface was compared with the transition temperature. If the temperature was greater than the transition temperature, the continuum vapor flow region was expanded to the location of the grid, and the vapor at this location was considered to be in the continuum state in the next time step computation. These two regions were solved separately and coupled via the interfacial parameters in both regions. During the iterations, the values of the interfacial parameters such as vapor temperature and velocity from the last iteration at the grids next to the interface in the rarefied region were treated as temporary boundary values when solving the continuum vapor flow region, which has been explicitly described by Eq. (22a). In the same way, the interfacial parameters such as vapor density and temperature in the continuum vapor region were treated as boundary parameters when solving the rarefied vapor region (Eq. (22b)). The overall numerical procedure for the heat pipe startup from the frozen state is as follows:

1 Initiate the numerical computation by applying the vapor self-diffusion model for the early startup period described by Cao and Faghri (1993).

2 Compare the vapor temperature at the evaporator exit with the rarefied-continuum transition temperature. If the vapor temperature is greater than the transition temperature, the continuum vapor flow model described by Eqs. (1)–(5) is applied in the evaporator region.

3 Compute the wick-vapor interfacial vapor velocity using Eq. (20), and the vapor velocity at the continuum-rarefied interface using the interfacial values of the rarefied vapor flow model from the last iteration.

4 Compute the vapor velocities and pressure in the continuum vapor region by applying the SIMPLE algorithm (Patankar, 1980, 1988) and the numerical treatment to the compressible continuum vapor flow described by Cao and Faghri (1990a).

5 Compute the vapor density and mass flux in the rarefied vapor region by applying the self-diffusion vapor flow model (Eqs. (6)–(9)), and treat the interfacial vapor density and temperature in the continuum region as the boundary values.

6 Solve for the vapor temperatures in the rarefied and continuum vapor regions.

7 Solve for the change of phase in the wick and the temperature distributions in the wick and wall along the entire heat pipe length.

8 If the solution is not converged, update the numerical values in the previous iteration as well as the diffusion coefficient and the phase-change properties in the wick. Repeat steps 3–7 until converged solutions are obtained within this time step.

9 Readjust the location of the rarefied-continuum vapor interface and return to step 3, starting computation for the next time step.

The coefficient of self-diffusion D_v was based on the Chapman-Enskog theory (Hirschfelder et al., 1966). The coefficient drops sharply with higher vapor density or pressure. During the transition from rarefied to continuum vapor flow in the evaporator region where the vapor density gradients were relatively small, it was found that the coefficient was too small, and sometimes presented a difficulty for a smooth transition. Since the coefficient of self-diffusion D_v was derived based on the dilute gas assumption and the Lennard-Jones empirical potential, it is a semi-empirical parameter in nature, and may not be adequate to describe the mass self-diffusion when the vapor density is relatively high during the transition period. Therefore, the coefficient of self-diffusion D_v was modified by a multiplicative factor

$$10^{(T/T_{tr})^5 - 1} \quad (\text{for } T > T_{tr})$$

where T_{tr} is the transition temperature from the free molecular flow to the intermediate flow, and can be found from Fig. 2. The multiplicative factor above has the feature that when T approaches T_{tr} , the factor reduces to unity, and when T is large and the vapor density is high, the factor is sufficiently large for the augmentation of the coefficient of self-diffusion. The modification factor was only used during the transition period in the evaporator region. Since the transition period is very short compared to the startup time, the modification factor has little effect on the overall numerical solution, and only helps to increase the coefficient of self-diffusion in the evaporator region when the vapor temperature is relatively high and the vapor density gradients are relatively small.

Numerical Results and Discussion

The numerical simulation for the entire heat pipe startup process was first performed for the heat pipe studied by Faghri et al. (1991a) and Buchko (1990), which was a multiple evaporator sodium heat pipe with a vapor core radius $R_v = 10.75$ mm, a wrapped screen wick of thickness $\delta_w = 0.456$ mm, and stainless steel wall of thickness $\delta_w = 2.15$ mm. The length of each individual evaporator is denoted by L_e . The heat pipe was

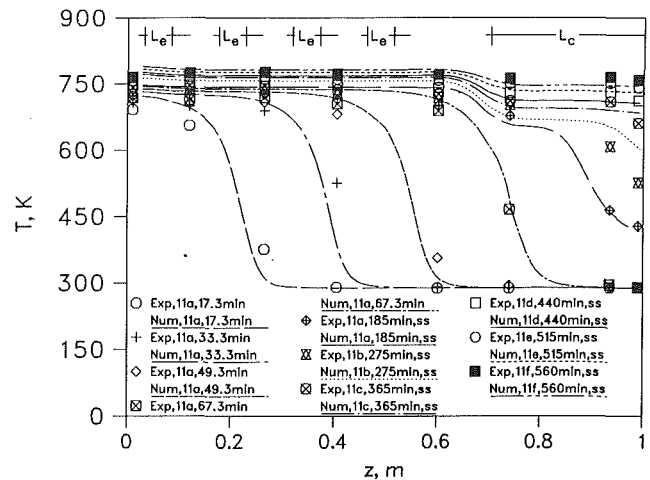


Fig. 3 The outer wall temperature compared with the experimental data for cases 11a–f, (Faghri et al., 1991)

tested in a vacuum chamber with a fluid charge of 30 g of sodium. The details of the heat pipe configuration and dimensions as well as the experimental setup are described by Buchko (1990). The heat inputs and outputs in different heat pipe regions for the different numerically simulated cases are given by Faghri et al. (1991a). Figure 3 compares the numerical and experimental outer wall temperatures at different times for experimental cases 11a–f with evaporator 1 active, which is closest to the evaporator end cap. The agreement between the numerical solutions and the experimental data is generally good. The time step and grid size used in the numerical calculation were $\Delta t = 20$ s and 14 (radial) \times 55 (axial). The numerical results were essentially independent of time step and grid sizes. A change of time step from $\Delta t = 10$ s to $\Delta t = 20$ s and a change of grid size from 14×55 to 28×110 resulted in a change in the numerical hot zone wall temperatures of about 1.5 and 3 percent, respectively. An estimated heat capacity of 3.75×10^6 J/(m³·K) has been added in the evaporator and adiabatic sections to account for the additional heat capacities due to the electrical resistance heaters and radiation shields. The total heat inputs in different cases were maintained at different levels in the active evaporator and incremented from 311 W (case 11a) to 598 W (case 11f). The corresponding power outputs at the condenser were 119 W (case 11a) and 298 W (case 11f). The hot zone moved from the active evaporator down to the condenser end cap with time. At $t = 185$ min, which corresponds to the steady state for case 11a, the hot zone had reached the condenser region, but the heat pipe wall temperature near the condenser end cap was still very low due to the insufficient heat input at the evaporator. For $t > 185$ min, the heat input to the heat pipe was increased to a higher level corresponding to case 11b, and the heat pipe wall temperature increased to a higher level. At the heat input level corresponding to case 11c, the hot zone filled the heat pipe completely, and the continuum vapor flow was established along the entire heat pipe length. Strictly speaking, cases 11a–c covered the heat pipe startup process. The heat pipe performance after case 11c is the transient heat pipe operation as described in the literature. The mass and energy balances over the vapor-wick interface and over the outer wall of the heat pipe were checked during the startup process. At the steady state, the total heat output at the condenser should be equal to the total heat input at the evaporator. This was the case in the present numerical solution at the steady states shown in the figure. The difference between the total heat input and output was within 1.5 percent in all cases. Figures 4 and 5 present the numerical outer wall temperature compared with the corresponding experimental data for cases 19a–d of Buchko (1990) and case 12 of Faghri et al. (1991a), respectively. The

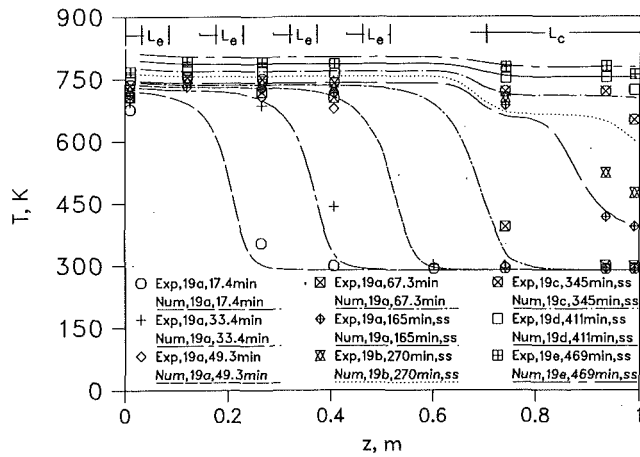


Fig. 4 The outer wall temperature compared with the experimental data for cases 19a-e, (Buchko, 1990)

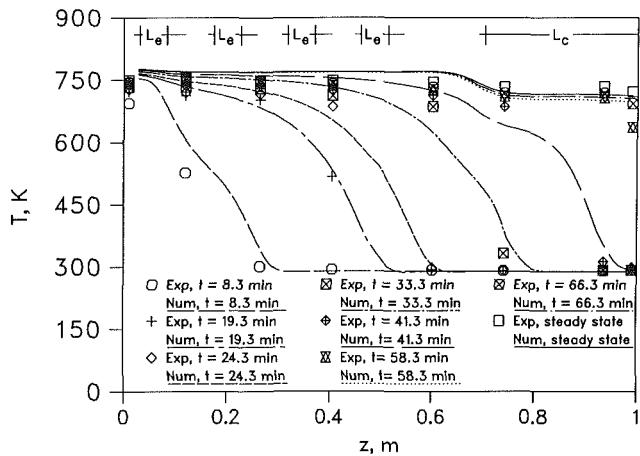


Fig. 5 The outer wall temperature compared with the experimental data for case 12 (Faghri et al., 1991)

agreement between the numerical solutions and experimental data is generally good.

The double-wall artery sodium heat pipe (Ponnappan, 1989) was then numerically simulated. The heat pipe studied by Ponnappan (1989) was a 2 m double-wall artery gas-loaded heat pipe with a vapor core radius $R_v = 6.35$ mm, an outer wall radius $R_o = 11.1$ mm, and a stainless steel wall of thickness $\delta_w = 1.65$ mm. The lengths of the evaporator, adiabatic, and condenser sections were 0.381 m, 0.737 m, and 0.914 m, respectively. The heat pipe was tested in a vacuum chamber with a fluid charge of 67.52 g in the screen and grooves. The details of the heat pipe dimensions, the cross-sectional view of the wick geometry, and the experimental setup are given by Ponnappan (1989). Although the primary objective of the experimental investigation by Ponnappan was to determine the performance of a gas-loaded sodium heat pipe, frozen startup tests in the vacuum mode were also conducted. Figures 6 and 7 present the numerical outer wall temperatures compared with the experimental data for heat rates of $Q_o = 289.6$ W and 354.4 W. The experimental data correspond to those in Figs. 46 and 49 of the technical report by Ponnappan (1989). The agreements between the numerical solutions and the experimental data are generally good, although the numerical values are consistently higher than the experimental data at the evaporator and adiabatic sections of the heat pipe. The heat was supplied via electrical resistance heaters at the evaporator, and radiation shields were used to prevent heat loss from the evaporator and adiabatic sections. Both the electrical resistance heaters and the radiation shields provided additional heat capacities during the heat pipe startup process. However, these

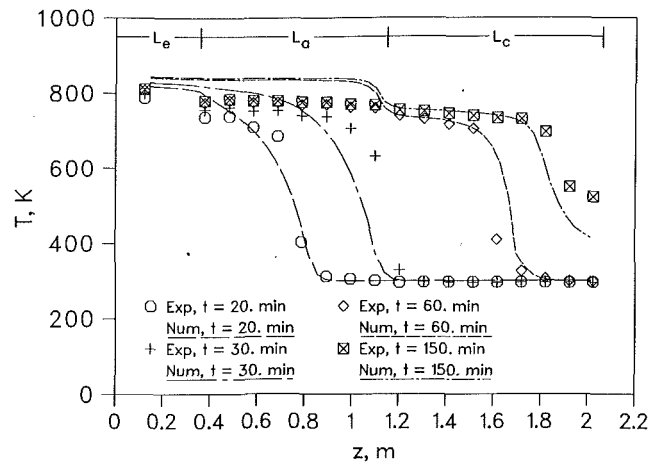


Fig. 6 The numerical outer wall temperature compared with the experimental data given by Ponnappan (1989) for $Q_o = 289.6$ W

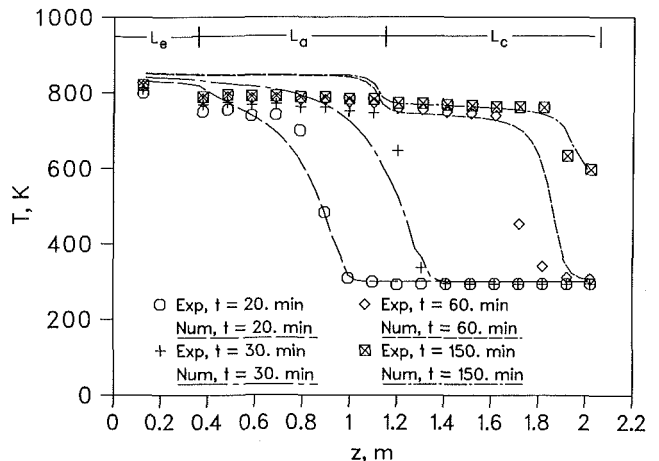


Fig. 7 The numerical outer wall temperature compared with the experimental data given by Ponnappan (1989) for $Q_o = 354.4$ W

additional heat capacities have not been accounted for in the numerical simulation due to the lack of detailed information. Thus, wall temperatures higher than the corresponding experimental data were predicted in the evaporator and adiabatic sections. Also, the radiation shutter in the condenser region was closed during the experiment, which also added an additional heat capacity over the condenser region. As a result, the numerical hot zone fronts moved faster than those of the experimental data.

The uncertainty involved in the experimental measurements by Faghri et al. (1991a) was about 5 percent, and the uncertainty was about 2-3 percent for the experimental data by Ponnappan (1989). The single most important uncertainty involved in the numerical simulations and comparisons with experimental data is the existence of additional heat capacities due to the electrical resistance heaters and radiation shields. These heat capacities are very difficult to estimate accurately because of the complex geometries and interfacial heat resistances between the heaters and the heat pipe wall. In addition, these heat capacities are dependent on the experimental setup, and change from experiment to experiment. A sensitivity analysis of these heat capacities revealed that the uncertainties involved in the maximum hot zone wall temperature and the startup time are about 5-7 percent. It should be pointed out that the use of the resistance heater and radiation shield, to a large extent, is to quantify the heat input at the evaporator or control heat pipe operation in the experiment. In real applications, the working environment may be much different from that in the laboratory. Additional heat capacities may not be

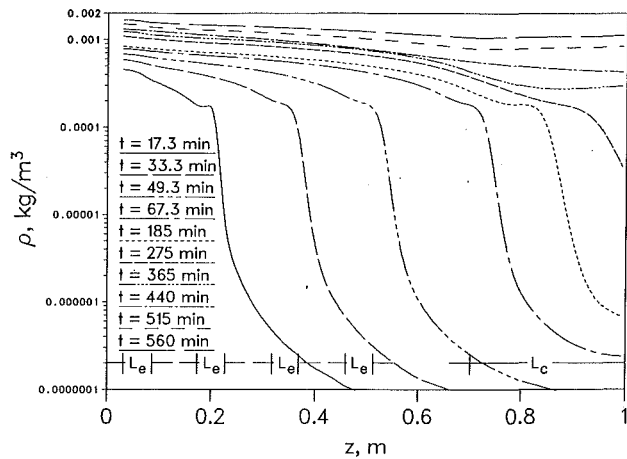


Fig. 8 The vapor density along the axial direction at different times for cases 11a-f (Faghri et al., 1991)

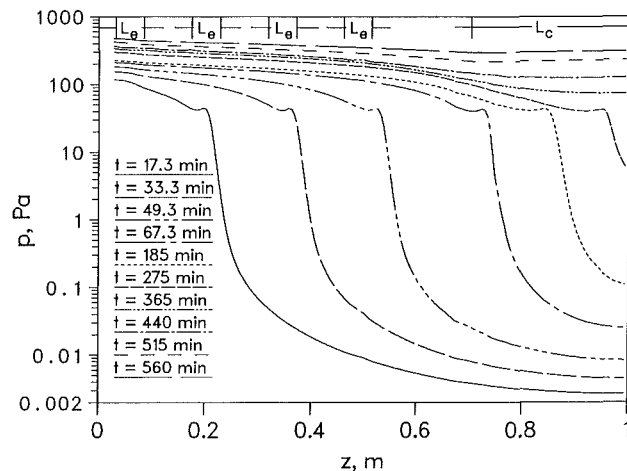


Fig. 9 The centerline vapor pressure along the axial direction at different times for cases 11a-f (Faghri et al., 1991)

involved, and therefore the related uncertainties may be relieved.

Figures 8 and 9 present the vapor density and pressure, respectively, along the heat pipe length at different times for cases 11a-f (Faghri et al., 1991a). During the startup process, both the vapor density and pressure in the continuum vapor region decreased along the heat pipe length with a slight recovery close to the continuum-rarefied interface, and then dropped sharply in the rarefied vapor flow region. After the hot zone reached the condenser end cap, both density and pressure became relatively uniform along the heat pipe length, indicating that the continuum vapor flow was established along the entire heat pipe length.

Figure 10 presents the centerline vapor temperatures at different times for cases 11a-f. Compared with the wall temperatures, the moving hot zone vapor temperature front is much steeper, and the vapor temperature is more uniform in the hot zone region. Figure 11 shows a comparison of the vapor and wall temperatures at different times for case 11a. For most of the previous investigations on heat pipe startup from the frozen state, the heat pipe wall temperatures were obtained from the experimental measurements and the vapor temperatures were considered to be of the same magnitude and trend as the wall temperature. This is not exactly true, however, especially in the slope region, as shown in Fig. 11. The vapor temperature front is always steeper and is located close to the middle of the slope region of the wall temperature distribution. In order for the hot zone of the wall temperature to move forward, heat must be supplied to the slope region to increase the tem-

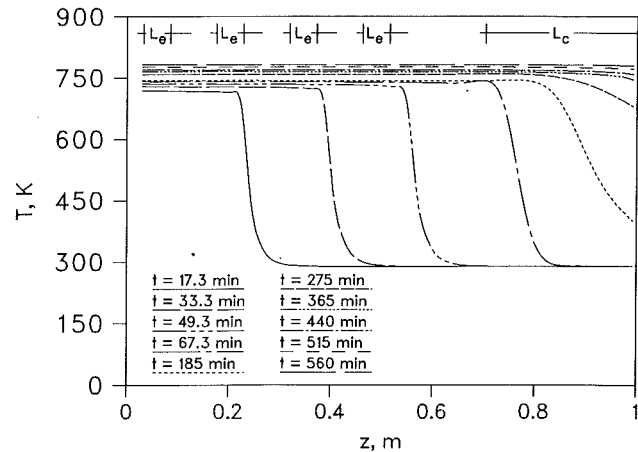


Fig. 10 The centerline vapor temperatures along the axial direction at different times for cases 11a-f (Faghri et al., 1991)

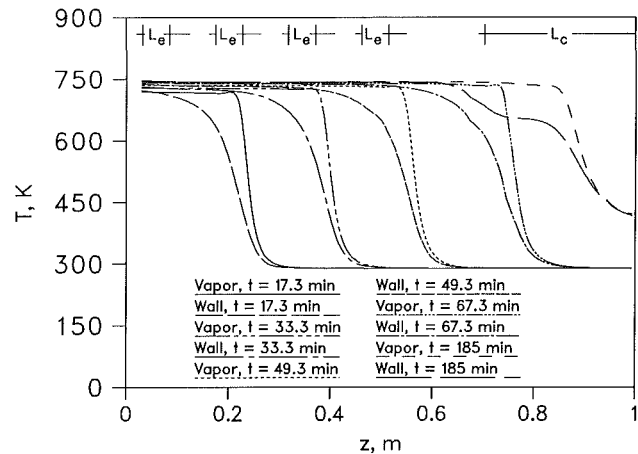


Fig. 11 Comparison of centerline vapor and wall temperatures at different times for case 11a (Faghri et al., 1991)

perature of heat pipe wall and wick there. This can be facilitated by intense condensation over the region. Therefore, a large temperature difference between the vapor and wall was required, as shown in Fig. 11. This can be further illustrated by examining the mass flux distributions at the vapor-wick interface. Figure 12 shows the radial interfacial mass flux of vapor, $\dot{m}_i = -\rho_i v_i$, along the axial direction at different times for cases 11a-f with evaporator 1 active, which is closest to the evaporator end cap. During the heat pipe startup periods, ($t \leq 275$ min), the maximum condensation mass flux always occurred in the continuum vapor flow region close to the continuum-rarefied interface.

Figure 13 shows the axial vapor Mach number along the heat pipe length at different times for cases 11a-f. During the startup period, the Mach number rose until approaching the region close to the continuum-rarefied interface. The Mach number dropped to a much lower value and then rose in the rarefied vapor region to a very large value before decreasing to zero at the condenser end cap. The trend of the vapor Mach number in the startup period can be explained by examining Figs. 8 and 12. At the active heater region, vapor was being accumulated due to evaporation at the vapor-wick interface, and the Mach number began to rise. After the vapor passed the exit of the active evaporator, the axial vapor mass flow rate in the heat pipe began to decrease due to the vapor condensation onto the vapor-wick interface. However, the vapor density also decreased significantly in this region. Since the vapor is compressible, $w = G_z / \rho_v$, the rate at which the density decreased exceeded the decrease of the axial mass flux G_z due to condensation. Therefore, the vapor velocity and the Mach

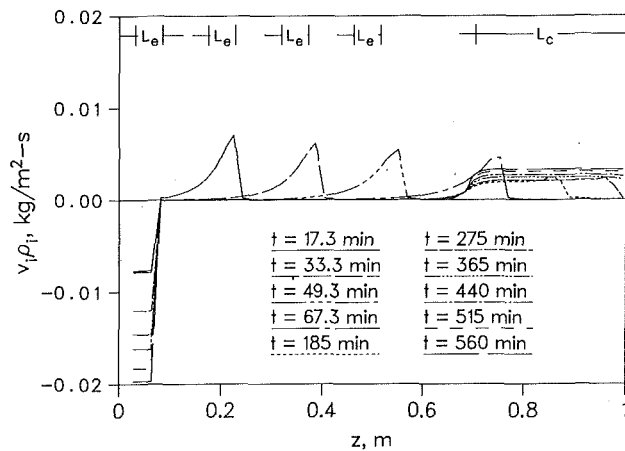


Fig. 12 The radial vapor interfacial mass flux along the axial direction at different times for cases 11a-f (Faghri et al., 1991)

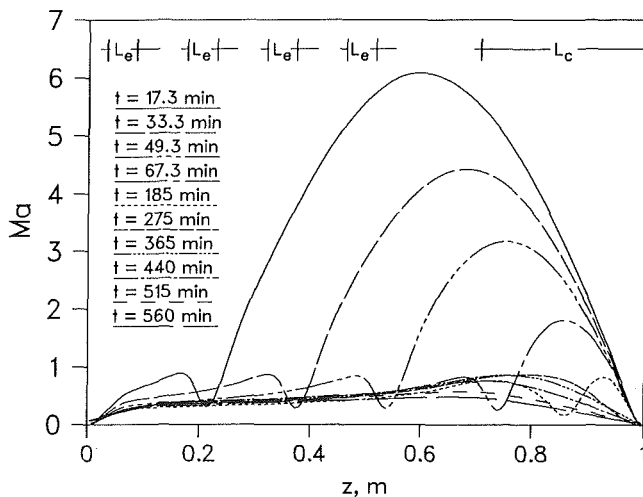


Fig. 13 Axial vapor Mach numbers along the heat pipe length at different times for cases 11a-f (Faghri et al., 1991)

number continued to rise. When the vapor approached the hot zone front of the heat pipe wall temperature, intense condensation occurred in that region, as shown in Fig. 12. The vapor Mach number dropped to a much lower value before entering the rarefied vapor region. As mentioned by Cao and Faghri (1993), the very large Mach number in the rarefied vapor flow is solely due to the extremely low vapor density in the heat pipe core. Although the vapor velocity is very high, the mass flux $G_z = w\rho_v$ in the axial direction is still very low.

Conclusions

A numerical method for the entire heat pipe startup process from the frozen state was presented in this paper. The continuum and rarefied vapor flows were linked with an appropriate interfacial treatment, and the conservation equations for the heat pipe wall, wick and vapor flow were solved as a conjugate problem. The numerical outer wall temperatures were compared with the corresponding experimental data in the literature with good agreement, indicating that the two-region model proposed in this paper is capable of simulating the entire heat pipe startup process. The numerical and experimental results showed that the high-temperature heat pipe startup process was characterized by a moving hot zone with relatively steep fronts. The numerical solution indicated that in the moving hot zone, the vapor temperature front was steeper than that for the wall temperature, and was located close to

the middle of the slope region of the wall temperature distribution.

Acknowledgments

Funding for this work was provided by a joint effort of the NASA Lewis Research Center and the Thermal Energy Group of the Aero Propulsion Laboratory of the U. S. Air Force under contract No. F33615-89-C-2820.

References

- Bowman, W. J., and Hitchcock, J., 1988, "Transient, Compressible Heat Pipe Vapor Dynamics," *Proc. 25th ASME National Heat Transfer Conf.*, Houston, TX, pp. 329-337.
- Buchko, M. T., 1990, "Experimental Investigation of Low and High Temperature Heat Pipes With Multiple Heat Sources and Sinks," Masters Thesis, Wright State University, Dayton, OH.
- Cao, Y., and Faghri, A., 1990a, "A Transient Two-Dimensional Compressible Analysis for High Temperature Heat Pipes With a Pulsed Heat Input," *Numerical Heat Transfer, Part A*, Vol. 18, pp. 483-502.
- Cao, Y., and Faghri, A., 1990b, "A Numerical Analysis of Phase-Change Problems Including Natural Convection," *ASME JOURNAL OF HEAT TRANSFER*, Vol. 112, pp. 812-816.
- Cao, Y., and Faghri, A., 1993, "Simulation of the Early Startup Period of High-Temperature Heat Pipes From the Frozen State by a Rarefied Vapor Self-Diffusion Model," *ASME JOURNAL OF HEAT TRANSFER*, Vol. 115, issue, pp. 239-246.
- Chang, W. S., and Colwell, G. T., 1985, "Mathematical Modeling of the Transient Operating Characteristics of a Low-Temperature Heat Pipe," *Numerical Heat Transfer*, Vol. 8, pp. 169-186.
- Chi, S. W., 1976, *Heat Pipe Theory and Practice*, Hemisphere, Washington, DC.
- Costello, F. A., et al., 1987, "Detailed Transient Model of a Liquid-Metal Heat Pipe," *Trans. 4th Symposium on Space Nuclear Power Systems*, CONF-870102-Summs, Albuquerque, NM., pp. 393-402.
- Faghri, A., Buchko, M., and Cao, Y., 1991a, "A Study of High Temperature Heat Pipes With Multiple Heat Sources and Sinks: Part I—Experimental Methodology and Frozen Startup Profiles," *ASME JOURNAL OF HEAT TRANSFER*, Vol. 113, No. 4, pp. 1003-1009.
- Faghri, A., Buchko, M., and Cao, Y., 1991b, "A Study of High Temperature Heat Pipes With Multiple Heat Sources and Sinks: Part II—Analysis of Continuum Transient and Steady State Experimental Data With Numerical Predictions," *ASME JOURNAL OF HEAT TRANSFER*, Vol. 113, pp. 1010-1016.
- Ganic, E. N., Hartnett, J. P., and Rohsenow, W. M., 1985, "Basic Concepts of Heat Transfer," in: *Handbook of Heat Transfer Fundamentals*, W. M. Rohsenow et al., eds., McGraw-Hill, New York.
- Hall, M. L., and Doster, J. M., 1990, "A Sensitivity Study of the Effects of Evaporation/Condensation Accommodation Coefficients on Transient Heat Pipe Modeling," *Int. J. Heat Mass Transfer*, Vol. 33, pp. 465-481.
- Hirschfelder, J. O., Curtiss, C. F., and Bird, R. B., 1966, *Molecular Theory of Gases and Liquids*, Wiley, New York.
- Ivanovskii, M. N., Sorokin, V. P., and Yagodka, I. V., 1982, *The Physical Principles of Heat Pipes*, Clarendon Press, Oxford, United Kingdom.
- Jang, J. H., Faghri, A., Chang, W. S., and Mahefkey, E. T., 1990, "Mathematical Modeling and Analysis of Heat Pipe Start-Up From the Frozen State," *ASME JOURNAL OF HEAT TRANSFER*, Vol. 112, pp. 586-594.
- Patankar, S. V., 1980, *Numerical Heat Transfer and Fluid Flow*, McGraw-Hill, New York.
- Patankar, S. V., 1988, "Elliptic Systems: Finite-Difference Method 1," in: *Handbook of Numerical Heat Transfer*, W. J. Minkowycz et al., eds., Wiley, New York.
- Pletcher, R. H., Minkowycz, W. J., Sparrow, E. M., and Schneider, G. E., 1988, "Overview of Basic Numerical Methods," in: *Handbook of Numerical Heat Transfer*, Wiley, New York.
- Ponnappan, R., 1989, "Studies on the Startup Transients and Performance of a Gas-Loaded Sodium Heat Pipe," Technical Report, WRDC-TR-89-2046, Universal Energy Systems, Inc., Dayton, OH.
- Seo, J. T., and El-Genk, M. S., 1988, "A Transient Model for Liquid Metal Heat Pipes," *Fifth Symposium on Space Nuclear Power Systems*, Albuquerque, NM, Jan. 11-14.
- Silver, R. S., and Simpson, H. C., 1961, "The Condensation of Super-Heated Steam," *Proceedings of a Conference held at the National Engineering Laboratory*, Glasgow, United Kingdom.
- Sukhatme, S. P., and Rohsenow, W. M., 1966, "Heat Transfer During Film Condensation of a Liquid Metal Vapor," *ASME JOURNAL OF HEAT TRANSFER*, pp. 19-28.
- Tien, C. L., and Lienhard, J. H., 1979, *Statistical Thermodynamics*, Hemisphere Publishing Corporation, New York.
- Wageman, W. E., and Guevara, F. A., 1960, "Fluid Flow Through a Porous Channel," *The Physics of Fluids*, Vol. 3, pp. 878-881.
- Yuan, S. W., and Finkelstein, A. B., 1956, "Laminar Pipe Flow With Injection and Suction Through a Porous Wall," *Transactions of the ASME*, Vol. 78, pp. 719-724.

Magnetized Fiber Orientation Control in Solidifying Composites: Numerical Simulation

G. S. Dulikravich

B. Kosovic

Department of Aerospace Engineering,
The Pennsylvania State University,
University Park, PA 16802

S. Lee

Agency for Defense Development,
Taejon, Republic of Korea

This work deals with the development of a numerical algorithm for the prediction of magnetic force lines inside a flowing solidifying melt with the ultimate purpose of simulating and controlling alignment of short nickel-coated fibers during the curing process in composites. A complete mathematical model and an accompanying computer program have been developed for the simulation of a steady laminar flow of an incompressible fluid with strong heat transfer (involving solidification) and a strong superimposed magnetic field. An extended form of the Boussinesq approximation allowing for temperature-dependent physical properties of the fluid and the solid including latent heat of phase change was incorporated. This formulation simultaneously predicts detailed velocity, pressure, and temperature fields in the moving fluid while capturing the forming solid phase by using a single computer code. The same code can simulate the reverse process of thawing or melting of the solid phase. The computed sample configurations involve a two-dimensional closed container, a straight and a U-shaped channel, and a passage of an arbitrary shape. It was found that the presence of an external steady magnetic field: (a) diminishes flow field vorticity, (b) causes higher velocity gradients within the boundary layers, (c) is able to orient magnetized fibers along the lines of local magnetic lines of forces.

Introduction

It is well known that the defects in short fiber composites that are mainly due to uncontrolled fiber orientation during composites manufacturing can reduce the strength of the composite (Cranston and Reitz, 1980; Hatta and Yamashita, 1988). Thus, it would be very desirable to perform a solidification of the resin where the local concentration and orientation of the fibers are fully controlled. The objective of this paper is to elaborate on a mathematical model and an accompanying numerical algorithm that are capable of simulating fully three-dimensional ferromagnetic fluid flow (representing the resin and the suspended nickel-coated fibers) and solidification under the influence of an arbitrarily distributed and oriented external magnetic field. The basic idea is that the coated fibers will align with the local magnetic lines of force, which are different from streamlines. The pattern of these lines depends on the flow field and the variation of the externally applied magnetic field.

During a controlled solidification process (Dulikravich and Hayes, 1988), it is very important to understand fully the process of solid phase formation. The accumulated solid phase effectively reduces and deforms the cross-sectional area of the passages and causes significant local variations in pressure and flow field shear stresses. During the solidification or melting process, secondary flows are generated due to strong thermal buoyancy forces. These processes can be controlled in the case of strong heat transfer if influenced by a global body force.

One such body force is the general electromagnetic Lorentz force, which is created in any electrically conducting fluid when either a magnetic field or an electric potential field is applied. It has been shown (Lee and Dulikravich, 1991a, 1991b; Lee et al., 1991a; Dulikravich et al., 1991a, 1991b; Kosovic et al., 1991; Dulikravich and Kosovic, 1992) that the magnetic field

can eliminate vorticity from the flow field, while the electric field can enhance it (Lee et al., 1991b). During the curing process in composites manufacturing, we usually work with weakly electrically conducting resins. Although very poorly, they do conduct electricity because of the presence of iron atoms, salts, or acids. At the same time, if fibers are coated with a thin layer of a ferromagnetic material, the fibers will respond to the applied electromagnetic fields by rotating and translating in the melt until they become aligned with the magnetic lines of force. This principle was demonstrated experimentally (Yamashita et al., 1989; Gandhi et al., 1989) and proven for a short nickel-coated carbon fiber analytically (Hatta and Yamashita, 1988). Thus, if a relatively strong magnetic field is applied, the flow field will respond (Heiser, 1964; Ievlev and Levin, 1989; Ozoe and Okada, 1989) and the solid/liquid front shape and the velocity field could be manipulated (Vives, 1989; Dulikravich et al., 1991b; Dulikravich and Kosovic, 1992). In this work we have formulated the entire problem as time dependent and three dimensional although our computational results will be for steady two-dimensional situations only.

In this first attempt at numerically simulating the process, we have assumed that the fluid is of a Newtonian type. In reality, local orientation of the short fibers and their volumetric concentration in the resin will make physical properties of the resin-fiber mixture (viscosity, heat conductivity, specific heat, electrical conductivity, magnetic permeability, etc.) tensor quantities. Moreover, due to the magnetic field imposed, the fibers will exert higher hydrodynamic resistance to the flowing resin. These physical effects have not been incorporated in the present study since they require development of a new complex mathematical model involving mixture theory and a complete electro-magneto-hydrodynamic formulation.

Analytical Model

From Maxwell's equations and a relationship between an induced electric current, J_i , an electric field, E_i , and an ex-

Contributed by the Heat Transfer Division and presented at the National Heat Transfer Conference, San Diego, California, August 9-12, 1992. Manuscript received by the Heat Transfer Division April 1992; revision received August 1992. Keywords: Mass Transfer, Materials Processing and Manufacturing Processes, Phase-Change Phenomena. Associate Technical Editor: Y. Bayazitoglu.

ternally applied magnetic field, H_i , in a moving medium given by Ohm's law

$$J_i = \sigma(E_i + \mu \epsilon_{ijk} v_j H_k) \quad (1)$$

where σ , μ , and v_j are the coefficient of electric conductivity, coefficient of magnetic permeability, and fluid velocity vector, respectively, we can derive the magnetic field transport equation (Chandrasekhar, 1961; Pai, 1962; Stuetzer, 1962; Jeffrey, 1966; Lee and Dulikravich, 1991a) as

$$H_{i,t} - (v_j H_i - v_i H_j)_{,j} = \frac{1}{\mu \sigma} H_{i,jj} \quad (2)$$

Subscripts after the comma designate partial differentiation with respect to the variable or variables that follow the comma. The entire set of Navier-Stokes partial differential equations for the fluid flow and a set of the partial differential equations for magnetic field transport can be nondimensionalized by introducing the relations

$$v_i^* = \frac{v_i}{v_o} \quad x_i^* = \frac{x_i}{l_o} \quad t^* = \frac{t v_o}{l_o} \quad p^* = \frac{p}{\rho_o v_o^2} \quad (3)$$

$$g^* = \frac{g}{g} \quad H_i^* = \frac{H_i}{H_o} \quad \theta = \frac{\Delta T}{\Delta T_o} \quad e^* = \frac{e}{c_{po} \Delta T_o} \quad (4)$$

where T_c is the temperature of the cold wall and T_h is the temperature of the hot wall, so that $\Delta T = T - T_c$, and $\Delta T_o = T_h - T_c$. Here, subscript zero designates reference values, while asterisk designates nondimensional variables.

In this work only incompressible Newtonian fluid flow will be considered, while accounting for thermal buoyancy via an extended Boussinesq approximation in the form that is valid even when fluid properties vary as a function of temperature (Gray and Giorgini, 1976). Fluid density and coefficients of specific heat, viscosity, and heat conduction can be expressed as general functions of temperature (Gray and Giorgini, 1976)

$$\rho = \rho_o \rho'(\theta) \quad c_p = c_{po} c_{pe}'(\theta) \quad (5)$$

$$\eta = \eta_o \eta'(\theta) \quad k = k_o k'(\theta) \quad (6)$$

where the primed values denote arbitrary functions of non-dimensional temperature, θ . Here, ρ , η , c_p , and k are fluid density, coefficient of viscosity, coefficient of specific heat at constant pressure, and coefficient of thermal conductivity, respectively. The nondimensional density ρ' can be expanded in a Taylor series while retaining only the first-order term

$$\rho' = 1 - \alpha \Delta T = 1 - \alpha^* \theta \quad (7)$$

so that

$$\alpha^* = \frac{\partial \rho'}{\partial \theta} = \frac{\Delta T_o \rho_o}{\rho_o \Delta T_o} \frac{\partial \rho'}{\partial \theta} = \frac{\Delta T_o}{\rho_o} \frac{\partial \rho}{\partial T} = \Delta T_o \alpha \quad (8)$$

It can be assumed that the coefficient of thermal expansion, α , is constant in the range of temperatures that are of interest in a particular case. When the term $(\Delta T_o \alpha) \ll 1$, equations more general than what is known as Boussinesq approximation can be derived for the fluid with nonconstant properties (Gray and Giorgini, 1976). For incompressible flows $c_p = c_p$. Thus, it follows that $de = c_v dT = c_p dT$. In the case of a liquid/solid mixture the enthalpy per unit mass of the mushy region becomes

$$dh = c_p dT + L dS \quad (9)$$

where L is the latent heat (enthalpy of solid/liquid phase change) and S is the volumetric fraction of the solid phase. Then

$$v_i h_{,i} = c_p v_i T_{,i} - L v_i S_{,i} = (c_p - L S_{,T}) v_i T_{,i} \quad (10)$$

Let $c_{pe} = c_p - L S_{,T}$ be an equivalent specific heat so that

$$c_{pe} = c_{po} c_{pe}' = c_{po} \left(c_p' - \frac{L S_{,\theta T}}{c_{po}} \right) \quad (11)$$

where S could be an arbitrary function of θ and c_{pe}' is the nondimensional equivalent specific heat. This approach is called the "enthalpy method" (Poirier and Salcudean, 1986). With the following nondimensional groups:

Nomenclature

c_p = specific heat at constant pressure, $\text{J kg}^{-1} \text{K}^{-1}$	Pm = magnetic Prandtl number	μ = magnetic permeability, H m^{-1}
c_v = specific heat at constant volume, $\text{J kg}^{-1} \text{K}^{-1}$	Pr = Prandtl number	ξ, η, ζ = nonorthogonal grid-following coordinates
\mathbf{E} = electric field, V m^{-1}	Re = hydrodynamic Reynolds number	ρ = density, kg m^{-3}
Ec = Eckert number	Rm = RePm = magnetic Reynolds number	σ = electrical conductivity, $\Omega^{-1} \text{m}^{-1}$
Fr = Froude number	S = volume fraction of the solid phase	ϕ = nondimensional gravity potential
g = gravity force per unit volume, m s^{-2}	t = time, s	Φ = viscous dissipation function, $\text{kg m}^{-1} \text{s}^{-3}$
Gr = Grashof number	T = absolute temperature, K	
\mathbf{H} = magnetic field, A m^{-1}	$\Delta T_o = T_h - T_c$ = temperature difference, K	
Ht = Hartmann number	$\mathbf{v} = (u, v, w)$ = velocity vector, m s^{-1}	
\mathbf{J} = electric current density, A m^{-2}	x, y, z = Cartesian coordinates, m	Subscripts
k = heat conductivity coefficient, $\text{W m}^{-1} \text{K}^{-1}$	α = thermal expansion coefficient, K^{-1}	c = cold wall
l = length, m	β = artificial compressibility coefficient	h = hot wall
L = latent heat of liquid/solid phase change, J kg^{-1}	η = coefficient of shear viscosity, $\text{kg m}^{-1} \text{s}^{-1}$	o = reference values
Mm = magnetic Mach number; $\text{Mm}^2 = \text{ReRm}/\text{Ht}^2$	θ = nondimensional temperature	
p = pressure, $\text{kg m}^{-1} \text{s}^{-2}$		Superscripts
		$*$ = nondimensional values
		$'$ = function of nondimensional temperature

Reynolds number	$Re = \frac{\rho_o v_o l_o}{\eta_o}$	$\frac{\partial \tilde{\mathbf{Q}}}{\partial t} + \frac{\partial \tilde{\mathbf{E}}}{\partial \xi} + \frac{\partial \tilde{\mathbf{F}}}{\partial \eta} + \frac{\partial \tilde{\mathbf{G}}}{\partial \zeta} = D^2 + \tilde{\mathbf{S}}$	(19)
Froude number	$Fr^2 = \frac{v_o^2}{g l_o}$		
Grashof number	$Gr = \frac{\rho_o^2 \alpha g l_o^3 \Delta T_o}{\eta_o^2}$		
Eckert number	$Ec = \frac{v_o^2}{c_{p_o} \Delta T_o}$		
Prandtl number	$Pr = \frac{\eta_o c_{p_o}}{k_o}$		
Magnetic Prandtl number	$Pm = \frac{\mu \sigma \eta_o}{\rho_o}$		
Hartmann number	$Ht = \mu l_o H_o \left(\frac{\sigma}{\eta_o} \right)^{1/2}$		
Magnetic Reynolds number	$Rm = Re Pm$		
Magnetic Mach number	$Mm^2 = \frac{Re Rm}{Ht^2} = \frac{\rho_o v_o^2}{\mu H_o^2}$		

where $\tilde{\mathbf{Q}}$ is the solution vector and $\tilde{\mathbf{E}}$, $\tilde{\mathbf{F}}$, and $\tilde{\mathbf{G}}$ are the flux vectors. The transformed source vector is denoted by $\tilde{\mathbf{S}}$. Definitions of these vectors will be given for both systems of equations (Navier–Stokes and magnetic transport) separately. For the Navier–Stokes equations, the generalized vectors are defined as

$$\tilde{\mathbf{Q}} = \frac{1}{J} \begin{bmatrix} \bar{p}/\beta \\ u \\ v \\ w \\ \theta \end{bmatrix} \quad \tilde{\mathbf{E}} = \frac{1}{J} \begin{bmatrix} U \\ Uu + \xi_{,x} \bar{p} \\ Uv + \xi_{,y} \bar{p} \\ Uw + \xi_{,z} \bar{p} \\ U\theta \end{bmatrix} \quad \tilde{\mathbf{F}} = \frac{1}{J} \begin{bmatrix} V \\ Vu + \eta_{,x} \bar{p} \\ Vv + \eta_{,y} \bar{p} \\ Vw + \eta_{,z} \bar{p} \\ V\theta \end{bmatrix}$$

$$\tilde{\mathbf{G}} = \frac{1}{J} \begin{bmatrix} W \\ Wu + \zeta_{,x} \bar{p} \\ Wv + \zeta_{,y} \bar{p} \\ Ww + \zeta_{,z} \bar{p} \\ W\theta \end{bmatrix} \quad \tilde{\mathbf{S}} = \begin{bmatrix} 0 \\ \tilde{d}_2 \\ \tilde{d}_3 \\ \tilde{d}_4 \\ \tilde{d}_5 \end{bmatrix} \quad \tilde{\mathbf{D}} = \frac{1}{Re} \begin{bmatrix} 0 \\ \eta' \\ \eta' \\ \eta' \\ k' \\ Pr c_p' \end{bmatrix}^T \quad (20)$$

the conservation laws in nondimensional form become

$$v_{i,i} = 0 \quad (13)$$

$$v_{i,i} + (v_i v_j)_{,j} = \frac{1}{Re} (\eta' v_{i,j})_{,j} - \bar{p}_{,i} + \frac{Gr\theta}{Re^2} g_i + \frac{Ht^2}{Rm Re} (H_{ik})_{,k} \quad (14)$$

$$\theta_{,i} + v_i \theta_{,i} = \frac{1}{Re Pr c_{pe}'} (k' \theta_{,i})_{,i} + \frac{Ec Ht^2}{Rm^2 Re c_{pe}'} \epsilon_{ijk} \epsilon_{ilm} H_{k,j} H_{m,l} \quad (15)$$

$$H_{,i} - (v_j H_i - v_i H_j)_{,j} = \frac{1}{Rm} H_{i,jj} \quad (16)$$

It should be pointed out that the viscous dissipation can be neglected from an order of magnitude analysis since

$$\frac{\rho_o c_{pe}'}{\Phi^{(i)}} \frac{\partial T}{\partial t} = \frac{Re}{Ec} \gg \gg 1 \quad (17)$$

The combination of nondimensional hydrodynamic, hydrostatic, and magnetic pressures is

$$\bar{p} = p + \frac{\phi}{Fr^2} + \frac{1}{Mm^2} H_i H_i \quad (18)$$

where ϕ is the nondimensional gravity potential defined as $g_i = \phi_{,i}$.

Numerical Algorithm

Equations (13)–(16) represent a global system of coupled nonlinear partial differential equations. The global system has been split in two subsystems in order to simplify programming. The Navier–Stokes equations, Eqs. (13)–(15), constitute the first subsystem and the magnetic field transport equations, Eq. (16), constitute the second subsystem. To integrate each subsystem, the explicit Runge–Kutta time stepping method (Jameson et al., 1981) was used in an alternating manner (Lee and Dulikravich, 1991a).

The general form of each subsystem is the same. The non-dimensional three-dimensional Navier–Stokes equations for incompressible flows in conservative form expressed in generalized curvilinear nonorthogonal coordinates are

where $J = \partial(\xi, \eta, \zeta)/\partial(x, y, z)$ is the Jacobian determination of the geometric transformation from physical Cartesian coordinates x, y, z into ξ, η, ζ computational space.

The system of equations given by Eqs. (13)–(16) is not hyperbolic since there is no physical time derivative term in the mass conservation equation. Consequently, the system cannot be integrated simultaneously. In order to integrate the system simultaneously and obtain a steady-state solution, an artificial compressibility (Chorin, 1967) term, $\partial/\partial t(\bar{p}/\beta)$, has been added to the mass conservation equation, Eq. (13). Here, β is an artificial compressibility coefficient, a user-specified parameter that depends on the problem geometry, grid, flow parameters, etc. (Lee and Dulikravich, 1991c). In the steady-state limit the artificial compressibility term tends to zero. Thus, it does not influence the steady-state solution.

The source vector $\tilde{\mathbf{S}}$ contains the influence of the ponderomotive force due to the magnetic field and the thermal buoyancy force. Its components are given as

$$\tilde{d}_2 = \frac{Ht^2}{Rm Re} \left(\frac{\partial}{\partial \xi} \left(\frac{\hat{H}_x H_x}{J} \right) + \frac{\partial}{\partial \eta} \left(\frac{\hat{H}_y H_y}{J} \right) + \frac{\partial}{\partial \zeta} \left(\frac{\hat{H}_z H_z}{J} \right) \right) + \frac{Gr\theta}{Re^2 J} g_x \quad (21)$$

$$\tilde{d}_3 = \frac{Ht^2}{Rm Re} \left(\frac{\partial}{\partial \xi} \left(\frac{\hat{H}_x H_y}{J} \right) + \frac{\partial}{\partial \eta} \left(\frac{\hat{H}_y H_x}{J} \right) + \frac{\partial}{\partial \zeta} \left(\frac{\hat{H}_x H_y}{J} \right) \right) + \frac{Gr\theta}{Re^2 J} g_y \quad (22)$$

$$\tilde{d}_4 = \frac{Ht^2}{Rm Re} \left(\frac{\partial}{\partial \xi} \left(\frac{\hat{H}_x H_z}{J} \right) + \frac{\partial}{\partial \eta} \left(\frac{\hat{H}_y H_z}{J} \right) + \frac{\partial}{\partial \zeta} \left(\frac{\hat{H}_x H_z}{J} \right) \right) + \frac{Gr\theta}{Re^2 J} g_z \quad (23)$$

$$\tilde{d}_5 = \frac{1}{c_{pe}'} \frac{Ec Ht^2 J}{Rm Re^2} \left(\bar{P}_1^2 + \bar{P}_2^2 + \bar{P}_3^2 \right) \quad (24)$$

where H_x, H_y, H_z are the components of the magnetic field vector in Cartesian coordinates, g_x, g_y, g_z are components of the unit vector in the direction of gravity force, and

$$\bar{P}_1 = \frac{\partial}{\partial \xi} \left(\frac{H_z \xi_{,y} - H_y \xi_{,z}}{J} \right) + \frac{\partial}{\partial \eta} \left(\frac{H_z \eta_{,y} - H_y \eta_{,z}}{J} \right) + \frac{\partial}{\partial \zeta} \left(\frac{H_z \zeta_{,y} - H_y \zeta_{,z}}{J} \right) \quad (25)$$

$$\bar{P}_2 = \frac{\partial}{\partial \xi} \left(\frac{H_x \xi_{,z} - H_z \xi_{,x}}{J} \right) + \frac{\partial}{\partial \eta} \left(\frac{H_x \eta_{,z} - H_z \eta_{,x}}{J} \right) + \frac{\partial}{\partial \zeta} \left(\frac{H_x \zeta_{,z} - H_z \zeta_{,x}}{J} \right) \quad (26)$$

Table 1 Nondimensional numbers

Passage	Closed	Straight	U-shaped	Arbitrary
Melt	(silicon)	(undefined)	(undefined)	(saline)
Gr	56.769x10 ⁶	0.0	0.0	0.0
Re	8300	100	20	234.44
Ec	7.869x10 ⁻⁸	1	1	6.46 x 10 ⁻⁸
Pr	0.0116	7.9	7.9	36.9
Pm	4.44x10 ⁻⁶	1	1	2.68 x 10 ⁻³
Ht	209.3B ₀ or 2093 B ₀	5 or 10	5 or 10	0.0 or 0.5027 B ₀

$$\bar{P}_3 = \frac{\partial}{\partial \xi} \left(\frac{H_y \xi_{,x} - H_x \xi_{,y}}{J} \right) + \frac{\partial}{\partial \eta} \left(\frac{H_y \eta_{,x} - H_x \eta_{,y}}{J} \right) + \frac{\partial}{\partial \zeta} \left(\frac{H_y \zeta_{,x} - H_x \zeta_{,y}}{J} \right) \quad (27)$$

The diffusion term in general curvilinear coordinates is

$$D^2 = \left(\frac{\bar{D}}{J} g_{ij} (J \bar{Q})_{,j} \right)_{,i} \quad (28)$$

The metric tensor is defined as

$$g_{ij} = \frac{\partial \bar{x}_i}{\partial \hat{x}_j} \frac{\partial \bar{x}_j}{\partial \hat{x}_i} \quad (29)$$

where \bar{x}_i is the Cartesian coordinate vector and \hat{x}_i is the curvilinear coordinate vector:

$$\bar{x}_i = (x, y, z)^T \quad \hat{x}_i = (\xi, \eta, \zeta)^T \quad (30)$$

Here, the superscript T represents a transpose. The contravariant components U, V, W of the velocity vector are related to the velocity components u, v, w in the Cartesian system as follows:

$$\begin{bmatrix} U \\ V \\ W \end{bmatrix} = \begin{bmatrix} \xi_{,x} & \xi_{,y} & \xi_{,z} \\ \eta_{,x} & \eta_{,y} & \eta_{,z} \\ \zeta_{,x} & \zeta_{,y} & \zeta_{,z} \end{bmatrix} \begin{bmatrix} u \\ v \\ w \end{bmatrix} \quad (31)$$

Similarly, the contravariant components $\hat{H}_\xi, \hat{H}_\eta, \hat{H}_\zeta$ of the magnetic field vector are defined as

$$\begin{bmatrix} \hat{H}_\xi \\ \hat{H}_\eta \\ \hat{H}_\zeta \end{bmatrix} = \begin{bmatrix} \xi_{,x} & \xi_{,y} & \xi_{,z} \\ \eta_{,x} & \eta_{,y} & \eta_{,z} \\ \zeta_{,x} & \zeta_{,y} & \zeta_{,z} \end{bmatrix} \begin{bmatrix} H_x \\ H_y \\ H_z \end{bmatrix} \quad (32)$$

For the subsystem containing the magnetic field transport equations, the solution vector \bar{Q} , the flux vectors $\bar{E}, \bar{F}, \bar{G}$, and the source vector \bar{S} are

$$\bar{Q} = \frac{1}{J} \begin{bmatrix} H_x \\ H_y \\ H_z \end{bmatrix} \quad \bar{E} = \frac{1}{J} \begin{bmatrix} H_x U - u \hat{H}_\xi \\ H_y U - v \hat{H}_\xi \\ H_z U - w \hat{H}_\xi \end{bmatrix} \quad \bar{F} = \frac{1}{J} \begin{bmatrix} H_x V - u \hat{H}_\eta \\ H_y V - v \hat{H}_\eta \\ H_z V - w \hat{H}_\eta \end{bmatrix} \quad (33)$$

$$\bar{G} = \frac{1}{J} \begin{bmatrix} H_x W - u \hat{H}_\zeta \\ H_y W - v \hat{H}_\zeta \\ H_z W - w \hat{H}_\zeta \end{bmatrix} \quad \bar{S} = 0 \quad \bar{D} = \frac{1}{\text{Rm}} \mathbf{I}$$

In the case of three-dimensional magnetohydrodynamics, the system of eight partial differential equations needs to be solved by integrating intermittently a subsystem of five fluid flow equations and a subsystem of three magnetic field transport equations and transferring the information through the sourcelike terms (Lee, 1990; Lee and Dulikravich, 1991a). The explicit Runge-Kutta time-stepping algorithm and finite difference scheme with artificial compressibility (Chorin, 1967)

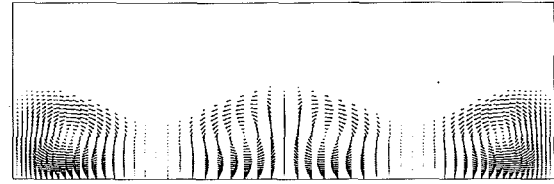


Fig. 1(a) Velocity vector field

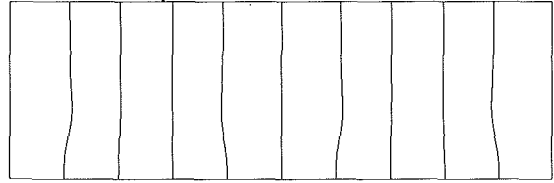


Fig. 1(b) Magnetic lines of force

Fig. 1 Closed container with a weak constant magnetic field

were used in the general nonorthogonal curvilinear boundary conforming coordinate system. The pressure boundary condition at the solid walls of the passages was enforced using a normal momentum equation, instead of the boundary layer approximation that the normal pressure gradient at the solid boundary is zero. Inlet and exit boundary conditions were treated using the method of characteristics (Lee and Dulikravich, 1991a). The explicit time integration scheme was used because it can be efficiently vectorized and because additional equations can be easily added to the system. The rate of convergence of explicit schemes is generally much lower than for implicit schemes, but when fully vectorized, these schemes need less central processor unit time to reach convergence than implicit schemes. This advantage of explicit schemes is more pronounced when three-dimensional problems with complex geometries are studied.

Computational Results

A computer code written in Fortran was developed for simulation of two-dimensional solidification processes under the influence of a steady externally applied magnetic field. Four configurations were tested numerically: a closed container cooled uniformly from above, a straight channel flow with nonuniformly cooled top and bottom walls, a U-shaped channel with nonuniformly cooled inner and outer walls, and an arbitrarily shaped channel nonuniformly cooled from top and the bottom. Nondimensional parameters used in the calculations are summarized in Table 1.

Closed Container. Mathematical and numerical models for solidification of a fluid flow were first tested in the case of a closed rectangular container of aspect ratio 3:1. It was discretized with 60 x 60 grid cells that were clustered toward the four walls. Vertical walls were thermally insulated, while the top wall had a uniform undercooling nondimensional temperature of $\theta = -10$. At the same time, the bottom wall had a uniform nondimensional temperature of $\theta = 1$. A uniform magnetic field of $Ht = 209.3 B_0$ was applied vertically downward. We have specified $B_0 = 1$ Tesla. The resulting velocity vector field (Fig. 1a) indicates strong recirculation of the melt due to thermal buoyancy. The solid accrued is visible toward the top wall. The resulting magnetic force lines (lines that are locally tangent to the magnetic force vector) are depicted in Fig. 1(b), indicating that the fluid motion has distorted the magnetic force lines. Notice that the magnetic force lines along which the short fibers would align have an entirely different pattern from the flow field streamlines.

When a stronger magnetic field ($Ht = 2093 B_0$) was applied, the thermal buoyancy flow was significantly suppressed (Fig.

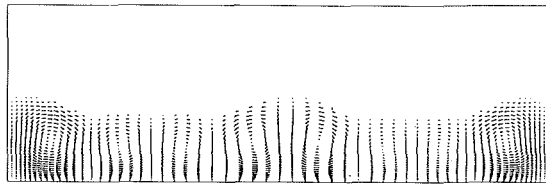


Fig. 2(a) Velocity vector field

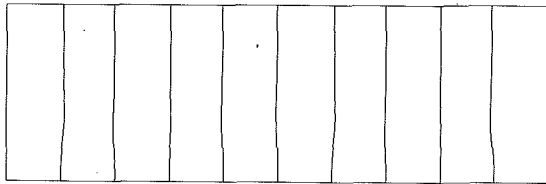


Fig. 2(b) Magnetic lines of force

Fig. 2 Closed container with a strong constant magnetic field

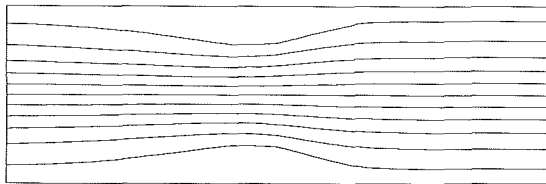


Fig. 3(a) Streamlines

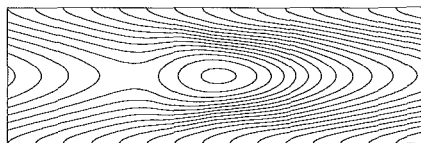


Fig. 3(b) Magnetic lines of force

Fig. 3 Straight channel with a weak constant magnetic field

2a) and the magnetic force lines straightened somewhat (Fig. 2b). The amount of solid accrued at the top wall is smaller than with $Ht = 209.3 B_o$.

Straight Channel. The second configuration studied was a straight two-dimensional channel of aspect ratio 3:1 with the flow direction from left to right (Fig. 3a). A uniform nondimensional temperature $\theta = 1$ was imposed at the inlet. Along the walls a smoothly varying cooling was specified as $\theta = 1 - 11 \sin(\pi x/3)$. Both velocity components were specified at the inlet, while a combination of hydrostatic, hydromagnetic and hydrodynamic pressure was specified at the exit. Properties of the fluid flow were defined by the nondimensional numbers, which are given in Table 1. All physical properties were assumed not to vary with temperature. The flow field was discretized with 60×60 nonclustered grid cells.

The first test case represents a solidifying flow field with an imposed uniform magnetic field of $Ht = 5$ acting vertically downward. The computed streamlines (Fig. 3a) clearly outline the solidified zones attached to the channel walls. Computed lines of magnetic force are given in Fig. 3(b), indicating that they have been strongly affected by the flow field. Notice how different the two patterns are. Magnetized fibers will align themselves according to the pattern in Fig. 3(b).

To test the influence of a stronger magnetic field on solidification, a test run was performed with the viscosity varying linearly in the mushy region and a vertically downward pointing constant magnetic field of $Ht = 10$. The computed velocity vector field (Fig. 4a) and the magnetic lines of force (Fig. 4b) demonstrate that the magnetic field is affected even further by the flow field. The presence of a magnetic field in an already

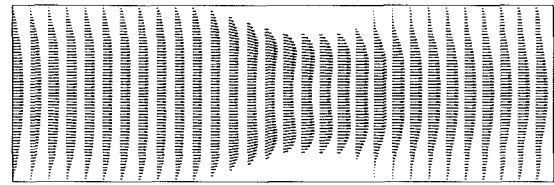


Fig. 4(a) Velocity vector field

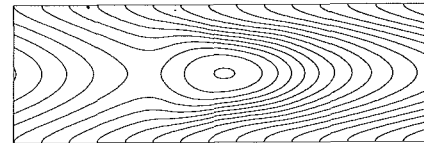


Fig. 4(b) Magnetic lines of force

Fig. 4 Straight channel with a strong constant magnetic field

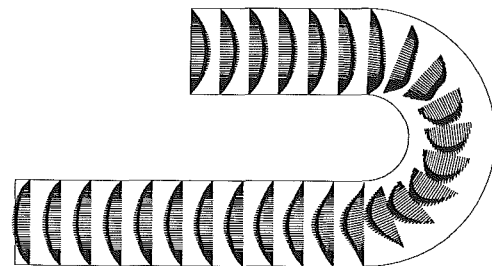


Fig. 5(a) Velocity vector field

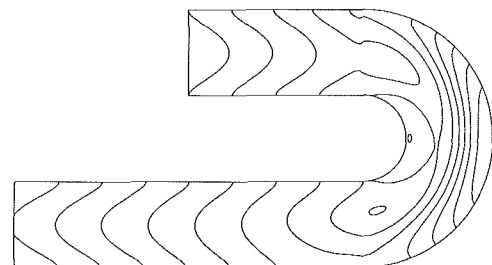


Fig. 5(b) Magnetic lines of force

Fig. 5 U-shaped channel with a weak constant magnetic field

existing mean flow inhibits the growth of the solid layers because of the higher speed of the fluid next to the solid/fluid interface. This is typical for magnetohydrodynamics.

U-Shaped Channel. The next test configuration represented a solidifying flow in a U-shaped channel of constant width where the fluid enters at the upper end and exits at the lower end. The same type of boundary condition was imposed on inlet temperature and velocity as in the case of a straight channel. Along the straight parts of the walls the temperature was kept constant ($\theta = 1$). Along the curved parts of the walls the nondimensional temperature varied according to $\theta = 1 - 11 \sin(\pi/2 - \omega)$ where ω is the angle between the wall point and the horizontal. The computational grid had 264×60 cells that were clustered toward the walls. Nondimensional numbers used with the U-shaped channel are given in Table 1.

In the first test case a uniform magnetic field ($Ht = 5$) was applied perpendicular to the walls of the entire U-shaped channel. The computed velocity vector field (Fig. 5a) demonstrates that the magnetic field effectively eliminates flow recirculation regions. The predicted magnetic force lines (Fig. 5b) are significantly distorted from the straight-line pattern that would connect inner and outer walls if there would be no flow through the channel.

In the second test case a stronger magnetic field ($Ht = 10$)

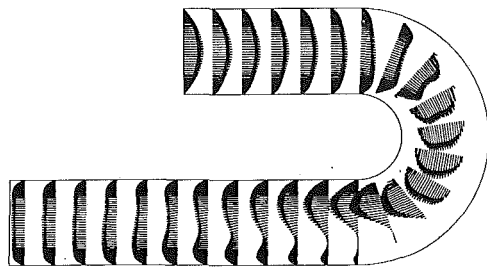


Fig. 6(a) Velocity vector field

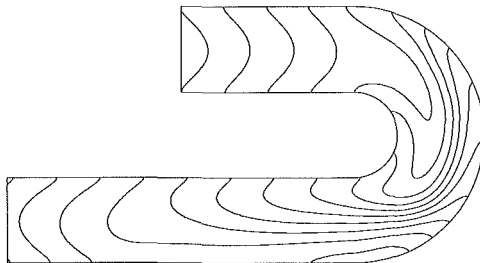


Fig. 6(b) Magnetic lines of force

Fig. 6 U-shaped channel with a strong constant magnetic field

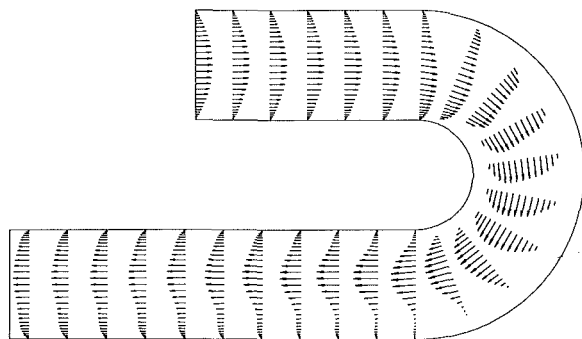


Fig. 7(a) Velocity vector field

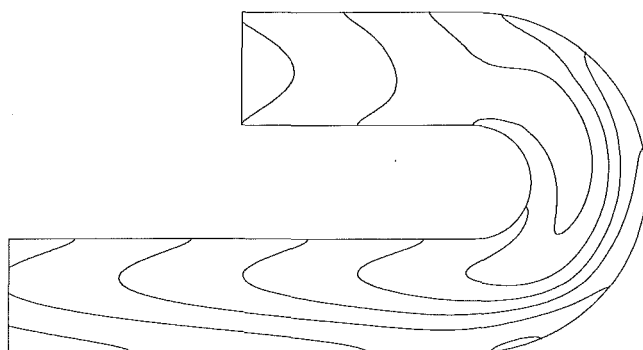


Fig. 7(b) Magnetic lines of force

Fig. 7 U-shaped channel with a variable magnetic field

was applied in the same manner, resulting in a dramatic change in the flow pattern (Fig. 6a). Plots of the magnetic lines of force (Fig. 6b) demonstrate their complex pattern that could be exploited to position and orient short ferromagnetically coated fibers in the flow field and, consequently, in the solidified layers.

In the case that the externally applied magnetic field is not uniform, but instead varies along the curved parts of the channel walls according to $Ht = 10 - 5 \sin(\pi/2 - \omega)$, the flow field pattern (Fig. 7a) and the magnetic lines of force (Fig. 7b) will

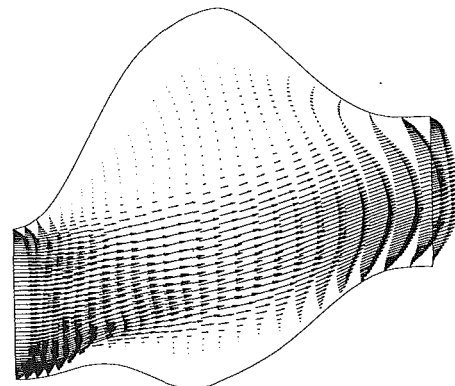


Fig. 8(a) Velocity vector field

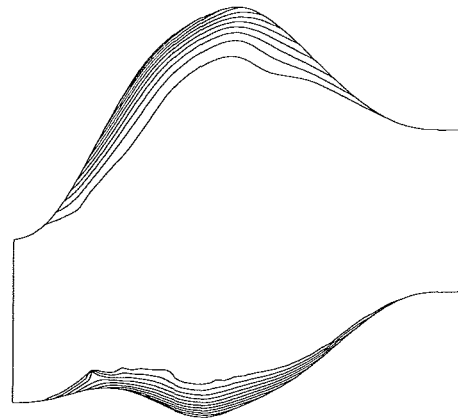


Fig. 8(b) Isotherms

Fig. 8 Arbitrary passage without magnetic field

be considerably different. This clearly demonstrates the conceptual feasibility of controlling not only the orientation, but also the concentration of the fibers in the resin during the curing process.

Arbitrary Channel. Finally, the mathematical model and the computer code were tested using a set of physical flow parameters corresponding to a saline solution flow in an arbitrary shaped channel with undercooled walls. As in the case of channel flow, the temperature of the walls from inlet to exit was varying according to a sinusoidal distribution $\theta = 1 - 11 \sin(\pi i / imax)$ where i is the grid cell index in the x direction ($1 < i < imax$). Fluid temperature at the inlet was a uniform $T = 283$ K corresponding to $\theta = 1$ since $T_h = 283$ K and $T_c = 273$ K so that $\Delta T_o = T_h - T_c = 10$ K. This made the coldest point on the wall have a temperature of -100°C . In the case when a steady uniform magnetic field was applied, it acted vertically downward between the inlet and 80 percent of the channel length, while no magnetic field was applied over the remaining 20 percent of the channel length. The characteristic quantities that were used for nondimensionalization are: $c_{po} = c_{po\ liq}$, $k_o = k_{o\ liq}$, $l_o = 0.01$ m, $v_o = 0.1$ m/s. Since the value for the magnetic permeability could not be found in the open literature, we have arbitrarily assumed it to be $\mu = 50 \mu_v$, where $\mu_v = 4 \pi \times 10^{-7}$ is the magnetic permeability for vacuum. If $B_o = \mu_v H_o$, the remaining terms in the equation for Ht can be grouped so that Ht is directly proportional to B_o , which is measured in Teslas. For example, if $Ht = 0.5 B_o$ and the value for B_o is 10, this means that the Hartmann number $Ht = 5$ can be achieved with the magnetic field of 10 T.

The nonorthogonal boundary-conforming computational grid consisted of 100×58 grid cells that were clustered toward the inlet and the passage top and bottom walls. The grid was

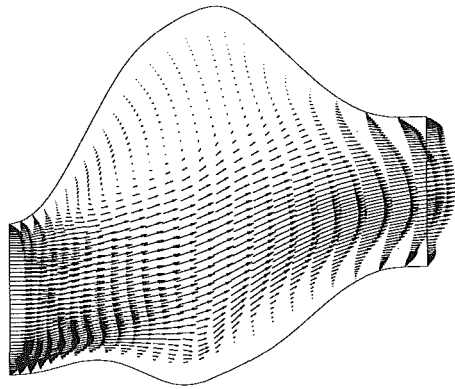


Fig. 9(a) Velocity vector field

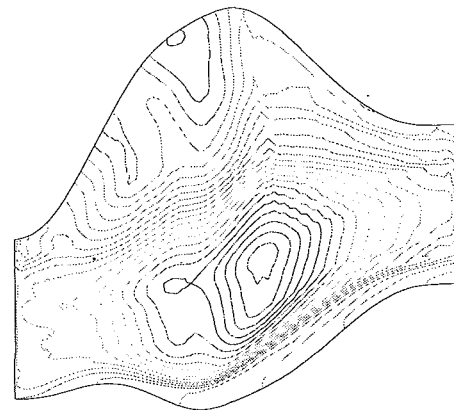


Fig. 10(a) Magnetic lines of force

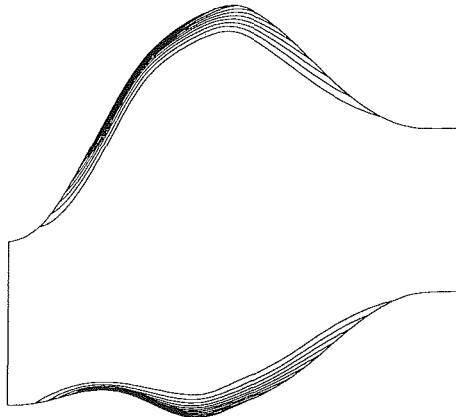


Fig. 9(b) Isotherms

Fig. 9 Arbitrary passage with a constant magnetic field

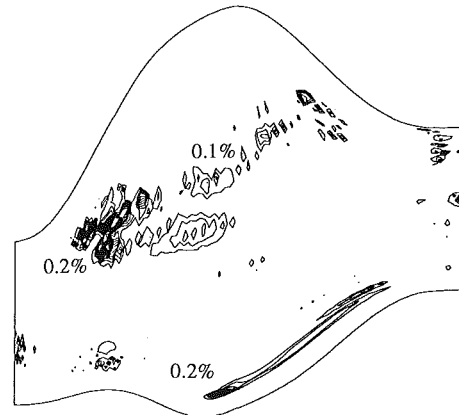


Fig. 10(b) Joule heating contours

Fig. 10 Arbitrary passage with a constant magnetic field

generated using our grid optimization algorithm (Kennon and Dulikravich, 1986).

A comparison of the computational results with and without an external magnetic field shows that the velocity profiles change under the influence of the magnetic field due to the ponderomotive force (Figs. 8a and 9a). More importantly, the solidified layers in the case where no external magnetic field was applied are thicker and differently shaped compared to the freezing with the magnetic field as indicated by the isotherms in the solid phase without (Fig. 8b) and with (Fig. 9b) the magnetic field. A very complex pattern of magnetic lines of force (Fig. 10a) clearly indicates that the coated short fibers could be manipulated using appropriately distributed magnetic field strength along the boundaries of the domain. It should be pointed out that it is the higher speed of the fluid close to the solid/liquid interface that decreases the residence time of the fluid particles in the mushy region, thus decreasing the rate of solid accretion. This increase in the fluid speed in the boundary layer regions is caused by the presence of the magnetic field. On the other hand, Joule heating (Fig. 10b) would have a profound influence on the solidification rate in the case of a lower electrical conductivity of the fluid and in flows generated purely by thermal buoyancy.

Conclusions

An analytical and a numerical formulation have been developed for the theoretical prediction of solidification processes in fluid flows inside undercooled passages with and without the influence of an externally applied steady magnetic field. Computational results confirm that the magnetic field has a profound influence on the solidifying flow field since it eliminates flow recirculation regions and causes distorted velocity profiles having pronounced overshoots close to the solid

boundaries. The temperature field also changes under the influence of the external magnetic field. This change influences heat transfer through the boundaries and consequently the amount of the solid phase accrued on undercooled walls. Specifically, the influence of the ponderomotive force and, to a much lesser extent, Joule heating are such that they tend to reduce the amount of the accrued solid phase. Combined with the predicted complex patterns of the magnetic field force lines, this indicates a possibility for the development of a computational inverse design/optimization algorithm capable of achieving desired configurations of the solidified layers and desired distribution and orientation of magnetized short fibers within the solidified layers.

Acknowledgments

All computations were performed remotely on the Cray-YMP computer at NASA Ames Research Center NAS facility and at Cray Research, Inc. in Eagan, Minnesota and post-processed at Penn State on equipment donated by Apple Computer, Inc. The authors are thankful to the reviewers for useful comments and to Mr. Scott G. Sheffer for correcting the grammar in this paper.

References

- Balasubramaniam, T. A., and Bowman, H. F., 1977, "Thermal Conductivity and Thermal Diffusivity of Biomaterials: A Simultaneous Measurement Technique," *Journal of Biomedical Engineering*, Aug., pp. 148-154.
- Chandrasekhar, S., 1961, *Hydrodynamic and Hydromagnetic Stability*, Dover Publication Inc., New York.
- Chorin, A. J., 1967, "A Numerical Method for Solving Incompressible Viscous Flow Problems," *Journal of Computational Physics*, Vol. 2, pp. 12-26.
- Cranston, J. J., and Reitz, J. A., III, 1980, "SMC Molding Techniques for

Optimized Mechanical Properties in Structural Applications," *Polymer and Plastics Technology and Engineering*, Vol. 15, pp. 97-114.

Diller, K. R., 1985, "The Influence of Controlled Ice Nucleation on Regulating the Thermal History During Freezing," *Cryobiology*, Vol. 22, pp. 268-281.

Dulikravich, G. S., and Hayes, L. J., 1988, "Control of Surface Temperatures to Optimize Survival in Cryopreservation," in: *Symposium on Computational Methods in Bioengineering*, R. L. Spilker and B. R. Simon, eds., ASME BED-Vol. 9, pp. 255-265.

Dulikravich, G. S., Kosovic, B., and Lee, S., 1991a, "Solidification of Variable Property Melts in Closed Containers: Magnetic Field Effects," *Proc. 13th IMACS World Congress on Computation and Applied Math.*, Dublin, Ireland, July 22-26.

Dulikravich, G. S., Kosovic, B., and Lee, S., 1991b, "Solidification in Reduced Gravity With Magnetic Fields and Temperature-Dependent Physical Properties," in: *Symposium on Heat and Mass Transfer in Solidification Processes*, G. S. Advani and C. Beckerman, eds., ASME HTD-Vol. 175/MD-Vol. 25, pp. 61-73.

Dulikravich, G. S., and Kosovic, B., 1992, "Solidification of Variable Property Melts Under the Influence of Low Gravity, Magnetic Fields and Electric Fields," AIAA Paper No. 92-0694.

Fazio, R. G., and Jacobs, H. R., 1974, "Heat Transfer Coefficients of Blood in Small Tubes and Capillaries," *AIChE Symposium Series 138*, Vol. 70, pp. 233-240.

Gandhi, M. V., Thompson, B. S., and Choi, S. B., 1989, "A New Generation of Innovative Ultra-advanced Intelligent Composite Materials Featuring Electro-Rheological Fluids: An Experimental Investigation," *Journal of Composite Materials*, Vol. 23, Dec., pp. 1232-1255.

Gray, D. D., and Giorgini, A., 1976, "The Validity of the Boussinesq Approximation for Liquids and Gases," *International Journal of Heat and Mass Transfer*, Vol. 19, pp. 545-551.

Hatta, H., and Yamashita, S., 1988, "Fiber Orientation Control by Means of Magnetic Moment," *Journal of Composite Materials*, Vol. 22, May, pp. 484-500.

Heiser, W. H., 1964, "Influence of Magnetic Fields Upon Separation," *AIAA Journal*, Vol. 2, No. 12, pp. 2217-2218.

Ievlev, V. M., and Levin, V. B., 1989, "Laminarization of a Submerged Jet of Electrically Conducting Fluid by Means of a Longitudinal Magnetic Field," *Izvestia Akademii Nauk SSSR, Mekhanika Zhidkosti i Gaza*, No. 6, Nov.-Dec., pp. 35-40.

Jameson, A., Schmidt, W., and Turkel, E., 1981, "Numerical Solution of the Euler Equations by Finite Volume Methods Using Runge-Kutta Time-Stepping Scheme," AIAA Paper No. 81-1259.

Jeffrey, A., 1966, *Magnetohydrodynamics*, University Mathematical Texts 33, Oliver & Royd Ltd., Edinburgh, United Kingdom.

Kennon, S. R., and Dulikravich, G. S., 1986, "Optimization of Computational Grids," *AIAA Journal*, Vol. 24, No. 7, pp. 1069-1073.

Kosovic, B., Dulikravich, G. S., and Lee, S., 1991, "Freezing Under the Influence of a Magnetic Field: Computer Simulation," *Proceedings of 1991 ICHMT Int. Symposium on Heat and Mass Transfer in Biomedical Engineering*, K. Diller, A. Shitzer, and S. Sideman, eds., Athens, Greece, Sept. 2-6.

Kosovic, B., and Dulikravich, G. S., 1992, "Unsteady Solidification in Microgravity," *Symposium on Topics in Heat Transfer*, Vol. 3, ASME HTD-Vol. 206-3, pp. 13-20.

Lee, S., and Dulikravich, G. S., 1991a, "Magnetohydrodynamic Steady Flow Computations in Three Dimensions," AIAA Paper No. 91-0388; also in *International Journal for Numerical Methods in Fluids*, Vol. 13, No. 8, Oct., pp. 917-936.

Lee, S., and Dulikravich, G. S., 1991b, "Computation of Magnetohydrodynamic Flow With Joule Heating and Buoyancy," *Proceedings of International Aerospace Congress*, Melbourne, Australia, May.

Lee, S., and Dulikravich, G. S., 1991c, "Performance Analysis of DMR Method for Acceleration of Iterative Algorithms," AIAA Paper No. 91-0241.

Lee, S., Dulikravich, G. S., and Kosovic, B., 1991a, "Interaction of a Magnetic Field With Blood Flow," *Proceedings of 17th Annual Northeast Bioengineering Conference*, University of Connecticut, Hartford, CT, Apr. 4-5.

Lee, S., Dulikravich, G. S., and Kosovic, B., 1991b, "Electrohydrodynamic (EHD) Flow Modeling and Computations," AIAA Paper No. 91-1469.

Ozoe, H., and Okada, K., 1989, "The Effect of the Direction of the External Magnetic Field on the Three-Dimensional Natural Convection in a Cubical Enclosure," *International Journal of Heat and Mass Transfer*, Vol. 32, No. 2, pp. 1939-1954.

Pai, S.-I., 1962, *Magnetogasdynamics and Plasma Dynamics*, Springer Verlag, Vienna.

Poirier, D., and Salcudean, M., 1986, "On Numerical Methods Used in Mathematical Modeling of Phase Change in Liquid Metals," ASME Paper No. 86-WA/HT-22.

Stuetzer, O. M., 1962, "Magnetohydrodynamics and Electrohydrodynamics," *The Physics of Fluids*, Vol. 5, No. 5, pp. 534-544.

Sud, V. K., Sekhon, G. S., and Mishra, R. K., 1977, "Pumping Action of Blood by a Magnetic Field," *Bulletin of Mathematical Biology*, Vol. 39, pp. 385-390.

Vives, C., 1989, "Effects of a Magnetically Forced Convection During the Crystallization in Mould of Aluminum Alloys," *Journal of Crystal Growth*, Vol. 94, pp. 739-750.

Yamashita, S., Hatta, H., Sugano, T., and Murayama, K., 1989, "Fiber Orientation Control of Short Fiber Composites: Experiment," *Journal of Composite Materials*, Vol. 23, pp. 32-41.

This section contains shorter technical papers. These shorter papers will be subjected to the same review process as that for full papers.

Laplace Transform Solution for Heat Transfer in Composite Walls With Periodic Boundary Conditions

M. F. Zedan¹ and A. M. Mujahid¹

Introduction

Composite walls are found in many engineering applications. The most familiar example is building walls, which usually consist of slabs made of materials with different thermophysical properties. The temperature inside most modern buildings is kept roughly constant by means of an air conditioning system. The sizing of such systems requires accurate evaluation of the maximum load, which requires hour-by-hour load calculations. One of the most important elements of load is the transmission of heat through walls and roofs.

The steady periodic heat flux at the inner wall surface due to periodic ambient temperature variation and solar radiation at the outside surface is usually the main objective. The need to calculate this flux as a function of time stems from the fact that the maximum flux does not occur at the time of maximum ambient temperature because of the thermal lag, which depends on the heat storage characteristics of the wall. Analytical solutions are only available for a single slab. For composite walls, numerical solutions are still necessary (McQuiston and Parker, 1988). Most calculation methods give the steady periodic response. However, the transient part of the solution can be important for some applications such as in calculating heat gain (loss) during the start-up of an air conditioning system in a massive building. The time to reach steady periodic conditions may exceed one full day. The thermal response of the structure under these conditions is required to study its effect on the performance of the equipment. The objective of this work is to develop an accurate and efficient method to calculate the transient (and steady periodic) response of a composite wall subjected to a fluid with periodic temperature variation on one side and a fluid with a constant temperature on the other side. Because of its analytic nature, the method is considered to be an efficient alternative to purely numerical methods.

¹Associate Professor, Mechanical Engineering Department, College of Engineering, King Saud University, Riyadh, Saudi Arabia.

Contributed by the Heat Transfer Division of THE AMERICAN SOCIETY OF MECHANICAL ENGINEERS. Manuscript received by the Heat Transfer Division August 20, 1991; revision received July 16, 1992. Keywords: Conduction, Thermal Energy Storage, Transient and Unsteady Heat Transfer. Associate Technical Editor: L. S. Fletcher.

Method of Analysis

Consider a composite wall made of n slabs as shown in Fig. 1(a). $T_{\infty n}$ is constant while $T_{\infty 1}$ is described by

$$T_{\infty 1}(t) = T_m + T_a \sin(\omega t + \phi) \quad (1)$$

where T_m and T_a are the mean and amplitude of variation of ambient temperature, ω is the frequency, t is the time, and ϕ is some phase angle. The unsteady one-dimensional heat conduction in a general slab " i " is governed by

$$\frac{\partial^2 \theta_i}{\partial X_i^2} = \gamma_i \frac{\partial \theta_i}{\partial \tau} \quad (2)$$

where

$$\theta_i(X_i, \tau) = \frac{T_i(X_i, t) - T_{\infty n}}{T_o - T_{\infty n}}; \quad X_i = x_i/L_i; \quad \tau = \alpha_i t/L_i^2 \quad (3)$$

T_o is the initial temperature (at $t = 0$); α_i and L_i are the thermal diffusivity and thickness of slab 1. The constant γ_i is given by

$$\gamma_i = \frac{\alpha_1 L_i^2}{\alpha_i L_i^2}$$

All slabs are assumed to be at uniform temperature T_o at $t = 0$, i.e.,

$$\theta_i(X_i, 0) = 1.0 \quad \text{for } i = 1 \text{ to } n \quad (4)$$

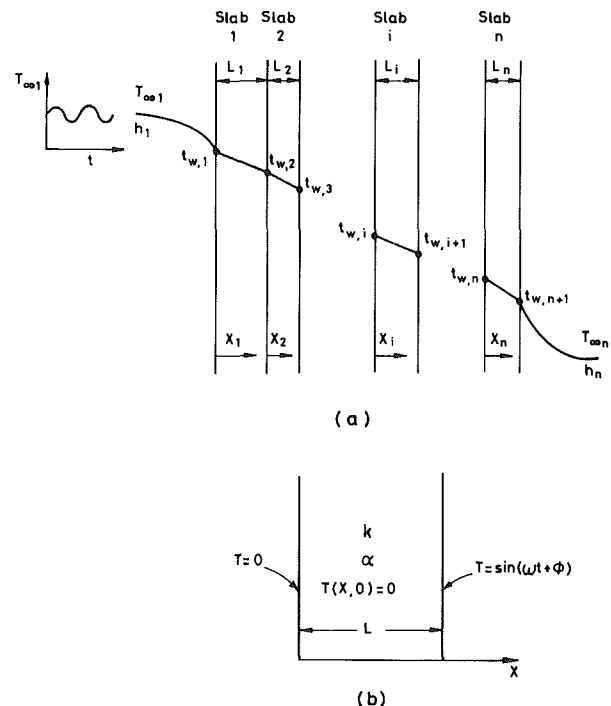


Fig. 1 Description sketch of problem and test case 3

Boundary Conditions. In this problem, we have $2n$ boundary conditions as follows:

$(n-1)$ conditions for the continuity of temperature distribution at the interfaces between the n slabs.

$(n-1)$ conditions for equal heat flux on each side of the $(n-1)$ interfaces between slabs.

2 convection conditions; one at the outer surface of slab 1 and one at inner surface of slab n .

The first $(n-1)$ conditions are represented by

$$\theta_{i-1}(1, \tau) = \theta_i(0, \tau) \quad \text{for } i=2 \text{ to } n \quad (5)$$

The second $(n-1)$ conditions are represented by

$$\frac{k_{i-1}}{L_{i-1}} \left(\frac{\partial \theta_{i-1}}{\partial X_{i-1}} \right)_{X_{i-1}=1} = \frac{k_i}{L_i} \left(\frac{\partial \theta_i}{\partial X_i} \right)_{X_i=0} \quad \text{for } i=2 \text{ to } n \quad (6)$$

where k_i is the thermal conductivity of slab i .

On the ambient side, the convection boundary condition is

$$\left(\frac{\partial \theta_1}{\partial X_1} \right)_{X_1=0} = -\beta_1 [\theta_{\infty 1}(\tau) - \theta_1(0, \tau)] \quad (7)$$

where β_1 is the Biot number for slab 1 ($\beta_1 = h_1 L_1 / k_1$) and $\theta_{\infty 1}(\tau)$ is the dimensionless ambient temperature, which is given by

$$\theta_{\infty 1}(\tau) = \theta_m + A \sin(\Omega \tau + \phi) \quad (8a)$$

where

$$\theta_m = (T_m - T_{\infty n}) / (T_o - T_{\infty n}); A = T_a / (T_o - T_{\infty n}); \quad \Omega = \omega L_1^2 / \alpha_1 \quad (8b)$$

On the other side of the composite wall (inner side), the convection boundary condition is expressed as

$$\left(\frac{\partial \theta_n}{\partial X_n} \right)_{X_n=1} = -\beta_n \theta_n(1, \tau) \quad (9)$$

where β_n is the Biot number for slab n ; $\beta_n = h_n L_n / k_n$.

Solution of Differential Equations in the s -Domain. The problem is described by the system of differential equations (2) subject to the initial condition of Eq. (4) and the boundary conditions of Eqs. (5), (6), (7), and (9). The approach adopted here is similar to that used by Mujahid and Zedan (1990) to solve the case of a three-slab composite wall subjected to a sudden change in ambient temperature. In this approach the equations are solved in the Laplace s -domain for the temperatures $\bar{\theta}_i(X, s)$, which are then transformed back to the time domain.

The Laplace transform of Eq. (2) is

$$\frac{d^2 \bar{\theta}_i}{dX_i^2} = \gamma_i (s \bar{\theta}_i(X_i, s) - \theta_i(X_i, 0)) \quad (10)$$

where $\bar{\theta}_i(X_i, s)$ is the Laplace transformation of $\theta_i(X_i, \tau)$ and $\theta_i(X_i, 0) = 1$ from the initial condition of Eq. (4). The solution of Eq. (10) is

$$\bar{\theta}_i(X_i, s) = a_i e^{\sqrt{s\gamma_i} X_i} + b_i e^{-\sqrt{s\gamma_i} X_i} + \frac{1}{s} \quad (11)$$

The $2n$ unknown coefficients a_i and b_i are determined from the $2n$ boundary conditions discussed above. In the s -domain, Eq. (5) becomes

$$\bar{\theta}_{i-1}(1, s) = \bar{\theta}_i(0, s)$$

Using Eq. (11), the above equation becomes

$$a_{i-1} e^{\sqrt{s\gamma_{i-1}}} - a_i + b_{i-1} e^{-\sqrt{s\gamma_{i-1}}} - b_i = 0 \quad \text{for } i=2 \text{ to } n. \quad (12)$$

The Laplace transform of Eq. (6) leads to

$$a_{i-1} \left(\sqrt{s\gamma_{i-1}} e^{\sqrt{s\gamma_{i-1}}} \right) - a_i \left(\sqrt{s\gamma_i} \frac{k_i}{k_{i-1}} \frac{L_{i-1}}{L_i} \right) - b_{i-1} \left(\sqrt{s\gamma_{i-1}} e^{-\sqrt{s\gamma_{i-1}}} \right) + b_i \left(\sqrt{s\gamma_i} \frac{k_i}{k_{i-1}} \frac{L_{i-1}}{L_i} \right) = 0 \quad (13)$$

for $i=2$ to n . The Laplace transform of Eq. (7) gives

$$\left. \frac{d\bar{\theta}_1}{dX_1} \right|_{X_1=0} = -\beta_1 (\bar{\theta}_{\infty 1}(s) - \bar{\theta}_1(0, s)) \quad (14)$$

The Laplace transformation of $\theta_{\infty 1}(\tau)$ is

$$\bar{\theta}_{\infty 1}(s) = \theta_m/s + A \left(\frac{\Omega \cos \phi + s \sin \phi}{s^2 + \Omega^2} \right) \quad (15)$$

Substituting for $\bar{\theta}_1$ from Eq. (11) into Eq. (14), then

$$a_1 (\sqrt{s\gamma_1} - \beta_1) - b_1 (\sqrt{s\gamma_1} + \beta_1) = -\beta_1 \bar{\theta}_{\infty 1}(s) + \beta_1/s \quad (16)$$

The remaining equation is the transformation of Eq. (9),

$$\left(\frac{d\bar{\theta}_n}{dX_n} \right)_{X_n=1} = -\beta_n \bar{\theta}_n(1, s)$$

Substituting for $\bar{\theta}_n$ from Eq. (11), this equation gives

$$a_n e^{\sqrt{s\gamma_n}} (\beta_n + \sqrt{s\gamma_n}) + b_n e^{-\sqrt{s\gamma_n}} (\beta_n - \sqrt{s\gamma_n}) = -\beta_n/s \quad (17)$$

Now the unknown $2n$ coefficients a_i and b_i are obtained by solving a system of $2n$ simultaneous linear algebraic equations. This system is set up by applying Eqs. (12) and (13) for $i=2$ to n giving $(2n-2)$ equations, while Eqs. (16) and (17) are used to complete the system. Once the coefficients a_i and b_i are known for all slabs, one can obtain $\theta_i(X_i, s)$ by using Eq. (11).

Transformation of Solution Back to Time Domain. The general inverse transform method known as the Fourier series technique (Chu et al., 1982) is used here to obtain $\theta_i(X_i, \tau)$ from $\theta_i(X_i, s)$. According to this work the inverse transformation $\phi(\tau)$ of a function $\phi(s)$ in the s -domain is approximated by

$$\phi(\tau) \cong \frac{e^{c\tau}}{\tau} \left[\frac{1}{2} \bar{\phi}(c) + R_e \left(\sum_{i=1}^N \bar{\phi} \left(c + \frac{ik\pi}{\tau} \right) (-1)^i \right) \right] \quad (18)$$

where N is the number of terms retained in the summation and c is a constant. This equation is used to obtain the temperature $\theta(X, \tau)$ in any slab from the solution in the Laplace domain $\theta(X, s)$. Chu et al. (1982) suggested that the optimum value of c is obtained when $c\tau$ is somewhere between 4 and 5 based on their results for a fin problem. Mujahid and Zedan (1990) used the known analytic solution of a single slab subjected to a sudden change in ambient temperature to obtain an optimum value for $c\tau = 3$. Results in agreement with the exact solution to plotting accuracy were obtained with N as little as 50.

Results and Discussions

The method described above was programmed on a PC-AT microcomputer. The performance of the method, which is exact except in the evaluation of the inverse Laplace transform, is examined using test cases with known solutions.

Steady Periodic Conduction in a Single Slab. An exact steady periodic solution for a single slab with boundary conditions similar to those in the present study was given by Kauschik et al. (1981). A separate program was developed based on the present Laplace transform method for this case. The results obtained from this "slab" program with $c\tau = 3.0$ and $N = 50$ are compared with the exact solution in Fig. 2 for a

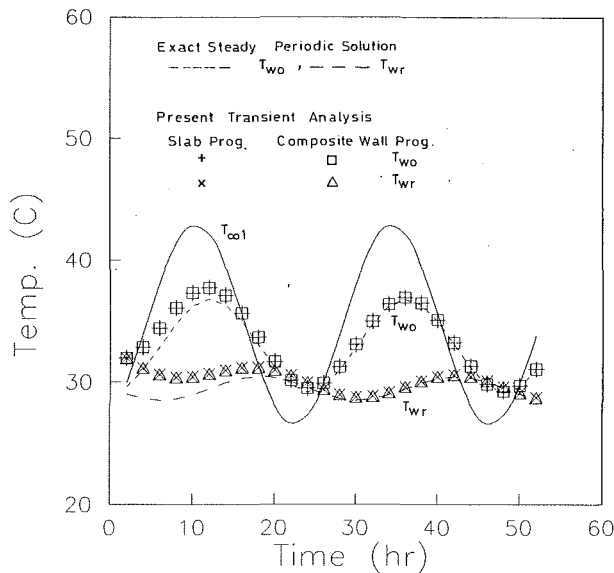


Fig. 2 Comparison of results of the single slab and the composite wall test cases for a typical summer ambient temperature

single slab with the following data: $L=0.2$ m, $k=1$ W/m \cdot K, $\alpha=0.45 \times 10^{-6}$ m 2 /s, $h_1=10$ W/m 2 \cdot K and $h_2=5$ W/m 2 \cdot K, for a typical summer ambient conditions in Riyadh (latitude = 24.6 $^\circ$ N): $T_m=34.72^\circ$ C, $T_a=8.14^\circ$ C, $\phi=-66.08$ deg, and of course ω is such that the period is 24 h. T_o was assumed equal to 34 $^\circ$ C. The results show perfect agreement with the exact solution for both the outside and inside wall surface temperatures after the present solution reaches steady periodic behavior. In the transient region, the results are different since the exact solution is for the steady periodic response only. The initial wall temperature was changed several times; as expected the transient part of the response changed while the steady part stayed the same.

Steady Periodic Conduction in a Composite Wall. Now we need to verify the method for a composite wall to make sure the boundary conditions at the slab interfaces are considered properly. Since there is no exact solution for this case, we considered a composite wall made of three slabs with the same properties and compared the results of the method with those obtained by the single "slab" program and by the exact solution for a slab with thickness $L=L_1+L_2+L_3$. A composite wall with $L_1=2$ cm, $L_2=17$ cm, and $L_3=1$ cm, $k_1=k_2=k_3=1$ W/m \cdot K, $\alpha_1=\alpha_2=\alpha_3=0.45 \times 10^{-6}$ m 2 /s, $h_1=10$ W/m 2 \cdot K and $h_3=5$ W/m 2 \cdot K was considered. Note that this composite wall is identical with the single slab considered in the previous test case. The composite wall program was run for this case with the same $T_{\infty 1}$ variation, T_o , and $T_{\infty 3}$ used before. The results shown in Fig. 2 for the composite wall and the single slab programs agree perfectly everywhere; the results of the exact solution, which agree with both in the steady periodic region, are represented by dashed lines. Similar comparisons made for different $T_{\infty 1}$ variations and different L_1 , L_2 , and L_3 and wall properties gave similar agreement indicating that the method is quite robust, at least in predicting the steady periodic response, over a wide range of parameters.

Transient Conduction in a Single Slab With Periodic Surface Temperature. The results of the previous two test cases showed some differences between the present solution and the exact solution for small times. This is attributed to transient effects, which are not accounted for in the exact solutions presented. In this test case, we verify the transient predictions

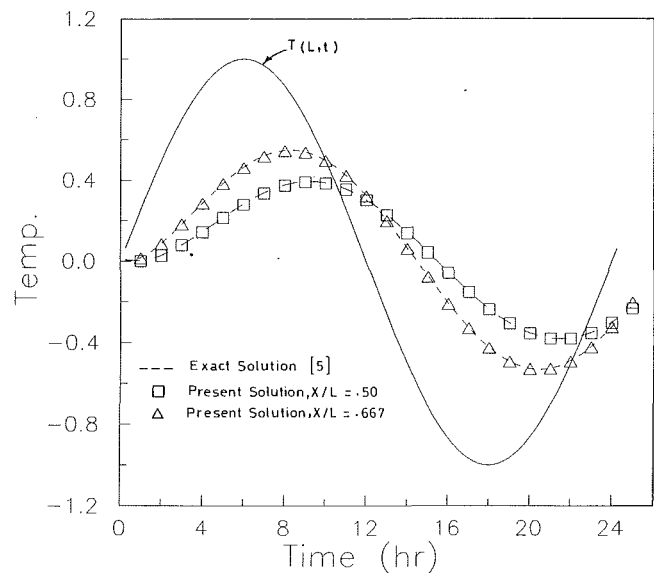


Fig. 3 Comparison of the computed transient response of a single slab with the exact solution

of the method for a single slab ($0 \leq x \leq L$) with the initial and boundary conditions shown in Fig. 1(b). The exact complete solution for this case is given by Carslaw and Jaeger (1972). The present method was adapted for a single slab with the above initial and boundary conditions and run for a case with $L=0.24$ m, $\alpha=0.5 \times 10^{-6}$ m 2 /s, $\omega=2\pi/(24 \times 3600)$ s $^{-1}$ and $\phi=0$. The results are compared with the exact solution in Fig. 3 at $x/L=0.5$ and 0.6667 . Excellent agreement is obvious at both locations and at all times indicating that the present method predicts the transient response with essentially the same accuracy with which it predicts the steady periodic response. The maximum error in the dimensionless temperature is about 0.004, which translates to about 0.7 percent near the peaks of the response.

Summary and Concluding Remarks

An analytic solution was developed for the heat transfer in a composite wall with periodic ambient temperature on one side and a constant-temperature fluid on the other side. A number of test cases with exact solutions showed that the method is accurate in predicting the transient and the steady periodic parts of the response. Computationally, the method is very efficient in the sense that the solution is only obtained at the points(s) of interest and not at all grid points as in finite difference methods.

References

- Carslaw, H. S., and Jaeger, J. C., 1972, *Conduction of Heat in Solids*, Oxford Press, pp. 105-109.
- Chu, H., Chen, C., and Weng, C., 1982, "Applications of Fourier Series Techniques To Transient Heat Transfer Problem," *Chem. Eng. Commun.*, Vol. 16, pp. 215-225.
- Kaushik, S. C., Sodha, M. S., Bhardwaj, S. C., and Kaushik, N. D., 1981, "Periodic Heat Transfer and Load Leveling of Heat Flux Through a PCCM Thermal Storage Wall/Roof in an Air-Conditioned Building," *Building and Environment*, Vol. 16, No. 2, pp. 99-108.
- McQuiston, F. C., and Parker, J. D., 1988, *Heating, Ventilating, and Air Conditioning: Analysis and Design*, 3rd ed., Wiley, New York, pp. 245-253.
- Mujahid, A. M., and Zedan, M. F., 1990, "Transient Heat-Conduction Response of a Composite Plane Wall," *Wärme- und Stoffübertragung*, Vol. 26, pp. 33-39.

Development of an Algebraic Model to Predict the Heat Transfer for Turbulent Flow in a Rod Bundle

Nae-Hyun Kim,¹ Sang-Keun Lee,² and Si-Hwan Kim²

Nomenclature

A = flow area, m²
 C_p = specific heat, J/kg K
 D = rod diameter, m
 D_h = hydraulic diameter, m
 f = friction factor
 h = heat transfer coefficient = $q''/(T_w - \bar{T})$, W/m²K
 k = thermal conductivity, W/mK
 L = half the rod spacing, m
 Nu = Nusselt number = $h D_h/k$
 p = rod pitch, m
 Pr = Prandtl number = $\mu C_p/k$
 q'' = heat flux, W/m²
 R = rod radius, m
 Re = Reynolds number = $\rho \bar{u} D_h/\mu$
 St = Stanton number = $h/\rho \bar{u} C_p$
 T = temperature, K
 T^+ = dimensionless temperature = $(T_w - \bar{T})\rho C_p u^*/q''$
 u = velocity, m/s
 u^+ = dimensionless velocity = u/u^*
 u^* = friction velocity = $\sqrt{\tau_w/\rho}$, m/s
 y = coordinate normal to the flow direction, m
 y^+ = dimensionless y coordinate = yu^*/ν
 μ = viscosity, Ns/m²
 ν = kinematic viscosity, m²/s
 τ_w = wall shear stress, N/m²
 ρ = density, kg/m³

Subscripts and Superscripts

h = based on hydraulic diameter
 i = related to the inlet
 m = measured data
 p = predicted value
 s = based on smooth tube
 w = related to the wall
 $\bar{\quad}$ = averaged value

1 Introduction

The fundamental theoretical work on rod bundle heat transfer was performed by Deissler and Taylor (1956). They obtained an expression for the friction and heat transfer coefficients of an infinite array. Further theoretical work was done by a number of investigators. The theoretical studies, however, referred to rod bundles of an infinite extension only, i.e., they excluded the influence of channel wall on heat trans-

fer. Heat transfer experiments are inevitably conducted in a channel with a limited number of rods. Thus, for correct interpretation of the results, the influence of channel wall should be accounted for. None of the above theoretical analyses considered the effect of channel wall.

Marek et al. (1973) presented the heat transfer data (shown in Fig. 7 in their paper). In the figure, measured Nusselt numbers were normalized by the Dittus-Boelter correlation, which is $Nu_{D-B} = 0.023 Re^{0.8} Pr^{0.4} (T_w/T_i)^{-0.2}$. The figure showed approximately ± 20 percent scatter of data. One possible cause of the scatter may be the wrong choice of the predictive correlation. The hydraulic diameter concept in the Dittus-Boelter correlation may not be adequate to represent the complex bundle geometry, e.g., rod pitch to diameter ratio (p/D) or wall gap to rod diameter ratio (W/D), on which the heat transfer should depend. In this study, an analytic model that accounts for those effects is developed assuming the validity of the universal velocity and temperature profile across the flow area.

2 Theoretical Development

Developed turbulent velocity profile measurements in pipe flow in a region outside the viscous sublayer ($y^+ > 26$) are well described by the universal velocity profile, that is,

$$u^+ = 2.5 \ln y^+ + 5.5 \quad (1)$$

By analogy, developed temperature profile may be expressed in a similar form:

$$T^+ = A_s \ln y^+ + B_s \quad (2)$$

Equation (2) is known as the universal temperature profile. Gowen and Smith (1967) measured the temperature profile for a range of Prandtl number ($0.7 < Pr < 14$), and obtained correlations for A_s and B_s . The values of A_s are given in the Gowen and Smith (1967) paper. They are approximately constant ($2.2 < A_s < 2.5$) over the Pr range. However, B_s is strongly dependent on Prandtl number, and is given by

$$B_s = 5 \ln \left(\frac{5Pr + 1}{30} \right) + 8.55 + 5 Pr \quad (3)$$

The friction factor in a circular tube is well predicted assuming Eq. (1) applies over the entire pipe radius. With the identity $\bar{u}/u^* = \sqrt{2/f}$ and $y^+ = yu^*/\nu = y/D Re \sqrt{f/2}$, Eq. (1) may be integrated over the entire radius

$$\frac{\bar{u}}{u^*} = \sqrt{\frac{2}{f}} = 2\pi \int_0^R \left[2.5 \ln \left(\frac{y}{D} \sqrt{\frac{f}{2}} Re \right) + 5.5 \right] (R - y) dy \quad (4)$$

The result is

$$\sqrt{2/f} = 2.5 \ln (Re \sqrt{f/2}) + 1.75 \quad (5)$$

The Nusselt number (or Stanton number) in circular tubes may be obtained by integrating Eqs. (1) and (2) over the entire pipe cross section.

$$\frac{1}{St} = \frac{Re Pr}{Nu} = \frac{1}{A} \int_A (2.5 \ln y^+ + 5.5)(A_s \ln y^+ + B_s) dA \quad (6)$$

The friction factor is needed for evaluation of y^+ in Eq. (6). The friction factor is obtained by solving Eq. (5) iteratively. The Stanton numbers predicted using Eq. (6) were compared with the well-accepted heat transfer correlations, and they agreed reasonably well.

The idea may also be applied to predict the heat transfer coefficients in a rod bundle. The cross-sectional flow channel (A) may be divided into a number of element channels ($A_1, A_2, A_3, \dots, A_n$). Writing the continuity equation assuming uniform density across the flow area,

¹Kum-Oh National Institute of Technology, 188 Shinpyung-Dong, Kumi-City, Kyungbuk, Korea.

²Korea Atomic Energy Research Institute, P.O. Box 7, Daeduck-Danji, Taejeon, Korea.

Contributed by the Heat Transfer Division of THE AMERICAN SOCIETY OF MECHANICAL ENGINEERS. Manuscript received by the Heat Transfer Division March 1991; revision received March 1992. Keywords: Forced Convection, Nucleonics. Associate Technical Editor: J. H. Kim.

$$\bar{u}A = \bar{u}_1 A_1 + \bar{u}_2 A_2 + \dots + \bar{u}_n A_n \quad (7)$$

Dividing by u^* and using the identity $\bar{u}/u^* = \sqrt{2/f}$, Eq. (7) becomes

$$\sqrt{2/f} = \frac{\bar{u}_1}{u^*} \frac{A_1}{A} + \frac{\bar{u}_2}{u^*} \frac{A_2}{A} + \dots + \frac{\bar{u}_n}{u^*} \frac{A_n}{A} \quad (8)$$

where

$$\frac{\bar{u}_i}{u^*} = \frac{1}{A_i} \int_{A_i} u^+ dA_i \quad (9)$$

The friction velocity u^* is defined as $\sqrt{\bar{\tau}_w/\rho}$. For a smooth tube, local wall shear stress τ_w is uniform peripherally, and is the same as the average wall shear stress $\bar{\tau}_w$. For a rod bundle, however, τ_w may vary along the rod periphery. The measurement by Subbotin et al. (1971) shows that τ_w varies significantly along the rod periphery when the pitch-to-diameter ratio p/D is close to 1. For $p/D > 1.2$, however, τ_w is almost uniform peripherally. In this study, the local wall shear stress τ_w is assumed to be the same as the bundle average wall shear stress $\bar{\tau}_w$. This may be a reasonable assumption for the rod bundles with $p/D > 1.2$. For $p/D < 1.2$, the assumption may cause some error. However, the error may not be significant, considering that the integration and addition process involved in evaluating the friction factor by Eq. (8) may smooth out the local effects. Then, the expressions for \bar{u}_i/u^* for each region may be obtained by integrating Eq. (1) over each region. The procedure is described below:

- 1 Divide the flow channel (A) into a number of element channels. The general rule involved in the channel division is described in the following section.
- 2 Formulate \bar{u}_i/u^* for each element channel. The integration is

$$\bar{u}_i/u^* = \int_{A_i} \left[2.5 \ln \left(\frac{y}{D_h} \text{Re} \sqrt{f/2} \right) + 5.5 \right] dA_i \quad (10)$$

In Eq. (10), the friction factor f is still unknown.

- 3 Substitute Eq. (10) into Eq. (8). The friction factor is obtained by iteratively solving the right-hand side and left-hand side of Eq. (8). Using the method, Kim et al. (1991) could predict the friction factors of various rod bundles reasonably well.

From the definition of mixing cup temperature \bar{T} , and assuming uniform density across the flow area,

$$\bar{u}(T_w - \bar{T})A = \bar{u}_1(T_w - \bar{T}_1)A_1 + \bar{u}_2(T_w - \bar{T}_2)A_2 + \dots + \bar{u}_n(T_w - \bar{T}_n)A_n \quad (11)$$

Multiplying by C_p/Aq'' , and using the definition of Stanton number and heat transfer coefficient h , Eq. (11) becomes

$$\frac{1}{St} = \frac{1}{St_1} \frac{A_1}{A} + \frac{1}{St_2} \frac{A_2}{A} + \dots + \frac{1}{St_n} \frac{A_n}{A} \quad (12)$$

where

$$\frac{1}{St_i} = \frac{1}{A_i} \int_{A_i} u^+ T^+ dA_i \quad (13)$$

In the preceding equations, the wall temperature T_w is assumed to be uniform peripherally. This may be a reasonable assumption for the rod bundles with $p/D > 1.2$. For $p/D < 1.2$, the assumption may cause some error. However, the error may not be significant based on the same reasoning we provided for the evaluation of the friction factor, i.e., the integration and averaging process may smooth out the local temperature variation effects.

To obtain the Stanton number from Eq. (12), temperature

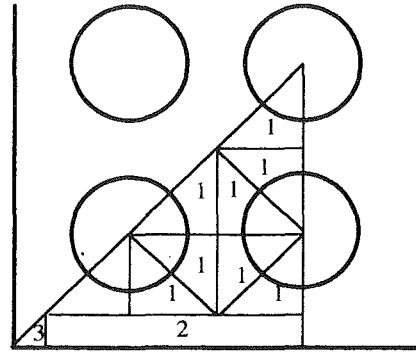


Fig. 1 Subarea division of a rod bundle tested by Dingee et al. (1955)

and velocity profiles in a rod bundle are needed. As a first approximation, smooth tube velocity and temperature profiles [Eqs. (1) and (2)] are used. The friction factors needed for the calculation of u^+ and T^+ are obtained from Eq. (8) following the procedure described previously. In the following sections, this procedure will be applied to various rod bundle geometries.

3 Application to a Rod Bundle

The current method is applied to predict the rod bundle heat transfer data. Rod bundle heat transfer experiments are inevitably conducted with heater rods enclosed by a channel wall. The wall region needs some treatments because the wall usually does not generate heat during the experiment. Wall region may be divided into two subareas: Area 1, which is affected by the rod, and Area 2, which is affected by the wall. In Area 1, smooth tube velocity and temperature profiles may be used to evaluate the Stanton number. In Area 2, smooth tube velocity profile may be assumed; however, we have trouble defining the temperature profile because the wall does not generate heat. In this study, T^+ in Area 2 is assumed zero following the suggestion by Dalle Donne and Meyer (1977). Then, the friction factor and the Stanton number at the wall region become

$$\frac{\bar{u}_{\text{wall}}}{u^*} = \frac{1}{\text{Area 1} + \text{Area 2}} \int_{\text{Area 1} + \text{Area 2}} u^+ dA \quad (14)$$

$$\frac{1}{St_{\text{wall}}} = \frac{1}{\text{Area 1} + \text{Area 2}} \int_{\text{Area 1}} u^+ T^+ dA \quad (15)$$

The bundle average friction and heat transfer coefficients are obtained by substituting Eqs. (14) and (15) as well as those of other element channels into Eqs. (8) and (12). The following example illustrates the usage of the current method.

Figure 1 shows a quarter section of the rod bundle tested by Dingee et al. (1955). The elemental subareas are also shown. The general rules applied to the division of subareas are: (1) The zero shear stress line is drawn whenever identifiable, (2) if not possible, a straightline is drawn at the shortest gap position. The zero shear stress line may be easily identified between rods. In the gap region, however, it is not easily identifiable, and thus, a straight line is drawn at the shortest gap position. The error associated with different element divisions at the wall gap region was estimated, and they were less than 1 percent in the measure of heat transfer coefficient.

Equations (1) and (2) are integrated for each subarea, and the friction factor and the Stanton number are obtained from Eqs. (8) and (12). For the Stanton number, only Area 1 in Fig. 1 needs to be considered. Areas 2 and 3 are the wall-affected sub channels, and assumed not to contribute to the heat transfer. The results are compared with the data of Dingee et al. (1955) in Fig. 2. The figure shows that current method predicts the data reasonably well.

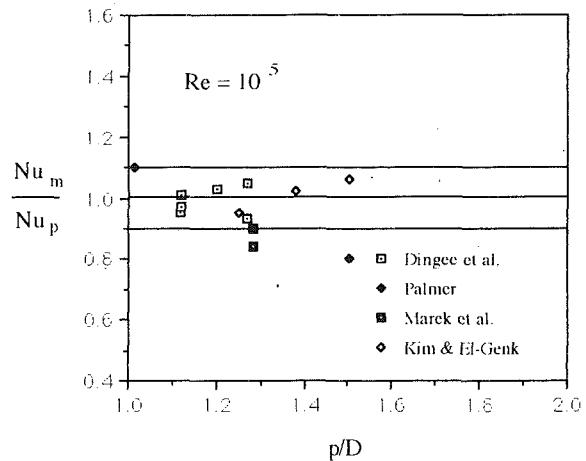


Fig. 2 Prediction of the available bundle heat transfer data

Table 1 Compilation of rod bundle heat transfer experiments

Author	Year	# of rods	p/D	W/D	Rod Array	Pr
Dingee et al.	1955	9 9 9	1.12 1.20 1.27	1.12 1.20 1.27	square and triangular	1.18 to 1.75
Palmer and Swanson	1962	7	1.015	1.015	triangular	1.1 - 2.6
Marek et al.	1973	9 16	1.283 1.283	1.23 1.27	square	0.7
Kim and El-Genk	1989	7 7 7	1.25 1.38 1.5	1.07 1.13 1.19	triangular	3.0 - 8.5

A number of heat transfer tests have been conducted for the past 30 years. The current method is applied to predict the available data. Table 1 is a compilation of studies available to the authors. The studies cover both square and triangular arrays, $1.015 \leq p/D \leq 1.462$ and $0.7 \leq Pr \leq 8.5$. Predictions were made at $Re = 10^5$, and the results are shown in Fig. 2. In the figure, experimental data (Nu_m) are normalized by the predicted values (Nu_p).

Figure 2 shows that the current method predicts most of the data within ± 10 percent, which is a significant improvement compared with the prediction by the Dittus-Boelter correlation [shown in Fig. 7 of Marek et al. (1973)]. Figure 2 shows that the current model reasonably predicts Palmer and Swanson's data. The p/D ratio of Palmer and Swanson's bundle is 1.015. It is well known that as the p/D ratio approaches to 1.0, wall shear stress and temperature distribution around the rod becomes highly nonuniform. In this study, uniform wall shear stress and temperature distribution is assumed. The integrating and additive nature of the current model may have smoothed out the peripheral nonuniformity.

The data by Marek et al. (1973) are about 15 percent overpredicted. Marek et al. used helium gas as a heat transfer medium, and the rod wall temperature was as high as 700°C . At such high temperatures, the temperature difference between the rod wall and the flowing medium would be considerable, and also the density variation across the flow area. The strong density variation may affect the temperature or velocity profile, and eventually make the current model overpredict the data. It is not clear how the density variation would affect the temperature or velocity profile. However, the resulting heat trans-

fer coefficients should decrease, compared with the case when uniform density is assumed. This point may also be confirmed from the fact that heat transfer correlations are usually modified when the temperature difference between the wall and the flowing medium is large. For example, the Dittus-Boelter correlation is multiplied by $(T_w/T_i)^{-0.2}$ to account for large temperature differences. When the ratio of T_w/T_i is large, the Nusselt number obtained from the original Dittus-Boelter correlation highly overpredicts the modified one. For example, the Nusselt number calculated from the modified Dittus-Boelter correlation at $T_w/T_i = 2.0$ is approximately 13 percent smaller than that calculated at $T_w/T_i = 1.0$. The T_w/T_i values of Marek et al. were not available to the authors. However, the fact that the rod wall temperature was as high as 700°C suggests that the value of T_w/T_i may have been considerable. To predict the data obtained at high rod wall temperatures, density variation should be taken into account in the predictive model. The current model assumes constant density across the flow area. Thus, caution should be taken when applying the current model to high wall temperature reactors such as gas-cooled reactors.

4 Conclusion

In this study, an analytic model was developed to predict the Nusselt number for turbulent flow in a rod bundle. A flow channel area is divided into several element channels, and the simple algebraic equations of the universal velocity profile and temperature profile are integrated over each element channel. The integral equations are then added to yield an analytic expression for the Nusselt number of a rod bundle. The analytic model predicts the available heat transfer data within ± 10 percent except for those of Marek et al. (1973). Their data are approximately 15 percent overpredicted. Marek et al. conducted experiments at high rod wall temperatures, and consequently large density variation should have occurred. The current model assumes uniform density across the flow area, which is not appropriate for the case of Marek et al. Besides, the strong density variation may affect the velocity or temperature profiles. Thus, caution should be taken when applying the current model to high wall temperature reactors such as gas-cooled reactors.

References

- Dalle Donne, M., and Meyer, L., 1977, "Turbulent Convective Heat Transfer From Rough Surfaces With Two-Dimensional Rectangular Ribs," *Int. J. Heat Transf. Vol. 20*, pp. 583-620.
- Deissler, R. G., and Taylor, M. F., 1956, "Analysis of Axial Turbulent Flow and Heat Transfer Through Banks of Rods or Tubes," *Proceedings of Reactor Heat Transfer Conference*, Pt. 1, Book 2, TID-7529, USAEC, pp. 416-461.
- Dingee, D. A. Bell, W. B., Chastain, J. W., and Fawcett, S. L., 1955, "Heat Transfer From Parallel Rods in Axial Flow," Report BMI-1026, TID-4500, USAEC.
- Gowen, R. A., and Smith, J. W., 1967, "The Effect of the Prandtl Number on Temperature Profiles for Heat Transfer in Turbulent Pipe Flow," *Chem. Eng. Sci.*, Vol. 22, pp. 1701-1711.
- Kim, N.-H., Chun, T.-H., Lee, S.-K., and Kim, S.-H., 1991, "Application of the Law of the Wall to Predict the Turbulent Friction Factor in Rod Bundles," *1st JSME/ASME Joint International Conference on Nuclear Engineering*, Tokyo, Japan, Nov. 4-7, Vol. 1, pp. 231-235.
- Kim, S.-H., and El-Genk, M. S., 1989, "Heat Transfer Experiments for Low Flow of Water in Rod Bundles," *Int. J. Heat Mass Transfer*, Vol. 32, No. 7, pp. 1321-1336.
- Marek, J., Maubach, K., and Rheme, K., 1973, "Heat Transfer and Pressure Drop Performance of Rod Bundles Arranged in Square Arrays," *Int. J. Heat Mass Transfer*, Vol. 16, pp. 2215-2228.
- Palmer, L. D., and Swanson, L. L., 1962, "Measurement of Heat Transfer Coefficients, Friction Factors and Velocity Profiles for Air Flowing Parallel to Closely Spaced Rods," *International Developments in Heat Transfer*, ASME, pp. 535-542.
- Subbotin, V. I., Ushakov, P. A., Levchenko, Yu. D., and Alexandrov, A. M., 1971, "Velocity Fields in Turbulent Flow Past Rod Bundles," *Heat Transfer—Soviet Research*, Vol. 3, No. 2, Mar.-April, pp. 9-35.

Solidification of a Flowing Liquid Inside a Pipe Subject to Radiation and Convection

B. T. F. Chung,¹ S. Gulati,¹ and A. K. Dalmia¹

Nomenclature

- Bi_f = Biot number based on flow radius = $h_1 R_f / k$
 Bi_R = Biot number based on pipe radius = $h_1 R / k$
 h_1 = combined outer heat transfer coefficient and pipe conductance [$1/h_1 = 1/h_0 + \ln(R_0/R)/k_0$]
 h_0, h_2 = outer and inner heat transfer coefficients, respectively
 k, k_0 = conductivity of solidified layer and pipe material, respectively
 P_h = phase change number, or inverse of Stefan number = $\alpha \rho L / k T_f$
 R, R_0, R_f = inner pipe radius, outer pipe radius, and flow radius, respectively
 T_a, T_f, T_s = environment, melting, and superheat temperatures, respectively
 $R1$ = dimensionless radiation parameter = $\sigma \epsilon T_f^3 / h_1$
 α = thermal diffusivity of solid phase
 η = dimensionless time = $h_1^2 t \alpha / k^2 P_h$
 θ_s = superheat parameter = T_s / T_f
 θ_a = dimensionless ambient temperature = T_a / T_f
 θ_{hr} = combined superheat and heat transfer ratio parameter = $(\theta_s - 1) h_2 / h_1$
 θ_{hrC} = critical value of θ_{hr}
 θ_{hrU} = limiting value of θ_{hr}

Introduction

Heat transfer with solidification of liquid involving initial superheat temperature and forced convection at the interface has significant applications in the thin-walled casting process. Recently, the concept of using a thin solidified layer of liquid metal inside a pipe to prevent contamination or reactions between the melting and the container material has attracted considerable attention in material processing. However, the maintenance of the solidified layer inside a pipe is difficult to achieve. As pointed out by Wang and Perry (1988), since the associated phase-change problem involves complete interaction between the material properties, the pipe sizes, and the processing conditions, the process window is extremely difficult to define without a systematic scheme to quantify the parametric relationships. These authors presented a mathematical model for understanding the parametric relationship in forming a stable solidified layer and identifying the criterion for process control. However, their model does not involve thermal radiation and leads to the conclusion that a stable solidified layer can never be formed if the Biot number based on the inner pipe radius is less than unity. Furthermore, the authors have

¹Department of Mechanical Engineering, The University of Akron, Akron, OH 44325-3903.

Contributed by the Heat Transfer Division of THE AMERICAN SOCIETY OF MECHANICAL ENGINEERS. Manuscript received by the Heat Transfer Division March 5, 1992; revision received July 10, 1992. Keywords: Forced Convection, Moving Boundaries, Radiation. Associate Technical Editor: Y. Bayazitoglu.

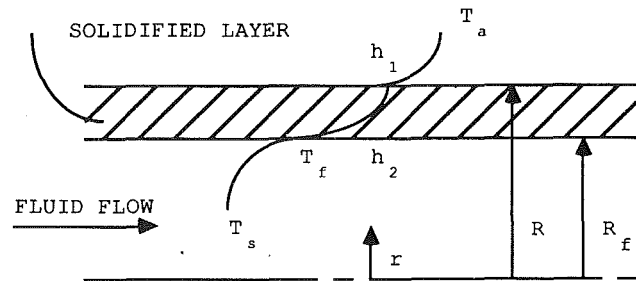


Fig. 1 Schematic diagram of the formation of a solidified layer in a fluid flowing through a pipe

not given any justification for the assumed first-order logarithmic temperature profile in their analysis.

This work extends the study of Wang and Perry (1988) by including the radiation effect and develops the process window for the case involving both radiation and forced convection at the outer surface of the pipe. Goodman's (1958) approximate analytical method is employed; the same problem is then solved using the finite element method in order to assess the accuracy of the first-order logarithmic temperature profile, as well as that of the integral method used. The problem is then further extended to include the axial conduction effect of the solid and the liquid. The transient solution for solidified layer is obtained numerically for various length to diameter ratios of the pipe.

Mathematical Analysis

Consideration is given to the system shown in Fig. 1 where a liquid initially at a superheat temperature T_s ($T_s > T_f$) flows inside a pipe. Due to the external cooling by simultaneous radiation and forced convection, solidification takes place inside the pipe. Forced convective heat transfer occurs at the interior phase interface due to the flow of the liquid inside the pipe. The following analysis and discussion aim at determining the transient buildup of the solidified layer with an emphasis on the formation of a stable layer. The following assumptions are made in the present analysis:

(1) Only radial heat transfer is considered in the part of the analysis using the integral approach, since the system under consideration is axisymmetric (axial conduction will be included in the numerical approach). (2) The internal heat transfer coefficient at the interface, h_2 , is constant. The assumption is reasonable if the solidified layer is thin, which is mostly true for a stable solidified layer. (3) All the thermal properties are temperature independent. (4) Without losing generality mathematically the ambient and environment temperatures are set equal. (5) The thermal entrance effect is neglected because the observed problems are in the fully developed region. (6) For completeness, the radial thermal conductance of the pipe is absorbed inside the expression of h_1 (see nomenclature) in which the external heat transfer coefficient h_0 is assumed constant.

The governing equation of the solidified layer at any time is

$$\frac{1}{r} \frac{\partial}{\partial r} \left(r \frac{\partial T}{\partial r} \right) = \frac{1}{\alpha} \frac{\partial T}{\partial t} \quad t > 0, R_f < r < R \quad (1)$$

where $t=0$ corresponds to the instant when the liquid at $r=R$ reaches T_f . Integrating the above equation with respect to r from R_f to R and utilizing Leibnitz's rule for the transient term gives

$$\frac{d\Theta}{dt} + R_f \frac{dR_f}{dt} - \alpha \left(R \frac{\partial \theta(R, t)}{\partial r} - R_f \frac{\partial \theta(R_f, t)}{\partial r} \right) = 0 \quad (2)$$

where

$$\theta = \frac{T}{T_f} \text{ and } \Theta = \int_{R_f}^R r \theta dr. \quad (3)$$

Let the temperature field within the solidified layer be approximated by a first-order logarithmic function of the following form:

$$\theta = a + b \ln(r/R_f) / \ln(R/R_f) \quad (4)$$

where b is a function of time. The applicable boundary conditions and the condition at the solid-liquid interface are

$$\theta = 1 \quad @r = R_f \quad (5)$$

$$-k \frac{\partial \theta}{\partial r} = h_1(\theta - \theta_a) + \sigma \epsilon T_f^3(\theta^4 - \theta_a^4) \quad @r = R, \eta > 0 \quad (6)$$

$$-k \frac{\partial \theta}{\partial r} + h_2(\theta_s - \theta) = \frac{\rho L}{T_f} \frac{dR_f}{dt} \quad @r = R_f, \eta > 0. \quad (7)$$

Equations (4) and (5) give $a = 1$. The second boundary condition represented by Eq. (6), when solved in conjunction with Eq. (4), yields, after simplification,

$$R1 \ln\left(\frac{Bi_R}{Bi_f}\right) C^4 + \left(\ln\left(\frac{Bi_R}{Bi_f}\right) + \frac{1}{Bi_R}\right) C - (R1 \ln\left(\frac{Bi_R}{Bi_f}\right) \theta_a^4 + \ln\left(\frac{Bi_R}{Bi_f}\right) \theta_a + \frac{1}{Bi_R}) = 0 \quad (8)$$

where $C = (1 + b)$. This equation will be used to find C or b , as we march in time. Simplifying Eq. (2) and using Eqs. (7) and (8) yields (see Dalmia, 1990)

$$\left(\frac{1}{2} \frac{b}{\ln(Bi_R/Bi_f)} Bi_f^2 + P_h Bi_f^2\right) \frac{dBi_f}{d\eta} - \left(\frac{Bi_R^2 - Bi_f^2}{4} \frac{b}{\ln(Bi_R/Bi_f)} (1 + 4R1(1 + b^3)) + \frac{Bi_R}{2} \frac{b}{\ln(Bi_R/Bi_f)}\right) \left(\frac{1}{(1 + 4R1(1 + b)^3 \ln\left(\frac{Bi_R}{Bi_f}\right) + \frac{1}{Bi_R})}\right) \cdot \frac{dBi_f}{d\eta} - P_h Bi_f \left(Bi_f \theta_{hr} + \frac{b}{\ln(Bi_R/Bi_f)}\right) = 0. \quad (9)$$

Equation (9) when solved in combination with Eq. (8) gives the dimensionless solid-liquid phase line Bi_f as a function of time. When θ_a and $R1$ are set equal to zero, Eqs. (8) and (9) give a solution identical to that of Wang and Perry (1988).

To determine the accuracy of the logarithmic temperature approximation for the solid region as well as the integral technique on solidification in pipes, a finite element solution is obtained for the above problem using the program ADINAT, which is based on the algorithm developed by Rolph and Bathe (1982). For the one-dimensional analysis, the model used is an axisymmetric one with 100 four-noded rectangular elements with each node having a single degree of freedom. Transient analysis is carried out using a lumped specific heat matrix and Euler's backward method of time integration.

The effect of axial conduction on the thickness of the solidified layer inside the pipe is considered next. In this case, as shown in Fig. 2, an axisymmetric model consisting of four-noded rectangular elements with 100 nodes along the radial direction and 10 nodes along the axis for the entire system is employed. Owing to the symmetry of the system with respect to the centerline of the pipe, a zero heat flux boundary condition is imposed along the section $A-B$ of the model. A prescribed temperature equal to the entering temperature of the flowing liquid, T_s , is input along the section $B-C$. A combined convection and radiation heat transfer to the ambient or environment is considered along the section $C-D$. Details of numerical procedures were reported by Gulati (1991).

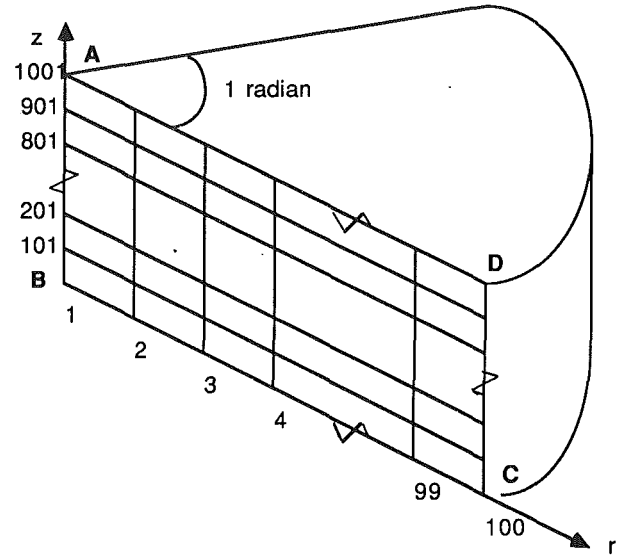


Fig. 2 Two-dimensional finite element model

Results and Discussion

Criteria for Achieving a Steady-State Solution. The criterion for achieving a steady-state solution to Eq. (9) can be derived by considering the transient and the steady-state terms separately. In the transient part, b is a dynamic variable. Numerical computations reveal that the coefficient of $dBi_f/d\eta$ is always positive for given values of $R1$ and θ_a ; therefore, the slope of the curve between Bi_f and η , i.e., $dBi_f/d\eta$, depends on the sign of the steady-state term. If the steady-state term is positive then the slope is positive and Bi_f increases with time, indicating remelting. If the steady-state term is negative then the slope is negative and Bi_f decreases with time, indicating solidification. Hence, the criterion becomes

$$Bi_f \theta_{hr} + b / (\ln(Bi_R/Bi_f)) = \begin{cases} 0 & \text{steady-state} \\ > 0 & \text{remelting} \\ < 0 & \text{solidifying.} \end{cases} \quad (10)$$

Solving the steady-state portion of Eq. (9) for θ_{hr} we have

$$\theta_{hr} = -b / (Bi_f \ln(Bi_R/Bi_f)). \quad (11)$$

The minimum point in the curve of θ_{hr} versus Bi_f specifies a critical value for θ_{hr} , i.e., θ_{hrC} . The value of θ_{hr} , for $Bi_f = Bi_R$, specifies the upper limit for θ_{hr} , i.e., θ_{hrU} . If the value of θ_{hr} is less than the critical value, then freeze-off (complete solidification) of the pipe will occur. This satisfies the solidifying criteria of Eq. (10) since it becomes less than zero. If the value of θ_{hr} is greater than the limiting value, then no layer will form, as this condition satisfies the remelting criterion in Eq. (10). Therefore a steady-state solution without freeze-off can only be achieved if the following condition is met:

$$\theta_{hrC} \leq \theta_{hr} \leq \theta_{hrU}. \quad (12)$$

The critical value of θ_{hr} is obtained by differentiating Eq. (11) with respect to Bi_f , or

$$-\frac{Bi_R[(C - \theta_a) + R1(C^4 - \theta_a^4)]}{1 + Bi_R \ln\left(\frac{Bi_R}{Bi_f}\right) (1 + 4C^3 R1)} + C - 1 - \frac{C - 1}{Bi_f \ln(Bi_R/Bi_f)} = 0. \quad (13)$$

The solution to this transcendental equation is obtained when it is solved in combination with Eq. (8). Solving for b and Bi_f from Eqs. (8) and (13) and substituting the results back in Eq. (11) gives θ_{hrC} .

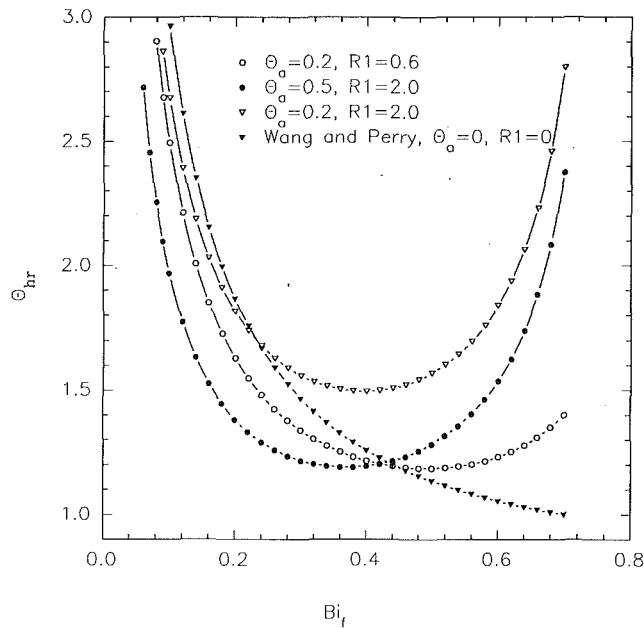


Fig. 3 Variation of θ_{hr} with Bi_f for $Bi_R = 0.7$

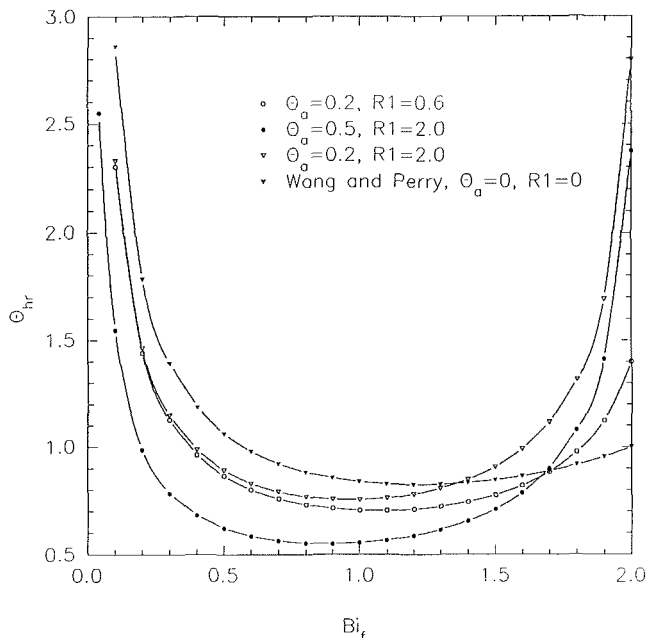


Fig. 4 Variation of θ_{hr} with Bi_f for $Bi_R = 2.0$

Since the maximum value for the flow radius cannot be greater than the pipe radius, the upper limit of θ_{hr} is obtained by setting $Bi_f = Bi_R$ in Eq. (11). Solution of Eq. (8) gives $b = 0$ under this condition and the right-hand side of equation (11) becomes an indeterminate expression. Applying L'Hospital's Rule gives

$$\lim_{Bi_f \rightarrow Bi_R} \frac{b}{\ln(R/R_f)} = -Bi_R[(1 - \theta_a) + R1(1 - \theta_a^4)] \quad (14)$$

Combining Eqs. (11) and (14) yields the upper limit of θ_{hr} for stable condition, i.e.,

$$\theta_{hrU} = [(1 - \theta_a) + R1(1 - \theta_a^4)] \quad (15)$$

with both θ_{hrU} and θ_{hrC} at hand, the steady-state region can be defined as specified by Eq. (12).

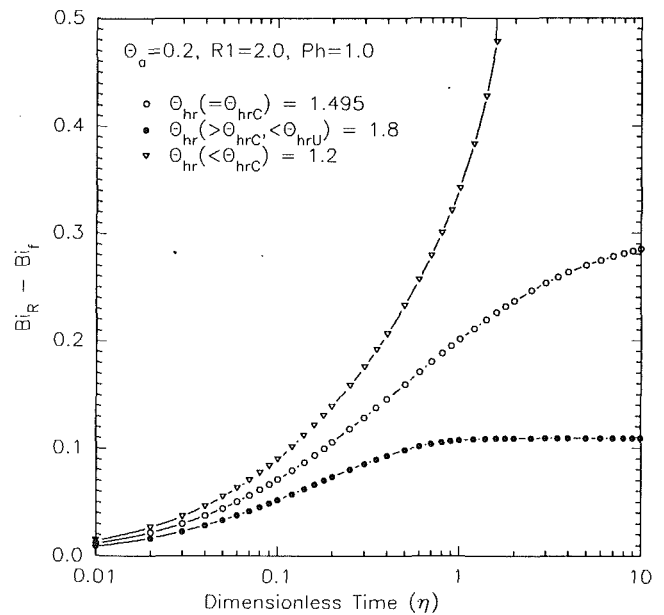


Fig. 5 Effect of θ_{hr} on the stable solidified layer for $Bi_R = 0.7$

Sensitivity Study on Dimensionless Parameters. Figure 3 shows a plot of θ_{hr} against Bi_f at $Bi_R = 0.7$. These curves have been generated by solving Eqs. (8) and (11) simultaneously. The minimum point in each curve indicates the critical value of θ_{hr} for a particular set of parameters. Figure 4 illustrates a similar case for $Bi_R > 1.0$. It is observed that as Bi_R increases from a value less than 1.0 to a value greater than 1.0, the range of Bi_f and θ_{hr} within which a stable solidified layer can be achieved also increases. From Eq. (15) it is seen that for a given value of the radiation parameter and dimensionless ambient temperature, θ_{hrU} does not change with Bi_R . Numerical computations reveal that the difference between the Biot numbers based on pipe radius and flow radius remains constant for an increasing pipe radius parameter, Bi_R .

Figure 5 shows the sensitivity of the combined superheat and heat transfer ratio parameter, θ_{hr} , on the solidified layer thickness. As θ_{hr} increases from its critical value θ_{hrC} , the thickness of the solidified layer decreases until no solidified layer is formed. However, if θ_{hr} is below the critical value, the freeze-off of the pipe occurs. It should be pointed out that the present analysis is based on the assumption of constant internal heat transfer coefficient, h_2 . If the solidified layer becomes thick, h_2 becomes large for a constant mass flow rate. The actual solidified layer can then be smaller than the predicted value and the freeze-off may not occur even if $\theta_{hr} < \theta_{hrC}$.

As the dimensionless radiation parameter increases, say from 1.5 to 2.0, the thickness of the solidified layer increases significantly. The change in this parameter also effects a change in the upper limit and the critical value of the combined superheat and heat transfer ratio parameter, θ_{hr} , as indicated by Eq. (15). For comparison purposes, the corresponding finite element solutions are also presented in Fig. 6. A maximum error up to 7 percent is found in the integral approach as compared to the finite element method. This figure also illustrates the effect of the axial heat conduction of the liquid and the solid on the thickness of the solidified layer. For a very small L/D ratio, say $L/D = 1$, a marked increase in the thickness of the solid region is detected as compared to the results of one-dimensional analysis. The effect of two-dimensional conduction, however, becomes less prominent for higher L/D ratios. When $L/D > 4$, the predicted solidified layer thickness almost equals that of one-dimensional conduction with radial heat transfer only.

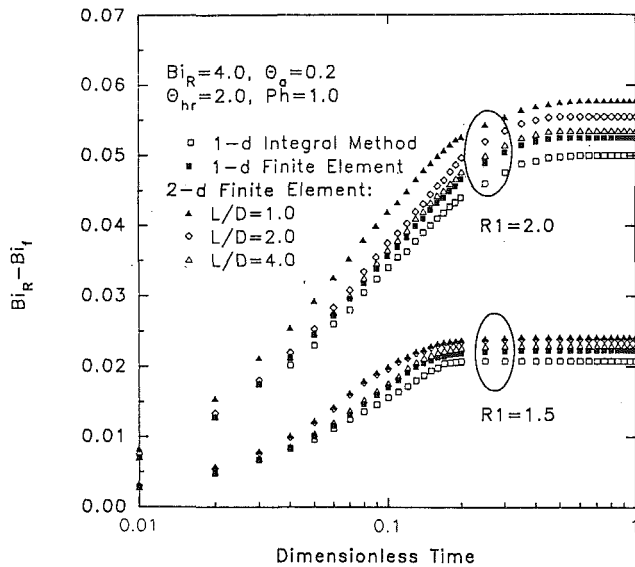


Fig. 6 Comparisons of buildup of solidified layer in a pipe based on integral method, one-dimensional, and two-dimensional finite element methods.

Conclusions

The present study indicates that regardless of the value of Bi_R , a stable solidified layer can always be formed as long as the value of the combined superheat and heat transfer ratio parameter, θ_{hr} , lies between θ_{hrC} and θ_{hrU} . This finding is different from the conclusion of Wang and Perry (1988), which indicated that a stable solidified layer can never be formed if $Bi_R < 1.0$. As the value of Bi_R increases from a value less than 1 to a value greater than 1, the range of Bi_f within which a stable solidified layer can be achieved increases. Furthermore, the critical value θ_{hrC} keeps decreasing, thus making the selection of the process parameters more flexible. It is also found that when θ_{hr} is greater than θ_{hrU} , no solidified layer is formed. Comparisons of the finite element solution and the integral solution of the aforementioned one-dimensional problem reveal that the first-order logarithmic temperature profile is a good approximation in the solidified layer for a cylindrical geometry. By including the effect of axial conduction, an increase in the solidified layer thickness of about 7 to 10 percent is noted over the corresponding one-dimensional solution. Finally, as is physically plausible, the solution of the one-dimensional phase change problem is observed to be a limiting case of that of the two-dimensional counterpart for values of L/D greater than 4.0.

References

- Dalmia, A. K., 1990, "Stable Layer of Solidified Metal Subject to Radiation and Convection," Master's Thesis, The University of Akron, Akron, OH.
- Goodman, T. R., 1958, "The Heat Balance Integral and Its Applications to Problems Involving a Change of Phase," *Trans. ASME*, Vol. 80, pp. 335-342.
- Gulati, S., 1991, "Finite Element Solution for One- and Two-Dimensional Heat Transfer With Solidification in a Pipe," Master's Thesis, The University of Akron, Akron, OH.
- Rolph, W. D., and Bathe, K. J., 1982, "An Efficient Algorithm for Analysis of Nonlinear Heat Transfer With Phase Changes," *International J. for Numerical Methods in Engineering*, Vol. 18, pp. 119-134.
- Wang, H. P., and Perry, E. M., 1988, "Criteria for Achieving a Stable Solidified Layer Inside a Nozzle Using Integral Solutions," *ASME HTD-Vol. 104*, pp. 129-135.

Relations for Local Radiative Heat Transfer Between Rectangular Boundaries of an Absorbing-Emitting Medium

R. Siegel¹

Nomenclature

- A_R = aspect ratio of rectangular region = d/b
- a = absorption coefficient of radiating medium; a_λ = spectral absorption coefficient
- B_0 = optical length of short side of rectangle = ab ; $B_{0,\lambda} = a_\lambda b$
- b, d = lengths of short and long sides of rectangle
- $e_{\lambda b}$ = blackbody hemispherical-spectral emissive power
- K_1 = modified Bessel function of order one
- q = local heat flux along sides of rectangle; q_λ = spectral values
- \tilde{q} = dimensionless local heat flux = $q/\sigma T^4$
- R_1, R_2, \dots = lengths defined in Eqs. (1)-(3)
- $S_n(\alpha)$ = integral function defined in Eq. (5)
- $S_{i-j}(\alpha)$ = difference of two S_n functions = $S_i(\alpha) - S_j(\alpha)$
- T = absolute temperature
- X, Y = dimensionless coordinates = $x/b, y/b$
- x, y, z = rectangular coordinates
- α, θ = argument and integration variable of S_n function, Eq. (5)
- $\beta = B_0 R_3$
- ϵ_{L-S} = emittance from long side to local positions along short sides
- η_1, η_2 = the quantities $B_0 Y$ and $B_0(A_R^2 + Y^2)^{1/2}$
- λ = wavelength
- ξ_1, ξ_2 = the quantities $B_0 X$ and $B_0(1 + X^2)^{1/2}$

Subscripts

- L, S = long and short sides of rectangle
- $L-L, L-S$ = from entire long side to local positions on opposite long and short sides
- M = the radiating medium within the rectangular region
- $M-L, M-S$ = from entire medium to local positions on long and short sides
- $S-L, S-S$ = from entire short side to local positions on long and opposite short sides
- λ = spectral values

Introduction

An analytical solution was obtained by Siegel (1991, 1992) for local boundary heat fluxes by a radiating medium at uniform temperature in a two-dimensional rectangular region. The

¹Research Scientist, NASA Lewis Research Center, Cleveland, OH 44135; Fellow ASME.

Contributed by the Heat Transfer Division of THE AMERICAN SOCIETY OF MECHANICAL ENGINEERS. Manuscript received by the Heat Transfer Division February 1992; revision received June 1992. Keywords: Furnaces and Combustors, Radiation. Associate Technical Editor: R. O. Buckius.

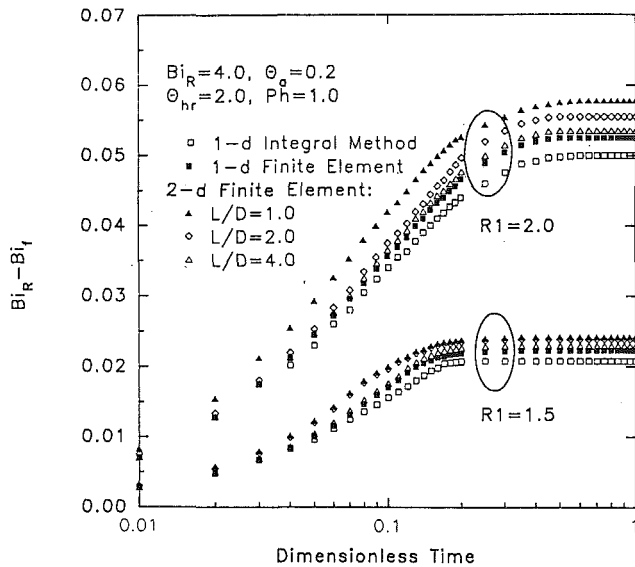


Fig. 6 Comparisons of buildup of solidified layer in a pipe based on integral method, one-dimensional, and two-dimensional finite element methods.

Conclusions

The present study indicates that regardless of the value of Bi_R , a stable solidified layer can always be formed as long as the value of the combined superheat and heat transfer ratio parameter, θ_{hr} , lies between θ_{hrC} and θ_{hrU} . This finding is different from the conclusion of Wang and Perry (1988), which indicated that a stable solidified layer can never be formed if $Bi_R < 1.0$. As the value of Bi_R increases from a value less than 1 to a value greater than 1, the range of Bi_f within which a stable solidified layer can be achieved increases. Furthermore, the critical value θ_{hrC} keeps decreasing, thus making the selection of the process parameters more flexible. It is also found that when θ_{hr} is greater than θ_{hrU} , no solidified layer is formed. Comparisons of the finite element solution and the integral solution of the aforementioned one-dimensional problem reveal that the first-order logarithmic temperature profile is a good approximation in the solidified layer for a cylindrical geometry. By including the effect of axial conduction, an increase in the solidified layer thickness of about 7 to 10 percent is noted over the corresponding one-dimensional solution. Finally, as is physically plausible, the solution of the one-dimensional phase change problem is observed to be a limiting case of that of the two-dimensional counterpart for values of L/D greater than 4.0.

References

- Dalmia, A. K., 1990, "Stable Layer of Solidified Metal Subject to Radiation and Convection," Master's Thesis, The University of Akron, Akron, OH.
- Goodman, T. R., 1958, "The Heat Balance Integral and Its Applications to Problems Involving a Change of Phase," *Trans. ASME*, Vol. 80, pp. 335-342.
- Gulati, S., 1991, "Finite Element Solution for One- and Two-Dimensional Heat Transfer With Solidification in a Pipe," Master's Thesis, The University of Akron, Akron, OH.
- Rolph, W. D., and Bathe, K. J., 1982, "An Efficient Algorithm for Analysis of Nonlinear Heat Transfer With Phase Changes," *International J. for Numerical Methods in Engineering*, Vol. 18, pp. 119-134.
- Wang, H. P., and Perry, E. M., 1988, "Criteria for Achieving a Stable Solidified Layer Inside a Nozzle Using Integral Solutions," *ASME HTD-Vol. 104*, pp. 129-135.

Relations for Local Radiative Heat Transfer Between Rectangular Boundaries of an Absorbing-Emitting Medium

R. Siegel¹

Nomenclature

- A_R = aspect ratio of rectangular region = d/b
- a = absorption coefficient of radiating medium; a_λ = spectral absorption coefficient
- B_0 = optical length of short side of rectangle = ab ; $B_{0,\lambda} = a_\lambda b$
- b, d = lengths of short and long sides of rectangle
- $e_{\lambda b}$ = blackbody hemispherical-spectral emissive power
- K_1 = modified Bessel function of order one
- q = local heat flux along sides of rectangle; q_λ = spectral values
- \tilde{q} = dimensionless local heat flux = $q/\sigma T^4$
- R_1, R_2, \dots = lengths defined in Eqs. (1)-(3)
- $S_n(\alpha)$ = integral function defined in Eq. (5)
- $S_{i-j}(\alpha)$ = difference of two S_n functions = $S_i(\alpha) - S_j(\alpha)$
- T = absolute temperature
- X, Y = dimensionless coordinates = $x/b, y/b$
- x, y, z = rectangular coordinates
- α, θ = argument and integration variable of S_n function, Eq. (5)
- $\beta = B_0 R_3$
- ϵ_{L-S} = emittance from long side to local positions along short sides
- η_1, η_2 = the quantities $B_0 Y$ and $B_0(A_R^2 + Y^2)^{1/2}$
- λ = wavelength
- ξ_1, ξ_2 = the quantities $B_0 X$ and $B_0(1 + X^2)^{1/2}$

Subscripts

- L, S = long and short sides of rectangle
- $L-L, L-S$ = from entire long side to local positions on opposite long and short sides
- M = the radiating medium within the rectangular region
- $M-L, M-S$ = from entire medium to local positions on long and short sides
- $S-L, S-S$ = from entire short side to local positions on long and opposite short sides
- λ = spectral values

Introduction

An analytical solution was obtained by Siegel (1991, 1992) for local boundary heat fluxes by a radiating medium at uniform temperature in a two-dimensional rectangular region. The

¹Research Scientist, NASA Lewis Research Center, Cleveland, OH 44135; Fellow ASME.

Contributed by the Heat Transfer Division of THE AMERICAN SOCIETY OF MECHANICAL ENGINEERS. Manuscript received by the Heat Transfer Division February 1992; revision received June 1992. Keywords: Furnaces and Combustors, Radiation. Associate Technical Editor: R. O. Buckius.

results have a convenient form in terms of S_n functions (Yuen and Wong, 1983) that occurs in two-dimensional radiation problems with absorbing-emitting media. The solution applies for a gray or spectral medium radiating to the surrounding walls. This is a useful test case to compare with results obtained numerically from computer programs written for more general conditions. Boundary heat flux values for a gray medium are given by Siegel (1991) for several optical dimensions and aspect ratios of the rectangular region. The walls were assumed cold relative to the temperature of the medium so radiation from the walls was not included.

The purpose of this note is to show that after the local fluxes from the medium to the walls have been evaluated, it is very easy to compute local fluxes arriving from the adjacent and opposite walls. This is because one of the integrals for exchange from the walls can be carried out to yield an exact analytical result that is readily evaluated. This extends the previous analysis, and provides convenient relations to include radiation from a black boundary, each side of the rectangle being at a different uniform temperature. Radiation from each side travels through the enclosed medium, and a portion reaches local positions on the other sides. This is given by integrals in the basic radiation equations. By using analytical transformations similar to those of Siegel (1991), one of the integrals is carried out in closed form to provide a very convenient result in terms of S_n functions. This yields final relations that can be rapidly evaluated by using interpolation of S_n tables; these expressions provide an alternative to evaluating the original integrals numerically. The integrated forms also show some of the basic mathematical behavior more easily than the integral forms. Since the final expressions can be evaluated quite rapidly, they are helpful in performing spectral calculations that must be made for many spectral bands.

Analysis

A rectangular region, Fig. 1, is filled with an absorbing-emitting medium at uniform temperature T_M . A gray medium is analyzed first; then the results are extended for a nongray medium. The boundary is black, and each side can be at a different uniform temperature. The geometry is long in the z -direction so the radiative behavior is two dimensional. Conduction and convection are assumed negligible compared with radiation.

The basic integral relations for the local heat fluxes arriving at the long and short sides by emission from a gray medium at uniform temperature T_M are given by the double integrals (Yuen and Wong, 1984; Siegel, 1989)

$$\frac{q_{M-L}(X)}{\sigma T_M^4} = B_0 \int_{X'=0}^{A_R} \int_{Y'=0}^1 S_2(B_0 R_2) \frac{1-Y'}{R_2^2} dX' dY'; \quad R_2^2 = (X-X')^2 + (1-Y')^2 \quad (1a)$$

$$\frac{q_{M-S}(Y)}{\sigma T_M^4} = B_0 \int_{X'=0}^{A_R} \int_{Y'=0}^1 S_2(B_0 R_1) \frac{A_R-X'}{R_1^2} dX' dY'; \quad R_1^2 = (A_R-X')^2 + (Y-Y')^2 \quad (1b)$$

The heat fluxes from an entire long side to a local position on either short side, and to a local position on the opposite long side are given by the integrals (Yuen and Wong, 1984)

$$\frac{q_{L-S}(Y)}{\sigma T_M^4} = Y \int_{X=0}^{A_R} \frac{A_R-X}{R_3^3} S_3(B_0 R_3) dX; \quad R_3^2 = (A_R-X)^2 + Y^2 \quad (2a)$$

$$\frac{q_{L-L}(X)}{\sigma T_M^4} = \int_{X'=0}^{A_R} \frac{S_3(B_0 R_4)}{R_4^3} dX'; \quad R_4^2 = (X-X')^2 + 1 \quad (2b)$$

Similarly, the heat fluxes from an entire short side to a local position on either long side, and to a local position on the opposite short side are

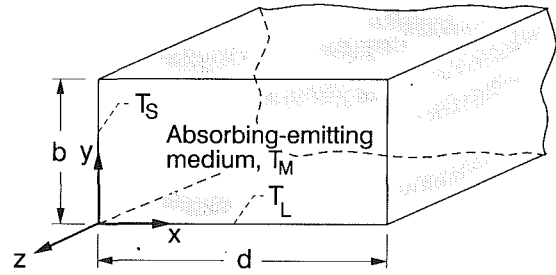


Fig. 1 Rectangular region with medium at temperature T_M and with black walls at differing temperatures

$$\frac{q_{S-L}(X)}{\sigma T_S^4} = X \int_{Y=0}^1 \frac{1-Y}{R_5^3} S_3(B_0 R_5) dY; \quad R_5^2 = X^2 + (1-Y)^2 \quad (3a)$$

$$\frac{q_{S-S}(Y)}{\sigma T_S^4} = A_R^2 \int_{Y'=0}^1 \frac{S_3(B_0 R_6)}{R_6^3} dY'; \quad R_6^2 = A_R^2 + (Y-Y')^2 \quad (3b)$$

Siegel (1991) gives the local heat fluxes found by the double integrals in Eqs. (1a) and (1b), which were transformed into more convenient forms having only a single integral in one term. These results are needed for part of the present analysis and are given by:

$$\frac{q_{M-L}(X)}{\sigma T_M^4} \equiv \tilde{q}_{M-L}(X) = 1 - S_{1-3}(B_0 X) - S_{1-3}[B_0(A_R - X)] - B_0 \int_{X'=0}^{A_R} S_{0-2}\{B_0[(X-X')^2 + 1]^{1/2}\} dX' \quad (4a)$$

$$\frac{q_{M-S}(Y)}{\sigma T_M^4} \equiv \tilde{q}_{M-S}(Y) = 1 - S_{1-3}(B_0 Y) - S_{1-3}[B_0(1 - Y)] - B_0 \int_{Y'=0}^1 S_{0-2}\{B_0[A_R^2 + (Y-Y')^2]^{1/2}\} dY' \quad (4b)$$

The notation is that $S_{1-3} = S_1 - S_3$ and $S_{0-2} = S_0 - S_2$, where the S_n are integral functions in two-dimensional radiative transfer. They are discussed and tabulated by Yuen and Wong (1983), and are readily evaluated by numerical integration of the relation

$$S_n(\alpha) = \frac{2}{\pi} \int_0^{\pi/2} e^{-\alpha/\cos\theta} \cos^{n-1}\theta d\theta \quad (5)$$

An integrated form for Eq. (2a) is now obtained. Let $\beta = B_0 R_3$; then Eq. (2a) becomes

$$\frac{q_{L-S}(Y)}{\sigma T_M^4} = B_0 Y \int_{\beta=B_0 Y}^{B_0 \sqrt{A_R^2 + Y^2}} \frac{S_3(\beta)}{\beta^2} d\beta \quad (6)$$

Since the derivative $dS_3(\beta) = -S_2(\beta)d\beta$, Eq. (6) is integrated by parts to yield

$$\int_a^b \frac{S_3(\beta)}{\beta^2} d\beta = \frac{S_3(a)}{a} - \frac{S_3(b)}{b} + \int_b^a \frac{S_2(\beta)}{\beta} d\beta \quad (7)$$

Siegel (1991) derives the following identity:

$$\frac{S_2(\beta)}{\beta} = \frac{2}{\pi} K_1(\beta) - S_1(\beta) \quad (8)$$

This yields the integral on the right-hand side of Eq. (7) as

$$\int \frac{S_2(\beta)}{\beta} d\beta = \int \left[\frac{2}{\pi} K_1(\beta) - S_1(\beta) \right] d\beta = -S_0(\beta) + S_2(\beta) \quad (9)$$

This is substituted into Eq. (6) and the result simplified to provide the final integrated form,

$$\frac{q_{L-S}(Y)}{\sigma T_L^4} \equiv \tilde{q}_{L-S}(\eta_1, \eta_2) = S_3(\eta_1) - \frac{\eta_1}{\eta_2} S_3(\eta_2) + \eta_1[-S_{0-2}(\eta_1) + S_{0-2}(\eta_2)] \quad (10)$$

where η_1 and η_2 are functions of Y defined in the nomenclature.

Equation (10) is for radiation from an entire long side to a local position on either of the adjacent short sides. By changing coordinates the relation is obtained for radiation from an entire short side to a local position on either of the adjacent long sides:

$$\frac{q_{S-L}(X)}{\sigma T_S^4} \equiv \tilde{q}_{S-L}(\xi_1, \xi_2) = S_3(\xi_1) - \frac{\xi_1}{\xi_2} S_3(\xi_2) + \xi_1[-S_{0-2}(\xi_1) + S_{0-2}(\xi_2)] \quad (11)$$

where the ξ_1 and ξ_2 are functions of X defined in the nomenclature.

From Eqs. (4a) and (11), expressions are now obtained for the radiation flux from an entire long side to a local position on the opposite long side. Note that the \tilde{q} are only functions of geometry. Hence relations between the \tilde{q} 's can be derived by considering the four sides and the medium to all be at the same temperature. For this condition the energy absorbed by the medium as radiation passes between the sides must equal that reemitted by the medium; the \tilde{q} for transmission between sides is thus related to the \tilde{q} for emission by the medium. Since the \tilde{q} 's do not depend on the temperatures, these relations continue to apply when the wall and medium temperatures are unequal. Then, using the enclosure equations of Siegel and Howell (1981, Sec. 17-3.2) yields the relation

$$\frac{q_{L-L}(X)}{\sigma T_L^4} \equiv \tilde{q}_{L-L}(X) = 1 - \tilde{q}_{M-L}(X) - \tilde{q}_{S_0-L}(X) - \tilde{q}_{S_{A_R}-L}(X) \quad (12)$$

where S_0 and S_{A_R} designate the short sides at $X=0$ and $X=A_R$. From Eq. (11) the last two terms in Eq. (12) are calculated from

$$\tilde{q}_{S_0-L}(X) = \frac{q_{S-L}(X)}{\sigma T_S^4} \quad (13a)$$

$$\tilde{q}_{S_{A_R}-L}(X) = \frac{q_{S-L}(A_R-X)}{\sigma T_S^4} \quad (13b)$$

where in Eq. (13b) the $\xi_n(X)$ in Eq. (11) become $\xi_n(A_R-X)$.

In a similar fashion the local flux along a short side received from the entire opposite short side is

$$\frac{q_{S-S}(Y)}{\sigma T_S^4} \equiv \tilde{q}_{S-S}(Y) = 1 - \tilde{q}_{M-S}(Y) - \tilde{q}_{L_0-S}(Y) - \tilde{q}_{L_1-S}(Y) \quad (14)$$

where L_0 and L_1 designate the long sides at $Y=0$ and 1. From Eq. (10)

$$\tilde{q}_{L_0-S}(Y) = \frac{q_{L_0-S}(Y)}{\sigma T_L^4} \quad (15a)$$

$$\tilde{q}_{L_1-S}(Y) = \frac{q_{L_1-S}(1-Y)}{\sigma T_L^4} \quad (15b)$$

When examining the local fluxes received along the walls, Eqs. (4), (10), and (11) are evaluated first; then Eqs. (12) and (14) are easily computed.

To extend the results to a nongray medium, the factors on the right sides of Eqs. (1), (10-12), and (14) are regarded as the emittances of the gray medium, a long side, and a short side, to local positions along the sides of the rectangle. The emittances depend on the optical length, B_0 , the local position

along the receiving side, and the aspect ratio. Then, for example, the heat flux from an entire long side that is received locally on either short side is

$$q_{L-S}(Y) = \sigma T_L^4 \epsilon_{L-S}(B_0, Y, A_R) \quad (16)$$

where ϵ_{L-S} is the right-hand side of Eq. (10). For a spectrally emitting medium $B_0 \rightarrow B_{0,\lambda} = a_\lambda b$. Using spectral quantities, Eq. (16) gives the local spectral flux in $d\lambda$ as

$$dq_{\lambda, L-S}(Y) = \epsilon_{\lambda, L-S}(\lambda, T_L) d\lambda \epsilon_{\lambda, L-S}(B_{0,\lambda}, Y, A_R) \quad (17)$$

By integrating over all wavelengths, the total local flux received along the short side is

$$q_{L-S}(Y) = \int_0^\infty dq_{\lambda, L-S}(Y) = \int_0^\infty \epsilon_{\lambda, L-S}(B_{0,\lambda}, Y, A_R) \epsilon_{\lambda, L-S}(\lambda, T_L) d\lambda \quad (18)$$

There are limiting expressions for Eqs. (10-12), and (14) as B_0 approaches zero. In this instance radiation leaving a side is not attenuated along its path to a local position on another side. Since the walls are black, the local flux arriving at the sides is given by the configuration factor. From Siegel and Howell (1981) the limiting relations are

$$\frac{q_{L-S}}{\sigma T_L^4} = \frac{1}{2} \left[1 - \frac{Y}{\sqrt{A_R^2 + Y^2}} \right] \quad (19a)$$

$$\frac{q_{L-L}}{\sigma T_L^4} = \frac{1}{2} \left[\frac{X}{\sqrt{1+X^2}} + \frac{A_R-X}{\sqrt{1+(A_R-X)^2}} \right] \quad (19b)$$

$$\frac{q_{S-L}}{\sigma T_S^4} = \frac{1}{2} \left[1 - \frac{X}{\sqrt{1+X^2}} \right] \quad (20a)$$

$$\frac{q_{S-S}}{\sigma T_S^4} = \frac{1}{2} \left[\frac{Y}{\sqrt{A_R^2 + Y^2}} + \frac{1-Y}{\sqrt{A_R^2 + (1-Y)^2}} \right] \quad (20b)$$

Results and Discussion

The local heat fluxes given by Eqs. (10-12) and (14) are rapidly evaluated by using tables of S_n values and spline interpolation. For a general test case involving both emission from the medium and from the boundary, the q_{M-L} and q_{M-S} are evaluated from Eqs. (4a, b). Then Eqs. (10) and (11), which are completely integrated forms of Eqs. (2a) and (3a), are evaluated for q_{L-S} and q_{S-L} . The q_{L-L} and q_{S-S} are then obtained from Eqs. (12) and (14).

Local dimensionless heat flux results for a square and a rectangular region of aspect ratio 2 are in Tables 1 and 2 for several values of the optical dimension B_0 . To check the analytical expressions, the basic integrals (2) and (3) were evaluated numerically for some cases, and agreement was obtained with the integrated forms. The results from Eqs. (10-12), and (14) as $B_0 \rightarrow 0$ agreed with values given by the limiting relations in Eqs. (19) and (20). The local boundary heat flux distributions for a square region along the side adjacent to the radiating side are in Fig. 2 as a function of B_0 .

At a corner the dimensionless flux radiated from an entire side to a local position on an adjacent side is 0.5. The flux along the adjacent side decreases with increased distance from the emitting side. This is the result of a decreased configuration factor and an increased path length through the medium that provides increased absorption. Although the received fluxes decrease as B_0 increases, the corner value remains at 0.5. As expected from the geometry, the local received fluxes are more uniform along the opposite side directly facing the emitting side. The lowest values are at the corners and there is symmetry about the center of the opposite side. At the corner there is a discontinuity in the fluxes on the adjacent and opposite sides.

Table 1 Local dimensionless heat fluxes to adjacent and opposite sides for radiation to one side of a square enclosure, $A_0 = d/b = 1$

Optical dimension, $B_0 = ab$				
	0	0.5	1	2
y/b	$q_{L-s}/\sigma T_L^4$			
0.0	0.500	0.500	0.500	0.500
0.1	0.450	0.386	0.336	0.261
0.2	0.402	0.315	0.251	0.166
0.3	0.356	0.259	0.193	0.111
0.4	0.314	0.214	0.150	0.077
0.5	0.276	0.178	0.117	0.053
0.6	0.243	0.147	0.092	0.038
0.7	0.213	0.123	0.073	0.027
0.8	0.188	0.102	0.057	0.019
0.9	0.166	0.085	0.046	0.014
1.0	0.146	0.072	0.036	0.010
x/b	$q_{L-l}/\sigma T_L^4$			
0.0	0.354	0.180	0.095	0.028
0.1	0.384	0.199	0.106	0.032
0.2	0.410	0.215	0.116	0.036
0.3	0.430	0.227	0.124	0.038
0.4	0.443	0.235	0.128	0.040
0.5	0.447	0.238	0.130	0.041

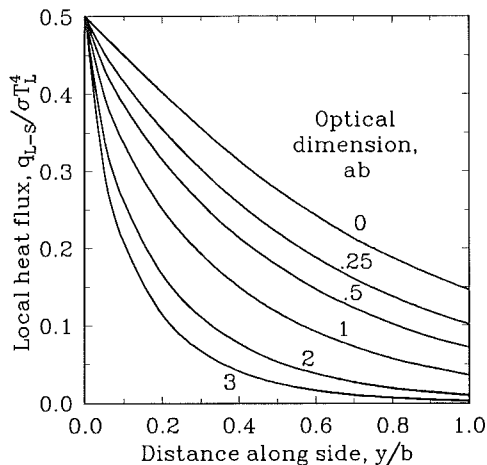


Fig. 2 Heat fluxes from an entire side of a square enclosure to local positions on an adjacent side, as a function of optical side length of the medium

The results illustrate how the analytical solution can readily provide exact boundary heat flux values for comparison as a test case with results from general computer programs. The spectral solution, Eqs. (16)–(18), can be rapidly evaluated, especially along an adjacent side where the local flux is expressed as a simple summation of tabulated S_n values.

References

Siegel, R., and Howell, J. R., 1981, *Thermal Radiation Heat Transfer*, Hemisphere, Washington, DC.
 Siegel, R., 1989, "Some Aspects of Transient Cooling of a Radiating Rectangular Medium," *International Journal of Heat and Mass Transfer*, Vol. 32, pp. 1955–1966.
 Siegel, R., 1991, "Analytical Solution for Boundary Heat Fluxes From a

Table 2 Local dimensionless heat fluxes to adjacent and opposite sides for a rectangle with aspect ratio $d/b = 2$

(a) Radiation from entire long side.

Optical dimension, $B_0 = ab$				
	0	0.5	1	2
y/b	$q_{L-s}/\sigma T_L^4$			
0.0	0.500	0.500	0.500	0.500
0.1	0.475	0.397	0.341	0.262
0.2	0.450	0.336	0.261	0.169
0.3	0.426	0.289	0.206	0.115
0.4	0.402	0.251	0.166	0.080
0.5	0.379	0.220	0.136	0.057
0.6	0.356	0.193	0.111	0.042
0.7	0.335	0.170	0.092	0.031
0.8	0.314	0.150	0.077	0.023
0.9	0.295	0.132	0.064	0.017
1.0	0.276	0.117	0.053	0.013
x/b	$q_{L-l}/\sigma T_L^4$			
0.0	0.447	0.214	0.108	0.030
0.2	0.535	0.264	0.137	0.039
0.4	0.610	0.306	0.161	0.047
0.6	0.664	0.337	0.177	0.052
0.8	0.697	0.355	0.187	0.055
1.0	0.707	0.360	0.190	0.056

(b) Radiation from entire short side.

Optical dimension, $B_0 = ab$				
	0	0.5	1	2
x/b	$q_{s-l}/\sigma T_s^4$			
0.0	0.500	0.500	0.500	0.500
0.2	0.402	0.315	0.251	0.166
0.4	0.314	0.214	0.150	0.077
0.6	0.243	0.147	0.092	0.038
0.8	0.188	0.102	0.057	0.019
1.0	0.146	0.072	0.036	0.010
1.2	0.116	0.051	0.023	0.005
1.4	0.093	0.037	0.015	0.003
1.6	0.076	0.027	0.010	0.002
1.8	0.063	0.020	0.007	0.001
2.0	0.053	0.015	0.005	0.001
y/b	$q_{s-s}/\sigma T_s^4$			
0.0	0.224	0.065	0.020	0.002
0.1	0.230	0.068	0.021	0.002
0.2	0.235	0.070	0.022	0.002
0.3	0.239	0.071	0.023	0.003
0.4	0.242	0.072	0.023	0.003
0.5	0.243	0.073	0.023	0.003

Radiating Rectangular Medium," ASME JOURNAL OF HEAT TRANSFER, Vol. 113, pp. 258-261.

Siegel, R., 1992, "Boundary Heat Fluxes for Spectral Radiation From a Uniform Temperature Rectangular Medium," *Journal of Thermophysics and Heat Transfer*, Vol. 6, pp. 543-545.

Yuen, W. W., and Wong, L. W., 1983, "Numerical Computation of an Important Integral Function in Two-Dimensional Radiative Transfer," *Journal of Quantitative Spectroscopy and Radiative Transfer*, Vol. 29, pp. 145-149.

Yuen, W. W., and Wong, L. W., 1984, "Analysis of Radiative Equilibrium in a Rectangular Enclosure With Gray Medium," ASME JOURNAL OF HEAT TRANSFER, Vol. 106, pp. 433-440.

Mass Transfer Effects on the Unsteady Forced and Free Convective Flow Through a Porous Medium Past an Infinite Vertical Isothermal Plate

V. M. Soundalgekar,¹ R. M. Lahurikar,² and S. G. Pohanerkar²

Introduction

Jahagirdar and Lahurikar (1989) studied the unsteady forced and free convection flow past an infinite isothermal plate. The mass transfer effects on this flow were studied by Soundalgekar (1989). Lahurikar et al. (1990) extended their work to include a porous medium. It is now proposed to study the effects of mass transfer on the unsteady mixed convection flow through a porous medium bounded by an infinite isothermal vertical plate. Following Gebhart and Pera (1972), we can show that the unsteady flow is governed by following equations in non-dimensional form:

$$\frac{\partial w}{\partial t} = \frac{\partial^2 w}{\partial y^2} + \lambda w - \theta - NC \quad (1)$$

$$Pr \frac{\partial \theta}{\partial t} = \frac{\partial^2 \theta}{\partial y^2}, \quad (2)$$

$$Sc \frac{\partial C}{\partial t} = \frac{\partial^2 C}{\partial y^2} \quad (3)$$

with initial and boundary conditions

$$\left. \begin{aligned} w=0, \quad \theta=0, \quad C=0 & \quad \text{for all, } y & \quad t \leq 0 \\ w=1, \quad \theta=1, \quad C=1 & \quad \text{at } y=0 \\ w=0, \quad \theta=0, \quad C=0 & \quad \text{as } y \rightarrow \infty & \quad t > 0 \end{aligned} \right\} \quad (4)$$

and the nondimensional quantities are defined as follows:

$$\begin{aligned} w' = U_o - u', \quad t = t' U_o^2 G / \nu, \quad y = y' U_o \sqrt{G} / \nu, \quad w = w' / U_o \\ \lambda = \nu^2 / \kappa U_o^2, \quad G = \nu g \beta (T_w' - T_\infty') / U_o^3, \quad \theta = (T' - T_\infty') / (T_w' - T_\infty') \\ Pr = \mu c_p / k, \quad C = (C' - C_\infty') / (C_w' - C_\infty'), \quad Sc = \nu / D, \\ N = \beta^* (C_w' - C_\infty') / \beta (T_w' - T_\infty') \quad (5) \end{aligned}$$

All the quantities are defined by Gebhart and Pera (1972) except that G is the Grashof number, t the time, y the axis normal to the plate; κ is the permeability of the porous medium. Here lateral and longitudinal dispersion in the porous medium

¹31A-12, Brindavan Society, Thane (400601) India; Mem. ASME.

²Department of Mathematics, Institute of Science, Aurangabad (431001) India.

Contributed by the Heat Transfer Division of THE AMERICAN SOCIETY OF MECHANICAL ENGINEERS. Manuscript received by the Heat Transfer Division March 1991; revision received March 1992. Keywords: Mass Transfer, Mixed Convection, Porous Media. Associate Technical Editor: W. A. Sirignano.

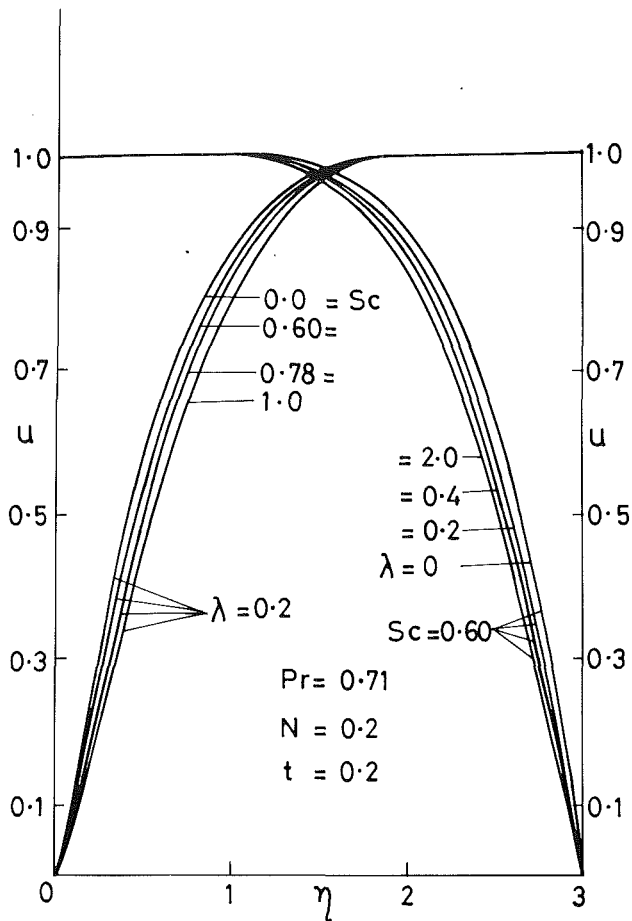


Fig. 1 Velocity profiles

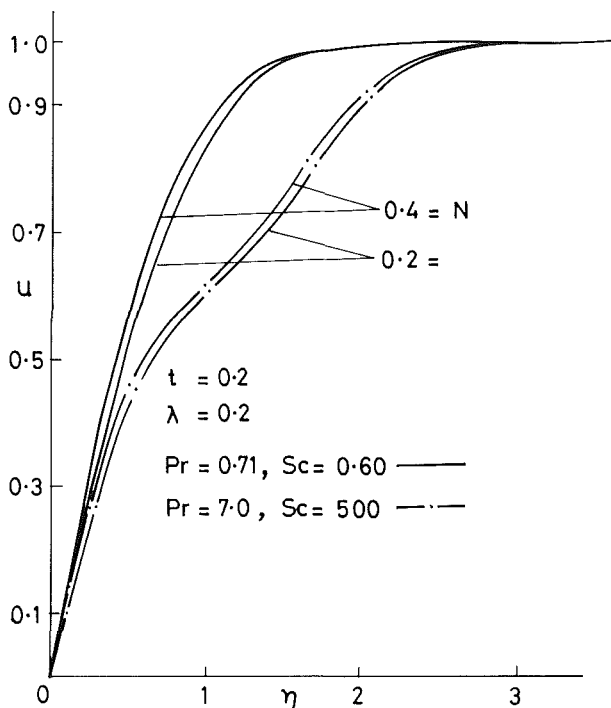


Fig. 2 Velocity profiles

is assumed to be negligible. Solutions are derived by the Laplace-transform technique and the velocity profiles are shown on Figs. 1-3. From Fig. 1, we observe that an increase in the Schmidt number Sc or the permeability parameter λ leads to

Radiating Rectangular Medium," ASME JOURNAL OF HEAT TRANSFER, Vol. 113, pp. 258-261.

Siegel, R., 1992, "Boundary Heat Fluxes for Spectral Radiation From a Uniform Temperature Rectangular Medium," *Journal of Thermophysics and Heat Transfer*, Vol. 6, pp. 543-545.

Yuen, W. W., and Wong, L. W., 1983, "Numerical Computation of an Important Integral Function in Two-Dimensional Radiative Transfer," *Journal of Quantitative Spectroscopy and Radiative Transfer*, Vol. 29, pp. 145-149.

Yuen, W. W., and Wong, L. W., 1984, "Analysis of Radiative Equilibrium in a Rectangular Enclosure With Gray Medium," ASME JOURNAL OF HEAT TRANSFER, Vol. 106, pp. 433-440.

Mass Transfer Effects on the Unsteady Forced and Free Convective Flow Through a Porous Medium Past an Infinite Vertical Isothermal Plate

V. M. Soundalgekar,¹ R. M. Lahurikar,² and S. G. Pohanerkar²

Introduction

Jahagirdar and Lahurikar (1989) studied the unsteady forced and free convection flow past an infinite isothermal plate. The mass transfer effects on this flow were studied by Soundalgekar (1989). Lahurikar et al. (1990) extended their work to include a porous medium. It is now proposed to study the effects of mass transfer on the unsteady mixed convection flow through a porous medium bounded by an infinite isothermal vertical plate. Following Gebhart and Pera (1972), we can show that the unsteady flow is governed by following equations in non-dimensional form:

$$\frac{\partial w}{\partial t} = \frac{\partial^2 w}{\partial y^2} + \lambda w - \theta - NC \quad (1)$$

$$Pr \frac{\partial \theta}{\partial t} = \frac{\partial^2 \theta}{\partial y^2}, \quad (2)$$

$$Sc \frac{\partial C}{\partial t} = \frac{\partial^2 C}{\partial y^2} \quad (3)$$

with initial and boundary conditions

$$\left. \begin{aligned} w=0, \quad \theta=0, \quad C=0 & \quad \text{for all, } y & \quad t \leq 0 \\ w=1, \quad \theta=1, \quad C=1 & \quad \text{at } y=0 \\ w=0, \quad \theta=0, \quad C=0 & \quad \text{as } y \rightarrow \infty & \quad t > 0 \end{aligned} \right\} \quad (4)$$

and the nondimensional quantities are defined as follows:

$$\begin{aligned} w' = U_o - u', \quad t = t' U_o^2 G / \nu, \quad y = y' U_o \sqrt{G} / \nu, \quad w = w' / U_o \\ \lambda = \nu^2 / \kappa U_o^2, \quad G = \nu g \beta (T_w' - T_\infty') / U_o^3, \quad \theta = (T' - T_\infty') / (T_w' - T_\infty') \\ Pr = \mu c_p / k, \quad C = (C' - C_\infty') / (C_w' - C_\infty'), \quad Sc = \nu / D, \\ N = \beta^* (C_w' - C_\infty') / \beta (T_w' - T_\infty') \quad (5) \end{aligned}$$

All the quantities are defined by Gebhart and Pera (1972) except that G is the Grashof number, t the time, y the axis normal to the plate; κ is the permeability of the porous medium. Here lateral and longitudinal dispersion in the porous medium

¹31A-12, Brindavan Society, Thane (400601) India; Mem. ASME.

²Department of Mathematics, Institute of Science, Aurangabad (431001) India.

Contributed by the Heat Transfer Division of THE AMERICAN SOCIETY OF MECHANICAL ENGINEERS. Manuscript received by the Heat Transfer Division March 1991; revision received March 1992. Keywords: Mass Transfer, Mixed Convection, Porous Media. Associate Technical Editor: W. A. Sirignano.

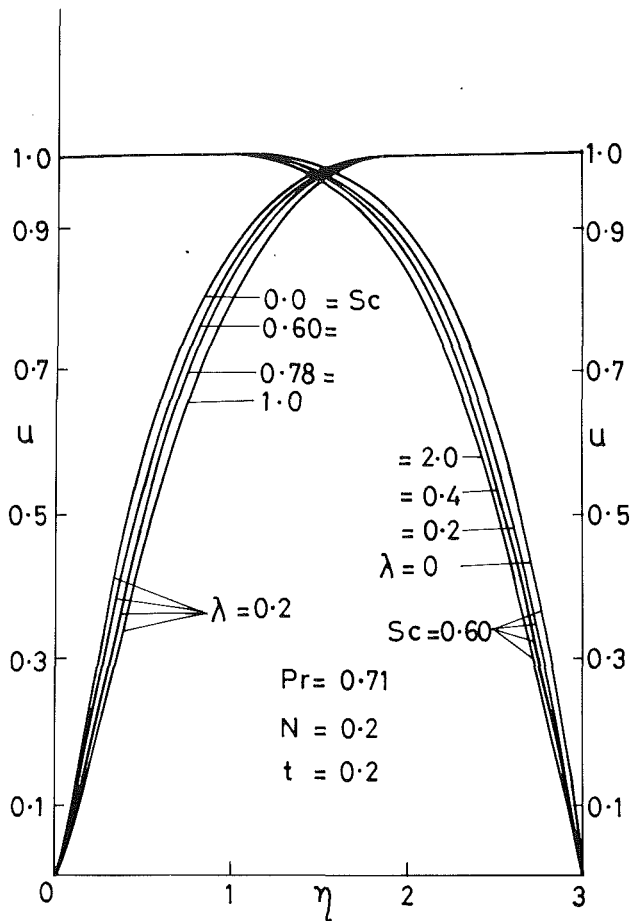


Fig. 1 Velocity profiles

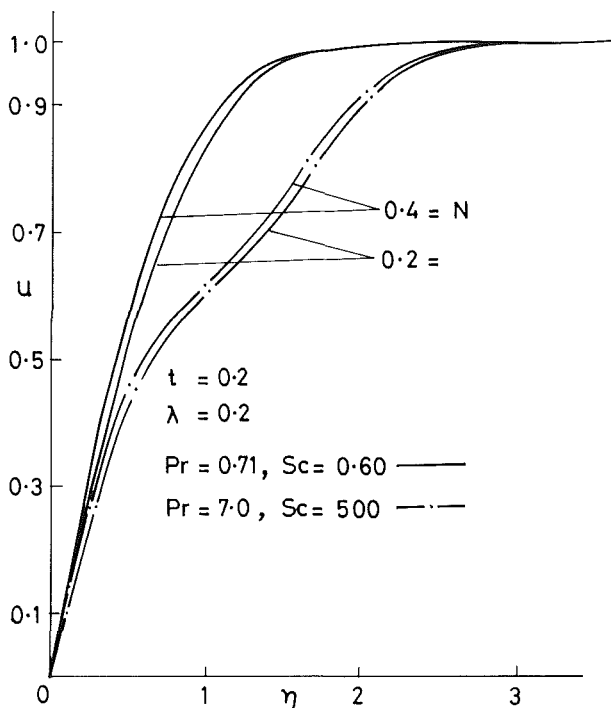


Fig. 2 Velocity profiles

is assumed to be negligible. Solutions are derived by the Laplace-transform technique and the velocity profiles are shown on Figs. 1-3. From Fig. 1, we observe that an increase in the Schmidt number Sc or the permeability parameter λ leads to

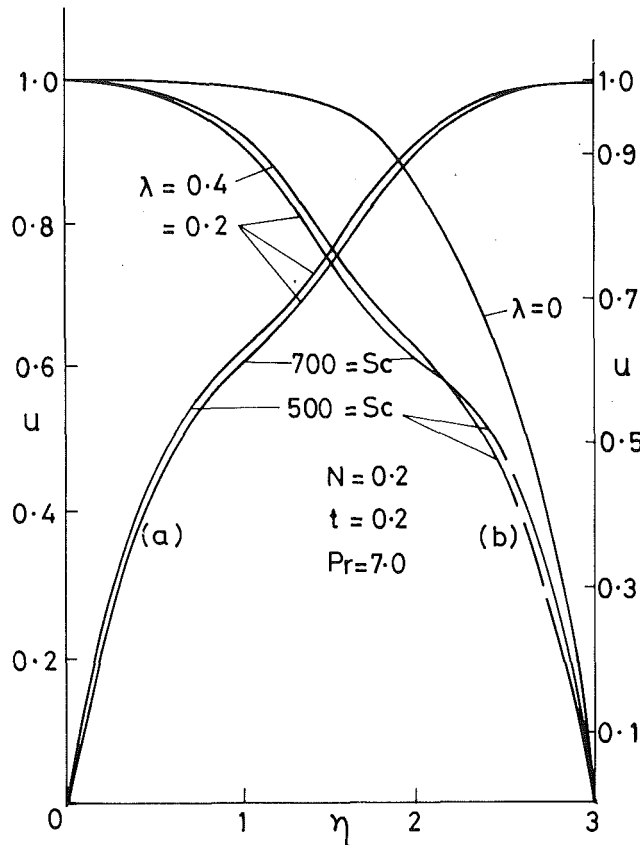


Fig. 3 Velocity profiles

Table 1 Values of the skin friction

t	Pr	N	Sc/λ	0.2	0.4
0.2	0.71	0.2	0.30	0.7685	1.0341
			0.60	0.7666	1.0249
			0.78	0.7623	1.0213
			1.0	0.7582	1.0180
0.4	0.71	0.2	0.60	0.8765	1.8975
			0.60	0.5423	0.9567
0.2	7.0	0.2	500	0.7037	0.9633
			700	0.7033	0.9633
0.4	7.0	0.4	500	0.7065	0.9665
			0.2	500	0.7135

a decrease in the velocity. Physically an increase in λ corresponds to a decrease in the permeability κ , which in turn corresponds to more resistance to the flow by porous medium and hence there is a decrease in the velocity of air in the presence of water vapor. The effect of a rise in the buoyancy force coefficient N leads to an increase in the velocity of both air and water (Fig. 2). The velocity profiles for water are shown in Fig. 3, which shows the existence of a point of inflection on the velocity curve between $\eta = 1$ and 2, and hence we can conclude that the flow of water may become unstable. This is prominently seen from Fig. (3b).

We now calculate the skin friction from

$$\tau = \tau' / \rho U_o^2 = \sqrt{G} \left. \frac{\partial u}{\partial \eta} \right|_{\eta=0} \quad (6)$$

We have derived the expression for τ and computed its values for air and for $Sc = 0.30$ (He), 0.60 (H₂O), 0.78 (NH₃), 1.0 (CO₂), and for water, $Sc = 500, 700$ as the value of the Schmidt number for water is always high. The values of τ are listed in Table 1.

We observe from this table that an increase in Sc or Pr leads

to a decrease in the skin friction. However, due to more resistance to the flow by the porous medium, the skin friction increases, which is true from the physical point of view.

Acknowledgments

We wish to thank the referees for some useful suggestions to improve our paper.

References

- Gebhart, B., and Pera, L., 1972, "The Nature of Vertical Natural Convection Flows Resulting From the Combined Buoyancy Effects on Thermal Mass Transfer," *International Journal of Heat and Mass Transfer*, Vol. 14, pp. 2025-2050.
- Jahagirdar, M. D., and Lahurikar, R. M., 1989, "Transient Forced and Free Convection Flow Past an Infinite Vertical Plate," *Indian Journal of Pure Applied Mathematics*, Vol. 20, pp. 711-715.
- Lahurikar, R. M., Pohanerkar, S. G., and Jahagirdar, M. D., 1990, "Unsteady Forced and Free Convective Flow Past an Infinite Vertical Plate Through a Porous Medium," *Indian Journal of Pure Applied Mathematics*, Vol. 21, pp. 396-402.
- Soundalgekar, V. M., 1989, "Transient Forced and Free Convection Flow With Mass Transfer Past an Infinite Vertical Plate," *Heat and Technology*, Vol. 7, pp. 96-105.

APPENDIX

The solution is given as:

For $Sc \neq 1$,

$$u = 1 - w = 1 - \frac{(\lambda - 1 - N)}{2\lambda} [e^{-2i\eta\sqrt{t\lambda}} \cdot \text{erfc}(\eta - i\sqrt{t\lambda}) + e^{2i\eta\sqrt{t\lambda}} \cdot \text{erfc}(\eta + i\sqrt{t\lambda})]$$

$$\begin{aligned} & - \frac{\exp\left(-\frac{t\lambda}{Pr-1}\right)}{2\lambda} \left[\exp\left\{-2i\eta\sqrt{\frac{Pr t\lambda}{Pr-1}}\right\} \text{erfc}\left(\eta - i\sqrt{\frac{Pr t\lambda}{Pr-1}}\right) \right. \\ & \quad \left. + \exp\left\{2i\eta\sqrt{\frac{Pr t\lambda}{Pr-1}}\right\} \text{erfc}\left(\eta + i\sqrt{\frac{Pr t\lambda}{Pr-1}}\right) \right] \\ & - \frac{N \exp\left(-\frac{t\lambda}{Sc-1}\right)}{2\lambda} \left[\exp\left\{-2i\eta\sqrt{\frac{Sc t\lambda}{Sc-1}}\right\} \text{erfc}\left(\eta - i\sqrt{\frac{Sc t\lambda}{Sc-1}}\right) \right. \\ & \quad \left. + \exp\left\{2i\eta\sqrt{\frac{Sc t\lambda}{Sc-1}}\right\} \text{erfc}\left(\eta + i\sqrt{\frac{Sc t\lambda}{Sc-1}}\right) \right] \\ & - \frac{1}{\lambda} \text{erfc}(\eta\sqrt{Pr}) - \frac{N}{\lambda} \text{erfc}(\eta\sqrt{Sc}) \\ & + \frac{\exp\left(-\frac{t\lambda}{Pr-1}\right)}{2\lambda} \left[\exp\left(-2i\eta\sqrt{\frac{Pr t\lambda}{Pr-1}}\right) \text{erfc}\left(\eta\sqrt{Pr} \right. \right. \\ & \quad \left. \left. - i\sqrt{\frac{\lambda t}{Pr-1}}\right) + \exp\left(2i\eta\sqrt{\frac{Pr t\lambda}{Pr-1}}\right) \text{erfc}\left(\eta\sqrt{Pr} + i\sqrt{\frac{\lambda t}{Pr-1}}\right) \right] \\ & + \frac{N \exp\left(-\frac{t\lambda}{Sc-1}\right)}{2\lambda} \left[\exp\left(-2i\eta\sqrt{\frac{Sc t\lambda}{Sc-1}}\right) \text{erfc}\left(\eta\sqrt{Sc} \right. \right. \\ & \quad \left. \left. - i\sqrt{\frac{t\lambda}{Sc-1}}\right) + \exp\left(2i\eta\sqrt{\frac{Sc t\lambda}{Sc-1}}\right) \text{erfc}\left(\eta\sqrt{Sc} + i\sqrt{\frac{t\lambda}{Sc-1}}\right) \right] \end{aligned} \quad (7)$$

For $Sc = 1$,

$$u = 1 - \frac{(\lambda - 1 - N)}{2\lambda} \left[\exp(-2i\eta\sqrt{t\lambda}) \operatorname{erfc}(\eta - i\sqrt{t\lambda}) + \exp(2i\eta\sqrt{t\lambda}) \cdot \operatorname{erfc}(\eta + i\sqrt{t\lambda}) \right]$$

$$- \frac{\exp\left(\frac{t\lambda}{1 - Pr}\right)}{2\lambda} \left[\exp\left(-2\eta\sqrt{\frac{Pr t\lambda}{1 - Pr}}\right) \operatorname{erfc}\left(\eta - \sqrt{\frac{Pr t\lambda}{1 - Pr}}\right) + \exp\left(2\eta\sqrt{\frac{Pr t\lambda}{1 - Pr}}\right) \operatorname{erfc}\left(\eta + \sqrt{\frac{Pr t\lambda}{1 - Pr}}\right) \right]$$

$$- \frac{1}{\lambda} \operatorname{erfc}(\eta\sqrt{Pr}) - \frac{N}{\lambda} \operatorname{erfc}(\eta)$$

$$+ \frac{\exp\left(\frac{t\lambda}{1 - Pr}\right)}{2\lambda} \left[\exp\left(-2\eta\sqrt{\frac{Pr t\lambda}{1 - Pr}}\right) \operatorname{erfc}\left(\eta\sqrt{Pr} - \sqrt{\frac{t\lambda}{1 - Pr}}\right) + \exp\left(2\eta\sqrt{\frac{Pr t\lambda}{1 - Pr}}\right) \operatorname{erfc}\left(\eta\sqrt{Pr} + \sqrt{\frac{t\lambda}{1 - Pr}}\right) \right] \quad (8)$$

where $\eta = y/2\sqrt{t}$.

Prediction of Spatial and Temporal Distributions of Frost Growth on a Flat Plate Under Forced Convection

Y.-X. Tao¹ and R. W. Besant¹

Nomenclature

- c_p = heat capacity at constant pressure
- d = diameter of the ice column
- D = vapor-air binary molecular diffusivity
- D_{eff} = effective diffusivity
- F = diffusion factor
- h = film heat transfer coefficient
- h_m = mass transfer coefficient
- k = thermal conductivity
- ℓ = length scale for nucleation sites
- Le = Lewis number = a/D
- Nu_x = Nusselt number = hx/k
- Re_x = Reynolds number = $u_\infty x/\nu$
- t = time
- t_{tr} = transition time to full growth of frost
- T_γ = gas temperature
- T_β = ice temperature
- T_c = cold plate temperature

¹Department of Mechanical Engineering, University of Saskatchewan, Saskatoon, Saskatchewan S7N 0W0, Canada.

Contributed by the Heat Transfer Division and presented at the National Heat Transfer Conference, San Diego, California, August 1992. Manuscript received by the Heat Transfer Division April 1992; revision received June 1992. Keywords: Moving Boundaries, Phase-Change Phenomena, Porous Media. Technical Editor: R. Viskanta.

- u_∞ = air velocity
- W = humidity ratio
- x = streamwise coordinate axis
- z = vertical coordinate axis
- δ_f = frost thickness
- ϵ_β = volume fraction of ice
- ϕ_∞ = air relative humidity
- ρ_f = frost density
- ρ_β = ice density

Introduction

In the literature dealing with the frost formation process on cold surfaces exposed to warm moist air, summarized by O'Neal and Tree (1985) and Padki et al. (1989), rigorous studies on theoretical predictions of frost growth and densification have received little attention. The majority of existing frost growth models average the frost density normal to the surface in the direction of frost growth. No variation of frost density and temperature within the frost layer is predicted (Padki et al., 1989). This is in part due to the complexity involved in formulating the problem, which requires accurate knowledge of transport phenomena within the frost layer, and a lack of sufficient experimental data on properties within the frost layer. At the molecular (microscopic) level, the transport of heat and mass within the frost layer is strongly dependent on the structure of the frost layer that is in turn related to many factors, such as the cold plate temperature, ambient air properties and flow characteristics, time duration of exposure, and solid surface properties. Among the few studies in which the spatial distribution of the frost density was considered, either a further simplification was imposed such that only the results of average frost density could be predicted (Sami and Duong, 1989) or the proposed model (Brian et al., 1970) failed to agree with the trend in the distributed frost density shown in experimental studies such as those by Cremers and Hahn (1978), and Bong et al. (1991). In a recent development, reported by Tao et al. (1992), attempts were made to establish a mathematical model that can predict both spatial and temporal variation of the frost density and temperature. The frost thickness and the heat flux through the frost layer can also be predicted. In that model, the frost is assumed to grow one dimensionally, perpendicular to the cold plate.

In this note, results are presented for the growth of a frost layer on a flat plate in which the spatial variation on the frost properties in the direction perpendicular to the cold plate as well as parallel to the direction of air flow is predicted; i.e., a transient, two-dimensional frost growth problem is analyzed. The results will be compared with the experimental data reported by Mao et al. (1992).

Numerical Model

The growth of a frost layer is divided into two stages, an initial stage with the ice-column frost structure followed by a fully developed porous frost layer, or full-growth, stage (Tao et al., 1992), as shown in Fig. 1. An ice-column numerical model on the cold plate is used to predict the frost behavior during the early growth stage with convective heat and mass transfer over the ice columns, rather than diffusion within the frost. After the ice columns grow to a certain height, or after a transition time, t_{tr} , a homogeneous porous medium model is applied to the frost layer full-growth stage. The physical nature of frost growth during the initial ice-column frost growth period was described by Hayashi et al. (1977). Using microscopic data, Tao et al. (1993) presented qualitative data on the transition time, t_{tr} , that agree well with the model by Tao et al. (1992). During the second stage, this porous medium is assumed to consist of the solid phase (ice crystals) and gaseous phase (a binary mixture of water vapor and air). Vapor diffusion is considered to be the mechanism for water vapor

$$\begin{aligned}
& \text{For } Sc = 1, \\
u = 1 - \frac{(\lambda - 1 - N)}{2\lambda} & \left[\exp(-2i\eta\sqrt{t\lambda}) \operatorname{erfc}(\eta - i\sqrt{t\lambda}) \right. \\
& \left. + \exp(2i\eta\sqrt{t\lambda}) \cdot \operatorname{erfc}(\eta + i\sqrt{t\lambda}) \right] \\
- \frac{\exp\left(\frac{t\lambda}{1 - Pr}\right)}{2\lambda} & \left[\exp\left(-2\eta\sqrt{\frac{Pr t\lambda}{1 - Pr}}\right) \operatorname{erfc}\left(\eta - \sqrt{\frac{Pr t\lambda}{1 - Pr}}\right) \right. \\
& \left. + \exp\left(2\eta\sqrt{\frac{Pr t\lambda}{1 - Pr}}\right) \operatorname{erfc}\left(\eta + \sqrt{\frac{Pr t\lambda}{1 - Pr}}\right) \right] \\
- \frac{1}{\lambda} \operatorname{erfc}(\eta\sqrt{Pr}) - \frac{N}{\lambda} & \operatorname{erfc}(\eta) \\
+ \frac{\exp\left(\frac{t\lambda}{1 - Pr}\right)}{2\lambda} & \left[\exp\left(-2\eta\sqrt{\frac{Pr t\lambda}{1 - Pr}}\right) \operatorname{erfc}\left(\eta\sqrt{Pr} - \sqrt{\frac{t\lambda}{1 - Pr}}\right) \right. \\
& \left. + \exp\left(2\eta\sqrt{\frac{Pr t\lambda}{1 - Pr}}\right) \operatorname{erfc}\left(\eta\sqrt{Pr} + \sqrt{\frac{t\lambda}{1 - Pr}}\right) \right] \quad (8)
\end{aligned}$$

where $\eta = y/2\sqrt{t}$.

Prediction of Spatial and Temporal Distributions of Frost Growth on a Flat Plate Under Forced Convection

Y.-X. Tao¹ and R. W. Besant¹

Nomenclature

c_p = heat capacity at constant pressure
 d = diameter of the ice column
 D = vapor-air binary molecular diffusivity
 D_{eff} = effective diffusivity
 F = diffusion factor
 h = film heat transfer coefficient
 h_m = mass transfer coefficient
 k = thermal conductivity
 ℓ = length scale for nucleation sites
 Le = Lewis number = a/D
 Nu_x = Nusselt number = hx/k
 Re_x = Reynolds number = $u_\infty x/\nu$
 t = time
 t_{tr} = transition time to full growth of frost
 T_γ = gas temperature
 T_β = ice temperature
 T_c = cold plate temperature

¹Department of Mechanical Engineering, University of Saskatchewan, Saskatoon, Saskatchewan S7N 0W0, Canada.

Contributed by the Heat Transfer Division and presented at the National Heat Transfer Conference, San Diego, California, August 1992. Manuscript received by the Heat Transfer Division April 1992; revision received June 1992. Keywords: Moving Boundaries, Phase-Change Phenomena, Porous Media. Technical Editor: R. Viskanta.

u_∞ = air velocity
 W = humidity ratio
 x = streamwise coordinate axis
 z = vertical coordinate axis
 δ_f = frost thickness
 ϵ_β = volume fraction of ice
 ϕ_∞ = air relative humidity
 ρ_f = frost density
 ρ_β = ice density

Introduction

In the literature dealing with the frost formation process on cold surfaces exposed to warm moist air, summarized by O'Neal and Tree (1985) and Padki et al. (1989), rigorous studies on theoretical predictions of frost growth and densification have received little attention. The majority of existing frost growth models average the frost density normal to the surface in the direction of frost growth. No variation of frost density and temperature within the frost layer is predicted (Padki et al., 1989). This is in part due to the complexity involved in formulating the problem, which requires accurate knowledge of transport phenomena within the frost layer, and a lack of sufficient experimental data on properties within the frost layer. At the molecular (microscopic) level, the transport of heat and mass within the frost layer is strongly dependent on the structure of the frost layer that is in turn related to many factors, such as the cold plate temperature, ambient air properties and flow characteristics, time duration of exposure, and solid surface properties. Among the few studies in which the spatial distribution of the frost density was considered, either a further simplification was imposed such that only the results of average frost density could be predicted (Sami and Duong, 1989) or the proposed model (Brian et al., 1970) failed to agree with the trend in the distributed frost density shown in experimental studies such as those by Cremers and Hahn (1978), and Bong et al. (1991). In a recent development, reported by Tao et al. (1992), attempts were made to establish a mathematical model that can predict both spatial and temporal variation of the frost density and temperature. The frost thickness and the heat flux through the frost layer can also be predicted. In that model, the frost is assumed to grow one dimensionally, perpendicular to the cold plate.

In this note, results are presented for the growth of a frost layer on a flat plate in which the spatial variation on the frost properties in the direction perpendicular to the cold plate as well as parallel to the direction of air flow is predicted; i.e., a transient, two-dimensional frost growth problem is analyzed. The results will be compared with the experimental data reported by Mao et al. (1992).

Numerical Model

The growth of a frost layer is divided into two stages, an initial stage with the ice-column frost structure followed by a fully developed porous frost layer, or full-growth, stage (Tao et al., 1992), as shown in Fig. 1. An ice-column numerical model on the cold plate is used to predict the frost behavior during the early growth stage with convective heat and mass transfer over the ice columns, rather than diffusion within the frost. After the ice columns grow to a certain height, or after a transition time, t_{tr} , a homogeneous porous medium model is applied to the frost layer full-growth stage. The physical nature of frost growth during the initial ice-column frost growth period was described by Hayashi et al. (1977). Using microscopic data, Tao et al. (1993) presented qualitative data on the transition time, t_{tr} , that agree well with the model by Tao et al. (1992). During the second stage, this porous medium is assumed to consist of the solid phase (ice crystals) and gaseous phase (a binary mixture of water vapor and air). Vapor diffusion is considered to be the mechanism for water vapor

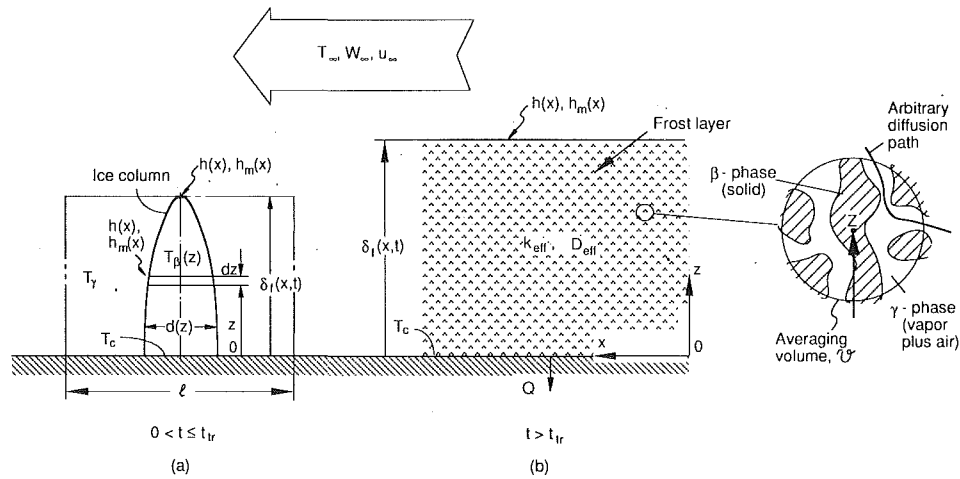


Fig. 1 Modeling of frost growth on a flat plate: (a) a unit cell for the ice column growth at the initial stage, and (b) the local volume averaging formulation at the full-growth period

transport within the porous frost layer, and phase change is due to ablation. The porous frost layer is treated as macroscopically one dimensional normal to the frost surface because the streamwise temperature gradient in the frost is at least an order of magnitude smaller than the temperature gradient perpendicular to the cold surface. The numerical model reported by Tao et al. (1992) is modified to include the variation of the frost properties parallel to the airflow direction. Readers are referred to the references of Tao et al. (1992) and Tao and Besant (1992) for details on the formulation and computational scheme. Consequently, only the modifications made for this study are discussed here.

First, in addition to the variation of frost properties in the direction perpendicular to the cold plate (z direction shown in Fig. 1), the streamwise variation of frost properties is considered (x direction in Fig. 1) and is believed to be caused primarily by the thermal and concentration boundary layers resulting from turbulent, warm air flow over the cold, frosting surface. This effect is included in the prescribed convective heat and mass transfer coefficients for heat and mass transfer in a fully developed turbulent flow as functions of the distance, x , from the leading edge of the thermal and mass transfer boundary layer (Kays and Crawford, 1980), i.e.,

$$Nu_x = 0.03 Re_x^{0.8} Pr^{0.6}, \quad (1)$$

where

$$Nu_x = \frac{h(x)x}{k} \quad \text{and} \quad Re_x = \frac{u_\infty x}{\nu},$$

and

$$h_m(x) = \frac{h(x)}{c_p L e^{2/3}}, \quad (2)$$

It is expected that the streamwise conduction and mass flow are important only for the cases where the temperature gradient along the cold plate is large and comparable to the normal temperature gradient and the pressure gradient in the flow direction is significant. For this study, we limit the model to the cases where there is a large temperature difference across the frost layer with no temperature gradient on the cold plate, and the streamwise pressure gradient is negligible.

The second modification is made to the effective mass diffusivity for the frost. It has been shown (Tao et al., 1992) that the effective vapor mass diffusivity, $D_{v,eff}$, used in the one-dimensional model of frost as a porous medium, can be approximated by

$$D_{eff} = \epsilon_\gamma D (1 + F), \quad (3)$$

where D is the air-vapor binary molecular diffusivity, m^2/s , ϵ_γ is the volume fraction of the gaseous phase, and F is called the diffusion factor, which takes into account the microscopically three-dimensional characteristics of mass diffusion in porous media (Whitaker, 1977). F is a structure-related property and can be a function of the cold plate temperature, as guided by the experimental data on frost growth and density (Tao et al., 1992). Experimental measurements of frost thickness, density, and heat flux showed that there are five independent test variables, namely, dimensionless distance from the leading edge, dimensionless temperature difference, humidity ratio, inlet Reynolds number, and Fourier number (Mao et al., 1992). This implies that F also depends on the ambient conditions such as T_∞ , Re_x , etc., i.e.,

$$F = f(T_c, T_\infty, x, u_\infty, \dots) \quad (4)$$

The above equation assumes that, due to the variation of frost density and thickness in the x direction, the microscopic structure of the frost layer varies in the streamwise direction. This assumption is justified later through the comparison of the predicted frost density variation along the x direction with the measured data.

It is also necessary to distinguish a frost surface diffusion factor, F_s , from the volumetric, internal frost layer diffusion factor, F , such that

$$D_{s,eff} = \epsilon_\gamma (z = \delta_f) D (1 + F_s), \quad (5)$$

The difference between the surface effective diffusivity and "volumetric" effective diffusivity (the one within the frost) results from the definition of the elementary averaging volumes within the control volume and at the interface between the porous medium and plain medium (Kaviany, 1991; Prat, 1989). Physically, this difference in the volumetric and surface diffusivities gives a measure of what a portion of the mass transfer of vapor from the ambient flow is contributing to the internal densification of the frost layer and the rest to the frost surface growth (i.e., the increase in the frost thickness). Based on the measured average density and thickness of frost (Mao et al., 1992), we derive the following empirical relations for F and F_s :

$$F = f \times \left[1.24694 - 0.79624 \log_{10} \left(\frac{x}{0.6} \right) \right], \quad (6)$$

$$F_s = f_s \times \left[-0.78 + 0.54 \left(\frac{x}{0.6} \right) - 0.36 \left(\frac{x}{0.6} \right)^2 \right], \quad (7)$$

where f and f_s are constant coefficients that depend on the cold plate temperature and ambient air velocity and temper-

Table 1 Values of f and f_s (Eqs. (6) and (7))

$T_c, ^\circ\text{C}$	$u_\infty, \text{m/s}$	f	f_s
-5	2	2.0	0.9
-10	2	1.0	1.0
-10	1	0.4	0.8
-15	2	0.12	1.4

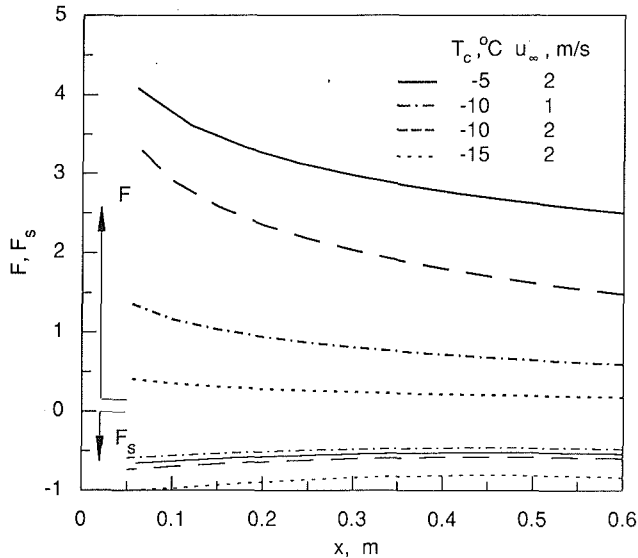


Fig. 2 Streamwise variations of the diffusion factors, D_{eff} and $D_{s,\text{eff}}$

ature. The values used in this study are listed in Table 1. The above functions for F and F_s allow us to predict the frost property distributions to such a satisfactory extent that the predicted average density and thickness of frost are in good agreement with the measured data, as will be discussed later.

Figure 2 shows the trends of F and F_s as functions of x . For the temperature and velocity ranges studied, F is within the range of 0 to 3.5, and F_s is between -1.0 and -0.33 (-1.0 being exclusive). That is, $D_{\text{eff}} > \epsilon_\gamma D$ at every point within the frost layer while $D_{s,\text{eff}} < \epsilon_\gamma (z = \delta_f) D$ on the frost-air interface. It should be noted that in the present study, Eqs. (6) and (7) should not be used beyond the applicable range, as indicated in Fig. 2. Although there are no direct measured data on the value of F , Yen (1969) and Yosida (1950) deduced F values between 2.2 and 3.5 in their studies of water vapor diffusion in snow subject to a constant temperature gradient, over a temperature range from 264 to 272 K. The justification of the values for F is also given by Christon (1990).

It should be mentioned that an empirical form of the effective thermal conductivity as a function of frost density (Yonko and Sepsy, 1967) is used in the model formulation. (For a detailed discussion the reader is referred to Tao et al., 1992, and Tao and Besant, 1992.)

Results and Discussion

From the numerical calculation, the spatial (along x and z directions) and temporal distributions of frost temperature, frost density, and rate of densification can be predicted for given boundary and initial conditions. The time variation of the frost thickness is also predicted. In Fig. 3, the typical distribution of ice volume fraction (note that $\rho_f = \epsilon_\beta \rho_\beta$) is shown for different times. Because no accurate experimental data are available for the frost properties within the frost layer, the results are compared with the empirical data for the frost thickness and frost density, averaged along the z direction (Mao et al., 1992), as shown in Fig. 4. A good agreement has been achieved. The largest discrepancy between the predicted and measured data occurs at the early stage, for example, for $t =$

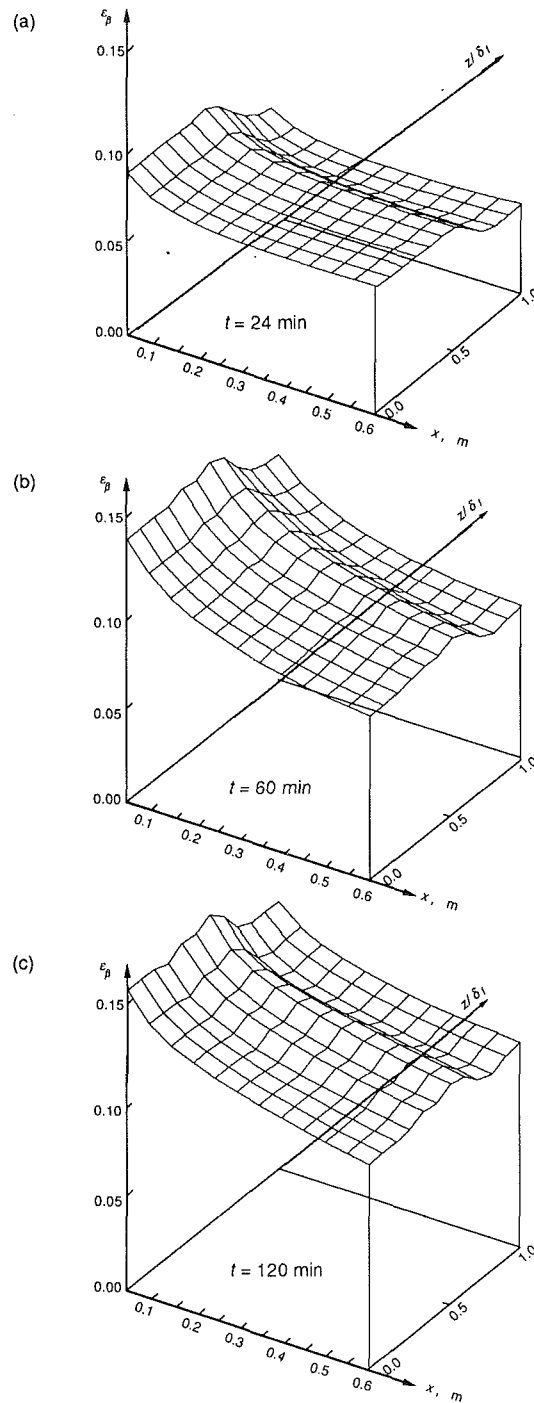


Fig. 3 Distributions of the ice volume fraction in the frost layer at different elapsed times: $T_c = -10^\circ\text{C}$, $T_\infty = 20^\circ\text{C}$, $\phi_\infty = 0.6$ and $u_\infty = 2.0 \text{ m/s}$, where $t_{\text{tr}} = 13.3 \text{ min}$

40 min in Fig. 4. This is partly attributed to limited experimental data at the early stage of frost growth, which are correlated with the full growth stage data (Mao et al., 1992). In addition, the experimental errors for small frost thicknesses are larger than those for thicker frost layers. In general, both experimental and predicted δ_f and $\bar{\rho}_f$ have higher values near the leading edge where more frost is accumulated. The exception is for the case with $T_c = -15^\circ\text{C}$ (Fig. 4a) in which a hump on the thickness curve for $t = 120 \text{ min}$ is shown. In this case, the predicted frost layer at the leading edge is slightly thinner. It reaches a maximum at about $x = 0.12 \text{ m}$, then decreases farther downstream. This phenomenon was observed

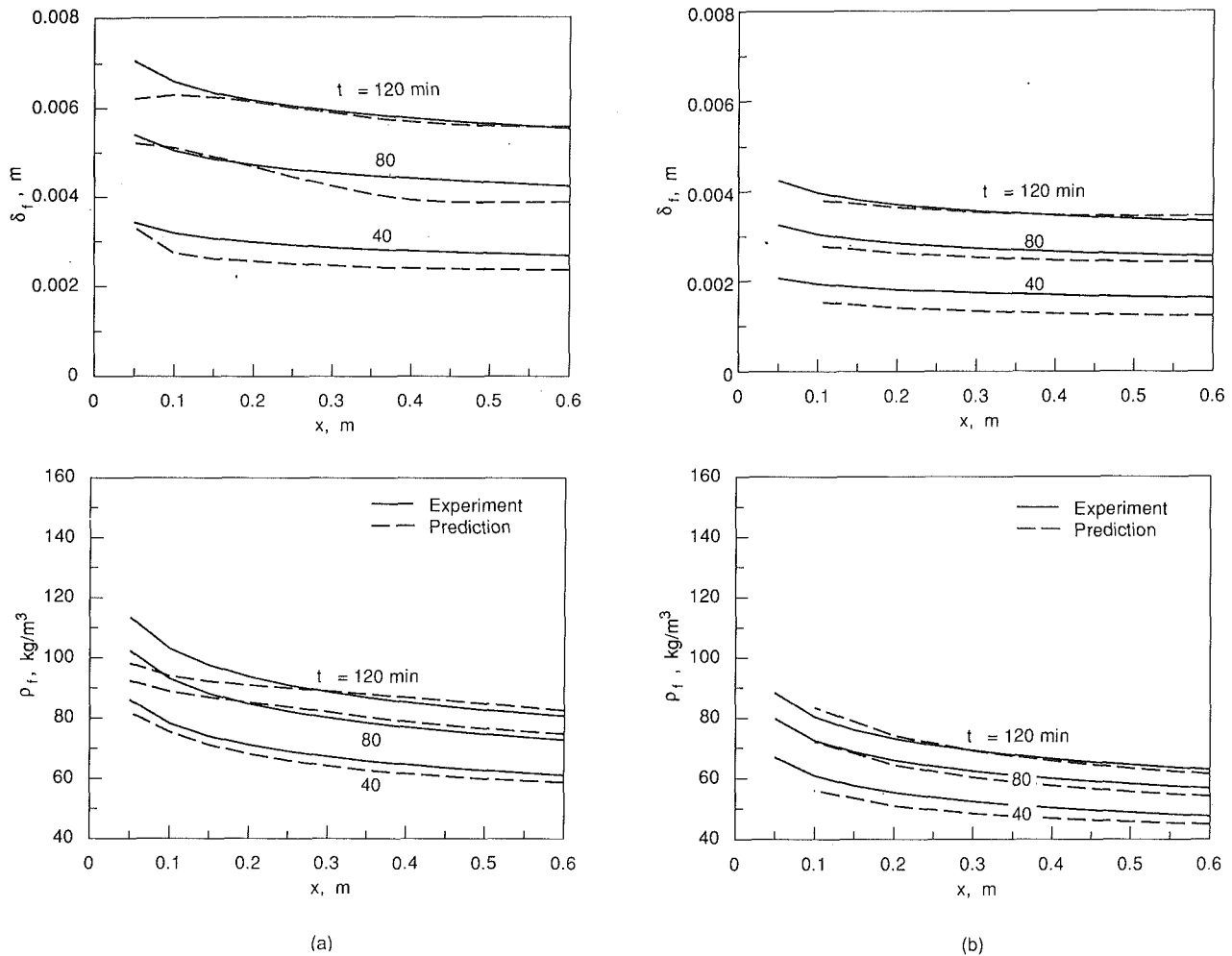


Fig. 4 Comparison of the predicted frost layer thickness and average frost density with the experimental data: (a) $T_c = -15^\circ\text{C}$, $T_\infty = 20^\circ\text{C}$, $\phi_\infty = 0.6$, and $u_\infty = 2.0$ m/s, where $t_{fr} = 9$ min, and (b) $T_c = -10^\circ\text{C}$, $T_\infty = 20^\circ\text{C}$, $\phi_\infty = 0.6$, and $u_\infty = 1.0$ m/s, where $t_{fr} = 13.3$ min

in some test runs by Mao et al. (1992), although the smoothly fitted empirical correlations of frost properties could not reflect this phenomenon for this particular case. Also, it was noted by Mao et al. (1992) that frost thickness growth of several millimeters in a fully developed air channel of 20 mm represents a significant step in the air flow right at the leading edge of the frost growth boundary layer. As a consequence, it is not expected that the correlations will fit the experimental data as well near the leading edge as they do farther downstream. In the same manner, this theoretical model does not consider coupling between the air flow and heat and mass transfer at the leading edge; therefore, it is expected that the prediction will improve in accuracy somewhat downstream of the leading edge.

References

- Bong, T. Y., Wijesundera, N. E., Saw, E. L., and Lau, K. O., 1991, "Comparison of Beta-Ray and Gamma-Ray Transmission Methods for Measurement of Frost Density Distribution," *Experimental Thermal and Fluid Science*, Vol. 4, pp. 567-576.
- Brian, P. L., Reid, T. R. C., and Shah, Y. T., 1970, "Frost Deposition on Cold Surfaces," *Ind. Eng. Chem. Fundam.*, Vol. 9, pp. 275-280.
- Christon, M. A., 1990, "3-D Transient Microanalysis of Multiphase Heat and Mass Transport in Ice Lattices," Ph.D. Thesis, Colorado State University.
- Cremers, C. J., and Hahn, O. J., 1978, "Frost Density Measurements on Vertical Cylinders by Gamma-Ray Attenuation," *Adv. Cry. Eng.*, Vol. 23, pp. 371-375.
- Kaviany, M., 1991, *Principles of Heat Transfer in Porous Media*, Springer-Verlag, New York, p. 141.
- Kays, W. M., and Crawford, M. E., 1980, *Convective Heat and Mass Transfer*, McGraw-Hill, New York, p. 217.
- Mao, Y., Besant, R. W., and Rezkallah, K. S., 1992, "Measurement and Correlations of Frost Properties With Air Flow Over a Flat Plate," *ASHRAE Trans.*, Vol. 98, Pt. 2.
- O'Neal, D. L., and Tree, D. R., 1985, "A Review of Frost Formation in Simple Geometries," *ASHRAE Trans.*, Vol. 91, p. 267.
- Padki, M. M., Sherif, S. A., and Nelson, R. M., 1989, "A Simple Method for Modeling the Frost Formation Phenomenon in Different Geometries," *ASHRAE Trans.*, Vol. 95, pp. 1127-1137.
- Prat, M., 1989, "On the Boundary Conditions at the Macroscopic Level," *Transp. Porous Media*, Vol. 4, pp. 259-280.
- Sami, S. M., and Duong, T., 1989, "Mass and Heat Transfer During Frost Growth," *ASHRAE Trans.*, Vol. 95, pp. 158-165.
- Tao, Y.-X., and Besant, R. W., 1992, "Prediction of Spatial and Temporal Distributions of Frost Growth on a Flat Plate Under Forced Convection," *Fundamentals of Heat Transfer in Porous Media*, ASME HTD-Vol. 193, pp. 131-139.
- Tao, Y.-X., Besant, R. W., and Rezkallah, K. S., 1992, "A Mathematical Model for Predicting the Densification and Growth of Frost on a Flat Plate," *Int. J. Heat Mass Transfer*, in press.
- Tao, Y.-X., Besant, R. W., and Mao, Y., 1993, "Characteristics of Frost Growth on a Flat Plate During the Early Growth Period," *ASHRAE Trans.*, Vol. 99, Pt. 1.
- Whitaker, S., 1977, "Simultaneous Heat, Mass and Momentum Transfer in Porous Media: a Theory of Drying," in: *Advances in Heat Transfer*, J. P. Hartnett and T. F. Irvine, Jr., eds., Vol. 13, Academic Press, New York.
- Yen, Y. C., 1969, "Recent Studies in Snow Properties," in: *Advances in Hydrosociences*, V. T. Chow, ed., Vol. 5, pp. 173-213, Academic Press, New York.
- Yonko, J. D., and Sepsy, C. F., 1967, "An Investigation of the Thermal Conductivity of Frost While Forming on a Flat Horizontal Plate," *ASHRAE Trans.*, Vol. 73, p. 11.
- Yosida, Z., 1950, "Heat Transfer by Water Vapor in Snow Cover," *Low Temp. Sci.*, Vol. 5, pp. 93-100.